

Lecture Notes in Electrical Engineering 1086

Hasmat Malik · Sukumar Mishra ·  
Y. R. Sood · Atif Iqbal ·  
Taha Selim Ustun *Editors*

# Renewable Power for Sustainable Growth

Proceedings of ICRP 2023

 Springer

# Lecture Notes in Electrical Engineering

## Volume 1086

### Series Editors

Leopoldo Angrisani, Department of Electrical and Information Technologies Engineering, University of Napoli Federico II, Napoli, Italy  
Marco Artega, Departament de Control y Robótica, Universidad Nacional Autónoma de México, Coyoacán, Mexico  
Samarjit Chakraborty, Fakultät für Elektrotechnik und Informationstechnik, TU München, München, Germany  
Jiming Chen, Zhejiang University, Hangzhou, Zhejiang, China  
Shanben Chen, School of Materials Science and Engineering, Shanghai Jiao Tong University, Shanghai, China  
Tan Kay Chen, Department of Electrical and Computer Engineering, National University of Singapore, Singapore, Singapore  
Rüdiger Dillmann, University of Karlsruhe (TH) IAIM, Karlsruhe, Baden-Württemberg, Germany  
Haibin Duan, Beijing University of Aeronautics and Astronautics, Beijing, China  
Gianluigi Ferrari, Dipartimento di Ingegneria dell'Informazione, Sede Scientifica Università degli Studi di Parma, Parma, Italy  
Manuel Ferre, Centre for Automation and Robotics CAR (UPM-CSIC), Universidad Politécnica de Madrid, Madrid, Spain  
Faryar Jabbari, Department of Mechanical and Aerospace Engineering, University of California, Irvine, CA, USA  
Limin Jia, State Key Laboratory of Rail Traffic Control and Safety, Beijing Jiaotong University, Beijing, China  
Janusz Kacprzyk, Intelligent Systems Laboratory, Systems Research Institute, Polish Academy of Sciences, Warsaw, Poland  
Alaa Khamis, Department of Mechatronics Engineering, German University in Egypt El Tagamoa El Khames, New Cairo City, Egypt  
Torsten Kroeger, Intrinsic Innovation, Mountain View, CA, USA  
Yong Li, College of Electrical and Information Engineering, Hunan University, Changsha, Hunan, China  
Qilian Liang, Department of Electrical Engineering, University of Texas at Arlington, Arlington, TX, USA  
Ferran Martín, Departament d'Enginyeria Electrònica, Universitat Autònoma de Barcelona, Bellaterra, Barcelona, Spain  
Tan Cher Ming, College of Engineering, Nanyang Technological University, Singapore, Singapore  
Wolfgang Minker, Institute of Information Technology, University of Ulm, Ulm, Germany  
Pradeep Misra, Department of Electrical Engineering, Wright State University, Dayton, OH, USA  
Subhas Mukhopadhyay, School of Engineering, Macquarie University, NSW, Australia  
Cun-Zheng Ning, Department of Electrical Engineering, Arizona State University, Tempe, AZ, USA  
Toyoaki Nishida, Department of Intelligence Science and Technology, Kyoto University, Kyoto, Japan  
Luca Oneto, Department of Informatics, Bioengineering, Robotics and Systems Engineering, University of Genova, Genova, Genova, Italy  
Bijaya Ketan Panigrahi, Department of Electrical Engineering, Indian Institute of Technology Delhi, New Delhi, Delhi, India  
Federica Pascucci, Dipartimento di Ingegneria, Università degli Studi Roma Tre, Roma, Italy  
Yong Qin, State Key Laboratory of Rail Traffic Control and Safety, Beijing Jiaotong University, Beijing, China  
Gan Woon Seng, School of Electrical and Electronic Engineering, Nanyang Technological University, Singapore, Singapore  
Joachim Speidel, Institute of Telecommunications, University of Stuttgart, Stuttgart, Germany  
Germano Veiga, FEUP Campus, INESC Porto, Porto, Portugal  
Haitao Wu, Academy of Opto-electronics, Chinese Academy of Sciences, Haidian District Beijing, China  
Walter Zamboni, Department of Computer Engineering, Electrical Engineering and Applied Mathematics, DIEM—Università degli studi di Salerno, Fisciano, Salerno, Italy  
Junjie James Zhang, Charlotte, NC, USA  
Kay Chen Tan, Department of Computing, Hong Kong Polytechnic University, Kowloon Tong, Hong Kong



The book series *Lecture Notes in Electrical Engineering* (LNEE) publishes the latest developments in Electrical Engineering—quickly, informally and in high quality. While original research reported in proceedings and monographs has traditionally formed the core of LNEE, we also encourage authors to submit books devoted to supporting student education and professional training in the various fields and applications areas of electrical engineering. The series cover classical and emerging topics concerning:

- Communication Engineering, Information Theory and Networks
- Electronics Engineering and Microelectronics
- Signal, Image and Speech Processing
- Wireless and Mobile Communication
- Circuits and Systems
- Energy Systems, Power Electronics and Electrical Machines
- Electro-optical Engineering
- Instrumentation Engineering
- Avionics Engineering
- Control Systems
- Internet-of-Things and Cybersecurity
- Biomedical Devices, MEMS and NEMS

For general information about this book series, comments or suggestions, please contact [leontina.dicecco@springer.com](mailto:leontina.dicecco@springer.com).

To submit a proposal or request further information, please contact the Publishing Editor in your country:

#### **China**

Jasmine Dou, Editor ([jasmine.dou@springer.com](mailto:jasmine.dou@springer.com))

#### **India, Japan, Rest of Asia**

Swati Meherishi, Editorial Director ([Swati.Meherishi@springer.com](mailto:Swati.Meherishi@springer.com))

#### **Southeast Asia, Australia, New Zealand**

Ramesh Nath Premnath, Editor ([ramesh.premnath@springernature.com](mailto:ramesh.premnath@springernature.com))

#### **USA, Canada**

Michael Luby, Senior Editor ([michael.luby@springer.com](mailto:michael.luby@springer.com))

#### **All other Countries**

Leontina Di Cecco, Senior Editor ([leontina.dicecco@springer.com](mailto:leontina.dicecco@springer.com))

**\*\* This series is indexed by EI Compindex and Scopus databases. \*\***

Hasmat Malik · Sukumar Mishra · Y. R. Sood ·  
Atif Iqbal · Taha Selim Ustun  
Editors

# Renewable Power for Sustainable Growth

Proceedings of ICRP 2023

 Springer

*Editors*

Hasmat Malik  
Department of Electrical Power  
Engineering, Faculty of Engineering  
Universiti Teknologi Malaysia (UTM)  
Johor Bahru, Malaysia

Y. R. Sood  
Department of Electrical Engineering  
National Institute of Technology Hamirpur  
Hamirpur, Himachal Pradesh, India

Taha Selim Ustun  
Advanced Industrial Science  
and Technology (FREA)  
Fukushima Renewable Energy Institute  
Koriyama, Japan

Sukumar Mishra  
Department of Electrical Engineering  
Indian Institute of Technology Delhi  
New Delhi, Delhi, India

Atif Iqbal  
Department of Electrical Engineering  
Qatar University  
Doha, Qatar

ISSN 1876-1100                      ISSN 1876-1119 (electronic)  
Lecture Notes in Electrical Engineering  
ISBN 978-981-99-6748-3              ISBN 978-981-99-6749-0 (eBook)  
<https://doi.org/10.1007/978-981-99-6749-0>

© The Editor(s) (if applicable) and The Author(s), under exclusive license to Springer Nature Singapore Pte Ltd. 2024

This work is subject to copyright. All rights are solely and exclusively licensed by the Publisher, whether the whole or part of the material is concerned, specifically the rights of translation, reprinting, reuse of illustrations, recitation, broadcasting, reproduction on microfilms or in any other physical way, and transmission or information storage and retrieval, electronic adaptation, computer software, or by similar or dissimilar methodology now known or hereafter developed.

The use of general descriptive names, registered names, trademarks, service marks, etc. in this publication does not imply, even in the absence of a specific statement, that such names are exempt from the relevant protective laws and regulations and therefore free for general use.

The publisher, the authors, and the editors are safe to assume that the advice and information in this book are believed to be true and accurate at the date of publication. Neither the publisher nor the authors or the editors give a warranty, expressed or implied, with respect to the material contained herein or for any errors or omissions that may have been made. The publisher remains neutral with regard to jurisdictional claims in published maps and institutional affiliations.

This Springer imprint is published by the registered company Springer Nature Singapore Pte Ltd. The registered company address is: 152 Beach Road, #21-01/04 Gateway East, Singapore 189721, Singapore

Paper in this product is recyclable.

# Preface

The papers presented at the 2nd International Conference on Renewable Power (ICRP-2023) held at Mewat Engineering College (Wakf), India, on March 28–29, 2023, are anthologized in this book. The ICRP-2023 mainly focuses on advanced research in the area of renewable power, which includes 10 sub-themes such as: (1) Smart Grid Technologies and Applications; (2) Renewable Power Systems including Solar PV, Solar Thermal, and Wind; (3) Power Generation, Transmission, and Distribution; (4) Transportation Electrification and Automotive Technologies; (5) Power Electronics and Applications in Renewable Power System; (6) Energy Management and Control System; (7) Energy Storage in Modern Power System; (8) Active Distribution Network; (9) Artificial Intelligence in Renewable Power Systems; and (10) Cyber-Physical Systems and Internet of Things in Smart Grid and Renewable Power. This conference provides a platform for sharing insights, experiences, and interaction on various facts of evolving technologies. The ICRP-2023 also provides a platform for leading academic scientists, researchers, scholars, and students to get together to share their research discovery and ideas. A total of 269 participants have participated in hybrid mode, out of them 33% of authors are from overseas and made technical presentations. More than **240** articles were submitted, out of which **68** were accepted. About 40% of articles are from overseas in the list of accepted articles, and these articles are from the following countries: Malaysia, Spain, Thailand, Indonesia, Brunei, Saudi Arabia, Qatar, Singapore, Japan, Nigeria, South Korea, and Italy.

We sincerely appreciate everyone who contributed to this book and helped create top-notch research material. We really appreciate the reviewers' prompt delivery of the reviews, comments, and recommendations.

We would like to express our sincere gratitude to Haryana Renewable Energy Development Agency (HAREDA) for providing financial support to make ICRP-2023 successful.

We would like to express our sincere gratitude to Springer LNEE for providing publishing opportunity. We would like to extend our sincere gratitude to **Mewat Engineering College (Wakf)** (a unique venture of Haryana Waqf Board, Government of Haryana, in district Nuh, Mewat, India) for providing a venue to host ICRP-2023.

We express our sincere gratitude to our **Chief Patron** Ch. Zakir Hussain, Administrator, Haryana Waqf Board, Government of Haryana; **Patron** Dr. Hanif Qureshi, IPS, Director General, HAREDA; Sh. Mohammed Shayin, IAS, Chief Executive Officer, Haryana Waqf Board and Managing Director, HVPNL, Government of Haryana, India; and Prof. Sukumar Mishra, IIT Delhi, India; **Conference General Chair** Prof. (Dr.) Khwaja M. Rafi, Director, Mewat Engineering College (Wakf); **Conference General Co-chair** Prof. Y. R. Sood, VC, JP University, Noida; Prof. Atif Iqbal, Professor, Qatar University, Qatar; Prof. Fausto Pedro Garcia Marquez, Universidad Castilla-La Mancha, Spain; and Prof. Nik Rumzi, Professor, UTM Malaysia, Malaysia; **Conveners** Dr. Shaheen Khan, HOD—ECED, MECW; Dr. Tazeem Ahmad Khan, HOD—EEED, MECW; and Dr. Hasmat Malik, UTM, Malaysia; **Organizing Secretaries** Dr. Mohd. Junaid Khan, Assistant Professor, EEED, MECW; Mr. Adil Zaidi, Assistant Professor, ECED, MECW; and Dr. Shafqat Nabi Mughal, HOD, Department EE, SoET BGSB University, Rajouri (J&K); **Finance Chair/Treasurer** Dr. Shamshad Ali, Assistant Professor, EEED, MECW; Dr. Nuzhat Fatema, UniSZA Malaysia; **Steering Committee** Prof. Moinuddin, Ex-Director, NIT Jalandhar; Prof. S. K. Chakarvarti, AICTE, Margadarshak and Ex-Dean Academic, Delhi; and Mr. K. K. Chakarvarti, Former Energy Economist, BEE, Ministry of Power, GoI; **Organizing Committee** Dr. Mohd. Shahid, MECW; Mr. Naseem Ahmed, MECW; Mr. Mohd Umar Khan, MECW; and Ms. Shahina Bano, MECW; **Publication Committee** Prof. Surender Reddy Salkuti, Woosong University, South Korea; Dr. Shimi, SL, EED, NITTTR Chandigarh, India; Dr. Ikhlaq Hussain, NIT Srinagar; and Publicity Committee Dr. Shadab Murshid, Rolls-Royce Corporate Lab, NTU Singapore; Dr. Samir Kumar, Korea University, the Republic of Korea; Mr. Waseem Akram, MECW; Mr. Ayaz Mahmood, AO, HWB, Government of Haryana, India; Dr. Azaz Khan, MECW; and Dr. Ahmed Riyaz, BGSB University, India.

We would like to extend our sincere gratitude to Dr. Shaheen Khan, HOD—ECED, MECW, and Dr. Mohd. Junaid Khan, Assistant Professor, EEED, MECW, for providing their valuable time and expertise to make ICRP success. We wish to acknowledge our gratitude to Intelligent Prognostic Private Limited Delhi, India for providing us technical and administrative support in the conference.

We sincerely acknowledge all the keynote speakers for disseminating their knowledge, experience, and thoughts. We express our sincere gratitude to the management of **Mewat Engineering College (Wakf)**, Conference Executive Chair, **International Advisory Committee, National Advisory Committee, and Technical Program Committee members** for their kind support and motivation.

We wish to thank our colleagues and friends for their insight and helpful discussion during the production of this book. We would like to highlight the contribution, suggestion, and motivation of Prof. Imtiaz Ashraf, Aligarh Muslim University, India; Prof. M. S. Jamil Asghar, Aligarh Muslim University, India; Prof. Salman Hameed, Aligarh Muslim University, India; Prof. A. H. Bhat, NIT Srinagar, India; Prof. Kouzou Abdellah, Djelfa University, Algeria; Prof. Jaroslaw Guzinski, Gdansk University of Technology; Prof. Mairaj Ud Din Mufti, NIT Srinagar, India; Prof. Majid Jamil, JMI, India; Prof. Majed A. Altotaibi, King Saud University, Saudi

Arabia; Prof. R. K. Jarial, NIT Hamirpur (HP), India; Prof. Rajesh Kumar, GGSIPU, India; Prof. Anand Parey, IIT Indore, India; and Prof. Yogesh Pandya, PIEMR Indore, India.

We would like to express our gratitude, our love, and our affection to our family members for their intense feeling of deep affection.

Johor Bahru, Malaysia  
New Delhi, India  
Hamirpur, India  
Doha, Qatar  
Koriyama, Japan

Dr. Hasmat Malik  
Prof. Sukumar Mishra  
Prof. Y. R. Sood  
Prof. Atif Iqbal  
Dr. Taha Selim Ustun

# Contents

<b>Editorial: Renewable Power for Sustainable Growth</b> .....	1
Hasmat Malik, Sukumar Mishra, Y. R. Sood, Atif Iqbal, and Taha Selim Ustun	
<b>An Efficient Algorithm for Energy Management in Smart Grid for Various Improvements</b> .....	31
Deepa Kumari and Ashish Sharma	
<b>Investigations and Validation of PV-Powered Unified Power Quality Conditioner for Electric Vehicle Smart Charger in Standard AC/DC Hybrid Microgrid Test System</b> .....	45
S. Sumana and R. Dhanalakshmi	
<b>Short-Term Electricity Load Forecasting Using Modified Hidden Markov Model</b> .....	61
Poras Khetarpal, Neelu Nagpal, Mahesh Kumar, D. Lakshmi, and Neelam Kassarwani	
<b>Microgrid Systems with Classical Primary Control Techniques—A Review</b> .....	75
Sujit Kumar, H. K. Yashaswini, Naveen Sharma, and Mohit Bajaj	
<b>Green Energy Solutions for Indoor Air Quality Improvement</b> .....	85
Saad Javed, Safdar Tanweer, Syed Sibtain Khalid, Naseem Rao, Jawed Ahmad, and Bhavya Alankar	
<b>Data Resource Library for Renewable Energy Prediction/ Forecasting</b> .....	99
Subeyr Bashir Ahmed, Hasmat Malik, Shahrin Md Ayob, Nik Rumzi Nik Idris, Awang Jusoh, and Fausto Pedro García Márquez	
<b>Solar Rooftop On-Grid Connected Net Metering System</b> .....	165
Sarfraz, Anju Gupta, and Rashmi Agarwal	

<b>Contemporary Maximum Power Point Tracking Methods of Solar Photovoltaic Modules</b> .....	177
Jyothi Tompala and Sravana Kumar Bali	
<b>Performance Analysis of Perturb &amp; Observe and Incremental Conductance Method of Maximum Power Point Tracking in Solar PV-Based Power Generation</b> .....	193
Avdhesh Kumar	
<b>The Airfoil Design for Small-Scale Wind Turbines in Maximizing Renewable Wind Energy</b> .....	205
S. A. H. Roslan, N. Umar, Z. A. Rasid, and A. K. Arifin	
<b>Comparative Study on Solar PV Module Performance with Sun Irradiance Trapping Mechanism: Power Generation Forecasting Using Machine Learning</b> .....	217
Rupendra Kumar Pachauri, Ashutosh Shukla, Ahmad Faiz Minai, Aryadhara Pradhan, Vinay Gupta, Mohit Kumar, and Shashikant	
<b>The Geometric Modelling and Linearization of Small-Scale Wind Turbine Blades for Optimized Renewable Energy</b> .....	229
S. A. H. Roslan, N. Umar, Z. A. Rasid, and A. K. Arifin	
<b>Performance Analysis of H-Type Vertical Axis Wind Turbine by Using Novelty Numerical Simulink Method</b> .....	245
Muhammad Radhiva, Muhammad Hasya Abdillah, Geordiano Devanaldy Khresna Putra, Muhammad Raihan Wajdi, Putri Wulandari, Wahyu Caesarendra, Ahmad Husin Lubis, and Ary Syahriar	
<b>Energy Production from Various Bio-wastes Under Different Electrode and Temperature Conditions: Experimental Study</b> .....	259
Rahul Anand, Rupendra Kumar Pachauri, Ahmad Faiz Minai, Akhlaque Ahmad Khan, Rajesh Singh, and Shashikant	
<b>Simulation and Prototype Design of Hybrid Renewable Energy Harvesting System</b> .....	271
Yanuar Z. Arief, Muhammad Syukri Nurulhak, and Hamzah Eteruddin	
<b>Design and Development of an Inexpensive Intelligent Device for Sag Measurement for Overhead Transmission Lines</b> .....	289
Manoj Kumar, Aman Kumar, Tushar Tomar, Anuj Dixit, Divya Asija, and R. K. Viral	
<b>Gradient Descent Back-Propagation Through Momentum (GDBPM) Endorsed <math>i \cos \phi</math> Control Technique-Based DSTATCOM Intended for Shunt Indemnification</b> .....	305
Mrutyunjaya Mangaraj, Kampara Ravisankar, Majji Satish, Kantubhukta Dinesh, and A. Praveena	



**Improvement in Voltage Stability of the System Due to Increased Penetration of Electric Vehicles Using Distributed Solar Photovoltaic Sources** ..... 319  
 Sheetal Deshmukh, Shirazul Islam, Atif Iqbal, and Md Fahim Ansari

**An Intelligent System for Furfural Estimation in the Power Transformers** ..... 339  
 Md. Manzar Nezami, Hythem Hashem, Md. Danish Equbal, Mohammad Junaid Khan, Md. Fahim Ansari, and Elfatih Elmubarak Mustafa

**Design of PID-Tuned Controller for Automatic Voltage Regulator for Frequency Stability in Thermal Power Plant** ..... 347  
 Md. Fahim Ansari, Atif Iqbal, and Md. Manzar Nezami

**Optimization of Distributed Generators in a Virtual Power Plan Using Mixed Integer Linear Programming Method** ..... 355  
 Ahmed Abubakar Elwan, Mohd Hafiz Habibuddin, Yanuar Z. Arief, Siti Nur Aisyah Mohd Sharan, Ahmad Safawi Bin Mokhtar, and Rasyidah Binti Mohamad Idris

**Solving Unit Commitment Problem Using Mixed Integer Linear Programming for Demand Side Management** ..... 367  
 Ahmed Abubakar Elwan, Mohd Hafiz Habibuddin, and Yanuar Z. Arief

**Deployment of Renewable Embedded Generation and Unified Power Quality Conditioner in Distribution System using Firefly Algorithm** ..... 377  
 Musa Mustapha, Madihah Binti Md. Rasid, Jasrul Jamani Bin Jamian, Ganiyu Ayinde Bakare, and Yau Shuaibu Haruna

**Application of Wind Power in Backwashing Filter Media** ..... 391  
 Deepak Juneja, Sushindra Kumar Gupta, and Aditya Rana

**Mixed Reality Accelerates the Designing Process in Automotive Industry** ..... 403  
 Mohamad Yahya Fekri Aladin, Ajune Wanis Ismail, and Fazliaty Edora Fadzli

**Design and Implementation of Solar Charging Electric Vehicle** ..... 417  
 Rahil Imtiyaz, Aman Kumar, Gitanjali Mehta, and Ruqaiya Khanam

**Modelling and Analysis of a Permanent Magnet DC Motor Fed Electric Vehicle Drive System** ..... 431  
 K. Subbaramaiah, Ravisankar Kampara, Majji Satish, Kantubhukta Dinesh, and Karthik Tamvada

**An Overview of Electric and Hybrid Vehicle Technology** ..... 441  
 V. S. Vishwanath Nagarajan, Vinay Kumar Jadoun,  
 N. S. Jayalakshmi, and Anubhav Kumar Pandey

**Performance Analysis of Classical Converter Using Different Control Strategies for Switched Reluctance Motor with Dynamic Loading** ..... 457  
 Ritika Asati and Deepak S. Bankar

**Design and Development Gear-Electric Bike and Performance Testing for Indian Road Conditions** ..... 469  
 Vinay Gupta, Jitesh Kumawat, Rupendra Kumar Pachauri, and Shashikant

**Design and Development of a Solar-Based Wireless Electric Vehicle Charging System** ..... 481  
 Sanyam Jain, Samyak Jain, Sanjay Kumar, Harsh Kaushik, Neelu Nagpal, and Ravi Sharma

**Design, Optimization, and Performance Enhancement of Switched Reluctance Motor for Pollution-Free Electric Vehicle Application** ..... 495  
 Kesar Ali, Arbaz Sherkhani Shaikh, Kirti Govind, Javid Navaj Shaikh, Yogesh B. Mandake, and Deepak S. Bankar

**Using Linear Regression Model to Predict the Wholesale of the Electric Car in Indonesia: What Can Be Learned from the Model?** ..... 513  
 Rosyid R. Al-Hakim, Nur F. Soelaiman, Sri Riani, and Yanuar Z. Arief

**Comparison of Thermoelectric Generator with Boost Converter and Single-Ended Primary-Inductance Converter** ..... 521  
 Megat Azri Irfan Adzmi, Mohd Zaki Daud, Shahrin Md Ayob, and Razman Ayop

**A Hybrid Maximum Power Point Tracking (MPPT) for Thermoelectric Generator (TEG) System** ..... 535  
 Naseem Mohd Arshad, Mohd Zaki Daud, Shahrin Md Ayob, and Razman Ayop

**Thermoelectric Generator (TEG) by Using Indirect Maximum Power Point (MPP) Algorithm** ..... 553  
 Ardrine Justin, Mohd Zaki Daud, Shahrin Md Ayob, and Razman Ayop

**Comprehensive Review on AC-DC, DC-DC, DC-AC-DC Converters Used for Electric Vehicles and Charging Stations** ..... 569  
 Utkarsh Shukla, Shekhar Yadav, Nitesh Tiwari, and Aayushi Priyadarshini

<b>Control and Performance Analysis for Active Islanding Detection Using q-Axis Control in Renewable Energy Sources Based Microgrid: A Review</b> .....	589
Avdhesh Kumar	
<b>Harmonics Analysis of Triple-Phase Induction Motor Drive</b> .....	601
Mohd. Rizwan Khan, Md. Nasim Akhter, and Mohd. Sartaj	
<b>Development of Witricity Based Wireless Power Transmission System</b> .....	619
Kanhaiya Mishra, Arjun Kushawaha, Neetigya Chaurasia, Sudhanshu Kumar, Gautam Kr. Singh, and Mohammad Shahid	
<b>Analysis of Three-Winding Transformer Configurations for Energy Storageless Dynamic Voltage Restorer</b> .....	635
Muhammad M. Roomi, S. M. Suhail Hussain, Mohd Tariq, and Taha Selim Ustun	
<b>Data Reliability Analysis for Early Fault Diagnosis of Air Handling Unit (AHU)</b> .....	649
Hasmat Malik, Shahrin Md Ayob, Nik Rumzi Nik Idris, Awang Jusoh, Fausto Pedro García Márquez, and Abdulaziz Almutairi	
<b>Use of Solar Energy in Treatment of Pulp and Paper Industry Effluent with Hemp: An Experimental Study</b> .....	675
Ambika Thakur, Deepak Juneja, and Yogyendra Narayan	
<b>Design of Radar-Based Portable System for Monitoring of Human Vital Signs with Renewable Energy Resources</b> .....	689
Pushparaj, Amod Kumar, and Garima Saini	
<b>Controlling Methods of Brushless DC Motor in Electrical Vehicle Drives</b> .....	717
Megha Sharma, Shailly Sharma, and Jayashri Vajpai	
<b>Effect of Number of Poles on IPMSM Performance for Electric Vehicle Drivetrain</b> .....	727
Vinod Kumar Kuttney and Sravana Kumar Bali	
<b>Offline Power Quality Management and Control Using Neural Networks</b> .....	737
Papia Ray, Surender Reddy Salkuti, and R. Aditya Kumar	
<b>Optimized Integral Sliding Mode Load Frequency Control of an Isolated Power System</b> .....	751
Neelam Kassarwani, Neelu Nagpal, Jagrat Sehgal, and Pierluigi Siano	

**Implementation of Supercapacitor-Battery-Based Energy Storage System in Hybrid Power System Incorporating Renewable Energy Resources** ..... 763  
 Jahid, Manaulah, and Sheeraz Kirmani

**Hybrid Waste to Energy Electricity Generation and Battery Storage System: The Economics and Environmental Emission in a Low-Income Community** ..... 773  
 Ahmed Abubakar Elwan, Mohd Hafiz Habibuddin, Yanuar Z. Arief, Ahmad Safawi Bin Mokhtar, and Rasyidah Binti Mohamad Idris

**Application of Solar Power in the Loopholes and Coverages of Buses in the Bus Rapid Transit System in Bhopal** ..... 785  
 Rajeev Kumar, Deepak Juneja, and Yogendra Narayan

**Forecasting of Carbon Emissions in India Using (ARIMA) Time Series Predicting Approach** ..... 799  
 Somesh Sharma, Amit Mittal, Manmohan Bansal, Bhagawati Prasad Joshi, and Ashish Rayal

**Peak Shaving Through Battery Storage for Photovoltaic Integrated Building Considering the Time of Day Pricing** ..... 813  
 A. Sharma, P. Mahajan, and R. Garg

**Economic Analysis of Renewable Energy Systems for Rural Electrification** ..... 827  
 Nikita Yadav, Rahul Sharma, and Yashwant Sawle

**Improved Voltage Regulation in Hybrid Photovoltaic/Wind Using Modified Dynamic Voltage Restorer with Hybrid Control Scheme** ..... 837  
 Preeti Rani, Ved Parkash, and Naveen Kumar Sharma

**Contingency Analysis for a Solar Energy Generation System Using Real-Time Data Analysis** ..... 853  
 Vishal V. Mehtre, Shivani Jitendra Khare, Swapnil Namekar, and D. S. Bankar

**Digital Twin in Extended Reality Applications for Industry 4.0** ..... 867  
 Ajune Wanis Ismail, Mohamad Yahya Fekri Aladin, and Nur Ameerah Abdul Halim

**Deep Image Coding in the Fractional Wavelet Transform Domain based on High-Frequency Sub-bands Prediction** ..... 881  
 Nadeem Ahmad, Zainul Abdin Jaffery, Irshad, and Shaheen Khan

**QIVIFS: Quaternion Approach of Interval-Valued Intuitionistic Fuzzy Sets with Applications in Renewable Energy System** ..... 899  
 Bhagawati Prasad Joshi, Madan Mohan Sati, Sanjay Oli, Deepak Kumar, Ashish Rayal, and Abhay Kumar

**Feminine Protection Wearable System Based on IoT** ..... 911  
 Shubham Kumar Verma, Udai Raj Tiwari, Utkarsh Rau,  
 Khadim Moin Siddiqui, Sandhya Srivastava, and Jayati Vaish

**Marine Predictors Algorithm Optimization Technique  
 to Estimate GMPP of PV Array Under Partial Shadowing  
 Conditions** ..... 923  
 Rupendra Kumar Pachauri, Rajesh Singh, Ahmad Faiz Minai,  
 and Shashikant

**Artificial Intelligence-Based Bearing Fault Diagnosis of Rotating  
 Machine to Improve the Safety of Power System** ..... 933  
 Mohmad Iqbal and A. K. Madan

**Stability Enhancement of AC Microgrid Using Discrete Mode  
 Controllers with Optimum Sampling Frequency** ..... 943  
 Amit Arora, Mahendra Bhadu, and Arvind Kumar

**Performance Analysis of Grid-Integrated Solar System Through  
 Interlinking Converter with Control Schemes** ..... 963  
 Preeti Rani, Ved Parkash, and Naveen Kumar Sharma

**Towards Achieving Net Zero Emissions in India by 2070** ..... 981  
 Akash Midha and Anuradha Tomar

**IOT-Based Monitoring and Controlling of Substation Parameters** ..... 993  
 P. Sai Kiran, B. Venkateswara Rao, G. Satyamohan Sarveswar,  
 and P. Manikanta

**Effectiveness of Resilience Index in Assessing Power System  
 Performance** ..... 1003  
 Hasna Satya Dini and Jasrul Jamani Jamian

**Author Index** ..... 1021

# About the Editors

**Dr. Hasmat Malik** (Senior Member, IEEE) is a Senior Lecturer at the Department of Electrical Power Engineering, Faculty of Electrical Engineering, Universiti Teknologi Malaysia (UTM) Johor, Malaysia. He served as an Assistant Professor for more than five years with the Division of Instrumentation and Control Engineering, Netaji Subhas Institute of Technology (NSIT), Government Delhi, India; and 3.5 years as a Postdoctoral scholar with the Berkeley Education Alliance for Research in Singapore (A research center of the University of California, Berkeley, USA) and the National University of Singapore (NUS), Singapore. He is currently a Chartered Engineer (CEng) and a Professional Engineer (PEng). He is a Fellow of the Institution of Electronics and Telecommunication Engineering (IETE), a Senior Member of the Institute of Electrical and Electronics Engineers (IEEE) USA, a Life Member of the Indian Society for Technical Education (ISTE), and a member of the Institution of Engineering and Technology (IET), UK and the Institute of Engineers (India). He has supervised 25 master's students and five Ph.D. are ongoing. He is involved in several large research and development projects. He has authored/co-authored more than 100 research articles, ten books, and 15 chapters in other books, published by IEEE, Springer, and Elsevier.

**Dr. Sukumar Mishra** (Senior Member, IEEE) received his M.Tech. and Ph.D. in Electrical Engineering from National Institute of Technology, Rourkela in 1992 and 2000 respectively. Presently, Dr. Mishra is a Professor at the Indian Institute of Technology Delhi and has been its part for the past 19 years. Professor Mishra has won many accolades such as Young Scientist award (1999) by Orissa Bigyan Academy, INSA medal for young scientist (2002), INAE Young Engineer award (2002), INAE Silver Jubilee Young Engineer award (2012), The Samanta Chandra Shekhar award (2016), Bimal Bose award (2019) and NASI-Reliance Platinum Jubilee award (2019), National Mission Innovation Championship award (2019) and INAE Outstanding Teachers award (2021). He has been granted fellowship from academies like NASI (India), INAE (India) and professional societies like IET (UK), IETE (India), IE (India). He has also been recognized as the INAE Industry Academic Distinguish

Professor. Professor Mishra is currently acting as ABB Chair professor and has previously delegated as the NTPC, INAE and Power Grid Chair professor.

**Dr. Y. R. Sood** (Senior Member, IEEE) has taken over as Vice-Chancellor with effect from 14 June 2021. Dr. Sood has an outstanding administrative, academic, research experience of more than 36 years. He obtained his B.Sc. degree from Government college for Men Chandigarh (Punjab University Chandigarh) in 1980, B.E. (Honours) Electrical Engineering in 1984 and M.E. Electrical Power System in 1987 from Punjab Engineering College Chandigarh, and Ph.D. from I.I.T. Roorkee in 2003. He has been a lecturer at Electrical Engineering Department of TIET Patiala from 6th January 1986 to 31st July 1986, at Electrical Engineering Department of N.I.T Kurukshetra (Haryana) from 1st August 1986 to 28th August 1991, Assistant Professor (equivalent to Associate Professor) at Electrical Engineering Department NIT Hamirpur (H.P.) from 29th August 1991 to 18th May 2003, Professor from 19th May 2003 to 27th April 2017 and Professor (HAG) w.e.f. 28th April 2017 to 13th June 2021. He has worked as Director, Chairman Board of Governors (BOG) at NIT Puducherry. He has worked as Dean (Research and Consultancy), Dean (Planning and Development), Dean (Faculty welfare) and Dean (Industrial Research Development and Consultancy), Head of Electrical Engineering Department, Member of BOG, Member of Senate, Coordinator/Chief Coordinator/Professor In-charge of TIFAC-CORE, Chief Vigilance Officer, Chairman Admission Committee, etc. at NIT Hamirpur and member of Senate, at NIT Calicut (Kerala). He has delivered more than 90 key notes/expert lectures in various international conferences, workshops, short term courses, etc., in India and abroad. He is the editor of three international books (two Springer Publisher and one Elsevier Publisher), many conference proceedings and technical reports. He has worked as Chairman/member of selection/interview boards for the various teaching and technical posts. He has organized and participated many short-term training programmes/short term courses and conferences. He has developed completely High Voltage Engineering Lab. from its very start and set up new experiments in various labs. He has successfully completed three MHRD research projects and one mega projects under TIFAC-CORE of Rs. 530 Lakhs. Twelve research scholars have already completed Ph.D. under his guidance. Two more research scholars are pursuing their Ph.D. under his guidance. He has Published more than 370 research papers in International and National Journals including several papers in SCI Journals, IEEE Transactions and conferences and many chapters in various international books.

**Dr. Atif Iqbal** (Senior Member, IEEE, Fellow IET, Fellow IE) received the B.Sc. and M.Sc. degrees in engineering (power system and drives) from Aligarh Muslim University (AMU), Aligarh, India, in 1991 and 1996, respectively, and Ph.D. degree from Liverpool John Moores University, Liverpool, UK, in 2006, and the D.Sc. degree (Habilitation) in control, informatics, and electrical engineering from the Gdansk University of Technology, in 2019. He is a Full Professor with the Department of Electrical Engineering, Qatar University, Doha, Qatar, and a former Full Professor with the Department of Electrical Engineering, AMU, Aligarh, India. He

has been a Lecturer with the Department of Electrical Engineering, AMU, since 1991, where he has served as a Full Professor, until August 2016. Dr. Iqbal has been listed in top 2% highly cited scientists of the world (data released by Stanford University, USA). The world ranking in 2019 was #649 and the current ranking is #622. He has published widely in international journals and conferences on his research findings related to power electronics, variable speed drives, and renewable energy sources. He has authored or co-authored more than 520 research articles and four books and several chapters in edited books. He has supervised several large research and development projects worth more than multi million USD. He was a recipient of the Maulana Tufail Ahmad Gold Medal for standing first at the B.Sc. Engg. (Electrical) Exams from AMU, in 1991. He was also a recipient of the Outstanding Faculty Merit Award academic year 2014–2015 and the Research Excellence Awards at Qatar University, in 2015 and 2019. He has received several best research papers awards, e.g., at IEEE ICIT-2013, IET-SEISCON-2013, SIGMA 2018, IEEE CENCON 2019, IEEE ICIOT 2020, ICSTEESSD-20, Springer ICRP 2020, IEEE GUCON 2021. He has also received the Gold Medal for his B.Sc. degree. He is the Vice-Chair of the IEEE Qatar Section. He is also an Associate Editor of the IEEE Transactions on Industrial Electronics and IEEE Access and the Editor-in-Chief of the *Journal of Electrical Engineering* (I'manager). He was a former Associate Editor of the IEEE Transactions on Industry Application and a former Guest Associate Editor IEEE Transactions on Power Electronics. He is head of the design team of Power Electronics and Drives equipment at Powerlab Instruments, Chennai, India His research interests include smart grid, complex energy transition, active distribution network, electric vehicles drivetrain, sustainable development and energy security, distributed energy generation, and multiphase motor drive systems.

**Dr. Taha Selim Ustun** (Senior Member, IEEE) received his Ph.D. degree in electrical engineering from Victoria University, Melbourne, VIC, Australia. Currently, he is a senior researcher at Fukushima Renewable Energy Institute, AIST (FREIA) and leads Smart Grid Cybersecurity Lab. Prior to that he was an Assistant Professor of Electrical Engineering with the School of Electrical and Computer Engineering, Carnegie Mellon University, Pittsburgh, PA, USA. His research interests include power systems protection, communication in power networks, distributed generation, microgrids, electric vehicle integration and cybersecurity in smart grids. He is a member of IEEE 2004, IEEE 2800 Working Groups and IEC Renewable Energy Management Working Group 8. He has edited several books and special issues with international publishing houses. He is a reviewer in reputable journals and has taken active roles in organizing international conferences and chairing sessions. He has been invited to run specialist courses in Africa, India and China. He delivered talks for Qatar Foundation, World Energy Council, Waterloo Global Science Initiative and European Union Energy Initiative (EUEI).



# Editorial: Renewable Power for Sustainable Growth



**Hasmat Malik, Sukumar Mishra, Y. R. Sood, Atif Iqbal,  
and Taha Selim Ustun**

**Abstract** Nowadays, the globe faces an urgent need to switch to sustainable and renewable sources of energy due to the rising concern over climate change and the finite supply of fossil fuels. Technologies for producing energy from renewable sources have become a viable option for achieving sustainable development and addressing environmental issues. This edited book provides a collection and overview of the role, advances, and different paradigms that renewable energy plays in promoting sustainable development, stressing both the potential advantages and difficulties. In this book, 68 are included, which represent the different types of applications in the area of renewable power for sustainable growth such as: (1) Smart Grid Technologies and Applications (5 chapters); (2) Renewable Power Systems including Solar PV, Solar Thermal, and Wind (10 chapters); (3) Power Generation, Transmission and Distribution (8 chapters); (4) Transportation Electrification and Automotive Technologies (10 chapters); (5) Power Electronics and Applications in Renewable Power System (8 chapters); (6) Energy Management and Control System (7 chapters); (7) Energy Storage in Modern Power System (5 chapters); (8) Active Distribution Network (4 chapters); (9) Artificial Intelligence in Renewable Power Systems (5 chapters); and (10) Cyber-Physical Systems and Internet of Things in Smart Grid and Renewable Power (5 chapters).

---

H. Malik (✉)

Department of Electrical Power Engineering, Faculty of Electrical Engineering, Universiti Teknologi Malaysia (UTM), Johor Bahru, Malaysia  
e-mail: [hasmat@utm.my](mailto:hasmat@utm.my)

S. Mishra

Department of Electrical Engineering, Indian Institute of Technology Delhi, Delhi, India

Y. R. Sood

Department of Electrical Engineering, National Institute of Technology - [NIT], Hamirpur, Himachal Pradesh, India

A. Iqbal

Department of Electrical Engineering, Qatar University, Doha, Qatar

T. S. Ustun

Fukushima Renewable Energy Institute, Advanced Industrial Science and Technology (FREA), Koriyama, Japan

**Keywords** Renewable power · Sustainable growth · Solar · Wind · Smart grid · Power generation · Transportation · Automation · Power electronics · Power and energy system · Energy management · Control system · Machine learning · Artificial intelligence · Data analytics · Advance computing · Prediction · Forecasting · Optimization · Smart city · Electric vehicle · Energy storage

## 1 Introduction

In the whole world, everyone is now willing to speak up in favor of a change that might improve the planet [1–3]. The topic of “Renewable Power” sources (RPS) is a ray of hope at a time when the effects of our unsustainable energy practices are becoming more and clearer. Because of our overwhelming reliance on fossil fuels (FF), the world is currently experiencing a climatic catastrophe of unparalleled scope. Rising carbon dioxide (CO<sub>2</sub>) emissions from the combustion of coal, oil, and natural gas have caused catastrophic climatic events and global warming. The moment has arrived for us to abandon this disastrous course and embrace a sustainable energy future fueled by renewable resources [2].

The key to a better and cleaner future for all of mankind is the utilization of RPS. These natural resources are hydro, tidal, solar, biomass, wind, geothermal, and wave power, which are never run out of power. They present us with a chance to satisfy our energy requirements without endangering the welfare of the next generations. Let’s start with solar energy, which is provided to us every day by the sun. Solar panels allow us to collect sunshine, which we can then turn into electricity to power homes, companies, and even towns. Imagine a world in which solar panels glisten on rooftops, harnessing the energy of the sun to illuminate our lives without emitting a single carbon dioxide (CO<sub>2</sub>) particle [4].

Another proponent of RPS is wind power [3], which is a monument to the strength of nature itself. Wind turbines whirl elegantly in the breeze, producing enough electricity to run large community. The wind spreads tales of a future devoid of smog and air pollution, where new generations may breathe pure air and play in fields free from the scars of industrialization. Apart of this, our planet’s lifeblood, water, contains the secret to achieving sustainable power through hydroelectricity. Dams allow rivers to cascade past them, turning massive turbines that generate electricity that powers our businesses while maintaining the sensitive ecosystems of the waterways.

A special chance to recycle nature’s gifts is provided by biomass, which is made of organic resources [5]. We decrease trash and dependency on FFs at the same time by transforming plant and agricultural waste into electricity. What was previously seen as waste is given new life via the procedure, much like a phoenix rising from the ashes. Moreover, the Earth’s interior heat, a testament to its enduring force, is harnessed via geothermal energy. Geothermal energy has the ability to heat our houses and produce power without leaving any traces on the surface, demonstrating the harmony we are capable of achieving with our earth [6].

Tidal and wave energy are provided by the huge and mighty seas [7]. These organic cycles carry the potential for unrelenting energy that may be wisely harnessed to dispel the impending darkness around us. Beyond its positive effects on the environment, RPS has other advantages. Investing in these technologies supports innovation and creativity as well as job creation and economic growth. It gives communities and countries the ability to become resilient in the face of international problems and energy independent.

Accepting RPS, nevertheless, is not without its difficulties. Coordination, tenacity, and long-term planning are needed to make the switch from FFs to RPS. It necessitates spending on research and development to advance technology and increase everyone's access to them. To eliminate barriers and encourage the transition to a greener society, governments, corporations, and individuals must work together. Although the journey ahead may be difficult, let's not forget that every great undertaking starts with a single step. Together, we can create a world where kids can imagine a future with clear sky, beautiful scenery, and an abundance of species.

To embrace the idea of RPS, we are here. Let's pledge to lessen our carbon footprint, promote clean energy regulations, and aid the advancement of renewable technology. By doing this, we not only protect our future but also show respect for the planet that has long provided for our needs. Let's select the route that will result in a world that is sustainable, prosperous, and driven by the unflinching grace of RPS as we stand at this historical crossroads.

Therefore, the harness of RP from RPS is a key research area to develop advanced approaches and models, which will be able to forecast/predict/identify the strength of the RP for a particular location/source. In this way, artificial intelligence (AI) and machine learning (ML) algorithms play important roles as we can see their advantages in different applications [8–154] without using system information. Generally, these AIML algorithms are dependent on data and the property of data only [155–164]. This edited book focuses on RPS, and advances in application using various computing techniques. It is a collection of 68 chapters (including this chapter of editorial), which demonstrate the different types of applications such as: (1) Smart Grid Technologies and Applications (5 chapters); (2) Renewable Power Systems including Solar PV, Solar Thermal, and Wind (10 chapters); (3) Power Generation, Transmission and Distribution (8 chapters); (4) Transportation Electrification and Automotive Technologies (10 chapters); (5) Power Electronics and Applications in Renewable power System (8 chapters); (6) Energy Management and Control System (7 chapters); (7) Energy Storage in Modern Power System (5 chapters); (8) Active Distribution Network (4 chapters); (9) Artificial Intelligence in Renewable Power Systems (5 chapters); and (10) Cyber-Physical Systems and Internet of Things in Smart Grid and Renewable Power (5 chapters).

In Chapter “[An Efficient Algorithm for Energy Management in Smart Grid for Various Improvements](#)” [165], Kumari et al. presented an efficient algorithm for energy management in smart grid for various improvements. The chapter discussed the application of artificial intelligence for obtaining an efficient energy management system in any electrical grid.

In Chapter “[Investigations and Validation of PV Powered Unified Power Quality Conditioner for Electric Vehicle Smart Charger in Standard AC/DC Hybrid Microgrid Test System](#)” [166], Sumana et al. provided the investigations and validation of PV powered unified power quality conditioner for electric vehicle smart charger in standard AC/DC hybrid microgrid test system. It is well known that increase of nonlinear load such as electric vehicles (EVs) has become the key aspect in booming the power quality (PQ) issues in the power distribution grid. In this chapter, the novelties are the analysis of PQ issues due to the penetration of EVs in AC/DC hybrid microgrid and its compensation by photovoltaic (PV)-powered UPQC. The simulation is carried out in MATLAB 2017b platform. Based on the action of UPQC, outcomes are analyzed for three different cases. In each case, three scenarios are discussed based on the charging condition of EV smart charger in both the modes of system operation, i.e., when it is coupled to the grid and also in off-grid mode.

In Chapter “[Short-Term Electricity Load Forecasting Using Modified Hidden Markov Model](#)” [167], Khetarpal et al. presented a short-term electricity load forecasting using modified hidden Markov model. This study proposes a modified hidden Markov model (HMM) as a method for predicting electricity on an hourly basis in the Delhi region. This study provides satisfactory prediction results even with limited data. Furthermore, the proposed modified HMM technique outperforms alternative techniques in terms of computational time and complexity.

In Chapter “[Microgrid Systems with Classical Primary Control Techniques—A Review](#)” [168], Kumar et al. presented a state of the art on microgrid system with classical primary control techniques. Key outcomes and potential patterns are presented. Using the hierarchical control architecture for DC MGs, this chapter summarizes the primary control approaches. Methods of primary control, such as inner loop and droop control, are specifically discussed. The authors also reviewed the pros and cons of a centralized, distributed, and decentralized approach to primary control.

In Chapter “[Green Energy Solutions for Indoor Air Quality Improvement](#)” [169], Javed et al. presented a study on green energy solutions for indoor air quality (IAQ) improvement. This chapter presents the design and implementation of an IAQ monitoring system using an Arduino microcontroller and various sensors to measure pollutants such as particulate matter, volatile organic compounds, and carbon monoxide. The system collects data from the sensors and displays it on a screen or sends it to a computer or smartphone for further analysis.

In Chapter “[Data Resource Library for Renewable Energy Prediction/Forecasting](#)” [170], Ahmed et al. developed a data resource library for renewable energy prediction/forecasting applications. The objective of this chapter is to develop a data resource library for renewable energy forecasting/prediction using the whole world’s available dataset of the solar and wind domains. A large volume of dataset information and resource files have been collected from Asia, Africa, Latin America, Oceania, and North America regions. Data library for 214 different locations in the world has been prepared.

In Chapter “[Solar Rooftop On-Grid Connected Net Metering System](#)” [171], Sarfraz et al. developed a solar rooftop on-grid connected net metering system.

The system performance analysis is demonstrated using DISCOM/State Boards for rooftop system under net metering.

In Chapter “[Contemporary Maximum Power Point Tracking Methods of Solar Photovoltaic Modules](#)” [172], Tompala et al. developed a contemporary maximum power point tracking methods of solar photovoltaic modules. This chapter presents a detailed analysis of different maximum power point tracking approaches for solar photovoltaic (PV) modules from traditional techniques. This chapter also details the design of different sections of solar PV simulation for research purposes.

In Chapter “[Performance Analysis of Perturb and Observe and Incremental Conductance Method of Maximum Power Point Tracking in Solar PV Based Power Generation](#)” [173], Kumar demonstrated the performance analysis of perturb and observe and incremental conductance method of maximum power point tracking in solar PV-based power generation. In this chapter, a study and performance analysis of perturb and observe (P&O) and incremental conductance (InC), method of MPPT control algorithms has been analyzed. Model has been tested under different environmental conditions. P&O, and InC algorithm has been analyzed.

In Chapter “[The Airfoil Design for Small-Scale Wind Turbines in Maximizing Renewable Wind Energy](#)” [174], Roslan et al. developed an airfoil design for small-scale wind turbines in maximizing renewable wind energy. In this study, a set of three airfoils specifically for low Re is obtained through geometric adjustments of a high-performance airfoil, WT180 that is suitable for large-scale wind turbines. At a low Re of 100,000, the newly adjusted airfoils were found to have  $L/D$  of up to 46 which is higher by 44% compared to the original WT180 and 4% compared to the SG6043 airfoil, the well-known airfoil designed for WT having low wind speed condition.

In Chapter “[Comparative Study on Solar PV Module Performance with Sun Irradiance Trapping Mechanism: Power Generation Forecasting Using Machine Learning](#)” [175], Pachauri et al. presented a comparative study on solar PV module performance with sun irradiance trapping mechanism: power generation forecasting using machine learning. In the presented study, an experimental investigation deliberates the performance analysis on a polycrystalline photovoltaic (PV) system with the manual arrangement using 2 mm thickness of acrylic sheet. Total three types of solar PV system-based experimental setups as (i) normal PV module/without sheet; (ii) integration of triangular shape of transparent sheet on PV module surface; and (iii) rectangular shape of transparent sheet. The experimental investigation performs for all three types of PV arrangements during the entire single-day window from morning to evening to monitor the electrical performance data in terms of voltage (open-circuit) and current (short-circuit) primarily.

In Chapter “[The Geometric Modelling and Linearization of Small-Scale Wind Turbine Blades for Optimized Renewable Energy](#)” [176], Roslan et al. developed a model for geometric modeling and linearization of small-scale wind turbine blades for optimized renewable energy. In this chapter, the power coefficient of a WT utilizing different blade geometries is determined and compared using the BEMT method. The blade geometries are obtained from the proposed formulas in literature and from the recommended polynomials that are based on experimental works. All

blades are analyzed using the extended BEMT that includes the tip loss effect, the axial induction correction factor,  $a$ , and the stall effect. At the same time, the obtained tapered blade is usually varies in its chord length and twist angle in a nonlinear manner with respect to radius of the blade. As this may cause manufacturing difficulty of the blade and increasing the wind turbine manufacturing cost, the best nonlinear distribution based on the BEMT analysis conducted has been linearized thru a process of linearization. A comparison is made on the aerodynamic performances of the WT for the linearized and nonlinear blades. The study shows that the geometry of the blade is better with the use of the empirical formula that gives high power at higher tip speed ratio (TSR) while having lower axial thrust.

In Chapter “[Performance Analysis of H-Type Vertical Axis Wind Turbine by Using Novelty Numerical Simulink Method](#)” [177], Radhiva et al. presented a detailed study for the performance analysis of H-type vertical axis wind turbine by using novelty numerical Simulink method. This chapter is a form of Darrieus VAWT research development. The demonstration of the numerical Simulink method can be found here to evaluate the performance of wind turbine such as the values of power coefficient, angular velocity, and torque. The input parameters are a symmetrical airfoil with 15% thickness, a radius of 0.5 m, a height of 1 m, and a chord length of 0.2 m. Numerical analysis using the novelty Simulink model is carried out.

In Chapter “[Energy Production from Various Bio-Waste Under Different Electrode and Temperature Conditions: Experimental Study](#)” [178], Anand et al. presented an experimental study on energy production from various bio-wastes under different electrode and temperature conditions. This chapter presents an analysis of the effects of various types of electrodes on the performance of microbial fuel cells (MFCs) under various test conditions. Electrical parameters are obtained from MFCs with different types of electrodes, e.g. carbon (C), aluminum (Al), zinc (Zn), and copper (Cu). The extensive performance is compared with different temperature levels during the study.

In Chapter “[Simulation and Prototype Design of Hybrid Renewable Energy Harvesting System](#)” [179], Arief et al. developed a simulation and prototype design of hybrid renewable energy harvesting system. This chapter focuses on the development of a hybrid renewable energy harvester system consisting of photovoltaic, piezoelectric, and wind energy. The system’s performance and capabilities are recorded and analyzed under different conditions and parameters.

In Chapter “[Design and Development of an Inexpensive Intelligent Device for Sag Measurement for Overhead Transmission Lines](#)” [180], Kumar et al. presented an approach for design and development of an inexpensive intelligent device for sag measurement for overhead transmission lines. This chapter mainly focus on the various factors affecting sag in overhead line while laying transmission lines. A high degree of stress in the conductor may be reached if the conductors are stretched too much between supports of two towers. In this, the author has worked upon the two physical parameters (i.e., temperature and tension). In order to prevent mechanical failure of the conductor (such as the breaking of cross arms or poles) and to allow for the use of less robust supports, proposed approach perform defectively.

In Chapter “[Gradient Descent Back Propagation Through Momentum \(GDBPM\) Endorsed  \$i \cos \phi\$  Control Technique Based dSTATCOM Intended for Shunt Indemnification](#)” [181], Mangaraj et al. developed a gradient descent back propagation through momentum (GDBPM)-endorsed  $i \cos \phi$  control technique-based dSTATCOM intended for shunt indemnification. The suggested organize approach is implemented within MATLAB/Simulink environment with the help of mathematical investigation with an appropriate learning rate and momentum behavior. This control technique follows the systematic process for obtaining the basic loading values of the active and reactive power, those are necessary for the efficiently generate perception currents.

In Chapter “[Improvement in Voltage Stability of the System Due to Increased Penetration of Electric Vehicles Using Distributed Photovoltaic Sources](#)” [182], Deshmukh et al. presented an approach for the improvement in voltage stability of the system due to increased penetration of electric vehicles using distributed photovoltaic sources. This chapter proposes a secondary coordinated control scheme (SCCS), including a centralized controller. The local controller communicates the information corresponding to various bus voltages to the secondary using the communication links.

In Chapter “[An Intelligent System for Furfural Estimation in the Power Transformers](#)” [183], Nezami et al. developed an intelligent system for furfural estimation in the power transformers. In the present work, an intelligent system is proposed and developed that predicts the level of furfural in the transformer oil. The system makes predictions using easily quantifiable parameters, enabling utilities to avoid suffering financial losses. The proposed system employs the Adaptive Neuro Fuzzy Inference System (ANFIS) technique with temperature and moisture as the input and 2-furfuraldehyde (2-FAL) as the output.

In Chapter “[Design of PID Tuned Controller for Automatic Voltage Regulator for Frequency Stability in Thermal Power Plant](#)” [184], Ansari et al. proposed a design of PID-tuned controller for automatic voltage regulator for frequency stability in thermal power plant. In this chapter, implementing three gain factors for integral, proportional, and differentiation at an acceptable degree of error as well as a dynamic response was the most crucial step in the construction of a PID. To acquire the necessary results, robustness and quick reaction were obtained.

In Chapter “[Optimization of Distributed Generators in a Virtual Power Plan Using Mixed Integer Linear Programming Method](#)” [185], Elwan et al. developed a framework for the optimization of distributed generators in a virtual power plan using mixed integer linear programming method. To find a solution that is both economical and sustainable, a virtual power plant is formed from diesel generators with a capacity of 5.6 MW, a waste-to-energy (WtE) power generating plant with a capacity of 1 MW, a wind power plant with a capacity of 0.6 MW, and a photovoltaic (PV) power plants with a capacity of 0.4 MW.

In Chapter “[Solving Unit Commitment Problem Using Mixed Integer Linear Programming for Demand Side Management](#)” [186], Elwan et al. developed a model for solving unit commitment problem using mixed integer linear programming for



demand side management. In this study, the cement industry was divided into operating units, simulated under two scenarios, and solved using mixed-integer linear programming (MILP) in an Excel solver. The result shows that there is a reduction in cost by 30% from \$1203 to \$880 for the same production requirement.

In Chapter “[Deployment of Renewable Embedded Generation and Unified Power Quality Conditioner in Distribution System Using Firefly Algorithm](#)” [187], Mustapha et al. proposed an intelligent approach for the deployment of renewable embedded generation and unified power quality conditioner in a distribution system using the firefly algorithm (FA). This chapter proposed the optimal allocation of DG and unified power quality conditioner (UPQC) simultaneously to improve the performance of an active distribution system. The effectiveness of the proposed optimal allocation of DG/UPQC using the FA method was evaluated by comparing it to the allocation of the DG system only and the base case system scenarios, respectively.

In Chapter “[Application of Wind Power in Backwashing Filter Media](#)” [188], Juneja et al. represented an application of wind power in backwashing filter media. In this chapter, a comparative study is represented.

In Chapter “[Mixed Reality Accelerates the Designing Process in Automotive Industry](#)” [189], Aladin et al. proposed a model for mixed reality accelerates the designing process in automotive industry. In this chapter, test application is introduced and its implementation is discussed to showcase how MR systems that utilize natural interaction can improve the design process in the automotive industry. The results of the experiment indicate that the combination of gesture and speech significantly impacts the user experience with MR, highlighting the potential of such systems for design in automotive industry.

In Chapter “[Design and Implementation of Solar Charging Electric Vehicle](#)” [190], Imtiyaz et al. represented a design and implementation of solar charging electric vehicle. In this chapter, the authors have proposed a photovoltaic (PV)-integrated electric vehicle (EV) instead of conventional EV with separate PV/grid/hybrid charging station. As starters, the goal is to execute our thought on an essential model and later with the assistance of this model, by building constant solar charging electric vehicle we may broaden our future.

In Chapter “[Modelling and Analysis of a Permanent Magnet DC Motor Fed Electric Vehicle Drive System](#)” [191], Subbaramaiah et al. represented a modeling and analysis of a permanent magnet DC motor fed electric vehicle drive system. In this chapter, a combined permanent magnet DC motor and electricity generator system is proposed to drive the vehicle and produces the electrical energy for the vehicle utilities. Permanent magnet DC motor find its advantage of simple construction and control, maintenance-free and high-power density.

In Chapter “[An Overview of Electric and Hybrid Vehicle Technology](#)” [192], Vishwanath Nagarajan et al. represented an overview of electric and hybrid vehicle technology. The aim of the study is to promote deeper understandings in the electric and hybrid vehicle technology by reviewing the current literature. Various types of EVs along with their basic principle and functioning are discussed based on their unique technology.



In Chapter “[Performance Analysis of Classical Converter Using Different Control Strategies for Switched Reluctance Motor with Dynamic Loading](#)” [193], Asati et al. demonstrated the performance analysis of a classical converter using different control strategies for switched reluctance motor with dynamic loading. This chapter represents the simulation of 7.5 kW, 8/6 pole, 4-phase SRM using asymmetric bridge converter with current hysteresis chopping and pulse width modulation (PWM) technique for dynamic load. Asymmetric bridge converter with current chopping or hysteresis current control offers better performance in terms of current as it is limited to 35 A under the range of peak current and appropriate speed–torque for dynamic loading.

In Chapter “[Design and Development Gear-Electric Bike and Performance Testing for Indian Road Conditions](#)” [194], Gupta et al. design and development gear-electric bikes and performance testing for Indian road conditions. In this chapter, authors presented the design steps and performance of the gear-electric bike. A 900 W motor, a 24 V brushless DC motor, a motor controller, four lead-acid batteries, and four gears are included in the proposed gear-electric bike. This electric bike can travel 150 km on a single charge and costs about 0.40 INR/km to operate.

In Chapter “[Design and Development of a Solar-Based Wireless Electric Vehicle Charging System](#)” [195], Jain et al. developed a design and development of a solar-based wireless electric vehicle charging system. This chapter proposes a design and implementation of a solar-based wireless EV battery charger where the objective is to charge a vehicle without connecting any wire through inductive coupling by simply parking of a car at the charging station. This study illustrates the applicability of WPT field technology for wireless charging of EV batteries in terms of charging time, range, and cost.

In Chapter “[Design, Optimization and Performance Enhancement of Switched Reluctance Motor for Pollution Free Electric Vehicle Application](#)” [196], Ali et al. represented a design, optimization, and performance enhancement of switched reluctance motor for pollution-free electric vehicle application. This chapter proposes 0.5 kW, 2000 rpm, and an 8/6 topology for designing and optimizing an efficient SRM configuration parameter of the stator and rotor. In EV-SRM material simulation, Ansys Maxwell software (RMxpvt tool) is used for analysis and optimization of power, torque density, losses, efficiency, and torque ripple.

In Chapter “[Using Linear Regression Model to Predict the Wholesale of the Electric Car in Indonesia: What Can Be Learned from the Model?](#)” [197], Al-Hakim et al. proposed an approach using linear regression model to predict the wholesale of the electric car in Indonesia: what can be learned from the model? The authors analyze wholesale datasets from Indonesian Automobile Industry Data for electric cars in Indonesia using statistical analysis to predict the electric cars used in the future. The authors apply a linear regression approach that adjusts the regression model according to wholesale electric cars between 2020 and 2022, as well as a statistical correlation test and the Wilcoxon test to support the regression result.

In Chapter “[Comparison of Thermoelectric Generator with Boost Converter and Single-Ended Primary-Inductance Converter](#)” [198], Adzmi et al. represented a comparison of thermoelectric generator with a boost converter and a single-ended

primary-inductance converter. In this research, the authors are studying the difference of using boost converter with single-ended primary-inductance converter (SEPIC) with a thermoelectric generator system. The contribution of the study is to determine the performance of TEG using different topology.

In Chapter “[A Hybrid Maximum Power Point Tracking \(MPPT\) for Thermoelectric Generator \(TEG\) System](#)” [199], Arshad et al. proposed a hybrid maximum power point tracking (MPPT) for thermoelectric generator (TEG) system. In this chapter, a hybrid MPPT for perturb and observe (P&O) and open-circuit method (OCV) is proposed to compare with the conventional direct method for P&O and OCV method, respectively. This research is initiated by modeling TEG system using MPPT algorithm with P&O method and OCV method using MATLAB/Simulink software.

In Chapter “[Thermoelectric Generator \(TEG\) by Using Indirect Maximum Power Point \(MPP\) Algorithm](#)” [200], Justin et al. developed a thermoelectric generator (TEG) by using indirect maximum power point (MPP) algorithm. In this chapter, the authors tried to study and compare indirect MPPT to the direct MPPT. This will help the authors to solve the problem that normal and direct MPPT such as P&O faces. Because of the inefficiency of the direct method, the indirect approach is favorable in solving this task. To overcome the problem of losing energy during sudden changes, the indirect MPPT will fix or constant one of its parameters that lead us to achieve high efficiency, desired power, and stability under sudden changes.

In Chapter “[Comprehensive Review on AC-DC, DC-DC, DC-AC-DC Converters Used for Electric Vehicles and Charging Stations](#)” [201], Shukla et al. represented a comprehensive review on AC-DC, DC-DC, DC-AC-DC converters used for electric vehicles and charging stations. This chapter reviews different converters, such as AC-DC converters, DC-DC converters, and DC-AC-DC converters.

In Chapter “[Control and Performance Analysis for Active Islanding Detection Using  \$q\$ -Axis Control in Renewable Energy Sources Based Microgrid: A Review](#)” [202], Kumar represented a review on control and performance analysis for active islanding detection using  $q$ -axis control in renewable energy sources based microgrid. In this chapter, control and performance of an active islanding detection method has been analyzed using  $q$ -axis controller. The detection approach is based on disturbance injection via  $q$ -axis controller, which measures the mean absolute frequency variation of the voltage at the point of common coupling (PCC).

In Chapter “[Harmonics Analysis of Triplen-Phase Induction Motor Drive](#)” [203], Khan et al. represented a harmonics analysis of triple  $n$ -phase induction motor drive. The present study uses a MATLAB/Simulink model in a stationary reference frame to examine induction motor drives’ transient and steady-state characteristics with three, six, and nine phases. The present investigation undertakes a comparative analysis of the harmonics in the stator and rotor currents of induction motors with three, six, and nine phases, all of which possess identical power ratings.

In Chapter “[Development of WiTricity Based Wireless Power Transmission System](#)” [204], Mishra et al. proposed a model for the development of WiTricity-

based wireless power transmission system. In this chapter, *the model has demonstrated encouraging results in terms of its efficiency and dependability, and significant progress has been made in overcoming these issues.*

In Chapter “[Analysis of Three-Winding Transformer Configurations for Energy Storage Less Dynamic Voltage Restorer](#)” [205], Roomi et al. represented a model for the analysis of three-winding transformer configurations for energy storage less dynamic voltage restorer. In this chapter, a new topology, wherein the DVR taps in energy through a three-winding transformer connected to the grid, is proposed. As different configurations are available for three-winding transformer, detailed analysis is conducted to find the best possible configuration of the three-winding transformer for a DVR-integrated system.

In Chapter “[Data Reliability Analysis for Early Fault Diagnosis of Air Handling Unit \(AHU\)](#)” [206], Malik et al. represented a data reliability analysis for early fault diagnosis of air handling unit (AHU) of ACMV/HVAC (air conditioning and mechanical ventilation/heating, ventilation, and air conditioning) system. In this chapter, data reliability analysis for early fault diagnosis is performed for AHU only, which includes fan degradation and return air duct leakage fault conditions. Data of the said faults are generated through the use of an expert system platform, OpenStudio (OS), and sensitivity analysis is performed to identify the most sensitive parameters with respect to the fault severity level starting from zero to 30% of deviation from healthy condition.

In Chapter “[Use of Solar Energy in Treatment of Pulp and Paper Industry Effluent with Hemp—An Experimental Study](#)” [207], Thakur et al. represented an experimental study for the use of solar energy in treatment of pulp and paper industry effluent with hemp. This chapter is dealing with the experimental study of P&P industry effluent with hemp so that the desired results can achieve and effluent can safely discharge into rivers without impacting aquatic and environmental elements.

In Chapter “[Design of Radar-Based Portable System for Monitoring of Human Vital Signs with Renewable Energy Resources](#)” [208], Pushparaj et al. represented a design model of radar-based portable system for monitoring of human vital signs with renewable energy resources. The system is user-friendly and applicable in various settings, such as hospitals, clinics, and homes. The design process involves several stages, including submodules, system requirements identification, design, prototype development, data collection and analysis, optimization, and validation.

In Chapter “[Controlling Methods of Brushless DC Motor in Electrical Vehicle Drives](#)” [209], Sharma et al. developed a controlling methods of brushless DC motor in electrical vehicle drives. In this chapter with the help of MATLAB simulations, authors have compared different approaches using pulse width modulation techniques to control Brushless DC motor parameters.

In Chapter “[Effect of Number of Poles on IPMSM Performance for Electric Vehicle Drivetrain](#)” [210], Kuttey et al. represented the effect of the number of poles on IPMSM performance for electric vehicle drivetrain. This chapter deals with analysis of the three different pole numbers and slot numbers of IPMSM. Three types of design structure, 6 pole, 8 pole, and 10 pole, are compared using FEM. The

results of these models are compared, and the trade-offs in selecting pole numbers are discussed.

In Chapter “[Offline Power Quality Management and Control Using Neural Networks](#)” [211], Ray et al. developed an intelligent model for offline power quality management and control using neural networks. In this chapter, the power quality (PQ) of a single-phase system is evaluated using a neural network (NN). The NN-based back-propagation (BP) technique is used to do offline assessment. The disturbances are produced using Simulink in MATLAB. The dyadic analysis filter bank receives these disturbances to acquire signal’s features.

In Chapter “[Optimized Integral Sliding Mode Load Frequency Control of an Isolated Power System](#)” [212], Kassarwani et al. developed an Optimized Integral Sliding Mode Load Frequency Control of an Isolated Power System. The system integrates multiple sources including conventional generators, renewable energy sources (RESs), and energy reserves to supply power demand.

In Chapter “[Implementation of Supercapacitor-Battery Based Energy Storage System in Hybrid Power System Incorporating Renewable Energy Resources](#)” [213], Jahid et al. proposed a model for the implementation of supercapacitor-battery based energy storage system in hybrid power system incorporating renewable energy resources. In this chapter, it is proposed that to counter mismatch between the power supplied by the renewable energy resources (RERs) and load connected to the system, a backup source/sink is needed.

In Chapter “[Hybrid Waste to Energy Electricity Generation and Battery Storage System: The Economics and Environmental Emission in a Low-Income Community](#)” [214], Elwan et al. developed a hybrid waste-to-energy electricity generation and battery storage system for the economics and environmental emission in a low-income community point of view. Using HOMERPro optimization software, this study assesses the economic, environmental, and technical impact of a waste-to-energy (WtE) hybrid plant with a storage device. The system’s net present cost (NPC) is estimated to be \$112,633 with a levelized cost of energy (LCOE) of 0.283 \$/kWh. The total energy generated is estimated to be 62,084 kWh/yr, with an excess of 1049 kWh/yr expected after consumption of 60,386 kWh/yr.

In Chapter “[Application of Solar Power in the Loopholes and Coverages of Buses in the Bus Rapid Transit System in Bhopal](#)” [215], Kumar et al. analyzed an application of solar power in the loopholes and coverages of buses in the Bus Rapid Transit System in Bhopal. This study is majorly dedicated to knowing the plans, routes, and transportation system of BRTS Bhopal to identify the coverage of areas, no. of stops and routes, congestion status, collision, and parallel routes.

In Chapter “[Forecasting of Carbon Emissions in India Using \(ARIMA\) Time Series Predicting Approach](#)” [216], Sharma et al. presented a study for forecasting of carbon emissions in India using (ARIMA) time-series predicting approach. The presented research focuses on predicting carbon emissions in India using autoregressive integrated moving average (ARIMA) models. The study uses time-series data from 1980 to 2021 to develop and validate the ARIMA models. The results of the analysis show that the ARIMA models are able to effectively capture the trend and seasonality of carbon emissions in India.

In Chapter “[Peak Shaving Through Battery Storage for Photovoltaic Integrated Building Considering the Time of Day Pricing](#)” [217], Sharma et al. presented a detailed study on peak shaving through battery storage for photovoltaic-integrated buildings considering the time of day pricing. This chapter has considered the feasibility of a battery storage system from peak demand reduction point of view under variable electricity energy pricing dynamics. The energy management approach described in this study seeks to reduce annual energy costs while maximizing battery energy throughput with grid restrictions acting as network demand limits for the performance evaluation of the investigated energy system in two scenarios. The analysis demonstrates that with an increase in storage size leads to a reduction in the energy cost till a certain point, and any further increase beyond the critical point will increase the energy cost due to an increase in investment cost.

In Chapter “[Economic Analysis of Renewable Energy Systems for Rural Electrification](#)” [218], Yadav et al. developed a model for economic analysis of renewable energy systems for rural electrification. With the use of HOMER software, this project aims to create an energy production model connected to an HRES combination at a location in Maharashtra, India. The outcomes of the study have been seen in NPC, O&M, COEs, and RF of energy systems. This study was conducted in Solapur, Maharashtra.

In Chapter “[Improved Voltage Regulation in Hybrid Photovoltaic/Wind Using Modified Dynamic Voltage Restorer with Hybrid Control Scheme](#)” [219], Rani et al. proposed a model for improved voltage regulation in hybrid photovoltaic/wind using a modified dynamic voltage restorer with a hybrid control scheme. This study analyzed the improvement in the voltage regulation of hybrid PV/wind systems using without energy storage (WES)-based dynamic voltage restorer (DVR) by inserting voltage at a common point of the network to maintain the supply value at the load side.

In Chapter “[Contingency Analysis for a Solar Energy Generation System Using Real Time Data Analysis](#)” [220], Mehtre et al. developed an intelligent model for contingency analysis for a solar energy generation system using real-time data analysis. This chapter also presents an overview of contingency analysis and the challenges faced in the field of renewable energy generation system. This chapter focuses on analysis of solar energy generation system using real-time data which has been visualized on Google Colab platform using the exploratory data analysis technique of machine learning.

In Chapter “[Digital Twin in Extended Reality Applications for Industry 4.0](#)” [221], Ismail et al. studied digital twin in extended reality applications for Industry 4.0. This chapter presents the overview of XR technologies in industry 4.0, and DT has become the mirrored copy of physical objects in the digital environment. This chapter also discovers the fundamentals of the XR applications implementation stages in the industry.

In Chapter “[Deep Image Coding in the Fractional Wavelet Transform Domain Based on High Frequency Sub-Bands Prediction](#)” [222], Ahmad et al. developed a deep image coding in the fractional wavelet transform domain based on high-frequency sub-band prediction. This chapter presents an image compression method

using deep convolutional neural networks and the fractional wavelet transform (FrWT) algorithm. Experimental results show that the proposed approach outperforms JPEG, JPEG2000, BPG, and some other neural network-based image coding techniques in terms of multi-scale structural similarity index measure (MS-SSIM).

In Chapter “[QIVIFS: Quaternion Approach of Interval-Valued-Intuitionistic-Fuzzy-Sets with Applications in Renewable Energy System](#)” [223], Joshi et al. developed a (QIVIFS) quaternion approach of interval-valued intuitionistic fuzzy sets with applications in renewable energy system. This chapter’s effort is to incorporate the concept of “quaternion numbers (QNs)” to “interval-valued” IFS (IVIFS) and hence present the concept of quaternion IVIFS (QIVIFS). These types of QIVIFS can capture mixed features and express multiple-dimensional IVIF information through the interval functions of real-belongingness, imaginary-belongingness, real non-belongingness, and imaginary non-belongingness.

In Chapter “[Feminine Protection Wearable System Based on IoT](#)” [224], Verma et al. proposed a feminine protection wearable system based on IoT. In this chapter, a GPS-based women’s security smart gloves are proposed.

In Chapter “[Marine Predictor’s Algorithm Optimization Technique to Estimate GMPP of PV Array Under Partial Shadowing Conditions](#)” [225], Pachauri et al. developed a marine predictor’s algorithm optimization technique to estimate GMPP of PV array under partial shadowing conditions. This study examines PV array reconfiguration, an effective shadow reduction strategy. This metaheuristics-based reconfiguration method is compared to series-parallel and total-cross-tied PV array setups.

In Chapter “[Artificial Intelligence-Based Bearing Fault Diagnosis of Rotating Machine to Improve the Safety of Power System](#)” [226], Iqbal et al. proposed an artificial intelligence-based bearing fault diagnosis of rotating machine to improve the safety of power system. This study proposes sophisticated vibration-based bearing fault defects in CNC machine tools. Early fault detection can also help identify energy-wasting issues such as electrical damage and overheating.

In Chapter “[Stability Enhancement of AC Microgrid Using Discrete Mode Controllers with Optimum Sampling Frequency](#)” [227], Arora et al. developed an approach for stability enhancement of ac microgrid using discrete mode controllers with optimum sampling frequency. This chapter examines the influence of discrete mode controllers with optimum sampling frequency to enhance the stability of the grid-integrated AC microgrid.

In Chapter “[Performance Analysis of Grid Integrated Solar System Through Interlinking Converter with Control Schemes](#)” [228], Rani et al. represented the performance analysis of grid-integrated solar system through interlinking converter with control schemes. This chapter analyzed the performance of PV panel integrated with the grid through interlinking converters at different attributes is the novelty in this article. The primary objective of the research included in this thesis is to contribute to the increased implementation of photovoltaic (PV) systems into electric networks.

In Chapter “[Towards Achieving Net Zero Emissions in India by 2070](#)” [229], Midha et al. presented a detailed overview on toward achieving net-zero emissions in India by 2070. India has set the target to reduce the emission intensity by 45%

by 2030 and to achieve the net zero emission by 2070. To meet the target of net zero, there is requirement of large investments and strong policies framework in the nation.

In Chapter “[IoT-Based Monitoring and Controlling of Substation Parameters](#)” [230], Sai Kiran et al. represented an IoT-based monitoring and controlling of substation parameters. In this chapter, in order to automate a modest 11 kV substation, the authors employ low-cost automation methods based on cutting-edge IoT innovations and embedded processors like the Raspberry Pi.

In Chapter “[Effectiveness of Resilience Index in Assessing Power System Performance](#)” [231], Dini et al. proposed a model to analyze the effectiveness of resilience index in assessing power system performance. This chapter attempts to evaluate several resilience metrics, namely RICD, Ri, Rt, and Rtime during a disaster in four different scenarios. The goal of this analysis was to seek the most appropriate index which able to capture the whole parameter of electrical system resilience. Typhoon Vicente is used as sample disaster on IEEE 6 bus power system which overlaid on South China area. The simulation shows that the resilience indices that is tested showing significant different value for all resilience index in each scenario.

In conclusion, the editors would like to take this opportunity to thank all of the individuals whose ongoing assistance and coordination have made the publication of this book successful. As editors, we would like to thank the authors in particular for their contributions. The reviewers’ insightful comments and timely replies are much appreciated. We really appreciate the help and advice provided by the Springer Nature staff during the whole process of producing this book.

**Acknowledgements** We would like to express our sincere gratitude to Haryana Renewable Energy Development Agency (HAREDA) to provide financial support to make ICRP-2023 successful. The editors extend their appreciation to the Intelligent Prognostic Private Limited, India, to provide all types of technical and non-technical facilities, cooperation, and support in each stage to make this book in real.

## References

1. International Energy Agency (IEA) report on renewable energy market update—June 2023, outlook for 2023 and 2024. Online. Available at: [https://iea.blob.core.windows.net/assets/63c14514-6833-4cd8-ac53-f9918c2e4cd9/RenewableEnergyMarketUpdate\\_June2023.pdf](https://iea.blob.core.windows.net/assets/63c14514-6833-4cd8-ac53-f9918c2e4cd9/RenewableEnergyMarketUpdate_June2023.pdf). Accessed 1 June 2023
2. ARENA’s regional market analysis. Online. Available at: <https://www.irena.org/Energy-Transition/Policy/Regional-Market-Analysis>. Accessed 1 June 2023
3. Our world in data, renewable energy. Online. Available at: <https://ourworldindata.org/renewable-energy>. Accessed 1 June 2023
4. The Paris Agreement. Online. Available at: <https://www.un.org/en/climatechange/paris-agreement>. Accessed 1 June 2023
5. NREL, USA information on biomass energy basics. Online. Available at: <https://www.nrel.gov/research/re-biomass.html>. Accessed 1 June 2023
6. Geothermal energy. Online. Available at: [https://en.wikipedia.org/wiki/Geothermal\\_energy](https://en.wikipedia.org/wiki/Geothermal_energy). Accessed 1 June 2023



7. Tidal energy. Online. Available at: <https://education.nationalgeographic.org/resource/tidal-energy/>. Accessed 1 June 2023
8. Malik H, Mishra S (2016) Application of gene expression programming (GEP) in power transformers fault diagnosis using DGA. *IEEE Trans Ind Appl* 52(6):4556–4565. <https://doi.org/10.1109/TIA.2016.2598677>
9. Ahmad MW et al (2020) A fault diagnostic and post-fault reconfiguration scheme for interleaved boost converter in PV-based system. *IEEE Trans Power Electron* 36(4):3769–3780. <https://doi.org/10.1109/TPEL.2020.3018540>
10. Malik H, Mishra S (2017) Artificial neural network and empirical mode decomposition based imbalance fault diagnosis of wind turbine using TurbSim, FAST and Simulink. *IET Renew Power Gener* 11(6):889–902. <https://doi.org/10.1049/iet-rpg.2015.0382>
11. Malik H, Mishra S (2018) Application of GEP to investigate the imbalance faults in direct-drive wind turbine using generator current signals. *IET Renew Power Gener* 12(3):279–291. <https://doi.org/10.1049/iet-rpg.2016.0689>
12. Malik H, Sharma R (2017) Transmission line fault classification using modified fuzzy Q learning. *IET Gener Transm Distrib* 11(16):4041–4050. <https://doi.org/10.1049/iet-gtd.2017.0331>
13. Yadav AK et al (2013) Application of neuro-fuzzy scheme to investigate the winding insulation paper deterioration in oil-immersed power transformer. *Electr Power Energy Syst* 53:256–271. <https://doi.org/10.1016/j.ijepes.2013.04.023>
14. Ahmad MW et al (2021) Non-invasive model-based open-circuit switch fault detection of AC-bypass leg switches in transformerless PV inverter. *IEEE J Emerg Sel Top Power Electron*. <https://doi.org/10.1109/JESTPE.2021.3098195>
15. Mishra S et al (2014) Selection of most relevant input parameters using Waikato environment for knowledge analysis for gene expression programming based power transformer fault diagnosis. *Int J Electr Power Compon Syst* 42(16):1849–1862. <https://doi.org/10.1080/15325008.2014.956952>
16. Malik H, Mishra S (2017) Selection of most relevant input parameters using principle component analysis for extreme learning machine based power transformer fault diagnosis model. *Int J Electr Power Compon Syst* 45(12):1339–1352. <https://doi.org/10.1080/15325008.2017.1338794>
17. Sharma R, Malik H (2017) EMD and ANN based intelligent fault diagnosis model for transmission line. *J Intell Fuzzy Syst* 32(4):3043–3050. <https://doi.org/10.3233/JIFS-169247>
18. Ahmaduddin SS, Malik H (2018) Gene expression programming (GEP) based intelligent model for high performance concrete comprehensive strength analysis. *J Intell Fuzzy Syst* 35(5):5403–5418. <https://doi.org/10.3233/JIFS-169822>
19. Shah AK et al (2018) EMD and ANN based intelligent model for bearing fault diagnosis. *J Intell Fuzzy Syst* 35(5):5391–5402. <https://doi.org/10.3233/JIFS-169821>
20. Malik H, Mishra S (2017) FAST and Simulink based simulation investigation of wind turbine faults. *Int J Renew Energy Technol* 8(3/4):286–304. <https://doi.org/10.1504/IJRET.2017.088970>
21. Malik H (2018) Wavelet and Hilbert Huang transform based wind turbine imbalance fault classification model using K-nearest neighbor algorithm. *Int J Renew Energy Technol* 9(1/2). <https://doi.org/10.1504/IJRET.2018.090105>
22. Alotaibi MA et al (2022) Power quality disturbance analysis using data-driven EMD-SVM hybrid approach. *J Intell Fuzzy Syst* 42(2):669–678. <https://doi.org/10.3233/JIFS-189739>
23. Kukker A et al (2020) Reinforcement learning based genetic fuzzy classifier for transformer faults. *IETE J Res* 1–12. <https://doi.org/10.1080/03772063.2020.1732844>
24. Alotaibi MA et al (2022) Cyberattacks identification in IEC 61850 based substation using proximal support vector machine. *J Intell Fuzzy Syst* 42(2):1213–1222. <https://doi.org/10.3233/JIFS-189783>
25. Ahmad MW et al (2022) Development of wide area monitoring system for smart grid application. *J Intell Fuzzy Syst* 42(2):827–839. <https://doi.org/10.3233/JIFS-189752>



26. Azeem A et al (2022) Real-time harmonics analysis of digital substation equipment based on IEC-61850 using hybrid intelligent approach. *J Intell Fuzzy Syst* 42(2):741–754. <https://doi.org/10.3233/JIFS-189745>
27. Sarita K et al (2022) Principal component analysis technique for early fault detection. *J Intell Fuzzy Syst* 42(2):861–872. <https://doi.org/10.3233/JIFS-189755>
28. Bisht VS et al (2022) A data-driven intelligent hybrid method for health prognosis of lithium-ion batteries. *J Intell Fuzzy Syst* 42(2):897–907. <https://doi.org/10.3233/JIFS-189758>
29. Nageswara Rao P et al (2020) Global sliding mode suspension control and condition monitoring of bearingless switched reluctance motor under eccentric faults. *Energies* 13(20):5485, 1–38. <https://doi.org/10.3390/en13205485>
30. Azeem A et al (2021) Design of hardware setup based on IEC 61850 communication protocol for detection & blocking of harmonics in power transformer. *Energies* 14(24):8284, 1–27. <https://doi.org/10.3390/en14248284>
31. Bhattacharjee T et al (2022) Hardware development and interoperability testing of a multivendor-IEC-61850-based digital substation. *Energies* 15(5):1785, 1–19. <https://doi.org/10.3390/en15051785>
32. Sharma R et al (2020) Fuzzy reinforcement learning based intelligent classifier for power transformer faults. *ISA Trans.* <https://doi.org/10.1016/j.isatra.2020.01.016>
33. Malik H, Almutairi A (2021) Modified fuzzy-Q-learning (MFQL)-based mechanical fault diagnosis for direct-drive wind turbines using electrical signals. *IEEE Access* 9:52569–52579. <https://doi.org/10.1109/ACCESS.2021.3070483>
34. Chandra R et al (2020) A survey of failure mechanisms and statistics for critical electrical equipment in buildings. In: *IECON 2020 the 46th annual conference of the IEEE industrial electronics society*, pp 1955–1961. <https://doi.org/10.1109/IECON43393.2020.9254225.63>
35. Pandya Y et al (2018) Feature extraction using EMD and classifier through artificial neural networks for gearbox fault diagnosis. In: *Applications of artificial intelligence techniques in engineering. Advances in intelligent systems and computing*, vol 697, pp 309–317. [https://doi.org/10.1007/978-981-13-1822-1\\_28](https://doi.org/10.1007/978-981-13-1822-1_28)
36. Kaushal P et al (2018) A hybrid intelligent model for power quality disturbance classification. In: *Applications of artificial intelligence techniques in engineering. Advances in intelligent systems and computing*, vol 697, pp 55–63. [https://doi.org/10.1007/978-981-13-1822-1\\_6](https://doi.org/10.1007/978-981-13-1822-1_6)
37. Reza MW et al (2018) Wide area monitoring system using integer linear programming. In: *Applications of artificial intelligence techniques in engineering. Advances in intelligent systems and computing*, vol 698, pp 23–30. [https://doi.org/10.1007/978-981-13-1819-1\\_3](https://doi.org/10.1007/978-981-13-1819-1_3)
38. Sharma T et al (2018) A novel intelligent bifurcation classification model based on artificial neural network (ANN). In: *Applications of artificial intelligence techniques in engineering. Advances in intelligent systems and computing*, vol 698, pp 53–61. [https://doi.org/10.1007/978-981-13-1819-1\\_6](https://doi.org/10.1007/978-981-13-1819-1_6)
39. Check D et al (2018) A novel intelligent transmission line fault diagnosis model based on EEMD and multiclass PSVM. In: *Applications of artificial intelligence techniques in engineering. Advances in intelligent systems and computing*, vol 698, pp 85–92. [https://doi.org/10.1007/978-981-13-1819-1\\_9](https://doi.org/10.1007/978-981-13-1819-1_9)
40. Singh KV et al (2017) Condition monitoring of wind turbine gearbox using electrical signatures. In: *IEEE ICMDCS 2017*, pp 1–6. <https://doi.org/10.1109/ICMDCS.2017.8211718>
41. Mishra S, Malik H (2016) Application of fuzzy Q learning (FQL) technique to wind turbine imbalance fault identification using generator current signals. In: *Proceedings of IEEE PIICON-2016*, 25–27 Nov 2016, pp 1–6. <https://doi.org/10.1109/POWERI.2016.8077283>
42. Mishra S, Malik H (2016) Application of gene expression programming (GEP) to investigate the health condition of direct-drive wind turbine using FAST and TurbSim. In: *Proceedings of IEEE IICPE-2016*, 17–19 Nov 2016, pp 1–6. <https://doi.org/10.1109/IICPE.2016.8079508>
43. Malik H, Aggarwal A, Sharma R (2016) Feature extraction using EMD and classification through probabilistic neural network for fault diagnosis of transmission line. In: *Proceedings of IEEE ICPEICES-2016*, pp 1–6. <https://doi.org/10.1109/ICPEICES.2016.7853709>

44. Sharma R et al (2016) Selection of most relevant input parameters using Weka for artificial neural network based transmission line fault diagnosis model. In: Proceedings of the international conference on nanotechnology for better living, vol 3, no 1, p 176. <https://doi.org/10.3850/978-981-09-7519-7nbl16-rps-176>
45. Mishra S, Malik H (2016) Application of extreme learning machine (ELM) in paper insulation deterioration estimation of power transformer. In: Proceedings of the international conference on nanotechnology for better living, vol 3, no 1, p 209. <https://doi.org/10.3850/978-981-09-7519-7nbl16-rps-209>
46. Kumar G et al (2016) Learning vector quantization neural network based external fault diagnosis model for three phase induction motor using current signature analysis. *Procedia Comput Sci* 93:1010–1016. <https://doi.org/10.1016/j.procs.2016.07.304>
47. Mishra S, Malik H (2015) Proximal support vector machine (PSVM) based imbalance fault diagnosis of wind turbine using generator current signals. *Energy Procedia* 90:593–603, IIT Bombay, 15–17 Dec 2015. <https://doi.org/10.1016/j.egypro.2016.11.228>
48. Sharma S et al (2015) External fault classification experienced by three-phase induction motor based on multi-class ELM. *Procedia Comput Sci* 70:814–820. <https://doi.org/10.1016/j.procs.2015.10.122>
49. Mishra S, Malik H (2015) Application of LVQ network in fault diagnosis of wind turbine using TurbSim, FAST and Simulink. In: Michael Faraday IET international summit 2015, pp 474–480. <https://doi.org/10.1049/cp.2015.1679>
50. Khatri A et al (2015) Probabilistic neural network based incipient fault identification using DGA dataset. *Procedia Comput Sci* 58:665–672. <https://doi.org/10.1016/j.procs.2015.08.086>
51. Mishra S, Malik H (2015) Application of probabilistic neural network in fault diagnosis of wind turbine using FAST, TurbSim and Simulink. *Procedia Comput Sci* 58:186–193. <https://doi.org/10.1016/j.procs.2015.08.052>
52. Mittal AP et al (2014) External fault identification experienced by 3-phase induction motor using PSVM. In: Proceedings of IEEE international conference on power India (PIICON 2014), New Delhi, India, 5–7 Dec 2014. <https://doi.org/10.1109/POWERI.2014.7117762>
53. Mishra S, Malik H (2014) Feature selection using RapidMiner and classification through probabilistic neural network for fault diagnostics of power transformer. In: Proceedings of IEEE international conference on emerging trends and innovation in technology (INDICON 2014), Pune, India, 11–13 Dec 2014. <https://doi.org/10.1109/INDICON.2014.7030427>
54. Mishra S, Malik H (2014) Fault identification of power transformers using proximal support vector machine (PSVM). In: Proceedings of IEEE international conference on power electronics (IICPE 2014), NIT Kurukshetra, India, 8–10 Dec 2014. <https://doi.org/10.1109/IICPE.2014.7115842>
55. Mishra S, Malik H (2014) Application of gene expression programming (GEP) in power transformers fault diagnosis using DGA. In: Proceedings of IEEE international conference on power India (PIICON 2014), New Delhi, India, 5–7 Dec 2014. <https://doi.org/10.1109/POWERI.2014.7117782>
56. Mishra S, Malik H (2015) Extreme learning machine based fault diagnosis of power transformer using IEC TC10 and its related data. In: Proceedings of IEEE India annual conference (INDICON-2015), pp 1–5. <https://doi.org/10.1109/INDICON.2015.7443245>
57. Singh S et al (2012) UV/VIS response based fuzzy logic for health assessment of transformer oil. *Procedia Engineering* 30:905–912. <https://doi.org/10.1016/j.proeng.2012.01.944>. ISSN: 1877-7058
58. Mahto T et al (2012) Make use of DGA to carry out the transformer oil-immersed paper deterioration condition estimation with fuzzy-logic. *Procedia Eng* 30:569–576. <https://doi.org/10.1016/j.proeng.2012.01.900>. ISSN: 1877-7058
59. Jarial RK et al (2012) Application research based on modern technology for transformer health index estimation. In: Proceedings of IEEE international multi conference on systems, signals and devices (SSD), Chemnitz, Germany, 20–23 Mar 2012, pp 1–7. <https://doi.org/10.1109/SSD.2012.6198012>

60. Mahto T et al (2019) Condition monitoring and fault detection & diagnostics of wind energy conversion system (WECS). In: *Soft computing in condition monitoring and diagnostics of electrical and mechanical systems*. Springer Nature, pp 121–154. [https://doi.org/10.1007/978-981-15-1532-3\\_5](https://doi.org/10.1007/978-981-15-1532-3_5)
61. Bakhsh FI et al (2019) Fault analysis of variable frequency transformer (VFT) for power transfer in-between synchronous grids. In: *Soft computing in condition monitoring and diagnostics of electrical and mechanical systems*. Springer Nature, pp 269–286. [https://doi.org/10.1007/978-981-15-1532-3\\_12](https://doi.org/10.1007/978-981-15-1532-3_12)
62. Mahto T et al (2011) An expert system for incipient fault diagnosis and condition assessment in transformers. In: *Proceedings of IEEE international conference on computational intelligence and communication networks*, pp 138–142. <https://doi.org/10.1109/CICN.2011.27>
63. Yadav AK et al (2011) Make use of UV/VIS spectrophotometer to determination of dissolved decay products in mineral insulating oils for transformer remnant life estimation with ANN. In: *Proceedings of IEEE international conference on engineering sustainable solutions, INDICON-2011*, pp 1–6. <https://doi.org/10.1109/INDCON.2011.6139574>
64. Jarial RK et al (2011) Application research based on modern technology to investigating causes and detection of failures in transformers on the bases of importance level. In: *Proceedings of IEEE international conference on engineering sustainable solutions, INDICON-2011*, pp 1–6. <https://doi.org/10.1109/INDCON.2011.6139577>
65. Kushwaha N et al (2011) Paper insulation deterioration estimation of power transformer using fuzzy-logic: part-2. In: *Proceedings of IEEE international conference on engineering sustainable solutions, INDICON-2011*, pp 1–5. <https://doi.org/10.1109/INDCON.2011.6139532>
66. Jarial RK et al (2011) Application of modern technology for fault diagnosis in power transformer energy management. In: *Proceedings of IEEE international conference on communication system's network technologies*, pp 376–381. <https://doi.org/10.1109/CSNT.2011.84>
67. Jarial RK et al (2011) Fuzzy-logic applications in cost analysis of transformer's main material weight. In: *Proceedings of IEEE international conference on computational intelligence and communication networks*, pp 386–389. <https://doi.org/10.1109/CICN.2011.81>
68. Yadav AK et al (2015) Application of rapid miner in ANN based prediction of solar radiation for assessment of solar energy resource potential of 76 sites in northwestern India. *Renew Sustain Energy Rev* 52:1093–1106. <https://doi.org/10.1016/j.rser.2015.07.156>
69. Yadav AK et al (2014) Selection of most relevant input parameters using WEKA for artificial neural network based solar radiation prediction models. *Renew Sustain Energy Rev* 31:509–519. <https://doi.org/10.1016/j.rser.2013.12.008>
70. Yadav AK et al (2018) Daily array yield prediction of grid-interactive photovoltaic plant using relief attribute evaluator based radial basis function neural network. *Renew Sustain Energy Rev* 81(Part 2):2115–2127. <https://doi.org/10.1016/j.rser.2017.06.023>
71. Azeem A et al (2018) K-NN and ANN based deterministic and probabilistic wind speed forecasting intelligent approach. *J Intell Fuzzy Syst* 35(5):5021–5031. <https://doi.org/10.3233/JIFS-169786>
72. Arora P et al (2018) Wind energy forecasting model for northern-western region of India using decision tree and MLP neural network approach. *Interdiscip Environ Rev* 19(1):13–30. <https://doi.org/10.1504/IER.2018.089766>
73. Fatema N et al (2022) Hybrid approach combining EMD, ARIMA and Monte Carlo for multi-step ahead medical tourism forecasting. *J Intell Fuzzy Syst* 42(2):1235–1251. <https://doi.org/10.3233/JIFS-189785>
74. Khursheed T et al (2022) Multi-step ahead time-series wind speed forecasting for smart-grid application. *J Intell Fuzzy Syst* 42(2):633–646. <https://doi.org/10.3233/JIFS-189736>
75. Fatema N et al (2022) Deterministic and probabilistic occupancy detection with a novel heuristic optimization and back-propagation (BP) based algorithm. *J Intell Fuzzy Syst* 42(2):779–791. <https://doi.org/10.3233/JIFS-189748>

76. Alotaibi MA et al (2022) A new hybrid model combining EMD and neural network for multi-step ahead load forecasting. *J Intell Fuzzy Syst* 42(2):1099–1114. <https://doi.org/10.3233/JIFS-189775>
77. Yadav AK et al (2020) A novel hybrid approach based on relief algorithm and fuzzy reinforcement learning approach for predicting wind speed. *Sustain Energy Technol Assess* 43. <https://doi.org/10.1016/j.seta.2020.100920>
78. Yadav AK et al (2021) Case study of grid-connected photovoltaic power system installed at monthly optimum tilt angles for different climatic zones in India. *IEEE Access* 9:60077–60088. <https://doi.org/10.1109/ACCESS.2021.3073136>
79. Yadav AK et al (2021) Novel approach to investigate the influence of optimum tilt angle on minimum cost of energy based maximum power generation and sizing of PV systems: a case study of diverse climatic zones in India. *IEEE Access* 9:110103–110115. <https://doi.org/10.1109/ACCESS.2021.3102153>
80. Yadav AK et al (2014) Comparison of different artificial neural network techniques in prediction of solar radiation for power generation using different combinations of meteorological variables. In: *Proceedings of IEEE international conference on power electronics, drives and energy systems (PEDES-2014)*, pp 1–5. <https://doi.org/10.1109/PEDES.2014.7042063>
81. Kumar G et al (2016) Generalized regression neural network based wind speed prediction model for western region of India. *Procedia Comput Sci* 93:26–32. <https://doi.org/10.1016/j.procs.2016.07.177>
82. Garg P et al (2016) Infogain attribute evaluator and ANN based wind speed prediction model for Rajasthan, north-west region of India. In: *Proceedings of the international conference on nanotechnology for better living*, vol 3, no 1, p 233. <https://doi.org/10.3850/978-981-09-7519-7nb116-rps-233>
83. Savita et al (2016) Wind speed and power prediction of prominent wind power potential states in India using GRNN. In: *Proceedings of IEEE ICPEICES-2016*, pp 1–6. <https://doi.org/10.1109/ICPEICES.2016.7853220>
84. Savita et al (2016) Application of artificial neural network for long term wind speed prediction. In: *Proceedings of IEEE CASP-2016*, 9–11 June 2016, pp 217–222. <https://doi.org/10.1109/CASP.2016.7746168>
85. Yadav AK et al (2018) Short term wind speed forecasting for power generation in Hamirpur, Himachal Pradesh, India, using artificial neural networks. In: *Applications of artificial intelligence techniques in engineering. Advances in intelligent systems and computing*, vol 697, pp 263–271. [https://doi.org/10.1007/978-981-13-1822-1\\_24](https://doi.org/10.1007/978-981-13-1822-1_24)
86. Vinoop P et al (2018) PSO-NN-based hybrid model for long-term wind speed prediction: a study on 67 cities of India. In: *Applications of artificial intelligence techniques in engineering. Advances in intelligent systems and computing*, vol 697, pp 319–327. [https://doi.org/10.1007/978-981-13-1822-1\\_29](https://doi.org/10.1007/978-981-13-1822-1_29)
87. Singh M et al (2018) Comparative study of different neural networks for 1-year ahead load forecasting. In: *Applications of artificial intelligence techniques in engineering. Advances in intelligent systems and computing*, vol 697, pp 31–42. [https://doi.org/10.1007/978-981-13-1822-1\\_4](https://doi.org/10.1007/978-981-13-1822-1_4)
88. Yadav V et al (2018) Forecasting of nitrogen dioxide at one day ahead using non-linear autoregressive neural network for environmental applications. In: *Applications of artificial intelligence techniques in engineering. Advances in intelligent systems and computing*, vol 698, pp 615–623. [https://doi.org/10.1007/978-981-13-1819-1\\_58](https://doi.org/10.1007/978-981-13-1819-1_58)
89. Yadav AK et al (2018) 10-min ahead forecasting of wind speed for power generation using nonlinear autoregressive neural network. In: *Applications of artificial intelligence techniques in engineering. Advances in intelligent systems and computing*, vol 698, pp 235–244. [https://doi.org/10.1007/978-981-13-1819-1\\_23](https://doi.org/10.1007/978-981-13-1819-1_23)
90. Garg S et al (2018) Long-term solar irradiance forecast using artificial neural network: application for performance prediction of Indian cities. In: *Applications of artificial intelligence techniques in engineering. Advances in intelligent systems and computing*, vol 697, pp 285–293. [https://doi.org/10.1007/978-981-13-1822-1\\_26](https://doi.org/10.1007/978-981-13-1822-1_26)

91. Azeem A et al (2016) Application of Waikato environment for knowledge analysis based artificial neural network models for wind speed forecasting. In: Proceedings of IEEE PIICON-2016, 25–27 Nov 2016, pp 1–6. <https://doi.org/10.1109/POWERI.2016.8077352>
92. Saad S et al (2016) Selection of most relevant input parameters using WEKA for artificial neural network based concrete compressive strength prediction model. In: Proceedings of IEEE PIICON-2016, 25–27 Nov 2016, pp 1–6. <https://doi.org/10.1109/POWERI.2016.8077368>
93. Azeem A et al (2016) Artificial neural network based intelligent model for wind power assessment in India. In: Proceedings of IEEE PIICON-2016, 25–27 Nov 2016, pp 1–6. <https://doi.org/10.1109/POWERI.2016.8077305>
94. Yadav AK et al (2015) ANN based prediction of daily global solar radiation for photovoltaics applications. In: Proceedings of IEEE India annual conference (INDICON), pp 1–5. <https://doi.org/10.1109/INDICON.2015.7443186>
95. Chimmula VKR et al (2021) Deep learning and statistical based daily stock price forecasting and monitoring. In: AI and machine learning paradigms for health monitoring system: intelligent data analytics. Studies in big data. Springer Nature, pp 203–216. [https://doi.org/10.1007/978-981-33-4412-9\\_13](https://doi.org/10.1007/978-981-33-4412-9_13)
96. Fatema N et al (2020) Metaheuristic algorithm based hybrid model for identification of building sale prices. In: Metaheuristic and evolutionary computation: algorithms and applications. Studies in computational intelligence. Springer Nature, pp 689–704. [https://doi.org/10.1007/978-981-15-7571-6\\_32](https://doi.org/10.1007/978-981-15-7571-6_32)
97. Fatema N et al (2020) Data-driven occupancy detection hybrid model using particle swarm optimization based artificial neural network. In: Metaheuristic and evolutionary computation: algorithms and applications. Studies in computational intelligence. Springer Nature, pp 283–297. [https://doi.org/10.1007/978-981-15-7571-6\\_13](https://doi.org/10.1007/978-981-15-7571-6_13)
98. Fatema N et al (2019) Data driven intelligent model for sales prices prediction and monitoring of a building. In: Soft computing in condition monitoring and diagnostics of electrical and mechanical systems. Springer Nature, pp 407–421. [https://doi.org/10.1007/978-981-15-1532-3\\_18](https://doi.org/10.1007/978-981-15-1532-3_18)
99. Yadav A et al (2011) Application research based on artificial neural network (ANN) to predict no load loss for transformer design. In: Proceedings of IEEE international conference on communication system's network technologies, pp 180–183. <https://doi.org/10.1109/CSNT.2011.45>
100. Mahto T et al (2012) Impact of usage duration on mobile phones EMI characteristics. In: Proceedings of IEEE international conference on communication system's network technologies, India, May 2012, pp 558–562. <https://doi.org/10.1109/CSNT.2012.126>
101. Vigya et al (2021) Renewable generation based hybrid power system control using fractional order-fuzzy controller. Energy Rep 7C:641–653. <https://doi.org/10.1016/j.egy.2021.01.022>
102. Jadoun VK et al (2021) Optimal scheduling of non-convex cogeneration units using exponentially varying whale optimization algorithm. Energies 14(4):1–30. <https://doi.org/10.3390/en14041008>
103. Mahto T et al (2021) Fractional order fuzzy based virtual inertia controller design for frequency stability in isolated hybrid power systems. Energies 14(6):1634. <https://doi.org/10.3390/en14061634>
104. Mahto T et al (2018) Load frequency control of a solar-diesel based isolated hybrid power system by fractional order control using particle swarm optimization. J Intell Fuzzy Syst 35(5):5055–5061. <https://doi.org/10.3233/JIFS-169789>
105. Nandan NK et al (2018) Solving nonconvex economic thermal power dispatch problem with multiple fuel system and valve point loading effect using fuzzy reinforcement learning. J Intell Fuzzy Syst 35(5):4921–4931. <https://doi.org/10.3233/JIFS-169776>
106. Devarapalli R et al (2022) An approach to solve OPF problems using a novel hybrid whale and sine cosine optimization algorithm. J Intell Fuzzy Syst 42(2):957–967. <https://doi.org/10.3233/JIFS-189763>

107. Rao BV et al (2022) Wind integrated power system to reduce emission: an application of bat algorithm. *J Intell Fuzzy Syst* 42(2):1041–1049. <https://doi.org/10.3233/JIFS-189770>
108. Bajaj M et al (2021) Optimal design of passive power filter using multi-objective pareto-based firefly algorithm and analysis under background and load-side's nonlinearity. *IEEE Access* 9:22724–22744. <https://doi.org/10.1109/ACCESS.2021.3055774>
109. Gupta S et al (2021) A hybrid Jaya–Powell's pattern search algorithm for multi-objective optimal power flow incorporating distributed generation. *Energies* 14(10):2831, 2–24. <https://doi.org/10.3390/en14102831>
110. Singh S et al (2021) Influence of wind power on modeling of bidding strategy in a promising power market with modified gravitational search algorithm. *Appl Sci* 11(10):4438, 2–16. <https://doi.org/10.3390/app11104438>
111. Singh S et al (2021) Strategic bidding in the presence of renewable sources for optimizing the profit of the power suppliers. *IEEE Access* 9:70221–70232. <https://doi.org/10.1109/ACCESS.2021.3078288>
112. Chankaya M et al (2021) Generalized normal distribution algorithm based control of 3-phase 4-wire grid-tied PV-hybrid energy storage system. *Energies* 14(14):4355, 1–22. <https://doi.org/10.3390/en14144355>
113. Singh S et al (2021) Impacts of renewable sources of energy on bid modeling strategy in an emerging electricity market using oppositional gravitational search algorithm. *Energies* 14(18):5726, 1–22. <https://doi.org/10.3390/en14185726>
114. Gupta S et al (2021) A robust optimization approach for optimal power flow solutions using Rao algorithms. *Energies* 14(17):5449, 1–28. <https://doi.org/10.3390/en14175449>
115. Chankaya M et al (2021) Multi-objective grasshopper optimization based MPPT and VSC control of grid-tied PV-battery system. *Electronics* 10(22):2770, 1–24. <https://doi.org/10.3390/electronics10222770>
116. Prakash P et al (2021) A novel hybrid approach for optimal placement of non-dispatchable distributed generations in radial distribution system. *Mathematics* 9(24):3171, 1–27. <https://doi.org/10.3390/math9243171>
117. Nagendra K et al (2021) Novel neural network-based load frequency control scheme: a case study of restructured power system. *IEEE Access* 9:162231–162242. <https://doi.org/10.1109/ACCESS.2021.3133360>
118. Shabbiruddin et al (2021) Fuzzy-based investigation of challenges for the deployment of renewable energy power generation. *Energies* 15(1):58, 1–16
119. Prakash P et al (2022) A novel analytical approach for optimal integration of renewable energy sources in distribution systems. *Energies* 15(4):1341, 1–23. <https://doi.org/10.3390/en15041341>
120. Chankaya M et al (2022) Stability analysis of chaotic grey-wolf optimized grid-tied PV-hybrid storage system during dynamic conditions. *Electronics* 11(4):567, 1–23. <https://doi.org/10.3390/electronics11040567>
121. Mohammad K et al (2022) Fuzzy-logic-based comparative analysis of different maximum power point tracking controllers for hybrid renewal energy systems. *Mathematics* 10(3):529, 1–28. <https://doi.org/10.3390/math10030529>
122. Kumar N et al (2022) Application of fractional order-PID control scheme in automatic generation control of a deregulated power system in the presence of SMES unit. *Mathematics* 10(3):521, 1–16. <https://doi.org/10.3390/math10030521>
123. Minai AF et al (2022) Performance analysis and comparative study of a 467.2 kWp grid-interactive SPV system: a case study. *Energies* 15(3):1107, 1–19. <https://doi.org/10.3390/en15031107>
124. Chimmula VKR et al (2019) Novel application of relief algorithm in cascade ANN model for prognosis of photovoltaic maximum power under sunny outdoor condition of Sikkim India: a case study. In: *Soft computing in condition monitoring and diagnostics of electrical and mechanical systems*. Springer Nature, pp 387–405. [https://doi.org/10.1007/978-981-15-1532-3\\_17](https://doi.org/10.1007/978-981-15-1532-3_17)



125. Yadav AK et al (2020) ANN- and multiple linear regression-based modelling for experimental investigation of photovoltaic module maximum power production under outdoor condition of mountainous region. In: *Modern maximum power point tracking techniques for photovoltaic energy systems*. Springer Nature, pp 229–245. [https://doi.org/10.1007/978-3-030-05578-3\\_8](https://doi.org/10.1007/978-3-030-05578-3_8)
126. Fatema N et al (2019) Big-data analytics based energy analysis and monitoring for multi-story hospital buildings: case study. In: *Soft computing in condition monitoring and diagnostics of electrical and mechanical systems*. Springer Nature, pp 325–343. [https://doi.org/10.1007/978-981-15-1532-3\\_14](https://doi.org/10.1007/978-981-15-1532-3_14)
127. Yadav AK et al (2018) Techno economic feasibility analysis of different combination of PV-wind-diesel-battery hybrid system, chap 11. In: *Hybrid-renewable energy systems in microgrids*. Elsevier, pp 203–218. <https://doi.org/10.1016/B978-0-08-102493-5.00011-X>
128. Minai AF et al (2020) Metaheuristics paradigms for renewable energy systems: advances in optimization algorithms. In: *Metaheuristic and evolutionary computation: algorithms and applications*. Studies in computational intelligence. Springer Nature, pp 35–61. [https://doi.org/10.1007/978-981-15-7571-6\\_2](https://doi.org/10.1007/978-981-15-7571-6_2)
129. Mahto T et al (2020) Traffic signal control to optimize run time for energy saving: a smart city paradigm. In: *Metaheuristic and evolutionary computation: algorithms and applications*. Studies in computational intelligence. Springer Nature, pp 491–497. [https://doi.org/10.1007/978-981-15-7571-6\\_21](https://doi.org/10.1007/978-981-15-7571-6_21)
130. Rahi OP et al (2012) Power system voltage stability assessment through artificial neural network. *Procedia Eng* 30:53–60. <https://doi.org/10.1016/j.proeng.2012.01.833>. ISSN: 1877-7058
131. Mahto T et al (2018) Fractional order control and simulation of wind-biomass isolated hybrid power system using particle swarm optimization. In: *Applications of artificial intelligence techniques in engineering*. Advances in intelligent systems and computing, vol 698, pp 277–287. [https://doi.org/10.1007/978-981-13-1819-1\\_28](https://doi.org/10.1007/978-981-13-1819-1_28)
132. Yadav AK et al (2016) Tilt angle calculation for installation of PV systems for mountainous regions of Himachal Pradesh India. In: *Proceedings of IEEE ICEPES 2016*, 14–16 Dec 2016, pp 205–209. <https://doi.org/10.1109/ICEPES.2016.7915931>
133. Yadav AK et al (2015) Optimization of tilt angle for installation of solar photovoltaic system for six sites in India. In: *Proceedings of IEEE international conference on energy economics and environment (ICEEE-2015)*, pp 1–4. <https://doi.org/10.1109/EnergyEconomics.2015.7235078>
134. Fatima K et al (2022) Intelligent approach-based maximum power point tracking for renewable energy system: a review. In: Malik H, Ahmad MW, Kothari D (eds) *Intelligent data analytics for power and energy systems*. Lecture notes in electrical engineering, vol 802. Springer, Singapore, pp 373–405. [https://doi.org/10.1007/978-981-16-6081-8\\_19](https://doi.org/10.1007/978-981-16-6081-8_19)
135. Kumar N et al (2022) Modeling and analysis of an intelligent approach for load frequency control in a deregulated power system: a case study based on different control schemes. In: Malik H, Ahmad MW, Kothari D (eds) *Intelligent data analytics for power and energy systems*. Lecture notes in electrical engineering, vol 802. Springer, Singapore, pp 61–83. [https://doi.org/10.1007/978-981-16-6081-8\\_4](https://doi.org/10.1007/978-981-16-6081-8_4)
136. Yadav AK et al (2020) Optimization of tilt angle for intercepting maximum solar radiation for power generation. In: *Optimization of power system problems (methods, algorithms and MATLAB codes)*. Springer Nature, pp 203–232. [https://doi.org/10.1007/978-3-030-34050-6\\_9](https://doi.org/10.1007/978-3-030-34050-6_9)
137. Gopal C et al (2022) Digital transformation through advances in artificial intelligence and machine learning. *J Intell Fuzzy Syst* 42(2):615–622. <https://doi.org/10.3233/JIFS-189787>
138. Shahid A et al (2018) Decrypting wrist movement from MEG signal using SVM classifier. *J Intell Fuzzy Syst* 35(5):5123–5130. <https://doi.org/10.3233/JIFS-169796>
139. Fatema N et al (2022) Data driven intelligent model for quality management in healthcare. *J Intell Fuzzy Syst* 42(2):1155–1169. <https://doi.org/10.3233/JIFS-189779>
140. Sanaullah A et al (2022) Analyzing impact of relationship benefit and commitment on developing loyalty using machine intelligence approach. *J Intell Fuzzy Syst* 42(2):699–712. <https://doi.org/10.3233/JIFS-189742>

141. Smriti S et al (2018) Intelligent tools and techniques for signals, machines and automation. *J Intell Fuzzy Syst* 35(5):4895–4899. <https://doi.org/10.3233/JIFS-169773>
142. Zhou L et al (2021) An optimal higher order likelihood distribution based approach for strong edge and high contrast restoration. *IEEE Access* 9:109012–109024. <https://doi.org/10.1109/ACCESS.2021.3101413>
143. Kumar D et al (2021) 6D-chaotic system and 2D fractional discrete cosine transform based encryption of biometric templates. *IEEE Access* 9:103056–103074. <https://doi.org/10.1109/ACCESS.2021.3097881>
144. Asyraf A et al (2021) Machine learning approach for targeting and recommending a product for project management. *Mathematics* 9(16):1958, 1–26. <https://doi.org/10.3390/math9161958>
145. Arvind D et al (2021) Likelihood estimation and wavelet transformation based optimization for minimization of noisy pixels. *IEEE Access* 9:132168–132190. <https://doi.org/10.1109/ACCESS.2021.3113857>
146. Jain H, Fatema N (2018) Layer recurrent neural network based intelligent user activity classification model using smartphone. *J Intell Fuzzy Syst (JIFS)* 35(5):5085–5097. <https://doi.org/10.3233/JIFS-169793>
147. Nuzhat F (2018) Application of neuro-fuzzy scheme to improve purchasing process in a hospital. *J Intell Fuzzy Syst (JIFS)* 35(5):5131–5146. <https://doi.org/10.3233/JIFS-169797>
148. Anil KB et al (2011) Application research based on fuzzy logic to predict minimum loss for transformer design optimization. In: *Proceedings of IEEE international conference on computational intelligence and communication networks*, pp 207–211. <https://doi.org/10.1109/CICN.2011.41>
149. Yadav AK et al (2011) Cost analysis of transformer's main material weight with artificial neural network (ANN). In: *Proceedings of IEEE international conference on communication system's network technologies*, pp 184–187. <https://doi.org/10.1109/CSNT.2011.46>
150. Khatri A et al (2012) Optimal design of power transformer using genetic algorithm. In: *Proceedings of IEEE international conference on communication system's network technologies*, pp 830–833. <https://doi.org/10.1109/CSNT.2012.180>
151. Goyal P et al (2019) Application of evolutionary reinforcement learning (ERL) approach in control domain: a review. In: *Smart innovations in communication and computational sciences*, vol 670, pp 273–288. [https://doi.org/10.1007/978-981-10-8971-8\\_25](https://doi.org/10.1007/978-981-10-8971-8_25)
152. Roy N et al (2018) Extreme learning machine-based image classification model using hand-written digit database. In: *Applications of artificial intelligence techniques in engineering. Advances in intelligent systems and computing*, vol 697, pp 607–618. [https://doi.org/10.1007/978-981-13-1822-1\\_57](https://doi.org/10.1007/978-981-13-1822-1_57)
153. Kukker A et al (2016) Forearm movements classification of EMG signals using Hilbert Huang transform and artificial neural network. In: *Proceedings of IEEE PIICON-2016*, 25–27 Nov 2016, pp 1–6. <https://doi.org/10.1109/POWERI.2016.8077417>
154. Fatema N (2019) Brain health assessment via classification of EEG signals for seizure and non-seizure conditions using extreme learning machine (ELM). In: Malik H, Srivastava S, Sood Y, Ahmad A (eds) *Applications of artificial intelligence techniques in engineering. Advances in intelligent systems and computing*, vol 697. Springer, Singapore. [https://doi.org/10.1007/978-981-13-1822-1\\_10](https://doi.org/10.1007/978-981-13-1822-1_10)
155. Tomar A et al (2020) Machine learning, advances in computing, renewable energy and communication. In: *LNEE*, vol 768. Springer Nature, Berlin, 659 pp. <https://doi.org/10.1007/978-981-16-2354-7>. ISBN: 978-981-16-2354-7
156. Iqbal A et al (2020) Renewable power for sustainable growth. In: *LNEE*, vol 723. Springer Nature, Berlin, 805 pp. <https://doi.org/10.1007/978-981-33-4080-0>. ISBN: 978-981-33-4082-4
157. Ahmad MW et al (2022) Intelligent data-analytics for power and energy systems. In: *LNEE*, vol 802. Springer Nature, Berlin, 641 pp. <https://doi.org/10.1007/978-981-16-6081-8>. ISBN: 978-981-16-6081-8
158. Fatema N et al (2021) Intelligent data-analytics for condition monitoring: smart grid applications. Elsevier, 268 pp. <https://www.sciencedirect.com/book/9780323855105/intelligent-data-analytics-for-condition-monitoring>. ISBN: 978-0-323-85511-2



159. Iqbal A et al (2020) Soft computing in condition monitoring and diagnostics of electrical and mechanical systems. Springer Nature, Berlin, 496 pp. <https://doi.org/10.1007/978-981-15-1532-3>. ISBN: 978-981-15-1532-3
160. Iqbal A et al (2020) Meta heuristic and evolutionary computation: algorithms and applications. Springer Nature, Berlin, 949 pp. <https://doi.org/10.1007/978-981-15-7571-6>. ISBN: 978-981-15-7571-6
161. Jafar A et al (2021) AI and machine learning paradigms for health monitoring system: intelligent data analytics. In: SBD, vol 86. Springer Nature, Berlin, 513 pp. <https://doi.org/10.1007/978-981-33-4412-9>. ISBN: 978-981-33-4412-9
162. Srivastava S et al (2019) Applications of artificial intelligence techniques in engineering, SIGMA 2018, vol 1. In: AISC, vol 698. Springer Nature, 643 pp. <https://doi.org/10.1007/978-981-13-1819-1>. ISBN: 978-981-13-1818-4
163. Srivastava S et al (2019) Applications of artificial intelligence techniques in engineering, SIGMA 2018, vol 2. In: AISC, vol 697. Springer Nature, 647 pp. <https://doi.org/10.1007/978-981-13-1822-1>. ISBN: 978-981-13-1821-4
164. Tomar A et al (2022) Proceedings of 3rd international conference on machine learning, advances in computing, renewable energy and communication. In: LNEE, vol 915. Springer Nature, Berlin, 781 pp. <https://doi.org/10.1007/978-981-19-2828-4>. ISBN: 978-981-19-2828-4
165. Kumari D et al (2023) An efficient algorithm for energy management in smart grid for various improvements. In: Proceedings of 2nd international conference on renewable power (ICRP). LNEE. Springer Nature
166. Sumana S et al (2023) Investigations and validation of PV powered unified power quality conditioner for electric vehicle smart charger in standard AC/DC hybrid microgrid test system. In: Proceedings of 2nd international conference on renewable power (ICRP). LNEE. Springer Nature
167. Khetarpal P et al (2023) Short-term electricity load forecasting using modified hidden Markov model. In: Proceedings of 2nd international conference on renewable power (ICRP). LNEE. Springer Nature
168. Kumar S et al (2023) Microgrid systems with classical primary control techniques—a review. In: Proceedings of 2nd international conference on renewable power (ICRP). LNEE. Springer Nature
169. Javed S et al (2023) Green energy solutions for indoor air quality improvement. In: Proceedings of 2nd international conference on renewable power (ICRP). LNEE. Springer Nature
170. Ahmed SB et al (2023) Data resource library for renewable energy prediction/forecasting. In: Proceedings of 2nd international conference on renewable power (ICRP). LNEE. Springer Nature
171. Sarfraz et al (2023) Solar rooftop on-grid connected net metering system. In: Proceedings of 2nd international conference on renewable power (ICRP). LNEE. Springer Nature
172. Tompala J et al (2023) Contemporary maximum power point tracking methods of solar photovoltaic modules. In: Proceedings of 2nd international conference on renewable power (ICRP). LNEE. Springer Nature
173. Kumar A (2023) Performance analysis of perturb & observe and incremental conductance method of maximum power point tracking in solar PV based power generation. In: Proceedings of 2nd international conference on renewable power (ICRP). LNEE. Springer Nature
174. Roslan SAH et al (2023) The airfoil design for small-scale wind turbines in maximizing renewable wind energy. In: Proceedings of 2nd international conference on renewable power (ICRP). LNEE. Springer Nature
175. Pachauri RK et al (2023) Comparative study on solar PV module performance with sun irradiance trapping mechanism: power generation forecasting using machine learning. In: Proceedings of 2nd international conference on renewable power (ICRP). LNEE. Springer Nature
176. Roslan SAH et al (2023) The geometric modelling and linearization of small-scale wind turbine blades for optimized renewable energy. In: Proceedings of 2nd international conference on renewable power (ICRP). LNEE. Springer Nature

177. Radhiva M et al (2023) Performance analysis of H-type vertical axis wind turbine by using novelty numerical Simulink method. In: Proceedings of 2nd international conference on renewable power (ICRP). LNEE. Springer Nature
178. Anand R et al (2023) Energy production from various bio-waste under different electrode and temperature conditions: experimental study. In: Proceedings of 2nd international conference on renewable power (ICRP). LNEE. Springer Nature
179. Arief YZ et al (2023) Simulation and prototype design of hybrid renewable energy harvesting system. In: Proceedings of 2nd international conference on renewable power (ICRP). LNEE. Springer Nature
180. Kumar M et al (2023) Design and development of an inexpensive intelligent device for sag measurement for overhead transmission lines. In: Proceedings of 2nd international conference on renewable power (ICRP). LNEE. Springer Nature
181. Mangaraj M et al (2023) Gradient descent back propagation through momentum (GDBPM) endorsed  $i \cos \phi$  control technique based dSTATCOM intended for shunt indemnification. In: Proceedings of 2nd international conference on renewable power (ICRP). LNEE. Springer Nature
182. Deshmukh S et al (2023) Improvement in voltage stability of the system due to increased penetration of electric vehicles using distributed photovoltaic sources. In: Proceedings of 2nd international conference on renewable power (ICRP). LNEE. Springer Nature
183. Nezami MM et al (2023) An intelligent system for furfural estimation in the power transformers. In: Proceedings of 2nd international conference on renewable power (ICRP). LNEE. Springer Nature
184. Ansari MF et al (2023) Design of PID tuned controller for automatic voltage regulator for frequency stability in thermal power plant. In: Proceedings of 2nd international conference on renewable power (ICRP). LNEE. Springer Nature
185. Elwan AA et al (2023) Optimization of distributed generators in a virtual power plan using mixed integer linear programming method. In: Proceedings of 2nd international conference on renewable power (ICRP). LNEE. Springer Nature
186. Elwan AA et al (2023) Solving unit commitment problem using mixed integer linear programming for demand side management. In: Proceedings of 2nd international conference on renewable power (ICRP). LNEE. Springer Nature
187. Mustapha M et al (2023) Deployment of renewable embedded generation and unified power quality conditioner in distribution system using firefly algorithm. In: Proceedings of 2nd international conference on renewable power (ICRP). LNEE. Springer Nature
188. Juneja D et al (2023) Application of wind power in backwashing filter media. In: Proceedings of 2nd international conference on renewable power (ICRP). LNEE. Springer Nature
189. Aladin MYF et al (2023) Mixed reality accelerates the designing process in automotive industry. In: Proceedings of 2nd international conference on renewable power (ICRP). LNEE. Springer Nature
190. Imtiyaz R et al (2023) Design and implementation of solar charging electric vehicle. In: Proceedings of 2nd international conference on renewable power (ICRP). LNEE. Springer Nature
191. Subbaramaiah K et al (2023) Modelling and analysis of a permanent magnet DC motor fed electric vehicle drive system. In: Proceedings of 2nd international conference on renewable power (ICRP). LNEE. Springer Nature
192. Vishwanath Nagarajan VS et al (2023) An overview of electric and hybrid vehicle technology. In: Proceedings of 2nd international conference on renewable power (ICRP). LNEE. Springer Nature
193. Asati R et al (2023) Performance analysis of classical converter using different control strategies for switched reluctance motor with dynamic loading. In: Proceedings of 2nd international conference on renewable power (ICRP). LNEE. Springer Nature
194. Gupta V et al (2023) Design and development gear-electric bike and performance testing for Indian road conditions. In: Proceedings of 2nd international conference on renewable power (ICRP). LNEE. Springer Nature

195. Jain S et al (2023) Design and development of a solar-based wireless electric vehicle charging system. In: Proceedings of 2nd international conference on renewable power (ICRP). LNEE. Springer Nature
196. Ali K et al (2023) Design, optimization & performance enhancement of switched reluctance motor for pollution free electric vehicle application. In: Proceedings of 2nd international conference on renewable power (ICRP). LNEE. Springer Nature
197. Al-Hakim RR et al (2023) Using linear regression model to predict the wholesale of the electric car in Indonesia: what can be learned from the model? In: Proceedings of 2nd international conference on renewable power (ICRP). LNEE. Springer Nature
198. Adzmi MAI et al (2023) Comparison of thermoelectric generator with boost converter and single-ended primary-inductance converter. In: Proceedings of 2nd international conference on renewable power (ICRP). LNEE. Springer Nature
199. Arshad NM et al (2023) A hybrid maximum power point tracking (MPPT) for thermoelectric generator (TEG) system. In: Proceedings of 2nd international conference on renewable power (ICRP). LNEE. Springer Nature
200. Justin A et al (2023) Thermoelectric generator (TEG) by using indirect maximum power point (MPP) algorithm. In: Proceedings of 2nd international conference on renewable power (ICRP). LNEE. Springer Nature
201. Shukla U et al (2023) Comprehensive review on AC-DC, DC-DC, DC-AC-DC converters used for electric vehicles and charging stations. In: Proceedings of 2nd international conference on renewable power (ICRP). LNEE. Springer Nature
202. Kumar A (2023) Control and performance analysis for active islanding detection using q-axis control in renewable energy sources based microgrid: a review. In: Proceedings of 2nd international conference on renewable power (ICRP). LNEE. Springer Nature
203. Khan MR et al (2023) Harmonics analysis of triplen-phase induction motor drive. In: Proceedings of 2nd international conference on renewable power (ICRP). LNEE. Springer Nature
204. Mishra K et al (2023) Development of WiTricity based wireless power transmission system. In: Proceedings of 2nd international conference on renewable power (ICRP). LNEE. Springer Nature
205. Roomi MM et al (2023) Analysis of three-winding transformer configurations for energy storage less dynamic voltage restorer. In: Proceedings of 2nd international conference on renewable power (ICRP). LNEE. Springer Nature
206. Malik H et al (2023) Data reliability analysis for early fault diagnosis of air handling unit (AHU). In: Proceedings of 2nd international conference on renewable power (ICRP). LNEE. Springer Nature
207. Thakur A et al (2023) Use of solar energy in treatment of pulp and paper industry effluent with hemp—an experimental study. In: Proceedings of 2nd international conference on renewable power (ICRP). LNEE. Springer Nature
208. Pushparaj et al (2023) Design of radar-based portable system for monitoring of human vital signs with renewable energy resources. In: Proceedings of 2nd international conference on renewable power (ICRP). LNEE. Springer Nature
209. Sharma M et al (2023) Controlling methods of brushless DC motor in electrical vehicle drives. In: Proceedings of 2nd international conference on renewable power (ICRP). LNEE. Springer Nature
210. Kuttay VK et al (2023) Effect of number of poles on IPMSM performance for electric vehicle drivetrain. In: Proceedings of 2nd international conference on renewable power (ICRP). LNEE. Springer Nature
211. Ray P et al (2023) Offline power quality management and control using neural networks. In: Proceedings of 2nd international conference on renewable power (ICRP). LNEE. Springer Nature
212. Kassarwani N et al (2023) Optimized integral sliding mode load frequency control of an isolated power system. In: Proceedings of 2nd international conference on renewable power (ICRP). LNEE. Springer Nature

213. Jahid et al (2023) Implementation of supercapacitor-battery based energy storage system in hybrid power system incorporating renewable energy resources. In: Proceedings of 2nd international conference on renewable power (ICRP). LNEE. Springer Nature
214. Elwan AA et al (2023) Hybrid waste to energy electricity generation and battery storage system: the economics and environmental emission in a low-income community. In: Proceedings of 2nd international conference on renewable power (ICRP). LNEE. Springer Nature
215. Kumar R et al (2023) Application of solar power in the loopholes and coverages of buses in the bus rapid transit system in Bhopal. In: Proceedings of 2nd international conference on renewable power (ICRP). LNEE. Springer Nature
216. Sharma S et al (2023) Forecasting of carbon emissions in India using (ARIMA) time series predicting approach. In: Proceedings of 2nd international conference on renewable power (ICRP). LNEE. Springer Nature
217. Sharma A et al (2023) Peak shaving through battery storage for photovoltaic integrated building considering the time of day pricing. In: Proceedings of 2nd international conference on renewable power (ICRP). LNEE. Springer Nature
218. Yadav N et al (2023) Economic analysis of renewable energy systems for rural electrification. In: Proceedings of 2nd international conference on renewable power (ICRP). LNEE. Springer Nature
219. Rani P et al (2023) Improved voltage regulation in hybrid photovoltaic/wind using modified dynamic voltage restorer with hybrid control scheme. In: Proceedings of 2nd international conference on renewable power (ICRP). LNEE. Springer Nature
220. Mehtre VV et al (2023) Contingency analysis for a solar energy generation system using real time data analysis. In: Proceedings of 2nd international conference on renewable power (ICRP). LNEE. Springer Nature
221. Ismail AW et al (2023) Digital twin in extended reality applications for industry 4.0. In: Proceedings of 2nd international conference on renewable power (ICRP). LNEE. Springer Nature
222. Ahmad N et al (2023) Deep image coding in the fractional wavelet transform domain based on high frequency sub-bands prediction. In: Proceedings of 2nd international conference on renewable power (ICRP). LNEE. Springer Nature
223. Joshi BP et al (2023) QIVIFS: quaternion approach of interval-valued-intuitionistic-fuzzy-sets with applications in renewable energy system. In: Proceedings of 2nd international conference on renewable power (ICRP). LNEE. Springer Nature
224. Verma SK et al (2023) Feminine protection wearable system based on IoT. In: Proceedings of 2nd international conference on renewable power (ICRP). LNEE. Springer Nature
225. Pachauri RK et al (2023) Marine predictors algorithm optimization technique to estimate GMPP of PV array under partial shadowing conditions. In: Proceedings of 2nd international conference on renewable power (ICRP). LNEE. Springer Nature
226. Iqbal M et al (2023) Artificial intelligence-based bearing fault diagnosis of rotating machine to improve the safety of power system. In: Proceedings of 2nd international conference on renewable power (ICRP). LNEE. Springer Nature
227. Arora A et al (2023) Stability enhancement of AC microgrid using discrete mode controllers with optimum sampling frequency. In: Proceedings of 2nd international conference on renewable power (ICRP). LNEE. Springer Nature
228. Rani P et al (2023) Performance analysis of grid integrated solar system through interlinking converter with control schemes. In: Proceedings of 2nd international conference on renewable power (ICRP). LNEE. Springer Nature
229. Midha A et al (2023) Towards achieving net zero emissions in India by 2070. In: Proceedings of 2nd international conference on renewable power (ICRP). LNEE. Springer Nature

230. Sai Kiran P et al (2023) IoT-based monitoring and controlling of substation parameters. In: Proceedings of 2nd international conference on renewable power (ICRP). LNEE. Springer Nature
231. Dini HS et al (2023) Effectiveness of resilience index in assessing power system performance. In: Proceedings of 2nd international conference on renewable power (ICRP). LNEE. Springer Nature

# An Efficient Algorithm for Energy Management in Smart Grid for Various Improvements



Deepa Kumari and Ashish Sharma

**Abstract** Set of algorithms are known as artificial intelligence (AI), and as per the current scenario, AI techniques, like expert systems (ESs), fuzzy logic (FL), and artificial neural networks (ANNs or NNWs), have changed the whole mode of operation by making power electronics and power engineering more advance in terms of their operation and control. With the introduction of this advancement, it has brought more efficient tools for blueprint, recreation, manage, evaluation, fault testing, and risk-tolerant control in recent smart grid (SG) and non-conventional power systems. The set of algorithms which we are talking about has achieved really quick development in the period of previous few years, and its impacts can be seen in the recent industrial applications. The implementation of different set of algorithms in smart power grids offers useful technical real-time support for the digital power system. Areas influenced by artificial intelligence in any smart power grid consist of energy management system, power generation, power supply, power system optimization, consumer behavior study, fault testing, etc. No enough data sample gathering, inadequate consistency, flawed infrastructure, need of special algorithm for power industry, etc., are the main problem which are still persisting for the existence of smart grid. Finding the solution and building the efficient algorithm for power industry can be the important tool to establish smart grid into the new era for electric network or power system. The paper will discuss the application of artificial intelligence for obtaining an efficient energy management system in any electrical grid.

**Keywords** Set of algorithms · Neural network · Customer behavior identification · Fuzzy logic (FL) · Neural network · Real-time data · Renewable energy systems (RESs) · Smart grid (SG) · Energy management system (EMS)

---

D. Kumari (✉) · A. Sharma  
Department of Electrical Engineering, Chandigarh University, Mohali, India  
e-mail: [deepa.e9647@cumail.in](mailto:deepa.e9647@cumail.in)

A. Sharma  
e-mail: [ashish.e10096@cumail.in](mailto:ashish.e10096@cumail.in)

# 1 Introduction

## 1.1 Smart Grid

Smart grid is one complete set of power system devices, computers, communication cyber technologies, and joint existence of recent information system and the conventional power grid [1]. As with the constant development in technology, we cannot stick to the old power generation system since they are superseded, unproductive, unpredictable and do not offer any efficient protection against the electric faults. Since smart grid is the one effective solution for all these conventional power systems, it can solve the problems of old power system like insufficient efficiency, poor load management, and poor fault analysis performance. The main area of focus by smart grid (SG) is as follows [2, 3]:

- Best possible resource deployment;
- Higher energy effectiveness;
- Higher system dependability;
- Higher system protection;
- Economically efficient electricity distribution

Keeping in view the current state of environmental health and climate change, smart grids can make hybrid power network system with different renewable energy systems (RESs) (solar, wind hydro, etc.) in addition to bulk conventional power plants (fossil, hydro, etc.) to overcome the problem [4]. It can also be installed with storage system (battery, pumped storage, flywheel, hydrogen, etc.) just because of unpredictable and fluctuating nature of renewable resources [5]. One of the best features offered by smart grid is its effective communication between supply and demand sides with the assistance of smart meters which helps to build the two-way communication between supplier and consumer and also decreases the use of bulk storage and offers economical tariff plans to the consumers [6, 7].

## 1.2 Algorithm

Algorithms mean “a method or group of rules to be obeyed in calculation or additional problems solving tasks”. Hence, algorithms are set of instructions which step-by-step explain the execution of work in order to get the desired results [8, 9]. As algorithms are one step-wise explanation to the solution hence they are easy to understand also in any algorithm obstacle it is first broken down into steps are smaller pieces it becomes easier for the programmer to translate it into an actual problem but at the same time creation on an algorithm requires vast time so the development is quite time intense also splitting and iteration to show in any set of algorithms is difficult [10, 11].

### 1.3 Energy Management System (EMS)

This system of any electrical grid is that part which majorly deals with the operation and control tasks. One of those major areas of EMS is to sustain the stability between load side demand and power generation setting up generation economically, switching the substations of high-voltage transmission, keeping up good security for the operation of transmission system, and providing aiding solution to diagnosing problems (Fig. 1).

To diagnosing problems, monitoring the  $N$ -numbers of operations at consumer's end and collecting the information among the various remote terminal units are the most efficient area of energy management system [12, 13]. We can conclude that the energy management system is most importantly a monitoring and estimation system as far more data enter the energy management system than leaves. As it is already proven that the integration of unstable resources (like photovoltaic cells, wind generation, electric vehicles, and energy storage system) affects the stable functioning of power and distribution system [14–18], it is being a big concern due the power ratio between the supply and demand is not balanced [19]. An extreme/over deficiency in power production or consumption may end up causing serious problems as in blackouts, voltage drop/rise in severe situations. Hence, to make the generation and consumption system effectively balanced and to minimize the peak load during unpredicted stages, energy management system can be taken into count [20]. Energy management can be implemented in two different bases that is one at supplier's end such as electric grid, where the generators can be made operated alternately according to the fluctuation of lode demand [21] (Fig. 2).

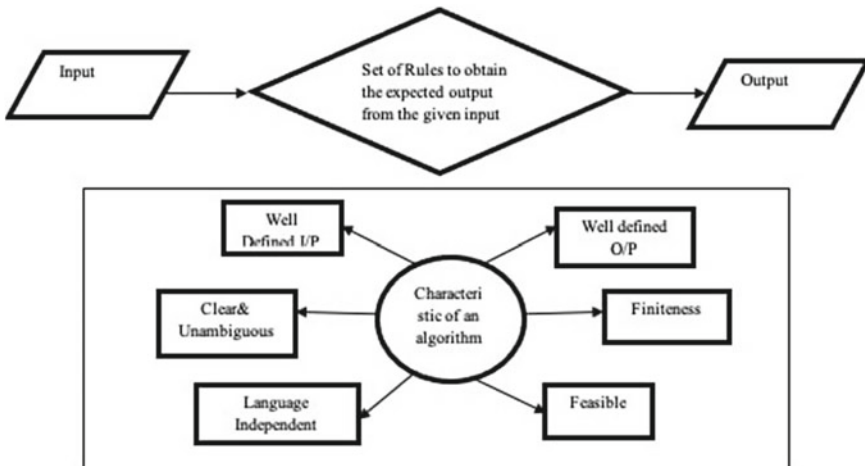


Fig. 1 Block representation of characteristics of algorithms



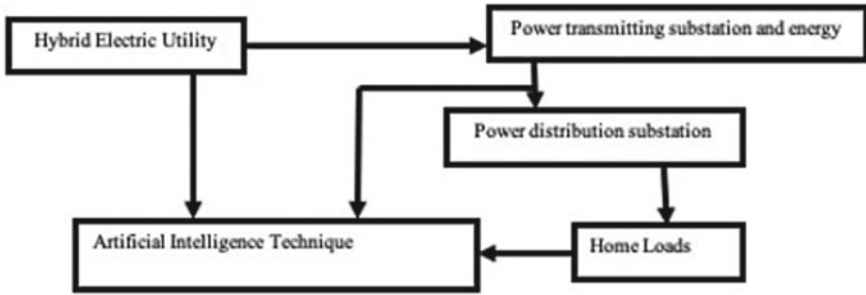


Fig. 2 Block diagram representation of dynamic regulation model with hybrid resources

## 2 Review of AI Techniques

There are basically four different areas to classify the AI techniques, i.e.,

- Expert systems (ESs);
- Fuzzy logic (FL);
- Artificial neural networks (ANNs or NNWs);
- Genetic algorithm (GA); or broadly evolutionary computation (EC).

As expert system, fuzzy logic, and neural network methods are normally used, these will be concisely reviewed [22, 23] under this segment. If there is any fastest evolving area in technology that we can say is an artificial intelligence and AI with its wide area of application is expected to serve its important features in the field of energy, transportation, health care, security etc. [24] (Fig. 3).

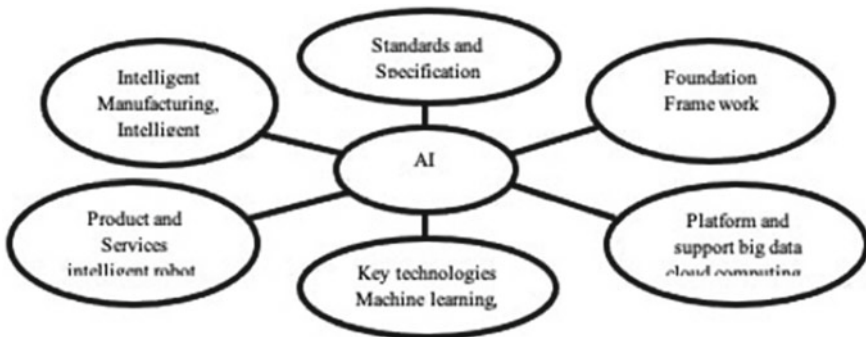


Fig. 3 Architecture of artificial intelligence

## 2.1 Expert System

Expert system is one of the intelligent computer programs which comprises Boolean logic function which is intended to insert the knowledge of human being in some specific areas as a result of which it can be implemented to crack the difficulty replacing human knowledge [25]. Although an expert system is an established technology, but so far it is not so applied in power system engineering [23]. We can trust the system in order to provide the high efficiency and performance to crack any difficult problem of a specific domain with high accuracy. User Interface, this is the feature with the help of which expert system interacts with the user, accepts the problem as an input in an editable format, and further processes it to the inference engine. Once the inference engine processes the data and gives response, it displays the response to the user [25]. So hence we can conclude that this that part of the system which allows the user to interconnect with expert system to find the resolution. Inference Engine (Rules of engine), this part of the system is acknowledged as the brain of the expert system as it is that unit which processes the main data. It implements rules of engine to the knowledge base to generate a result or to obtain new information. As the accuracy of expert system is very high, so it also helps to drive the most accurate solution of the query asked by the user. It is also that unit where the knowledge is extracted from the knowledge base [26]. Knowledge Base, it is that storage system of the system which stores the knowledge from the distinctive specialists of the particular area. It is then called as big packing of knowledge. The more the knowledge stored in knowledge base, more accurate the expert system will. It has similarity with database that contains information and rules of a particular domain. This can also be expressed as accumulation of objects and their attributes [27]. The use of expert system in energy management system: The encoding of information and implementing it to support operators require the integration of expert system inside the energy management system to such a level not currently conceived. In order to make applications' operation more expert system oriented, the run and sequencing logic of these application programs need to be changed [28]. In effect, any algorithm in the energy management system talks about the application of specific information regarding electric utility operation. For instance, almost every energy management system needs the existence of some logic that runs a condition estimator and security analysis on a habitual clock period with an supersede if switching events have occurred within a few seconds of the start additional [29]. The operative can call for an implementation of the condition estimator and safety analysis every time desired. With an expert system scheming, the state estimator and safety analysis events can be taken based on what type of switching accomplishment has taken place (Fig. 4).

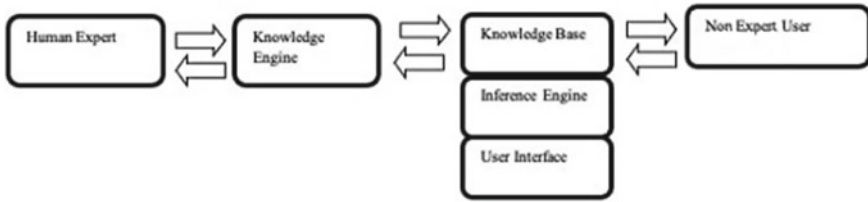


Fig. 4 Architecture of expert system

## 2.2 Fuzzy Logic

It is a way of thinking that pairs the human thinking. This procedure is alike to how human takes different decisions and it exhibits all intermediate possibilities between Yes and No [30]. It is a way of thinking that pairs the human thinking. This procedure is alike to how human takes different decisions and it exhibits all intermediate possibilities between Yes and No [31]. The old logic commands as per the computer understanding take exact input unit and generate a certain output as FALSE or TRUE which is exactly similar to human response as NO or YES. This algorithm was conceived after observing that human reacts in multiple ways under different conditions unlike computers where the output is limited between TRUE and FALSE, such as: can be as flexible as it can be fit for any size and proficiencies like microcontrollers, large networked or workstation-based organizations, and also it can be suitable for any hardware software or mixture of both [32]. Fuzzy logic has wide area of application; it can be suitable for commercial as well as practical purposes like:

- Fuzzy logic is one of the ways to command products of machine and consumer (Fig. 5).
- In accordance to human thinking if fuzzy logic is not able to provide exact thinking, it anyways can provide the satisfactory thinking.
- It benefits in commerce with the ambiguity in engineering rules. It comprehends search-required procedures and the necessary if-then statements presented by the



Fig. 5 Basic working of fuzzy

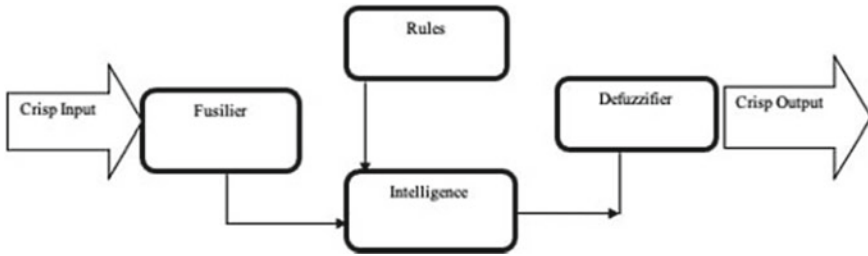


**Fig. 6** Architecture of fuzzy logic

specialists to control any decision-making scheme. The current apprise in this algorithm offers multiple effective ways for the designing and modification of fuzzy logic controllers. Generally, this improvement minimizes the numeral of fuzzy rules [33].

Fuzzification is a conversion unit where the input or crisp numbers are converted into fuzzy sets. These crisp inputs can be processed by control system once measured by the sensors [33].

Inference Engine Amount of balance among fuzzy input and rules as per the input field is determined by this unit, and this unit will then choose the rules that need to be excited [33]. Defuzzification is the process of conversion of the given fuzzy sets into the crisp value. To do defuzzification, it has multiple types of practices present and the best-suited one is required to be selected with an expert system [15] (Fig. 6).

**The Use of Fuzzy Logic in EMS**

Fuzzy logic consists of input variables, and in fuzzy modeling, every input unit is first transformed to a fuzzy variable over a method termed as fuzzification. Fundamentally, this process converts any mathematical input into linguistic value. One specific variable in terms of using fuzzy logic for EMS is employed by the fuzzy logic energy management system (EMS) to make the electricity more economically affordable. It must be distinguished that the standardization progression utilized for charges—separating by the highest cost of the past few days—may allow the standardized value to be larger than one. Thus, the creation of dialogue in this fuzzy logic system is chosen to satisfy the desired range [25], which sufficiently covers the level for this variable.

**2.3 Artificial Neural Network (ANN)**

Set of algorithms forming Neural Network [34] is the very generic version of artificial intelligence; it is most likely to follow the genetic nervous system as associated to Expert system and Fuzzy Logic that is used to imitate the developmental nature of brain by means of the rule base. This algorithm (NNW) has the feature of nonlinear

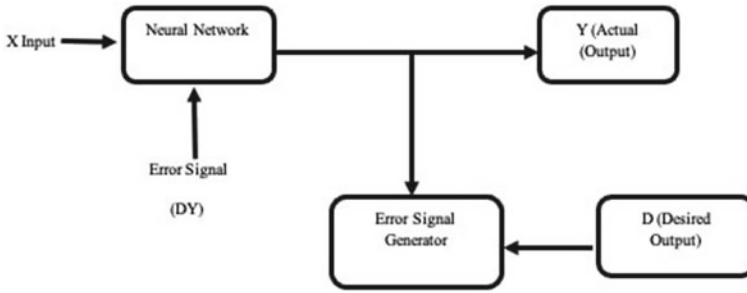


**Fig. 7** Architecture of artificial neural network

*i/p–o/p* mapping or arrangement identification property which basically imitates the linking memory property of the human brain. This is the very significant part of artificial intelligence and is very well-organized in terms of solving pattern acknowledgment or image-processing mode troubles that are kind of tough to crack with conventional methods [35]. The combination or interconnectedness of manmade neurons can be termed as Neural Network, which further can serve its application in numerous engineering scientific and real-life problems [21, 22]. These NNW are of two main categories feedforward and feedback as per the flow of direction [16] (Fig. 7).

### Feedforward Network

This is non-repeatable network having processing segments/node and these sections in a layer are joint along with the segments of preceding layer. The connections have dissimilar loads on them. Feedforward type does not have and response loop which means that the signal can stream in single direction, i.e., from input to output. Further, it may be described as follows [17].

#### Single-Layered Feedforward Network

Here, under this type, input layer is completely connected to output layer and this is that one of the concepts of feedforward ANN (Fig. 8).

#### Multilayer Feedforward Network

This is the idea of feedforward artificial neural network (ANN) having numerous subjective layers. As in this type there are more than one layer present between input and output layers, it is also called hidden layers [17, 18] (Fig. 9).

### Feedback Network

As it is clear from its name, there will a feedback path which means that the direction of flow of signals can be in both the directions using loops. This makes the system dynamic and nonlinear. It changes uninterruptedly until it touches a state of steadiness [16, 17].

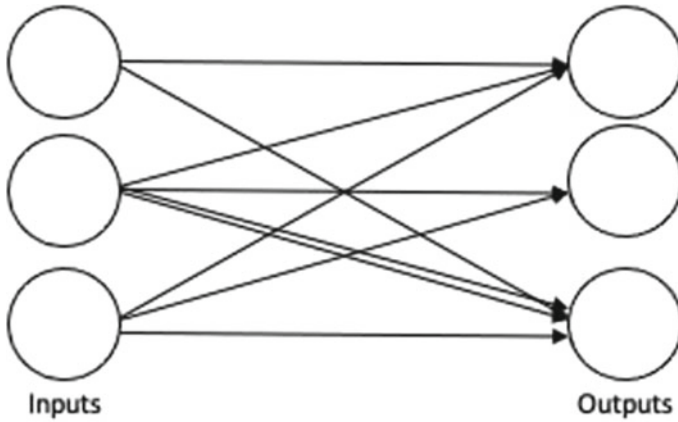


**Fig. 8** Single-layer feedforward

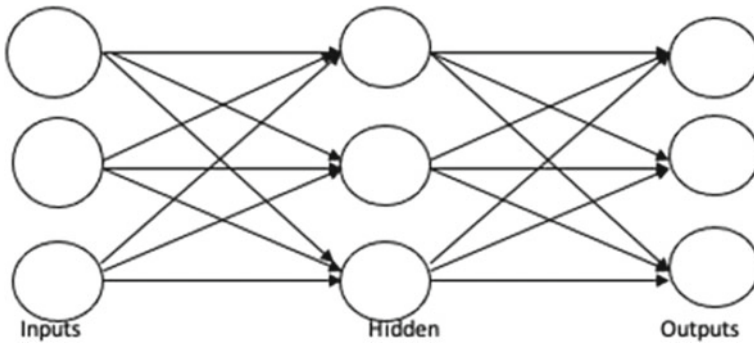


**Fig. 9** Multilayer feedforward network

**Recurrent Network**

This is the greenest Neural Network design as all the nodes are linked to one another and every node functions as both input and output [22] (Fig. 10).

**Jordan Network**

It is a close path network where the outcome will get back to the input again as feedback as displayed in Fig. 11 [23, 24].

**The Use of Artificial Neural Network in Energy Management System**

Artificial neural network is one of the predicting algorithms which when utilized in any smart grid system can be used for predicting the consumption of energy. By implementing feedforward type of neural network, the prediction is according to as training function is TRAINLM, learning function LEARNGDM, performance function is MSE and LOGSIG as transfer function. In the whole process of artificial neural

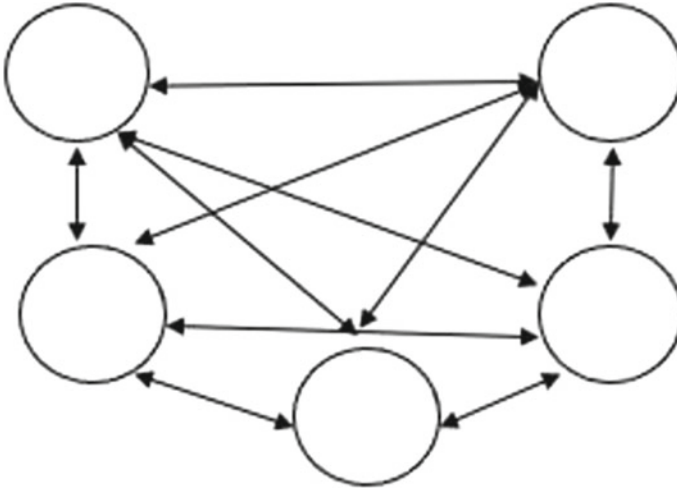


Fig. 10 Recurrent network

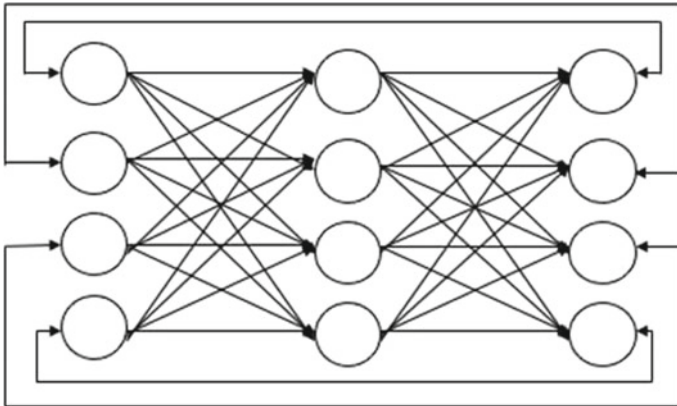


Fig. 11 Jordan network

network, consumption of power, number of experiments run, experiment hours, and cost of electricity act as input parameters and energy consumption is the output data.

### 3 Conclusion

As we know that the set of different algorithms will result into some artificial techniques and the artificial techniques are one most powerful tool for application in smart grid and non-conventional sources. This work gives as an idea about the

existing algorithms and their different types such as Expert system, Fuzzy logic, and artificial neural network; these are the significant branches of artificial intelligence, which is then trailed by the brief explanation of block architecture of AI and their different types? These discussions and explanations of different AIs are very interesting and can be implemented over a wide range of applications in smart grid. The algorithms' examples labeled in the paper can be stretched to cover various other functions in smart grid in integration with renewable resources. The implementation and consumption of any novel energy technologies impress more than a few challenges associated to this field (power management) of recent constructions that take the shape of prosumers. Allowing for substantial and time limitations of power management related to individuals, there is a requirement for smart energy management systems that accomplish an extra competent power depletion and decreased to achievable point of electricity bill autonomously of the atmosphere and weather circumstances.

**Acknowledgements** The authors would like to acknowledge The University Institute of Engineering, Electrical Engineering Department at Chandigarh University and UCRD (University Center for Research Development Academic Science), for encouraging research work and providing financial help to carry forward the research work.

## References

1. Jiao J (2020) Application and prospect of artificial intelligence in smart grid. IOP Conf Ser Earth Environ Sci 510(2):022012. IOP Publishing
2. Gharavi H, Ghafurian R (eds) (2011) Smart grid: the electric energy system of the future, vol 99. IEEE, Piscataway, NJ
3. Bose BK (2002) Modern power electronics and AC drives, vol 123. Prentice Hall, Upper Saddle River, NJ
4. Bose B (2006) Power electronics and motor drives—advances and trends, 915 pp
5. Bose BK (2017) Artificial intelligence techniques in smart grid and renewable energy systems—some example applications. Proc IEEE 105(11):2262–2273
6. Cheung V, Westland S, Connah D, Ripamonti C (2004) A comparative study of the characterisation of colour cameras by means of neural networks and polynomial transforms. Color Technol 120(1):19–25
7. Alamaniotis M, Heifetz A, Raptis AC, Tsoukalas LH (2013) Fuzzy-logic radioisotope identifier for gamma spectroscopy in source search. IEEE Trans Nucl Sci 60(4):3014–3024
8. Das UK, Tey KS, Seyedmahmoudian M, Mekhilef S, Idris MYI, Van Deventer W, Horan B, Stojcevski A (2018) Forecasting of photovoltaic power generation and model optimization: a review. Renew Sustain Energy Rev 81:912–928
9. Zieher M, Lange M, Focken U (2015) Variable renewable energy forecasting—integration into electricity grids and markets—a best practice guide. In: Proceedings of Deutsche Gesellschaft Internationale Zusammenarbeit (GIZ), July 2015, pp 1–8
10. Anuradha MA, Massoud A (2013) IEEE vision for smart grid controls: 2030 and beyond: roadmap. In: IEEE CSS
11. Mikkili S, Panda AK, Prattipati J (2015) Review of real-time simulator and the steps involved for implementation of a model from MATLAB/SIMULINK to real-time. J Inst Eng (India) Ser B 96:179–196



12. Bose BK (2017) Power electronics, smart grid, and renewable energy systems. *Proc IEEE* 105(11):2011–2018
13. Meijer F, Visscher HENK, Nieboer N, Kroese R (2012) Jobs creation through energy renovation of the housing stock. *Neujobs*. Retrieved 7 July 2017
14. Bose BK (2007) Neural network applications in power electronics and motor drives—an introduction and perspective. *IEEE Trans Ind Electron* 54(1):14–33
15. Chhaya SM, Bose BK (1995) Expert system aided automated design, simulation and controller tuning of AC drive system. In: *Proceedings of IECON'95—21st annual conference on IEEE industrial electronics*, vol 1. IEEE, pp 712–718
16. Jang J-SR (1993) ANFIS: adaptive-network-based fuzzy inference system. *IEEE Trans Syst Man Cybern* 23(3):665–685
17. Ssekulima EB, Anwar MB, Al Hina A, El Moursi MS (2016) Wind speed and solar irradiance forecasting techniques for enhanced renewable energy integration with the grid: a review. *IET Renew Power Gener* 10(7):885–989
18. Bhandari B, Lee K-T, Lee G-Y, Cho Y-M, Ahn S-H (2015) Optimization of hybrid renewable energy power systems: a review. *Int J Precis Eng Manuf Green Technol* 2(1):99–112
19. Chaouachi A, Kamel RM, Andoulsi R, Nagasaka K (2012) Multiobjective intelligent energy management for a microgrid. *IEEE Trans Ind Electron* 60(4):1688–1699
20. Nilsson NJ (2010) The quest for artificial intelligence: a history of ideas and achievements. <https://doi.org/10.1017/CBO9780511819346>
21. Russel S, Norvig P (2013) *Artificial intelligence: a modern approach*, vol 256. Pearson Education Limited, London
22. Sugeno and Mamdani fuzzy inference systems, *MATLAB 2021a documentation* (2021). Accessed 31 Mar 2021
23. El-Bayeh CZ, Alzaareer K, Gabbar AH (2019) Issue on smart grid management systems features. In: *Energy management in smart grid*. IEEE Press
24. Yang Y, Wang S (2021) Resilient residential energy management with vehicle-to-home and photovoltaic uncertainty. *Int J Electr Power Energy Syst* 132:107206
25. Sousa M, Saraiva F (2019) A fuzzy system applied to photovoltaic generator management aimed to reduce electricity bill. In: *Progress in artificial intelligence: 19th EPIA conference on artificial intelligence*, EPIA 2019, Vila Real, Portugal, 3–6 Sept 2019, proceedings, Part I 19. Springer International Publishing, pp 450–461
26. Varzaneh SG, Raziabadi A, Hosseinzadeh M, Sanjari MJ (2021) Optimal energy management for PV-integrated residential systems including energy storage system. *IET Renew Power Gener* 15(1):17–29
27. Nizami MSH, Hossain MJ, Mahmud K, Ravishankar J (2018) Energy cost optimization and der scheduling for unified energy management system of residential neighborhood. In: *2018 IEEE international conference on environment and electrical engineering and 2018 IEEE industrial and commercial power systems Europe (EEEIC/I&CPS Europe)*. IEEE, pp 1–6
28. Athari MH, Ardehali MM (2016) Operational performance of energy storage as function of electricity prices for on-grid hybrid renewable energy system by optimized fuzzy logic controller. *Renew Energy* 85:890–902
29. Mohsenzadeh A, Pang C (2018) Two stage residential energy management under distribution locational marginal pricing. *Electr Power Syst Res* 154:361–372
30. Prajwal KT, Sitaram Gupta VSNV (2018) Smart home energy management system using fuzzy logic for continuous power supply with economic utilisation of electrical energy. In: *2018 2nd international conference on inventive systems and control (ICISC)*. IEEE, pp 274–279
31. Zafar R, Mahmood A, Razaq S, Ali W, Naeem U, Shehzad K (2018) Prosumer based energy management and sharing in smart grid. *Renew Sustain Energy Rev* 82:1675–1684
32. Dimitroulis P, Alamaniotis M (2020) Residential energy management system utilizing fuzzy based decision-making. In: *2020 IEEE Texas power and energy conference (TPEC)*. IEEE, pp 1–6
33. Kanwar N et al (2022) Fuzzy-based investigation of challenges for the deployment of renewable energy power generation. *Energies* 15(1):58

34. Ahmad MW et al (eds) (2022) Intelligent data analytics for power and energy systems. Springer Singapore, pp XXII, 641. ISBN: 978-981-16-6081-8. <https://doi.org/10.1007/978-981-16-6081-8>
35. Tomar A et al (eds) (2022) Proceedings of 3rd international conference on machine learning, advances in computing, renewable energy and communication: MARC 2021, vol 915. Springer Nature, pp XV, 781. ISBN: 978-981-19-2830-7. <https://doi.org/10.1007/978-981-19-2828-4>
36. Bush SF (2014) Network theory and smart grid distribution automation. *IEEE J Sel Areas Commun* 32(7):1451–1459
37. Abu-Rub H, Malinowski M, Al-Haddad K (2014) Power electronics for renewable energy systems, transportation and industrial applications. Wiley. Bose BK (2015) Energy environment and power electronics. In: Proceedings of IEEE industrial electronics society distinguished lecture
38. Bose BK (2015) Advance technologies, applications and trends of power electronics and motor drives. In: Proceedings of keynote presentation conference on power, control, communication and computational technologies for sustainable growth (PCCCTSG), Kurnool, India, Dec 2015
39. Ricalde LJ, Ordoñez E, Gamez M, Sanchez EN (2011) Design of a smart grid management system with renewable energy generation. In: 2011 IEEE symposium on computational intelligence applications in smart grid (CIASG). IEEE, pp 1–4
40. Dimian GC, Marin E, Jablonsky J (2019) Investigating the long and short-run salary-employment relationship in Romania: a sectorial approach using the ARDL model. *Econ Comput Econ Cybern Stud Res* 53(1)

# Investigations and Validation of PV-Powered Unified Power Quality Conditioner for Electric Vehicle Smart Charger in Standard AC/DC Hybrid Microgrid Test System



S. Sumana and R. Dhanalakshmi

**Abstract** It is well known that increase of nonlinear load such as electric vehicles (EVs) has become the key aspect in booming the power quality (PQ) issues in the power distribution grid. The application of AC/DC hybrid microgrid has become one of major trends in power transmission and distribution. The electric vehicle smart charger in the hybrid AC/DC microgrid (MG) causes PQ issues in the power system and also at the customer end. To uphold the quality of the power according to its standard, series of devices called custom power devices (CPDs) are accustomed. Unified power quality conditioner (UPQC) provides better solution in resolving the PQ-related issues and is emerged as powerful tool in enhancing the standards of power that is supplied to the end user. Novelty in this paper is the analysis of PQ issues due to the penetration of EVs in AC/DC hybrid microgrid and its compensation by photovoltaic (PV)-powered UPQC. The simulation is carried out in MATLAB 2017b platform. Based on the action of UPQC, outcomes are analyzed for three different cases. In each case, three scenarios are discussed based on the charging condition of EV smart charger in both the modes of system operation, i.e., when it is coupled to the grid and also in off-grid mode. Comparative investigation is achieved on the Performance of the PV powered UPQC for compensating the PQ issues caused by the EV charger in AC/DC hybrid microgrid test system and as well as in the standard IEEE 14 bus microgrid (MG) system for validation.

**Keywords** AC/DC hybrid microgrid · PV-powered UPQC · EV charger · Dynamic load · IEEE 14 bus

---

S. Sumana (✉) · R. Dhanalakshmi  
Department of Electrical and Electronics, Dayananda Sagar College of Engineering, Bengaluru, India  
e-mail: [sumana-eee@dayanandasagar.edu](mailto:sumana-eee@dayanandasagar.edu)

R. Dhanalakshmi  
e-mail: [dhanalakshmi-eee@dayanandasagar.edu](mailto:dhanalakshmi-eee@dayanandasagar.edu)

## 1 Introduction

The hypothesis of PQ is explaining the efficacy of the power grid to supply authentic, absolute electricity to customers [1]. In modern power system, some standards such as IEEE and IEC indicate the importance of power quality [2–5]. A correlation between benchmarks related to PQ concept is represented in [6, 7]. Effect of most frequently used power electronic devices in modern distribution network is discussed in [8]. Due to the rapid growth of the Distributed Generation (DG) units to the grid, which increases the power quality issues, this would be the new topic of research in upcoming years. Several examinations were performed on diminishing the argumentative impact of nonlinear loads mainly power electronic (PE)-based DGs in microgrids, despite the fact that still much upgradation has to be done in this area [9–12]. A new configuration of AC/DC microgrid which comprises generation together with storage that is interconnected with AC and DC loads has emerged as one of the best infrastructures which can provide the integration of AC/DC technologies [13, 14]. A decisive review has been accomplished on PQ issues due to nonlinear loads in AC/DC hybrid microgrid and also suggested that still there is room for improvement [15–17]. The future trend of transportation sector is that conventional vehicles are replaced by electric vehicle (EV). Charging of EVs both in grid-coupled and island means of working, of power system using PV and wind, is considered in [18]. Basically, PE converter alike EV chargers are nonlinear load, its characteristics not only disturb the voltage configuration of the system but also initiate harmonics in the current, and the elimination of harmonics by UPQC using modified optimization techniques is presented in [19, 20]. Mitigation of power quality by multi-level inverter while using the electric vehicles is presented in [21]. The custom power device whose construction is based on the fundamentals of p–q theory and is emerged as most promising device in intensifying the PQ of both voltage as well as current is unified power quality conditioner (UPQC). Considering to the effective standards of the component existing in UPQC, it can be applied to both single and for three-phase supplies, but there arises stability issues when three individual single-phase apparatuses are resemblant to get a three-phase UPQC [22]. Numerous ways of solving the power quality problems using UPQC when it is connected to grid and off-grid have been studied, but these solutions are not turned as global solution [23–26]. Still, a promising solution is required for power quality intensification in the area of hybrid microgrid using custom power devices. The gaps explored from the above researches in diminishing the PQ riddles owing to the variation caused by unpredictable loads in distribution system are as follows: (i) Though review suggests the advantages of hybrid AC/DC microgrid in energy system, but the invent of power electronics devices modified the load characteristics of customer. Therefore, investigation on PQ issues in hybrid AC/DC MGs is still an area of research. (ii) Several ways of resolving the power quality problems using UPQC when it is connected to grid and off-grid have been studied, but these solutions are not turned as global solution. Still, a promising solution is required for PQ enrichment in the area of hybrid AC/DC microgrid using custom power devices in the presence of nonlinear loads.

In this work, the proposed system power quality is enhanced by using two-level inverters, i.e., UPQC when the EVs are connected as load. Simulation is performed in MATLAB 2017b context for three cases and three scenarios for each case. The results are validated in IEEE 14 bus microgrid environment. The novelty of this work is as follows: (i) Designing of hybrid AC/DC MG by modeling the DC grid using PV with effective converter, (ii) Modeling of PV-powered UPQC for enhancement of power quality in hybrid AC/DC microgrid, (iii) Modeling of EV charger and dynamic load, (iv) Testing and validating the PV-based UPQC under the standard IEEE 14 bus microgrid test environment for power quality issues caused by EV charger and dynamic load. This paper is mainly organized into three sections: Sect. 1 provides introduction about power quality issues due to the EV charger, hybrid AC/DC microgrid architecture, and custom power devices. In Sect. 2 block diagram of the proposed network and standard IEEE 14 bus system, its control scheme and design of the dynamic load are discussed in comprehensive. Section 3 provides the outcome and discussion of the proposed evaluating system and the standard IEEE 14 bus system.

## 2 Proposed Methodology

PQ issues of the proposed system as a consequence of penetration of EV smart charger and dynamic loads are analyzed for grid coupled as well as in off-grid mode. The analysis is carried in the following way: At first, the proposed analysis system is examined for three cases and three scenarios with EV smart charger and the same system is validated in standard IEEE 14 bus microgrid model distribution system.

Figure 1 represents the schematic outline of proposed hybrid AC/DC MG system. The comprehensive narration of the schematic structure is discussed in this way.

### 2.1 Modeling of AC Grid System

The principal AC grid is modeled in MATLAB tool by way of a configurable three-phase voltage source, a switch, a three-phase 200 kVA distribution transformer with a minimal power capacity of 1 MVA and delta-star connected. This traditional AC distribution network comprises distribution conduit, operating, susceptible, and harmonic loads. The loads, i.e., three commercially available EVs with single-phase 16 A (230 V) charger and 24 kWh lithium-ion (Li-ion) battery are placed at the tail end of the distribution lines. Also, a dynamic load of 45 kW resistive load (15 kW per phase) tractable per single phase in 1 kW steps is placed at the end of distribution lines.

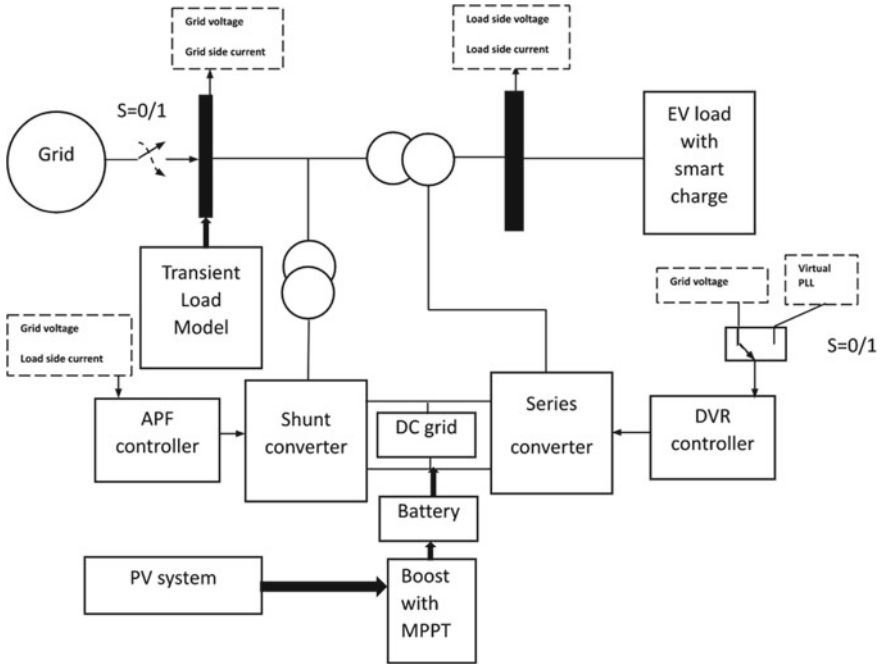


Fig. 1 Block diagram of proposed AC/DC hybrid microgrid system

## 2.2 Modeling of DC Distribution System

For the DC microgrid, the primary source of energy is the PV arrays that gives the utmost beneficial power, with a magnitude of 800 V in the DC network using a step-up DC/DC converter. The simulated DC segment of the AC/DC hybrid MG comprises 700 kW PV arrays that are controlled by Perturb and observe maximum power point (MPPT) tracing approach and a 600 V/500 Ah Li-ion battery [27].

## 2.3 Load

The operation of EV battery charge controller is like a droop controller. The EV intelligent charge regulator directs prescribed current to the charger as per electric mains' voltage dip state. It is a unidirectional charger whose charging rate can be modulated between 6 and 16 A. Figure 2 shows the closed-loop system of smart EV charger.

- A simple transient load of 45 kW is considered in this test system and is made it to run for 1 s. At initial, the 1/6th of 45 kW is connected. Then, the 2/6th time the 2/6th of the load is connected. The notion is given as the numerical model [28].

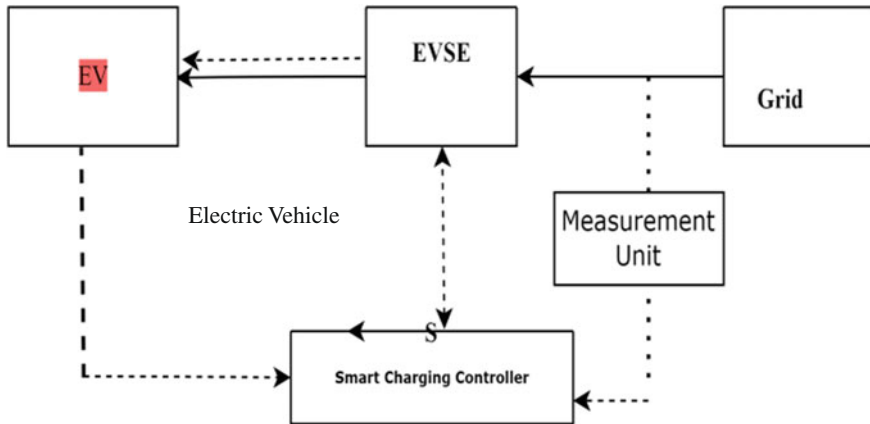


**Fig. 2** Control scheme of EV smart charger

$$P_{\text{load}}(i) = \left(\frac{i}{6}\right) * P; \text{ here } i = 1, \dots, 6; P \text{ is the load.} \quad (1)$$

## 2.4 Proposed Approach

If the switch  $S = 1$  then the proposed AC/DC hybrid microgrid operates in grid attached mode which indicates that three phase locked loop (PLL) is active, which is shown in the schematic diagram in Fig. 1. If  $S = 0$  then the proposed system operates in islanded mode. The power from the DC grid to the load through the UPQC, which functions as the synchronizing inverter. The energy to the DC grid is supplied by solar panel which is attached to the DC/DC converter, which in turn ties up with battery storage. This configuration contributes the steady DC link potential. Synchronizing inverter, i.e., UPQC avails this voltage for the enhancement of PQ in grid-connected way and converts the DC to AC in off-grid manner.

## 2.5 Control Scheme

The UPQC is a combo of shunt active power filter (SAPF) and series-controlled inverter, i.e., DVR. UPQC resolves PQ problems related to voltage and current.

Figure 3 shows the regulation strategy of UPQC. The control method of APF identifies the estimated values and generates the required compensation alert. These signals are then linked with hysteresis controller and the desired control signals are initiated. Similarly, series-connected DVR determines the signal associated with

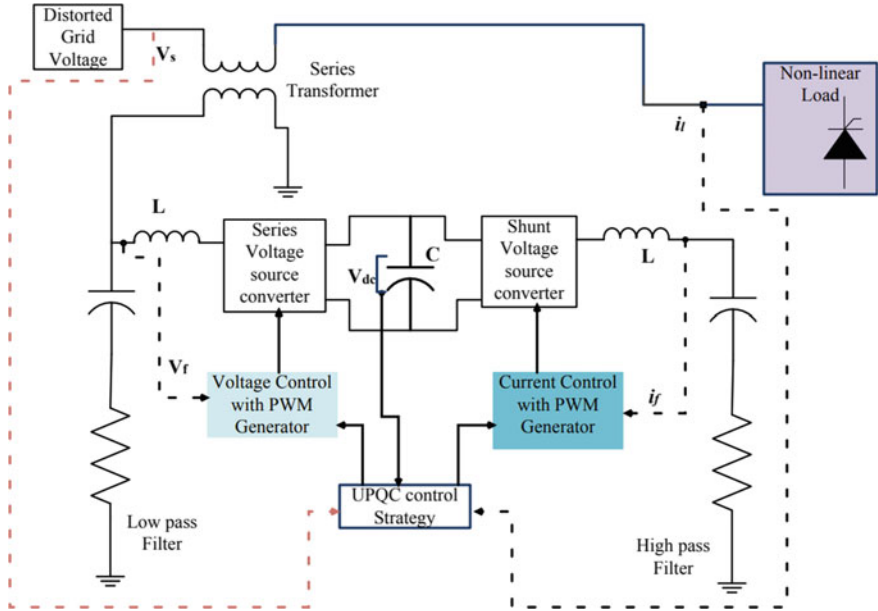


Fig. 3 Control scheme of UPQC

input voltage for sag/swell identification. This identified signals are then fed in pulse duration modulation regulator and the desired gate signals are originated.

### 2.6 Modeling of AC/DC Hybrid Microgrid in IEEE 14 Bus System

IEEE 14 bus system is test bed which constitutes a simple estimation of the United States (US) Electric Power system. It includes 14 buses, 5 generators, and 11 loads.

One-line illustration of IEEE 14 bus MG model distribution network is represented in Fig. 4. The main grid is of 69 kV, 100 MVA electrical transmission system, with  $X/R$  ratio of 10, which in turn is stepped down to a voltage of 13.8 kV. In this work, Bus number 13 is of 13.8 kV which is stepped down to 220 V using a step-down transformer. Buses which is indicated in blue color are 13.8KV and indicated in green color are of 220V. The green color buses 2 and 5 represents the voltage at distribution side, which forms the DC grid. Bus 13 is the AC grid, and the PV-powered UPQC is connected between Buses 2 and 5. The simulation is carried out in MATLAB 2017b environment, for three cases and three scenarios with EV load and dynamic load. The consequence of including PV-powered UPQC is examined in the standard IEEE 14 bus platform. MATLAB 2017b is considered for analyzing and indicating the simulation results [27, 28]. Figure 4 represents the IEEE 14 bus system modelled as





**Scenario 3 (SCN 3):** The smart charger is in charging condition only at single phase [28].

**Scenario 1, Case 1: EV smart charger is in charging mode with minimum of 6 A current**

It is noticed from Fig. 5 that in the absence of UPQC, smart charger has helped to boost the voltage at the grid side, but every second increase in the dynamic load increases the smart charger current to maintain the grid voltage. In this case, the grid voltage is maintained at 194 V.

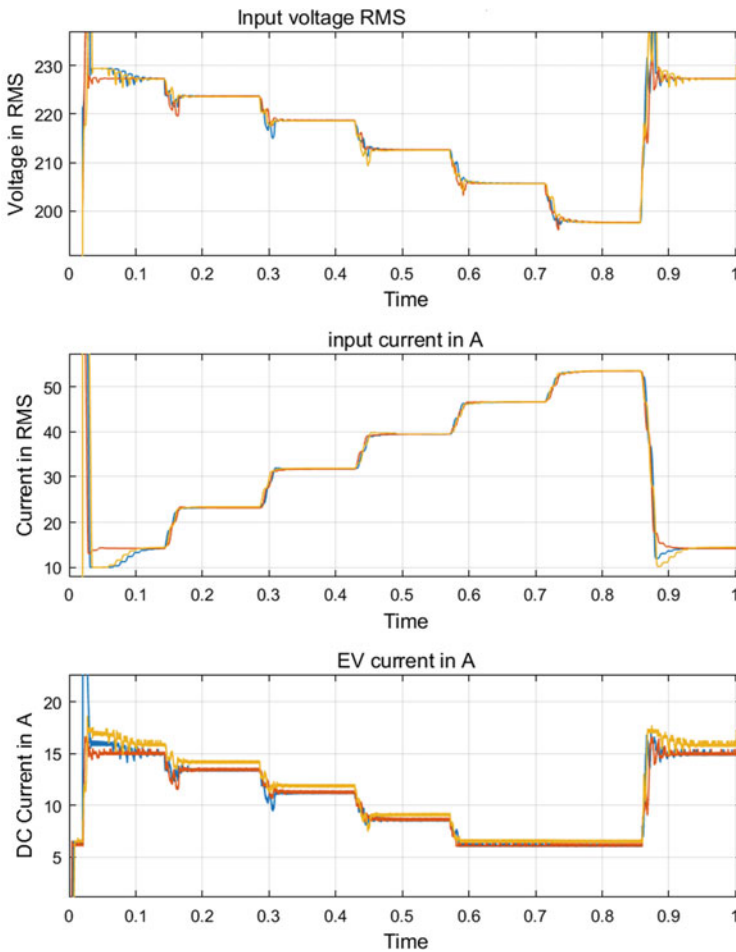


**Fig. 5** Voltage, current of grid and EV current in RMS value: SCN 1, Case 1

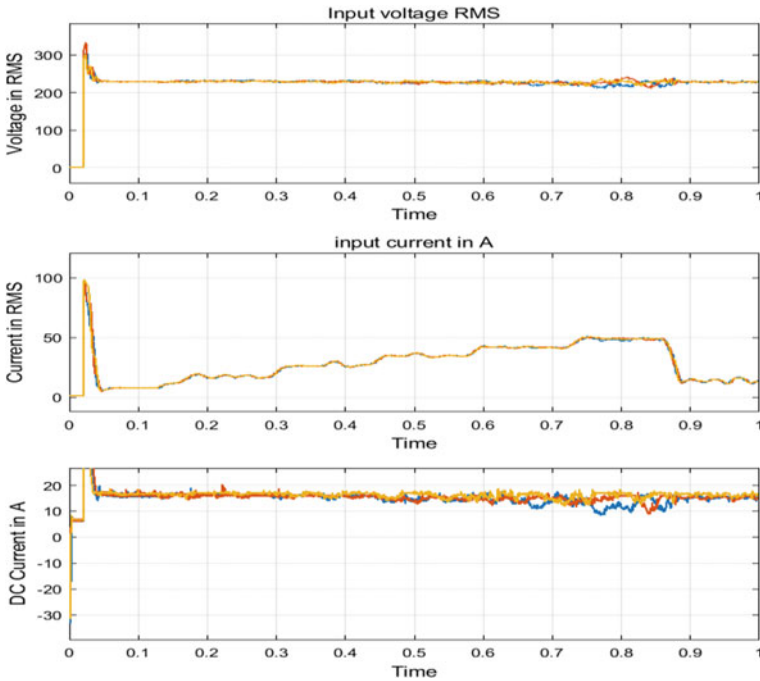


Fig. 6 RMS values of voltage and current of grid and EV current: Scenario 1, Case 2

**Scenario 1, Case 2: The UPQC is connected to the network and the smart EV charger is in charging condition**

In Case 2, the combination of UPQC and the smart EV charger action maintains the voltage at 220 V which is shown in Fig. 6.

**Scenario 1, Case 3: In Case 3, the system is detached from the grid, but the UPQC is connected to the system**

It can be seen from Fig. 7 that the smart charger work efficiently and maintains the grid voltage to 230V in case 3.

The values of EV current, grid voltage, current and voltage harmonics, power factor of scenario 1 for all the three cases are estimated and is tabulated in Table 1.

**Scenario 2: The smart EV charger is in action at two phases only**

The proposed system is tested under unstable status. Here, smart EV charger and the transient load operate at two phases. This invents instability in the system.

In Case 1, i.e., in the absence of UPQC, the voltage is slightly improved to 196 V. The voltage is improved slightly compared to Scenario 1. In Case 2, UPQC and smart EV charger action maintain the grid voltage at 220 V, i.e., within the safer limit. The grid is detached and the outcomes are same as Scenario 1 in Case 3. The values of

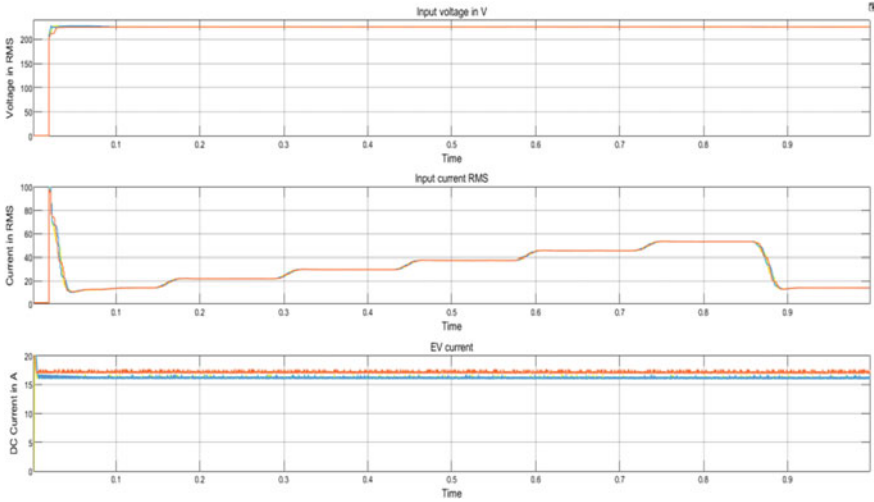


**Fig. 7** Voltage, current of grid and EV current in RMS: Scenario 1, Case 3

**Table 1** Comparative analysis of AC/DC hybrid microgrid system [26]

Cases	Parameters	SCN 1	SCN 2	SCN 3
Case 1	Grid voltage (V)	194	196	199
	Grid current (A)	55	55	56
	Percentage voltage THD	19.52	5.38	12.21
	Percentage current THD	20.38	3.81	3.95
	EV charger current (A)	6	6	6
	P.f (min)	0.5	0.65	0.72
Case 2	Grid voltage (V)	220	210	213
	Grid current (A)	50	35	28
	Percentage voltage THD	4.39	4.07	1.72
	Percentage current THD	4.06	6.13	5.08
	EV charger current (A)	9	9	10
	P.f (min)	0.78	0.84	0.8
Case 3	Grid voltage (V)	220	220	220
	Grid current (A)	30	30	28
	Percentage voltage THD	2.59	5.38	0.47
	Percentage current THD	3.29	3.81	5.61
	EV charger current (A)	9	9	9
	P.f (min)	0.95	0.94	0.93

grid voltage, EV current, voltage and current harmonics, power factor of Scenario 2 for all the three cases are tabulated in Table 1.

### **Scenario 3: EV smart charger is in action with only single phase**

The Scenario 3 discusses the unbalancing due to EV charger in charging condition for only one phase. The C phase is connected with dynamic load which creates the sag in voltage. In Case 1, the grid voltage is little bit compensated; it reached up to 199 V, because of the connection of EV smart charger, but it is not within safer limit. In Case 2, the UPQC and smart EV charger are connected and the voltage is steady between the phases. The RMS value of voltage is 213 V. PV based DC grid provides the power to the load through UPQC and the voltage is maintained at 220V within safe limit in the islanding operation of case 3. The values of grid voltage, EV current, voltage and current harmonics, power factor of scenario 2 for all the three cases are tabulated in Table 1.

Three colors in the graph indicate three-phase colors (i.e., R Y B or A B C).

## ***3.2 Performance Analysis of UPQC in Standard IEEE 14 Bus Microgrid Model Distribution System***

**Scenario 1, Case 1:** EV charger is in charging state with minimal current of 6 A in all the three phases and the UPQC is not connected.

Due to the EV charger in charging state, the grid voltage is managed at 106 V which is shown in Fig. 8. The grid current is 103 A and the EV current is 6 A.

**Scenario 1, Case 2:** EV smart charger is in operation with minimum current of 6 A in all the three phases and the UPQC is connected to the system.

In Case 2, when UPQC is brought into action, there is an improvement in the voltage. Due to the effect of UPQC, the RMS value of voltage is maintained at 127 V and decreases the current to 100 A which is shown in Fig. 9.

**Scenario 1, Case 3:** EV smart charger is in charging mode, and the UPQC is attached to the system, but the grid is disconnected from the main supply.

In Case 3, during island mode, PV-powered UPQC maintains the grid voltage to nearly equal RMS value of the voltage, i.e., at 120 V which is shown in Fig. 10. All other parameters such as power factor, EV current, Voltage and current harmonics are in safer limit and is tabulated in Table 2.

### **Scenario 2: EV smart charger operates at two phases only**

The proposed system is tested under unbalanced condition in standard IEEE 14 bus microgrid environment. This scenario functions for only two phases. In Case 1 without UPQC, there is voltage sag, and it is maintained at 104 V, whereas in Case 2 and Case 3, in the presence of UPQC system, voltage is maintained at its RMS value. All remaining parameters are within the limit as tabulated in Table 2.

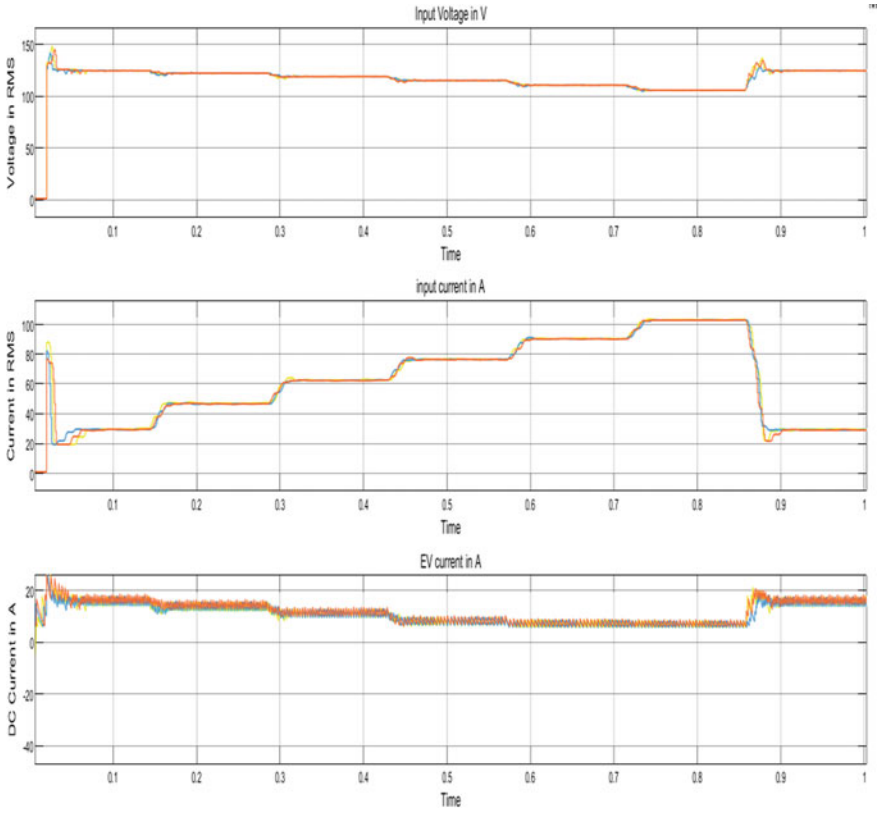


Fig. 8 RMS voltage and current of grid and EV current: Scenario 1, Case 1

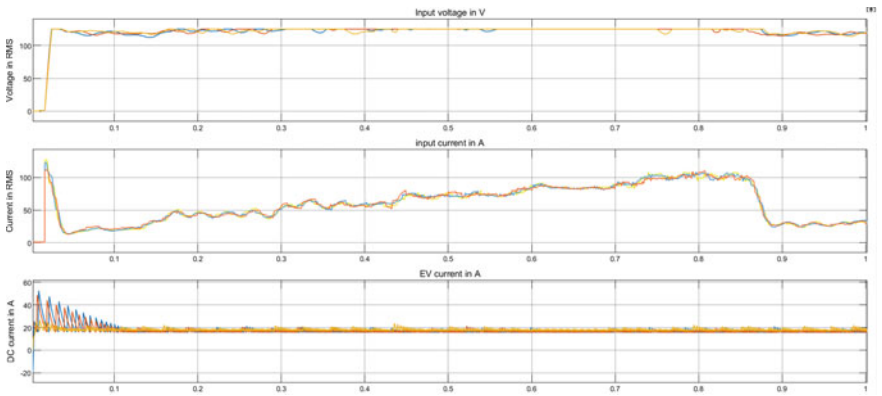
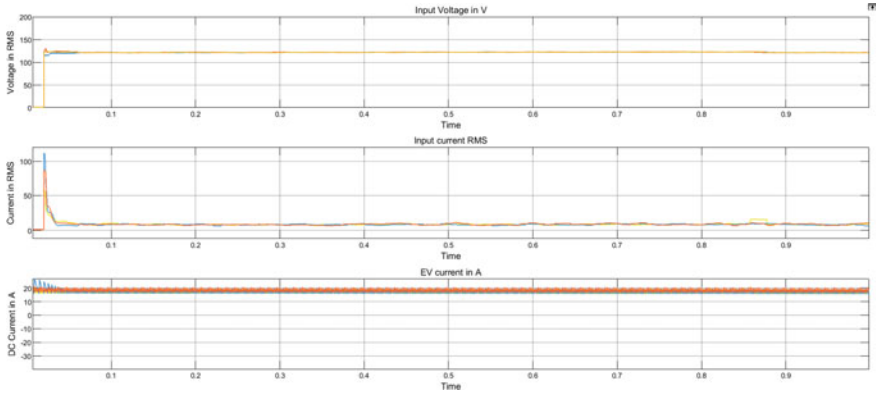


Fig. 9 Voltage and current of grid in RMS: Scenario 1, Case 2



**Fig. 10** RMS values of voltage and current of grid and EV current: Scenario 1, Case 3

**Table 2** Comparative analysis of scenarios in IEEE 14 bus

Cases	Parameters	Scenario 1	Scenario 2	Scenario 3
Case 1	Grid voltage (V)	106	104	104
	Grid current (A)	103	98	100
	Percentage voltage THD	4.91	4.6	4.6
	Percentage current THD	2.39	4.64	2.39
	EV charger current (A)	6	6	6
	P.f (min)	0.7	0.5	0.72
Case 2	Grid voltage (V)	127	127	125
	Grid current (A)	96	80	50
	Percentage voltage THD	1.91	3.85	2.25
	Percentage current THD	5.55	4.02	6.07
	EV charger current (A)	16	16	16
	P.f (min)	0.5	0.5	0.8
Case 3	Grid voltage (V)	121	123	121
	Grid current (A)	10	12	10
	Percentage voltage THD	3.52	9.44	4.27
	Percentage current THD	4.58	4.58	6.40
	EV charger current (A)	16	16	12
	P.f (min)	0.5	0.65	0.7

**Scenario 3: The smart charger is in charging condition at only one phase**

The Scenario 3 operates at only one phase, where both the loads are connected at C. In the absence of UPQC (Case 1), there is voltage sag, and even though smart charger is in charging mode, it can able to maintain 104 V, whereas in Case 2 and

Case 3, in the presence of UPQC system, voltage is maintained at its RMS value. All remaining parameters are within the limit as tabulated in Table 2.

## 4 Conclusion

PQ issues due to the penetration of EV charger in the proposed AC/DC hybrid microgrid system is analyzed for three cases and three scenarios. PV-powered UPQC is capable of resolving these issues in the grid system. System is analyzed for both in coupled to grid as well as in island modes.

Voltage and harmonic-related issues have raised in the grid system due to the attachment of EV smart charger. These analyses are done for grid-coupled and isolated mode with and without PV-powered UPQC. From the results, it is evident that voltage levels are improved, power factor is also in the acceptable limit, and also voltage and current harmonics are also within the safer range. Power quality issues due to EV charger are also analyzed and tested for the same cases and scenarios in the standard IEEE 14 bus microgrid environment. The results of all scenarios for the three cases are tabulated for the proposed AC/DC hybrid microgrid network in Table 1, and the validated results for the standard IEEE 14 bus microgrid environment are listed in Table 2. From these outcomes, it is evident that voltages are below the RMS value (i.e., below 200 V in test system and it is below 120 V in the standard system) for Case 1 (i.e., when UPQC is not inaction). There is an improvement in the voltage stability both in test as well as in standard IEEE 14 bus system when UPQC is connected (i.e., in Case 2). In the off-grid mode, the DC power is supplied to the load via battery. The PV and accumulator are acting at one time to satisfy both EV and the transient load. UPQC is performed well comparatively in off-grid mode, i.e., in Case 3. In both the system power factors, EV currents are in acceptable limit. Thus, the performance of PV-powered UPQC is validated in standard IEEE 14 bus microgrid and provides better performance.

## References

1. Agarwal A, Kumar S, Ali S (2012) A research review of power quality problems in electrical power system. *MIT Int J Electr Instrum Eng* 2:88–93
2. IEEE recommended practice and requirements for harmonic control in electric power systems—redline. *IEEE Std 519-2014 (revision of IEEE Std 519-1992)—redline (2014)*, pp 1–213
3. Sakthivel K, Das SK, Kini K (2003) Importance of quality AC power distribution and understanding of EMC standards IEC 61000-3-2, IEC 61000-3-3 and IEC 61000-3-11. In: *Proceedings of the 8th international conference on electromagnetic interference and compatibility, INCEMIC*. IEEE, pp 423–430
4. IEEE draft guide for testing the electrical, mechanical, and durability performance of wildlife protective devices on overhead power distribution systems rated up to 38 kV. *IEEE P1656/D10*, Aug 2010, pp 1–14



5. Compatibility E (2008) Part 4-30: testing and measurement techniques—power quality measurement methods. IEC Standard, p 61000
6. Halpin SM (2005) Comparison of IEEE and IEC harmonic standards. In: IEEE power engineering society general meeting, vol 3, pp 2214–2216
7. Balasubramaniam P, Prabha S (2015) Power quality issues, solutions and standards: a technology review. *J Appl Eng Sci* 18:371–380
8. Mauthe G, Heinemann L, Westermann D (2001) Economical power quality enhancement in MV distribution networks by power electronics solutions. In: Proceedings of the 16th international conference and exhibition on electricity distribution. Part 1: contributions CIRED (IEE conference publ no 482), vol 2, p 5
9. Temerbaev S, Dovgun V (2014) Improvement of power quality in distributed generation systems using hybrid power filters. In: Proceedings of the 16th international conference on harmonics and quality of power (ICHQP). IEEE, pp 694–698
10. Lee T-L, Yang S-S, Hu S-H (2014) Design of decentralized voltage control for PV inverters to mitigate voltage rise in distribution power system without communication. In: 2014 international power electronics conference (IPEC-Hiroshima 2014-ECCE-ASIA). IEEE, pp 2606–2609
11. Elbaset AA, Hassan M (2016) Design and power quality improvement of photovoltaic power system. Springer; Tiwari AK, Jhala A. Improvement of power quality in distribution system with grid connected RES
12. Zin AAM, Naderipour A, Habibuddin MB, Khajehzadeh A (2006) Design a new compensation control strategy for grid-connected WT and MT inverters at the microgrid
13. Wang P, Goel L, Liu X, Choo FH (2013) Harmonizing AC and DC: a hybrid AC/DC future grid solution. *IEEE Power Energy Mag* 11(3):76–83. <https://doi.org/10.1109/MPE.2013.2245587>
14. Karabiber A, Keles C, Kaygusuz A, Alagoz B (2013) An approach for the integration of renewable distributed generation in hybrid DC/AC microgrids. *Renew Energy* 52:251–259
15. Kaushik RA, Pindoriya NM (2014) A hybrid AC-DC microgrid: opportunities & key issues in implementation. In: IEEE 2014 international conference on green computing communication and electrical engineering (ICGCCEE), Coimbatore, India, 6–8 Mar 2014. <https://doi.org/10.1109/icgccee.2014.6922391>
16. Singh B, Chandra A, Al-Haddad K (2015) Power quality problems and mitigation techniques, 1st edn. Wiley
17. Durante L, Nielsen M, Ghosh P (2017) Analysis of non-sinusoidal wave generation during electric vehicle charging and their impacts on the power system. *Int J Process Syst Eng* 4(2–3):138–150
18. Kurfirt M, Kaspirek M, Hlavnicka J (2019) E-mobility impact on supply in distribution grid. In: 2019 20th international scientific conference on electric power engineering (EPE), pp 1–4
19. Karmaker AK, Roy S, Ahmed R (2019) Analysis of the impact of electric vehicle charging station on power quality issues. In: International conference on electrical, computer and communication engineering, pp 7–9
20. Ye J, Gooi HB, Wu F (2018) Optimal design and control implementation of UPQC based on variable phase angle control method. *IEEE Trans Ind Inform* 14(7):3109–3123
21. Kushwaha R, Singh B (2019) Power factor improvement in modified bridgeless landsman converter fed EV battery charger. *IEEE Trans Veh Technol*
22. Han B et al (2006) Combined operation of unified power quality conditioner with distributed generation. *IEEE Trans Power Delivery* 21(1):330–338
23. Reddy GS (2010) Feasibility analysis of DGSC-UPQC. *Int J Res Rev Appl Sci* 4(1):32–47
24. Khorasani PG, Joorabian M, Seifossadat SG (2017) A new proposal for the design of hybrid AC/DC microgrids toward high power quality. *Turk J Electr Eng Comput Sci* 25:4033–4049. <https://doi.org/10.3906/clk-1609-74>
25. Malik H, Ahmad MW, Kothari DP (eds) (2022) Intelligent data analytics for power and energy systems. Springer Singapore, pp XXII, 641. ISBN: 978-981-16-6081-8. <https://doi.org/10.1007/978-981-16-6081-8>

26. Tomar A et al (eds) (2022) Proceedings of 3rd international conference on machine learning, advances in computing, renewable energy and communication: MARC 2021, vol 915. Springer Nature, pp XV, 781. ISBN: 978-981-19-2830-7. <https://doi.org/10.1007/978-981-19-2828-4>
27. Sumana S, Dhanalakshmi R, Dhamodharan S (2022) Validation of photovoltaics powered UPQC using ANFIS controller in a standard microgrid test environment. *Int J Electr Comput Eng* 12(1):92–101. ISSN: 2088-8708. <https://doi.org/10.11591/ijece.v12i1>
28. Ortiz L, Orizondo R, Aguila A, Gonzalez JW, Lopez GJ, Isaac I. Hybrid AC/DC microgrid test system simulation: grid-connected mode. <https://doi.org/10.1016/j.heliyon.2019.e02862>
29. Martinenas S, Knezovic K, Marinelli M. Management of power quality issues in low voltage networks using electric vehicles: experimental validation. *IEEE Trans Power Delivery*. <https://doi.org/10.1109/tpwrd.2016.2614582>
30. Rao SS, Rangaswamy D (2021) Power quality mitigation and transient analysis in AC/DC hybrid microgrid for electric vehicle charging. *Indones J Electr Eng Comput Sci* 24(3):1315–1322. ISSN: 2502-4752. <https://doi.org/10.11591/ijeecs.v24.i3>

# Short-Term Electricity Load Forecasting Using Modified Hidden Markov Model



Poras Khetarpal, Neelu Nagpal, Mahesh Kumar, D. Lakshmi,  
and Neelam Kassarwani

**Abstract** This study proposes a modified Hidden Markov Model (HMM) as a method for predicting electricity on an hourly basis in the Delhi region. Typically, load prediction involves utilizing statistical techniques that need significant modifications in the data to adapt to the random nature of the energy demand. Alternatively, data-based methods like artificial neural networks (ANNs) rely heavily on data to deliver reliable findings. An attempt is made to implement HMM taking into account short-term electricity demand as a non-stationary time series. This provides satisfactory prediction results even with limited data. Furthermore, the proposed modified HMM technique outperforms alternative techniques in terms of computational time and complexity.

**Keywords** Electricity demand · Hidden Markov Model · Short-term electricity forecasting

## 1 Introduction

Short-term demand for electricity forecasting is vital for power generation and distribution. It is useful for the electricity sector in demand estimation, distribution planning, scheduling, demand side management, etc. Electricity forecasts are categorized as long-term, medium, and short-term forecasts. Long-term electricity prediction is obtained using several months of data. Long-term electricity demand forecasts are

---

P. Khetarpal · M. Kumar

IT Department, Bharati Vidyapeeth's College of Engineering, New Delhi 110063, India

N. Nagpal (✉) · N. Kassarwani

EEE Department, Maharaja Agrasen Institute of Technology, Delhi 110086, India

e-mail: [nagpalneelu1971@ieee.org](mailto:nagpalneelu1971@ieee.org)

D. Lakshmi

School of Computing Science and Engineering, VIT Bhopal University, Bhopal, MP 466114, India

e-mail: [lakshmi.d@vitbhopal.ac.in](mailto:lakshmi.d@vitbhopal.ac.in)

© The Author(s), under exclusive license to Springer Nature Singapore Pte Ltd. 2024

H. Malik et al. (eds.), *Renewable Power for Sustainable Growth*,

Lecture Notes in Electrical Engineering 1086,

[https://doi.org/10.1007/978-981-99-6749-0\\_4](https://doi.org/10.1007/978-981-99-6749-0_4)

generally easier to obtain than short-term forecasts since seasonal patterns are clearly visible in the long-term data. Hence, this type of data is easier than a forecast model. On the other hand, short-term electricity demand, especially hourly and half-hourly demand is highly stochastic in nature showing no such clear trends as compared to long-term electricity demand forecasting [1]. Hourly short-term forecast is required for manufacturing and planning-related purposes so that the demand is not under- or over-valued. A variety of methodologies have been developed to estimate short-term demand including intelligent methods [2–4], statistical methods [5], machine learning methods [6, 7], and many more. In the case of statistical technique, detrending and other modifications to the non-stationary data are necessary. In recent years, other methods are used such as artificial neural networks (ANNs). ANN requires years of data and high computational power to produce forecasts [8].

HMM is suitable for application in the non-stationary nature of the time series and stochastic processes. It has found applications in various fields such as stock market prediction, speech recognition, and other varied fields [9–14]. In this study, the HMM algorithm is modified using Bayesian inference for better performance. In addition, the Markov Chain Monte Carlo (MCMC) approach is utilized to determine the parameters of forecasting model rather than the conventional Baum–Welch procedure. The HMM and its modified version are used for short-term electricity prediction using hourly electricity demand of 2 years (2018–2019) for Delhi city. Following parameter estimation using these HMM methods, forecast results are compared to test data in terms of mean absolute error (MAE) and root mean square error (RMSE). In addition, other forecasting models based on auto-regression (AR), auto-regressive moving average (ARIMA), exponential moving average (EMA), and long short-term memory networks (LSTM) techniques are used. The workflow structure of the proposed model is shown in Fig. 1. The main contributions of work are summarized below:

- This study explores the application of a modified HMM technique to perform the STLF forecasting model which is simple and requires limited training data and less computational time.
- This study looks at how well the suggested forecast model performs for STLF in a metropolitan city with variable weather, including excessive heat in the summer and extreme cold in the winter. Further, the load pattern in this city is unstable due to its fast-paced urban development.
- Viterbi algorithm (VA) is used to train the model by determining the parameters using the Baum–Welch algorithm.
- Comparative analysis with various alternative forecasting approaches such as AR, ARIMA, EMA, LSTM, and HMM to validate the suggested forecasting technique's superior performance over others.

The paper is structured as: The introduction and background of the present work are presented in Sect. 1. A description of HMM method is presented in Sect. 2. The proposed electricity forecasting approach and its implementation are discussed in Sect. 3. A simulation study and result analysis are presented in Sect. 4 to validate the performance of the modified HMM forecasting approach. Section 5 presents the conclusion along with the future direction of this work.

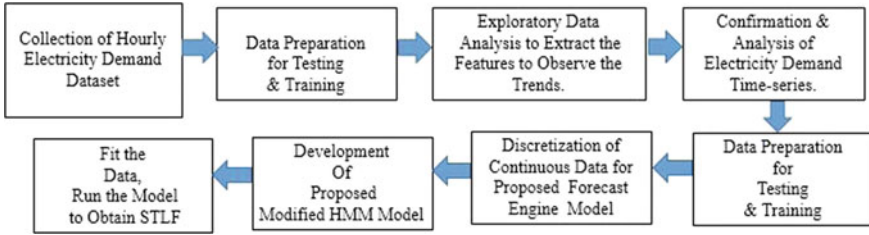


Fig. 1 Workflow structure of proposed forecasting model

## 2 Hidden Markov Model

HMM is useful for non-stationary data due to its stochastic nature. Being a probabilistic model, it is applicable to a time series which can be assumed as a Markov process. This is a kind of process in which the probability of each event happening in a particular sequence is determined only by its preceding state. The distribution of conditional probabilities for the subsequent state depends entirely on the previous state. It is mathematically represented as:

$$\begin{aligned}
 \text{Prob}(Y_n = y_n | Y_{n-1} = y_{n-1}, \dots, Y_0 = y_0) \\
 = \text{Prob}(Y_n = y_n | Y_{n-1} = y_{n-1})
 \end{aligned}
 \tag{1}$$

In HMM, the input sequence is assumed to be the “hidden” state as the input variable is not actually being directly observed. The observed variables are calculated based on the transition probabilities of the input (or hidden) sequence. The HMM can be represented with its parameters in Fig. 2. The observable  $Y$  (forecast output) is obtained by a sequence of hidden states,  $y$  (sequenced input). Assume that the transitions between hidden states have the Markov property. They are obtained by the transition probability matrix,  $A$ , by the emission probability matrix,  $B$  (sometimes  $\theta$ ). Also,  $\pi$  denotes the initial probability. With the following model parameters and observed data, the sequence of hidden states is estimated. The model parameters are determined by the iterative Baum–Welch algorithm [15] for expectation–maximization where the forward–backward technique is used. The Baum–Welch method identifies local maxima as follows:

$$\theta^* = \arg \max_{\theta} \text{Prob}(Y | \theta)
 \tag{2}$$

where  $\theta$  maximizes the probability of observing  $X$ . Viterbi algorithm [16] discovers the most probable sequence of hidden states. For an observation  $i$ , this algorithm computes the likelihood in terms of probability of observing  $i$ th element in state  $l$  which is  $e_l(i)$  as below

$$p_l(i, x) = e_l(i) \max_k (p_k(j, x - 1) \cdot p_{kl})
 \tag{3}$$

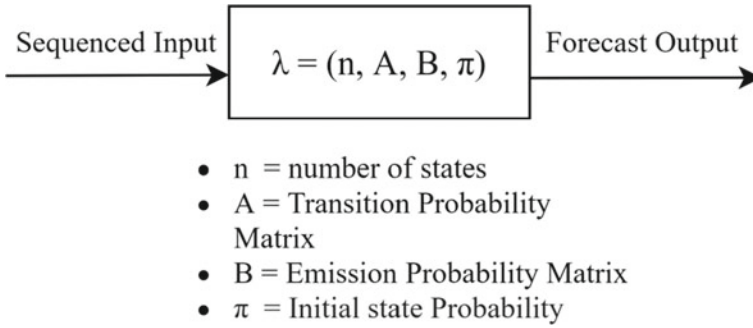


**Fig. 2** HMM

This algorithm calculates the likelihood that, given observation  $i$ , the path would end in state  $k$ .  $p_k(j, x - 1)$  = Likelihood of the most plausible path endpoint in position  $x - 1$  and in the state  $k$  with the  $i$ th element.  $p_{kl}$  = probability of transition from state  $l$  to state  $k$ .

The Viterbi method is used in the model to extract the sequence of hidden states with a series of observations. HMM parameters are then obtained using an observation likelihood matrix with the Baum–Welch procedure (known as the forward–backward algorithm). It begins with some given initialized values of the HMM parameters, and it follows the two steps for multiple iterations. This method involves two steps as follows:

**E-step: The expectation step**

$$\chi = \frac{\gamma_l(i)\sigma_l(j)}{\gamma_T q_F}, \quad \forall t, j$$

$$\xi_t(i, j) = \frac{\gamma_l(i)\alpha_{ij}\beta_j(o_{t+1}\sigma_{t+1}(j))}{\gamma_T(q_F)}, \quad \forall t, i, \text{ and } j$$
(4)

**M-step: The maximization step**

$$\hat{\alpha}_{ij} = \frac{\sum_{t=1}^{T-1} \xi_t(i, j)}{\sum_{t=1}^{T-1} \sum_{k=1}^N \xi_t(i, k)}$$

$$\hat{\beta}_{v_k} = \frac{\sum_{t=1}^T \text{s.t. } o_t=v_k \gamma_t(j)}{\sum_{t=1}^T \gamma_t(j)}$$
(5)

During E-step, “A” parameter is used for expected state occupancy counts, and “B” parameter is used for expected state transition counts. And further during the M-step, they are utilized to recalculate the probability for A and B. In the modified HMM, Bayesian HMM with inference performed via MCMC is used [17]. The Baum–Welch algorithm is not used to determine parameters in this case; instead, MCMC is used. HMM is a dynamic model as the probability of a state change is a function of

time, and it is subject to change. The number of latent or hidden states in modified HMM varies as part of the fitting process. This is done using hierarchical Dirichlet prior (HDP), and then MCMC sampling is done on the hidden states to estimate the model parameters. MCMC updates the multinomial regression coefficients  $\sigma$ , the state model parameter  $\theta$ , and the hidden variable  $Z$ .

Let  $Z_t = (Z_1, \dots, Z_t)$  be the past observed process and  $\zeta_t = (\zeta_1, \dots, \zeta_t)$  represent the order of states from time = 1 to time =  $t$ .  $f_z(\cdot)$  denotes the normal probability density function of  $Z_t \vee Z_t = s, s \in S$ , then the formulation of the joint likelihood function considering the observed data is represented as

$$\begin{aligned} \pi(y^T, z^T | \theta, \sigma) &= \pi(y^T | z^T \theta, \sigma) \pi(z^T | \theta, \sigma) \\ &= f_{z1}(y1) p_{z1}^{(1)}, z2(y2) \dots p_{zT-1, zT}^{(T-1)}, f_{zT}(yT) \\ P_{ij}^t &= \frac{\exp(x_t \sigma_j)}{\sum_{l=1}^m \exp(x_t \sigma_{il})}; \quad \text{for } i, j = 1, \dots, m. \end{aligned} \quad (6)$$

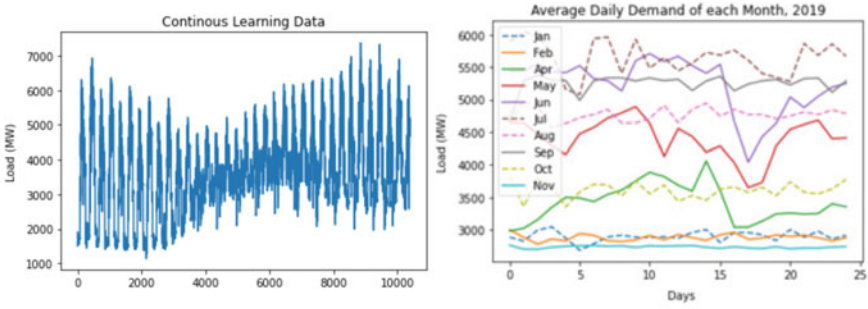
The time-dependent values of the transition matrix are obtained based on the parameter  $\sigma$  from the presented equations.

### 3 Proposed HMM as Forecasting Model

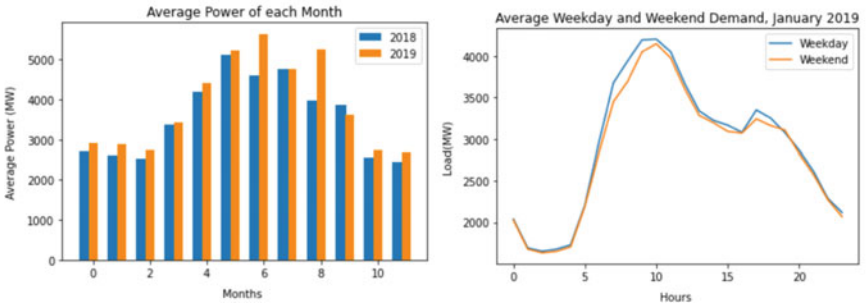
The dataset of hourly electricity demand used was obtained from the state load dispatch center, Delhi. This center is responsible for scheduling and distributing power within Delhi, exercising supervision and control over the intrastate transmission system, and monitoring grid operations, among other responsibilities. The data size was hourly electricity demand for 24 months from January 2018 to December 2019. It was divided into training and learning data (10,000 and 4000 dataset points). After exploratory data analysis, long-term and short-term trends were analyzed within the electricity demand. Since Delhi has fairly consistent and distinct seasons, long-term seasonality is observed right away. Then feature engineering and selection are done based on the observed data's tendencies.

#### 3.1 Exploratory Analysis

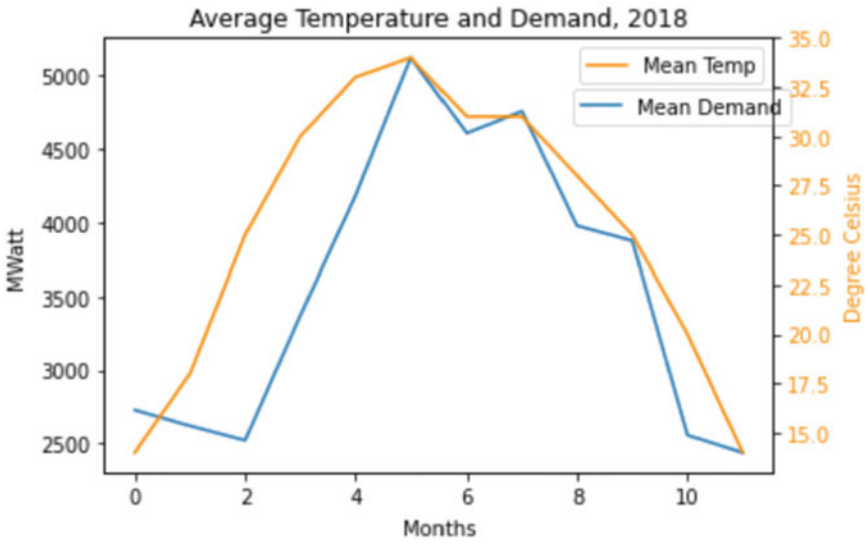
The long-term trends in Delhi's electricity demand are notably visible because of the seasonal weather changes [18]. The monthly change in demand is drastic from the lowest demand being in the winter months (November, December, January) to the highest demand being in the hottest summer months (June, July). The monthly trends are fairly consistent throughout the years. The daily and weekly electricity demands were also found to be consistent within the same month of different years as shown in Fig. 3a–f. The weekend demand was found to be only slightly less than



(a) Hourly electricity demand of Delhi. (b) Average daily demand of each month.



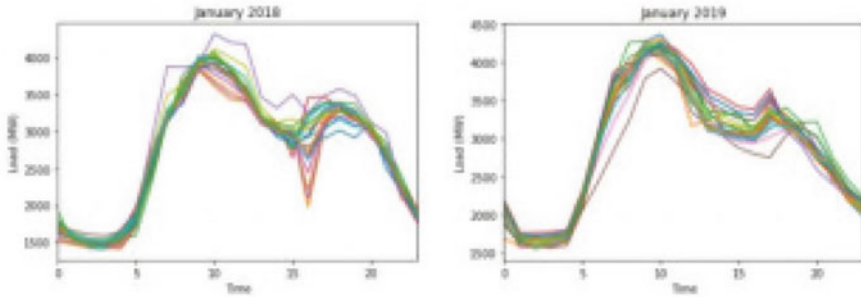
(c) Total average power of each month. (d) Weekend vs weekday demand.



(e) Average monthly temperature and demand

Fig. 3 Data preparation





(f) Daily demand of January.

Fig. 3 (continued)

the weekday demand and with the same trends. The daily and monthly temperatures were found to have a high correlation with the electricity demand. It is pertinent to mention that seasonal temperature effects as well as hourly temperature effects were prominent.

### 3.2 Data Preparation

First of all, the non-stationary nature of hourly electricity demand time series was confirmed using two methods: (i) augmented Dickey–Fuller (ADF) [19]; (ii) testing and plotting rolling mean and standard deviation.

As shown in Fig. 4, the results of the ADF test have proved the non-stationarity of the time series with a  $P$ -value significantly greater than 0.05. The rolling mean and

```

Augmented Dickey-Fuller Test Results:
ADF Test Statistic      -0.942611
P-Value                 0.773616
# Lags Used             0.000000
# Observations Used    23.000000
Critical Value (1%)    -3.752928
Critical Value (5%)    -2.998500
Critical Value (10%)   -2.638967
dtype: float64
Is the time series stationary? False
    
```

Fig. 4 ADF test on demand of a single day

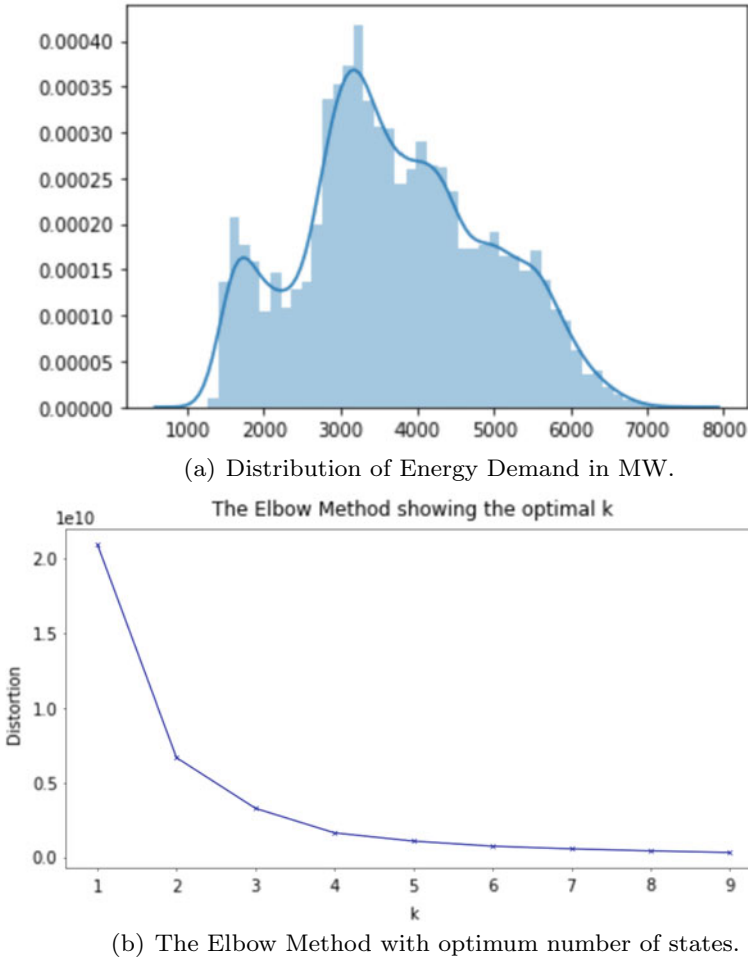


**Fig. 5** Data analysis

standard deviation were also found to be nonlinear. Since the statistical properties changed over time, it is a non-stationary time series. As illustrated in Fig. 5a, the distribution of demand was then analyzed in order to discretize the continuous data, as the HMM requires input in discrete sequences of states. An optimum number of states are computed with the use of K-means clustering [20] and the period for discretization. The elbow curve method was employed to confirm the ideal number of states for the present data as shown in Fig. 5b.

### 3.3 Modified HMM

The model was trained with the Viterbi algorithm, and the parameters ( $A$ ,  $B$ ) were determined by the Baum–Welch algorithm. The test data of 10,000 dataset points was used to train the model. The transition matrix obtained along with the emission probability matrix is shown in Fig. 6.

The number of EM algorithm iterations in the training proceeds until it reaches convergence. The number of iterations converged the EM algorithm, and this is confirmed using the HMM learn library as shown in Fig. 7.

After obtaining all the parameters, the future values are predicted and compared against test data. The modified HMM is then implemented; initially, Markov Chain Monte Carlo (MCMC) sampling is utilized to generate the starting-state probabilities, emission probabilities, and transition probability matrix as shown in Fig. 8.

Transition matrix

```
[[9.93734167e-01 1.29894375e-72 6.26583284e-03 6.04369063e-62]
 [1.96383902e-97 9.91559259e-01 2.39588751e-04 8.20115240e-03]
 [8.87642934e-03 8.25881303e-04 9.87849052e-01 2.44863708e-03]
 [2.30126829e-04 7.59934718e-03 1.38695936e-03 9.90783567e-01]]
```

Fig. 6 Emission probability matrix

```
from hmmlearn.base import ConvergenceMonitor
model.monitor_
ConvergenceMonitor(0.01,100,verbose=False)
model.monitor_.converged
```

True

Fig. 7 HMM learn library

Transition Probability

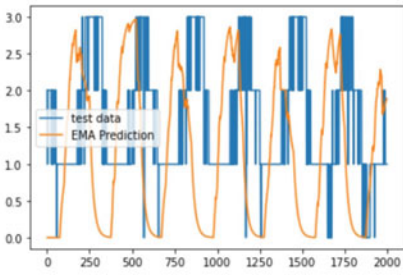
```
[0.925, 0.001, 0.002, 0.072]
[0.039, 0.015, 0.032, 0.913]
[0.174, 0.042, 0.319, 0.466]
[0.237, 0.383, 0.063, 0.316]
```

Fig. 8 Transition probability matrix

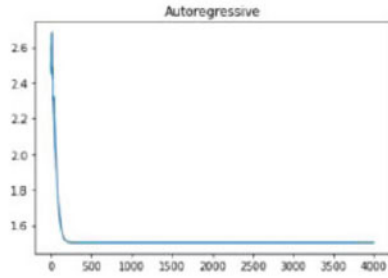
It is seen in this section that the acquired transition and emission probabilities are used to predict future electricity demand values based on training data using the HMM. The obtained model parameters from MCMC are then used to forecast the next values using this HMM, and this is termed a modified HMM approach.

## 4 Results

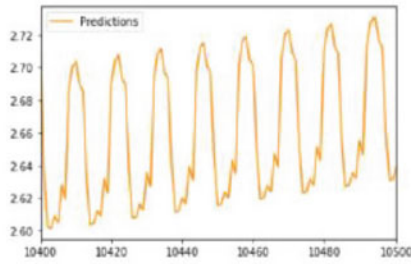
The program is developed in Python programming language on Google Colaboratory web IDE. The IDE offers a 2.30 GHz CPU clock, Haswell as the CPU family, and 2 Core CPUs. Pmdarima, Statsmodel, Pandas, and Bokeh packages are used for statistical models, whereas NumPy, Pandas, Bokeh, Sklearn, and XGBoost packages are used for machine learning models. The program is developed using the available data (refer to Sect. 3.1) on a personal computer. Different forecast approaches (such as AR, ARIMA, and EMA, as well as the LSTM and HMM) are developed and simulated, and the corresponding results are shown in Fig. 9a–f. A study is conducted to compare the forecasting performance of the recommended modified HMM with other traditional models, including LSTM and HMM. As mentioned above, the modified HMM with MCMC obtained transition and emission probabilities that are used to obtain the forecast as shown in Fig. 9f. From the results, it is indicated that statistical methods AR and ARIMA fail to perform well (as expected) on non-stationary time series. Each forecast outcome is compared to the test data, and the error metrics obtained for these models, namely MAE and RMSE, are displayed (refer Table 1). LSTM and the modified HMM have the lowest error metrics out of the five which can be inferred from Fig. 10 and Table 1. This comparative analysis validates the superior modified HMM forecast, which has the lowest MAE = 0.616 and RMSE = 0.165, respectively. In contrast, the LSTM [21–24] is known to produce the most accurate forecasts and performs well, but it required significantly more computation time and processing power than the HMM and modified HMM. LSTM model produces the best accuracy of 97.765%, and then modified HMM performed with the accuracy of 97.446. HMM has comparable error metrics to LSTM with a higher MAE and the lowest RMSE. On the other hand, LSTM, being a deep learning-based method, requires a huge dataset, and its computational time is large as compared to HMM and modified HMM which requires less data and puts less computational burden on the processor. Also, the modified HMM method is very near to accuracy as compared to LSTM. Further, the temporal complexity of the two algorithms, LSTM and MCMC for parameter estimation in modified HMM, are compared using empirical values of the runtime of the algorithms. Considering the size of the present training data, the forecast model upon which the program is run, 100 iterations of LSTM take 30–40 min to train, while 100 MCMC steps take 8 s per iteration making 13 min in total. It is known that for even larger-sized data, LSTM and other RNN models



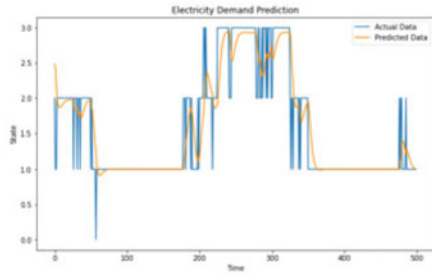
(a) EMA forecast result.



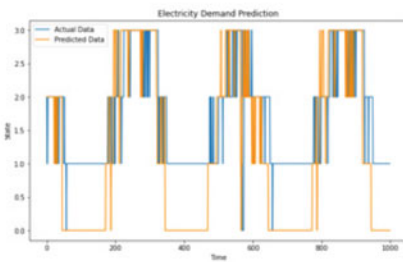
(b) AR forecast result.



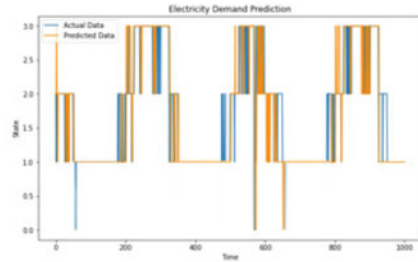
(c) ARIMA forecast result.



(d) LSTM forecast result.t.



(e) HMM forecast result



(f) Modified HMM forecast.

**Fig. 9** Forecast results using different approaches

take a lot of training time. This result analysis concludes the work in the following section.

## 5 Conclusion

This research proposes a modified HMM for short-term electricity demand forecasting. HMM is modified using Bayesian inference, using MCMC sampling to obtain the model parameters, as short-term electricity demand is a non-stationary time series with stochastic nature. From the result analysis, the overall performance of HMM

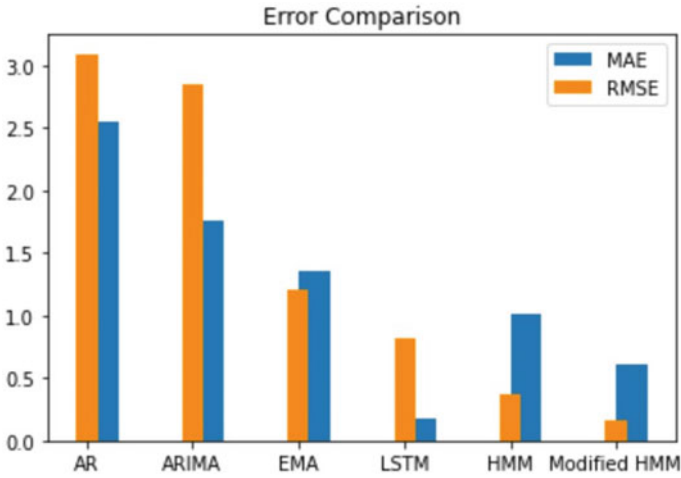


**Fig. 10** Comparative analysis using MAE and RMSE

**Table 1** Comparative performance analysis of forecasting models

Performance indices ↓	AR	ARIMA	EMA	LSTM	HMM	Proposed HMM
MAE	2.557	1.76	1.357	0.177	1.016	0.616
RMSE	3.094	2.849	1.2	0.815	0.371	0.165
% Accuracy	86.675	91.138	93.108	97.765	96.411	97.446

and its modification proves better in predicting the future electricity forecast values than all other statistical methods if accuracy, computation time, and dataset size are considered together. Also, modified HMM and LSTM have better error metrics, but LSTM is way more time-consuming, computationally complex, and takes a lot of processor power and time as compared to the HMM, whereas the MCMC sampling takes considerable computational time as compared to Baum–Welch HMM. Subsequently, it is concluded that the proposed modified HMM is capable of performing efficient short-term electricity load forecasting with limited training data, lower complexity, and overall ease of use. With the addition of weather conditions, the performance of the modified HMM approach can be improved even further. As a future direction of work, other inference methods can also be investigated for improved results. Furthermore, HMM can be incorporated into AI-based models to improve forecast accuracy into AI-based models to improve forecast accuracy when used for real-time applications.

## References

1. Alhelou HH, Parthasarathy H, Nagpal N, Agarwal V, Nagpal H, Siano P (2022) Decentralized stochastic disturbance observer-based optimal frequency control method for interconnected power systems with high renewable shares. *IEEE Trans Ind Inform* 18(5):3180–3192. <https://doi.org/10.1109/TII.2021.3107396>
2. Nilakanta Singh K, Robindro Singh K (2021) A review on deep learning models for short-term load forecasting. In: Choudhary A, Agrawal AP, Logeswaran R, Unhelkar B (eds) *Applications of artificial intelligence and machine learning. Lecture notes in electrical engineering*, vol 778. Springer, Singapore. <https://doi.org/10.1007/978-981-16-3067-5-53>
3. Sadaei HJ, de-Lima e-Silva PC, Guimarães FG, Hisyam LM (2019) Short-term load forecasting by using a combined method of convolution neural networks and fuzzy time series. *Energy* 175:365–377. ISSN 0360-5442
4. Saravanan S, Kannan S, Thangaraj C (2012) Forecasting India's electricity demand using artificial neural network. In: *IEEE-international conference on advances in engineering, science and management (ICAESM-2012)*, Tamil Nadu, pp 79–83
5. Taylor JW, McSharry PE (2007) Short-term load forecasting methods: an evaluation based on European data. *IEEE Trans Power Syst* 22(4):2213–2219
6. Son M, Moon J, Jung S, Hwang E (2019) A short-term load forecasting scheme based on auto-encoder and random forest. In: Ntalianis K, Vachtsevanos G, Borne P, Croitoru A (eds) *Applied physics, system science and computers III. APSAC 2018. Lecture notes in electrical engineering*, vol 574. Springer, Cham. <https://doi.org/10.1007/978-3-030-21507-1-21>
7. Subbiah SS, Chinnappan J (2022) Short-term load forecasting using random forest with entropy-based feature selection. In: Raje RR, Hussain F, Kannan RJ (eds) *Artificial intelligence and technologies. Lecture notes in electrical engineering*, vol 806. Springer, Singapore. <https://doi.org/10.1007/978-981-16-6448-9-8>
8. Singhal R, Choudhary NK, Singh N (2020) Short-term load forecasting using hybrid ARIMA and artificial neural network model. In: Dutta D, Kar H, Kumar C, Bhadauria V (eds) *Advances in VLSI, communication, and signal processing. Lecture notes in electrical engineering*, vol 587. Springer, Singapore. <https://doi.org/10.1007/978-981-32-9775-3-83>
9. Gupta A, Dhingra B (2012) Stock market prediction using hidden Markov models. In: *Students conference on engineering and systems*, Allahabad, Uttar Pradesh, pp 1–4
10. Varga AP, Moore RK (1990) Hidden Markov model decomposition of speech and noise. In: *International conference on acoustics, speech, and signal processing*, Albuquerque, NM, vol 2, pp 845–848
11. Starner T, Pentland A (1995) Real-time American sign language visual recognition from video using hidden Markov models. Master's thesis, MIT, Feb 1995. Program in Media Arts
12. Jia L, Najmi A, Gray RM (2000) Image classification by a two-dimensional hidden Markov model. *IEEE Trans Signal Process* 48(2):517–533. <https://doi.org/10.1109/78.823977>
13. Chen MY, Kundu A, Zhou J (1994) Off-line handwritten word recognition using a hidden Markov model type stochastic network. *IEEE Trans Pattern Anal Mach Intell* 16(5):481–496. <https://doi.org/10.1109/34.291449>
14. Srivastava A, Kundu A, Sural S, Majumdar A (2008) Credit card fraud detection using hidden Markov model. *IEEE Trans Depend Secure Comput* 5(1):37–48. <https://doi.org/10.1109/TDSC.2007.70228>
15. Turin W (1998) Unidirectional and parallel Baum–Welch algorithms. *IEEE Trans Speech Audio Process* 6(6):516–523. <https://doi.org/10.1109/89.725318>
16. David G, Forney J (2005) The Viterbi algorithm: a personal history. <https://arxiv.org/pdf/cs/0504020>
17. Djuric PM, Chun J (2002) An MCMC sampling approach to estimation of non-stationary hidden Markov models. *IEEE Trans Signal Process* 50(5):1113–1123. <https://doi.org/10.1109/78.995067>

18. Hor CL, Watson SJ, Majithia S (2005) Analyzing the impact of weather variables on monthly electricity demand. *IEEE Trans Power Syst* 20(4):2078–2085. <https://doi.org/10.1109/TPWRS.2005.857397>
19. Fuller WA (1976) *Introduction to statistical time series*. Wiley, New York. 0-471-28715-6
20. Kanungo T, Mount DMN, Netanyahu S, Piatko CD, Silverman R, Wu AY (2002) An efficient k-means clustering algorithm: analysis and implementation. *IEEE Trans Pattern Anal Mach Intell* 24(7):881–892. <https://doi.org/10.1109/TPAMI.2002.1017616>
21. Sepp H, Schmidhuber J (1997) Long short-term memory. *Neural Comput* 9(8):1735–1780. <https://doi.org/10.1162/neco.1997.9.8.1735>. PMID 9377276
22. Kong W, Dong ZY, Hill DJ, Luo F, Xu Y (2018) Short-term residential load forecasting based on resident behaviour learning. *IEEE Trans Power Syst* 33(1):1087–1088. <https://doi.org/10.1109/TPWRS.2017.2688178>
23. Tomar A et al (eds) (2022) *Proceedings of 3rd international conference on machine learning, advances in computing, renewable energy and communication: MARC 2021*, vol 915. Springer Nature, pp XV, 781. ISBN: 978-981-19-2830-7. <https://doi.org/10.1007/978-981-19-2828-4>
24. Ahmad MW et al (eds) (2022) *Intelligent data analytics for power and energy systems*. Springer Singapore, pp XXII, 641. ISBN: 978-981-16-6081-8. <https://doi.org/10.1007/978-981-16-6081-8>



# Microgrid Systems with Classical Primary Control Techniques—A Review



Sujit Kumar, H. K. Yashaswini, Naveen Sharma, and Mohit Bajaj

**Abstract** Present scenario of power engineering the fast production of energy electronics has rendered the idea of microgrid (MG) generally acknowledged. Direct current MGs have grown in popularity despite the fact that DC delivery techniques, which cause less damage and quickly align energy loading resources, are the current standard. A DCMG containing many fonts is becoming increasingly relevant as distributed output increases. The goal of this multi-source DCMG is to provide voltage support and robust value distribution. An inclusive evaluation of “state-of-the-art” processes in DCMGs is an integral part of the control methodology that provides consistent MG power and performance. This section details the DCMG’s primary and secondary control methods. Internal loop and droop control, in particular, are examined, along with their fundamental control methodologies. The supplementary rulemaking is a decentralised, self-governing system. Key outcomes and potential patterns are now finally presented. Using the hierarchical control architecture for DC MGs, this study summarises the primary control approaches. Methods of primary control, such as inner loop and droop control, are specifically discussed. We go over the pros and cons of a centralised, distributed, and decentralised approach to primary control. Both the most important results and the most likely developments in the future are laid forth.

**Keywords** Regulations · Control procedures · Primary control

---

S. Kumar (✉)

Department of Electrical and Electronics Engineering, Dayananda Sagar College of Engineering, Bengaluru, India

e-mail: [sujit-eee@dayanandasagar.edu](mailto:sujit-eee@dayanandasagar.edu)

H. K. Yashaswini

Department of Electrical and Electronics Engineering, Jain (Deemed-to-be University), Bengaluru, India

N. Sharma

Department of Electrical Engineering, IKGPTU Main Campus, Jalandhar, India

M. Bajaj

Department of Electrical Engineering, Graphic Era (Deemed to be University), Dehradun, India

© The Author(s), under exclusive license to Springer Nature Singapore Pte Ltd. 2024

H. Malik et al. (eds.), *Renewable Power for Sustainable Growth*,

Lecture Notes in Electrical Engineering 1086,

[https://doi.org/10.1007/978-981-99-6749-0\\_5](https://doi.org/10.1007/978-981-99-6749-0_5)

# 1 Introduction

Modern power networks have changed extensively in the last two decades and are dynamic adaptive structures. As the suitable solution for grid installation of dispersed sources, microgrids (MGs), a novel distributor network layout, have been developed [1, 2]. Alternative current (AC) dominates electrical networks, but it is evident that high-voltage and low-voltage systems have realised a growth in the number of DC systems in power system [3]. DC voltage networks, including storage, delivery, and energy usage stages, were rapidly expanded by the technology of electric power. The benefits of DCMGs can be drawn as follows contrasted with AC MGs [3–5]:

1. Solar panels and fuel cells are only two examples of the renewable technologies used to provide DC electricity. Because of the absence of need for further power conversions, the DC grid may be a better fit for wind turbines, which generate AC electricity by design.
2. Reactive power and frequency modulation are not required.
3. Even DC in design is the bulk of energy storage units. With an existing DC–DC transformer, battery technology can quickly be incorporated into a DC bus with lower costs and improved performance.

Provided the above benefits, DCMGs are generally acknowledged, not only for public grids, but also for further travel through electricity such as more hybrid aircraft [6]. In Fig. 1, we see the typical DCMG configuration using a single DC bus. Electric panels, wind turbines, and ESSs may all be connected to one DC bus using these electronic converters (ECs) [6].

The DCMG has many power sources; therefore, its control device must deal with maintaining a consistent control voltage, distributing the load evenly, and conserving energy. These issues necessitate a hierarchical approach to management, which

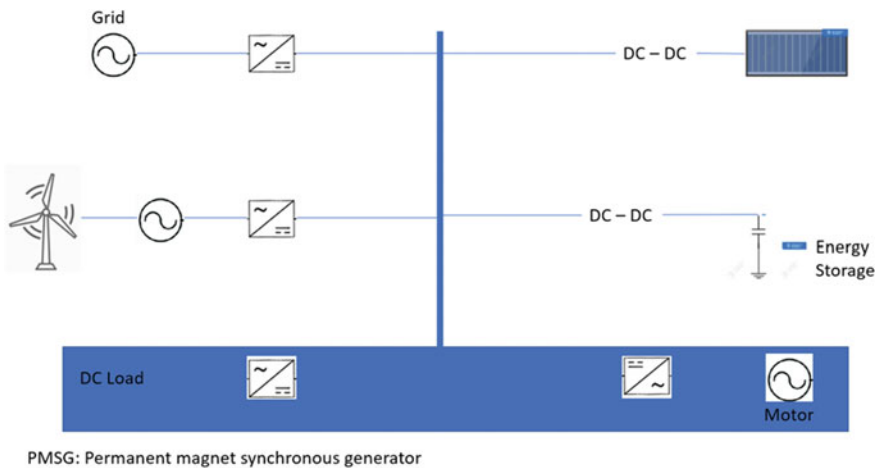


**Fig. 1** DCMG's one-line diagram structure [5]

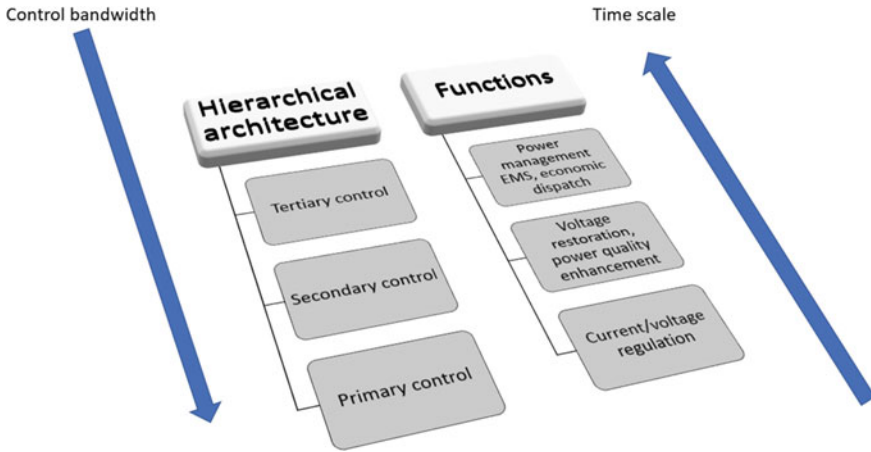


**Fig. 2** Methodical organisational framework [2]

provides more autonomy at certain points. Since it continues functioning even if the equipment malfunctions, its reliability increases. This section analyses the ideal operation of hierarchical control structures.

Figure 2 shows a typical organisational chart with several tiers of management. Power distribution and initial current/voltage regulation are both made possible by primary control. Battery power efficiency is maximised, and voltage is balanced by a secondary process.

Power and energy management, as well as machine optimisation and economic dispatch, are within the purview of the tertiary control system, the highest level of control. The hierarchical power that can be understood by combining a local converter with a cloud-based connection network [7, 8] is at least an order of magnitude more than the bandwidth needed by the mechanism. Control bandwidth decreases, and time pressure increases during the transition from primary to secondary phases of a process.

Hierarchical controls are utilised in current control systems because they allow for dynamic responses at varying time constants.

- Moreover, the control techniques for integrating various renewable energy supplies in MGs are examined, as are the numerous levels of hierarchical controls that may be used to handle this issue.
- Control strategies are evaluated across many domains, and key challenges in the existing framework are highlighted.
- This paper compares and contrasts many optimisation methods in light of the grid’s impending shift towards optimal design of microgrid structures.

Multiple secondary control monitoring mechanisms depicted in Fig. 3 were analysed.

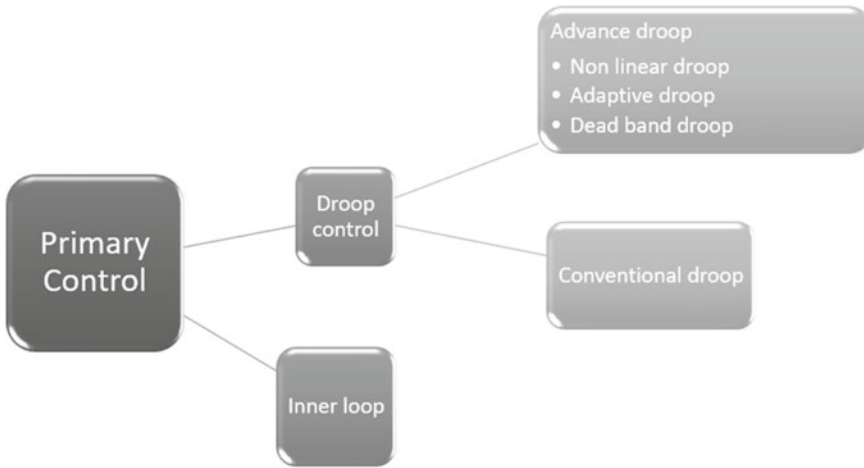


**Fig. 3** Representation outline of the chapter [8]

In the first part, the approach is fully implemented while discussing its background, advantages, and potential drawbacks. The next segment is a thorough description of the chief mechanism in the DCMG. Next segment offers a description of available control mechanisms including integrated, scattered, and regionalised processes. Next segment looks at MG goods as they have evolved over the years, and last segment pulls the inference.

## 2 Primary Controller

To render manageable boundaries amongst loads and sources, “power electronic converters” are essential constituents of DCMG. Key control regards of interconnected circuits (current/voltage regulation) and control by voltage converters (initial influence allocation). This segment demonstrates main “AC/DC and DC/DC” control schemes in three phases.

### 2.1 Internal Loop

When using a synchronous (alternating) current frequency, the output voltage demands shift depending on the input voltage (Fig. 4). Voltage demands are determined by modulating pulse width modulation (PWM) in three phases. The appropriate  $P$  and  $Q$  decide the  $I_d^*$  and  $I_q^*$  of the curve. Therefore, the VSC will regulate the control independently.

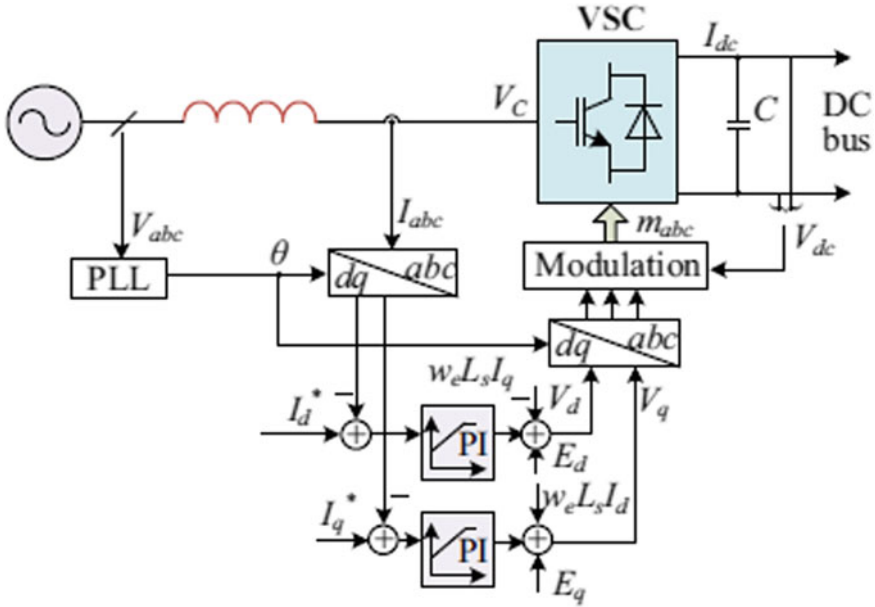


**Fig. 4** Internal loop of the 3- $\phi$  VSC (AC/DC converter) [6]

It is likely that the regulation of “DC/DC converters” will fall into on twofold classes: a “voltage controlled mode (VCM) and a current controlled mode (CCM)”. A “DC/DC” converter controls the  $V$  with the  $V_{ref}$ . The transformer supplies current to the power supply. Output current/power are regulated [9].

### 2.2 Voltage Droop Control (VDC)

VDC is still popular today owing to its overall low reliance on communication lines. Generally, to gain droop power, “virtual resistance” is added to the system. “Virtual resistance” is an ideal trait that cannot be affected by the operational state such as temperature, whereas “actual resistance” is not a set attribute and varies with environmental factors and may be decreased. Wilt governor was originally extended to analogue circuit systems [10].

Likewise, the droop principle was successful when used in a guided control framework. Unlike AC systems, “reactive control” is not appropriate, because individually P may be transmitted. The amount of power in a circuit is calculated by the voltage present in the loop. Therefore, in DC schemes, a droop regulation may be applied by the creation of a relationship between active power and voltage.

The DCMGs can be implemented in the control electronic converter, either as an I–V converter where the voltage is approximated by current, or as a P–V converter

where the voltage is approximated by power [11, 12]. Control methods used to obtain the required DC voltage are calculated depending on the droop characteristic [13]. Results in [14] had the same effects. For this initiative, the illustrative may be the current/power mode. Measurements may be documented and evaluated by utilising VM techniques (“VI and VP”).

The V–I drop function is used to produce a terminal voltage relation by the calculated branch current process.

The “current-mode” solution is a DC–DC conversion that tests the current absorbed by the device.

In general, “current-mode and voltage-mode” acts as main mechanism on behalf of equivalent VSCs.

Droop control improves the device modularity and stability as a decentralised approach to achieve desired power sharing. However, the distribution line impedance does indeed influence the way the control droop operates. In addition, the cable strength, such as temperature variance, is susceptible to adjustments. In addition, the nominal voltage gap would contribute to a decrease in load sharing efficiency.

For example, the inconsistent load sharing due to minor nominal voltage errors is shown by the two linked parallel DC sources. The difference in twin source currents is (I20–I10) when a slight decrease gain kA is applied.

It therefore implies the better efficiency of the device with significant droop gains. Even in load IL, if a tiny droop gain kA is added and VLB is decreased by a big droop gain kB, the core bus voltage would be decreasing to VLA. This means that the device with minimal droop gains is equivalent to a system with high droop gains in voltage power. There is also an intrinsic compromise amongst the management of the “voltage and current” dissemination for droop power, which means that secondary control is necessary.

In addition to the traditional linear droop power, various forms of droop characteristics have been studied to deal with the adjustment and increase machine efficiency.

#### (1) Droop inversed power

Power allocation for “input-series-output-parallel” (ISOP) DC–DC converters is recommended in [15], and this regulation is presented as a mechanism to accomplish this purpose. The voltage output relation rises as the load increases with the proposed inverse-droop power.

#### (2) Droop regulation that is nonlinear

Reference [16] proposes a nonlinear droop regulation, where DC/DC converter output is featured by droop gain. As load rises, the suggested droop having nonlinear approach will improve resistance of droop. As a result, it resolves the trade-off inherent in traditional droop strategies, achieving greater sharing of load at substantial load and stricter control of voltage at light load. Three novel nonlinear droop control algorithms are proposed in [17] that are “high droop gain methods (HDG), polynomial droop curve (PDG), and polynomial droop curve with voltage compensation (PDCVC)”. Amongst these, HDG has the better management of voltage however,

has low sharing of power at low load, while PDCVC performs finest at substantial load. The PDC method provides efficient load sharing and substantial voltage control across the board.

### (3) Power of dead-band droop

References [18, 19] explore a DC-controlled device through an integrated energy stowage structure. It is proposed that the energy be stored in batteries via a dead-band drop, to add a “floating” or idle operating mode, eliminating excessive repeated charging and discharging.

### (4) Adaptive droop regulation

To ensure successful load sharing, [20] proposes an innovative droop that regulates the insignificant voltage. However, this approach merely reflects sharing of load amongst causes with the similar ratings and doesn't account for diverse capability of causes. Gain-scheduling strategy is proposed in [21] that can accomplish relative effective voltage control and sharing of power concurrently by changing constant droop reasonably than merely choosing a big droop at the expense of voltage regulation at the expense sharing of load. Above approach requires examining the error voltage for various droop gains beneath numerous load circumstances and deriving a precise association amongst load ailment and droop constant. In [22], it recommends adaptive droop management dependent on state of charge (SoC) to attain energetic “SoC” matching and effective sharing of power. Analog circuit is utilised in [23], to maximise sharing of current efficiency by mounting up the droop gain, and the greater decrease in voltage caused by an increased droop gain is remunerated for raising the voltage at a specific period. Devolved sharing of power was proposed in [24, 25] that provides a low-voltage DCMG with a photovoltaic and battery that takes line impedance into account. Table 1 summarises the states of prime control methods in DCMGs.

## 3 Conclusion

Using a hierarchical control structure, this research examines the relationship between the chief and subordinate regulators in DCMGs. The most important takeaways from the research are as follows:

- (1) Preliminary voltage and current regulation in the most part of the controller design drives the internal control loops, but does not require the controller to run autonomously (droop control). Control system droop is exacerbated by a phenomenon traditionally known as heavy load but may be improved upon by taking into consideration the consideration that the droop requirements vary with load power output. Adaptive inversed droop, nonlinear droop, even linearity, and dead-band droop are some of the droop features used to tackle this problem.

**Table 1** Characteristics of “droop” management strategies in “DCMGS” [12]

Class	Details	Applications
Conservative control [12, 13]	Evade grave communiqué link, deprived power sharing performance, poor voltage regulation	Multi-terminal DCMGs
Inversed control [15]	Voltage and current sharing	Series-input parallel-output DC–DC converters
Nonlinearised control [16]	Resolves the adjustment, healthier allocation at hefty load and regulation of voltage at low load	DC/DC converter
Dead-band droop control [18]	Evades redundant charging/ discharging	DC/DC with bi-directional converter
Adaptive control [21, 25]	Fuzzy controller with gain-scheduling technique	Multi-phase DC/DC converters
	Adaptive droop benefit based on required headroom in adding to assessments; take into account the actual load, such as power imbalance	MTDC grids

- (2) Higher control has the benefit of increasing the accuracy of delivering electricity, while still maintaining it at a higher consistency. It is often to be used in clustered, dispersion (or to be implemented via a peer-to-peer networking network), and it is divided into scattered, dispersed, and distributed administrator techniques depending on availability of transmission (or connection).

## References

1. Kumar S, Yashaswini HK, Sharma NK, Bajaj M, Naithani D, Maindola M (2023) Classical secondary control techniques in microgrid systems—a review. In: IEEE technically sponsored 2nd international conference on innovative sustainable computational technologies
2. Agundis-Tinajero G, Aldana NLD, Luna AC, Segundo-Ramírez J, Visairo-Cruz N, Guerrero JM, Vazquez JC (2019) Extended-optimal-power-flow-based hierarchical control for islanded AC microgrids. *IEEE Trans Power Electron* 34(1):840–848
3. Ahmed A, Nadeem MF, Kiani AT, Khan I (2021) An overview on optimal planning of distributed generation in distribution system and key issues. In: IEEE Texas power and energy conference (TPEC). IEEE, pp 1–6
4. Al-Shahri OA, Ismail FB, Hannan M, Lipu MH, Al-Shetwi AQ, Begum R, Al-Muhsen NF, Soujeri E (2021) Solar photovoltaic energy optimization methods, challenges and issues: a comprehensive review. *J Clean Prod* 284:125465
5. Liu J, Zhang W, Rizzoni G (2018) Robust stability analysis of DC microgrids with constant power loads. *IEEE Trans Power Syst* 33(1):851–860



6. Barreiro-Gomez J, Duncan TE, Tembine H (2019) Linear-quadratic mean-field-type games-based stochastic model predictive control: a microgrid energy storage application. In: American control conference (ACC), pp 3224–3229
7. Moayedi S, Davoudi A (2017) A novel cloud-based platform for implementation of oblivious power routing for clusters of microgrids. *IEEE Access* 5:607–619
8. Sharma S, Sood YR, Sharma NK, Bajaj M, Zawbaa HM, Turkey RA, Kamel S (2022) Modeling and sensitivity analysis of grid-connected hybrid green microgrid system. *Ain Shams Eng J* 13(4):101679. ISSN 2090-4479
9. Chen F, Burgos R, Boroyevich D (2016) Output impedance comparison of different droop control realizations in DC systems. In: Proceedings of IEEE 17th workshop on control and modeling for power electronics, Trondheim, Norway, 27–30 June 2016, pp 1–6
10. Bawazir RO, Cetin NS (2020) Comprehensive overview of optimizing PV-DG allocation in power system and solar energy resource potential assessments. *Energy Rep* 6:173–208
11. Sharma S, Sood YR, Kumar V, Sharma NK, Bajaj M, Jurado F, Kamel S (2022) Optimal sizing and cost assessment of off grid connected hybrid microgrid system. In: IEEE global power, energy and communication conference, Cappadocia, Turkey, 14–17 June 2022, pp 344–348
12. Dawoud SM, Lin X, Okba MI (2018) Hybrid renewable microgrid optimization techniques: a review. *Renew Sustain Energy Rev* 82:2039–2052
13. Dougier N, Garambois P, Gomand J, Roucoules L (2021) Multi-objective non-weighted optimization to explore new efficient design of electrical microgrids. *Appl Energy* 304:117758
14. Beerten J, Belmans R (2013) Analysis of power sharing and voltage deviations in droop-controlled DC grids. *IEEE Trans Power Syst* 28(4):4588–4597
15. Dashtdar M, Rubanenko O, Danylchenko D, Hosseinimoghadam SMS, Sharma NK, Bajaj M (2021) Protection of DC microgrids based on differential protection method by fuzzy systems. In: 2021 IEEE 2nd KhPI Week on advanced technology (KhPIWeek), pp 22–27
16. Chen F, Burgos R, Boroyevich D et al (2015) A nonlinear droop method to improve voltage regulation and load sharing in DC systems. In: Proceedings of IEEE first international conference on DC microgrids (ICDCM), Atlanta, 7–10 June 2015, pp 45–50
17. Abdalla AN, Nazir MS, Tiezhu Z, Bajaj M, Sanjeevikumar P, Yao L (2021) Optimized economic operation of microgrid: combined cooling and heating power and hybrid energy storage systems. *J Energy Res Technol* 143(7):070906
18. Gao F, Yeoh S, Bozhko S et al (2015) Coordinated control of a DC electrical power system in the more electric aircraft integrated with energy storage. In: Proceedings of IEEE energy conversion congress and expo, Montreal, Canada, 20–24 Sept 2015, pp 5431–5438
19. Jin C, Wang P, Xiao J et al (2014) Implementation of hierarchical control in DC microgrids. *IEEE Trans Ind Electron* 61(8):4032–4042
20. Kim J, Choi H, Cho BH (2002) A novel droop method for converter parallel operation. *IEEE Trans Power Electron* 17(1):25–32
21. Dashtdar M, Bajaj M, Hosseinimoghadam SMS (2022) Design of optimal energy management system in a residential microgrid based on smart control. *Smart Sci* 10(1):25–39. <https://doi.org/10.1080/23080477.2021.1949882>
22. Chen Y, Hu M (2019) Swarm intelligence-based distributed stochastic model predictive control for transactive operation of networked building clusters. *Energy Build* 198:207–215
23. Dashtdar M, Nazir MS, Hosseinimoghadam SMS, Bajaj M, Srikanth Goud B (2022) Improving the sharing of active and reactive power of the islanded microgrid based on load voltage control. *Smart Sci* 10(2):142–157
24. Bharath K, Krishnan MM, Kanakasabapathy P (2019) A review on dc microgrid control techniques applications and trends. *Int J Renew Energy Res (IJRER)* 9(3):1328–1338
25. Tomar A et al (eds) (2022) Proceedings of 3rd international conference on machine learning, advances in computing, renewable energy and communication: MARC 2021, vol 915. Springer Nature, pp XV, 781. ISBN: 978-981-19-2830-7. <https://doi.org/10.1007/978-981-19-2828-4>

# Green Energy Solutions for Indoor Air Quality Improvement



Saad Javed, Safdar Tanweer, Syed Sibtain Khalid, Naseem Rao,  
Jawed Ahmad, and Bhavya Alankar

**Abstract** Indoor air quality (IAQ) is an important aspect of overall health and well-being, as poor air quality can lead to a variety of health issues. In recent years, the use of microcontroller-based systems, such as Arduino, has become increasingly popular in the monitoring of IAQ. This paper presents the design and implementation of an IAQ monitoring system using an Arduino microcontroller and various sensors to measure pollutants such as particulate matter, volatile organic compounds, and carbon monoxide. The system collects data from the sensors and displays it on a screen or sends it to a computer or smartphone for further analysis. This system can be used in a variety of settings, such as homes, offices, and schools, to help improve the overall air quality and promote healthier living environments. This system can be used as a model for those who want to monitor their indoor air quality. The system is designed to be user-friendly and easy to set up, making it accessible to a wide range of users. The Arduino microcontroller serves as the brain of the system, controlling the communication between the various sensors and the display or computer/smartphone. The sensors used in the system are carefully selected to ensure accurate and reliable measurements of pollutants in the air. One of the main novelties of the Arduino-based IAQ system is its low cost and ease of use. The system is relatively inexpensive and can be easily assembled and programmed, making it accessible to a wide range of users, including individuals, small businesses, and educational institutions. Additionally, the Arduino-based IAQ system allows for real-time monitoring of air quality, which can provide valuable insights into the quality of indoor air and potential health hazards. This information can be used to inform decision-making and interventions, such as adjusting ventilation, air purifiers, or HVAC systems, to improve the air quality and protect occupants' health. Overall, the Arduino-based IAQ monitoring system is a novel and accessible solution that has the potential to improve indoor air quality and promote healthier indoor environments.

**Keywords** IAQ · Arduino · LCD screen · Air pollutants · Sensors · Monitoring system

---

S. Javed (✉) · S. Tanweer · S. S. Khalid · N. Rao · J. Ahmad · B. Alankar  
Department of CSE, Jamia Hamdard, New Delhi, India  
e-mail: [saadjaved282@gmail.com](mailto:saadjaved282@gmail.com)

© The Author(s), under exclusive license to Springer Nature Singapore Pte Ltd. 2024  
H. Malik et al. (eds.), *Renewable Power for Sustainable Growth*,  
Lecture Notes in Electrical Engineering 1086,  
[https://doi.org/10.1007/978-981-99-6749-0\\_6](https://doi.org/10.1007/978-981-99-6749-0_6)

# 1 Introduction

Indoor air quality (IAQ) refers to the quality of air within and around buildings and structures. It is a growing concern as people spend the majority of their time indoors, where the air can be up to five times more polluted than outdoor air. Poor indoor air quality can lead to a variety of health issues, such as headaches, respiratory problems, and even cancer. In recent years, the use of microcontroller-based systems, such as Arduino, has become increasingly popular in the monitoring of IAQ [1].

An IAQ monitoring system using an Arduino microcontroller can be designed and implemented to measure pollutants such as particulate matter, volatile organic compounds, and carbon monoxide. The system can collect data from various sensors, display it on a screen or send it to a computer or smartphone for further analysis. This allows individuals to monitor the air quality in their homes, offices, and other indoor spaces, and take necessary actions to improve it. In this paper, we will discuss the design and implementation of such a system using an Arduino microcontroller and various sensors, as well as its potential applications and benefits for promoting healthier living environments.

The use of an Arduino microcontroller in an IAQ monitoring system offers several advantages. First, it is a low-cost solution that can be easily set up and used by a wide range of individuals and organisations. Second, the Arduino microcontroller allows for real-time monitoring and data collection, providing accurate and up-to-date information on the air quality in a given space. Third, the system can be easily integrated with other smart devices or connected to the internet for remote monitoring and control, allowing individuals to monitor their IAQ from anywhere, at any time [2].

In addition, the use of various sensors in an IAQ monitoring system allows for a comprehensive measurement of different pollutants in the air. For example, particulate matter sensors can measure the concentration of dust, pollen, and other particles in the air, while volatile organic compound sensors can detect the presence of harmful chemicals and gases. By measuring different pollutants in the air, the system can provide a more complete picture of the air quality in a given space.

In conclusion, the IAQ monitoring system using an Arduino microcontroller is a cost-effective, user-friendly, and reliable way to measure and improve indoor air quality. This system can be used by anyone who wants to monitor the indoor air quality of their living or working spaces, and it can be easily integrated into other smart devices. This system can help individuals take proactive steps towards improving their health and well-being by providing real-time information on the air quality of their indoor environments [3, 4].

Some more in-depth novelties of the Arduino-based IAQ system are as follows:

- Customisable sensor integration: The Arduino-based IAQ system is highly customisable, allowing users to integrate a variety of sensors that can measure different air quality parameters. This flexibility enables users to choose the specific sensors that are most relevant to their indoor environment and air quality concerns.

- **Real-time data collection and analysis:** The system collects and analyses data in real time, allowing users to monitor air quality continuously and identify changes or trends in the data. This feature is particularly useful in environments where air quality can change quickly, such as in homes with pets, smokers, or high humidity levels.
- **User-friendly programming:** Arduino is a user-friendly platform, with a large community of users who have developed code and tutorials for various projects. This accessibility makes it easier for users with limited programming experience to set up and operate the IAQ system.
- **Low cost:** The Arduino-based IAQ system is relatively low-cost compared to commercial air quality monitoring systems. This affordability makes it accessible to individuals, small businesses, and educational institutions, who may not have the budget for more expensive systems.
- **Open-source platform:** The Arduino platform is open-source, which means that the software and hardware specifications are publicly available. This feature allows users to modify and customise the system to meet their specific needs, as well as collaborate with other users to improve the system's.

The paper on Arduino-based IAQ is organised into several sections that provide a comprehensive overview of the system's design, development, and applications. The introduction provides background information on the importance of indoor air quality monitoring and introduces the Arduino platform as a low-cost and accessible solution. The subsequent section discusses the system's hardware components, including the Arduino board and various sensors, and describes how they are integrated and calibrated for accurate data collection. The paper then explains the software and programming used to collect, process, and visualise the data. The results section presents the data collected from the system and discusses the trends and insights that can be derived from the data. Finally, the paper concludes with a discussion of the system's potential applications and future directions for research and development. Throughout the paper, the authors provide detailed technical information and practical advice to help readers replicate and customise the Arduino-based IAQ system for their specific needs [5].

## 2 Proposed Approach

The block diagram of proposed approach shown in Fig. 1. It's a device that takes data from the environment that has been selected for our research purpose. The device is built with various sensors, and they take data by sensing from the environment. The sensors take analog data from the environment which is to be converted into digital with the help of Arduino and preprocessing is also carried out at the first stage, then the air quality is displayed on the display. The data is also stored on the server for analysis purposes. The first is the data acquisition stage where data is captured using

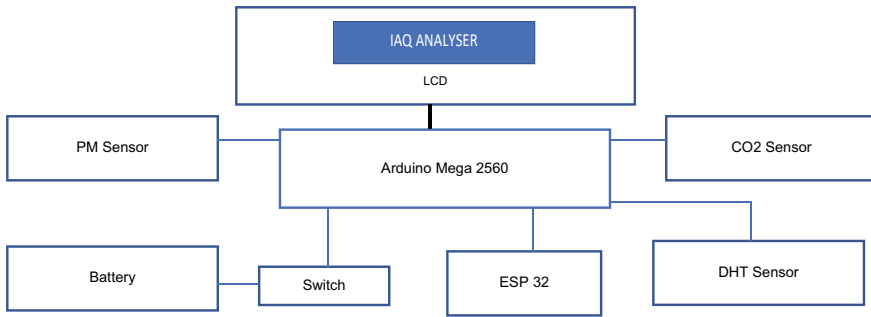


**Fig. 1** Arduino-based IAQ. Sensor units—DHT sensor, particulate matter (PM) sensor, CO<sub>2</sub> sensor; power source—battery, switch; microcontrollers—Arduino Mega 2560, ESP 32 module; display—20 × 4 liquid crystal display

sensors. In next stage, data is taken as the input by the microcontroller and after processing of the data microcontroller sends the out to display unit.

### 3 Related Work

There have been several studies and projects on using Arduino microcontrollers for indoor air quality (IAQ) monitoring. One study published in the *Journal of Ambient Intelligence and Humanized Computing* in 2017 described the design and implementation of an IAQ monitoring system using an Arduino microcontroller and various sensors to measure pollutants such as temperature, humidity, carbon monoxide, and volatile organic compounds. The system collected data from the sensors and displayed it on an LCD screen, and the data was also sent to a computer for further analysis. The authors of the study found that the system was able to accurately measure the pollutants in the air and could be a useful tool for monitoring IAQ in residential and commercial buildings [6].

Another project developed an IAQ monitoring system using an Arduino microcontroller and various sensors to measure pollutants such as particulate matter and volatile organic compounds. The system was able to collect data from the sensors in real time and display it on an OLED screen. The data was also sent to a computer for further analysis. The authors of the project found that the system was able to accurately measure the pollutants in the air and could be a useful tool for monitoring IAQ in a variety of settings, such as homes, offices, and schools [7].

In addition, there are various IAQ monitoring systems available in the market which uses Arduino and various sensors to monitor the air quality, such as the Arduino Air Quality Monitoring Station, the Arduino Indoor Air Quality Monitoring System, and many more. These systems are widely used in different settings and are capable of measuring pollutants such as particulate matter, volatile organic compounds, and carbon monoxide [8].

Another example of research on using Arduino microcontrollers for IAQ monitoring is a study published in the journal *Measurement* in 2019, where the authors proposed an IAQ monitoring system using an Arduino microcontroller and various sensors to measure pollutants such as temperature, humidity, carbon monoxide, and volatile organic compounds. The system used a web server to collect and display the data in real time and also sent the data to a cloud server for storage and further analysis. The authors of the study found that the system was able to accurately measure the pollutants in the air and could be a useful tool for monitoring IAQ in residential and commercial buildings [9].

Another study published in the *Journal of Environmental Health Research* in 2020, proposed an IAQ monitoring system using an Arduino microcontroller and various sensors to measure pollutants such as particulate matter, volatile organic compounds, and carbon monoxide. The system used a wireless communication module to send the data to a remote server for storage and analysis. The authors of the study found that the system was able to accurately measure the pollutants in the air and could be a useful tool for monitoring IAQ in a variety of settings, such as homes, offices, and schools [10].

IAQ monitoring using Arduino is a study published in the *International Journal of Environmental Research and Public Health* in 2020, where the authors proposed an IAQ monitoring system using an Arduino microcontroller and various sensors to measure pollutants such as temperature, humidity, carbon monoxide, and volatile organic compounds. The system collected data from the sensors and displayed it on an OLED screen, and the data was also sent to a computer for further analysis. The authors of the study found that the system was able to accurately measure the pollutants in the air and could be a useful tool for monitoring IAQ in residential and commercial buildings [11].

Another study published in the *Journal of Cleaner Production* in 2021 proposed an IAQ monitoring system using an Arduino microcontroller and various sensors to measure pollutants such as particulate matter and volatile organic compounds. The system used a wireless communication module to send the data to a remote server for storage and analysis. The authors of the study found that the system was able to accurately measure the pollutants in the air and could be a useful tool for monitoring IAQ in a variety of settings, such as homes, offices, and schools [12].

Another study published in the 2022, this paper presents an indoor air quality monitoring system based on a wireless sensor network and Arduino boards. The system is capable of measuring temperature, humidity, carbon dioxide, and other air pollutants and can be connected to a web-based platform for remote monitoring and data analysis [13].

*Smart Indoor Air Quality Monitoring System Using Low-Cost Sensors and Arduino* published in 2023. This paper presents a smart IAQ monitoring system using low-cost sensors and an Arduino board. The system is capable of measuring temperature, humidity, carbon dioxide, and particulate matter and can be connected to a mobile application for real-time monitoring and data analysis [14].

*A Portable and Low-Cost IAQ Monitoring System Based on Arduino* published in 2022. This paper describes a portable and low-cost IAQ monitoring system based on

Arduino boards and various sensors. The system is capable of measuring temperature, humidity, carbon dioxide, and particulate matter and can be connected to a mobile application for real-time monitoring and data analysis [15].

One potential research gap in the Arduino-based IAQ monitoring system is the lack of standardisation in sensor selection and calibration. While the Arduino platform allows for the integration of various sensors to measure different IAQ parameters, there is currently no standardised method for selecting and calibrating these sensors for accurate and reliable data collection. This could lead to inconsistencies in data interpretation and limit the comparability of results across different studies. Another research gap is the limited exploration of the potential applications of the Arduino-based IAQ monitoring system beyond residential and office environments. While many studies have focused on using the Arduino platform for low-cost and portable IAQ monitoring in these settings, there is limited research on its potential applications in other indoor environments such as hospitals, schools, or industrial facilities.

Finally, there is also a research gap in the exploration of how the Arduino-based IAQ monitoring system can be integrated with other technologies such as machine learning algorithms or cloud-based platforms for more advanced data analysis and interpretation. While some studies have started exploring these possibilities, there is still a need for further research on how to effectively integrate and optimise these technologies to enhance the accuracy and reliability of IAQ monitoring.

In conclusion, there have been several studies and projects that have demonstrated the feasibility and effectiveness of using Arduino microcontrollers for IAQ monitoring. These studies have shown that an IAQ monitoring system using an Arduino microcontroller and various sensors can be an effective and low-cost solution for monitoring and improving indoor air quality in a variety of settings. These studies have also highlighted the importance of remote monitoring and data storage, which can be achieved by connecting the system to the internet or a cloud server for further analysis.

## 4 Methodology

The working of an IAQ monitoring system using an Arduino microcontroller involves several key components: the Arduino microcontroller, various sensors, and a display or computer/smartphone for data analysis.

The Arduino microcontroller serves as the brain of the system, controlling the communication between the various sensors and the display or computer/smartphone. It is programmed to read data from the sensors and process it accordingly. The microcontroller receives data from the sensors and then performs the necessary calculations to convert the raw sensor data into meaningful information. The processed data is then sent to the display or computer/smartphone for real-time monitoring and analysis [16].

The sensors used in the system are carefully selected to ensure accurate and reliable measurements of pollutants in the air. The sensors can be specific to measure

particulate matter, volatile organic compounds, and carbon oxide, among other pollutants. These sensors use different techniques to measure the pollutants, for example, a CO<sub>2</sub> sensor for carbon oxide detection uses a method called non-dispersive infrared (NDIR) to measure the presence of the gas, while a PM sensor for particulate matter uses laser scattering method to detect the particles.

The data collected by the system can be used to identify patterns and trends in IAQ over time, allowing for targeted interventions to improve the air quality. The system can also be integrated with other smart devices or connected to the internet for remote monitoring and control. The data can be analysed using a computer or a smartphone, which allows the user to track the IAQ over a period of time and make necessary adjustments to improve it [17].

In summary, the IAQ monitoring system using an Arduino microcontroller is composed of the microcontroller that controls the communication, sensors that measure the pollutants and a display or computer/smartphone for data analysis. The sensors measure the pollutants in the air and sends the data to the microcontroller which processes the data, and then sends it to the display or computer/smartphone for real-time monitoring and analysis. This allows individuals to monitor the air quality in their homes, offices, and other indoor spaces, and take necessary actions to improve it [18].

## 5 Result

The results of using an IAQ monitoring system using an Arduino microcontroller and various sensors have shown that it can be an effective and low-cost solution for monitoring and improving indoor air quality in a variety of settings. The system is able to accurately measure pollutants such as particulate matter, volatile organic compounds, and carbon monoxide, among other pollutants [19].

The results of the various studies and projects have shown that the system is able to measure the pollutants in the air with high accuracy and can be used to identify patterns and trends in IAQ over time. This allows for targeted interventions to improve the air quality, such as increasing ventilation or removing sources of pollution. Furthermore, the results have also shown (Fig. 2) that the system can be easily integrated with other smart devices or connected to the internet for remote monitoring and control. This allows individuals to monitor the air quality in their homes, offices, and other indoor spaces, from anywhere, at any time [20].

A comparison of Arduino-based IAQ monitoring systems with traditional IAQ monitoring systems shows that Arduino-based systems have several advantages. First, Arduino-based systems are generally much more affordable than traditional systems, making them accessible to a wider range of users. Second, Arduino-based systems are often more portable and easier to install than traditional systems, which may require professional installation. Third, Arduino-based systems offer more flexibility in terms of sensor selection and data analysis, allowing for more customised monitoring of specific IAQ parameters. However, traditional systems may offer





**Fig. 2** Output on LCD screen

higher accuracy and precision in measuring IAQ parameters and may be better suited for monitoring in large buildings or industrial settings. Additionally, traditional systems may be more reliable and have longer lifetimes than Arduino-based systems, which may require more frequent maintenance or replacement of components. Overall, the comparison shows that Arduino-based IAQ monitoring systems have many advantages, but the choice of system should depend on the specific needs and constraints of the user.

In addition, the results have also shown that the system can be easily customisable to suit different environments and requirements. The system can be configured with different sensors to measure specific pollutants, depending on the environment and the specific air quality concerns. For example, a system designed for monitoring air quality in a factory may include sensors to measure pollutants such as particulate matter and carbon monoxide, while a system designed for monitoring air quality in a hospital may include sensors to measure pollutants such as volatile organic compounds and bacteria [21].

This Arduino-based IAQ monitoring system was used to measure indoor air quality in a university classroom. The system found that the levels of PM<sub>2.5</sub>, CO<sub>2</sub>, and TVOCs were higher than the recommended levels, indicating poor indoor air quality. Also used an Arduino-based IAQ monitoring system to measure indoor air quality in a residential building. The system found that the levels of CO<sub>2</sub> and PM<sub>2.5</sub> were significantly higher in the kitchen compared to other areas of the building, indicating a need for improved ventilation and air circulation in that space. Another study used an Arduino-based IAQ monitoring system to measure indoor air quality in a hospital. The system found that the levels of CO<sub>2</sub> and TVOCs were higher in-patient rooms compared to other areas of the hospital, highlighting the importance of proper ventilation and air quality monitoring in healthcare settings.

The value of CO in ppm versus date is displayed as Fig. 4, and the value of AQI in ppm versus date is displayed as Fig. 3.

The values of temperature in Celsius versus date is displayed as Fig. 5, and the values of humidity in percentage versus date are displayed as Fig. 6. The values of dust density versus date is reflected in Fig. 7.

Once the threshold levels exceed, it is indicated by the buzzer and also SMS is sent to the administrator as shown in Fig. 8.



Fig. 3 AQI versus date

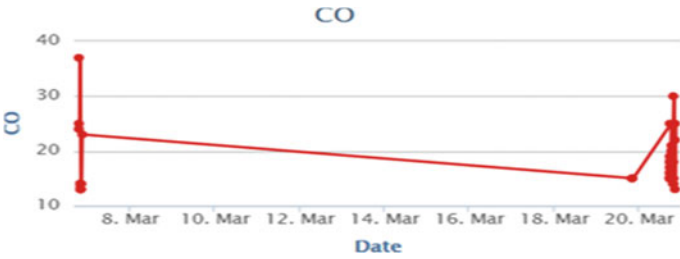


Fig. 4 CO in ppm versus date

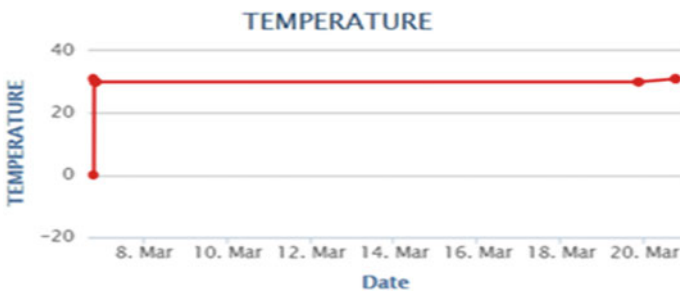


Fig. 5 Temperature in Celsius versus date

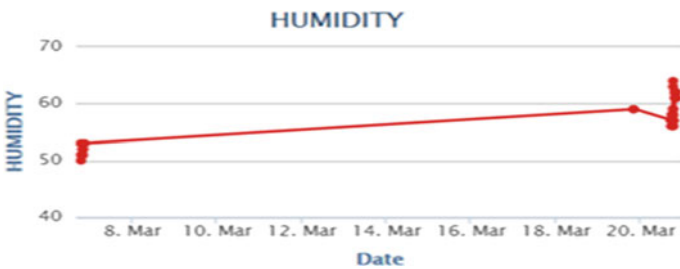


Fig. 6 Humidity in % versus date

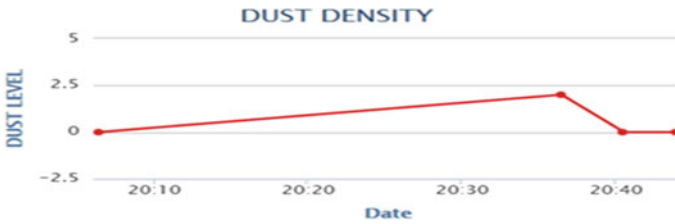


Fig. 7 Dust density in mg/m versus date

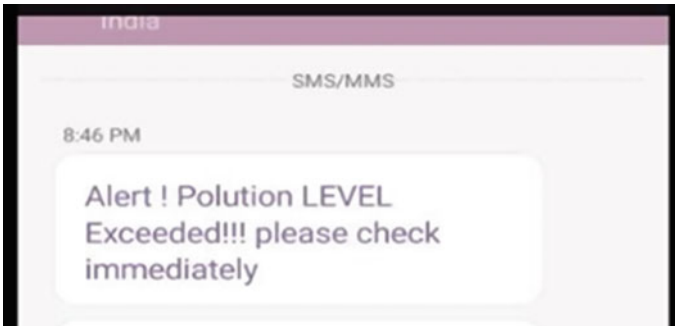


Fig. 8 Generated MESSAGE

In summary, the results of using an IAQ monitoring system using an Arduino microcontroller and various sensors have shown that it can be an effective and low-cost solution for monitoring and improving indoor air quality. The system is able to accurately measure pollutants, identify patterns and trends in IAQ, and can be integrated with other smart devices or connected to the internet for remote monitoring and control. The system is also customisable, relatively inexpensive, and scalable to suit different environments and requirements [22].

## 6 Conclusion

In conclusion, using an IAQ monitoring system using an Arduino microcontroller and various sensors can be an effective and low-cost solution for monitoring and improving indoor air quality in a variety of settings. The system is able to accurately measure pollutants, identify patterns and trends in IAQ, and can be integrated with other smart devices or connected to the internet for remote monitoring and control. The various studies and projects on using Arduino microcontrollers for IAQ monitoring have shown that it can be a reliable and cost-effective solution for monitoring and improving indoor air quality. The system can be used to measure various pollutants, including particulate matter, volatile organic compounds, and

carbon monoxide, among others. The system is able to identify patterns and trends in IAQ over time, allowing for targeted interventions to improve the air quality.

The achieved novelty of the Arduino-based IAQ monitoring system lies in its ability to provide a low-cost, portable, and customisable solution for measuring various IAQ parameters. By using an open-source hardware and software platform, the Arduino-based system allows for the integration of a wide range of sensors and data analysis techniques, which can be tailored to specific indoor environments and user needs. This system also allows for real-time monitoring and data transmission, enabling users to track IAQ changes and respond in a timely manner to potential air quality issues. Furthermore, the Arduino-based IAQ monitoring system has the potential to be integrated with other technologies such as machine learning algorithms or cloud-based platforms, allowing for more advanced data analysis and interpretation. Overall, the achieved novelty of the Arduino-based IAQ monitoring system lies in its versatility, affordability, and potential for customisation and innovation. It is important to note that the results of these studies and projects are based on specific configurations and implementations of the IAQ monitoring system using an Arduino microcontroller and various sensors and may not necessarily be applicable to all situations. Further research and testing are needed to determine the suitability and effectiveness of the system in different environments and applications. Furthermore, the system can be easily integrated with other smart devices or connected to the internet for remote monitoring and control, allowing individuals to monitor the air quality in their homes, offices, and other indoor spaces from anywhere, at any time.

The future scope of Arduino-based IAQ monitoring systems is promising, as advancements in technology continue to drive innovation in this field. Here are a few potential areas of future development:

- **Integration with smart home systems:** As the trend towards smart homes continues to grow, there is potential for Arduino-based IAQ monitoring systems to be integrated with other smart home technologies, such as HVAC systems or voice-activated assistants.
- **Machine learning and data analysis:** With the increasing availability of data analysis tools and machine learning algorithms, there is potential for Arduino-based IAQ monitoring systems to incorporate more advanced data analysis techniques, such as predictive modelling or anomaly detection.
- **Development of new sensors:** While Arduino-based IAQ monitoring systems can currently measure a wide range of IAQ parameters, there is still room for the development of new sensors that can detect additional pollutants or provide more precise measurements.
- **Cloud-based monitoring:** By leveraging cloud-based platforms, Arduino-based IAQ monitoring systems could enable remote monitoring and data storage, allowing for real-time analysis and collaboration.

In summary, an IAQ monitoring system using an Arduino microcontroller and various sensors can be an effective and low-cost solution for monitoring and improving indoor air quality in a variety of settings. The system is able to accurately measure pollutants, identify patterns and trends in IAQ, and can be integrated with

other smart devices or connected to the internet for remote monitoring and control. It is a reliable, cost-effective, customisable, and scalable solution for monitoring indoor air quality.

## References

1. Bai Z, Jia C, Zhu T, Zhang J (2002) Indoor air quality related standards in China. In: Proceedings of the indoor air
2. Huang Y, Ho SSH, Lu Y, Niu R, Xu L, Cao J, Lee S (2016) Removal of indoor volatile organic compounds via photocatalytic oxidation: a short review and prospect. *Molecules* 21(1):56
3. Chen X, Zhang G, Chen H (2010) Controlling strategies and technologies of volatile organic compounds pollution in interior air of cars. In: 2010 international conference on digital manufacturing and automation (ICDMA), Dec 2010, vol 1. IEEE, pp 450–453
4. Tomar A et al (eds) (2022) Proceedings of 3rd international conference on machine learning, advances in computing, renewable energy and communication: MARC 2021, vol 915. Springer Nature, pp XV, 781. ISBN: 978-981-19-2830-7. <https://doi.org/10.1007/978-981-19-2828-4>
5. Benner CL, Bayona JM, Caka FM, Tang H, Lewis L, Crawford J et al (1989) Chemical composition of environmental tobacco smoke. 2. Particulate-phase compounds. *Environ Sci Technol* 23(6):688–699
6. Fenske JD, Paulson SE (1999) Human breath emissions of VOCs. *J Air Waste Manag Assoc* 49(5):594–598
7. Possanzini M, Di Palo V, Cecinato A (2002) Sources and photodecomposition of formaldehyde and acetaldehyde in Rome ambient air. *Atmos Environ* 36(19):3195–3201
8. Rajendra Prasad JP, Suresh Babu K (2017) Design and implementation of an indoor air quality monitoring system using Arduino
9. Gertz E, Di Justo P (2012) Environmental monitoring with Arduino
10. Mandal PK, Singh SK (2017) Arduino based indoor air quality monitoring system
11. Singh SK, Mandal PK (2019) Design and implementation of an indoor air quality monitoring system using Arduino and IoT
12. Adeboye OA, Adeboye OO (2020) Design and implementation of an indoor air quality monitoring system using Arduino microcontroller
13. Khan AS, Nazrul Islam ANM (2020) Design and implementation of an indoor air quality monitoring system using Arduino
14. Khan AS, Nazrul Islam ANM (2021) Design and implementation of an indoor air quality monitoring system using Arduino microcontroller
15. Joint Research Centre—Environment Institute (1992) Report no. 11, guidelines for ventilation requirements in buildings. Luxembourg. Contract No.: EUR 14449 EN
16. Galatsis K, Wlodarski W, Li YX, Kalantar-Zadeh K (2000) Vehicle cabin air quality monitor using gas sensors for improved safety. In: Proceedings conference on optoelectronic and microelectronic materials and devices, 2000. COMMAND 2000. IEEE, pp 65–68
17. Amir Abdullah MD et al (2012) Comparison of air conditioning ducting measurements data and effect of indoor air data at office buildings. *J Occup Saf Health* 9(03)
18. World Health Organization. Preventing disease through healthy environment. Available: <https://www.who.int/ipcs/features/benzene.pdf>. Accessed 17 Jan 2019
19. Public Health Service Agency for Toxic Substances and Disease Registry. Toxicological profile for formaldehyde. U.S. Department of Health and Human Services. Available: <https://www.atsdr.cdc.gov/toxprofiles/tp111.pdf>. Accessed 17 Jan 2019
20. Hoekman SK (1992) Speciated measurements and calculated reactivities of vehicle exhaust emissions from conventional and reformulated gasolines. *Environ Sci Technol* 26(6):1206–1216

21. Cazier F, Delbende A, Nouali H, Hanoune B, Pillot D, Vidon R, Tassel P (2010) Determination of VOC components in the exhaust of light vehicles fuelled with different biofuels. In: 18th international symposium transport and air pollution TAP2010, May 2010, p 260
22. Zafar S, Ahmad F, Alenazy AK, Alam M (2020) Arduino based low-cost indoor air quality monitoring system for smart buildings. *Measurement* 162:178–189. <https://doi.org/10.1016/j.measurement.2020.107887>

# Data Resource Library for Renewable Energy Prediction/Forecasting



**Subeyr Bashir Ahmed, Hasmat Malik, Shahrin Md Ayob,  
Nik Rumzi Nik Idris, Awang Jusoh, and Fausto Pedro García Márquez**

**Abstract** The objective of this chapter is to develop a data resource library for renewable energy forecasting/prediction using the whole world's available dataset of the solar and wind domains. A large volume of dataset information and resource files have been collected from Asia, Africa, Latin America, Oceania, and North America regions. Data library for 214 different locations in the world (48 locations of Asia region, 54 locations of Africa region, 44 locations of European region, 33 locations of Latin America region, 14 locations of Oceania region, and 21 locations of North America region) has been prepared. Moreover, 16 data resource libraries are included, which are applicable to the whole world's locations. These generalized 16 data resource libraries are very useful to collect renewable energy data for those locations where the installation of a metrological station is not feasible.

**Keywords** Data resource · Wind speed data library · Solar radiation data library · Renewable data library · Data for prediction · Data for forecasting

---

S. B. Ahmed · H. Malik (✉) · S. M. Ayob · N. R. N. Idris · A. Jusoh  
Department of Electrical Power Engineering, Faculty of Electrical Engineering, Universiti  
Teknologi Malaysia (UTM), Skudai, Malaysia  
e-mail: [hasmat@utm.my](mailto:hasmat@utm.my)

S. B. Ahmed  
e-mail: [ahmed.subeyr@graduate.utm.m](mailto:ahmed.subeyr@graduate.utm.m)

S. M. Ayob  
e-mail: [e-shahrin@utm.my](mailto:e-shahrin@utm.my)

N. R. N. Idris  
e-mail: [e-nrumzi@utm.my](mailto:e-nrumzi@utm.my)

A. Jusoh  
e-mail: [awang@utm.my](mailto:awang@utm.my)

F. P. G. Márquez  
Ingenium Research Group, Department, Universidad Castilla-La Mancha, 13071 Ciudad Real,  
Spain  
e-mail: [faustopedro.garcia@uclm.es](mailto:faustopedro.garcia@uclm.es)

# 1 Introduction

With the ability to generate a sustainable energy supply and act as a cornerstone element for microgrids in a way that contributes to the smart grid infrastructure, renewable energy is crucial among low-carbon energy technologies [1–10]. The widespread use of renewable energy (wind and solar power) is confronted with a number of difficulties due to the unpredictable and intermittent nature of its output [11–14]. As renewable energy sources become more prevalent, these uncertainties associated with renewable energy sources could jeopardize the system's dependability and power quality, raising concerns about key grid integration issues such as balancing management and reserve capacities [15, 16].

The use of renewable energy (wind speed and solar radiation) and power generation projections can reduce the requirement for energy balancing and enable the scheduling and dispatch of power generation using wind speed [17–28] and solar radiation [29–39]. Additionally, by minimizing the requirement for renewable energy curtailments and resulting increase in revenue from electricity market operations, projections can be crucial in maintaining costs at a level that is competitive [40–49]. It is, however, very challenging to precisely anticipate renewable energy (wind speed and solar radiation) and power accurately. This is due to the unpredictable and unstable properties of renewable energy (wind speed/solar radiation). Therefore, various energy and environment-related research organizations have invested significant resources in the creation and improvement of renewable energy (wind speed and solar radiation) and/or power forecasting systems [15–28].

Numerous forecasting strategies have been researched and put forth in the literature [50–55]; each makes use of a distinct technique and performs well with a particular prediction horizon depending on the data availability conditions. Recent studies in the area of renewable energy prediction/forecast are predominantly focused on the development of the data library for the focusing of wind and solar in whole world. In order to make precise forecasts/predictions about the generation of future renewable energy, forecasting and prediction for renewable energy involve analyzing historical and current data. In forecasting renewable energy, the following categories of data library are presented in this paper:

- Historical energy generation data can be used to understand seasonal patterns, trends, and changes in energy output. Examples of historical renewable energy generating data include solar irradiation, wind speed, and hydroelectric flow rates. For training forecasting models, this information is essential.
- Weather information data: Because it has a direct impact on the production of solar, wind, and hydropower, weather information is a crucial part of forecasting for renewable energy sources. To precisely anticipate the output of renewable energy, variables such as temperature, humidity, wind speed, wind direction, cloud cover, and precipitation are gathered from weather stations or meteorological models.
- Data on solar irradiance: Information on solar irradiance, such as global horizontal irradiance (GHI), direct normal irradiance (DNI), and diffuse horizontal irradiance (DHI), quantifies the amount of solar energy that is present at a specific location.



This information, which is essential for predicting solar energy, is gathered from measurements made by satellites or ground-based sensors.

- **Wind speed data:** Wind speed and direction data reveal the direction and force of the wind at a particular location. This information is obtained via anemometers, wind masts, or remote sensing tools like LiDAR or SODAR (Light Detection and Ranging). For forecasting wind energy, it is crucial.

The organization of this paper is comprised of four sections. Section 1 represents the introduction of data resource libraries. Multiple domains of data resources are represented in Sect. 2, which includes generalist data repositories as well as specialized data repositories as per discipline. Section 3 includes the data resources for renewable energy prediction/forecasting for 214 locations of the world. Finally, conclusion is represented in Sect. 4.

## 2 Multiple Domains of Data Resources

A platform/system that can centrally store and manage data from various areas or domains is referred to as a “multiple domain data resource/repository”. Data from different sources and industries, including commerce, science, medicine, finance, social media, and more, can be accommodated by data repository. Data resources/repositories have several key characteristics such as centralized storage, data integration, data organization, data security, data sharing and collaboration, scalability, metadata management, data governance, data analysis and exploration. There are several types of data repositories, available in the digital domain. A few of the data repositories are generalist repositories and specialized repositories as shown in Tables 1 and 2, respectively.

### 2.1 *Re3data (Registry of Research Data Repositories)*

An open science resource that provides researchers, funding agencies, libraries, and publishers with a list of current international repositories for research data is the Registry of Research Data Repositories ([re3data.org](http://re3data.org)) [56]. A global directory of research data archives from all academic fields can be found at [re3data.org](http://re3data.org). In order to assist researchers in choosing an appropriate repository for their data and thereby meet the criteria outlined in data regulations, it gives an overview of the current research data repositories. In May 2013, the registration was formally introduced.

The registered data at re3data platform are in following different domains such as AID systems, API certificates, content types, data access, data access restrictions, database access, database access restrictions, database licenses, data licenses, data upload, data upload restrictions, enhanced publication, institution country, institution responsibility type, institution type, keywords, metadata standards, PID systems,

**Table 1** Generalist data repositories

S. No.	Name of repository	Access	Allowable space	Access link	Brief information
1	Science Data Bank	Free access	8 GB per file	<a href="https://www.scidb.cn/en">https://www.scidb.cn/en</a>	Open datasets: 6,959,643 Deposited datasets: 7,090,794 Data volume: 343,964 + GB Page views: 63,691,554 File downloads: 21,184,109
2	Harvard Dataverse	Free of cost	2 GB per file	<a href="https://dataverse.harvard.edu/">https://dataverse.harvard.edu/</a>	Social sciences (61,629), arts and humanities (36,414), earth and environmental sciences (12,313), medicine, health and life sciences (9262), law (5804), agricultural sciences (5415), other (3501), computer and information science (3083), physics (2308), engineering (2121), business and management (1636), astronomy and astrophysics (1251), chemistry (862), mathematical sciences (636)

(continued)

Table 1 (continued)

S. No.	Name of repository	Access	Allowable space	Access link	Brief information
3	Zenodo	Free of cost	50 GB per file	<a href="https://zenodo.org/">https://zenodo.org/</a>	Publication (1,795,418) + image (804,708) + dataset (196,004), software (103,967), presentation (40,172), other (19,822), poster (16,734), video (8072), lesson (4738), physical object (1093)
4	TU.ResearchData	Beyond 10 GB, paid	Limit to 10 GB yearly (free)	<a href="https://data.4tu.nl/">https://data.4tu.nl/</a>	Datasets: 8945 Most of available data are research data only
5	Dryad Digital Repository	Free of cost	300 GB per dataset	<a href="https://datadryad.org/stash">https://datadryad.org/stash</a>	50,000 data from 70,000 international institutions and collaboration
6	Figshare	Free of cost	Limit to 1 TB (free)	<a href="https://figshare.com/">https://figshare.com/</a>	Allowable single file up to 20 GB
7	Mendeley Data	Free of cost	10 GB per dataset	<a href="https://data.mendeley.com/">https://data.mendeley.com/</a>	Cloud-based repository managed by Elsevier
8	Open Science Framework	Free of cost	5 GB per file	<a href="https://osf.io/">https://osf.io/</a>	Managed by Center for Open Science

Table 2 Specialized data repositories as per discipline

S. No.	Disc	ToD	Name of repository	Access	Access link	Brief information
1	Physical sciences	Astrophysics research data	Astrophysics Source Code Library (ASCL)	Free of cost	<a href="https://ascl.net/">https://ascl.net/</a>	Source codes: astronomers and astrophysicists, solar system astronomers
2		Scattering data	High-energy physics data (HEP data)	Free of cost	<a href="https://www.hepdata.net/">https://www.hepdata.net/</a>	Search on 9965 publications and 126,302 data tables
3		High-energy physics data	Durham High-Energy Physics Database (HEPDdata)	Free of cost		
4	Computer sciences	Code	<i>GitHub</i>	Free of cost	<a href="https://github.com/">https://github.com/</a>	Written in Ruby, JavaScript, Go, C, Rust
5		Code	Software heritage	Free of cost	<a href="https://www.softwareheritage.org/">https://www.softwareheritage.org/</a>	Source files: 15,781,836,577 Projects: 241,590,736
6		Code and data	<i>RunMyCode</i>	Free of cost	<a href="http://www.runmycode.org/">http://www.runmycode.org/</a>	Openly share the code and data
7	<i>Neuroscience</i>	Computational neuroscience models	ModelDB	Free of cost	<a href="https://modeldb.science/">https://modeldb.science/</a>	1818 models
8		Neuroimaging data	Brain Analysis Library of Spatial maps and Atlases (BALSA)	Need to check	<a href="https://balsa.wustl.edu/">https://balsa.wustl.edu/</a>	Available 70 records
9		MRI and EEG data	<i>OpenfMRI</i>	Free of cost	<a href="https://openfmri.org/">https://openfmri.org/</a>	Number of currently available datasets: 95 Number of subjects across all datasets: 3372
10		MRI, PET, MEG, EEG, and iEEG data	<i>OpenNeuro</i>	Free of cost	<a href="https://openneuro.org/">https://openneuro.org/</a>	856 public datasets of "MRI, PET, MEG, EEG, and iEEG data"
11		Maps, parcellations, and atlases of the brain	NeuroVault	Free of cost	<a href="https://neurovault.org/">https://neurovault.org/</a>	All collected data 7225

(continued)

Table 2 (continued)

S. No.	Disc	ToD	Name of repository	Access	Access link	Brief information
12		DICOM and NIFTI images with normal and diagnoses	NeuroImaging Tools and Resources Collaboratory (NITRC)	Free of cost	<a href="https://www.nitrc.org/">https://www.nitrc.org/</a>	Data domain: CT (86), clinical (110), computational (229), ECG (13), EEG/MEG (165), imaging (89), MR (893), optical (65), PET/SPECT (97), other (146)
13	Chemistry	Crystal structures organic, inorganic, metal-organic compounds, and minerals' data (excluding biopolymers)	<i>Crystallography Open Database (COD)</i>	Free of cost	<a href="http://www.crystallography.net/cod/">http://www.crystallography.net/cod/</a>	502,986 data entries
14		Computational chemistry files	<i>ioChem-BD Computational Chemistry Datasets</i>	Free of cost	<a href="https://www.iochem-bd.org/">https://www.iochem-bd.org/</a>	344,006 collections available
15		Bioassay data	<i>ChEMBL</i>	Free of cost	<a href="https://www.ebi.ac.uk/che/mb/">https://www.ebi.ac.uk/che/mb/</a>	Assays 1,610,596 items
16		Functional enzymology data	<i>STRENDA-DB</i>	Free of cost	<a href="https://www.beilstein-strenda-db.org/strenda/index.xhtml">https://www.beilstein-strenda-db.org/strenda/index.xhtml</a>	Driven by 15 scientists of biochemistry, enzyme nomenclature, bioinformatics, systems biology, modeling, mechanistic enzymology, and theoretical biology areas
17		Compounds, substances, and bioassays data	<i>NCBI PubChem</i>	Free of cost	<a href="https://pubchem.ncbi.nlm.nih.gov/">https://pubchem.ncbi.nlm.nih.gov/</a>	925 data sources
18		Nanomaterial samples	<i>catNanoLab</i>	Free of cost	<a href="https://cmano1lab.cancer.gov/#">https://cmano1lab.cancer.gov/#</a>	Search samples 1566, 222 sample sources, 7434 characterizations, 1714 physico-chemical, 2800 in vitro, 170 in vivo, 2750 other
19	Social sciences	Archeology (isotope data)	<i>IsoArch</i>	Free of cost	<a href="https://isoarch.eu/">https://isoarch.eu/</a>	More than 50,000 + standardized isotopic data

(continued)

Table 2 (continued)

S. No.	Disc	ToD	Name of repository	Access	Access link	Brief information
20		Qualitative data	<i>Qualitative Data Repository</i>	Free of cost	<a href="https://qdr.syr.edu/">https://qdr.syr.edu/</a>	Collections (6), data projects (161), files (14,281)
21		Archeological data	<i>The Digital Archaeological Record (IDAR)</i>	Free of cost	<a href="https://www.tdar.org/about/">https://www.tdar.org/about/</a>	439,760 records
22		Heritage data	<i>Archaeology Data Service</i>	Free of cost	<a href="https://archaeologydataservice.ac.uk/">https://archaeologydataservice.ac.uk/</a>	1.4 million metadata
23		Archeology (radiocarbon data)	<i>Canadian Radiocarbon Date Database (CARD) database</i>	Free of cost	<a href="https://www.canadianarchaeology.ca/">https://www.canadianarchaeology.ca/</a>	Over 104,000 dates from the lower 48 US states
24		Social science data	<i>Inter-university Consortium for Political and Social Research (ICPSR)</i>	Free of cost	<a href="https://www.icpsr.umich.edu/web/pages/">https://www.icpsr.umich.edu/web/pages/</a>	18,798 studies, 6,208,878 variables
25	<i>Health and Medical Sciences</i>	Human subjects' data related to mental health research	<i>Research Domain Criteria Database (RDoCdb)</i>	Freely accessible	<a href="https://www.nimh.nih.gov/research/research-funded-by-nimh/rdoc">https://www.nimh.nih.gov/research/research-funded-by-nimh/rdoc</a>	Data of following domain: mental illness, any anxiety disorder, attention-deficit/hyperactivity disorder (ADHD), autism, spectrum disorder (ASD), bipolar disorder, eating disorders, major depression, obsessive-compulsive disorder (OCD), personality disorders, post-traumatic stress disorder (PTSD), schizophrenia, suicide
26		Clinical studies data	<i>ClinicalTrials.gov</i>	Freely accessible	<a href="https://clinicaltrials.gov/">https://clinicaltrials.gov/</a>	Data from 50 states and over 200 countries. Available API, study data, CSV

(continued)

Table 2 (continued)

S. No.	Disc	ToD	Name of repository	Access	Access link	Brief information
27		Medical research data	<i>PhysioNet</i>	Freely + restricted data	<a href="https://physionet.org/">https://physionet.org/</a>	Provide data, software. Open databases, restricted databases (18), credentialled databases (54), contributor review databases (3)
28		Medical image data	SICAS Medical Image Repository	Freely accessible	<a href="https://www.smir.ch/">https://www.smir.ch/</a>	Mortem CT images of 50 subjects
29		Clinical, demographic, and phenotypic data associated with autism spectrum disorder	<i>National Database for Autism Research (NDAR)</i>	Freely accessible	<a href="https://nda.nih.gov/about.html">https://nda.nih.gov/about.html</a>	151,831 subjects by age, 95,929 individuals ( <a href="https://www.re3data.org/repository/r3d100010717">https://www.re3data.org/repository/r3d100010717</a> )
30		Patient data	<i>Synapse</i>	Free up to 10 GB	<a href="https://www.synapse.org/">https://www.synapse.org/</a>	Data can be accessed through AD knowledge portal, dHealth digital health knowledge portal, BSMN 3IPortal, NF data portal, ARK portal, Ca32Incer complexity knowledge portal, psychencode knowledge portal
31		Clinical trial data related to mental illness	<i>National Database for Clinical Trials related to Mental Illness (NDCT)</i>	Freely accessible	<a href="https://catalog.data.gov/dataset/national-database-for-clinical-trials-related-to-mental-illness-ndct">https://catalog.data.gov/dataset/national-database-for-clinical-trials-related-to-mental-illness-ndct</a>	Data at all levels of biological and behavioral organization
32		De-identified medical images of cancer	<i>The Cancer Imaging Archive</i>	Freely accessible	<a href="https://www.cancerimagingarchive.net/">https://www.cancerimagingarchive.net/</a>	196 data entries
33		Drug abuse and HIV data	<i>National Addiction and HIV Data Archive Program (NAHDAP)</i>	Free of charge	<a href="https://www.icpsr.umich.edu/web/pages/NAHDAP/index.html">https://www.icpsr.umich.edu/web/pages/NAHDAP/index.html</a>	578 studies, 1,140,711 variables

(continued)

Table 2 (continued)

S. No.	Disc	ToD	Name of repository	Access	Access link	Brief information
34	BMDS data	Social, economic, and population data	<i>UK Data Service</i> (social, economic and population data)	Free of charge	<a href="https://ukdataservice.ac.uk/">https://ukdataservice.ac.uk/</a>	Data theme is: aging, COVID-19, crime, economics, environment and energy, education, ethnicity, food, health, housing, information and communication, labor, politics, and poverty
35	Materials science	Computational materials science data	<i>Materials Cloud</i>	Freely accessible	<a href="https://www.materialscloud.org/home">https://www.materialscloud.org/home</a>	Available 29,306,745 crystal structures data
36		Materials data	<i>NoMaD Repository</i>	Freely accessible	<a href="https://nomad-lab.eu/nomad-lab/">https://nomad-lab.eu/nomad-lab/</a>	Available data entries 12,529,831 and represented materials 2,976,441
37	Earth and planetary sciences	Marine data	<i>Sea scientific open data publication (SeanoE)</i> Open access (1175), on demand (127)	Freely accessible	<a href="https://www.seanoe.org/">https://www.seanoe.org/</a>	Data: physical oceanography (508), biological oceanography (261), chemical oceanography (196), environment (196), marine geology (135), fisheries and aquaculture (132), cross-discipline (94), atmosphere (49), administration and dimensions (43), economy (22), cryosphere (11), terrestrial (6)
38		Oceanic, atmospheric, and geophysical data; restricted data deposit	<i>NOAA National Centers for Environmental Information</i>	Freely accessible	<a href="https://www.ngdc.noaa.gov/">https://www.ngdc.noaa.gov/</a>	Data with several variables

(continued)



Table 2 (continued)

S. No.	Disc	ToD	Name of repository	Access	Access link	Brief information
39		Atmospheric radiation data	<i>Atmospheric Radiation Measurement (ARM) Data Archive</i>	Freely accessible	<a href="https://www.archive.arm.gov/discovery/">https://www.archive.arm.gov/discovery/</a>	Aerosols (668), atmospheric state (1394), atmospheric carbon (203), cloud properties (1509), radiometric (696), surface properties (496), non-geophysical (82)
40		Ecological/environmental research data	<i>ESS-DIVE archive</i>	Freely accessible	<a href="https://ess-dive.lbl.gov/about/">https://ess-dive.lbl.gov/about/</a>	Data with several variables
41		Ecological data	<i>KNB: The Knowledge Network for Biocomplexity</i>	Freely access up to 5 GB	<a href="https://knb.econinformatics.org/">https://knb.econinformatics.org/</a>	28,923 datasets, 28,923 metadata files
42			<i>Environmental Data Initiative</i>	Freely accessible	<a href="https://edirepository.org/">https://edirepository.org/</a>	Data with several variables
43		Rock and paleomagnetic data	<i>Magnetics Information Consortium (MagIC)</i>	Freely accessible	<a href="https://www2.earthref.org/MagIC">https://www2.earthref.org/MagIC</a>	Contribution (4422), locations (13,410), sites (229,136), samples (119,524), specimens (139,832), experiments (386,469), measurements (8,262,765)
44		Data concerning the Tibetan Plateau and surrounding regions	<i>National Tibetan Plateau/Third Pole Environment Data Center</i>	Freely accessible	<a href="https://data.tpdc.ac.cn/en/">https://data.tpdc.ac.cn/en/</a>	Data 5933, number of open datasets (3857)
45		Hydrologic data	<i>HydroShare (CUAHSI)</i>	Freely accessible	<a href="https://www.hydroshare.org/">https://www.hydroshare.org/</a>	Data with several variables
46		Marine geoscience data	<i>Marine Geoscience Data System (MGDS)</i>	Freely accessible	<a href="https://data.ess-dive.lbl.gov/">https://data.ess-dive.lbl.gov/</a>	794 datasets, 942 GB of content
47		Earth science data	<i>Interdisciplinary Earth Data Alliance</i>	Freely accessible	<a href="https://www.iiedata.org/">https://www.iiedata.org/</a>	Data with several variables

(continued)

Table 2 (continued)

S. No.	Disc	ToD	Name of repository	Access	Access link	Brief information
48			PANGAEA	Freely accessible	<a href="https://www.pangaea.de/">https://www.pangaea.de/</a>	Chemistry (72,786), lithosphere (49,622), biological (33,904), atmosphere (31,207), paleontology (25,691), ocean (22,101), ecology (20,313), land surface (8289), biosphere (4484), geophysics (4128), cryosphere (1737), lakes and rivers (802), human dimensions (578), fisheries (302), agriculture (160)
49		Atmospheric composition, water and energy cycles, and climate variability data	<i>Interdisciplinary Earth Data Alliance</i>	Freely accessible	<a href="https://di.sc.gsfc.nasa.gov/">https://di.sc.gsfc.nasa.gov/</a>	Archive size: 5,504,279 TB Archived data files: 203,648,342 Files distributed*: 4,365,225,776 Data volume distributed*: 52,472.643 TB
50	<i>Biological Sciences-I</i>	Immunology data	<i>Immunology Database and Analysis Portal (ImmPort)</i>	Freely accessible	<a href="https://docs.immport.org/">https://docs.immport.org/</a>	Over 6 million experimental results across 100+ diseases and conditions
51		Protein sequence	<i>Universal Protein Resource Knowledgebase (UniProt)</i>	Freely accessible	<a href="https://www.uniprot.org/">https://www.uniprot.org/</a>	Swiss-prot (569,516), TrEMBL (249,308,459)
52		Transcriptomic and cistromic data	<i>Signaling Pathways Project</i>	Freely accessible	<a href="http://signalingpathways.org/index.jsf">http://signalingpathways.org/index.jsf</a>	1642 datasets
53		Flow cytometry	FlowRepository	Freely accessible	<a href="http://flowrepository.org/">http://flowrepository.org/</a>	Public datasets, OMIP datasets, community datasets
54		Imaging data	<i>Coherent X-ray Imaging Data Bank (CXIDB)</i>	Freely accessible	<a href="https://www.cxidb.org/">https://www.cxidb.org/</a>	215 datasets are available

(continued)

Table 2 (continued)

S. No.	Disc	ToD	Name of repository	Access	Access link	Brief information
55			<i>Cell Image Library</i>	Freely accessible	<a href="http://www.cellimagelibrary.org/home">http://www.cellimagelibrary.org/home</a>	12,000 unique datasets and 30 TB of data
56			<i>Image Data Resource</i>	Freely accessible	<a href="http://idr.openmicroscopy.org/">http://idr.openmicroscopy.org/</a>	120 studies, 13,666,889 images, 361 TB
57		Metabolomics	<i>MetaboLights</i>	Freely accessible	<a href="http://www.ebi.ac.uk/metaboblights/">http://www.ebi.ac.uk/metaboblights/</a>	Complete file
58		Raw sequencing data, genome assemblies, annotated sequences, and sample metadata	<i>Genome Sequence Archive (GSA)</i>	Freely accessible	<a href="https://ngdc.cncb.ac.cn/gsa/">https://ngdc.cncb.ac.cn/gsa/</a>	682,346 projects, 24,803,103 experiments, 33,895,331 samples
59			<i>INSDC repositories</i>	Freely accessible	<a href="https://www.insdc.org/">https://www.insdc.org/</a>	Data available at: DDBJ ( <a href="https://www.ddbj.nig.ac.jp/index-e.html">https://www.ddbj.nig.ac.jp/index-e.html</a> ), EMBL-EBI ( <a href="https://www.ebi.ac.uk/">https://www.ebi.ac.uk/</a> ) and NCBI ( <a href="https://www.ncbi.nlm.nih.gov/">https://www.ncbi.nlm.nih.gov/</a> )
60		Genetic sequences	<i>GenBank</i>	Freely accessible	<a href="http://www.ncbi.nlm.nih.gov/genbank">http://www.ncbi.nlm.nih.gov/genbank</a>	By June 2023: bases (1,966,479,976,146), sequences (243,560,863)
61		Proteomics	<i>ProteomeXchange</i>	Freely accessible	<a href="http://www.proteomexcha.ngc.org/">http://www.proteomexcha.ngc.org/</a>	Total datasets: 28,190
62			<i>PRIDE</i>	Freely accessible	<a href="https://www.ebi.ac.uk/pride/">https://www.ebi.ac.uk/pride/</a>	Datasets (23,565)
63			<i>Panorama Public</i>	Freely + restricted data	<a href="https://panoramaweb.org/home/project-begin.view?">https://panoramaweb.org/home/project-begin.view?</a>	Total datasets: 527, public: 455, private: 72
64			<i>MASSIVE</i>	Freely accessible	<a href="https://massive.ucsd.edu/ProteoSAFe/static/massive.jsp">https://massive.ucsd.edu/ProteoSAFe/static/massive.jsp</a>	Public datasets: 13,858, number of files: 8,381,648
65	<i>Biological Sciences-2</i>	Genetic data per organism/family	<i>The Zebrafish Model Organism Database (ZFIN)</i>	Freely accessible	<a href="https://zfin.org/">https://zfin.org/</a>	Data with several variables
66			<i>FungiDB</i>	Freely accessible	<a href="https://fungidb.org/fungidb/app">https://fungidb.org/fungidb/app</a>	Data with several variables

(continued)

Table 2 (continued)

S. No.	Disc	ToD	Name of repository	Access	Access link	Brief information
67			<i>WormBase</i>	Freely accessible	<a href="https://blog.wormbase.org/">https://blog.wormbase.org/</a>	Brief communication (232), community (62), external website news (133), featured papers (28), grants (3), meetings (81), new datasets (60), new features (99), new labs (3), news (733), paper of interest (76), positions available (14), release notes (144), service status (46), tutorials (28), uncategorized (35), wormboard (8), wormbook (6)
68			<i>Solanaceae Genomics Network</i>	Freely accessible	<a href="https://solgenomics.net/">https://solgenomics.net/</a>	Data with several variables
69			<i>Xenopus Genomics Database (Xenbase)</i>	Freely accessible	<a href="http://www.xenbase.org/entry/">http://www.xenbase.org/entry/</a>	Data field: Xenopus stock center, Xenopus ontologies, community, genes with phenotypes and diseases, orthology, reagents, sequences, expression, genes
70			<i>The Arabidopsis Information Resource database (TAIR)</i>	Freely accessible	<a href="https://www.arabidopsis.org/">https://www.arabidopsis.org/</a>	Data with several variables
71			<i>Fly Base</i>	Freely accessible	<a href="https://flybase.org/">https://flybase.org/</a>	Data with several variables
72			<i>Saccharomyces Genome Database (SGD)</i>	Freely accessible	<a href="https://www.yeastgenome.org/">https://www.yeastgenome.org/</a>	Data with several variables
73			<i>Rat Genome Database (RGD)</i>	Freely accessible	<a href="https://rgd.mcw.edu/">https://rgd.mcw.edu/</a>	Data with several variables
74			<i>TriTrypDB</i>	Freely accessible	<a href="https://tritrypdb.org/tritrypdb/app">https://tritrypdb.org/tritrypdb/app</a>	Data with several variables

(continued)

Table 2 (continued)

S. No.	Disc	ToD	Name of repository	Access	Access link	Brief information
75			<i>PlasmODB</i>	Freely accessible	<a href="https://plasmodb.org/plasmo/app">https://plasmodb.org/plasmo/app</a>	Data with several variables
76			<i>Mouse Genome Informatics (MGI)</i>	Freely accessible	<a href="https://www.informatics.jax.org/">https://www.informatics.jax.org/</a>	Data with several variables
77			<i>Mycobank</i>	Freely accessible	<a href="https://www.mycobank.org/">https://www.mycobank.org/</a>	383,177 records
78			<i>Xenopus Genomics Database (Xenbase)</i>	Freely accessible	<a href="https://zfin.org/">https://zfin.org/</a>	Data with several variables
79			<i>ToxoDB</i>	Freely accessible	<a href="https://toxodb.org/toxo/app">https://toxodb.org/toxo/app</a>	Data with several variables

*BMDS* Business, Management, and Decision Sciences

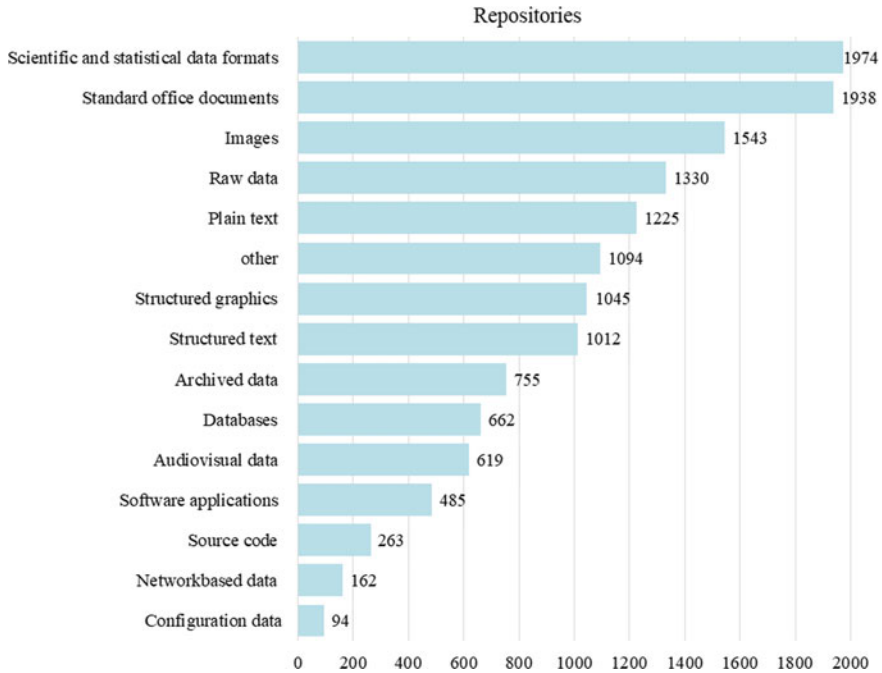


**Fig. 1** Available content types in Re3data repository [56]

provider types, quality management, repository languages, software, subjects, syndications, repository types, versioning. The service renders all registration metadata freely used under the Creative Commons CC0 deed. Data of different types of contents are represented in Fig. 1. API includes the following types of APIs: FTP (318), NetCDF (89), OAI-PMH (291), OpenDAP (50), REST (637), SOAP (56), SPARQL (42), SWORD (104), and other (330). Re3data repository includes following categories of data access such as closed (267), embargoed (468), open (2688), and restricted (1519). Re3data repository also includes following categories of software information such as CKAN (97), DSpace (126), Dataverse (168), DigitalCommons (5), EPrints (34), Fedora (48), MySQL (90), Nesstar (19), Opus (3), dLibra (3), eSciDoc (5), other (649), unknown (1187).

## 2.2 FAIRsharing

A resource on data and metadata standards that is curated, instructive, and educational that is connected to databases and data policies. FAIRsharing platform [57]

provides the 1622 standards (775—terminology artifact, 557—model/format, 244—reporting guidelines, 32—identifier schema, etc.), 2033 databases (1050—repositories, 836—knowledge bases, 147—knowledge bases’ repositories, etc.), and 166 policies. Available data on FAIRsharing platform are categorized into three categories such as humanities social sciences, natural sciences, and engineering sciences.

### 2.3 *DataONE*

In order to promote data sharing, data discovery, and open science, DataONE [58] is a network of interoperable data repositories. One of the first DataNet programs was first funded in 2009 with \$21.2 million from the US National Science Foundation.

For member, the three coordinating members offer network-wide functions. They have mirrored content, entire copies of science metadata, and geographical replication. The project was supervised by William Michener at the University of New Mexico (UNM), and UNM is one of the coordinating members. UNM, Oak Ridge Campus (a collaboration between University of Tennessee and Oak Ridge National Laboratory, ORNL), and University of California, Santa Barbara, serve as coordinating nodes.

### 2.4 *IEEEDataPort*<sup>TM</sup>

The *IEEEDataPort*<sup>TM</sup> [59] provides the dataset of multi-disciplinary domains dataset categories such as Artificial Intelligence (879), Astronomy (12), Biomedical and Health Sciences (307), Biophysiological Signals (104), Cloud Computing (55), Communications (333), Computational Intelligence (213), Computer Vision (350), COVID-19 (91), CRAWDAD (177), Demographic (22), Ecology (14), Education and Learning Technologies (46), Environmental/Climate Change (61), Financial (27), Geoscience and Remote Sensing (125), Image Fusion (43), Image Processing (477), IoT (232), Machine Learning (921), Other (433), Power and Energy (376), Reliability (69), Security (187), Sensors (226), Signal Processing (410), Social Sciences (87), Standards Research Data (260), Transportation (132), and Wireless Networking (226). The access of the datasets through *IEEEDataPort*<sup>TM</sup> is open access as well as payment basis. Few datasets are available based on open access. Following are the few examples for prediction and forecasting: Prediction of Energy Consumption Using Smart Meter Data (<https://iee-dataport.org/sites/default/files/analysis/38040/Prediction%20Of%20Energy%20Consumption%20Using%20Smart%20Meter%20Data.docx>), Power System Oscillation Mode Prediction Data

([https://iee-dataport.s3.amazonaws.com/data/13900/Power%20System%20Oscillation%20Mode%20Prediction%20Data.mat?response-content-disposition=attachment%3B%20filename%3D%22Power%20System%20Oscillation%20Mode%20Prediction%20Data.mat%22&X-Amz-Algorithm=AWS4-HMAC-SHA256&X-Amz-Credential=AKIAJOHYI4KJCE6Q7MIQ%2F20230326%2Fus-east-1%2Fs3%2Faws4\\_request&X-Amz-Date=20230326T101124Z&X-Amz-SignedHeaders=Host&X-Amz-Expires=3600&X-Amz-Signature=3377a7197fb123b036d3a367a139a66f3d5f56d20812bf7171d4aefbca9a4402&KDV9HX7OKbVhvX5aWTb7qVD6nkTzmegF](https://iee-dataport.s3.amazonaws.com/data/13900/Power%20System%20Oscillation%20Mode%20Prediction%20Data.mat?response-content-disposition=attachment%3B%20filename%3D%22Power%20System%20Oscillation%20Mode%20Prediction%20Data.mat%22&X-Amz-Algorithm=AWS4-HMAC-SHA256&X-Amz-Credential=AKIAJOHYI4KJCE6Q7MIQ%2F20230326%2Fus-east-1%2Fs3%2Faws4_request&X-Amz-Date=20230326T101124Z&X-Amz-SignedHeaders=Host&X-Amz-Expires=3600&X-Amz-Signature=3377a7197fb123b036d3a367a139a66f3d5f56d20812bf7171d4aefbca9a4402&KDV9HX7OKbVhvX5aWTb7qVD6nkTzmegF)), Data for Article Electricity Load Forecast Considering Search Engine Indices ([https://iee-dataport.s3.amazonaws.com/data/41148/Data%20for%20Article%20Electricity%20Load%20Forecast%20Considering%20Search%20Engine%20Indices.zip?response-content-disposition=attachment%3B%20filename%3D%22Data%20for%20Article%20Electricity%20Load%20Forecast%20Considering%20Search%20Engine%20Indices.zip%22&X-Amz-Algorithm=AWS4-HMAC-SHA256&X-Amz-Credential=AKIAJOHYI4KJCE6Q7MIQ%2F20230326%2Fus-east-1%2Fs3%2Faws4\\_request&X-Amz-Date=20230326T101156Z&X-Amz-SignedHeaders=Host&X-Amz-Expires=3600&X-Amz-Signature=21ec4136ce4da50c37d2cfdb952a8263cca98f440536b285b9385ec5d89e1344&PJpNnqa4jgVjXYajiNU1UPCWwR8BVLmV](https://iee-dataport.s3.amazonaws.com/data/41148/Data%20for%20Article%20Electricity%20Load%20Forecast%20Considering%20Search%20Engine%20Indices.zip?response-content-disposition=attachment%3B%20filename%3D%22Data%20for%20Article%20Electricity%20Load%20Forecast%20Considering%20Search%20Engine%20Indices.zip%22&X-Amz-Algorithm=AWS4-HMAC-SHA256&X-Amz-Credential=AKIAJOHYI4KJCE6Q7MIQ%2F20230326%2Fus-east-1%2Fs3%2Faws4_request&X-Amz-Date=20230326T101156Z&X-Amz-SignedHeaders=Host&X-Amz-Expires=3600&X-Amz-Signature=21ec4136ce4da50c37d2cfdb952a8263cca98f440536b285b9385ec5d89e1344&PJpNnqa4jgVjXYajiNU1UPCWwR8BVLmV)), Solar Irradiance Data Under Dynamic Weather Conditions (sunny and cloudy days) ([https://iee-dataport.s3.amazonaws.com/data/1129731/Solar\\_Irradiance\\_Data.zip?response-content-disposition=attachment%3B%20filename%3D%22Solar\\_Irradiance\\_Data.zip%22&X-Amz-Algorithm=AWS4-HMAC-SHA256&X-Amz-Credential=AKIAJOHYI4KJCE6Q7MIQ%2F20230326%2Fus-east-1%2Fs3%2Faws4\\_request&X-Amz-Date=20230326T101855Z&X-Amz-SignedHeaders=Host&X-Amz-Expires=3600&X-Amz-Signature=5e8a66b4e4fc2da1af9a949503c2d64b245bf60fec3f2778866dfd39f6ddb46f](https://iee-dataport.s3.amazonaws.com/data/1129731/Solar_Irradiance_Data.zip?response-content-disposition=attachment%3B%20filename%3D%22Solar_Irradiance_Data.zip%22&X-Amz-Algorithm=AWS4-HMAC-SHA256&X-Amz-Credential=AKIAJOHYI4KJCE6Q7MIQ%2F20230326%2Fus-east-1%2Fs3%2Faws4_request&X-Amz-Date=20230326T101855Z&X-Amz-SignedHeaders=Host&X-Amz-Expires=3600&X-Amz-Signature=5e8a66b4e4fc2da1af9a949503c2d64b245bf60fec3f2778866dfd39f6ddb46f)), Day-Ahead Electricity Demand Forecasting: Post-COVID Paradigm, Bayesian CNN-BiLSTM and Vine-GMCM Based Probabilistic Forecasting of Hour-Ahead Wind Farm Power Outputs (Input dataset), Short-Term Photovoltaic Power Forecasting Based on Long Short-Term Memory Neural Network and Attention Mechanism, Energy Forecasting in Fuel Cell, Short-Term Load Forecasting Data with Hierarchical Advanced Metering Infrastructure and Weather Features, The Use of Extreme Value Theory for Forecasting Long-Term Substation Maximum Electricity Demand, etc.

## 2.5 UCI Machine Learning Repository

UCI Machine Learning (ML) Repository is created by the Center for Machine Learning and Intelligent System, Bren School of Information and Computer Science, University of California, Irvine. As of now, UCI-ML Repository includes 622 datasets [60], which are freely available (open access) to download and further analysis. These datasets have been categorized as per task (named as classification, regression, clustering, and other), attribute type (i.e., categorical, numerical, and mixed), data type (i.e., multivariate, univariate, sequential, time series, text, domain theory,



and other), area (i.e., life science, physical science, CS/Engineering, social science, business, game, and other), number of attributes (less than 100, 100–1000, greater than 1000), and format type (i.e., matrix and non-matrix). Moreover, few examples of forecast and prediction datasets are available for analysis, such as Traffic Flow Forecasting, Daily Demand Forecasting Orders, Bias correction of numerical prediction model temperature forecast, Demand Forecasting for a store, Indoor User Movement Prediction from RSS data, Appliances energy prediction, Bias correction of numerical prediction model temperature forecast, Water Quality Prediction.

## ***2.6 Data in Brief of Science Direct Digital Library***

Data in Brief (DIB) is a multi-disciplinary, open access, peer-reviewed journal of ScienceDirect [61], which provides research data. DIB provides the platform for original dataset of simulated data, negative data, questionnaires/survey data, published raw data complete dataset to be used as a workbench to evaluate the profitability of an offshore wind farm.

# **3 Data Resources for Renewable Energy Prediction/Forecasting**

## ***3.1 Data Resources for Renewable Energy Prediction/Forecasting for Asian Countries***

Asian countries are categorized into five sub-categories such as Central Asia (5 countries: Uzbekistan, Kazakhstan, Tajikistan, Kyrgyzstan, and Turkmenistan), Eastern Asia (5 countries: China, Japan, South Korea, North Korea, and Mongolia), South-eastern Asia (11 countries: Indonesia, Philippines, Vietnam, Thailand, Myanmar, Malaysia, Cambodia, Laos, Singapore, Timor-Leste, Brunei), Southern Asia (9 countries: India, Pakistan, Bangladesh, Iran, Afghanistan, Nepal, Sri Lanka, Bhutan, Maldives), and Western Asia (18 countries: Turkey, Iraq, Saudi Arabia, Yemen, Syria, Jordan, Azerbaijan, United Arab Emirates, Israel, Lebanon, Oman, State of Palestine, Kuwait, Georgia, Armenia, Qatar, Bahrain, Cyprus). Data Resources for Renewable Energy Prediction/Forecasting for Asian Countries are represented in sub-sequence sections.

**Table 3** Data resources for Southern Asia countries

S. No.	Name of country	Name of repository	Access	Access link	Solar/wind	Brief information
1	India	National Institute of Wind Energy	Restricted	<a href="https://niwe.res.in/downloads.php">https://niwe.res.in/downloads.php</a>	S, W	<ul style="list-style-type: none"> <li>– Data available for different heights of station: 50, 80, 100, and 120 m</li> <li>– Data are available per minute, hour, day, week</li> <li>– Data available 2005–till date</li> <li>– Variables in the data are: wind speed, solar radiation, dew point, latitude, long., height from sea</li> <li>– Data from 448 stations</li> </ul>
2	Pakistan	▼	▼	▼	▼	▼
3	Bangladesh	Bangladesh Meteorological Department	Restricted	<a href="http://www.bmddataportal.com/">http://www.bmddataportal.com/</a>	W	<ul style="list-style-type: none"> <li>– The data of 20–25 km resolution in three horizons: 3 h, daily, and month</li> </ul>
4	Iran	▼	▼	▼	▼	▼
5	Afghanistan	▲	▲	▲	▲	▲
6	Nepal	Department of Hydrology and Meteorology	Restricted	<a href="https://www.dhm.gov.np/downloads">https://www.dhm.gov.np/downloads</a>	S, W	<ul style="list-style-type: none"> <li>– Data are measured in different stations scattered whole country, which has different horizons hourly, daily, and monthly</li> </ul>
7	Sri Lanka	Department of Meteorology—Sri Lanka	Restricted	<a href="https://www.meteo.gov.lk/index.php?option=com_content&amp;view=article&amp;id=100&amp;Itemid=321&amp;lang=en">https://www.meteo.gov.lk/index.php?option=com_content&amp;view=article&amp;id=100&amp;Itemid=321&amp;lang=en</a>	W	<ul style="list-style-type: none"> <li>– Daily parameters per station</li> <li>– Daily average per station</li> <li>– 3 h data per station</li> <li>– 10 min interval per station</li> <li>– Hourly data per station</li> <li>– Monthly average per station</li> </ul>

(continued)

Table 3 (continued)

S. No.	Name of country	Name of repository	Access	Access link	Solar/wind	Brief information
8	Bhutan	National Center for Hydrology and Meteorology	Available on request	<a href="https://www.nchm.gov.bt/">https://www.nchm.gov.bt/</a>	S, W	<a href="https://www.nchm.gov.bt/attachment/ckfinder/userfiles/files/NCHM%20Hydromet%20Data%20Request%20Form%20_2020.pdf">https://www.nchm.gov.bt/attachment/ckfinder/userfiles/files/NCHM%20Hydromet%20Data%20Request%20Form%20_2020.pdf</a> – Data can be in hourly, daily, monthly, and annually
9	Maldives	Maldives Meteorological Service	Freely accessible	<a href="https://www.meteorology.gov.mv/climate-data">https://www.meteorology.gov.mv/climate-data</a>	W	
10	Afghanistan	World Bank Group	Freely accessible	<a href="https://globalsolaratlas.info/download/afghanistan">https://globalsolaratlas.info/download/afghanistan</a>	S	Solar resource (GHI, DNI, DIF, GTI, OPTA), PV power potential (PVOUT), and other parameters are provided in the form of raster (gridded) data in two formats: GeoTIFF and AAIGRID (Esri ASCII Grid)
		SolarGIS	Restricted	<a href="https://solargis.com/maps-and-gis-data/download/afghanistan">https://solargis.com/maps-and-gis-data/download/afghanistan</a>	S	More specific and customized than World Bank Group data
		National Renewable Energy Laboratory (NREL)	Freely accessible	<a href="https://nsrdb.nrel.gov/data-viewer">https://nsrdb.nrel.gov/data-viewer</a>	S, W	– The first dataset is in 15, 30, 60 min timestamps with 4 km resolution and is collected in 2017–2019 – The second dataset is in 60 min timestamp in the years between 2000 and 2014 – Parameters in both datasets are temperature, clearsky DHI, clearsky DNI, clearsky GHI, cloud type, dew point, DHI, DNI, fill flag, GHI, ozone, relative humidity, solar zenith angle, surface albedo, pressure, precipitable water, wind direction, wind speed

▼: Data resource is given in Table 25, ▲: Data resource is given in this table

### **3.1.1 Data Resources for Southern Asia Countries**

Total nine countries (India, Pakistan, Bangladesh, Iran, Afghanistan, Nepal, Sri Lanka, Bhutan, and Maldives) are available in southern part of Asia. Data resources of all nine Southern Asia Countries are represented in Table 3.

### **3.1.2 Data Resources for Western Asia Countries**

Total 18 countries (Turkey, Iraq, Saudi Arabia, Yemen, Syria, Jordan, Azerbaijan, UAE-United Arab Emirates, Israel, Lebanon, Oman, State of Palestine, Kuwait, Georgia, Armenia, Qatar, Bahrain, Cyprus) are available in western part of Asia. Data resources of all 18 western Asia countries are represented in Table 4.

### **3.1.3 Data Resources for Southeastern Asia Countries**

Total 11 countries (Indonesia, Philippines, Vietnam, Thailand, Myanmar, Malaysia, Cambodia, Laos, Singapore, Timor-Leste, Brunei) are available in Southeastern part of Asia. Data resources of all 11 Southeastern Asia countries are represented in Table 5.

### **3.1.4 Data Resources for Central Asia Countries**

Total 5 countries (Uzbekistan, Kazakhstan, Tajikistan, Kyrgyzstan, and Turkmenistan) are available in Central part of Asia. Data resources of all five Central Asia countries are represented in Table 6.

### **3.1.5 Data Resources for Eastern Asia Countries**

Total 5 countries (China, Japan, South Korea, North Korea, and Mongolia) are available in Eastern part of Asia. Data resources of all five Eastern Asia countries are represented in Table 7.

## ***3.2 Data Resources for Renewable Energy Prediction/ Forecasting for Africa Countries***

All 54 African countries are categorized in to five sub-categories such as eastern Africa (18 countries: Ethiopia, Tanzania, Kenya, Uganda, Mozambique, Madagascar, Malawi, Zambia, Somalia, Zimbabwe, Rwanda, Burundi, South Sudan, Eritrea, Mauritius, Djibouti, Comoros, Seychelles), Middle Africa (9 countries: DR Congo, Angola, Cameroon, Chad, Congo, Central African Republic, Gabon, Equatorial Guinea, Sao Tome and Principe), Northern Africa (6 countries: Egypt, Algeria, Sudan, Morocco, Tunisia, Libya), Southern Africa (5 countries: South

**Table 4** Data resources for West Asia countries

S. No.	Name of country	Name of repository	Access	Access link	Solar/ wind	Brief information
1	Turkey	Turkish State Meteorological Service	Freely accessible	<a href="https://mgm.gov.tr/eng/for-ecast-5days.aspx">https://mgm.gov.tr/eng/for-ecast-5days.aspx</a>	S, W	<a href="http://www.omn.urv.cat/MEDARE/docs/3wo-rkshop/20_turkey.pdf">http://www.omn.urv.cat/MEDARE/docs/3wo-rkshop/20_turkey.pdf</a> (detailed information) <a href="http://www.solar-med-atlas.org/solarmed-atlas/download.htm">http://www.solar-med-atlas.org/solarmed-atlas/download.htm</a> (Solar Atlas for the Mediterranean)
2	Iraq	Iraqi Agrometeorological Center	Freely accessible	<a href="https://www.agromet.gov.iq/eng/document.php">https://www.agromet.gov.iq/eng/document.php</a>	S, W	Data will be sent to your email after request at least after one week
3	Saudi Arabia	▼	▼	▼	▼	▼
4	Yemen	▼	▼	▼	▼	▼
5	Syria	Solar Atlas for the Mediterranean	Freely accessible	<a href="http://www.solar-med-atlas.org/solarmed-atlas/download.htm">http://www.solar-med-atlas.org/solarmed-atlas/download.htm</a>	S	Download ready-made static GIS packages (for QGIS software) for nine countries
6	Jordan	▼	▼	▼	▼	▼
7	Azerbaijan	Carto	Restricted	<a href="https://carto.com/spatial-data-catalog/browser/dataset/ws_historic_f274d7b4/">https://carto.com/spatial-data-catalog/browser/dataset/ws_historic_f274d7b4/</a>	S, W	Historical data for 2000 to present with a lot of parameter include wind speed and solar radiation. The data are 22 km spatially and hourly resolution

(continued)

Table 4 (continued)

S. No.	Name of country	Name of repository	Access	Access link	Solar/wind	Brief information
8	UAE	▼	▼	▼	▼	▼
9	Israel	Israel Meteorological Service	Freely accessible	<a href="https://ims.gov.il/en/data_gov">https://ims.gov.il/en/data_gov</a>	S, W	Solar radiation and wind speed in different horizons and different stations to choose
10	Lebanon	▼	▼	▼	▼	▼
11	Oman	▼	▼	▼	▼	▼
12	State of Palestine	▼	▼	▼	▼	▼
13	Kuwait	▼	▼	▼	▼	▼
14	Georgia	▼	▼	▼	▼	▼
15	Armenia	Global Solar Atlas	Freely accessible	<a href="https://energydata.info/dataset/armenia-solar-radiation-measurement-data">https://energydata.info/dataset/armenia-solar-radiation-measurement-data</a>	S	Hourly direct normal irradiance and global horizontal solar irradiance data, 1990–July 2016
16	Qatar	Civil Aviation Authority	Freely accessible	<a href="https://www.data.gov.qa/explore/dataset/msl-pressure-and-scalar-wind-speed/information/">https://www.data.gov.qa/explore/dataset/msl-pressure-and-scalar-wind-speed/information/</a>	W	Monthly average speed average between 2011 and 2018 <a href="https://ds.data.jma.go.jp/tcc/RaiInfoshare/mem/ber/qatar.html">https://ds.data.jma.go.jp/tcc/RaiInfoshare/mem/ber/qatar.html</a>
17	Bahrain	▼	▼	▼	▼	▼
18	Cyprus	Cyprus Department of Meteorology	Available on request	<a href="http://www.moa.gov.cy/moa/dm/dm.nsf/meteorstations_en?OpenDocument">http://www.moa.gov.cy/moa/dm/dm.nsf/meteorstations_en?OpenDocument</a>	S, W	<a href="https://www.data.gov.cy/node/3900?langua=ge=en">https://www.data.gov.cy/node/3900?langua=ge=en</a> (request online)

▼: Data resource is given in Table 25

**Table 5** Data resources for Southeastern Asian countries

S. No.	Name of country	Name of repository	Access	Access link	Solar/wind	Brief information
1	Indonesia	(1) EMD International A/S (2) BMKG (Meteorological, Climatological and Geophysical Agency)	Freely accessible	(1) <a href="http://indonesia.windprospecting.com/">http://indonesia.windprospecting.com/</a> (2) <a href="http://dataonline.bmkg.go.id/home">http://dataonline.bmkg.go.id/home</a>	S, W	Average wind speed, power density, temperature, wind direction, solar radiation for the 50, 75, 100, 150 m height. Download at: <a href="http://dataonline.bmkg.go.id/akses_data">http://dataonline.bmkg.go.id/akses_data</a>
2	Philippines	▼	▼	▼	▼	▼
3	Vietnam	▼	▼	▼	▼	▼
4	Thailand	▼	▼	▼	▼	▼
5	Myanmar	▼	▼	▼	▼	▼
6	Malaysia	Malaysia Meteorological Department (MMD)	Freely accessible	<a href="https://www.met.gov.my/en/">https://www.met.gov.my/en/</a>	S, W	<a href="https://aeesj.com/wp-content/uploads/2021/05/AEEESJ28316-1.pdf">https://aeesj.com/wp-content/uploads/2021/05/AEEESJ28316-1.pdf</a>
7	Cambodia	▼	▼	▼	▼	▼
8	Laos	▼	▼	▼	▼	▼
9	Singapore	Meteorological Service Singapore	Freely accessible	<a href="http://www.weather.gov.sg/client-historical-daily/">http://www.weather.gov.sg/client-historical-daily/</a>	S, W	Daily data from 2010 until today from different stations throughout the country
10	Timor-Leste	▼	▼	▼	▼	▼
11	Brunei	Brunei Darussalam Meteorological Department (BDMD)	Available on request	<a href="http://www.bruneweather.com.bn/downloads">http://www.bruneweather.com.bn/downloads</a>	S, W	<a href="http://www.met.gov.bn/admin/upload/downloads/1678780148.pdf">http://www.met.gov.bn/admin/upload/downloads/1678780148.pdf</a>

▼: Data resource is given in Table 25

**Table 6** Data resources for Central Asia countries

S. No.	Name of country	Name of repository	Access	Access link	Solar/wind	Brief information
1	Uzbekistan	▼	▼	▼	▼	▼, <a href="https://data.egov.uz/eng/statistics">https://data.egov.uz/eng/statistics</a>
2	Kazakhstan	▼	▼	▼	▼	▼, <a href="https://www.kazhydromet.kz/en/">https://www.kazhydromet.kz/en/</a>
3	Tajikistan	▼	▼	▼	▼	▼, <a href="https://www.meteo.tj/en">https://www.meteo.tj/en</a>
4	Kyrgyzstan	▼	▼	▼	▼	▼, for more information ( <a href="https://www.jma.go.jp/jma/jma-eng/satellite/ra2wigosprojec/documents/5th_meeting_program_presentation/CountryReport/Kyrgyz.pdf">https://www.jma.go.jp/jma/jma-eng/satellite/ra2wigosprojec/documents/5th_meeting_program_presentation/CountryReport/Kyrgyz.pdf</a> )
5	Turkmenistan	▼	▼	▼	▼	▼, for more information ( <a href="https://en.ilmati.teenlaitos.fi/weather/turkmenistan/ashgabat">https://en.ilmati.teenlaitos.fi/weather/turkmenistan/ashgabat</a> )

▼: Data resource is given in Table 25



**Table 7** Data resources for Eastern Asia countries

S. No.	Name of country	Name of repository	Access	Access link	Solar/wind	Brief information
1	China	National Tibetan Plateau Data Center (TPDC)	Freely accessible	<a href="https://data.tpdc.ac.cn/home">https://data.tpdc.ac.cn/home</a>	S, W	A lot of datasets in deferent timestamps and resolution
		China Meteorological Data Service Centre	Available on request	<a href="http://data.cma.cn/">http://data.cma.cn/</a>	S, W	Public datasets for request granted users
2	Japan	Japan Meteorological Agency	Freely accessible	<a href="https://www.data.jma.go.jp/gmd/env/radiation/en/data_rad_e.html">https://www.data.jma.go.jp/gmd/env/radiation/en/data_rad_e.html</a>	S, W	Data of direct and diffuse solar radiation are given in text format recorded in six stations in Japan. Resolution of the data is daily
			Freely accessible	<a href="https://www.data.jma.go.jp/obd/stats/etm/view/monthly_s3_en.php?block_no=47401&amp;view=11">https://www.data.jma.go.jp/obd/stats/etm/view/monthly_s3_en.php?block_no=47401&amp;view=11</a>	S, W	Monthly data of global solar radiation, temperature, wind speed, air pressure, relative humidity, vapor pressure, sunshine duration, precipitation, snowfall depth
3	South Korea	▼	▼	▼	▼	▼, for more information ( <a href="https://www.kma.go.kr/eng/index.jsp">https://www.kma.go.kr/eng/index.jsp</a> )
4	North Korea	▼	▼	▼	▼	▼
5	Mongolia	Mongolia Meteorological Agency	Restricted	<a href="http://w.tsag-agaar.gov.mn/eng">http://w.tsag-agaar.gov.mn/eng</a>	S, W	Daily, monthly, yearly data

▼: Data resource is given in Table 25

Africa, Namibia, Botswana, Lesotho, Eswatini), and Western Africa (16 countries: Nigeria, Ghana, Côte d'Ivoire, Niger, Burkina Faso, Mali, Senegal, Guinea, Benin, Togo, Sierra Leone, Liberia, Mauritania, Gambia, Guinea-Bissau, Cabo Verde). Data resources for renewable energy prediction/forecasting for all African countries are represented in sub-sequence sections.

### **3.2.1 Data Resources for Northern Africa**

Total 5 countries (Egypt, Algeria, Sudan, Morocco, Tunisia, and Libya) are available in Northern part of Africa. Data resources of all five Northern Africa countries are represented in Table 8.

### **3.2.2 Data Resources for Western Africa**

Total 16 countries (Nigeria, Ghana, Côte d'Ivoire, Niger, Burkina Faso, Mali, Senegal, Guinea, Benin, Togo, Sierra Leone, Liberia, Mauritania, Gambia, Guinea-Bissau, and Cabo Verde) are available in Western part of Africa. Data resources of all 16 Western Africa countries are represented in Table 9.

### **3.2.3 Data Resources for Central/Middle Africa**

Total nine countries (DR Congo, Angola, Cameroon, Chad, Congo, Central African Republic, Gabon, Equatorial Guinea, and Sao Tome and Principe) are available in Central/Middle part of Africa. Data resources of all nine Central/Middle Africa countries are represented in Table 10.

### **3.2.4 Data Resources for Eastern Africa**

Total 18 countries (Ethiopia, Tanzania, Kenya, Uganda, Mozambique, Madagascar, Malawi, Zambia, Somalia, Zimbabwe, Rwanda, Burundi, South Sudan, Eritrea, Mauritius, Djibouti, Comoros, and Seychelles) are available in Eastern part of Africa. Data resources of all 18 Eastern Africa countries are represented in Table 11.

### **3.2.5 Data Resources for Southern Africa**

Total five countries (South Africa, Namibia, Botswana, Lesotho, and Eswatini) are available in Southern part of Africa. Data resources of all five Southern Africa countries are represented in Table 12.

**Table 8** Data resources for Northern Africa countries

S. No.	Name of country	Name of repository	Access	Access link	Solar/wind	Brief information
1	Egypt	Solar Atlas for the Mediterranean	Freely accessible	<a href="http://www.solar-med-atlas.org/solarmed-atlas/download.htm">http://www.solar-med-atlas.org/solarmed-atlas/download.htm</a>	S	GHI For more information click <a href="http://nwp.gov.eg/">http://nwp.gov.eg/</a> <a href="http://nwp.gov.eg/category/weather.php">http://nwp.gov.eg/category/weather.php</a>
2	Algeria	Solar Atlas for the Mediterranean	Freely accessible	<a href="http://www.solar-med-atlas.org/solarmed-atlas/download.htm">http://www.solar-med-atlas.org/solarmed-atlas/download.htm</a>	S	GHI For more information click <a href="https://www.aps.dz/en/algéria/tag/National%20Meteorological%20Office">https://www.aps.dz/en/algéria/tag/National%20Meteorological%20Office</a>
3	Sudan	▼	▼	▼	▼	▼
4	Morocco	Solar Atlas for the Mediterranean	Freely accessible	<a href="http://www.solar-med-atlas.org/solarmed-atlas/download.htm">http://www.solar-med-atlas.org/solarmed-atlas/download.htm</a>	S	For more information: <a href="http://www.marocmeteo.ma/">http://www.marocmeteo.ma/</a>
5	Tunisia	Solar Atlas for the Mediterranean	Freely accessible	<a href="http://www.solar-med-atlas.org/solarmed-atlas/download.htm">http://www.solar-med-atlas.org/solarmed-atlas/download.htm</a>	S	For more information: <a href="https://www.meteo.tn/en">https://www.meteo.tn/en</a>
6	Libya	Solar Atlas for the Mediterranean	Freely accessible	<a href="http://www.solar-med-atlas.org/solarmed-atlas/download.htm">http://www.solar-med-atlas.org/solarmed-atlas/download.htm</a>	S	For more information: (1) <a href="https://www.state.gov/joint-statement-on-the-situation-in-libya-4/">https://www.state.gov/joint-statement-on-the-situation-in-libya-4/</a> (2) <a href="https://www.worlddata.info/africa/libya/climate.php">https://www.worlddata.info/africa/libya/climate.php</a>

▼: Data resource is given in Table 25

**Table 9** Data resources for Western Africa countries

S. No.	Name of country	Name of repository	Access	Access link	Solar/wind	Brief information
1	Nigeria	▼	▼	▼	▼	▼, more information at <a href="https://mimet.gov.ng/">https://mimet.gov.ng/</a>
2	Ghana	Ghana Meteorological Agency	Available on request	Access link: <a href="https://www.meteo.gov.gh/gmet/category/frequently-asked-questions/faq-s-on-meteorological-agency/">https://www.meteo.gov.gh/gmet/category/frequently-asked-questions/faq-s-on-meteorological-agency/</a>	S, W	Data are available after formal request to the email and address mention in the link
3	Côte d'Ivoire	▼	▼	▼	▼	▼
4	Niger	▼	▼	▼	▼	▼
5	Burkina Faso	Augsburg University—Jan Bliefernicht	Freely accessible	<a href="https://dataportal.pauwes.dz/geonetwork/srv/api/records/340c37ba-bf77-4b82-b481-c0bdbbf8ec42">https://dataportal.pauwes.dz/geonetwork/srv/api/records/340c37ba-bf77-4b82-b481-c0bdbbf8ec42</a>	S, W	Half-hourly data of precipitation, air temperature, radiation, wind speed, air pressure, radiation
6	Mali	▼	▼	▼	▼	▼
7	Senegal	Agence Nationale de l'Aviation Civile et de la Météorologie	Freely accessible	<a href="http://www.anacim.sn/spip.php?article67">http://www.anacim.sn/spip.php?article67</a>	S, W	
8	Guinea	Direction Nationale de la Meteorologie	Available on request	<a href="https://meteoguinnee.net/commande/">https://meteoguinnee.net/commande/</a>	S, W	Need request but they do not publish what type of data they have available
9	Benin	▼	▼	▼	▼	▼, more info at: <a href="https://meteobenin.bj/">https://meteobenin.bj/</a>
10	Togo	▼	▼	▼	▼	▼

(continued)

Table 9 (continued)

S. No.	Name of country	Name of repository	Access	Access link	Solar/wind	Brief information
11	Sierra Leone	Sierra Leone Meteorological Agency	Freely accessible	<a href="https://slmet.gov.sl/">https://slmet.gov.sl/</a>	S, W	Temperature, wind direction, wind speed, dew point, cloud cover, precipitation, surface pressure
12	Liberia	▼	▼	▼	▼	▼
13	Mauritania	Mauritius Meteorological Services	Freely accessible	<a href="http://metservice.intnet.mu/cli-mate-services/climate-info-and-data.php">http://metservice.intnet.mu/cli-mate-services/climate-info-and-data.php</a>	S, W	Over 50 years of climate data for a good number of stations fairly well distributed spatially over the Republic. Other data at: <a href="http://www.solar-med-atlas.org/solarmed-atlas/download.htm">http://www.solar-med-atlas.org/solarmed-atlas/download.htm</a>
14	Gambia	▼	▼	▼	▼	▼
15	Guinea-Bissau	▼	▼	▼	▼	▼
16	Cabo Verde	NOVELTIS	Restricted	<a href="https://dataportal.pauwes.dz/geonetwork/srv/api/records/871ee576-d4e0-4c1e-9f42-7ebc9de78e0a">https://dataportal.pauwes.dz/geonetwork/srv/api/records/871ee576-d4e0-4c1e-9f42-7ebc9de78e0a</a>	S	Average GHI

▼ : Data resource is given in Table 25

**Table 10** Data resources for Central Africa countries

S. No.	Name of country	Name of repository	Access	Access link	Solar/wind	Brief information
1	DR Congo	▼	▼	▼	▼	▼
2	Angola	▼	▼	▼	▼	▼
3	Cameroon	Department of National Meteorology	Available on require	Data link <a href="https://meteocameroun.gov.cm/en/">https://meteocameroun.gov.cm/en/</a>	W	Temperature, precipitation, humidity, wind <a href="https://meteocameroun.gov.cm/en/demande-de-donnees/">https://meteocameroun.gov.cm/en/demande-de-donnees/</a>
4	Chad	▼	▼	▼	▼	▼
5	Congo	▼	▼	▼	▼	▼
6	Central African Republic	▼	▼	▼	▼	▼
7	Gabon	▼	▼	▼	▼	▼
8	Equatorial Guinea	▼	▼	▼	▼	▼
9	Sao Tome and Principe	▼	▼	▼	▼	▼

▼: Data resource is given in Table 25

**Table 11** Data resources for Eastern Africa countries

S. No.	Name of country	Name of repository	Access	Access link	Solar/wind	Brief information
1	Ethiopia	Harvard Dataverse	Freely accessible	<a href="https://dataverse.harvard.edu/dataset.xhtml?persistentId=doi:10.7910/DVN/IKMU6A">https://dataverse.harvard.edu/dataset.xhtml?persistentId=doi:10.7910/DVN/IKMU6A</a>	S, W	Daily, monthly, yearly data <a href="https://www.worlddata.info/africa/libya/climate.php">https://www.worlddata.info/africa/libya/climate.php</a>
2	Tanzania	National Meteorological Agency	Restricted	<a href="http://www.ethiomet.gov.et/data_access/request_form">http://www.ethiomet.gov.et/data_access/request_form</a>	S, W	Solar and wind data from many stations throughout the whole country
3	Kenya	Tanzania Meteorological Authority	Freely accessible	<a href="https://www.meteo.go.tz/">https://www.meteo.go.tz/</a>	S, W	<a href="https://www.meteo.go.tz/publications/34">https://www.meteo.go.tz/publications/34</a>
4	Uganda	Kenya Meteorological Department	Freely accessible	<a href="https://meteo.go.ke/">https://meteo.go.ke/</a>	S, W	Daily, 5 days, 7 days, monthly data. Data will be shared upon request. <a href="https://meteo.go.ke/resources/data-request">https://meteo.go.ke/resources/data-request</a>
5	Mozambique	Uganda National Meteorological Authority	Freely accessible	<a href="https://www.unma.go.ug/research-reports/">https://www.unma.go.ug/research-reports/</a>	W	▼
		National Institute of Meteorology (INAM)	Freely accessible	<a href="https://www.inam.gov.mz/index.php/pt/services/pedido-de-dados">https://www.inam.gov.mz/index.php/pt/services/pedido-de-dados</a>	S, W	This organization is responsible for recording climatological data in the country. The Institute started activities in 1910 and presently has a network of 288 climatological stations spread over the country

(continued)

Table 11 (continued)

S. No.	Name of country	Name of repository	Access	Access link	Solar/wind	Brief information
6	Madagascar	University of La Reunion	Freely accessible	<a href="https://zenodo.org/record/7092861—Y_TzTuxBz6s">https://zenodo.org/record/7092861—Y_TzTuxBz6s</a> <a href="https://zenodo.org/record/4408678">https://zenodo.org/record/4408678</a>	S, W	Solar and meteorological data collected from the Ouani station (Comores) by the ENERGY-lab at the University of La Reunion between December 2019 and September 2022 <a href="https://doi.org/10.1016/j.soler.2005.08.007">https://doi.org/10.1016/j.soler.2005.08.007</a>
7	Malawi	Department of Climate Change and Meteorological Services	Freely accessible	<a href="https://www.metmalawi.gov.mw/">https://www.metmalawi.gov.mw/</a>	S	<a href="https://doi.org/10.1016/j.soler.2005.08.007">https://doi.org/10.1016/j.soler.2005.08.007</a>
8	Zambia	▼	▼	▼	▼	▼, for details are available at: <a href="https://www.mgee.gov.zm/?page_id=1181">https://www.mgee.gov.zm/?page_id=1181</a>
9	Somalia	▼	(▼) Available on request	▼	▼	▼, <a href="https://moewr.gov.so/en/departments/hydro-meteorology">https://moewr.gov.so/en/departments/hydro-meteorology</a>
10	Zimbabwe	▼	(▼) Available on request	▼	▼	▼, more information at: <a href="http://www.zim.gov.zw/index.php/en/">http://www.zim.gov.zw/index.php/en/</a>
11	Rwanda	Rwanda Meteorology Agency	Available on request	<a href="http://mis.meteorwanda.gov.rw/data-request-requirements">http://mis.meteorwanda.gov.rw/data-request-requirements</a>	S, W	Data will shared upon request after you fill the 'data request' form and upload all the document needed
12	Burundi	▼	▼	▼	▼	▼

(continued)



Table 11 (continued)

S. No.	Name of country	Name of repository	Access	Access link	Solar/wind	Brief information
13	South Sudan	▼	▼	▼	▼	▼, more information at: <a href="https://climis-southsudan.org/userguide/agromet">https://climis-southsudan.org/userguide/agromet</a>
14	Eritrea	▼	▼	▼	▼	▼
15	Mauritius	University of La Reunion	Freely accessible	<a href="https://zenodo.org/record/7092861-Y_TzTuxBz6s">https://zenodo.org/record/7092861-Y_TzTuxBz6s</a> <a href="http://metservice.intnet.mu/">http://metservice.intnet.mu/</a>	S, W	Solar and meteorological data collected from the Ouani station (Comores) by the ENERGY-lab at the University of La Reunion between December 2019 and September 2022
16	Djibouti	▼	▼	▼	▼	▼
17	Comoros	University of La Reunion	Freely accessible	<a href="https://zenodo.org/record/7092861-Y_TzTuxBz6s">https://zenodo.org/record/7092861-Y_TzTuxBz6s</a>	S	December 2019–September 2022, gridded data
18	Seychelles	▼	▼	▼	▼	▼

▼: Data resource is given in Table 25

**Table 12** Data resources for Southern Africa countries

S. No.	Name of country	Name of repository	Access	Access link	Solar/wind	Brief information
1	South Africa	South Africa Weather Services	Freely accessible	<a href="https://www.weathersa.co.za/">https://www.weathersa.co.za/</a>	W	Temperature, humidity, wind speed, rain, wind direction
2	Namibia	Namibia Meteorological Service	Freely accessible	<a href="http://www.meteona.com/index.php/">http://www.meteona.com/index.php/</a>	W	Temperature, humidity, wind speed, rain, wind direction
3	Botswana	Department of Meteorological Services	Available on request	<a href="https://www.gov.bw/natural-resources/request-climatological-data">https://www.gov.bw/natural-resources/request-climatological-data</a>	S, W	No cost, 3 working days
4	Lesotho	▼	▼	▼	▼	(▼), <a href="https://www.lesmet.org.ls/">https://www.lesmet.org.ls/</a>
5	Eswatini	Eswatini Meteorological Service	Available on request	<a href="https://www.swazimet.gov.sz/index.php">https://www.swazimet.gov.sz/index.php</a>	S, W	<a href="https://www.swazimet.gov.sz/index.php?page=data">https://www.swazimet.gov.sz/index.php?page=data</a>

▼: Data resource is given in Table 25

### ***3.3 Data Resources for Renewable Energy Prediction/Forecasting for Europe Countries***

All 44 European countries are categorized into four sub-categories such as Eastern Europe (10 countries: Russia, Ukraine, Poland, Romania, Czech Republic (Czechia), Hungary, Belarus, Bulgaria, Slovakia, Moldova), Northern Europe (10 countries: the UK, Sweden, Denmark, Finland, Norway, Ireland, Lithuania, Latvia, Estonia, Iceland), Southern Europe (15 countries: Italy, Spain, Greece, Portugal, Serbia, Croatia, Bosnia and Herzegovina, Albania, North Macedonia, Slovenia, Montenegro, Malta, Andorra, San Marino, Holy See), and Western Europe (9 countries: Germany, France, Netherlands, Belgium, Austria, Switzerland, Luxembourg, Monaco, Liechtenstein). Data Resources for Renewable Energy Prediction/Forecasting for all African countries are represented in sub-sequence sections.

#### **3.3.1 Data Resources for Eastern Europe**

Total ten countries (Russia, Ukraine, Poland, Romania, Czech Republic (Czechia), Hungary, Belarus, Bulgaria, Slovakia, Moldova) are available in Eastern part of Europe. Data resources of all ten Eastern Europe countries are represented in Table 13.

#### **3.3.2 Data Resources for Northern Europe**

Total ten countries (the UK, Sweden, Denmark, Finland, Norway, Ireland, Lithuania, Latvia, Estonia, Iceland) are available in Northern part of Europe. Data resources of all ten Northern Europe countries are represented in Table 14.

#### **3.3.3 Data Resources for Southern Europe**

Total 15 countries (Italy, Spain, Greece, Portugal, Serbia, Croatia, Bosnia and Herzegovina, Albania, North Macedonia, Slovenia, Montenegro, Malta, Andorra, San Marino, Holy See) are available in Southern part of Europe. Data resources of all 15 Southern Europe countries are represented in Table 15.

#### **3.3.4 Data Resources for Western Europe**

Total five countries (Germany, France, Netherlands, Belgium, Austria, Switzerland, Luxembourg, Monaco, Liechtenstein) are available in Western part of Europe. Data resources of all five Western Europe countries are represented in Table 16.

**Table 13** Data resources for Eastern Europe countries

S. No.	Name of country	Name of repository	Access	Access link	Solar/wind	Brief information
1	Russia	DataONE	Freely accessible	<a href="https://search.dataone.org/view/%7BADB7EF81-B5EB-4409-ADF9-B941F00317BD%7D">https://search.dataone.org/view/%7BADB7EF81-B5EB-4409-ADF9-B941F00317BD%7D</a>	S, W	
2	Ukraine	Ukrainian Hydrometeorological Center	Freely accessible	<a href="https://www.meteo.gov.ua/en/">https://www.meteo.gov.ua/en/</a>	S, W	Temperature, cloudiness, precipitation, wind <a href="https://uhmi.org.ua/eng/">https://uhmi.org.ua/eng/</a>
3	Poland	Public data	Freely accessible	<a href="https://danepubliczne.img.w.pl/">https://danepubliczne.img.w.pl/</a>	S, W	Download at: <a href="https://danepubliczne.img.w.pl/data/">https://danepubliczne.img.w.pl/data/</a>
4	Romania	National Meteorological Administration of Romania	Restricted	<a href="https://www.meteoromania.ro/produse-si-servicii/">https://www.meteoromania.ro/produse-si-servicii/</a>	W	Direct, diffuse, global, reflected solar radiation of hourly values, daily, monthly, annual averages are available
5	Czech Republic (Czechia)	Earth System Science Data	Freely accessible	<a href="https://doi.pangaea.de/10.1594/PANGAEA.879722">https://doi.pangaea.de/10.1594/PANGAEA.879722</a>	S, W	Database contains irradiance of 10-min measurement from July 2014 to December 2016. For two stations, there are additional data: PM10, SO <sub>2</sub> , NO <sub>x</sub> , NO, NO <sub>2</sub> concentrations, air temperature and relative humidity, air pressure, wind speed, and wind direction

(continued)

Table 13 (continued)

S. No.	Name of country	Name of repository	Access	Access link	Solar/wind	Brief information
		Czech Hydrometeorological Institute	Available on request	<a href="https://www.chmi.cz/o-nas/organizacni-struktura/usek-meteorologie-a-klimatologie/odbor-klimatologie/zakladni-informace">https://www.chmi.cz/o-nas/organizacni-struktura/usek-meteorologie-a-klimatologie/odbor-klimatologie/zakladni-informace</a>	S, W	Data are shared upon request
6	Hungary	National Meteorological Service	Freely accessible	<a href="https://www.met.hu/en/ido-jaras/">https://www.met.hu/en/ido-jaras/</a>	S, W	Temperature, wind, pressure, precipitation, humidity, snow depth
7	Belarus	Belarus weather	Freely accessible	<a href="https://www.belarus.by/en/">https://www.belarus.by/en/</a>	S, W	Temperature, wind speed, atmospheric pressure, precipitation, humidity, snow depth, wind direction
8	Bulgaria	Department of weather forecasts	Freely accessible	<a href="https://weather.bg/0index.php?lng=1">https://weather.bg/0index.php?lng=1</a>	S, W	National Institute of Meteorology and Hydrology. Download at: <a href="https://plovdiv.meteo.bg/en/">https://plovdiv.meteo.bg/en/</a>
9	Slovakia	Slovak Hydrometeorological Institute	Freely accessible	<a href="https://www.shmu.sk/en/?page=1">https://www.shmu.sk/en/?page=1</a>	S, W	Temperature, wind speed, atmospheric pressure, precipitation, humidity
10	Moldova	Serviciul Hidrometeorologic de Stat	Available on request	<a href="https://www.meteo.md/">https://www.meteo.md/</a>	S, W	Temperature, wind speed, atmospheric pressure, precipitation, humidity

▼: Data resource is given in Table 25

**Table 14** Data resources for Northern Europe countries

S. No.	Name of country	Name of repository	Access	Access link	Solar/wind	Brief information
1	UK	NERC Data Catalogue Service The CEDA Archive	Freely accessible Freely accessible	<a href="https://data-search.nerc.ac.uk/geonet/work/srv/eng/catalog.search/home">https://data-search.nerc.ac.uk/geonet/work/srv/eng/catalog.search/home</a> <a href="https://archive.ceda.ac.uk/">https://archive.ceda.ac.uk/</a>	S, W S, W	NERC data catalogue service Many datasets
2	Sweden	Swedish Meteorological and Hydrological Institute	Freely accessible	<a href="https://www.smhi.se/data/meteorologi/ladda-ner-meteorologiska-observationer-param=maxMeanWindSpeed,station=core">https://www.smhi.se/data/meteorologi/ladda-ner-meteorologiska-observationer-param=maxMeanWindSpeed,station=core</a>	S, W	Solar radiation, wind speed, and other parameter historical data in many different horizons from many measuring stations
3	Denmark	Danish Meteorological Institute	Freely accessible	<a href="http://research.dmi.dk/data/">http://research.dmi.dk/data/</a>	S, W	Cordex (CMIP5—climate model data): <a href="http://cordex.dmi.dk/joomla/">http://cordex.dmi.dk/joomla/</a> Ensembles (CMIP3—climate model data): <a href="http://ensemblesr3.dmi.dk/">http://ensemblesr3.dmi.dk/</a> ROM SAF (radio occultation data): <a href="http://www.romsaf.org/">http://www.romsaf.org/</a>
4	Finland	Climate4impact portal Finnish Meteorological Institute	Freely accessible Freely accessible	<a href="https://www.climate4impact.eu/c4i-frontend/search?project=CMIP6">https://www.climate4impact.eu/c4i-frontend/search?project=CMIP6</a> <a href="https://www.ilmatieteenlaitos.fi/havaintojen-lataus">https://www.ilmatieteenlaitos.fi/havaintojen-lataus</a>	S, W S, W	Temperature, precipitation, humidity, wind, radiation, pressure, evaporation – Solar radiation, wind speed data, and many other parameter in a minute to month horizons from 2010 until present – Many stations to choose from
5	Norway	Skipheia Meteorological Station	Freely accessible	<a href="https://zenodo.org/record/2557500—Y_inSOxBzUs">https://zenodo.org/record/2557500—Y_inSOxBzUs</a>	W	The data were gathered between years 2009 and 2015

(continued)

Table 14 (continued)

S. No.	Name of country	Name of repository	Access	Access link	Solar/wind	Brief information
		Norwegian Meteorological Institute	Freely accessible	<a href="https://seklima.met.no/">https://seklima.met.no/</a>	W	Download wind data in different ranges and horizons. Choose many measuring stations also
6	Ireland	Ireland open data portal	Freely accessible	<a href="https://data.gov.ie/dataset/suggest/aa445e7e-c53a-4183-8d89-9d50fea5a546">https://data.gov.ie/dataset/suggest/aa445e7e-c53a-4183-8d89-9d50fea5a546</a>	S, W	This resource includes several different datasets too
		University of Galway	Freely accessible	<a href="https://data.gov.ie/organization/nui-galway?q=wind&amp;sort=score+desc.+metadata_modified+desc">https://data.gov.ie/organization/nui-galway?q=wind&amp;sort=score+desc.+metadata_modified+desc</a>	W	Hourly wind speed datasets
7	Lithuania	Lithuania Meteorological Service	Restricted	<a href="http://www.meteo.lt/lt/prasymai">http://www.meteo.lt/lt/prasymai</a>	S, W	Solar and wind data are available in many horizons and ranges
8	Latvia	Latvian Environment, Geology and Meteorology Center	Restricted	<a href="https://www.meteo.lv/en/lapas/observations/meteorology/meteorology_introduction?id=1928&amp;mid=680">https://www.meteo.lv/en/lapas/observations/meteorology/meteorology_introduction?id=1928&amp;mid=680</a>	S, W	Dataset of 33 stations (1 station per 1500 km <sup>2</sup> ), 23 observations is recorded
9	Estonia	EUMETSAT	Freely accessible	<a href="https://www.imateenistus.ee/klirma/solar-atlas/?lang=en">https://www.imateenistus.ee/klirma/solar-atlas/?lang=en</a>	S, W	Temperature, precipitation, humidity, wind, radiation, pressure, sea water level, snow
10	Iceland	Icelandic Meteorological Office	Freely accessible	<a href="https://en.vedur.is/">https://en.vedur.is/</a>	S, W	Wind, temperature, precipitation, cloud cover, dew point

▼ : Data resource is given in Table 25

**Table 15** Data resources for Southern Europe countries

S. No.	Name of country	Name of repository	Access	Access link	Solar/wind	Brief information
1	Italy	Meteo Italian Supercomputing Portal	Freely accessible	<a href="https://www.mistralportal.it/">https://www.mistralportal.it/</a>	W	Precipitation, temperature, wind, pressure, cloud coverage, relative humidity, snow
2	Spain	Meteorological State Agency of Spain	Freely accessible	<a href="https://datos.gob.es/cat-alogo/01462508-datos-horarios-de-calidad-del-aire-desde-2016">https://datos.gob.es/cat-alogo/01462508-datos-horarios-de-calidad-del-aire-desde-2016</a>	S, W	<ul style="list-style-type: none"> <li>- Hourly air quality data from the stations of the surveillance network of the city of Valencia since 2016</li> <li>- Stations: Avda. Francia, Bulevar Sud, Moll del Sol, Pista Silla, Polytechnic, Viveros, Centro, Conselleria Meteo, Nazaret Meteo, Puerto Valencia</li> <li>- Parameters: PM1, PM2.5, PM10, NO, NO<sub>2</sub>, NO<sub>x</sub>, O<sub>3</sub>, SO<sub>2</sub>, CO, NH<sub>3</sub>, C<sub>7</sub>H<sub>8</sub>, C<sub>6</sub>H<sub>6</sub>, C<sub>8</sub>H<sub>10</sub>, noise, wind speed, wind direction, temperature, relative humidity, pressure, solar radiation, precipitation, maximum wind speed</li> </ul>
3	Greece	Hellenic National Meteorological Service	Freely accessible	<a href="http://climatlas.hnms.gr/sdi/">http://climatlas.hnms.gr/sdi/</a>	S, W	Lot of data available starting from 1971
4	Portugal	Instituto Português do Mar e da Atmosfera	Freely accessible	<a href="https://www.ipma.pt/en/otempop/prev.localidade.hora/">https://www.ipma.pt/en/otempop/prev.localidade.hora/</a>	S, W	Precipitation, temperature, wind, pressure, cloud coverage, relative humidity
5	Serbia	▼	▼	▼	▼	▼
6	Croatia	Croatian Meteorological and Hydrological Service	Freely accessible	<a href="https://meteo.hr/proizvodi_e.php?section=proizvodi_usluge&amp;param=services">https://meteo.hr/proizvodi_e.php?section=proizvodi_usluge&amp;param=services</a>	S, W	Based on request for the data to the email shared in the official website and that will be sent to him/her. It is charged if data are used for private use. Universities and science research are free of charge
7	Bosnia and Herzegovina	National Oceanic and Atmospheric Administration	Restricted	<a href="https://doi.pangaea.de/10.1594/PANGAEA.886522">https://doi.pangaea.de/10.1594/PANGAEA.886522</a>	W	Old data from 1953 to 1984
8	Albania	Meteorology Network	Restricted	<a href="https://www.geo.edu.al/">https://www.geo.edu.al/</a>	S, W	▼
9	North Macedonia	Wind power	Freely accessible	<a href="https://www.thewindpower.net/country_en_93_north-macedonia.php">https://www.thewindpower.net/country_en_93_north-macedonia.php</a>	S, W	Wind and generation data ▼

(continued)



Table 15 (continued)

S. No.	Name of country	Name of repository	Access	Access link	Solar/wind	Brief information
10	Slovenia	National Meteorological Service of Slovenia	Freely accessible	<a href="https://meteo.arso.gov.si/met/en/">https://meteo.arso.gov.si/met/en/</a>	W	Temperature, wind speed, wind gust, pressure, rain, pressure tendency
11	Montenegro	Institute of Hydrometeorology and Seismology	Freely accessible	<a href="http://www.meteo.co.me/">http://www.meteo.co.me/</a>	S, W	Temperature, wind speed, wind gust, pressure, rain, radiation
12	Malta	Malta International Airport	Freely accessible	<a href="https://www.maltairport.com/weather/detailed-forecast/">https://www.maltairport.com/weather/detailed-forecast/</a>		Humidity, wind, sun rays, pressure, dew points
13	Andorra	National Meteorological Service	Freely accessible	<a href="http://www.meteo.ad/en/stations">http://www.meteo.ad/en/stations</a>	S	Provides list of Andorra weather stations with further provision of weather data, wind speed, wind direction and tower altitude
14	San Marino	Weather in San Marino		<a href="https://en.ilmatieteemaitos.fi/weather/san%20marino">https://en.ilmatieteemaitos.fi/weather/san%20marino</a>	S, W	Also wind and solar data can be downloaded through ▼
15	Holy See	▼	▼	▼	▼	▼

▼: Data resource is given in Table 25

**Table 16** Data resources for Western Europe countries

S. No.	Name of country	Name of repository	Access	Access link	Solar/wind	Brief information
1	Germany	Deutscher Wetterdienst	Freely accessible	<a href="https://opendata.dwd.de/climate_environment/">https://opendata.dwd.de/climate_environment/</a>	S, W	Provides historical and current meteorological data for numerous parameters, e.g., for air temperature together with humidity, soil temperature, precipitation height, pressure, wind speed and direction, visibility, solar radiation, sunshine duration, and cloud cover in 10-min, hourly, daily, monthly, annual or multi-year (e.g.: 30-year average) resolution
2	France	Meteo France	Freely accessible	<a href="https://meteonet.umr-cnrm.fr/">https://meteonet.umr-cnrm.fr/</a>	S, W	Hundreds of observation stations are built throughout the French territory, each one fitted with several sensors measuring parameters such as temperature, pressure, wind. Each parameter is measured every 6 min and each file contains 1 month of data for each geographical area ('NW' for North-West of France and 'SE' for South-East of France)

(continued)

Table 16 (continued)

S. No.	Name of country	Name of repository	Access	Access link	Solar/wind	Brief information
3	Netherlands	The Dutch PV Portal	Freely accessible	<a href="https://www.tudelft.nl/en/ewi/over-de-faculteit/afdeling/elektrical-sustainable-energy/photovoltaic-materials-and-devices/dutch-pv-portal/meteorological-data">https://www.tudelft.nl/en/ewi/over-de-faculteit/afdeling/elektrical-sustainable-energy/photovoltaic-materials-and-devices/dutch-pv-portal/meteorological-data</a>	S, W	Data for one year in 10 min resolution
		Royal Netherlands Meteorological Institute	Restricted	<a href="https://www.knmi.nl/data-services/knmi-producten-ovorzicht/klimatologische-gegevens/data-product-1">https://www.knmi.nl/data-services/knmi-producten-ovorzicht/klimatologische-gegevens/data-product-1</a>		Hourly data More data info: <a href="https://www.knmi.nl/data-services/knmi-producten-ovorzicht/klimatologische-gegevens">https://www.knmi.nl/data-services/knmi-producten-ovorzicht/klimatologische-gegevens</a>
4	Belgium	Royal Meteorological Institute	Freely accessible	(1) <a href="http://www.meteo.be">www.meteo.be</a> (2) <a href="https://www.meteo.be/en/weather/forecasts/weather-model-alarm/temperature">https://www.meteo.be/en/weather/forecasts/weather-model-alarm/temperature</a> (3) <a href="https://www.meteo.be/en/weather/observations/belgium">https://www.meteo.be/en/weather/observations/belgium</a> (temperature, precipitation, rel. humidity, wind, pressure, solar radiation)	S, W	<a href="https://www.belspo.be/belspo/invent/sproj.asp?l=en">https://www.belspo.be/belspo/invent/sproj.asp?l=en</a> Temperature, dew point temperature, relative humidity, pressure, cloudiness low, cloudiness medium, cloudiness high, cloudiness total, wind precipitation, windchill (3) W, S data can be downloaded through link 3 directly

(continued)

Table 16 (continued)

S. No.	Name of country	Name of repository	Access	Access link	Solar/wind	Brief information
5	Austria	The Sonnblick Observatory of GeoSphere Austria	Freely accessible	<a href="https://www.sonnblick.net/en/data/download-portal/sbo-data-portal/">https://www.sonnblick.net/en/data/download-portal/sbo-data-portal/</a>	S, W	One should register and request to access the data
		ERA5-Land data, Austrian government	Freely accessible	<a href="https://zenodo.org/record/6812067—Y_—OADuxBz6s">https://zenodo.org/record/6812067—Y_—OADuxBz6s</a>	S, W	Historical data in daily resolution from 2014 to 2021 for Graz, Austria

▼: Data resource is given in Table 25

### ***3.4 Data Resources for Renewable Energy Prediction/Forecasting for Latin America and the Caribbean Countries***

All 33 Latin America and the Caribbean Countries are categorized into three sub-categories such as Caribbean (13 countries: Haiti, Cuba, Dominican Republic, Jamaica, Trinidad and Tobago, Bahamas, Barbados, Saint Lucia, Grenada, St. Vincent and Grenadines, Antigua and Barbuda, Dominica, Saint Kitts and Nevis), Central America (8 countries: Mexico, Guatemala, Honduras, Nicaragua, El Salvador, Costa Rica, Panama, Belize), and Southern America (12 countries: Brazil, Colombia, Argentina, Peru, Venezuela, Chile, Ecuador, Bolivia, Paraguay, Uruguay, Guyana, Suriname). Data resources for renewable energy prediction/forecasting for all Latin America and the Caribbean Countries are represented in sub-sequence sections.

#### **3.4.1 Data Resources for Caribbean**

Total 13 countries (Haiti, Cuba, Dominican Republic, Jamaica, Trinidad and Tobago, Bahamas, Barbados, Saint Lucia, Grenada, St. Vincent and Grenadines, Antigua and Barbuda, Dominica, Saint Kitts, and Nevis) are available in Caribbean part. Data resources of all 13 Caribbean countries are represented in Table 17.

#### **3.4.2 Data Resources for Central America**

Total eight countries (Mexico, Guatemala, Honduras, Nicaragua, El Salvador, Costa Rica, Panama, Belize) are available in Central America part of LA. Data resources of all eight Central America countries are represented in Table 18.

#### **3.4.3 Data Resources for Southern America**

Total 12 countries (Brazil, Colombia, Argentina, Peru, Venezuela, Chile, Ecuador, Bolivia, Paraguay, Uruguay, Guyana, Suriname) are available in Southern America part of LA. Data resources of all 12 Southern America countries are represented in Table 19.

**Table 17** Data resources for Caribbean countries

S. No.	Name of country	Name of repository	Access	Access link	Solar/wind	Brief information
1	Haiti	University of Alabama in Huntsville	Freely accessible	<a href="https://pragwater.com/solar-radiation-data-for-pr-dr-and-haiti/">https://pragwater.com/solar-radiation-data-for-pr-dr-and-haiti/</a>	S	Hourly and daily-integrated solar radiation data
2	Cuba	University of Alabama in Huntsville	Freely accessible	<a href="https://pragwater.com/solar-radiation-data-for-pr-dr-and-haiti/">https://pragwater.com/solar-radiation-data-for-pr-dr-and-haiti/</a>	S, W	Hourly and daily-integrated solar radiation data Wind data at: <a href="https://windy.app/forecast2/spot/4897561/cuba/status">https://windy.app/forecast2/spot/4897561/cuba/status</a>
3	Dominican Republic	University of Alabama in Huntsville	Freely accessible	<a href="https://pragwater.com/solar-radiation-data-for-pr-dr-and-haiti/">https://pragwater.com/solar-radiation-data-for-pr-dr-and-haiti/</a>	S, W	Hourly and daily-integrated solar radiation data Wind data at: <a href="https://windy.app/forecast2/spot/881647/Rep%C3%BAblica+dominicana">https://windy.app/forecast2/spot/881647/Rep%C3%BAblica+dominicana</a>
4	Jamaica	University of Alabama in Huntsville	Freely accessible	(1) <a href="https://pragwater.com/solar-radiation-data-for-pr-dr-and-haiti/">https://pragwater.com/solar-radiation-data-for-pr-dr-and-haiti/</a> (2) <a href="https://metervice.gov.jm/local-forecast/">https://metervice.gov.jm/local-forecast/</a>	S, W	Hourly and daily-integrated solar radiation data Wind data at: <a href="https://windy.app/forecast2/spot/378827/Jamaica/status">https://windy.app/forecast2/spot/378827/Jamaica/status</a>
5	Trinidad and Tobago	Trinidad and Tobago Meteorological Service	Available on request	<a href="https://www.metoffice.gov.tt/">https://www.metoffice.gov.tt/</a>	S, W	On request
6	Bahamas	Department of Metrology	Freely accessible	<a href="https://met.gov.bs/">https://met.gov.bs/</a>	S, W	<a href="https://www.bahamasreality.com/blog/posts/2020/11/24/going-green-the-growth-of-solar-energy-in-the-bahamas/">https://www.bahamasreality.com/blog/posts/2020/11/24/going-green-the-growth-of-solar-energy-in-the-bahamas/</a>
7	Barbados	Barbados weather	Freely accessible	<a href="https://www.barbadosweather.org/">https://www.barbadosweather.org/</a>	S, W	Solar data: <a href="https://energy.at-site.be/pygis/SA/Barbados/?menu=3">https://energy.at-site.be/pygis/SA/Barbados/?menu=3</a>

(continued)

Table 17 (continued)

S. No.	Name of country	Name of repository	Access	Access link	Solar/wind	Brief information
8	Saint Lucia	Saint Lucia Meteorological Services	Freely accessible	<a href="https://met.gov.lc/">https://met.gov.lc/</a>	S, W	▼
9	Grenada	Metrological Services	Freely accessible	<a href="https://weather.gd/">https://weather.gd/</a>	S, W	▼
10	St. Vincent and Grenadines	▼	▼	▼	▼	▼
11	Antigua and Barbuda	Antigua and Barbuda Meteorological Services	Freely accessible	<a href="http://www.antiguamet.com/">http://www.antiguamet.com/</a>	S, W	▼
12	Dominica	Government of the Commonwealth of Dominica	Data on request	<a href="https://www.weather.gov.dm/cliente/climate-request-data-form">https://www.weather.gov.dm/cliente/climate-request-data-form</a>	W	Wind, humidity, pressure, rain fall, solar radiation
13	Saint Kitts and Nevis	▼	▼	▼	▼	▼

▼: Data resource is given in Table 25

**Table 18** Data resources for Central America countries

S. No.	Name of country	Name of repository	Access	Access link	Solar/wind	Brief information
1	Mexico	National Centers for Environmental Information	Freely accessible	<a href="https://www.ncei.noaa.gov/products">https://www.ncei.noaa.gov/products</a>	S, W	Provides several datasets
2	Guatemala	▼	▼	▼	▼	▼
3	Honduras	▼	▼	▼	▼	▼
4	Nicaragua	Nicaraguan Institute of Territorial Studies	Available on request	<a href="https://www.ineter.gob.ni/Catalogo.html">https://www.ineter.gob.ni/Catalogo.html</a>	S, W	▼
5	El Salvador	▼	▼	▼	▼	▼
6	Costa Rica	Instituto Meteorológico Nacional de Costa Rica	Restricted	<a href="https://www.imm.ac.cr/en/web/imm/solicitud-de-servicios">https://www.imm.ac.cr/en/web/imm/solicitud-de-servicios</a>	S, W	Data will be shared upon request
7	Panama	Panama Canal Authority	Freely accessible	<a href="https://smithsonian.fgshare.com/articles/dataset/Panama_Canal_Meteorological_Data_Agua_Salud/11794575">https://smithsonian.fgshare.com/articles/dataset/Panama_Canal_Meteorological_Data_Agua_Salud/11794575</a>	W	January 2008–December 2019 data
8	Belize	Parque Natural Metropolitano	Restricted	<a href="https://search.dataone.org/view/ess-dive-0894f32557f576b-20211202T054533831751">https://search.dataone.org/view/ess-dive-0894f32557f576b-20211202T054533831751</a>	W	Wind speed data in any horizon
		National Meteorological Service of Belize	Restricted	<a href="https://mms.gov.bz/">https://mms.gov.bz/</a>	S, W	Solar and wind data

▼: Data resource is given in Table 25



**Table 19** Data resources for Southern America countries

S. No.	Name of country	Name of repository	Access	Access link	Solar/wind	Brief information
1	Brazil	National Institute for Space Research (INPE)	Freely accessible	<a href="http://labren.cesr.inpe.br/atlas_2017.html">http://labren.cesr.inpe.br/atlas_2017.html</a> —mod	S	Contains the annual and monthly averages of the daily total of the global horizontal, diffuse, direct normal, tilted plane, and PAR irradiation
2	Colombia	Instituto Nacional de Meteorología	Freely accessible	<a href="https://bdmep.inmet.gov.br/">https://bdmep.inmet.gov.br/</a>	W	Many resolution from any station in the whole country
3	Argentina	Instituto de Hidrología, Meteorología y Estudios Ambientales de Colombia	Freely accessible	<a href="http://www.ideam.gov.co/">http://www.ideam.gov.co/</a>	S, W	Several data available
4	Peru	Instituto SMN Argentina	Freely accessible	<a href="https://halo-db.pa.op.dlr.de/mstutute/62">https://halo-db.pa.op.dlr.de/mstutute/62</a>	S, W	Download at: <a href="https://www.smn.gob.ar/">https://www.smn.gob.ar/</a>
5	Venezuela		▼	▼	▼	▼
6	Chile	Chile Navy Weather Service	On request	<a href="https://web.directemar.c/met/jurno/indice/english.htm">https://web.directemar.c/met/jurno/indice/english.htm</a>	S, W	Available bunch of different data
7	Ecuador		▼	▼	▼	▼
8	Bolivia		▼	▼	▼	Image data: <a href="https://www.meteoblue.com/en/country/weaather/satellite/bolivia_bolivia_3923057">https://www.meteoblue.com/en/country/weaather/satellite/bolivia_bolivia_3923057</a>
9	Paraguay	Dirección de Meteorología e Hidrología	Restricted	<a href="https://www.meteorologia.gov.py/servicio-publico/">https://www.meteorologia.gov.py/servicio-publico/</a>	W	Wind speed data in any horizon
10	Uruguay	El Instituto Uruguayo de Meteorología	On request	<a href="https://www.inumet.gub.uy/ins-titucional/transparencia/solicitud-informacion-meteorologica">https://www.inumet.gub.uy/ins-titucional/transparencia/solicitud-informacion-meteorologica</a>	S, W	Data will be shared upon request and documents are needed

(continued)

**Table 19** (continued)

S. No.	Name of country	Name of repository	Access	Access link	Solar/wind	Brief information
11	Guyana	Hydrometeorological Service	On request	<a href="https://hydromet.gov.gy/">https://hydromet.gov.gy/</a>	S, W	<a href="https://hydromet.gov.gy/data-request/">https://hydromet.gov.gy/data-request/</a>
12	Suriname	▼	▼	▼	▼	▼

▼: Data resource is given in Table 25

### ***3.5 Data Resources for Renewable Energy Prediction/ Forecasting for Oceania Countries***

All 14 Oceania Countries are categorized in to four sub-categories such as “Australia and New Zealand” (two countries: Australia and New Zealand), Melanesia (four countries: Papua New Guinea, Fiji, Solomon Islands, Vanuatu), Micronesia (five countries: Micronesia, Kiribati, Marshall Islands, Palau, Nauru), and Polynesia (three countries: Samoa, Tonga, Tuvalu). Data resources for renewable energy prediction/forecasting for all Oceania Countries are represented in sub-sequence sections.

#### **3.5.1 Data Resources for Australia and New Zealand**

Total two countries (Australia and New Zealand) are available in this region. Data resources of both Oceania Countries are represented in Table [20](#).

#### **3.5.2 Data Resources for Melanesia**

Total four countries (Papua New Guinea, Fiji, Solomon Islands, Vanuatu) are available in Melanesia region. Data resources of five Melanesia Countries are represented in Table [21](#).

#### **3.5.3 Data Resources for Micronesia**

Total five countries (Micronesia, Kiribati, Marshall Islands, Palau, Nauru) are available in Melanesia region. Data resources of five Micronesia Countries are represented in Table [22](#).

#### **3.5.4 Data Resources for Polynesia**

Total three countries (Samoa, Tonga, Tuvalu) are available in Melanesia region. Data resources of three Polynesia Countries are represented in Table [23](#).

**Table 20** Data resources for Australia and New Zealand countries

S. No.	Name of country	Name of repository	Access	Access link	Solar/wind	Brief information
1	Australia	Bureau of Meteorology	Freely accessible	<a href="http://www.bom.gov.au/climate/how/IDCIAD/0111.shtml">http://www.bom.gov.au/climate/how/IDCIAD/0111.shtml</a>	S	Hourly direct normal and hourly global horizontal solar irradiance data for the period 1990–July 2016
		Queensland government, Australia	Freely accessible	<a href="https://www.lon.gpaddock.qld.gov.au/silo/about/access-data/">https://www.lon.gpaddock.qld.gov.au/silo/about/access-data/</a>	S	Daily solar radiation data from 1889 to 2023 in any point in the country
		The Desert Knowledge Australia Solar Centre	Freely accessible	<a href="https://dkasolarcentre.com.au/download?location=alice-springs">https://dkasolarcentre.com.au/download?location=alice-springs</a>	S	The flagship project of the DKASC, Alice Springs or the Yulara Solar System containing live data from solar generating plants in Central Australia. You can also explore the NT Solar Resource project's high-grade irradiance and climate data from meteorological stations across the NT Data resolution can be 5 min, hourly, daily, or monthly in range of 2008–2013
		Bureau of Meteorology	Restricted	<a href="http://www.bom.gov.au/climate/data-services/charges.shtml">http://www.bom.gov.au/climate/data-services/charges.shtml</a>	W	Wind speed and direction in any resolution and range of year
2	New Zealand	National Institute of Water and Atmospheric Research	Available on request	<a href="https://cliffo.niwa.co.nz/">https://cliffo.niwa.co.nz/</a>	S, W	Solar radiation and wind speed data from different station with different horizons include hour, days and months in many years of recording

▼: Data resource is given in Table 25

**Table 21** Data resources for Melanesia countries

S. No.	Name of country	Name of repository	Access	Access link	Solar/wind	Brief information
1	Papua New Guinea	Papua New Guinea National Weather Service	Freely accessible	<a href="https://www.pngmet.gov.pg/">https://www.pngmet.gov.pg/</a>	S, W	Includes both costal and ocean data
2	Fiji	Fiji Meteorological Service	Freely accessible	<a href="https://www.met.gov.fj/index.php?page=datarequest">https://www.met.gov.fj/index.php?page=datarequest</a>	S, W	Solar and wind data in the years between 2014 and present in any horizon including minutes and hours
3	Solomon Islands	Solomon Islands Meteorological Services	Freely accessible	<a href="https://met.gov.sb/">https://met.gov.sb/</a>	S, W	Hourly data
4	Vanuatu	Vanuatu Meteorology Services	Freely accessible	<a href="http://www.vmgd.gov.vu/">http://www.vmgd.gov.vu/</a>	S, W	Rainfall, temperature, pressure, wind, solar radiation, humidity, sunshine hours, direction. Available at: <a href="http://www.vmgd.gov.vu/vmgd/index.php/climate/cli-mate-information-services/data-services">http://www.vmgd.gov.vu/vmgd/index.php/climate/cli-mate-information-services/data-services</a>

▼: Data resource is given in Table 25

**Table 22** Data resources for Micronesia countries

S. No.	Name of country	Name of repository	Access	Access link	Solar/wind	Brief information
1	Micronesia	National Weather Service	Freely accessible	<a href="https://www.weather.gov/gum/WSOPohnpei">https://www.weather.gov/gum/WSOPohnpei</a>	S, W	Temperature, precipitation, wind speed, direction, sky cover, wind gust, dew point <a href="https://graphical.weather.gov/sectors/guam.php">https://graphical.weather.gov/sectors/guam.php</a>
2	Kiribati	Kiribati Meteorological Service	Freely accessible	<a href="https://www.met.gov.ki/">https://www.met.gov.ki/</a>	S, W	Solar and wind data ▼
3	Marshall Islands	National Weather Service	Freely accessible	<a href="https://www.weather.gov/gum/Majuro">https://www.weather.gov/gum/Majuro</a>	S, W	▼
4	Palau	Climate Statistics	Freely accessible	<a href="https://www.palau.gov.pw/executive-branch/ministries/finance/budgetandplanning/climate-statistics/">https://www.palau.gov.pw/executive-branch/ministries/finance/budgetandplanning/climate-statistics/</a>	S, W	<a href="http://www.palauweather.org/">http://www.palauweather.org/</a> Data at: <a href="https://www.windguru.cz/126261">https://www.windguru.cz/126261</a>
5	Nauru	▼	▼	▼	▼	▼

▼: Data resource is given in Table 25

**Table 23** Data resources for Polynesia countries

S. No.	Name of country	Name of repository	Access	Access link	Solar/wind	Brief information
1	Samoa	Samoa Meteorological Service	Freely accessible	<a href="http://www.samet.gov.ws/">http://www.samet.gov.ws/</a>	S, W	▼
2	Tonga	▼	▼	▼	▼	▼
3	Tuvalu	Tuvalu Meteorological Service (TMS)	Freely accessible	<a href="https://tuvmet.tv/">https://tuvmet.tv/</a>	W	▼

▼: Data resource is given in Table 25

### ***3.6 Data Resources for Renewable Energy Prediction/ Forecasting for Northern America Countries***

Total 41 countries are available in Northern America. Data resources of all 21 Northern America countries are represented in Table 24, whereas data resources of rest 20 America countries (Mexico, Guatemala, Haiti, Cuba, Dominican Republic, Honduras, Nicaragua, El Salvador, Costa Rica, Panama, Jamaica, Trinidad and Tobago, Belize, Bahamas, Barbados, Saint Lucia, Grenada, Antigua and Barbuda, Dominica, Saint Kitts and Nevis) are represented in Sect. 3.4.

## **4 Conclusion**

In this chapter, data resource library of 214 locations of the world has been developed for the renewable energy forecasting/prediction. Developed data resource library covers six regions (Asia, Africa, Europe, Latin America, Oceania, and North America) of the world. In this data library, 48 locations of Asian region (i.e., 5 locations: central Asia, 5 location: Eastern Asia, 11 locations: Southeastern Asia, 9 locations: Southern Asia, 18 locations: Western Asia), 54 locations of Africa region (i.e., 18 locations: eastern Africa, 9 locations: Middle Africa, 6 locations: Northern Africa, 5 locations: Southern Africa, and 16 locations: Western Africa), 44 locations of Europe region (i.e., 10 locations: Eastern Europe, 10 locations: Northern Europe, 15 locations: Southern Europe, and 9 locations: Western Europe), 33 locations of Latin America and the Caribbean region (i.e., 13 locations: Caribbean region, 8 locations: Central America, and 12 locations: Southern America), 14 locations of Oceania region (i.e., 2 locations: Australia and New Zealand region, 4 locations: Melanesia region, 5 locations: Micronesia region, and 3 locations: Polynesia region), and 21 locations of Northern America region are included. Moreover, 16 general data resource libraries are included, which are applicable for whole world's location. These data libraries are very useful for those locations where metrological station is not feasible to install.



**Table 24** Data resources for Northern America countries

S. No.	Name of country	Name of repository	Access	Access link	Solar/wind	Brief information
1	USA	Oak Ridge National Laboratory	Freely accessible	<a href="https://midcdmz.nrel.gov/apps/daily.pl?site=ORNL&amp;start=20070912&amp;yr=2019&amp;mo=11&amp;dy=20">https://midcdmz.nrel.gov/apps/daily.pl?site=ORNL&amp;start=20070912&amp;yr=2019&amp;mo=11&amp;dy=20</a>	S, W	Data are available in years between 2007 and 2019 with 1 min, hourly, and daily. All solar resource parameters (GHI, DHI, DNI) are available with wind speed and direction
		National Solar Radiation Database		<a href="https://nsrdb.nrel.gov/data-viewer">https://nsrdb.nrel.gov/data-viewer</a>		The NSRDB is a serially complete collection of hourly and half-hourly values of the three most common measurements of solar radiation—global horizontal, direct normal, and diffuse horizontal irradiance—and meteorological data. The current NSRDB is modeled using multi-channel measurements from geostationary satellites
		NASA		<a href="https://power.larc.nasa.gov/data-access-viewer/">https://power.larc.nasa.gov/data-access-viewer/</a>		Any location in USA with hourly, daily, monthly, and yearly timestamps in range of 1981–2023. The data have a lot of other parameters other than solar radiation and wind speed
2	Puerto Rico					▼

(continued)

Table 24 (continued)

S. No.	Name of country	Name of repository	Access	Access link	Solar/wind	Brief information
3	Canada	Government of Canada	Freely accessible	<a href="https://climate.weather.gc.ca/">https://climate.weather.gc.ca/</a>	W	The data on the whole country horizon on many different measuring stations. The range of data is from 1840s to today
			Freely accessible	<a href="https://natural-resources.canada.ca/energy/sources-distribution/renewables/solar-photovoltaic-energy/solar-resource-data-available-canada/14390">https://natural-resources.canada.ca/energy/sources-distribution/renewables/solar-photovoltaic-energy/solar-resource-data-available-canada/14390</a>	S	Here is a lot of datasets from particular stations and satellite on all the parameters of solar energy resource such as GHI, DHI, DNI. Most of datasets are from years between 1953 and now and they are available in any horizontal range which includes minutely and hourly
4	Guadeloupe	▼	▼	▼	▼	▼
5	Martinique	▼	▼	▼	▼	▼
6	Curacao	▼	▼	▼	▼	▼
7	Saint Vincent and Grenadines	▼	▼	▼	▼	▼
8	Aruba	▼	▼	▼	▼	▼
9	United States Virgin Islands	▼	▼	▼	▼	▼
10	Cayman Islands	▼	▼	▼	▼	▼
11	Bermuda	▼	▼	▼	▼	▼

(continued)

**Table 24** (continued)

S. No.	Name of country	Name of repository	Access	Access link	Solar/wind	Brief information
12	Greenland	▼	▼	▼	▼	▼
13	Sint Maarten	▼	▼	▼	▼	▼
14	Turks and Caicos Islands	▼	▼	▼	▼	▼
15	Saint Martin	▼	▼	▼	▼	▼
16	British Virgin Islands	▼	▼	▼	▼	▼
17	Caribbean Netherlands	▼	▼	▼	▼	▼
18	Anguilla	▼	▼	▼	▼	▼
19	Saint Barthélemy	▼	▼	▼	▼	▼
20	Saint Pierre and Miquelon	▼	▼	▼	▼	▼
21	Montserrat	▼	▼	▼	▼	▼

▼ : Data resource is given in Table 25

**Table 25** Data resources applicable for whole world's countries

S. No.	Repository name	Access	Access link	Solar/wind
1	National Solar Radiation Database	Freely accessible	<a href="https://nstrdb.nrel.gov/data-viewer">https://nstrdb.nrel.gov/data-viewer</a>	S, W
2	Global Solar Atlas	Freely accessible	<a href="https://globalsolaratlas.info/download">https://globalsolaratlas.info/download</a>	S
3	Photovoltaic Geo4graphical Information System	Freely accessible	<a href="https://re.jrc.ec.europa.eu/pvg_tools/en/">https://re.jrc.ec.europa.eu/pvg_tools/en/</a>	S
4	Global Wind Atlas	Freely accessible	<a href="https://globalwindatlas.info/en">https://globalwindatlas.info/en</a>	S
5	NOAA Central Library Foreign Climate Data	Freely accessible	<a href="https://library.noaa.gov/Collections/Digital-Documents/Foreign-Climate-Data-Home">https://library.noaa.gov/Collections/Digital-Documents/Foreign-Climate-Data-Home</a>	S, W
6	Meteonorm	Restricted	<a href="https://meteonorm.com/en">https://meteonorm.com/en</a>	S, W
7	SOLCAST	Restricted	<a href="https://solcast.com/">https://solcast.com/</a>	S, W
8	SoDa	Restricted	<a href="https://www.soda-pro.com/">https://www.soda-pro.com/</a>	S, W
9	Weatheronline, UK	Restricted	<a href="https://qfds.weatheronline.co.uk/historical_data/weather_statistics_download/#forward">https://qfds.weatheronline.co.uk/historical_data/weather_statistics_download/#forward</a>	S, W
10	Wind prospecting	Restricted	<a href="https://www.windprospecting.com/">https://www.windprospecting.com/</a>	W
11	SolarAnywhere	Restricted	<a href="https://www.solaranywhere.com/products/solaranywhere-data/">https://www.solaranywhere.com/products/solaranywhere-data/</a>	S
12	Windy.App	Freely accessible	<a href="https://windy.app/">https://windy.app/</a>	W
13	SolarGIS	Freely accessible	<a href="https://solargis.com/">https://solargis.com/</a>	S
14	Climate change knowledge portal	Freely accessible	<a href="https://climateknowledgeportal.worldbank.org/">https://climateknowledgeportal.worldbank.org/</a>	S, W
15	Met Office	Freely accessible	<a href="https://www.metoffice.gov.uk/">https://www.metoffice.gov.uk/</a>	S, W
16	Our World in Data	Freely accessible	<a href="https://ourworldindata.org/">https://ourworldindata.org/</a>	S, W

**Acknowledgements** This study was supported by the Universiti Teknologi Malaysia—“Development of Adaptive and Predictive ACMV/HVAC Health Monitoring System Using IoT, Advanced FDD, and Weather Forecast Algorithms” (Q.J130000.3823.31J06).

## References

1. Malik H et al (2021) Intelligent data-analytics for condition monitoring: smart grid applications. Elsevier. ISBN: 978-0-323-85510-5. <https://doi.org/10.1016/C2020-0-02173-0>
2. Iqbal A et al (2020) Soft computing in condition monitoring and diagnostics of electrical and mechanical systems. Springer Nature, 496 pp. ISBN: 978-981-15-1532-3. <https://doi.org/10.1007/978-981-15-1532-3>
3. Iqbal A et al (2020) Meta heuristic and evolutionary computation: algorithms and applications. Springer Nature, 849 pp. ISBN: 978-981-15-7571-6. <https://doi.org/10.1007/978-981-15-7571-6>
4. Fatema N et al (2021) AI and machine learning paradigms for health monitoring system: intelligent data analytics. Springer Nature, 513 pp. ISBN: 978-981-334-412-9
5. Iqbal A et al (2021) Renewable power for sustainable growth. Springer Nature, 805 pp. ISBN: 978-981-334-080-0
6. Smriti S et al (2018) Applications of artificial intelligence techniques in engineering, vol 1. Springer Nature, 643 pp. ISBN 978-981-13-1819-1. <https://doi.org/10.1007/978-981-13-1819-1>
7. Smriti S et al (2018) Applications of artificial intelligence techniques in engineering, vol 2. Springer Nature, 647 pp. ISBN: 978-981-13-1822-1. <https://doi.org/10.1007/978-981-13-1822-1>
8. Tomar A et al (2021) Machine learning, advances in computing, renewable energy and communication. Springer Nature, 659 pp. ISBN: 978-981-16-2354-7. <https://doi.org/10.1007/978-981-16-2354-7>
9. Waseem M et al (2022) Intelligent data-analytics for power and energy systems: advances in models and applications. Springer Nature, 641 pp. ISBN: 978-981-16-6080-1. <https://doi.org/10.1007/978-981-16-6080-1>
10. Tomar A et al (2022) Machine learning paradigm: advances in computing, renewable energy and communication. Springer Nature, 781 pp. <https://doi.org/10.1007/978-981-19-2828-4>
11. Chankaya M et al (2021) Generalized normal distribution algorithm based control of 3-phase 4-wire grid-tied PV-hybrid energy storage system. *Energies* 14(14):4355, 1–22. <https://doi.org/10.3390/en14144355>
12. Chankaya M et al (2021) Multi-objective grasshopper optimization based MPPT and VSC control of grid-tied PV-battery system. *Electronics* 10(22):2770, 1–24. <https://doi.org/10.3390/electronics10222770>
13. Chankaya M et al (2022) Stability analysis of chaotic grey-wolf optimized grid-tied PV-hybrid storage system during dynamic conditions. *Electronics* 11(4):567, 1–23. <https://doi.org/10.3390/electronics11040567>
14. Chankaya M et al (2022) Seamless capable PV power generation system without battery storage for rural residential load. *Electronics* 11(15):2413, 1–19. <https://doi.org/10.3390/electronics11152413>
15. Alotaibib MA et al (2022) Power quality disturbance analysis using data-driven EMD-SVM hybrid approach. *J Intell Fuzzy Syst* 42(2):669–678. <https://doi.org/10.3233/JIFS-189739>
16. Kaushal P et al (2018) A hybrid intelligent model for power quality disturbance classification. In: Applications of artificial intelligence techniques in engineering. Advances in intelligent systems and computing, vol 697, pp 55–63. [https://doi.org/10.1007/978-981-13-1822-1\\_6](https://doi.org/10.1007/978-981-13-1822-1_6)

17. Azeem A et al (2018) K-NN and ANN based deterministic and probabilistic wind speed forecasting intelligent approach. *J Intell Fuzzy Syst* 35(5):5021–5031. <https://doi.org/10.3233/JIFS-169786>
18. Khurshheed T et al (2022) Multi-step ahead time-series wind speed forecasting for smart-grid application. *J Intell Fuzzy Syst* 42(2):633–646. <https://doi.org/10.3233/JIFS-189736>
19. Yadav AK et al (2021) A novel hybrid approach based on relief algorithm and fuzzy reinforcement learning approach for predicting wind speed. *Sustain Energy Technol Assess* 43. <https://doi.org/10.1016/j.seta.2020.100920>
20. Yadav AK et al (2022) Novel application of relief algorithm in cascaded artificial neural network to predict wind speed for wind power resource assessment in India. *Energy Strat Rev* 41(100864):1–14. <https://doi.org/10.1016/j.esr.2022.100864>
21. Kumar G et al (2016) Generalized regression neural network based wind speed prediction model for western region of India. *Procedia Comput Sci* 93:26–32. <https://doi.org/10.1016/j.procs.2016.07.177>
22. Garg P et al (2017) Infogain attribute evaluator and ANN based wind speed prediction model for Rajasthan, north-west region of India. In: *Proceedings of the international conference on nanotechnology for better living*, vol 3, no 1, p 233. <https://doi.org/10.3850/978-981-09-7519-7nb116-rps-233>
23. Savita et al (2016) Wind speed and power prediction of prominent wind power potential states in India using GRNN. In: *Proceedings of IEEE ICPEICES-2016*, pp 1–6. <https://doi.org/10.1109/ICPEICES.2016.7853220>
24. Savita et al (2016) Application of artificial neural network for long term wind speed prediction. In: *Proceedings of IEEE CASP-2016*, 9–11 June 2016, pp 217–222. <https://doi.org/10.1109/CASP.2016.7746168>
25. Azeem A et al (2016) Application of Waikato environment for knowledge analysis based artificial neural network models for wind speed forecasting. In: *Proceedings of IEEE PIICON-2016*, 25–27 Nov 2016, pp 1–6. <https://doi.org/10.1109/POWERI.2016.8077352>
26. Yadav AK et al (2018) 10-min ahead forecasting of wind speed for power generation using nonlinear autoregressive neural network. In: *Applications of artificial intelligence techniques in engineering. Advances in intelligent systems and computing*, vol 698, pp 235–244. [https://doi.org/10.1007/978-981-13-1819-1\\_23](https://doi.org/10.1007/978-981-13-1819-1_23)
27. Vinoop P et al (2018) PSO-NN-based hybrid model for long-term wind speed prediction: a study on 67 cities of India. In: *Applications of artificial intelligence techniques in engineering. Advances in intelligent systems and computing*, vol 697, pp 319–327. [https://doi.org/10.1007/978-981-13-1822-1\\_29](https://doi.org/10.1007/978-981-13-1822-1_29)
28. Yadav AK et al (2018) Short term wind speed forecasting for power generation in Hamirpur, Himachal Pradesh, India, using artificial neural networks. In: *Applications of artificial intelligence techniques in engineering. Advances in intelligent systems and computing*, vol 697, pp 263–271. [https://doi.org/10.1007/978-981-13-1822-1\\_24](https://doi.org/10.1007/978-981-13-1822-1_24)
29. Yadav AK et al (2015) Application of rapid miner in ANN based prediction of solar radiation for assessment of solar energy resource potential of 76 sites in northwestern India. *Renew Sustain Energy Rev* 52:1093–1106. <https://doi.org/10.1016/j.rser.2015.07.156>
30. Yadav AK et al (2014) Selection of most relevant input parameters using WEKA for artificial neural network based solar radiation prediction models. *Renew Sustain Energy Rev* 31:509–519. <https://doi.org/10.1016/j.rser.2013.12.008>
31. Mahto T et al (2018) Load frequency control of a solar-diesel based isolated hybrid power system by fractional order control using particle swarm optimization. *J Intell Fuzzy Syst* 35(5):5055–5061. <https://doi.org/10.3233/JIFS-169789>
32. Minai AF et al (2022) Performance evaluation of solar PV-based Z-source cascaded multilevel inverter with optimized switching scheme. *Electronics* 11(22):3706, 1–28. <https://www.mdpi.com/2079-9292/11/22/3706>
33. Tajjour S et al (2022) Novel metaheuristic approach for solar photovoltaic parameter extraction using manufacturer data. *Photonics* 9(11):858, 1–21. <https://www.mdpi.com/2304-6732/9/11/858>

34. Prasad D et al (2023) A novel ANROA based control approach for grid-tied multi-functional solar energy conversion system. *Energy Rep* 9:2044–2057. <https://doi.org/10.1016/j.egy.2023.01.039>
35. Yadav AK et al (2020) Optimization of tilt angle for intercepting maximum solar radiation for power generation. In: *Optimization of power system problems (methods, algorithms and MATLAB codes)*. Springer Nature, pp 203–232. [https://doi.org/10.1007/978-3-030-34050-6\\_9](https://doi.org/10.1007/978-3-030-34050-6_9)
36. Yadav AK et al (2014) Comparison of different artificial neural network techniques in prediction of solar radiation for power generation using different combinations of meteorological variables. In: *Proceedings of IEEE international conference on power electronics, drives and energy systems (PEDES-2014)*, pp 1–5. <https://doi.org/10.1109/PEDES.2014.7042063>
37. Yadav AK et al (2015) ANN based prediction of daily global solar radiation for photovoltaics applications. In: *Proceedings of IEEE India annual conference (INDICON)*, pp 1–5. <https://doi.org/10.1109/INDICON.2015.7443186>
38. Yadav AK et al (2015) Optimization of tilt angle for installation of solar photovoltaic system for six sites in India. In: *Proceedings of IEEE international conference on energy economics and environment (ICEEE-2015)*, pp 1–4. <https://doi.org/10.1109/EnergyEconomics.2015.7235078>
39. Garg S et al (2018) Long-term solar irradiance forecast using artificial neural network: application for performance prediction of Indian cities. In: *Applications of artificial intelligence techniques in engineering. Advances in intelligent systems and computing*, vol 697, pp 285–293. [https://doi.org/10.1007/978-981-13-1822-1\\_26](https://doi.org/10.1007/978-981-13-1822-1_26)
40. Upma S et al (2022) Wind energy scenario, success and initiatives towards renewable energy in India—a review. *Energies* 15(6):2291, 1–39. <https://doi.org/10.3390/en15062291>
41. Vigya et al (2021) Renewable generation based hybrid power system control using fractional order-fuzzy controller. *Energy Rep* 7C:641–653. <https://doi.org/10.1016/j.egy.2021.01.022>
42. Singh S et al (2021) Strategic bidding in the presence of renewable sources for optimizing the profit of the power suppliers. *IEEE Access* 9:70221–70232. <https://doi.org/10.1109/ACCESS.2021.3078288>
43. Singh S et al (2021) Impacts of renewable sources of energy on bid modeling strategy in an emerging electricity market using oppositional gravitational search algorithm. *Energies* 14(18):5726, 1–22. <https://doi.org/10.3390/en14185726>
44. Shabbiruddin et al (2021) Fuzzy-based investigation of challenges for the deployment of renewable energy power generation. *Energies* 15(1):58, 1–16. <https://doi.org/10.3390/en15010058>
45. Prakash P et al (2022) A novel analytical approach for optimal integration of renewable energy sources in distribution systems. *Energies* 15(4):1341, 1–23. <https://doi.org/10.3390/en15041341>
46. Khan AA et al (2022) Optimal sizing, control and management strategies for hybrid renewable energy systems: a comprehensive review. *Energies* 15(17):6249, 1–29. <https://www.mdpi.com/1996-1073/15/17/6249>
47. Yadav AK et al (2018) Techno economic feasibility analysis of different combination of PV-wind-diesel-battery hybrid system, chap 11. In: *Hybrid-renewable energy systems in microgrids*. Elsevier, pp 203–218. <https://doi.org/10.1016/B978-0-08-102493-5.00011-X>
48. Minai AF et al (2020) Metaheuristics paradigms for renewable energy systems: advances in optimization algorithms. In: *Metaheuristic and evolutionary computation: algorithms and applications. Studies in computational intelligence*. Springer Nature, pp 35–61. [https://doi.org/10.1007/978-981-15-7571-6\\_2](https://doi.org/10.1007/978-981-15-7571-6_2)
49. Fatima K et al (2022) Intelligent approach-based maximum power point tracking for renewable energy system: a review. In: Malik H, Ahmad MW, Kothari D (eds) *Intelligent data analytics for power and energy systems. Lecture notes in electrical engineering*, vol 802. Springer, Singapore, pp 373–405. [https://doi.org/10.1007/978-981-16-6081-8\\_19](https://doi.org/10.1007/978-981-16-6081-8_19)
50. Arora P et al (2018) Wind energy forecasting model for northern-western region of India using decision tree and MLP neural network approach. *Interdiscip Environ Rev* 19(1):13–30. <https://doi.org/10.1504/IER.2018.089766>

51. Fatema N et al (2022) Hybrid approach combining EMD, ARIMA and Monte Carlo for multi-step ahead medical tourism forecasting. *J Intell Fuzzy Syst* 42(2):1235–1251. <https://doi.org/10.3233/JIFS-189785>
52. Alotaibib MA et al (2022) A new hybrid model combining EMD and neural network for multi-step ahead load forecasting. *J Intell Fuzzy Syst* 42(2):1099–1114. <https://doi.org/10.3233/JIFS-189775>
53. Chimmula VKR et al (2021) Deep learning and statistical based daily stock price forecasting and monitoring. In: *AI and machine learning paradigms for health monitoring system: intelligent data analytics*. Studies in big data. Springer Nature, pp 203–216. [https://doi.org/10.1007/978-981-33-4412-9\\_13](https://doi.org/10.1007/978-981-33-4412-9_13)
54. Yadav V et al (2018) Forecasting of nitrogen dioxide at one day ahead using non-linear autoregressive neural network for environmental applications. In: *Applications of artificial intelligence techniques in engineering*. Advances in intelligent systems and computing, vol 698, pp 615–623. [https://doi.org/10.1007/978-981-13-1819-1\\_58](https://doi.org/10.1007/978-981-13-1819-1_58)
55. Singh M et al (2018) Comparative study of different neural networks for 1-year ahead load forecasting. In: *Applications of artificial intelligence techniques in engineering*. Advances in intelligent systems and computing, vol 697, pp 31–42. [https://doi.org/10.1007/978-981-13-1822-1\\_4](https://doi.org/10.1007/978-981-13-1822-1_4)
56. Re3data (Registry of Research Data Repositories). <https://www.re3data.org/>. Accessed 26 Jan 2023
57. FAIRsharing platform. <https://fairsharing.org/>. Accessed 26 Jan 2023
58. DataONE. <https://www.dataone.org/>. Accessed 26 Jan 2023
59. IEEEDataPortTM. Online. Available at: <https://iee-dataport.org/>. Accessed 26 Jan 2023
60. UCI Machine Learning Repository. Online. Available at: <https://archive.ics.uci.edu/ml/index.php>. Accessed 26 Jan 2023
61. Data in Brief. Online. Available at: <https://www.sciencedirect.com/journal/data-in-brief>. Accessed 26 Jan 2023



# Solar Rooftop On-Grid Connected Net Metering System



Sarfraz, Anju Gupta, and Rashmi Agarwal

**Abstract** Net metering is an arrangement that rewards solar energy users with credits for the extra electricity they supply to the grid. When solar energy generates extra electricity, it is routed to the grid and is available for use even when solar plants are not operating. A bidirectional meter is used to take measurements while solar energy that has been net metered is being consumed. The customers are only billed for net energy they have consumed. The solar energy plays a vital role for net metering system. By the use of on grid net metering system which produces more energy saving and also reduction of the customer money. As we know that solar energy is renewable energy source, the use of this pollution becomes zero and thus makes planet green. A NEM system helps user with grid connected net metering system that reduces their electricity units. This type of system motivates a number of people to move toward to install solar rooftop system. For the net metering systems, users are allowed to install solar plants at their open area, whether it is in their roofs or anywhere in the ground area and thus used for electricity generation through solar panels. This system has a bidirectional meter for net energy consumed units during both day and night time. This meter records final net readings of unit consumed. The customer's primary service providing PVs meter connects the solar panels to the grid. When producing more energy than is required, sites return excess energy to the grid via the net meter. As we know that the net meter is bidirectional, it calculates both the units, generated unit and consumed units by the customers. The customer pays the net of both the transactions. The net metering system is also known as net energy management system, NEM. The net metering a particular type of billing system or tool uses consumer's/users excess generated solar power and reverts back to the electricity grid and thus net meter calculates the net payable units which we consume during cloudy or rainy sessions. Thus, we can say that on-grid solar net metering system is pollution-free energy source and beneficial to the producers and customers.

---

Sarfraz (✉) · A. Gupta · R. Agarwal  
EE Department, JCBoseust, YMCA (HR), Faridabad, India  
e-mail: [sarfarazilahee@gmail.com](mailto:sarfrazilahee@gmail.com)

**Keywords** Renewable energy resources · Pollution-free system · Solar energy · Smart energy meter net energy meters · Solar inverter · Charge controller · Solar PV cells · On-grid system

## 1 Introduction

In net metering process, if a domestic customer has installed an on-grid solar system more than their domestic load on their roof, it will produce more power than their use. The excess generated electricity then sends back/adds to the grid via net meter. This type of system is called net metering system. This is the systematic process that consumers are paid for the price of net electrical power which is sent back out to the gridding by the use of on-grid PV system.

In net metering process in an average, only 15–45% of a solar energy output power goes into the grid and this solar PV generated electricity sends to the nearby customers' loads. In the current net metering system, a singular bidirectional metering is used for readings. This system gives an option to their users for saving electrical power and makes the electricity bill zero and sometimes DISCOM reverts back to the customers for their generated power through on-grid solar photo voltaic system [1] (Fig. 1).

The net metering system is mainly a combination of solar rooftop system on-grid inverter bidirectional energy meter and grid interconnection. Net metering is procedure which reduces in the cost of consumer's electricity bill. Also if the load of the consumers is less in comparison with the rooftop generated power, it works as money provider to the consumers by providing excess amount of electricity to the govt. electricity boards. Under the net metering systems, the electric energy produced by the rooftop solar panels that we don't use is credited back to us by reducing the overall consumed electricity units in the monthly bills.

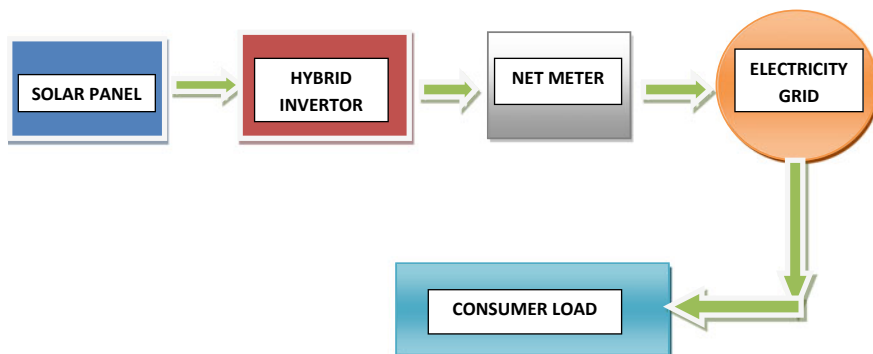


Fig. 1 Net metering system

When the rooftop installed solar systems produce more electricity power when compared with our use at any point of the sunny day, this produced generated solar power is reverted to the electricity board, and in cloudy, rainy conditions and in the night time we pull back this power again running the net energy meter forward that is the so called “net metering”. Here correct size of rooftop solar system is very important if the rooftop solar panel system is more than our required load; in these circumstances this net metering system works in a smooth way if the installed rooftop solar panels power is less than our required load, then this net metering system is not so effective. So, well-planned rooftop system should be installed as per govt. electricity board rules and regulations. Smart meters may play vital role in the net meter policies, playing major roles in make-out net metering system fully and successfully in Haryana and India too [2, 3].

## 2 On-Grid Solar System

The on-grid system works only day time. The on-grid solar system is that system which works along with the grid, without the use of any storage unit like batteries, etc. This means that any excess electrical power can be fed back to the grid through net metering process. Any domestic or industrial customers have options for an on-grid solar system. These customers can be paid back by Govt. Electricity’s Boards for the generated excess power and save on their electricity bills. By the use of the on-grid solar photo voltaic system, we can get electrical power for domestic or industrial use without use of batteries, thus it saves money which will be invested for purchasing of the batteries [4, 5] (Fig. 2).

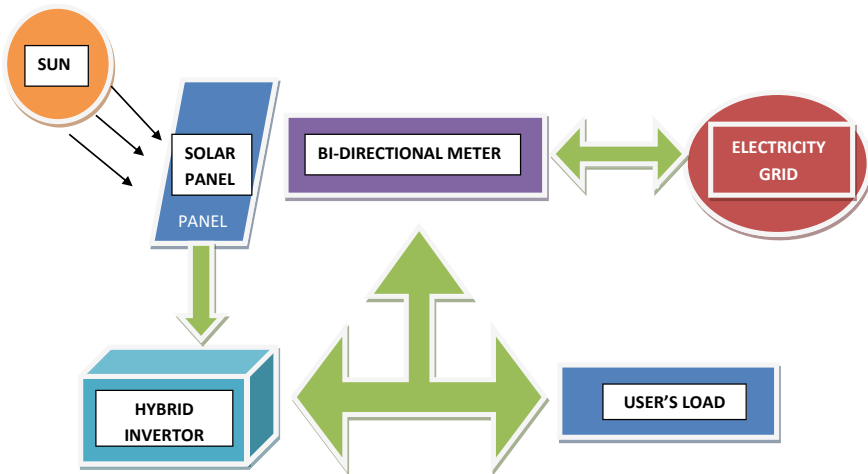


Fig. 2 On-grid net metering system

The on-grid solar systems have hybrid solar inverter without battery storage system. The on-grid system works only in day time with good sunlight. If the weather is cloudy or rainy day, then the on-grid solar system efficiency reduced much that it will work along with govt. board's grid [6].

### 3 Block Diagram of Net Metering System [7]

The net metering system is combination of many components. The net metering generally occurs between renewable source generated energy like solar photo voltaic, wind turbines, etc., and grid. In this system, a solar PV system, solar inverter, a charger controller connects solar generated power to the domestic use through solar inverters (Fig. 3).

After that, a bidirectional net meter is installed between solar power and grid connection. The excess electrical power generated by the solar system/renewable sources is feedback to the grid, this process takes place in day time only. The net meter is electronics device which measures the solar generated electric energy units with respect grid [7].

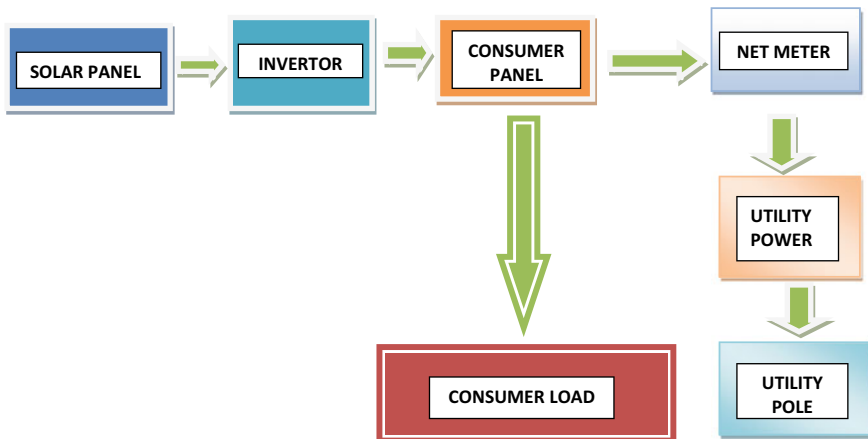


**Fig. 3** Block diagram of net metering system [7]

## 4 How On-Grid Solar Net Metering System Works

When solar energy production begins, the loads use the energy first. The leftover energy will be exported to the grid after the load demand has been met. Grid alone functions as a fictitious battery, absorbing all the extra energy that has been exported. The banking of energy is what is meant by this.

When there is no sunlight throughout the night, the loads can import the stored energy, similar to how electricity is imported from the grid when solar energy production is lower due to overcast circumstances. A bidirectional meter will be used to determine the net of the export and import billing at the conclusion of each billing cycle [8]. The classic unidirectional meter and the bidirectional meter are different, in that the traditional meter simply shows the total consumed energy that was taken from the state. The bidirectional meter, however, keeps track of these readings where the total energy comes into the meter and goes out from the meter (in kWh) [9, 10].

## 5 Connection Flowchart of Net Metering System

The flowchart of the net metering system is a combination of many electrical components. These are renewable sources (solar PV), inverter/charger controller, consumer/user panels (loads), net meter, utility power system and utility pole, etc. These all components make a net metering system. These all components have different functions (Fig. 4).

## 6 Metering Arrangement

There are two meters in the configuration:

1. Solar energy meter to measure the solar power generated
2. Bidirectional energy meter used for calculation of net export and import of energy in the consumer units [11, 12].

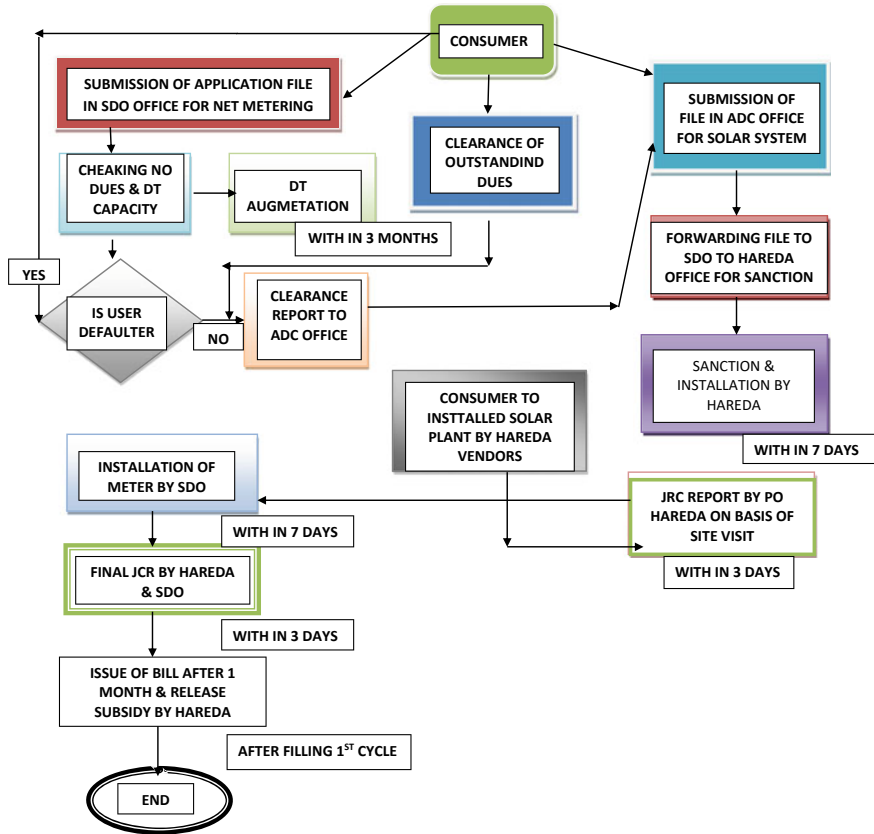


Fig. 4 Flowchart of net metering systems [this flowchart is taken from HAREDA official website]

## 7 Implementation of Net Metering in Haryana

### 7.1 HAREDA (Haryana Renewable Energy Development Agency)

In Haryana, HAREDA is the govt. organization which deals with all renewable energy-related work. In the net metering arrangement, a rooftop solar system is installed at consumer premises, which delivers solar power simultaneously with the power supplied by the Electricity Board [taken from HAREDA official website].

In this system, the power generated through solar roof top arrangement offsets the power imported by the consumer from the Electricity Board. Accordingly, consumer receives a net import/export bill from the Electricity Board as per the net consumption.

## 7.2 Haryana Solar Subsidy Scheme 2022

Haryana Solar System Subsidy with the introduction of this program, the government introduced 300 or 500 W solar inverters. The government also gave the farmers a 40% subsidy. The government has offered discounts for the purchase of solar inverters under this program in the amounts of Rs. 6000 for 300 watts and Rs. 10,000 for 500 watts. Government of Haryana gives 75% subsidy on solar water pump set and at present 15% subsidy on solar inverter charger system and so many other important schemes [taken from HAREDA official website].

## 8 Who Can Get Benefit from On-grid Solar Net Metering System in Haryana

According to the Haryana solar Net Metering policy, Haryana Renewable Development Agency (HAREDA) offers the benefit to the Haryana state. Haryana's people can avail the benefit of Net Metering system. Both UHBVN and DHBVN electricity boards support for installation of net meters. Consumers that have these types of system in Haryana will only pay for the difference in electrical power consumed and send back to the electricity boards [taken from HAREDA official website].

Here, I took survey of 7 kW rooftop solar energy net metering system in Gurugram-based domestic user who has low day time electric Table 1. Power consumption has an electricity monthly billing of Rs. 10,500 sets by 7 kW solar PV system; the net billable units import and export are as = 127 (1146 – 239 – 780) resulting in an 897 rupees monthly energy cost reduction, saving 9603 rupees each month (Table 2).

**Table 1** Monthly solar, grid energy generated and consumed

1	Monthly power consumed	1146 Units (kWh)
2	Monthly solar energy generated	1019 Units
3	Solar power consumed by the user	239 Units
4	Remaining solar energy	780 Units (1019–239)
5	New monthly units get back from grid	907 Units (1146–239)

**Table 2** Monthly unit consumptions solar and grid [taken from HAREDA official website]

Category	Connection of electricity	Units after NEM
Unit in a month (kWh)	1146	907
Net billable units	1146	127
Grid electricity bill	10,500	897

## 9 Benefits of Net Metering

The net metering system has many benefits/advantages:

- a. The use of net metering system **reduced electricity bills**. It is environment-friendly as it uses renewable energy sources for generation of electric power with respect to grid.
- b. It will provide protection to the grid. In this system, **there is no need to install heavy cost batteries for power storage**.
- c. The net metering removes **the electricity load from the power grid in peak load conditions**.
- d. It required very less maintenance [13, 14].

Thus, we can say that it will pressure off from the live grid. It will encourage people to move toward to use green energy sources (renewable energy like solar, wind, hydro, etc.) for power generation. It will help to preserve natural energy sources, thus saving planet. Provided further that for each unit (kWh) of energy generated and injected into the grid by eligible consumers shall be paid by the DISCOMs in Haryana at Rs. 3.11/- per kWh [taken from HAREDA official website].

The said rate has been determined by the Commission for the solar power projects setup/to be setup in Haryana under PM Kusum Scheme, wherein the cost of land/lease rental and higher O & M expenses are included. Further, the tariff discovered for solar energy through competitive bidding is continuously below Rs 3/- per unit. Nonetheless, given the high cost of land in Haryana including its limited availability, rooftop solar system can only drive the solar in Haryana.

Hence, the tariff shall be Rs. 3.11/- per unit for five years without any escalation, despite market asymmetry. The Commission may revise/re-determine the tariff after a period of five years from the notification of these regulations [taken from HAREDA official website].

## 10 Drawbacks of Net Metering

The net metering system has very less drawbacks:

- a. It necessitates that consumers have a precise electricity meter in order to monitor both the energy consumed and the energy generated by their renewable sources.
- b. Due to the frequent high cost and ongoing maintenance associated with metering systems, this may be pricey for some customers.
- c. The on-grid solar PV connected net metering works only in day time [13, 15].



**Table 3** Financial implication to the DISCOM/state boards for rooftop system under net metering [6]

Months	Billed demand/ consumptions from grid (units) (A)	Units generated by the rooftop solar system (B)	Net energy (units) (B – A = C)	Net monthly payment by DISCOM/boards lets (C*APPPC@RS 4/kWh)		Net monthly payment by consumer to DISCOM/ electricity boards	
January	1000	1200	200	800	10.8	– 800	– 11
February	1200	1000	200	0	0.0	1800	24
March	1300	1050	250	0	0.0	2250	30
Total	3500		650				
Net amount received by DISCOM/boards during a quarter under net metering						3250	44

### 11 Performance Analysis

From the above Table 3, I took analysis of units generated by solar rooftop system (B) and units consumed from grid (A) during three months of year. By the use of net metering bidirectional meter, I can get the net consumed unit by the household load denoted by C.

According to an analysis of Table 3 above, using a rooftop net metering system can reduce electricity costs to zero, and in some cases, it can even go down to a negative bill, which means the electricity board will add extra solar generation to the subsequent bill [1, 7].

Here it also calculated that if we would not have rooftop net metering system and consumed all units from grid, then we would have to pay for 3500 units (3500\*4 = Rs. 14,000).

But after installing rooftop net metering system, we just pay for 650 units (650\*4 = Rs. 2600) only. From this analysis, we saved an amount 14,000–2600 = Rs. 11,400, that’s a huge reduction on bills. Thus, we can conclude that rooftop net metering system is not only helps us to reduce in electricity bills but also cleans up our earth and drastically lowers carbon emissions.

### 12 Results

The performance of net metering depends upon the solar PV use for generation of electric power. The generation of the solar PV is directly proportional to the sunlight falls on the solar panels. The environmental conditions also affect the performance of the solar PVs, like dusty surface of the solar photo voltaic. The performance of the solar panels directly affects the net metering system as it is fully based on the renewable energy sources [7, 16–22].

**Table 4** Load consumption for home electronic devices

Sr. No	Items	Power (watts)	No. s	Hours of operations	W/h/day	W/h
1	Led	10	10	7	700	100
2	Fan	150	4	6	3600	600
3	TV	100	1	4	400	100
4	Freeze	200	1	8	1600	200
5	Mixer	500	1	1	500	500
6	Comp	300	1	4	1200	300
7	Pump	500	1	1	500	500
8	Iron	1000	1	1	1000	1000
9	Total	P = 2760W			W/h/day = 9500	W/h = 3300

From the above Table 4 [taken from HAREDA official website] I can conclude that:

$$\begin{aligned}
 \text{Total electrical power consumed as per daily load} &= 9500 \text{ W/h/day} \\
 &= 9.5 \text{ KWh/day} \\
 &= 9.5 \text{ units/day hourly Load} \\
 &= 3300 \text{ W/h} = 3.3 \text{ KW/h} \\
 &= 4 \text{ KW/h.}
 \end{aligned}$$

Monthly/annually (15–20 years) is Rs. 2284/Rs. 27,412.5/Rs. 685,312.5. Carbon dioxide emissions is ~ 74 tons. This process leads to planting ~ 121 teak like trees over the lifetime.

### 13 Conclusions

Net metering plays a very important role to save energy for our future and will influence the users and for rooftop-based electrical power generations. In this paper, we mainly focus on green energy utilizations with the help of net metering method. The renewable energy depends on the availability of the natural resource.

The net metering concept is very good option for use of solar energy by the use of on-grid solar system through net metering. In net metering, users generate their own electrical power pollution freely and efficiently at their rooftops during the day, most solar users generate through solar photovoltaic on-grid more electrical power than they consumed, net metering allows the users/customers to send back the power to the grid and reduce their future electricity bills.

Solar-powered energy plays an important role in the development of a country. Thus we can say that, net metering gives an idea of clean and green electrical energy

by the use of net metering systems at their rooftops. By the use of rooftop on-grid net metering system, we can conclude that the net metering is one of the great initiatives of government to electricity consumers/users in the way of using rooftop solar system with net metering mechanism to the amount of credits in their electricity consumption bills and sometimes makes the electricity bills units to zero and negative to give back money to the consumers/users from the electricity boards.

From the point of future scope of the on-grid rooftop net metering systems is that, at present, there is great boost in installation of rooftop solar system almost at every house of the big cities; it also increases in remote areas too, it's just a onetime investment to the consumers/users, then it gives back a lot of profits by reducing in daily consumable electricity units. For this scheme, the government also provides a good subsidy to their consumers.

The net metering system helps Indian Government to overcome load shielding problem throughout entire country. It provides help to the consumers, also it helps to reduce in their huge amount of electric bills. It can play a wonderful role in stabilizing nation and regional power grids. This system helps state electricity boards to reduce their financial losses. Also, it lowers the per-person energy footprint and aggregate technical and commercial losses. So, this can conclude that the net metering system has huge horizon in near future era of rooftop solar system.

## References

1. Abdel-Raouf O, Elsisy MA, Kelash E (2020) A survey of game theory applications in electrical power micro-grid systems. *Int J Comput Appl* 177(37):25–34. <https://doi.org/10.5120/ijca2020919871>
2. Poullikkas A, Kourtis G, Hadjipaschalis I (2013) A review of net metering mechanism for electricity renewable energy sources. *Int J Energy Environ*
3. Ahmad MW et al (eds) (2022) *Intelligent data analytics for power and energy systems*. Springer, New York, p 641. <https://doi.org/10.1007/978-981-16-6081-8>
4. Tomar A et al (eds) (2022) *Proceedings of 3rd international conference on machine learning, advances in computing, renewable energy and communication: MARC 2021*, vol 915. Springer, New York, p 781. <https://doi.org/10.1007/978-981-19-2828-4>
5. Minai AF et al (2022) Performance analysis and comparative study of a 467.2 kWp grid-interactive SPV system: a case study. *Energies* 15(3):1107
6. Ahmad A (2021) Distributed energy cost recovery for a fragile utility: the case of Électricité du liban. *Util Policy* 68:101138. <https://doi.org/10.1016/j.jup.2020.101138>
7. Bedi HS, Singh N, Singh M (2016) A technical review on solar-net metering. In: *Proceedings of the 2016 7th India international conference on power electronics (IICPE)*, Patiala, India
8. Sajjad IA, Napoli R, Chicco G, Martirano L (2016) A conceptual framework for the business model of smart grids. In: *Proceedings of the 16th IEEE international conference on environment and electrical engineering (EEEIC 2016)*, Florence, Italy, pp 1–5. <https://doi.org/10.1109/EEEIC.2016.7555684>
9. Spertino F, Di Leo P, Cocina V (2014) Which are the constraints to the photovoltaic grid-parity in the main European markets? *Sol Energy* 105:390–400
10. Hirth L (2015) Market value of solar power: is photovoltaics cost-competitive? *IET Renew Power Gener* 9(1):37–45

11. Liu M, Quilumba FL, Lee WJ (2015) A collaborative design of aggregated residential appliances and renewable energy for demand response participation. *IEEE Trans Ind Appl* 51(5):3561–3569
12. Tsarakis G, Thomson RC, Collin AJ, Harrison GP, Kiprakis AE, McLaughlin S (2016) Assessment of the cost and environmental impact of residential demand-side management. *IEEE Trans Ind Appl* 52(3):2486–2495
13. Syed MH, Burt GM, Kok JK, D'Hulst R (2015) Demand side participation for frequency containment in the web of cells architecture. In: Proceedings of the international symposium on smart electric distribution systems and technologies (EDST), pp 588–592. Gantz JM, Massoud Amin S, Giacomoni AM (2014) Optimal capacity partitioning of multi-use customer-premise energy storage systems. *IEEE Trans Smart Grid* 5(3):1292–1299
14. Ratnam EL, Weller SR, Kellett CM (2015) Scheduling residential battery storage with solar PV: assessing the benefits of net metering. *Appl Energy* 155:881–891
15. Paterakis NG, Erdinç O, Pappi IN, Bakirtzis AG, Catalão JPS (2016) Coordinated operation of a neighborhood of smart households comprising electric vehicles, energy storage and distributed generation. *IEEE Trans Smart Grid* 7(6):2736–2747
16. Thakura J, Chakrabortya B, Mishra R (2016) Sustainable net metering model for diversified India. *Energy Proced* 88:336–340
17. Sajjad A, Napoli R, Chicco G (2014) Future business model for cellular microgrids. In: Proceedings of the 4th international symposium on business modeling and software design (BMSD), pp 209–216
18. Bronski P, Creyts J, Guccione L, Madrazo M, Mandel J, Rader B, Seif D, Lilienthal P, Glassmire J, Abromowitz J, Crowdis M, Richardson J, Schmitt E, Tocco H (2014) The economics of grid defection. Rocky Mountain Institute. Boulder, CO. [www.rmi.org](http://www.rmi.org)
19. Breyer C, Gerlach A (2013) Global overview on grid-parity. *Prog Photovolt* 21(1):121–136
20. European Commission (2015) Delivering a new deal for energy consumers. European Commission, Brussels, p 141. Sajjad IA, Chicco G, Napoli R (2016) Definitions of demand flexibility for aggregate residential loads. *IEEE Trans Smart Grid* 7(6):2633–2643
21. Leiva J, Palacios A, Aguado JA (2016) Smart metering trends, implications and necessities: a policy review. *Renew Sustain Energy Rev* 55:227–233
22. Abapour S, Nazari-Heris M, Mohammadi-Ivatloo B, Tarafdar Hagh M (2020) Game theory approaches for the solution of power system problems: a comprehensive review. *Arch Comput Methods Eng* 27(1):81–103. <https://doi.org/10.1007/s11831-018-9299-7>

# Contemporary Maximum Power Point Tracking Methods of Solar Photovoltaic Modules



Jyothi Tompala and Sravana Kumar Bali

**Abstract** This paper presents a detailed analysis of different maximum power point tracking approaches for solar photovoltaic (PV) modules from traditional techniques. This paper also details the design of different sections of solar PV simulation for research purposes. The benefits and limitations of different approaches brief the researchers to propose novel techniques for extracting maximum power point under different operating conditions. The results presented in this paper will give a brief about the upcoming approaches in the considered research problem solutions. Novel artificial intelligence-based controllers and their implementation on the maximum power point tracking of a solar photovoltaic has been discussed which will abridge the research gap between the existing MPPT methods and the novel algorithms.

**Keywords** MPPT · Solar photovoltaic · Partial shading · P and O algorithm

## 1 Introduction

Renewable energy sources are the most sought-after areas because of their availability and affordability. Non-renewable energy sources get easily exhausted, unlike renewable energy available in large amounts. Conventional energy sources expel out carbon and sulphur emissions into the atmosphere, which can cause damage to the environment as well as human beings. Solar energy is one of the cleanest sources of energy, i.e. there are no carbon or sulphur emissions, requires less maintenance and is an economical energy source compared with other energy sources [1]. PV systems are used to convert solar energy to electrical energy. PV systems are divided into two groups based on their applications, i.e. stand-alone PV systems (electric cars, street lights, battery charging, etc.) and utility shared PV system (hybrid power system, power plant, etc.) [2, 3].

---

J. Tompala (✉) · S. K. Bali  
Department of EEE, GITAM Deemed to be University, Visakhapatnam 530045, India  
e-mail: [jtompala@gitam.in](mailto:jtompala@gitam.in)

© The Author(s), under exclusive license to Springer Nature Singapore Pte Ltd. 2024  
H. Malik et al. (eds.), *Renewable Power for Sustainable Growth*,  
Lecture Notes in Electrical Engineering 1086,  
[https://doi.org/10.1007/978-981-99-6749-0\\_9](https://doi.org/10.1007/978-981-99-6749-0_9)

The devices that are used for PV conversion is called solar cells. When solar irradiation falls on solar cell, it is directly converted into DC current. Major advantages are that there is no moving part, it requires less maintenance, works quite adequately with beam or diffused irradiation and can be adapted for various power requirements. But the limitation is that solar cells have minimal efficiency and require storage, and the initial cost of solar cells is high. A single solar cell cannot be used alone for the generation of energy where high power is required, like powering a household. The output of a single solar cell is very small, i.e. only 0.5 V, and the solar cell requires protection to protect it from moisture, mechanical shock, dust and harsh outdoor conditions. Solar cells are connected in series and parallel in a solar module. They are connected in series to build up the voltage and in parallel in order to supply the required amount of current. A group of cells connected in series is called a solar cell string. Most commercial modules have a connection of 32 or 36 silicon cells, making them capable of charging a 1-V battery. The power output from the installed solar PV modules also plays key role in its effective utilization. There are several methods proposed by the researchers [2–5], and further research is recommended for improved performance characteristics.

The paper is organized as, design aspects are listed in Sect. 2, MPPT techniques are presented in Sect. 3, and Sect. 4 provides different configurations of solar PV and finally conclusion and references.

## **2 Design Aspects of Solar PV Module**

### ***2.1 Solar Panel***

The PV model consists of solar arrays composed of several solar panels connected in series and parallel. They are laminated with plastic to protect against environmental damage. And the PV array is composed of several photovoltaic panels and modules to generate power. Based on standard test conditions (STC), the maximum power output for a PV array is determined. Generally, the PV modules used are very safe and there are very few chances of failure. As well it has a long lifetime of 20 or more years. Depending upon our description of necessity, we choose the desired PV modules.

### ***2.2 Buck Boost DC/DC Converter***

The PV model uses a buck boost DC/DC converter. As we can derive by its name, it combines the function of a buck converter (steps down DC voltage) and a boost converter (steps up DC voltage). The converter comprises of capacitor, diode, inductor and a switching MOSFET. Based upon the duty cycle, voltage value can be

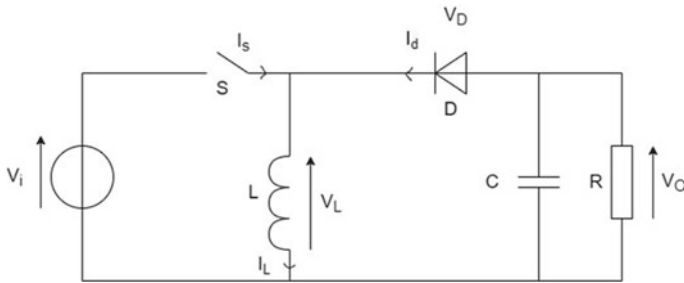


**Fig. 1** Buck boost converter

incremented or decremented. The inductor stores energy in its magnetic field when the MOSFET is turned on. No current flows through load due to the reverse biasing of the diode (Fig. 1).

The capacitor functions when the diode is reverse biased, the inductor is removed from the source, and the MOSFET is switched off. Reverse biasing causes the current to decrease instantaneously. The step-down duty ratio is below 50% and the step-up duty ratio is above 50%. This converter is used in PV system because when there is un-uniform illumination, the output voltage produced by the solar panel varies. So, with the help of buck boost converter, we may increase or decrease its value to our desired output value. The output voltage equations can be given by Eq. 1.

$$V_o = -\frac{DV_i}{1 - D} \tag{1}$$

### 2.3 PWM Modulator

PWM stands for pulse width modulation. This modulator is a switch connected between solar array and battery bank. This modulator decreases the current supplied to the battery, depending upon its charged state and reduces power supplied as it reaches its fully charged state. This increases the battery life and reduces duty cycle. It keeps batteries in floating condition, i.e. fully charged during the working period. It is used in solar PV system so that the charge stored does not again flow back into the solar array from the batteries during the night or a cloudy day because the output voltage is zero. Its efficiency lies in the range of 65–85%. It is especially useful when employed for small systems. Its operation is unaffected by the solar array size and works at constant efficiency.

## **2.4 MPPT Controller**

It is a charge controller with an in-built MPPT also which sees maximum power being drawn into the battery from the solar panels. This is mostly useful in off-grid solar systems such solar pumps, solar home system, etc. It helps in studying the solar V–I characteristics. It is used in PV system such that it maintains the voltage close to the maximum power point value, so that the system always draws maximum power. It simplifies the system and increases efficiency. Its output value directly controls the DC–DC converter. It regulates the voltage difference and provides optimization for DC load. It is most suitable for large systems with comparatively larger output voltage than battery voltage.

## **2.5 Capacitors**

The MPPT value is affected by the value of the variable capacitance of a capacitor. We assume that the capacitor is connected in parallel with the PV array, so the transfer function for the buck boost converter is derived and reduces source impedance.

## **2.6 Filters**

Usually, low pass filters are used in PV systems that only pass the waveform's fundamental component and appear in the output component. It also prevents the passage of components consisting of harmonics. We need to use a resonant filter if we use an inverter that works for a single fixed frequency and supplies power for that particular frequency.

## **2.7 Inverter**

They are used to convert the DC current generated at solar panels to AC. This current can be used for household purposes or in an electrical grid. If the power generated finds application in grid, it needs a special inverter called a grid-tie inverter. This grid tie works by matching the phase of generated current and the current required by grid. Else if this condition is not satisfied, it can get quite dangerous for the workers fixing the power lines. As soon as there is a power cut, it shuts down the supply in solar panel.



## ***2.8 Series and Parallel Combination of Solar PV***

To increase the voltage required, the solar PV modules are connected in series. The voltage of a single PV module is very small, and after connecting  $n$  number of PV modules we get desired voltage required by power plant. The open circuit voltage of the array is given by algebraic sum of individual open circuit voltages. We connect the solar cells in parallel to generate a large power, since increasing the voltage doesn't satisfy the purpose, so we have to increase the current. In parallel combination, the current of individual PV modules gets added. While designing a PV array, we combine parallel- and series-connected solar modules to get maximum power because power is a product current and voltage.

## ***2.9 PWM Pulse Signals***

The buck boost converter generates the pulse with modulation signals. An inverter is used to convert DC voltage generated by PV module to a variable or fixed AC voltage of the required frequency and magnitude. We can get variable AC voltage output by keeping the inverter gain constant and changing the DC value. Or if we keep the input DC value constant and want a variation AC output voltage, we have to vary the gain constant of the inverter. Sinusoidal output waveform is desired, but practical inverters fail to achieve it due to harmonics present in low and medium power applications. So, we receive square wave or quasi square wave voltage for these applications. We need nearly sinusoidal waves with the least distortion in high-power applications. This is achieved by switching techniques that cuts away the harmonic components in the output voltage wave.

## ***2.10 Bypass Diodes***

These diodes allow one directional flow of current and it is generally connected in parallel to the solar array. Its function is to present the generated power to flow from healthy solar cells to non-illuminated solar cells and not burn it in the process. These are designed to carry the short circuit current smoothly. There are two types of bypass diodes. They are Schottky barrier diode and PN-junction silicon diode. Their designing matches that of blocking diodes, but its function makes it different. Blocking diode is connected in series and its function is to allow the current to flow from PV array to the load and prevents the current to flow back into the array. We use this diode when we have several parallel branches of PV arrays, so we connect a blocking diode in each branch to prevent charged batteries from discharging at nightfall. Generally, manufacturers make both types of diodes in wide ranging current capacities.

## 2.11 Load

The term load refers to the devices that consumes the generated energy. The PV system comprises of variable load. The MPPT draws maximum power during operation but if this much power is not absorbed by load, then MPPT automatically adjusts at operating point. The buck boost converter enables us to match the load demand with the solar module with the help of a transformer. If the PV works under constant power factor and is connected to a grid, then the MPPT doesn't change with load change.

## 3 Maximum Power Point Tracking of Solar Cell

The solar radiation falling on the solar PV module will release free electrons which will result in the generation of voltage across the module, resulting in the flow of current through the closed circuit. The maximum power point of a solar cell is the point on the power curve (I–V curve) at which the highest value of the maximum net power output can be obtained. Different techniques are used to track the MPP to improve solar panel efficiency [3–7].

The offline methods that allow the PV system to work around its estimated MPP are:

- Fractional open circuit voltage method
- Fractional short circuit current method

These types of offline techniques determine the MPP on the basis of appropriate data. The PV panel is disconnected from the load, so offline parameters such as open circuit voltage and short circuit current can be noted. Because the PV panel is isolated from the rest of the system at the time of measurement, these are called offline maximum power point trackers. Here, continuous tracking of voltage and current is not carried out. The data usually consists of typical current–voltage curves for different temperatures and irradiances. The main advantage here is the requirement of a fairly lesser number of current and voltage sensors (Fig. 2).

### 3.1 Fractional Open Circuit Voltage Method

This method makes use of the fact that the relationship is almost linear between the open circuit voltage  $V_{OC}$  and the PV array voltage, corresponding to the maximum power point  $V_{MPP}$  for different irradiance and temperature levels.

$$V_{MPP} = K_{PV} V_{OC} \quad (2)$$

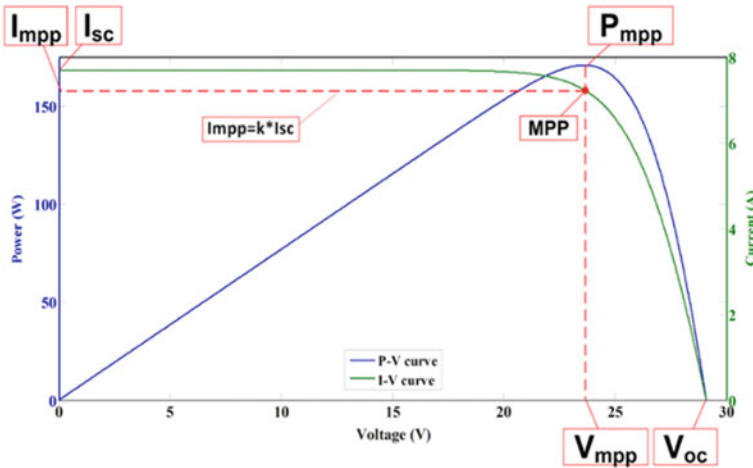


Fig. 2 Variation of solar PV module power and current w.r.t. voltage

Here,  $K_{PV}$  is a constant and is termed as voltage factor.  $K_{PV}$  value is usually provided in the datasheet of panels. It typically lies between 0.7 and 0.9. This value can also be determined using panel  $V-I$  curves. The main aim here is to estimate the value of voltage at MPP. To do so, the  $V_{OC}$  is found out periodically by isolating the panel from the load at certain time intervals and it is then multiplied with the voltage factor, i.e.  $K_{PV}$ . A precise estimation of the voltage at maximum power point can be made with the help of  $V_{OC}$  measurement, because the value of voltage factor given by  $V_{MPP}/V_{OC}$  does not change much with the temperature and irradiance. By opening the switch at regular instants, the  $V_{OC}$  is sampled periodically. The duration of the process of sampling and its frequency determines the accuracy of estimation of  $V_{MPP}$ . If high frequency is there and duty cycles are large, the quality of estimation is improved. But this comes at a cost, high frequency of sampling results in increased power loss. The FOCV method faces two major challenges, first that the panel can never really operate at true MPP and second, preventing the occurrence of power loss. At every time interval, the load is disconnected from the panel and the open circuit voltage is measured at those instants. The value of  $V_{OC}$  is then multiplied with voltage factor  $K$  which gives the voltage at MPP. The PI controller then compares the actual PV operating voltage when it is connected to the load with the voltage at MPP, treats the difference between these two values as error and tries to reduce it by adjusting the duty cycle of converter.

### 3.2 Fractional Short Circuit Current Method

By observing the current–voltage curve of a solar module, we get that the current corresponding to maximum power point and the panel’s short circuit current lie near

each other. So, the main idea here is to find the ISC at different temperature and irradiance levels and then multiply it by voltage factor  $K$  to find IMPP. This way, we can approximate the value of IMPP and make the solar panel deliver power at higher efficiency.

Mathematically, this can be written as,

$$I_{MPP} = K * I_{SC} \quad (3)$$

The voltage factor  $K$  is mentioned in the datasheet of panels and usually ranges between 0.8 and 0.92.

At the start of the operation, to measure the ISC, the switch between the panel and converter is closed, so that the panel gets short circuited and no power gets delivered to the load. The current sensor at this point measures the ISC. After that, the switch is opened and current starts flowing to the load. The same current sensor now measures the IPV. The difference between IPV and IMPP is that the PI controller calculates the error and then the required duty cycle is computed and fed to the DC–DC converter. Now according to the duty cycle fed to the converter, it starts delivering power to the load. This way, the error is rectified every few minutes and the solar panel is made to operate somewhat near the maximum power point.

### ***3.3 Advantages of Offline MPP Tracking***

The methods discussed above yield approximate MPP tracking, yet they have some advantages as mentioned below.

The fractional open circuit voltage method requires only one voltage sensor and the fractional short circuit current method requires only one current sensor. This way, this technique becomes economical to implement. They are easier to implement when compared with other MPPT methods. The speed of their convergence is fast. Oscillations around maximum power point is not faced in these methods.

### ***3.4 Disadvantages of Offline MPP Tracking***

These methods have been limited to use because of several disadvantages. Because these are approximated techniques, using them, we cannot make the solar panel operate at the exact MPP because they are not suitable for highly efficient PV system applications. During the course of a day, the temperature and irradiance level varies a number of times. So, periodic measurements of VOC and ISC have to be taken quite a number of times. The PV panel gets isolated from the system and power is cut off from the load many times. This consequently results in significant power loss. This particular drawback is being worked upon by a few improvement measures such as making the intermittent measurement process not time-based. The measurements of

offline parameters are taken only when the difference between the stored value (at the starting time of the system) and the instantaneous values crosses a certain value. In this way, the amount of power loss can be reduced. So, these were the conventional offline techniques to track the MPP of a solar panel. They are economical and easy to implement, but are a bit low in terms of efficiency. There are some other techniques in which the maximum power point (MPP) is captured online where a steady operating area is set by designing its control strategy. The duty cycle is kept constant when the operating point is within the stable operating area, i.e. aperiodic perturbation, and when the operating point is outside the stable operating area, maximum power point capturing is triggered to capture a new MPP with a different steady operating area. Some online techniques [4, 5] of MPPT are:

- Perturb and observe method
- Incremental conductance.

### 3.5 *Perturb and Observe Algorithm for Maximum Power Point Tracking*

It is one of the most basic methods of tracking maximum power point. It is also known by two other names like hill-climbing and two point power comparison method. This method can only track the maximum power point when the irradiance is uniform on the solar PV panel. This method is not applicable when the irradiance on the solar PV panel is non-uniform, i.e. when it is partially shaded.

Let us suppose the solar irradiance is uniform and we draw a PV curve, this curve will have only one maximum power point which is both the local and global maxima (for now, we're keeping aside the partial shading condition).

The graph for power versus voltage for perturb and observe algorithm is shown in Fig. 3.

From the graph, we can see that on the left-hand side of the MPP, the change in power with respect to voltage is positive, so when the voltage in this region is increased, the power increases and when it is decreased the power decreases. But on the right-hand side, the change in power with respect to voltage is negative, so if the voltage is increased the power decreases, and if it is decreased the power increases. At the MPP stage, the change in power with respect to voltage is zero, which is the condition for maxima.

As a result, the perturb and observe algorithm checks the power to voltage slope. If it is positive that means we're on the left-hand side of MPP, we're on the right side of the MPP if it is negative and we're at MPP if it is zero, i.e.

$$dP/dV = 0 \text{ At MPP} \tag{4}$$

$$dP/dV > 0 \text{ Left side of MPP} \tag{5}$$

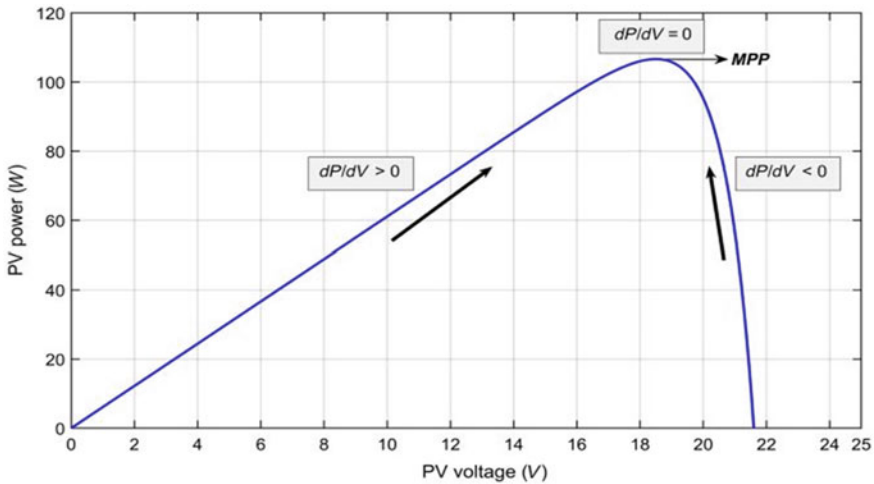


**Fig. 3** Change in power magnitude corresponding the changes in voltage of a solar PV module

$$dP/dV < 0 \text{ Right side of MPP} \quad (6)$$

This logic can be used to make a flowchart in which the voltage of the panel is perturbed and the corresponding change in power is observed. The flowchart is shown in Fig. 4. From the flowchart, we can observe that if the perturbation results in power increase, then the perturbation is repeated in the same direction, otherwise it is repeated in the opposite direction. This perturbation is done repeatedly during each sampling period, until the slope is zero and MPP is reached. Finally, we save the value of the voltage and power at which MPP was reached. Now, this voltage is compared with the voltage of the solar panel to calculate the error which is the difference in the two voltages. The controller receives this error and converts it to the duty ratio 'D', the PWM generator receives this duty ratio and generates a PWM signal. In this hill climbing method, the duty ratio is directly perturbed. In order to increase the panel's voltage, the duty ratio is decreased and vice versa when it is increased. We can stop perturbing the duty ratio and set it to one value as MPP is reached.

Some advantages of P&O method are that it has low hardware and software complexity, reasonable dynamic, analog and digital implementation. Some disadvantages of the P&O method are power oscillations, does not work under partial shading conditions and sudden change in lighting conditions results in drifting of the MPP to another point.

We cannot neglect the effect of weather condition for considering the efficiency of PV developed power [7, 8]. The generated power is mainly influenced by irradiance and temperature. The graph is different in shading conditions. As we can see from the Fig. 5, when there are shading conditions, the PV graph will have many local maxima

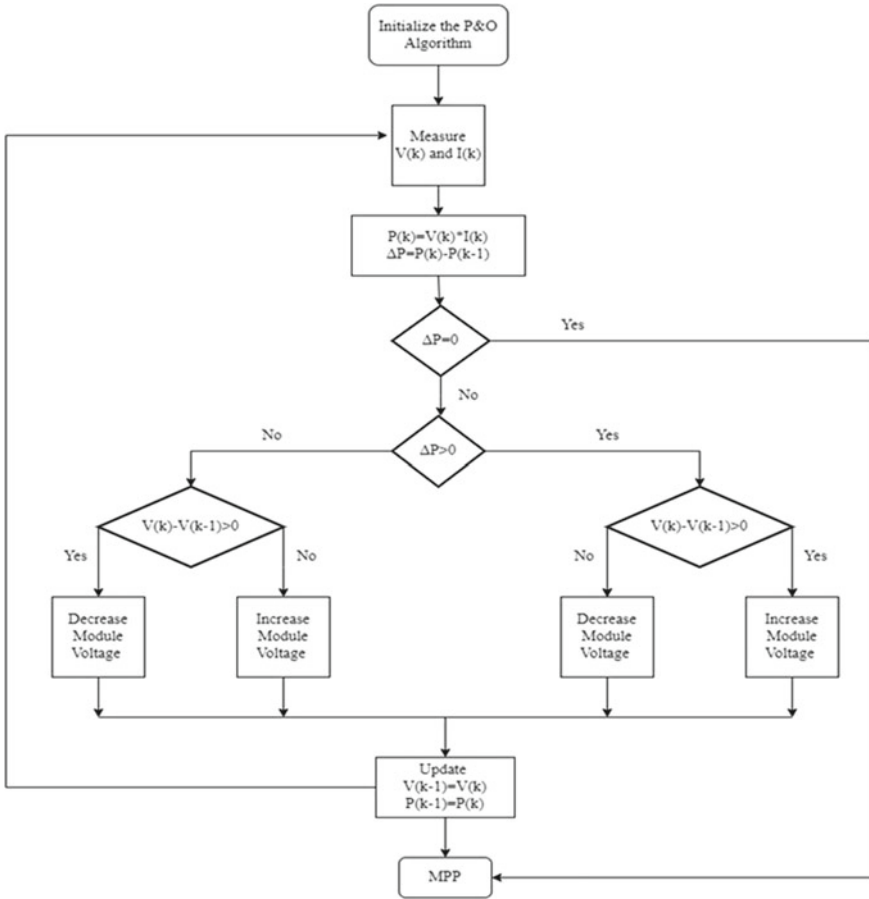
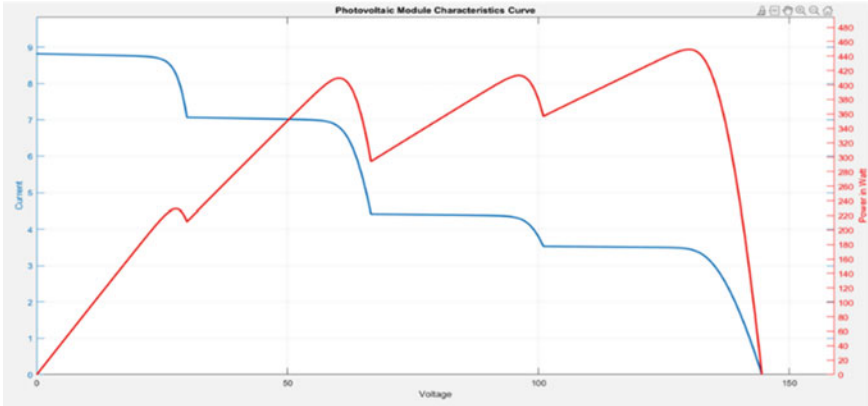


Fig. 4 Flowchart of perturb and observe algorithm

and one global maxima, so while tracking we may get stuck at a local maxima. Hence, this method fails for shading conditions and we go for other advanced techniques.

### 3.6 Incremental Conductance Maximum Power Point Tracking Algorithm

The incremental conductance (IC) method helps in overcoming the shortcomings of perturb and observe method. The P&O method cannot properly track the maximum power under quick varying environmental conditions, which can be overcome by the incremental conductance method. The IC method ensures that the MPPT works at its maximum efficiency and helps control the buck boost converter duty cycle. It



**Fig. 5** PV characteristics of solar photovoltaic module under partial shading conditions

improves the tracking time and produces more energy for vast irradiance change in environment. The algorithm of incremental conductance is obtained by differentiating the power of PV array/module with respect to voltage and equating the result to zero.

$$dP/dV = 0 \tag{7}$$

$$d(V * I)/dV = 0 \tag{8}$$

$$I + VdI/dV = 0 \tag{9}$$

By rearranging the solution, we get:

$$dI/dV = -I/V \tag{10}$$

where  $dI/dV$  is the incremental conductance.

So, at MPP the above equation should satisfy and depending upon the relationship between  $dI/dV$  and  $-I/V$ , we will obtain the MPPT operating point.

Hence,

$$dI/dV = -I/V \text{ at MPP} \tag{11}$$

$$dI/dV > -I/V \text{ left of MPP} \tag{12}$$

$$dI/dV < -I/V \text{ right of MPP} \tag{13}$$



If  $dI/dV > -I/V$ , the PV array operating point is towards the left of the maximum power point, so we need to increase the PV array voltage to reach the MPP. If  $dI/dV < -I/V$ , the PV array operating point is towards the right of the maximum power point, so we need to decrease the PV array voltage to reach the MPP. The flowchart of incremental conductance maximum power point tracking is shown below.

We obtain the maximum power through this method and directly control the PV's extracted power. The advantages of this method are that it can determine when the MPPT has reached the maximum power point, whereas P&O oscillates around the MPP. It is more accurate in determining the increase or decrease in irradiance level when compared with P&O method, it is highly responsive and power output can be controlled.

This method assumes that the ratio of change in output conductance equals the negative of the instantaneous conductance. The disadvantage of this method is the complexity and cost of implementation is higher. So now we work on obtaining a condition such that  $(dI/dV) + (I/V)$  equals zero. The PWM control signal of the DC-DC boost converter is regulated by MPPT until the condition:  $(dI/dV) + (I/V) = 0$  is obtained. This algorithm depends on PV curve slope and depends upon solar irradiance level and load resistance.

## 4 Solar PV System Configurations

The solar PV system configurations are of mainly,

- Stand-alone SPV systems
- Grid-interactive PV system
- Small systems for consumer applications
- Centralized PV station or PV power station
- Hybrid system.

### 4.1 Centralized PV Power Station or PV Power Station

This accounts for wide ranging applications in supplying power from solar PV system to the electric grid. It resembles conventional central power plant. It finds applications in solar farm, solar plant, etc. The peak value of solar energy is usually at 1 MWp. Many big PV power stations are owned and operated by self-sustaining producers. The world's largest solar park is Bhadla Solar Park (2020) and has a storage of 2245 MW and is occupied over 5700 ha (14,000 acres) in Jodhpur district of Rajasthan.

## **4.2 Distributed PV System**

This type of configuration is used for small-scale power generation such as residential loads (2–10 kW) and commercial loads (20–200 kW). They are usually set-up on the top of the roofs of houses or mounted on ground if space is available. These are mainly generated for personal use of owners, but if produced in large quantity it is sold. They are further classified as:

- (a) Stand-alone PV system
- (b) Grid-interactive PV system
- (c) Small systems for consumer applications.

## **4.3 Stand-Alone PV System**

This PV system is not dependent on the electricity grid; the generated energy is stored in batteries. This is mainly produced in areas that do not have easy access to electric grid. It also comprises an inverter that converts the DC power produced by the PV modules to AC as used in household or industrial purposes.

The functions of some of its components are that the voltage and current characteristics enable the MPPT to set its operating point to extract maximum power and the DC/AC converter converts the DC energy received from the solar PV module to AC and feeds it into the load. When the battery is fully charged and has more charge, it is transferred to dump load. With the help of inverter, the battery provides power to load during night time. The battery does not get overcharged when the charger is removed, because it is discharged by diode DB. When the sun has set the diode, DA does not allow the current to flow into the array through the battery by isolating it. Mode controller receives all system signals and keeps a check on the charging or discharging of batteries. Thus, it acts as a centralized controller.

## **4.4 Grid-Interactive PV System**

It functions along with the electric utility grid. It supports power generation in the range of hundreds of watts from one PV array to tens of megawatts from a large set-up. If power generated becomes excess, it is directed to electric grid and we don't require a dump load. The battery is not needed for power stored at night time.

MPPT studies the current and voltage characteristics in this system and sets its operating point to withdraw maximum power. It consists of a power conditioner that converts the DC current to AC and removes the harmonics before feeding it into the electric grid. Some grid-interactive systems employ a battery to be used at times of power shortage or at low illumination conditions.

## 4.5 Hybrid Systems

Hybrid systems are composed of two or more than two types of generating stations. It provides more storage and employs advanced technologies compared with any individual energy generating station. One of its applications lies in mining, where diesel power plant is integrated with solar and wind power plants. This reduces the transportation as well as material cost considerably.

As we know, since the past few years, solar and wind costs have greatly decreased. And now the solar energy is utilized at great per cent and the wind mills have become taller which is an advantage to this power system. So, generally we combine diesel plants with renewable energy sources. Solar wind hybrid power systems are used widely nowadays, because we know the peak power for individual power systems occurs at different times of the day and when employed together, they provide less fluctuations in energy generations. It provides power back up of 6–7 h when there is power cut. And this system does not support more than one air conditioner.

## 5 Conclusion

This paper provides detailed description in the solar photovoltaic system simulation and analysis research area. The basic modelling of different components involved in simulations has been demonstrated. Contemporary methods on maximum power point tracking methods starting from offline and online methods with their advantages and disadvantages have been described. The connection of solar photovoltaic modules for the different applications have been presented in this paper. The paper presents the scope of the work in the solar PV maximum point tracking and the application of solar energy. Hence, the future scope of the paper is to adopt numerous state-of-the-art techniques in extracting maximum power from the existing solar PV modules in the industries and household applications.

## References

1. Ram Babu N et al (2022) A comprehensive review of recent strategies on automatic generation control/load frequency control in power systems. *Arch Comput Methods Eng* 30:543–572. <https://doi.org/10.1007/s11831-022-09810-y>
2. Saberian A, Hizam H, Radzi MAM, Ab-Kadir MZA, Mirzaei M (2014) Modelling and prediction of photovoltaic power output using artificial neural networks. *Int J Photoenergy* 2014:e469701
3. Mishra VL, Chauhan YK, Verma KS (2022) A critical review on advanced reconfigured models and metaheuristics-based MPPT to address complex shadings of solar array. *Energy Conver Manag* 269:116099
4. Kamran M et al (2020) Implementation of improved Perturb and Observe MPPT technique with confined search space for standalone photovoltaic system. *J King Saud Univ Eng Sci* 32:432–441
5. Ahmad MW et al (eds) (2022) *Intelligent data analytics for power and energy systems*. Springer, Singapore, p 641. <https://doi.org/10.1007/978-981-16-6081-8>

6. Tomar A et al (eds) (2022) Proceedings of 3rd international conference on machine learning, advances in computing, renewable energy and communication: MARC 2021, vol 915. Springer, New York, p 781. <https://doi.org/10.1007/978-981-19-2828-4>
7. Nagadurga T, Narasimham PVRL, Vakula VS, Devarapalli R (2022) Gray wolf optimization-based optimal grid connected solar photovoltaic system with enhanced power quality features. *Concurr Comput Pract Exper* 34:e6696
8. Nagadurga T, Narasimham PVRL, Vakula VS, Devarapalli R, Márquez FPG (2021) Enhancing global maximum power point of solar photovoltaic strings under partial shading conditions using chimp optimization algorithm. *Energies* 14:4086

# Performance Analysis of Perturb & Observe and Incremental Conductance Method of Maximum Power Point Tracking in Solar PV-Based Power Generation



Avdhesh Kumar

**Abstract** In this paper, study and performance analysis of perturb and observe (P&O) and incremental conductance (InC), method of maximum power point tracking (MPPT) control algorithms has been performed. It has been tested under different environmental conditions, viz. standard test condition, varying insolation and temperature in the MATLAB/Simulink 2018(a) environment. P&O and InC algorithm has been analyzed. It is found that performance using incremental conductance algorithm is efficient in terms of less perturbation in the duty cycle and slightly more power output, i.e. 100 W for developed 10.25 kW solar PV system in the MATLAB/Simulink.

**Keywords** Incremental conductance · Solar photovoltaic · Perturb and observe

## 1 Introduction

The integration of renewable energy sources, semiconductor devices and partial shading of SPV array results in several losses that are significant enough to be taken into account while designing the system for supplying a specific load. Thus, the efficiency still ranges between 14 and 16%, due to above aforementioned restrictions [1]. Figure 1 shows the schematic representation of the system consisting of a SPV system, boost converter embedded with maximum power tracking method and load [2].

Solar photovoltaic energy is suitable as one of the key options for supplying electricity to remote areas. Output power of solar PV is influenced by different environmental conditions. To achieve the optimal power output irrespective of dynamic nature of environmental conditions, MPPT is required. MPPT aims to achieve the

---

A. Kumar (✉)

Electrical Engineering Department, Delhi Technological University, Delhi, India

e-mail: [avdhesh\\_phd2k17@dtu.ac.in](mailto:avdhesh_phd2k17@dtu.ac.in)

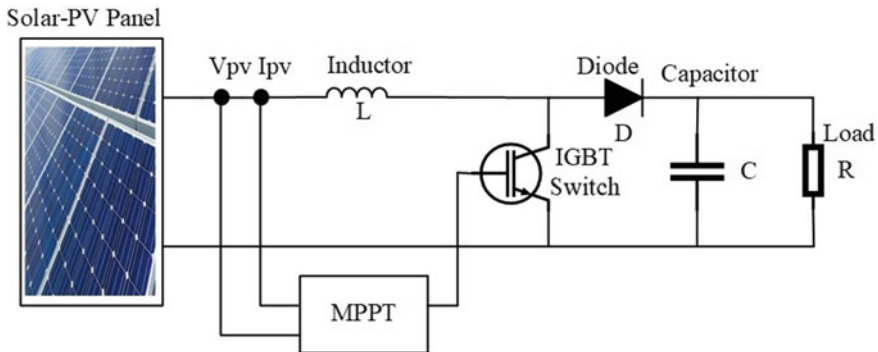


**Fig. 1** Test system

optimal power output irrespective of environmental conditions [3]. The most popular techniques, namely P&O and InC algorithms have been used. P&O and InC technique evaluate the point of the MPP by shifting it back and forth and injecting a disturbance in the PV voltage/current based on the nonlinear properties of the PV [4].

In the literature [5], different MPPT have been thoroughly discussed in order to obtain maximum power like simple and efficient P&O and InC, grey wolf optimization (GWO) and particle swarm optimization (PSO). All of the MPPT techniques based on artificial intelligence show fast convergence speed, less oscillation under steady state and high performance. These methods are highly computational and expensive to develop. The problem associated with MPPT algorithm has been addressed in various literature, but P&O is the furthestmost commonly used method due to, its comfort of implementation, particularly for low-cost implementations [6]. Further research is ongoing to enhance the existing MPPT techniques to handle temperature and varying irradiance conditions. Grid integration of PV system is realized using a VSC. The operation of the PV system requires switching pulses given to the VSC. The generation of switching pulses requires the reference current which helps in elimination of harmonics, compensation of reactive power and maintaining power balance at the PCC. The main aim of pulses given to VSC is to reduce the distortion level at grid side.

There are a number of techniques for the conventional MPPT [7], InC, hill climbing, P&O and improved P&O method. Because the algorithms for these strategies are less sophisticated, they are simple to implement. Since the PV will only produce one GMPP under uniform irradiation, these conditions will maximize their efficiency.

Fuzzy logic control and artificial neural network-based MPPT are examples of intelligent-based approaches [7]. These methods are designed to be extremely accurate under dynamic, ever-changing weather circumstances. Their tracking effectiveness and speed are really high. Complexity in control technique and enormous

data processing for the system's initial training are additional drawbacks of these techniques.

Cuckoo search-based and artificial bee colony are examples of optimization methodologies [7–10]. These approaches also tend to hunt for real MPP in changing environmental situations. The PSO technique is a faster tracking method with less steady-state oscillations [10].

In the present studies, PV-based microgrid has been implemented using Perturb & Observe and incremental conductance MPPT control. Performance analysis and comparison of P&O and InC MPPT algorithms have been performed under standard test condition, varying insolation and temperature in the MATLAB/Simulink 2018(a) environment.

## 2 System Configuration

Figure 1 shows that test set-up consists of a 10.25 kW SPV system, as well as a boost converter and a consumer load(R). SPV power is not constant and fluctuates with environmental situations, P&O and InC algorithms have been modelled and simulated to achieve optimum efficiency of the SPV array.

## 3 Solar PV Configuration

Output of PV array are constantly changing owing to environmental variations, it is essential to track the optimum power using algorithm. In this study, the MPP is tracked using the P&O and InC control method. Using the maximum power transfer theory, the MPPT algorithm maintains the solar PV operating point corresponding to maximum power by varying the duty ratio. Characteristics of the SPV array varied solar insolation and temperature are depicted in Figs. 2 and 3, respectively.

## 4 MPPT Control Technique

The output of a PV array is not continuous and varies, depending on the environment. In order to monitor the optimum power, P&O and InC MPPT algorithm has been implemented in MATLAB/Simulink (2018) environment.

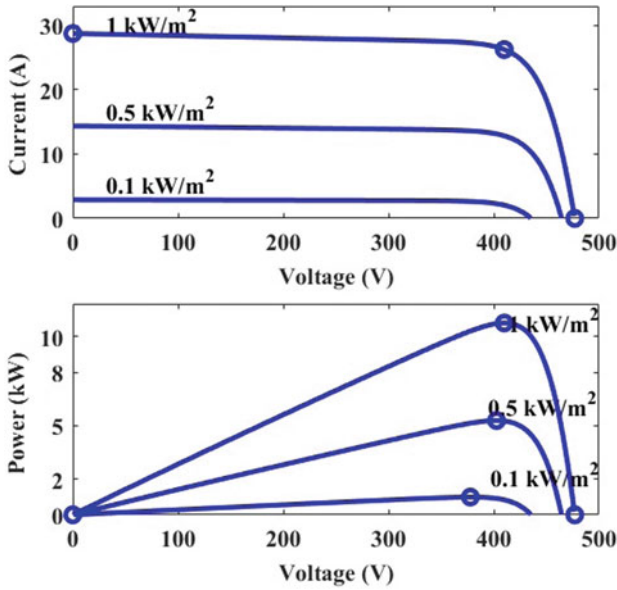


Fig. 2 *I-V* and *P-V* curve of PV array at variable insolation

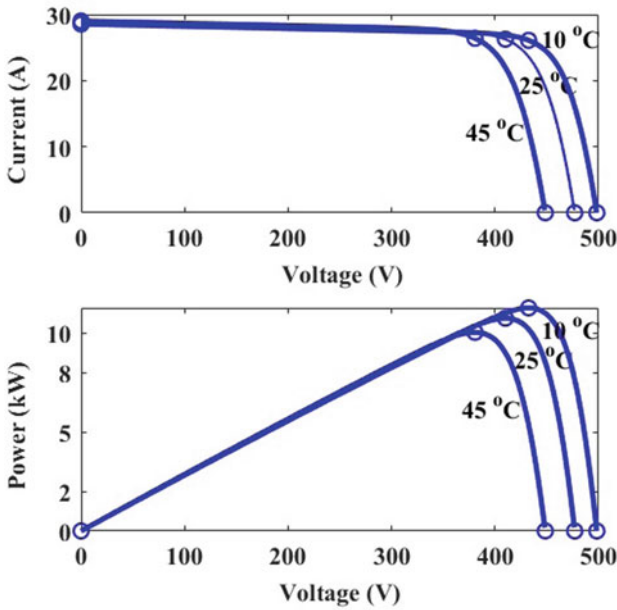


Fig. 3 *I-V* and *P-V* curve of PV array at variable temperature



### 4.1 P&O

This P&O MPPT is user-friendly, has the simplest algorithm and is simple to implement on any microcontroller, making it ideal for most authors to utilize in their applications. P&O calculations compare the voltage position after comparing, with obtained power at two places on a  $P-V$  curve. The voltage is then changed appropriately to follow the MPP (either to the left or right of the  $P-V$  curve).

Flowchart of P&O has been depicted in Fig. 4. Fundamentally, this method first looks for a  $(\Delta P)$ , then it looks for a sign of  $(\Delta V)$ . Fundamentally, this method first looks for a change in  $(dP)$ , then it looks for a sign of  $(dV)$ . To examine the actual movement of the operational point,  $P-V$  curve data is used. Furthermore, procedure continues until  $(dP = dV)$  equals zero. Furthermore, algorithm comprises an adjustment in converter's duty cycle as well as an adjustment in the output voltage. The changes in the PV array voltage, maximum power point tracking algorithm of the SPV system, varies the duty cycle of the DC-DC converter.

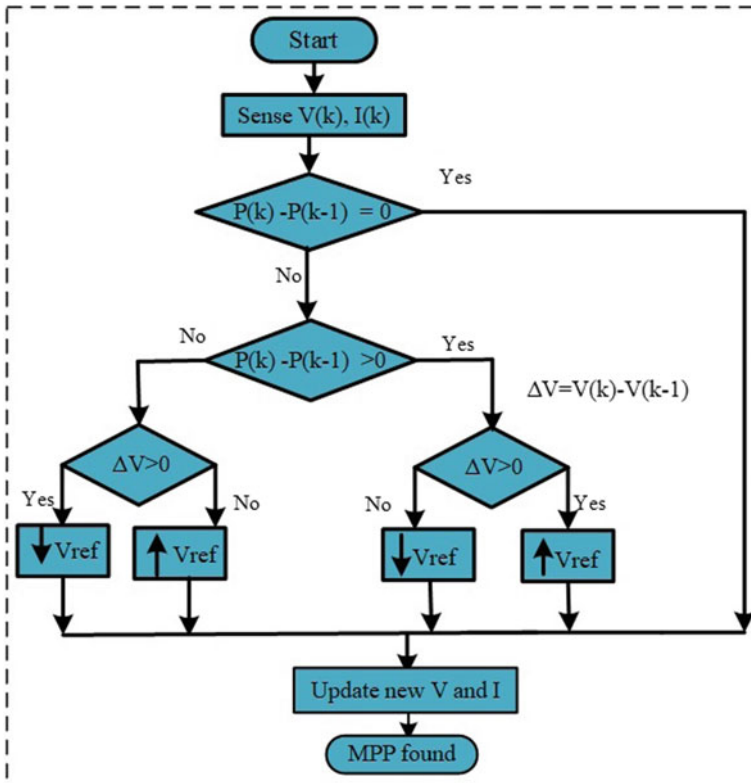


Fig. 4 P&O: flowchart

### 4.2 InC

Flowchart of InC has been depicted in Fig. 5, this approach largely follows the same path from P&O to MPP, but makes use of the special relationship between the  $I-V$  curve. This calculation measures the PV cell current and voltage. Furthermore, InC algorithm, estimates derivative of current ( $dI$ ) and voltage ( $dV$ ) of PV cells. The InC method, requires ( $dP/dP = 0$ ) at MPP. The  $P-V$  curve will be used as the basis for all data in this approach, which uses that data to track the MPP. Only the tracking procedure is completed if either the PV array power's derivative ( $dP = dV$ ) or the  $P-V$  curve's slope are both zero.

$P-V$  curve has a zero slope at MPP, increasing to the left of MPP and decreasing to right. Following are fundamental equations for this technique:

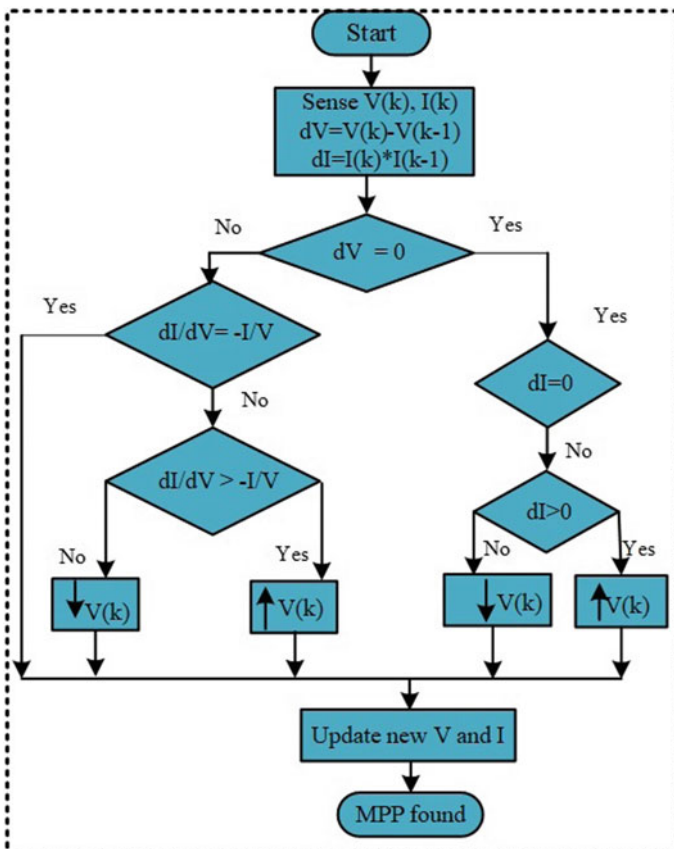


Fig. 5 InC: flowchart

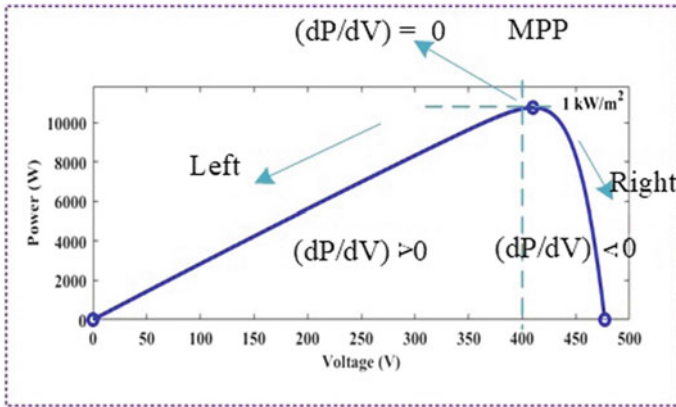


Fig. 6 *P–V* curve

$$\text{At MPP, } \frac{dI}{dV} = -\frac{I}{V}$$

$$\text{Left of MPP, } \frac{dI}{dV} > -\frac{I}{V}$$

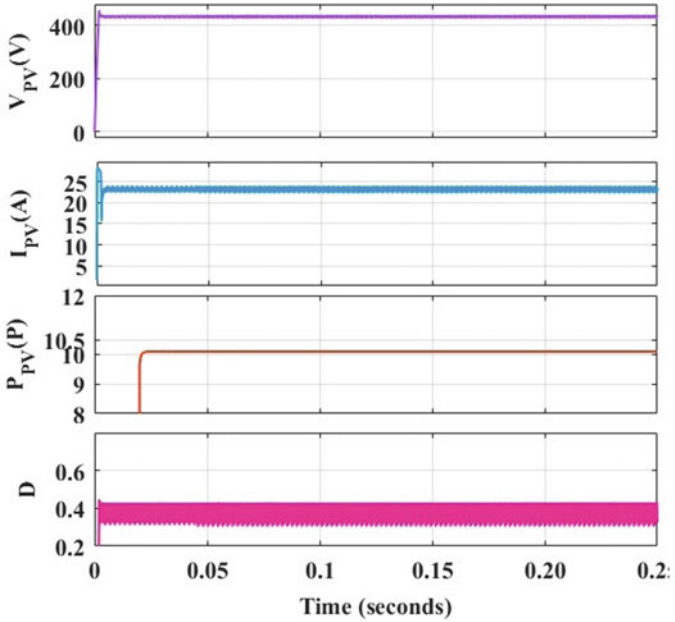
$$\text{Right of MPP, } \frac{dI}{dV} < -\frac{I}{V}.$$

Equations’ left side signifies the InC of the *P–V* module and their right side signifies its instantaneous conductance. In the case when the ratio of output conductance change equals the negative output conductance, SPV operates at its MPP that can be seen from *P–V* curve of the SPV system as depicted in the Fig. 6.

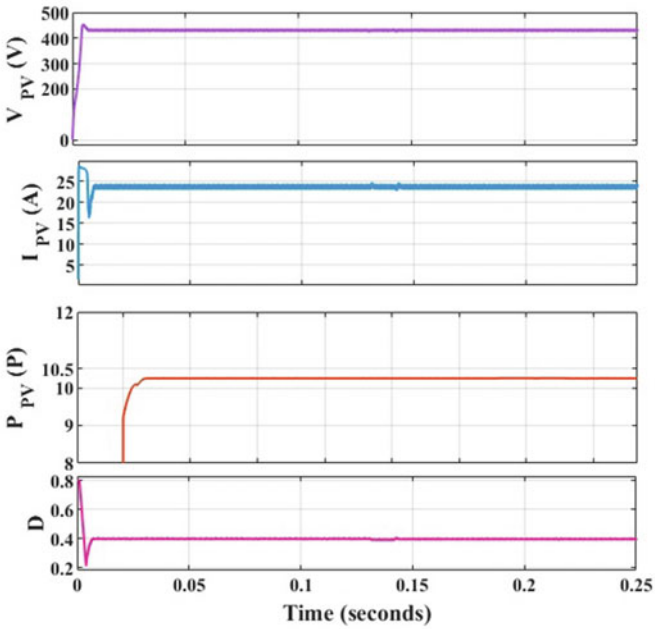
## 5 Results and Discussions

Performance under different environmental conditions have been analyzed and compared. Microgrid system is modelled in MATLAB/Simulink. The performance of P&O and InC at standard test condition (STC), variable insolation and variable temperature has been analyzed and presented. Various parameter of the system, viz. voltage, current and power are depicted in Figs. 7, 8, and 9, respectively. It has been observed from Fig. 7b that in the developed system, incremental conductance is efficient and has less perturbation in the duty cycle when compared with P&O at STC [1000 W/m<sup>2</sup> and 25 °C] and extracting slightly more power, i.e.100 W for the developed solar PV system (10.25 kW).

The system’s performance is evaluated by varying the external circumstances, such as insolation and temperature to further validate the efficacy of the two control

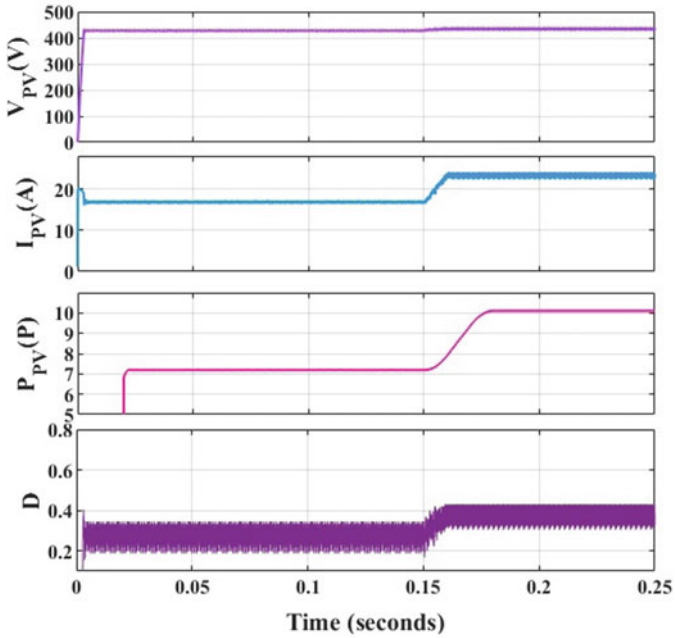


(a)

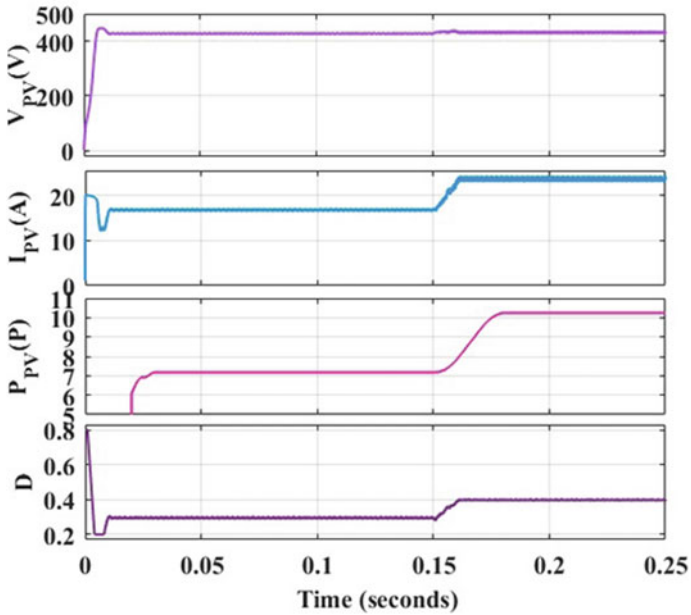


(b)

Fig. 7 Simulation result at STC [ $1000 \text{ W/m}^2$  and  $25 \text{ }^\circ\text{C}$ ] using: **a** P and O, **b** InC

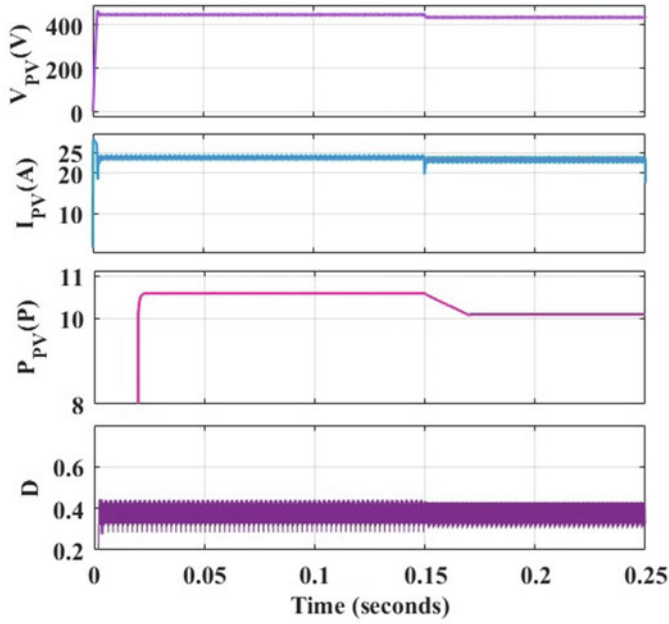


(a)

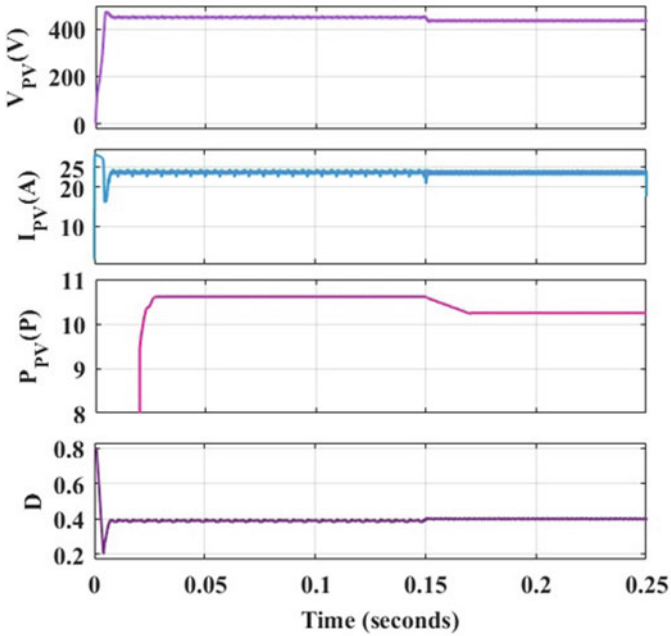


(b)

Fig. 8 Simulation result variable insolation using: a P&O, b InC



(a)



(b)

Fig. 9 Simulation result variable temperature from 15 to 25 [°C], using: a P&O, b InC

algorithms. At 0.15 s, the solar insolation intensity has been changed from 700 to 1000 W/m<sup>2</sup> and performance is depicted in the Fig. 8. It has been observed from Fig. 8b that incremental conductance is efficient and has less perturbation in the duty cycle when compared with P&O at variable insolation and extracting slightly more power, i.e. 100 W for the developed solar PV system (10.25 kW).

The system's performance is evaluated by changing external circumstances such as temperature to further validate the efficacy of the two control algorithms; at 0.15 s, the temperature has been changed from 15 to 25 [°C], performance is depicted in the Fig. 9. It can be seen from the Fig. 9b that InC has less perturbation/oscillations in the duty cycle when compared with P&O at variable temperature and also extracting slightly more power, i.e. 100 W for the developed solar PV system (10.25 kW).

## 6 Conclusions

In this paper, PV-based standalone microgrid has been developed and implemented in the MATLAB/Simulink 2018(a). P&O and InC method of the MPPT control algorithm have been used as MPPT. It has been tested under different environmental conditions, viz. standard test condition, varying insolation and temperature. Performance of the implemented method has been analyzed. It is found that performance using incremental conductance algorithm is efficient in terms of less perturbation in the duty cycle and slightly more power output, i.e. 100 W for developed 10.25 kW solar PV system in the MATLAB/Simulink.

## References

1. Zhang X, Gamage D, Wang B, Ukil A (2021) Hybrid maximum power point tracking method based on iterative learning control and perturb and observe method. *IEEE Trans Sustain Energy* 12(1):659–670. <https://doi.org/10.1109/TSTE.2020.3015255>
2. Kumar A, Garg R, Mahajan P (2021) Harmonics mitigation techniques in grid integrated PV based microgrid: a comparative analysis, pp 1–6. <https://doi.org/10.1109/icaect49130.2021.9392631>
3. Liu L, Meng X, Liu C (2016) A review of maximum power point tracking methods of PV power system at uniform and partial shading. *Renew Sustain Energy Rev* 53:1500–1507. <https://doi.org/10.1016/j.rser.2015.09.065>
4. Yap KY, Sarimuthu CR, Lim JM (2020) Artificial intelligence based MPPT techniques for solar power system: a review. *J Mod Power Syst Clean Energy* 20(20):1–18
5. Femia N, Petrone G, Spagnuolo G, Vitelli M (2005) Optimization of perturb and observe maximum power point tracking method. *IEEE Trans Power Electron* 20(4):963–973. <https://doi.org/10.1109/TPEL.2005.850975>
6. (2019) Array in solar applications: a review. *Renew Sustain Energy Rev* 101, 82–102
7. de Brito MAG, Galotto L, Sampaio LP, Melo GDA, Canesin CA (2013) Evaluation of the main MPPT techniques for photovoltaic applications. *IEEE Trans Ind Electr* 60(3):1156–1167

8. Tomar A et al (eds) (2022) Proceedings of 3rd international conference on machine learning, advances in computing, renewable energy and communication: MARC 2021, vol 915. Springer, New York, p 781. <https://doi.org/10.1007/978-981-19-2828-4>
9. Ahmad MW et al (eds) (2022) Intelligent data analytics for power and energy systems. Springer, Singapore, p 641. <https://doi.org/10.1007/978-981-16-6081-8>
10. Bollipo RB, Mikkili S, Bonthagorla PK (2021) Hybrid, optimal, intelligent and classical PV MPPT techniques: a review. CSEE J Power Energy Syst 7(1):9–33



# The Airfoil Design for Small-Scale Wind Turbines in Maximizing Renewable Wind Energy



S. A. H. Roslan, N. Umar, Z. A. Rasid , and A. K. Arifin

**Abstract** As one alternative of renewable energy sources, wind turbine (WT) has risen to dominate the energy source with its large-scale wind turbine. Of late however, there are growing appeals for small-scale wind turbine (SSWT) that operates in urban areas and territories with minimal wind speed as a complement to its large counterparts. However, the SSWT comes with challenging problems of low wind speed that not only gives low lift force,  $F_L$  but also low Reynold's number,  $Re$  that leads to drag controlled flow. Both are the primary reasons for the SSWT to have low glide ratio,  $L/D$ , power coefficient and power. Airfoil design plays a crucial role in accomplishing the maximum possible  $L/D$  over a longer range of angle of attacks (AOAs) that gives the highest achievable power coefficient and power. In current situation, with the increasing trend of WT usage in regions with low wind speed, the SSWT can still benefit from new airfoil designs. As such in this study, a set of three airfoils specifically for low  $Re$  are obtained through geometric adjustments of a high-performance airfoil, WT180 that is suitable for large-scale wind turbine. At low  $Re$  of 100,000, the newly adjusted airfoils were found to have  $L/D$  of up to 46 which is higher by 44% compared with the original WT180 and 4% compared with the SG6043 airfoil, the well-known airfoil designed for WT having low wind speed condition.

**Keywords** Renewable energy · Small-scale wind turbine · Airfoil design · Glide ratio · Drag controlled flow

---

S. A. H. Roslan · N. Umar · Z. A. Rasid (✉)  
Universiti Teknologi Malaysia, Jalan Sultan Yahaya Petra, 54100 Kuala Lumpur, Malaysia  
e-mail: [arzainudin.kl@utm.my](mailto:arzainudin.kl@utm.my)

A. K. Arifin  
Universiti Kebangsaan Malaysia, 43600 Bangi, Malaysia  
e-mail: [kamal3@ukm.edu.my](mailto:kamal3@ukm.edu.my)

## 1 Introduction

The growing concern over the effects of carbon-based energy in the last decades has materialized with the energy and climate crisis that shackles the world today. In addition, with the increase in population and industries, there comes environment and sustainability issues that require quick solutions, covering areas among others, energy production [1–3], material designs [4, 5], structural failures [6, 7] and manufacturing process [8, 9]. In terms of energy production, the utilization of supplies of renewable energy [10], including solar energy and wind energy is one of the most efficacious answers to deal with these problems. And wind, the free energy source obtained through the wind turbine (WT) machine, has been dominating the renewable energy's world with its increasingly large-scale wind turbine (LSWT) [11]. Unlike the LSWT field that is matured [12], with a wealth of well-understood solutions to problems faced, the SSWT as a small machine having low wind speed that has to operate at low Reynold's number,  $Re$ , requires more attention [13] and works to improve challenging problems of low power coefficient, low starting capability and low cost [14–16].

Thus, in designing a SSWT, the objective is to have high coefficient of power,  $C_P$ , power, annual energy production and AEP at lower cost of energy [17]. One key factor to reach this is to have an airfoil that gives high and consistent glide ratio,  $L/D$  covering a broad span of angle of attack (AOA),  $\alpha$ . This depends on the shape of the blade profile that can give high lift force,  $F_L$  and avoid high drag force,  $F_D$ , as the effect of the low  $Re$ . The shape of the airfoil is such that it gives high pressure variation between the upper and the lower sides of the airfoil as air flows through the profile, thus providing the  $F_L$  and the operation of the WT. But the airfoil shape also produces the adverse pressure gradient (APG), especially for the SSWT that operates in low  $Re$  which results in flow separation, separation bubbles and drag-dominated flow.

An airfoil is shaped by three significant shape parameters which are thickness,  $t$ , chamber,  $C$ , and nose-angle of the leading edge. High airfoil thickness offers sound mechanical strength of the blade, but causes an elevated friction. On the other hand, low thickness averts flow separation by reducing the APG on the airfoil upper part and thus increases lift [18]. A turbulator or a transition ramp can be added to the design of an airfoil to avoid flow separation and separation bubble [19, 20]. Furthermore, by escalating the leading edge's nose radius, the reduction of the APG can also occur. Simultaneously, the lift and  $C_L$  can be improved by airfoil's trailing edge cusping [21]. The increase of airfoil chamber and the maximum gap between mean chamber line and chord line causes an increase in pressure disparity and thus multiplying the lift [22].

A choice is to be made by a designer to design a new profile or modify the currently available airfoil or simply uses the currently available airfoils. However, currently available airfoils specifically for SSWT are not common such that new airfoil design can still benefit the SSWTs [23–25]. Nikhade et al. [26] made an impressive design of an airfoil called AFN2016 that delivers  $L/D$  greater than several airfoils including

the SG6041. The new airfoil has thickness of 12.93% at chord position of 27.4 and 4.76% chamber at chord position of 47.1%. New airfoils created by Birajdar et al. [27] applied a continuing transition ramp on the profile's upper side, reducing the laminar separation effects. Impressively, the airfoil was determined to provide the greatest glide ratio measured up to other profiles in the study. Singh and Ahmed [19] successfully developed a new airfoil with a flatback trailing edge that improved start-up problem, structural strength and having a high stall angle of  $14^\circ$ .

The designs of new airfoils as explained above are all based on the trial and error. For more accurate finding, optimization method in designing the airfoil has been suggested. The importance of special tailored airfoils had inspired Chen et al. [28] to conduct optimization process in designing a WT family airfoil. The objective function was the maximum  $L/D$  in normal and in rough surface condition. High-order polynomial series of Taylor were the base for the shape function, while airfoil shape function's second to ninth coefficients were used as the design variables. The upper and lower limits of the design variables were taken as the design constraints. The results suggest that the WT family airfoil showed better performances when compared with some typically applied WT profiles. Furthermore, the experimental tests at a wind tunnel conducted on the WT100 airfoil verified the high values  $L/D$  and  $C_L$ . Yang et al. [29] conducted multi-objective optimization considering the airfoil, aerodynamic and structural effects. In a recent study by Yin et al. [30], multi-objective optimization was conducted on an airfoil based on the NACA4412 airfoil using the NSGA-II method before aerodynamic analysis was conducted on a wind turbine, applying the optimized airfoil using the Wilson method. The objective of the optimization was to obtain the highest  $L/D$  while avoiding extreme changes in the thickness and surface area of the shape. The method of airfoil parameterization used was the Hicks–Henne shape functions, where the optimization variables to alter the airfoil shape are the coefficients of the shape functions. The optimization process was a success with the new airfoil called NACA4412-OPT that provides  $C_L$  and  $L/D$  ratio; those are 8 and 14% higher than the original NACA4412 airfoil, respectively. Furthermore, the stall angle was increased and  $L/D$  was maintained over a broad span of AOA.

Whether it is the adjustment method or the optimization method being applied, designing new airfoils is still needed for specific purpose such as for low wind speed application in the SSWT. In this study, new airfoils for SSWT are designed through adjustments of a high-performance airfoil for large-scale wind turbine. The airfoil taken for adjustments is the optimized airfoil, WT180 [28], designed for high-speed condition. The adjustments made include the thickness and the chamber of the airfoil such that the new airfoils will be suitable for SSWT. The new profiles are then tested for lift coefficient,  $C_L$  and glide ratio,  $L/D$ . The aerodynamic attributes of these modified profiles are related to accomplishments of the original WT180 profile and the SG6043 profile, known for its suitability for SSWT.

The importance of airfoil design has been stressed in the introduction of this paper. In the following methodology section, the design procedure for getting the WT180 airfoil suitable for LSWT is explained. With that, the method for adjusting this WT180 to give three airfoils that are suitable for SSWT are given. The three

airfoils are tested for their aerodynamic performances at  $Re = 100,000$ . The results are compared with the original WT180 and also the SG6043 airfoils that are suitable for SSWT. The conclusion and future research are given at the end.

## 2 Methodology

The WT180 airfoil was designed through an optimization procedure where the design variables are the coefficients of the Taylor's polynomial that controls the shape of the airfoils. As such, this design method allows the creation of a number of airfoils by controlling the coefficients of the polynomial. In this section, the optimization method of the blade profile is initially discussed. The modification process of the airfoil to suit the low  $Re$  condition is then explained. Following that, the aerodynamic traits of the modified airfoils are determined through the XFOIL software. The steps in this research can be clearly seen in the flowchart in Fig. 1.

### 2.1 The Transformation of the Airfoil

Wind turbine airfoil was produced through a transformation process applying a shape function in a form of high-order Taylor series. The airfoil was then optimized utilizing the genetic algorithm (GA) optimization method. Initially, an airfoil shape can be transformed from a circular shape using conformal transformation called Joukowski transformation. The following derivation is based on the works of Chen et al. [28]

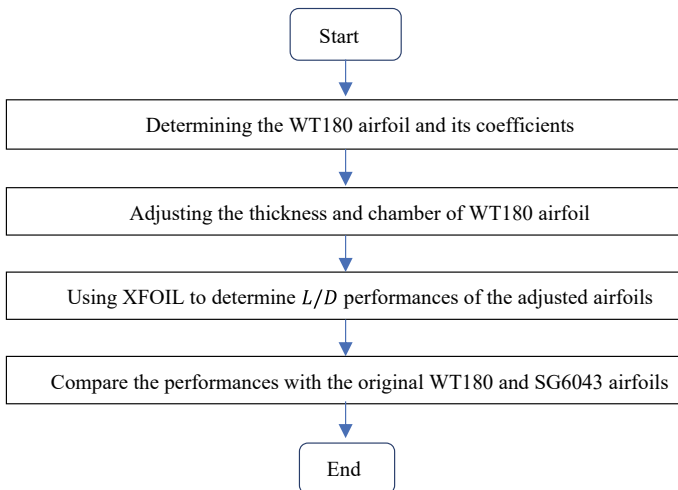


**Fig. 1** Stops in methodology of the study

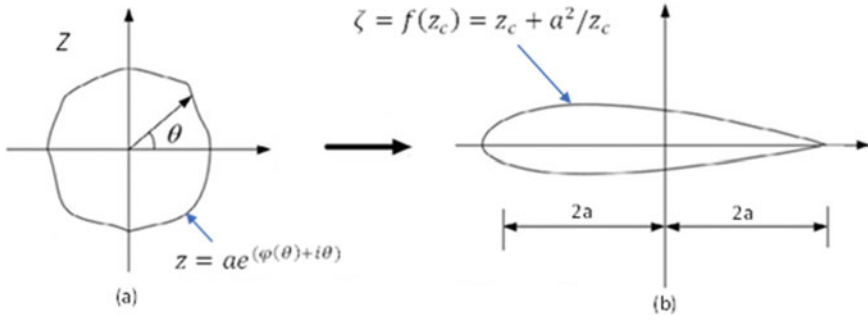


**Fig. 2** Circle to airfoil shape transformation: **a** Circle domain **b** Airfoil domain [29]

and Yang et al. [29]. The coordinates in the  $\zeta$  (airfoil) domain as a function of the  $z_c$  (circle) domain is such as.

$$\zeta = f(z_c) = z_c + a^2/z_c \tag{1}$$

where  $a$  is a parameter related to the airfoil size (see Fig. 2).

The  $z_c$  coordinate is defined as

$$z_c = ae^{\varphi+i\theta} \tag{2}$$

where  $\theta$  is the angle of any points in  $Z$  domain with respect to  $x$ -axis. Defining a shape function,  $\rho(\theta) = e^\varphi$ , a function that depends on  $\theta$  such as

$$z_c = a\rho(\theta)e^{i\theta} \tag{3}$$

where  $a\rho(\theta)$  is the position vector of the matching circle.

Substitute Eq. (3) into Eq. (1), we have a coordinate of the airfoil in terms of the shape function.

$$\zeta = f(z_c) = a[\rho e^{i\theta} + \rho^{-1}e^{-i\theta}] \tag{4}$$

The shape function in Eq. (3) can be expanded to a higher order polynomial according to Taylor's expansion such as

$$\rho(\theta) = C_0 + C_1\theta + C_2\theta^2 + C_3\theta^3 + \dots + C_k\theta^k + \dots \tag{5}$$

where  $k = 0, 1, 2, \dots, n$ ;  $C_0, C_1, C_2, C_k$  are coefficients of the shape function and  $\theta \in [0, 2\pi]$ . Equation (5) describes the airfoil, where changing the coefficients of the shape function will give the desired airfoil and the coefficients will be the design variables of the optimization process. The objective function of the optimization process is to have maximum glide ratio,  $L/D$  of the airfoil which can be stated as

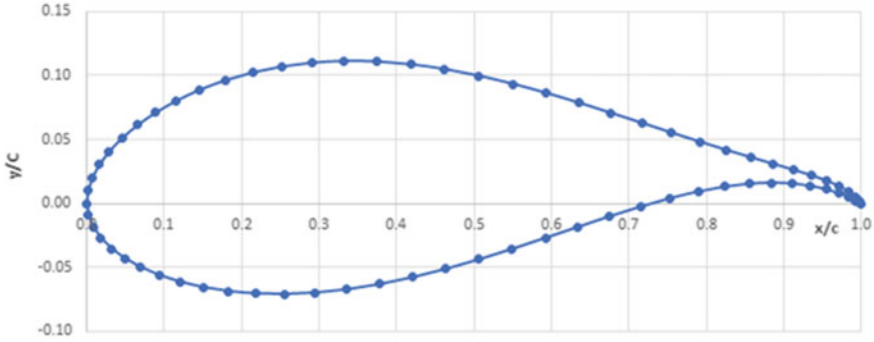


Fig. 3 WT180 airfoil [28]

Table 1 Coefficients [28]

C1	C2	C3	C4	C5	C6	C7	C8
0.135179	0.169777	- 0.650805	0.526446	- 0.199565	0.0399258	- 0.00407183	0.000167

$$f(X) = \text{Max}(L/D) \tag{6}$$

where  $X$  is the design variable consisting of coefficients of the shape function such as

$$X = C(C_0, C_1, C_2, C_3, C_4, C_5, C_6, C_7)^T \tag{7}$$

With several design constraints considered, the process resulted in high-performance airfoils suitable for LSWT, one of them is the WT180 airfoil shown in Fig. 3. Table 1 gives the values of coefficients following the optimization process.

### 2.2 The Adjustment Process

The WT180 shows high performance of  $C_L$  and  $L/D$  at high  $Re$  but the performances are greatly reduced at low wind speed, i.e., at low  $Re$ . This is shown in Fig. 4 where at  $Re = 100,000$ , the maximum  $L/D$  for WT180 is merely 32.8 when compared with  $L/D = 43.6$  for SG6043, the well-known airfoil for the SSWT. In this study, following the direct designing method [18], the geometry of the WT180 airfoil is adjusted several times. Each time, the modified airfoil is tested through XFOIL software to determine its  $C_L$  and  $L/D$  at low wind speed with  $Re = 105$ . Improvements in the  $C_L$  and  $L/D$ , compared with the WT180 are recognized until the performances are at par with the performances of the SG6043 airfoil.

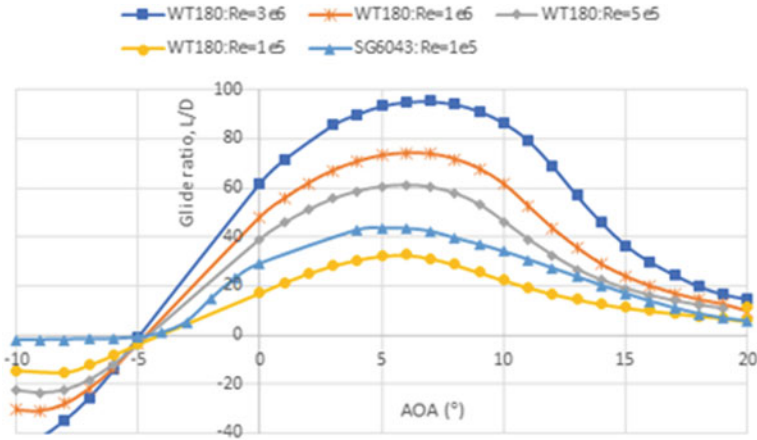


Fig. 4 Aerodynamic performances of WT180 airfoil at several  $Re$

### 3 Results and Discussions

In this section, the results from the modification of the WT180 airfoil are given, including the aerodynamic characteristics of the modified airfoils. With these chosen airfoils, the performances are described in terms of its lift coefficient, glide ratio and coefficient of pressure,  $C_p$ .

#### 3.1 The Airfoil Modification

Following several modifications of the original WT180 airfoil, three generated airfoils are considered for having encouraging  $C_L$  and  $L/D$ . Table 2 gives the thickness and chamber of the three airfoils, namely the WT180-a, WT180-b and WT180-c along with the original WT180 and the SG6043 airfoils for comparison purpose. Figure 5 shows the configurations of the three modified airfoils.

Table 2 Modifications made to the WT180 airfoil

Airfoils	Thickness	@	Chamber	@
WT180	17.99	29.5	3.04	67.5
WT180-a	14.99	29.4	3.16	50.6
WT180-b	11.99	29.4	4.28	67.6
WT180-c	9.1	29.2	5.34	67.6
SG6043	10.02	32.1	5.5	49.7

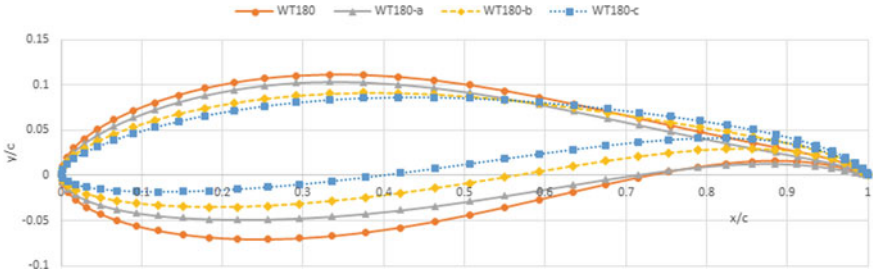


Fig. 5 Original WT180 airfoil and its three generated airfoils

Using the XFOIL codes, the aerodynamic performances of the airfoils at  $Re = 100,000$  are shown in Figs. 6 and 7. Furthermore, the maximum lift coefficient and the maximum glide ratio of these airfoils are compared in Table 3. It can be seen from Fig. 6 that the highest  $L/D = 46$  occurring at AOA of  $5^\circ$  comes from WT180-c airfoil which is higher by 44% and 4% compared with the WT180 and SG6043 airfoils, respectively. However, sudden drop of the  $L/D$  can be seen after its maximum point. WT180-a and WT180-b show good performances of  $L/D = 39$  and  $L/D = 43$ , respectively which are improvements of 34 and 22% compared with WT180, respectively. It can be said that the WT180-b gives the best performance among the three airfoils due to its ability to provide high and stable glide ratio over a higher range of AOAs, compared with the WT180-c. Figure 7 shows the similar trend of increasing performances of lift coefficients,  $C_L$  for modified airfoils starting from WT180-a to WT180-c. The WT180-c gives the highest improvement of  $C_L$  when compared with the WT180 at 34.2%, while the WT180-a and WT180-b give improvements of 8.6 and 24.7%, respectively.

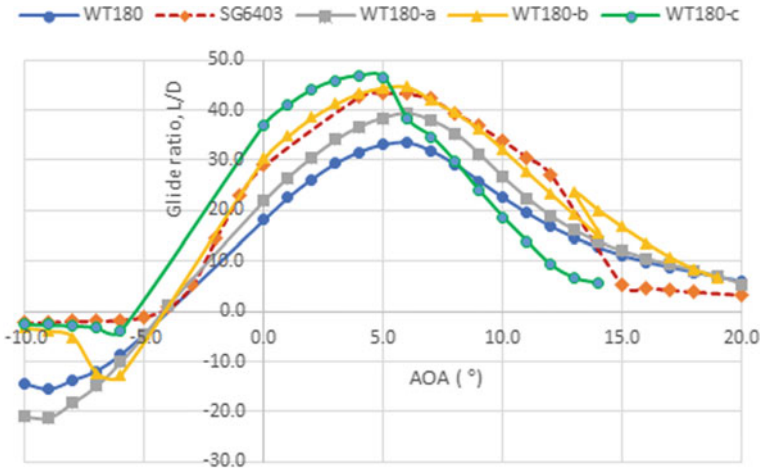


Fig. 6 Glide ratio against the AOA for modified airfoils



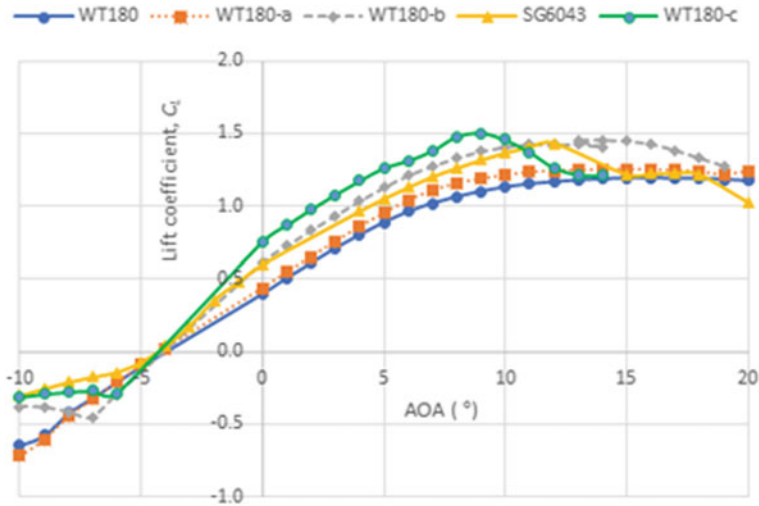


Fig. 7 Lift coefficient against the AOA for modified airfoils

Table 3 Aerodynamic performances of the airfoils at  $Re = 100,000$

Airfoils	$L/D, \max$	@	$C_{L, \max}$	@
WT180	32	6	1.18	14.81
WT180-a	39	6	1.251	14.96
WT180-b	43	6	1.4214	12.5
WT180-c	46	5	1.4687	8.96
SG6043	44	6	1.452	14.48

Figure 8 shows the pressure distribution along the best modified airfoil, the WT180-b airfoil for three operating AOAs. The pressure difference between the top (lower) and bottom surface (higher) of the airfoil can be seen around the leading edge of the airfoil that provides the lift force to the wind turbine. This can be seen to be especially true at operating point of  $\alpha = 12^\circ$  where the lift coefficient is maximum. Figure 9 further looks at the performance of the WT180-b at different  $Re$ 's. It shows that the airfoil can provide an increase in  $L/D$  with an increase in  $Re$ . Furthermore, as the  $Re$  is increased, the maximum  $L/D$  comes with increasing AOA range which indicates a good airfoil in dealing with occurrence of stall.

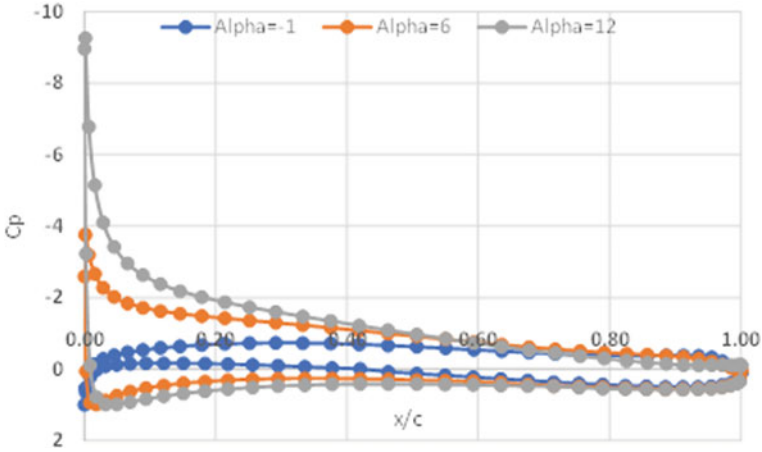


Fig. 8 Pressure distribution along the airfoil for three AOAs

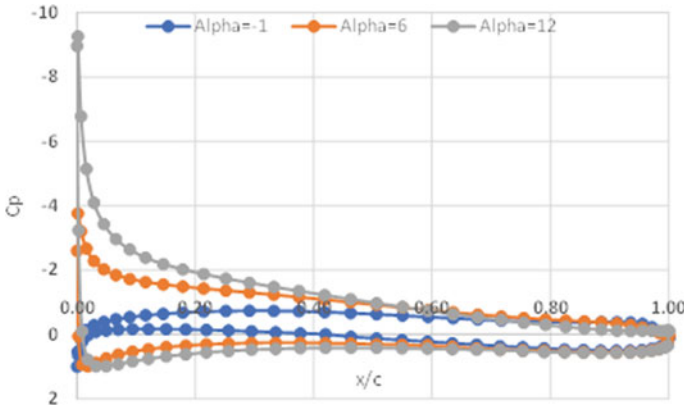


Fig. 9 L/D of WT180-b for several Re

### 4 Conclusion

A WT180 airfoil, suitable for large-scale wind turbine has been modified to suit the small-scale wind turbine. The WT180 airfoil was designed through optimization of coefficients of Taylor’s series polynomial that acts as shape controller to the airfoil. The results of the modification are three airfoils, namely WT180-a, WT180-b and WT180-c that perform well in terms of providing high lift to glide ratio. Through the application of XFOIL codes, the WT180-b has shown the performance of having  $L/D = 43$ , which gives improvement of 34% compared with the original WT180 airfoil. Most importantly, the maximum glide ratio comes with higher range of AOAs. The WT180-b is also shown to give improved glide ratio with the increase of Reynold’s

number. In the following study, optimization method will be applied through the transformation process applying the shape function in the airfoil design, specifically for small-scale wind turbines.

**Acknowledgements** This work is funded by the UTMER Scheme grant “Q.K.130000.2656.18J24”, provided by the Malaysia-Japan International Institute of Technology, a faculty of the Universiti Teknologi Malaysia, Skudai, Malaysia. The authors acknowledge this support.

## References

1. Razak MA et al (2019) Energy consumption clustering analysis in residential building. Symposium on intelligent manufacturing and mechatronics. Springer, Melaka, pp 436–450
2. Roslan SAH, Rasid ZA, Ariffin AK (2022) The aerodynamic performance of the small-scale wind turbine blade with NACA0012 airfoil. *CFD Lett* 14(10):87–98
3. Roslan SAH, Rasid ZA, Ariffin AK (2023) Extended blade element momentum theory for the design of small-scale wind turbines. *J Adv Res Appl Mech* 101(1):62–75
4. Rasid ZA, Zahari R, Ayob A (2014) The instability improvement of the symmetric angle-ply and cross-ply composite plates with shape memory alloy using finite element method. *Adv Mech Eng* 6:632825
5. Roslan S et al (2019) Dynamic instability response of smart composite material. *Materialwiss Werkstofftech* 50(3):302–310
6. Rasid ZA et al (2011) Thermal buckling and post-buckling improvements of laminated composite plates using finite element method. *Key Eng Mater* 471–472:536–541
7. Wahab A et al (2018) Dynamic instability of high-speed rotating shaft with torsional effect. *Int J Autom Mech Eng* 15(4):6034–6051
8. Ren H et al (2020) Development of a green and sustainable manufacturing process for gefapixant citrate (MK-7264) part 1: introduction and process overview. *Organ Process Res Develop* 24(11):2445–2452
9. Bhatt Y, Ghuman K, Dhir A (2020) Sustainable manufacturing: bibliometrics and content analysis. *J Clean Product* 260:120988
10. Lattief FA et al (2021) Performance analysis of a solar cooling system with equal and unequal adsorption/desorption operating time. *Energies* 14(20):6749
11. Zhao Z et al (2022) A review: approaches for aerodynamic performance improvement of lift-type vertical axis wind turbine. *Sustain Energy Technol Assessm* 49:101789
12. Chehouri A et al (2015) Review of performance optimization techniques applied to wind turbines. *Appl Energy* 142:361–388
13. Akbari V et al (2022) Multi-objective optimization and optimal airfoil blade selection for a small horizontal-axis wind turbine (hawt) for application in regions with various wind potential. *Machines* 10(8):687
14. Wood D (2011) Small wind turbines. *Advances in wind energy conversion technology*. Springer, New York, pp 195–211
15. Pourrajabian A et al (2012) Choosing an appropriate timber for a small wind turbine blade: a comparative study. *Renew Sustain Energy Rev* 100:1–8
16. Rahgozar S et al (2020) Performance analysis of a small horizontal axis wind turbine under the use of linear/nonlinear distributions for the chord and twist angle. *Energy Sustain Develop* 58:42–49
17. Mehta PR, Kale RV (2022) Parameters affecting design of wind turbine blade: a review. In: Chaurasiya PK, Singh A, Verma TN, Rajak U (eds) *Technology innovation in mechanical engineering*. Lecture notes in mechanical engineering. Springer, Singapore

18. Shah H, Mathew S, Lim CM (2014) A novel low Reynolds number airfoil design for small horizontal axis wind turbines. *Wind Eng* 38(4):377–391
19. Shah H et al (2012) Low Reynolds number airfoil for small horizontal axis wind turbine blades. In: *Sustainable future energy 2012 and 10th SEE forum on innovations for sustainable and secure energy*. Brunei Darussalam, pp 1–12
20. Singh RK et al (2012) Design of a low Reynolds number airfoil for small horizontal axis wind turbines. *Renew Energy* 42:66–76
21. McGranahan B, Selig M (2004) Aerodynamic tests of six airfoils for use on small wind turbines. University of Illinois at Urbana-Champaign Urbana, Illinois
22. Osei EY et al (2020) Development of high performance airfoils for application in small wind turbine power generation. *J Energy* 128:1–9
23. Pang X, Wang H, Chen J (2019) Intelligence algorithm for optimization design of the low wind speed airfoil for wind turbine. *Cluster Comput* 22(Suppl 4):8119–8129
24. Kale V, Shah P, Gupta S, Prabhune Y, Katira V (2023) Design and shape optimization of a NACA0018 airfoil vertical axis wind turbine for highway applications. In: Vasudevan H, Kottur VKN, Raina AA (eds) *Proceedings of international conference on intelligent manufacturing and automation*. Lecture notes in mechanical engineering. Springer, Singapore
25. Kumar S, Raghav G, Sharma L, Tiwari S (2023) Comparative analysis of different airfoil profiles for wind turbine blades. In: Siddiqui NA, Baxtiyarovich AS, Nandan A, Mondal P (eds) *Recent advances in recycling engineering*. AIR 2021. Lecture notes in civil engineering, vol 275. Springer, Singapore
26. Nikhade SD, Kongare SC, Kale SA (2017) Design of an airfoil for low wind horizontal axis micro wind turbine. In: *Proceedings of the 2017 2nd international conference for convergence in technology (I2CT)*. IEEE, Mumbai, pp 850–853
27. Birajdar M, Kale S, Sapali S (2015) Effects of design parameters on aerodynamic performance of new profile small wind turbine blades. *ASME international mechanical engineering congress and exposition*. ASME, Houston, pp 1–8
28. Chen J et al (2016) A new direct design method of wind turbine airfoils and wind tunnel experiment. *Appl Math Model* 40(3):2002–2014
29. Yang H et al (2019) A new aero-structural optimization method for wind turbine blades used in low wind speed areas. *Compos Struct* 207:446–459
30. Yin R, Xie J-B, Yao J (2022) Optimal design and aerodynamic performance prediction of a horizontal axis small-scale wind turbine. *Math Probl Eng* 2022:1–19

# Comparative Study on Solar PV Module Performance with Sun Irradiance Trapping Mechanism: Power Generation Forecasting Using Machine Learning



Rupendra Kumar Pachauri , Ashutosh Shukla, Ahmad Faiz Minai, Aryadhara Pradhan, Vinay Gupta, Mohit Kumar, and Shashikant

**Abstract** In present study, an experimental investigation deliberates the performance analysis on poly-crystalline photovoltaic (PV) system with the manual arrangement using 2 mm thickness of acrylic sheet. Total three types of solar PV system-based experimental setup are as: (i) normal PV module/without sheet (ii) integration of triangular shape of transparent sheet on PV module surface (iii) rectangular shape of transparent sheet. The experimental investigation performs for all three types of PV arrangements during the entire single-day window from morning to evening to monitor the electrical performance data in terms of voltage (open-circuit) and current (short circuit) primarily. In addition, meteorological data in terms of sun irradiance and solar PV surface temperature is measured during the experimentation. Based on experimental study, the electrical performance comparison shows that the integration of triangular sheet with the solar PV module is responsible for

---

R. K. Pachauri (✉) · A. Shukla  
Electrical Cluster, School of Engineering, University Petroleum and Energy Studies,  
Dehradun 248007, India  
e-mail: [rpachauri@ddn.upes.ac.in](mailto:rpachauri@ddn.upes.ac.in)

A. F. Minai  
Electrical Engineering Department, Integral University, Lucknow, India

A. Pradhan  
School of Electrical Engineering, KIIT University, Bhubaneswar, India  
e-mail: [aryadhara.pradhanfel@kiit.ac.in](mailto:aryadhara.pradhanfel@kiit.ac.in)

V. Gupta  
Electrical Engineering Department, National Institute of Technology, Jalandhar, Punjab, India  
e-mail: [vinra\\_20@rediff.com](mailto:vinra_20@rediff.com)

M. Kumar  
Department of Electrical Engineering, Manipal University, Jaipur, India

Shashikant  
Electrical Engineering Department, Babu Banarasi Das University, Lucknow, India

R. K. Pachauri  
Asian Institute of Technology, Khlong Luang, Pathum Thani, Thailand

higher performance (22.064W, 1.12A) compared with rectangular shape arrangement (20.4W, 1.02A). The percentage increment of triangular arrangement integration of PV system reveals as 8.92% compared with other approaches. The machine learning algorithm proves the validation of concept and forecasting the power generation.

**Keywords** Solar photovoltaic system · Sun irradiance · Power loss · Machine learning · Power forecasting

## 1 Introduction

The solar photovoltaic (PV) sector is attracting more and more attention throughout the world. To increase the effectiveness of solar PV as a grid, the intelligent grid includes load control and the delivery of storage devices. It is projected that the global PV technology sector has grown by an average of 30% per year over the past few decades [1]. Since it is common knowledge that the current state of PV system technology results in poor conversion efficiency, experimental methods are employed to extract as much energy as possible in a practical PV power system.

PV power-producing systems have various issues. The PV cell's short circuit (SC) current fluctuates for several different reasons related to technology and the environment. While progress in PV cells and modules may help alleviate technological concerns, environmental concerns cannot be ignored [2]. Partially shaded PV array (due to filthy, dusty panels, shadows on the tablet from passing clouds, nearby trees and buildings, etc.) is the primary atmospheric explanation for erratic SC current. The authors of [3, 4] discussed the improvement of PV cells' electric efficiency using concentration and cooling methods. To solve the cooling operations of two PV cells, a heat pipe method for straight cooling systems and cooling was initially implemented. Rising temperatures in PV cells lead to a drop in terminal voltage. Thin-film silicone PV cells have recently undergone a series of optimizations aimed at increasing their efficiency [5]. The basic PV cell should control short circuit current for performance. In [6, 7], the authors showed that simple flat mirrors, cooling technologies, and sun concentration improved solar panel performance. In [8], the writers employed reflectors and a sun tracker device to improve solar PV production. A comparative study was done on a diffused reflector and solar power tracker. Researchers must enhance solar PV system production to meet maximum sun irradiation and focus on novel approaches to do so [9]. In [10], the authors discussed solar PV system efficiency changes utilizing the flat hybrid PV/thermal solar system. Solar PV system performance with reflectors relies on tilt-angle, panel length, and reflectivity [11, 12].

### 1.1 Novelty of Work

Based on the aforementioned literature study, the solar irradiation trapping strategies are:

- The rectangular and triangular solar irradiance trapping systems are used to compare and study how well they work.
- The performance study in terms of power voltage and current is observed for a single-day window.
- For power generation forecasting, the machine learning method is used. This method is based on the real-time performance parameters from the experimental study.
- Overall, the triangular trapping mechanism was observed to be more suitable to enhance the PV system performance during the experimental study and the machine learning approach as well.

## 2 Experimental Study and System Description

Present experimentation work is carried out in the month of March, 2020 at Dehradun, Uttarakhand. During the experiment, the environment is partially cloudy at identified geographical longitude and latitude location ( $30.3165^\circ$  N and  $78.0322^\circ$  E). The experimental set as shown in Fig. 1 comprised the 20W three poly-crystalline PV modules with defined specifications as given in Table 1. The rectangular and triangular sun irradiance trappers are fixed with the two PV modules individually, and the third PV module is considered normal or without any trapping mechanism for comparative study.

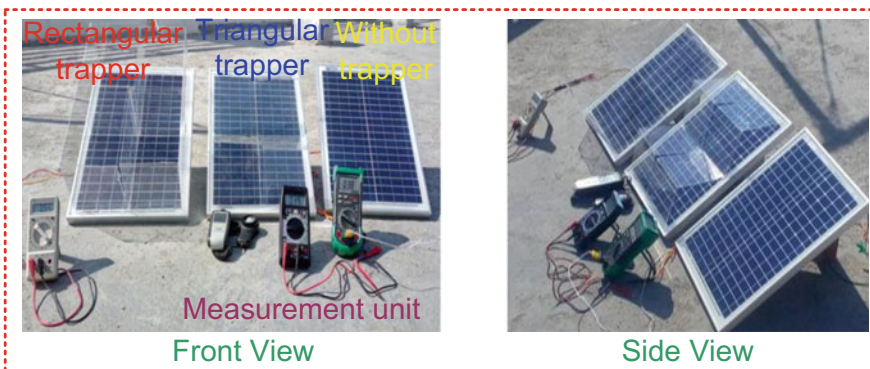


**Fig. 1** Experimental setup

**Table 1** PV module specifications (Manuf.: Spark Solar)

PV performance parameters	Values
Maximum power ( $P_{\max}$ )	20 W
Maximum voltage ( $V_{\max}$ )	18.25 V
Maximum current ( $I_{\max}$ )	1.10 A
Open-circuit voltage ( $V_{oc}$ )	21.96 V
Short circuit current ( $I_{SC}$ )	1.17 A

### 3 Machine Learning Model

SVMs are used for machine learning framework to analyze accordance with statistical learning theory. The SVM can boost the learning machine's advancement as well. Even if the gathered discriminant function is based on limited data, the prediction error of the independent test set might be tiny. The SVM is a convex quadratic optimization problem; hence its extreme solution is global optimum. These two traits make SVM a good machine learning method and useful component of statistical theory [13–16]. The mathematical formulation constraints with approach through the flowchart are shown in Fig. 2.

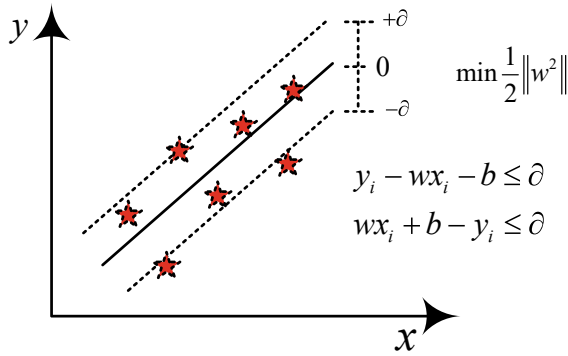
### 4 Results and Discussion

The electrical performance of PV systems in the selected geographic area of Dehradun, India, is measured manually and with multimeters from 8 a.m. to 4 p.m. The experimental data is used to forecast power generation based on the experimental work. The true experimental data and the predicted data in terms of power are given in Table 2. In addition, a comparative study to determine the error analysis in terms of root mean square error, mean absolute percentage error, and regression analysis is given in Table 3.

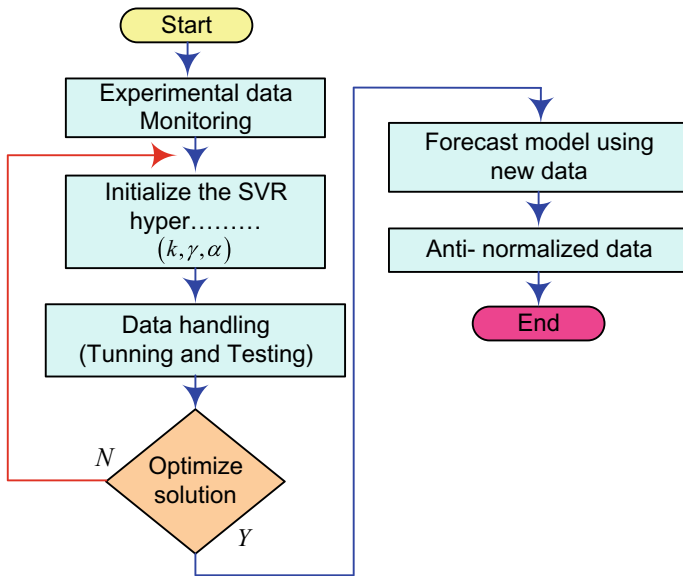
The PV module temperature and available irradiation level patterns are shown in Fig. 3. The higher level of irradiation and temperature are found between 11:30 a.m. and 14 p.m., which is responsible for the higher power performance of the PV module with the experimental setup. Figure 3 depicts the temperature and irradiation variation pattern as.

A comparative study is being conducted to extract the electrical performance of all PV module arrangements. The higher power generated from triangular trapper integrated mechanisms is compared with standard and rectangular trapper arrangements. The transient behavior is shown in Fig. 4a. In addition, the machine learning approach is applied to obtain the forecasted value of power generation, which is shown in Fig. 4b and compared with all the PV arrangements.





(a)



(b)

**Fig. 2** a Mathematical constraints b SVR flowchart

The error between the true experimental and forecasted power values for all three PV module arrangements is calculated as RMSE and MAPE. Table 4 and Fig. 5 show the regression values for all of the arrangements.

**Table 2** Electrical performance parameters observed during experimental study

Sample	Time (IST)	Experimental data										Environmental data				
		WT					TT					RT			Irradiance (W/m <sup>2</sup> )	Temp. (°C)
		V (V)	I (A)	P (W)	V (V)	I (A)	P (W)	V (V)	I (A)	P (W)	V (V)	I (A)	P (W)			
1	08:00	17.4	0.24	4.152	17.5	0.36	6.264	17.4	0.28	4.90	410	24				
2	08:15	17.9	0.36	6.444	18.1	0.48	8.592	17.9	0.44	7.964	440	26				
3	08:30	18.6	0.43	7.912	18.6	0.55	10.23	18.6	0.48	8.928	510	28				
4	08:45	19.4	0.51	9.894	19.6	0.63	12.222	19.4	0.59	11.564	640	29				
5	09:00	20.1	0.64	13.05	20.6	0.76	15.276	20.1	0.74	15.244	722	32				
6	09:15	20.2	0.71	14.48	20.6	0.83	16.766	20.2	0.75	15.450	783	35				
7	09:30	20.2	0.79	16.03	20.5	0.91	18.382	20.2	0.77	15.785	796	37				
8	09:45	20.2	0.86	17.28	20.3	0.98	19.796	20.2	0.8	16.24	826	39				
9	10:00	20	0.91	18.29	20.3	1.03	20.6	20	0.81	16.443	865	40				
10	10:15	19.9	0.94	18.89	20.3	1.06	21.094	19.9	0.84	17.052	870	40				
11	10:30	19.7	0.96	19.20	20.2	1.08	21.276	19.7	0.88	17.776	889	40				
12	10:45	19.6	0.96	19.00	20	1.08	21.168	19.6	0.9	18	920	41				
13	11:00	19.78	0.99	19.70	20.1	1.11	21.955	19.78	0.92	18.492	928	41				
14	11:15	19.65	0.99	19.8	20.2	1.11	21.81	19.65	0.92	18.584	942	41				
15	11:30	19.7	1.01	20.09	20.1	1.13	22.26	19.7	1.01	20.301	977	40.5				
16	11:45	19.73	0.99	19.60	20	1.11	21.90	19.73	1.08	21.6	998	40				
17	12:00	19.7	1	19.8	20	1.12	22.06	19.7	1.02	20.4	1012	41				
18	12:15	19.6	0.96	19.00	20	1.08	21.16	19.6	0.91	18.2	1025	42				
19	12:30	19.5	0.92	18.12	19.9	1.08	21.16	19.5	0.91	18.1	1045	41				
20	12:45	19.8	0.9	17.82	20	1.02	20.19	19.8	0.9	18	1023	40				

(continued)

Table 2 (continued)

Sample	Time (IST)	Experimental data										Environmental data			
		WT					TT					RT		Irradiance (W/m <sup>2</sup> )	Temp. (°C)
		V (V)	I (A)	P (W)	V (V)	I (A)	P (W)	V (V)	I (A)	P (W)	V (V)	I (A)	P (W)		
21	13:00	19.7	0.88	17.33	19.9	1	19.7	19.7	0.89	17.71	19.7	0.89	17.71	1016	40
22	13:15	19.6	0.8	15.84	20	1.003	19.66	19.6	0.87	17.4	19.6	0.87	17.4	1018	41
23	13:30	19.8	0.74	14.72	20.1	0.965	19.11	19.8	0.81	16.4	19.8	0.81	16.4	965	40
24	13:45	19.7	0.65	13	20.2	0.942	18.56	19.7	0.76	15.342	19.7	0.76	15.342	950	41
25	14:00	19.7	0.57	11.34	20.1	0.874	17.22	19.7	0.74	14.88	19.7	0.74	14.88	890	40
26	14:15	19.8	0.51	10.2	20.2	0.836	16.55	19.8	0.63	12.742	19.8	0.63	12.742	886	39
27	14:30	19.73	0.463	9.22	20.1	0.766	15.11	19.9	0.60	12.11	19.9	0.60	12.11	844	39
28	14:45	19.86	0.414	8.33	20.3	0.710	14.11	20.1	0.55	11.165	20.1	0.55	11.165	755	38
29	15:00	19.82	0.364	7.32	20.3	0.656	13	20.1	0.52	10.556	20.1	0.52	10.556	704	38
30	15:15	19.84	0.293	5.89	20.3	0.554	11	20.1	0.44	9.11	20.1	0.44	9.11	665	38
31	15:30	19.85	0.27	5.373	20.1	0.445	8.84	19.9	0.40	8.11	19.9	0.40	8.11	638	38
32	15:45	19.84	0.26	5.096	19.8	0.38	7.5392	19.6	0.35	7	19.6	0.35	7	618	37
33	14:00	19.78	0.24	4.632	19.5	0.36	7.1208	19.3	0.30	6	19.3	0.30	6	580	34

\* Without trapper = WT, Triangular trapper = TT, Rectangular trapper = RT

**Table 3** Electrical performance parameters observed during forecasting study

Sample	Time (IST)	Forecasting data using SVR		
		WT	TT	RT
		$P$ (W)	$P$ (W)	$P$ (W)
1	08:00	4.5906249	6.1410149	5.5858388
2	08:15	5.7652925	7.6987276	7.2325199
3	08:30	7.2612135	9.4398967	8.4622183
4	08:45	10.374651	12.152065	11.657484
5	09:00	12.676912	14.758457	14.255046
6	09:15	13.727214	16.305408	14.783275
7	09:30	14.220749	17.282527	14.796424
8	09:45	14.873917	18.38324	15.138605
9	10:00	15.830703	19.29917	15.677255
10	10:15	16.223859	19.612227	16.060883
11	10:30	16.725155	19.954244	16.723566
12	10:45	16.93679	20.308483	17.146113
13	11:00	17.429941	20.808074	17.518717
14	11:15	17.736079	20.920884	17.786273
15	11:30	18.657494	21.60869	19.288684
16	11:45	18.92427	21.706287	20.360538
17	12:00	19.019273	21.971932	19.802053
18	12:15	18.600944	21.694366	18.727743
19	12:30	18.786207	21.955909	19.174293
20	12:45	18.491554	21.184573	18.956174
21	13:00	18.121235	20.844093	18.700396
22	13:15	17.149261	20.849201	18.397006
23	13:30	15.881336	19.875311	17.238299
24	13:45	14.48273	19.400825	16.291876
25	14:00	12.814986	17.939455	15.291391
26	14:15	12.430797	17.552924	14.339131
27	14:30	11.170881	16.278045	13.358462
28	14:45	9.3550283	14.603544	11.65754
29	15:00	7.9151301	13.374762	10.545943
30	15:15	6.485208	11.859517	9.2057506
31	15:30	5.7317619	10.422809	8.2784639
32	15:45	5.4872715	9.5094959	7.5869962
33	14:00	5.3405895	8.8022067	7.0257527

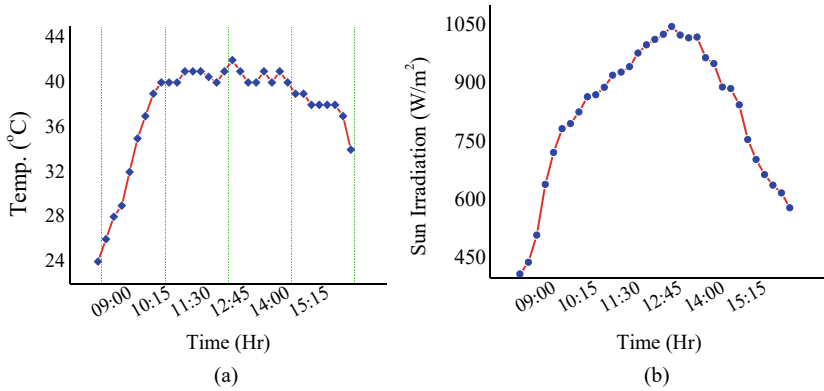


**Fig. 3** a Temperature b Sun irradiation during the experimental work

**Fig. 4** a Actual power  
b Forecasted power

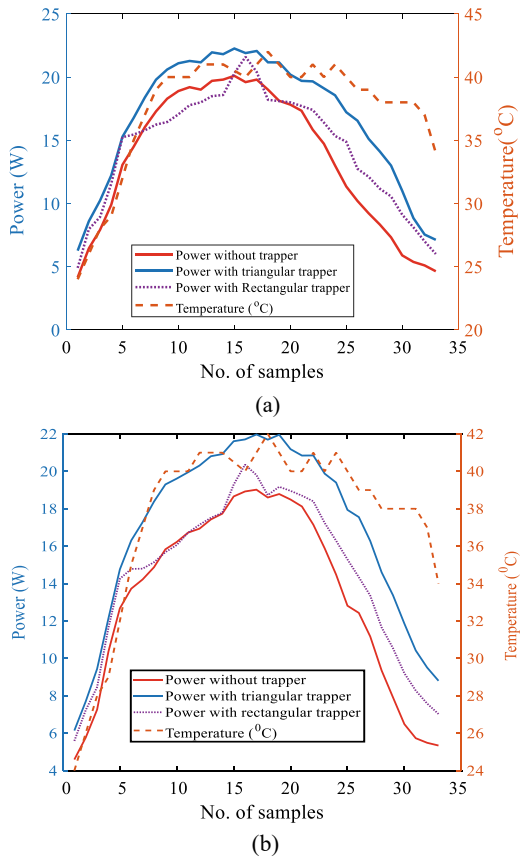


**Table 4** Error analysis

	WT	TT	RT
RSME	1.432	1	0.864
MAPE	9.44	5.98	5.715
R	0.97	0.981	0.981

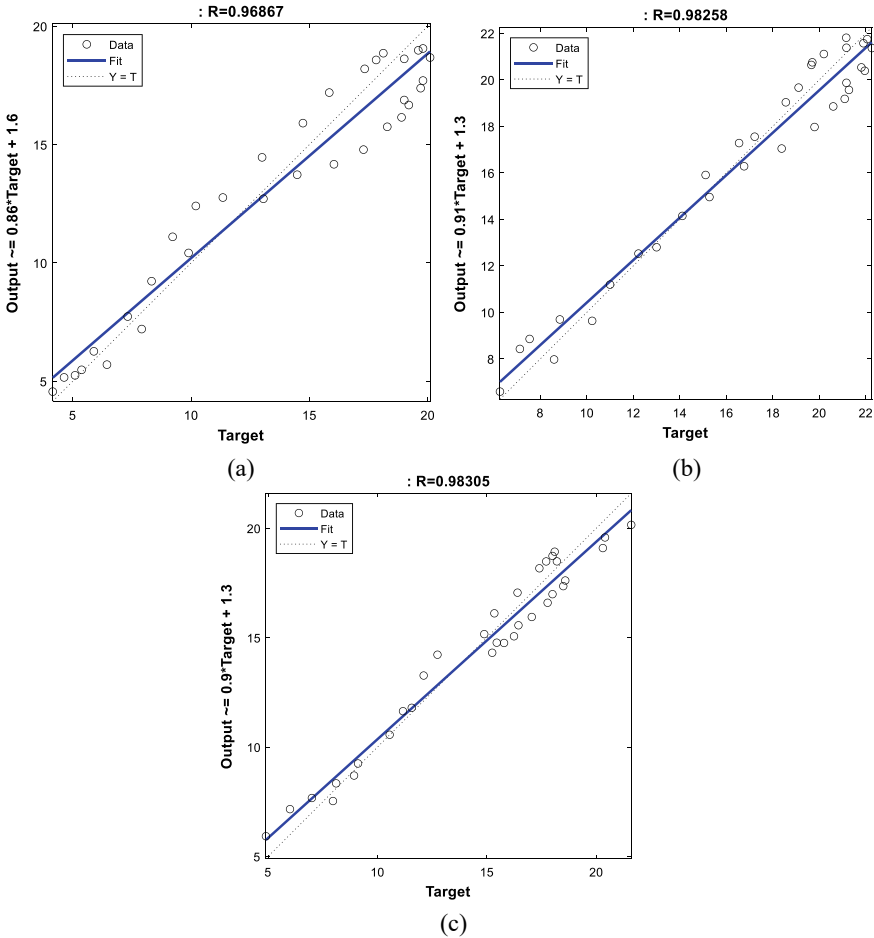


**Fig. 5** Regression values **a** Without trapper **b** Triangular trapper **c** Rectangular trapper

## 5 Conclusion

Experimental monitoring is carried out in the current study during the variable irradiation and temperature ranges. The following highlights are illustrated as follows,

- Under similar environmental conditions, solar panels with triangular trapper mechanisms outperform those with normal and rectangular trapper mechanisms in terms of peak power value.
- The integrated triangular trapper mechanism PV system provided 22.064 watts of power at 12 a.m., whereas the rectangular trapper-based PV module provided 20.4 watts at the same time. Overall, an 8.92% increment in power generation is observed.
- For triangular and rectangular mechanisms, error analysis like RMSE, MAPE, and regression analysis are done and compared with the standard arrangement.

Overall, the present study is helpful to new learners for the real-time experimental monitoring and comparative analysis of power prediction through the machine learning approach.

## References

1. Gupta AK, Chauhan YK, Maity T (2018) Experimental investigations and comparison of various MPPT techniques for photovoltaic system. *Shadna* 43(8):1–32
2. Kumar A, Pachauri RK, Chauhan YK (2015) Analysis and performance improvement of solar PV system by solar irradiation tracking. In: *Proceeding IEEE conference on energy economic and environment*, pp 7–12
3. Beck ME, Wiedeman S, Huntington R, Van Alsburg J, Kanto E, Butcher R, Britt JS (2007) Advancements in flexible CLGS module manufacturing. In: *Proceeding IEEE international conference on photovoltaic specialist*, pp 211–214
4. Farhat MA (2004) Improvement the thermal electric performance of photovoltaic cells by cooling and concentration techniques. In: *Proceeding IEEE international conference on power engineering*. Bristol, pp 623–628
5. Eymard MB, Boccard M, Bugnon G, Meillaud F, Despeisse M, Haug FJ, Ballif C (2013) Current matching optimization in high-efficiency thin-film silicon tandem solar cells. In: *Proceeding IEEE international conference on photovoltaic specialist*. Tampa, pp. 184–187
6. Arshad R, Tariq S, Niaz MU, Jamil M (2014) Improvement in solar panel efficiency using solar concentration by simple mirrors and by cooling. In: *Proceeding IEEE international conference on robotics and emerging applied technologies in engineering*. Islamabad, pp 2092–2095
7. Huang BJ, Sun FS (2007) Feasibility study of one axis three positions tracking solar PV with low concentration ratio reflector. *Energy Conver Manag* 48:1273–1280
8. Ajayi AB, Majekodunmi OA, Shittu AS (2013) Comparison of power output from solar PV panels with reflectors and solar tracker. *J Energy Technol Policy* 3(7):70–77
9. Ahmed Z, Kazem HA, Sopian K (2012) Effect of dust on photovoltaic performance: review and research status. *Latest Trends Renew Energy Environ Inform* 34(6):193–199
10. Palaskar VN, Deshmukh SP (2013) A critical review on enhancement in system performance of flat plate hybrid PV/thermal solar collector system. *Int J Energy Sci* 3(6):395–402
11. Anand VP, Khan MM, Ameen E, Amuthan V, Pesala B (2014) Performance improvement of solar module system using flat plate reflectors. In: *Proceeding IEEE international conference on advances in electrical engineering*, pp 1–4
12. Kabeel A, Abdelgaied M, Sathyamurthy R (2019) A comprehensive investigation of the optimization cooling technique for improving the performance of PV module with reflectors under Egyptian conditions. *Sol Energy* 186:257–263
13. Tomar A et al (eds) (2022) *Proceedings of 3rd international conference on machine learning, advances in computing, renewable energy and communication: MARC 2021*, vol 915. Springer, New York, p 781. <https://doi.org/10.1007/978-981-19-2828-4>

14. Ahmad MW et al (eds) (2022) Intelligent data analytics for power and energy systems. Springer, Singapore, p 641. <https://doi.org/10.1007/978-981-16-6081-8>
15. Li J, Ward JK, Tong J, Collins L, Platt G (2016) Machine learning for solar irradiance forecasting of photovoltaic system. *Renew Energy* 90:542–553
16. Zazoum B (2022) Solar photovoltaic power prediction using different machine learning methods. *Energy Rep* 8:19–25



# The Geometric Modelling and Linearization of Small-Scale Wind Turbine Blades for Optimized Renewable Energy



S. A. H. Roslan, N. Umar, Z. A. Rasid , and A. K. Arifin

**Abstract** The modelling of blade geometry is the first step to be taken before the boundary element momentum theory (BEMT) analysis can be conducted on the wind turbine (WT). Yet it is a crucial step in establishing the best aerodynamic achievement the WT can give. In this paper, the power coefficient of a WT utilizing different blade geometries are determined and compared using the BEMT method. The blade geometries are obtained from the proposed formulas in literature and from the recommended polynomials that are based on experimental works. All blades are analyzed using the extended BEMT that includes the tip loss effect, the axial induction correction factor,  $a$  and the stall effect. At the same time, the obtained tapered blade usually varies in its chord length and twist angle in a nonlinear manner with respect to radius of the blade. As this may cause manufacturing difficulty of the blade and increasing the wind turbine manufacturing cost, the best nonlinear distribution based on the BEMT analysis conducted has been linearized through a process of linearization. A comparison is made on the aerodynamic performances of the WT for the linearized and nonlinear blades. The study shows that the geometry of the blade is better with the use of the empirical formula that gives high power at higher tip speed ratio (TSR) while having lower axial thrust. Furthermore, comparing the linear and nonlinear blade, it can be concluded that linearizing the chord length and twist angle is a good practice because with its simpler construction, the maximum power of 200 W that was produced is at par with the nonlinear one, while the axial thrust is much lower at 125N when compared with 225N in the case of nonlinear blade.

**Keywords** Geometric modelling · Geometric distribution · Linearization · Renewable energy

---

S. A. H. Roslan · N. Umar · Z. A. Rasid (✉)  
Universiti Teknologi Malaysia, Jalan Sultan Yahaya Petra, 54100 Kuala Lumpur, Malaysia  
e-mail: [arzainudin.kl@utm.my](mailto:arzainudin.kl@utm.my)

A. K. Arifin  
Universiti Kebangsaan Malaysia, 43600 Bangi, Malaysia

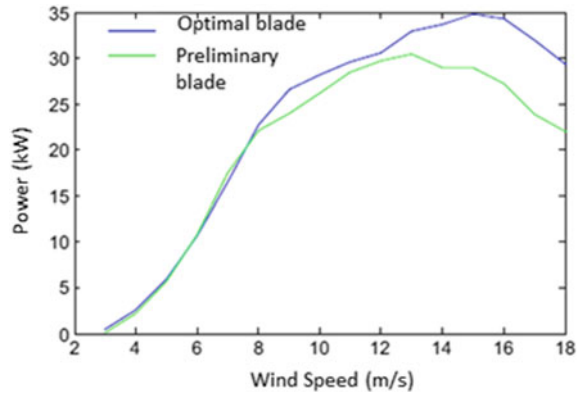
## 1 Introduction

In today's world, with the rapid growing and evolving of technology, the environmental issues have become one of the top priorities to be considered, especially in areas of green manufacturing processes [1, 2], failure of structures [3, 4] and design of materials [5, 6] and renewable energy [7, 8]. Following this, wind energy has developed into one key green energy source throughout the world in an effort to replace the carbon-based energies [9]. At the same time, research on the small-scale wind turbine (SSWT) that works in low wind speed regions has been gradually broadened in catching up with its widely used large counterpart [10]. In the analysis part, the blade element momentum theory (BEMT) has been widely adopted in the field of wind turbine design due to its simplicity and accuracy. In conducting the BEMT analysis, one early step is to assign dimensions of chord length and twist angle along the blade length before shape optimization process can be conducted to determine the designed aerodynamic performance values of the wind turbine. These chord length and twist angle values can be drawn from formulas such as proposed in literature [11–15]. Going through the iteration process in the BEMT analysis, the blade has been proven suitable to be tapered and twisted, especially for low wind speed applications [11, 16, 17] so that the maximum coefficient of power,  $C_p$  can be reached. The purpose of twisting the blade is to adjust the wind direction such that the angle of attack (AOA) is always closed to the critical AOA,  $\alpha_{cr}$  where glide ratio,  $L/D$  is maximum. In addition, a blade is tapered to reduce drag and bending stress so that the blade is stronger and lighter, where the later effect can also improve the starting capability of the wind turbine.

Improvements made by tapering and twisting have been demonstrated by many researchers [18–20]. In a comparison study made between experimental [21] and numerical work, blades with and without tapering and twisting were compared, [18] where tapered and twisted blade showed 50% of  $C_p$  improvement. NACA4418 airfoil was used by Hsiao et al. [19] to study aerodynamic performance of blades with and without tapering and twisting, using the extended BEMT method, computational fluid dynamic (CFD) method and experiment. It was verified that the best blade in having the consistently highest  $C_p$  for over an extensive span of tip speed ratio (TSR) was the blade having tapering and twisting.

The tapering and twisting of the blades however, come with disadvantages as well. Both actions have caused the distribution of the chord length and the twist angle throughout the length of the blade to become nonlinear. The nonlinear distribution will lead to the increase in difficulty in fabrication, increase in cost of material and reduce in accuracy of the turbine blade. In a research study [22], it was indicated that the nonlinear distribution obtained after the shape optimization process did not guarantee better performance compared with the linearized one. In this study, a new approach was applied in a SSWT design in relation to linearize the blade geometry. Based on the optimization method, the best linear blade's geometry was decided among the 589 combinations of chord and twist angle that provided the best annual

**Fig. 1** Output power of preliminary and optimal blades [22]



energy production. The results demonstrated that the linearized distribution gave some improved performances of the WT as shown in Fig. 1.

Tahani et al. [23] made tangent line crossing that passes through every point on the preliminary lines in order to linearize the blade geometry. The line that gave the lowest decrease in  $C_p$ , applying the BEMT method was decided as the best linearized line. The smallest decrease in  $C_p$  was determined through this method when measured up to the previous work [22, 24]. Rahgozar et al. [25] studied optimization power maximization and starting time minimization by combining linear and nonlinear distribution of chord length and angle of twist. The linear distribution was determined to enhance power. The starting time of the WT was improved by the nonlinear distribution.

Abdelsalam et al. [26] compared experimentally the  $C_p$  of a SSWT equipped with linear and nonlinear distribution of the blade geometry. Only one airfoil was used, i.e. the RISØ-A-24 profile. The linearized blades were found to have volume reduction of 26% while having  $C_p$  closed to the nonlinear blades. Further, the starting ability of the linearized blade was improved.

It can be observed from literature review that the BEMT study on a certain blade geometry is common. However, comparison studies between several of these geometric modelling of the blade that will show the effectiveness of each model, to our knowledge are rare. Similarly, it can be said that only few studies have been conducted to compare the aerodynamic performances of wind turbine operating with nonlinear and linear distributions of the chord length and the twist angle. This is however important in designing such blades that give the maximum power and power coefficient. As such, in this study, a comparison is made on the aerodynamic performances of a SSWT having chord length and twist angle with four different distributions. The best geometric distribution in terms of the resulting aerodynamic performances is then linearized through optimization method. Following that, a comparison is made between the nonlinear and linear distributions of the blade dimensions. The airfoil, SG6043, has been chosen for this study for having the highest  $L/D$  compared with several well-known airfoils for SSWT applications. The aerodynamic analysis was

conducted using the extended BEMT method applying the Prandtl's tip loss factor, the axial induction correction factor,  $a$  and the high AOA in post-stall region to uncover the best WT performances between the geometric dimensions of the blade and also between the linear and nonlinear distributions.

This paper starts with the discussion on the importance of selecting the geometry of the blades and its linearization that ends with the objective of the paper. Following that, the methodology used for this study that includes the elaboration on formulas used for determining blade geometries, the discussion on the method of linearization and the BEMT analysis of the blades. Following that, the results on the best geometry, the linearization of the best blades and the comparison on the aerodynamic performances of the linear and nonlinear blades are given. Finally, the conclusion of the paper is given along with the future work to be conducted.

## 2 Methodology

The specifications of the WT, profile and blade are presented in this section. Furthermore, the formulas for chord lengths and twist angles are given. The simplified version of the BEMT is explained where the method is extended to include the Prandtl's factor of tip loss, thrust influence due to elevated axial induction factor,  $a$  and the interpolated  $C_L$  and  $C_D$  at high AOAs. This study is on the SSWT with two number of blades, i.e.  $N = 2$ . The radius of rotor is 1.5 m. The wind speed and tip speed ratio (TSR) are varied to find both minimum values that meet the minimum requirement of power,  $P$  required per household which is about 600 W [27].

### 2.1 The Airfoil

Referring to Fig. 2, the profile applied here is the SG6043. The SG6043 airfoil is recognized to have high maximum glide ratio, maximum  $L/D$  which is the most critical factor to obtain the best power coefficient,  $C_p$  and power,  $P$ .

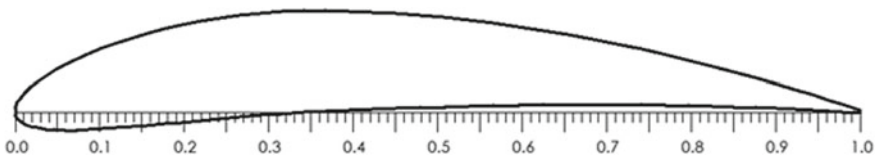


Fig. 2 SG6043 airfoil

**Table 1** Chord length formulae

No	Formulae	References
1	$c(r) = \frac{8\pi r}{BC_L}(1 - \cos\phi), \phi(r) = \frac{2}{3}\tan^{-1} \frac{2}{3\lambda_r}, \theta(r) = \phi(r) - \alpha_D$	Manwell 1 [11]
2	$c(r) = \frac{8\pi r \sin\phi}{3BC_L\lambda_r}, \phi(r) = \tan^{-1} \frac{2}{3\lambda_r}, \theta(r) = \phi(r) - \alpha_D$ (w/o wake rotation)	Manwell 2 [11]
3	$c(r) = \frac{16\pi r}{B(C_L)_D} \sin^2\left(\frac{1}{3}\tan^{-1} \frac{R}{r\lambda_D}\right), \phi(r) = \frac{2}{3}\tan^{-1} \frac{R}{r\lambda_D}, \theta(r) = \phi(r) - \alpha_D$	Schmitz [14]
4	$c(r) = \frac{16\pi/C_L}{9N\lambda_D\sqrt{\frac{4}{9} + \left[\lambda_r + \frac{2}{9\lambda_r}\right]^2}}, \phi(r) = \tan^{-1} \frac{2}{3\lambda_r + \frac{2}{\lambda_r}}, \theta(r) = \phi(r) - \alpha_D$	Burton [15]

### 2.2 The Formulas for Chord Length and Twist Angle

Table 1 gives the formulae for chord length and twist angle that are available in literature. Four Eqs. (1–4) are estimated based on AOAs, while the last equation is obtained from fitting the experiment data.

The empirical formulas for chord length and twist angle as applied by Anderson [18] are

$$c(r) = 5 * (0.162 - r/R * (0.585 - r/R * (1.033 - r/R * (0.876 - r/R * 0.284))))/3 \tag{1}$$

$$\theta(r) = \begin{cases} 54.17 - \frac{r}{R}(307.43 - \frac{r}{R} * (719.55 - \frac{r}{R} * (785.97 - \frac{r}{R} * 326.67))) & \frac{r}{R} < 0.7 \\ 5.32 - \frac{r}{R}(7.06) & \frac{r}{R} \geq 0.7 \end{cases} \tag{2}$$

### 2.3 The Linearization of the Geometric Distribution

The linearization process in this study follows the work of Liu et al. [21]. The chord length and twist angle values are fixed at the tip of the blade. The end values at the root of the blade are changed according to the following equations to give huge numbers of linearized spreadings of the length and angle to choose from.

$$c_{i,n} = c_{t,o} + (0.7c_{r,0} - c_{t,0})\frac{(n - 1) r_i}{N} \frac{r_i}{R} \quad n = 1, 2, \dots, N + 1 \tag{3}$$

$$\theta_{i,n} = \theta_{t,o} + (0.7\theta_{r,0} - \theta_{t,0})\frac{(n - 1) r_i}{N} \frac{r_i}{R} \quad n = 1, 2, \dots, N + 1 \tag{4}$$

For reasonable varying steps of the twist angle and chord length of about 1° and 0.025 m, respectively, the number of divisions *n* in this study are taken as 18 and 30 for chord length and twist angle linearization, respectively. For each linear distribution, the optimization is conducted by calculating for the blade geometry the annual energy production (AEP), where the distribution with the highest AEP will be taken as the

best distribution. With air density ( $\rho$ ), the transmission efficiency ( $\eta$ ), swept area ( $A$ ), rotor power coefficient of the wind turbine ( $C_{PR}$ ) and the wind speed Rayleigh distribution ( $f_{\text{Raleigh}}$ ), the AEP can be calculated as

$$E = 8760 \times \frac{1}{2} \eta \rho A \int_{v_{\text{cin}}}^{v_{\text{cout}}} v^3 C_{PR}(v) \times f_{\text{Raleigh}}(v) dv \quad (5)$$

where  $\eta$  is the transmission efficiency (in percentage) of both mechanical and electronic systems of the wind turbine,  $\rho$  is the air density,  $A$  is the swept area of the wind turbine rotor and  $C_{PR}$  is the rotor power coefficient of the wind turbine derived from the BEMT as a function of velocity,  $v$ .

## 2.4 The BEMT

In the BEMT analysis, iterations are necessary to determine the axial and tangential induction factors  $a$  and  $a'$ , respectively. After making assumptions of these two values in the first iteration,  $a$  and  $a'$  can be calculated using the following formulae in the following iterations until the values converged.

$$a = \frac{1}{\frac{4F \sin^2 \phi}{\sigma C_a} + 1} \quad (6)$$

$$a' = \frac{1}{\frac{4F \sin \phi \cos \phi}{\sigma C_t} + 1} \quad (7)$$

where  $\phi$  and  $\sigma$  are the flow angle and the solidity of the wind turbine, respectively and  $C_a$  and  $C_t$  are the axial and tangential force coefficients. Furthermore,  $F$  is the Prandtl's tip loss factor that is the first correction made to the BEMT.  $F$  is defined as

$$F = \frac{2}{\pi} \cos^{-1} \left[ \exp \left( - \frac{0.5B(r-R)}{r \sin \phi} \right) \right] \quad (8)$$

The second correction factor is the effect of low axial thrust,  $F_a$  at high value of  $a$ . While there are several corrective models, in this study, the model of Glauert's, such as in the following is used. Defining the two parameters  $Y_1$  and  $Y_2$ :

$$Y_1 = \frac{4F \sin^2 \phi}{\sigma C_a} \quad (9)$$

$$Y_2 = \frac{4F \sin \phi \cos \phi}{\sigma C_d} \quad (10)$$

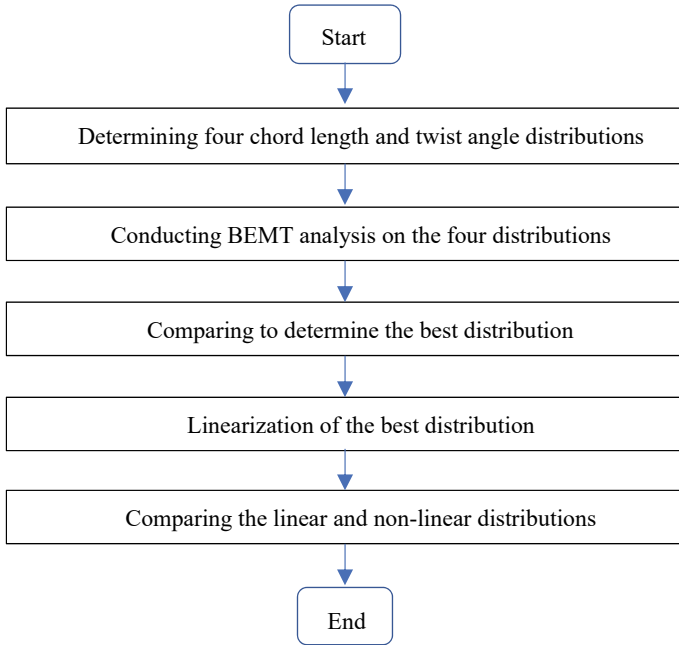


Fig. 3 Flowchart of the work

The new induction factor,  $a_n$  is then set to be:

$$a_n = \begin{cases} \frac{2+Y_1-\sqrt{4Y_1(1-F)+Y_1^2}}{2(1+FY_1)} & Y_1 \geq 2 \\ \frac{(2+Y_1c_r-\sqrt{((Y_1c_r+2)^2-4(1-\frac{1}{9}FY_1)})})}{2} & Y_1 < 2 \end{cases} \quad (11)$$

And the new radial induction factor,

$$a' = \frac{1}{\frac{(1-aF)Y_2}{(1-a)} - 1}. \quad (12)$$

The BEMT analysis in this study is conducted using MATLAB’s codes following the paper’s work steps that can be easily understood from the flowchart in Fig. 3.

### 3 Results and Discussions

In this section, the differences in the chord length and twist angles among different blades are given. With this, the BEMT analysis is conducted on the blades to determine and compare the power coefficient and power of each blade. The best model

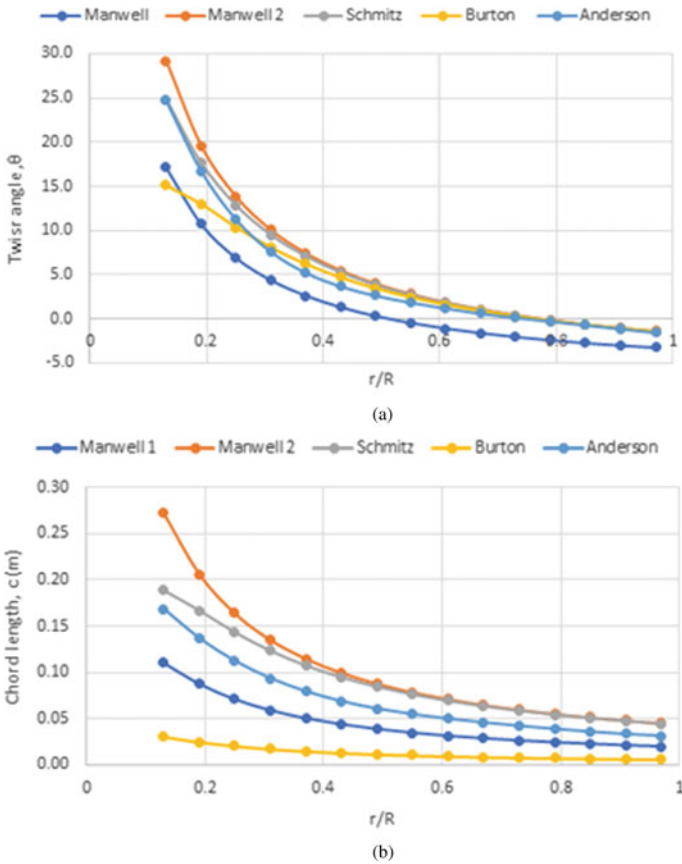


**Fig. 4** **a** Twist angle and **b** Chord length along the blade radius

is selected to go through linearization process of the chord length and angle of twist distributions. It is followed by the comparison on the aerodynamic performances between the blade with nonlinear and its linearized distributions.

### 3.1 The Chord Length and Twist Angle Distributions

Based on the given formulae in Table 1, the plots of the chord length and twist angle against blade’s radius are shown in Fig. 4 which correspond to the five geometric formulae, including one that is based on empirical relationship [14]. All formulas give parallel distribution throughout the length except for the Burton’s twist angle distribution. It can be seen that different formulae provide different sizes of chord length and twist angle, where the Manwell’s formula without considering the wake



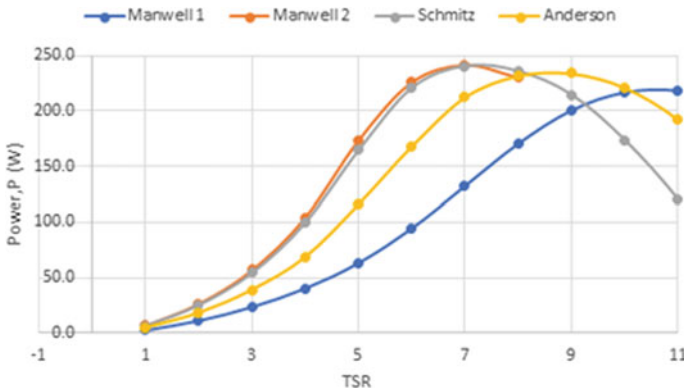


Fig. 5 Glide ratio against the AOA for modified airfoils

rotation gives the highest values of twist angle and chord length throughout the blade length.

### 3.2 The Aerodynamic Performances for Different Blade Geometries

The aerodynamic performances of the five wind turbines correspond to five different blade’s chord length, and twist distributions are given. Figure 5 shows the plots of power versus tip speed ratio, TSR. It shows the typical plot of the achievement criteria having a maximum value at a certain TSR value, where the Schmitz and Manwell 1 plots are almost identical. Note that due to convergence problem, the plot for Manwell 1 is only up to TSR = 8. The Schmitz’s, Manwell 1’s and Anderson’s plots show almost the same value of maximum power, except that in the Anderson’s plot, maximum  $P$  occurs at higher TSR.

Figure 6 shows the comparison of thrust plots for the blades that correspond to the applied formulas. It shows that the Anderson’s formula gives such lower values of thrust throughout the TSR. Recall that the Anderson’s formula has given almost similar maximum  $P$  and  $C_p$  to Schmitz’s and Manwell 1’s formulae which occur at higher TSR. With these advantages, the Anderson’s blade is taken to the next step of linearization of the chord length and twist angle distributions.

### 3.3 The Linearization of the Distributions

Here, the distributions provided by Anderson’s empirical formulae have been chosen to be linearized. Based on Eqs. (3) and (4), the value of  $n$  chosen here is 15 and 25

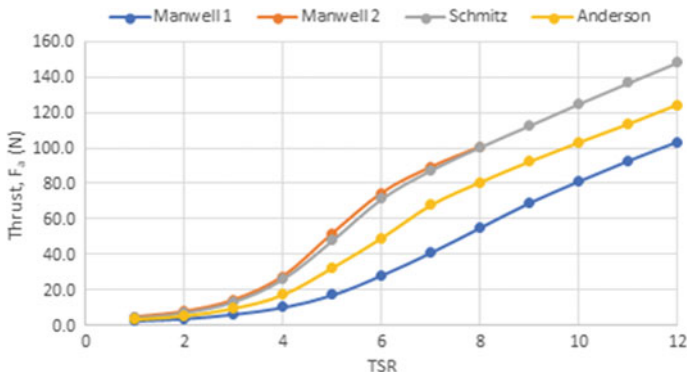
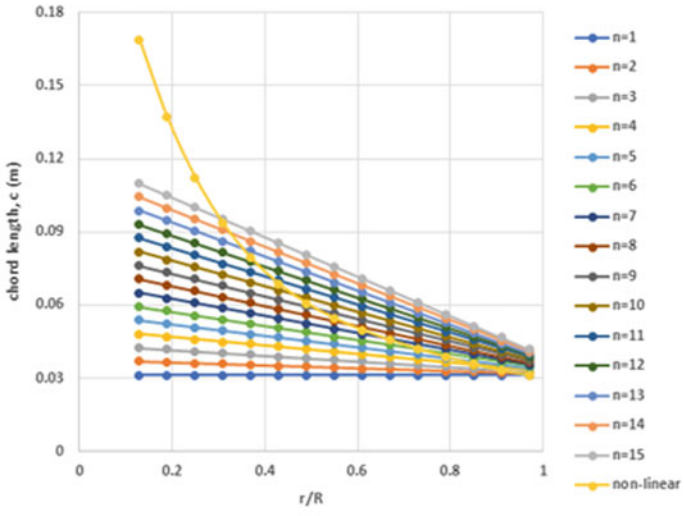


**Fig. 6** Plots of thrust,  $F_a$  against TSR

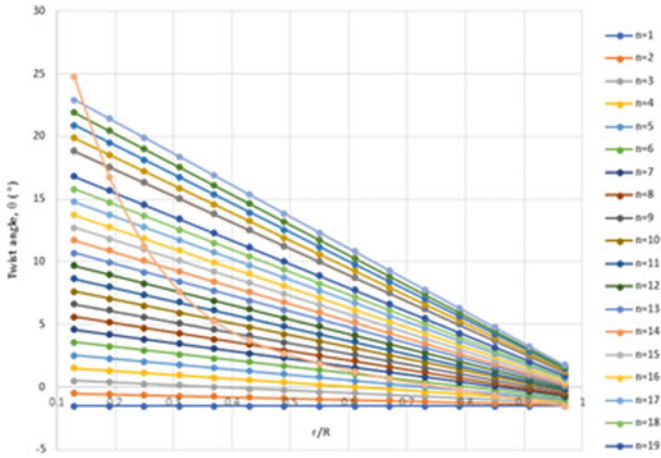
for chord length and twist angle, respectively. Figure 7a shows all the 15 possible linear distributions along with the nonlinear distributions of the chord length, while similar plots of 25 linear distribution for twist angle can be seen in Fig. 7b. In the following optimization process, the BEMT analysis has been conducted on turbine blades, each having combination of 15 chord length and 25 twist angle distributions that makes it all 375 possible combinations of twist angle and chord length.

Figure 8 shows the plot of power that corresponds to all combinations of chord lengths and twist angles. The dimensions of the chord length and twist angles are referring to the values at the roots of the blades. It shows that as the chord length is increased in sizes, the power and power coefficient performances are increased as well. However, the effect of the twist angle can be seen to give maximum power for the blade having root's twist angle of  $7.6^\circ$ . As such, the optimal values of chord length and twist angles are the chord length with linear distribution of  $n = 15$  and the twist angle with linear distribution of  $n = 10$ .

The BEMT analysis has been conducted on the blade equipped with the chosen linear distributions of the chord length and twist angle. Comparison is made between the performances of the blades with linear and nonlinear (Anderson's) distributions of chord length and twist angle. Figure 9 shows the plots of power and thrust versus TSR for blades having linear and nonlinear chord length and twist angle distribution. It shows that with the simplified linear distributions, the linear blade gives almost the same maximum power as the nonlinear blade as shown in Fig. 9a. Furthermore, Fig. 9b shows one desired result of the linear distribution blade that shows lower values of thrust load,  $F_a$ .



(a)



(b)

Fig. 7 Linearization of the **a** Chord length **b** Twist angle distribution

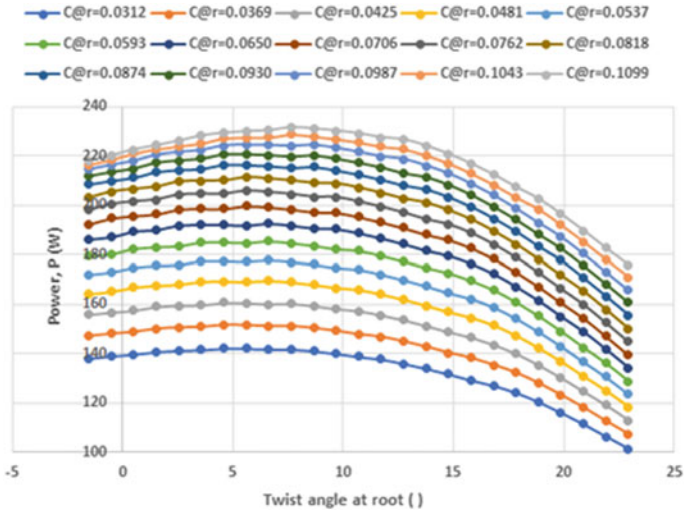


**Fig. 8** Power against the linearized twist angle distribution

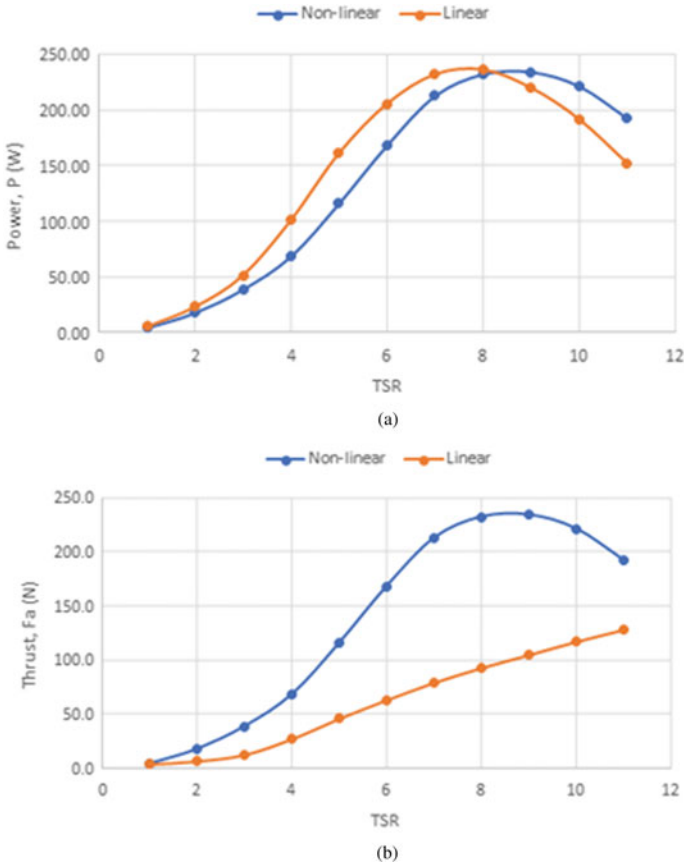


Fig. 9 Performance comparison for linear and nonlinear distribution: **a** Power **b** Thrust

## 4 Conclusion

A study has been conducted on comparing for the best nonlinear distribution of the chord length and twist angle that gives the best aerodynamic performance of the blade. This best distribution is then linearized to study the effect of the linearization on the performances of the blades. It was found that the distribution given by empirical formulas gives the highest power and power coefficient at high TSR and at the same time gives the lowest axial thrust force. Furthermore, by linearizing this distribution, the more simplified blade design with cheaper manufacturing cost has been determined that gives similar power to the nonlinear blades while it produces much less maximum thrust force of about 125N when compared with 225N for its nonlinear counterpart. The logical next course of action is to determine the best

blade geometry through the available optimization methods, such as genetic algorithm (GA) and particle swarm optimization (PSO) to apply a more systematic way in finding the best blade geometry.

**Acknowledgements** This work is funded by the UTMER Scheme grant “Q.K.130000.2656.18J24”, provided by the Malaysia-Japan International Institute of Technology, a faculty of the Universiti Teknologi Malaysia, Skudai, Malaysia. The authors acknowledge this support.

## References

1. Ren H et al (2020) Development of a green and sustainable manufacturing process for gefapixant citrate (MK-7264) part 1: introduction and process overview. *Organ Process Res Develop* 24(11):2445–2452
2. Bhatt Y, Ghuman K, Dhir A (2020) Sustainable manufacturing: bibliometrics and content analysis. *J Clean Prod* 260:120988
3. Rasid ZA et al (2011) Thermal buckling and post-buckling improvements of laminated composite plates using finite element method. *Key Eng Mater* 471–472:536–541
4. Wahab A et al (2018) Dynamic instability of high-speed rotating shaft with torsional effect. *Int J Autom Mech Eng* 15(4):6034–6051
5. Rasid ZA, Zahari R, Ayob A (2014) The instability improvement of the symmetric angle-ply and cross-ply composite plates with shape memory alloy using finite element method. *Adv Mech Eng* 6:632825
6. Roslan S et al (2019) Dynamic instability response of smart composite material. *Mater Wissenschaft und Werkstofftechnik* 50(3):302–310
7. Razak MA et al (2019) Energy consumption clustering analysis in residential building. *Symposium on intelligent manufacturing and mechatronics*. Springer, Melaka, pp 436–450
8. Roslan SAH, Rasid ZA, Ariffin AK (2023) Extended blade element momentum theory for the design of small-scale wind turbines. *J Adv Res Appl Mech* 101(1):62–75
9. Mehta PR, Kale RV (2022) Parameters affecting design of wind turbine blade: a review. In: Chaurasiya PK, Singh A, Verma TN, Rajak U (eds) *Technology innovation in mechanical engineering*. Lecture notes in mechanical engineering. Springer, Singapore
10. More A, Roy A (2020) Design and weight minimization of small wind turbine blade for operation in low-wind areas. In: Singh S, Ramadesigan V (eds) *Advances in energy research*. Springer proceedings in energy 2. Springer, Singapore
11. Manwell JF, McGowan JG, Rogers AL (2010) *Wind energy explained: theory, design and application*. Wiley
12. Ingram G (2011) *Wind turbine blade analysis using the blade element momentum method*, version 1.1. Durham University, Durham
13. Jamieson P (2018) *Innovation in wind turbine design*. Wiley
14. Bakırcı M, Yılmaz S (2018) Theoretical and computational investigations of the optimal tip-speed ratio of horizontal-axis wind turbines. *Eng Sci Technol Int J* 21(6):1128–1142
15. Burton T et al (2011) *Wind energy handbook*. Wiley
16. Batu T, Lemu HG (2020) Comparative study of the effect of chord length computation methods in design of wind turbine blade. In: Wang Y, Martinsen K, Yu T, Wang K (eds) *Advanced manufacturing and automation IX*. IWAMA 2019. Lecture notes in electrical engineering, vol 634. Springer, Singapore
17. Jha D, Singh M, Thakur AN (2021) A novel computational approach for design and performance investigation of small wind turbine blade with extended BEM theory. *Int J Energy Environ Eng* 12:563–575

18. Lee MH, Shiah YC, Bai CJ (2016) Experiments and numerical simulations of the rotor-blade performance for a small-scale horizontal axis wind turbine. *J Wind Eng Ind Aerodyn* 149:17–29
19. Hsiao FB, Bai CJ, Chong WT (2013) The performance test of three different horizontal axis wind turbine (HAWT) blade shapes using experimental and numerical methods. *Energies* 6(6):2784–2803
20. Madi M et al (2021) Comparative analysis of taper and taperless blade design for ocean wind turbines in Ciheras coastline, West Java. *Kapal Jurnal Ilmu Pengetahuan dan Teknologi Kelautan* 18(1):8–17
21. Anderson M, Milborrow D, Ross J (1982) Performance and wake measurements on a 3 m diameter horizontal axis wind turbine. Comparison of theory, wind tunnel and field test data. In: *International symposium on wind energy system, processing (United Kingdom)*
22. Liu X, Wang L, Tang X (2013) Optimized linearization of chord and twist angle profiles for fixed-pitch fixed-speed wind turbine blades. *Renew Energy* 57:111–119
23. Tahani M et al (2017) Aerodynamic design of horizontal axis wind turbine with innovative local linearization of chord and twist distributions. *Energy* 131:78–91
24. Sedaghat A, Mirhosseini M, Moghimi Zand M (2014) Aerodynamic design and economical evaluation of site specific horizontal axis wind turbine (HAWT). *Energy Equip Syst* 2(1):43–56
25. Rahgozar S et al (2020) Performance analysis of a small horizontal axis wind turbine under the use of linear/nonlinear distributions for the chord and twist angle. *Energy Sustain Develop* 58:42–49
26. Abdelsalam AM et al (2021) Experimental study on small scale horizontal axis wind turbine of analytically-optimized blade with linearized chord twist angle profile. *Energy* 216:119304
27. Sena B et al (2021) Determinant factors of electricity consumption for a Malaysian household based on a field survey. *Sustainability* 13(2):818

# Performance Analysis of H-Type Vertical Axis Wind Turbine by Using Novelty Numerical Simulink Method



Muhammad Radhiva, Muhammad Hasya Abdillah,  
Geordiano Devanaldy Khresna Putra, Muhammad Raihan Wajdi,  
Putri Wulandari, Wahyu Caesarendra, Ahmad Husin Lubis,  
and Ary Syahriar

**Abstract** Renewable energy is a solution to displace non-renewable energy resources with the wind turbine being one of the prominent the renewable energy sources. Research on wind turbines still ongoing to be advanced. The Horizontal Axis Wind Turbines (HAWTs) are more widely utilized for electricity production, Vertical Axis Wind Turbines (VAWTs) offer distinct advantages not found in HAWTs. However, VAWT has several benefits that are not present in HAWT, so research on VAWT must continue with the aim that VAWT can be developed into a commercial power generator. This paper is a form of Darrieus VAWT research development. The demonstration of Numerical Simulink Method can be found here to evaluate the performance of Wind Turbine such as the values of power coefficient, angular velocity, and torque. The input parameters are a symmetrical airfoil with 15% thickness, a radius of 0.5 m, a height of 1 m, and a chord length of 0.2 m. Numerical analysis using the Novelty Simulink Model is carried out so that engineers or scientists can evaluate VAWT performance under various conditions for further research. This paper also presents a graph depicting a relationship between all output parameters with wind speeds starting from 1 m/s until 12 m/s. According to the study's outcome, these have a relation with increasing wind speed. Moreover, this research provides evidence that the VAWT can work properly at low wind speeds (less than 12 m/s).

**Keywords** VAWT · Start-up ramp condition · Airfoil NACA 0015 · Torque · Coefficient of power · Low wind speed

---

M. Radhiva · M. H. Abdillah · G. D. K. Putra · M. R. Wajdi · P. Wulandari · A. H. Lubis ·  
A. Syahriar (✉)  
Faculty of Science and Engineering, University Al-Azhar, Jakarta, Indonesia  
e-mail: [ary@uai.ac.id](mailto:ary@uai.ac.id)

W. Caesarendra  
Faculty of Integrated Technologies, Universiti Brunei Darussalam, Bandar Seri Begawan, Brunei



## 1 Introduction

Demand of electrical energy has increased significantly along with the increase in population and demand for industry and so on. Currently the fuel used to produce electrical energy is fossil fuels such as coal, natural gas, and oil. Fossil fuels are hydrocarbons that have an environmental impact when used. When more fossils are extracted from the earth, the great of greenhouse gases that pollute the air on earth will increase. These harmful gases produced by fossil fuels have impacts on global warming [1].

Global warming is a situation in which the Earth's temperature rises due to a multitude of factors. The increase in greenhouse gases is the most influential factor in global warming. Fossil fuel combustion sources such as transportation and non-renewable power plants are factors that cause excessive toxic gases such as CO<sub>2</sub>, methane, nitrous oxide, and SO<sub>2</sub> to be produced [2]. In addition, living creatures on earth are sure to be affected, directly or indirectly, because the gases produced are very dangerous to the environment and health. In terms of the environment, the intensity of natural disasters will increase, as extreme weather occurs more frequently as a result of rising temperatures. Not only that, life in the oceans and freshwater systems is also affected. Life in the oceans and freshwater systems is affected because CO<sub>2</sub> can dissolve, causing a decrease in water pH. In addition, the heat from greenhouse gases is trapped and absorbed by water, causing it to heat up [3]. In terms of health, there are various diseases caused by global warming because, fundamentally, global warming contributors are not only CO<sub>2</sub>, so it can be said to be directly proportional to air pollution. For children, the effects of air pollution include infant mortality, low birth weight, allergies, asthma, nerve development damage, disabilities, and cancer, which some of these effects can be experienced by adults [4].

The Paris Agreement, enacted in 2015, was created in response to the extensive impact of global warming. In this agreement, 197 countries concurred to limit the maximum temperature rise to no more than 2 °C [5]. This means that the use of fossil fuels is increasingly restricted, as they contribute to the production of dangerous gases and rising air temperatures, in order to keep the global surface temperature increase to only 1.5 °C, which is better than the targeted 2 °C. Oil, natural gas, and coal are therefore expected to remain unexploited, leaving only 58%, 56%, and 89% respectively by 2050 [6]. Therefore, there is a need for special attention to be given to renewable energy like wind, solar, water, biomass, and geothermal so they can be used more massively as they are more environmentally friendly, have lower usage costs, and are not exhaustible. Wind power utilization is one of many solution for reducing the use of non-renewable energy. Wind energy converted into electrical energy through a generator has been proven to produce relatively low air pollution, resulting in lower impacts on living beings and the environment. Furthermore, in terms of the economy, the benefits of adopting renewable energy steadily escalate. In the year 2015, the proportion of renewable energy attained 15%. It is predicted that by 2050, the share of renewable energy will continue to grow given the public's concerns about environmental health issues, reaching 63% of energy production revenue [7].

Nowadays, there are two common categories of wind turbines which are distinguished according to the direction of their axis, To be precise, it was the Horizontal-Axis Wind Turbine (HAWT) and the Vertical-Axis Wind Turbine (VAWT). HAWT has a shape similar to aircraft propellers, which are Aligned with the wind flow, thus requiring a special mechanism to direct the blades according to the movement of the wind. The other type is VAWT, which has its axis orthogonal to the wind flow. The advantage of VAWT is that no matter where the wind comes from, it will continue to rotate, so no special mechanism is needed to rotate its blades. Both types of turbines are still being developed in order to achieve a high level of efficiency [8].

In generating electricity from a steady wind flow with sufficient speed, HAWT is clearly superior and can produce much more energy than VAWT. Additionally, HAWT exhibits more efficient performance than VAWT [9]. HAWT is commonly used in large wind farms, remote access areas, and offshore locations where the wind speed is stable and uninterrupted. On the other hand, wind patterns in urban areas tend to be unstable with low wind speeds, unpredictable wind directions, and full of turbulence which make HAWT relatively ineffective. Therefore, VAWT can be a better choice for urban areas [10]. However, VAWT is more effective when the wind direction is constantly changing because VAWT does not require a mechanism to adjust to changing wind direction. Because of this, VAWT can be utilized in other areas such as in the middle of a highway, which can be used to power the lighting system [11]. Another advantage of VAWT is that more VAWTs can be installed on a single piece of land compared to HAWT, resulting in greater energy density for VAWT usage on that land [12].

The research uses the four-digit NACA series from the National Aeronautics and Space Administration (NASA) as an airfoil of the wind turbine. Symmetrical airfoils have better efficiency but worse self-starting ability than chambered airfoils [13]. A symmetrical airfoil called the NACA 0015, which has a thickness of 15%, was used in the experiment because it can produce a maximum power coefficient at the optimum tip speed ratio ( $\lambda$ ) higher than 3 [14, 15]. Based on Song's simulation, it was found that NACA 0015 and 0018 are more suitable for use in VAWT. Moreover, it was also found that the torque produced by NACA 0015 is not too bad, although NACA 0018 is the best [16].

This research was conducted to determine the characteristics of a vertical axis Darrieus type wind turbine using the Simulink Numerical Method. Research related to simulation methods is necessary, as a lightweight and accurate simulation method is still being sought. So far, there are two simulation methods that are often used, namely Double Multiple Streamtube (DMST) and Computational Fluid Dynamic (CFD) [17]. Although they are simulation methods that meet the needs of VAWT simulation, research on numerical methods with Simulink is very likely to be the initial step towards eventually surpassing both methods. Another advantage of this method is that we can apply control systems and generators within it. However, in this paper, we will only review its aerodynamic performance and ensure that the model has shown correct calculations [18].

## 2 Research Theory

In the concept of wind turbine efficiency, it is related to the betz limit. The betz limit is the maximum efficiency value that can be achieved on a wind turbine. This concept was first introduced by a physicist from Germany named Albert Betz in 1919. The value of the betz limit is 16/27 or 59.3%, which means that the maximum limit of wind kinetic energy that can drive a turbine is only 59.3% as shown in Fig. 1. But in fact, no wind turbine can reach the maximum limit of this betz limit. The average wind turbine efficiency value is only 35–45%. [19]

However, according to Divakaran [21] there are many studies which prove that the Betz limit does not apply to VAWT. Other research says that the Betz limit still applies with a different maximum. The maximum efficiency value that applies to VAWT is 63%. Of course, it seems impossible if the efficiency of a wind turbine is close to 100%. therefore, in this study, it is assumed that the maximum possible efficiency is 64% [22].

The power in the wind turbine is the result of the conversion of wind energy that drives the rotor and generator. The amount of power in a wind turbine is highly dependent on the speed of the wind that drives the rotor. The power equation for the wind turbine is as follows:

$$P = \frac{1}{2} \rho C_p A V o^3 \tag{1}$$

with

$$A = H d \tag{2}$$

where  $P$  is wind turbine power (watts),  $\rho$  is air density (1.225 kg/m<sup>3</sup>),  $C_p$  is Coefficient of Power,  $V_o$  is freestream wind speed (m/s),  $A$  is rotor area (m<sup>2</sup>),  $H$  is the height of the wind turbine (m), and  $d$  is the diameter of the rotor (m) [23].

Coefficient of power ( $C_p$ ) is a coefficient that determines the amount of power performance of the wind turbine. This  $C_p$  is basically influenced by two factors, namely the yield power of the wind turbine and the kinetic energy of the wind flow

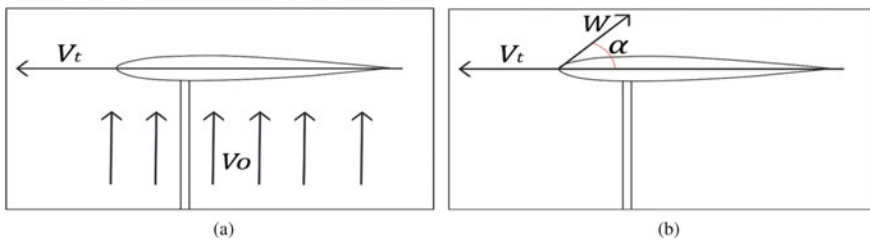


**Fig. 1** **a** Illustration of freestream wind flow through the blade and **b** Illustration of relative wind flow [20]

itself. This  $C_p$  has a directly proportional relationship with the performance of the wind turbine, the greater the  $C_p$ , the better the performance of the wind turbine. The Coefficient of Power ( $C_p$ ) equation is as follows:

$$C_p = \frac{Pr}{Pw} = \frac{\tau\omega}{\frac{1}{2}\rho AVo^3} \quad (3)$$

where  $C_p$  is the Coefficient of Power,  $Pr$  is the actual turbine power (Watts), and  $Pw$  is the Power of the theoretical wind speed (Watts) [19].

Tip speed ratio ( $\lambda$ ) is one of the crucial factors in determining the design of wind turbine.  $\lambda$  may be defined as the ratio of wind speed with wind turbine blade tip velocity.  $\lambda$  is a dimensionless quantity that states the relationship between wind speed and the average rotation of the rotor [24]. The equation can be written as:

$$\lambda = \frac{\omega R}{Vo} \quad (4)$$

where  $\lambda$  is Tip speed ratio,  $\omega$  is turbine rotor rotation speed,  $R$  is rotor radius (m),  $Vo$  is freestream windspeed (m/s) [25].

The force experienced by the blade in the direction from the trailing edge to the leading edge is the simple definition of tangential force. The tangential force can be found by the following equation:

$$F_t = C_t \frac{1}{2} \rho ch W^2 \quad (5)$$

where  $F_t$  is tangential force (N),  $C_t$  is tangential force coefficient, is air density ( $1.225 \text{ kg/m}^3$ ),  $c$  is cord length,  $h$  is turbine height, and  $W$  is relative wind flow.

Tangential force can be obtained from the accumulation of lift and drag forces, so that the tangential coefficient  $C_t$  is a constant value that accumulates constant values of drag and lift forces. To find the tangential force, the value  $C_t$  can be calculated with the following equation:

$$C_t = C_d \sin(\alpha) - C_l \cos(\alpha) \quad (6)$$

where  $C_t$  is tangential coefficient,  $C_d$  is coefficient drag force,  $C_l$  is coefficient lift force, and  $\alpha$  is angle of attack.

Angle of Attack is the angle between the relative windflow ( $Vo$ ) vector line and the tangential moving blade direction vector  $Vt$ . angle of attack has an effect on  $C_t$ . Therefore, the angle of attack also has a very significant effect on the torque value on the blade.

To find the angle of attack on this wind turbine, we can use the following equation:

$$\alpha = \tan^{-1} \left( \frac{\cos \theta}{\frac{\lambda}{(1-u)} + \sin \theta} \right) \quad (7)$$

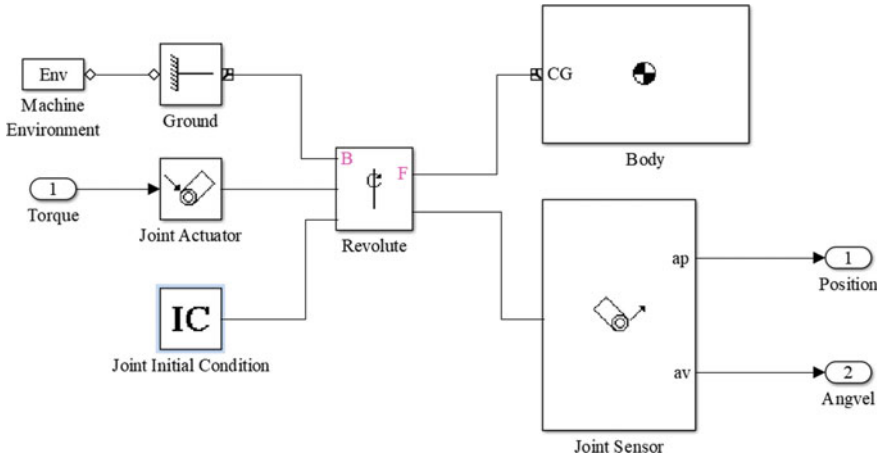


Fig. 2 Subsystem of dynamic measurement [26]

where  $\tau$  is the angle of attack,  $u$  is induction factor, and  $\theta$  is angular position (rad).

Relative Windflow is the wind flow in terms of the blade. Figure 1a shows freestream windflow heading towards a moving blade. While Fig. 1b shows us the direction of the wind flow when viewed from a moving blade. The value of the Relative Windspeed can be calculated by the following equation:

$$W = V_o \sqrt{[\lambda + (1 - u) \sin(\theta)]^2 + [(1 - u) \cos(\theta)]^2} \tag{8}$$

$$u = \frac{Nc\omega}{2\pi V_o} \sin(\theta) \tag{9}$$

where  $N$  is number of blade,  $c$  is blade chord length (m),  $h$  is height (m),  $W$  is relative wind flow,  $\theta$  is angular position (rad),  $\lambda$  is tip speed ratio,  $\omega$  is angular sepeed (rad/s),  $V_o$  is freestream windspeed (m/s),  $u$  is induction factor, and  $R$  is rotor radius (m) [27].

Torque is the value of the moment of force that states the object is rotating on its axis. Therefore, the torque value can be calculated as

$$\tau = \frac{\rho \times H \times C_t \times W^2 \times c}{2} \tag{10}$$

where is the torque (Nm), where  $C_t$  tangential force coefficient,  $W$  is relative wind speed (m/s),  $H$  is blade height (m),  $\rho$  is air density [28].

### 3 Methodology

Simulink is an additional part of the Matlab software that can be used as a means of modeling, simulating and analyzing dynamic systems using a graphical interface (GUI) [29]. In this study, Simulink is used to determine the value of angular velocity, torque, and power coefficient at start-up ramp condition. Matlab is also used to plot comparison charts based on parameters on Table 1. the equations that are used are applied to the Simulink that have been compiled. Finally, the angular velocity, torque, and power coefficient are shown. The parameters used in this experiment are listed in Table 1. The air pressure at the wind turbine location is assumed to be an average temperature in the world at the industrial revolution (1850) had just begun, 15 degrees Celsius, so the air density equal to  $1.225 \text{ kg/m}^3$  [30]. The minimum wind speed used is 1 m/s and the maximum is 12 m/s. The rest of the specifications of the VAWT will be determined based on the results of this test. Table 1 is a lists of the parameters.

To calculate the angular velocity and angular position of the VAWT that being analyzed, the block set from Woods [26] will be used, as shown in Fig. 2. This subsystem block describes how the 3D shape of the turbine is used to calculate a rotational object using momentum theory. The sensor will calculates the VAWT and displays it to the user in the form of numbers.

Still based on Woods' presentation, it has been explained that a coefficient called a Simple Model Generator exists. During the experiment, it was found that this Simple

**Table 1** Parameters of VAWT simulation

Parameters	Value
Air density	$1.225 \text{ kg/m}^3$
Reynold number	80,000
Wind velocity	1 – 12 m/s
Blade number	3
Radius	0.5 m
Height	1 m
Airfoil	NACA 0015
Chord length	0.2 m

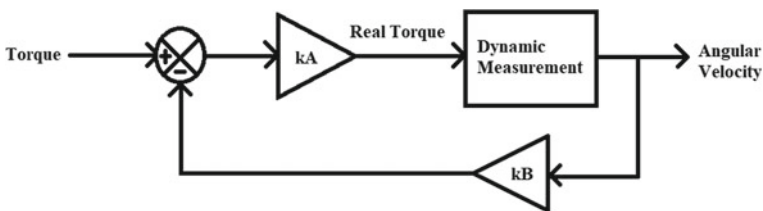


**Fig. 3** System for finding a real torque and angular velocity [26]

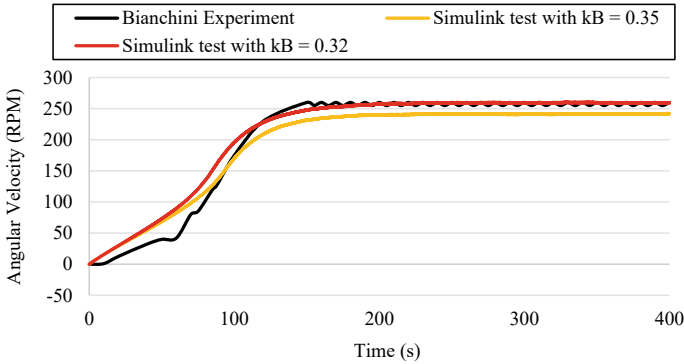


**Fig. 4** Comparison between different  $k_B$  of Simulink model test and Bianchini Experiment [31]

Model Gen has an influence on the maximum angular speed of the wind turbine. In addition, additional gain is also needed to match the wind turbine torque with the results of existing wind turbine research. Figure 3 illustrates the system that been found in this research. Coefficient A ( $k_A$ ) and the value of the coefficient B ( $k_B$ ) can be adjusted for generate a close enough result compared to another or real experiment test result.

Until the time of writing this paper, the nature of this coefficient had not yet been fully understood. A provisional hypothesis is that there may be a relationship between these two coefficients and the theory of momentum. This is because when using other wind turbine parameters, even with the same H-type and airfoil, the results do not match immediately with other resources such as real experiments or data from other journals. The calculation results only match when adjusting these two coefficients to fit at least one condition. For this study,  $k_A = 0.08$  and  $k_B = 0.35$  are used.

Figure 4 is a graph produced by the Simulink test and Bianchini experiment. There are three graphs, namely the model test with  $k_B = 0.35$  and  $0.32$ . Of course, the  $k_A$  used for both is the same. Two graphs produced by Simulink are compared with the graph from Bianchini's test, where he tested with the same VAWT parameters used in this experiment. When compared, the graph results closely approximate the graph obtained by Biancini, who used a Wind Tunnel Test to test his wind turbine. This comparison result shows that the model used for simulation in this paper is valid.

## 4 Research and Discussion

The research will be carried out by running a Simulink model that contains the previously determined parameters and discovered equation which it applied at the Simulink models with the end of the model to calculate angular velocity was shown in Fig. 2. The resulting data of angular velocity,  $C_p$ , and torque will be analyzed.

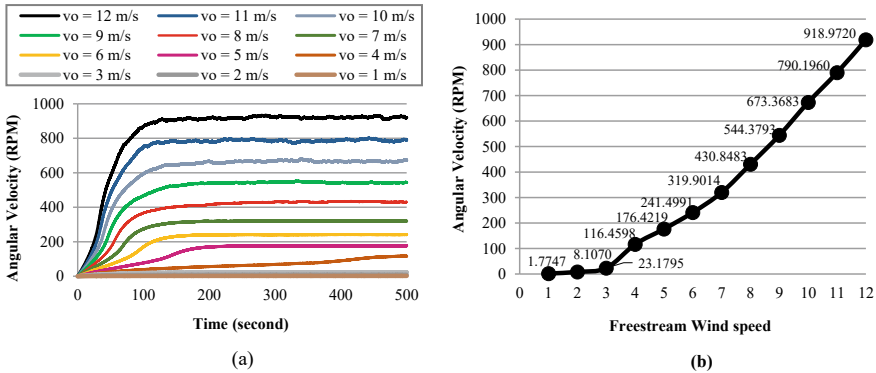


**Fig. 5** **a** Angular velocity plot while turbine at start up condition. **b** Angular velocity at  $t = 500$  s versus freestream wind speed [32]

The phenomenon of angular velocity will be observed while the wind turbine runs for 200 s with freestream wind speeds ( $V_o$ ) ranging from 1 to 12 m/s.

Figure 5 depicts the relationship between Angular Velocity and wind speed. In Fig. 5a, it is evident that the turbine attains a steady state condition when the wind speed is at its maximum for every given speed. Although the angular velocity increases with wind speed, the time required to reach steady state is not always linear. However, the steady state time is always proportional to wind speed. Figure 5b illustrates that the angular velocity exhibits an almost linear trend with wind speed. The maximum angular velocity of 918.9720 rpm is observed at a wind speed of 12 m/s, while the minimum angular velocity of 1.7747 rpm is recorded at a wind speed of 1 m/s.

Certain aspects of wind turbine performance can be determined by analyzing the torque generated during rotation. Greater torque indicates that the turbine will have difficulty stopping. Figure 6 presents a plot of  $C_p$  and torque during the turbine’s initial rotation until 200 s of operation. From the figure, it can be observed that both variables exhibit a common feature of rising and falling as if oscillating at a high frequency.

The simulation was carried out through multiple iterations until a total time of 500 s was reached. When plotting the torque and  $C_p$  values at the 200-s mark, the calculations was conducted for a total of 4689 iterations. Due to the high frequency of the torque and  $C_p$  values, a moving average of 50 iterations was employed to determine whether these variables tended towards a positive or negative trend.

Figure 6, shows that both have a peak value when the time is around 100 s. After that, the red line which is the moving average is decreasing. When  $t = 120$  s, the moving average line no longer decreases and stays around the value torque and  $C_p$  equals to 0. This means that when the time shows 100 s, the value of the angular velocity is increasing and starting to enter a steady state. Only when the time shows 120 s, the steady state starts and the value of the angular velocity no longer increases.



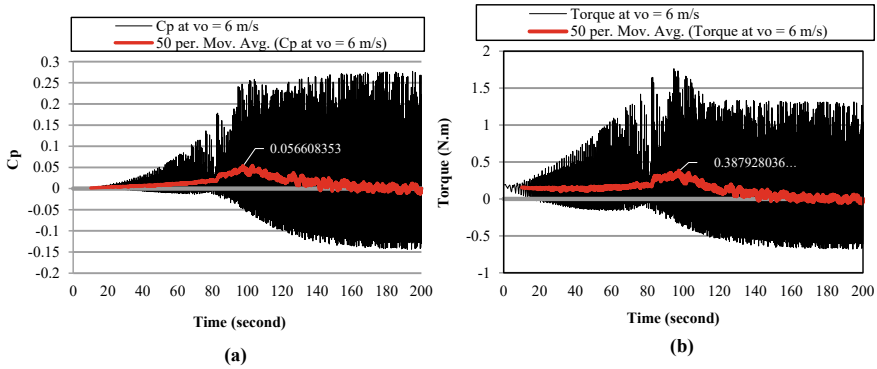


**Fig. 6** a  $C_p$  and b torque plot during start-up ramp until the angular velocity is steady [33]

To understand why the torque and  $C_p$  oscillate very quickly, the influence of the azimuth angle on torque and  $C_p$  was investigated. The experimental results are shown in Fig. 6, which illustrate the influence of the azimuthal angle on torque and  $C_p$  at times  $t = 99$  s and  $t = 199$  s. Referring to Fig. 5, the time  $t = 99$  s is the peak of the moving average torque and  $C_p$  values, which represents the final start-up ramp condition. The torque test and  $C_p$  experiment were conducted at the end of 199 s, at which time the turbine was already in steady condition.

From Fig. 7, both (a) and (b), show us that the turbine will have a negative value of torque and  $C_p$  when the Azimuthal Angle is between 0 to 180 degrees, while the positive value is in the position of 180° to 360°. There are two points where the value of torque and  $C_p$  is 0, which is around 180° and 300°. The two 0 points where the three blade torques have positive and negative values, so they eliminate each other. Please note that the wind is blowing from 180° and moving to 360°.

Additionally, the torque and  $C_p$  values were examined as the freestream wind speed varied from 1 to 12 m/s. Although the experiment yielded a similar plot shape, the

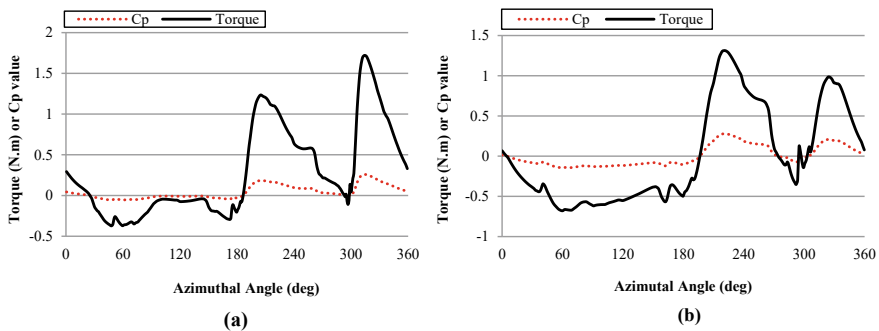


**Fig. 7**  $C_p$  and torque versus Azimuthal angle at a final start-up ramp condition and b steady condition [34]

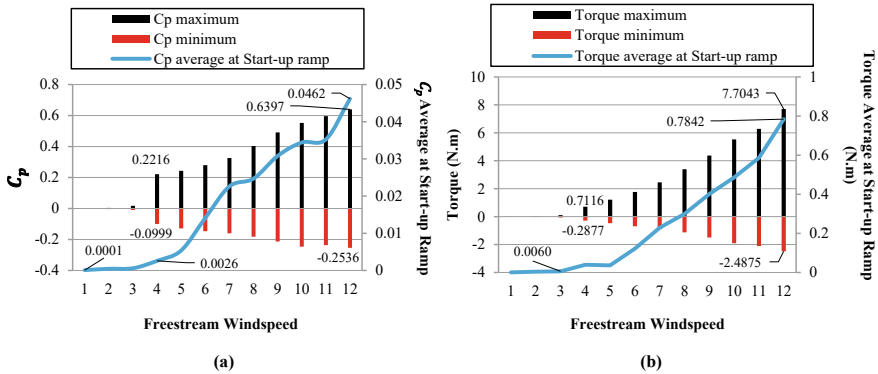


Fig. 8 a  $C_p$  and b Torque versus wind speed [33]

maximum and minimum values were different. Figure 8 displays the maximum and minimum torque values and  $C_p$  for various freestream windspeeds. To determine the actual performance of the wind turbine during rotation, an average value of the torque and  $C_p$  was calculated solely during the start-up ramp conditions.

Figure 8a depicts that the amplitude of torque and  $C_p$  plots is directly proportional to the freestream wind speed. At  $v_0 = 12$  m/s, the  $C_p$  amplitude reaches its maximum value of 63.97%. However, the maximum  $C_p$  at average start-up ramp condition is only 4.6%. Figure 8b shows the amplitude values and average torque at start-up ramp conditions. The results indicate that during start-up in ramp conditions, the average torque has a maximum value of 0.78 N.m. Both plots in Figure 8 illustrate that the torque and  $C_p$  values are significantly small when the  $v_0$  values are between 1 and 3 m/s. It suggests that even the slightest disturbance can stop the turbine.

## 5 Conclusion

The performance of a Novel Simulink model shows that it can provide sufficiently accurate results when compared to Bianchini’s experimental results. The VAWT with NACA 0015 airfoil has been evaluated using the model created, where some of the input parameters such as the number of blades, wind speed, radius, and chord length are used to produce outputs in the form of angular velocity and torque at start-up conditions, these results can be used to observe the phenomenon of wind turbine movement during start-up conditions. For further research, the created model can also be used for analyzing installed generator performance in the VAWT. According to the simulation results, the best operating condition for a VAWT is when the freestream wind speed is at 12 m/s, but it can still operate when the freestream wind speed is below 4. When the freestream wind speed is less than 4, it would be challenging for the VAWT to generate energy due to the slightest disturbance that can cause the turbine to stop as a result of the small torque acting on it. It is also observed that the

freestream wind speed has an influence on the speed of the turbine to reach a steady state.

This paper demonstrates that a low-speed wind turbine ( $vo < 12$ ) can be operated with the NACA 0015 symmetrical airfoil. The analysis conducted using the Simulink model is just the first step towards a more in-depth analysis of wind turbines. However, further development and testing are necessary, especially in determining  $k_A$  and  $k_B$  in Dynamic Measurement. Without knowing  $k_A$  and  $k_B$ , data from other simulations or experiments from the actual device must be compared to determine them. This poses a challenge to the use of the model. If  $k_A$  and  $k_B$  can be determined, this model can potentially develop further to simulate all situations and conditions, including when the device is connected to the generator.

## References

1. Pata UK (2021) Renewable and non-renewable energy consumption, economic complexity, CO<sub>2</sub> emissions, and ecological footprint in the USA: testing the EKC hypothesis with a structural break. *Environ Sci Pollut Res* 28(7):846–861
2. Mehmood I et al (2020) Carbon cycle in response to global warming. *Environ Climate Plant Vegetation Growth* 1–15
3. Al-Ghussain L (2019) Global warming: review on driving forces and mitigation. *Environ Prog Sustain Energy* 38(1):13–21
4. Perera FP (2017) Multiple threats to child health from fossil fuel combustion: impacts of air pollution and climate change. *Environ Health Perspect* 125(2):141–148
5. Iyer GC et al (2015) The contribution of Paris to limit global warming to 2 °C. *Environ Res Lett* 10(12):125002
6. Welsby D et al (2021) Unextractable fossil fuels in a 1.5 °C world. *Nature* 597(7875):230–234
7. Gielen D et al (2019) The role of renewable energy in the global energy transformation. *Energy Strat Rev* 24:38–50
8. Augusta FA et al (2020) Vertical axis wind turbine analysis using MATLAB. *J Phys Conf Ser* 1517(1):012065
9. Johari MK, Jalil M, Shariff MFM (2018) Comparison of horizontal axis wind turbine (HAWT) and vertical axis wind turbine (VAWT). *Int J Eng Technol* 7(4.13):74–80
10. Shah SR et al (2018) Design, modeling and economic performance of a vertical axis wind turbine. *Energy Rep* 4:619–623
11. Liew HF et al (2020) Review of feasibility wind turbine technologies for highways energy harvesting. *J Phys Conf Ser* 1432(1):012059
12. Brownstein ID, Wei NJ, Dabiri JO (2019) Aerodynamically interacting vertical-axis wind turbines: performance enhancement and three-dimensional flow. *Energies* 12(14):2724
13. Maleki Dastjerdi S et al (2021) Application of simultaneous symmetric and cambered airfoils in novel vertical axis wind turbines. *Appl Sci* 11(17):8011
14. Rogowski K, Hansen MOL, Bangga G (2020) Performance analysis of a H-Darrieus wind turbine for a series of 4-digit NACA airfoils. *Energies* 13(12):3196
15. Wang Y et al (2018) Investigation on aerodynamic performance of vertical axis wind turbine with different series airfoil shapes. *Renew Energy* 126:801–818
16. Song C et al (2020) Study on aerodynamic characteristics of darrieus vertical axis wind turbines with different airfoil maximum thicknesses through computational fluid dynamics. *Arab J Sci Eng* 45:689–698
17. Jang H et al (2021) Performance evaluation and validation of H-darrieus small vertical axis wind turbine. *Int J Precision Eng Manuf Green Technol* 1–11

18. Rodrigues G, Valério D, Melicio R (2022) Controller development and experimental validation for a vertical axis wind turbine. *Sustainability* 14(20):13498
19. Ranjbar MH et al (2019) Reaching the betz limit experimentally and numerically. *Energy Equip Syst* 7(3):271–278
20. Safarov A, Mamedov R (2021) Study of effective omni-directional vertical axis wind turbine for low speed regions. *IIUM Eng J* 22(2):149–160
21. Divakaran U et al (2021) Effect of helix angle on the performance of Helical Vertical axis wind turbine. *Energies* 14:393–417
22. Castillo J (2012) Small-scale vertical axis wind turbine design. Bachelor's thesis, Universitat Politècnica de Catalunya
23. Chabane F, Barkat MA, Arif A (2022) Aerodynamic shape optimization of a vertical-axis wind turbine with effect number of blades. *DYNA: revista de la Facultad de Minas. Universidad Nacional de Colombia. Sede Medellín* 89(220):154–162
24. Wang Z, Zhuang M (2017) Leading-edge serrations for performance improvement on a vertical-axis wind turbine at low tip-speed-ratios. *Appl Energy* 208:1184–1197
25. Chen Y, Lian Y (2015) Numerical investigation of vortex dynamics in an H-rotor vertical axis wind turbine. *Eng Appl Comput Fluid Mech* 9(1):21–32
26. Damon Woods L (2014) Simulation of VAWT and hydrokinetic turbines with variable pitch foils. Master's thesis, Boise State University
27. Manwell JF, McGowan JG, Roger AL (2009) *Wind energy explained—theory, design, and application*, 2nd edn. Wiley, London, pp 147–148
28. Hasan A (2015) Model-based design and development of a vertical axis wind turbine computational model. Master's thesis, De Monfort University
29. Daowd M et al (2011) Passive and active battery balancing comparison based on MATLAB simulation. In: 2011 IEEE vehicle power and propulsion conference. IEEE, pp 1–7
30. Radha R (2022) Analysis of increase in average temperature on earth, its causes and wildfire using machine learning techniques. In: 2022 2nd Asian conference on innovation in technology (ASIANCON). IEEE, pp 1–13
31. Bianchini A, Ferrari L, Magnani S (2011) Start-up behavior of a three-bladed H-Darrieus VAWT: experimental and numerical analysis. In: *Turbo expo: power for land, sea, and air*, pp 811–820
32. Maalouly M et al (2022) Transient analysis of H-type vertical axis wind turbines using CFD. *Energy Rep* 8:4570–4588
33. Cai X et al (2020) Performance and effect of load mitigation of a trailing-edge flap in a large-scale offshore wind turbine. *J Marine Sci Eng* 8(2):72
34. Pucci M et al (2022) A DMST-based tool to establish the best aspect ratio, solidity and rotational speed for tidal turbines in real sea conditions. *J Ocean Eng Marine Energy* 8(3):285–303

# Energy Production from Various Bio-wastes Under Different Electrode and Temperature Conditions: Experimental Study



Rahul Anand, Rupendra Kumar Pachauri, Ahmad Faiz Minai, Akhlaque Ahmad Khan, Rajesh Singh, and Shashikant

**Abstract** This paper presents an analysis of the effects of various types of electrodes on the performance of microbial fuel cells (MFCs) under various test conditions. Electrical parameters are obtained from MFCs with different types of electrodes, e.g., carbon (C), aluminum (Al), zinc (Zn), and copper (Cu). The extensive performance is compared with different temperature levels during the study. Great and sufficient results are obtained and analyzed with electro-microorganisms' electrical properties and the bio-fuel cell performance, i.e., voltage and current characteristics with respect to time under variable temperature conditions. The voltage and current have been obtained with different types of electrodes, sewage wastes, and temperature values of sludge (sewage and rice water).

**Keywords** Bio-fuel cell · Energy generation · Waste to energy · Electrical performance

---

R. Anand  
School of Engineering, Gautam Buddha University, Greater Noida 201312, India

R. K. Pachauri (✉)  
Electrical Cluster, School of Engineering, University of Petroleum and Energy Studies,  
Dehradun 248007, India  
e-mail: [rpachauri@ddn.upes.ac.in](mailto:rpachauri@ddn.upes.ac.in)

A. F. Minai · A. A. Khan  
Electrical Engineering Department, Integral University, Lucknow, Uttar Pradesh, India

R. Singh  
Uttaranchal Institute of Technology, Uttaranchal University, Dehradun 248007, India

Shashikant  
Electrical Engineering Department, School of Engineering, Babu Banarasi Das University,  
Lucknow 226028, India

R. K. Pachauri  
Asian Institute of Technology, Khlong Luang, Pathum Thani, Thailand

## 1 Introduction

As a result of these bio-electrical energy and performance situations, MFCs have seen tremendous change in the previous several decades. MFCs are one of the electro-microbiology resources. It is capable of having a lower impact on the environment and causing less pollution, presenting various innovative technologies, having a lower cost influence, and so on. Bio-MFCs are highly capable of biotic microorganisms with suitable clean and bearable features.

Energy production from bio-waste is an important area of research that has gained increasing attention in recent years. Bio-waste can be defined as any organic waste material that is generated from agricultural, industrial, or municipal activities, which can be used as a feedstock for the production of energy.

One important aspect of bio-waste energy production is the use of electrodes and temperature conditions to enhance the efficiency of the conversion process. Electrodes can be used to facilitate the transfer of electrons in microbial processes, such as anaerobic digestion, while temperature conditions can influence the rate of biochemical reactions that are involved in the conversion of bio-waste into energy.

## 2 Literature Review

Mounika et al. [1] have studied and investigated the use of different types of catalysts for better performance through electrochemical electricity. Using a better quality catalyst, they obtained maximum power density and increased solution conductivity. Kai et al. [2] have shown that microbial alliances are an important factor in the surface of the MFC anode, organic compounds, and power generation. Mohan et al. [3] have studied ammonium removal with success in an MFC. When this method is used, it increases the flow of electrons and current generation. Aliraeza et al. [4] have used carbon nanotubes (CNTs) as a prospective collection device that can be used alone for physical and electrical properties. The MFC department strictly adheres to the bio-source recovery and minimum theoretical limit energy production requirements. Moreover, the authors have studied the current research to separate and screen potential biological power generation and biological plant diseases from tea plantation clay samples held in MFC waste. After some time, obtain the maximum voltage at room temperature. Chih et al.'s [5] work has led to the development of an innovative bio-trickling microbial fuel cell. Power production and venting of ethyl acetate (EA) from gas flow and voltage are increased. Haixia et al. [6] have studied incontestably the aptitude of MFC for more useful treatment with potato slurry and more efficient power generation. Nannan et al. [7] have shown that stacked connections of MFCs are an effective way to increase the performance of the MFCs' electrical output. This study tested a glycerol-driven self-stacking submerged MFC to gain large, more efficient voltage reaches and increase the current density. Mohan et al. [8] discovered that the salt bridge MFC is the most basic bio-fuel cell that can be designed and

studied. To maximize MFC power generation, all of these factors must be optimized. Carlo and colleagues [9] investigated electro-active biofilms and electron transfer mechanisms involving solid electrodes. The final category is MFCs, which describe the actual implementation of energy output. Nur et al. [10] investigated MFCs as a new method of obtaining electrical energy from biochemical waste. While removing some chemicals from wastewater, highly efficient power was obtained. Dongdong et al. [11] investigated MFCs with graphite electrodes and discovered that they have a high current efficiency in comparison to the other metal, platinum, with a low catalyst cathode. Hanyu et al. [12] investigated another process for electrochemical decomposition using electrochemical bacteria on MFCs. Biocatalysts are enzymes that decompose organic matter while producing bioelectricity. The concentration of COD in wastewater was found to have the greatest impact on performance by Weihua et al. [13]. It had a significant impact on power generation but had no effect on COD removal rates. Rusli et al. [14] used bio-cathode material to improve bio-electrochemical mechanisms and improve MFC performance. Compare the performance of bio-cathodes in MFCs for bioelectricity generation and wastewater treatment. Zainab and Ismail [15] worked in a dual-chamber MFC to create electricity by processing sewage water from potato chips. Chen et al. [16] developed a chemical formula for poly-pyrrole nanowires, which were used as anodes to obtain the best electrical parameters from MFCs. Walter et al. [17] investigated various types of electrolytes immersed at various heights and fueled with human urine. Among the various heights obtained are the cathode and overall performance.

Wenfang et al. [18] investigated ILP-coated carbon electrodes designed for microorganism habitats and found that they significantly improved current performance in MFCs. Seokheun [19] studied recent advances in electronic microbiology from the study of MFCs and discovered a more reliable sewage treatment method. Liu et al. [20] created a high-performance tungsten carbide electrode for a MFC with free atmospheric causes. Tungsten carbide has good biocompatibility, is inexpensive, and has a high conductivity [21].

The authors have done work in the present study and the following points are given to show the novelty as (i) different anode and cathode materials are used to explore the performance of bio-fuel cell in terms of electrical parameters. (ii) Temperature variation is one of the important aspects to obtain the system performance.

Section 1 explored the introduction of the present study. Literature review is given in Sect. 2. Furthermore, Sect. 3 is dedicated to experimental setup and wastewater samples. Section 4 explores about the results and discussion. In last, Sect. 5 concludes the study.

### 3 Experimental Setup

#### 3.1 System Description

In this designed MFC's setup, one and two plastic containers (900 ml) are used for the cathode electrode, which is used as a zinc electrode (Zn), an aluminum electrode (Al), and a copper electrode (Cu), and for the anode electrode, which is used as carbon (C), and different types of bio-waste from various locations. The copper wire serves as a connecting wire between the electrodes of MFCs. A wire is generally used because of its higher conductivity and good mechanical strength. It is used for varying mechanical and electrical parameter loads. The multimeters used here are the voltmeter and ammeter for the measurement of voltage and current on the MFC model. A typical multimeter is used to measure voltage, current, and resistance during experimentation. Infrared thermometer, digital (measurement range:  $-50$ – $380$  °C, display resolution:  $0.1$  °C). The layout of the experimental setup is shown in Fig. 1a.

#### 3.2 Electrode Used

MFC is employed with various electrodes that are used to generate electrical energy from sediment that has organic and inorganic matter, i.e., aluminums and copper, zinc and carbon, and copper and carbon. Figure 1b depicts various electrodes used in the study.

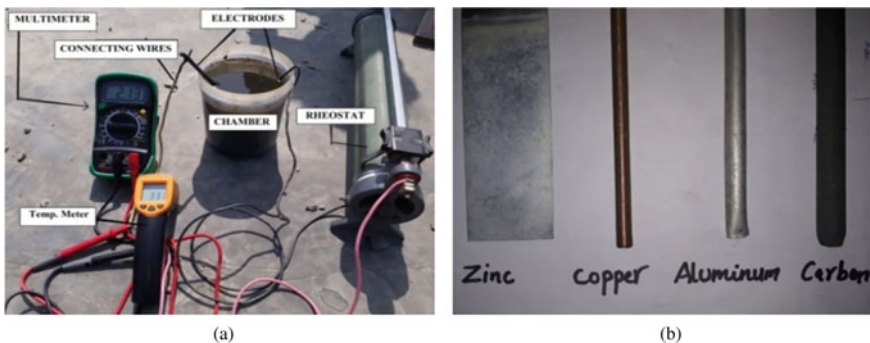


**Fig. 1** a Experimental setup b types of electrodes



### **3.3 Waste Material Sewage Sludge**

This waste sewage sludge material is obtained from the municipal and authorized storage wastewater plants and is usually treated with calcium hydroxide ( $\text{CaOH}_2$ ) stabilization, coagulation, flocculation, sedimentation, some ion exchangers, etc. As with the electron exchanger process, the single-chamber MFC with sewage sludge helps generate electricity, and microorganisms play an important role in breaking down the excess sludge.

### **3.4 Waste Material Slurry Water**

Slurry water is obtained from the thin mixture of liquid in contaminated and wastewater. Some microorganism sludge is mostly found in domestic waste, restaurants, rice water, beverage plants, and the bleaching industry. In addition, other changes in pH, moisture, and temperature, such as surfactants and disinfectants, help to grow microbial areas and also increase the biodegradability of waste.

## **4 Results and Discussion**

When attempting to sketch the characteristics of voltage and current with regard to time, it is vital to have both the measured voltage and current of the MFC along with their changes. During the course of the research, the load has acted as a  $4 \Omega$  resistance.

### **4.1 MFC Performance with Sewage Sludge Wastage**

#### *(i) Effect of Time and Temperature with Copper and Carbon Electrodes*

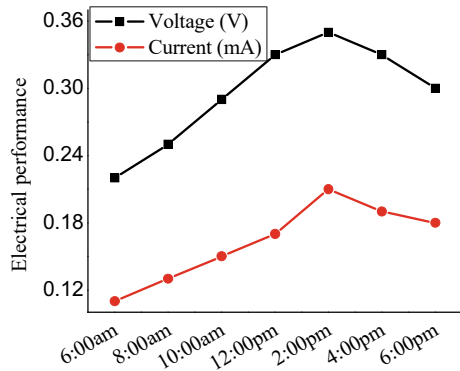
The voltage and current characteristics vary with respect to time and temperature at different levels. The obtained quantitative results at different time and temperature values are shown in Table 1, and electrical performance in terms of voltage and current with respect to time is shown in Fig. 2 as follows.

From the obtained result, it is observed that the system started its work at a temperature of  $15.3^\circ\text{C}$  and the minimum voltage and current of  $0.22\text{ V}$  and  $0.11\text{ mA}$ , respectively. The temperature was increased up to  $26.9^\circ\text{C}$  and the maximum voltage and current of  $0.35\text{ V}$  and  $0.21\text{ mA}$ , respectively. At the end of the day, when the temperature was  $24.3^\circ\text{C}$ , the voltage and current were decreased again to  $0.30\text{ V}$  and  $0.18\text{ mA}$ , respectively.

**Table 1** Electrical performance and temperature

Time (h)	Voltage (V)	Current (mA)	Temp. (°C)
6:00 am	0.22	0.11	15.3
8:00 am	0.25	0.13	18.6
10:00 am	0.29	0.15	20.5
12:00 pm	0.33	0.17	23.7
2:00 pm	0.35	0.21	26.9
4:00 pm	0.33	0.19	25.6
6:00 pm	0.30	0.18	24.3

**Fig. 2** Voltage and current analysis (copper and carbon electrodes)



(ii) *Effect of Time and Temperature with Zinc and Carbon Electrodes*

At different levels, the voltage and current characteristics change with time and temperature. Table 2 shows the quantitative results obtained at various time and temperature values, and Fig. 3 shows the electrical performance in terms of voltage and current with respect to time.

The system began working at a temperature of 15.3 °C and provided the minimum voltage and current, 0.26 V and 0.31 mA, as shown in the plot above. The temperature is raised to 26.9 °C, and the maximum voltage and current, 0.52 V and 0.42 mA, are

**Table 2** Electrical performance at different temperatures

Time (h)	Voltage (V)	Current (mA)	Temp. (°C)
6:00 am	0.26	0.31	15.3
8:00 am	0.29	0.33	18.6
10:00 am	0.35	0.35	20.5
12:00 pm	0.46	0.37	23.7
2:00 pm	0.52	0.42	26.9
4:00 pm	0.44	0.39	25.6
6:00 pm	0.39	0.34	24.3

**Fig. 3** Voltage and current performance (zinc and carbon electrodes)

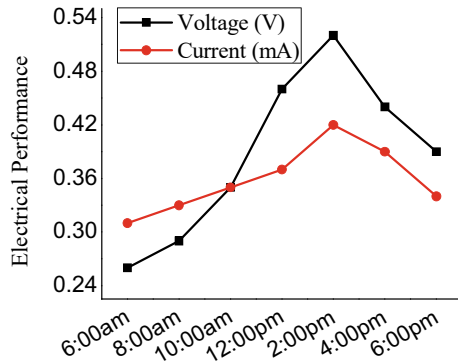


**Table 3** Electrical performance at different temperature

Time (h)	Voltage (V)	Current (mA)	Temp. (°C)
6:00 am	0.35	0.31	15.3
8:00 am	0.45	0.33	18.6
10:00 am	0.52	0.35	20.5
12:00 pm	0.58	0.39	23.7
2:00 pm	0.65	0.45	26.9
4:00 pm	0.59	0.41	25.6
6:00 pm	0.53	0.38	24.3

provided. When the temperature reached 24.3 °C at the end of the day, the voltage and current were reduced to 0.39 V and 0.34 mA, respectively.

(iii) *Effect of Time and Temperature with Aluminum and Carbon Electrodes*

Voltage and current characteristics change with time and temperature at different levels. Table 3 displays the quantitative results obtained at various time and temperature values, and Fig. 4 depicts the electrical performance in terms of voltage and current as a function of time.

**4.2 MFC Performance with Slurry Water Wastage**

(i) *Effect of Time and Temperature with Copper and Carbon Electrodes*

At various levels, voltage and current characteristics change with time and temperature. Table 4 shows the quantitative results obtained at different time and temperature values, and Fig. 5 shows the electrical performance in terms of voltage and current as a function of time.

**Fig. 4** Voltage and current performance (aluminum and copper electrodes)

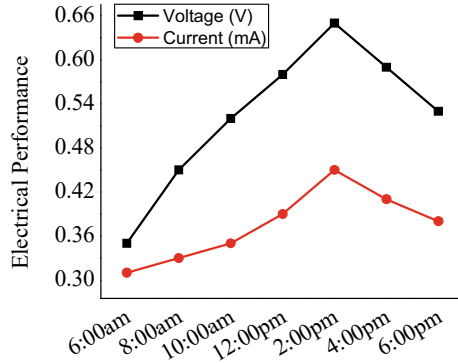
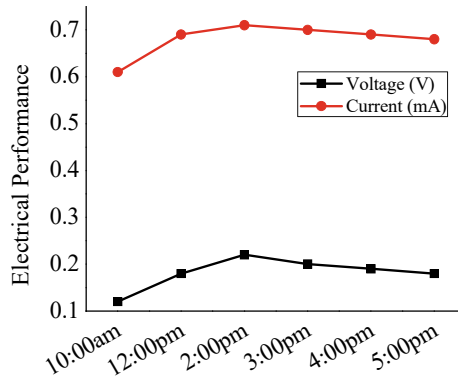


**Table 4** Electrical performance at different temperatures

Time (h)	Voltage (V)	Current (mA)	Temp. (°C)
10:00 am	0.12	0.61	28
12:00 pm	0.18	0.69	33
2:00 pm	0.22	0.71	36
3:00 pm	0.20	0.70	35
4:00 pm	0.19	0.69	35
5:00 pm	0.18	0.68	34

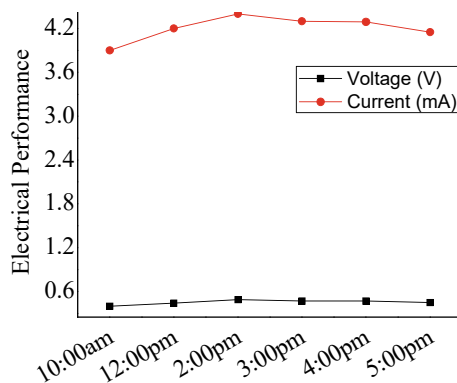
**Fig. 5** Voltage and current performance (copper and carbon electrodes)



The system began working at a temperature of 28 °C and provided the minimum voltage and current, 0.12 V and 0.61 mA, as shown in the plot above. The temperature is raised to 36 °C, and the maximum voltage and current, 0.22 V and 0.71 mA, are provided. When the temperature reached 34 °C at the end of the day, the voltage and current were reduced to 0.18 V and 0.68 mA, respectively.

**Table 5** Electrical performance at different temperatures

Time (h)	Voltage (V)	Current (mA)	Temp. (°C)
10:00 am	0.40	3.9	28
12:00 pm	0.44	4.2	33
2:00 pm	0.49	4.4	36
3:00 pm	0.47	4.3	35
4:00 pm	0.47	4.29	35
5:00 pm	0.45	4.15	34

**Fig. 6** Voltage and current analysis (copper and aluminum electrodes)

## (ii) Effect of Time and Temperature with Copper and Aluminum Electrodes

Voltage and current characteristics change with time and temperature at different levels. Table 5 displays the quantitative results obtained at various time and temperature values, and Fig. 6 depicts the electrical performance as a function of time in terms of voltage and current.

The system began working at a temperature of 28 °C and provided the minimum voltage and current, 0.40 V and 3.9 mA, as shown in the plot above. The temperature is raised to 36 °C, and the maximum voltage and current, 0.49 V and 4.4 mA, are provided. When the temperature reached 34 °C at the end of the day, the voltage and current were reduced to 0.45 V and 4.15 mA, respectively.

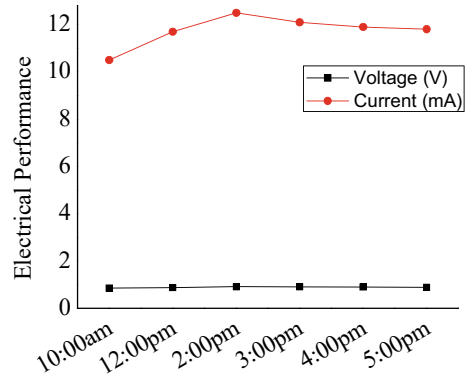
## (ii) Effect of Time and Temperature with Copper and Zinc Electrodes

Table 6 shows the electrical performance in terms of voltage and current as a function of time in Fig. 7, which shows the electrical performance in terms of voltage and current as a function of time.

**Table 6** Compare voltage and current at different times and temperatures

Time (h)	Voltage (V)	Current (mA)	Temp. (°C)
10:00 am	0.86	10.5	28
12:00 pm	0.88	11.7	33
2:00 pm	0.92	12.5	36
3:00 pm	0.91	12.1	35
4:00 pm	0.90	11.9	35
5:00 pm	0.89	11.8	34

**Fig. 7** Voltage and current response (copper and zinc electrodes)



## 5 Conclusion

An MFC has the capability to produce power from various types of sewage water. Electrical parameters are obtained by observing the various effects of the four types of electrodes on the self-assembled experimental setup of MFC at different temperatures and times. A detailed examination of the physical properties of the metal electrode, as well as the obtained results in voltage and current characteristics, demonstrates the performance of the MFC. Following the note, the results of this study are summarized as follows:

- In the investigation, copper and aluminum electrodes generated the maximum voltage and current.
- In the case of zinc and copper electrodes, their performance is less affected by microbial fuel cells (MFCs) compared to copper and aluminum electrodes.
- Compared to other metals, copper and carbon electrodes produce very little voltage and current.
- The amount of electricity generated in the MFC is directly dependent on the rate of bacterial metabolic reactions and the anode and cathode surface areas.

## References

1. Mounika K, Carlo S, Alexey S (2017) Air breathing cathodes for microbial fuel cell using Mn-, Fe-Co and Ni containing platinum group metal-free catalyst. *Electrochim Acta* 231:115–124
2. Kai C, Jingping H et al (2017) Aerobic granular sludge inoculated microbial fuel cells for enhanced epoxy reactive diluent wastewater treatment. *Bioresour Technol* 229:126–133
3. Mohan Q, Ibrahim M, Abu R, Zhen H (2016) Effects of current generation and electrolyte pH on reverse salt flux across thin film composite membrane in osmotic microbial fuel cells. *Water Res* 105:583–590
4. Aliraeza YA, Lorenzo AD et al (2016) Carbon nanotube modification of microbial fuel cell electrodes. *Biosens Bioelectron* 85:536–552
5. Chih WH, Jing SC, Chi LW (2016) Continuous production of power using microbial fuel cells with integrated biotrickling filter for ethyl acetate-contaminated air stream treatment. *Int J Hydrogen Energy* 4:21945–21954
6. Haixia D, Fusheng L (2016) Effects of varying the ratio of cooked to uncooked potato on the microbial fuel cell treatment of common potato waste. *Sci Total Environ* 42:541–849
7. Nannan Z, Irini A, Yifeng Z (2017) Electricity generation and microbial community in response to short-term changes in stack connection of self-stacked submersible microbial fuel cell powered by glycerol. *Water Res* 109:367–374
8. Mohan Y, Kumar MMS, Das D (2008) Electricity generation using microbial fuel cells. *Int J Hydrogen Energy* 33:423–426
9. Carlo S, Catia A, Benjamin E, Ioannis I (2017) Microbial fuel cells: from fundamentals to applications: a review. *J Power Sources* 356:225–244
10. Nur HNS, Shahrom ZM et al (2013) Microbial fuel cell using different types of waste water for electricity generation and simultaneously removed pollutant. *J Eng Sci Technol* 8(3):316–325
11. Dongdong Z, Zhiling L et al (2017) Phenol degrading anode bio-film with high coulombic efficiency in graphite electrodes microbial fuel cell. *J Biosci Bioeng* 123(3):364–369
12. Hanyu W, Fang Q, Yat L (2014) Solar assisted microbial fuel cells for bioelectricity and chemical fuel generation. *Nano Energy* 8:264–273
13. Weihua H, Maxwell WJ et al (2016) The effect of flow modes and electrode combinations on the performance of a multiple module microbial fuel cell installed at wastewater treatment plant. *Water Res* 105:351–360
14. Rusli NFS, Bakar AHM et al (2019) Review of high performance biocathode using stainless steel and carbon based material in microbial fuel cells for electricity and water treatment. *Int J Hydrogen Energy* 44:30772–30787
15. Zainab RYAZ, Ismail (2019) Polarization model of microbial fuel cell for treatment of actual potato chips processing wastewater associated with power generation. *J Electroanal Chem* 836:176–181
16. Chen Y, Zhao Z, Weng Z, Joang H (2019) Performance study of polypyrrole-nanowires based microbial fuel cells. In: *Proceedings of IEEE international conference on circuit, system and simulation*, pp 1–6
17. Walter AX, Carlo S, Geenman J, Ioannis I (2019) Self stratifying microbial fuel cell: the importance of the cathode electrode immersion height. *Int J Hydrogen* 44:4524–4532
18. Lu Y, Wenfang D, Yueming T et al (2017) Boosting current generation in microbial fuel cells by an order of magnitude by coating an ionic liquid polymer on carbon anodes. *Biosens Bioelectron* 91:644–649
19. Seokheun C (2015) Microscale microbial fuel cells: advances and challenges. *Biosens Bioelectron* 69:8–25
20. Liu D, Chang Q, Gao Y, Huang W, Sun Z, Yan M, Guo C (2020) High performance of microbial fuel cell afforded by metallic tungsten carbide decorated carbon cloth anod. *Electrochim Acta* 330:1–11

21. Tomar A et al (eds) (2022) Proceedings of 3rd international conference on machine learning, advances in computing, renewable energy and communication (MARC 2021), vol 915. Springer, Berlin, 781pp. ISBN: 978-981-19-2830-7. <https://doi.org/10.1007/978-981-19-2828-4>



# Simulation and Prototype Design of Hybrid Renewable Energy Harvesting System



Yanuar Z. Arief, Muhammad Syukri Nurulhak, and Hamzah Eteruddin

**Abstract** In this era of globalization, the energy harvesting technology for renewable energy has improved to combat the concerns about energy conservation, global warming, and excessive waste materials. Additionally, the problem of getting continuous and reliable energy and power supply will become a real issue in the future. The energy harvesting technology can be an alternative to the current power generation and can lead to the potential of getting a more reliable power supply for everyone. By combining multiple renewable energy harvesting systems, more power can be continuously generated, and the efficiency of energy output will increase. This paper focuses on the development of a hybrid renewable energy harvester system consisting of photovoltaic, piezoelectric, and wind energy. The system's performance and capabilities are recorded and analyzed under different conditions and parameters.

**Keywords** Energy harvester · Hybrid renewable energy · Photovoltaic · Piezoelectric · Wind energy · Power supply

## 1 Introduction

Energy harvesting refers to the harnessing of readily available energy from the surrounding into electrical energy [1]. Some of the energy harvesting technology covers the conversion of light, kinetic, thermal, and radio frequency via various mechanisms such as photovoltaic, piezoelectric, and thermoelectric [2]. The electrical energy gathered can be used directly or stored for later use. The energy harvesting

---

Y. Z. Arief (✉) · M. S. Nurulhak

Faculty of Engineering, Department of Electrical and Electronic Engineering, Universiti Malaysia Sarawak (UNIMAS), Kota Samarahan, Sarawak, Malaysia

e-mail: [ayzulardiansyah@unimas.my](mailto:ayzulardiansyah@unimas.my)

H. Eteruddin

Faculty of Engineering, Department of Electrical Engineering, Universitas Lancang Kuning (UNILAK), Rumbai, Riau Province, Indonesia

e-mail: [hamzah@unilak.ac.id](mailto:hamzah@unilak.ac.id)

© The Author(s), under exclusive license to Springer Nature Singapore Pte Ltd. 2024

271

H. Malik et al. (eds.), *Renewable Power for Sustainable Growth*,

Lecture Notes in Electrical Engineering 1086,

[https://doi.org/10.1007/978-981-99-6749-0\\_16](https://doi.org/10.1007/978-981-99-6749-0_16)

technology can be an alternative for places with no power grid or places that are not suitable for solar panels and wind turbine installation. Energy harvesting also has become one of the most-rapid growing technologies in the current year. It is estimated that the market size of energy harvesting can reach up to USD 817.2 Million by 2026 [3]. The motivation for adopting the energy harvesting technology for renewable energy comes from the concern about energy conservation, global warming, and excessive waste materials.

However, the energy harvested is in small amounts and adequate for low-power applications such as remote sensing, body implants, and most wireless applications [4]. For start, some of the IoT devices can integrate the energy harvester system for their sustainability since it can be operated at low power. The Internet of Things or IoT can be described as billions of physical devices that are linked to the Internet to connect and exchange data [5, 6]. IoT devices can be everything if it connected to the Internet and can be interacted with or controlled. It can be as small as switching on the lamps using a smartphone application or exchanging massive data back and forth using thousands of sensors for the monitoring system.

The self-sustainable operation of IoT devices is one of the main importance that has been discussed by many researchers. For long-term accessibility, the usage of a disposable battery can be ignored, and it can be charged by itself. The energy harvesters are divided into four groups that are based on their power output, which is high power (more than 2–10 W), medium power (between 1 and 10 W), low power (between 1 mW and 1 W), and ultra-low power (below 1 mW) [7–11]. From the low-power devices, the energy harvesting system can move on to powering up the medium to high-power devices. This can lead to the integration of energy harvesting technology into various industries such as transportation, automotive, power generation, and more. There are already some existing energy harvesting devices and applications such as photovoltaic solar energy at rooftops that convert light into electric energy or use wind energy to convert mechanical energy to electrical energy [11].

This paper presents the study of four types of energy harvesters which are photovoltaic, piezoelectric, thermoelectric, and radio frequency. The energy harvester will be combined and merged to create a hybrid energy harvester. The energy harvester will be tested using simulation, and some of them will be implemented into hardware design depending on the availability and convenience.

## 2 Research Method

### 2.1 *Simulation of Hybrid Renewable Energy Harvesting System*

Figure 1 shows the process flowchart for MATLAB simulation for this project. It is divided into two parts, which are for photovoltaic energy harvester and wind energy harvester simulation.

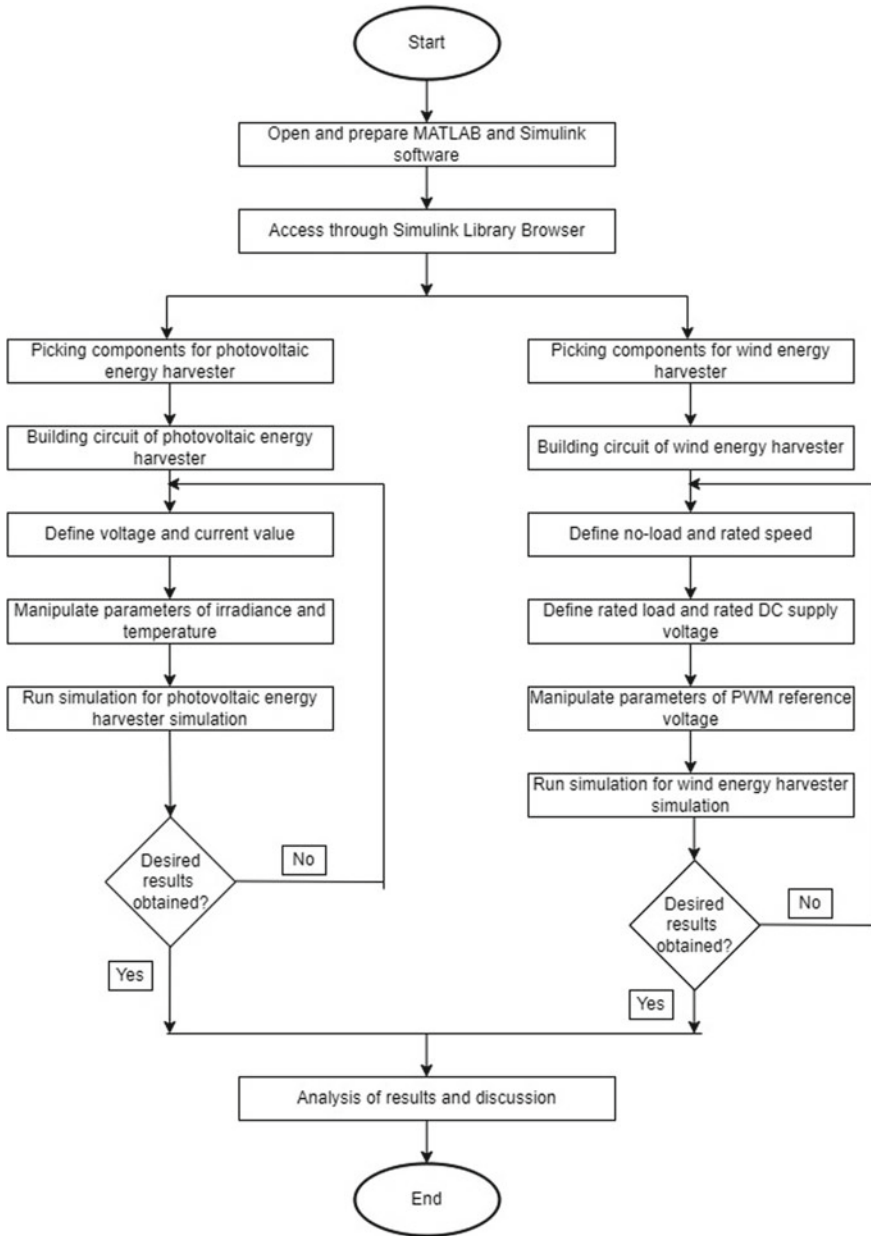


Fig. 1 Flowchart for MATLAB simulation of energy harvesting system

The renewable hybrid energy harvesting system can be simulated using MATLAB. MATLAB is a programming software designed for scientists and engineers to design, simulate, and analyze systems. It contains another add-on software called Simulink which is a graphical programming environment for modeling and simulating that will be used for this project.

Simulink is important software that can do modeling, coding, simulation, and analysis at the same time. It has a user-friendly interface that is easy to navigate and has modern look compared to other software. Simulink also provides a wide variety of hardware components and libraries that can be accessed and used for this project. Photovoltaic, piezoelectric, and wind energy can be designed with the libraries provided and simulated at the same time. Moreover, it can run large-scale simulations without a problem.

Simulink also can pinpoint the error made in the design and help the user by providing a guide. The results of the simulation can be represented in two ways which are graph and number. Users can control the output and results by altering the parameters in the model design. This versatility gives freedom to the user to modify the design and result as the user wanted in Simulink.

## ***2.2 Prototype of Hybrid Renewable Energy Harvesting System***

Figure 2 shows the process flowchart for the hardware prototype for this research work. It is divided into three parts, which are a photovoltaic energy harvester, a piezoelectric energy harvester, and a wind energy harvester.

For the hardware prototype, three renewable energy harvesters will be used which are photovoltaic, wind energy, and piezoelectric. The three renewable energy harvesters will be connected in parallel to the energy storage. The INA219 sensor module is integrated into each of the renewable energy harvesters to measure the current and voltage output of the energy harvesters. The piezoelectric utilized rectifier because the output current is in AC. Each of the sensor modules will send the information to Arduino Uno to display the information through an LCD monitor.

On the other hand, the energy storage uses a lithium-ion battery with TP4056 module integration. The TP4056 is important to charge and protect the battery during and after the charging is completed. At the same time, the battery with TP4056 will also manage to power up the Arduino Uno. Then, the power will go battery and to the load directly. Figure 3 shows the overall block diagram for the hybrid renewable energy harvesting system prototype. Figure 4 shows the prototype circuit of the hybrid renewable energy harvesting system, while Fig. 5 shows the actual representation of similar flow components.

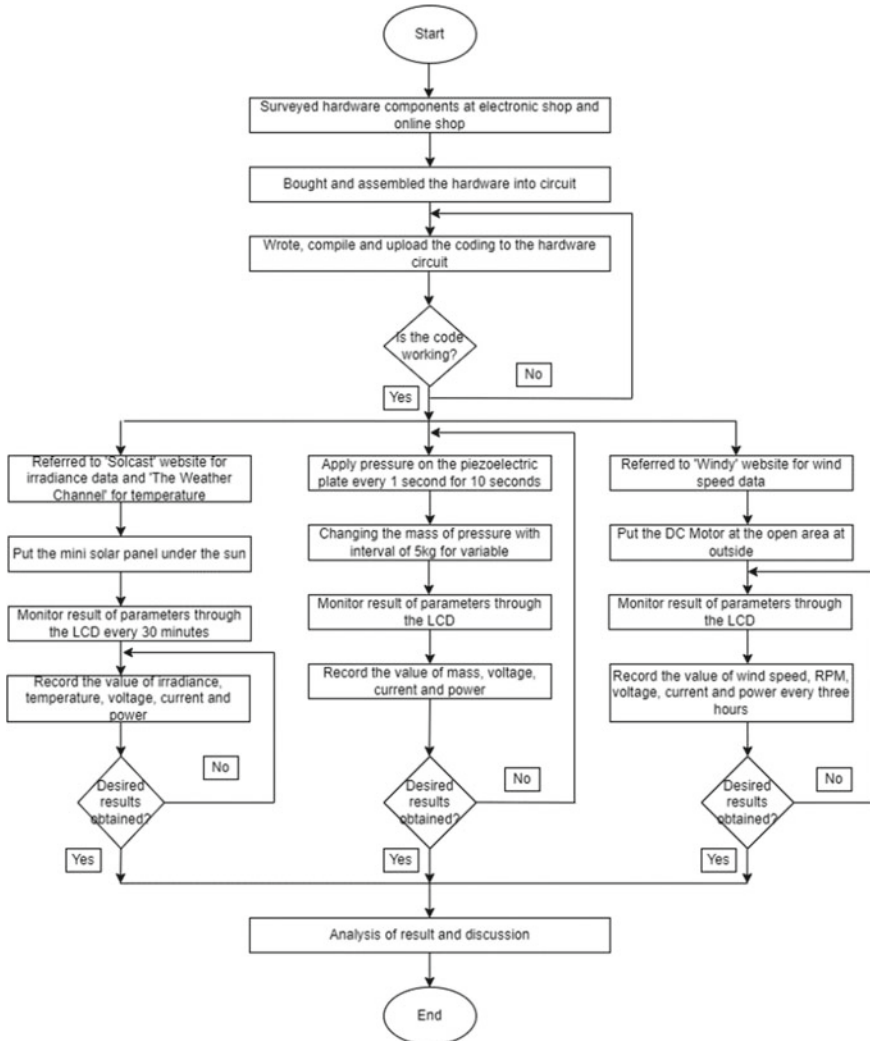


Fig. 2 Flowchart for the hardware of the energy harvesting system prototype

### 3 Results and Discussion

The circuit was tested individually to show the output results for each renewable energy harvester. The results consist of the output values of the simulation such as current, voltage, power output, and energy. The parameters of the circuit are changing to show that the circuit is working as intended with certain specifications. The specification of both energy harvesters was made close to the hardware of the

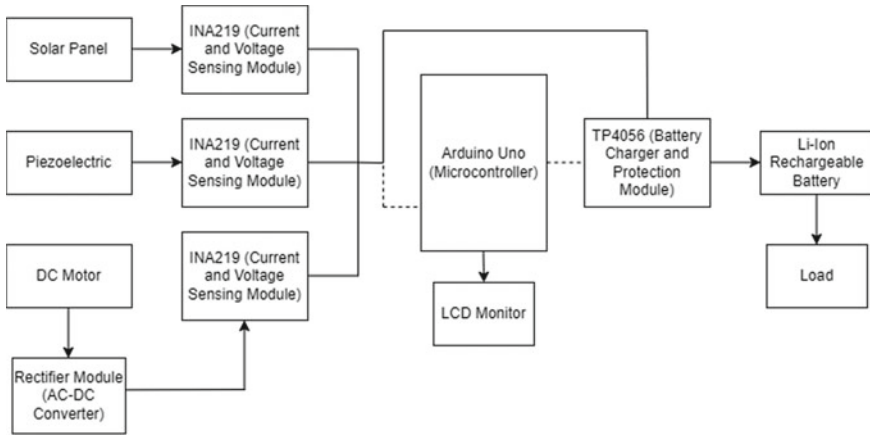


Fig. 3 Block diagram for the prototype of a hybrid renewable energy harvesting system

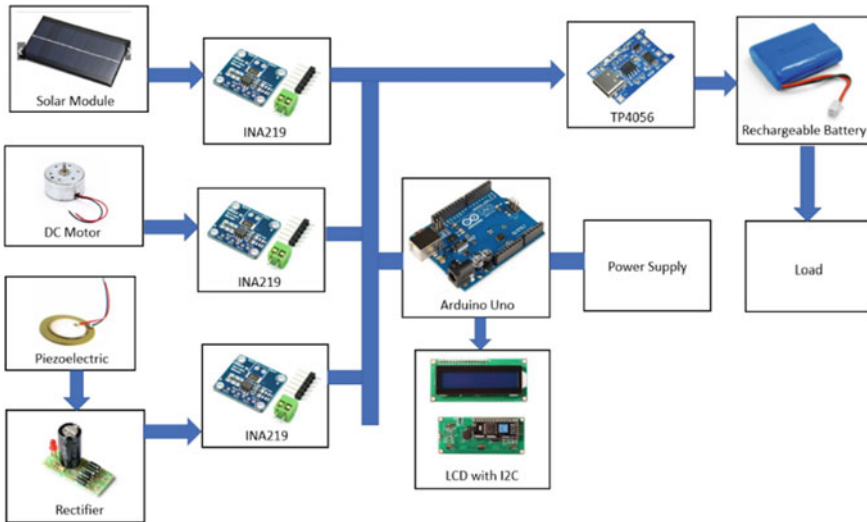


Fig. 4 Conceptual design of the actual project prototype

prototype. Figures 6 and 7 show the circuit for simulation of the photovoltaic energy harvester and wind energy harvester, respectively.

The results of the hardware prototype of photovoltaic, piezoelectric, and wind energy harvesters are also shown and discussed. For photovoltaics, the results of the hardware prototype were compared with the simulation based on the irradiance. The three-day results for photovoltaics were also compared with each other to show the effect of weather conditions.

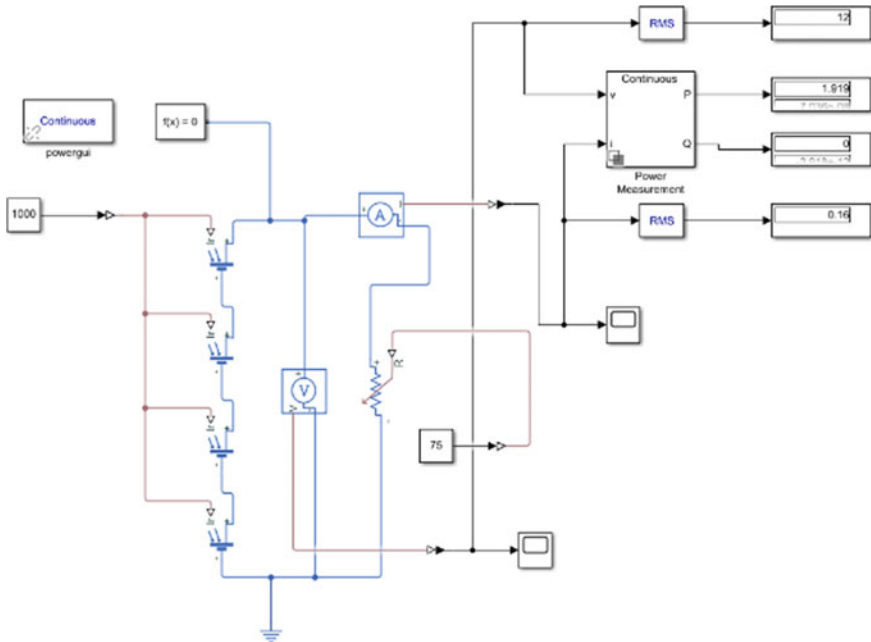


Fig. 5 Circuit for simulation of photovoltaic energy harvester

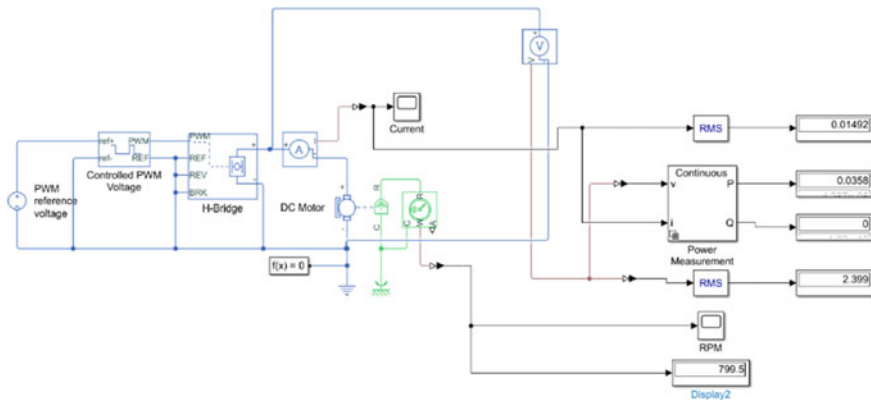


Fig. 6 Circuit for simulation of wind energy harvester

For the piezoelectric energy harvester, different mass of pressure was applied on the piezoelectric plate for 10 s with an interval of 1 s for each pressure. The result for each different mass was compared with each other. For the wind energy harvester, the results of the hardware prototype were compared with the simulation based on the RPM of the DC motor. After that, all the hardware prototype results are combined to show the continuity of the hybrid renewable energy harvester to continue harvesting

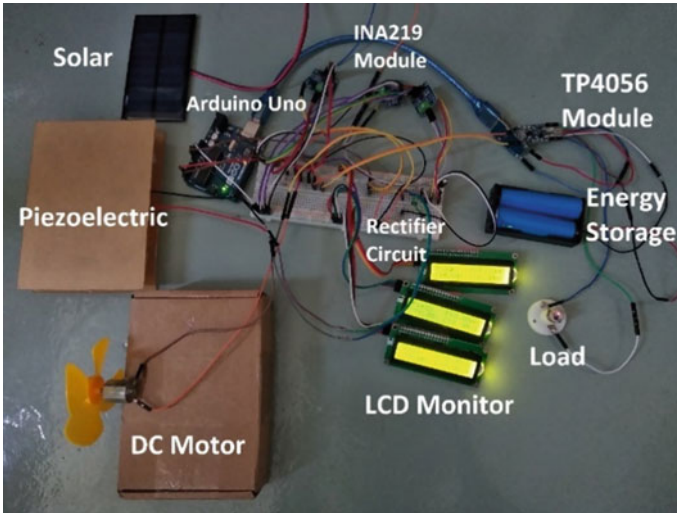


Fig. 7 Completed circuit for the prototype of the hybrid renewable energy harvester

energy throughout the day. Figure 7 shows the completed circuit for the prototype of the renewable energy harvester.

### 3.1 Simulation Results of Photovoltaic Energy Harvester

The results for photovoltaic simulations are shown in Tables 1 and 2. For this photovoltaic simulation, two simulations were run with different parameters setting. The first simulation ran with fixed temperature and the second simulation ran with fixed irradiance. Two parameters can change the output of the photovoltaic which are irradiance and temperature.

Table 1 shows the first photovoltaic simulation with a fixed temperature of 25 °C. It is found that when the irradiance decreases, the power output also decreases. This

Table 1 Results of photovoltaic energy harvester simulation with fixed temperature

Irradiance (W/ m <sup>2</sup> )	Temperature (°C)	Current (A)	Voltage (V)	Power Output (W)	Energy (Wh)
1000	25	0.0800	6.000	0.4797	1726.92
800	25	0.0795	5.964	0.4742	1707.12
600	25	0.0789	5.918	0.4670	1681.20
400	25	0.0781	5.855	0.4570	1645.20
200	25	0.0766	5.744	0.4399	1583.64



**Table 2** Result of photovoltaic energy harvester simulation with fixed irradiance

Temperature (°C)	Irradiance (W/m <sup>2</sup> )	Current (A)	Voltage (V)	Power Output (W)	Energy (Wh)
25	500	0.0785	5.890	0.4625	1665.00
30	500	0.0783	5.869	0.4593	1653.48
35	500	0.0780	5.849	0.4562	1642.32
40	500	0.0777	5.830	0.4532	1631.52
45	500	0.0774	5.812	0.4504	1621.44

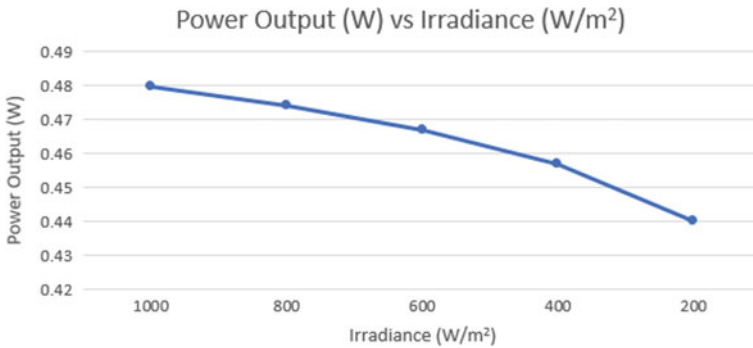


**Fig. 8** Graph of power output versus irradiance for photovoltaic energy harvester simulation

shows that when there is more radiant energy, it will create more output power. Irradiance directly affects the performance of solar cells. Figure 8 shows the downward trends of power output when the irradiance is decreased.

Table 2 shows the second photovoltaic simulation with fixed irradiance of 500 W/m<sup>2</sup>. It is found that when the temperature increases, the power output also decreases. The other parameters such as current and voltage are also decreasing. This shows that when the temperature of the solar cells increases, the solar panel efficiency is declining. Figure 9 shows the downward trends of power output when the temperature is increased.

### 3.2 Simulation Results of Wind Energy Harvester

To simulate the wind speed hitting the wind turbine, the PWM reference voltage is used as a variable value. When the PWM reference voltage increases, the turbine rotation is also increasing. Other than that, the other parameters such as current, voltage, and power output are also increasing as the turbine rotates faster. The power output is very small because it follows the small DC motor model with the lower

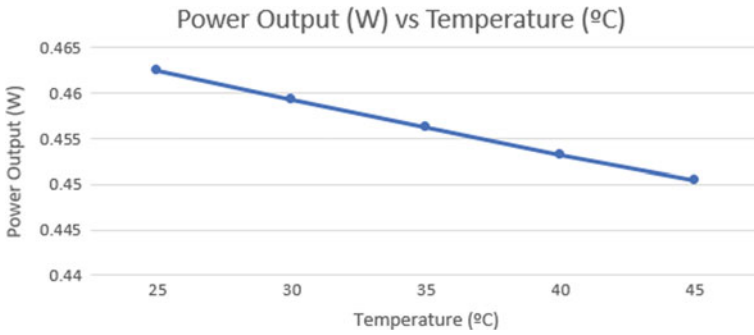


Fig. 9 Graph of power output versus temperature for photovoltaic energy harvester simulation

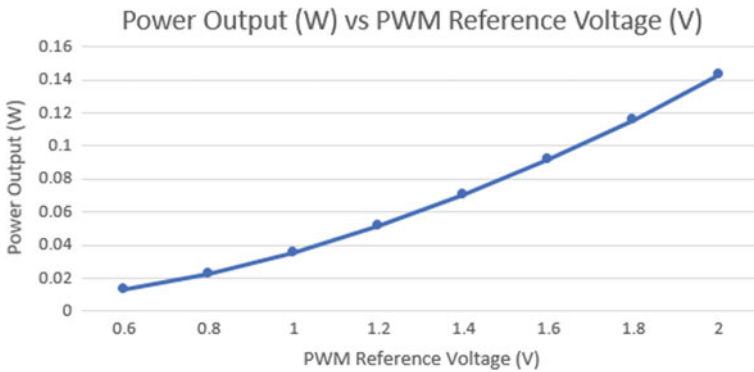


Fig. 10 Graph of power output versus PWM reference voltage for wind energy harvester simulation

specification that is used for the prototype. Figure 10 shows the upward trends of power output when the PWM reference voltage is increased.

### 3.3 Prototype Results of Photovoltaic Energy Harvester

For the prototype result of the photovoltaic energy harvester, the data collection was done for three days from 16/05/2022 until 18/05/2022. Each day had different weather conditions, which were cloudy, rainy, and sunny, respectively. For each day, the duration of data collection was from 07:00 a.m. until 6:30 p.m. which referred to the Solcast website’s active time.

As shown in Fig. 11, power output peaked two times at around 1230 and 1500 h. That is when the weather gets sunny, the sun irradiance peaks during that time. There is a dip in power output at around 1330 h when the weather gets very cloudy, so the sun irradiance cannot reach the solar panel at full coverage.

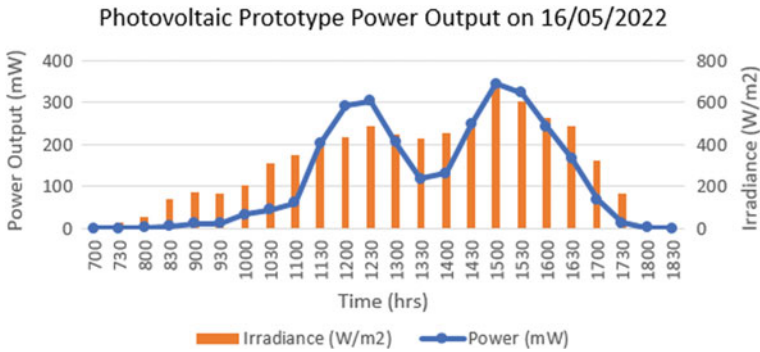


Fig. 11 Graph of power output from photovoltaic energy harvester prototype on 16/05/2022

The graph also shows that the irradiance correlates with the power output of the solar panel. The average irradiance for 16/05/2022 was 306.670W/m<sup>2</sup>. The peak output power was at 345.210 mW which gives around 1242.760 Wh of energy, and it happened at 1500 h with 675.000 W/m<sup>2</sup> irradiance. The average output power that was generated was 117.525 mW for an entire day, and the average energy produced was 423.092 Wh.

Figure 12 shows that power output peaked two times at around 1030 and 1530 h. The weather was still cloudy, but there was enough irradiance that made the power output peak during that time. There is a massive drop in power output and irradiance at around 1200 h due to dark clouds and rain. The condition continued until 1430 h when the rain stopped.

On 17/05/2022, the average irradiance for on was 246.750 W/m<sup>2</sup>. The peak output power was at 108.420 mW which gives around 390.300 Wh of energy, and it happened at around 1100 h with 588.000 W/m<sup>2</sup> irradiance, an hour before it started raining. The

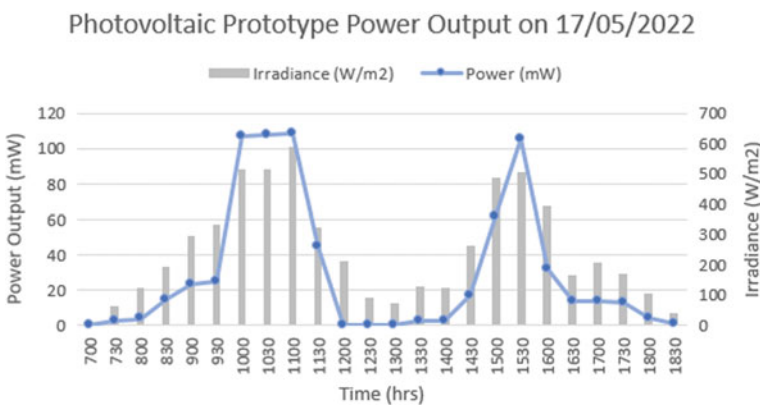
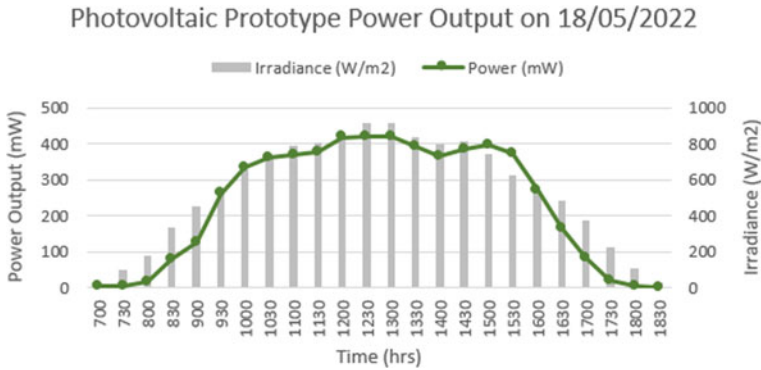


Fig. 12 Graph of power output from photovoltaic energy harvester prototype on 17/05/2022



**Fig. 13** Graph of power output from photovoltaic energy harvester prototype on 18/05/2022

average output power generated was 29.217 mW for an entire day, and the average energy produced was 105.181 Wh.

As shown in Fig. 13, the power output was consistent throughout the day according to the irradiance of the sun. The irradiance given stayed above 600 W/m<sup>2</sup> from 1100 to 1600 h and only went down slowly when the sun was also going down.

The average irradiance on 18/05/2022 was 537.875 W/m<sup>2</sup>. The peak output power was at 421.200 mW which gives around 1516.320 Wh of energy, and it happened at 1230 h with 918.000 W/m<sup>2</sup> irradiance. The average output power that was generated was 235.141 mW for an entire day, and the average energy produced was 846.508 Wh.

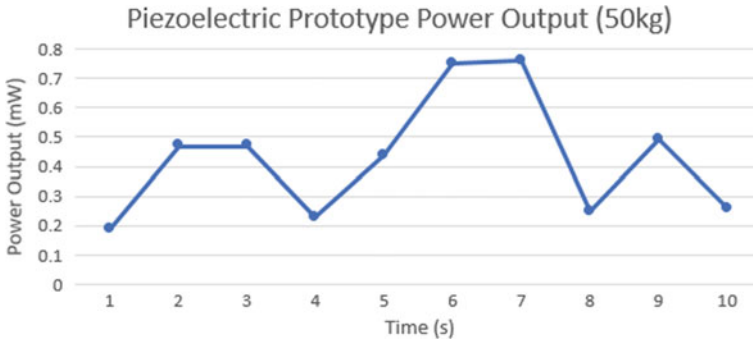
### 3.4 Prototype Results of Piezoelectric Energy Harvester

For the prototype result of the photovoltaic energy harvester, the data collection was done by applying different amounts of mass on the piezoelectric plate. Three people with each different masses of 50, 55, and 60 kg step on the piezoelectric plate, respectively. The amount of voltage, current, power, and energy was recorded.

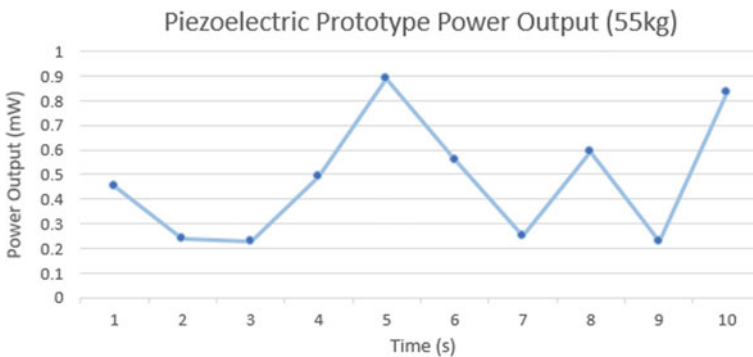
The obtained data show that the output parameters of piezoelectric energy when people with a mass of 50 kg applied the pressure on the piezoelectric plate by stepping on it for 10 s.

As shown in Fig. 14, the output power when 50 kg of mass was applied is fluctuating every second. The peak power output was 0.760 mW which gives around 2.740 Wh of energy. The average power output produced for 10 s is 0.431 mW, and the average energy produced is 1.551 Wh.

Figure 15 shows the output power when 55 kg of mass was applied is fluctuating every second. The peak power output was 0.890 mW which gives around 3.210 Wh of energy. The average power output produced for 10 s is 0.476 mW, and the average energy produced is 1.715 Wh.



**Fig. 14** Graph of power output from piezoelectric energy harvester prototype with 50 kg pressure



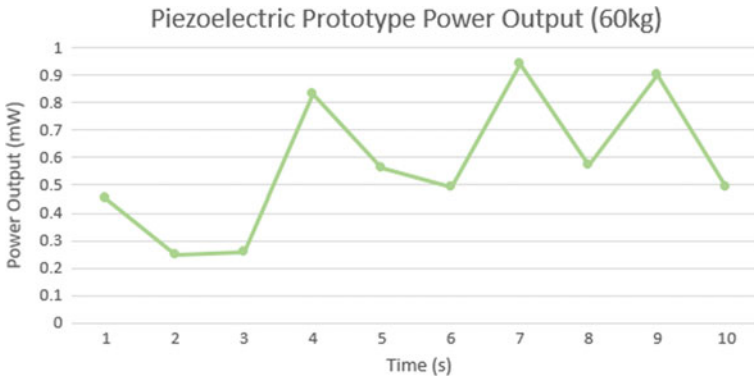
**Fig. 15** Graph of power output from piezoelectric energy harvester prototype with 55 kg pressure

Figure 16 shows the output power when 60 kg of mass was applied is fluctuating every second. The peak power output was 0.940 mW which gives around 3.370 Wh of energy. The average power output produced for 10 s is 0.574 mW, and the average energy produced is 2.064 Wh.

### 3.5 Prototype Results of Wind Energy Harvester

For the prototype result of the wind energy harvester, the data collection was done for 3 days from 16/05/2022 until 18/05/2022. The collection of data was done every 3 h for three days straight. The wind speed data was referred to the windy website. During this day, the wind is not too strong from early morning until night. There is a spike of high wind speed at around 0800 h with 10 km/h wind speed.

Figure 17 shows the power output peaked one time at around 0800 h. The wind speed is decreasing in the next 6 h until 1400 h, and thus, the output power is also



**Fig. 16** Graph of power output from piezoelectric energy harvester prototype with 60 kg pressure

decreasing. From 1700 h until 2300 h, the wind is at a constant 3 km/h which also gives constant power output at around 0.040 mW.

On 16/05/2022, the average wind speed was 4.875 km/h throughout the day. The peak output power was at 0.627 mW which gives around 2.257 Wh of energy, and it happened at around 0800 h with 10 km/h wind speed. The average output power that was generated was 0.180 mW for an entire day, and the average energy produced was 0.649 Wh.

Figure 18 shows the power output peaked two times at around 1400 and 2300 h. The first peak at 1400 h had a wind speed of 13 km/h, which is the highest throughout the day, and it gives a peak power output of 0.952 mW with a peak energy of 3.427 Wh. The second peak at 2300 h has a wind speed of 8 km/h, and it gives a power output of 0.408 mW with an energy of 1.469 Wh. At the other time, the wind speed is averaging between 3 and 4 km/h and gives around 0.070 mW of power output.

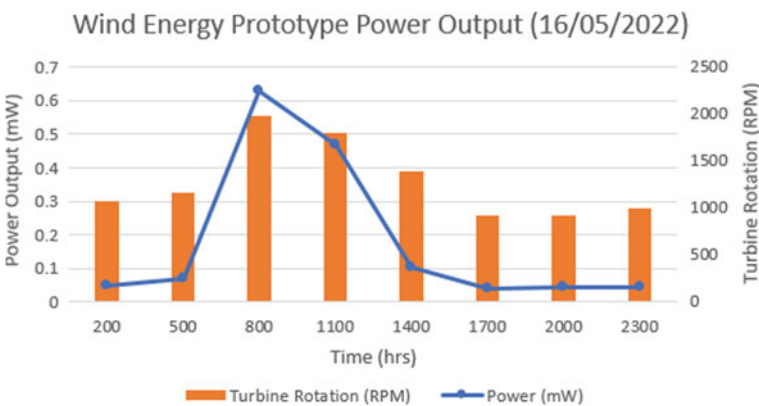


**Fig. 17** Graph of power output from wind energy harvester prototype on 16/05/2022

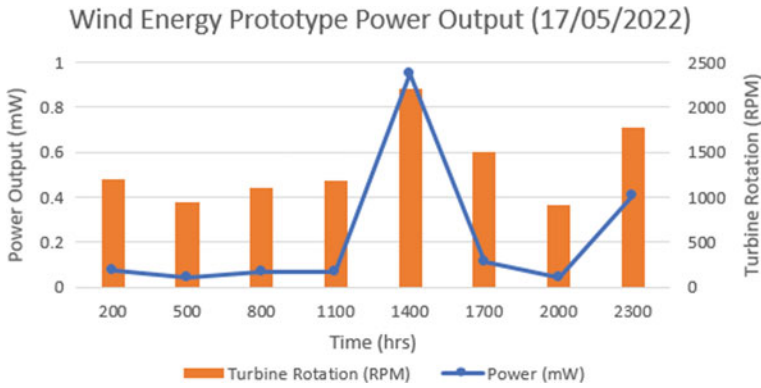
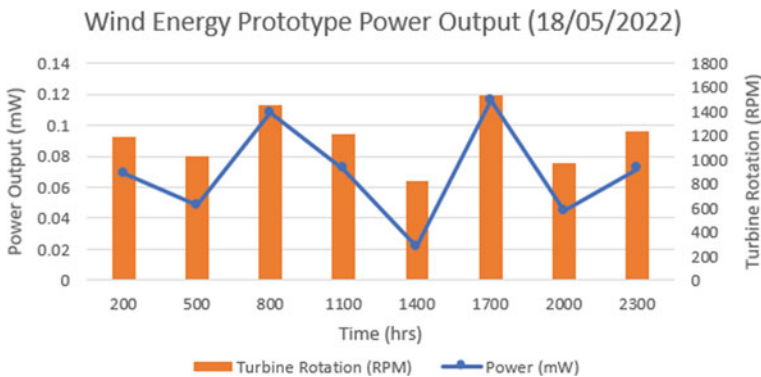


**Fig. 18** Graph of power output from wind energy harvester prototype on 17/05/2022

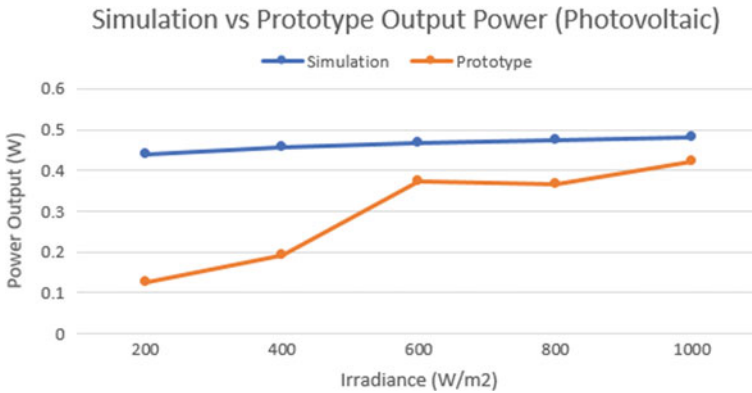
On 17/05/2022, the average wind speed was 5.625 km/h throughout the day. The average output power that was generated was 0.221 mW for an entire day, and the average energy produced was 0.795 Wh.

Figure 19 shows that no significant peak power output is outstanding since it is almost the same. However, there is little power output peaking two times at around 0800 and 1700 h. The first small peak at 0800 h is the second highest, which gave power output of 0.108 mW and 0.389 Wh energy. The second small peak occurred at 1700 h is the highest throughout the day, which gave power output of 0.116 mW and 0.418 Wh energy. At the other time, the wind speed is averaging between 3 and 4 km/h and gives around 0.070 mW of power output.

On 18/05/2022, the average wind speed was 3.875 km/h throughout the day. The average output power generated was 0.069 mW for an entire day, and the average energy produced was 0.2484 Wh.



**Fig. 19** Graph of power output from wind energy harvester prototype on 18/05/2022



**Fig. 20** Comparison between simulation and hardware results for photovoltaic energy harvester

### 3.6 Results Comparison of Photovoltaic Energy Harvester

Figure 20 shows that there are slight differences in power output against the irradiance for simulation and prototype. The value of power output for the prototype was taken by calculating the average power output of a certain value of irradiance from all the results.

At 200 W/m<sup>2</sup>, the prototype has lower power output than the simulation where it dropped below 0.1244 mW compared to 0.4399 mW. The value of power output for the prototype becomes closer to the simulation starting from 600 W/m<sup>2</sup>, where the power output is 0.3725 mW compared to 0.4670 mW at simulation. Continuing toward 800 and 1000 W/m<sup>2</sup>, the value of power output becomes stable and constant like the simulation even though it is slightly lower. At 1000 W/m<sup>2</sup>, there is a difference of 0.0580 mW between the simulation and prototype power output. From the comparison below, it is seen that the behavior of the prototype photovoltaic panel is that it is not very sensitive to the light at lower irradiance; hence, it generated low-power output. The photovoltaic panel worked more efficiently at higher irradiance value.

Figure 21 shows the comparison of power output for the prototype of a photovoltaic energy harvester for a three-day period which all have different weather conditions. The three weather conditions were cloudy, rainy, and sunny, respectively.

On 16/05/2022, it had the second-highest average power output at 117.53 mW and 423.00 Wh energy with an unstable pattern on the graph. Meanwhile, on 17/05/2022, it had the lowest average power output at 29.22 mW and 105.18 Wh energy. The pattern of the graph stayed at the below part, indicating that there is almost no irradiance to generate power output. Lastly, on 18/05/2022, it had the highest average power output with 235.15 mW and 846.51 Wh energy. The pattern of the graph is stable throughout the day indicating that it continuously gets irradiance and generates high-power output. From this comparison, it can be said that rainy days



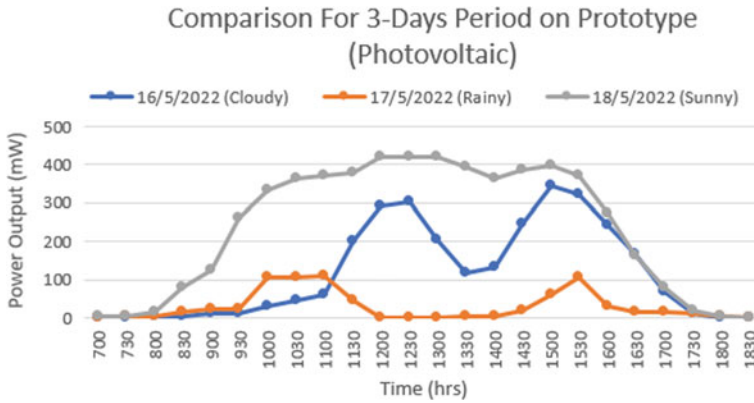


**Fig. 21** Photovoltaic energy harvester output power comparison for three days

produced less power output due to low irradiance and sunny days had a higher power output due to high irradiance.

## 4 Conclusion

The circuit for the simulation and hardware prototype of the hybrid renewable energy harvesting system was successfully created. In this work, the simulation of a hybrid renewable energy harvesting system, consisting of a photovoltaic and wind energy harvesting system. The hardware prototype consisting of a photovoltaic, piezoelectric, and wind energy harvesting system.

The results revealed that the photovoltaic energy harvester can harvest energy from 0700 to 1830 h. The piezoelectric energy harvester can harvest energy from 0700 to 2200 h, and the wind energy harvester can harvest energy for 24 h. Based on the time, the hybrid renewable energy harvesting system can always harvest energy continuously.

The performance of hybrid renewable energy harvester vary depending on different conditions and parameters. Photovoltaic energy harvesters can harvest energy optimally on a sunny day with high irradiance. Piezoelectric energy harvesters can harvest more energy with higher mass, and wind energy harvesters can harvest energy on a rainy day with the windier conditions. Based on the performance of three energy harvesters, the photovoltaic energy harvester has the biggest potential to generate large power output. Piezoelectric and wind energy are not feasible to utilize since the power generated is less than 1–2% of the overall power generation.

Overall, there is a potential for improvement of overall output power generation for hybrid renewable energy harvesters on a larger scale.

**Acknowledgements** This work was supported/funded by the Universiti Malaysia Sarawak under International Matching Grant (GL/F02/UNILAK/2020).

## References

1. Sanislav T, Mois GD, Zeadally S, Folea SC (2021) Energy harvesting techniques for internet of things (IoT). *IEEE Access* 9:39530–39549. <https://doi.org/10.1109/ACCESS.2021.3064066>
2. Bai Y, Jantunen H, Juuti J (2021) Hybrid, multi-source, and integrated energy harvesters. *Front Mater* 5. <https://doi.org/10.3389/fmats.2018.00065>
3. GlobesNewswire (2021) Energy harvesting system market size to reach USD 817.2 million by 2026—Report by Market Research Future (MRFR). Market Research Future, 27 Oct 2021. Accessed on 18 Oct 2021 [Online]. Available: <https://www.globenewswire.com/news-release/2021/10/27/2321811/0/en/Energy-Harvesting-System-Market-Size-to-Reach-USD-817-2-Million-by-2026-Report-by-Market-Research-Future-MRFR.html>
4. Amos K (2016) The how and why of energy harvesting for low-power applications, all about circuits, 23 June 2016. Accessed on 18 Oct 2021 [Online]. Available: <https://www.allaboutcircuits.com/technical-articles/how-why-of-energy-harvesting-for-low-power-applications/>
5. Steve R (2020) What is the IoT? Everything you need to know about the internet of things right now. ZDNet, 3 Feb 2020. Accessed on 18 Oct 2021 [Online]. Available: <https://www.zdnet.com/article/what-is-the-internet-of-things-everything-you-need-to-know-about-the-iot-right-now/>
6. Oracle (2021) What is IoT? Oracle. Accessed on 18 Oct 2021 [Online]. Available: <https://www.oracle.com/internet-of-things/what-is-iot/>
7. Saha CR, Huda MN, Mumtaz A, Debnath A, Thomas S, Jinks R (2020) Photovoltaic (PV) and thermo-electric energy harvesters for charging applications. *Microelectron J* 96:104685. <https://doi.org/10.1016/j.mejo.2019.104685>
8. Mohsen S, Zekry AA, Youssef KY, Ebrahim MA (2020) Design and implementation of hybrid energy harvesting system for medical wearable sensor nodes. Ph.D. dissertation, Department of Electronics and Communication Engineering, Ain Shams University, Cairo, Dec 2020 [Online]. Available: [https://www.researchgate.net/publication/346381943\\_Design\\_and\\_Implementation\\_of\\_Hybrid\\_Energy\\_Harvesting\\_System\\_for\\_Medical\\_Wearable\\_Sensor\\_Nodes](https://www.researchgate.net/publication/346381943_Design_and_Implementation_of_Hybrid_Energy_Harvesting_System_for_Medical_Wearable_Sensor_Nodes)
9. Akin-Ponnle E, Carvalho NB (2021) Energy harvesting mechanisms in a smart city—a review. *Smart Cities* 4(2):476–498 (2021). <https://doi.org/10.3390/smartcities4020025>
10. Tomar A et al (eds) (2022) Proceedings of 3rd international conference on machine learning, advances in computing, renewable energy and communication (MARC 2021), vol 915. Springer, Berlin, 781pp. ISBN: 978-981-19-2830-7. <https://doi.org/10.1007/978-981-19-2828-4>
11. Weddell AS, Magno M (2018) Energy harvesting for smart city applications. In: 2018 International symposium on power electronics, electrical drives, automation and motion (SPEEDAM), June 2018, pp 111–117 [Online]. <https://doi.org/10.1109/SPEEDAM.2018.8445323>

# Design and Development of an Inexpensive Intelligent Device for Sag Measurement for Overhead Transmission Lines



Manoj Kumar, Aman Kumar, Tushar Tomar, Anuj Dixit, Divya Asija, and R. K. Viral

**Abstract** This paper mainly focus on the various factors affecting sag in overhead line while laying transmission lines. A high degree of stress in the conductor may be reached if the conductors are stretched too much between supports of two towers. In this the author has worked upon the two physical parameters (i.e. Temperature and Tension). In order to prevent mechanical failure of the conductor, such as the breaking of cross arms or poles, and to allow for the use of less robust supports, it is preferable that tension be kept low in the conductor. From the topmost portion of the transmission tower on which install the transmission line, distance from top of the tower to the bottom part of the transmission line called Sag. This study takes a look at a variety of sag measuring approaches that use physical characteristics including vibration, temperature, and others. It is noted that the current methods of measuring sag have a number of drawbacks. Several solutions are suggested to the problems highlighted. This all-encompassing analysis of sag measurement methods will pave the way for the development of cutting-edge, time-saving systems for measuring and monitoring sag in real-time. Also from results we get to know that the elongation in the overhead transmission line due to increase in temperature will result in the sag formation, therefore with the increase temperature of overhead transmission line sag increases. Similarly, increase in tension result in increase in the sag percentage.

**Keywords** Conductors · Transmission lines · Sag · Measurement techniques · Temperature

---

M. Kumar (✉) · A. Kumar · T. Tomar · A. Dixit · D. Asija · R. K. Viral  
Department of Electrical Engineering, ASET, Amity University, Noida, Uttar Pradesh, India  
e-mail: [manojkumar5685657@gmail.com](mailto:manojkumar5685657@gmail.com)

D. Asija  
e-mail: [dasija@amity.edu](mailto:dasija@amity.edu)

R. K. Viral  
e-mail: [rviral@amity.edu](mailto:rviral@amity.edu)

# 1 Introduction

A transmission system is the infrastructure that moves energy from its source of production to its ultimate consumer. Overhead Transmission lines are an important aspect of the power grid because they link power generators to consumers in a reliable and efficient manner. Power outages may have a significant impact if transmission lines are disrupted or faulty. Transmission lines and substations play a central role in the transmission of electricity to the load [1]. These thermal stresses will cause elongation in the conductors of transmission line which will result in transmission line sag [2]. Regarding the tension that the conductor is subjected to, it is crucial to provide a reasonable safety factor while building overhead transmission lines [3]. Wind, ice loading, and temperature changes all have an impact on the conductor's tension. When stress on a transmission line is too great, it may damage the transmission towers, snap the cross arm of the towers, and even break the conductor. To prevent this, sags are intentionally installed between line supports. Because of the temperature variation and heat dissipation while power flow through conductors of transmission line, transmission line sag can differ [4]. For security purpose a minimum ground clearance is given while installing a new transmission line. The current carrying capacity of the conductor will also get affected by the transmission line sag [5, 6]. Thus, real-time monitoring of transmission line sag is critical for ensuring the safe and efficient functioning of the power transmission and distribution system. Current sag measuring methods concentrate on leveraging the correlation of sag with a number of physical factors that may be directly monitored by a variety of sensors. In order to model the sag of a transmission line, the authors of [7] have developed state equations that take into account several factors, including temperature, span, and initial measurement of sag, elasticity modulus, and weight per unit length. These equations likely allow for the prediction of the sag at any given point along the transmission line, based on the inputs provided.

In this paper the Author has new techniques for sag measurement of overhead transmission line based on physical parameter i.e. Temperature and Tension. Here author has measured sag at different temperature and different tension. It is noticed that after a certain temperature and tension the graph become constant and does not increase further.

- In this sag can be measured without visiting the site.
- The measured sag can be known automatically at the substation.
- Fault can also be detected using these techniques.

The paper is organized in following way firstly there is Abstract followed by introduction and then brief theory about sag and different sag measurement techniques followed by proposed method and block diagram. Conclusion, future work and result at the end.

## 2 Sag Measurement

The span of the overhead conductor affects how sag and tension are calculated in transmission lines. The term “level span” refers to a tower with equal level supports, or towers of the same height. On the other hand, an unequal level span is one that has uneven heights of support [8]. This is so that it can shield the conductor from too much strain. Rather of being fully stretched, conductors are permitted to have sagged in order to provide for an acceptable degree of strain [9]. The conductor has a potential to break or get disconnected from its end support if it is completely stretched during installation due to wind pressure. Sag is therefore permitted to exist when the conductor is suspended.

### 2.1 Sag Calculation Can Be Express for Tower Support Placed at Two Levels as Discussed Below

#### 2.1.1 Sag Calculation for Supports is at Equal Levels

From Fig. 1, imagine *AOB* is leading the orchestra. The points *A* and *B* provide stability. The lowest and central point is point *O*.

“Let, *L* = distance of wire between two poles”, i.e., *AB*.

“*w* = it is defined weight/ length of conductor”.

“*T* = tension in the wire”.

“A point is chosen on the overhead transmission line, let the point is *P*”.

“*x* = the distance of point *p* from the bottom point *O*”.

“*y* = vertical distance from point *O* to point *P*”.

As seen in the accompanying diagram, when we compare the moments of two forces acting on point *O*, we obtain [10]

$$Ty = wx * \frac{x}{2} \tag{1}$$

$$\text{Now, } y = \frac{wx^2}{2T}, \text{ when } y = S \text{ and } x = \frac{L}{2} \tag{2}$$

#### 2.1.2 Calculation of Sag for Supports at Unequal Levels

From Fig. 2, let *AOB* is the line of which the bottom point is *O*.

*L* = span of wire.

*H* = distance between the points at which they are at two supports.

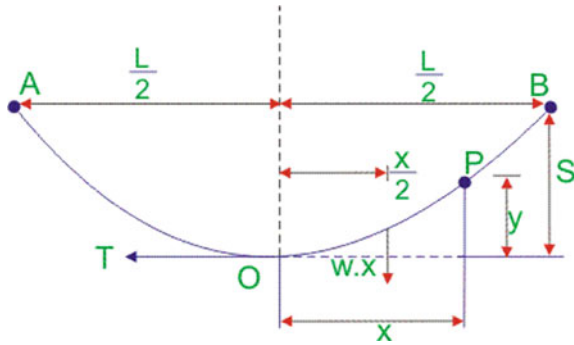


Fig. 1 Supports at equal levels

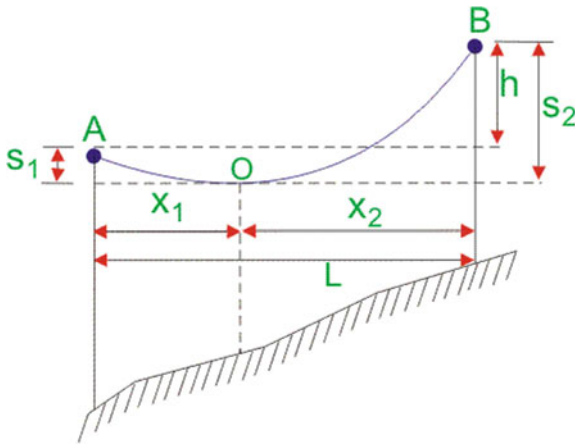


Fig. 2 Supports at unequal levels

$x_1$  = distance which is from the bottom-level of point A from O.

$x_2$  = distance of point B from O.

$T$  = tension of the Overhead transmission line.

$w$  = weight/length of wire.

Now,

$$\text{Sag } S_1 = \frac{wx_1^2}{2T} \quad \text{and} \quad \text{Sag } S_2 = \frac{wx_2^2}{2T} \tag{3}$$

Also,

$$x_1 + x_2 = L \quad (4)$$

Now,

$$S_2 - S_1 = \frac{w}{2T}(x_2^2 - x_1^2) = \frac{w}{2T}(x_2 - x_1)(x_2 + x_1) \quad (5)$$

So,

$$S_2 - S_1 = \frac{wL}{2T}(x_2 - x_1) \quad (6)$$

Again,

$$S_2 - S_1 = h$$

So,

$$h = \frac{wL}{2T}(x_2 - x_1) \quad (7)$$

Or,

$$(x_2 - x_1) = \frac{2Th}{wL} \quad (8)$$

Solving Eqs. (4) and (8), we get

$$x_1 = \frac{L}{2} - \frac{Th}{wL} \quad \text{and} \quad x_2 = \frac{L}{2} + \frac{Th}{wL} \quad (9)$$

Inputting the values for  $x_1$  and  $x_2$  into the Sag equation allows us to quickly calculate the corresponding values for  $S_1$  and  $S_2$ .

The aforementioned Sag equations hold true only under perfect conditions. When there is no wind and no ice loading is present, we have reached the “ideal state,” as defined in [11]. However, in real practice, wind pressure is constantly present on the conductor, and ice loading is most often seen in cold areas [12–14]. India is one of the few places in the world where ice loading on transmission lines is seldom seen.

### 3 Sag Measurement Techniques

S. No.	Technique name	Merits	Demerits	Remarks
1	Temperature, vibration, load cell	Sag varies with temperature, therefore measuring how much the conductor is heated may provide a rough approximation of the sag	The accuracy of systems based on heating of conductor, vibration, and load cells (tension measurement) is poor	Heating of line varies in Both axial and radial in power cables. As a result, sag readings at various positions along a line may differ from one another. In This particular aspect, this method is very suitable to be used
2	Laser based	Improved accuracies	Complex and expensive	It carries out measurements from the ground at a distance of about 30 m from the line. So, in this type of measurement, it can be used as a method
3	Tension based	Error is just 2% in this	Sag in the overhead transmission line is inversely proportional to tension in the conductor	The inclination angle, which varies with stress, has an impact on sag. If a result, if the line sag increases, the tension line will also decrease. Utilizing this strategy will be the most effective course of action
4	Optical techniques	The laser-based system's precision is more than 5 cm	It is not possible to ensure automated data collection without human intervention	This specific kind of sag measuring technique can be employed if the needed precision is better than 5 cm
5	Magnetic field based	A large operational range, high detecting accuracy, low power need, and affordable price	A potential pitfall of this method is that it is susceptible to inaccuracy	With the transmission line's sag and current, the flux density value rises. Therefore, this may be applied to that specific element
6	GPS signal based	Reduced error in the calculated sag	So many things to maintain	So, the suitability of the method is dependent on the way of sag which needs to be measured

(continued)



(continued)

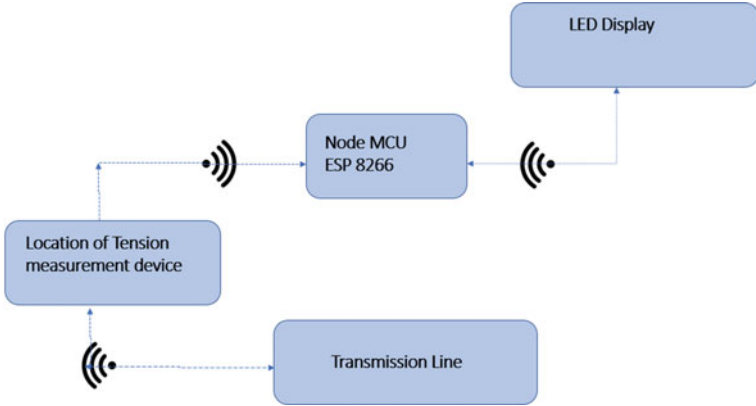
S. No.	Technique name	Merits	Demerits	Remarks
7	Robot based method	Additionally, it can keep an eye on the line's temperature, vibration, obstructions, and humming sound	More error chances as humans are not involved in this	It is ideal for detecting changes in temperature, vibration, obstructions, and line humming

### 3.1 Proposed System Description

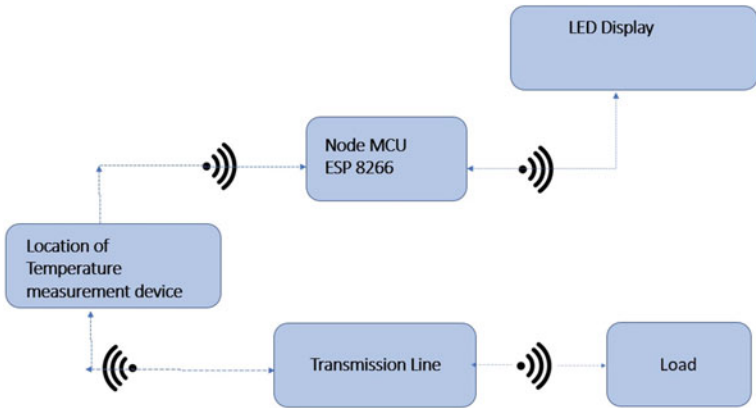
In this paper we measure sag with two main technique first is tension-based technique and second temperature-based technique showed in flow chart. And we add some miscellaneous technique in this paper ex—laser based technique, optical based technique, magnetic field based technique, GPS based technique, Robot based technique, Phasor measurement unit based technique. But we will measure sag in this paper with tension and temperature-based technique. We prepare the block diagram and hardware of both techniques. We use to prepare hardware many components ex- Node MCU 8266, LCD module, Resistor, Transformer, Capacitor. These components are the main component to use in this project. After completing the hardware we check the result and plot the graph of tension based technique and temperature based technique. In tension based technique we plot the graph between sag and tension and in temperature based technique we plot graph between length and temperature. we have calculated expand in length of overhead transmission line with increase in temperature and increase in sag percentage along with tension. The elongation in the overhead transmission line due to increase in temperature will result in the sag formation, therefore with the increase temperature of overhead transmission line sag increases. Similarly, increase in tension result in increase in the sag percentage. This is going to be very useful in the future because there is a lot of difficulty in checking the sag by going from place to place and at the same time it takes a lot of time to find the sag, through this we can detect the sag by sitting at one place, both by vibration and temperature. We do not even go to many places with technology, like in hilly areas, in the forest, but with this technique, we can easily find out and solve the problem as soon as possible. With the help of this, a lot of expenses will be saved, such as going to check the sag, in which the cost of the vehicle along with our manpower is also saved, through this many accidents will be saved, many times the wire breaks due to excessive sag.

### 3.2 Block Diagram

#### (a) Tension Based

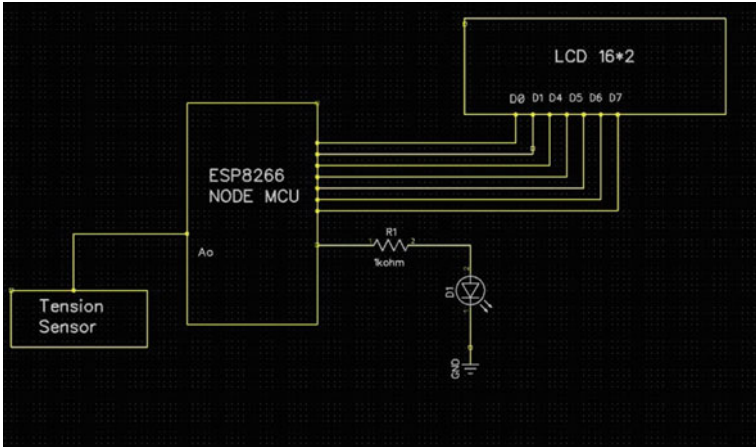


#### (b) Temperature Based

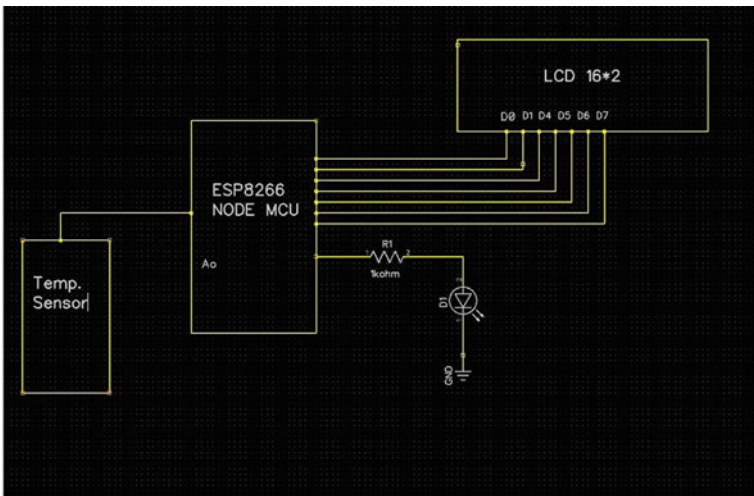


### 3.2.1 Diptrace Diagram

#### (a) Tension Based



#### (b) Temperature Based



## Component List

S. No.	Item name	Specification	Quantity
1	Node MCU ESP8266	3.3 V	2
2	LCD module	16X2, 5 V $\pm$ 10%	2
3	Transformer	500 mA, 12 V	1
4	Variable resistance		2

## Component Rating

S. No.	Component name	Rating
1	Transformer	500ma / 12 V
2	Capacitor	1000 micro farad
3	Resistor	1 k ohm

### 3.2.2 Solution Methodology

### 3.2.3 Tension Based Device

We made a device which will measure the sag between two poles in overhead transmission line. In this device we used many components ex- Node MCU8266, LCD display, Tension measurement device, Diode and other components. A quick glance at the hardware (depicted in the image below) reveals that connecting the display to the NODE MCU8266 device kit was a breeze; we simply wired the display's ground pin to one of the NODE MCU's ground pins and the LCD display's voltage pin to the board's Vin pin. With NODE MCU, you can build Internet-of-Things platforms. It bases both its hardware and software on the ESP8266 Wi-Fi System-on-a-Chip (SoC) that is manufactured by Espressif, as well as the ESP-12 module. By default, the firmware that is included with the NODE MCU is used rather than the development kits. Within the ESP8266 firmware, the programming language known as Lua is used. It was constructed using the Espressif Non-OS SDK for ESP8266, and the Lua homework served as the primary inspiration for it. First we connect supply to NODE MCU, Tension Measure device is connected to NODE MCU8266 which measures tension of the overhead transmission line and value will display on LCD as we can see the value of sag tension in laptop or mobile phone with the help of Wi-Fi web page and for calculating the values of sag data we have to measure the distance wire between two poles and the weight of the wire, then we will put the value in this formula,

$$S = \frac{wl^2}{8T}$$

From this formula we can see clearly, the sag of overhead transmission line is inversely proportional to the sag tension.

### 3.3 *Temperature Based Device*

The supply is connected to transformer to step down the voltage level which is then connected to full wave rectifier to convert Ac supply to Dc, a capacitor is connected for filtration and connected to a regulator which regulates the voltage. Capacitor is connected with regulator for further filtration and then it is connected to node mcu, and a temperature sensor is connected to node mcu which detects the temperature from the overhead transmission line on which the loads are connected which is displayed on the led which is connected to node mcu. As the load vary, different values of temperature will be obtained which results in different values of Sag.

## 4 Experimental Setup and Result

As shown in the Fig. 3 (pic of setup), the supply (220 V) is given to the transformer which step down the voltage level to 12 V, is connected to full wave rectifier which convert ac into dc (as the node mcu circuit will work on dc). Capacitor is connected for filtration of harmonics. Then voltage regulator is connected to regulate the voltage to 5 V and then is connected to node mcu, A temperature sensor is connected to node mcu which measures the temperature of the overhead transmission line, which will be displayed on the LED (Fig. 4).

In the device below we used many components ex- Node MCU8266, LCD display, Tension measurement device, Diode and other components. As we can see in the

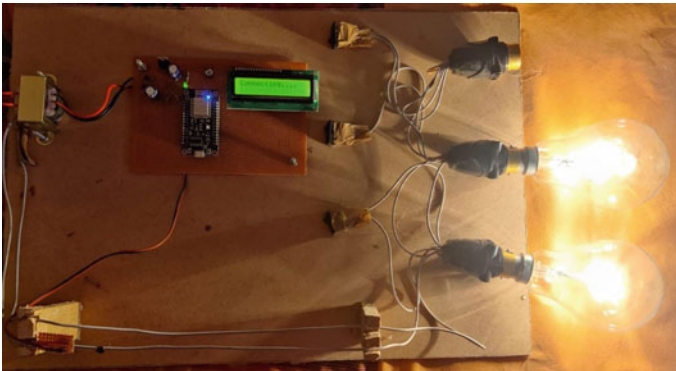


**Fig. 3** Temperature based model with load

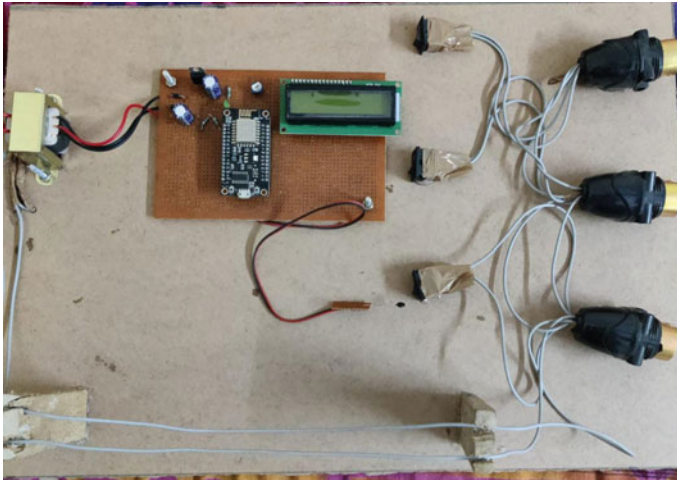


**Fig. 4** Temperature based model with no load

hardware (below in the figure), we connected the display to NODE MCU8266 device kit in pretty straight forward, connect the GND pin to the display to one of GND pins on the NODE MCU and connect the V pin the LCD display to the Vin pin on the NODE MCU.

The results here, we have calculated expand in length of overhead transmission line with increase in temperature and increase in sag percentage along with tension. The elongation in the overhead transmission line due to increase in temperature will result in the sag formation, therefore with the increase temperature of overhead transmission line sag increases. Similarly, increase in tension result in increase in the sag percentage (Figs. 5 and 6).

**Table of temperature-based device**

S. No.	Initial temperature (°C)	Final temperature (°C)	Change in temperature (°C)	Change in length (delta L) = alpha * delta T * L (cm)
1	19	19.5	0.5	0.000299
2	19.5	20.5	1	0.000598
3	20.5	22	1.5	0.000897
4	22	24	2	0.001196
5	24	26.5	2.5	0.0014954
6	26.5	29	2.5	0.0014956

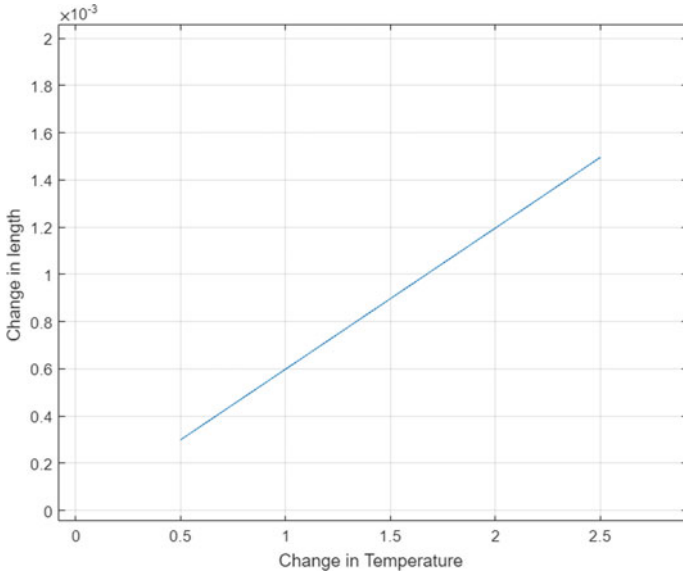


Fig. 5 Temperature based model result graph

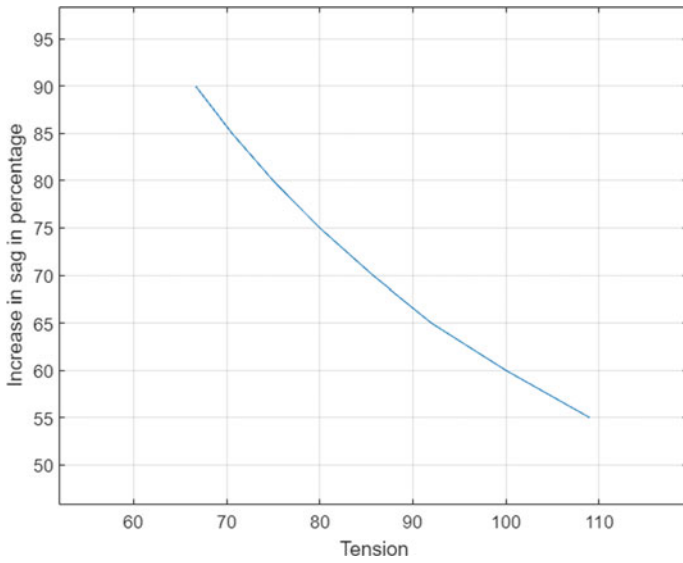


Fig. 6 Tension based model result graph

**Table of tension-based device**

S. No.	Tension ( $N$ )	Increase in Sag (in percentage)
1	66.67	90
2	70.58	85
3	75	80
4	80	75
5	85.71	70
6	92	65
7	100	60
8	109	55

## 5 Conclusion and Future Work

Here, a number of research on evaluating the sag of overhead electricity lines have been compared using a variety of performance indicators, and the results of these comparisons are discussed. However, the results of this analysis show that there is a significant need for more research and development in the field of sag measuring methodologies. It is common known that sag measurement systems come with their fair share of challenges and restrictions. In the process of developing technology for detecting and monitoring sag in smart grids, researchers may investigate methods that are both efficient and accurate for estimating the DLR of overhead transmission lines. This article will go over a number of different direct ways that may be used to determine the temperature of wires in the atmosphere. It has been abundantly evident, via the process of comparing numerous approaches, that not only are there large differences in the method that is employed, but also in the interpretation of the temperature that is recorded for a conductor. It's possible that the temperature is only an estimate, and that it just applies to a certain stretch of line or a single site. When viewed in a radial direction, the value may alternatively be interpreted as representing the temperature of the conductor's surface, core, or average. Each proposed technology that might prevent exact conductor temperature measurements in practise comes with its own set of benefits and drawbacks.

This is going to be very helpful in the future because checking the sag requires a lot of difficulty by going from place to place, and it also takes a lot of time to find the sag. With this, we can detect the sag while sitting in one place, both by vibration and temperature. This is going to be very useful because checking the sag requires a lot of difficulty. We don't even travel to many locations with technology, such as steep regions or the forest, but with this approach, we can simply find out what the issue is and fix it as quickly as we can. Through the use of this, a significant amount of money will be saved. One example of this is the cost of going to check the sag, which will save us not only the cost of the vehicle but also the cost of our manpower.



In addition, this will prevent a significant number of accidents, as excessive sag is often the cause of wire breaks. Additionally, there is a possibility of mishaps for the persons emerging from below; nevertheless, accidents will be reduced as a result of this measure. Because we can see that many things break down when the storm arrives, the amount of damage that is inflicted by the storm may be mitigated to some degree by lowering the sag in the infrastructure before it arrives.

## References

1. Industrial-Electronics.com (2021) Ultimate guide to electric power engineering: Transmission system: transmission line construction and maintenance. Accessed 10 June 10. [https://www.industrial-electronics.com/elec\\_pwr\\_3e\\_12.html](https://www.industrial-electronics.com/elec_pwr_3e_12.html)
2. Prabhu VA, Tiwaria A (2014) Dynamic alignment control using depth imagery for automated wheel assembly. *Procedia CIRP* 25:161–168 (2014)
3. Padegaonkar A, Brahme M, Bangale M (2014) Implementation of machine vision system for finding defects in wheel alignment. *Int J Comput Technol.* He CG, Huang YB (2015) Experimental investigation on the effect of tangential force on wear and rolling contact fatigue behaviors of wheel material
4. Josef M (2009) Identification of accident location by use of GPS and possibilities of application. In: Proceedings of the 4th IRTAD conference, Seoul, South Korea
5. Mintsis G et al (2004) Applications of GPS technology in the land transportation system. *Eur J Oper Res* 152(2):399–409
6. Maurer P (1998) The use of a satellite navigation system (GPS) to register locations of traffic accidents. In: Proceedings of the seventh report of International Cooperation on Theories and Concepts in Traffic Safety, Budapest, Hungary
7. Malhara S, Vittal V (2010) Mechanical state estimation of overhead transmission lines using tilt sensors. *IEEE Trans Power Syst* 25(3):1282–1290
8. Guide for Application of Direct Real Time Monitoring Systems, Cigre Technical Brochure (N° 498) (2010)
9. Cloet E, Lilien J (2011) Upgrading transmission lines through the use of an innovative real-time monitoring system. In: 2011 IEEE PES 12th International conference on transmission and distribution construction, operation and live-line maintenance (ESMO), Providence, RI, pp 1–6
10. Kiessling F, Nefzger P, Nolasco JF, Kaintzyk U (2003) Overhead power lines planning design construction. Springer, Berlin
11. Ahmad MW et al (eds) (2022) Intelligent data analytics for power and energy systems. Springer, Singapore, 641pp. ISBN: 978-981-16-6081-8. <https://doi.org/10.1007/978-981-16-6081-8>
12. Tomar A et al (eds) (2022) Proceedings of 3rd international conference on machine learning, advances in computing, renewable energy and communication (MARC 2021), vol 915. ISBN: 978-981-19-2830-7. Springer, Berlin, 781pp. <https://doi.org/10.1007/978-981-19-2828-4>
13. IEEE subcommittee 15.11 (1993) IEEE guide to the installation of overhead transmission line conductors. IEEE Standard 524
14. CIGRE Technical Brochure N° 299 (2006) Guide for selection of weather parameters for bare conductor ratings, Aug 2006

# Gradient Descent Back-Propagation Through Momentum (GDBPM) Endorsed $i \cos \phi$ Control Technique-Based DSTATCOM Intended for Shunt Indemnification



Mrutyunjaya Mangaraj, Kampara Ravisankar, Majji Satish,  
Kantubhukta Dinesh, and A. Praveena

**Abstract** This article is mainly based on model feature and designing a control approach for 3- $\phi$  three wire (3P3W) static compensator (DSTATCOM) by incorporating gradient descent back-propagation through momentum (GDBPM) suggested  $i \cos \phi$  algorithm. The suggested organized approach is implemented within MATLAB/Simulink Environment with the help of mathematical investigation with an appropriate learning rate and momentum behavior. This control technique follows the systematic process for obtaining the basic loading values of the active and reactive power, and those are necessary for efficiently generating perception currents. Harmonic dampening, voltage regulation profile, power factor improvement, balancing of load, and rating of VSC are presented under different conditions of load. In this work, instantaneous digital-simulator (RTD-S) is used for existing centralization of DSTATCOM. The effectiveness of a DSTATCOM among the anticipated control approach originates to be satisfactory and follows the standards of IEEE-519 and IEC-61000-3.

**Keywords** DSTATCOM · GDBPM control algorithm ·  $i \cos \phi$  control algorithm · VSC

---

M. Mangaraj · K. Ravisankar · M. Satish · K. Dinesh (✉) · A. Praveena  
Lendi Institute of Engineering and Technology, Vizianagaram, Andhra Pradesh, India  
e-mail: [dineshk1710@gmail.com](mailto:dineshk1710@gmail.com)

© The Author(s), under exclusive license to Springer Nature Singapore Pte Ltd. 2024  
H. Malik et al. (eds.), *Renewable Power for Sustainable Growth*,  
Lecture Notes in Electrical Engineering 1086,  
[https://doi.org/10.1007/978-981-99-6749-0\\_18](https://doi.org/10.1007/978-981-99-6749-0_18)

## 1 Introduction

The major makes use of distributed FACTS (D-FACTS) controller in the current power distribution system has eliminated drawbacks of electromechanical-based controllers, such as slower operation speed, decreased switching safety, a heavy VA load, a uni-facial feature, low-efficiency because of an excessive loss, and unpredictable. In order to absorb or inject the reactive element of current by associating inductors next to the site of common-coupling, a DSTATCOM device is linked to the D-FACTS device in shunt. This type of actuator is also known as a static synchronous condenser or a “advanced static VAR compensator” (ASVC). It is sufficiently competent to provide effective corrective measures and affordable remedies for the distribution system’s poor power quality issues [1–3]. To organize the real behavior of DSTATCOM [4–6], various modeling designs of the organizer procedures are evolved [7–9].  $i \cos \phi$  control technique [10, 11] are outlined in the specified literature.

In addition to an algorithm is constructed using neural networks, which includes a neural network supervisor [12–15], Hopfield neural network approach [16, 17], neural network-based algorithm for intelligent identification of signatures [18], and the back-propagation approach. Adaptive RBF and generalized expanding cutting-radial-based function (GGP-RBF) have all been used. Developed neural network approaches have certain distinct benefits over other control methods, including supervised, feed-forward, back up training and rationalization principles, etc. [13–19]. This control technique is used for various tasks, including image recognition, delineate information, statistics investigation, industrialized operations, earth-shattering signal categorization, and correction of power quality matters. Hence, neural network is providing a suitable solution to analyze the functions associated with the load in a distributed system which are both regular and nonlinear. A number of scientists and researchers are stepping advance to combine methods from flexible computing through predictable algorithms for enhanced performance as contrasted with simple normal algorithms in light of the changing scenario according to restructured electricity systems.

In this investigation, a three-phase, two-level DSTATCOM is employed to implement a GDBPM-based  $i \cos \phi$  control methodology to derive the reactive component and the active element scaled quantities of load current during balanced and asymmetrical nonlinear loads. This control approach implements a method that splits training weight through three levels:  $i/p$  signal training, estimation of error information, and amending of training weights. Each of these steps includes various training weight qualities, such as regularity, differentiability, structural stability adaptability, steady repetitiveness, and strong illustrative abilities. In real practice, the proposed control technique is presented with the help of mathematical analysis which depends on the GDBPM principle effects. This is actually put into reality. In this work the recommended methodology is utilized to demonstrate voltage source converter (VSC), DC voltage regulation, phase balancing, load compensation for the nonlinear loads in both balance loading and unbalanced loading cases.

## 2 Configuration of the System with Control Algorithm

Figure 1 exhibits the suggested DSTATCOM incorporated with the existing distribution network system. The major components in the developed systems are 3- $\phi$  DSTATCOM, source, and loads in nonlinear nature. The distribution STATCOM is regarded as 3- $\phi$  3Wire 2 level VSC.  $Z_{ca}, Z_{cb}, Z_{cc}$  are the three impedances attached in sequences at the o/p of VSC to make available without ripple currents.  $i_{ca}, i_{cb}, i_{cc}$  are remunerate currents to retract the power constituents and diminish the generating currents' distortions ( $i_{sa}, i_{sb}, i_{sc}$ ).

Figure 2 shows a diagrammatic characterization of the GDBPM-based  $i \cos \phi$  control method. The projected control strategy reduces the major distortion of input making it highly resilient through its learning methods. The whole methodology

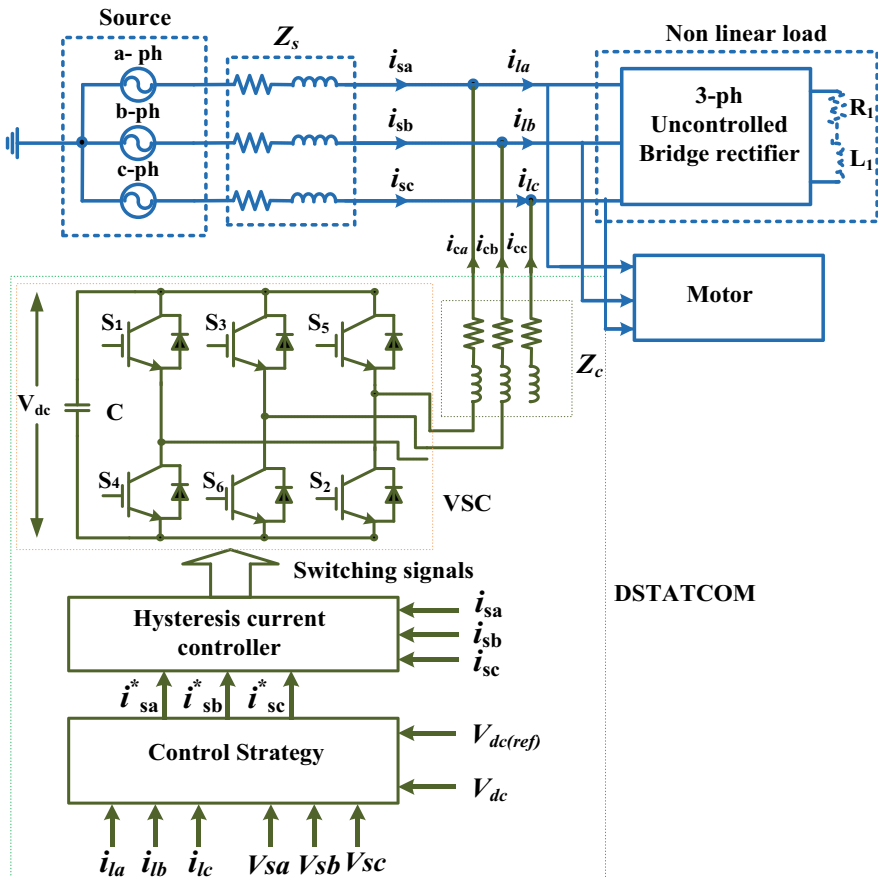


Fig. 1 Diagrammatic characterization of electrical distribution system through suggested DSTATCOM

is used to estimate switching signal production. Computation of biased worth of essential active and reactive works of weighted load current by using GDBPM-based  $i \cos \phi$  control technique reactive and active power elements is computed by its updated values. This strategy is effective in upgrading the complex weights, and bias in equal way to the presentation function is indicated in Fig. 3

$$i_{lap} = w_0 + i_{la} \cos \phi_{la} u_{ap} + i_{lb} \cos \phi_{lb} u_{bp} + i_{lc} \cos \phi_{lc} u_{cp} \tag{1}$$

$$i_{lbp} = w_0 + i_{la} \cos \phi_{la} u_{ap} + i_{lb} \cos \phi_{lb} u_{bp} + i_{lc} \cos \phi_{lc} u_{cp} \tag{2}$$

$$i_{lcp} = w_0 + i_{la} \cos \phi_{la} u_{ap} + i_{lb} \cos \phi_{lb} u_{bp} + i_{lc} \cos \phi_{lc} u_{cp} \tag{3}$$

At the point of common coupling (PCC), the following equations are obtained

$$\left. \begin{aligned} u_{ap} &= \frac{v_{sa}}{v_t} \\ u_{bp} &= \frac{v_{sb}}{v_t} \\ u_{cp} &= \frac{v_{sc}}{v_t} \end{aligned} \right\} \tag{4}$$

and the amplitude at the PCC voltages is obtained as

$$v_t = \sqrt{\frac{2(v_{sa}^2 + v_{sb}^2 + v_{sc}^2)}{3}} \tag{5}$$

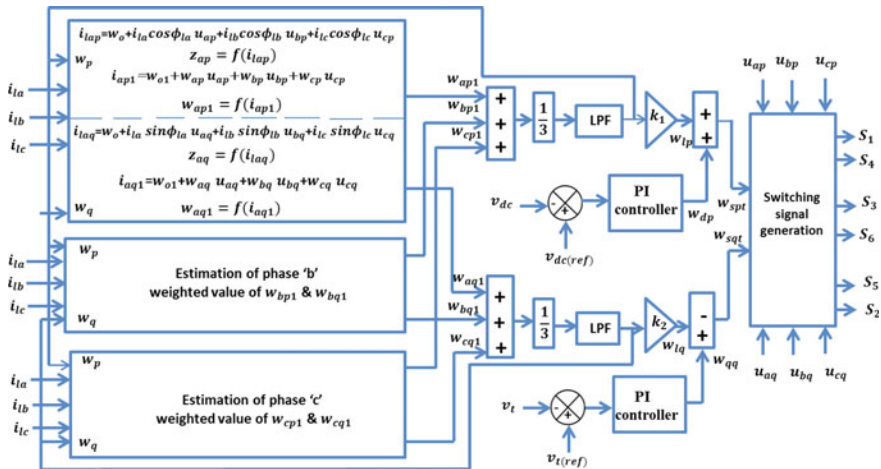


Fig. 2 Schematic diagram of signals generation switching of voltage. Source Converter (VSC) using GDBPM-based  $i \cos \phi$  control technique

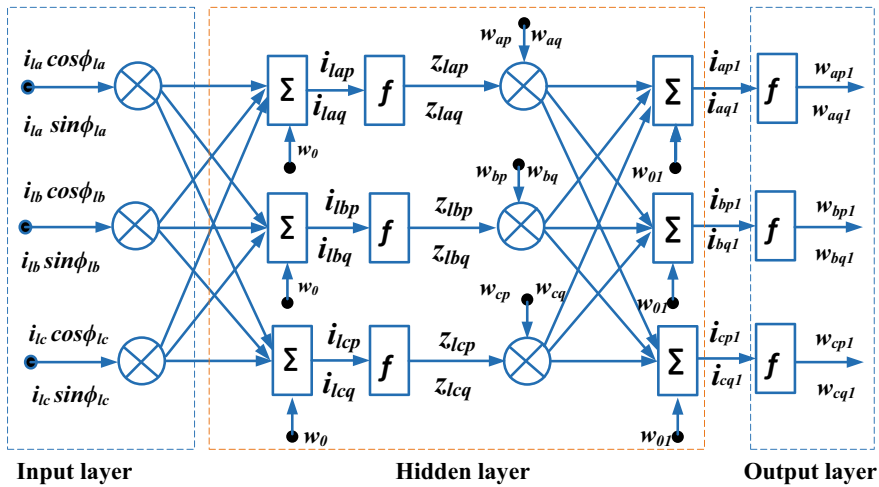


Fig. 3 Assessment of weighted standards by means of GDBPM-based  $i \cos \phi$  control technique

The extricated 3- $\phi$  currents of ( $i_{lap}$  and  $i_{lbp}$  and  $i_{lcp}$ ) are sent through uninterrupted sigmoid task. It describes a mathematical representation having in S-shape curve. If  $i_{lap} \rightarrow +ve\infty$ ,  $Z_{ap} = 1$  and  $i_{lap} \rightarrow -ve\infty$ ,  $Z_{ap} = -1$ . As a result, it may be considered an activation function with a range of  $-1$  to  $1$ . The output signals  $Z_{ap}$ ,  $Z_{bp}$ , and  $Z_{cp}$ . The following equations can be used to determine how input signals are handled by the hidden layer.

$$\left. \begin{aligned} Z_{ap} &= f(i_{lap}) = \frac{1}{1+e^{-i_{lap}}} \\ Z_{bp} &= f(i_{lbp}) = \frac{1}{1+e^{-i_{lbp}}} \\ Z_{cp} &= f(i_{lcp}) = \frac{1}{1+e^{-i_{lcp}}} \end{aligned} \right\} \tag{6}$$

The 3- $\phi$  outputs of this layer of fundamental element ( $i_{ap1}$ ,  $i_{bp1}$  and  $i_{cp1}$ ) are expressed as

$$i_{ap1} = w_{01} + w_{ap}Z_{ap} + w_{bp}Z_{bp} + w_{cp}Z_{cp} \tag{7}$$

$$i_{bp1} = w_{01} + w_{ap}Z_{ap} + w_{bp}Z_{bp} + w_{cp}Z_{cp} \tag{8}$$

$$i_{cp1} = w_{01} + w_{ap}Z_{ap} + w_{bp}Z_{bp} + w_{cp}Z_{cp} \tag{9}$$

The drawbacks of GDBP are overcome by GDBPM algorithm. In this proposed algorithm, the concept of momentum is included. The momentum allows not only the gradient but also weight changes [15]. So that weight updating will not be stuck in

local minimum. It allows weight update which is mediated by a momentum constant “ $\alpha$ ”. The updated weight  $w_{ap}$  of active component for phase-a can be expressed as

$$w_{ap} = w_p + \mu \{w_p - w_{ap1}\} f'(i_{ap1}) + \alpha w_{p-1} \quad (10)$$

where  $w_{ap1}$  is the Phase-A fundamental subjective assessment of active element,  $f'(i_{ap1})$  is the first derivative of  $i_{ap1}$ , and  $w_{p-1}$  is the earlier value common biased assessment of the dynamic element, etc.

Similarly, the updated weight for b-phase and c- $\phi$  is written as

$$w_{bp} = w_p + \mu \{w_p - w_{bp1}\} f'(i_{bp1}) + \alpha w_{p-1} \quad (11)$$

$$w_{cp} = w_p + \mu \{w_p - w_{cp1}\} f'(i_{cp1}) + \alpha w_{p-1} \quad (12)$$

The fundamental values  $i_{ap1}$ ,  $i_{bp1}$  and  $i_{cp1}$  are processed with the sigmoid function, which acts as an activation function, may written as  $w_{ap1}$ ,  $w_{bp1}$  and  $w_{cp1}$

$$\left. \begin{aligned} w_{ap1} &= f(i_{ap1}) = \frac{1}{1+e^{-i_{ap1}}} \\ w_{bp1} &= f(i_{bp1}) = \frac{1}{1+e^{-i_{bp1}}} \\ w_{cp1} &= f(i_{cp1}) = \frac{1}{1+e^{-i_{cp1}}} \end{aligned} \right\} \quad (13)$$

The active element of a basic weighted average can be computed as

$$w_p = \frac{w_{ap1} + w_{bp1} + w_{cp1}}{3} \quad (14)$$

The low-frequency elements are divided by employing the first-order low-pass filters (LPF). This extracted active power component is reduced by linearized scaled factor “ $k_1$ ” to acquire the definite value ( $w_{lp}$ ); it is shown in Fig. 2.

Correspondingly, the subjective standards of the reactive works of load current in input level be specified as

$$i_{laq} = w_0 + i_{la} \sin \phi_{la} u_{aq} + i_{lb} \sin \phi_{lb} u_{bq} + i_{lc} \sin \phi_{lc} u_{cq} \quad (15)$$

$$i_{lbq} = w_0 + i_{la} \sin \phi_{la} u_{aq} + i_{lb} \sin \phi_{lb} u_{bq} + i_{lc} \sin \phi_{lc} u_{cq} \quad (16)$$

$$i_{lcq} = w_0 + i_{la} \sin \phi_{la} u_{aq} + i_{lb} \sin \phi_{lb} u_{bq} + i_{lc} \sin \phi_{lc} u_{cq} \quad (17)$$

The quadrature unit voltage template of a, b, and c-phase is mentioned as

$$\left. \begin{aligned} u_{aq} &= \frac{u_{bp} + u_{cp}}{\sqrt{3}} \\ u_{bq} &= \frac{3u_{ap} + u_{bp} - u_{cp}}{2\sqrt{3}} \\ u_{cq} &= \frac{-3u_{ap} + u_{bp} - u_{cp}}{2\sqrt{3}} \end{aligned} \right\} \quad (18)$$

Therefore, the mentioned weighted standards of  $i_{laq}$ ,  $i_{lbq}$ , and  $i_{lcq}$  be processed during sigmoid task to estimate the weighted standards of the reactive rudiments of load current  $Z_{aq}$ ,  $Z_{bq}$ , and  $Z_{cq}$ , which may be represented through the equations below.

$$\left. \begin{aligned} Z_{aq} &= f(i_{laq}) = \frac{1}{1+e^{-i_{laq}}} \\ Z_{bq} &= f(i_{lbq}) = \frac{1}{1+e^{-i_{lbq}}} \\ Z_{cq} &= f(i_{lcq}) = \frac{1}{1+e^{-i_{lcq}}} \end{aligned} \right\} \quad (19)$$

The hidden layer processes the  $Z_{aq}$ ,  $Z_{bq}$ , and  $Z_{cq}$  acts, which are i/p signals.  $i_{aq1}$ ,  $i_{bq1}$ , and  $i_{cq1}$  are the 3- $\phi$  basic output components of this layer.

$$i_{aq1} = w_{01} + w_{aq}Z_{aq} + w_{bq}Z_{bq} + w_{cq}Z_{cq} \quad (20)$$

$$i_{bq1} = w_{01} + w_{aq}Z_{aq} + w_{bq}Z_{bq} + w_{cq}Z_{cq} \quad (21)$$

$$i_{cq1} = w_{01} + w_{aq}Z_{aq} + w_{bq}Z_{bq} + w_{cq}Z_{cq} \quad (22)$$

Here  $w_{aq}$ ,  $w_{bq}$  and  $w_{cq}$  are upgraded weighted standards of reactive element of load current in a, b, and c- $\phi$  employed as feedback signal.

The upgraded weight “ $w_{aq}$ ” of reactive element of a- $\phi$  can be expressed as

$$w_{aq} = w_q + \mu \{w_q - w_{aq1}\} f'(i_{aq1}) + \alpha w_{q-1} \quad (23)$$

where  $w_{aq1}$  is the a-phase original subjective amplitude of the reactive element  $f'(i_{aq1})$  is the primary derivative of  $i_{aq1}$  element and  $w_{q-1}$  is the earlier worth average subjective worth of the reactive component, etc.

Similarly, two equations for b and c- $\phi$  can be viewed as

$$w_{bq} = w_q + \mu \{w_q - w_{bq1}\} f'(i_{bq1}) + \alpha w_{q-1} \quad (24)$$

$$w_{cq} = w_q + \mu \{w_q - w_{cq1}\} f'(i_{cq1}) + \alpha w_{q-1} \quad (25)$$

The basic variables  $i_{aq1}$ ,  $i_{bq1}$  and  $i_{cq1}$  are processed by the sigmoid function, which can be represented in terms of  $w_{aq1}$ ,  $w_{bq1}$  and  $w_{cq1}$  as an activation function.



$$\left. \begin{aligned} w_{aq1} &= f(i_{aq1}) = \frac{1}{1+e^{-i_{aq1}}} \\ w_{bq1} &= f(i_{bq1}) = \frac{1}{1+e^{-i_{bq1}}} \\ w_{cq1} &= f(i_{cq1}) = \frac{1}{1+e^{-i_{cq1}}} \end{aligned} \right\} \quad (26)$$

The weighted average of fundamental reactive element can be calculated as

$$w_q = \frac{w_{aq1} + w_{bq1} + w_{cq1}}{3} \quad (27)$$

The little frequency works are divided by employing first-order low-pass filters. This extracted reactive power element of current is reduced by a linearized scaled factor “ $k_2$ ” the actual value ( $w_{lq}$ ) which is shown in Fig. 2. Two linearizing components,  $k_1$  and  $k_2$ , are employed to assure the stability margin of closed-loop control systems when taking direct and quadrature axis weighted data, which are then sent via a low-pass filter. This filter preserves system dynamics at low frequencies while rejecting noise.

The feasibility of the controller is tested under distorted source voltage, balanced and unbalanced loading conditions. It is observed to perform satisfactorily under all these disturbed conditions and the THD is maintained within the limit (below 5%), satisfying IEEE guidelines. This confirms the stable operation of the controller.

#### A. Calculation of the Active Element of Mentioned Basis Currents

The DC voltage error ( $v_{de}$ ) is the difference between actual DC voltage and mention DC voltage, and it can be uttered as

$$v_{de} = v_{dc (ref)} - v_{dc} \quad (28)$$

The dissimilarity is handled by the PI regulator to supervise the invariable DC bus voltage. The output of PI controller may be represented as

$$w_{dp} = k_{pdp} v_{de} + k_{idp} \int v_{de} dt \quad (29)$$

The amount of output of PI regulator and the common amount of active component is the entirety active components of the mentioned basis current that can be uttered as

$$w_{spt} = w_{dp} + w_{lp} \quad (30)$$

#### B. Calculation of the Reactive Component of Reference Source Currents

$$v_{te} = v_t (ref) - v_{ta} \quad (31)$$

The dissimilarity is handled by the PI regulator in order to supervise the invariable AC bus voltage. The o/p of proportional integral controller represented as

$$w_{qq} = k_{pq} v_{te} + k_{iq} \int v_{te} dt \quad (32)$$

The variation of average magnitude and o/p of PI controller of reactive element is the whole reactive elements of the suggested basis current and can be viewed as

$$w_{sqt} = w_{qq} - w_{lq} \quad (33)$$

### C. Calculation of Signal Generation Switching

3- $\phi$  Instant mention source active element is calculated by means of multiply in phase unit voltage pattern and active power current element, and these are named as

$$\left. \begin{aligned} i_{sap} &= w_{spt} u_{ap} \\ i_{sbp} &= w_{spt} u_{bp} \\ i_{scp} &= w_{spt} u_{cp} \end{aligned} \right\} \quad (34)$$

Comparably the 3- $\phi$  the reactive element of a 3- $\phi$  simultaneous reference source is calculated by multiplying the quadrature element voltage model and the reactive current element and is given as

$$\left. \begin{aligned} i_{saq} &= w_{sqt} u_{aq} \\ i_{sbq} &= w_{sqt} u_{bq} \\ i_{scq} &= w_{sqt} u_{cq} \end{aligned} \right\} \quad (35)$$

Reference source currents are defined as total reactive and active components of a phase, which are obtained as

$$\left. \begin{aligned} i_{sa}^* &= i_{sap} + i_{saq} \\ i_{sb}^* &= i_{sbp} + i_{sbq} \\ i_{sc}^* &= i_{scp} + i_{scq} \end{aligned} \right\} \quad (36)$$

The definite basis currents ( $i_{sa}, i_{sb}, i_{sc}$ ) and the mentioned source currents ( $i_{sa}^*, i_{sb}^*, i_{sc}^*$ ) of various phases are differentiated then the error.

## 3 Opal-RT Results

Users can utilize RT-LAB for quick transform Simulink models through synchronized workshop (RTW) and then execute immediate simulations on several objective computers among multicore personal computer processors. In order to have a smooth operation RT-LAB transparency controls, the following units such as:

- (1) Synchronization
- (2) User interference
- (3) Real-world interfacing via input–output boards
- (4) Data transfers.

One among the crucial parts that constitute Opal-RT Systems’ flexible OP5000 Interface Output device is the OP5142. This permits the decentralized processing of H–D–L–Hardware specification language operations and more-speed, higher-density digitized Input–output in actual time simulations using FPGA technology within RT-LAB simulated groups. Employing a peripheral constituent interconnect—Advanced ultra-low-latency actual time network user interface, it communicates with the desired PC.

Simulations be approved out to give you an idea about how the DSTATCOM system operates as it is controlled by the  $i \cos \phi$  and GDBPM-based  $i \cos \phi$  methods under various loading circumstances. The evaluations that followed were conducted in actual time on a PC operating Opal-RT-LAB software [19]. Figures 4, 5, 6, 7, 8, 9, 10, and 11 exhibit the Opal-Real-Time Laboratory simulation waveforms attained by using the DSO.

The real-time digital simulation findings are consistent with results in simulation, confirming improved functionality of DSTATCOM based on GDBPM controlled

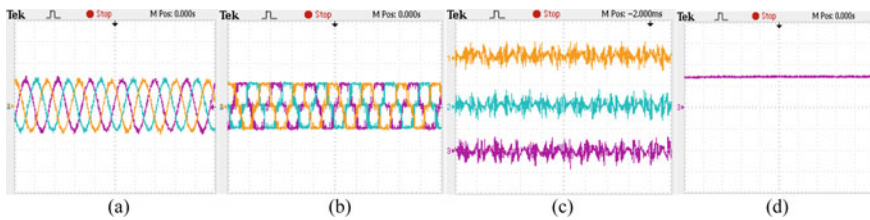


**Fig. 4** Experimental waveforms for DSTATCOM-based  $i \cos \phi$  procedure under steady-state condition of converter (rectifier) **a** supply current, **b** load current, **c** compensating current, **d** DC voltage

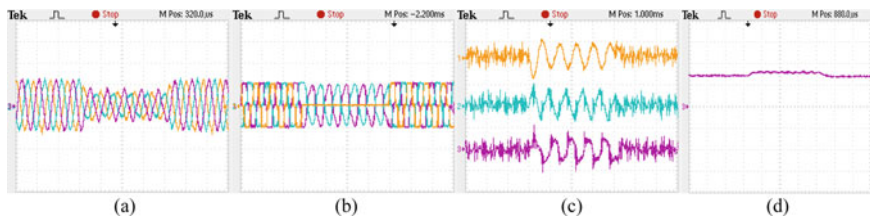


**Fig. 5** Experimental waveforms for DSTATCOM-based  $i \cos \phi$  procedure under dynamic loading condition of converter (rectifier) **a** supply current, **b** load current, **c** compensating current, **d** DC voltage

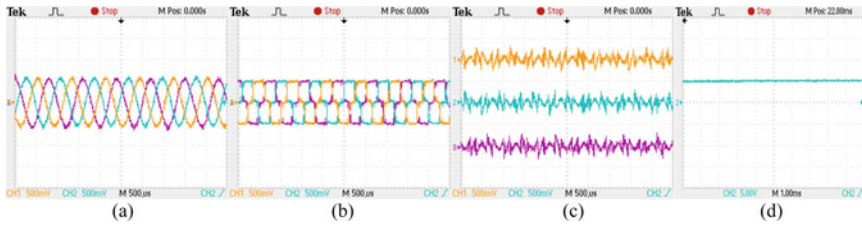


**Fig. 6** Experimental waveforms for DSTATCOM-based GDBPM supported  $i \cos \phi$  procedure under steady-state condition of converter (rectifier) **a** supply current, **b** load current, **c** compensating current, **d** DC voltage

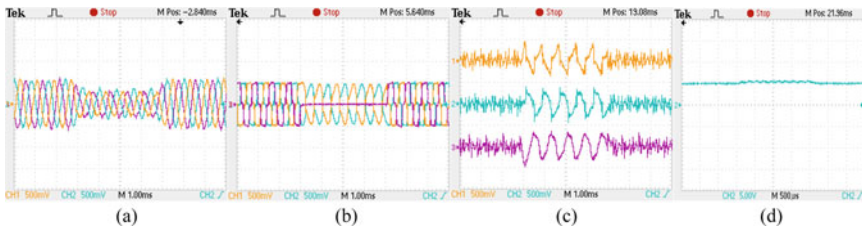


**Fig. 7** Experimental waveforms for DSTATCOM-based GDBPM supported  $i \cos \phi$  procedure under dynamic loading condition of converter (rectifier) **a** supply current, **b** load current, **c** compensating current, **d** DC voltage

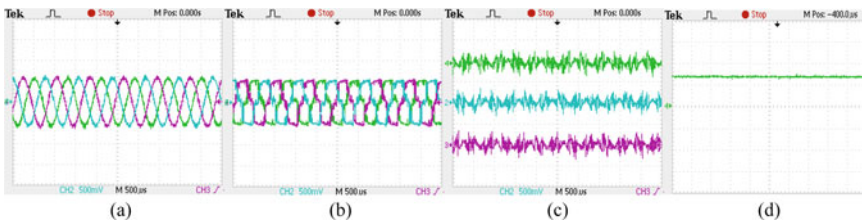


**Fig. 8** Experimental waveforms for DSTATCOM-based  $i \cos \phi$  technique under steady-state condition of both converter (rectifier) and DC-motoring load **a** source current, **b** load current, **c** compensating current, **d** DC voltage

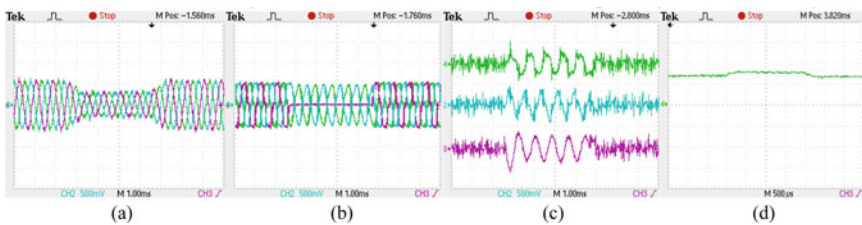


**Fig. 9** Experimental waveforms for DSTATCOM-based  $i \cos \phi$  technique under dynamic condition of both converter (rectifier) and DC-motoring load **a** source current, **b** load current, **c** compensating current, **d** DC voltage

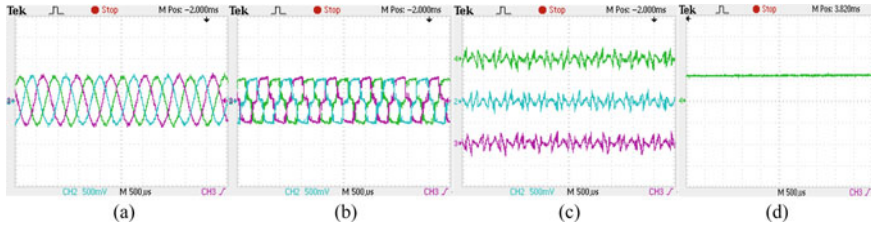


**Fig. 10** Experimental waveforms for DSTATCOM-based GDBPM supported  $i \cos \phi$  procedure under steady-state loading condition of both converter (rectifier) and motoring load **a** supply current, **b** load current, **c** compensating current, **d** DC voltage

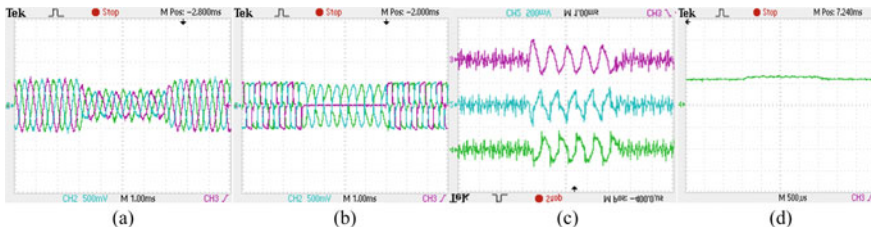


**Fig. 11** Experimental waveforms for DSTATCOM-based GDBPM supported  $i \cos \phi$  procedure under dynamic condition of both converter (rectifier) and DC-motoring load **a** source current, **b** load current, **c** compensating current, **d** DC voltage

$i \cos \phi$  method. The Appendix contains a list of the various block parameters that were used in the simulation investigations.

### 4 Conclusion

The comprehensive design and execution of DSTATCOM by GDBPM-based proposed control technique under unbalanced and balanced loading have been introduced and presented in this work. This control method effectively allows previous weights to acquire new weight through the use of momentum constants. From the simulation outputs, we can observe that by using the proposed control architecture the total harmonic distortion of source current of phases a, b, c are 4.12, 4.34, 4.04 and 4.26, 4.47, 4.54 under various cases. In comparison with the other conventional technique, this topology performs best shunt compensation, with minimization of harmonics, improvement in power factor, load balancing with voltage regulation. Real-time digital laboratory modelling results have been applied to corroborate the efficacy of the experimental results. These presentations of the projected system can be enhanced by incorporating advanced artificial intelligence-based controllers in DSTATCOM for obtaining reference currents.

## References

1. Ghosh A, Ledwich G (2002) Power quality enhancement using custom power devices. Kluwer, Norwell
2. Dugan RC, Mcgranaghan MF, Antoso S, Beaty HW (2003) Electrical power systems quality. McGraw Hill, New York
3. Cai J, Zhao H (2021) performance comparison of dSTATCOM using SRF,IRP control algorithm. In: IEEE 16th conference on industrial electronics and applications (ICIEA), pp 1984–1989
4. Zaveri T, Bhavesh B, Zaveri N (2011) Control techniques for power quality improvement in delta connected load using DSTATCOM. In: Electrical machine drives conference, pp 1397–1402
5. Singh B, Jayaprakash P, Kumar S, Kothari DP (2011) Implementation of neural network controlled three-leg VSC and a transformer as three-phase four-wire dSTATCOM. IEEE Trans Ind Appl 47(4):1892–1901
6. Qian L, Cartes DA, Li H (2008) An improved adaptive detection method for power quality improvement. IEEE Trans Ind Appl 44(2):525–533
7. Ahmed T, Waqar A, Essam A, Ammar A et al (2021) Energy management of a battery storage & DSTATCOM integrated power system using the fractional order sliding mode control. CSEE J Power Energy Syst 7(5)
8. Chenchireddy K, Kumar V, Sreejyothi KR, Tejaswi P et.al (2021) A review on D-STATCOM control techniques for power quality improvement in distribution. In: 2021 5th International conference on electronics, communication and aerospace technology (ICECA)
9. Aredes M, Akagi H, Watanabe EH, Salgado EV, Encarnacao LF (2009) Comparisons between the P-Q & P-Q-R theories in three-phase four-wire systems. IEEE Trans Power Electron 24(4):924–933
10. Talaat N, Ilic M (2008) ANNs based on subtractive cluster feature for classifying power quality. In: Power symposium, 40th North American, Calgary, AB, pp 1–7
11. Singh B, Jayaprakash P, Kumar S, Kothari DP (2011) Implementation of neural-network-controlled three-leg VSC and a transformer as three-phase four-wire dSTATCOM. IEEE Trans Ind Appl 47(4):1892–1901
12. Kalagotla H, Jegathesan V, Ashok Kumar L (2020) Different topologies of inverter: a literature survey. In: Innovations in electrical and electronics engineering, pp 35–43
13. RT-Lab Professional. <http://www.opal-rt.com/product/rt-lab-professional>.
14. Mikkili S, Panda AK (2012) Real-time implementation of PI and fuzzy logic controllers based shunt active filter control strategies for power quality improvement. Int J Electr Power Energy Syst 43:1114–1126
15. Panda AK, Mangaraj M (2017) DSTATCOM employing hybrid neural network control technique for power quality improvement. IET Power Electron 10(4):480–489
16. Ahmad MW et al (eds) (2022) Intelligent data analytics for power and energy systems. Springer, Singapore, 641pp. <https://doi.org/10.1007/978-981-16-6081-8>. ISBN: 978-981-16-6081-8
17. Tomar A et al (eds) (2022) Proceedings of 3rd international conference on machine learning, advances in computing, renewable energy and communication (MARC 2021), vol 915, 781pp. Springer, Berlin. ISBN: 978-981-19-2830-7. <https://doi.org/10.1007/978-981-19-2828-4>
18. Mikkili S, Panda AK (2013) Simulation and real-time implementation of shunt active filter id-iq control strategy for mitigation of harmonics with different fuzzy membership functions. IET Power Electron. 5(9):1856–1872
19. Panda AK, Mikkili S (2013) FLC based shunt active filter ( $p-q$  and  $Id-Iq$ ) control strategies for mitigation of harmonics with different fuzzy MFs using MATLAB and real-time digital simulator. Int J Electr Power Energy Syst 47:313–336

# Improvement in Voltage Stability of the System Due to Increased Penetration of Electric Vehicles Using Distributed Solar Photovoltaic Sources



Sheetal Deshmukh , Shirazul Islam , Atif Iqbal ,  
and Md Fahim Ansari 

**Abstract** Aiming to improve bus voltage profile and to enhance its voltage stability limit in a given power system including loads and increased penetration of Electric Vehicles (EVs), a distributed PV system injects both active and reactive powers. However, the uncoordinated operation of these PVs may increase the line losses. To resolve this issue, distributed PV sources are integrated at different locations of the IEEE-9 bus system which inject the active and reactive in such a way that the losses in the transmission lines are minimized. This paper proposes a secondary coordinated control scheme (SCCS), including a centralized controller. The local controller communicates the information corresponding to various bus voltages to the secondary using the communication links. If voltage deviation at a given bus becomes more than a specified limit, the secondary controller commands the nearest PV source that can inject the required active and reactive power to reduce losses occurred during power injection by the PV source. The proposed secondary controller scheme maintains the bus voltages within the specified limits. This control scheme is validated using Matlab/Simulink. Further, the maximum loadability margin of a given bus in the grid is calculated using MATPOWER. A comparison of the proposed scheme's performance with those reported in the literature demonstrates its effectiveness.

**Keywords** Voltage stability · Voltage control · Loadability margin · PV–QV curves

---

S. Deshmukh (✉) · S. Islam · A. Iqbal  
Department of Electrical Engineering, Qatar University, Doha, Qatar  
e-mail: [sd1912817@student.qu.edu.qa](mailto:sd1912817@student.qu.edu.qa)

S. Islam  
e-mail: [shiraz.ulislam@qu.edu.qa](mailto:shiraz.ulislam@qu.edu.qa)

A. Iqbal  
e-mail: [atif.iqbal@qu.edu.qa](mailto:atif.iqbal@qu.edu.qa)

M. F. Ansari  
Department of Electrical Engineering, Graphic Era Deemed to be University, Dehradun, India  
e-mail: [drfahim.ee@geu.ac.in](mailto:drfahim.ee@geu.ac.in)



## 1 Introduction

Solar photovoltaics (PVs), wind turbines, and fuel cells are currently being integrated into transmission and distribution grids at a large scale. The schematic of a single-line diagram in which renewable energy sources and EV loads are integrated into the sub-transmission network is shown in Fig. 1. The main bus 1 is fed from the conventional power plant. Here, two solar PV farms are connected to the transmission line at buses 2 and 5 at the point of common coupling (PCC). The industrial load and EV load are connected to the buses 3 and 4. Voltage control is a major issue faced due to the integration of these renewable sources. Some of the issues that are faced in networks are voltage fluctuations, voltage stability, cascading tripping faults, and fault-induced delayed voltage recovery (FIDVR) [1]. To quickly assist renewable sources, it is important to understand how the transmission/distribution network system interacts with renewable sources. It is important to maintain voltage stability among these sources by implementing a smart and coordinated control scheme. Voltage stability is referred to as the ability to maintain constant voltages in all grid buses under usual circumstances and during disturbances. This problem of voltage stability occurs due to the system being heavily loaded, faulty, or inadequate amount of reactive power [2, 3]. Various voltage control schemes implemented in transmission grids like optimal control, and three-level automatic voltage control (AVC), are implemented in Europe [4–7]. The adaptive zone division method and security-constrained optimal power flow (SCOPF) are used in China and the USA, respectively [4]. In [5], the base method uses a convex relaxation technique that solves nonlinear non-convex problems. It is crucial to integrate renewable sources to enhance the bus voltage of various buses. It is important to maintain bus voltages within an acceptable range while also maintaining voltage stability [6–8].

PV/wind sources are generally installed at sub-transmission and distribution levels. These networks are resistive lines with an  $r/x$  ratio greater than 1. Hence, in this type of network, both active and reactive powers are required to maintain the voltage [9–11]. In the literature, voltage control schemes are categorized as communication and non-communication based. Some of the voltage control schemes that are non-communication based are discussed in [12–14]. These schemes maintain

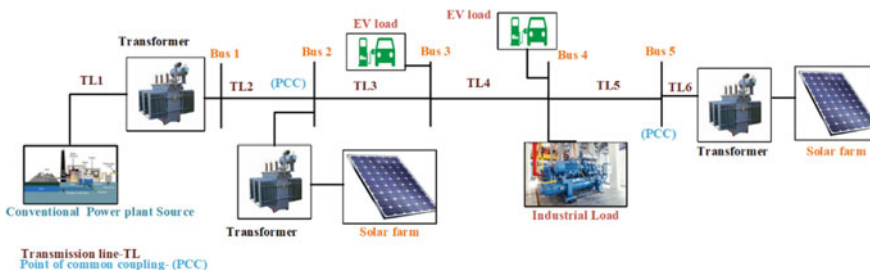


**Fig. 1** Single-line diagram with the integration of solar farm and EV and industrial load



the bus voltage by injecting active and reactive powers. A  $P$ - $Q$ - $V$  droop method is proposed in which the voltage is maintained by curtailing the active power, allowing for more reactive power to be injected when the inverter is running at its nominal capacity [12]. The  $P$  reference ( $P_{\text{ref}}$ ) and  $Q$  reference ( $Q_{\text{ref}}$ ) are calculated from droop characteristics. Another method discussed in [13] uses a reverse calculation which is used to estimate the grid voltage magnitude without the PV inverter, and the deviation from the nominal value is used to calculate the  $P$  and  $Q$  references. An optimization technique is used that will generate  $P_{\text{ref}}$  and  $Q_{\text{ref}}$  with the aim of minimization of line losses and power curtailment [14]. The author proposed an adaptive  $PQ$  management which derived a relation between voltage and  $P/Q$  of the inverter. The relationship between  $V$  and  $P$  and  $Q$  of the inverter is non-monotonic in nature. The main role is to find the reactive power required to make the voltage within the limit. The reference for  $Q$  is from the adaptive algorithm [15]. In [16], the voltage stability is improved using the integration of a renewable PV source. This scheme is implemented in the IEEE-14 and IEEE-30 bus systems. In addition, it generates a voltage stability profile for a full day that helps to identify the safe operating margin throughout the day. Some of the control schemes based on communication are [17–20]. In [17], an online supervisory voltage control scheme (OSVC) is proposed which improves voltage stability that having one PV source connected to one bus. In this technique, voltage stability is maintained through the reactive current division algorithm and control scheme (OSVC). Here, all the bus voltages are sensed using a wide-area measurement system (WAMS). Depending on the sensed value, the controller assigns the reactive current references to the PV plant as per the rated capacity. In this way, the bus voltages are maintained in a specific range. However, the limitation of this scheme is that the losses increase in the feeders. In addition, if multiple DGs (PV plants) are included in the system, the behavior of the system is not discussed. In [18, 19], an IEEE-118 bus system is partitioned among different zones and the coordination between them is discussed. In [20], an IEEE-9 bus system is integrated with three renewable sources and highlights that the voltage profile can be improved. The analysis is carried out through MATPOWER software. These lacks of coordination between the renewable sources and losses in the transmission lines are not discussed. The positive and negative aspects of all schemes are given in Table 1. The above limitation is overcome by the proposed control scheme and its key features are listed below.

- A secondary coordinated controller scheme (SCCS) is proposed.
- The proposed controller generates  $P_{\text{ref}}$  and  $Q_{\text{ref}}$  for each source.
- This controller can maintain the voltage within the limit by finding the nearest PV which will inject active and reactive power which will result in reduced power losses in transmission lines.
- Ease of implementation.
- In addition, the voltage stability study for the IEEE-9 system with and without the integration of DG (PV) sources is performed.

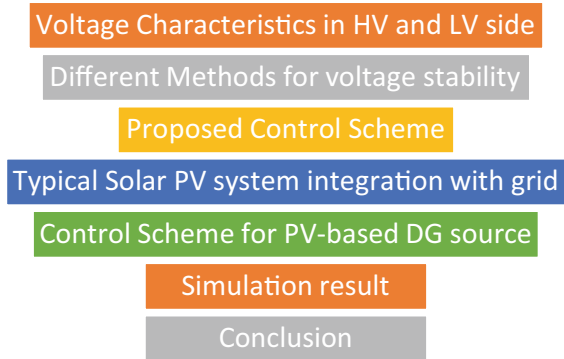
**Table 1** Advantages and limitations of the existing control schemes

S. No.	Objective	System used for validation	Communication	Generation of $P_{ref}$ and $Q_{ref}$	Advantages	Limitation
[12]	The voltage at PCC is controlled by injecting active and reactive power (droop method)	Loop 2-11 KV-feeder	No	Look-up table	Simple to implement and cost-effective	<ul style="list-style-type: none"> <li>Control action is local</li> <li>Performance deteriorates in case of power system reconfiguration</li> </ul> Difficult to implement
[13]	Line loss minimization and curtailment of active power using an optimization approach	Radial IEEE-37	Yes	$P_{ref}$ and $Q_{ref}$ using an optimization approach	Excellent performance and losses are reduced	Difficult to implement
[14]	Controls PCC voltage by allocation of reactive power	Radial 8-bus	Yes	The dual ascent method generates $P_{ref}$ and $Q_{ref}$	<ul style="list-style-type: none"> <li>Simple to implement</li> <li>Costly</li> </ul>	<ul style="list-style-type: none"> <li>Partial coordinated control</li> <li>More line losses</li> <li>Slower dynamic response</li> </ul>
[15]	Controls PCC voltage by finding the amount of $Q$ required to bring voltage within the limit	Radial-UKGDS 95-bus	No	Adaptive PQ + technique used to generate $P_{ref}$ , $Q_{ref}$	Simple to implement and cost-effective	<ul style="list-style-type: none"> <li>Control action is limited to local bus</li> <li>More losses in lines</li> <li>Limited range to improve voltage profile</li> </ul>
[16]	Controls the PCC voltage by injecting $P_{ref}$ and $Q_{ref}$	IEEE-14	No	Monte Carlo simulation method is used to generate $P_{ref}$ and $Q_{ref}$	<ul style="list-style-type: none"> <li>Consider uncertainties and intermitances of PV array</li> </ul>	<ul style="list-style-type: none"> <li>Locally controlled</li> <li>Difficult to implement</li> </ul>

(continued)

**Table 1** (continued)

S. No.	Objective	System used for validation	Communication	Generation of $P_{ref}$ and $Q_{ref}$	Advantages	Limitation
[20]	Controls PCC voltage by injecting $P_{ref}$ and $Q_{ref}$	IEEE-9	No	Feedforward control of three-phase CSI generates $P_{ref}$ and $Q_{ref}$	<ul style="list-style-type: none"> <li>Simple to implement, full converter utilization, Low cost</li> </ul>	<ul style="list-style-type: none"> <li>Control action is local</li> <li>Losses in transmission lines are not minimized</li> </ul>
[Proposed]	The voltage profile of PCC is improved by the nearest PV source and both $P_{ref}$ and $Q_{ref}$ (coordinated control)	IEEE-9	Yes	Secondary coordinated control scheme (SCCS) generates $P_{ref}$ and $Q_{ref}$	<ul style="list-style-type: none"> <li>Reduced line losses and increase efficiency</li> </ul>	<ul style="list-style-type: none"> <li>Capacity of PV Converters is utilized one by one not simultaneously</li> </ul>

**Fig. 2** Structure of the paper

The organization of the paper is depicted in Fig. 2. The voltage characteristics on HV and LV sides are followed by different methods of voltage stability. Section 2 explains the proposed control scheme and typical integration of solar PV systems in Sect. 3. Section 4 is about the results of the scheme in various scenarios which are discussed. Section 5 concludes the chapter.

### ***1.1 Voltage Characteristics in High Voltage (HV) and Low Voltage (LV)***

The PV source is followed by an inverter injecting power into the grid through impedance  $Z$ . The phasor diagram relating the sending end voltage,  $V_s$ , and receiving end,  $V_r$  in the high-voltage grid area is shown in Fig. 3. The receiving end voltage,  $V_r$ , is assumed as the reference phasor.

The voltage drop equation is given by (1)

$$\begin{aligned} \Delta V &= ((P + jQ)/V_r)(R + jX) \\ &= ((PR + QX)/V_r) + j((PX - QR)/V_r). \end{aligned} \quad (1)$$

For the system in which the  $R/X$  ratio is low, the voltage drop has been given as (2) by neglecting the imaginary component. While for the system in which the  $R/X$  ratio is high, the effect of resistance is large, and the equation of voltage drop equation is given as Eq. (3)

$$\Delta V = (QX/V_r) + j(PX/V_r), \quad (2)$$

$$\Delta V = (PR + QX)/V_r. \quad (3)$$

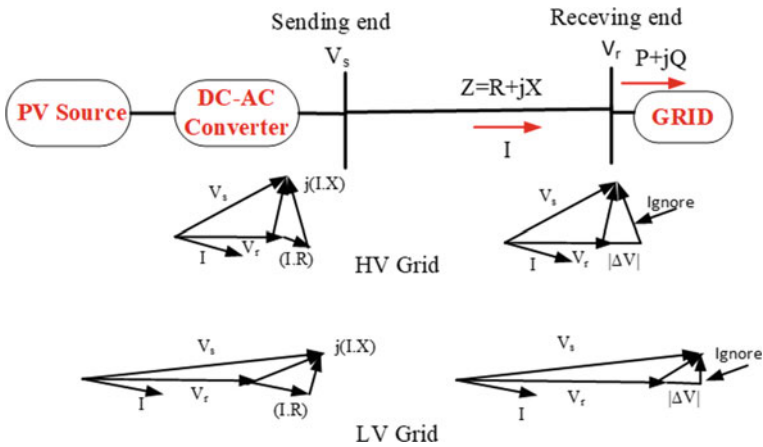


Fig. 3 Voltage phasor in HV and LV sides

### 1.2 Different Methods for Voltage Stability

There are two forms of voltage stability: small disturbance voltage stability and high disturbance voltage stability. The small disturbance voltage stability is due to an increase in the load. On the other side, the large disturbance voltage stability may be tripping offline or power plant. Voltage stability can last from a few seconds to several minutes. These small and large disturbances can have long-term and short-term stabilities. Static and dynamic analyses are the two basic techniques for determining voltage stability. The static analysis of a power system considers only static aspects. The time-variant differential equations are therefore set to zero. The load flow analysis is used in static analysis. The commonly used static method is PV, QV, and VQ sensitivity analysis [21–23]. The dynamic voltage stability analysis is transient stability of the power system. Here, by using differential equations and algebraic equations, the system is represented. However, there is no indication of how near the system is to voltage collapse. The detailed classification of voltage stability analysis methods is depicted in Fig. 4.

## 2 Proposed Control Schemes

The proposed secondary coordinated control scheme working is given in Fig. 5. In this bus voltages are sensed, and the data are given to the central controller. Here this controller detects whether the system is operating at ideal or undervoltage/overvoltage and takes appropriate action. If the voltages are operating above 0.95 p.u., then the central controller is operating in idle mode. Whenever the bus voltages drop below 0.95 p.u., the secondary controller detects its undervoltage mode. Furthermore,

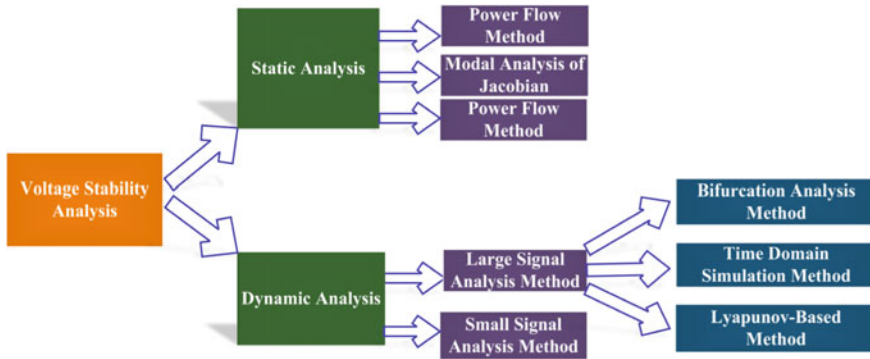


**Fig. 4** Different methods of voltage stability analysis

the SCCS central controller finds the nearest DG source that can compensate for voltage deviation which will result in lower losses. The SCCS central controller communicates to the local controller which is first nearest to that bus to inject power. Now, the local controller will change its  $P_{ref}$  and  $Q_{ref}$  values. However, if the DG cannot support voltage deviation, then it communicates to the SCCS central controller. Further, the SCCS central controller will identify the second nearest DG source that can compensate for this voltage deviation and communicate with the local controller of that DG source. Now, the corresponding local controller will compensate for the voltage deviation. When the bus voltages are above 1.05 p.u, the central controller operates in overvoltage operating mode. The central controller will find the nearest DG source that absorbs the reactive power and sends the signal to that local controller only. Figure 6 depicts the flowchart for this SCCS design. Whenever there is voltage deviation, each source local controller sets  $P_{ref-1}$  and  $Q_{ref-1}$  in four steps as given below. Here, ref-1, 2, and 3 indicate for local controllers 1, 2, and 3 in four steps as given below.

1.  $P_{ref-1} = 0.05 * S_{rated}$  and  $Q_{ref-1} = 0$  (initial state).
2.  $P_{ref-1} = 0.05 * S_{rated}$  and  $Q_{ref-1} = 0.11 * S_{rated}$ .
3.  $P_{ref-1} = 0.15 * S_{rated}$  and  $Q_{ref-1} = 0.44 * S_{rated}$ .
4.  $P_{ref-1} = 0.80 * S_{rated}$  and  $Q_{ref-1} = 0$ .

### 3 Typical Solar PV System Integration with Grid

Figure 7 shows a solar PV integration block diagram with a local and central controller. A DG source (PV), two converters (DC–DC and DC–AC), filters, a step-up transformer, and a local controller are the major elements. The output of the PV source is given to the first DC–DC converter, which employs maximum power point tracking (MPPT). Mostly used MPPT is (P&O) method. The output of the first stage is given to the second DC–AC inverter and then passed to the filter to

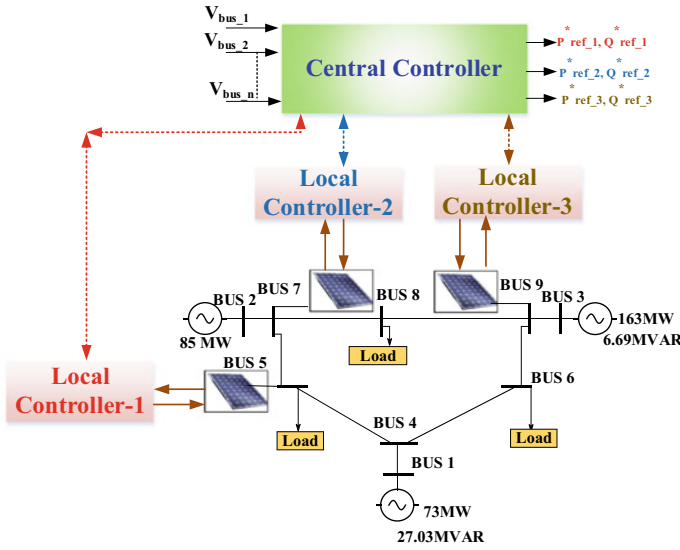


Fig. 5 Proposed secondary coordinated control scheme (SCCS)

remove unwanted signals. This inverter can provide both active and reactive powers by varying the DC–AC output current waveform with respect to the output voltage waveform. The DC–AC converter output is fed to the step-up transformer voltages from (11/230 kV). The central controller senses the bus voltages and sends the bus voltages value to the local controller.

The local controller sets the active and reactive power references as discussed in the proposed control scheme section. The rating and size of the PV array decide the amount of active power injection that can be injected. The output that a PV array can generate is determined by solar irradiation ( $G_{max}$ ) and the end temperature ( $T_{min}$ ) (4). The power corresponding to maximum power point ( $V_{MPP}$ ,  $I_{MPP}$ ) is  $W^{max} = (G^{max} T^{min})$ . Considering the inverter efficiency, the equation can be written as (5). The reactive power injection capacity is given by (6)

$$P_{array,DCI}^{max} W^{max} = V_{MPP}(W^{Max})I_{MPP}(W^{max}), \tag{4}$$

$$S_{PV}^{max} = P_{max} = \eta P_{array DCI}^{max} W^{max}, \tag{5}$$

$$Q_{available|W} = \sqrt{S_{PV}^{max 2} - P_{PV}|w^2}. \tag{6}$$

Grid operators have created grid codes (GCs) to support grid stability when there is a disturbance in the grid. GC Australian mandated that PV systems should increase reactive power supply by 4% if their voltage drops 1% at the point of common coupling (PCC). According to IEEE-STD-1547-2018, all distributed energy

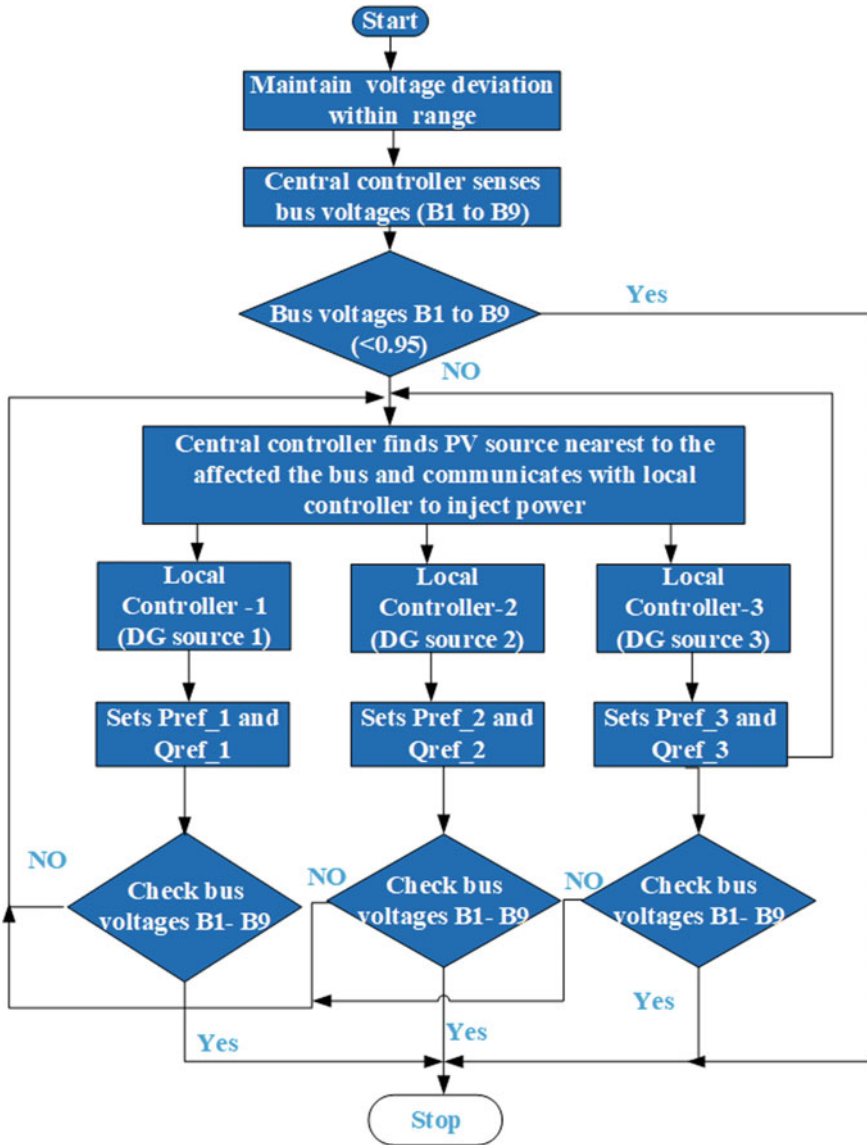


Fig. 6 Flowchart of the proposed scheme

resources (DER) can inject/absorb reactive power within defined restrictions. The types of DER are Category A and Category B depending upon the reactive power capability. Category A is the DER that is non-inverter based with lesser active and reactive power control abilities, while Category B is an inverter-based PV, battery energy storage system (BESS) with increased capacity of active and reactive control.



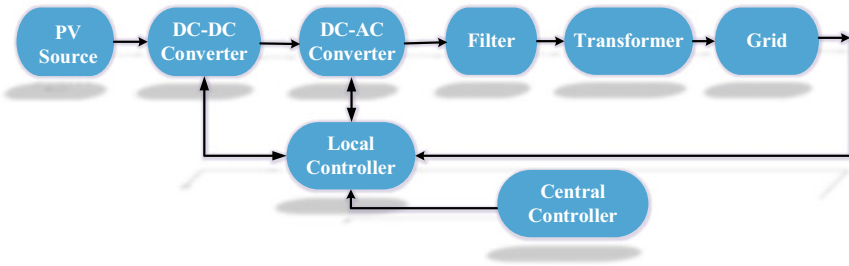


Fig. 7 Solar PV integration block diagram with a local and central controllers

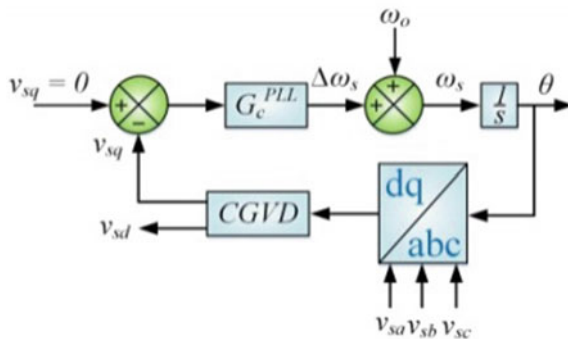
If the DER operates at 20% active power, then categories A and B can inject reactive power which is 44% of  $S_{rated}$ . On the contrary side, the reactive power absorption is 25% of  $S_{rated}$  for Category A and 44% of  $S_{rated}$  for Category B [24].

### 3.1 Control Scheme for PV-Based DG Source

The DGs source amplitude and phase angle need to be synchronized with the utility grid. This is carried out with the help of PLL as given in Fig. 8 Compensator for grid voltage disturbance (CGVD) reduces the disturbance in the grid voltage.

The block diagram of the integration of the PV source with the grid through a three-phase inverter is shown in Fig. 9. In this scheme, the three-phase current is detected and transformed to two-phase quantities using the theta value generated by the three-phase PLL. This two-phase quantity ( $I_d$  and  $I_q$ ) is compared with the reference value of active power and reactive power. The output of the comparator is given to the PI controller that is compared that generates ( $v_d^*$  and  $v_q^*$ ). This two-phase voltage quantity is again converted to  $abc$  which acts as input for the switches.

Fig. 8 Schematic of three-phase PLL used for acquiring phase information of grid



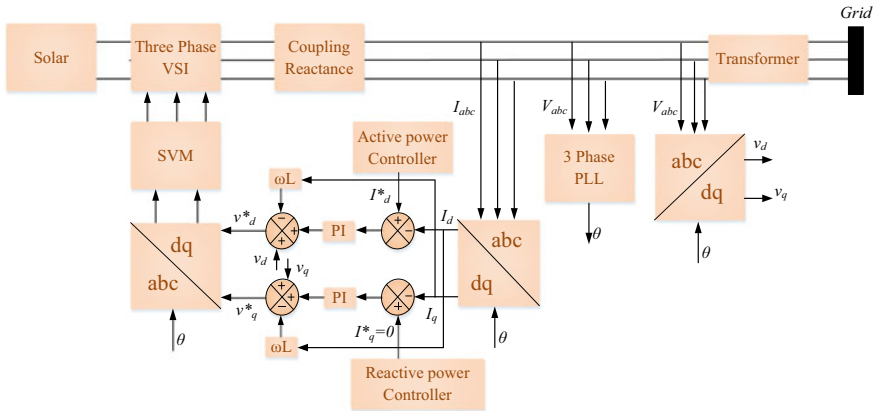


Fig. 9 Integration of PV source with the grid through a three-phase inverter

### 4 Simulation Result

The IEEE-9 bus system illustrated in Fig. 10 consists of three sources, loads (5, 6, and 8), and nine buses. In this system, three PV sources are connected at buses no 5, 7, and 9. PV-based DG system is simulated in MATLAB as per the given parameters in Table 2. Each PV source based is implemented as shown in Fig. 9 of 100 MW. The loads connected at the buses 5, 6, and 8 are 90 MW, 30 MVAR; 125 MW, 50 MVAR; and 100 MW, 35 MVAR, respectively. Working of the proposed control scheme SCCS is tested by varying the load variation as given in Table 3.

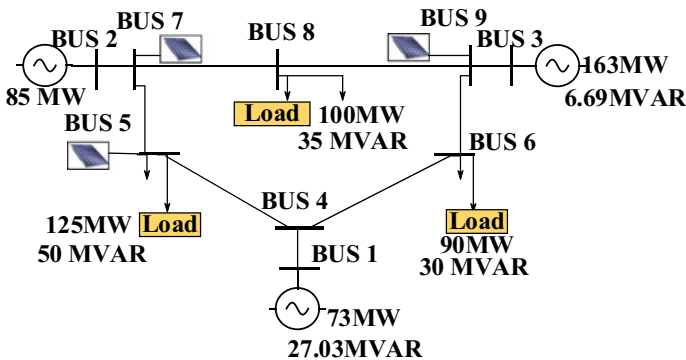


Fig. 10 PV integration with the IEEE-9 bus system

**Table 2** Simulation parameters of PV Sources

Parameters	Value
The power rating of PV source-5, 7, and 9	100 MW
Main grid voltage ( $L-L$ )	11 kV
Inductance ( $L_1, L_2,$ and $L_3$ )	2 mH
Capacitances ( $C_1, C_2,$ and $C_3$ )	500 $\mu$ F
Switching frequency ( $f_s$ )	10 kHz
Grid frequency( $f$ )	50 Hz

**Table 3** Cases

Case 1	Case 2
L5-189 MW, 76 MVAR	L5-125 MW, 50 MVAR
L6-90 MW, 3 0MVAR	L6-90 MW, 30 MVAR
L8-100 MW, 35 MVAR	L8-166 MW, 58 MVAR

#### 4.1 Case 1

In this case, the load of bus 5 is increased while keeping the rest loads as it is in Table 3. The active and reactive power injections for every source and bus voltages are shown in Fig. 11. Before  $t = 0.1$  s in Fig. 11b, the voltage profile is below 0.95 p.u. The central controller communicates with the PV source at bus 5 to support the grid. The local controller of that source will change the reference accordingly and inject power. The PV source at 5 is connected at  $t = 0.1$  s; for this time, the  $p = 5$  MW and  $q = 0$  MVAR. At  $t = 0.3$  s, the local controller injects only reactive power while keeping active power constant ( $p = 5$  MW and  $q = 11$  MVAR). The voltage profile of the bus is improved however still below 0.95 p.u. At  $t = 0.4$  s, the PV source at 5 injects both  $p$  and  $q$  ( $p = 20$  MW and  $q = 44$  MVAR). For this duration, the voltage profile is enhanced. From Fig. 11a at  $t = 0.5$  s, the injection of  $p = 80$  MW and  $q$  is constant 44 MVAR and it is observed that after  $t = 0.6$  s. all bus's voltages are above 0.95 p.u, except bus 9. Further, the local controller communicates with the central controller and its capacity is fully utilized. Hence, the central controller sends the signal to the PV source connected at 7 to inject the first  $q = 11$  MVAR at  $t = 0.7$  s and then at  $t = 0.7$  s  $q = 44$  MVAR. It can be observed that the voltage profile after  $t = 0.7$  s is below 0.95 s. Hence,  $p = 30$  MW is injected at  $t = 0.8$  s. For this case, the still the capacity of the DG source at 7 is not fully utilized, while the PV source at 9 is totally unused.

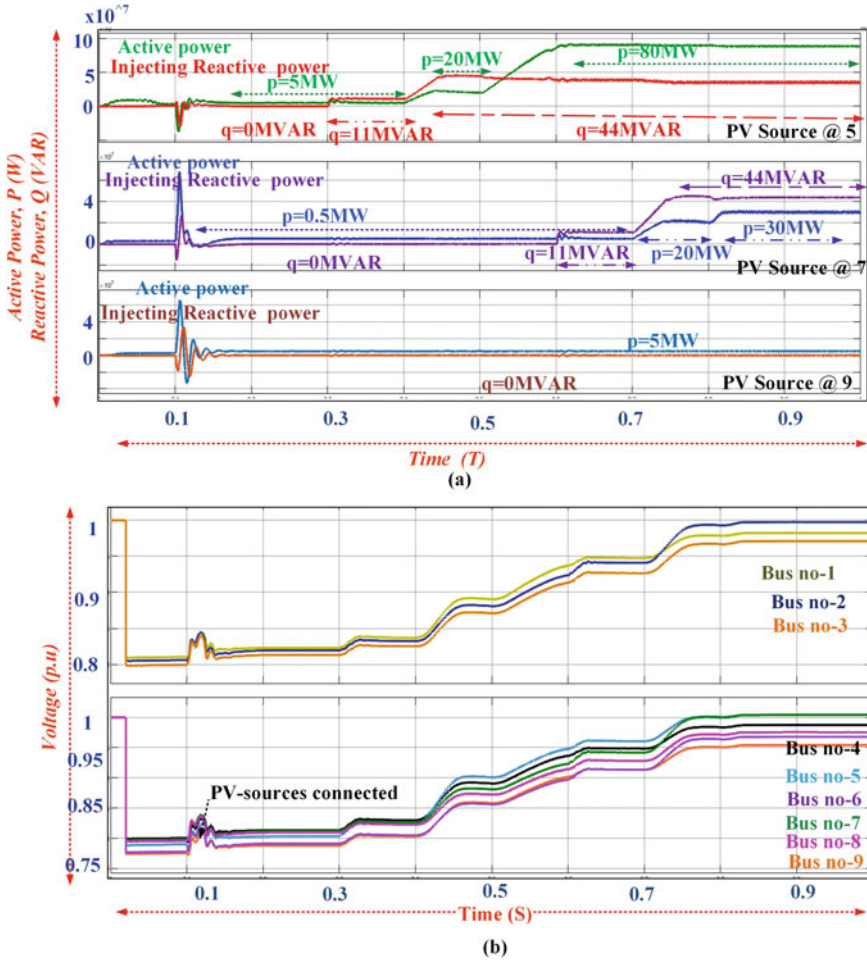


**Fig. 11** a PV sources 5, 7, and 9 active and reactive power injections (case 1), b voltage profile (case 1)

### 4.2 Case 2

In this case, the load is varied at bus 8 as given in Table 3. The active and reactive power injections for PV sources and voltage profile for this case are given in Fig. 12. The central controller communicates with the DG source 9 to inject the required power demand by the load. This PV source 9 will start injecting at  $t = 0.1$  s initial ( $p = 5$  MW and  $q = 0$ ), while at that time other PV sources are operating at ( $p = 5$  MW and  $q = 0$ ). The PV source now further injects at  $t = 0.3$  s ( $p = 5$  MW and  $q = 11$  MVAR); there is an improvement in the voltage profile. The master controller communicates further with the controller to change the  $P_{ref}$  and  $Q_{ref}$  signal ( $p =$

20 MW and  $q = 44$  MVAR). At  $t = 0.5$  s, the local controller of PV source-5 injects active power  $0.8 \cdot S_{\text{rated}}$  (80 MW). Now the central controller sends  $P_{\text{ref}}$  and  $Q_{\text{ref}}$  signal to PV source connected at bus 7 that injects ( $p = 5$  MW,  $q = 0$ ), ( $p = 5$  MW,  $q = 11$  MVAR), ( $p = 20$  MW,  $q = 44$  MVAR), and ( $p = 80$  MW,  $q = 44$  MVAR). After  $t = 0.8$  s, all the bus voltages are above 0.95 p.u

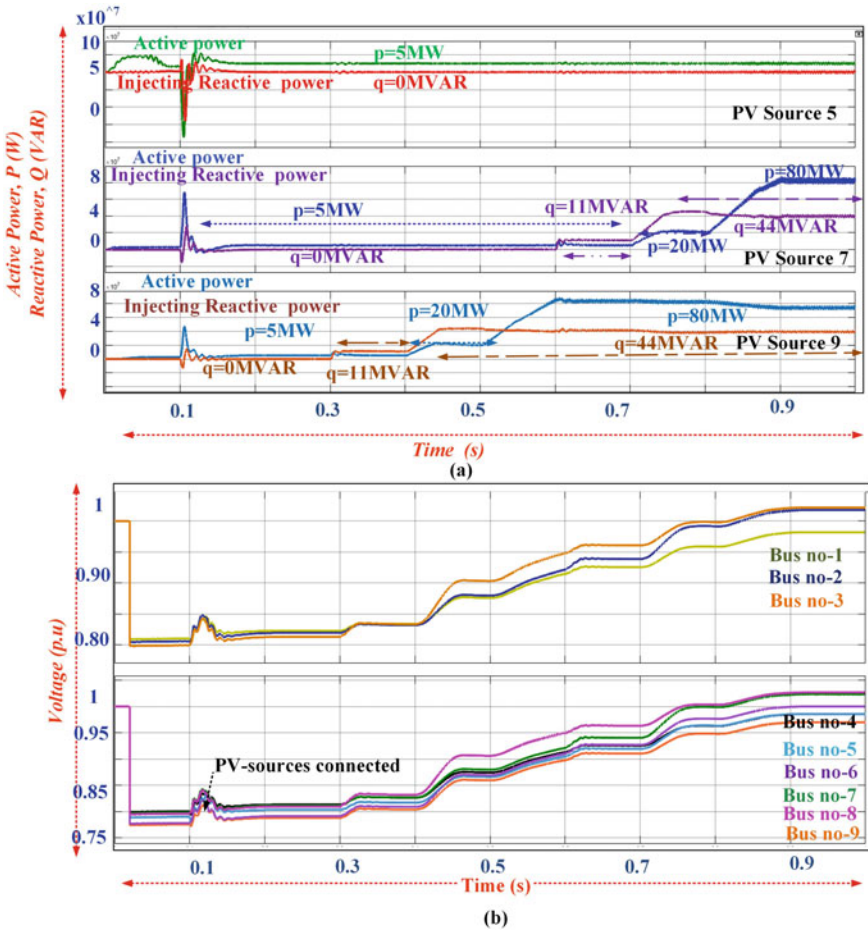
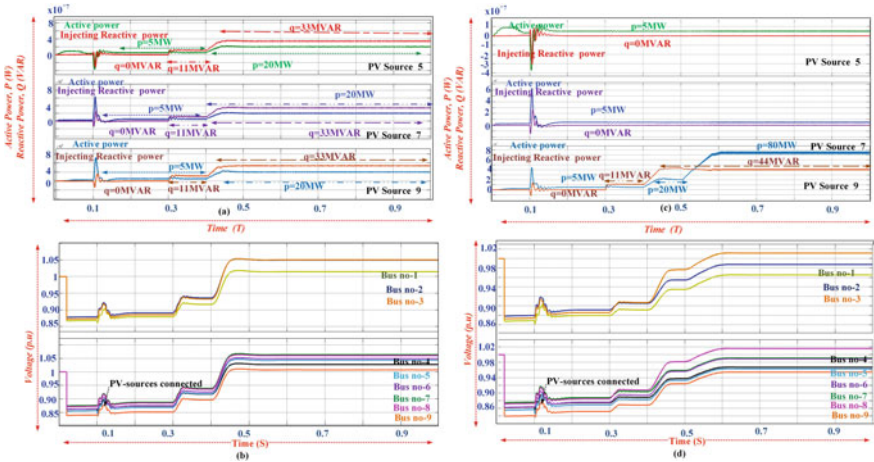


Fig. 12 a PV sources 5, 7, and 9 active and reactive power injections (case 2). b Voltage profile (case 2)

### 4.3 To Determine the SCCS Control Scheme Effectiveness with the Existing Schemes

To validate the working of the proposed SCCS control scheme, its performance is compared with the other uncoordinated schemes. For this scenario suppose an increase in load demand at bus 6 is considered. The voltage profile and corresponding injection of active and reactive different sources are displayed in Fig. 13a, b. The action of uncoordinated PV control scheme leads to production of overvoltage at buses 6, 7, and 8. In addition, it increases the losses, and all the sources are utilized. However, for the proposed control scheme, it was observed that only the PV source at bus 9 injects active and reactive powers as it is near bus 6 depicted in Fig. 13c, d. The PV source connected at bus 9 is utilizing its full capacity by injecting rated active and reactive power, while other PV sources connected at bus 5, 7 are still available for backup. The waveform for the SCCS proposed scheme is illustrated in Fig. 13d. A comparison is given in Table 4.



**Fig. 13** a Uncoordinated PV sources 5, 7, and 9 active and reactive power injection. b Voltage profile (uncoordinated), c the coordinated PV sources 5, 7, and 9 active and reactive power injections, d voltage profile (coordinated)

**Table 4** Comparison table between uncoordinated and coordinated schemes

Scheme	No PV sources utilized	Under voltage	Over voltage
Uncoordinated	1, 2, and 3	✗	✓
Coordinated (proposed)	1	✗	✗

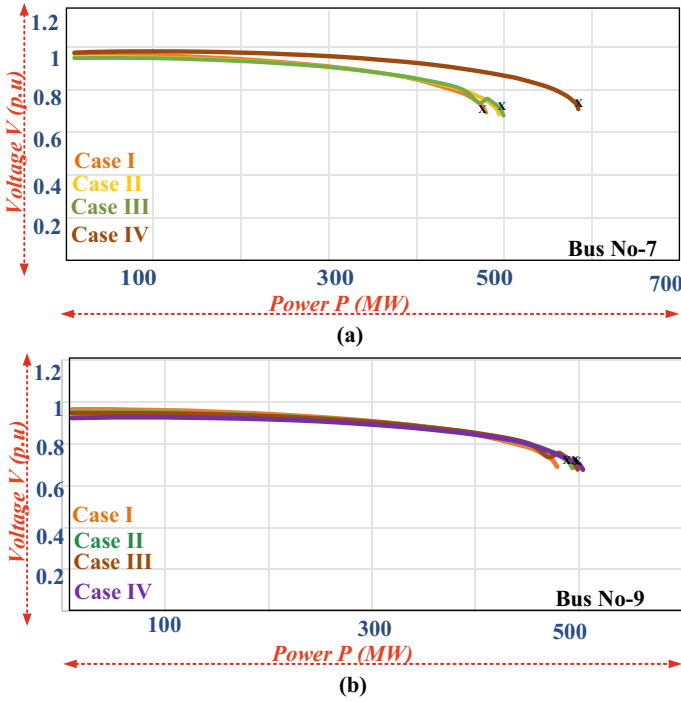


Fig. 14 PV curve analysis for a bus 7 and b bus 9

#### 4.4 Voltage Stability Analysis Using PV and QV Curves

In this subsection, the PV and QV curves analyses are carried out to find the maximum loadability margin of the bus in the IEEE-9 bus system with the integration of PV sources and without PV sources. The P–V curve of buses’ no. 7 and 9 is analyzed with the integration of only two PV sources 70 MW connected at bus 6 and bus 8 for different cases as mentioned below:

- Case I: when no PV plant source is connected in the IEEE-9 bus system.
- Case II: when one PV plant source is connected at bus 6 of the IEEE-9 bus system.
- Case III: when the PV plant source is connected at bus 8 of the IEEE-9 bus system.
- Case IV: when DG sources are connected at buses 6 and 8 of the IEEE-9 bus system.

The PV and QV curves for buses 7 and 9 for all four cases are shown in Figs. 14 and 15. From these figures, the following points are observed. There was a significant increase in the maximum load ability limit of the line when the PV sources are integrated into the system.

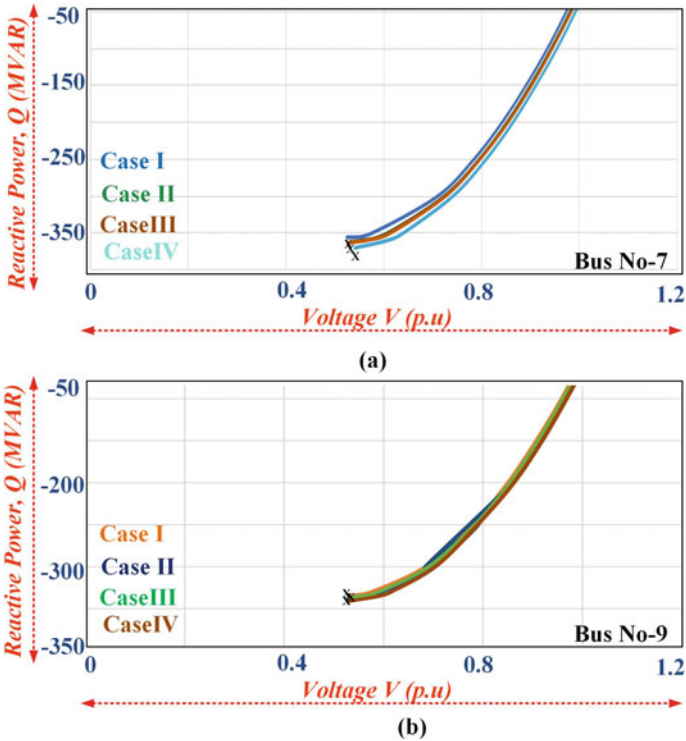


Fig. 15 QV curve analysis a bus no. 7 b bus no. 9

- PV Analysis: Case I has a maximum loadability limit of 510 MW, while Cases II and III have load ability and increased the margins by 5.68%. The voltage stability margin for Case IV is 584 MW. Above this point, the voltage is unstable. In each case, the point “X” indicates the point of voltage collapse. It is observed that for Case IV, the PV margin is increased by 14.5% for bus 7 and 5.21% for bus 9 as shown in Fig. 14. There was a significant increase in the maximum load ability limit of the line when the PV plant sources are integrated into the system.

## 5 Conclusion

In this paper, a centralized secondary controller is discussed which is utilized to enhance the voltage profile of the buses in an IEEE-9 bus system. This proposed control scheme maintains the bus voltages by injecting active and reactive power from the PV sources that are connected to the IEEE-9 bus system. The active and reactive power injections are carried out as per IEEE standard 1547. To validate the efficacy of the controller, the loads on buses 5 and 8 are increased by 51% from their normal values. Whenever the bus voltage drops below 0.95 p.u, the proposed



SCCS schemes identify the nearest PV sources and inject active and reactive powers to maintain the voltage. Initially, the active and reactive power references are set as  $P_{\text{ref-1}} = 0.05 * S_{\text{rated}}$  and  $Q_{\text{ref-1}} = 0$ . The voltage profile is constantly monitored by the centralized controller. If the voltage profile does not reach 0.95 p.u, the active and reactive power references of source-1 are changed to  $P_{\text{ref-1}} = 0.05 * S_{\text{rated}}$  and  $Q_{\text{ref-1}} = 0.11 * S_{\text{rated}}$ . Furthermore, if bus voltages do not increase, the local controller sets new  $P_{\text{ref-1}} = 0.15 * S_{\text{rated}}$  and  $Q_{\text{ref-1}} = 0.44 * S_{\text{rated}}$ . Still, if the bus voltages do not reach the prescribed limit, the  $P_{\text{ref-1}} = 0.80 * S_{\text{rated}}$  and  $Q_{\text{ref-1}} = 0$  are set. Here, one PV source's active and reactive power injection capacities are fully utilized. The secondary controller commands the nearest PV sources one by one to decrease the losses in transmission lines. The voltage deviation which is less than 5% of the base value of grid voltage is achieved across each bus of the IEEE-9 bus system. According to the results, the suggested controller ensures coordinated control of PV sources and increases the loadability margin. The active and reactive power injection capacity of each PV plant is fully utilized one by one. The active power injection takes place in such a way that the losses in the transmission lines are minimized. When the SCCS scheme performance is compared to that of uncoordinated schemes, it is concluded that the uncoordinated schemes produce overvoltage in certain of the buses. All PV sources are not properly utilized which leads to more transmission losses. The future scope is to implement the SCCS proposed control scheme in Real-Time Digital Simulator (RTDS).

**Acknowledgements** This publication was made possible by an NPRP grant [13S- 0108-200028] from the Qatar National Research Fund (a member of Qatar Foundation). The statements made herein are solely the responsibility of the authors.

## References

1. Sun H et al (2019) Review of challenges and research opportunities for voltage control in smart grids. *IEEE Trans Power Syst* 34(4):2790–2801 (2019). <https://doi.org/10.1109/TPWRS.2019.2897948>. Maxwell JC (1892) A treatise on electricity and magnetism, 3rd edn, vol 2. Clarendon, Oxford (1892), pp 68–73
2. Corsi S (2015) Voltage control and protection in electrical power systems: from system components to wide-area control. Springer
3. Definition and classification of power system stability (2004)
4. Corsi S, Pozzi M, Sforna M, Dell'Olio G (2004) The coordinated automatic voltage control of the Italian transmission Grid-part II: control apparatuses and field performance of the consolidated hierarchical system. *IEEE Trans Power Syst* 19(4):1733–1741. <https://doi.org/10.1109/TPWRS.2004.836262>
5. Sun H, Guo Q, Zhang B, Wu W, Wang B (2013) An adaptive zone-division-based automatic voltage control system with applications in China. *IEEE Trans Power Syst* 28(2):1816–1828. <https://doi.org/10.1109/TPWRS.2012.2228013>
6. Guo Q, Sun H, Zhang M, Tong J, Zhang B, Wang B (2013) Optimal voltage control of PJM smart transmission grid: study, implementation, and evaluation. *IEEE Trans Smart Grid* 4(3):1665–1674. <https://doi.org/10.1109/TSG.2013.2256938>

7. Low SH (2014) Convex relaxation of optimal power flow—part I: formulations and equivalence. *IEEE Trans Control Netw Syst* 1(1):15–27. <https://doi.org/10.1109/TCNS.2014.2309732>
8. Sharma G, Narayanan K, Adefarati T et al (2022) Frequency regularization of a linked wind-diesel system using dual structure fuzzy with ultra-capacitor. *Prot Control Mod Power Syst* 7:12. <https://doi.org/10.1186/s41601-022-00233-2>
9. Jahangiri P, Aliprantis DC (2013) Distributed Volt/VAR control by PV Inverters. *IEEE Trans Power Syst* 28(3):3429–3439. <https://doi.org/10.1109/TPWRS.2013.2256375>
10. Singhal A, Ajarapu V, Fuller J, Hansen J (2019) Real-time local Volt/Var control under external disturbances with high PV penetration. *IEEE Trans Smart Grid* 10(4):3849–3859. <https://doi.org/10.1109/TSG.2018.2840965>
11. Jabr RA (2019) Robust Volt/VAr control with photovoltaics. *IEEE Trans Power Syst* 34(3):2401–2408. <https://doi.org/10.1109/TPWRS.2018.2890767>
12. Moawwad A, Khadkikar V, Kirtley JL (2013) A New P-Q-V droop control method for an interline photovoltaic (I-PV) power system. *IEEE Trans Power Delivery* 28(2):658–668. <https://doi.org/10.1109/TPWRD.2013.2242906>
13. Liu Y et al (2018) Distribution network voltage control by active power/reactive power injection from PV inverters. In: 2018 13th IEEE conference on industrial electronics and applications (ICIEA), Wuhan, China, 2018, pp 543–547. <https://doi.org/10.1109/ICIEA.2018.8397776>
14. Li J, Xu Z, Zhao J, Zhang C (2019) Distributed online voltage control in active distribution networks considering PV curtailment. *IEEE Trans Indus Inf* 15(10):5519–5530. <https://doi.org/10.1109/TII.2019.2903888>
15. Das A, Batzelis EI, Anand S, Sahoo SR (2022) Network-agnostic adaptive PQ adjustment control for grid voltage regulation in PV systems. *IEEE Trans Indus Appl* 58(5):5792–5804 (2022). <https://doi.org/10.1109/TIA.2022.3180280>
16. Rahman S et al (2021) Analysis of power grid voltage stability with high penetration of solar PV systems. *IEEE Trans Indus Appl* 57(3):2245–2257 (2021). <https://doi.org/10.1109/TIA.2021.3066326>
17. Xiao W, Torchyan K, El Moursi MS, Kirtley JL (2014) Online supervisory voltage control for grid interface of utility-level PV plants. *IEEE Trans Sustain Energy* 5(3):843–853. <https://doi.org/10.1109/TSTE.2014.2306572>
18. Mehrjerdi H, Lefebvre S, Saad M, Asber D (2013) Coordinated control strategy considering effect of neighborhood compensation for voltage improvement in transmission systems. *IEEE Trans Power Syst* 28(4):4507–4515. <https://doi.org/10.1109/TPWRS.2013.2262007>
19. Mehrjerdi H, Lefebvre S, Saad M, Asber D (2013) A decentralized control of partitioned power networks for voltage regulation and prevention against disturbance propagation. *IEEE Trans Power Syst* 28(2):1461–1469. <https://doi.org/10.1109/TPWRS.2012.2225154>
20. Gore S, Iqbal A, Mehrjerdi H, Meraj M (2021) Voltage profiling and control of a sub-transmission network with integrated renewable energy sources—a case study. In: 2021 IEEE 4th international conference on computing, power and communication technologies (GUCON), 2021, pp 1–6. <https://doi.org/10.1109/GUCON50781.2021.9573790>
21. Aththanayake L, Hosseinzadeh N, Mahmud A, Gargoom A, Farahani EM (2020) Comparison of different techniques for voltage stability analysis of power systems. *Australas Univ Power Eng Conf (AUPEC) 2020*:1–6
22. Tomar A et al (eds) (2022) Proceedings of 3rd international conference on machine learning, advances in computing, renewable energy and communication: MARC 2021, vol 915, p XV, 781. ISBN: 978-981-19-2830-7. Springer Nature. <https://doi.org/10.1007/978-981-19-2828-4>
23. Ahmad MW et al (eds) (2022) Intelligent data analytics for power and energy systems. Springer, Singapore, pp 22, 641. ISBN: 978-981-16-6081-8. <https://doi.org/10.1007/978-981-16-6081-8>
24. IEEE standard for interconnection and interoperability of distributed energy resources with associated electric power systems interfaces. In: *IEEE Std 1547-2018 (Revision of IEEE Std 1547-2003)*, vol. pp.1–138 (2018). <https://doi.org/10.1109/IEEESTD.2018.8332112>

# An Intelligent System for Furfural Estimation in the Power Transformers



**Md. Manzar Nezami, Hythem Hashem, Md. Danish Equbal,  
Mohammad Junaid Khan, Md. Fahim Ansari,  
and Elfatih Elmubarak Mustafa**

**Abstract** Power transformers are supposed to be an expensive and critical component of a power system and so its schedule maintenance is an important aspect near the utilities. The cellulose paper used as the solid insulating material of the transformer deteriorates regularly due to progressive aging. As a result, it produces several degradation by-products of cellulose insulation into the transformer oil. Furfurals are among the major by-product of cellulose and are exploited to estimate the physical state of the transformer's dielectric and the electrical insulation directly and noninvasively. In the present work, an intelligent system is proposed and developed that predicts the level of furfural in the transformer oil. The system makes predictions using easily quantifiable parameters, enabling utilities to avoid suffering financial losses. The proposed system employs the Adaptive Neuro Fuzzy Inference System (ANFIS) technique with temperature and moisture as the input and 2-Furfuraldehyde

---

Md. M. Nezami (✉)

Department of Electronics and Communication Engineering, GLA University, Mathura 281406, India

e-mail: [manzar.nezami@gla.ac.in](mailto:manzar.nezami@gla.ac.in)

H. Hashem · E. E. Mustafa

Department of Computer Science, Faculty of Science and Arts at Belqarn, University of Bisha, 61985, Sabt-Al-Alaya, Saudi Arabia

e-mail: [hythemo@ub.edu.sa](mailto:hythemo@ub.edu.sa)

E. E. Mustafa

e-mail: [eemustafa@ub.edu.sa](mailto:eemustafa@ub.edu.sa)

Md. D. Equbal

Department of Electrical Engineering, Galgotias College of Engineering and Technology, Greater Noida, India

M. J. Khan

Department of Electrical and Electronics Engineering, Mewat Engineering College (Wakf), Nuh, Haryana, India

Md. F. Ansari

Department of Electrical Engineering, Graphic Era University, Dehradun, India

e-mail: [drfahim.ee@geu.ac.in](mailto:drfahim.ee@geu.ac.in)

(2-FAL) as the output. An optimum arrangement of the developed model to find accurate outputs has been achieved by the suitable selection of number and types of the membership functions of the network. Also, an exhaustive study is made to optimize the training data points to achieve the accurate predictions at minimum iterations. The proposed system is validated with nine test conditions of temperature and moisture, and the output thus obtained is verified through existing life models in the literature.

**Keywords** 2-Furfuraldehyde · Aging · ANFIS · Cellulose · Degradation · Power transformer

## 1 Introduction

The mineral oil-filled power transformers are considered critical and costly constituent of the power system [1]. The regular power supply is maintained on the cost of transformer's scheduled condition monitoring. Generally, the liquid and solid materials are used to provide the insulation between core and windings. The solid insulation uses the thermally upgraded kraft (TUK) papers made of cellulose. The performance of the transformers is mostly reliant over the condition of insulating cellulosic paper (solid). The transformers undergo successive aging when it confronted to factors like temperature and moisture [2, 3]. These causes hasten aging, create acids and unwanted sludge components that affect the cellulose insulation straight [4]. A continuous negligence in transformer maintenance not only has negative effects on utilities' finances, but also lowers the functionality and dependability of the equipment [5]. For maintenance purposes, a thorough inspection of the transformer provides a better understanding of its condition. Utilities must therefore frequently check on the physical state of the power transformers in order to estimate their valuable lifespan.

The status of the transformer can be readily inferred from how much the insulation made of cellulose paper has decomposed. The cellulose used to manufacture insulating paper is the linear polymer comprised glucose (monomer) units that are linked up all together to form a chain structure [6]. Every polymeric chain's number of glucose units is called the Degree of Polymerization (DP), that is the most reliable parameter to measure the extent of cellulosic insulation decomposition [7]. DP is measured through viscometric technique, and it is an invasive and destructive process of measurement and thereby avoided. The thermal aging of the cellulosic insulation in the company of moisture/water generates few degradation by-products into the transformer oil [8–11]. They most likely include carbon oxides and furfurals. Furfurals have referred to a family of six heterocyclic compound, that includes 2-Furfuraldehyde (2-FAL), 5-Methyl-2-Furfuraldehyde, Furfuryl Alcohol, 2-Furoic Acid, 5-Hydroxymethyl-2-Furfuraldehyde, and 2-Acetyl Furan [12]. The 2-FAL dissipates in transformer oil in large proportion and it is thermally more stable than the other furanic derivatives and thereby considered as the more reliable and prominent aging indicator of the cellulosic insulation [13].

In accordance with the transformer paper insulation's DP value, numerous research studies have been conducted to evaluate the transformer health. But, the DP measurement required intrusion into the transformer to cause a severe outage that will not be economical near the utilities. On the other hand, several empirical models have been found in the literature to calculate the value of DP based on the concentration of 2-FAL, such as Chendong, Stebbin, De-Pablo, and Pahlavanpour. These models take the 2-FAL concentrations (ppb or ppm) and estimate the value of DP, based on which the current physical state of cellulosic insulation is identified. However, numerous soft computing techniques, including support vector machines, wavelet networks, fuzzy logic, neural fuzzy systems, and neural networks, have been documented in the literature to evaluate the health of transformers based on different parameters (especially, DP), and 2-FAL computation has not yet been attempted [14–21]. In this work, an Adaptive Neural Fuzzy Inference System (ANFIS) has been exploited to implement the utility of easily measurable parameters to estimate the molecules (in ppm) of 2-FAL in the transformer insulating oil. The system takes temperature and moisture as the inputs to estimate the value of 2-FAL which ultimately give the DP values and hence the status of the cellulose. The proposed method facilitates the utilities for developing a web-based real-time health assessment system. This not only makes the distribution transformers complete their designed life but also overcomes the revenue losses for the utilities. The system has also an advantage that it avoids the destructive measurement for the transformer's health assessment and thus the severe outages.

The paper is organized in the chronological order. The first section is the introduction part followed by ANFIS system description in the second section. The proposed methodology and development of the system are detailed thereafter. Finally, the result and discussion and conclusion are included in the last section.

## 2 ANFIS

The ANFIS employed hybrid input–output mapping technique that utilizes the benefits of neural network's capability for learning within framework of FIS. The ANFIS's generalized structure, which consists of nodes connected by directional links, is represented in Fig. 1. ANFIS structure consists of five layers, each having such nodes that can be either static or adjustable. The output obtained at the adaptive square nodes relies at the parameters that are used to create them, whereas spherical nodes responded as the stationary one and their output is reliant over the outcomes of preceding layers. The one-to-one linkage offers conduit the signal without altering its form [22, 23]. Here, Layer 1 is made up of the four nodes  $A_1$ ,  $A_2$ ,  $B_1$ , and  $B_2$ . These nodes stand for a particular fuzzy set which maps the input toward the output as per that how firmly it bears a resemblance to the define fuzzy sets. The shape of circular nodes in Layer 2 indicates its fixed nature. These circular-shaped nodes provide an output by multiplying the input signals by the product. Nodes that formed Layer 3 conduct the normalizing function for Layer 2's output. Nodes in the Layer 4 are

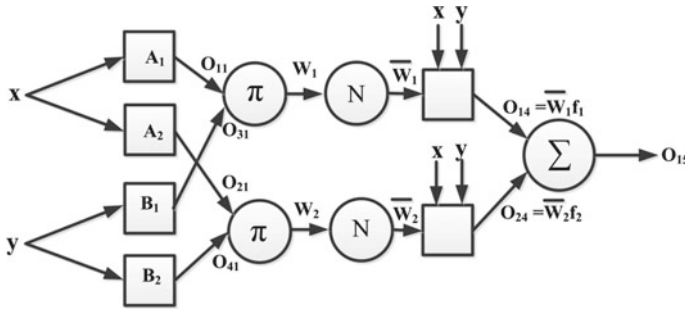


**Fig. 1** Generalize five-layered ANFIS structure

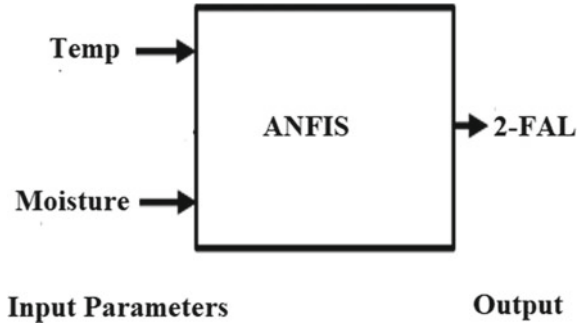
of adaptive type, meaning that their output relies on node’s ensuing parameter. The results for the layer, therefore, integrate the results of the prior layer. To create the concluding output, the Layer 5 applies the summing function of incoming signals.

### 3 Proposed Intelligent System for 2-FAL Estimation

The kraft paper is used to provide the insulation inside the transformers and made usually of cellulose (C<sub>6</sub>H<sub>10</sub>O<sub>5</sub>). The cellulose is polymer of glucose monomers in linear structure which breakdowns under successive aging. Due to overloading condition in the transformers, the temperature rises and distresses the cellulosic insulation [24–27]. The presence of moisture in the transformer accelerates this distress and thereby produces cellulose degradation by-products. The furanic derivatives and carbon oxides are released into transformer oil as the aging (due to decomposition of cellulose) by-products of the cellulosic paper breakdown. Among furanic derivatives, 2-FAL is dissipated in oil in large proportion and thermally stable and thereby predicts the cellulose condition accurately. The ANFIS model proposed here estimates the concentration of 2-FAL as the straight function of moisture and the temperature (ambient). The design of the proposed structure is depicted in the block diagram of Fig. 2.

The proposed ANFIS system takes temperature and moisture as the inputs and estimates 2-FAL as the output. The values of temperature were lying in the range from 90 to 130 °C and moisture (%) varies from 1 to 3%. A dataset which comprises 100 input–output points has been given to the system for the training. To obtain an optimal ANFIS system, different types and number of membership functions have been attempted. Trapezoidal membership function is found to be the best membership function with least error of 0.0024. The model is tested and validated for ten samples comprised different temperature and moisture values.

**Fig. 2** Schematic of proposed ANFIS-based intelligent system



### 4 Result and Discussion

The ANFIS structure is designed and implemented using the MATLAB environment to estimate the concentrations of 2-FAL against easily measurable parameters. The optimal ANFIS model has been found using hit-and-trial method, i.e., by varying the type and number of the membership functions. The external experimental data available in literature are then tested using the optimal ANFIS model [11]. Table 1 displays the experimental data points used to evaluate the ANFIS model’s performance. Observing Table 1, one can conclude that the rise in temperature directly affects the evolution of 2-Furfuraldehyde in the transformer’s insulating oil. However, the increase in the moisture accelerated the 2-FAL generation more rapidly. As a result, the proposed ANFIS model was found to be more accurate for the detection of transformers’ cellulose degradation product more appropriately.

**Table 1** Estimated output of the developed ANFIS system as the function of temperature and moisture

Input		Output
temperature (°C)	Moisture (%)	2-Furfuraldehyde (2-FAL) ppm
90	1	0.11
90	2	0.32
90	3	1.99
110	1	2.50
110	2	2.93
110	3	2.92
130	1	2.44
130	2	2.95
130	3	2.84

## 5 Conclusion

The paper successfully implemented the ANFIS model for 2-Furfuraldehyde (2-FAL) estimation. The model employs the parameters like temperature and moisture to measure the 2-FAL. The parameters used to develop the system are easily measurable and thereby make the system more economical for the utilities. The ANFIS structure easily correlates the input and the output by appropriately tuning the membership function. The system has been tested and validated with the available data in the literature and found to estimate more precise and accurate outcomes. As a result, the ANFIS model offers us a productive substitute for measuring the values of DP with the help of diagnostic parameters while restricting the intrusive measurements approach.

## References

1. Wu S, Zhang H, Wang Y, Luo Y, He J, Yu X, Zhang Y, Liu J, Shaug F (2022) Concentration prediction of polymer insulation aging indicator—alcohols in oil based on genetic algorithm—optimized support vector machines. *Polymers* 4:1449
2. Yoo J, Kang S, Lee J et al (2023) Electrical characteristics of high-performance ultrasonic transducer for non-destructive testing. *Trans Electr Electron Mater.* <https://doi.org/10.1007/s42341-023-00432-0>
3. Fan X, Liu J, Lai B, Zhang Y, Zhang C (2021) FDS measurement-based moisture estimation model for transformer oil-paper insulation including the aging effect. *IEEE Trans Instrum Meas* 70:1–10
4. Pradhan MK (2006) Assessment of the status of insulation during thermal stress accelerated experiments on transformer prototypes. *IEEE Trans Dielectr Electr Insul* 13:227–237
5. Kherif O, Benmahamed Y, Tegar M, Boubakeur A, Ghoneim SSM (2021) Accuracy improvement of power transformer faults diagnostic using KNN classifier with decision tree principle. *IEEE Access* 9:81693–81701 (2021)
6. Kachler AJ, Hohlein I (2015) Aging of cellulose at transformer service temperatures. Part 1: influence of type of oil and air on the degree of polymerization of pressboard, dissolved gases, and furanic compounds in oil. *IEEE Elect. Insul Mag* 21:15–21 (2015)
7. Saha TK, Darveniza M, Yao ZT, Hill DJT, Yeung G (1999) Investigating the effects of oxidation and thermal degradation on electrical and chemical properties of power transformers insulation. *IEEE Trans Power Del* 14:1359–1367
8. Feng DW, Yang LJ, Liao RJ, Zhou LW, Lin YD (2018) Effect of moisture content on the production and partitioning of furfural in oil-paper insulation. *IEEE Trans Dielectr Electr Insul* 25:2389–2397
9. Unsworth J, Mitchell F (1990) Degradation of electrical insulating paper monitored with high performance liquid chromatography. *IEEE Trans Electr Insul* 25:737–746
10. Ali M, Emsley AM, Herman H, Heywood RJ (2001) Spectroscopic studies of the ageing of cellulosic paper. *Polymer* 42:2893–2900
11. Mandlik M, Ramu TS (2014) Moisture aided degradation of oil impregnated paper insulation in power transformers. *IEEE Trans Dielectr Electr Insul* 1:21
12. Nezami MM, Wani SA, Khan SA, Khera N, Sohail S (2018) An MIP-based novel capacitive sensor to detect 2-FAL concentration in transformer oil. *IEEE Sens J* 18(19):7924–7931
13. Nezami MM, Wani SA, Khan SA, Khera N, Sohail S (2020) A comb type capacitive 2-FAL sensor for transformer oil with improved sensitivity. *IEEE Trans Instr Meas* 69(7):4524–4532



14. Ghunem RA, Assaleh K, El-hag AH (2012) Artificial neural networks with stepwise regression for predicting transformer oil furan content. *IEEE Trans Dielectr Electr Insul* 19:414–420
15. Nezami MM, Eqbal MD, Khan SA, Sohail S, Ghoneim SSM (2021) Classification of cellulosic insulation state based on smart life prediction approach (SLPA). *Processes* 9:981
16. Chaturvedi D, Satsangi PS, Kalra PK (1999) Flexible neural network models for electrical machine. *J. Inst Engg* 80:53–58
17. Abu-Elanien AEB, Salama MMA, Ibrahim M (2012) Calculation of a health index for oil-immersed transformers rated under 69 kV using fuzzy logic. *IEEE Trans Power Deliv* 27:2029–2036
18. Talpur N, Abdulkadir SJ, Alhussian H et al (2023) Deep neuro-fuzzy system application trends, challenges, and future perspectives: a systematic survey. *Artif Intell Rev* 56:865–913
19. Nezami MM, Eqbal MD, Khan SA, Sohail S (2021) An ANFIS based comprehensive correlation between diagnostic and destructive parameters of transformer's paper insulation. *Arab J Sci Eng* 46:1541–1547
20. Nezami MM, Wani SA, Khan SA, Khera N, Khan MA (2017) Fuzzy approach for residual life assessment of paper insulation. In: 3rd International conference on condition assessment techniques in electrical systems (CATCON), pp 26–30, Ropar, India (2017)
21. Goyal D, Choudhary A, Sandhu JK, Srivastava P, Saxena KK (2022) An intelligent self-adaptive bearing fault diagnosis approach based on improved local mean decomposition. *Int J Interact Des Manuf*. <https://doi.org/10.1007/s12008-022-01001-0>
22. Khan SA, Eqbal MD, Islam T (2015) A comprehensive comparative study of DGA based transformer fault diagnosis using fuzzy logic and ANFIS models. *IEEE Trans Dielectr Electr Insul* 22(1):590–596
23. Forouhari S, Abu-Siada A (2018) Application of adaptive neuro fuzzy inference system to support power transformer life estimation and asset management decision. *IEEE Trans Dielectr Electr Insul* 25(3):845–852
24. Ahmad MW et al (eds) (2022) *Intelligent data analytics for power and energy systems*. Springer, Singapore, p 22, 641, ISBN: 978-981-16-6081-8. <https://doi.org/10.1007/978-981-16-6081-8>
25. Tomar A et al (eds) (2022) *Proceedings of 3rd international conference on machine learning, advances in computing, renewable energy and communication: MARC 2021*, vol 915. ISBN: 978-981-19-2830-7. Springer, pp 15, 781. <https://doi.org/10.1007/978-981-19-2828-4>
26. Heywood RJ, Emsley A, Ali M (2000) Degradation of cellulosic insulation in power transformers. Part 1: factors affecting the measurement of the average viscometric degree of polymerization of new and aged electrical papers. *IEE Proc Sci Meas Technol* 147(2):86–90 (2000)
27. Mian T, Choudhary A, Fatima S (2022) Vibration and infrared thermography based multiple fault diagnosis of bearing using deep learning. *Nondestr Test Eval*. <https://doi.org/10.1080/10589759.2022.2118747>

# Design of PID-Tuned Controller for Automatic Voltage Regulator for Frequency Stability in Thermal Power Plant



Md. Fahim Ansari, Atif Iqbal, and Md. Manzar Nezami

**Abstract** The current work is centered on the construction of a tuned controller's proportional integral and derivative (PID) to achieve consistent voltage and frequency and hence reliable power. Implementing three gain factors for integral, proportional, and differentiation at an acceptable degree of error as well as a dynamic response was the most crucial step in the construction of a PID. To acquire the necessary results, robustness and quick reaction were obtained.  $P = 0.1943$ ,  $I = 0.1827$ ,  $D = 0.0338$ ,  $N = 8.267$  were the PID controller settings that were quickly acquired in a settling time of 0.6316 s. The robustness is reduced for faster reactions that settle in less than 0.6316 s. Fast response time of 0.632 s and the highest level of system robustness yield the best result.

**Keywords** PID controller · Tune PID · Robustness

---

Md. F. Ansari  
EED, Graphic Era Deemed to Be University Dehradun, Dehradun, India  
e-mail: [drfahim.ee@geu.ac.in](mailto:drfahim.ee@geu.ac.in)

A. Iqbal  
Qatar University Qatar, Doha, Qatar

Md. M. Nezami (✉)  
GLA Mathura, Chaumuhan, India  
e-mail: [manzar.nezami@gla.ac.in](mailto:manzar.nezami@gla.ac.in)

## 1 Introduction

The PID controller is also known as the Proportional (P), Integral (I), and Derivative (D) controller (D). Closed-loop control can provide appropriate performances with a simple algorithm for a variety of processes, using proportional integral derivative (PID) controllers which have been found to be the best controllers utilized in the process of industries [1–4]. Moreover, this controller is very durable and cost-effective [5–7]. Finding the proper controller setting modifications is quite challenging; the required closed-loop system performance can only be attained after a lot of trial and error. Controller tuning is the term used to describe the procedure. Many tools, methods, and theories can be used to fine-tune the PID controller [8–10]. It is still difficult to determine the PID controller's ideal parameters. The paper has been designed to get proper response for a tuned controller, which has wide application for selecting proper parameters of the circuit. The main factor to solve the issues with thermal power plant is its settling time whenever a sudden change in load demand takes place.

The paper work has been designed to obtain an optimized value of  $P$ ,  $I$ ,  $D$  values when a sudden change of load is applied.

## 2 Robustness Consideration

The ability of the closed-loop system to be resistant to component changes is known as robustness [11, 12], that is one of the most advantageous aspects of feedback. They can also create feedback systems based on strongly simplified models thanks to it. It is necessary to use quantitative techniques to evaluate how well a feedback system functions. The resilience of any system affects how well it performs. To assess a system's robustness, testing engineers induce defects and monitor the system's resiliency. Test engineers can develop efficient methods to aid fault injection in locating critical system defects. The choice of a PID controller can be challenging. The next stage in configuring a PID controller is selecting or tweaking PID parameter values. The letters  $P$ ,  $I$ , and  $D$  are used to control various parameters. The responses have been enhanced in a number of ways, including by tweaking the hit-and-trial method first, and then the PID, or control gains, later. Because the proportional term compensation grows with error size, larger proportional gains ( $P$ ) imply that faster production is possible [13]. Moreover, as big also denotes oscillation and instability, integral gains ( $I$ ) have been used to lessen oscillations while also indicating that steady-state errors are corrected more quickly [14]. There may be severe overshoot because any negative error introduced during the transient reaction must be balanced out by a positive error before steady state can be reached. Finally, derivative gain

(D) reduces overshoot while considerably improving the slow transient response [15, 16]. This paper aims to find the following results:

- Comparison of tuned and block response.
- Reducing settling time and improving the robustness of the system.
- Designing of controller parameters such as  $P$ ,  $I$ ,  $D$  and  $N$ .

### 3 Simulation Results

Figure 1 depicts the simulation model used to calculate the output voltage in per unit and in kV. It has been found that PID-tuned controllers respond more quickly than PID controllers. Figure 2 displays the PID controller’s tuned and block responses.

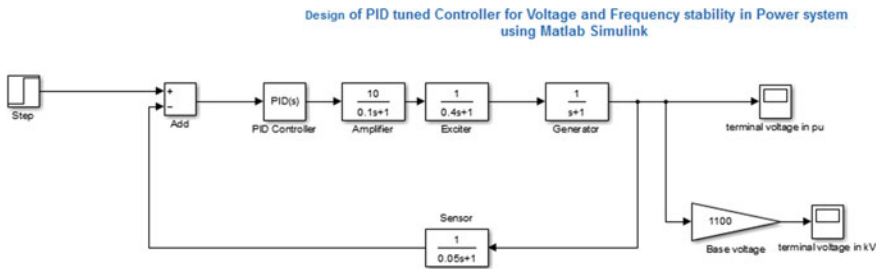


Fig. 1 PID controller for voltage and frequency stability

Table 1 compares various parameters acquired using PID-tuned and block controllers and demonstrates how the value of tuned parameters has been significantly decreased as compared to block controller parameters. Also, the robustness parameters have been enhanced.

Figure 3 graph for rapid reaction makes it abundantly evident that the settling time has been slashed to 0.632 s.

For fast settling time, the response of tuned PID and block PID has been given in Table 2, which indicates that for fast settling time, robustness of system is reduced.

Finally, taking into account the system’s resilience and speed, a plot of their optimal values is shown in Fig. 4. This picture demonstrates that the parameters for  $P$ ,  $I$ , and  $D$  have been supplied in Table 3 for robustness and speed.

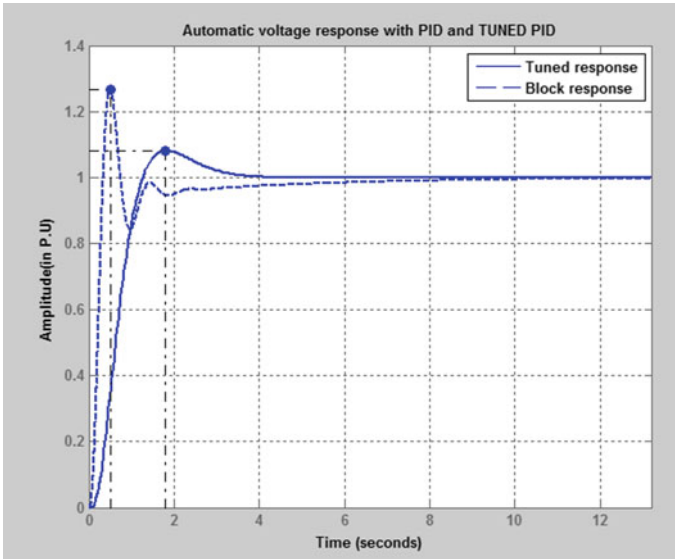
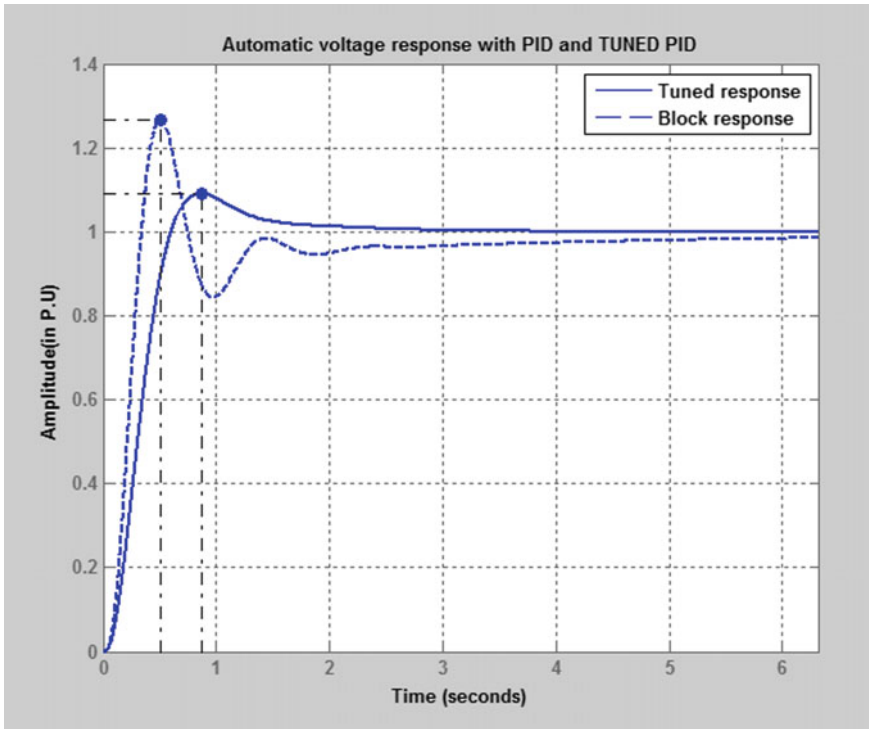


Fig. 2 Voltage response with tuned PID and block response

Table 1 PID-tuned and block parameters for AVR along with their robustness

Controller parameters		
	Tuned	Block
<i>P</i>	0.19423	1
<i>I</i>	0.18269	0.25
<i>D</i>	0.033803	0.25
<i>N</i>	3.2667	100
<i>Performance and robustness</i>		
	Tuned	Block
Rise time	0.731 s	0.206 s
Settling time	3.01 s	5.11 s
Overshoot	8.03%	26.8%
Peak	1.03	1.27
Gain margin	16.3 dB @ 6.35 rad/s	10.6 dB @ 12.1 rad/s
Phase margin	60° @ 1.52 rad/s	39.4° @ 5.76 rad/s
Closed-loop stability	St a b l e	Stable



**Fig. 3** Fast response with settling time 0.632S

**Table 2** For fast settling time tuned PID and block PID response along with the robustness of system

<i>Controller parameters</i>		
	Tuned	Block
<i>P</i>	0.48544	1
<i>I</i>	0.4156	0.25
<i>D</i>	0.13336	0.25
<i>N</i>	361.9086	100
<i>Performance and robustness</i>		
	Tuned	Block
Rise time	0.377 s	0.206 s
Settling time	1.6 s	5.11 s
Overshoot	9.12%	26.8%
Peak	1.09	1.27
Gain margin	18.2 dB @ 13.5 rad/s	10.6 dB @ 12.1 rad/s
Phase margin	60° @ 3.17 rad/s	39.4° @ 5.76 rad/s
Closed-loop stability	Stable	Stable

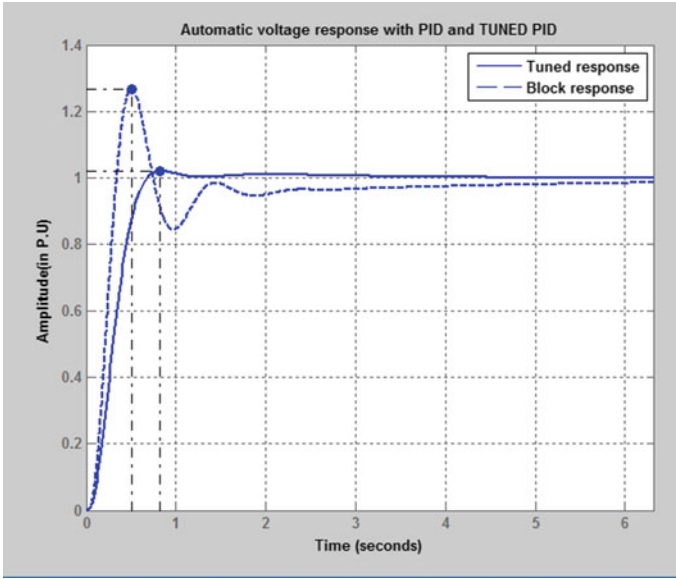


Fig. 4 Improved robustness and fastness

Table 3 Optimized value of fastness and robustness of the parameters for  $P$ ,  $I$ , and  $D$

<i>Controller parameters</i>		
	Tuned	Block
$p$	0.44602	1
$I$	0.34299	0.25
$D$	0.14425	0.25
$N$	361.9086	100
<i>Performance and robustness</i>		
	Tuned	Block
Rise time	0.399 s	0.206 s
Settling time	0.633 s	5.11 s
Overshoot	1.99%	26.8%
Peak	1.02	1.27
Gain margin	18.2 dB @14 rad/s	10.6 dB @12.1 rad/s
Phase margin	67° @3.17 rad/s	39.4° @5.76 rad/s
Closed-loop stability	Stable	Stable

## 4 Conclusion

The study discusses a thermal power plant model whose voltage and frequency profiles are tracked using AVR. Three factors have been taken into consideration; in one, the system's speed was examined, and in another, its robustness. Both fastness and robustness have been examined in the third section. It has been noted that the robustness has decreased for very quick settling times of 0.632 s. The system's robustness and settling time have been determined to have an optimal value for  $P$ ,  $I$ , and  $D$ , as shown in Table 3.

## References

1. Chen P, Luo Y (2023) Analytical fractional-order PID controller design with Bode's ideal cutoff filter for PMSM speed servo system. *IEEE Trans Industr Electron* 70(2):1783–1793. <https://doi.org/10.1109/TIE.2022.3158009>
2. Dai C, Guo T, Yang J, Li S (2021) A disturbance observer-based current-constrained controller for speed regulation of PMSM systems subject to unmatched disturbances. *IEEE Trans Ind Electron* 68(1):767–775
3. Seo D, Bak Y, Lee K (2020) An improved rotating restart method for a sensorless permanent magnet synchronous motor drive system using repetitive zero voltage vectors. *IEEE Trans Ind Electron* 67(5):3496–3504
4. Shenbagalakshmi R, Shelar SD (2018) Design PID controller for positive output voltage converter. In: 2018 International conference on advances in communication and computing technology (ICACCT), 2018, pp 455–458. <https://doi.org/10.1109/ICACCT.2018.8529655>
5. Wibawa U, Mardiana E, Ardhenta L (2020) Design and performance analysis of PID controller for extended output voltage buck-boost converter. In: 2020 10th electrical power, electronics, communications, controls and informatics seminar (EECCIS), 2020, pp 31–36. <https://doi.org/10.1109/EECCIS49483.2020.9263458>
6. Gopi Krishna Rao PV, Subramanyam MV, Satyaprasad K (2014) Study on PID controller design and performance based on tuning techniques. In: 2014 international conference on control, instrumentation, communication and computational technologies (ICCICCT), 2014, pp 1411–1417. <https://doi.org/10.1109/ICCICCT.2014.6993183>
7. Saini P, Kumar R, Rajput N (2016) Cascade—PID control of nonlinear chemical process. *Nonlinear Stud (Scopus Indexed)* 23(4):561–568
8. Hote YV, Jain S (2018) PID controller design for load frequency control: Past, present and future challenges, *IFAC-PapersOnLine*, 51(4):604–609. ISSN 2405-8963. <https://doi.org/10.1016/j.ifacol.2018.06.162>
9. Ansari MF, Afzal A (2022) Sensitivity and performance analysis of 10 MW solar power plant using MPPT technique. In: Mekhilef S, Shaw RN, Siano P (eds) *Innovations in electrical and electronic engineering*. ICEEE 2022. Lecture notes in electrical engineering, vol 894. Springer, Singapore. [https://doi.org/10.1007/978-981-19-1677-9\\_46](https://doi.org/10.1007/978-981-19-1677-9_46)
10. Rawat A, Jha SK, Kumar B, Mohan V (2020) Nonlinear fractional order PID controller for tracking maximum power in photo-voltaic system. *J Intell Fuzzy Syst* 38(5):6703–6713. <https://doi.org/10.3233/JIFS-179748>
11. Yoneya A, Kondo T, Hashimoto Y, Togari Y (1998) Two-valued PID controller. *IEEE Trans Industr Electron* 45(1):183–184. <https://doi.org/10.1109/41.661321>
12. El-Sousy FFM (2010) Hybrid  $h_\infty$ -based wavelet-neural-network tracking control for permanent-magnet synchronous motor servo drives. *IEEE Trans Ind Electron* 57(9):3157–3166



13. Kosut RL (1983) Design of linear systems with saturating linear control and bounded states. *IEEE Trans Autom Control* 28(1):121–124
14. Sharma G, Narayanan K, Adefarati T, Sharma S (2022) Frequency regularization of a linked wind–diesel system using dual structure fuzzy with ultra-capacitor. *Prot Control Mod Power Syst* 7(1):1–9
15. Tomar A et al (eds) (2022) Proceedings of 3rd international conference on machine learning, advances in computing, renewable energy and communication: MARC 2021, vol 915, pp 15, 781. ISBN: 978-981-19-2830-7. Springer. <https://doi.org/10.1007/978-981-19-2828-4>
16. Yamamoto T, Takao K, Yamada T (2009) Design of a data-driven PID controller. *IEEE Trans Control Syst Technol* 17(1):29–39. <https://doi.org/10.1109/TCST.2008.921808>

# Optimization of Distributed Generators in a Virtual Power Plan Using Mixed Integer Linear Programming Method



Ahmed Abubakar Elwan, Mohd Hafiz Habibuddin, Yanuar Z. Arief,  
Siti Nur Aisyah Mohd Sharan, Ahmad Safawi Bin Mokhtar,  
and Rasyidah Binti Mohamad Idris

**Abstract** Power utilities worldwide face capacity expansion challenges due to costs, land availability, and environmental sustainability. Increased demand and the need to build a reliable and resilient network have compelled power utilities to organize competitively distributed generators to compensate for any supply surge. These distributed power generation units are small and dispersed, making control difficult. To find a solution that is both economical and sustainable, a virtual power plant is formed from diesel generators with a capacity of 5.6 MW, a waste-to-energy (WtE) power generating plant with a capacity of 1 MW, a wind power plant with a capacity of 0.6 MW, and a photovoltaic (PV) power plants with a capacity of 0.4 MW. The distributed generators were optimally integrated into a virtual power plant and for the best integration solution, a Deming wheel, also known as the plan, do, check, and act (PDCA) method and mixed integer linear programming (MILP) were used in an Excel solver. The simulation results show that the total VPP power generated from the sources is 6.33 MW, with renewable energy sources accounting for 1.6 MW (25% of the total) and a cost estimate of 0.5\$/kW. Diesel and wind contribute the least in comparison with their capacities, while others contribute the most (100% of the capacities).

---

A. A. Elwan · M. H. Habibuddin · S. N. A. M. Sharan · A. S. B. Mokhtar · R. B. M. Idris  
Department of Electrical Power Engineering, Universiti Teknologi Malaysia (UTM), Johor Bahru,  
Malaysia

e-mail: [mdhafiz@utm.my](mailto:mdhafiz@utm.my)

A. S. B. Mokhtar

e-mail: [safawi@utm.my](mailto:safawi@utm.my)

R. B. M. Idris

e-mail: [rasyidahidris@utm.my](mailto:rasyidahidris@utm.my)

Y. Z. Arief (✉)

Department of Electrical and Electronic Engineering, Faculty of Engineering, Universiti Malaysia  
Sarawak (UNIMAS), Kota Samarahan, Sarawak, Malaysia

e-mail: [ayzulardiansyah@unimas.my](mailto:ayzulardiansyah@unimas.my)

© The Author(s), under exclusive license to Springer Nature Singapore Pte Ltd. 2024

355

H. Malik et al. (eds.), *Renewable Power for Sustainable Growth*,

Lecture Notes in Electrical Engineering 1086,

[https://doi.org/10.1007/978-981-99-6749-0\\_22](https://doi.org/10.1007/978-981-99-6749-0_22)

**Keywords** Virtual power plant · Mixed integer linear programming · Waste to energy · Distributed generator · Renewable energy

## 1 Introduction

With the current decentralization, deregulation, and environmental concerns in the electrical power sector, there has been a massive integration of diverse sources of electrical power into the system, making management difficult. Because they must be close to the source, most of these resources have limited capacity and are dispersed. Power system operators are investigating various options for integrating such resources, and virtual power plants (VPP) can play a significant role in integrating these dispersed low-capacity power plants into a single entity that is both secure and market competitive. This commitment should allow small players to enter the power sector [1]. However, VPPs may be required to operate at lower load factors, posing the risks of high per kWh GHG emissions and high cost per unit production, resulting in low competitiveness [2] and sector coordination. It will become even more critical in the coming years, as more renewable energies (RE) are expected to be added to the electricity grid between now and 2050 [3].

Like all other power systems, a virtual power plant schedules generators and loads in a way that allows the system operator to achieve cheap and reliable operation while maintaining competitiveness and cost. However, this is frequently challenged due to their lack of competitive capacity, remoteness, and sporadic nature [4]. More can be accomplished in a VPP by optimizing the integration of various distributed energy resources. Several researchers have conducted studies on the optimal integration of distributed energy resources in a VPP, as shown in [5–8]. VPP has been classified into two broad categories, as described in [9, 10]: commercial and technical virtual power plants (CVPP and TVPP), each with its own application and scope. Examples of these applications include reserve power, price stabilization, and so on. Zhang et al. [11] investigated optimization of VPPs, whereas [12] investigated dynamic integration and performance of dispersed resources in a VPP using both linear and nonlinear programming.

The goal of this research is to integrate distributed resources into a VPP and investigate the performance of a VPP plant to ensure adequate resource allocation to maximize capacity output while keeping costs low. The PCDA method and a mixed integer linear program (MILP) method are used in this study to optimize distributed sources. Figure 1 depicts the basic VPP configuration for the studies.

Figure 1 depicts the distributed resources, which include PV, diesel power generators, a waste-to-energy power plant, and a wind power plant. The management and resource allocation center coordinate these resources, and the power generated is fed to the various load units, as shown in Fig. 1.

To optimally integrate the distributed resources, this study employs the PDCA (Demming wheel) method Fig. 2 and a mixed integer linear program (MILP) solution. PDCA allows for significant “improvements” in performance (“breakthroughs”)

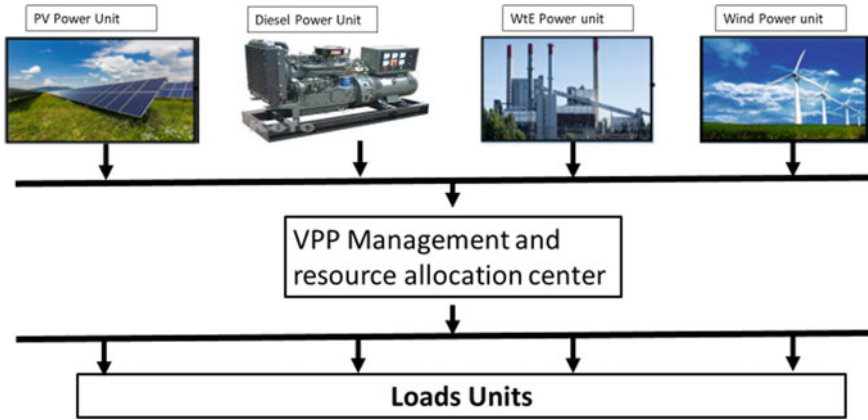
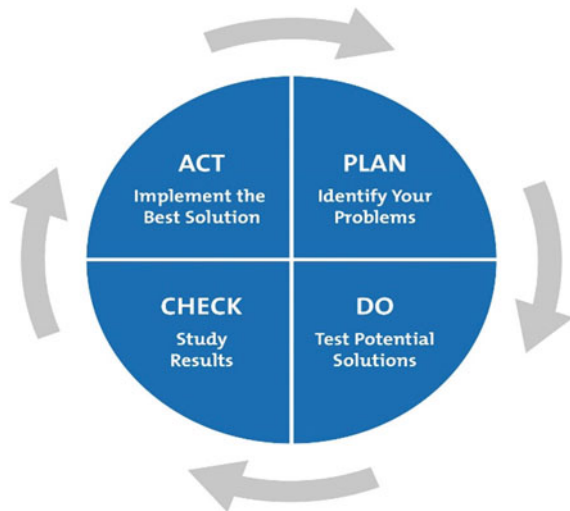
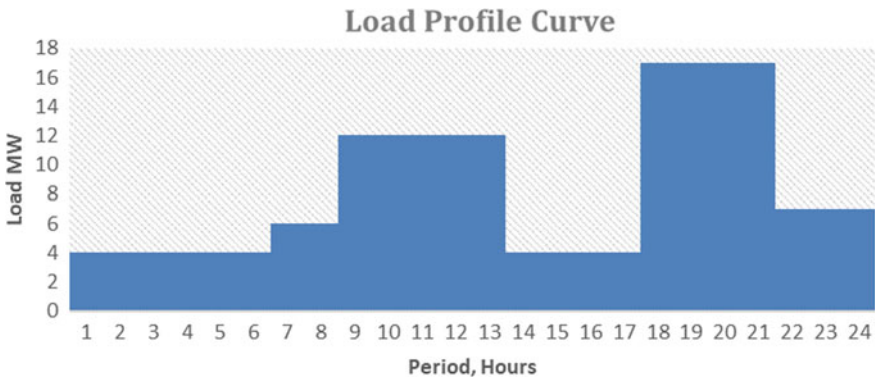


Fig. 1 VPP configuration showing the various distributed resources

[13]. While MILP is a mathematical model used to reduce risks (e.g., cost, energy loss, errors, etc.) or maximize opportunities (e.g., profit, quality, efficiency, etc.), it is subject to some constraints [14]. The study’s findings are expected to be used by policymakers to encourage more participation from distributed energy resources in the power sector in a profitable and sustainable manner, reflecting the anticipated contributions from VPP plants to a sustainable energy system.

Fig. 2 PDCA cycle





**Fig. 3** Demand load profile curve

## 2 Proposed Method

### 2.1 Topology of the VPP

The VPP under consideration is a collection of distributed diesel generators (dg) and renewable energy sources (RES) units (PV and wind). WtE stands for waste-to-energy electrical generator. The goal is to create a VPP portfolio that can manage the technical capability of its distributed energy resources at the lowest possible cost. Other generalized assumptions made in the formulation of the VPP for this study include the fact that all structural capabilities of active, passive, and storage resources in terms of size and location were determined during the VPP planning stage and cannot be changed in the short term, keeping in mind that decisions made during the planning stage considered all environmental and efficiency principles in terms of energy sources and conversion technologies, particularly when using fossil fuels.

### 2.2 Load Profile and Distribution

Figure 3 depicts the load profile. According to the data, demand ranges from a high of 16 MW between 18:00 and 21:00 h and a low of 4 MW between 01:00 and 06:00 h and 14:00 to 17:00 h.

### 2.3 PDCA Implementation Framework

Figure 4 depicts the detailed framework used in the study's implementation. The PDCA cycle is a never-ending cycle of planning, doing, checking, and acting. The

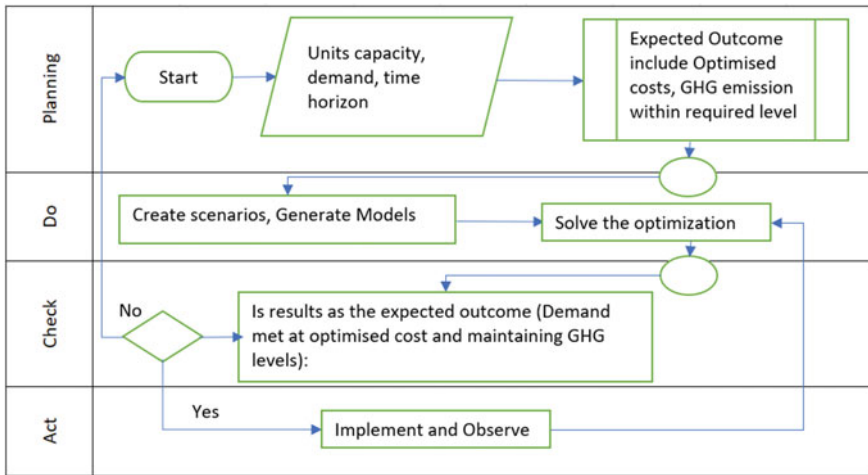


Fig. 4 PDCA implementation framework flowchart

framework in Fig. 4 has been broken down into smaller steps or development stages of the activities, and ways to improve each one has been explored.

### 2.4 Distributed Resources

As previously stated, the distributed resources considered for the VPP fall into two categories: (1) fossil fuel-based (diesel generators) and (2) renewable energy resources (PV, wind, and WtE). Figure 5 depicts the daily generator availability. The yellow shaded area represents low sunshine for a PV generator, amber represents low wind speed, light red indicates an emergency shutdown, dark red indicates a generator is on reliability maintenance, and blue indicates a generator is scheduled for planned maintenance.

### 2.5 Equations

Each unit is expected to be either available or unavailable ( $u = 1$  or  $0$ ). The generated power ( $P_i$ ) is between the minimum and maximum capacities. Although fossil fuel generators have a higher capacity, renewable energy is expected to contribute significantly due to low GHG emissions. The main goal is to have a power supply mix with a variety of capacities and characteristics that can contribute to demand at a low cost and in a sustainable manner. The mix should be in a proportion that strikes a balance between RE and fossil-based generation, allowing GHG emissions to be

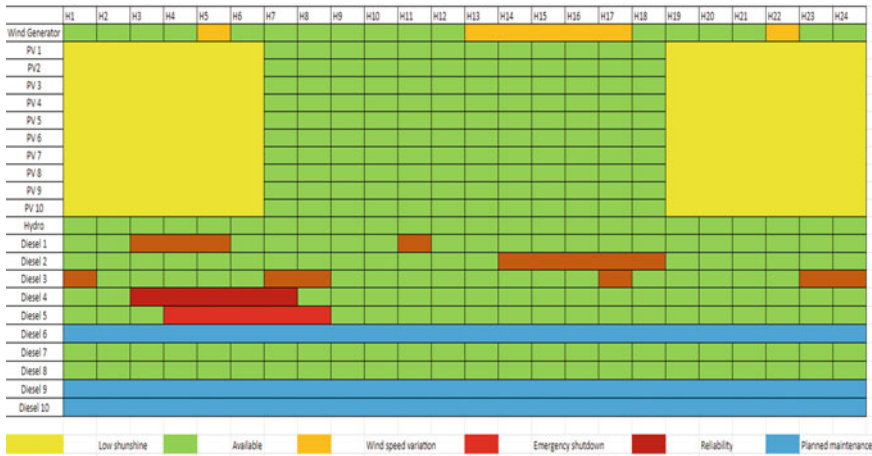


Fig. 5 VPP generator availability chart

kept to a minimum. The goal is to maximize output while keeping supply mix costs as low as possible.

(a) **Objective Function and Variables**

The objective function is made of two power components. The first power component is determined by the availability of the plant based on Fig. 5, i.e., if a unit is in operation or not at the time of the decision. The second power component is the contribution of renewable generators. They are also dependent on the amount of power generated at that period, greatly impacted by weather conditions as in Fig. 5. The objective function is formulated as in Eq. (1).

The optimization problem is presented in (1) and it is expected to maximize the total power from all generating plants. Unlike renewables and WtE, the total power expected is given in Eq. (2). Power generation for all other sources is at maximum when it is available except for diesel generators whose generation is usually between the maximum and minimum capacity as shown in (3). Constraints associated with the solution are given in Eqs. (4–6).

$$\min(P_i) \left\{ \sum_{n=t}^{N-1} P^{dg} + \sum_{n=t}^{N-1} P^{reg} + P^{WtE} \right\} \tag{1}$$

$$P_{vpp} = \sum_{n=t}^{N-1} P^{dg} + \sum_{n=t}^{N-1} P^{reg} + P^{WtE} \tag{2}$$

$$U(t) > 0 \tag{3}$$

where

- $P^{dg}$  diesel power (kW)
- $P^{reg}$  renewable power (kW)
- $P^{WtE}$  WtE power (kW)
- $U(t)$  availability index (1 or 0).

(b) **Constraints**

The optimization is subject to the following constraints.

$$P_{max}^{dg} \geq P^{dg} \geq P_{min}^{dg} \tag{4}$$

where

- $P_{max}^{dg}$  Maximum diesel power (kW)
- $P_{min}^{dg}$  Minimum diesel power (kW)

$$P^{reg} = \sum_{n=t}^{N-1} P^{pv} + P^{wind} \tag{5}$$

where

- $P^{pv}$  PV power (kW)
- $P^{wind}$  Wind power (kW).

$$0.5 = \left\{ \sum_{n=t}^{N-1} Cp^{dg}(n) + \sum_{n=t}^{N-1} Cp^{reg}(n) + \sum_{n=t}^{N-1} Cp^{Wte}(n) \right\} \tag{6}$$

### 3 Results and Discussion

Results from the simulation are presented in tables. In the simulation, total power generation, VPP contribution, and renewable penetration are presented based on the constraints given. After modeling and simulation, Table 1 gives the optimal power contribution from VPP and the contribution from respective generation modes.

Table 2 gives the power distribution, renewable energy penetration, and cost. It is shown that wind and diesel contribution has been capped because of the cost constraint, while other sources were maximized. The wind has about 75% of its rated capacity as slack and diesel has about 21% as slack.

In Table 3, sensitivity analysis of the simulation showed that while some generation sources have room to adjust costs and still have an optimal condition, other



**Table 1** VPP power from simulation results

S/No	Optimal power from VPP components		
	Plant	Original value	Power (MW)
1.	Total power (VPP)	0	6.333333333
2.	PV generator	0	0.4
3.	Wind gen	0	0.2
4.	WtE gen	0	1
5.	Diesel	0	4.733333333

**Table 2** Power distribution with slacks

S/No	Constraints used for simulation			
	Name	Cell value	Slack	Total
1.	RE penetration < =	1.6	0	0
2.	Total cost = < =	0.5	0	0
3.	PV generator	0.4	0	0
4.	Wind generator	0.2	0.4	0.6
5.	WtE generator	1	0	0
6.	Diesel generator	4.733333333	1.266666667	6
7.	External	0	18	18

sources have absolutely no room for that. The reduced costs tell us how much the objective can be increased or decreased before the optimal solution changes.

Table 4 gives the sensitivity analysis of constraints on this table, the shadow price is an important function to reckon with. The shadow prices tell us how much the optimal solution can be increased or decreased by changing the value of the constraints with one unit.

**Table 3** Sensitivity analysis of variable simulation

S/No	Sensitivity analysis				
	Name	Final value	Reduced cost	Allowable increase	Allowable decrease
1.	PV generation	0.4	0.67	1E + 30	0.67
2.	Wind generation	0.2	0	0.22	1E + 30
3.	WtE generation	1	0.22	1E + 30	0.22
4.	Diesel generation	4.73	0	1E + 30	0.5
5.	External	0	- 1.22	1.22	1E + 30

**Table 4** Sensitivity analysis of constraints simulation

S/No	Sensitivity analysis					
	Name	Final value	Shadow price	Constraint	Allowable increase	Allowable decrease
1.	RE penetration < =	1.6	- 0.33333333	1.6	0.4	0.2
2.	Total cost = < =	0.5	22.22222222	0.5	0.114	0.426

### 3.1 Optimal Power Solution

According to the simulation results in Tables 1 and 2, the VPP’s ideal power is 6.33 MW, with a 1.6 MW RE penetration. Due to its size, the diesel contribution is more than predicted, but not all of its capacity is used. Table 2 gives that 1.23 MW, or about 20% of the overall capacity for diesel generators, as well as roughly 75% of the wind capacity, are underutilized. The best power is obtained by completely utilizing other sources. This scenario can be linked to the need to keep costs at a specific level and the higher cost of power from the two sources.

### 3.2 Sensitivity Analysis

It is optimal to have 0.4 MW of PV generation, 0.2 MW of wind generation, 1 MW of WtE generation, and 4.73 MW of diesel generation. This solution gives the maximum VPP generation of 6.33 MW (see Table 1). This solution uses all the resources available for PV and wind at 100% (0.4 MW of capacity and 1 MW of capacity) and 33% of wind (capacity and 78% of diesel capacity).

- **Reduced Cost:** Table 3 gives how much the objective coefficients can be increased or decreased before the optimal solution changes. Only wind generator units can be increased by (0.22) based on the results, while other sources can only be decreased before the optimal value changes. As a result, if there is a need to increase any output while still maintaining the optimal solution, it may be possible to do so solely through wind generation capacity.
- **Shadow Price:** The shadow prices indicate how much the optimal solution can be increased or decreased if the constraint values (RE contribution and cost) are changed by one unit. According to Table 4, the shadow price is only valid between “22.2 - 0.42 and 22.2 + 0.11,” and anything outside of this range will cause the optimal solution to change.

## 4 Conclusion

This research has investigated the optimal integration of distributed resources into a VPP plant successfully. The Deming wheel (PDCA) method was used in model formulation, and the optimization was solved using mixed integer linear programming (MILP). It is demonstrated that optimal integration is possible by optimizing power and constraining cost at a specific value. The two elements that were constrained in the solution were RE penetration and contribution. The optimal solution generates 6.33 MW of power from the VPP, with a RE contribution of 1.6 MW and a cost of 0.5 \$/kW. Diesel and wind were found to contribute less to total VPP power, with wind contributing only **33%** and diesel contributing **78%**.

**Acknowledgements** This work was supported/funded by the Ministry of Higher Education under Fundamental Research Grant (Grant FRGS/1/2018/TK07/UTM/02/6).

## References

1. Akasiadis C, Chalkiadakis G (2016) Decentralized large-scale electricity consumption shifting by prosumer cooperatives. In: ECAI. August 2016, pp 175–183
2. Vale Z, Pinto T, Morais H, Praça I, Faria P (2011) VPP's multi-level negotiation in smart grids and competitive electricity markets. In: 2011 IEEE power and energy society general meeting. IEEE. July 2011, pp 1–8
3. Elwan AA, Habibuddin MH (2021) Techno-economic analysis of a grid-connected waste to energy gasification plant: a case study. *Energy Eng* 118(6):1681–1701
4. Yang Q, Wang H, Wang T, Zhang S, Wu X, Wang H (2021) Blockchain-based decentralized energy management platform for residential distributed energy resources in a virtual power plant. *Appl Energy* 294:117026
5. AbuJarad SY, Mustafa MW, Jamian JJ (2017) Recent approaches of unit commitment in the presence of intermittent renewable energy resources: a review. *Renew Sustain Energy Rev* 70:215–223
6. Emovon I (2020) A fuzzy multi-criteria decision-making approach for power generation problem analysis. *J Eng Sci* 7(2):E26-31
7. Kanagasabai L (2021) Heat transfer and simulated coronary circulation system optimization algorithms for real power loss reduction. *J Eng Sci* 8(1):E1–E8
8. Sikorski T, Jasiński M, Ropuszyńska-Surma E, Węglarz M, Kaczorowska D, Kostyła P, Leonowicz Z, Lis R, Rezmer J, Rojewski W, Sobierajski M (2019) A case study on distributed energy resources and energy-storage systems in a virtual power plant concept: economic aspects. *Energies* 12(23):4447
9. Wang X, Liu Z, Zhang H, Zhao Y, Shi J, Ding H (2019) A review on virtual power plant concept, application and challenges. In: 2019 IEEE innovative smart grid technologies-Asia (ISGT Asia). May 2019, pp 4328–4333
10. Teixeira R, Cerveira A, Baptista J (2021) Optimized management of renewable energy sources in smart grids in a VPP context. In: 2021 international conference on electrical, computer and energy technologies (ICECET). IEEE. December 2021, pp 1–6
11. Zhang G, Jiang C, Wang X (2019) Comprehensive review on structure and operation of virtual power plant in electrical system. *IET Gener Transm Distrib* 13(2):145–156
12. Othman MM, Hegazy YG, Abdelaziz AY (2015) A review of virtual power plant definitions, components, framework, and optimization. *Int Electr Eng J* 6(9):2010–2024

13. Schmidt H (2019) Explosive precursor safety: an application of the Deming cycle for continuous improvement. *J Chem Health Saf* 26(1):31–36
14. Alauddin N, Yamada S (2019) Overview of Deming criteria for total quality management conceptual framework design in education services. *J Eng Sci Res* 3(5):12–20

# Solving Unit Commitment Problem Using Mixed Integer Linear Programming for Demand Side Management



Ahmed Abubakar Elwan, Mohd Hafiz Habibuddin, and Yanuar Z. Arief

**Abstract** The implementation of demand side management (DSM) for an industrial plant by solving a unit commitment problem (UCP) is hoped to solve imbalances between electricity supply limitations and demand requirements which many times lead to a partial or total shutdown of production plants because of trips due to under voltage or high frequency when the supply is overloaded or a unit is suddenly stopped, while there is a need to maintain production. For this study, the cement industry was divided into operating units, simulated under two scenarios, and solved using mixed integer linear programming (MILP) in an Excel solver. The result shows that there is a reduction in cost by 30% from \$1203 to \$880 for the same production requirement.

**Keywords** Unit commitment problem · Mixed integer linear programming · Demand side management · Electricity supply · Production plants

## 1 Introduction

Manufacturing plants are energy intensive, consuming about 54% of the world's total delivered energy [1]. The cement sub-sector alone is consuming approximately 12–15% of total industrial energy use (electrical energy) [2, 3]. According to [3] energy cost constitutes about 60–75% of the direct manufacturing cost of cement. To sustain profitability and balance demand and supply that guarantee cost-effective manufacturing and availability of products to consumers, a detailed review of energy

---

A. A. Elwan · M. H. Habibuddin

Department of Electrical Power Engineering, Universiti Teknologi Malaysia (UTM), Johor Bahru, Malaysia

e-mail: [mdhafiz@utm.my](mailto:mdhafiz@utm.my)

Y. Z. Arief (✉)

Department of Electrical and Electronic Engineering, Faculty of Engineering, Universiti Malaysia Sarawak (UNIMAS), Kota Samarahan, Sarawak, Malaysia

e-mail: [ayzularadiansyah@unimas.my](mailto:ayzularadiansyah@unimas.my)

use to identify improvement in areas of demand/supply balance and cost optimization becomes necessary.

Due to the increasing demand for cement production [4] and the epileptic source of supply in Nigeria, most cement manufacturing industries hardly meet up with customer demands. To boost the electricity supply for the industries, various distributed generations (DGs) were integrated into the electrical system either as self-generation or purchased power. However, this action increases the cost of production because of the return on the investment required and usually takes a long time to implement. A short-term but sustainable solution is required by harnessing available opportunities to balance demand and supply as well as reduce costs through adequate production planning, taking advantage of having storage facilities for inventory in the cement plants.

Several energy management strategies have been adopted by manufacturing plant operators, the most common strategies in practice include (1) the use of energy-efficient machines [5] and (2) applying scheduling strategies [6, 7]. While the use of an energy-efficient machine approach requires an extra investment that imposes huge pressure on companies for early return on investment (ROI), the application of scheduling strategies helps in reducing energy consumption as well as reducing financial costs and attracts less or no investments to execute. The most commonly practiced scheduling strategy in the Nigerian cement industries is load shedding or power-down. The power-down strategy means that a machine cannot be idle for a certain amount of time between two consecutive processing tasks [8], it has to be shut down immediately after use. Therefore, when a machine is shut down energy may be saved based on the assumption that not all jobs are available at the same time. However; this may not be applicable in a high-demand continuous manufacturing plant like cement industries, where continuous operation is desirable or at least to have all storage facilities filled up. Another strategy used is the speed-scaling technique [9], this technique has to do with the selection of the right processing speed for an operating machine. But this technique also requires some level of equipment investment and will increase the cost burden on the production plant.

The dynamic management of electricity demand, also referred to as demand side management (DSM), emerges as an effective approach to energy management. Industrial DSM helps to improve power supply performance and optimize production to meet up with customer demands [6]. Related studies [10, 11] considered electrical energy cost minimization through classical deadlines and pre-emptive schedules to reduce consumption. The authors in [12] use mathematical models to minimize costs in a variable electricity price. While [11] deals with different consumption at different machine states, [12] was concerned with job ordering and processing and optimal scheduling of machine states, respectively, by using heuristics and genetic algorithms.

Authors in [13] applied the model from [12] to a real-time plant and a 20% improvement in profit was recorded after the implementation to a CHP plant. Using discrete time representation in a continuous power-intensive non-dispatchable demand response program, [9] developed a MILP model for inter-operating modes transition and [14] developed a general discrete time model for the scheduling of

power-intensive process networks with various power contracts. A two-step integer/constraint programming approach was used to solve an industrial case study involving energy constraints and objectives linked to electric power consumption [15].

Industrial DSM needs flexibility in production and energy management, to explore this authors in [7] made schedules based on sequencing and timing of production tasks, giving particular attention to waiting for time constraints between consecutive production stages. Scheduling considering the inventory of a plant was studied by [16]. The emphasis was on the impact of storage in industrial DSM. For the same purpose state-task network (STN) and resource-task network (RTN) was used by [17] using a well-known concept from [18], where state nodes were used to represent features of the operations (final product, intermediates, and feeds). Modeling of industrial schedules by considering both production and power consumption was first proposed by [19], where the production and consumption characteristics vary within the same process depending on the state in which the process is operating [20].

The objective of this paper is to propose a demand side energy management (DSM) technique by solving a unit commitment problem for an industrial case study. The unit commitment problem aims at the scheduling of units to achieve optimal production to satisfy the inventory needs and also balance power supply/demand at a minimum cost, while other studies focused on minimizing cost by scheduling waiting time optimization, reduction in consumption, sequencing of production, and constraints between stages and electricity prices. A mix integer linear programming approach is used to solve the unit commitment problem (UCP). This approach tends to solve the difficulty of integrating energy constraints (DSM) into production scheduling.

## 2 Research Method

The industrial plant to be addressed is a cement manufacturing plant and the problem to be addressed is optimizing the available power supply for production to satisfy demand at a minimized cost. The plant is divided into four main operating units' codes named OPU1...4. The properties for each unit are displayed in Table 1.

Each operating unit requires a large amount of electricity to turn huge machinery into production. Each unit is equipped with storage facilities, maximum and minimum storage levels are identified in Table 2. The plant operation is expected to be updated in real-time depending on the frequency. The peak supply demand for the operating units is 25 MW.

**Table 1** Plant properties

Properties	OPU1	OPU2	OPU3	OPU4
Operating cost	30	25	45	60
Idling cost	20	30	50	10
Start-up cost	800	650	200	80
Min cons level	4	2	5	5
Max cons level	9	3	10	10
Minimum up time	46	5	150	71
Minimum down time	86	3	43	13
Power allocation (%)	35	5	25	30

**Table 2** Plant inventory parameters

Parameter	OPU1	OPU2	OPU3	OPU4
Production rate	260	20	80	140
Consumption rate	70	16	140	240
Maximum capacity	13,000	100	14,000	12,000
Minimum capacity	4000	40	5000	3000
Min Inv. to start	6000	40	6000	3000
Max Inv. to stop	12,000	90	12,000	10,000
Variance to stop	1000	10	2000	2000
Variance to start	6000	60	8000	7000
Min up time	46	5	150	71
Min down time	86	3	43	13

## 2.1 Model Description

Each unit is expected to be in any of the three states, the ON state, the OFF state, and the IDLE state. The duration of the ON state is  $\geq$  minimum operating time and the duration for OFF  $\leq$  minimum downtime the idle time is when the unit is kept running without any output and should be minimized. Both minimum operating time and minimum down time are evaluated based on inventory stock level and restocking requirements. Each stage of operation consumes power referred to as operational power ( $P_{op}$ ) which depends on the state of the units whether the unit is ON or OFF and idle power when the overall unit is not active but some amount of power is required to run some critical equipment for cooling and other related functions. The shortest ON duration has to be met before a unit is shut down and the shortest OFF duration is also required before a unit is restarted up.



## 2.2 Equations

The objective function is made of two cost components. The first cost component is determined by real-time status decisions termed as the operation cost, i.e., if a unit is in operation or not at the time of the decision. The second cost component comes when the units are not in active operation. This idling cost is usually incurred when the units are turned off and there must be some residual elements that will be allowed to continue operating for cooling and other non-productive activities. The objective function is formulated as in (1).

$$\min[e(n)] \left\{ \sum_{n=t}^{N-1} e^o(n) P_{op} \cdot \hat{U}(t) + \sum_{n=t}^{N-1} e^{id} [P_{id}](n) \right\} \tag{1}$$

where

- $e^o$  Operating cost for the units after start-up and before shutdown
- $e^{id}$  Cost incurred from non-operation activities when units are idling
- $P_{op}$  Operating power
- $P_{id}$  Idling power.

The following constraints apply.

### (a) Operating Time Constraints

$$\hat{U}(t) - \hat{U}(t - 1) \leq \hat{U}(t + T_{up}) \tag{2}$$

$$\hat{U}(t - 1) - \hat{U}(t) \leq \hat{U}(t + Td) \tag{3}$$

where

$$TU_i = T_{on} \text{ if } T_{op,i} < MT_{up} \tag{4}$$

$$TD_i = T_{off} \text{ if } T_{id,i} < MT_{down} \tag{5}$$

For any operating unit OPU,

$$MT_{up} \geq \varphi / \delta \text{ (h)} \tag{6}$$

$$MT_{down} \leq \gamma / \mu \text{ (h)} \tag{7}$$

where

- $\delta$  Rate of production
- $\mu$  Rate of consumption

- $\gamma$  Minimum stock
- $\varphi$  Maximum stock
- $U(t - 1), U(t)$  status of a unit at a time  $(t - 1)$  and time  $(t)$ .

**(b) Mass Balance Constraints (Inventory Constraints)**

We define the variable  $I_{i,t}$  which represents the product stored at each time period  $t$  as a balance of consumption from the amount produced by each unit  $i$ . By mass balance, the following relationships hold [21].

$$I_{i,t} = I_o + \sum_s P_{s,t} - \mu_t \quad \forall t \in T : t = 1 \tag{8}$$

$$I_{i,t} = I_{t-1} + \sum_s P_{s,t} - \mu_t \quad \forall t \in T : t > 1 \tag{9}$$

And the inventory limits are given as follows

$$\gamma \leq I_{i,t} \leq \varphi \tag{10}$$

where

- $I_{i,t}$  Product stored at each time period  $t$
- $I_o$  Initial inventory position
- $P_{s,t}$  Production at time  $t$
- $\mu_t$  Consumption rate.

**(c) Energy Balance (Demand/Supply) Constraints**

The demand limit of each operating unit is between the maximum and minimum power levels of each unit as given in (11) a period of time  $(t)$ .

$$P_{itmax} \geq P_{dit} \geq P_{itmin} \tag{11}$$

$$P_d = U(t) * P_{op} + h * P_{id} \tag{12}$$

where

- $P_{di,t}$  Total demand power
- $P_{itmax}$  Maximum power demand for each unit at a time  $(t)$
- $P_{itmin}$  Minimum power demand for each unit at a time  $(t)$
- $P_{op}$  Operation power
- $P_d$  Demand power
- $P_{id}$  Idling power
- $U(t)$  Operating status of the plant
- $h$  Hours of operation to produce.

### 3 Results and Analysis

Results from the simulation are presented in two scenarios: the business as usual (BAU) and the constraints. In the business-as-usual scenario, the restriction is just on the power limits, hence a unit can be started or kept down as long as the power required is within the limits. After modeling and simulation, Table 3 gives the cost objective and Table 4 is the power for the BAU.

From the result in Table 3, idling cost is about 33% of the total cost, this is because some equipment was running even when the plant is not in production. Operating cost is the actual cost incurred from power used during production and this accounts for 67% of the overall cost of production.

From Table 4, the total idling power consumed by all the units is 15 MW, while the power used in the actual production (operating power) is 19.1 MW representing 44% and 56%, respectively. An almost equal amount of power is required by the units during idling and when the plant is in normal operations. There is a huge need to be controlled for good optimization.

In the constraint scenario, the restriction is on both power and utilization status limits. A unit can only consume power within its limit and only when it is in operation. When the unit is not in operation, then it incurs additional costs for idling as seen in the outcome of the simulation results. After modeling and simulation, Table 5 gives the cost values, and Table 6 gives the power values required by the respective units.

In the constraint scenario, power is only consumed when the unit is in production mode, hence the reduction in the total cost from \$1203 in the BAU to a total cost of \$880.00. To achieve this, unit 2 has to be down while other units 1, 3, and 4 are onboard as given in Table 7.

**Table 3** BAU cost distribution values

Name	Original value	Actual value	Contribution (%)
Total cost (\$)	0	1203.94	100
Operation cost (\$)	0	797.74	67
Idling cost (\$)	0	406.20	33

**Table 4** BAU power distribution values

Name	Original value	Actual value
The total power consumed (MW)	0	34.1
Operating power (MW)	0	19.1
Idling power (MW)	0	15

**Table 5** Constraints scenario cost distribution values

Name	Original value	Actual value
Cost (\$)	1230	880

**Table 6** Constraints scenario power values

Name	Actual value
Power OPU1 (MW)	8
Power OPU2 (MW)	0
Power OPU3 (MW)	8
Power OPU4 (MW)	6

**Table 7** Operating status of the units in the constraint scenario

Name	Actual value
Operating status OPU1	1
Operating status OPU2	0
Operating status OPU3	1
Operating status OPU4	1

The total power consumed in the constraint scenario is 32 MW compared with the 34.1 MW of the BAU scenario under the same period and condition of operation. This resulted in the reduction of the total power cost for the process.

## 4 Conclusion

This study presents a mixed-integer linear programming formulation (MILP) to solve unit commitment (UC) for energy management while considering the production and power constraints in an industrial plant. It is shown that this is possible by modeling the operating parameters based on the amount of inventory required to be produced at any time. The study also shows that by committing the units following some constraints, the cost has been reduced by **27%** from the BAU scenario maintaining all other limits. Application of the method of this study is expected to reduce electricity demand and allow prompt response to supply/demand mismatch. By incorporating DSM in production planning and unit scheduling for maintenance and other intervention purposes in a manufacturing plant, it is possible to control power cost and energy efficiency throughout the process.

**Acknowledgements** This work was supported/funded by the Ministry of Higher Education under Fundamental Research Grant (Grant FRGS/1/2018/TK07/UTM/02/6).

## References

1. Conti J, Holtberg P, Diefenderfer J, LaRose A, Turnure JT, Westfall L (2016) International energy outlook 2016 with projections to 2040. USDOE Energy Information Administration (EIA), Washington, DC (United States). Office of Energy Analysis
2. Madloul NA, Saidur R, Hossain MS, Rahim NA (2011) A critical review on energy use and savings in the cement industries. *Renew Sustain Energy Rev* 15(4):2042–2060
3. Fadayini OM, Madu C, Oshin TT, Obisanya AA, Ajiboye GO, Ipaye TO, Rabi TO, Akintola JT, Ajayi SJ, Kingsley NA (2021) Energy and economic comparison of different fuels in cement production. *Cem Ind Optim Charact Sustain Appl* 3:105
4. Unachukwu GO (2003) Energy efficiency measures investigation in cement company: BCC case study. *Niger J Renew Energy*. 10(1–2):85–92
5. Menghi R, Papetti A, Germani M, Marconi M (2019) Energy efficiency of manufacturing systems: a review of energy assessment methods and tools. *J Clean Prod* 10(240):118276
6. Yin Y, Wang Y, Cheng TC, Liu W, Li J (2017) Parallel-machine scheduling of deteriorating jobs with potential machine disruptions. *Omega* 1(69):17–28
7. Wang DJ, Liu F, Jin Y (2017) A multi-objective evolutionary algorithm guided by directed search for dynamic scheduling. *Comput Oper Res* 1(79):279–290
8. Liang P, Yang HD, Liu GS, Guo JH (2015) An ant optimization model for unrelated parallel machine scheduling with energy consumption and total tardiness. *Math Probl Eng* 1:2015
9. Zhang Q, Grossmann IE (2016) Planning and scheduling for industrial demand side management: advances and challenges. *Altern Energy Sources Technol* 383–414
10. Zhang X, Hug G, Kolter JZ, Harjunkoski I. Model predictive control of industrial loads and energy storage for demand response. In: 2016 IEEE power and energy society general meeting (PESGM) 2016 Jul 17. IEEE, pp 1–5
11. Weckmann S, Kuhlmann T, Sauer A (2017) Decentral energy control in a flexible production to balance energy supply and demand. *Procedia Cirp*. 1(61):428–433
12. Xu W, Tang L, Pistikopoulos EN (2018) Modeling and solution for steelmaking scheduling with batching decisions and energy constraints. *Comput Chem Eng* 4(116):368–384
13. Mitra S, Sun L, Grossmann IE (2013) Optimal scheduling of industrial combined heat and power plants under time-sensitive electricity prices. *Energy* 1(54):194–211
14. Harjunkoski I, Maravelias CT, Bongers P, Castro PM, Engell S, Grossmann IE, Hooker J, Méndez C, Sand G, Wassick J (2014) Scope for industrial applications of production scheduling models and solution methods. *Comput Chem Eng* 5(62):161–193
15. Pattison RC, Touretzky CR, Johansson T, Harjunkoski I, Baldea M (2016) Optimal process operations in fast-changing electricity markets: framework for scheduling with low-order dynamic models and an air separation application. *Ind Eng Chem Res* 55(16):4562–4584
16. Uddin M, Romlie MF, Abdullah MF, Abd Halim S, Kwang TC (2018) A review on peak load shaving strategies. *Renew Sustain Energy Rev* 1(82):3323–3332
17. Castro PM, Dalle Ave G, Engell S, Grossmann IE, Harjunkoski I (2020) Industrial demand side management of a steel plant considering alternative power modes and electrode replacement. *Ind Eng Chem Res* 59(30):13642–13656
18. Melouk S, Damodaran P, Chang PY (2004) Minimizing makespan for single machine batch processing with non-identical job sizes using simulated annealing. *Int J Prod Econ* 87(2):141–147
19. Artigues C, Lopez P, Hait A (2013) The energy scheduling problem: industrial case-study and constraint propagation techniques. *Int J Prod Econ* 143(1):13–23
20. Tomar A et al (eds) (2022) Proceedings of 3rd international conference on machine learning, advances in computing, renewable energy and communication: MARC 2021, vol 915. ISBN: 978-981-19-2830-7. Springer, pp 15, 781. <https://doi.org/10.1007/978-981-19-2828-4>
21. Ierapetritou MG, Wu D, Vin J, Sweeney P, Chigirinskiy M (2002) Cost minimization in an energy-intensive plant using mathematical programming approaches. *Ind Eng Chem Res* 41(21):5262–5277

# Deployment of Renewable Embedded Generation and Unified Power Quality Conditioner in Distribution System using Firefly Algorithm



Musa Mustapha , Madihah Binti Md. Rasid, Jasrul Jamani Bin Jamian, Ganiyu Ayinde Bakare, and Yau Shuaibu Haruna

**Abstract** The efficiency and operation of current distribution systems have been enhanced by the insertion of renewable distributed generation (RDG). However, the placement of DG does not satisfy the network's need for reactive power, which keeps the voltage of the buses at a level that maximizes the uncontrolled real and reactive variations of power systems. This paper proposed the optimal allocation of DG and Unified Power Quality Conditioner (UPQC) simultaneously to improve the performance of an active distribution system. The most advanced custom power device is the UPQC which combined with the capability of shunt and series compensator features allows for voltage and current compensation in distribution systems. A suitable optimization method is needed to address the challenge of selecting the capacity and position of these compensators. The Firefly Algorithm (FA) is a promising solution to the challenges of multi-objective optimization. The intended objective is active and reactive power loss reduction while improving the voltage profile without violating any system constraints. The effectiveness of the proposed optimal allocation of DG/UPQC using the FA method was evaluated by comparing

---

M. Mustapha (✉)

Department of Electrical and Electronics Engineering, University of Maiduguri, Maiduguri, Nigeria

e-mail: [musamustyy@unimaid.edu.ng](mailto:musamustyy@unimaid.edu.ng)

M. B. Md. Rasid · J. J. B. Jamian

Faculty of Electrical Engineering, Universti Teknologi Malaysia (UTM), 81310 Johor Bahru, Malaysia

e-mail: [madihahmdrasid@utm.my](mailto:madihahmdrasid@utm.my)

J. J. B. Jamian

e-mail: [Jassrul@utm.my](mailto:Jassrul@utm.my)

G. A. Bakare · Y. S. Haruna

Department of Electrical and Electronics Engineering, Abubakar Tafawa Balewa University, Bauchi, Nigeria

e-mail: [gabakare@atbu.edu.ng](mailto:gabakare@atbu.edu.ng)

Y. S. Haruna

e-mail: [ysharuna@atbu.edu.ng](mailto:ysharuna@atbu.edu.ng)

it to the allocation of the DG system only and the base case system scenarios, respectively. The results revealed a significant percentage reduction in active and reactive power losses, reaching 72.01% and 66.57% with the optimal DG/UPQC allocation combination, respectively. In comparison to the Artificial Bee Colony Optimization (ABC) method, the results revealed the FA method is more efficient regarding both convergence speed and solution quality. The MATLAB 2021b environment served as the platform for the simulation, and it was tested it using the IEEE 33-bus radial distribution system method.

**Keywords** Unified Power Quality Conditioner · Firefly Algorithm · Distributed generation · Distribution system

## 1 Introduction

Recent years have seen a lot of interest in distributed generation (DG) sources, particularly solar and wind energies because of their potential to replace traditional sources of energy. Integrating DG systems into utility grid systems raises power quality issues, jeopardizing network stability. The integration challenge is expected to worsen as more large-scale DGs gain access to the distribution network. As a result, the distribution system's overall power quality may be affected by technical problems caused by this scenario [1]. This has led to challenges in identifying their optimal capacity and position in the power distribution systems (DS). Sambaiah, Shuaibu Hassan et al. [2, 3] reviewed optimization methods for the optimal DG allocation in the power DS for power loss reduction.

Custom power devices (CPDs) are equipment that use power electronics to enhance DS's efficiency, reliability, and quality. Unified Power Quality Conditioner (UPQC) an advanced CPD, addresses power quality issues in the electricity DS. It is a combination of two devices; a series voltage compensator and a shunt current compensator. It can compensate for voltage sags/swells, voltage unbalances, reactive power support, and harmonic distortion [4]. UPQC is typically positioned between the utility grid and the load, where the current and voltage are monitored at the point of common coupling (PCC). It generates compensating voltages and currents injected into the system network to mitigate any disturbances and enhance the overall power quality. A reviewed article on the optimal allocation of CPD in the electrical DS can be found in [5]. The UPQC's equivalent circuit diagram is shown in Fig. 1.

According to Fig. 1, the series and shunt compensators of the UPQC's voltage and current injections are designated by  $V_{SE}$  and  $I_{SH}$ . With the aid of series- and shunt-connected voltage source converters, it can inject both real and reactive powers. The  $V_s$ ,  $V_L$ , and  $V_P$  signified the source, load, and the terminal voltages at PCC, while  $I_s$  and  $I_L$  signified the source and load currents, respectively. Refer [7] for a complete analysis of the UPQC model.

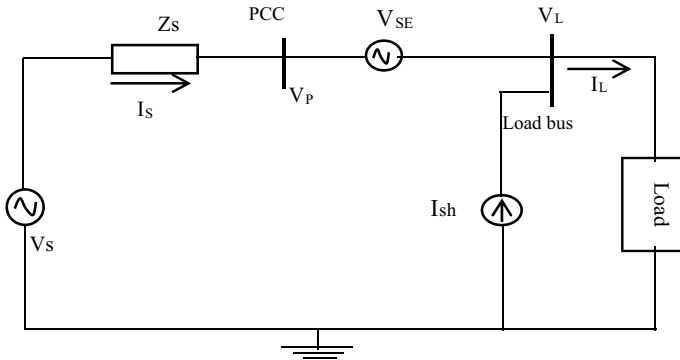


Fig. 1 UPQC equivalent circuit [6]

Following are the remaining sections of this article: Sect. 2 offers an overview of the literature; In Sect. 3, the problem formulation for multi-objective optimization problems is presented. After that, Sect. 4 provides the methodology. Section 5 provides the simulation results and discussion. Section 6 offers concluding remarks and recommends further research.

## 2 Literature Review

The optimal placement of UPQC in DS was discussed in many research studies that were previously published employing various methods and purposes. Musa et al. [8] studied optimal position and rating of UPQC in DS using a Bacteria Foraging Algorithm. Its effectiveness was demonstrated on the IEEE 33-bus test system and practical 50-bus Canteen feeder by improved total feeder voltage profile and real power loss reduction; [9] proposed UPQC intelligent controller-based model for load balancing and voltage profile enhancement in the DS. Also, [10] studied the optimal deployment of a UPQC in a smart grid for power loss reduction. The capability of UPQC for providing reactive power compensation was demonstrated in [6]. Moth-flame optimization algorithm was utilized for UPQC allocation to solve issues related to current and voltage by the shunt and series compensations.

To fully benefit from DG deployment, distribution network operators must strive hard to overcome some of the key challenges. However, with growth in the number of nonlinear loads added to the distribution networks, a lack of reactive power will result in uncontrolled voltage magnitude which eventually induces voltage collapse. Recently, various authors have worked toward improving the reactive power of the active DS by optimizing the allocation of combined DG and D-STATCOM. A Cuckoo search optimization algorithm was formulated for optimal DG/D-STATCOM allocation for voltage correction and power loss reduction in radial DS [11]. A whale optimization algorithm is proposed in [12] to determine the optimal placement of



D-STATCOM and DG at a specific bus based on the loss sensitivity factor. The algorithm considers multiple objectives, including minimizing power loss and reducing operating costs. Frahat et al. [13] presented a Grasshopper optimization algorithm for DG and D-STATCOM optimal capacity planning. To reduce power loss and enhance voltage stability, the device's location was determined using a multi-objective formulation based on the voltage stability index. Hariprasad et al. [14] studied two meta-heuristic algorithms, namely Artificial Fish Swarm Optimization (AFSOA) and Ant Colony Optimization (ACO) for combined DG/D-STATCOM allocation in radial DS. The objective was to enhance the quality of voltage and minimize power loss. The research findings indicated that AFSOA performed better than ACO in achieving these outcomes.

## 2.1 Motivation

Reactive power compensation and stability study for power distribution systems are described as the major contributing factors in a survey of current research work. At some points, the heavily congested lines keep the bus voltage at a level that maximizes the uncontrolled exchange of power systems. UPQC is one of the advanced CPD's potential load flow management devices. It is a combination of two devices; a series voltage compensator and a shunt current compensator. The device can control both active and reactive power flows simultaneously, along with nodal voltage. Most study attempts were made to overcome the DG and D-STATCOM optimum planning problem using various methods. Utilizing an efficient overall DS, it is crucial to merge DG and UPQC in the DS to reduce the overall system power loss and enhance the voltage profile. There have been unsuccessful attempts to merge these compensators in the literature. These drawbacks and challenges serve as inspiration for this effort.

Furthermore, regarding the proposed optimization technique for DG/UPQC allocation, Firefly Algorithm (FA) was found to be a promising solution in the quest to solve this multi-objective optimization problem, as it is truly robust to noisy and multimodal objective functions, and it can find high-quality solutions even in difficult optimization scenarios [15].

## 3 Problem Formulation

High power losses in the radial distribution networks are caused by issues related to voltage issues and stability limitation problems [16]. Classical load flow models like Gauss–Seidel, Newton–Raphson, etc., do not apply to the DS load flow analysis because of the high R/X ratio, radiality nature, large number of buses and lines in the radial DS. These methods are unable to provide exact line flows and voltage values [17]. Several techniques have been suggested in the literature for DS load flow analysis. The Bus Injection to Branch Current (BIBC) Matrix and Forward Sweep

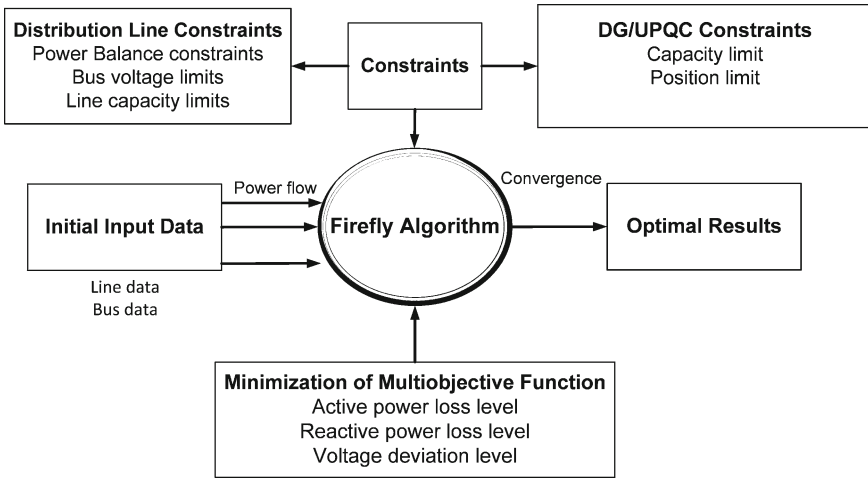


**Fig. 2** Optimization process summary

approach was successfully applied for the power flow analysis of the DS. Refer to [18] for a detailed analysis of the BIBC and forward sweep power flow method.

Figure 2 depicts a summary of the optimization process. The optimal deployment of DG/UPQC problems is described as minimization problems. It is required to formulate and optimize the objective function while meeting the operational constraints. This effort considers reducing the system’s real and reactive power loss and correcting the voltage profile as its objectives.

### 3.1 Objective Function

Simultaneous DG/UPQC allocation aims to select the optimal position and dosage of these compensators for system power loss reduction.

#### 3.1.1 Power Loss Reduction

The reduction in power loss due to the deployment of DG/UPQC is computed as:

$$J_1 = \frac{P_{t,loss \text{ after DG/UPQC}}}{P_{t,loss \text{ before DG/UPQC}}}, \tag{1}$$

where  $P_{t,loss \text{ after DG/UPQC}}$  is the total power loss reduction after DG/UPQC allocation and  $P_{t,loss \text{ before DG/UPQC}}$  is the system overall power loss before placement.

### 3.1.2 Minimization of Total Voltage Deviation for Improved Voltage Profile

The distribution system's voltage profile is improved by optimal DG/UPQC allocation. To demonstrate the DG/UPQC superiority in voltage profile enhancement of the DS, the concept of the minimum bus voltage deviation is given as:

$$J_2 = \Delta V_D = \sum_{i=1}^{N_{\text{Bus}}} (V_i - V_i^{\text{lim}})^2, \quad (2)$$

where  $V_i$  and  $V_i^{\text{lim}}$  are the bus  $i$  reference and the actual voltages, respectively. The voltage deviation index  $\Delta V_D$  is, therefore, the deviation of the bus voltage to the nominal voltage.

The equation for the objective function can be found in Eq. (3) and is formulated mathematically as follows:

$$\text{Minimize}(F_1) = \text{Min}(\alpha_1 \cdot J_1 + \alpha_2 \cdot J_2), \quad (3)$$

where  $\alpha_1$  and  $\alpha_2$  are the weight factors used for constraint handling. Authors have selected weights for the system loss and voltage profile correction as ( $\alpha_1 = 0.4$ ) and ( $\alpha_2 = 0.3$ ). The objective function constraints are;

Power balance equality constraints:

$$\sum_{i=1}^{N_{\text{bus}}} P_{\text{DG/UPQC}} = \sum_{i=1}^{\text{Bus}} P_{Di} + P_L, \quad (4)$$

$$\sum_{j=1}^{N_{\text{bus}}} Q_{\text{DG/UPQC}} = \sum_{j=1}^{\text{Bus}} Q_{Dj} + Q_L, \quad (5)$$

where  $P_{\text{DG/UPQC}}$  and  $Q_{\text{DG/UPQC}}$  represent the amount of real and reactive powers generated by the DG/UPQC;  $P_{Di}$  and  $Q_{Di}$  denote real and reactive power demands of the load bus, while the real and reactive power losses of the line are represented by  $P_L$  and  $Q_L$ , respectively.

The voltage and DG/UPQC capacity limits are the inequality constraints which are given as:

$$V_i^{\text{min}} \leq V_i \leq V_i^{\text{max}} \text{ for } i = 1 \dots N_{\text{Bus}}, \quad (6)$$

$$P_{\text{DG,min}} \leq P_{(i)\text{DG/UPQC}} \leq P_{\text{DG,max}}, \quad (7)$$

$$q_{\text{DG,min}} \leq q_{(i)\text{DG/UPQC}} \leq Q_{\text{DG,max}}. \quad (8)$$

Here, the terms min and max signify the lowest and highest values allowed for the parameters, respectively.

In this study, UPQC provides reactive power, while the PV-DG source delivers constant active power.

### 4 Methodology

In 2009, Yang developed the Firefly Algorithm (FA), a new metaheuristic algorithm inspired by the behavior of fireflies [19]. It is utilized to resolve multi-objective continuous optimization problems based on this natural phenomenon [20]. It has higher efficiency and success rates for discrete and continuous problems and has been proven to be very effective for searching the pareto-optimality set [15].

The FA was developed based on three idealized rules [15].

Given a specific medium and constant absorption coefficient  $\gamma$ , the light intensity is given as

$$I_i = I_0 \ell^{(-\gamma r^2)}, \tag{9}$$

where

$I_i$  is the light intensity during the  $i$ th iteration.

$I_0$  is the initial light intensity.

$r$  and  $\gamma$  denote the distance between two fireflies and the light absorption coefficient, respectively.

Equation (10) is used to alter the light intensity equation to define the attractiveness.

$$\beta = \beta_0 \ell^{(-\gamma r^2)}, \tag{10}$$

where  $\beta_0$  is the attractiveness at  $r = 0$ , and  $\beta$  is the attractiveness at  $i$ th iteration. A firefly's movement is thus determined by its brightness. Equation (11) describes the movement of a less bright firefly  $i$  that is drawn to a firefly  $j$  that is brighter.

$$x_{i(t+1)} = x_{i(t)} + \beta_0 \ell^{(-\gamma r_{ij}^2)} \cdot (x_{j(t)} - x_{i(t)}) + \alpha \xi, \tag{11}$$

where

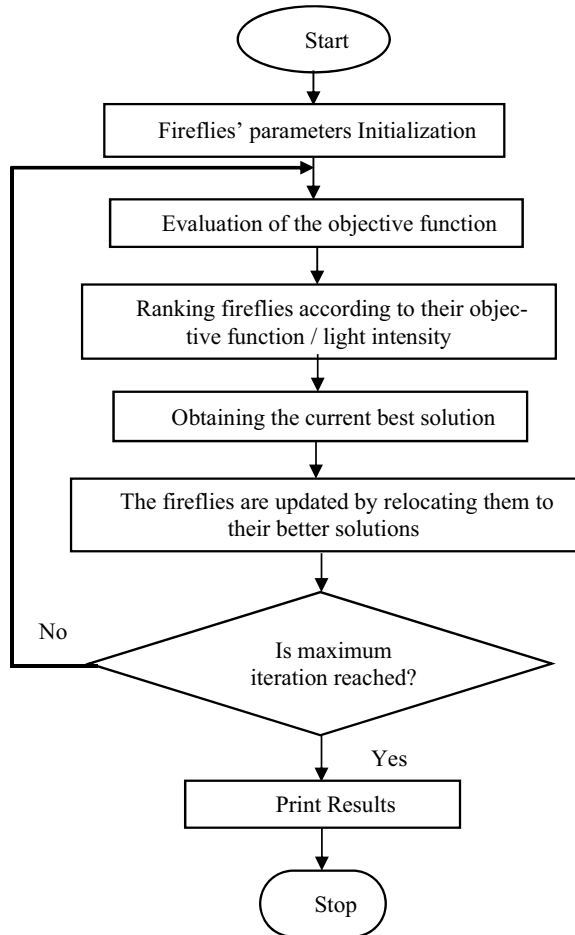
$x_{i(t+1)}$  and  $x_{i(t)}$ , respectively, denote the firefly's positions  $i$  at  $(t + 1)$  and  $(t)$  iteration.

$\alpha$  is the random step length and controls the algorithm parameter from exceeding the specified solution space.

$\xi$  is a vector of randomly generated numbers that were taken from Gaussian distributions.

Figure 3 displays the flowchart of the FA optimization method.

**Fig. 3** Firefly algorithm flowchart



#### ***4.1 Steps Involved in Implementing the Optimal Allocation of DG/UPQC Using Firefly Algorithm***

Here are the steps for implementing the optimal DG/UPQC deployment with FA:

**Step 1:** Define the FA parameters which include the number of fireflies, the maximum number of generations, the scaling parameter, the stopping criteria, the absorption coefficient, and the minimum value of attractiveness.

**Step 2:** Read the system data including receiving and sending bus, branch number, line resistance, line reactance, and bus active and reactive power loads.

**Step 3:** To acquire the initial voltages and power losses at each bus, the base case power flow was executed.

**Step 4:** The parameters of the firefly are initialized.

**Step 5:** Using Eq. (3) to formulate the objective function for each firefly.

**Step 6:** For each candidate bus, the FA technique is applied to obtain the best position and rating of DG/UPQC.

**Step 7:** According to Eq. (10), attractiveness increases with light intensity, which indicates the best values of DG/UPQC position and capacity as calculated.

**Step 8:** Equation (11) determines the best value of DG/UPQC position and capacity of firefly  $i$  that is not bright is attracted to a firefly  $j$  that is brighter.

**Step 9:** To determine the updated light intensity, the new solutions were evaluated, i.e., best values of DG/UPQC position and capacity.

**Step 10:** The fireflies are ranked by their light intensity and their optimal position and capacity was determined.

**Step 11:** Repeat steps 4 through 9 until the prescribed number of iterations is reached.

**Step 12:** The final power flow was performed with the DG/UPQC optimum capacity and position to determine the corresponding losses of active and reactive power as well as the voltage profiles of the system, respectively.

## 5 Results of the Simulation and Discussion

The results of the evaluation and simulation of the FA technique used to allocate DG and UPQC for reducing power loss and correcting voltage profiles in distribution systems are presented in this section. To test the effectiveness of the FA technique, it was compared with the Artificial Bee Colony (ABC) optimization method. The program is set at 100 iterations with a population size of 50. Other FA parameter settings are randomness ( $\alpha = 0.2$ ), absorption coefficient ( $\gamma = 1$ ), and attractiveness ( $\beta = 2$ ). Performance evaluation of the approach was carried out using the IEEE 33-bus radial distribution test system. The 33-bus system's single-line schematic, bus data, and lines were provided in [21]. Three case studies are taken into consideration for simulation in the DS. They are

- System without DG and UPQC (base case).
- Optimal DG allocation without UPQC.
- Optimal DG/UPQC allocation.

To determine the initial bus voltage magnitude and loss of active and reactive power, the base case power flow was run using BIBC and a forward sweep approach. The simulation results of the test system for the three cases are summarized in Table 1. We found that the base case resulted in an active and reactive power loss of 201.7749 kW and 134.9912 kVAR, respectively.

The following case is the optimal DG allocation without UPQC. The proposed FA method was applied to determine the optimal position and capacity of embedded DG with the objective of minimizing system loss and correcting voltage profile. The findings in Table 1 indicates that the system's performance was enhanced, with a 49.76 and 45.99% decrease in active and reactive power losses after DG was

**Table 1** Results from the simulation and performance evaluation

Case study	Base case	Optimal DG allocation		Optimal DG/UPQC allocation	
		FA	ABC	FA	ABC
Optimization method		FA	ABC	FA	ABC
Optimal location	–	25	25	25	5
Optimal DG size (kW)	0	2706	2711	–	–
Optimal DG/UPQC sizes (kw, kVAR)	–	–	–	2006, 1353	2510, 977
Loss in active power (kW)	201.7749	101.3768	101.3768	56.4783	56.4905
Percentage active loss reduction (%)	–	49.76	49.76	72.01	72.00
Reactive power loss (kVAR)	134.9912	72.9023	72.9192	45.1269	45.2320
Percentage reactive loss reduction (%)	–	45.99	45.98	66.57	66.49
Minimum voltage (p.u) @ 33 bus	0.9134	0.950	0.950	0.9666	0.9636
Minimum voltage deviation index	0.119168	0.03098	0.03098	0.012116	0.0146384

optimally sized and sited. Likewise, the DG optimal position and size were found to be at bus 25 with a size of 2706 kW.

By utilizing the proposed FA method and combining DG/UPQC, a significant improvement was observed in the reduction of real and reactive power loss by 72.01% and 66.57%, respectively. The optimal position of DG and UPQC were equally found to be at bus 25 with sizes of 2006 kW and 1353 kVAR, respectively. Further, it was also noted that the DG size was scaled down to 2006 kW when considering the impact of UPQC allocation. Furthermore, regarding the bus voltage performance, Bus 33 specifically recorded the least value of bus voltage at 0.9134 p.u when the base case was considered. But with DG allocation, the bus voltage profile improved to 0.950 p.u and improved further to 0.9666 p.u with combined DG/UPQC approach. Table 1 provides and compares the results realized from the proposed FA and the ABC optimization method considering the three cases.

Furthermore, the voltage deviation index captured in Table 1 indicates the variation between the expected and actual bus voltages. Hence, the closer this index is to zero, the more efficiently the system voltage operates. It was also observed that the combined DG/UPQC approach has the least voltage deviation index value of 0.012116 with the proposed FA method compared to the base case and DG without UPQC case as reported in Table 1. This has also proved the performance of the proposed DG/UPQC approach.

Figure 4a and b show the convergence graphs which compared the power loss reduction mode of FA and ABC algorithms for optimal DG and combined DG/UPQC problems, respectively.

As captured in Fig. 4a and b, the proposed FA method converges faster than the ABC method in both cases, reaching the optimal solution in fewer than six iterations.

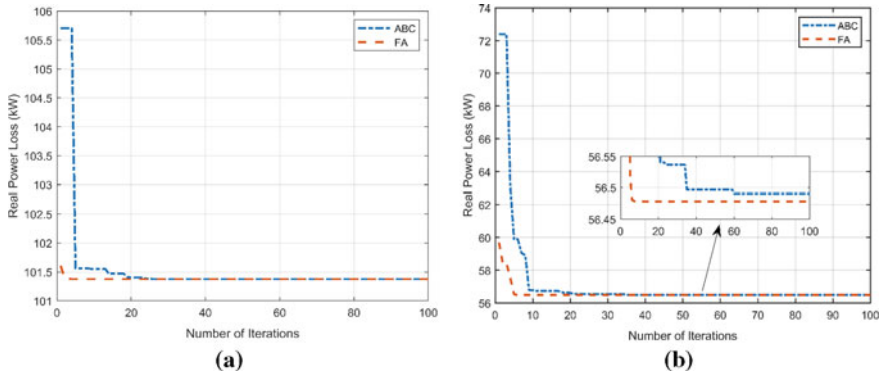


**Fig. 4** Convergence curve comparability of ABC and FA for optimal power loss reduction **a** DG allocation **b** DG/UPQC allocation

It also offered better solution quality (minimum objective function value) compared to the ABC method as captured in Fig. 4b.

Figure 5a and b provide the simulation results for the test system’s bus voltage performance with DG allocation and simultaneous DG/UPQC allocation approaches, respectively. Furthermore, the result also displayed the performance of both FA and ABC algorithms in both scenarios.

In Fig. 5a, it is demonstrated how the system bus voltage increased after the optimal allocation of DG to a minimum bus voltage of 0.950 p.u reached. However, some buses still lie along the defined lower threshold limit of 0.95 p.u, which is the minimum bus voltage limit set as captured in Fig. 5a. On the other hand, Fig. 5b demonstrates that optimal DG/UPQC allocation led to more significant voltage improvement than the system of DG without UPQC. With the combined DG/UPQC

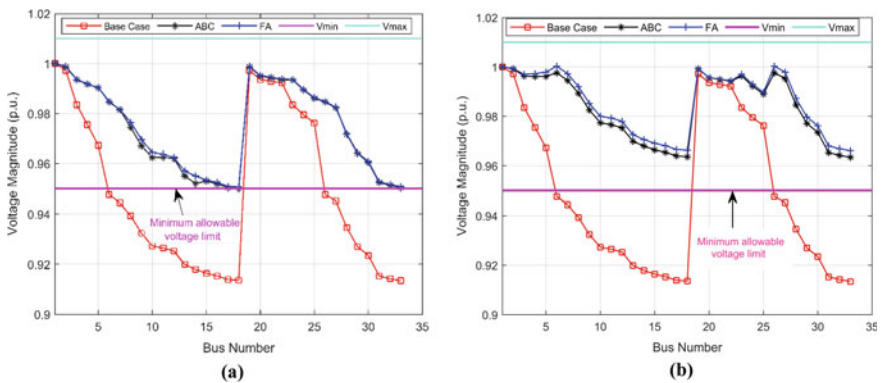


**Fig. 5** Comparison of the system voltage profile with ABC and FA algorithm. **a** With DG allocation, **b** with DG/UPQC allocation



approach, the minimum bus voltage has increased from a threshold limit of 0.95–0.9666 p.u. This result also highlights the effectiveness of the FA method in providing a superior voltage profile compared to the ABC method.

## 6 Conclusion

The performance of the active power DS was improved by implementing an optimal allocation of DG and UPQC approach. Through analysis and comparison of simulation outcomes using the proposed FA method and the ABC optimization method, it was found that the FA method was effective in improving the voltage profile and reducing overall system loss. The efficacy and applicability of using the FA method for the optimal allocation of DG/UPQC were compared with the base case and DG without the UPQC case. Results showed significant improvements of 72.01 and 66.57% in loss reduction of real and reactive powers with the combined DG/UPQC allocation, compared to 49.76 and 45.98% loss reductions for the DG system without UPQC. The minimum bus voltage @ bus 33 also improved to 0.9666 p.u with optimal DG/UPQC allocation compared to 0.950 p.u for the system without UPQC. These results suggest that the simultaneous DG/UPQC allocation approach can greatly enhance the active electrical DS performance. Future research could consider the operational costs of UPQC/DG for real-time radial distribution systems.

## References

1. Machowski J, Bialek JW, Bumby JR (2011) Power system dynamics: stability and control. John Wileys & Sons, Ltd. [https://doi.org/10.1007/978-1-4471-2291-3\\_5](https://doi.org/10.1007/978-1-4471-2291-3_5)
2. Sambaiiah KS (2018) A review on optimal allocation and sizing techniques for DG in distribution systems. *Int J Renew Energy Res* 8:1236–1256
3. Shuaibu Hassan A, Sun Y, Wang Z (2020) Optimization techniques applied for optimal planning and integration of renewable energy sources based on distributed generation: recent trends. *Cogent Eng* 7
4. Kadam PM, Kushare BE (2017) A survey on unified power quality conditioner for power quality improvement. In: National conference on emerging trends in engineering & technology, pp 2320–3331
5. Farhoodnea M, Mohamed A, Shareef H, Zayandehroodi H (2012) A comprehensive review of optimization techniques applied for placement and sizing of custom power devices in distribution networks. *Prz Elektrotechniczny* 88:261–265
6. Ramanaiah ML, Reddy MD (2018) Moth flame optimization method for unified power quality conditioner allocation. *Int J Electr Comput Eng* 8:530–537
7. Taher SA, Afsari SA (2012) Optimal location and sizing of UPQC in distribution networks using differential evolution algorithm. *Math Prob Eng* 2012
8. Musa U, Mati AA, Mohammed A, Mas AA (2020) Implementation of bacterial foraging algorithm based model for unified power quality conditioner placement in a practical distribution feeder. *Coven J Eng Technol* 4:49–65

9. Jayalakshmi D, Sankar S, Venkateshkumar M (2019) An analysis of load management system by using UPQC for distribution network. *Emerging trends expert application and security advance intelligence system computer*, vol 841. Springer Singapore, pp 261–272
10. Dehnavi E, Afsharnia S, Gholami K (2019) Optimal allocation of unified power quality conditioner in the smart distribution grids. *Electr. Eng. Springer* 101:1277–1293
11. Yuvaraj T, Ravi K, Devabalaji KR (2017) Optimal allocation of DG and DSTATCOM in radial distribution system using cuckoo search optimization algorithm. *Model. Simul. Eng.* 2017
12. Yuvaraj T, Devabalaji KR, Thanikanti SB (2019) Simultaneous allocation of DG and DSTATCOM using whale optimization algorithm. *Iran J Sci Technol Trans Electr Eng* 0123456789
13. Frahat M, Hatata AY, Saadawi MM, Kaddah SS (2022) Grasshopper optimization-based optimal sizing of DG/DSTATCOM in distribution networks. *MANSOURA Eng J* 47:6–16
14. Hariprasad C, Kayalvizhi R, Karthik N (2022) Optimum restructuring of radial distribution network with integration of DG and DSTATCOM using artificial fish swarm optimization technique. In: *International conference on sustainable energy and future electric transportation*. IEEE, pp 4–6. <https://doi.org/10.1109/SeFeT55524.2022.9909394>
15. Durbhaka GK, Selvaraj B, Nayyar A (2019) Fire fly swarm : metaheuristic swarm intelligence technique for mathematical optimization. Springer Singapore. <https://doi.org/10.1007/978-981-13-1274-8>
16. Iqbal F, Khan MT, Siddiqui AS (2018) Optimal placement of DG and DSTATCOM for loss reduction and voltage profile improvement. *Alex Eng J* 57:755–765
17. Singh B, Chandra A, Al-Haddad K (2015) *Power quality: problems and mitigation techniques (Book News)*. IEEE Ind Electr Mag. 9
18. Raj AF, Saravanan AG (2023) An optimization approach for optimal location & size of DSTATCOM and DG bus injection to branch current. *Appl Energy* 336:120797
19. Yang XS (2009) Firefly algorithms for multimodal optimization. *Lect Notes Comput Sci (including Subser Lect Notes Artif Intell Lect Notes Bioinformatics)* 5792:169–178
20. Yang XS (2010) Firefly algorithm, stochastic test functions and design optimization. *Int J Bio-Inspired Comput* 2:78–84
21. Vita V (2017) Development of a decision-making algorithm for the optimum size and placement of distributed generation units in distribution networks. *Energies*. <https://doi.org/10.3390/en10091433>

# Application of Wind Power in Backwashing Filter Media



Deepak Juneja, Sushindra Kumar Gupta, and Aditya Rana

**Abstract** Water harvesting can solve many issues ranging from flooding to declining water table. It is also need of the hour looking at the water stress due to increase in demand and a reduction infiltration. Clogging of harvester is a limitation which needs to be addressed. If the water is brought to harvesting unit after proper sedimentation, the clogging time can be increased. Further amount of sedimentation depends on detention time in desilt chamber and also on flow velocities. A comparison of clogging time and area of desilt chamber shows a linear relationship. When we increase the area of desilt chamber, the TSS in harvested water is reduced and this increases the clogging time.

## 1 Introduction

Rapid urbanization has changed the hydrology of region surrounding Punjab. This change in hydrology has been due to increase in impermeable surfaces as well as increase in pumping out of water from the aquifers. There is a demand for 135 lpcd of demand for water. As the cities grow in size, this demand is met partially by canal water and partially by pumping out of water [9, 10]. Early civilizations settled mostly on river banks and depended solely on river water. But as the population exploded after advancement in technology and industrial revolution, people started to build homes at all places. It has resulted in reduced infiltration and increased withdrawal of water from aquifers. Many big cities and towns are water stressed and unable to meet the growing demands for water. Water table has gone to 1000 feet in some areas in

---

D. Juneja (✉) · S. K. Gupta · A. Rana  
Department of Civil Engineering, Chandigarh University, Mohali, Punjab, India  
e-mail: [Junejadeepash@gmail.com](mailto:Junejadeepash@gmail.com)

S. K. Gupta  
e-mail: [sushindra.e11729@cumail.in](mailto:sushindra.e11729@cumail.in)

A. Rana  
e-mail: [adityae7590@cumail.in](mailto:adityae7590@cumail.in)

Mohali districts. Environmental protection is a key concern in WSUD technologies for urban storm water strategies.

Our environment is a legacy which we inherited from our ancestors. It is therefore our duty to pass it to the next generations in a manner similar to or better than what we received from our ancestors. Increased economic activities in the past has severely depleted our environment. Sustainability of environment is not only our responsibility, but also our duty.

In a bid to create employment, provide comforts and luxuries to the people, create wealth, there had been lot of thrust by governments on innovations and industrialization. Unplanned growth coupled with increased population has severely depleted the air and water quality. Whereas particulate matter pollution has increased in air due to suspended dust and ash in the air, pollutants in water and declining water table are a major concern in water for environmentalists. Many places have turned into water stressed places. Any place where more than 20% of the total water requirement is met by pumping of water from aquifers and having a declining water table is known as a water stressed. Water stress in area of Punjab is primarily due to these reasons. Growing of paddy to reap economic benefits is one reason why we pump out so much water from our aquifers. Paddy requires 150 cm of water for irrigation. More than half of this water requirement is met by pumping of water from aquifers. This causes a drawdown in the aquifers.

To add to the woes, it is sown in summer season and evaporation losses are to the tune of 4 mm/h. Another reason for water withdrawal is due to supply of 135 lpd of water for domestic need. Increasing population and also movement of people from villages to urban areas also increase this demand for public supply. Another reason for water stress is increased runoff and reduced infiltration. Due to unplanned and haphazard growth of cities, the permeable area for infiltration in an urban watershed is just 10%. This reduces infiltration and increases runoff. This paper discusses how we can increase clogging time of infiltration systems by changing the characteristics of storm water. The paper helps in solving maintenance issues of harvesting system. Harvesting systems get clogged over a period of time.

The paper is divided into four sections: Introduction, Material and method, Results and discussion, and finally, there is Conclusion. The clogging time of the harvester is checked by varying characteristics of storm water.

## **2 Pollutants in Storm Water**

There are many different types of pollutants in storm water. These pollutants range from suspended solids, metals, oils and surfactants, nutrients, microorganisms to other chemical and biological impurities. Presence of these impurities in water causes turbidity and adversely affects aquatic life. Different pollutants have different effects on people who consume this water.

## ***2.1 Suspended Solids***

These are particles with diameter less than 2  $\mu\text{m}$ . Due to their small size and low weight, they remain suspended in water causing turbidity. They cause turbidity in water. The allowable limit of turbidity for potable water supply is 1 NTU. These sediments are the biggest pollutants by weight in any water [2]. Hydrocarbons and nutrients are attached to these sediments [3]. Removal of suspended impurities removes many nutrients as other impurities are attached to them. This suspended matter can be removed either by aggregate filter media or by primary treatment of sedimentation and coagulation.

## ***2.2 Nutrients***

Nutrients in water are added as water from fields. They are present in water as potassium, nitrogen, and phosphorous. These are present in fields either due to application of chemical fertilizers or are present due to decomposition of organic matter. Their presence in water encourages growth of algae duckweed or phytoplankton. They consume the dissolved oxygen in water and adversely impact aquatic life [7]. This phenomenon is known as eutrophication. They are responsible for biological clogging and can retard the infiltration rates of aggregate filter media.

## ***2.3 Metals***

Metals are added to storm water as effluents from industries and also as sweeps from various workshops. Presence of heavy metals in water adversely affect the quality of water [1]. Cancer which is the leading cause of death is caused due to presence of heavy metals in water. Water can be polluted by addition of copper, cadmium, zinc, nickel, iron, lead, and manganese. Presence of zinc is although not harmful for human consumption but is harmful for aquatic life. Microorganisms in soil are sensitive to cadmium. Birth defects in animals and various other harmful effects on aquatic life are there due to chromium [11].

## ***2.4 Oils and Surfactants***

They are added to road surfaces due to leakages in various hydraulic systems of vehicles. They may be added to storm water due to spills on petrol stations. Their presence can reduce dissolved oxygen and can be detrimental to existence of aquatic

life. High levels of hydrocarbons and oils are toxic to fish, invertebrates, and macrophytes, which result in lessening in photosynthesis which affects growth of algae and phytoplanktons.

## **2.5 Organic Matter**

Organic matter is mainly present in top soil and is added to as soil erosion. Top soil contains organic matter. Excess of organic matter can induce algae growth and can reduce dissolved oxygen in water. This can affect aquatic life and can be detrimental to the growth of lentic and lotic ecosystem [5].

## **2.6 Microorganisms**

They are added to water as sewerage water is mixed to storm drains. They are also added from human excreta and also from bird feces. Most of the waterborne diseases like cholera and E.coli are due to presence of microorganisms in water. They can cause a variety of other diseases also [8]. Pathogens in storm water cause a serious health issue to those who consume contaminated water.

Several studies by researchers have found that characteristics of storm water are area specific and depend largely on type of surface and type of water shed and also on urbanization of area.

Further research on pollutant iterates those sediments which are the largest contributors of pollutants by weight. Most of the other pollutants are attached to sediments and removal of sediments can remove most of the pollutants [6]. These sediments can be removed by simple primary treatment of sedimentation and coagulation.

## **3 Urban Storm Water Management**

Urban storm water is considered as an overlooked resource. Most of the times, it is added to receiving waters. New modern concept of urban storm water management emphasizes importance of zero discharge or completely harvesting the water to aquifers.

Whereas water from storm water is harvested to aquifers, sewerage water is recycled for irrigation or for flushing after treating from treatment plants. Urban storm water treatment is based on structural measures and non-structural measures.

### **3.1 *Non-structural Measures***

#### **3.1.1 Wetlands**

They are used in storm water management either as standalone facilities or in combination with other WSUD systems, such as storm water detention ponds. These are relatively shallow vegetated waterbody treatment systems that are designed to detain water for treatment on a periodic or permanent basis. They are designed to trap sediment, nutrients, bacteria, and toxins and also promote oxygen recovery [12]. Water treatment is performed as a combination of sedimentation, filtration, and biological nutrient uptake.

They can provide recreation facilities and provide aesthetic appearance to area. Vegetation can help in lowering the velocities and also in desilting the water. They are amenable for areas with low density of population. They can help prevent flooding and erosion, and also, they do not require any infrastructure. They have low infiltration rates but large are siphon off the effects of low rates.

#### **3.1.2 Ponds**

They are a type of artificial lakes which mainly treat water by sedimentation and desilting. The depth of lake is generally more than 1.5 m. Water is detained in these ponds before being discharged to receiving bodies. The main principle behind the treatment is detention and treatment by sedimentation. The treatment train provided by lakes includes sedimentation, biological uptake, and exposure to ultraviolet disinfection. Lakes' design and maintenance are important to avoid the risk of algal blooms and pre-treatment is a requirement to avoid this risk [4].

#### **3.1.3 Pollutant Traps**

They use screens, stalling flow, settlement, skimming tanks, and flow separation as a measure for treatment. However, they cannot remove dissolved solids and very fine impurities. They can also remove free-floating oils before the water is finally discharged to receiving bodies.

### **3.2 *Structural Measures***

They consist of infiltration system with desilt chamber. They are suitable for areas with stressed infrastructure. They are also very cheap to build and solve multiple issues ranging from flooding, runoff control, soil erosion, and distresses on pavements. A simple system is shown in Fig. 1.

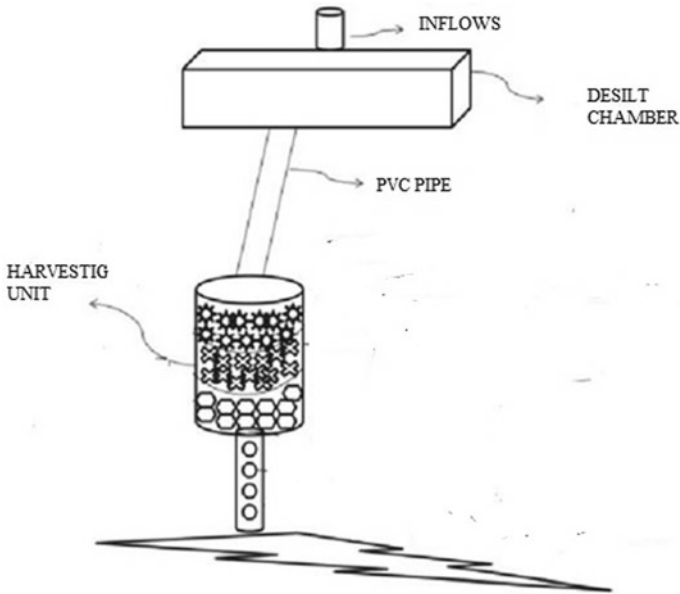


**Fig. 1** Infiltration trench

But, clogging of these system is a limitation. Most of these systems tend to clog in one season. The clogging time can increase if water from detention pond is brought to these systems. Detention ponds and desilt chambers have a similar type of function.

#### 4 Working of Harvester

Water comes first to desilt chamber where the velocity is retarded. The desilt chamber removes TSS from the water by simple process of sedimentation. Desilt chamber can be cylindrical or cuboidal in shape. Generally, cuboidal shapes are preferred as it is amenable to space restrictions that the water goes to harvesting unit. Harvesting unit is a pit circular in shape and depth is up to first sand strata encountered but minimum of ten feet. It is plastered with cement mortar on sides after brick lining with masonry. Bottom of the pit is Kutcha. It is backfilled with aggregate of size 2 mm at the top and then gradually increasing size to 10 mm at the bottom conforming to Terzaghi criterion of filter media requirements. Thickness of 2 mm aggregate should be 50 cm. Aggregate of size 10 mm and thickness of 50 cm forms drainage layer which is at the bottom. There is a reverse well point at the bottom which takes the water from drainage layer to second sand strata, as the water from drainage layer finds its way to second sand strata. Suction pressure is generated inside the well point. This pressure has a tendency to negate the effects of clogging and pull the water in harvesting unit



downward. This type of infiltration system is economical and costs few thousand rupees compared to others which cost much more difficult to understand and less affective in harvesting water. Simply replacing the top 50 cm of clogged filter media makes this system operational again restoring back the infiltration rates.

## 5 Material and Method

Experiments were conducted in field to find the relationship between area of desilt chamber and clogging time. Experiment was compressed in time by performing the experiment with semi-synthetic storm water of known TSS. Artificial storm water was created with harvested sediments. Storm water has a concentration of 2–300 (mg/l) depending on storm event. Synthetic storm water was created with TSS of 150 mg/liter which is a mean value of TSS in storm water. Clogging time was further noted at a time when the infiltration rate was reduced to half of the infiltration rate at the beginning of the experiment. This was also done to further compress the experiments in time. Normally, clogging is assumed to have occurred when the infiltration rate is reduced to 5% of infiltration rate at the beginning of experiment. Vibrator was installed inside storm water tank to prevent the sediments from settling. Area of the chamber was kept as 2, 4, and 6 m<sup>2</sup>. Experiment was done thrice for each different areas for desilt chamber. Mean value of the results was taken and graph was plotted. There was very less coefficient of variation in the results as the experiment was done with semi-synthetic storm water. Graph was plotted with clogging time on ordinate and area of desilt chamber on abscissa. The graph showed a linear relationship and positive correlation. From the experiments, it can be concluded that flow velocities in desilt chamber reduce in proportion to the increase in area of the chamber. Further, the sedimentation in desilt chamber depends on detention time which depends on flow velocities. As such clogging issues in any infiltration system can be addressed by passing the storm water through a pond or through a desilt chamber.

## 6 Results and Discussions

With other parameters remaining the same, it was observed that there was a direct correlation between clogging time and the area of the chamber. It clearly shows that the amount of sedimentation increased in proportion to the reduction in velocity. Further, the reduction in velocity is a factor of the area (Fig. 2).

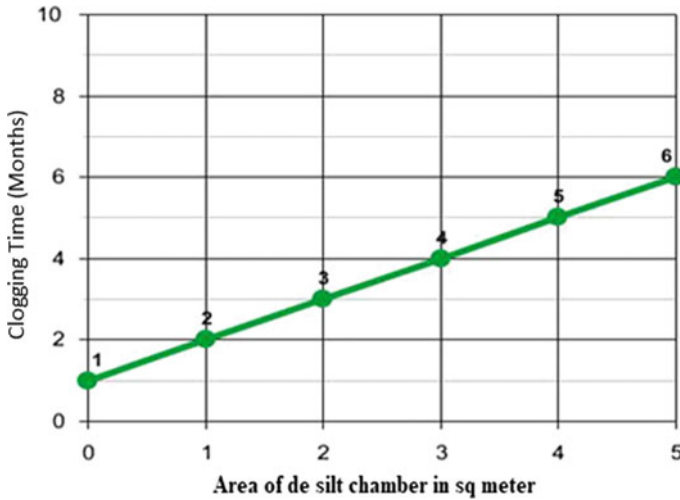


Fig. 2 Graph showing variation of clogging time with area of desilt chamber

### 6.1 Clogging Time and Area of Desilt Chamber

Clogging issues in any harvester can be addressed by passing the storm water through a detention pond or by proper sedimentation of the storm water. There is an inverse and linear relationship between flow velocities and sedimentation. As the velocity retards, very fine particles also start settling down.

There were many interesting observations. One of the interesting observations was that clogging time is increased to 4 times by joining two harvesters at the top. Further, this design is amenable to space constraints and very economical. These harvesters can be made with less than Rs 1 lac compared to 3 lacs for other designs. They are more practical and easy to understand and operate. A simple replacing the top 50 cm of filter media can make these harvesters operational again and restores the infiltration rate.

The clogging time increases if the area of the desilt chamber is increased. Clogging time of filter media is also a variable of void ratio and porosity of filter media.

### 6.2 Clogging Time versus TSS

Further clogging time of any harvester has inverse correlation with TSS in storm water. As the TSS in storm water increases, the clogging time has inverse square relationship. The TSS in storm water can be up to 300 mg/l. Semi-synthetic storm water was used to find out the correlation between clogging time and TSS (Fig. 3).

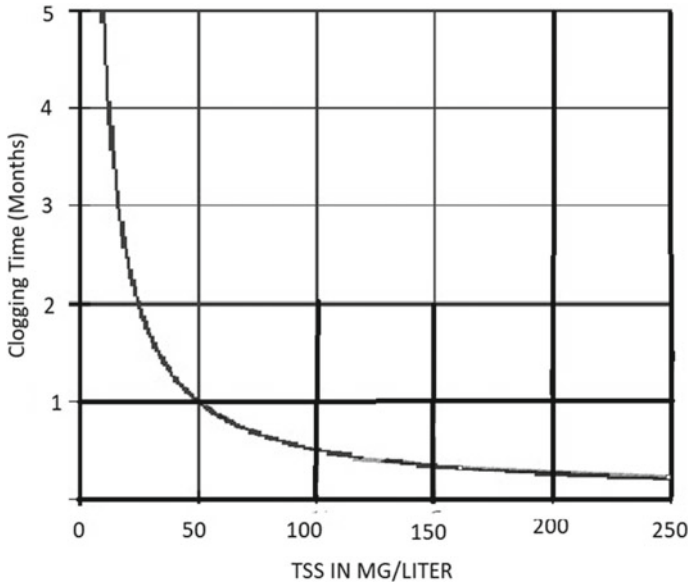
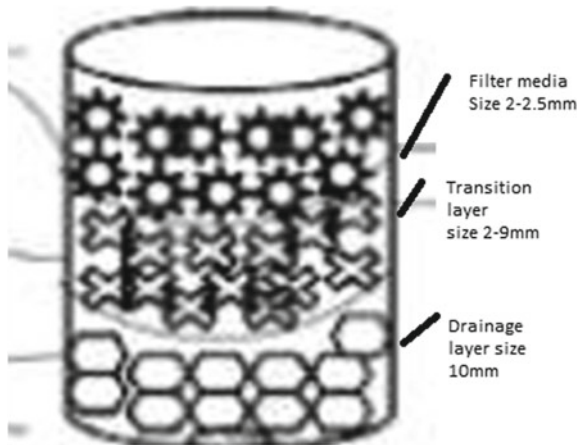


Fig. 3 Clogging time versus TSS (inverse square relationship)

Further angularity and shape have no effect on the filter media performance. Filtration system can be divided into three layers. The top-most layer consists of fine media of particles in the range of 2–2.5 mm. This size media is suitable from the point of view of hydraulic conductivity as well as treatment performance. If we use smaller size, the permeability is reduced and the infiltration trench may get clogged quickly. Bigger size will have an impact on treatment performance of the media. This size is a tradeoff between permeability and treatment efficiency. The second layer in filtration system is a transition layer which has particles of gradually increasing size with 2 mm particles at the interface of filter media and 9 mm size at the interface of drainage layer.

Further drainage layer has particles of the size of 10 mm with a reverse well point collecting water from drainage layer. Thickness of each filter media should be from 50 to 100 cm. Transition layer can have a thickness of 25–50 cm. Similarly, drainage layer can have a thickness of 50–100 cm (Fig. 4).

There is a reverse well point in the drainage layer. Reverse well point is a perforated pipe with a geotextile wrapped on it. Whereas the infiltration occurs in the harvester, reverse well point takes the water from harvester to second sand layer. In spite of all these, if there is a water in the first harvesting unit above the filtration system, it flows to the second harvesting unit. Second harvesting unit works in a similar fashion as the first unit except for the fact that water to the second unit has less turbidity and TSS. So, the water is being harvested to first and second sand layers in both the units. Even if the first unit gets clogged, there is a generation of suction pressure in the drainage layer of first unit which pulls the water standing in the first unit. Twin

**Fig. 4** Filtration system**FILTRATION SYSTEM**

harvester has a clogging time of four or five seasons compared with clogging time of one season for single unit.

After the unit is clogged, we can replace the top 50 cm of sand in the filter media, and from literature review studies, it has been found that the clogged materials remain in the top 50 cm of filter media.

## 7 Conclusions

Storm water harvesting can help solve the problem of declining water table, flooding, soil erosion, and also on distresses on roads. Further, our storm water drains cannot be designed to carry peak flows without harvesting the water to aquifers. Structural measures for harvesting are more suitable for countries with stressed infrastructure.

There is a limitation of these measures in terms of clogging. We need to do sedimentation of water before passing it through aggregate filter media. We can change the storm water characteristic by passing it through desilt chamber.

As the velocity in a desilt chamber is retarded, there is settlement of sediments and clogging time is enhanced in proportion of size of desilt chamber.

**Acknowledgements** The authors acknowledge financial support from the Chandigarh university UCRD department.

**Conflicts of Interest** The authors declare that there are no conflicts of interest regarding the publication of this paper.

## References

1. Brown JN, Peake BM (2006) Sources of heavy metals and polycyclic aromatic hydrocarbons in urban stormwater runoff. *Sci Total Environ* 359:145–155
2. Burton GA, Pitt RE (2002) Stormwater effects handbook—A toolbox for watershed managers, scientists, and engineers. Lewis, Boca Raton, Fla
3. Deletic A, Orr DW (2005) Pollution build-up on road surfaces. *J Environ Eng* 131(1):49–59
4. Francey M, Fletcher TD, Deletic A, Duncan HP (2010) New insights into water quality of urban stormwater in South Eastern Australia. *J Environ Eng* 136(4):381390
5. Karnena MK, Saritha V (2021) Water treatment by green coagulants—nature at rescue. In: Vaseashta A, Maftei C (eds) *Water safety, security and sustainability. Advanced sciences and technologies for security applications*. Springer, Cham
6. Makepeace DK, Smith DW, Satanley SJ (1995) Urban stormwater quality: summary of contaminant data. *Critic Rev Environ Sci Technol* 25
7. Mayer T, Marsalek J, Reyes ED (1996) Nutrients and metal contaminants status of urban stormwater ponds. *Lake Reser Manage* 12(3):348–363
8. McCarthy DT, Mitchell VG, Deletic A, Diaper C (2009) The first flush of E. coli in urban stormwater runoff. *Water Sci. Technol.* 60(11):2749–2757
9. Ahmad MW et al. (eds) (2022) *Intelligent data analytics for power and energy systems*. Springer Singapore, p 22, 641. ISBN: 978-981-16-6081-8. <https://doi.org/10.1007/978-981-16-6081-8>
10. Tomar A et al. (eds) (2022) *Proceedings of 3rd international conference on machine learning, advances in computing, renewable energy and communication: MARC 2021, vol 915*. Springer Nature, p 15, 781. ISBN: 978-981-19-2830-7. <https://doi.org/10.1007/978-981-19-2828-4>
11. Popa M, Glevitzky I (2021) Security standards applied to drinking water. In: Vaseashta A, Maftei C (eds) *Water safety, security and sustainability. Advanced sciences and technologies for security applications*. Springer, Cham
12. Vaseashta A (2021) Introduction to water safety, security and sustainability. In: Vaseashta A, Maftei C (eds) *Water safety, security and sustainability. Advanced sciences and technologies for security applications*. Springer, Cham

# Mixed Reality Accelerates the Designing Process in Automotive Industry



Mohamad Yahya Fekri Aladin, Ajune Wanis Ismail,  
and Fazliaty Edora Fadzi

**Abstract** Mixed Reality (MR) technologies offer the potential to revolutionize the manufacturing process of the automotive industry by providing intelligent interfaces that enable more efficient approaches to design. However, to fully leverage the benefits of MR, natural and intuitive interactions such as gesture and speech must be explored. While natural user interactions can improve efficiency, inappropriate design can lead to longer task completion times. In order to address this challenge, robust real hand gestures have been explored to accelerate the design process and produce more efficient results when combined with speech. In this chapter, test application is introduced and its implementation is discussed to showcase how MR systems that utilize natural interaction can improve the design process in the automotive industry. The results of the experiment indicate that the combination of gesture and speech significantly impacts the user experience with MR, highlighting the potential of such systems for design in automotive industry.

**Keywords** Speech interaction · Real-time gesture tracking · Mixed Reality

---

M. Y. F. Aladin · A. W. Ismail · F. E. Fadzi (✉)  
Mixed and Virtual Reality Research Lab, ViCubeLab, Faculty of Computing, Universiti Teknologi  
Malaysia, 81310 Johor, Malaysia  
e-mail: [fazliaty.edora@utm.my](mailto:fazliaty.edora@utm.my)

M. Y. F. Aladin  
e-mail: [myfekri2@graduate.utm.my](mailto:myfekri2@graduate.utm.my)

A. W. Ismail  
e-mail: [ajune@utm.my](mailto:ajune@utm.my)

## 1 Introduction

Transitioning to renewable energy sources is essential for reducing carbon emissions and combating the global climate crisis. However, the process of designing and implementing renewable energy systems can be complex and challenging. Fortunately, Mixed Reality (MR) technology is emerging as a valuable tool for accelerating the design and development of renewable energy solutions. Designing new vehicles and components in the automotive industry can be a time-consuming and costly operation, but with the emergence of MR technology, designers and engineers now have a promising new tool at their disposal that can accelerate the design process and improve the quality of the final product by enabling them to visualize and interact with virtual 3D models of their designs in real-world environments, making the design process more immersive and intuitive.

Nowadays, there is a large knowledge to explore based on numerous extended reality (XR) topics. When working with interaction, the XR technologies have focused on natural ways, especially using gesture and speech to accelerate interaction [1]. XR technologies consist of MR. The field of MR is commonly divided into two technologies: Augmented Reality (AR) and Virtual Reality (VR), which involve the creation of computer-generated images. In recent times, MR has proven to be a valuable tool for improving the interface and understanding of complex data systems [2]. When comparing XR with MR, it can be observed that AR and VR are subsets of MR. However, XR is considered an umbrella term that encompasses these three environments. AR technology allows for the overlay of digital content onto the real world without the need for an in-depth understanding of physical surroundings [3]. XR technologies can produce the intelligent interfaces and aim for a more efficient approach that could benefit the manufacturing process of the automotive industry. In the automotive industry, XR technologies such as AR and MR, able to produce the initial pilots and prototypes, have been used across industries. However, very less exploring on what MR can do for manufacturing. Figure 1 shows examples of AR/VR/MR in the automotive industry [4]. In MR, customers can feel presence, and they experience the way how to be a part of the design process. The standard time for most companies to design a vehicle from scratch to its commercialization is around 2–3 years. Now, MR along with the headset device has gained great traction in the automobile industry. Google Tilt Brush, Gravity Sketch, and Vector Suite are a few software available across various VR devices such as Oculus, HTC Vive, and Windows Mixed Reality [5], whether it is for automakers to visualize the complex design or for training new technicians or for supporting the service professionals and creating a more detailed model, or for better customer experiences.

Sketching in 3D with VR enables better visualization [6], and the ability to sketch symmetry in 3D, real-time manipulation, the ability to transfer the lines sketched for 3D modeling, and quicker ideation not only reduce the time required for generating concepts but also decrease the overall time required in designing the vehicle.

Fekri and Wanis [7] have reviewed the previous works in multimodal that use gestures and speech. Advanced interaction multimodal has been explored in the MR



**Fig. 1** Examples of AR/VR/MR in the automotive

system by [8]. Table 1 shows the related research [9–19] in the automotive industry that utilizes MR technologies, including using HoloLens, since HoloLens is the MR device that can create AR/MR interface. Research has demonstrated that MR has the potential to enhance the effectiveness of various activities, such as assembly and inspection, leading to improved efficiency. Hoover [10] evaluated the use of Microsoft HoloLens in a manufacturing-guided assembly task and found that MR technology can enhance the assembly process by providing visual guidance. A MR assistant system for post-final car assembly inspection was suggested by [11], which can assist inspectors in identifying potential defects and reducing the time required for inspection.

Schwarz et al. [12] examined the utilization of immersive VR training environments for automotive assembly and indicated that compared to traditional training methods, these environments can substantially enhance learning outcomes. Dalle Mura and Dini [15] introduced an AR-based to assist with panel alignment during car body assembly. Fernández-Caramés and Fraga-Lamas [19] discussed the potential of AR and MR for shipbuilding, highlighting the benefits of MR technology in shipbuilding processes. Overall, these studies suggest that MR technology has significant potential to enhance various processes in the automotive industry, from manufacturing and assembly to inspection and maintenance.



**Table 1** List of related works in the automotive field in Industry 4.0

Year	Title	Citation
2017	Microsoft HoloLens for interacting with automotive vehicle objects	[9]
2018	Microsoft HoloLens for a manufacturing-guided assembly task	[10]
2019	MR assistance system for the inspection after final car assembly	[11]
2020	Learning success in immersive Virtual Reality training environments	[12]
2021	ViXAssist and HoloLens 2 for automotive service and maintenance	[13]
2021	Virtual Reality in the automotive field in Industry 4.0. materials	[14]
2022	AR supporting panel alignment in car body assembly	[15]
2022	Review paper for instruction in manual assembly, training and repair	[16]
2022	XR-OOM: Mixed Reality	[17]
2022	CFD in Industry 4.0: a manufacturing design paradigm	[18]
2023	Augmented and Mixed Realities for shipbuilding	[19]

The development of AR and MR applications is primarily driven by the goal of constructing environments enriched with information. The potential for advanced interaction methods in these environments is also driving the development of these technologies. This chapter focuses on:

- Exploring the use of gesture and speech recognition to accelerate the design process in the automotive industry.
- The advancement of gesture and speech interaction implementation with aim to showcase the impact and improvement of MR technology on car designing.
- Examines the use of free-hand gestures in MR combined with speech recognition as a means to accelerate user interaction and create a more intuitive and natural design process.
- Contributes to the expanding body of research focused on the utilization of MR technology for designing and developing products in automotive industries.

This chapter presents a study on the use of MR technology for designing in the automotive industry. The paper is organized into four main sections: the introduction, the proposed system, the test application, and the conclusion. The introduction provides an overview of the use of MR technology for automotive design and highlights the need for more efficient interaction methods. The proposed system section discusses the use of gesture and speech recognition to improve the design process and reduce task completion time. It also outlines the technical specifications of the system and its implementation. The test application section presents a case study of the proposed system applied to car assembly, demonstrating its effectiveness in improving the design process. Finally, the conclusion summarizes the main findings of the study and discusses the potential for MR technology to transform the automotive industry.

## 2 Proposed System

In this section, we explain the design and construction of the MR system that has been proposed. We delve into the interaction aspects between MR and 3D objects, including gestures and speech with 3D objects. Furthermore, we present the workflow and detail the experiments conducted as part of this research.

### 2.1 Natural Hand Gesture Recognition in MR Space

By attaching the Leap Motion device to the Oculus Rift in its current head position, it becomes convenient for the device to accurately track the movement of both hands. The 3D hands have been mapped to human real hand to see the real-time gesture recognition. The both hands have been tracked and captured as demonstrated in Fig. 2.

Figure 2 shows virtual hand aligned correctly to user's real hands. Figure 2a shows the real environment with the user wears the HMD, the both hands have tracked by the device. His palm up gesture has been detected (as shown in Fig. 2b). With the palm up and palm down (as in Fig. 2c), using gestures user can modify the objects in the MR world. As illustrated in Fig. 3a, the user performs a tap gesture to collide with the 3D object while Fig. 3b illustrate the user is performing grasp gesture to grab the object. The interaction features in the prototypes include the following gestures: palm up, palm down, touch, pinch, grasp and hover. However, this research does not apply all gesture inputs, but only the listed inputs.

Besides the pinch gesture, the grasping gesture is implemented with the same algorithm as in Fig. 3b to allow the user to manipulate the 3D object. If more than two fingers collide with the 3D object, the grasping gesture is triggered. With grasp (as in Fig. 3b) or pinch (as in Fig. 4a), he can hold the object with his right hand. A 6DOF 3D object manipulation is accomplished because the user can translate and rotate the object in 6DOF, and user can release it by disengaging the grasp or pinch gesture (as in Fig. 4b).



**Fig. 2** Palm up and palm down gesture inputs



(a) User in MR space with tap and swap Gesture



(b) User in MR space with grasp gesture to perform grabbing

**Fig. 3** Tap and grasp gesture inputs

Pinch algorithm was executed when the interface successfully detected that the hands' fingertips are less than a specified threshold distance between thumb and index fingertip positions. The pinch is used to trigger a grab function. After pinch gesture method has found the collided object, the gesture is performed to grab an object by obtaining the difference of time when a pinching is activated, and grab is detected. The detection of a pinch gesture involves measuring the distance between the fingertips of the thumb and the index finger. To perform pinch gesture, the thumb finger collider and index finger collider must collide with the 3D object. If collide, the pinch gesture is performed, and a force vector is applied to the 3D object. It was to release the 3D object when the pinch gesture is no longer collide with the 3D object collider.

This research has practically applied a depth camera (DC), a depth-sensing technology, in order to acquire the depth data. The device is a passive stereovision-based camera that uses two lenses to capture the real-world environment. Through running a specific sensor-based tracking algorithm, it is possible to do spatial mapping, also called 3D reconstruction. To operate the motion data that have been acquired by Leap

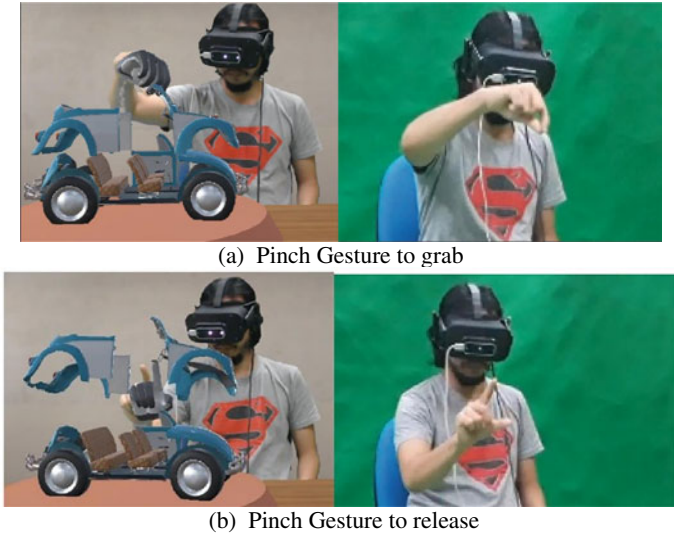
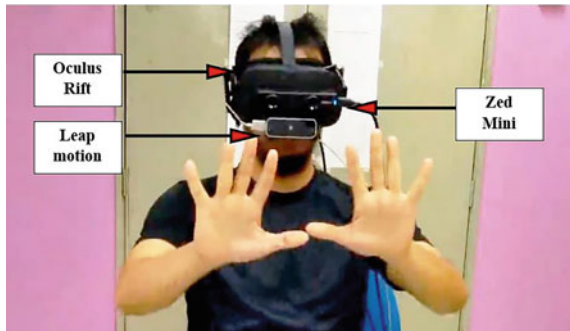


Fig. 4 Pinch gesture inputs to grab and release object

Motion, a proper gesture recognition process has been applied. Next, the gesture recognition process is presented in Fig. 5, and an HMD (head-mounted display) is attached with a depth camera device, ZED Mini. ZED Mini uses to capture the real environment for the depth mapping, while the Leap Motion uses to capture the skeleton of user's hands.

The recognition of gestures occurs during pose detection when the Leap Motion device sends a signal to initiate skeleton calibration, enabling the tracking of free-hand gestures. This skeleton-based tracking differs from vision-based tracking, as illustrated in Fig. 6.

Fig. 5 Gesture recognition device setup



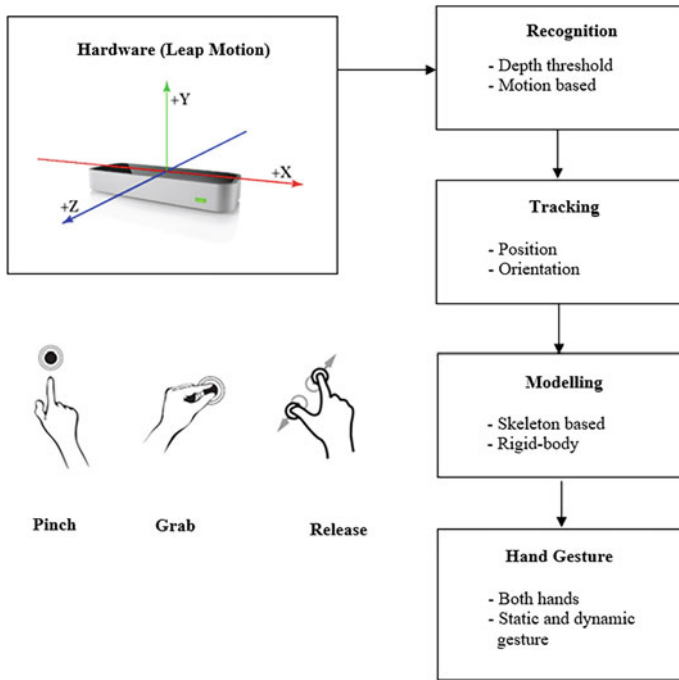


Fig. 6 Skeleton-based tracking process

## 2.2 Gesture with Speech Input Interaction

The system is designed to implement grasp and pinch gesture, so the user can naturally hold the 3D object. Another gesture being checked is hover, indicating the user intent to perform uniform object manipulation. The gesture input is found; the system will continue performing the looping to acquire the gesture data. After the gesture has found, then the system will allow the speech input to be invoked. Figure 7 illustrates the representation for gesture–speech to be executed using gesture and speech. The captured modalities inputs are determined between gesture and speech. Grammar list or dictionary where the speech inputs were stored, such as “change to red”, “select all”, and “copy” were used to check for the correct command. While the gesture was deactivated, the system was able to run speech-only during speech recognition process. While the speech was deactivated, the system was able to execute gesture-only.

Speech input has a maximum of three words, for example, “change to blue” and “change to yellow”. The implementation of speech inputs using standard.NET framework with C# language. The speech recognizer is initialized, and the grammar

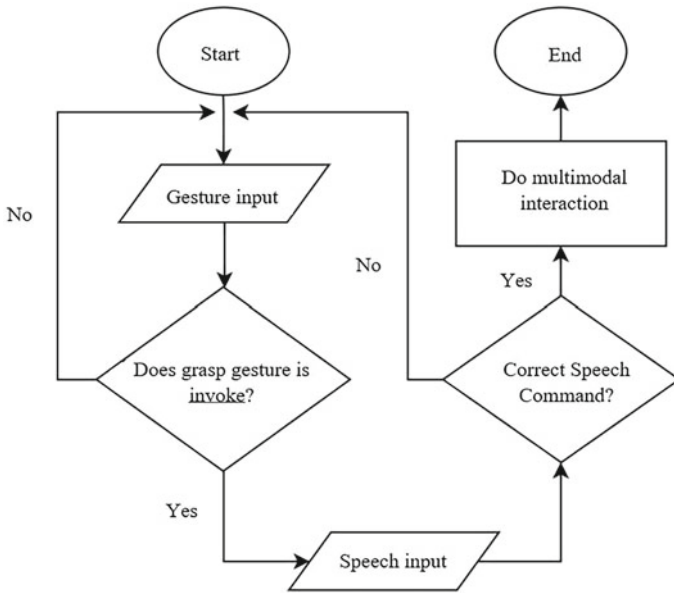


Fig. 7 Gesture with speech input interaction

has been defined in an instance of the grammar lists. The commands updated asynchronously. Grammar list or dictionary where the speech inputs were stored, such as “change to red”, “select all”, and “copy”. While the gesture was deactivated, the system was able to run speech-only during speech recognition process. While the speech was deactivated, the system was able to execute gesture-only.

### 3 Test Application

For the prototype, a model of a car is used and the car is made up of several car parts to test for automotive. To make the UI for this prototype, Adobe Photoshop is used, and in order to create or edit 3D objects, Autodesk Maya 2012 is used. The development process runs in the desktop machine, with an OS of Windows 10, ROG STRIX GeForce RTX 2016 graphics card, 16 GB of random access memory (RAM), and a 2.50 GHz Intel Core i7-8700 CPU. Oculus Rift acts as a display device.

For the test application, the user is given the freedom to use any defined gesture inputs that they seem suitable to be used for a particular task such as grasping to grab the 3D object. The user is also given a set of speech to be spoken, which is “increase size by one” and “change this” for scaling and changes the car part. Speech command “change this” allows user to change the selected 3D object to the new 3D object, while for “increase size by one”, it increases the scaling value by one. Both of these speech commands are triggered multimodal interaction since the

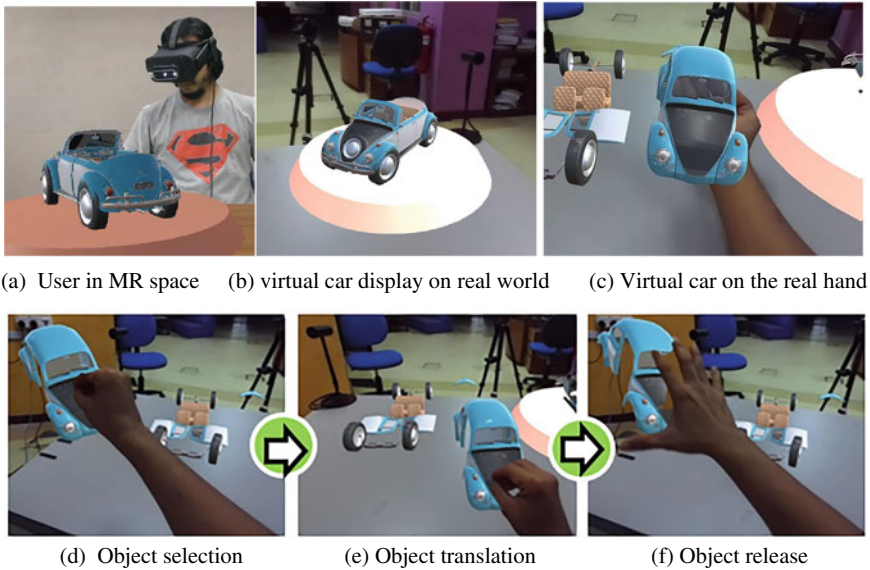


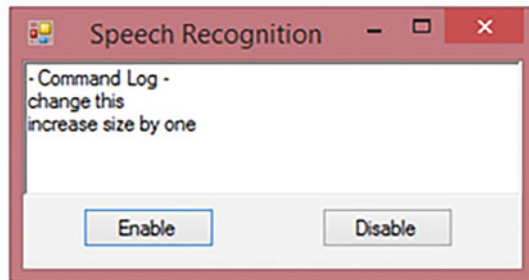
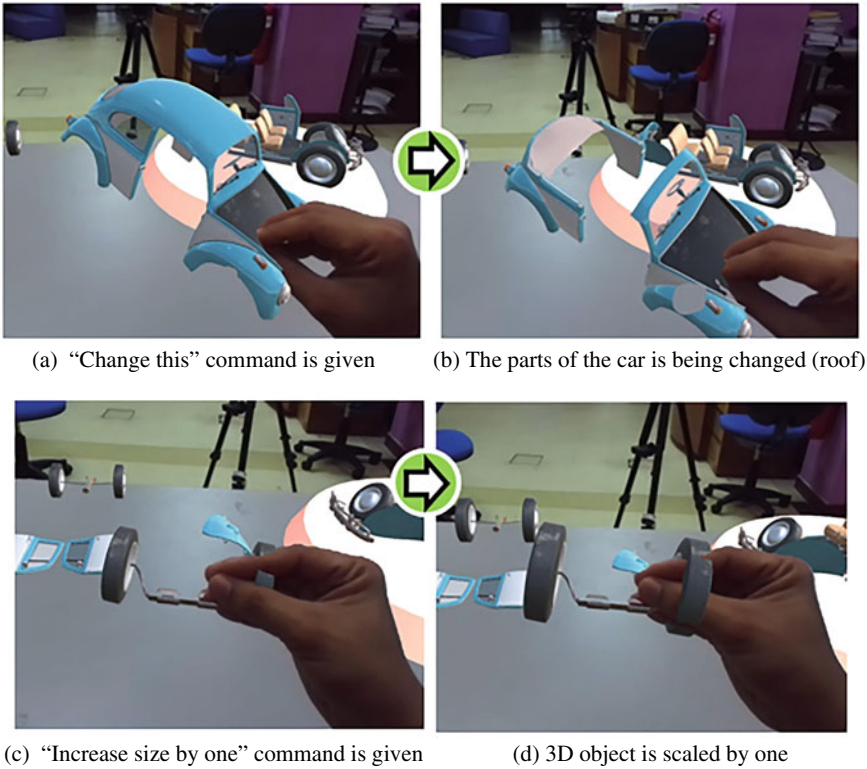
**Fig. 8** MR automotive assembly car

commands both come after the gesture command, right after the user grabs the 3D object. The threshold for the depth estimation and the resolution for the depth data are also determined in this pilot test. In this prototype, 3D car parts are utilized as visual aids, allowing users to manipulate and assemble the parts into their appropriate positions. Figure 8a illustrates the car parts that need assembly, and Fig. 8b and c illustrate the finish looks of when all the car parts are assembled correctly.

To manipulate 3D object, it can be done without speech by using gesture-only. The user is able to grasp or pinch to perform object selection. The selection, translation, and rotation have been designed in this test application. Rotation and changing the 3D object are done with MMI. Figure 8 illustrates the gesture being used to perform translation. Grasp gesture uses to select the object (as in Fig. 8d), while the grasp gesture is still active, the user dragging the 3D object to move or translate the object for 3D object manipulation (as in Fig. 8e). Figure 8f shows that the user releases the selected 3D object by opening their hands. For rotation, the user performs 3D object rotation, but translation and rotation concurrently as the gesture used support six degrees of freedom (DOF) movement [20].

Figure 9a shows that the user holds the car and speaks the command “change this”. The car part: A roof has been removed (as in Fig. 9b). It can be seen that the user scales up the object tires (as in Fig. 9c) by saying “increase size by one”. In Fig. 9d, the tires have been scaled up to one scalar factor. As demonstrated in Fig. 9e, the speech panel displays the command log, and the panel is triggered to show the speech commands list. Panel is popping out to show that the speech recognition is successfully executed.





(e) Speech command

Fig. 9 Gesture–speech interaction

## 4 Conclusion

The contribution of this chapter is the exploration of a more intuitive way to interact with Mixed Reality (MR) content using speech and gesture. The use of gesture and speech in MR applications has the potential to greatly enhance the user’s experience and accelerate the automotive design process. To accomplish this, the proposed



system and test application integrate natural user interactions by combining gesture recognition through Leap Motion and speech commands. We have examined various forms of gesture inputs, and alongside that, we have identified suitable commands for speech recognition to complement the gesture interaction.

The effectiveness of the proposed method has been demonstrated in enabling real-time gesture interaction for 6DOF object manipulations, augmented by speech commands. The findings of the study demonstrate that the combination of speech and gesture in the MR test application significantly influences the user experience. Additionally, this chapter provides a future work that involves removing the need for a headset and instead utilizing hologram technology to provide an even more immersive experience. Overall, this research emphasizes the significance of intuitive interaction in MR and showcases the potential of integrating gesture and speech for achieving it. Furthermore, it contributes to the expanding body of research focused on enhancing the efficiency and intuitiveness of MR applications in diverse industries, including the automotive industry.

## References

1. Aladin MYF, Ismail AW (2019) Designing user interaction using gesture and speech for mixed reality interface. *Int J Innov Comput* 9(2)
2. Ismail AW, Aladin MYF, Halim NAA, Manaf MSA (2023, Feb) Augmented reality using gesture and speech accelerates user interaction. In: *Advanced communication and intelligent systems: first international conference, ICACIS 2022, Virtual Event, Revised Selected Papers*. Cham: Springer Nature Switzerland, pp 233–244
3. Ismail AW, Billinghamurst M, Sunar MS, Yusof CS (2018, Sep) Designing an augmented reality multimodal interface for 6DOF manipulation techniques. In: *Proceedings of SAI intelligent systems conference*. Springer, Cham, pp 309–322
4. Narayanan S, Ramesh NN, Tyagi AK, Anbarasi LJ, Raj BE (2021) Current trends, challenges, and future prospects for augmented reality and virtual reality. *Multimedia Sens Input Augmented, Mixed, Virtual Reality* 275–281
5. Jiang Y, Zhang C, Fu H, Cannavò A, Lamberti F, Lau HY, Wang W (2021, May) HandPainter-3D sketching in VR with hand-based physical proxy. In: *Proceedings of the 2021 CHI conference on human factors in computing systems*, pp 1–13
6. Darwish M, Kamel S, Assem A (2023) Extended reality for enhancing spatial ability in architecture design education. *Ain Shams Eng J* 102104
7. Fekri AMY, Wanis IA (2019, Aug) A review on multimodal interaction in mixed reality environment. In: *IOP conference series: materials science and engineering*, vol 551, no 1. IOP Publishing, p 012049
8. Szczurek KA, Prades RM, Matheson E, Rodriguez-Nogueira J, Di Castro M (2023) Multimodal multi-user mixed reality human-robot interface for remote operations in hazardous environments. *IEEE Access*
9. Kulanthaivetpillai N, Gorges G (2017) Implementing an augmented reality application to use on microsoft HoloLens to interact with automotive vehicle objects
10. Hoover M (2018) An evaluation of the microsoft HoloLens for a manufacturing-guided assembly task. *Doctoral dissertation*, Iowa State University
11. Pattke M, Martin M, Voit M (2019, July) Towards a mixed reality assistance system for the inspection after final car assembly. In: *International conference on human-computer interaction*. Springer, Cham, pp 536–546

12. Schwarz S, Regal G, Kempf M, Schatz R (2020, Oct) Learning success in immersive virtual reality training environments: practical evidence from automotive assembly. In: Proceedings of the 11th nordic conference on human-computer interaction: shaping experiences. Shaping Society, pp 1–11
13. Chow H (2021) Augmented reality using ViXAssist and HoloLens 2 for automotive service and maintenance. In: XR case studies. Springer, Cham, pp 59–66
14. Firu AC, Tapîrdea AI, Feier AI, Drăghici G (2021) Virtual reality in the automotive field in industry 4.0. *Mater Today: Proc* 45:4177–4182
15. Dalle Mura M, Dini G (2021) An augmented reality approach for supporting panel alignment in car body assembly. *J Manuf Syst* 59:251–260
16. Wang Z, Bai X, Zhang S, Billingham M, He W, Wang P, Lan W, Min H, Chen Y (2022) A comprehensive review of augmented reality-based instruction in manual assembly, training and repair. *Rob Comput-Integr Manufact* 78:102407
17. Goedicke D, Bremers AW, Lee S, Bu F, Yasuda H, Ju W (2022, Apr) XR-OOM: MiXed Reality driving simulation with real cars for research and design. In: CHI conference on human factors in computing systems, pp 1–13
18. Mourtzis D, Angelopoulos J, Panopoulos N (2022) Integration of mixed reality to CFD in industry 4.0: a manufacturing design paradigm. *Proc CIRP* 107:1144–1149
19. Fernández-Caramés TM, Fraga-Lamas P (2023) Augmented and mixed reality for shipbuilding. In: Springer handbook of augmented reality. Cham: Springer International Publishing, pp 643–667
20. Aladin MYF, Ismail AW, Ismail NA, Rahim MSM (2020, Nov) Object selection and scaling using multimodal interaction in mixed reality. In: IOP conference series: materials science and engineering, vol 979, no 1. IOP Publishing, p 012004

# Design and Implementation of Solar Charging Electric Vehicle



Rahil Imtiyaz, Aman Kumar, Gitanjali Mehta , and Ruqaiya Khanam

**Abstract** The accessibility of non-renewable energy sources will diminish to increment popularity and will be depleted in the near future. Along these lines, it is important to track down the substitute fuel to work the vehicles. As a sustainable power source, solar energy is utilized to make solar charging electric vehicle (SCEV) that is our venture. This kind of vehicle would be fit to supplant conventional ignition engines for ordinary vehicle exercises. The utilization of solar-based energy to control the vehicle takes into account greater appropriateness and a method for utilizing environmentally friendly power energy. Standardization of the vehicle this kind would drastically decrease the harmful emissions delivered by the vehicles and diminish the oil demand. The authors have proposed a photovoltaic (PV) integrated electric vehicle (EV) instead of conventional EV with separate PV/grid/hybrid charging station. As starters, the goal is to execute our thought on an essential model and later with the assistance of this model, by building constant solar charging electric vehicle we may broaden our future.

**Keywords** Solar charging electric vehicle · Photovoltaics · Renewable energy

## 1 Introduction

In the current circumstance, due to the increase in population, usage of assets like petrol, coal and diesel are continuously increasing. The availability of these non-environmentally friendly power source will decrease accordingly, and it will be exhausted in sometime leading to a future with fuel and mineral deficit. In this way, present patterns in energy utilization, particularly oil, cannot be supported any longer

---

R. Imtiyaz · A. Kumar · G. Mehta (✉)  
Electrical and Electronics Engineering, Galgotias University, Greater Noida, India  
e-mail: [gitanjali.iitr@gmail.com](mailto:gitanjali.iitr@gmail.com)

R. Khanam  
Computer Science and Engineering, Center for Artificial Intelligence in Medicine, Imaging and Forensic, Sharda University, Greater Noida, India

[1–3]. Additionally, the use of conventional energy sources is the major cause behind environmental imbalance, ozone layer consumption and global warming which thus is a major danger to the future human race. Once more, considering the chance of a worldwide temperature alteration, these assets are assuming a negative part. Along these lines, under the present situation, it is very important to make another investigation of the common asset of energy. It is viable, more affordable or more all, it is an unending wellspring of energy. With well-enhanced energy productivity, a shift to an energy-based wealth capable of supporting predicted global economic growth is possible [4, 5].

Power can be produced utilizing environmentally friendly power sources, for example, solar, wind and biomass. Sun-based energy is the cleanest and most abundant ecologically friendly power source available. Sunlight-based solar panels convert the sunlight rays into usable solar energy. The process of turning light (photons) into electricity (voltage) is defined as the photovoltaic effect. Solar panels convert the majority of visible light and a small amount of brilliant infrared light into electricity. Solar charging innovations can harness this energy for a variety of purposes, including generating electricity, providing light or a pleasant indoor atmosphere, and warming water for domestic, commercial or industrial usage [6–8].

The authors propose to decrease the utilization of natural fuel-controlled vehicle and plan climate-amicable electric vehicle. Sunlight-oriented vehicle is principally controlled by direct sun rays. On the solar vehicle, photovoltaic (PV) cells are utilized to capture the PV rays and convert the solar-oriented energy form into electric energy form. Silicon and mixtures of indium, gallium and nitrogen are used to create this product. The semiconductors assimilate light and afterwards discharge it, creating a progression of electrons that produce power which charges 24 V battery associated with it, which runs the 375 W Brushless DC (BLDC) motor to send the ability to drive the vehicle. We are using high-strength iron square pipes for good mechanical strength. The configuration is made with the end goal that vehicle has appropriate weight to power proportion and is light in weight and strong, which is a must for any solar charging vehicle.

Habib et al. [9] have discussed the present and future status of electric vehicle (EV) and charging system implementation. The EV batteries are charged during the day by PV charging stations in parking area. Khalid et al. [10] have reviewed EV charging infrastructures and the impact it has on power quality of grid. Savio et al. [11] have analysed the energy management strategy of hybrid microgrid structured EV charging station. Tazay and Miao [12] have proposed a hybrid converter for PV charging station. Ramadhani et al. [13] have reviewed the different PV-based charging techniques for EV. Abdelsalam et al. [14] have presented the modelling and simulation of PV-powered EV charging station. Tiano et al. [15] have evaluated the potential of PV panel installation on EV body.

Most of the work proposes EV with PV charging stations. Our study designs and implements PV integrated EV system so as to improve the driving range and reduce battery storage size. The authors have designed and implemented PV-based EV system instead of conventional EV with PV charging stations. The advantages

offered by the proposed solar charging EV system are reduced grid energy demand, increased EV driving range and reduced carbon emissions.

The paper is organized as given. Section 2 discusses the modelling of solar charging electric vehicle. Section 3 focuses on the design calculation of the EV. Section 4 discusses the design vehicle specifications and a comparison with the conventional vehicles. Section 5 gives the conclusion along with future scope of work.

## 2 Proposed Work

The block diagram of solar charging electric vehicle with a battery charge/discharge controller is shown in Fig. 1. The SCEV project was at first begun in the fall of 2021. The required number of parts were bought, and associations were done with the creation shop close by for joint welding to the edges of the vehicle: 3 × 6 ft length 1.5" square iron pipe body, 2-rods at the end, 1-steering for 2 front wheel, 1-solar plate, 1 steering set, 1-brake build near to handle, 4 small wheels, 2 battery, 1 reverse switch, 1 chain set, 375 W BLDC motor, controller, 7 × bearings and 1 brake cable [16–18].

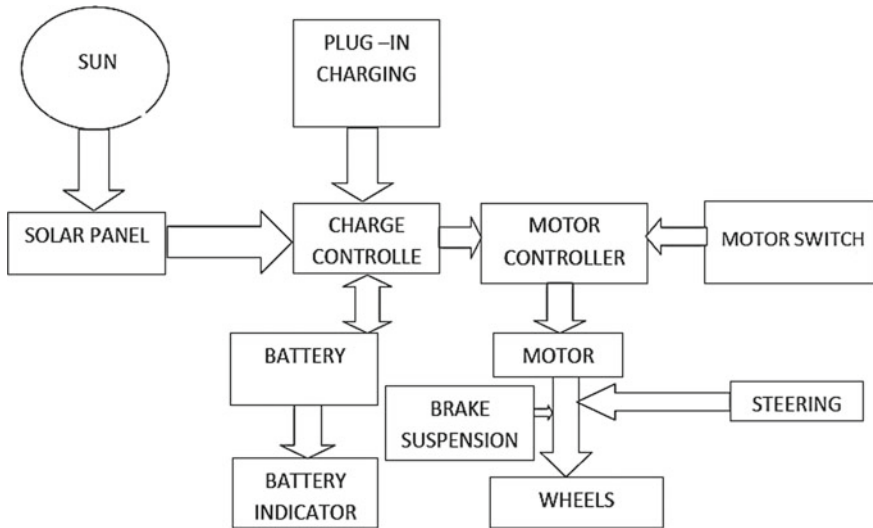
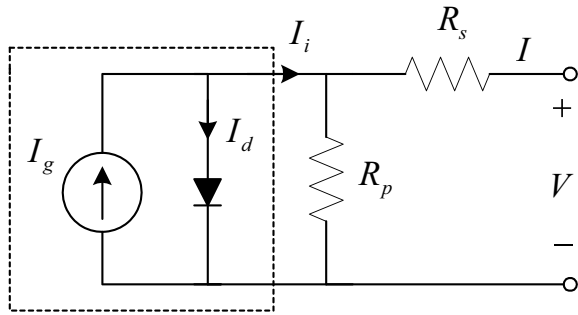


Fig. 1 Block diagram of solar charging electric vehicle

**Fig. 2** Equivalent circuit of a single PV cell



### 2.1 Solar Panel

Solar cells are generally constructed of silicon that has been specially processed to shape an electric field. The back is heavily doped with boron, while the phosphorus-doped negative side is exposed to the sun. At the point when photons from sun rays hit the solar cells, making electron-opening sets, electrons are extracted from the particles in the semiconductor material. Figure 2 shows the block diagram of a single PV cell. Assuming electrical conduits are connected to the +ve and -ve sides, an electrical circuit is shaped and the moving electrons make electric flow  $I_g$  (photocurrent). The more noteworthy the power of daylight, the more prominent is the progression of power [19–24].

When there is no daylight, the sunlight-based cell is certainly not a functioning gadget, and it fills in as a diode. In the event that it is associated with an outer stockpile, it creates a current,  $I_d$ , called diode current. Figure contains a flow source,  $I_g$ , the diode and an arrangement opposition addressing the inner obstruction of a cell  $R_s$ . As a result, the difference between  $I_g$  and  $I_d$  is the net current  $I$  expressed as:

$$I = I_g - I_d = I_g - I_0 \left( e^{\frac{\beta(V+R_s I)}{\alpha}} - 1 \right), \tag{1}$$

where  $\alpha$  is the diode ideality factor,  $\beta$  is the inverse thermal voltage,  $k$  is Boltzmann’s gas constant,  $V$  is cell voltage and  $I_0$  is the diode reverse saturation current.

### 2.2 Battery

A battery is an electrical component that changes chemical energy into electrical energy and the other way around. Positive cathode and negative anode are the two terminals that it usually possesses. During a prospective shift (charging or releasing) the framework relies on the synthetic response of electrolyte (fluid or glue arrangement). Particles will pass between the two terminals because of the electrolyte

(cathode and anode) or the dynamic materials of the battery, enabling electricity to flow from the battery in order to complete necessary tasks.

The battery’s applications are limitless. For all electrical devices that necessities high energy stockpiling limit or for any gadget that requirements low energy yield (versatile gadgets like cell, PC and so forth), battery is utilized for either to capacity energy or to go about as a force supply. Along with technological advancements that increase the capacity limit, size and lifetime of batteries, new battery applications are gradually emerging [17–20].

For the solar-based vehicle, we were utilizing battery for a backup to store energy which has ceaseless yield. To do that we need explicit determination of battery to play out our undertaking effectively which require clear comprehension of its boundaries just as its inclination of conduct.

State of charge (SOC) is a statement of the current battery limit as a level of greatest limit. SOC is for the most part determined utilizing current incorporation to decide the adjustment of battery limit over the long run. It can likewise be clarified as:

$$SOC = \frac{\text{Available Capacity}}{\text{Nominal Capacity}} \tag{2}$$

Depth of discharge (DOD) defines the level of battery capacity that has been discharged with respect to the most extreme limit. Figure 3 shows the charging and discharging of the battery. The SOC represents an alternative form of DOD measurement, and hence, DOD is expressed as:

$$DOD = 1 - SOC \tag{3}$$

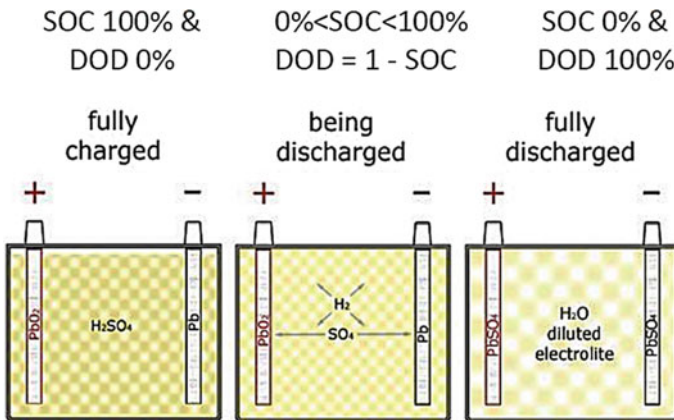


Fig. 3 Battery charging and discharging (SOC vs. DOD)

### 3 Design Calculation for Solar Charging Electric Vehicle

The solar vehicle is manufactured at the cost of INR 30,000. The vehicle has a wheelbase of 1066 mm (42 in.). The vehicle uses four wheels, two wheels in front and two in rear. The body material uses seamless square iron pipe for better mechanical strength. The ground clearance from the driver seat is 101.4 mm (4 in.). The ground clearance is decided as per the vehicle structure. There is square iron pipe bumper in the front and the rear of the vehicle. Two jack point is provided near the rear wheel. The driver's exit is so easy that he/she can exit from the vehicle within 5 s. Driver visibility is two hundred degrees ( $200^\circ$ ) field of vision and one hundred degrees ( $100^\circ$ ) to both sides of the driver. Steering system is well connected with the front two wheels. Proper braking system is attached with the rear wheels supporting by the disc. The BLDC motor is used with the power 375 W, and running voltage is limited to 24 V. Battery capacity is 24 V and 30 Ah all the time. Figure 4 shows the overview of the developed solar charging electric vehicle. Figure 5 displays the different parts of the SCEV. Figure 5a shows the braking system with the rear wheel, and Fig. 5b shows the wheel side view. Figure 5c shows the battery charge/discharge controller, and Fig. 5d shows the solar panel. Figure 5e shows the battery pack and Fig. 5f the chain set. Table 1 shows the dimensions of the designed solar charging electric vehicle. Table 2 gives the solar charging electric vehicle specifications. Table 3 shows the calculated values for angular velocity, frequency, peak torque, peak power, continuous torque, continuous power, continuous speed, air resistance and rolling resistance derived from Eqs. (4) to (12).



Fig. 4 Overall view of solar charging electric vehicle

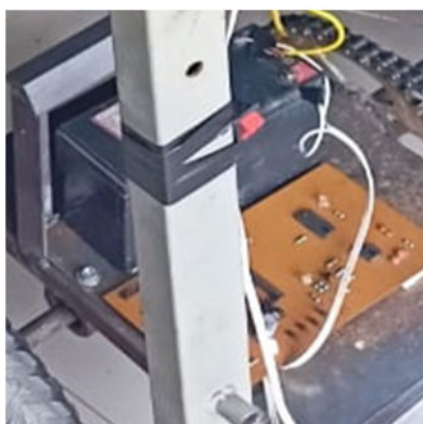




(a) Braking system with the rear wheel



(b) Wheel Side View



(c) Battery Charge / Discharge Controller



(d) Solar Panel



(e) Battery Pack



(f) Chain set

Fig. 5 View of different parts of solar charging electric vehicle

**Table 1** Dimensions of the designed solar charging electric vehicle

Parameter	Value (m)
Length	1.828
Width	0.914
Height	1.219
Ground clearance	0.101
Wheelbase	1.066

**Table 2** Solar charging electric vehicle specifications

Parameter	Value
Weight of the vehicle	80 kg
Speed	20–25 km/h
Diameter of wheel	0.4 m
Weight of battery	20 kg
Average speed	20 km/h
Range	20 m

**Table 3** Calculation results

Parameter	Value
Angular velocity	27.75 rad/s
Frequency	265.12 RPM
Peak torque	19.6 N-m
Peak power	543.9 W
Air resistance	32 W
Rolling resistance	147.2 W
Continuous power	179.2 W
Continuous speed	104.66 RPM
Continuous torque	16.34 N-m

• **Wheel angular velocity calculation**

Considering Linear Velocity = 20 km/h  
 Speed =  $20 \times (5/18)$  m/s = 5.55 m/s  
 Wheel Diameter = 0.4 m

$$\begin{aligned}
 \text{Angular Velocity} &= \text{Linear Velocity} \div \text{Radius} \\
 &= 5.55/0.2 = 27.75 \text{ rad/s}
 \end{aligned}
 \tag{4}$$

$$\text{Angular Speed} = 2 \times \text{frequency} \times \pi$$

$$\begin{aligned} \text{Frequency} &= \text{Angular Speed} / 2\pi \text{RPS} = \text{Angular Speed} \times 60 / (\pi \times 2) \text{RPM} \\ &= 27.75 \times 60 / (3.14 \times 2) \text{RPM} = 265.12 \text{RPM} \end{aligned} \tag{5}$$

- **Peak torque calculation**

$$\begin{aligned} \text{Peak Torque Wheel} &= (\text{Wt. of Vehicle} + \text{Wt. of Battery}) \\ &\quad \times \text{Acceleration due to gravity} \\ &\quad \times \text{Slope\%} \times \text{Radius of wheel} \\ &= (80 + 20) \times 9.8 \times 0.2 \times 0.1 \text{ N-m} = 19.6 \text{ N-m} \end{aligned} \tag{6}$$

$$\begin{aligned} \text{Power Required} &= \text{Angular Velocity} \times \text{Torque} \\ &= 27.75 \times 19.6 \text{ W} = 543.9 \text{ W} \end{aligned} \tag{7}$$

- **Air resistance calculation**

$$\begin{aligned} \text{Air Resistance} &= (5/100,000) \times \text{Wt. of vehicle} \times (\text{Average Speed})^3 \\ &= (5/100,000) \times 80 \times 203 = 32 \text{ W} \end{aligned} \tag{8}$$

- **Rolling resistance calculation**

$$\begin{aligned} \text{Rolling Resistance} &= 0.092 \times \text{average speed} \times \text{Wt. of the vehicle} \\ &= 0.092 \times 20 \times 80 = 147.2 \text{ W} \end{aligned} \tag{9}$$

- **Continuous power calculation**

$$\begin{aligned} \text{Power Required (Continuous)} &= \text{Rolling Resistance} + \text{Air Resistance} \\ &= 147.2 + 32 = 179.2 \text{ W} \end{aligned} \tag{10}$$

- **Continuous speed calculation**

$$\begin{aligned} \text{Continuous Speed} &= \text{Average Speed} \times 60 / (2 \times \text{Wheel Radius} \times \pi) \\ &= 20 \times (5/18) \times 60 / (2 \times 0.2 \times \pi) = 104.66 \text{ RPM} \end{aligned} \tag{11}$$

**Table 4** SWOT analysis

Strength	Weakness	Opportunities	Threats
Light in weight and long-lasting chassis	Not suitable for long drives	Environment-friendly vehicle	Bad weather condition and not getting proper sunlight rays
Directly run-on solar power	Performance varies with change in weather	Directed towards a green and clean future	Roads are not settled everywhere

- **Continuous torque calculation**

$$\begin{aligned}
 \text{Torque Required} &= (\text{Air Resistance} + \text{Rolling Resistance}) \\
 &\quad \times 60 / (2 \times \text{Continuous Speed} \times \pi) \\
 &= (32 + 147.2) \times 60 / (2 \times 104.66 \times \pi) = 16.34 \text{ N-m} \quad (12)
 \end{aligned}$$

## 4 Solar Charging Electric Vehicle Specifications

It's just a DC transformer with a chopper circuit that allows it to go up or down in voltage. We can increase the yield voltage by changing the semiconductor switch's obligation pattern. To avoid a sudden shift in current, we may simply charge the battery through an inductor. We may connect the DC motor to the circuit in a similar manner. Table 4 presents the SWAT analysis for SCEV. Table 5 gives a comparison of solar charging electric vehicle with petrol vehicle and electric vehicle. Table 6 provides a comparison of running cost for petrol vehicle, electric vehicle and solar electric vehicle.

## 5 Conclusions

A four-wheeled minimal expense photovoltaic integrated electric vehicle is achievable and practicable. Our SCEV, a solitary situated vehicle controlled by 375 W BLDC-centred motor can be a decent decision for the Asian market. A multivariate specialized gathering has improved the design and manufacturing of our SCEV, ensuring that it stays a safe, elite and cost-effective electric sun-based vehicle. Utilization of square iron pipes for strong mechanical strength, utilization of ergonomically planned solar vehicle inside, moving on direct sunlight-based energy without

**Table 5** Comparison of solar charging electric vehicle with petrol vehicle and electric vehicle

Petrol versus solar charging electric vehicle	Solar charging electric vehicle versus electric vehicle	Environment-friendliness
Fixed number of non-renewable resources and will end in coming years	Not possible to charging on shadow or any covered halt	No pollution and CO <sub>2</sub> emit
Too costly	For charging using power supply required rated power supply	Better use of sun rays
Not safe/dangerous	On moving constant charging not possible due to uneven sunlight rays	Will be helpful to reduce global warming
Environment disaster	If charging on EVs charging stations is time taking	The vehicle is manufactured of eco-friendly material
Very high running cost and maintenance are expensive	Should not be best for long-distance travel	
	Maintenance cost is less but once after battery dies replacement of battery is expensive	
	It is environment-friendly but not be best for every place	

**Table 6** Comparison of running cost

Parameters	Petrol vehicle	Electric vehicle	Solar vehicle
Fuel	Petrol	Electricity	Solar electricity
Rate of fuel	INR 98/L	INR 28/Full charge	Free
Vehicle mileage	12–20 km/L	100–200 km/charge	50–200 km/charge
Running cost per km	INR 4–7	INR 0.2	Free
Running cost per year (18,000 km)	INR 72,000–126,000	INR 3600	Free
Yearly saving	–	INR 68,400–122,400	INR 72,000–126,000

external source, utilization of a few electronic gadgets like solar board heat sensors, advanced cooling framework and so forth have reinforced the vehicle as a high-level SCEV ready for worldwide market. Thus, the authors have designed a photovoltaic integrated electric vehicle which has numerous advantages when compared with conventional EV with the requirement of separate charging station.

## References

1. Spina MA, de la Vega RJ, Rossi SR (2012) Source issues on the design of a solar vehicle based on hybrid energy system. *Int J Energy Eng* 2:15–21
2. Mehta G, Yadav VK (2018) Impact of renewable distributed generators in competitive electricity markets considering economic factors. In: *IEEE international conference on power electronics, drives and energy systems*, Chennai
3. Saxena N, Hussain I, Singh B, Vyas AL (2018) Implementation of a grid-integrated PV-battery system for residential and electrical vehicle applications. *IEEE Trans Ind Electron* 65(8):6592–6601
4. Gobhinath S, Boobalan S, Ashwin R, Meshach J, Rajkumar K (2020) A practical approach in design and fabrication of solar-powered four-wheeled electric vehicle. In: *Innovations in electrical and electronics engineering. Lecture notes in electrical engineering*, vol 626. Springer, Singapore
5. Chellaiah C, Thangamani K, Subin PG, Rathinakumar P, Muthukrishnan P (2013) Design of a fuel free electric vehicle. In: *Mobile communication and power engineering. Communications in computer and information science*, vol 296. Springer, Berlin
6. Surya S, Williamson SS (2022) Energy storage devices and front-end converter topologies for electric vehicle applications. In: *E-Mobility. EAI/Springer innovations in communication and computing*. Springer, Berlin
7. Ben Said-Romdhane M, Skander-Mustapha S (2021) A review on vehicle-integrated photovoltaic panels. *Advanced technologies for solar photovoltaics energy systems*. In: *Green energy and technology*. Springer, Berlin
8. Duan et al (2018) A solar power-assisted battery balancing system for electric vehicles. *IEEE Trans Transp Electrification* 4(2):432–443
9. Habib S, Khan MM, Abbas F, Sang L, Shahid MU, Tang H (2018) A comprehensive study of implemented international standards, technical challenges, impacts and prospects for electric vehicles. *IEEE Access* 6:13866–13890
10. Khalid MR, Alam MS, Sarwar A, Asghar MJ (2019) A comprehensive review on electric vehicles charging infrastructures and their impacts on power quality of the utility grid. *E-Transportation* 1:100006
11. Savio DA, Juliet VA, Chokkalingam B, Padmanaban S, Holm-Nielsen JB, Blaabjerg F (2019) Photovoltaic integrated hybrid microgrid structured electric vehicle charging station and its energy management approach. *Energies* 12(1):168
12. Tazay A, Miao Z (2018) Control of a three-phase hybrid converter for a PV charging station. *IEEE Trans Energy Convers* 33(3):1002–1014
13. Ramadhani UH, Shepero M, Munkhammar J, Widén J, Etherden N (2020) Review of probabilistic load flow approaches for power distribution systems with photovoltaic generation and electric vehicle charging. *Int J Electr Power Energy Syst* 120:106003
14. Abdelsalam MA, Obaid W, Ahmad FF, Hamid AK, Ghenai C (2020) Modeling and simulation of a solar powered golf cart charging station in Sharjah. In: *Advances in science and engineering technology international conferences*
15. Tiano FA, Rizzo G, Marino M, Monetti A (2020) Evaluation of the potential of solar photovoltaic panels installed on vehicle body including temperature effect on efficiency. *E-Transportation* 5:100067
16. Mehta G, Singh M, Dubey S, Uzair, Mishra Y (2021) Design of auto-braking system for accident prevention and accident detection system using IoT. In: *Smart sensors for industrial internet of things*. Springer, Berlin
17. Mi C, Masrur A (2018) *Hybrid electric vehicles principles and applications*, 2nd edn. Thomas Kurfess
18. Taha Z, Md Sah J, Passarella R, Abd Rahim N (2014) A review on energy management system of solar car

19. Dwivedi M, Mehta G, Iqbal A, Shekhar H (2017) Performance enhancement of solar PV system under partial shaded condition using PSO. In: International conference on computing, communication and networking technologies
20. Ahmad MW et al (eds) (2022) Intelligent data analytics for power and energy systems. Springer, Singapore, p XXII, 641. ISBN: 978-981-16-6081-8. <https://doi.org/10.1007/978-981-16-6081-8>
21. Tomar A et al (eds) (2022) Proceedings of 3rd international conference on machine learning, advances in computing, renewable energy and communication: MARC 2021, vol 915, p XV, 781. ISBN: 978-981-19-2830-7. Springer Nature. <https://doi.org/10.1007/978-981-19-2828-4>
22. Bhavnani SH (1994) Design and construction of a solar-electric vehicle. ASME J Sol Energy Eng 116(1):28–34
23. Giannouli M, Yianoulis P (2012) Study on the incorporation of photovoltaic systems as an auxiliary power source for hybrid and electric vehicles. Sol Energy 86:441–451
24. Araki K, Ota Y, Yamaguchi M (2020) Measurement and modeling of 3-D solar irradiance for vehicle-integrated photovoltaic. Appl Sci 2020(10):872

# Modelling and Analysis of a Permanent Magnet DC Motor Fed Electric Vehicle Drive System



K. Subbaramaiah, Ravisankar Kampara, Majji Satish, Kantubhukta Dinesh, and Karthik Tamvada

**Abstract** Modern transportation has evolved from internal combustion engine to electric drive system due to the reasons that rise in demand for fossil fuels, environmental pollution and government stringent regulations. The electric vehicle technology requires an efficient system which makes it more suitable and reliable function. Thus, design and analysis of the electric vehicle drive system are a vital part to further enhance the e-vehicle technology. In this article, a combined permanent magnet DC motor and electricity generator system are proposed to drive the vehicle and produce the electrical energy for the vehicle utilities. Permanent magnet DC motor finds its advantage of simple construction and control, maintenance free and high-power density. Permanent magnet (PM) motor drives have been successfully developed to fulfil the special requirements for electric vehicles such as high-power density, high efficiency, high starting torque and high cruising speed. The components selection criteria along with the system description are given in detail. A permanent magnet DC motor (PMDC) fed electric vehicle drive system is modelled using the MATLAB/Simulink tool, and the simulated results of its static and dynamic performance have been analysed under various conditions.

**Keywords** DC motor · Electric drive · Electric vehicle · Fossil fuels · Permanent magnet

## 1 Introduction

Global warming, pollution of environment and shortage of fossil fuels are the factors which create the distress in the modern society. The above-said factors are interrelated so as one factor which could affect the others [1–3]. When the high usages of fossil fuel results in CO<sub>2</sub> emission, polluting the environment thus increases

---

K. Subbaramaiah · R. Kampara · M. Satish (✉) · K. Dinesh · K. Tamvada  
Department of Electrical and Electronics Engineering, Lendi Institute of Engineering and Technology, Jonnada, Vizianagaram, Andhra Pradesh, India  
e-mail: [majji.satish486@gmail.com](mailto:majji.satish486@gmail.com)



the global warming. Transportation and electricity generation are the two processes which consume more fossil fuels [4]. Nowadays, the electricity generation through the burning of fossil fuels has been drastically reduced through the alternative way of resources such as renewable energy sources-based and atomic power [5, 6]. However, the transportation still uses the fossil fuel since the vehicles use internal combustion engine (ICE). Nowadays, the major portion of fossil fuel consumed by the transportation is changeover from internal combustion engine-based technology to electric vehicle technology. This technology transfer helps in the reduction of fossil fuel consumption and thereby drastically reduces the global warming and environmental pollution. Also, threatening of shortage of fossil fuel also can be addressed in a smarter way. Apart from the countries of entire world committed towards the replacing the existing ICE-based vehicles to e-vehicles, the e-vehicle technology becomes more popular [7, 8].

Electric vehicle uses different components like battery, motor, controller and other utilities. The selection of these components is based on the requirements such as speed, carrying power, torque and charging time. Many different kinds of motors have been adopted for the e-vehicle. Direct current motor, induction motor, switched reluctance motor (SRM) and permanent magnet (PM) motor are the different variations in that [9]. Here a PMDC motor is selected suitable to drive system due to its simplicity and controlling counterpart [10].

The energy storage part is the vital one in e-vehicle drive system since it supplies the required power to the drive, i.e. motor. Batteries are commonly classified as non-rechargeable batteries, i.e. primary batteries and rechargeable batteries, i.e. secondary batteries [11]. The non-rechargeable batteries kind of batteries are not suitable for e-vehicle, and hence, the rechargeable batteries are being utilized. Nickel and cadmium (Ni-Cd) batteries, lead-acid (LA) batteries, nickel-metal hydride batteries (NiMH), lithium ion (Li-ion) and lithium ion polymer (LIPO) rechargeable batteries are the types of rechargeable batteries. Amongst which lithium ion polymer batteries are performing well and have high-power density; however, it is costlier than any other batteries [12]. Whereas the performance of lithium ion batteries is more than lead-acid (LA) batteries, Ni-Cd, NiMH batteries and near to the lithium ion polymer batteries, and hence, it is widely adopted as the energy storage unit for the electric vehicle [12].

### **Novelty of the Work:**

- Permanent magnet (PM) motor drives have been successfully developed to fulfil the special requirements for electric vehicles such as high-power density, high efficiency, high starting torque and high cruising speed.
- The permanent magnets are permanently magnetized. So the rotor runs synchronously to the switching AC current. The slippage necessary in induction motors is eliminated, which improves mechanical and heat efficiency of the motor in the vehicle.

This article proposes the combined permanent magnet DC motor and electricity generator system along with the lithium ion energy storage unit. A permanent magnet

DC motor fed electric vehicle drive system is modelled using the MATLAB/Simulink tool, and simulation results for the static and dynamic conditions have been reported.

Further, the article is organized with different sections as, Sect. 2 describes the system components, Sect. 3 explains the modelling of a PMDC motor fed electric vehicle system, simulation results of a permanent magnet DC motor fed electric vehicle drive system is given in detail; Sects. 4 and 5 reveal the conclusion.

## 2 Proposed Approach

Figure 1 shows the functional block diagram of a PMDC motor fed electric vehicle system. The proposed electric vehicle drive system comprises of the components such as permanent magnet DC motor, alternator, wheel hub and battery. Permanent magnet motor has many types such as permanent magnet direct current motor, permanent magnet synchronous motor, permanent magnet brushless DC motor and permanent magnet hybrid excitation motor. Amongst which the permanent magnet direct current motor is a simple and efficient mechanism. Here, permanent magnet DC motor is coupled with both alternator and wheel hub. This motor translates power taken from battery into a mechanical output power which will drive the wheel. The energy generated from the alternator is given to the rectifier unit as input. This rectifier converts 3 $\phi$  AC supply into DC output and gives to the battery to charge and other utilities like front lamp and charging port.

The description of the different components used in the system is specified in Table 1.

The rectifier output voltage should be 48 V for the charging of battery so that peak voltage generated from the generator should be more than 48 V. Hence, the alternator rms output voltage set be 40 V so as the maximum value of the generated voltage is obtained as 56 V which is more than battery voltage. 20 Ah battery has been selected for the electric drive system. It takes the rated current of 2.5 A, and

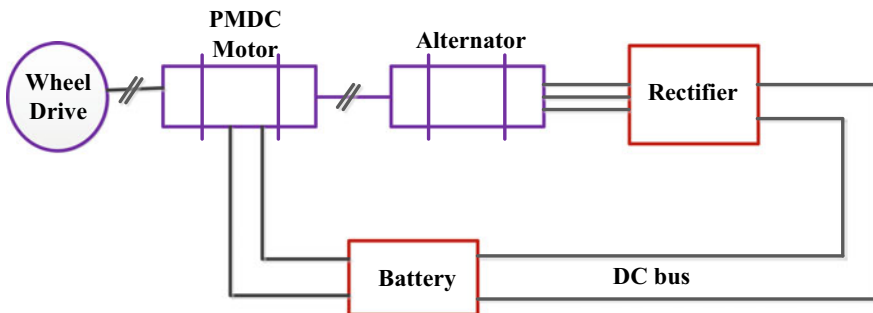


Fig. 1 Functional block diagram of a permanent magnet DC motor fed electric vehicle drive system

**Table 1** Specification of components

S. No.	Components name	Specification
1	PMDC motor	250 W 48 V 5.2 A 400 RPM
2	Alternator	3 $\phi$ output 40 V
3	Battery	Lithium ion 48 V 20 Ah
4	Loads	Lamps and other utilities

complete charging time will be 8 h. A PMDC motor offers the rated power of 250 W at 48 V, and the rated speed is 400 rpm.

### 3 Modelling of a Permanent Magnet DC Motor Fed Electric Vehicle Drive System

The PMDC motor fed electric vehicle drive system has been modelled through MATLAB/Simulink platform and the same is shown in Fig. 2.

As shown in Fig. 2, torque and angular speed of PMDC motor are fed into the generator as inputs. A 3 $\phi$  generator is incorporated with the control circuit of field current regulation to have a control on its output voltage. The battery is connected across the output of the rectifier unit. The appropriate measuring units are connected to measure the various parameters from the electric vehicle drive system. The closed-loop control system is essential in e-vehicle to keep constant the DC bus voltage

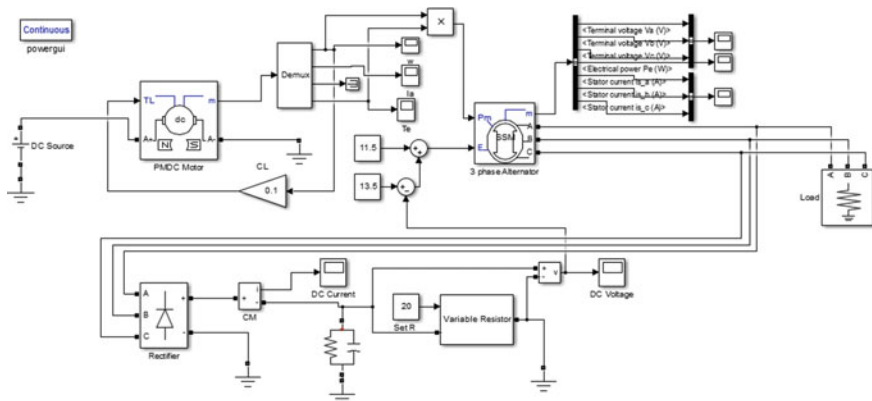


**Fig. 2** Modelling of a permanent magnet DC motor fed electric vehicle drive system

value. Thereby it doesn't affect the illumination of level of the front light of the vehicle when other electrical loads are turned ON. The closed-loop controller has been designed and implemented in the electric vehicle drive system as shown in Fig. 2. The closed-loop control continuously monitors the DC bus voltage, takes as feedback, and checks with the minimum and maximum prefixed values of the voltage. Based on this, the field current of the three-phase synchronous generator is adjusted so as to maintain the DC bus voltage as constant. The constant value of this DC bus voltage is maintained even during different speeds of the drive and other vehicle's electrical loading conditions. The modelling of PMDC motor is explained with the help of the following equations (Eqs. 1–5).

The angular speed of a permanent magnet DC motor is expressed as,

$$\omega_{\text{rad}} = n \frac{2\pi}{60} \tag{1}$$

The speed of the motor is directly proportional to the supply voltage as given in Eq. 2,

$$\omega_m = \frac{V_a - R_a I_a}{k_a \Phi} \text{ rad/s,} \tag{2}$$

where  $V_a$  is the supply voltage,  $R_a$  is the armature resistance,  $I_a$  is the armature current,  $\Phi$  is the permanent magnet flux.

The relationship amongst the speed, torque and the conversion factor is given in below expression,

$$P_{\text{mech}} = Mn \frac{2\pi}{60}, \tag{3}$$

where  $n$  is the speed in rotation per minute and  $M$  is the torque in N m.

Twice the reluctances are presented in the motor, one flows through the laminated iron part ( $R_i$ ) and the another one is due to the flux which flows in the air between two laminations ( $R_L$ ).

$$R_i = \frac{L}{\mu_r \mu_o c W} \tag{4}$$

$$R_L = \frac{L}{\mu_o (1 - c) W} \tag{5}$$

where  $L$  and  $W$  are the length and width of the path and  $c$  is the fraction of the path filled with iron.

## 4 Simulation Results of a Permanent Magnet DC Motor Fed Electric Vehicle Drive System

The model developed in the software environment is simulated for various conditions and the same has been analysed in various aspects in this section. The different cases and its results are as follows:

**Case 1:** In this case, the rated supply voltage is provided to the PMDC motor and the battery is charging with its rated capacity.

From Fig. 3, it is understand that, since the rated supply voltage is provided to the PMDC motor it offers the constant speed of 450 rpm. The generator rectifier output voltage and current are 40 V and 1.76 A, respectively. The rectifier output voltage is maintained as 48 V, and the current is 2.5 A to charge the battery with rated capacity.

**Case 2:** Figure 4 shows the results corresponding to case 2. In this case, the two different supply voltages are provided to the PMDC motor, i.e. 48 V and 45 V, and the battery is charging with its rated capacity.

As shown in Fig. 4, the dynamic condition during the supply voltage change from 48 to 45 V and the corresponding speed varies from 420 to 380 rpm (refer Fig. 4b), respectively. Since the motor is directly coupled with the alternator, the alternator output voltage varies from 40 to 35 V. However, there is no change in rectifier output current, DC bus voltage (battery voltage) and charging current. The DC bus voltage never changes due to the closed-loop control system. If it changes, then it will get damage the electronic loads which are connected with the electric vehicle. The rectifier output current, battery voltage and charging current are 1.76 A, 48 V and 2.5 A, respectively (refer Fig. 4d–f).

**Case 3:** In this case, the rated supply voltage is given to the drive. However, the additional load is turned ON along with the charging of battery operation.

From Fig. 5, it is understand that during sudden increase of load, the current taken by the DC bus is increased with step change. The output current from the generator changes from 1.76 to 2.12 A (refer Fig. 5c). Similarly, the DC current consumption increases from 2.5 to 3 A as shown in Fig. 5d. At all the three above cases even during speed and load variations, the DC bus voltage is maintained as 48 V and this will ensure the battery performance.

## 5 Conclusion

A combined permanent magnet DC motor and electricity generator system are proposed in this article. A 250 W, 48 V, 400 rpm PMDC motor is selected, and this PMDC motor is used to drive the vehicle. The 3 $\phi$  alternator produces the electricity that will be being utilized for battery charging and other vehicle utilities, and its rated output voltage is 40 V. A lithium ion battery has been selected with the rated voltage of 48 V with the rating of 20 Ah. A permanent magnet DC motor fed

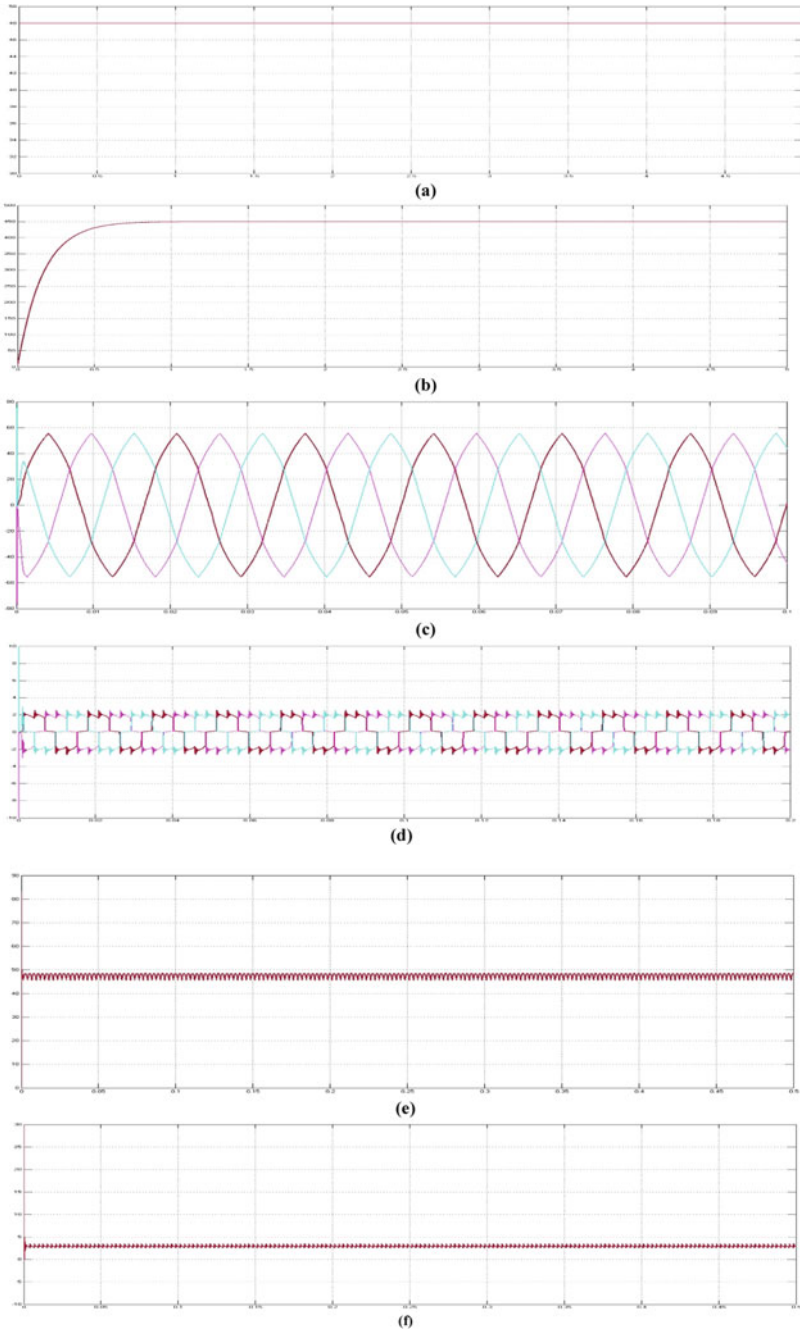


**Fig. 3 Case 1:** At fixed speed condition, **a** supply voltage, **b** speed of a motor, **c** alternator voltage, **d** alternator current, **e** battery voltage, **f** battery current

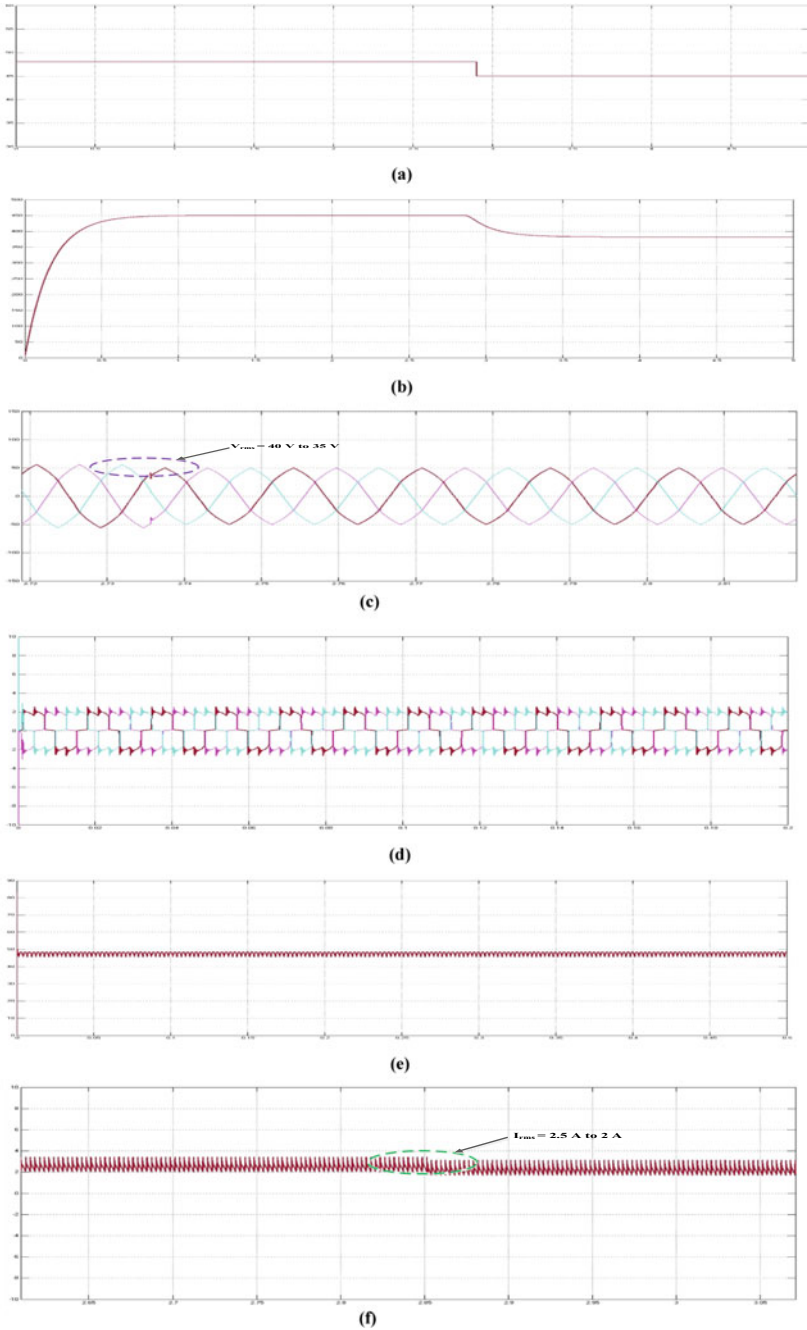


**Fig. 4 Case 2:** At two different speed conditions, **a** supply voltage, **b** speed of motor, **c** alternator voltage, **d** alternator current, **e** battery voltage, **f** battery current

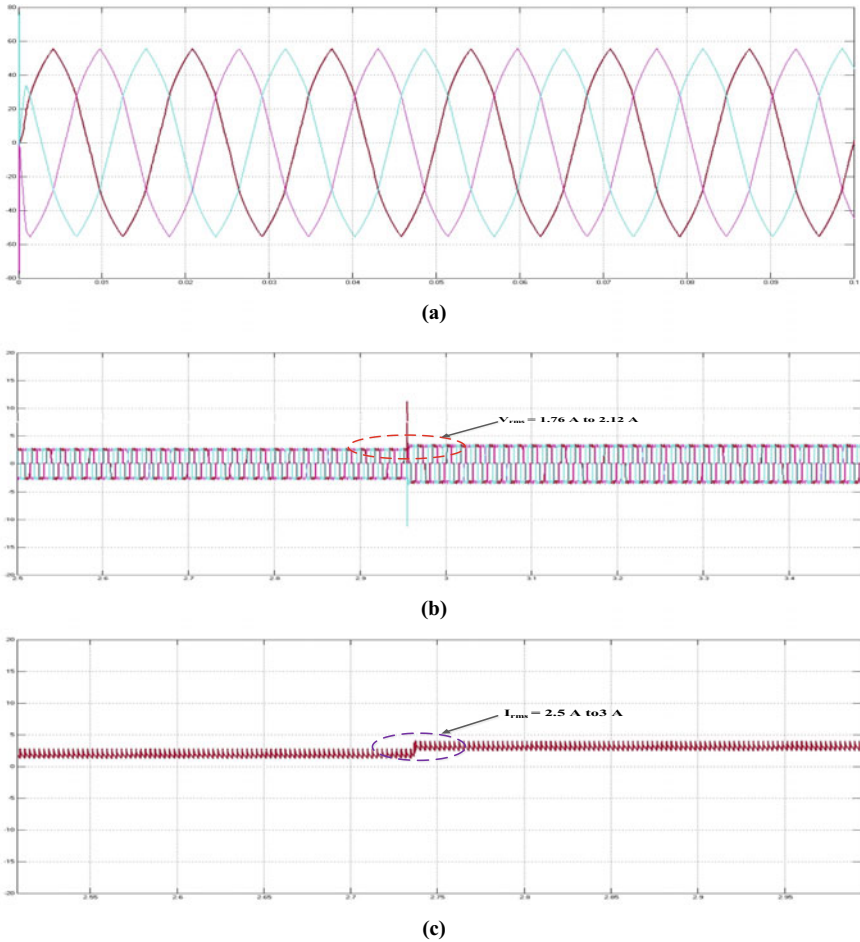


**Fig. 5 Case 3:** During the addition of load with the battery charging, **a** alternator voltage, **b** alternator current, **c** battery voltage, **d** battery current

electric vehicle drive system is modelled using the MATLAB/Simulink tool, and the simulated results under three different conditions, i.e. rated supply voltage, changing supply voltage and sudden change in load, are presented. Further, the performance of the proposed system can be improved by incorporating various latest battery management techniques.



## References

1. Rana LB, Shrestha A, Phuyal S, Mali B, Lakhe O, Maskey RK (2020) Design and performance evaluation of series hybrid electric vehicle using backward model. *J Eng* 14:1–10
2. Kommula BN, Kota VR (2020) Direct instantaneous torque control of brushless DC motor using firefly algorithm based fractional order PID controller. *J King Saud Univ Eng Sci* 32:133–140
3. Suarez C, Martinez W (2019) Fast and ultra-fast charging for battery electric vehicles—a review. In: *Proceedings of the 2019 IEEE energy conversion congress and exposition (ECCE)*, Baltimore, MD, USA, 29 Sept–3 Oct 2019, pp 569–575
4. Lee W, Li S, Han D, Sarlioglu B, Minav TA, Pietola M (2018) A review of integrated motor drive and wide-band gap power electronics for high-performance electro hydrostatic actuators. *IEEE Trans Transp Electrif* 3(4):684–693
5. Sun X, Diao K, Yang Z, Lei G, Guo Y, Zhu J (2019) Direct torque control based on a fast modeling method for a segmented-rotor switched reluctance motor in HEV application. *IEEE J Emerg Sel Top Power Electron* 9(1):232–241
6. Cai W, Gong J, Zhang Z et al (2020) Chapter 7: technology roadmap of electric drive. In: *Technology roadmap of energy saving and new energy vehicle*. China Machine Press. ISBN 978-7-1111-67009-4
7. Kaban B, Vinot E, Yuan C, Trigui R, Dumand C, Hajji TE (2019) Efficiency improvement of a series-parallel hybrid electric powertrain by topology modification. *IEEE Trans Veh Technol* 12(68):11523–11531
8. Li J, Jin X, Xiong R (2017) Multi-objective optimization study of energy management strategy and economic analysis for a range-extended electric bus. *Appl Energy* 194:798–807
9. Kim K, Kim K, Kim HJ, Lee J (2009) Demagnetization analysis of permanent magnets according to rotor types of interior permanent magnet synchronous motor. *IEEE Trans Magn* 45(6):2799–2802. <https://doi.org/10.1109/TMAG.2009.2018661>
10. Rubaai, Yalamanchili R (1992) Dynamic study of an electronically brushless DC machine via computer simulation. *IEEE Trans Energy Convers* 7:132–138
11. Tomar A et al (eds) (2022) *Proceedings of 3rd international conference on machine learning, advances in computing, renewable energy and communication: MARC 2021*, vol 915, p XV, 781. ISBN: 978-981-19-2830-7. Springer Nature. <https://doi.org/10.1007/978-981-19-2828-4>
12. Ahmad MW et al (eds) (2022) *Intelligent data analytics for power and energy systems*. Springer, Singapore, p XXII, 641. ISBN: 978-981-16-6081-8. <https://doi.org/10.1007/978-981-16-6081-8>

# An Overview of Electric and Hybrid Vehicle Technology



V. S. Vishwanath Nagarajan, Vinay Kumar Jadoun , N. S. Jayalakshmi ,  
and Anubhav Kumar Pandey 

**Abstract** The aim of the study is to promote deeper understandings in the Electric and Hybrid Vehicle Technology by reviewing the current literature. Various types of EVs along with their basic principle and functioning are discussed based on their unique technology. The Hybrid Electric Vehicles which are emerging as the alternative to ICE Vehicles are discussed with their types. The facets for different Drivetrains within the research sector are extensive. This article also outlines the vital knowledge on various architectures of Drivetrain for meeting the desired requirement in the application and highlights the expertise of Drivetrain. A quick glance of main components required for functioning of EV such as Electric motors, energy storage devices, power electronics, battery management system is also summed up. It also covers an important part of EV, which is Energy management systems, which manages the available energy optimally for efficient use. Further, the overview of powertrain topology is also included for better understandings on the functioning of various systems in Electric Vehicles. Unlike an ICE Vehicle, there are new systems in Electric Vehicles, which were discussed with their functionality in the perspective of EV application at the end of the study.

**Keywords** Hybrid Vehicles · Electric Vehicles · Drivetrain · Drivetrain architecture · Series · Parallel Drivetrain · Mild hybrid · Micro hybrid · Full hybrid · PHEV · BEV · EMS · Topology

---

V. S. Vishwanath Nagarajan (✉) · V. K. Jadoun · N. S. Jayalakshmi · A. K. Pandey  
Department of Electrical and Electronics Engineering, Manipal Institute of Technology, Manipal  
Academy of Higher Education, Manipal, Karnataka 576104, India  
e-mail: [vishwanathnagarajan199@gmail.com](mailto:vishwanathnagarajan199@gmail.com)

V. K. Jadoun  
e-mail: [vinay.jadoun@manipal.edu](mailto:vinay.jadoun@manipal.edu)

N. S. Jayalakshmi  
e-mail: [jayalakshmi.ns@manipal.edu](mailto:jayalakshmi.ns@manipal.edu)

A. K. Pandey  
e-mail: [anubhav.pandey@learner.manipal.edu](mailto:anubhav.pandey@learner.manipal.edu)

# 1 Introduction

Since the world is moving into the next era and all sectors are booming with latest innovations, the invention of Electric Vehicle (EV) and Hybrid Electric Vehicles (HEVs) is causing revolution in the automobile sector [1–5]. The increased amount of pollution from fossil fuel vehicle causing global warming due to greenhouse effect and the long-term result of shortage of resources for fossil fuel has constrained us to take up the adoption of Electric Vehicle in market. The EVs are found to be a best alternative as they are less pollutant and efficient in operations [6–9]. This efficiency is achieved since there are very fewer moving parts and the replacement of mechanical parts with electrical/electronic parts which are equipped and controlled by a Controller/Program. The Drivetrain of an EV/HEV is an art of engineering since it does not involve any transmission box or a complex mechanism as present in an Internal Combustion Engine (ICE) vehicle. The HEVs are found similar to the ICE vehicle but are equipped with Electric motor and additional Energy management system. The Regenerative braking is an important part in the HEV and EV which assist the vehicle in battery charging by effectively using the lost energy during braking. The Battery Electric Vehicle, Plug-In Hybrid Electric Vehicles are the types of Electric Vehicles whose functionality and operations vary on each type [10–12]. The hybrids are basically of three types a Mild type, Micro type, and Full hybrid type whose efficiency varies on each type as they are designed with limited features only. The Energy management system is an essential part in an EV which plays a vital role of managing energy to have an efficient operation in the vehicle. The powertrain topology is the overall view of a Drivetrain of a vehicle with the systems and parts inbuilt in it. The Planetary Gearset used in HEVs acts as a transmission path between engine and the differential. The Electronic Differential also called as E-Diff is a differential replacing the traditional mechanical differential which is controlled electronically [13–17]. The architecture of different Hybrid Vehicles is described in this review along with their salient feature.

The contributions of this paper are as follows:

- A review of Electric Vehicle, Hybrid Vehicles, Energy management systems, Powertrain Topology, different Hybrid Vehicle types based on Hybridization.
- An overview of Plug-In HEVs, Battery Electric Vehicle, and Hybrid Electric Vehicle and a glance on component of Electric Vehicle.
- An overview of Drivetrain architectures such as Parallel, Series, and Series–Parallel along with the basic understanding of Planetary.
- Various new systems used in Electric Vehicles such as Gearset, Inverter, and Electronic Differential used in Hybrid Vehicles.

Section 1 includes the Introduction of this study with the purpose the study and some basic information required for understanding this paper. Section 2 includes the proposed approach which describes the various areas covered in this section along with their subsection which includes their types. Section 3 describes the Discussion/Descriptions part of the study in which all topics covered in this study are discussed

briefly. Section 4 describes the powertrain topology of an Electric Vehicle for understanding their topology. Section 5 describes in detail about the various components of Electric Vehicle. The various architectures of Hybrid and Electric Vehicles are discussed in Sect 6. And few of the new systems used in Electric and Hybrid Vehicles are discussed in detail in Sect. 7. Sections 8, 9, and 10 are followed by Summary, Future Scope, and Conclusion, respectively. All references along with the details were included in the section eleven.

## 2 Proposed Approach

Figure 1 shows the flowchart representation of various topics and areas covered in this study. On the first part, Plug-In Hybrid Vehicles, Hybrid Vehicles, and Battery Electric Vehicles are the types of EVs covered while the Mild Hybrid, Micro Hybrid, and Full Hybrid are covered under HEVs. While the Components of EV's part include an Electric motor, Energy management system, Energy storage devices, power electronics, battery management system. In-between, the powertrain topology of EVs is also discussed. On the other part, the study on the Drivetrain technology covers the various Drivetrain architectures popularly used in EVs and HEVs which are Parallel type, Series type and the Series-Parallel type, while on technology path, some important systems of Electric Vehicles required for the better understanding on functioning of EV concepts such as Torque converter, Planetary Gearset, E-Differential, and Invertor are also covered in this study.

## 3 Descriptions/Discussion

### 3.1 Electric Vehicle (EV)

In an EV, the main source of power for propulsion is given by Electric motor. The power required to drive the motor is primarily supplied by the battery source which is charged directly or through an alternative source based on their types. Even though the motor efficiency is found to be more than 80%, the limited storage capacity of battery restricts its range. Unlike an Internal Combustion Engine (ICE) vehicle, the EV can also produce high torque at very low speeds due to the presence of powerful Electric motors. The battery capacity, motor size, and Powertrain are the main factors which influence the performance and efficiency of the vehicle. The three main subsystems upon which the Electric Vehicle is built are as follows:

- (1) Electric Propulsion subsystem composing of Controller, Power Converter, Electric motor, differential.
- (2) Energy management subsystem composing of battery, Energy management system, charging system.

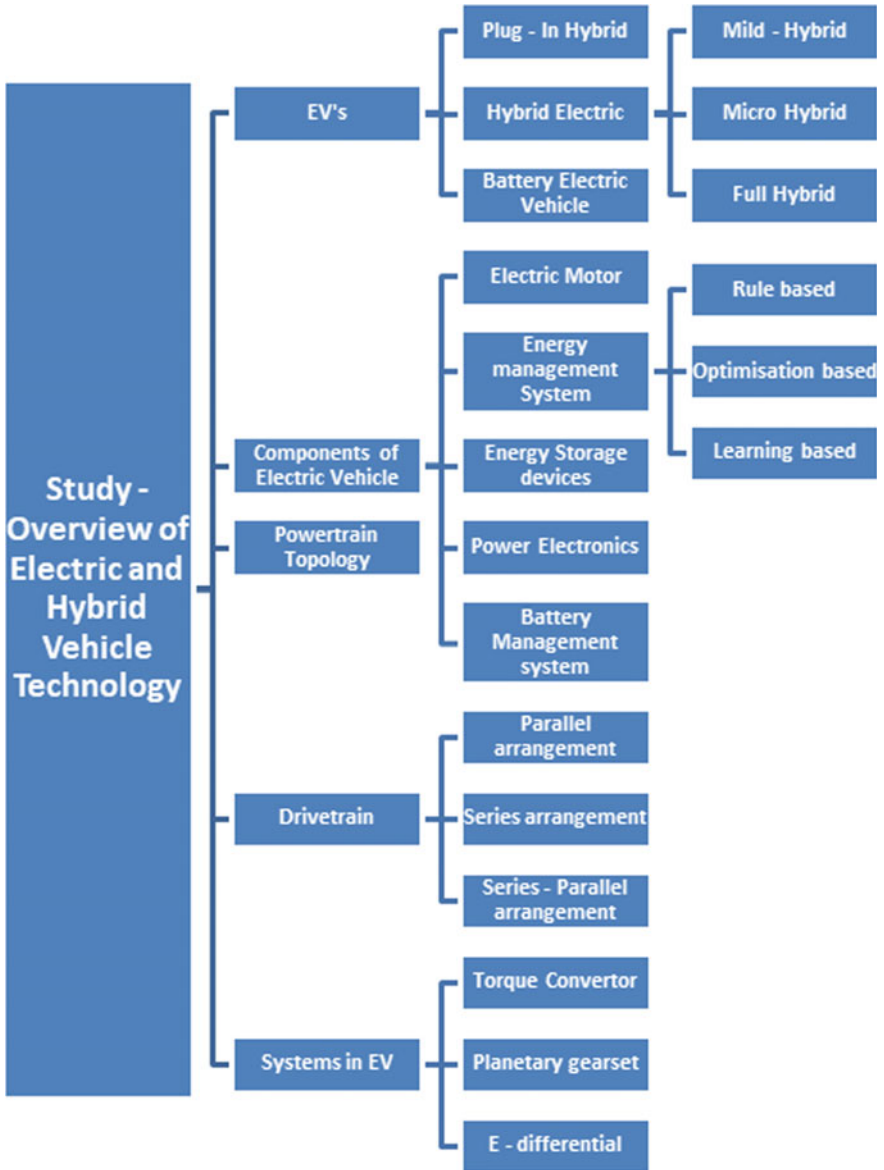


Fig. 1 Flowchart representation of paper [14, 15]

- (3) Auxiliary subsystem composing of auxiliary power supply, power steering unit, temperature control unit.

The Battery Electric Vehicle (BEV), Plug-In Hybrid Electric Vehicles (PHEVs), and Hybrid Electric Vehicles (HEVs) are the types of Electric Vehicle which are explained in continuation.

### **3.1.1 Battery Electric Vehicle (BEV)**

In a BEV type, the battery is the only source of power for driving the Electric motor. The battery can be charged through charging station/Grid and can be supported by a Regenerative braking. The propulsion of wheels can be done only through power generated by Electric motors.

### **3.1.2 Plug-in Hybrid Electric Vehicle (PHEV)**

A PHEV type is an advanced type of vehicles similar to Hybrid Vehicles on which the battery can be charged directly through Grid or Power Stations. All other operations are similar to that of a HEV. Usually, the PHEV gets a bigger sized battery than that of a HEV since they can be recharged through an external source.

### **3.1.3 Hybrid Electric Vehicles (HEVs)**

In a HEV layout, the propulsion of wheels can be either through ICE or EM or through both. The source for battery charging is through Engine power and supported by Regenerative braking. The ICE power can be used either to drive the wheels directly nor to charge the battery alone based on the Drivetrain configurations. The main difference between an EV and HEV is that in a HEV, there are two or more sources of energy for propulsion say Internal Combustion Engine (ICE), Electric motor (EM), Fuel Cell (FC), while in an EV, there is only source of propulsion, i.e., Electric motor. Here, the wheels can be driven through ICE or EM or either by both sources at the same time. HEVs are better in efficiency and performance since they have two sources of power. The main challenge existing in the HEVs is the management of power since they can be switched between their available sources or can be driven by both sources at the same time. Generally, the HEVs are found to be costly. Based on hybridization level and functionality, there are three types of HEVs which are as follows.

## **3.2 Hybrid Electric Vehicles**

### **3.2.1 Micro Hybrid**

These are the entry-level hybrid cars which employ motor of small power ranging from 3 to 5 kW. They do not interfere on any other operation and are just like an add-on in an ICE vehicle. Their main work is to save energy by switching on and off the engine based on the vehicle running condition. For instance, in case of a city driving situation during signal stoppage. They are more beneficial for city driving vehicles like Mofussil buses. They also assist on Regenerative braking and their hybridization factor is 5–10%.

### **3.2.2 Mild Hybrid**

These are mid-level Hybrid Vehicles where the motor can assist to provide added torque to engine during operation in addition in supporting propulsion, regenerative braking. Since they assist the vehicle on multiple operations, they are equipped with motor ranging from 7 to 15 kW's. The hybridization factor for this type is 10–30%.

### **3.2.3 Full Hybrid**

This is a complete Hybrid Vehicle which is capable of running on Electric power alone. Here, in order to meet the needs, powerful motors of size 30–50 kW's are used. Hybridization factor is 30–50%. Amid, the Regenerative braking in this model is highly efficient than others in capturing the power without much losses.

## **4 Powertrain Topology**

The Hybrid Vehicle generally uses an ICE and EM to generate power required to drive a vehicle. The tractive power required for wheel is given by the EM to drive the vehicle in all Drivetrains and in some instance given by the ICE based on the mode of operation, in cases such as Parallel Drivetrain and Series–Parallel Hybrid Vehicle. Figure 2 represents the overall topology of a powertrain used in vehicles. Generally, the inputs from driver end are sensed by the sensors present there and these inputs have been captured by both Controller as well as Energy management system. The EMS manages the energy efficiently and directs it to system during requirement. The Controller is the main part which is integrated with all other units to receive inputs. The Energy management system controlled by a Controller plays a vital role in managing the Regenerative braking. The Kinetic Energy generated during braking is effectively captured through Regenerative braking and then converted into Electric

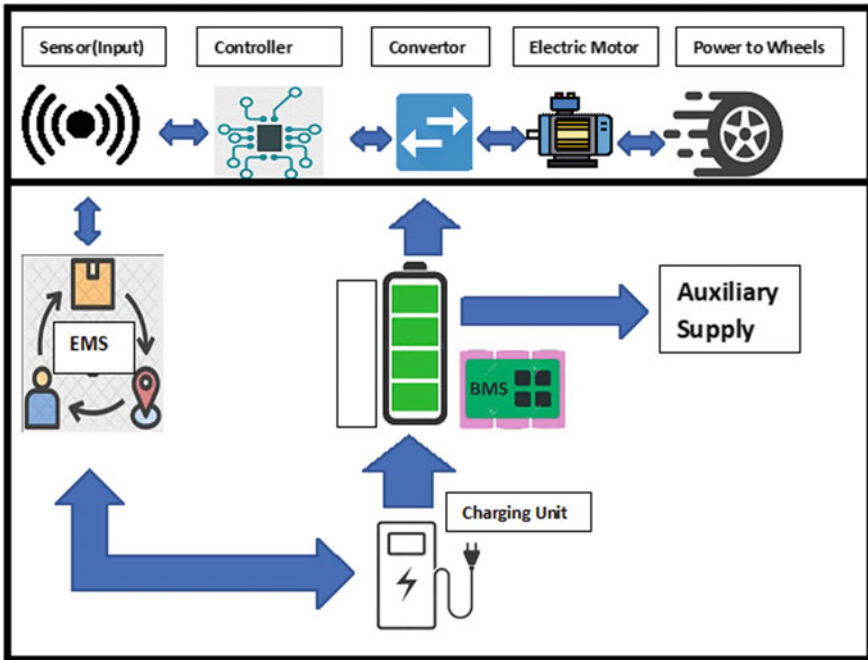


Fig. 2 Powertrain topology

power by the generator which is then stored in battery. A power electronic converter is provided in between a battery and motor to step up. An Onboard charging unit is provided on vehicle which can be used for charging the battery. The power required to auxiliary units is provided by the auxiliary supply since each auxiliary system functions on different voltage levels. Overall, the EMS is integrated with both inputs from driver end as well as input from vehicle end with updated information based on which it works and manages efficiently. The power received from battery is used to drive the vehicle through the Electric motor.

### 5 Component of Electric Powertrain

The main components of Electric Powertrain are Electric motor, Energy storage devices, Power Electronics, battery management system, and the Energy management system which are discussed in the following subsections.



## 5.1 *Electric Motor/Generator*

An Electric motor is an important part of an EV which causes propulsion of a vehicle by consuming Electric power from a storage device, while a generator plays a vital role of power generation by capturing the energy generated during braking by converting and sending it to storage devices. In simple terms, motor is a power-consuming device which consumes Electrical energy, while a generator is a power generation device which produces Electrical energy. In some configuration, a single EM can act as a motor/generator based on the requirement.

The two classifications of motor are AC motor and DC motor which works based on their name as specified; the DC motor functions on Direct Current, while an AC motor functions on Alternating Current. For a long run, the AC motors are found to be cheaper, while DC motor is bit costlier. The DC motor is very effective and compact in size, while an AC motor has the ability to function as both motor/generator and also specializes effectively on speed control. AC motor is very effective in speed and torque control.

There are different motor types existing in the market, among which the popular motors used on EVs are divided below

- Brushed DC motor—These are capable of producing high torque at low speed and was popular on entry-level EV like two wheelers. But, the high heat generation reduces their efficiency.
- Permanent Magnet Brushless DC motor—These are brushless DC motor which has permanent magnet to achieve high efficiency and power density. But, they have limited constant power speed range making it not suitable for mass adoption.
- Permanent Magnet Synchronous Motor (PMSM)—These are able to achieve high efficiency during a predefined cycle. They are operatable at different speeds without gear systems. They are even able to operate in wheel application and can be used in four-wheel drive application also.
- Induction motor (IM)—They are popular type which are able to achieve high efficiency even under high-speed cruise conditions. They are a cheaper one.
- Switch Reluctance Motor (SRM)—They are simpler, fault tolerant and has good efficiency. They have long constant power range and high-power density. But are found large, heavy and complex as they require a control system for operation.

## 5.2 *Energy Storage Devices*

It is an important part of EV which stores the required energy for functional application of vehicles. The main factors to be considered for Energy storage systems are total energy capacity, ability to provide high power output, life cycle, behavior during functional failures, etc. Traditionally and popularly used one is a battery, but there are also other emerging technologies which are as follows:

- Capacitors—These are high energy density storage devices. They can be used as a secondary storage device for supporting purposes. They have high discharge rate. Supercapacitors and Ultracapacitor are the types among them.
- Fuel Cell—These are devices in which Electrical energy is created by the proton release of fuel with composition  $C_xH_yO_z$ . Most commonly used Fuel Cells are hydrogen in which they are split into protons and hydrogen electrons. They are capable of delivering high efficiency.

### ***5.3 Power Electronics***

These are electronic devices which are used for power conversion purpose in a vehicle. It may be a DC/DC convertor in the case where it ensures a stable output to EM or else a DC/AC convertor which is also called inverter in case if we use an AC motor in vehicle. The inverters are capable of providing variable frequency AC power which makes the motors to be controlled and allows it to rotate on different speeds. Meanwhile, they also assist in converting the AC power generated during Regen braking to DC power for storage in battery.

### ***5.4 Battery Management System***

Batteries are generally made up of pack of cells connected together. There are an imbalance and possibility for parametric variation while operating during practical application. This has to be continuously monitored and corrective action is to be taken to prevent any hazard. So, BMS is a system which effectively monitors all the parameters for ensuring stable functioning. In addition, it always maintains the battery in a state which can fulfill functional requirement.

### ***5.5 Energy Management Systems (EMS)***

Energy management has an important path in bringing out an efficient Electric Vehicle. In spite of the technology deployed and Drivetrain type used, they decide on amount of power to be supplied from sources and split it to the drive in order to have an optimal system. They play a crucial part in vehicle performance, fuel efficiency, and driver comfort. Generally, integrated within the Controller of a vehicle, they must be designed to be fast and quick reactive at times. They have control over the power supply to the wheels, and since the power withdrawn is directly proportional to the battery SOC, deployment of an optimal EMS system is mandatory in order to keep the vehicle to be efficient. The most prominent EMS techniques are discussed below along with their simple workings.

- Rule based (RB)—Works on the concept of predefined rules/preprogrammed conditions in spite of the different conditions prevailing at the time.
- Optimization based (OB)—Works based on the info level of driving conditions prevailing during drive, considering it as an input before taking decisions which makes it optimum than RB.
- Learning type (LB)—An advance type which employs Machine Learning and Artificial Intelligence for online data-based storage and training approach.

An RB is a simple one which can execute functionalities successfully for the real-time application, but due to its constraints on design level, it could not be used for advanced level. Since the technology is emerging day by day, the OB-based and LB-based EMS will emerge as the future technology for building a sustainable vehicle.

## 6 Drivetrain Architecture

The three different types of Drivetrain architecture followed in Electric and Hybrid Vehicles are Parallel type, Series type, and the Series–Parallel type which are discussed in the following subsections.

### 6.1 *Parallel Hybrid*

Figure 3 represents the Parallel type of architecture. In this type of architecture, the ICE and Electric motor are arranged Parallel in the Drivetrain. It means that they can operate individually or else combinedly. Power to the wheel can be received from either of the one source or else from the both sources at the same time. It is said to be more powerful since the Engine can assist for more power generation when required during times. Since both the powers have to be combined, the arrangement is quite complex. Regenerative braking acts as a source for charging the battery. Torque coupling plays an important role in Parallel HEV. The power from both sources EM and ICE is received in Torque coupling and coupled to single power and sent to Final Drive through Shaft. Here, the engine is more powerful than EM since most of the powers are generated by the ICE and vehicle is run by it.

Through the Road-Parallel HEVs—here the same Parallel HEV is arranged in such a way like two wheels are powered by ICE and the other two wheels by EM's. Vehicles when either operated in a single source of Power is considered to be a two-wheel drive and when operated from both power sources it will be considered as All-Wheel Drive.

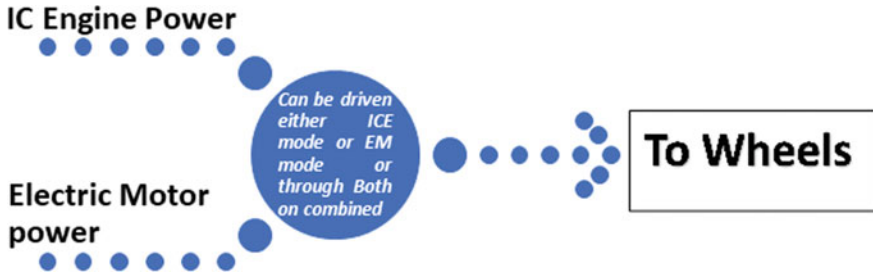


Fig. 3 Parallel type of architecture

### 6.2 Series HEV

Figure 4 represents the Series type of architecture. In this type of architecture, the ICE and EM are arranged in the Series connection. Even though both sources are available, the power to the wheels is given only by the Electric motor. The Mechanical power generated in ICE is converted into Electrical power to drive the EM which are connected in Series. Since there will be more losses during conversion, the additional power required is withdrawn from battery source to meet its requirement and needs. The battery is charged by the ICE through generator in addition to Regenerative braking. Unlike in PHEV, the Series HEV ICE will be always working on a constant speed and generates a constant power. Usually, only small Engine size is required here since they only act as a supporting unit to meet the power requirement. This type of vehicles is found to be expensive in cost since we have to rely on large size Batteries and powerful motors since Engine is used here only for charging purposes. They are optimal only for city usages and are used mostly in City buses which use stop and go concepts. Easier to control and simpler in arrangement since the source for the wheel or actuation is only from a single source, i.e., Electric motor power.

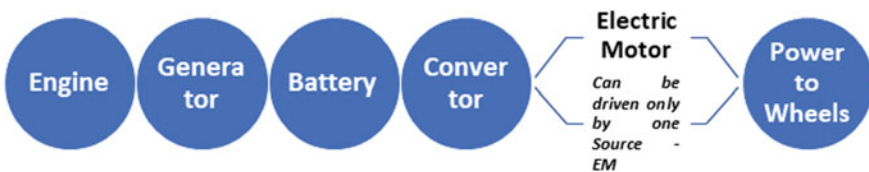


Fig. 4 Series type of architecture

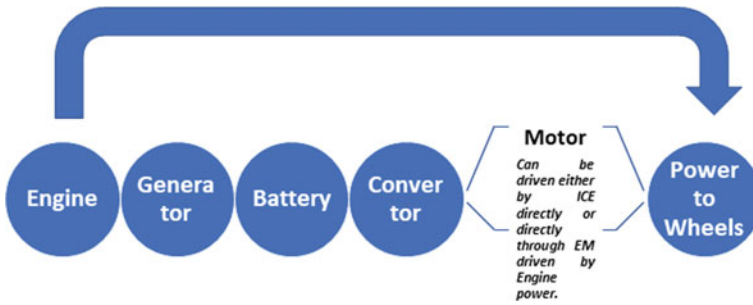


Fig. 5 Series–Parallel type of architecture

### 6.3 Series–Parallel Hybrid

Figure 5 represents the Series–Parallel type of architecture. This Series–Parallel hybrid are the combination of both Series type and Parallel type of Hybrid architectures integrated together on a single system. Thus, it can operate as Series hybrid type in time, Parallel hybrid types in time and also on both type at a time based on the requirement or operation. When the vehicle has to be run by one type of drive, the other type is decoupled by the decoupler. The integration of power received from both the Drivetrains is a crucial part which is done by a Planetary gear. This type of DT has two motor, one which acts as generator to generate Electric power from ICE and the other to run the wheels by using Electric power. This type of Drivetrain helps us to overcome the disadvantage existing on this each type of operation by the application of integration of two methods of power sources (i.e.) overcome the low torque issues during initial speed faced by ICE by operating on EM and to overcome the constraints of High speed faced in EM by operating in ICE. This makes it to be a more fuel-efficient type even though this complex architecture is found to be expensive and occupies a huge space in Powertrain system. This type of Drivetrain can operate only on CVT type of Transmission. Only challenge existing is the power flow management since they can operate on four modes—Series type, Parallel type, ICE heavy, and Electric motor heavy.

## 7 Systems in Electric and Hybrid Vehicles

### 7.1 Torque Converter

The Torque converter is an important part of Hybrid Vehicle which performs the function of Torque multiplication/reduction since all HEVs and EVs come with an automatic transmission only. Meantime, they can also assist the vehicle in motion

isolation to avoid any failure during the time of braking. Made up of a simple construction with parts such as pump, turbine and reactor, this helps to produce high torque/speed based on the vehicle requirement. They are housed in a casing with fluids. The reactor placed in between the pump and turbine in TC helps in achieving their functionality during different conditions.

## **7.2 Planetary Gearset**

Also, called as Epicyclic gear train, they are used in HEVs and Automatic transmission vehicles. Made up of a simple construction—Sun Gear, Planet Gear, Ring Gear & a Carrier. With Sun gear placed in middle and ‘n’ planet gears placed upon them, the arrangement is kept inside the Ring gear meshed on them and the Carrier attached to the planetary gear. With the Sun Gear connected to the Output shaft and Carrier connected to the input shaft, they are able to transfer motion, reverse it and arrest the motion based on the functional requirement by making each gears stationery.

## **7.3 E-Differential (E-Diff)**

An Electronic Differential is the latest type of differential replacing the conventional differential used in modern cars and EVs. In the cases of EV, this E-Diff comes into picture only when two or more motors drive the wheels individually. The E-Diff considers various inputs such as speed of car, steering wheel angle positions, throttle positions, power received out of powerhouse. An Electronic Controller (EC) is built within them which decides on the amount of power to be sent to each wheel based on the inputs received. Analysis has been made based on the inputs received to understand the driving condition and actions are provided accordingly to get an optimal result. Since they have to be quickly responsive, they keep getting the feedback of input from all end through sensors and at the same time perform corrective action ‘n’ number of times per second. They keep tracking the driving behavior and play a vital role in torque distribution and avoiding understeer, oversteer, wheel spinning.

## **8 Summary**

The EV and HEV are much efficient than the ICE Vehicle. They are capable of producing high torque at low speeds. The BEVs operate only on battery power, and they are suitable only for limited range applications. The HEVs are more powerful due to its multiple sources but are expensive due to it. The PHEV is a viable one for adoption due to its Plug-In technology and added ICE source in it. The Micro

hybrid is more similar to that of an ICE Vehicle due to limited features. The Mild hybrid is the hybrid models which are normally adopted in the market due to added features and moderate cost in implementation. The Full hybrids are having found to be highly efficient, but the cost is also similar to its efficiency. The EMS of the vehicle must be effective in spite of technology adopted. The suitable Drivetrain architecture selection for a vehicle makes it to perform better on the application and to be efficient. Parallel hybrids are capable of running the vehicle through two sources, but managing the power sources is quite complex. The capability of Series hybrid to run the vehicle through single source in spite of presence of multiple sources is attractive, but huge losses occur during conversion of the power. The Series-Parallel hybrid which is a combination of both types is effective but found to be heavier since it employs a greater number of parts in it. Torque convertor helps out in multiplication/reduction of torque generated from source. The different types of motors are suited and selected based on the application of vehicle. The simple construction of Epicyclic gear train helps us to perform the transmission of power easily. The BMS of the battery manages the battery effectively and ensures smooth functioning of the vehicle. Power Electronics is the important part in the EV which converts the power based on the type of motor used or the type of power supplied. E-Diff is the next-generation differential system which works instantaneously based on the inputs and takes immediate corrective action ensuring a stable movement.

## 9 Future Scope

Even though EVs are found to be advantageous in some aspects, the limited energy storage capacity restricts it from becoming predominant in the market. The battery has high energy density but is found to be very expensive contributing the major cost of the vehicle. So, we have to develop the available alternative storage device like Supercapacitors, Ultracapacitors, Fuel Cells and conduct real-time study for understanding the viability for real-world implementation. Vehicles can be modeled and analyzed on software with different Drivetrain architectures to study the different parameter conditions and for comparison in EVs, HEVs. The different types of motor can be implemented on various applications and studied to find an optimum one for exact application for different segments of vehicles such as SUV, MUV, Sedans and Hatchbacks. The Battery EV and Fuel Cell EV can be implemented on application basis and studied to find the practical difficulties existing and the exact area where the research can be extended for overcoming the barriers. Case studies can be conducted on small mini level EVs by implementing the learning-based and optimization-based types of EMS. Each Hybrid Vehicle type can be modeled and simulated to find their efficiency and effectiveness.

## 10 Conclusion

The Electric Vehicles are found to be emerging due to its several advantages, but we would be able to achieve the important goal only if all powers required for their functioning are met out from renewable or non-polluting source. This is the high time to concentrate and develop cost-effective high-energy storage device in order to keep the EV adoption to be successful on long run. The motor, which is considered as important part of EV, plays a major role in determining the level of hybridness and functioning. All passenger segment vehicle manufacturers should at least implement Mild hybrid across all the models as part of implementation in a phased manner. Even though we have limited the discussion of motors in this study, in real time, the cost-effective motor based on the application requirement will boost the EV implementation. The Fuel Cell is seen to be highly effective, but researches are still undergoing on safety aspects and effective storage part for processing the same. The battery has several advantages, but there are several difficulties when it comes to different applications such Heavy machineries, Commercial vehicles. So, we are constrained to work on other devices which can produce highly efficient large storage devices at a cost effective as well as compact in size. The rule-based EMS is predominantly used in EVs, but the real-world effectiveness of Advancement in Engineering can be seen only on proper implementation of learning and optimization-based EMS. Hybrid Vehicles can be an intermediary option to fill in the gap between ICE vehicle and EV implementation, but focusing more on HEV part practically may lead to a threat to adoption of EV. The introduction of Planetary Gearset, Torque converter and E-Differential has caused drastic reduction in number of moving parts to reduce losses and increase efficiency. Moreover, the recent findings of huge volume of Lithium material source in India are expected to boost the EV sector. Overall, the succession of EVs can be seen only based on the performance on the real world, as usually a new product takes time for attaining their expected goal as it undergoes several challenges and corrective action in between for fulfilling the needs of market expectation.

## References

1. Hilgers M, Achenbach W (2021) Hybrid vehicles. In: Alternative powertrains and extensions to the conventional powertrain. Commercial vehicle technology. Springer, Heidelberg. [https://doi.org/10.1007/978-3-662-60832-6\\_3](https://doi.org/10.1007/978-3-662-60832-6_3)
2. Elgowainy A. Electric, hybrid, and fuel cell vehicles. Springer Link, ESSTS. <https://doi.org/10.1007/978-1-0716-1492-1>
3. Varga BO (2012) Energy management of electric and hybrid vehicles dependent on powertrain configuration. Cent Eur J Eng 2:253–263. <https://doi.org/10.2478/s13531-011-0066-x>
4. Singh KV, Bansal HO, Singh D (2019) A comprehensive review on hybrid electric vehicles: architectures and components. J. Mod. Transport. 27:77–107. <https://doi.org/10.1007/s40534-019-0184-3>
5. Chan CC (2002) The state of the art of electric and hybrid vehicles. Proc IEEE 90(2):247–275. <https://doi.org/10.1109/5.989873>



6. Vidyanandan KV (2018) Overview of electric and hybrid vehicles. *Energy Scan (A House Journal of Corporate Planning, NTPC Ltd., India) III*:7–14. Kamil Çağatay Bayindir, Mehmet Ali Gözüküçük, Ahmet Teke. A comprehensive overview of hybrid electric vehicle: powertrain configurations, powertrain control techniques and electronic control units, Elsevier—Energy Conversion and Management (2011)
7. Namirian Z (2020) Comprehensive overview of hybrid vehicle drivetrains. *Int J Eng Technol* 07. <https://doi.org/10.5281/zenodo.4561583>
8. Yousaf M, Wang T, Li G, Chen D, Al-Nehari M (2022) A study of advanced efficient hybrid electric vehicles, electric propulsion and energy source. *J Power Energy Eng* 10:1–12. <https://doi.org/10.4236/jpee.2022.107001>
9. Tran D-D, Vafaeipour M, El Baghdadi M, Barrero R, Van Mierlo J, Hegazy O (2020) Thorough state-of-the-art analysis of electric and hybrid vehicle powertrains: topologies and integrated energy management strategies. In: *Renewable and sustainable energy reviews*
10. Bapodra Y, Rajamanickam U (2021) A review on hybrid electric vehicle and simulation on hybrid electric vehicle drivetrain. *IOP Conf Ser: Earth Environ Sci* 633:012007. <https://doi.org/10.1088/1755-1315/633/1/012007>
11. Lanzarotto D, Marchesoni M, Passalacqua M, Pini Prato A, Repetto M (2018) Overview of different hybrid vehicle architectures. *IFAC-PapersOnLine* 51(9):218–222. ISSN 2405-8963. <https://doi.org/10.1016/j.ifacol.2018.07.036>
12. Prajapati KC, Sagar R, Patel R (2014) Hybrid vehicle: a study on technology. *Int J Eng Res Technol (IJERT)* 03(12)
13. Aggarwal A (2013) Electronic differential in electric vehicle. *Int J Sci Eng Res* 4
14. Ahmad MW et al (eds) (2022) *Intelligent data analytics for power and energy systems*. Springer Singapore, page XXII, 641. ISBN: 978-981-16-6081-8. <https://doi.org/10.1007/978-981-16-6081-8>
15. Tomar A et al (eds) (2022) *Proceedings of 3rd international conference on machine learning, advances in computing, renewable energy and communication: Mar 2021, vol 915, Pages XV, 781*. ISBN: 978-981-19-2830-7. Springer Nature. <https://doi.org/10.1007/978-981-19-2828-4>
16. De Carlo M, Mantriota G (2020) Electric vehicles with two motors combined via planetary gear train. *Mech Mach Theor* 148:103789. ISSN 0094-114X. <https://doi.org/10.1016/j.mechmach.2020.103789>
17. Cao Z, Mahmoudi A, Kahourzade S, Soong WL (2021) An overview of electric motors for electric vehicles. In: *2021 31st Australasian Universities power engineering conference (AUPEC)*, Perth, Australia, pp 1–6. <https://doi.org/10.1109/AUPEC52110.2021.9597739>

# Performance Analysis of Classical Converter Using Different Control Strategies for Switched Reluctance Motor with Dynamic Loading



Ritika Asati and Deepak S. Bankar

**Abstract** Among the researchers, switched reluctance motor (SRM) is generating a lot of interest as it is a permanent magnet-free motor which significantly differs from the other polyphase machines. Due to the absence of brushes, windings, and permanent magnet on rotor, its structure is lightweight. Other than the structure, it has many other attractive characteristics suitable for variable speed applications. Special applications include aerospace, renewable and electric vehicle (EV). Lack of reserves of permanent magnet and continuous rise in its price are forcing motor manufacturers to look for an alternate motor which does not require permanent magnet. SRM is the best alternate solution to mitigate these challenges. Performance of SRM drive depends on the type of power converter and control technique used. Over the years, many converters have been developed and analyzed; among those, asymmetric bridge converter gives the highest performance in terms of independent switch control, good fault tolerance capability, and easy power regeneration. This paper represents the simulation of 7.5 kW, 8/6 pole, four-phase SRM using asymmetric bridge converter with current hysteresis chopping and pulse-width modulation (PWM) technique for dynamic load. Asymmetric bridge converter with current chopping or hysteresis current control offers better performance in terms of current as it is limited to 35 A under the range of peak current and appropriate speed–torque for dynamic loading.

**Keywords** Asymmetric bridge converter (ABC) · Switched reluctance motor (SRM) · Hysteresis current control (HCC) · Pulse-width modulation (PWM) · Dynamic load

---

R. Asati (✉) · D. S. Bankar

Department of Electrical Engineering, Bharati Vidyapeeth (Deemed to be) University, College of Engineering, Pune, India

e-mail: [rasati-ext@bvucoep.edu.in](mailto:rasati-ext@bvucoep.edu.in)

D. S. Bankar

e-mail: [dsbankar@bvucoep.edu.in](mailto:dsbankar@bvucoep.edu.in)

## 1 Introduction

Switched reluctance drive (SRD) is gaining significant traction in the field of renewable energy, electric vehicles, aerospace, and other variable speed application due to its lightweight rotor. Switched reluctance motor (SRM) is a permanent magnet-free motor with no brushes and windings on its rotor [1]. The origin of the nomenclature (switched reluctance) comes from the fact that the rotor of SRM continuously changes its position with respect to the variable reluctance path. Construction of SRM is different from the other multi-phase machines because of the doubly salient structure [2]. SRM's primary advantage lies in the fact that it does not need permanent magnet for its construction unlike most of the other motors which require permanent magnet for their construction. Permanent magnets are manufactured from rare-earth element which usually involves high cost of refining and mining, thereby increasing the cost of the motors. Very few countries around the world have these rare-earth elements reserve.

SRM is characterized by its wide speed range, good fault tolerance, high speed in a wide constant power range, low cost, simple, and light structure motor. Due to these characteristics, constant advancements are being made with the consideration that SRM can be used as an alternative to permanent magnet motors [3]. In spite of many attractive features and suitability to EV application, doubly salient structure of SRM creates noise, vibration, and torque ripple which limit its acceptance.

Figure 1 shows the basic components of SRM drive giving input to a dynamic load. Battery and its management system supply DC power for the motor through power electronics converter. For the movement of the rotor, stator winding needs to be energized in steps with the help of power electronic converters. Switching pulses for this converter excite each phase of the motor to conduct independently [4]. Motor controller block controls all the switching signals applied to the power converter. Different control techniques can be used on the same type of power converter based on the performance requirement of the load.

Multiple current and torque control methods have already been discussed in literature for asymmetric bridge converter like commutation angle control, torque sharing function (TSF), model predictive control (MPC), direct instantaneous torque control (DITC), and many more. Commutation angle control has wide torque adjustment range and suitable for higher speed. By controlling the dwell angle and advanced angle of switching devices, regulated phase current waveform can be obtained, but this angle control causes changes in other phase current waveforms and also makes it non-suitable for low-speed operation [5, 6]. TSF is generally discussed and analyzed in literature, and it uses the SRM flux linkage characteristics for current reference profiling purpose [7]. This method is effective at both base speed and above the base speed as well. TSF needs larger memory size and exhaustive computation [8]. MPC predicts the future nature of the controlled variables by predefining the criterion of optimization. Motor can work both with voltage and current controls but requires large memory to store these data and is sensitive for system variable changes [9]. In

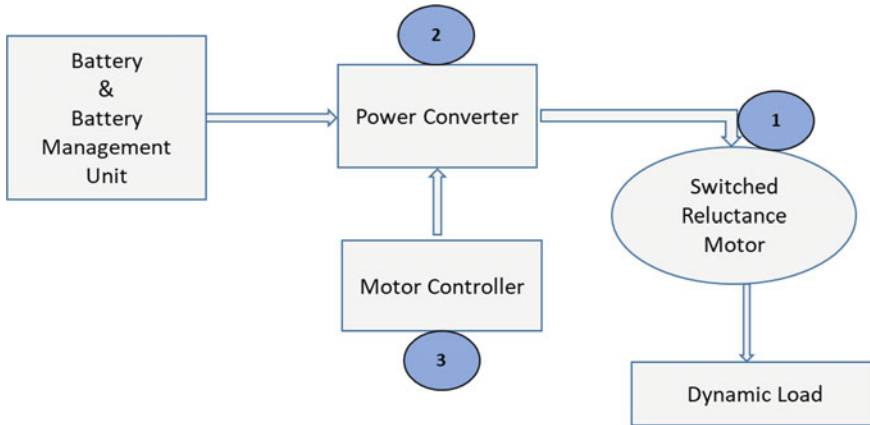


**Fig. 1** Basic components of switched reluctance motor drive

DITC technique, controller maintains the torque within hysteresis band by controlling the switching pulses of converter to energize the incoming and outgoing phase [10], but fixed commutation angles are unable to avoid the negative torque in DITC method [11]. PWM voltage control provides fixed frequency operation but is not suitable for dynamic load as current is very high during the starting because of the absence of current limiter [5].

Hysteresis current control technique provides better response and has good current control to protect the switches and windings of motor [12]. The starting and running torque provided by this method is sufficient to drive dynamic load in an electric vehicle. Table 1 lists the SRM specification used in the MATLAB simulation of asymmetric bridge converter for the comparison of commonly used PI (proportional plus integral)-based current chopping or pulse-width modulation control techniques. Here, simulation waveform presented that the hysteresis or current chopping control is the simple control technique which provides both current and speed controls.

**Table 1** Switched reluctance motor specifications

Parameters	Value
Type	8/6
Stator resistance (ohm)	0.5
Inertia (Kg m <sup>2</sup> )	200 * 0.28 * 0.28
Friction (N-m s)	0.02
Unaligned inductance (H)	9.15 × 10 <sup>-3</sup>
Aligned inductance (H)	145.9 × 10 <sup>-3</sup>
Saturated aligned inductance (H)	0.15 × 10 <sup>-3</sup>
Maximum current (A)	35
Maximum flux linkage (V s)	0.9

The paper is arranged in different segments as follows: Here, Sect. 2 presents role and requirement of converter, SRM, and EV specification; Sect. 3 will give overview of asymmetric bridge converter with its operation mode; detailed block diagram and working of hysteresis and PWM control technique are demonstrated in Sect. 4; waveform comparison and simulation result discussion are shown in Sect. 5; and at last, Sect. 6 presents the conclusion and scope of extension of this work.

## 2 SRM Requirements

Input DC voltage to SRM is obtained from a battery through power electronics converter to excite the respective stator phase which offers low reluctance path [13]. In SR motor, it is assumed that the mutual coupling between the different phases is negligible, which helps each phase of the motor to be independently controlled [14].

$$V = R_s i + L(\theta, i) \frac{di}{dt} + \frac{dL(\theta, i)}{d\theta} \omega_m i. \quad (1)$$

Equation 1 [3] shows the voltage applied across each phase of the motor winding. First two components on the right side of Eq. 1 denote voltage drop in resistance and inductance of the motor winding, and the third component of Eq. 1 indicates the generated back emf, which primarily depends on the variable inductance with rotor position and speed.

The instantaneous torque produced in SRM is given by:

$$T = \frac{1}{2} i^2 \frac{dL}{d\theta}. \quad (2)$$

As per the torque Eq. 2 [3], it is observed that SRM torque can be controlled by the following parameters:

- (1) By controlling the current in the stator winding.
- (2) By controlling DC voltage to stator.
- (3) By advanced or dwell angle control [5].

Based on these parameters, speed or torque can be controlled using commonly used or advanced control methods.

## 3 Asymmetric or Classical Converter

Asymmetric bridge converter (ABC) is the highly flexible, four-quadrant commonly used converter for SR motor drive. Figure 2 is showing the classical asymmetric bridge converter for a four-phase SRM drive where each phase is using two power

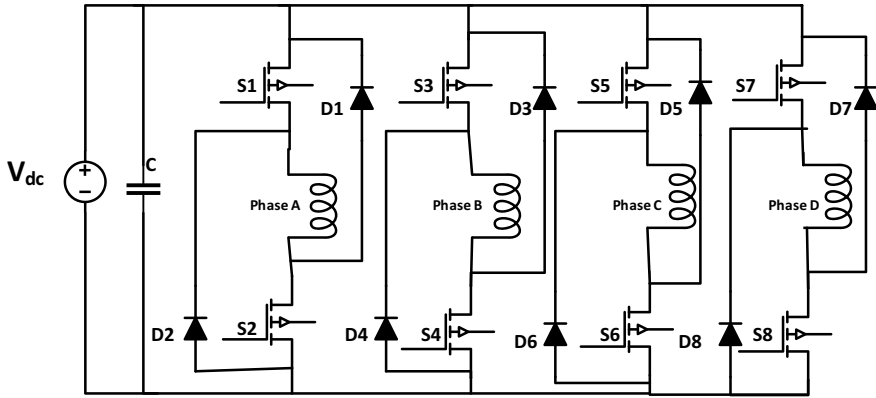


**Fig. 2** Classical asymmetric bridge converter for four-phase SRM

switches and two diodes. The voltage stress experienced by each switch is equal to dc link supply voltage.

The supply voltage (+U, -U, and zero) appears across the phases and can be controlled independently which makes this converter suitable for high-speed application [15, 16]. The asymmetric bridge converter can work in two modes by using three different means of current conduction magnetization, demagnetization, and freewheeling.

- (i) **Hard chopping mode:** In Fig. 2, if we will turn on both the switches  $S_1$  and  $S_2$ , phase A will be energized and current will start flowing through  $V_{dc}$ ,  $S_1$ , Phase A,  $S_2$ . For turning off the phase A, both the switches  $S_1$  and  $S_2$  will turn off and diodes  $D_1$  and  $D_2$  will be on, and the phase A energy will be supplied back to source in this mode called regeneration as negative supply voltage will appear across the winding and current will decrease rapidly bringing it below the commanded value [6].
- (ii) **Soft chopping mode:** In soft chopping mode for turning off phase A, only one switch say  $S_2$  will be off, while  $S_1$  will remain on and diode  $D_1$  will be forward-biased, and this will circulate the current through phase winding,  $D_1$  and  $S_1$ . The voltage appeared across the winding will be zero during this mode (assuming voltage drop across switches and diodes is negligible) that will assist in reduction of current rate in comparison with the hard chopping mode. This mode will help in reducing the switching frequency and later the switching losses [6, 14].

Asymmetric bridge converter does not need any additional winding or commutation circuit, that helps in decreasing the copper loss and high heat loss [15]; this converter is highly flexible in controlling the phase current value and also has good fault tolerance capability that can effectively improve the reliability of the SRM drive.

## 4 Control of SRM

Control techniques for SRM are different than the other permanent magnet motor due to the extremely nonlinear behavior of it. Salient pole stator–rotor and no magnet on rotor create variable inductance to produce torque [7]. From Eq. 1, we can see that torque is controlled by controlling the amplitude of current. As by changing the supply voltage, phase current can also be changed. Therefore, voltage and current controls can be used for controlling the speed or torque of the SRM. By proper selection of control scheme, performance of the SRM drive can be enhanced for dynamic loading condition.

### 4.1 Hysteresis Current or Current Chopping Control Technique

Current chopping or hysteresis current control is the most commonly applied control method in SRM with asymmetric bridge converter due to its fast dynamic response, model independence, and it requires to set only current band for control [4]. Various parameters of motor mainly current, speed, and torque have significantly affected by the choice of current controller [7]. The block diagram of a hysteresis or current chopping control approach is presented in Fig. 3 [6]. For the SRM operation below base speed and at a suitable DC voltage, current control technique is levied. In this control hysteresis band  $\Delta I$  is set as per the maximum value of phase winding current. The winding current is limited around the set reference current  $I^*$ . Power converter gets switching pulses from the control circuit when the current is lower than the set value and turns off the switches when current reaches upper limit of hysteresis band [17].

In current chopping technique, frequency of gate pulse varies with the speed. Therefore, speed monitoring and reference current are required to achieve steady-state speed. Speed controller block in Fig. 3 compares reference speed with actual measured speed to produce speed error. This error is processed through the speed

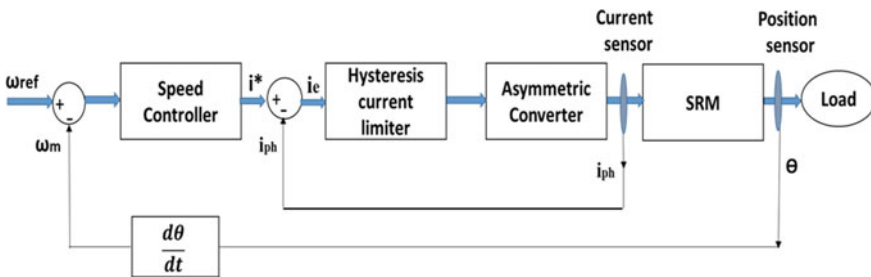


Fig. 3 Closed-loop hysteresis current control with asymmetric bridge converter

controller block to generate reference current. Current limit needs to be set in the speed controller. By proper selection of pulses, required phase can be turned on to control the value of torque and speed. Selecting the value of hysteresis band is a cumbersome task, which also affects the performance of the drive. Here, a PI controller is used to process the speed error, so by adjusting the proper value of  $K_p$ ,  $K_i$ , and reference speed, desired closed-loop performance can be achieved [6].

The main characteristics of the current chopping control are: It is simple and direct method, smooth torque, and appropriate for low-speed operation [5]. The current ripples in SRM are much prominent at low-speed operation. Variation in switching frequency affects the hysteresis band of current. [7] These current ripples can be reduced by narrow down the hysteresis band  $\Delta I$  [17]. The main purpose of the controller in this system is to use the information from position and current sensor and compared with the set value [18].

## ***4.2 Pulse-Width Modulation (PWM) or Voltage Chopping Control Technique***

In this closed loop, voltage chopping method by keeping  $\theta_{on}$  and  $\theta_{off}$  unchanged; reference speed is set into the controller as input, instead of PWM duty cycle. Continuous motor speed can be obtained either by differentiating the rotor position or position sensor. PWM control method can be applied to the winding voltage [5]. By varying the duty cycle of the pulses in PWM, average output DC voltage to the phase winding can be controlled. This in turn controls the phase current of the winding and regulates the torque and speed of the SR motor drive. This control method is usually employed when rotor position is available. The actual motor speed is derived by differentiating the rotor position. All the power switches in the converter operate in the pulse-width modulation (PWM) mode [6].

In closed-loop PWM control system shown in Fig. 4, reference and actual speeds are compared and generated speed error (difference between two speeds) is processed through speed controller. This speed controller adjusts the PWM duty cycles to reduce the speed error to zero. Speed controller will continuously adjust the duty cycle to get the desired reference speed. It provides the desired performance in terms of settling time and no overshoot in speed. But sudden increase in the duty cycle during starting condition leads to high value of phase current which can damage the stator windings [6]. This method is appropriate for low- and high-speed operation, but at low-speed torque ripple produced through this control technique is more. There are always some benefits and limitations of using any new technique [19–21].



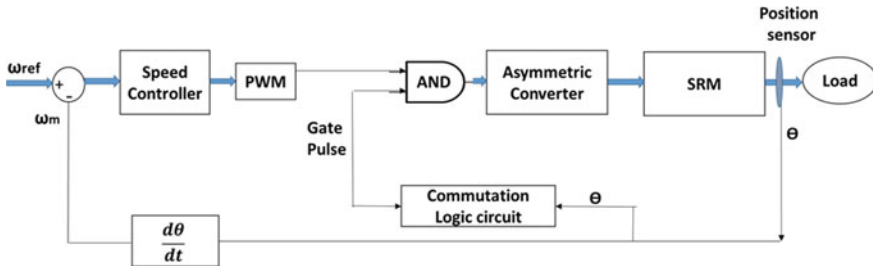
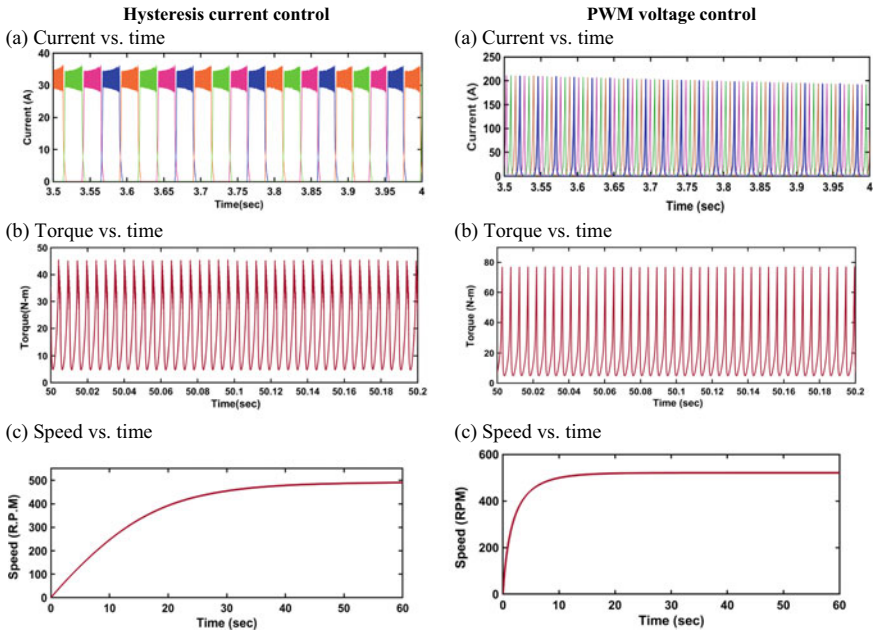


Fig. 4 Closed-loop voltage PWM control

## 5 Results and Discussion on Waveform

In this section, MATLAB simulation model of a four-phase, 7.5 kW, 8/6 pole SR motor with closed-loop hysteresis current control and pulse-width modulation technique are presented as shown in Fig. 5. The load used for these simulations is 200 kg weight dynamic load model. Current limit set in both the controllers is 35 A. For the entire speed range, angle of turn on is  $40^\circ$  and angle of turn off is  $55^\circ$  during the entire speed range. In both the control techniques, supply DC voltage to SRM is 200 V and these control techniques are implemented on asymmetric or classical converter. The simulation has been run for 60 s, and Fig. 5 is representing simulation waveform of current, torque, and speed of asymmetric bridge converter with hysteresis current and PWM voltage control technique.

It can be deduced from the simulation results given by comparative table in Fig. 5. In Fig. 5a, current waveforms are shown which indicating that in hysteresis current control, initial current is 35 A under set hysteresis band, while in PWM voltage control, initial current peak is too high and goes around 500 A for short duration as no current limiter is applied in this technique after 15 s current value reaches to 70 A. From the torque waveform in Fig. 5b, it can be monitored that initial torque peak is 58 N-m in current control latter this torque becomes constant near 45 N-m in 50 s. Though, initial torque peak is extremely high around 680 N-m in PWM voltage control, latter it is settled near 80 N-m in 15 s. Maximum speed reached is 490 RPM or 51.6 km/h and time required to settle at this constant speed is 50 s using current control approach; for voltage control approach, maximum speed is 520 RPM or 54.8 km/h and settling time for this speed is 20 s and can be observed from Fig. 5c for dynamic load. In both the control approaches, speed is almost same, but time to settle speed is more in current control technique.



**Fig. 5** Comparison of the simulation results of hysteresis current control and PWM voltage control for four-phase SRM

Table 2 shows the comparison of two different control techniques based on the frequency, settling time, maximum torque, maximum current, and speed. From this comparison, it is observed that both of these SRM control techniques have their own advantages and drawbacks. The simulation waveforms in Fig. 5 for torque and speed of SRM motor drive using both the control techniques substantiated the objective of this research paper. Speed waveform indicating that with increasing time, speed settles and becomes constant. The torque waveform demonstrates that, under dynamic load condition, the torque has a high initial value before becoming constant.

**Table 2** Comparative of control techniques for four-phase SRM

Type of control scheme	Hysteresis current control	Pulse-width modulation (PWM)
Frequency	Variable	Fixed
Speed settling time	More (50 s)	Less (15–20 s)
Initial peak current	Set in hysteresis controller (35 A)	No current limiter (very high)
Maximum torque	Good starting torque of (80 N-m)	Very high initial peak torque (680 N-m)
Maximum speed	490 RPM or 51.6 km/h	521 M or 54.8 km/h

## 6 Conclusions and Scope of Extension

The work in this research paper presented the comparison of a four-phase, SRM drive to analyze the performance of classical asymmetric bridge converter with hysteresis current and PWM voltage control technique. For desired performance of SRM drive with dynamic load, selection of a control technique for any converter is an important task. It is perceived from the simulation waveform that average and maximum torque in PWM technique is higher than the current control technique and as required for a dynamic loading condition. Also, the initial high peak current can destroy the motor phase winding and switches in converter unit. The important benefit of using hysteresis current control is that it protects phase winding and switching device from high current peaks and reduces the power losses. Torque provided by hysteresis control is less compared to voltage control but sufficient to drive the dynamic load. The simulation results demonstrate that asymmetric bridge or classical converter with hysteresis current control is appropriate for better performance of dynamic load in comparison with the voltage PWM control.

From simulation result, observations are made that PWM voltage control technique fulfills all the desired features for dynamic loading and only high inrush current is an issue. In future work, current limiter or any advance control can be added along with the PWM voltage control technique to enhance its performance.

## References

1. Xu S, Chen H, Yang J, Dong F (2019) Performance evaluation and reliability enhancement of switched reluctance drive system by a novel integrated power converter. *IEEE Trans Power Electron* 34(11):11090–11102. <https://doi.org/10.1109/TPEL.2019.2900328>
2. Rani GC, Santosh Kumar M (2021) Modelling and reduction of torque ripple in SRM drive using SVM based converter. *Int J Modern Trends Sci Technol* 7:172–176. <https://doi.org/10.46501/IJMTST0709027>
3. Asati R, Bankar DS, Nehete AL (2022) Comparative analysis of converter topologies used in switched reluctance motor for high torque electric vehicle application. In: *Materials today: proceedings*. ISSN 2214-7853. <https://doi.org/10.1016/j.matpr.2022.08.497>
4. Taylor J, Valencia DF, Bilgin B, Narimani M, Emadi A (2020) Comparison of current control strategies for low- and high-power switched reluctance motor drives. *IEEE Transp Electrification Conf Expo (ITEC) 2020*:198–203. <https://doi.org/10.1109/ITEC48692.2020.9161762>
5. Gao X, Wang X, Li Z, Zhou Y (2015) A review of torque ripple control strategies of switched reluctance motor. *Int J Control Autom* 8(4):103–116
6. Makwana JA (2021) *Fundamentals of switched reluctance motor & drive*. ISBN 9798547055058, 1st edn
7. Fang G, Scalcon FP, Xiao D, Vieira RP, Gründling HA, Emadi A (2021) Advanced control of Switched Reluctance Motors (SRMs): a review on current regulation, torque control and vibration suppression. *IEEE Open J Ind Electron Soc* 2:280–301. <https://doi.org/10.1109/OJIES.2021.3076807>
8. Li H, Bilgin B, Emadi A (2019) An improved torque sharing function for torque ripple reduction in switched reluctance machines. *IEEE Trans Power Electron* 34(2)

9. Xu A, Shang C, Chen J, Zhu J, Han L (2019) A new control method based on DTC and MPC to reduce torque ripple in SRM. *IEEE Access* 7:68584–68593. <https://doi.org/10.1109/ACCESS.2019.2917317>
10. Pratapgiri S (2016) Comparative analysis of hysteresis current control and direct instantaneous torque control of switched reluctance motor. In: *International conference on electrical, electronics, and optimization techniques (ICEEOT)*, pp 2856–2860. <https://doi.org/10.1109/ICEEOT.2016.7755219>
11. Singh SK, Tripathi RK (2013) Minimization of torque ripples in SRM drive using DITC for electrical vehicle application. In: *Students conference on engineering and systems (SCES)*, pp 1–5
12. Peng F, Ye J, Emadi A (2016) A digital PWM current controller for switched reluctance motor drives. *IEEE Trans Power Electron* 31(10):7087–7098. <https://doi.org/10.1109/TPEL.2015.2510028>
13. Indira D, Venmathi M (2021) Comparative assessment of converter topologies for switched reluctance motor drives. *IETE J Res* 1–19. <https://doi.org/10.1080/03772063.2021.1977187>
14. Krishnan R (2001) *Switch reluctance motor drives: modelling, simulation, analysis, design and applications*. CRC Press, New York
15. Mahmoud Sm, El-Sherif MZ, Abdel-Aliem ES, Nashed MNF (2013) Studying different types of power converters fed switched reluctance motor. *Int J Electron Electr Eng* 1(4):281–290. <https://doi.org/10.12720/ijeee.1.4.281-290>
16. Pires VF, Pires Aj, Cordeiro A, Foito D (2020) A review of the power converter interfaces for switched reluctance machines. *Energies* 13:3490. Online ISSN: 1996-1073. <https://doi.org/10.3390/en13133490>
17. Kurian S, Nisha GK (2015) Torque ripple minimization of SRM using torque sharing function and hysteresis current controller. In: *2015 international conference on control communication & computing India (ICCC)*, pp 149–154. <https://doi.org/10.1109/ICCC.2015.7432884>
18. Lu C, Zhang G, Du C, Cheng J, Wu C (2018) Design and simulation of switched reluctance motor control system. In: *Proceedings of the 3rd international conference on electrical and information technologies for rail transportation (EITRT) 2018*. *Lecture Notes in Electrical Engineering*, vol 482. Springer, Singapore. [https://doi.org/10.1007/978-981-10-7986-3\\_64](https://doi.org/10.1007/978-981-10-7986-3_64)
19. Ahmad MW et al (eds) (2022) *Intelligent data analytics for power and energy systems*. Springer Singapore, page XXII, 641. ISBN: 978-981-16-6081-8. <https://doi.org/10.1007/978-981-16-6081-8>
20. Tomar A et al (eds) (2022) *Proceedings of 3rd international conference on machine learning, advances in computing, renewable energy and communication: MAR 2021*, vol 915, Pages XV, 781, ISBN: 978-981-19-2830-7. Springer Nature. <https://doi.org/10.1007/978-981-19-2828-4>
21. Kumar VM, Vinoth Kumar K, Saravanakumar R (2020) Switched reluctance motor converter topologies: review. In: *Innovations in electrical and electronics engineering*. *Lecture Notes in Electrical Engineering*, vol 626. Springer, Singapore. [https://doi.org/10.1007/978-981-15-2256-7\\_6](https://doi.org/10.1007/978-981-15-2256-7_6)

# Design and Development Gear-Electric Bike and Performance Testing for Indian Road Conditions



Vinay Gupta, Jitesh Kumawat, Rupendra Kumar Pachauri, and Shashikant

**Abstract** Due to rising environmental concerns about pollution and the preservation of fuel supplies globally, the automotive industry has entered a new phase with the development of more fuel-efficient, low-emission vehicles and innovative technology. Electric vehicles are one of the most innovative technologies. The existing two-wheeler has a limited speed range and cannot support a heavy passenger load in Indian road conditions. This paper's major goal is to design and create a two-wheeler that is appropriate for Indian road conditions and enhances vehicle performance. In this paper, we present the design steps and performance of the gear-electric bike. A 900W motor, a 24 V brushless DC motor, a motor controller, four lead-acid batteries, and four gears are included in the proposed gear-electric bike. This electric bike can travel 150 km on a single charge and costs about 0.40 INR/km to operate.

**Keywords** Electric vehicles · Geared electric bike · Lead-acid batteries · Electric two-wheeler

---

V. Gupta · J. Kumawat  
Department of Electrical Engineering, Manipal University, Jaipur 303007, India  
e-mail: [vina\\_20@rediff.com](mailto:vina_20@rediff.com)

R. K. Pachauri (✉)  
Electrical Cluster, School of Advanced Engineering, University of Petroleum and Energy Studies,  
Dehradun 248007, India  
e-mail: [rpachauri@ddn.upes.ac.in](mailto:rpachauri@ddn.upes.ac.in)

Department of Energy, Environment and Climate Change, SERD, Asian Institute of Technology,  
Pathum Thani, Thailand

Shashikant  
Electrical Engineering Department, Babu Banarasi Das University, Lucknow, India

## 1 Introduction

One of the most important innovations of all time is the internal combustion engine (ICE). Traditional ICE vehicles have a long operational range and solid performance. However, their low fuel efficiency, environmental contamination, and threat to human life have led to and continue to be major issues. One of the primary objectives of contemporary design is the elimination of fuel use and pollutants. Due to rising environmental concerns about pollution and the preservation of fuel supplies globally, the automotive industry has entered a new phase with the development of more fuel-efficient, low-emission vehicles, and innovative technology. The electric vehicle (EV) is one of the best technologies. A significant issue that the modern world is now dealing with is global warming. Electrical vehicles (EVs) provide a significant solution to this. A well-planned and fuel-efficient bike has to be created, taking India's urban and rural demographics into account. The electric bike is a type of motorcycle that is propelled by an electric motor and battery.

Because the supplies for gasoline, diesel, and natural gas are quickly running out, the energy crisis is one of the biggest issues facing the globe today. These critical issues have been attempted to be solved by this effort. V-Elph 2.01, a simulation and modelling programme established at Texas AM University, was introduced by Karen et al. in 1999 [1]. The visual modelling language MATLAB/Simulink, which is supported by the majority of computer platforms, was used to create V-Elph. They also talked about the V-Elph package's process for constructing vehicle drivetrains. The simulation software has been used to build an EV, a series HEV, a parallel HEV, and a traditional internal combustion engine-powered powertrain. For each vehicle, simulation findings related to fuel usage, vehicle emissions, and complexity are compared and analysed. For EVs with high power densities, Xianmin [2] created a unique propulsion system design approach. According to the dynamic features of the vehicle, theoretical analysis and mathematical models of EVs are first constructed. The system is then separated into seven function blocks in accordance with power flow, and simulation models are created in the MATLAB programming language. The simulation results are validated in a PDM AC-AC converter, demonstrating the appropriateness of the recommended approach for EV.

Fan [3] developed a model in MATLAB and ADAMS to show how much more fuel-efficient it is than a standard automobile. He used the Honda Integrated Motor Assistant (IMA) architecture, which uses the electric motor to increase the torque of the engine. He gave an example of how the motor unit turns into a generator when braking with regenerative power. He utilized a seven-basic power management algorithm in the power management controller that he designed for the automobile. The significance of vehicle simulations in the design of hybrid electric cars was explored by Bauml and Simic [4]. Modelica, a simulation language, was used to create a hybrid electric car simulation. They outlined the simulation methodology. Some of the simulation findings were used to support their conclusion, highlighting the value of simulation. Simulink was used by Zhou and Chang [5] to create a powertrain dynamic simulation model for a hybrid electric vehicle (HEV) with an

integrated starter/generator (ISG). Research and design went into the parallel electric assist control technique (PEACS). The FTP driving cycle was used to evaluate the model's dynamics performance and fuel efficiency, which could be used as a design guide for the powertrain test bench. The findings demonstrate that by employing the planned PEACS and keeping the battery's state of charge within a specific range, fuel consumption may be efficiently decreased.

Several research studies [6, 7] focus on energy estimates and system design for solar-powered E-bike pools. Other research concentrates on data loggers for electric vehicles to evaluate the performance of electric vehicles [7, 8]. Gupta et al. focused on the charging infrastructures of electric vehicles using super capacitors and BNS-driven systems [9–11]. Due to the poor road conditions in India, we have seen that vehicles without gears take more time to operate at constant speed. We frequently take breaks, which results in excessive energy use. The driving range is thereby reduced. An electric vehicle carrying two people moves at a relatively slow speed without gears and encounters difficulties on sloping terrain. To address these problems, we created the gear-electric bike. The performance and pickup of this suggested electric bike have been enhanced by the inclusion of a gear box. An advanced electric motor drive combined with the electrification of a vehicle instead of a conventional combustion engine may result in improved fuel economy and reduced pollutants. A well-designed and fuel-efficient pure electric bike has been created, taking into account India's urban and rural state. The primary goals of this project are,

- To design and fabricate an electric bike with gears.
- To examine an evolved electric vehicle's driving cycle.

## 2 Designing Methodology and Technological Calculation of an Electric Powertrain

An electric bike works essentially the same way an IC engine-powered bike works: it is propelled by an engine, and that engine requires fuel such as gasoline. The main difference is that the gasoline in a conventional bike is replaced by batteries, which may be lithium or lead-acid batteries in an electric version. An IC engine's working principle and that of an electric motor are relatively similar. Bikes are propelled by mechanical energy in both situations, but only in one of them are rechargeable batteries used. Electric vehicles are powered by electricity, which causes a pole to be inserted into the motor, causing it to spin. When the battery is on, current flows to the motor, and the power is transmitted to the wheels with the help of the chain drive shaft. The methodology for designing a geared electric bike is shown in Fig. 1.

According to the design idea, an electric drivetrain for a single-track vehicle with a peak speed of 50 km/h and a range of around 150 km would be developed. The preliminary calculations were done to determine the required power output using straightforward physics equations.

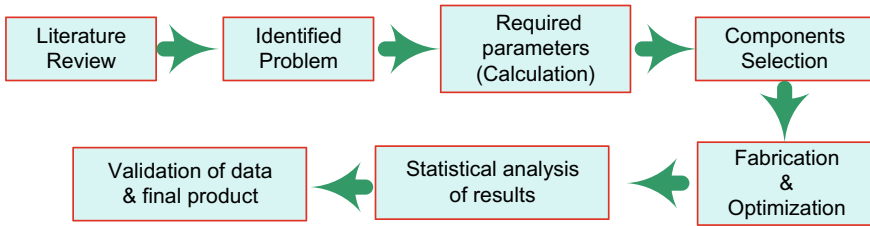


Fig. 1 PV cell (electrical circuit) [10]

$$P_C = \frac{\left(mgf_t + C_x \left(\frac{\rho V^2}{2}\right) A\right) V}{\eta_P} \tag{1}$$

where  $m$  = bike mass including driver and passenger (380 kg),  $g$  = Earth’s gravitational acceleration,  $f_t$  = rolling friction coefficient (0.015),  $C_x$  = drag coefficient (0.65),  $\rho$  = air density,  $A$  = reference area (0.6 m<sup>2</sup>),  $V$  = vehicle speed,  $\eta$  = power transmission efficiency coefficient (0.98).

### 3 Components Description of the Proposed Bike

This gear-electric bike is proposed to have 900 W, 48 V, a brushless D-C motor, a motor controller, four lead-acid batteries, and four gears. The block diagram shows the components and the connections between them, so they can be easily identified. The parts are as follows: charger, battery, key or switch, controller, BLDC motor, transmission with gears, chain drive system, wheels, and throttle (Fig. 2).

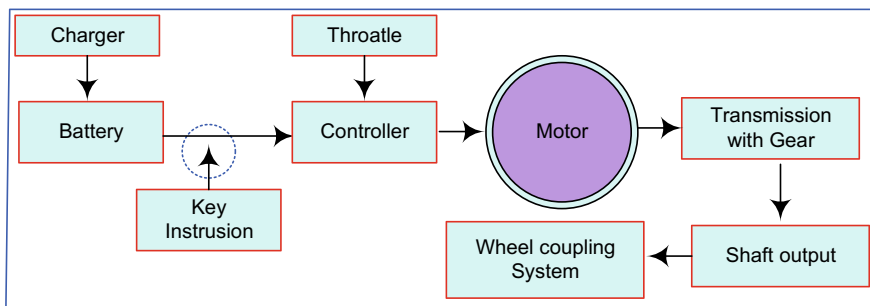
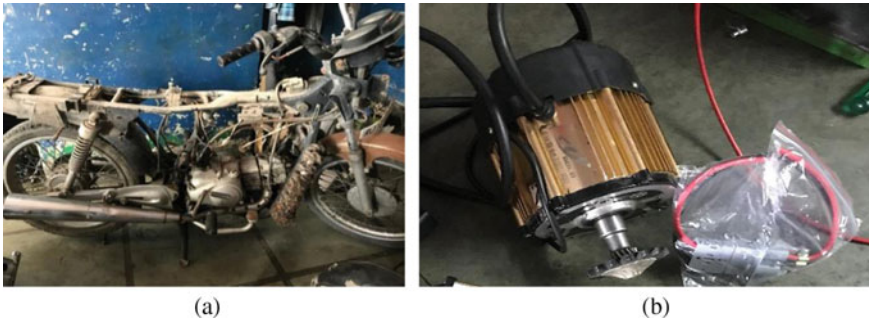


Fig. 2 Schematic diagram for proposed gear-electric bike





**Fig. 3** a Bike chassis and b brushless DC motor

### 3.1 Chassis

The main support structure of a motorbike is its frame. It supports the motor, contains the steering and rear suspension, and holds the rider, any additional passengers, and any baggage. The battery and energy storage device are also mounted to the frame. The pivot point for the swing arm suspension motion is at the rear of the frame, while the steering head tube, which supports the pivoting front fork, is placed at the front. Figure 3a shows the chassis of the bike used in this proposed project.

### 3.2 Brushless DC Motor

A BLDC motor is used in this proposal. Magnets and windings are found in the stator and rotor, respectively, of a brushless motor. Since there are no brushes, as the name implies, commutation in this case is carried out electronically by a drive amplifier that modifies the current in the windings depending on feedback from the rotor position. The BLDC motor is analogous to a reversed DC commutate motor in this regard, where the conductors are fixed, and the magnet revolves. As a result, internal or external position sensors are frequently used in BLDC motors to sense the real rotor position. The specifications of the BLDC motor used in the proposed bike are given in Table 1. Figure 3b shows the BLDC motor used in this proposed project.

**Table 1** Specifications of BLDC motor

Parameters	Value
Type	Brushless
Power	900 W
Voltage	24 V
Coolant	Air cool

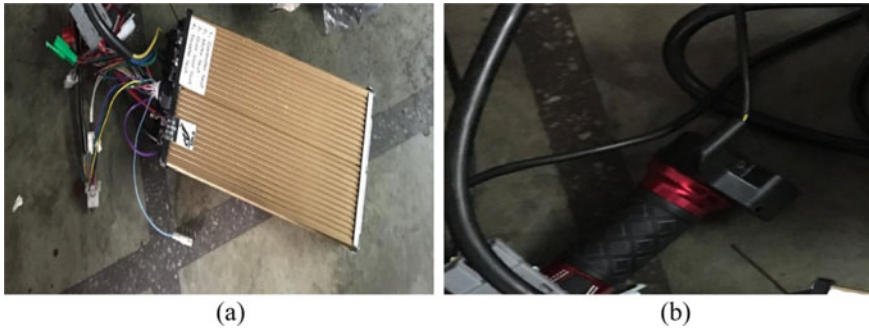


**Fig. 4** **a** BLDC motor controller and **b** bike throttle

### 3.3 Motor Controller

Brushless motors operating at currents of up to 90 A are used by controllers. These controllers use both internal signals and orders to regulate the speed, smooth start, and abrupt stop of brushless motors as shown in Fig. 4a. Speed control is provided by the BLD and BLSD series controllers in accordance with the voltage input signal (0–5 V DC) or the position of the internal potentiometer. It is also feasible to use an external potentiometer to regulate speed. Start/stop input is meant to initiate and halt motor spinning. The motor begins or stops according to the front edge of the signal at the “start/stop” input if this input is set to pulse logic by default (clean contact). Level logic may be substituted for input logic at the client’s request. Additionally conceivable is an open collector for PLC connections. A button on the controller’s casing serves as a replica of the start/stop input.

### 3.4 Throttle

There are several types of electric bikes with numerous options for turning on the electric aid. There are several varieties of throttles, including twist grip, thumb, push button, and pedal assist (torque sensor and cadence sensor). The motor supplies power and moves the bike forward when the throttle is opened. Several of the various throttle designs that may be seen on electric motorcycles include. This is the bike’s half-grip twist throttle. Similar to a motorbike or scooter, the throttle is opened by twisting it. The most typical e-bike throttle is this one. Figure 4b shows the throttle used in this proposed project.

**Table 2** Battery specifications

Parameters	Value
Type	Lead-acid
Voltage	12 W
Amp-hr	40
Nos	4

### 3.5 Battery

Two or more electric cells connected together form a battery. Chemical energy is transformed into electrical energy by the cells. A positive electrode and a negative electrode are connected by an electrolyte to form the cell. DC electricity is produced by a chemical interaction between the electrodes and the electrolyte. Lead-acid batteries, nickel-based batteries like nickel iron, nickel cadmium, and nickel metal hydride, lithium-based batteries like lithium polymer and lithium-ion batteries, and lithium-ion batteries are all possible options for EV batteries. We used four lead-acid batteries in this project, two in series and two in parallel, for a total of 24 V and 80 Ah. Table 2 shows the specifications of the batteries used in the proposed bike.

### 3.6 Mechanical Coupling

A coupling is a mechanical component that joins two shafts at their ends in order to convey power. The main function of couplings is to connect two pieces of spinning machinery while allowing some degree of end movement, misalignment, or both. Normal couplings prevent the separation of shafts while they are in use; however, some torque-limiting couplings can slide or detach if a predetermined torque limit is exceeded. Coupling selection, installation, and maintenance may cut down on maintenance time and expense. Figure 5a shows the mechanical coupling used in the proposed bike.

### 3.7 Gear Box

A bike's engine cannot operate at all speeds like it can in a traditional car. It has a speed limit below which it cannot operate smoothly and a speed limit over which it cannot rotate. The torque is quite low when the engine is spinning quickly. So, the wheels cannot be turned by the engine. In addition, when the engine turns slowly, the torque enables the engine to turn the wheels without difficulty. The engine must operate at a modest pace in order to provide the most torque upon starting. However, if we run the engine at a very low pace, it will shut off. In order to get maximum



**Fig. 5** a Mechanical coupling and b gear box

torque and start the wheel rolling, we thus employed gears to decrease the speed as shown in Fig. 5b.

The performance and pickup of this suggested electric bike have been enhanced by the inclusion of a gear box. Due to the poor road conditions in India, we have seen that vehicles without gears take more time to operate at constant speed. We frequently take breaks, which results in excessive energy use. The driving range is thereby reduced. An electric vehicle carrying two people moves at a relatively slow speed without gears and encounters difficulties on sloping terrain.

### 3.8 Chain and Sprocket

A toothed wheel that attaches to a shaft is called a sprocket. A key that inserts into keyways in the sprocket and shaft prevents it from rotating on the shaft. Two sprockets are joined together by a chain. The driver sprocket is one of the sprockets. From one shaft to another, and consequently from one sprocket to another, motion and force may be transferred via the chain. Power transmission chains are used to transfer motion and force from one sprocket to another. Figure 6 shows the assembly of different parts of the proposed electric bike.

## 4 Results and Discussion

A 900 W motor, a 24 V brushless DC motor, a motor controller, four lead-acid batteries, and four gears are included in this proposed gear-electric bike. This electric bike can run 140 km per charge, and the running cost is approx. 0.40 Rs. /Km with batteries (80 Ah). Gear increases the efficiency of the electric bike. Figure 7 depicts



**Fig. 6** Assembling of different part of the proposed electric bike

the proposed gear bike. Tables 3 and 4 illustrated the difference between bikes with and without gears.



**Fig. 7** Actual image of proposed geared electric bike

**Table 3** Performance parameters for without and with gear-bike (driver only)

Parameters	Without gear-bike	Proposed gear-bike
Top speed	40 km/hr	50 km/hr
Driving range	96 km/full charging	150 km/full charging
Pick up	Low	High
Cost/km	0.85 Rs	0.40 Rs
Charging time	8 h	8 h
Battery	Lead-acid 80 Ah	Lead-acid 80 Ah

**Table 4** Performance parameters for without and with gear-bike (two people)

Parameters	Without gear-bike	Proposed gear-bike
Top speed	34 km/hr	50 km/hr
Driving range	76 km/full charging	141 km/full charging
Pick up	Low	High
Cost/km	0.98 Rs	0.45 Rs
Charging time	8 h	8 h
Battery	Lead-acid 80 Ah	Lead-acid 80 Ah

The above results show that the proposed bike has significant parameter values when compared to a bike without gears. This electric bike can run 150 km per charge, and the running cost is approx. 0.40 INR/km with batteries (80 Ah). Hence, gear increases the efficiency of the electric bike. Figure 7 shows the actual image of the proposed gear-electric bike.

## 5 Conclusion

The purpose of this study is to design an efficient electric bike. Various performance parameters of two bikes (with and without gear) were recorded. Both bikes were run in similar road conditions. The performance of the proposed gear-electric bike was investigated by obtaining different parameters. The comparative analysis of the proposed gear-electric bike and one without an electric bike led us to understand the benefit of gears. After analysing the parameters, it was observed that gear not only increases the driving range of the bike and load capacity but also decreases the running cost. The overall cost of a gear bike, however, rises.

There is scope to enhance the performance of the proposed electric bike using lithium-ion batteries. Lithium-ion batteries not only improve the performance of the proposed bike but also reduce the vehicle's weight and space.

- To increase range and speed.
- Reducing the noise level.
- Sensor for start.
- Reduce charge time.
- More effective by reducing extra energy waste.
- Automation may be added.

The present study is explore the development of electric gear bike and also helpful for new learner.

## References

1. Butler KL, Ehsani M, Kamath P (1999) A MATLAB based modeling and simulation package for electric and hybrid electric vehicle design. *IEEE Trans Veh Technol* 48(6):1770–1778
2. Xianmin M (2022) Propulsion system control and simulation of electric vehicle in MATLAB software environment. In: Proceedings of IEEE world congress on intelligent control and automation on 10–14 June 2002 at Shanghai, China, pp 815–818
3. Fan BSM (2007) Modeling and simulation of a hybrid electric vehicle using MATLAB/Simulink. Master's thesis, University of Waterloo
4. Bauml T, Simic D (2008) Simulation and comparison of different energy management strategies of a series hybrid electric vehicle. In: Proceedings of IEEE vehicle power and propulsion conference (VPPC), 3–5 Sept 2008, Harbin, China, pp 1–5
5. Yafu Z, Cheng C (2008) Study on the powertrain for ISG mild hybrid electric vehicle. In: Proceeding of IEEE vehicle power and propulsion conference on 3–5 Sept 2008 at Harbin, pp 1–6
6. Barve DS (2016) Design and development of solar hybrid bicycle. *Int J Curr Eng Technol* 4:377–380
7. Karthi A, Afridhin N, Aravind D, Kamalesh G, Kumar KR (2020) Design and fabrication of an electric bike. *Int Res J Eng Technol* 7(2):2377–2383
8. Gupta V, Sharma N, Maram D, Priyadarshi H (2020) IOT enabled data acquisition system for electric vehicle. *AIP Conf Proc* 2294(1):1–8
9. Gupta V, Priyadarshi H, Goyal V, Singh K, Shrivastava A, Akhtar J (2020) BMS-driven onsite insolation charging infrastructure for electric vehicles. *AIP Conf Proc* 2294(1):1–10
10. Gupta V, Priyadarshi H, Goyal V, Singh K, Shrivastava A, Akhtar J (2020) Energy exchange modeling of super-capacitors for E-mobility applications. *AIP Conf Proc* 2294(1):1–10
11. Tomar A et al (eds) (2022) Proceedings of 3rd international conference on machine learning, advances in computing, renewable energy and communication: MARC 2021, vol 915, Pages XV, 781. ISBN: 978-981-19-2830-7. Springer Nature. <https://doi.org/10.1007/978-981-19-2828-4>



# Design and Development of a Solar-Based Wireless Electric Vehicle Charging System



Sanyam Jain, Samyak Jain, Sanjay Kumar, Harsh Kaushik, Neelu Nagpal, and Ravi Sharma

**Abstract** A new era of automobiles is upon us, with the industry rapidly transitioning from internal combustion engines to electric vehicles (EVs). The demand for EVs is growing, which has led to an increase in charging stations. Recently, wireless power transmission (WPT) technology has developed rapidly so the power ranges from milli-watts to kilo-watts, power transmission distances extend from millimeters to hundreds of millimeters, and load efficiencies exceed 90%. With this advancement, wireless power transmission (WPT) becomes very popular for deploying EV charging during both static and dynamic charging situations. This work proposes a design and implementation of a solar-based wireless EV battery charger where the objective is to charge a vehicle without connecting any wire through inductive coupling by simply parking of a car at the charging station. This study illustrates the applicability of WPT field technology for wireless charging of EV batteries in terms of charging time, range, and cost. The proposed charging system's performance is evaluated using black box and unit testing. Furthermore, the power efficiency of wireless charging systems is evaluated, with the conclusion that this charging outperforms wired charging.

**Keywords** Wireless charging · Electric vehicle · Solar energy · Sustainable

---

S. Jain (✉) · S. Jain · S. Kumar · H. Kaushik · N. Nagpal · R. Sharma  
EEE Department, Maharaja Agrasen Institute of Technology, Delhi 110086, India  
e-mail: [sanyam.04514804919@eee.mait.ac.in](mailto:sanyam.04514804919@eee.mait.ac.in)

S. Jain  
e-mail: [samyak.03814807820@eee.mait.ac.in](mailto:samyak.03814807820@eee.mait.ac.in)

S. Kumar  
e-mail: [sanjay.03914807820@eee.mait.ac.in](mailto:sanjay.03914807820@eee.mait.ac.in)

H. Kaushik  
e-mail: [harsh.04014804919@eee.mait.ac.in](mailto:harsh.04014804919@eee.mait.ac.in)

N. Nagpal  
e-mail: [neelunagpal@mait.ac.in](mailto:neelunagpal@mait.ac.in)

R. Sharma  
e-mail: [Ravisharma@mait.ac.in](mailto:Ravisharma@mait.ac.in)



# 1 Introduction

Road transport is the most widely used mode of transport worldwide. Car use has increased significantly, increasing demand for petrol and diesel. The widespread adoption of EVs is one of the key drivers for the sustainable transportation revolution. Recently, EVs have become more popular as they bring down the dependence on fossil fuels and carbon footprints. The issue with EVs is energy storage technology, which has a low energy density, a short service life, and a high cost. In this world of technological progress, latest technologies are emerging every day that make the civilian lives more convenient. Despite all this, we still rely on classic and traditional wired systems to charge our everyday electronic devices. Therefore, in this work, a new idea is proposed to wirelessly charge electric vehicles through the principle of inductive energy transfer using transmitting and receiving coils, reducing the size of the battery without the need for cables, and increasing convenience improve sexuality. EVs can be charged using either static wireless power transfer (SWPT) or dynamic wireless power transfer (DWPT). Traditional cable systems create confusion when charging multiple EVs simultaneously. It also occupies a lot of sockets on the charging port. Questions may arise at this point. “What if we could use a single technology to charge these electric vehicles simultaneously without using wires and without clutter?” We thought about it and came up with an idea of inductive coupling, a simple and effective way to transmit power wirelessly.

## 1.1 *Wireless Power Transmission (WPT)*

The effective transmission of electrical energy from one point to another through a vacuum/ atmosphere without the use of any conducting wire or materials is referred as WPT. It can be implemented where the conventional wire is inaccessible for instantaneous and continuous supply of energy. Thus, the issue of inconvenient, costly, dangerous, undesirable, or impossible power transfer can be overcome using (i) inductive coupling for short distances, (ii) resonance induction for medium distances, and (iii) electromagnetic wave power transmission for long distances. The basic theory developed with the concept of inductive power transfer has been utilized for WPT, and using this technology, power can be transmitted to those locations which are otherwise inaccessible or impractical. The technology of magnetic resonance WPT eliminates the need of bulky cables and facilitates the wireless transfer of electrical energy from a source to a consumer remotely following the Nikola Tesla’s greatest invention.

## ***1.2 Solar Energy***

The proposed charging system is solar-powered using solar panels. Solar panels are used to power the proposed charging system. This ensures a completely clean renewable energy source, free of air and water pollution and harmful emissions, obviating the need for any finite resources. Furthermore, the solar panel system is extremely durable, with some systems having a production life of more than 25 years and requiring little to no maintenance. The main maintenance required for these panels is an occasional dusting to remove dirt, leaves, or other debris that must be cleaned by a professional on a regular basis.

## ***1.3 Requirement***

The advancement of civilization has exacerbated global warming due to the release of greenhouse gases and the use of fossil fuels, which is a serious issue. This has made energy conservation and emission reduction even more important. In this regard, the transport sector is gaining attention all over the world because it is a major contributor to greenhouse gas emissions. As a well-known clean energy source, electrical energy can be obtained from renewable energy sources such as solar and wind. Contrast to conventional vehicles (powered by fossil fuels), EVs are powered by electrical energy have the unique advantage of zero emissions. In contrast to conventional vehicles (which use fossil fuels), electric vehicles (EVs) have the distinct advantage of emitting no emissions. As a result, EVs have emerged as a viable option for the transportation sector to drive the optimization of its energy requirements. The high cost, limited capacity, and range of EV battery packs, on the other hand, limit further EV promotion. If the charging procedure is compared, then alternative to the conventional plug-in charging, WPT charging is preferred as there is no physical contact between the source and the load during charging. Thus, the proposed WPT method results more flexible and safe charging process and classified as SWPT and DWPT. DWPT charging is developed on the basis of SWPT charging, which can effectively reduce the capacity of the vehicle's battery pack, extend the driving range, and further improve the convenience of charging. The main goal of the work is to install Wireless Charging Paths (WCP) on Electric Vehicle Service Roads (EVSR) in order to facilitate service roads for wireless charging of EVs while driving. This framework provides a cable less system that reduces the complexity of the EV charging process. It is already mentioned that in the proposed work, the power required to charge EVs is generated from solar panels.

## ***1.4 Existing System***

In existing systems, charging modules are installed under park road slots in public places. The drawback of this system is that the electric vehicle can only be charged when it is parked at a specific location with charging stations. This causes many serious problems. First, in order to use the charging point for another EV, the EV must leave the dedicated parking space immediately after charging. This doesn't always happen. Second, with the proliferation of electric vehicles, every parking lot may need to be equipped with a charging station. This increases the cost of installing charging infrastructure that is not 100.

## ***1.5 Objective***

The goal of this work is to design and develop an EV charging infrastructure that will function as a charging platform for wirelessly transmitting electrical energy through space and charging batteries. The system works by using inductive coupling to transfer energy from the transmitter to the electric vehicle's resistive load or battery. The method proposed here simplifies the procedure of charging EV batteries by eliminating the need for cables. It also ensures battery safety by removing the possibility of battery damage.

## **2 Literature Review**

The investigation of Supriyadi et al. [1] has shown that the effect of wire diameter (AWG) and the number of turns used is directly proportional to the power that can be transmitted. The greater the number of turns, the more power is transferred. Assume an enameled copper wire with a diameter of 0.5 mm is used with 26 turns and an input frequency of 470 kHz. At 1 cm distance, the power efficiency is approximately 1.51. Uthaya Banu et al. [2] have represented a variety of technologies related to WPT systems. These systems have been used to avoid flux loss during power transmission, make vehicles run with high efficiency, and improve quality parameters. The study also demonstrates progress in generating electricity from renewable sources. Further, Yatnalkar and Narman [3] have outlined the limited charging time of EVs. As a result, wireless charging of EVs can solve the problem of charging time. This document also included the most recent wireless charging scenarios for EVs, as well as the parameters required for the charging section. The most important parameters for wireless charging of EVs are the distance between the transmitting and receiving coils, the position of the EV coils, the size of the battery, and the charging time. Electric cars need charging stations, and like current fuel cars, they need gas pumps, and of course charging takes time, so charging while parked is more efficient. It can

be combined with IoT technology that makes the system easy to use where particulars can be transferred to the cloud and smartphone at the same time. Parked car safety is one of the problems individuals face. The health of WPT systems can be monitored using the IoT that offers broader connectivity, change detection, intelligence processing, and flexibility [4]. Thus while parking, the involvement of IoT has provided easily monitoring of parking and charging at the same time that helps synchronous parking. Another key factor in leveraging IoT is the ability to store data in the cloud that can be accessed anytime, anywhere, making life easier and simpler. To charge a car, one needs a charging station so that he can incorporate his assigned parking lot concept as an electric station where he can park and charge his car [5]. Thus, this system has many advantages. Timpner and Wolf [6] also noted that the current transport infrastructure and parking facilities cannot keep up with the influx of vehicles on the streets, causing great damage to the environment and the economy, such as the time it takes to find a parking space gain. Therefore, we need an approach that can support electric vehicles and their charging needs and use parking and charging infrastructure as efficiently as possible. A centralized planning system for electric vehicle (EV) charging in car parks has been developed by Kuran et al. [7]. The system is based on realistic vehicle parking patterns focused on individual parking spaces. Based on mobility, consider two types of electric vehicles. One is regular electric car, and the other is non-regular electric car. EVs need plenty of time to charge. In this work, a PLRS system is suggested that records vehicle departure and arrival times, EV battery status, and mileage. The system then creates a unique charging plan for an EV. This system works day and night and can increase the number of EV charging units and parking revenue. The proposed system features a two-layer PLRS system for charging electric vehicles based on their parking patterns. Sultanbek et al. [8] have given an overview of intelligent wireless charging stations for EVs and concluded that inductive or magnetic coupling techniques are suitable methods for WPT for EV charging.

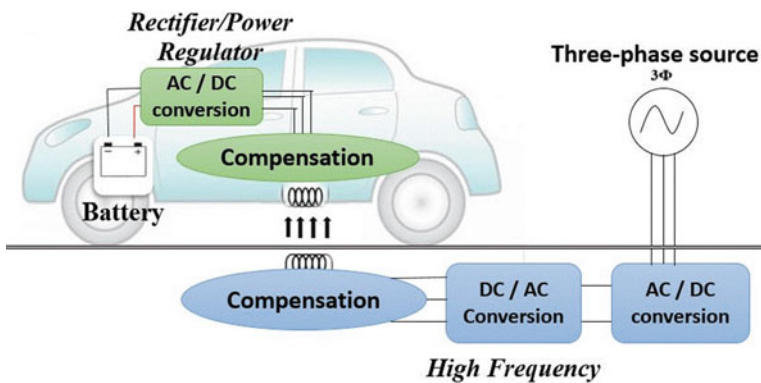


Fig. 1 Picture demonstration of wireless charging

In this study, an intelligent WPT system for charging electric vehicles is presented and simulated. Misalignment affects charging, so innovative ways to improve the flexibility of EV wireless charging are needed. This technology uses fingerprinting to automatically align transmit and receive coils. The proposed system saves the necessary time, minimizes human error, minimizes energy consumption, and can also charge the car based on real-time information about the system. It is very useful for EV customers to save energy and reduce electricity bills. Wireless charging is a new development area for EV charging. This article demonstrates the efficiency of resonant inductive coupling in EV charging and explains techniques that upgrade wireless charging performance for high frequency and high-power applications. Various coil-hi alignment methods were discussed and fingerprinting was presented as an economical technique for generating WPT intelligence. Another procedure to the EV charging planning problem is presented in [9]. In this article, we'll look at parking billing issues where you need to make the most of your time. When the electric vehicle comes at the garage entrance, it gets details such as estimated arrival time, estimated departure time, current and required battery SOC, and garage charging management system (CMS) [10]. This CMS can decide whether to accept or reject the customer's statement. Manage desired performance based on decisions. Once the process is complete, the power will be disabled. All charging units are controlled by a clever charging network. Power is managed by CMS, and all charging activities are switched automatically. EVs that are not being serviced by the system will be parked in non-charging areas. The following are some important points of the work:

- This paper provides a research overview of static and dynamic wireless charging systems for EVs that contains information on proposed wireless charging for high-power applications, including EVs. Wireless charging has many precedence over plug-in charging due to its simplicity, reliability, and ease of use. A con is that it can be used when the vehicle is in non-moving mode.
- The paper mentions that EVs would make electricity an integral part of transportation. Wireless charging plays a key role in facilitating the charging of EVs, providing efficient and flexible charging methods. Also, the standardization of this technology is underway, providing more ease of use and freedom when charging vehicles in wireless parking lots.
- As the number of EVs grows, new charging infrastructure must be built. Wireless charging is more efficient than plugs and cables. This article describes the basic principles of resonant inductive energy transfer commonly used in wireless charging. As the number of these EVs increases, the problems associated with them must be resolved. There are basically three types of charging methods: battery replacement, conductive charging, and wireless charging transmission. Currently, the EV industry is developing at full speed around the world, bringing various charging infrastructures to market. However, wireless power transfer faces several challenges in the absence of complete and comprehensive standards.
- This article releases a report on intelligent parking systems. The proposed system implements an intelligent parking system, an on-site deployment of slot models used to monitor vacant spaces and reserve parking spaces. Smart parking can

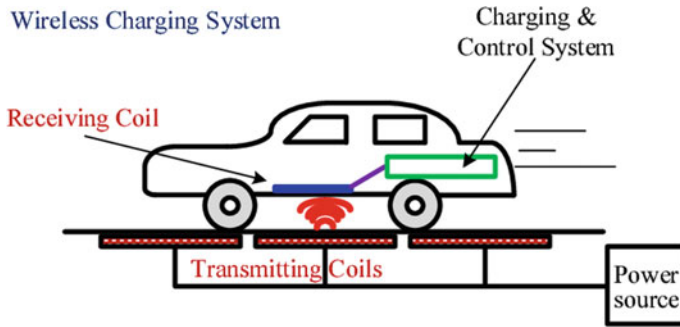


Fig. 2 Picture demonstration of wireless charging of an electric vehicle using transmitter coils and receiver coils

improve economics by doing less fuel consumption and pollution in city. Smart parking can be an application of IoT. It also offers the possibility to reserve slots. As soon as you enter the slot period, users start leaving the slot later. The user has to pay the amount for the period his car is slotted (Fig. 2).

### 3 Design and Implementation

#### 3.1 Block Diagram

The output of timer IC is applied to an inverter circuit to invert the oscillating signal and represent it as signal 2. Signal 1, on the other hand, represents the non-inverted oscillating signal. This oscillating signal, both original and inverted, is applied to the MOSFET driver IC to generate high and low pulses to trigger the gate of the MOSFET terminal. It is formed as a driver circuit. This driver circuit sent AC power to the LC circuit. This current flowing through the inductor and capacitor creates a magnetic field (Fig. 3).

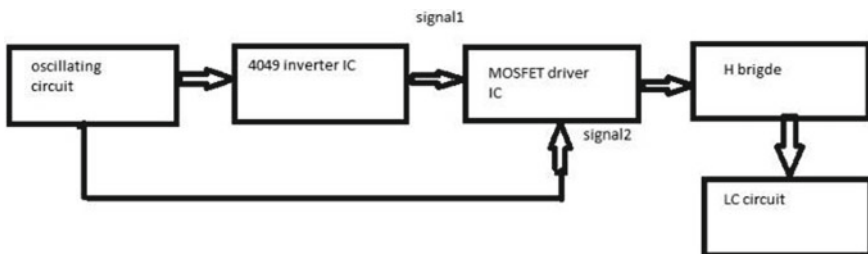
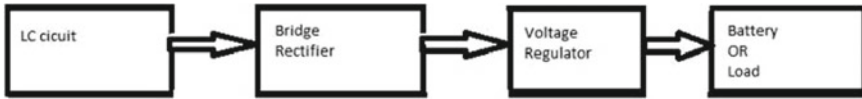


Fig. 3 Block diagram of primary circuit of WPT



**Fig. 4** Block diagram of secondary circuit of WPT

A coil from the primary receives energy and creates a magnetic field around the coil. Due to the use of high frequency output, the magnetic flux is very strong. When the magnetic flux from the primary coil connects to the secondary or receiving coil, a current is induced in the parallel connected inductor and capacitor. The voltage generator across the LC circuit is AC and this AC signal is applied to the bridge rectifier circuit. This circuit converts AC to DC and connects a capacitor to the output to generate a smooth DC signal. A voltage regulator is used to limit the voltage to prevent damage to the load (Fig. 4).

### **3.2** *Circuit Diagram*

See Fig. 5.

### **3.3** *Code*

See Fig. 6.

## **4** *Performance Analysis*

### **4.1** *System Testing*

A sensitive product framework is to look at a fully integrated machine to assess its suitability for precise requirements. Device testing also falls into the realm of darkroom viewing, and this method does not require any data or code about the inner workings of mind beings. Its conscious diamond lettering is absolutely comparable. Within the check case label, it should be possible to match the situation of the check case with the use case beyond it.

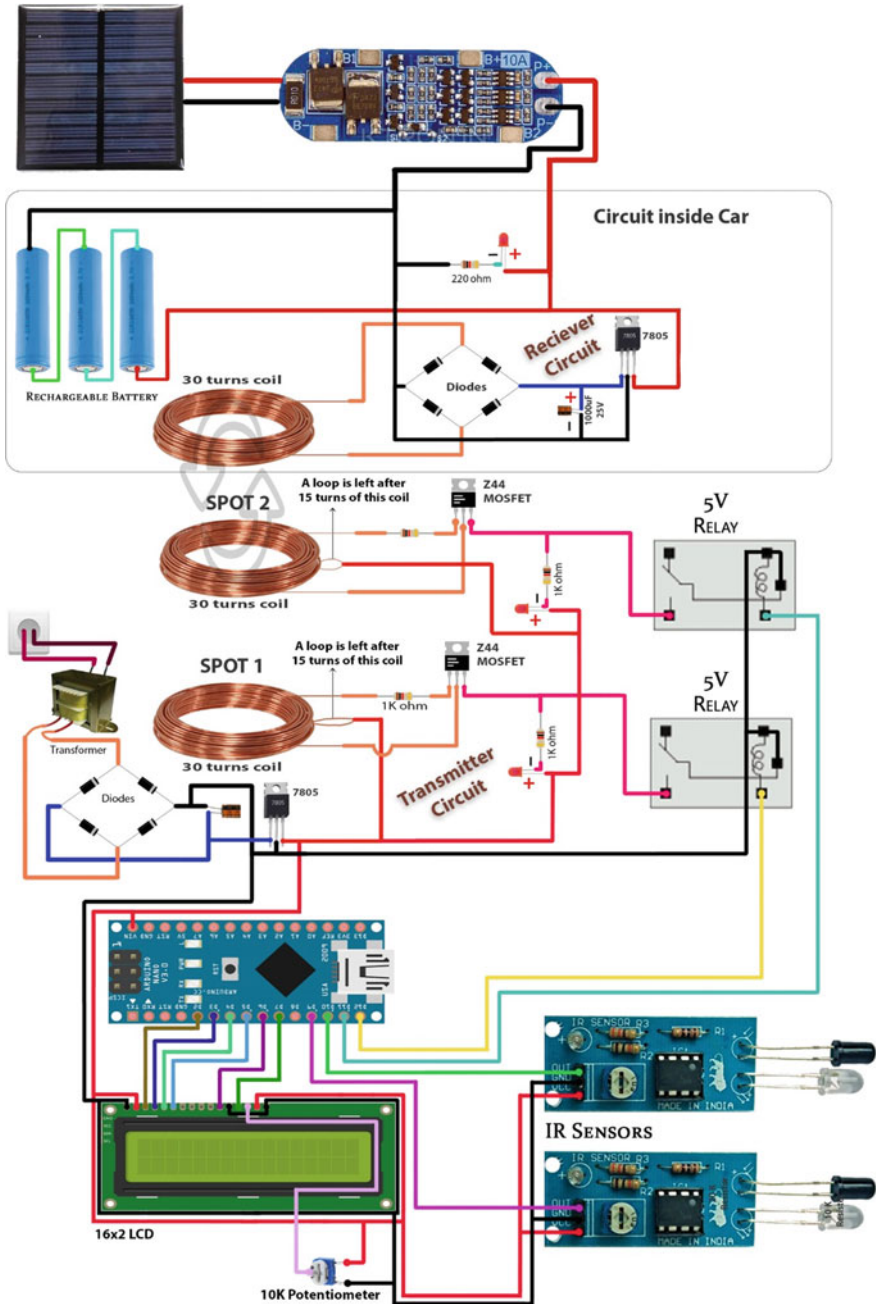


Fig. 5 Circuit diagram



```

1  #include<LiquidCrystal.h>
2  LiquidCrystal lcd(2, 3, 4, 5, 6, 7);
3
4  int ir[2] = {9,10};
5  int re[2] = {11,12};
6
7  void setup() {
8      lcd.begin(16, 2);
9      lcd.clear();
10     lcd.setCursor(0, 0);
11     lcd.print("Wireless Vehicle");
12     lcd.setCursor(0, 1);
13     lcd.print("Charging System");
14     pinMode(ir[0],INPUT);
15     pinMode(ir[1],INPUT);
16     pinMode(re[0],OUTPUT);
17     pinMode(re[1],OUTPUT);
18     delay(3000);
19     lcd.clear();
20     lcd.setCursor(1, 0);
21     lcd.print("Spot1");
22     lcd.setCursor(10, 0);
23     lcd.print("Spot2");
24 }
25
26 void loop() {
27     if(digitalRead(ir[0])) {
28         digitalWrite(re[0],HIGH);
29         lcd.setCursor(0, 1);
30         lcd.print("Charge");
31     }
32     else {
33         digitalWrite(re[0],LOW);
34         lcd.setCursor(0, 1);
35         lcd.print(" OFF ");
36     }
37
38     if(digitalRead(ir[1])) {
39         digitalWrite(re[1],HIGH);
40         lcd.setCursor(9, 1);
41         lcd.print("Charge");
42     }
43     else {
44         digitalWrite(re[1],LOW);
45         lcd.setCursor(9, 1);
46         lcd.print(" OFF ");
47     }
48 }

```

Fig. 6 Code

## 4.2 Black Box Testing

Black box analysis is “an approach to test programming that reveals the functionality and behavior of a product without examining its inner workings or behavior. Understanding of the product’s form, code, and programming is typically not required.”

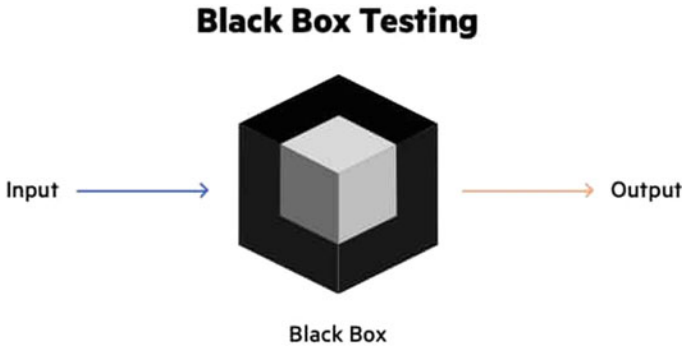


**Fig. 7** Black box testing

Furthermore, the analyzer happily responds that in this case the final infinite yield can be recovered by careful input, but I'm not sure how to do it in general. Elements convey yields at key points (Fig. 7).

### 4.3 Unit Testing

Throughout PC programming and coding, these unit tests are used to process specific units or fixed units of shipping code and possibly additional PC programming components and associated control record procedures and experienced work practices. We will help you how to deal with which product testing. Analyze whether it is suitable for use. You can also instinctively find the unit as the smallest testable component of your device. In this procedural programming context, our unit may be an entire module, but it is much more common to be of a masculine or feminine type or trait. The goal of the unit review is to isolate all the details of this system and show that the human factor is correct (Fig. 8).

## 5 Power Efficiency

Plugin loading is not 100% efficient. Energy losses, mainly in the form of heat, occur at every step from the grid to the battery. Additionally, regardless of brand, plug-in EV chargers consist of many components, each of which may be more or less efficient than similar components in another charger. So the "efficiency" of transferring energy from the grid to the battery includes a range. A typical Level 2 home charger operates in the range of about 83–94% efficiency from mains to battery, depending on what you buy. In an electric vehicle plug-in AC charging scenario, the onboard charger (OBC) does the heavy lifting for the vehicle. This includes rectifier PFC, inverter,

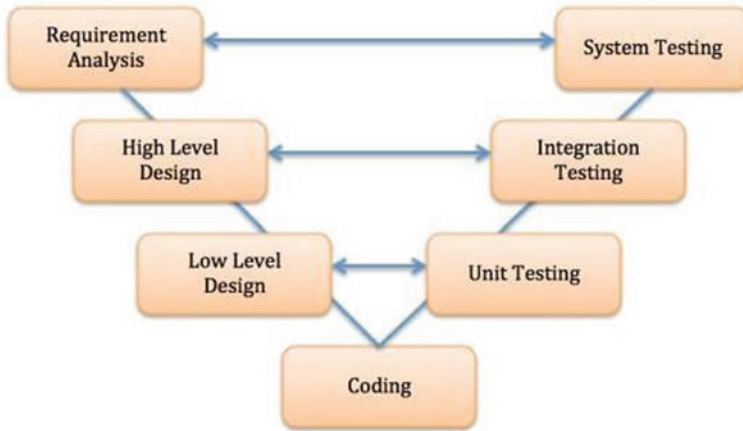


**Fig. 8** Unit testing

transformer, and rectifier. The main power source is electricity that can be used by electric vehicle batteries. However, wireless charging reduces the complexity of onboard charging by eliminating the need for an onboard charger (OBC). Be careful with the gap. So why isn't the "gap" between the floor panel and the vehicle a loss? It seems counter-intuitive that space doesn't lead to inefficiency.

Ground Pads and Vehicle Pads convert alternating current into a magnetic field and transfer the energy to the air gap. It also uses magnetic resonance to transfer energy in specially designed low-loss resonators, resulting in very low losses. In fact, the air gap between the ground and the vehicle serves the same safety function as the isolation created by the isolation transformer (in the OBC between the mains connection and vehicle) during plug-in charging. Due to the wireless charger's high resonance design, it is nearly as efficient as the isolation transformer used for plug-in charging. The wireless charging operates in a narrow efficiency band (88–93%) equivalent to Level 2 plug-in charging, giving you the extra efficiency of not having to spend time plugging and unplugging your vehicle. Last but not least, every time during park and charge wireless, it is more likely to operate in the 20–80% state-of-charge (SOC) range that the battery prefers, which is the most efficient. With plug-in charging, drivers tend to forget about plugging in or don't care even though they know they have plenty of spare batteries for the next trip, so 20–80% of his SOC range is less likely to be maintained. In fact, many people plug-in once a week, drive all week, and plug-in on weekends. Not only is this less efficient but it's harder on the battery.

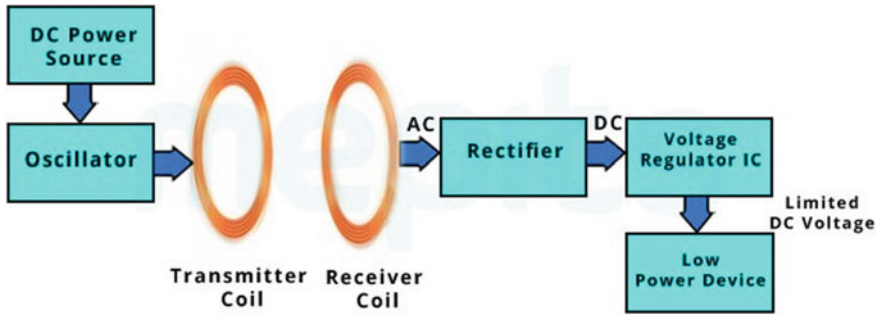


Fig. 9 Block diagram of tested working system

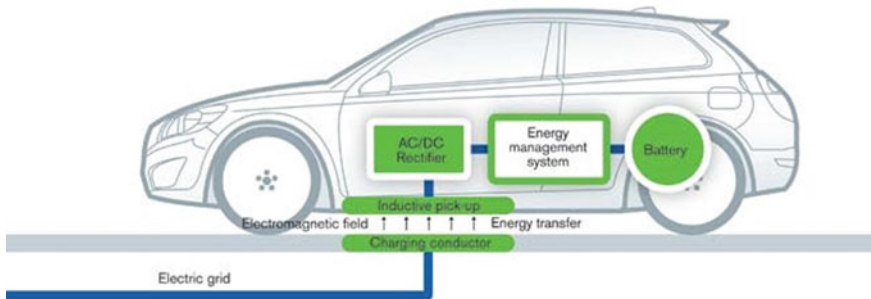


Fig. 10 Tested working system

## 6 Conclusion

This system introduces wireless energy transfer. Just as electric vehicles are on the rise in the market. You can charge your vehicle using the wireless charging system. This system demonstrates the performance and implementation of charging stations in the future technologies. Overall, this paper compares different intelligent parking, charging, and combined charging and parking systems to solve a variety of related problems. The paper has a comparative table of various research papers. It tells about the different types of procedures and techniques used for parking and charging. This system does not require human intervention, and wireless power supply has the potential to become one of the technologies that will take a step into the future. This research can open up new possibilities for wireless charging that can be used in everyday life (Figs. 9 and 10).

## References

1. Supriyadi, Rakhman E, Suyanto, Rahman A, Basjaruddin NC (2018) Development of a wireless power transfer circuit based on inductive coupling. *TELKOMNIKA* 16(3):1013–1018
2. Uthaya Banu N, Arun Kumar U, Gokula Kannan A, Hari Prasad MK, Shathish Sharma AB (2018) Wireless power transfer in electric vehicle by using solar energy. *Asian J Electr Sci* 7(1)
3. Yatnalkar G, Narman H (2018) Survey on wireless charging and placement of stations for electric vehicles. In: Conference: 2018 IEEE international symposium on signal processing and information technology (ISSPIT), Dec 2018
4. Rana MdM, Xiang W (2018) Internet of things infrastructure for wireless power transfer systems. *IEEE Access* 6:19295–19303
5. Rupani S, Doshi N (2019) A review on smart parking using internet of things (IOT). In: The 3rd international workshop on recent advances on internet of things: technology and application approaches (IoT-T and A 2019), Nov 2019, Coimbra, Portugal
6. Timpner J, Wolf L (2012) A back-end system for an autonomous parking and charging system for electrical vehicles. In: International electrical vehicle conference, Greenville, SC, USA. IEEE
7. Kuran M, Viana A, Iannone L, Kofman D, Mermoud G, Vasseur JP (2015) A smart parking lot management system for scheduling the recharging of electric vehicles. *IEEE Trans Smart Grid* 6:1–1. <https://doi.org/10.1109/TSG.2015.2403287>
8. Sultanbek A, Khassenov A, Kanapyanov Y, Kenzhegaliyeva M, Nagheri M (2017) Intelligent wireless charging station for electrical vehicles. In: International Siberian conference on control and communication. IEEE
9. Wei Z, Li Y, Zhang Y, Cal L (2018) Intelligent parking garage EV charging scheduling considering battery charging characteristic. *IEEE Trans Ind Electron* 65
10. Tomar A et al (eds) (2022) Proceedings of 3rd international conference on machine learning. Advances in computing, renewable energy and communication: MARC 2021, vol 915, p XV, 781. Springer Nature. <https://doi.org/10.1007/978-981-19-2828-4>, ISBN: 978-981-19-2830-7

# Design, Optimization, and Performance Enhancement of Switched Reluctance Motor for Pollution-Free Electric Vehicle Application



Kesar Ali, Arbaz Sher Khan Shaikh, Kirti Govind, Javid Navaj Shaikh, Yogesh B. Mandake, and Deepak S. Bankar

**Abstract** Recent years have seen an increase in global air pollution, and citizens in urban areas suffer grave health problems. In India, transportation accounts for 24% of India's carbon emissions, exacerbated by the use of motor vehicles and petroleum consumption. Research and development on new propulsion systems have resulted from the need for clean energy and carbon emissions reduction. Greenhouse gas emissions can be reduced by using electric vehicles. Furthermore, it promotes the use of renewable energy on a large scale, thereby reducing dependence on fossil fuels. The majority of electric vehicles with two or three wheels utilize BLDC motors. Electric cars use several kinds of three-phase induction motors. Using less magnets reduces our dependence on China, which is the largest exporter of rare Earth magnets. In the electric vehicle market, SRM will facilitate "MAKE IN INDIA". A magnet-free design, high speed, fault tolerance, and reliable structure make SRMS ideal for electric vehicles. This paper proposes 0.5 kW, 2000 rpm and an 8/6 topology for designing and optimizing an efficient SRM configuration parameter of the stator and rotor. In EV-SRM material simulation, Ansys Maxwell software (RMxprt tool) is

---

K. Ali (✉) · A. S. Shaikh · K. Govind · J. N. Shaikh · Y. B. Mandake · D. S. Bankar  
Department of Electrical Engineering, Bharati Vidyapeeth (Deemed to be University) College of Engineering, Pune, India  
e-mail: [kali20-elect@bvucoep.edu.in](mailto:kali20-elect@bvucoep.edu.in)

A. S. Shaikh  
e-mail: [sasher Khan20-elect@bvucoep.edu.in](mailto:sasher Khan20-elect@bvucoep.edu.in)

K. Govind  
e-mail: [kirit1-coep@bvucoep.edu.in](mailto:kirit1-coep@bvucoep.edu.in)

J. N. Shaikh  
e-mail: [jnshaikh20-elect@bvucoep.edu.in](mailto:jnshaikh20-elect@bvucoep.edu.in)

Y. B. Mandake  
e-mail: [yogesh.mandake@bvucoep.edu.in](mailto:yogesh.mandake@bvucoep.edu.in)

D. S. Bankar  
e-mail: [dsbankar@bvucoep.edu.in](mailto:dsbankar@bvucoep.edu.in)

used for analysis and optimization of power, torque density, losses, efficiency, and torque ripple.

**Keywords** Global air pollution · Carbon emissions · Renewable energy · Switched reluctance motor (SRM) · Brushless direct current motors (BLDC) · Make in India · Ansys Maxwell software (RMxpert tool) · Electrical vehicle (EV)

## 1 Introduction

### 1.1 Environmental Impact

Global air pollution accounts for seven million deaths every year, which makes it the world's biggest environmental health risk. Rapid economic growth brings increased vehicle ownership, which contributes to environmental problems. For instance, the usage of combustion engine vehicles has led to an increase in petroleum consumption, air pollution, and global warming. New propulsion systems have been developed in response to the need for clean energy and the reduction of carbon emissions from internal combustion engines. Electrical vehicles powered by electric motors contribute significantly to the reduction of greenhouse gas emissions. This encourages the widespread use of renewable energy sources and lessens reliance on fossil fuels while also decreasing ozone-depleting.

### 1.2 Comparative Study of IC Engine and EV Motors

In the current day, there is no doubt that conventional internal combustion engines (ICEs) are less fuel-efficient and generate significant amounts of greenhouse gases (GHGs); however, electrifying vehicles can be both a solution to these issues as well as a means of reducing fossil fuel consumption.

Figure 1 shows Indian oil consumption. ICEV owners spend a lot of money on fuel consumption, and according to data collected by the Census and Economic Information Center (CEIC), the country consumes 4,878,175 barrels of oil per year, most of which is imported. The costs spent on fossil fuels have been increasing rapidly in the past few years. Smart Grid Technology (SGT) can manage the increased electricity costs that result from EVs efficiently by reducing energy wastage by communication and keeping it to a minimum. It is observed that ICEVs have a lower power conversion efficiency since the engine power is transferred through various channels before reaching the wheels, resulting in huge mechanical losses. In contrast, electric vehicles use a simple channel to transfer power to the wheels, reducing mechanical losses and increasing transmission efficiency. Because the electric vehicle system uses a battery to power it, greenhouse gas emissions are negligible.

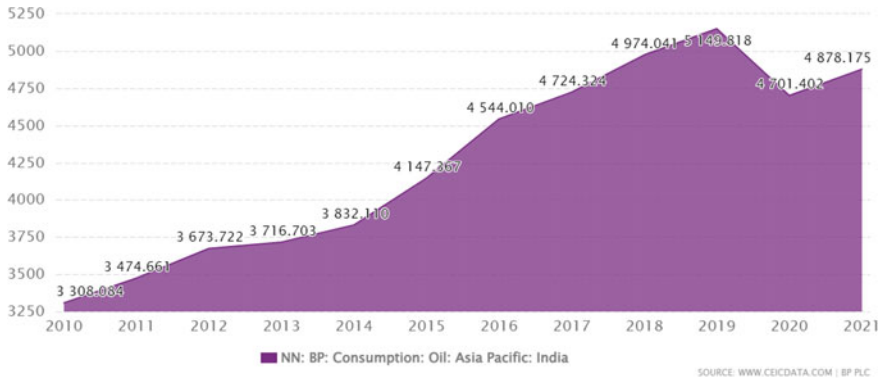


**Fig. 1** Oil consumption in India [1]

### 1.3 Motor Used in Electrical Vehicle

In the last few years, electrification of vehicles has surged, especially when it comes to “last mile connectivity”, where three-wheelers are most useful. Two- and three-wheeled electric vehicles use BLDC motors about 90% of the time. Induction motors power electric cars. In permanent magnet synchronous motors (PMSM) and brushless direct current motors (BLDC), rare Earth magnets are required, and they are therefore more expensive. As China is the largest exporter of rare Earth magnets in the world, reducing our use of magnets directly leads to a reduction in our dependency on them. E-Vehicles must be produced with a motor that is low cost, highly reliable, and has a high-power density over the long term in order to achieve mass production and long-term productivity. In comparison with BLDC and PMSM, SRM is more promising, low cost, low inertia rotor, no rotor loss, high reliability, small size, robust in construction, easy to cool, high pickup, high operating speed, etc. [2]. Furthermore, SRM doesn’t use rare Earth magnets and reduces dependence on countries that manufacture them [3].

### 1.4 Switched Reluctance Motor (SRM)

In SRMs, the separate phase windings are invigorated sequentially by rotor position switches. It is plausible that a wide range of speeds will be possible. It must be ensured that the rotor moves to a location where the lowest reluctance is found, so that torque can be produced. In EVs, SRMs are suitable since they can handle non-critical faults easily and have a high starting torque. There is a progressive progression of phases in the current flowing through the lead edge of the stator. This progression determines how the activity of uniform power is influenced by the phase progression of the current in the lead edge in the Fig. 2.



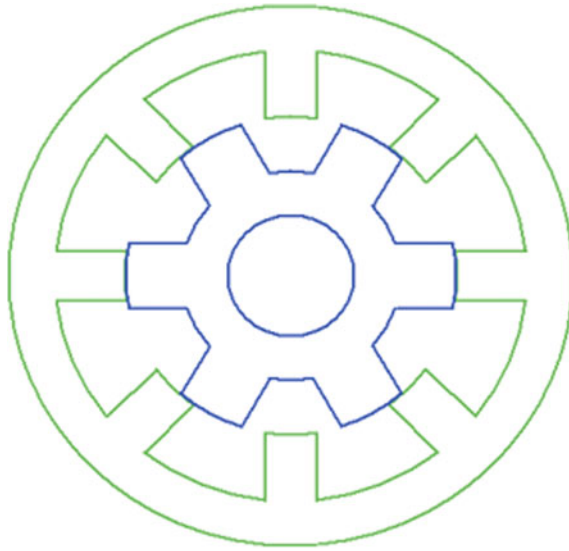


**Fig. 2** Schematic diagram of SRM

## 2 Problem Identification

- In India, there are currently 15 lakh electric rickshaws, and about 11,000 new ones are added each month. These numbers could be much higher as a large percentage is yet to be registered. The market is expected to sell 9.25 lakh E-Vehicles by 2024.
- The BLDC motors currently used in E-Vehicles are made of rare Earth magnets imported mainly from China. Rare Earth magnets are produced in about 60% of the world.
- There are many major problems associated with mining of magnets, such as health issues for laborers involved in extraction, environmental pollution, etc. [4].
- SRMs have high torque ripple, low-power density, low-power factor, etc.
- Torque ripple creates acoustic noise and vibration that degrades performance.

So, this research work is focused on design optimization and performance enhancement of switched reluctance motor for E-Vehicle application.

### 3 Various Techniques to Enhancing the Performance

- Commutation Angle Optimization: Torque ripple reduction methods begin with commutation angle optimization. Online or offline optimizations of the commutation angle are possible [5].
- The slot shapes of the switched reluctance motor (SRM) with double stator axial field (AF) were developed for automotive fan applications to achieve higher efficiency [6].
- Annealing removes the damage and increases the grain size, resulting in a reduction in iron losses and an increase in permeability after annealing. The measured performance of the two SRMs shows that the motor with the annealed steel has higher torque and power density, with higher efficiency at high torque loads [7].
- Direct instantaneous torque control (DITC) techniques are used for minimization of torque ripple in switched reluctance motor drive [8].
- Torque Sharing Function (TSF): This method controls the rate of change of torque rather than the change of current during commutation [9, 10].
- Sliding-mode control method (SMCM) and intelligent fuzzy technique (FIT) have proposed methods to reduce the torque ripple of SRM [11].
- A nonlinear  $k(\theta, i)$ —factor-based technique for minimizing torque ripple in 8/6 four-phase SRM drives. Torque ripple is reduced by modifying the incoming phase current reference based on the outgoing current [12].
- Torque ripple minimization of switched reluctance motor using sense coils [13].

### 4 Selection of Stator and Rotor Poles

There is a direct relationship between the number of rotor poles and that of stator poles on SRM performance parameters such as torque ripple and peak torque. The torque ripple in non-saturated operating regions is decreased for SRMs with more poles. A SRM is often used where  $(N_s) > (N_r)$ . There are three topologies (10/8, 8/6, and 6/4) and different topologies are used for different applications [14]. Two opposite poles correspond to one phase in all topologies, like as 10/8 according to topology, there are five phases, whereas in the 8/6 SRM, there are four phases, etc. It is recommended to use 10/8 and 8/6 rather than 6/4 for electric vehicles. Using the 10/8 topology requires many switches for its drive, which is expensive. 8/6 topology is affected by torque ripple. We selected a motor topology 8/6 in order to solve this problem, since it was tuned properly according to the application.

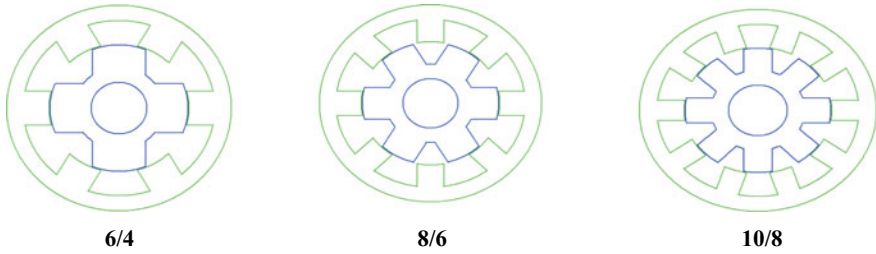


**Fig. 3** Common SRM topologies

**Table 1** Model

Sr. No	Model	Number of phases	Total loss (W)	Rated torque (Nm)	Rated speed (rpm)	Efficiency (%)
1	6/4	3 phases	79.5347	1.91478	2483.75	86.2293
2	8/6	4 phases	63.232	2.32666	2040.88	88.7184
3	10/8	5 phases	58.2793	2.66488	1778.18	89.4899

### 5 An E-Vehicle SRM Design Approach

A SRM’s design specification includes the power output  $P_{kW}$  in kW, the speed  $N$  in rpm, allowable peak phase current  $i_p$  in amps, and the supply voltage  $V_{ac}$  in volts. Automatic torque development is determined by knowing the speed and power output (Table 2),

$$T_{req} = \frac{P_{kW}}{2\pi (N \div 60)} \text{ N m}$$

$$T_{req} = \frac{0.5 \times 1000}{2\pi \times 2000} \times 60$$

$$T_{req} = 2.38732 \text{ N m}$$

**Table 2** Specifications of SRM

General data			
Sr. No	Parameters	Evaluated value	Units
1	Rated output power	0.5	kW
2	Rated voltage	48	V
3	Poles ratio	8/6	–
4	Rated speed	2000	rpm

### 5.1 Frame Size Selection

SRMs are designed based on a comparison with equivalent induction motors [IEC71] when determining their physical dimensions. Designed to comply with IEC recommendations, the machine has a frame size of 63 mm (Figs. 4 and 5).

- The stator’s outer diameter can be given by,

$$D_o = (\text{Frame size} - 3) \times 2$$

$$D_o = (63 - 3) \times 2 = 120 \text{ mm}$$

The standard configuration for electric vehicle applications consists of  $N_s = 8$  and  $N_r = 6$ . This configuration is the most efficient and economical configuration for the application of electric vehicles (Table 3).

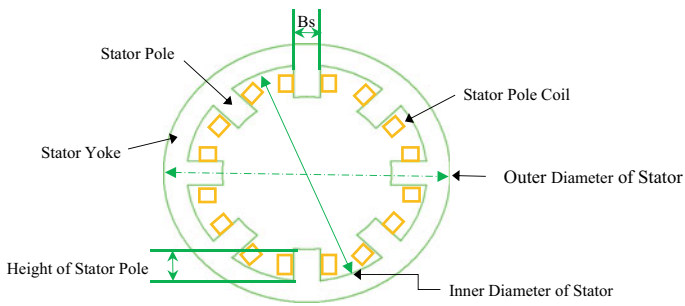


Fig. 4 Stator dimension

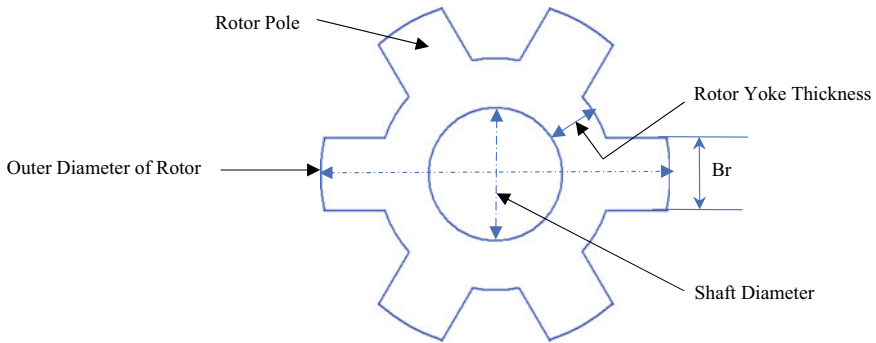


Fig. 5 Rotor dimension

**Table 3** Stator and rotor dimension

Stator and rotor core data			
Sr. No	Parameters	Evaluated value	Units
1	Number of stator poles	8	No
2	Outer diameter of stator	120	mm
3	Inner diameter of stator	65	mm
4	Length of stator core	85	mm
5	Number of rotor poles	6	No
6	Rotor outer diameter	64.6	mm
7	Inner diameter of rotor	22	mm
8	Length of air gap	0.2	mm
9	Length of rotor core	90	mm

### 6 Drive Circuit

The conventional drive circuit of the SRM is shown in Fig. 6. Ansys Maxwell software is used to obtain this information. The kind of circuit used is a full voltage circuit that is driven by a constant power load at a constant voltage. Based on analyzing the system, the trigger pulse width is 120°, the diode loss is 2.18662 W, and the transistor loss is 8.02588 W.

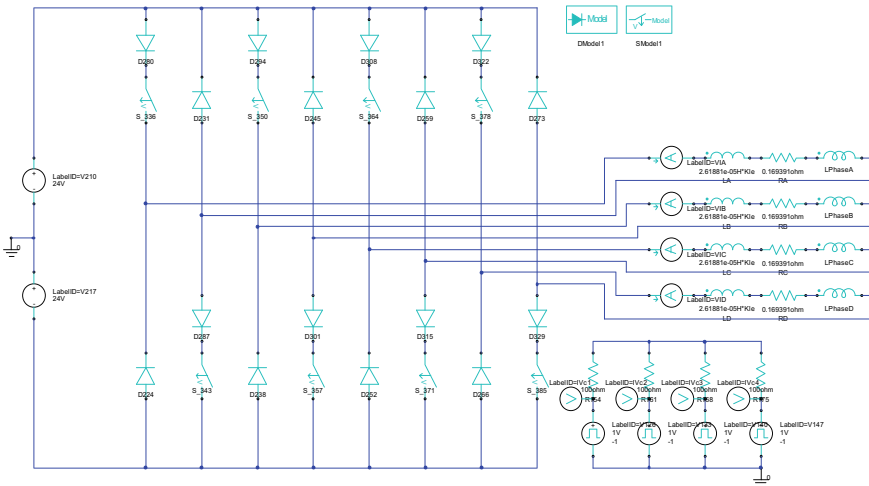


**Fig. 6** Drive circuit for SRM

## 7 Performance Analysis

An analysis of the efficiency, torque, speed, and losses can be attributed to the number of turns per pole and wire diameter. As a result of the analysis, we can see that it is possible to achieve maximum efficiency, minimum losses, and an extremely close value for the average torque for the number of turns per pole (38) and the wire diameter (1.628 mm) (Tables 4, 5 and 6).

**Table 4** In-depth examination of five possible number of turns per pole

Sr. No	Number of turns per pole	Wire diameter (mm)	Total loss (W)	Rated torque (Nm)	Rated speed (rpm)	Efficiency (%)
1	34	1.828	59.2693	1.91219	2486.53	89.3627
2	35	1.828	58.1185	1.99366	2378.44	89.5222
3	36	1.828	57.4204	2.10315	2259.66	89.6557
4	37	1.828	56.7708	2.20886	2151.6	89.7611
5	38	1.828	56.176	2.29488	2069.2	89.8497

**Table 5** In-depth examination of six possible number of wires diameter

Sr. No	Wire diameter (mm)	Number of turns per pole	Total loss (W)	Rated torque (Nm)	Rated speed (rpm)	Efficiency (%)
1	1.024	38	146.76	1750.3	2.71719	77.2393
2	1.15	38	115.898	2.58328	1845	81.1551
3	1.291	38	94.7071	2.51326	1912.35	84.1631
4	1.45	38	77.1761	2.39152	1980.51	86.5353
5	1.628	38	64.9115	2.32197	2032.9	88.3925
6	1.828	38	56.176	2.29488	2069.2	89.8497

**Table 6** In-depth examination of five possible numbers of stacking factor

Sr. No	Stacking factor	Total loss (W)	Rated torque (Nm)	Rated speed (rpm)	Efficiency (%)
1	0.75	65.3983	2.19234	2185.06	88.4669
2	0.8	64.1899	2.20124	2155.79	88.5606
3	0.85	63.5505	2.24237	2113.02	88.6462
4	0.9	63.1376	2.27833	2075.49	88.6915
5	0.95	63.232	2.32666	2040.88	88.7184

The stacking factor should be set at 0.95 in order to maximize efficiency, yield maximum torque output, and minimize losses. A stacking factor of more than one is generally prohibited.

An analysis of the yoke thickness. It is clear that in order to achieve the required efficiency, there is a need to have less losses and to achieve the required torque in the output, and when we take the yoke thickness (12 mm) into account, we would achieve maximum efficiency, minimum losses, and a very close value for the average torque (Table 7).

Using nominal torque, power, loss, flux distribution density, load torque, and efficiency values, the performance of non-oriented M19, M43, and super core JNX materials is investigated. Compared with other materials, this proposed design achieves maximum efficiency with grain-oriented silicon laminates to minimize weight reduction. As a result of the high efficiency of silicon core materials (steel\_1010), optimized EV-SRMs at rated speed and power were compared with the rated EV-SRMs at 2000 rpm and 500 watts, respectively, for their peak efficiency. The grain-oriented material achieved a rated torque of 2.32666 Nm, an efficiency of 88.7184%, and a core weight reduction to minimize vibration for high-speed EV applications. Future work will focus on thermal and noise analysis to improve the accuracy of the core material for weight reduction for EV-SRM applications (Table 8).

An analysis of the airgap. To achieve the required efficiency, less losses, and output torque, an airgap of 0.2 mm should be used.

**Table 7** In-depth examination of five possible numbers of yoke thickness

Sr. No	Yoke thickness	Total loss (W)	Rated torque (Nm)	Rated speed (rpm)	Efficiency (%)
1	8	66.0771	2.34182	2022.69	88.2448
2	9	64.9115	2.32197	2032.9	88.3925
3	10	64.1512	2.31758	2035.22	88.5053
4	11	63.5938	2.31881	2039.4	88.6198
5	12	63.232	2.32666	2040.88	88.7184

**Table 8** In-depth examination of four possible types of materials

Sr. No	Materials analysis	Total loss (W)	Rated torque (Nm)	Rated speed (rpm)	Efficiency (%)
1	Non-oriented material M19-29G	68.5479	2.29035	2065.86	87.8468
2	JFE Steel Super Core 10JNEX900	65.1553	2.28538	2066.3	88.3583
3	M43_29G	72.9213	2.31663	2044.82	87.1841
4	Steel_1010	63.232	2.32666	2040.88	88.7184

**Table 9** In-depth examination of six possible airgaps

Sr. No	Airgap (mm)	Total loss (W)	Rated torque (Nm)	Rated speed (rpm)	Efficiency (%)
1	0.2	63.232	2.32666	2040.88	88.7184
2	0.3	73.6725	2.28768	2067.48	87.0516
3	0.4	85.6543	2.2956	2061.25	85.2617
4	0.5	99.0954	2.31425	2052.15	83.3852
5	1	189.777	2.51682	1894.1	72.4556
6	1.5	341.771	2.88702	1652.62	59.3809

### 7.1 General Data

To start a simulation, the designer should enter the aforementioned parameters in the General Data field, as shown in Fig. 7.

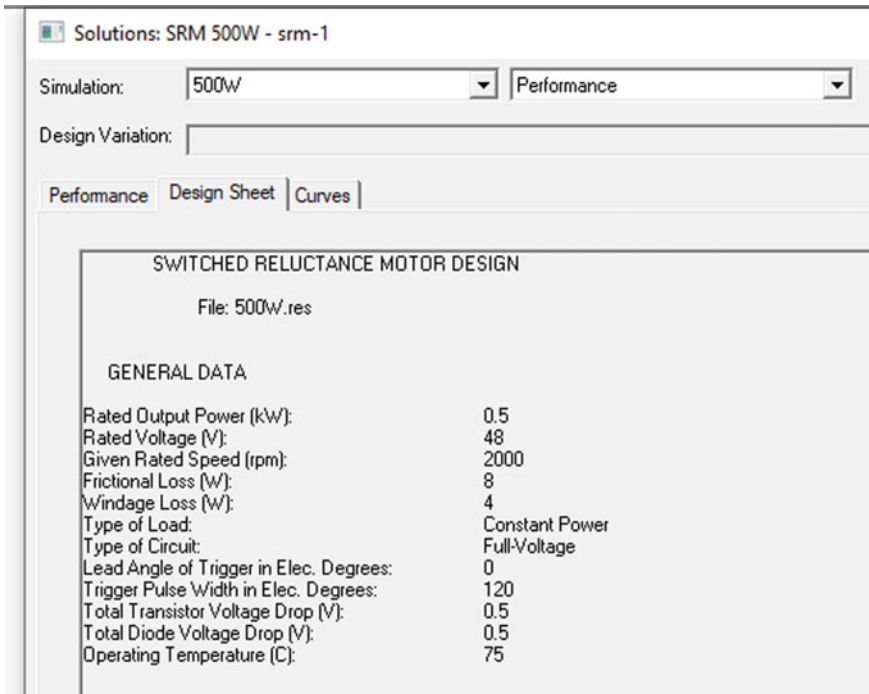


**Fig. 7** General data



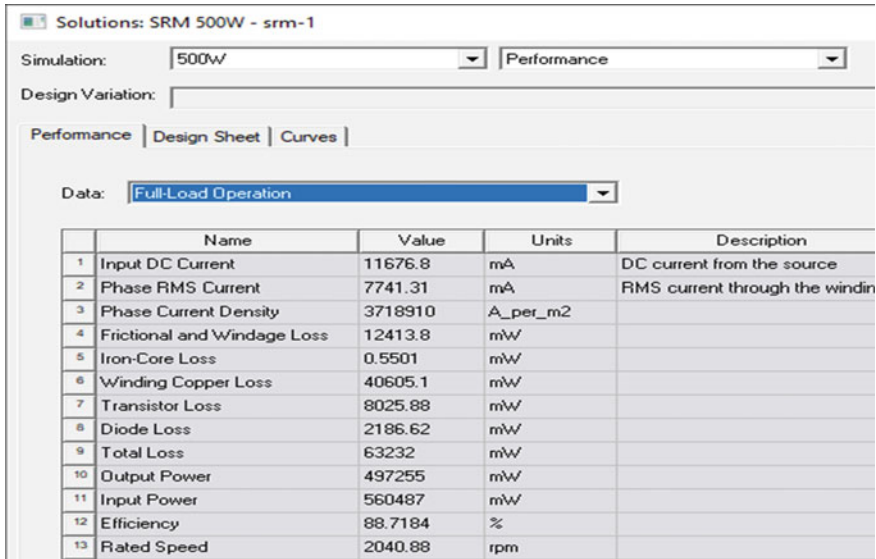


Fig. 8 Full load operation

### 7.2 Full Load Operation

A detailed illustration of several key parameters can be found in Fig. 8, such as output power, efficiency, and peak torque, among others.

### 7.3 Material Consumption

This Fig. 9 shows the results of the material consumption calculation based on the stator and rotor data that were provided by the motor manufacturer.

## 8 Simulation Results

We have obtained some significant graphs from our proposed SRM motor (500 W, 48 V) and discussed them in the following paragraphs.

Figure 10 shows the efficiency of the process. There is 88.7184% efficiency achieved, based on the nominal speed of 2000 RPM. Efficiency decreases with increasing speed, according to the graph.

Solutions: SRM 500W - srm-1

Simulation: 500W Performance

Design Variation:

Performance | Design Sheet | Curves

Data: Material Consumption

	Name	Value	Units	Description
1	Stator Copper Density	8900	kg_per_m3	Mass Density
2	Stator Core Steel Density	7872	kg_per_m3	Mass Density
3	Rotor Core Steel Density	7872	kg_per_m3	Mass Density
4	Stator Copper Weight	2.40829	kg	
5	Stator Core Steel Weight	3.39182	kg	
6	Rotor Core Steel Weight	1.37238	kg	
7	Total Net Weight	7.1725	kg	
8	Stator Core Steel Consumption	7.09654	kg	
9	Rotor Core Steel Consumption	2.22654	kg	

Fig. 9 Material consumption

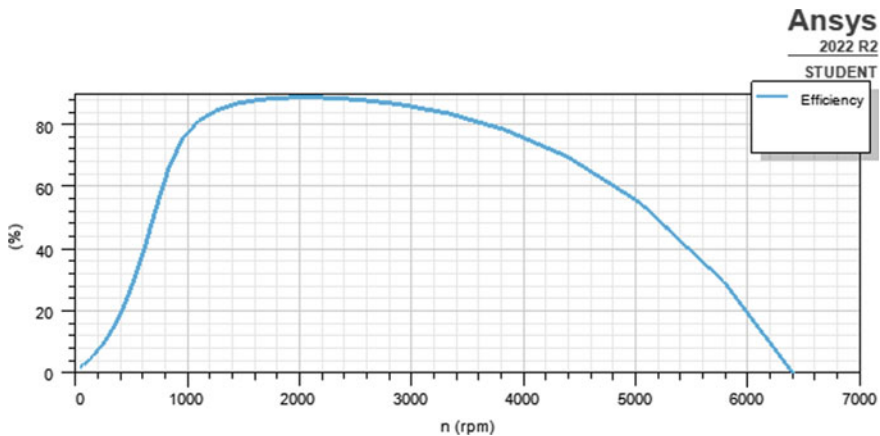


Fig. 10 Efficiency versus speed

This plot of output torque versus speed is shown in Fig. 11. A rated speed of 2000 rpm results in an output torque of 2.32666 Nm when the motor is running at its rated speed. Increasing speed results in decreasing torque (Figs. 12, 13, 14, 15 and 16).

After examining all parameters, some important parameters resulting from the simulation are summarized in Table 10.

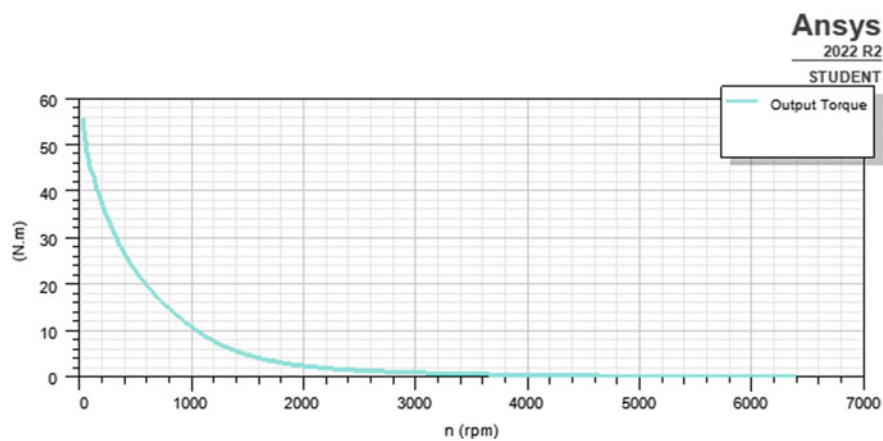


Fig. 11 Output torque versus speed

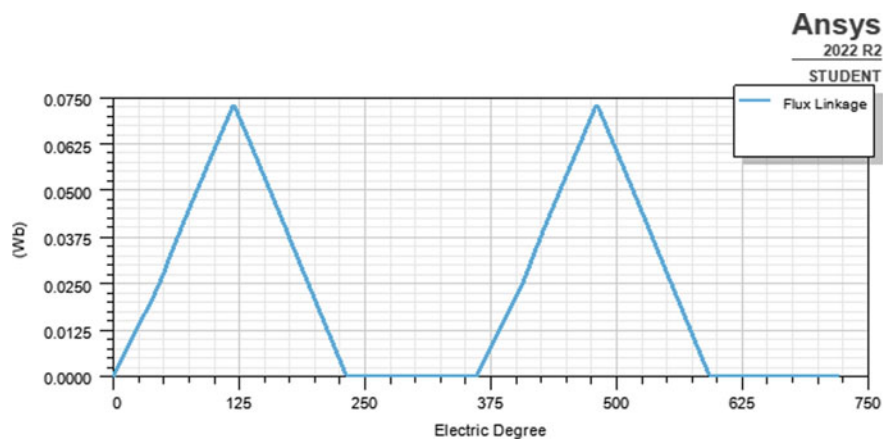


Fig. 12 Flux linkage

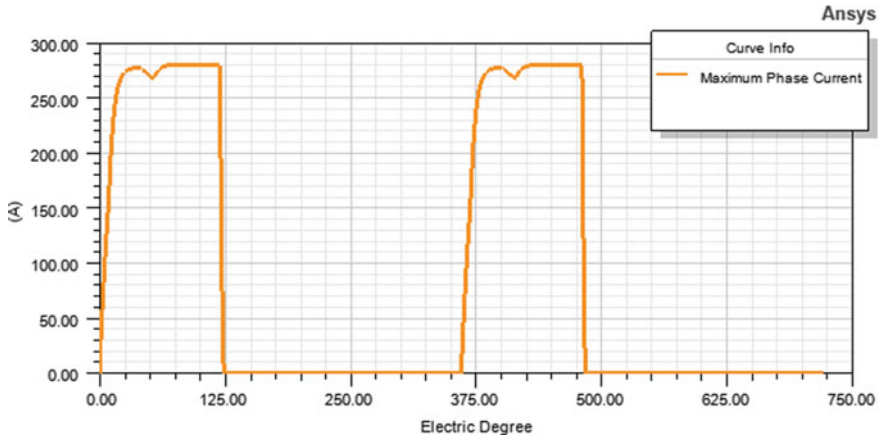


Fig. 13 Maximum phase current

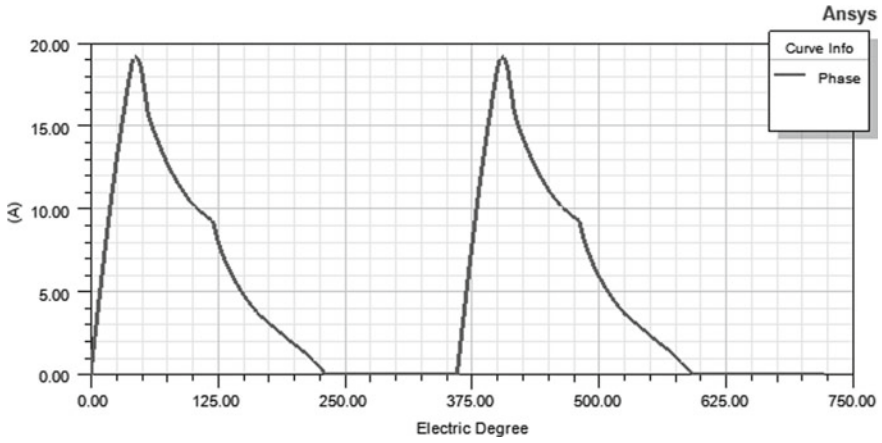


Fig. 14 Rated phase current

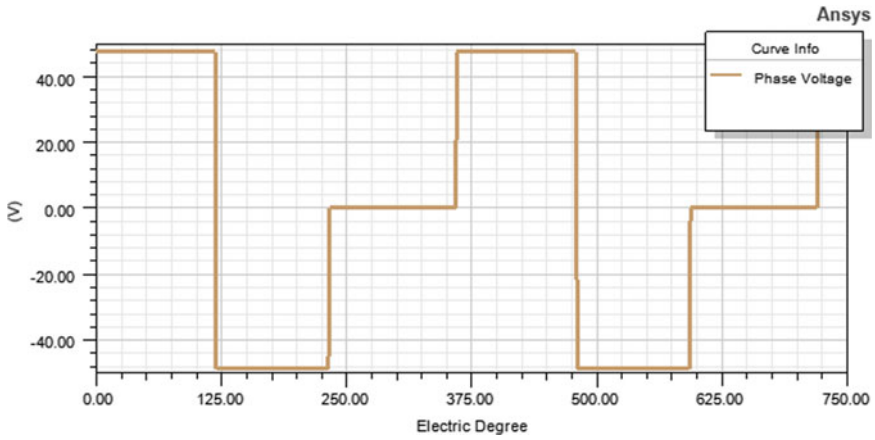


Fig. 15 Phase voltage

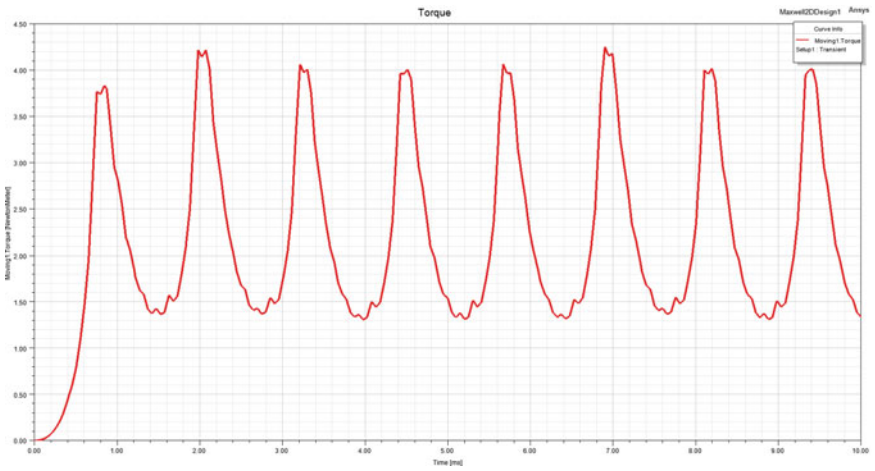


Fig. 16 Torque ripple

Table 10 Parameters

Sr. No	Parameter	Evaluated value	Units
1	Number of turns per pole	38	No
2	Wire diameter	1.628	mm
3	Stacking factor	0.95	–
4	Yoke thickness	12	mm
5	Type of material	steel_1010	–
6	Efficiency ( $\eta$ ) %	88.7184	%
7	Rated torque	2.32666	Nm
8	Rated speed (rpm)	2040.88	rpm

## 9 Conclusion

To design the optimized geometry of the 8/6 SRM E-Vehicles, a switched reluctance motor is presented in this dissertation for low- power electric three-wheelers. The nominal torque, power loss, flux distribution density, load torque, and efficiency of high-performance non-oriented materials such as M19, M43, super core materials and grain-oriented materials (steel\_1010) are examined with the nominal values of these materials. When compared with other materials, grain-oriented silicon (steel 10) fin materials improve efficiency and reduce core loss in this proposed design for E-Vehicle. The efficiency of the silicon high-core material was compared with optimized EV-SRM at a rated speed and power of 2000 rpm and 500 W for the 8/6 SRM configuration. Grain-oriented material achieves rated torque of 2.32666 Nm, efficiency of 88.7184%, stator and rotor core weights of 3.39182 and 1.37238 kg to minimize vibration. We will focus on improving core material accuracy and reducing weight for EV-SRM applications through thermal and noise analysis. We compared the results received from Ansys Maxwell (RMXpert tool) software, SRMs advantages include small size, low cost, low inertia of the rotor, high reliability, no rotor loss, robustness, and, most importantly, no use of rare grounded magnets. Although SRM for E-Vehicles has certain limitations such as torque ripple and acoustic noise, these can be eliminated with proper tuning. In the coming future, SRM-driven will be commonly encountered as it meets the requirements for an efficient, reliable, and environmentally friendly design of the electric tricycle segment. The introduction of a switched reluctance motor would be a great alternative to the current BLDC and PMSM motors for E-Vehicles.

## 10 Future Scope

These results of the proposed SRM prototype can be used to find and analyze simulation results required for the application of e-rickshaws. The area of mechanical design of switched reluctance machines focused on reducing the noise level, which can also be addressed, which in turn will allow the researcher to design a complete drive system for a switched reluctance motor that includes the controller and the motor.

Innovative current profile optimization algorithms to lessen auditory vibrations and noise in SRMs. The re-search offers guidelines and an outline for additional research for upcoming projects.

- Utilizing the SRM's torque, rotor angle, along with current for drive control.
- Optimizing and creating an appropriate phase current for the drive system.
- The most suitable angles for turning on and off the drive system.
- Each phase shift is accompanied by a torque ripple. This results from the actual phase currents' inability to keep up with the abrupt changes in reference [12].

## References

1. Poornesh K (2020) A comparative study on electric vehicle and internal combustion engine vehicles, ICOSSEC 2020. <https://doi.org/10.1109/ICOSSEC49089.2020.9215386>
2. Zabihi N, Gouws R (2016) A review on switched reluctance machines for electric vehicles. In: 2016 IEEE 25th international symposium on industrial electronics (ISIE), pp 799–804. <https://doi.org/10.1109/ISIE.2016.7744992>
3. Kurian S, Nisha GK (2014) State of the art of switched reluctance motor for torque ripple minimization. *Int J Ind Electron Electr Eng* 02(12):68–74. Available from: [http://pep.ijeee.org.in/journal\\_pdf/11-97-141758891168-74.pdf](http://pep.ijeee.org.in/journal_pdf/11-97-141758891168-74.pdf)
4. Binnemans K, Jones PT, Müller T et al (2018) Rare Earths and the balance problem: how to deal with changing markets? *J Sustain Metall* 4:126–146. <https://doi.org/10.1007/s40831-018-0162-8>
5. Mademlis C, Kioskeridis I (2003) Performance optimization in switched reluctance motor drives with online commutation angle control. *IEEE Trans Energy Convers* 18(3):448–457
6. Lee D-H, Ahn J-W (2017) Department of Mechatronics Engineering Kyungsoong University Busan, Korea, 2017 IEEE, ITECASIA. <https://doi.org/10.1109/ITEC-AP.2017.8080987>
7. Chiang C-C (2014) *IEEE Trans Magn* 50(11). <https://doi.org/10.1109/TMAG.2014.2329708>
8. Singh SK, Tripathi RK (2013) Students conference on engineering & systems (SCES). <https://doi.org/10.1109/SCES.2013.6547569>
9. Shaked NT, Rabinovici R (2005) New procedures for minimizing the torque ripple in switched reluctance motors by optimizing the phase-current profile. *IEEE Trans Magn* 41(3):1184–1192
10. Gan C, Wu J, Sun Q, Kong W, Li H, Hu Y (2018) A review on machine topologies and control techniques for low-noise switched reluctance motors in electric vehicle applications. *IEEE Access* 6:31430–31443
11. Shahgholian G, Sahafi AR (2021) <https://www.researchgate.net/publication/348407711>
12. Department of Electrical Engineering Indian Institute of Technology Ropar (2021). <https://doi.org/10.1109/TIE.2021.3063871>
13. Reddy BP, Vemula JR, Keerthipati S (2020) *IET Journal*, 25 Feb 2020. <https://doi.org/10.1049/iet-epa.2019.0787www.ietdl.org>
14. Krishnan R (2001) *Switched reluctance motor drives: modeling, simulation, analysis, design, and applications*. CRC Press. Available from: <https://doi.org/10.1201/9781420041644>.

# Using Linear Regression Model to Predict the Wholesale of the Electric Car in Indonesia: What Can Be Learned from the Model?



Rosyid R. Al-Hakim, Nur F. Soelaiman, Sri Riani, and Yanuar Z. Arief

**Abstract** We analyze wholesale datasets from Indonesian Automobile Industry Data for electric cars in Indonesia using statistical analysis to predict the electric cars used in the future. We apply a linear regression approach that adjusts the regression model according to wholesale electric cars between 2020 and 2022, as well as a statistical correlation test and the Wilcoxon test to support the regression result. We find a strong positive relationship for electric cars bought in the future, with a not significantly different population median of the total number of wholesale electric cars. It might be 210 cars estimated per year. Among the regression model, it is more effective for policymakers, as well as car industries. We estimate that there are various reasons and conditions for Indonesian people regarding buying electric cars inside conventional ones.

---

R. R. Al-Hakim · Y. Z. Arief (✉)

Department of Electrical Engineering, Faculty of Information Sciences and Engineering, Jakarta Global University, Kota Depok, Indonesia  
e-mail: [ayzularadiansyah@unimas.my](mailto:ayzularadiansyah@unimas.my)

R. R. Al-Hakim

e-mail: [rosyidridlo@student.jgu.ac.id](mailto:rosyidridlo@student.jgu.ac.id)

R. R. Al-Hakim

Graduate School, IPB University, Bogor, Indonesia

N. F. Soelaiman

Department of Computer and Informatics, Jakarta State Polytechnic, Depok, Indonesia

Faculty of Information and Communication Technology, Universiti Teknikal Melaka, Malacca, Malaysia

S. Riani

Department of Biology, International Women University, Bandung, Indonesia

Faculty of Biology, Universitas Jenderal Soedirman, Purwokerto, Indonesia

Y. Z. Arief

Department of Electrical and Electronic Engineering, Faculty of Engineering, Universiti Malaysia Sarawak, Kota Samarahan, Sarawak, Malaysia

© The Author(s), under exclusive license to Springer Nature Singapore Pte Ltd. 2024

513

H. Malik et al. (eds.), *Renewable Power for Sustainable Growth*,

Lecture Notes in Electrical Engineering 1086,

[https://doi.org/10.1007/978-981-99-6749-0\\_34](https://doi.org/10.1007/978-981-99-6749-0_34)



**Keywords** Electric vehicles · Hybrid vehicles · Energy policy · Electric car consumption · Car industry

## 1 Introduction

Indonesian regulations related to new and renewable energy [1] would optimize the green or renewable energy used in all sectors. One of the challenges regarding its policy includes EV [2]. Besides, since 2020 Indonesia has launched electric vehicles (EVs) in the transportation industry. Migrating to EV from a conventional vehicle (CV) based on oil-fueled or gasoline-powered fuel must be concerned in the context of green energy, as well as zero-emission missions [3, 4].

The car dealership plays the leading role in supplying the EV in the vehicle market [5]. The most common EV types are fully fueled by electricity, including battery electric vehicles (BEVs). It is reported that the overall selling market of this EV must be the attention of policymakers [6, 7]. Most people would choose an alternative fuel vehicle, BEV, caused of its crucial element of sustainable development, as well as electromobility factors [8]. Car industries would encourage buyers to adopt electromobility to improve EV uptakes [9, 10]. Besides, various choice reasons influenced EV buyers [11–13]. EV ownership is adopted mainly for lower costs than other fuel vehicles [14].

We tried to analyze within providing the statistical model for predicting the total number of EV wholesale in Indonesia. Besides, Indonesia is a developing country, and the emergence of EVs in the vehicle market has given rise to fluctuating purchases. The first year intensified the massive use and legalization of EVs in Indonesia since 2020. This study was conducted to statistically model the possible number of EV wholesale in the future.

## 2 Research Method

### 2.1 Data Collection

We collected the primary wholesales electric car (car electric vehicle, CEV) dataset from Indonesian Automobile Industry Data (<https://files.gaikindo.or.id/>) between 2020 and 2022, as well as reported electric cars began to be marketed in Indonesia in 2020. The data was collected for all car providers that sell fully electrical-based fuel, including battery electric vehicle (BEV) and Fuel-Cell Vehicle (FCEV), as well as not included Hybrid Electric Vehicle (HEV) and Plug-in Hybrid Electric Vehicle (PHEV) that is already used oil-based fuel. We are concerned with oil free and fully electrical-based fuel for this study, according to support zero emissions and fossil-free use, especially in the vehicle industries [15].

## 2.2 Data Analysis

The collected dataset was analyzed using linear regression to predict future electric vehicles (EVs), especially car electric vehicles (CEVs). The regression equation was obtained by regression analysis for the proposed mathematical prediction modeling. To support the regression result, we also used statistical correlation Kendall-Tau for analyzing the correlation between month wholesale quantity and the year of product sale. Besides, the Wilcoxon test was used to determine the future probability of total CEV sales in Indonesia obtained from the population median from the dataset.

## 3 Results and Discussion

### 3.1 Statistical Analysis Results

Tables 1 and 2 show the regression analysis results to predict the future wholesale total of car electric vehicle (CEV) (Fig. 1) based on the wholesale data from 2020 and 2022 in Indonesia. The regression analysis shows a significant ( $p$ -value  $< 0.050$ , one-tailed) difference between wholesale and year of sales in Indonesia. The future CEV industry in Indonesia would be proposed from the regression model as shown in Fig. 1, such as market optimization.

Meanwhile, the Kendall-Tau statistical correlation test shows the value of  $r$ -correl = 1.00, indicating that wholesale total CEV and year of sale have strong positive relationships. Besides, the regression model can be predictable for future wholesale total CEV in Indonesia, as well as supported by strong positive relationships. In addition, the Wilcoxon test shows that the number of CEV sales in the future is not significantly different from the population median of 201 cars estimated per year ( $p$ -value  $0.054 > 0.050$ , one-tailed) in Indonesia.

**Table 1** Regression summary of this study

Regression statistics	
<i>R</i> square	0.8852
Adjusted <i>R</i> square	0.7703

**Table 2** Regression test results of this study

Regression analysis	Std. error	<i>t</i> stat	<i>F</i>	Sig. <i>F</i>	<i>p</i> -value	Lower 95%	Upper 95%
Wholesale (2020–2022)	0.392	5150.868	7.7087	0.220	0.000*	2015.245	2025.212

\*  $p$ -value  $< 0.050$ , one-tailed

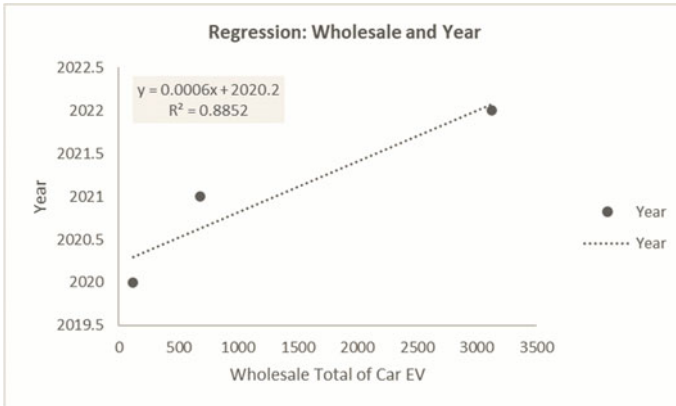


Fig. 1 Regression equation of the total wholesale EV car in Indonesia against the year of sales

### 3.2 Discussion

The regression model shown in Eq. (1) indicates that the prediction of wholesale total CEV in the future in Indonesia is optimistic when the constant value of 2020.2 is affected (increased) by wholesale total car electric vehicle (WTCEV). The increase in the year also affected the number of wholesale CEV products in Indonesia. The Kendall-Tau correlation test also supports strong positive relationships between them.

$$y = 0.0006 \times \text{WTCEV} + 2020.2, \tag{1}$$

where

- y prediction of wholesale total CEV in the future in Indonesia;
- WTCEV number of wholesale total car electrical vehicle (CEV).

Based on the prediction model, the estimated wholesale total number of CEVs in the future is about 210 cars per year in Indonesia’s population median. It might be fluctuating conditions, such as pandemic policy [16]. This model would be influenced by infrastructure development and government policy conditions according to Mali et al. [3] stated that in Nepal as a developed country, there are various influences, such as several accomplished initiatives, problems, tried-and-true regulations, and infrastructure development are all examples of this. Indonesia is also a developed country, so those factors probably influenced our study model, especially in the availability of charging station infrastructure [15] and policy implications [17], as well as techno-economic study [18]. Regarding the EV policy, we can learn from a previous study by Lebrouhi et al. [6]. Lemme et al. [19] proposed a model for evaluating electric vehicles as a fleet composition option in station-based car-sharing systems, and it can be applied in infrastructure development. Besides, Jakarta used photovoltaic (PV) integrated with electric vehicles (EVs) as the battery to reduce

energy costs by 33–34% in 2030 [20], so if this concept plan to be spreading to other cities in Indonesia, it is an alternative to make efficient use of green energy sources. In addition, the Indonesian government must provide a new policy regarding energy sources for EVs; like China [21], as well as the development of a vehicle-to-grid operations policy [22, 23], it is crucial to regulate gasoline-powered vehicles (conventional cars), so they can be used for the reason of migrating conventional vehicle to electric vehicle (EV) [24].

The trend in Istanbul–Turkey stated that subsidizing electric vehicle parking and hybrid car bridge and tunnel crossing tolls is more efficacious [11]. Based on the dataset obtained, non-fully electric batteries, including hybrid cars and oil-fueled cars (conventional cars), are the most consumed in Indonesia. Besides, Brazil reported that factors influencing EV usage intention include charging infrastructure, charging time, car autonomy, and purchasing price [12]. If these factors concern the Indonesian government, it would be an excellent way to educate about using the EV inside the conventional car.

The study shows that many unidentified factors in the statistical analysis influenced the regression model. It would probably be the factors of family decisions to buy the EV [25], economic and safety opinions [26], EV subsidy [27], EV buyer willingness regarding solar energy aspects [28], three together aspects: electrification, shared mobility, and automation [4], driver's preferences [7], transport actors and behavior [29], electrification level optimization for the passenger [30], total cost ownership [31], incentives for buying an EV [32], and technology-based as well as industrialization aspects [33].

## 4 Conclusion

We proposed the prediction model based on the statistical analysis for the number of total wholesale of car electric vehicles (CEVs) in Indonesia for the future. This study reported the preliminary report regarding the factors that probably influence the Indonesian people to buy an EV. Our model predicted that increased years would increase the number of buying an EV. The predicted total number of wholesale CEVs in the future might fluctuate, based on various factors, including economics, policy, willingness, and behavior of Indonesian people. Hopefully, this study can be used to determine the next new energy vehicle as well as the electric vehicle (EV) strategy. This study is limited to analyzing the wholesale number of EVs in Indonesia and predicting the future. We were also grateful for any feedback on this study. It is suggested for future works to extend the duration of wholesale year as well as the manufacturers to give comprehensive results.

## References

1. Al Hakim RR, Ariyanto E, Arief YZ, Sungkowo A, Trikolos T (2022) Preliminary study of juridical aspects of renewable energy draft law in Indonesia: an academic perspectives. *ADLIYA J Huk dan Kemanus* 16(1):59–72. <https://doi.org/10.15575/adliya.v16i1.14063>
2. Al Hakim RR (2020) Model Energi Indonesia, Tinjauan Potensi Energi Terbarukan untuk Ketahanan Energi di Indonesia: Sebuah Ulasan. *ANDASIH J Pengabdian Kpd Masy* 1(1):11–21 [Online]. Available: <http://www.jurnal.umitra.ac.id/index.php/ANDASIH/article/view/374>
3. Mali B, Shrestha A, Chapagain A, Bishwokarma R, Kumar P, Gonzalez-Longatt F (2022) Challenges in the penetration of electric vehicles in developing countries with a focus on Nepal. *Renew Energy Focus* 40:1–12. <https://doi.org/10.1016/J.REF.2021.11.003>
4. Roca-Puigròs M, Marmy C, Wäger P, Müller DB (2023) Modeling the transition toward a zero emission car fleet: integrating electrification, shared mobility, and automation. *Transp Res Part D Transp Environ* 115:103576. <https://doi.org/10.1016/J.TRD.2022.103576>
5. Tromaras A, Aggelakakis A, Margaritis D (2017) Car dealerships and their role in electric vehicles' market penetration—a Greek market case study. *Transp Res Procedia* 24:259–266. <https://doi.org/10.1016/J.TRPRO.2017.05.116>
6. Lebrouhi BE, Khattari Y, Lamrani B, Maaroufi M, Zeraoui Y, Kousksou T (2021) Key challenges for a large-scale development of battery electric vehicles: a comprehensive review. *J Energy Storage* 44(Part B):103273. <https://doi.org/10.1016/J.EST.2021.103273>
7. Danielis R, Rotaris L, Giansoldati M, Scorrano M (2020) Drivers' preferences for electric cars in Italy. Evidence from a country with limited but growing electric car uptake. *Transp Res Part A Policy Pract* 137:79–94. <https://doi.org/10.1016/J.TRA.2020.04.004>
8. Kowalska-Pyzalska A, Michalski R, Kott M, Skowrońska-Szmer A, Kott J (2022) Consumer preferences towards alternative fuel vehicles. Results from the conjoint analysis. *Renew Sustain Energy Rev* 155:111776. <https://doi.org/10.1016/J.RSER.2021.111776>
9. Matthews L, Lynes J, Riemer M, Del Matto T, Cloet N (2017) Do we have a car for you? Encouraging the uptake of electric vehicles at point of sale. *Energy Policy* 100:79–88. <https://doi.org/10.1016/J.ENPOL.2016.10.001>
10. Scorrano M, Danielis R (2022) Simulating electric vehicle uptake in Italy in the small-to-medium car segment: a system dynamics/agent-based model parametrized with discrete choice data. *Res Transp Bus Manag* 43:100736. <https://doi.org/10.1016/J.RTBM.2021.100736>
11. Inci E, Tatar Taspınar Z, Ulingen B (2022) A choice experiment on preferences for electric and hybrid cars in Istanbul. *Transp Res Part D Transp Environ* 107:103295. <https://doi.org/10.1016/J.TRD.2022.103295>
12. de Oliveira MB, da Silva HMR, Jugend D, Fiorini PDC, Paro CE (2022) Factors influencing the intention to use electric cars in Brazil. *Transp Res Part A Policy Pract* 155:418–433. <https://doi.org/10.1016/J.TRA.2021.11.018>
13. Wicki M, Brückmann G, Bernauer T (2022) How to accelerate the uptake of electric cars? Insights from a choice experiment. *J Clean Prod* 355:131774. <https://doi.org/10.1016/J.JCLEPRO.2022.131774>
14. Goetzel N, Hasanuzzaman M (2022) An empirical analysis of electric vehicle cost trends: a case study in Germany. *Res Transp Bus Manag* 43:100825. <https://doi.org/10.1016/J.RTBM.2022.100825>
15. Gönül Ö, Duman AC, Güler Ö (2021) Electric vehicles and charging infrastructure in Turkey: an overview. *Renew Sustain Energy Rev* 143:110913. <https://doi.org/10.1016/J.RSER.2021.110913>
16. Wen W, Yang S, Zhou P, Gao SZ (2021) Impacts of COVID-19 on the electric vehicle industry: evidence from China. *Renew Sustain Energy Rev* 144:111024. <https://doi.org/10.1016/J.RSER.2021.111024>
17. Mastoi MS et al (2022) An in-depth analysis of electric vehicle charging station infrastructure, policy implications, and future trends. *Energy Rep* 8:11504–11529. <https://doi.org/10.1016/J.EGYR.2022.09.011>

18. Mohideen MM et al (2023) Techno-economic analysis of different shades of renewable and non-renewable energy-based hydrogen for fuel cell electric vehicles. *Renew Sustain Energy Rev* 174:113153. <https://doi.org/10.1016/J.RSER.2023.113153>
19. Lemme RFF, Arruda EF, Bahiense L (2019) Optimization model to assess electric vehicles as an alternative for fleet composition in station-based car sharing systems. *Transp Res Part D Transp Environ* 67:173–196. <https://doi.org/10.1016/J.TRD.2018.11.008>
20. Dewi RG, Siagian UWR, Asmara B, Anggraini SD, Ichihara J, Kobashi T (2023) Equitable, affordable, and deep decarbonization pathways for low-latitude developing cities by rooftop photovoltaics integrated with electric vehicles. *Appl Energy* 332:120507. <https://doi.org/10.1016/J.APENERGY.2022.120507>
21. Li Y, Taghizadeh-Hesary F (2022) The economic feasibility of green hydrogen and fuel cell electric vehicles for road transport in China. *Energy Policy* 160:112703. <https://doi.org/10.1016/J.ENPOL.2021.112703>
22. Prencipe LP, Theresia van Essen J, Caggiani L, Ottomanelli M, Homem de Almeida Correia G (2022) A mathematical programming model for optimal fleet management of electric car-sharing systems with vehicle-to-grid operations. *J Clean Prod* 368:33147. <https://doi.org/10.1016/J.JCLEPRO.2022.133147>
23. Caggiani L, Prencipe LP, Ottomanelli M (2021) A static relocation strategy for electric car-sharing systems in a vehicle-to-grid framework. *Transp Lett* 13(3):219–228. <https://doi.org/10.1080/19427867.2020.1861501>
24. Krishnan R, Butt B (2022) “The gasoline of the future:” points of continuity, energy materiality, and corporate marketing of electric vehicles among automakers and utilities. *Energy Res Soc Sci* 83:102349. <https://doi.org/10.1016/J.ERSS.2021.102349>
25. Kannchen M (2021) Using the PVM-VSI (Preference Vector Method-Vector Space of Increments) method in supporting the decision related to the purchase of an electric family car. *Procedia Comput Sci* 192:2199–2209. <https://doi.org/10.1016/J.PROCS.2021.08.233>
26. Hu JW, Javaid A, Creutzig F (2021) Leverage points for accelerating adoption of shared electric cars: perceived benefits and environmental impact of NEVs. *Energy Policy* 155:112349. <https://doi.org/10.1016/J.ENPOL.2021.112349>
27. Vivanco DF, Nechifor V, Freire-González J, Calzadilla A (2021) Economy-wide rebound makes UK’s electric car subsidy fall short of expectations. *Appl Energy* 297:117138. <https://doi.org/10.1016/J.APENERGY.2021.117138>
28. Stauch A (2021) Does solar power add value to electric vehicles? An investigation of car-buyers’ willingness to buy product-bundles in Germany. *Energy Res Soc Sci* 75:102006. <https://doi.org/10.1016/J.ERSS.2021.102006>
29. Corradi C, Sica E, Morone P (2023) What drives electric vehicle adoption? Insights from a systematic review on European transport actors and behaviours. *Energy Res Soc Sci* 95:102908. <https://doi.org/10.1016/J.ERSS.2022.102908>
30. Shafiei E, Dauphin R, Yugo M (2022) Optimal electrification level of passenger cars in Europe in a battery-constrained future. *Transp Res Part D Transp Environ* 102:103132. <https://doi.org/10.1016/J.TRD.2021.103132>
31. Danielis R, Giansoldati M, Rotaris L (2018) A probabilistic total cost of ownership model to evaluate the current and future prospects of electric cars uptake in Italy. *Energy Policy* 119:268–281. <https://doi.org/10.1016/J.ENPOL.2018.04.024>
32. Deuten S, Vilchez JGG, Thiel C (2020) Analysis and testing of electric car incentive scenarios in the Netherlands and Norway. *Technol Forecast Soc Change* 151:119847. <https://doi.org/10.1016/J.TECHFORE.2019.119847>
33. Du J, Meng X, Li J, Wu X, Song Z, Ouyang M (2018) Insights into the characteristics of technologies and industrialization for plug-in electric cars in China. *Energy* 164:910–924. <https://doi.org/10.1016/J.ENERGY.2018.09.060>

# Comparison of Thermoelectric Generator with Boost Converter and Single-Ended Primary-Inductance Converter



Megat Azri Irfan Adzmi, Mohd Zaki Daud, Shahrin Md Ayob,  
and Razman Ayop

**Abstract** Thermoelectric generator (TEG) is a clean and noiseless renewable energy source from heat source, and it can become an alternative way of generating electricity consciously. Building a thermoelectric generator converter can consist of different parts. In this research, we are studying the difference of using boost converter with single-ended primary-inductance converter (SEPIC) with the thermoelectric generator system. The contribution of the study is to determine the performance of TEG using different topology. It is done using a simulation using Matlab Simulink with varying temperature flux and load resistance. Varying the temperatures can give a consistent output, while varying load resistance by increasing can lower the performance of the thermoelectric generator system. It can also be seen that the settling time increases when the load increases. The performance of the boost converter (98.7% efficiency) is better than SEPIC (97.4% efficiency), but it is also according to the designer's desired outcome. The output can also be manipulated by having different settling time by designing the load resistance value.

**Keywords** TEG · SEPIC · P&O · Boost converter · Matlab/Simulink

---

M. A. I. Adzmi · M. Z. Daud (✉) · S. M. Ayob · R. Ayop  
Faculty of Electrical Engineering, Universiti Teknologi Malaysia, 81310 Johor Bahru, Malaysia  
e-mail: [mdzaki@utm.my](mailto:mdzaki@utm.my)

M. A. I. Adzmi  
e-mail: [megat.azri.irfan@graduate.utm.my](mailto:megat.azri.irfan@graduate.utm.my)

S. M. Ayob  
e-mail: [e-shahrin@utm.my](mailto:e-shahrin@utm.my)

R. Ayop  
e-mail: [razman.ayop@utm.my](mailto:razman.ayop@utm.my)

## 1 Introduction

People are looking for an alternative way of generating electricity without depleting Earth's resources. Thermoelectric generators (TEG) can be the solution for that as it would produce electricity that is clean and noiseless without any moving parts [1]. TEG is a semiconductor device that converts temperature flux between surfaces into electrical energy directly [2]. There are many different parts inside a TEG for it to work efficiently.

With many different parts into a TEG, there can be many different variations that could be made. In this research, we are going to implement the most widely known maximum power point tracking (MPPT) algorithm which is "Perturb & Observe" (P&O). The MPPT is important as it tracks the maximum power point and minimizes impedance imbalance of the DC-DC converter that is being used [2].

The research in this area is commonly focused on using boost converter only. However, the study on the type of converter used for the TEG converter is still new. Since single-ended primary-inductor converter (SEPIC) is good in other application, the performance may improve if the SEPIC converter is used in TEG converter, instead of boost converter. Boost converter is known as a step-up converter with voltage output in excess of the voltage input [3]. SEPIC can be both step-up and step-down converter and instead of the output being inverted such as buck-boost converter, the outcome of this is positive.

This paper analyzed the performance of TEG converter using SEPIC converter. The performance is then compared with the boost converter. In this research, we are going to see which converter is better or if there are even any differences in performances at all. In next section, the methodology of the TEG model and MPPT is shown. Next, the design of both boost and SEPIC converters is discussed. Then, the results of the simulation are illustrated and discussed. The last section is the conclusion.

## 2 Methodology

Matlab Simulink is used in order to run this research. Only simulation is done and no hardware components are used. For the TEG, the power we want to achieve is not low. As mentioned in future work in [1], it is to run the experiment using a practical sized TEG which is better presented in [2].

In order to get a better understanding of a TEG system and what it consists of, it can be referred to Fig. 1. The block diagram shows the full system and what needs to be realized in order to get the desired outcome. In this research, the manipulated variable would be the temperature of the hot source and load resistance  $R_L$ .



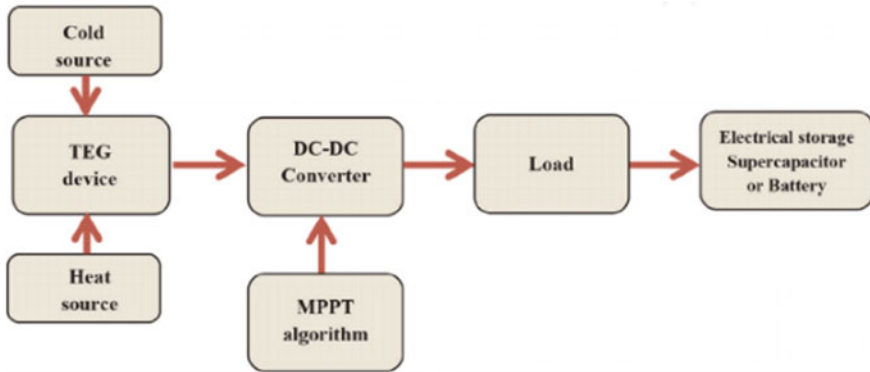


Fig. 1 TEG block diagram [4, Fig. 7]

### 2.1 Thermoelectric Generator Device

As mentioned earlier, we wanted to have a TEG device that is practical. Having a singular TEG module can only obtain low power [2]. The design of the TEG device has been modified. The modules are arranged in series and parallel so that it could produce a higher power with the total internal resistance,  $R_{int}$ , becoming  $7 \Omega$ . Figure 2 shows the modules in parallel.

From the left side of the figure we can also see the hot surface temperature ( $T_h$ ), cold surface temperature ( $T_c$ ), Seebeck coefficient and also module in series. The values for  $T_h$ ,  $T_c$  and Seebeck coefficient are set by TEG properties manufactured by TEG thermoelectric systems as referred in [2].

### 2.2 P&O MPPT

Discussion of the best MPPT algorithm is still an ongoing research for people in the field of power electronics. The most common one that is being used right now is P&O. This is due to the effectiveness and simplicity of the algorithm. Figure 3 shows the flowchart of the P&O algorithm. It is very helpful in writing the code that is needed.

The P&O MPPT calculates the power of the TEG device by taking the current and voltage value of the current time and also the previous time. From there, it would compute whether the duty cycle needs to increase or decrease, it depends on the graph that can be seen in Fig. 4.

Figures 5 and 6 present the subsystem inside the Simulink that shows where and how the P&O coding is implemented into the TEG system.

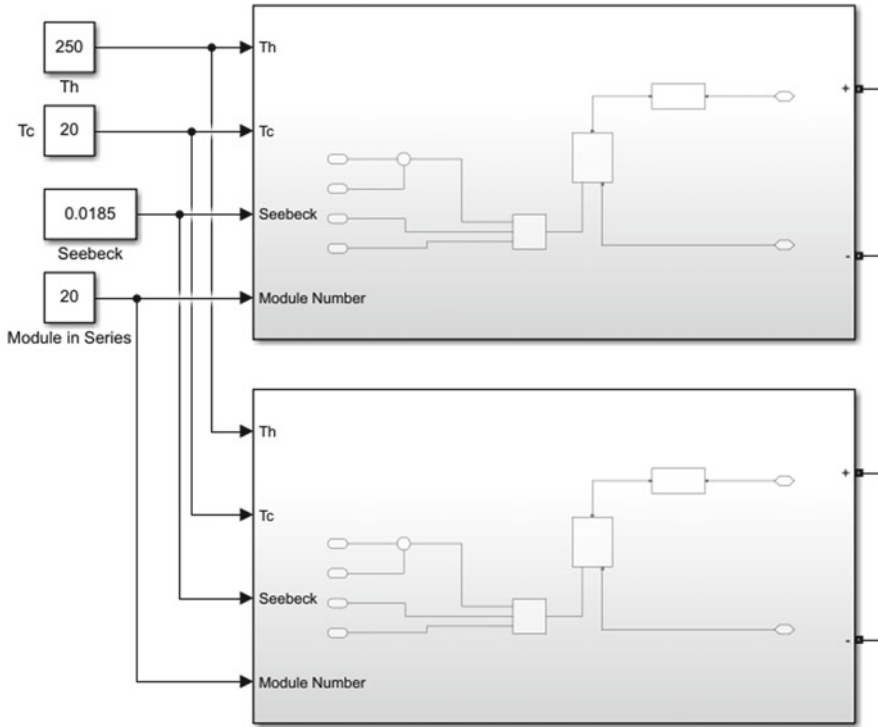


Fig. 2 TEG modules in parallel

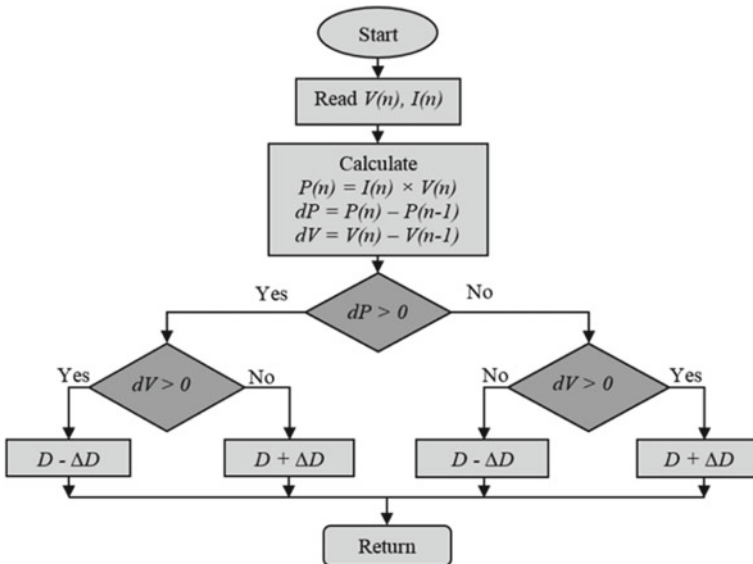


Fig. 3 Flowchart of P&O algorithm [2, Fig. 2b]

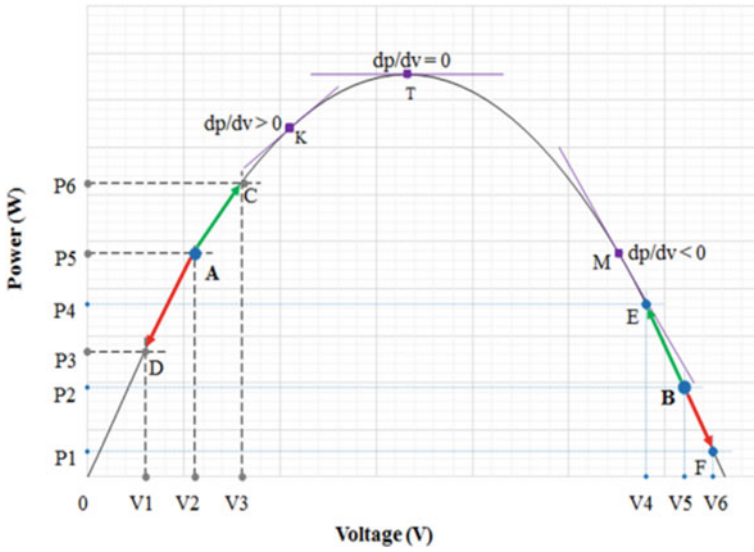


Fig. 4 MPPT graph principle [2, Fig. 2a]

Fig. 5 Subsystem of P&O MPPT

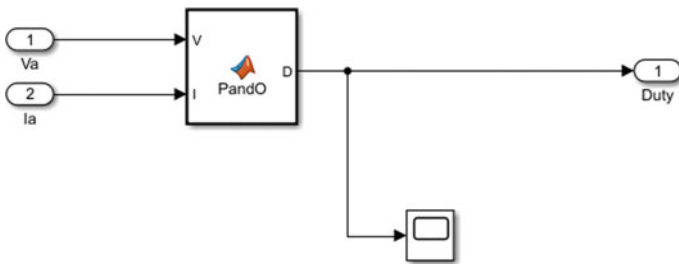


Fig. 6 Inside the subsystem of P&O MPPT

### 3 DC-DC Converter

There are many different converters that are available to be used inside a TEG system. The two converters that are being used in this research are boost converter and SEPIC converter. Both will go head-to-head by varying the  $T_h$  and  $R_L$ .

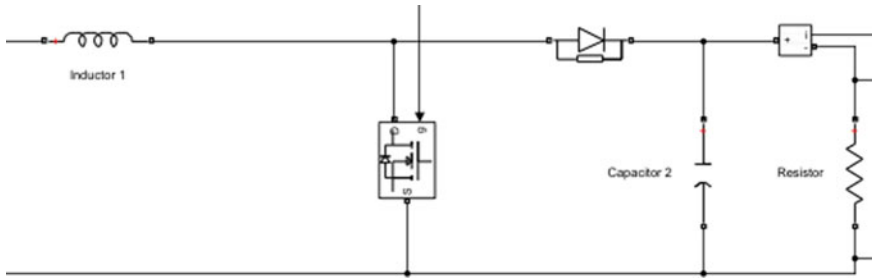


Fig. 7 Boost converter in simulink

### 3.1 Boost Converter

Boost converters are known to step up the voltage. Using the converter would give an output that is higher than the input voltage. It is ideal for generating a bigger voltage with a small source and easy to control and is efficient [5].

One factor that could decrease the efficiency of the converter is the high input current. An option to reduce ripple current is to make it operate in continuous current mode (CCM), but this would increase the weight and volume of the converter [6].

As we can see from (1), i.e. the ratio for boost converter where we can see what desired outcome we want to achieve.  $V_{out}$  is the output voltage,  $V_{in}$  is the input voltage and  $D$  is the duty cycle. The MPPT manipulates the  $D$  of the converter to the maximum power point needed at the moment of time. Therefore, it keeps changing according to the P&O algorithm.

$$V_{out}/V_{in} = 1/(1 - D) \quad (1)$$

Figure 7 shows the Simulink circuit for the boost converter. It consists of an inductor, with a MOSFET as the semiconductor, a diode and also capacitor. The values for each components are  $L = 1$  mH,  $C = 3000$   $\mu$ F and MOSFET with a snubber resistance of  $R_s = 1$  M $\Omega$ . The MOSFET is connected to the subsystem of P&O MPPT as in Fig. 5. What the P&O MPPT does is, it generates duty cycle in and creates switching signals for converter [7]. Figure 8 shows the whole TEG system with boost converter.

### 3.2 SEPIC

The single-ended primary-inductor converter is similar to both buck-boost and boost converter. It is identical with buck-boost in terms of output, as it can be both step up and step down. The upside of SEPIC over buck-boost converter is the output is not

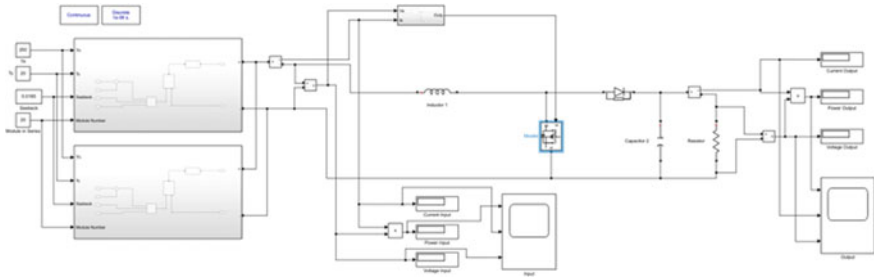


Fig. 8 TEG system with boost converter

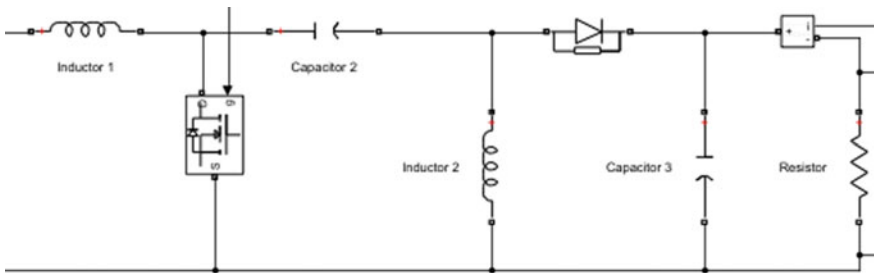


Fig. 9 SEPIC in simulink

inverted. It is akin to a boost converter in its structure, but with adding a buck-boost converter after it.

Figure 9 shows the SEPIC inside the Matlab Simulink. There are a total of two capacitors, two inductors, MOSFET and diode. The values for each components are  $L1 = L2 = 5 \text{ mH}$ ,  $C2 = 300 \text{ }\mu\text{F}$ ,  $C3 = 470 \text{ }\mu\text{F}$  and  $R_s = 1 \text{ M}\Omega$ . Similar to boost converter, MOSFET is connected to the P&O MPPT subsystem as in Fig. 5, small source, easy to control and is efficient [5].

The reason why MOSFET is chosen for both of these converters is because it has low gate threshold voltage that allows better compatibility with microcontrollers and lower power requirements.

SEPIC's duty cycle ratio is known in (2). The principle of it is similar to boost's which is the duty cycle is manipulated using the P&O MPPT algorithm. Figure 10 shows the whole TEG system with boost converter.

$$V_{\text{out}}/V_{\text{in}} = D/(1 - D) \tag{2}$$

The use of SEPIC is also known to have less electrical stress on components that can result in device failure and overheating [8].

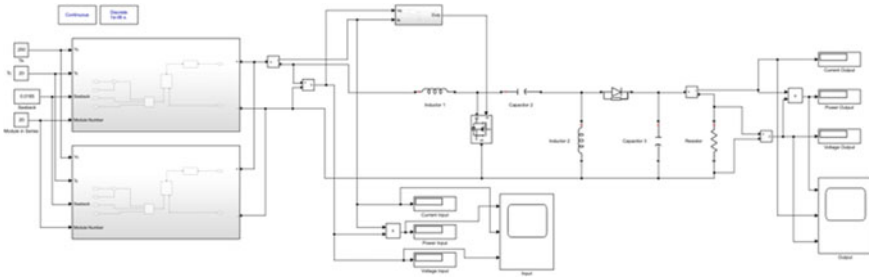


**Fig. 10** TEG system with SEPIC

## 4 Results and Discussion

Since the scope of this research is simulation, the results gotten are also coming from the simulation of Matlab Simulink. Manipulated variable that is mentioned was temperature of  $T_h$  and resistance  $R_L$ . The experiment done was that when the  $T_h$  is differing, the  $R_L$  is kept the same and vice versa. The values are  $T_h = 30, 80, 100, 150$  and  $250\text{ }^\circ\text{C}$  and  $R_L = 3, 7, 20, 80$  and  $100\ \Omega$ .

### 4.1 TEG with Boost Converter Waveforms

The waveforms that are illustrated have the manipulated variable of  $T_h = 250\text{ }^\circ\text{C}$  and  $R_L = 7\ \Omega$ .

Figures 11 and 12 show the simulation on the Matlab Simulink. From the waveform, we can get the settling time,  $T_s = 0.038\text{ s}$  for the power of output. The efficiency of the TEG system for this particular variable is also very good which is 100%. Even though 100% efficiency is not possible, this is fine because we wanted to get the waveform for this section. The different efficiencies will be tabulated in the later section. This may be due to the similar resistance value of internal resistor inside the TEG module and with the  $R_L$ .

### 4.2 TEG with SEPIC Waveforms

The waveform that is illustrated has the manipulated variable of  $T_h = 250\text{ }^\circ\text{C}$  and  $R_L = 7\ \Omega$ .

Figures 13 and 14 show the simulation of SEPIC. From the waveform, we can see that settling time,  $T_s$ , is around  $0.076\text{ s}$ . The settling time is more than for boost converter. This may be due to the values of the inductors and capacitors, but it is still acceptable and very fast in terms of itself, rendering it useful for the industry. The

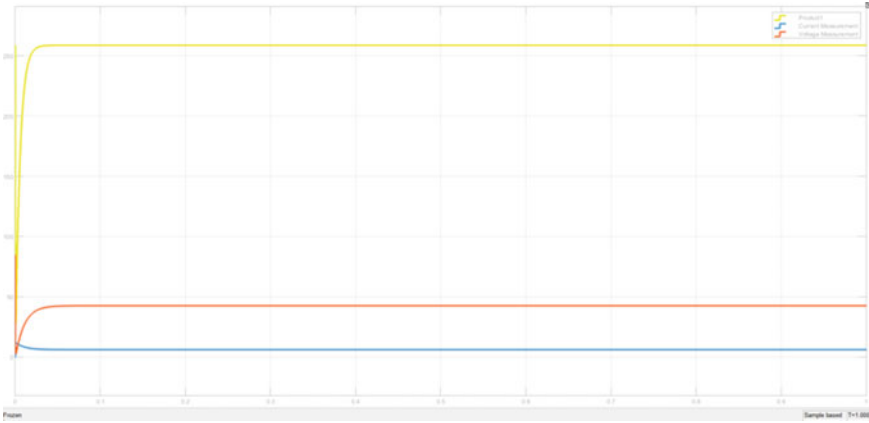


**Fig. 11** Input graph simulated for boost converter

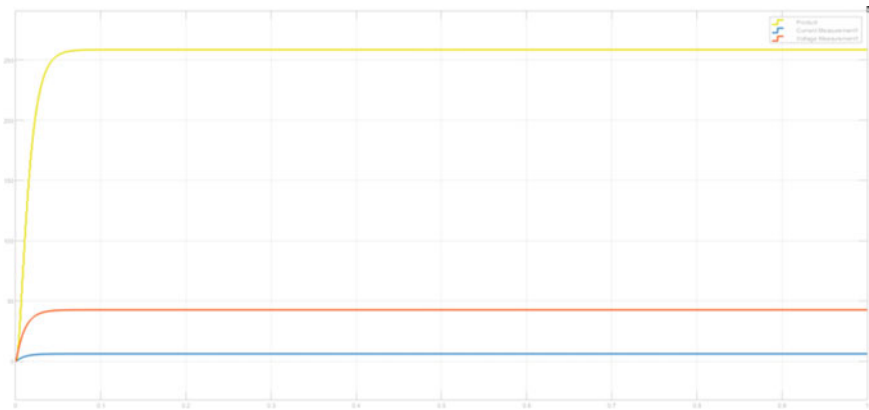


**Fig. 12** Output graph simulated for boost converter

efficiency for this particular variable is 97.21% which is quite high and acceptable value. When the output graph is zoomed in, as shown in Fig. 15, we can see the ripple voltage. It sways between  $V_{\max} = 260.8 \text{ V}$  and  $V_{\min} = 247.1 \text{ V}$ .

### 4.3 Tabulation of Simulation

The simulations were not only tapped into an oscilloscope, but also with the readings. The readings are then tabulated into four different tables which show the efficiency of each converter with different  $T_h$  and  $R_L$ .

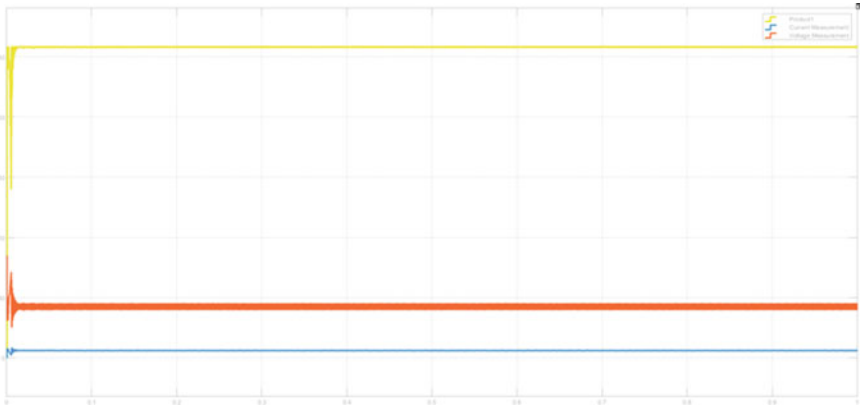


Fig. 13 Input graph simulated for SEPIC

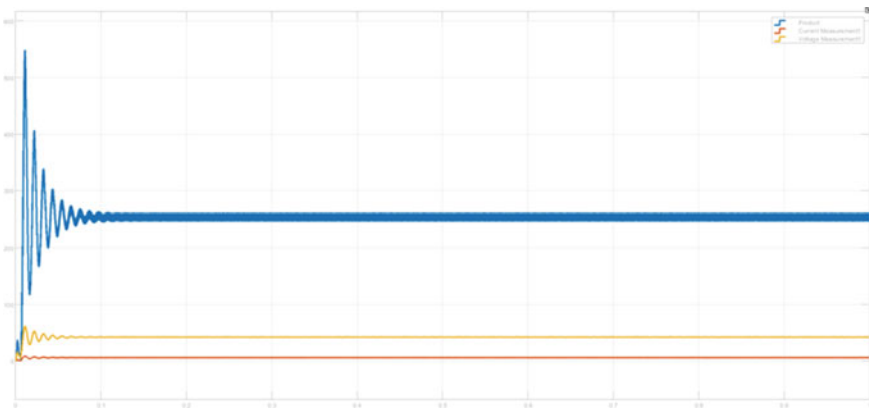


Fig. 14 Output graph simulated for SEPIC

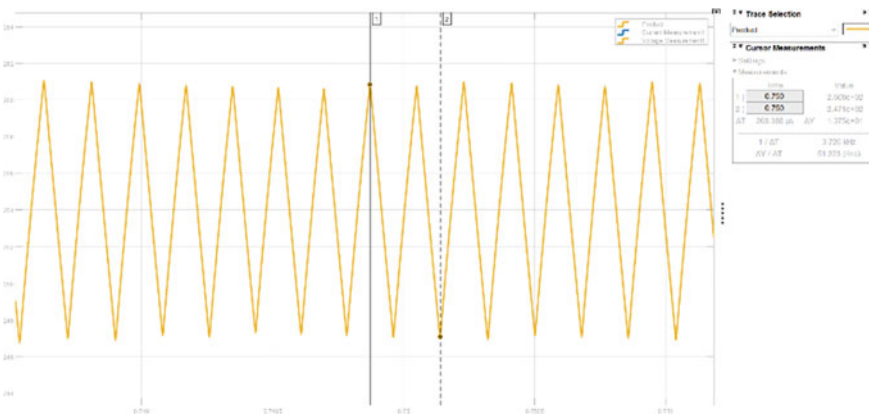
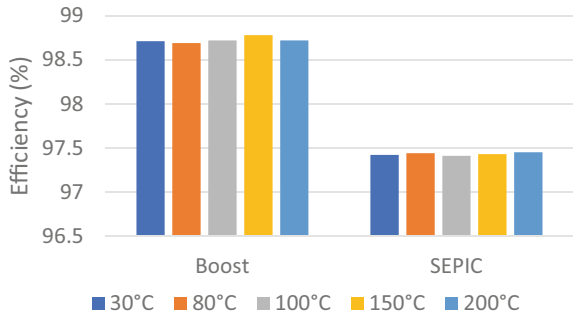


Fig. 15 Output power of SEPIC



**Fig. 16** MPPT efficiency of boost and SEPIC converters when the  $T_h$  changes



Figures 16 and 17 show the efficiency and performance of each varying temperature and load. It can be seen that the performance for changing  $T_h$  is very stable, while increasing the loads will lower the performance. If we would see further, the waveform shows that the settling time of the output is also longer as seen in Fig. 18 comparing with Fig. 12.

**Fig. 17** MPPT efficiency of boost and SEPIC converters when the  $R_L$  changes

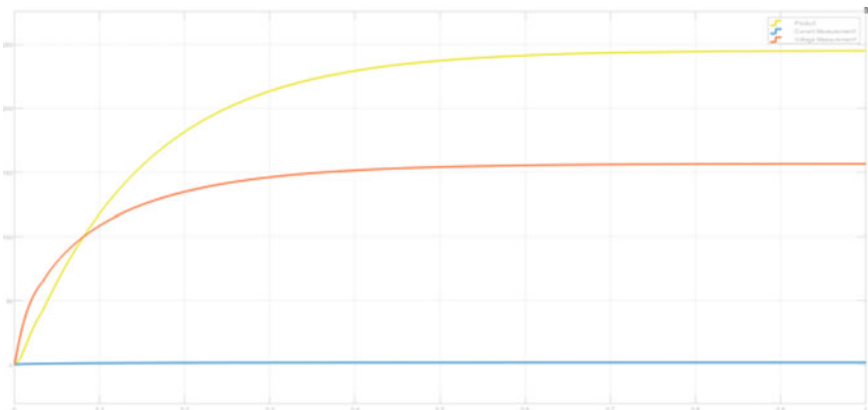
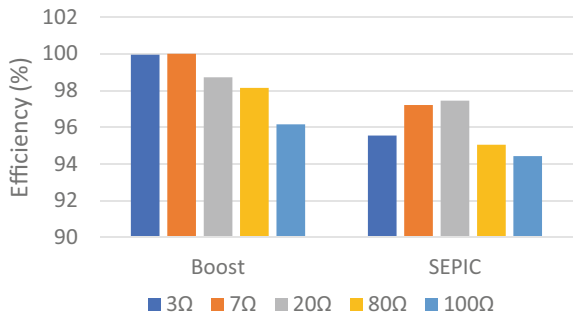


**Fig. 18** Output waveform for boost converter  $R_L = 100 \Omega$

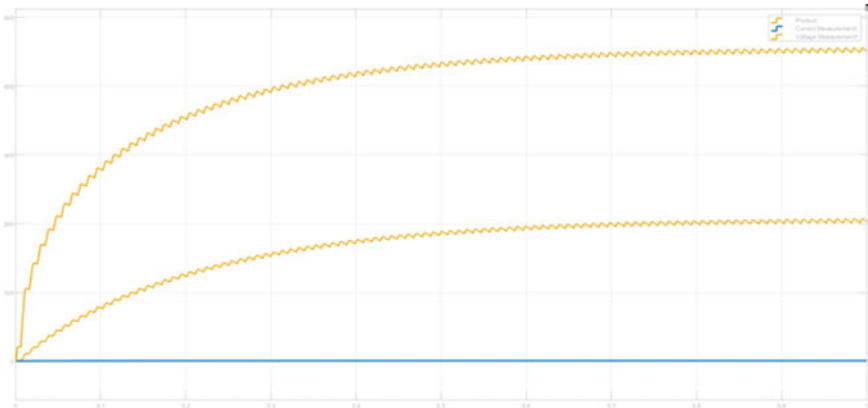


**Fig. 19** Output waveform for SEPIC  $R_L = 100 \Omega$

Figures 16 and 17 show the result for SEPIC. Here we see the same pattern as boost converter. Varying the temperature of the hot surface makes the performance pretty consistent. Meanwhile, increasing the load affects the performance drastically. The performance decreases except when the load is lower than internal resistor of TEG module which is  $3 \Omega$ . The power output is higher than the input, which is probably false. This is due to the load being smaller than internal resistance. The same goes with the settling time, which is increasing as the load increases. It can be observed by comparing Fig. 19 which is for 2 s instead of 1 s with Fig. 14.

## 5 Conclusion

Using different DC-DC converters can give us different results and different shapes of waveform. It all depends on the application and what type of design that is needed inside a system. The boost converter is one that can convert pretty smoothly with less components than in SEPIC. Boost converters only consist of four components, while SEPIC has six components. This can be looked upon during costing of the design. SEPIC is very convenient in having both option of stepping up and stepping down but it might need to have longer settling time. SEPIC will always be a choice of manufacturers to do battery-operated devices. We also have learnt that the value of resistance is important. In getting the desired result, lowering the  $R_L$  for SEPIC is the right way. Having the higher resistance also increases the settling time, therefore taking longer time to fulfil the desired output. The efficiency for the boost converter is also on average 1.3% higher compared with the SEPIC converter. Based on the results, it shows that the SEPIC is not a suitable replacement for the TEG application. In the future recommended work, the boost and SEPIC converters need to be designed properly to operate at critical continuous current mode and specified ripple factor. This ensures a fairer comparison.

**Acknowledgements** The authors would like to thank Universiti Teknologi Malaysia (UTM) and Ministry of High Education Malaysia (MOHE) for funding this research under UTM Encouragement Research (UTMER) Grant (Cost Centre No.: Q.J130000.3851.19J23).

## References

1. Kwan T, Wu X (2017) TEG maximum power point tracking using an adaptive duty cycle scaling algorithm. *Energy Procedia* 105:14–27. Available: <https://doi.org/10.1016/j.egypro.2017.03.274>. Accessed 15 Jan 2022
2. Mamur H, Çoban Y (2020) Detailed modeling of a thermoelectric generator for maximum power point tracking. *Turk J Electr Eng Comput Sci* 28(1):124–139. Available: <https://doi.org/10.3906/elk-1907-166>. Accessed 15 Jan 2022
3. Faraj K, Hussain J (2020) Analysis and comparison of DC-DC boost converter and interleaved DC-DC boost converter. *Eng Technol J* 38(5):622–635. Available: <https://doi.org/10.30684/etj.v38i5a.291>. Accessed 18 May 2022
4. Enescu D (2019) Thermoelectric energy harvesting: basic principles and applications. In: *Green energy advances*. Available: <https://doi.org/10.5772/intechopen.83495>. Accessed 5 Feb 2022
5. Man E, Schaltz E, Rosendahl L (2014) Thermoelectric generator power converter system configurations: a review. In: *Proceedings of the 11th European conference on thermoelectrics*, pp 151–166. Available: [https://doi.org/10.1007/978-3-319-07332-3\\_18](https://doi.org/10.1007/978-3-319-07332-3_18). Accessed 18 May 2022
6. Ni L, Sun K, Zhang L, Xing Y, Chen M, Rosendahl L (2011) A power conditioning system for thermoelectric generator based on interleaved boost converter with MPPT control. In: *2011 international conference on electrical machines and systems*. Available: <https://doi.org/10.1109/icems.2011.6073395>. Accessed 16 May 2022
7. Islam M, Merabet A, Beguenane R, Ibrahim H (2014) Simulation based study of maximum power point tracking and frequency regulation for stand-alone solar photovoltaic systems. In: *International conference on renewable energies and power quality, Cordoba, Spain*
8. Sharp G (2014) *Sepic converter design and operation*

# A Hybrid Maximum Power Point Tracking (MPPT) for Thermoelectric Generator (TEG) System



Naseem Mohd Arshad, Mohd Zaki Daud, Shahrin Md Ayob,  
and Razman Ayop

**Abstract** Thermoelectric generators (TEG) convert heat energy into electricity in a quantity dependent on the temperature difference across them and the electrical load applied. It is critical to track the optimum electrical operating point using power electronic converters controlled by a maximum power point tracking (MPPT) algorithm. In this paper, a hybrid MPPT for perturb and observation (P&O) and open-circuit method (OCV) are proposed to compare with the conventional direct method for P&O and OCV methods, respectively. This research is initiated by modelling TEG system using MPPT algorithm with P&O method and OCV method using MATLAB/Simulink software. Then, it is followed by modelling a hybrid MPPT for both methods. In addition, a boost converter having this MPPT algorithm was added to the TEG modelling system. Every modelled system will be analysed and compared in the percentage of power transferred and response time. As conclusion, P&O method responds poorly to a fast-changing operating condition, and OCV method suffers disadvantages such as temporary power loss. The proposed hybrid method results in a very fast-tracking speed and the energy losses are improved compared to conventional direct method.

**Keywords** Hybrid · P&O · OCV · MPPT algorithm

---

N. M. Arshad · M. Z. Daud (✉) · S. M. Ayob · R. Ayop  
Faculty of Electrical Engineering, Universiti Teknologi Malaysia, 81310 Johor Bahru, Malaysia  
e-mail: [mdzaki@utm.my](mailto:mdzaki@utm.my)

N. M. Arshad  
e-mail: [naseemmohdarshad@graduate.utm.my](mailto:naseemmohdarshad@graduate.utm.my)

S. M. Ayob  
e-mail: [e-shahrin@utm.my](mailto:e-shahrin@utm.my)

R. Ayop  
e-mail: [razman.ayop@utm.my](mailto:razman.ayop@utm.my)

## 1 Introduction

Nowadays, ensuring the increasing global energy demand can be met is very crucial part to avoid affecting the environment in a detrimental way and it can be solved by developing sustainable and non-polluting electrical energy. There are many types of energy sources and conversion devices that were being used in various kinds of applications to overcome this issue such as small distributed networks, centralized generation, and system energy recovery [1]. It is very important to find the energy from resources that are renewable and easy to find at the environment [2]. One of the conversion devices that show potential for waste heat recovery applications is using thermoelectric generator (TEG) [3].

TEG is semiconductor device that converts the particular temperature difference between surfaces into electrical power directly [4]. In this case, it cannot deliver the maximum power automatically besides it has the behaviour of nonlinear dynamic and it can represent in nonlinear  $I-V$  curve. So, it is very important to track and achieve MPP on  $I-V$  curve and it can be done in MPPT technique. The MPPT is implemented in the system to get the maximum efficiency and operate the system around MPP [5].

There are a lot of MPPT methods that have recently been developed and integrated. The strategy is varied, and it includes complexity, sensors essential, convergence speed, price, selection of effectiveness, execution hardware, popularity, plus in other aspects [6]. In terms of techniques, the most widely used is perturb and observe (P&O) and open-circuit voltage (OCV) technique [7]. The particular comparison between these types of common MPPT strategies and describe variations between them need to be done so that the efficient power versus voltage ( $P-V$ ) characteristic curve can be obtained [7, 8].

To overcome the disadvantages of these two methods, a novel hybrid MPPT technique that is combination of P&O and OCV methods is proposed in this paper. To justify this proposed technique, the new MPPT should be figured out and keep consider the stated problem for both methods. The technique of hybrid of P&O and OCV methods is very suitable for this solution as it includes the advantages for both techniques and rejects their drawbacks. The limitation of this research is the MPPT is only involve P&O and OCV methods only. The comparison made is only between both methods and does not compare besides this. There might be a better solution for MPPT using modern technology and has improved a lot in terms of efficiency.

## 2 Literature Review

### 2.1 TEG Device

Combining high figure of merit p- and n-type semiconductors yields a thermoelectric (TE). Figure 1 shows the schematic diagram of TEG module. To increase the voltage, the TE is connected in series with one another. To increase heat conductivity, TEGs are built by linking TEGs in parallel using ceramic plates. Heat flow from the hot surface to the cold surface when a temperature difference between the ceramic plates is created. Electron flow from n-type to p-type semiconductors is caused by heat transfer [6, 7].

As a result, the parameters from this circuit can be produced as follows:

$$V_{OC} = \alpha \Delta T \tag{1}$$

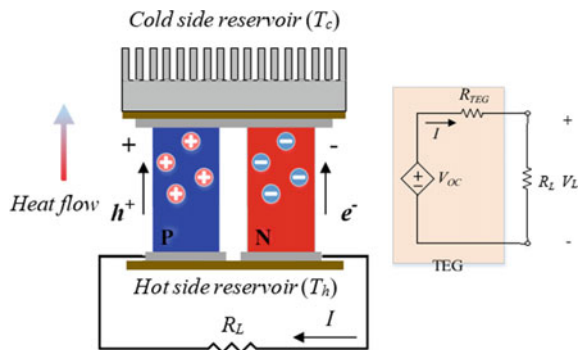
$$\Delta T = T_H - T_C. \tag{2}$$

VOC represents the TEG’s open-circuit voltage (V),  $\alpha$  denotes the Seebeck coefficient (V/K), and  $\Delta T$  is the different temperature between two surfaces (K).  $T_H$  represents hot temperature (K), and  $T_C$  represents cold temperature (K). By choosing a great material, a Seebeck coefficient can be obtained in the range between 100 and 300  $\mu\text{V/K}$  [4].

The equivalent circuit of a TEG module includes of a temperature-dependent voltage source and an internal resistor,  $R_{TEG}$ . The connection of a load,  $R_L$ , into TEG system is purposely to generate power. By using the fundamental of basic circuit theory, the power generated by the TEG can be derived as:

$$P_{TEG} = (\alpha \Delta T)^2 \times \frac{R_L}{R_L + R_{TEG}}. \tag{3}$$

Fig. 1 Equivalent circuit of a TEG module [7]



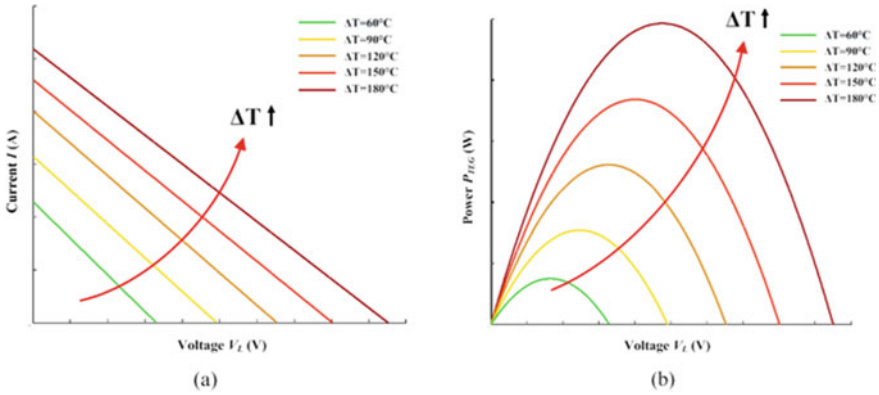


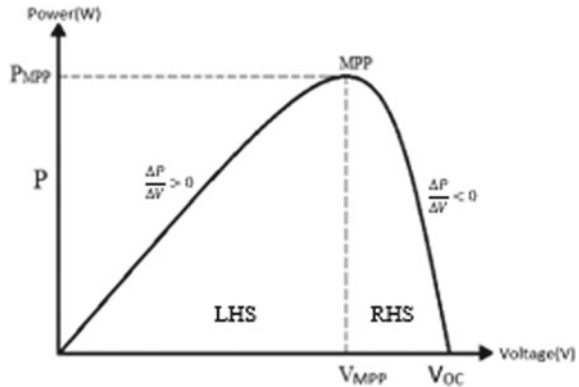
**Fig. 2** Characteristic curves of TG 12-6 under different temperature gradients, **a**  $I-V$  curves, **b**  $P-V$  curves [7]

The graph of current versus voltage ( $I-V$ ) can be obtained based on the difference of temperature, the curve is linear, and the power generated can be plotted based on ( $I-V$ ) curve. Figure 2a shows the simulated  $I-V$  curves of the TG 12-6 TEG module under various temperature gradients, whereas Fig. 2b shows the associated  $P-V$  curves for various temperature gradients. The parabolic  $P-V$  characteristic is produced by the linear  $I-V$  characteristic, with its maximum placed at half of the open-circuit voltage. For any given thermal operating point (OP), the output power produced by the TEG varies according to the current (voltage) drawn by the load, as shown in Fig. 2b; thus, optimizing the energy harvest from TEGs using an MPPT technique is important for TEG applications. To achieve this purpose, a power converter with MPPT control is typically installed between the TEG and the external load [7].

### 2.2 MPPT Algorithm: P&O Method

P&O method is one of the simplest methods to track maximum power point tracking. Figure 3 shows the power-voltage graph. Voltage at maximum power point,  $V_{MPP}$ , is located at the peak of the curve; meanwhile, maximum voltage is called as open-circuit voltage,  $V_{OC}$ . From the curve, it can be divided into three regions which is at maximum power point (MPP), left-hand side (LHS) and right-hand side (RHS). For MPP, the change of power with respect to voltage is zero where the power will always at maximum point.

Fig. 3 P-V curve



On the LHS region, the change of power with respect to voltage is always greater than zero (positive slope) when observing from 0 V to  $V_{MPP}$ . When the voltage is increased, power also increases and vice versa for this region. On the RHS region, the change of power with respect to voltage is always less than zero (negative slope) when observing from  $V_{MPP}$  to  $V_{OC}$ . When the voltage is increased, power will decrease, and when voltage is decreased, power will increase for this region.

From the derivative of power with respect to voltage, the logic can be used to create a flowchart by perturbing the voltage to observe the changing power. The purpose is to alter the current situation of the derivative to move close to the MPP. Figure 4 shows the flowchart of the MPPT: P&O. The algorithm is initiated by getting the value of voltage,  $V(k)$  and current,  $I(k)$ . Then the power is calculated using the formula,  $P(k) = V(k) \times I(k)$ . Next, the change of power and voltage is calculated by subtracting with the previous sample which are  $\Delta P = P(k) - P(k - 1)$  and  $\Delta V = V(k) - V(k - 1)$ . By comparing  $\Delta P$  and  $\Delta V$  with Fig. 4, if  $\Delta P$  and  $\Delta V$  are greater than zero, it indicates the curve is in LHS region. So, the voltage has to be increased and it can be done by adding duty cycle in boost converter and is given by  $D(k) = D(k - 1) + \Delta D$ . If  $\Delta P$  is greater than zero and  $\Delta V$  is less than zero, it indicates the curve is in RHS region. So, the voltage has to be decreased and it can be done by reducing duty cycle in boost converter, and it given by  $D(k) = D(k - 1) - \Delta D$ . If  $\Delta P$  and  $\Delta V$  are less than zero, it indicates the curve is in LHS region. So the voltage has to be increased, and it can be done by adding duty cycle in boost converter and is given by  $D(k) = D(k - 1) + \Delta D$ . If  $\Delta P$  is less than zero and  $\Delta V$  is greater than zero, it indicates the curve is in RHS region. So, the voltage has to be decreased, and it can be done by reducing duty cycle in boost converter and is given by  $D(k) = D(k - 1) - \Delta D$ .



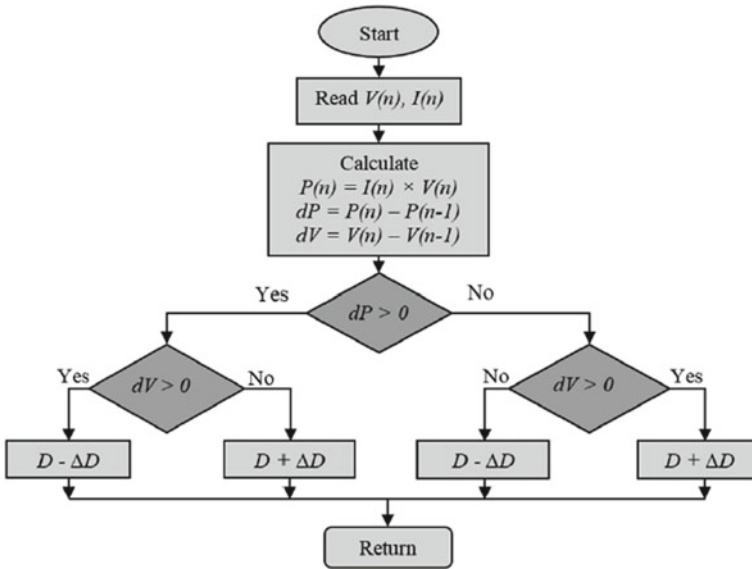


Fig. 4 Flowchart of MPPT P&O [4]

### 2.3 MPPT Algorithm: OCV Method

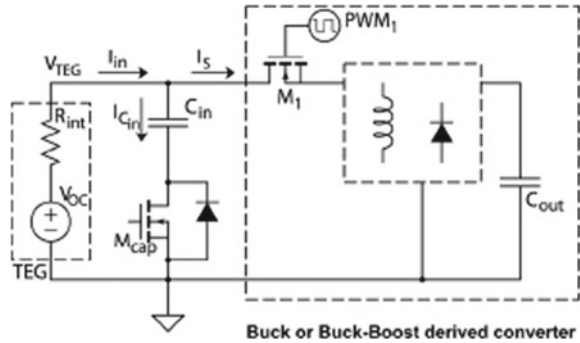
The fractional open-circuit voltage (FOCV) algorithm can be classified as indirect or offline method since it requires electrical parameters such as voltage and current to track the maximum power point. There are two approaches to implement this method. First, the method is known as the mathematical approach. Fractional open-circuit voltage, more commonly known as constant voltage in some literature due to the relation between open-circuit voltage ( $V_{OC}$ ) and the  $V_{MPP}$ , is almost linear. The equation between these parameters is as follows:

$$V_{MPP} = k \times V_{OC}, \tag{4}$$

where  $k$  is a constant proportionally. Based on the  $I-V$  characteristic of TEG, the value of the constant is usually in between 70 and 87% of the open-circuit voltage. The algorithm operates by periodically disconnecting the TEG from the power converter and  $V_{OC}$  can be measured.  $V_{MPP}$  can be calculated by using Eq. (4) (Fig. 5).

As second method, it can be known as switching approach. Figure 6 shows the schematic diagram of OCV. To understand more about the algorithm, Fig. 6 shows the timing diagram during the running time. During normal operation,  $M_{cap}$  is closed, and  $C_{in}$  contributes to the pulsing input current that the converter needs during  $t_{on}$ . When a measurement of the voltage in an open circuit is needed,  $M_{cap}$  is opened. The bottom part of Fig. 6 shows a closer look at what happens in this situation. During  $t_{off}$ ,  $M_1$  is open, and the TEG is temporarily disconnected from the converter.

**Fig. 5** Schematic drawing of the components required for OCV method [9]



Since the current can't flow into  $C_{in}$ , the potential at the TEG's terminals rises to the open-circuit voltage  $V_{OC}$ , which usually happens within tens of nanoseconds. The microcontroller is set to measure  $V_{TEG}$  during  $t_{off}$  while the converter is still in a pseudonormal state, and both the TEG and  $C_{in}$  are still giving power to the converter during  $t_{on}$ . The open-circuit measurement is repeated every  $T_{meas}$ , which depends on the TEG system's thermal time constant. The time is normally between 0.1 and 1 s. In between measurements of  $V_{OC}$ , a digital control loop keeps changing the duty cycle of the converter to keep  $V_{TEG}$  at half of  $V_{OC}$ .

Even though method has the ability to track maximum power tracking, it also faces few disadvantages. The fact that the equation provided is an approximation which means that this technique does not deliver accurate maximum power point. Besides, there is power loss during the formation of  $V_{OC}$ . It is because the voltage is obtained from the generating open circuit by disconnecting the load during a fraction of second. So this method should be modified so that efficiency can be improved.

However, this method possess has advantages of being simple to implement due to no added circuit will be used. Besides, the cost to implement this method is very low because no DSP or microcontrollers are required. As a result, because it is not a precise procedure, it is used when precision is not a concern. It's also can be considered as fast technique to reach maximum power because doesn't require a lot of sensors.

#### 2.4 MPPT Algorithm: Hybrid P&O and OCV Methods

Hybrid of maximum power point tracking methods is one of the alternatives used to overcome the drawbacks of single-method approaches and able to generate much better outcomes. Hybrid MPPT approaches have been presented in the literature to address the shortcomings of both traditional and advanced methods. Combining two conventional methods, a hybrid soft computing-based algorithm with a conventional-based algorithm, or two soft computing-based algorithms are examples of hybrid methods.

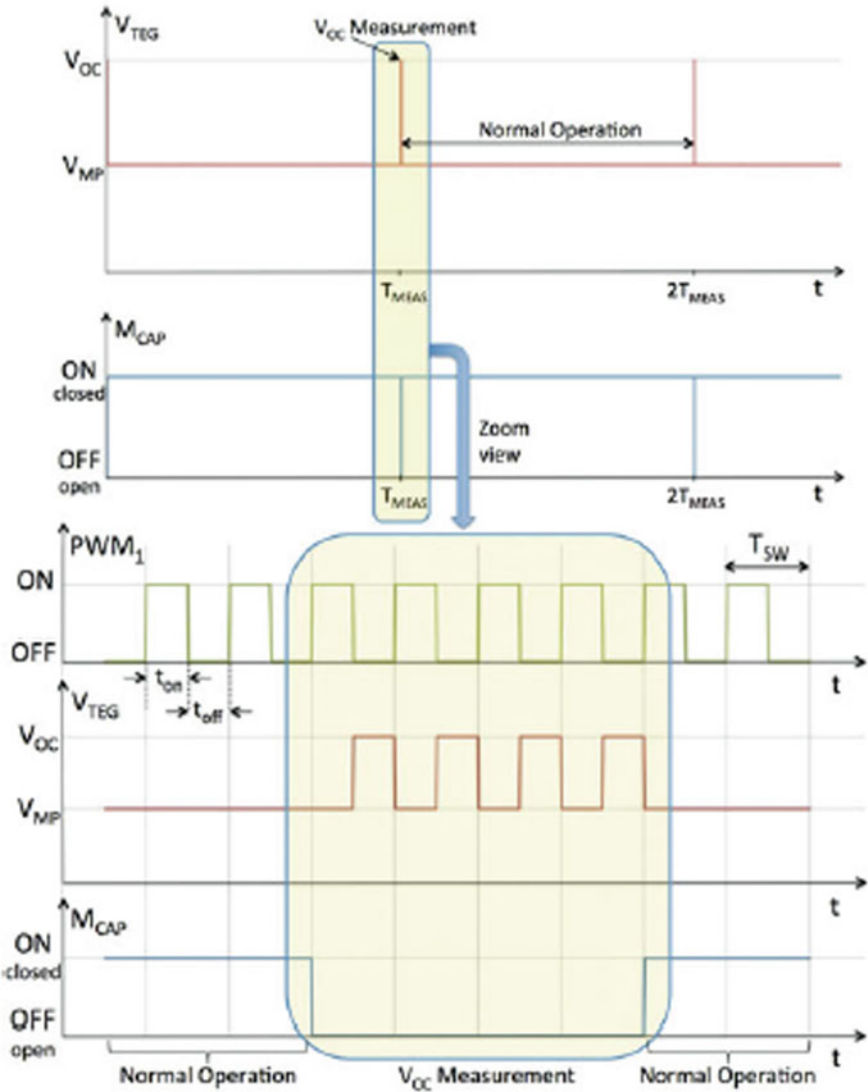


Fig. 6 Timing diagram for OCV measurement is achieved [9]

A hybrid of open-circuit voltage and the P&O approach is proposed as shown in Fig. 7. The proposed method’s working principle is that these two approaches are defined as two working loops, the set point computation and fine-tuning loops. The maximum power point, MPP, is approximated using the open-circuit voltage method. The fine-tuning loop tracks the precise amount MPP using the traditional P&O method. During start-up and in reaction to fast changes in atmospheric conditions, the suggested approach exhibits acceptable efficiency and high performance.

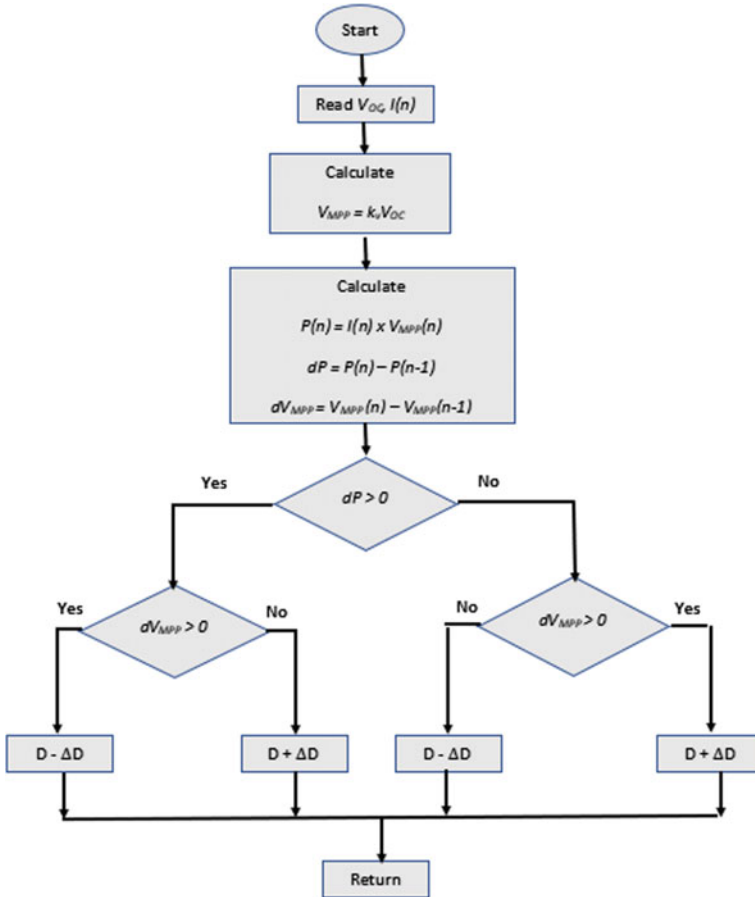
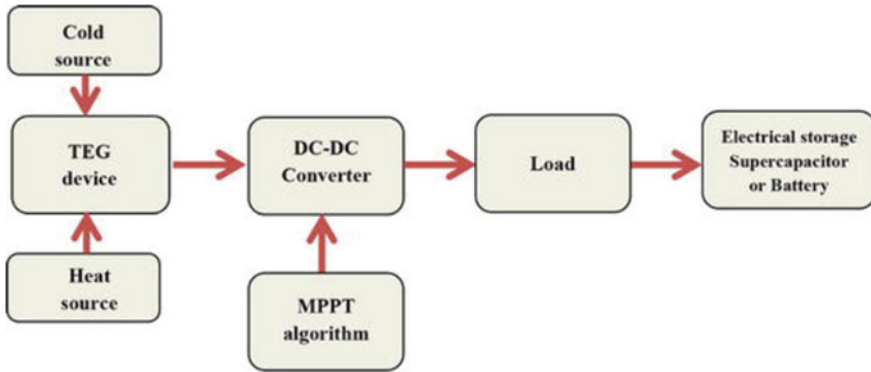


Fig. 7 Flowchart of MPPT hybrid P&O and OCV

In this algorithm, it possesses fast-tracking time and no energy loss during OCV sampling are two advantages of this proposed technique.

### 3 Methodology

Understanding the general overview of TEG is necessary so that all the processes can be done separately and able to analyse well. From this overview, it starts with implementing boost converter which include circuit design and software simulation. Next is to implement MPPT with P&O method and followed by MPPT with OCV method. Next, hybrid of this method will be done. After all the design and simulation



**Fig. 8** General view of TEG system

is successful, analysis and discussion of these simulations include comparison will be briefly explained.

### 3.1 Design Overview

From the general view of TEG block diagram, the research is mainly focused on DC-DC converter and MPPT algorithm. For DC-DC converter, boost converter is used for this research as to step up the voltage. Besides, MPPT algorithm will be more focused on P&O method and OCV method. These algorithms will be designed and analysed separately before implementing hybrid for both methods. The rest of the block diagram is not the main component for this research, but it is necessary and required for the simulation as every block diagram has its own function so that it can form a complete system. Figure 8 shows the block diagram for TEG system. For the software simulation, MATLAB/Simulink is being used to simulate and analyse these blocks. The blocks will be simulated separately which include boost converter, MPPT P&O method, MPPT OCV method, and hybrid of P&O and OCV methods.

### 3.2 MPPT: P&O

In the modelling TEG system with MPPT: P&O method, the schematic diagram is shown in Fig. 9. The structure is sketched based on block diagram of TEG system that is referred to Fig. 9, and simulation is made via MATLAB/Simulink. From the schematic diagram for simulation, the parameters of every component will be shown in Table 1.

For TEG module, it consists of two models which is connected in parallel which is shown in Fig. 10a and the internal structure of TEG model is shown in Fig. 10b. The

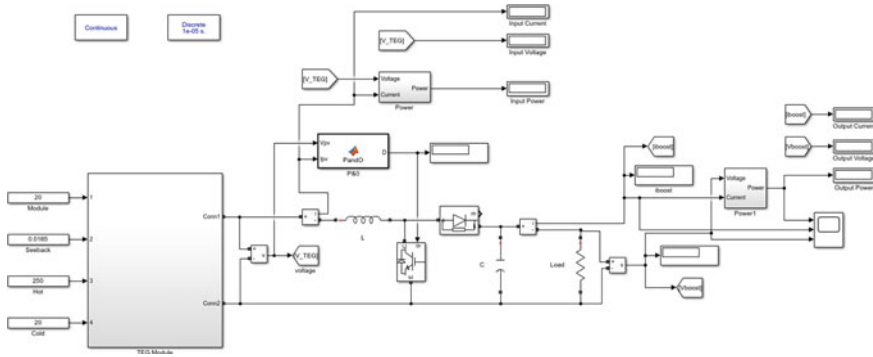


Fig. 9 Schematic diagram of TEG system using P&O

Table 1 Parameters for TEG module using P&O

Properties	Value
Hot surface temperature, $T_H$	80–250 °C
Cold surface temperature, $T_C$	20 °C
Load matching each resistance, $R_{in} = R_L$	0.7 $\Omega$
Seebeck coefficient	185 $\mu\text{V/K}$

connection of modules is in series parallel type. At default, the number of connected modules in TEG modelling is 20 in series. So the total resistance that is connected in series is  $0.7 \times 20 = 14 \Omega$ . When connected in parallel, total resistance is  $14/2 = 7 \Omega$ . So, total resistance in series parallel is  $7 \Omega$ . In this system, boost converter with MPPT: P&O was included where the inductor,  $L$  is 1 mH and capacitor,  $C$  is 3300  $\mu\text{F}$ .

In this simulation, temperature will be varied at 80–250 °C hot temperature,  $T_H$ . Meanwhile, the value of cold temperature,  $T_C$  and load,  $R_L$  will be constant which are 25 °C and 7  $\Omega$ , respectively. From the schematic diagram shown in Fig. 12, the input current, input voltage, and input power refer to parameter before having MPPT: P&O. Meanwhile, the output current, output voltage, and output power refer to the parameter after having MPPT: P&O. All these values will be tabulated. Besides, the

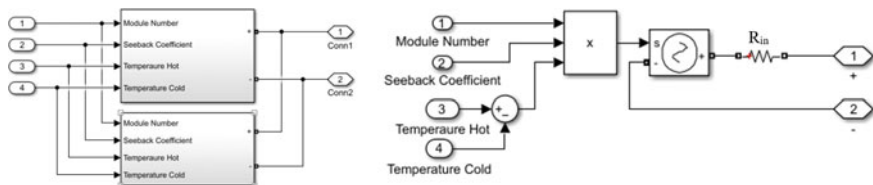


Fig. 10 Connection of TEG, a parallel, b internal structure

percentage is power transferred and is calculated by division of output power with respect to input power.

### 3.3 MPPT: OCV

The schematic diagram for OCV method is shown in Fig. 11. The structure is sketched based on Fig. 5. From this schematic diagram, the parameters of every component will be shown in Table 2.

In this simulation, the parameters of Seebeck’s coefficient will be kept constant at  $185 \mu\text{V/K}$ . Besides, switching frequency,  $f_{s1}$  will be set at 250 kHz at 90% of pulse width. For switching frequency,  $f_{s2}$  it also will be set at 250 kHz but pulse width only at 50%. The temperature difference will be varied from 60 to 250 °C. From these variables, percentage of power transferred from TEG sources to the load will

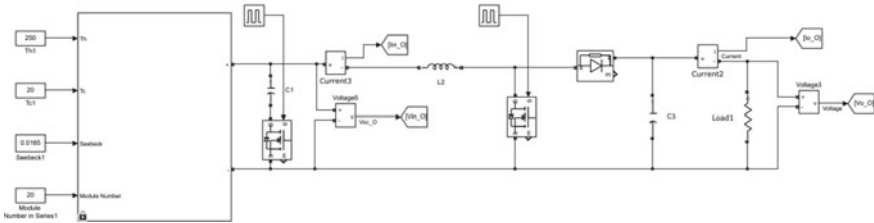


Fig. 11 Schematic diagram of TEG system using OCV

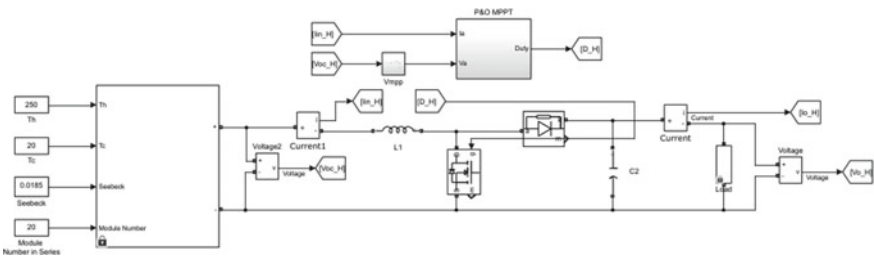


Fig. 12 Schematic diagram of TEG system using hybrid P&O and OCV

Table 2 Parameters for TEG module using OCV

Properties	Value
Switching frequency, $f_{s1}$	250 kHz at 90% pulse width
Switching frequency, $f_{s2}$	250 kHz at 50% pulse width
Hot surface temperature, $T_H$	80–250 °C
Cold surface temperature, $T_C$	20 °C

**Table 3** Parameters for TEG module using hybrid P&O and OCV

Properties	Value
Hot surface temperature, $T_H$	80–250 °C
Cold surface temperature, $T_C$	20 °C
Constant, $k_v$	0.76

be calculated and tabulated. The power is calculated from the TEG module which refers to input side and boost converter as output side. The parameter for voltage and current from both sides will be tabulated. This simulation will be repeated six different temperatures.

### 3.4 MPPT: Hybrid P&O and OCV

The schematic diagram for hybrid of P&O and OCV methods is shown in Fig. 12. The structure is sketched based on Fig. 7. From this schematic diagram, the parameters of every component will be shown in Table 3.

In this simulation, the parameters of Seebeck's coefficient will be kept constant at  $185 \mu\text{V/K}$ . The temperature difference will be varied from 60 to 250 °C. From these variables, percentage of power transferred from TEG sources to the load will be calculated and tabulated. The power is calculated from the TEG module which refers to input side and boost converter as output side. The parameter for voltage and current from both sides will be tabulated. This simulation will be repeated at six different temperatures.

## 4 Result

After the text edit has been completed, the paper is ready for the template. Duplicate the template file by using the Save As command and use the naming convention prescribed by your conference for the name of your paper. In this newly created file, highlight all of the contents and import your prepared text file. You are now ready to style your paper; use the scroll-down window on the left of the MS Word Formatting toolbar.

Figure 13 shows the waveform of power generated from three different methods at  $\Delta T = 230 \text{ }^\circ\text{C}$ . All waveforms show that the system achieved stability but at different time. The analysis will be explained in the tabulated data (Tables 4, 5, and 6).



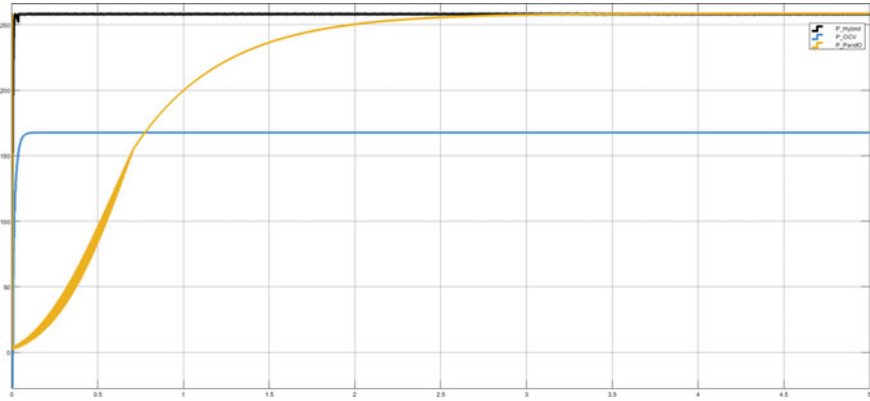


**Fig. 13** Power generated at for every method at  $\Delta T = 230\text{ }^\circ\text{C}$

**Table 4** Result of P&O methods

Surface temperature ( $^\circ\text{C}$ )		Load, $R_L$ ( $\Omega$ )	Current, $I$ (A)		Voltage, $V$ (V)		Power, $P$ (W)		MPPT (%)
$T_H$	$T_C$		Input	Output	Input	Output	Input	Output	
80	20	7	1.545	1.512	11.38	10.58	17.59	16.00	90.96077
100			2.08	2.035	15.04	14.24	31.28	28.98	92.64706
150			3.415	3.342	24.15	23.39	82.63	78.17	94.60244
180			4.217	4.126	29.68	28.88	125.2	119.2	95.20767
200			4.751	4.649	33.34	32.54	158.4	151.3	95.51768
250			6.087	5.956	42.49	41.69	258.6	248.3	96.01701

**Table 5** Result of OCV methods

Surface temperature ( $^\circ\text{C}$ )		Load, $R_L$ ( $\Omega$ )	Current, $I$ (A)		Voltage, $V$ (V)		Power, $P$ (W)		MPPT (%)
$T_H$	$T_C$		Input	Output	Input	Output	Input	Output	
80	20	7	2.489	1.245	4.76	8.718	11.85	10.86	91.64557
100			3.334	1.668	6.24	11.68	20.8	19.48	93.65385
150			5.446	2.725	9.94	19.08	54.14	51.98	96.01034
180			6.714	3.359	12.16	23.51	81.64	78.99	96.75404
200			7.559	3.782	13.64	26.47	103.1	100.1	97.0902
250			9.671	4.839	17.34	33.87	167.7	163.9	97.73405

**Table 6** Result of hybrid P&O and OCV methods

Surface temperature (°C)		Load, $R_L$ ( $\Omega$ )	Current, $I$ (A)		Voltage, $V$ (V)		Power, $P$ (W)		MPPT (%)
$T_H$	$T_C$		Input	Output	Input	Output	Input	Output	
80	20	7	1.31	0.7825	13.03	21.48	17.07	16.81	98.47686
100			1.828	1.225	16.8	24.58	30.72	30.11	98.01432
150			3.115	2.435	26.3	33.04	81.91	80.44	98.20535
180			3.894	3.192	31.94	38.34	124.4	122.4	98.39228
200			4.445	3.703	35.48	41.92	157.7	155.2	98.41471
250			5.77	4.993	44.71	50.95	258	254.4	98.60465

From this result, the percentage of power transferred is almost stable for hybrid of P&O and OCV which is 98% and above for all different temperature. For conventional method which are P&O and OCV methods, the percentage of power transferred increase proportionally to the temperature difference. The higher the temperature difference, the more efficient percentage of power transferred. Besides, the generated power from hybrid and P&O methods is much higher compared to OCV methods which is around 30–35% of difference.

Table 7 shows the settling time for on three different simulation which from P&O, OCV, and hybrid of both methods. It can be observed that the settling time is almost same for each method even occurred at difference temperature. Hybrid methods show the fastest settling time which is around 0.028 s in average. P&O method shows the slowest of settling time which is 2.59 s in average.

Table 8 shows the summary of outcome for all simulation. There are three concerns in this simulation which are generated power, settling time, and stability. P&O methods produce a high-power generation but suffer slow settling time. OCV methods produce a very fast settling time but suffer low power generation. For both conventional methods, the efficiency increases when difference temperature increase. For hybrid of P&O and OCV methods, overcome all the disadvantages for both conventional method without any additional circuit.

**Table 7** Response time for every method

Temperature difference, ( $\Delta T = T_H - T_C$ )	Settling time of MPPT algorithm, $T_s$ (s)		
	P&O	OCV	Hybrid
$\Delta T = 60^\circ$	2.018	0.060	0.017
$\Delta T = 80^\circ$	2.082	0.060	0.021
$\Delta T = 130^\circ$	2.169	0.061	0.028
$\Delta T = 160^\circ$	2.175	0.062	0.031
$\Delta T = 180^\circ$	2.195	0.063	0.033
$\Delta T = 230^\circ$	2.218	0.063	0.038

**Table 8** Summary of results

Methods	Advantages	Disadvantages
P&O	<ul style="list-style-type: none"> <li>• High-generated power</li> </ul>	<ul style="list-style-type: none"> <li>• Slow settling time</li> <li>• Efficiency increases when difference temperature increase</li> </ul>
OCV	<ul style="list-style-type: none"> <li>• Fast settling time</li> </ul>	<ul style="list-style-type: none"> <li>• Low-generated power</li> <li>• Efficiency increases when difference temperature increase</li> </ul>
Hybrid	<ul style="list-style-type: none"> <li>• Fast settling time</li> <li>• High-generated power</li> <li>• Stable is efficiency of power transferred for all different temperature</li> </ul>	

## 5 Conclusion

In conclusion, three outcomes that have been observed which include power generation, response time, and efficiency. P&O methods suffer slow settling time while OCV methods suffer low-generated power. Besides both conventional methods face low power transferred during low-temperature difference. The proposed hybrid of P&O and OCV methods has overcome the disadvantages of conventional methods for P&O and OCV methods, respectively. Furthermore, it does not require additional circuits to implement so it can reduce the cost of installation.

**Acknowledgements** The authors would like to thank Universiti Teknologi Malaysia (UTM) and the Ministry of High Education Malaysia (MOHE) for funding this research under the UTM Encouragement Research (UTMER) Grant (Cost Centre No.: Q.J130000.3851.19J23).

## References

1. Laird I, Lu DD (2013) High step-up DC/DC topology and MPPT algorithm for use with a thermoelectric generator. *IEEE Trans Power Electron* 28(7):3147–3157. <https://doi.org/10.1109/TPEL.2012.2219393>
2. Alonso G, Osipova Elena A (2017) Maximum power point tracking algorithms for solar photovoltaic systems
3. Nadeem A, Sher HA, Murtaza AF, Ahmed N (2020) An online fractional open-circuit voltage maximum power point tracking (MPPT) algorithm based on sliding mode control. In: 2020 international symposium on recent advances in electrical engineering & computer sciences (RAEE & CS), pp 1–6. <https://doi.org/10.1109/RAEECS50817.2020.9265809>
4. Mamur H, Çoban Y (2020) Detailed modeling of a thermoelectric generator for maximum power point tracking. *Turk J Electr Eng Comput Sci* 28(1)
5. Murtaza AF, Sher HA, Chiaberge M, Boero D, Giuseppe MD, Addoweesh KE (2012) A novel hybrid MPPT technique for solar PV applications using perturb & observe and fractional open circuit voltage techniques. In: Proceedings of 15th international conference Mechatronika, pp 1–8

6. ESRAM T, CHAPMAN PL (2007) Comparison of photovoltaic array maximum power point tracking techniques. *IEEE Trans Energy Convers* 22(2):439–449. <https://doi.org/10.1109/tec.2006.874230>
7. LIU Y-H, CHIU Y-H, HUANG J-W, WANG S-C (2016) A novel maximum power point tracker for thermoelectric generation system. *Renew Energy* 97
8. BAIMEL D, TAPUCHI S, LEVRON Y, BELIKOV J (2019) Improved fractional open circuit voltage MPPT methods for PV systems. *Electronics* 8(3). <https://doi.org/10.3390/electronics8030321>
9. ALONSO AEG (2017) Maximum power point tracking algorithms for solar photovoltaic systems

# Thermoelectric Generator (TEG) by Using Indirect Maximum Power Point (MPP) Algorithm



Ardrine Justin, Mohd Zaki Daud, Shahrin Md Ayob, and Razman Ayop

**Abstract** Heat is one of the most important energy that exists and has drove many civilizations to achieve greatness. When we use it in daily life, we can use thermoelectric generator to power our electrical appliances at home from the heat we produce domestically. The heat is absorbed by the thermoelectric generator (TEG) module and since the other surface of the module is cold, it will create a gradient in temperature. If the load linked to the TEG is equal to the internal resistance, the maximum power that it can produce is achieved. To produce this result, we must design the circuit properly by using the suitable MPPT such as direct MPPT like Perturb and Observe (P&O) or indirect maximum power point tracking (MPPT) like constant voltage. There are many types of MPPT that we can classify based on the methods used. In this study, we tried to study and compare indirect MPPT to the direct MPPT. This will help us to solve the problem that normal and direct MPPT such as P&O faces. Because of the inefficiency of the direct method, the indirect approach is favourable in solving this task. To overcome the problem of losing energy during the sudden changes, the indirect MPPT will fix or constant one of its parameter that leads us to achieve high efficiency, desired power and stability under sudden changes.

**Keywords** Boost converter · Buck converter · MPPT · TEG · Indirect MPPT

---

A. Justin · M. Z. Daud (✉) · S. M. Ayob · R. Ayop  
Faculty of Electrical Engineering, Universiti Teknologi Malaysia, 81310 Johor Bahru, Malaysia  
e-mail: [mdzaki@utm.my](mailto:mdzaki@utm.my)

A. Justin  
e-mail: [megat.azri.irfan@graduate.utm.my](mailto:megat.azri.irfan@graduate.utm.my)

S. M. Ayob  
e-mail: [e-shahrin@utm.my](mailto:e-shahrin@utm.my)

R. Ayop  
e-mail: [razman.ayop@utm.my](mailto:razman.ayop@utm.my)

## 1 Introduction

Human has harnessed the power of heat since beginning of time and helps us progress further into more progress and advanced future. Since invention of steam engine that drove the first industrial revolution, we had used more energy and created carbon footprint in 100 years than any human and in history. Our desire for energy makes us want to conserve more energy and use it efficiently, so that we will use all of it without wasting any of it. That is why technology like TEG is introduced. TEG is a technology that uses heat energy to produce electricity without having to use any mechanical part. This is one of the reasons why it is a very efficient technology. The usage is very simple, at one end it is heated and one end is cold. The movement of electrons created by the temperature difference is going to create electrical energy, without having to move anything or mechanical movement. One of the reasons is it is very efficient. TEG can produce electricity without having to produce any noise which is one of its many advantages. However, TEG is subject to disadvantages to like any technology that it produces a very small voltage especially if it operates without MPPT. Even with MPPT like P&O MPPT, it still suffered from inefficiency especially when the load surpasses certain value and when the value of the load suddenly changes or the condition was suddenly changed. It will suffer from energy loss and the steady state power oscillation that will reduce the efficiency. However, we can solve this problem by using indirect MPPT method that will eliminate the problem and allow rapid track the desired MPPT with various operating conditions. In this method, when operational, the system will work at maximum power, is either measured or predicted the current or voltage by using experimental data. This is because in this 2 method, the duty ratio is controlled or fixed to produce only the maximum power for a specific operating condition. A constant current or voltage is quite popular that produces a desired control outcome. Because of this, the system is simple structured and very optimum. It also is not sensitive to any sudden changes from outside elements or conditions. This report aims to study the working principle of TEG and P&O MPPT and gather the result of it, so we can use it later in the next part of this study, where we will be comparing the data in this study with the data that we will get from the indirect MPPT. Our focus is at their efficiency, power and stability under sudden changes.

## 2 Objectives

The objectives of the TEG project are:

- I. To design a TEG system and a boost converter by using direct MPPT algorithm.
- II. To design a TEG system and a boost converter by using indirect MPPT algorithm.

- III. To simulate the TEG by using MATLAB/Simulink.
- IV. To compare the performance of the TEG with indirect MPPT and direct MPPT algorithm.

### 3 Literature Review

#### (A) *Thermoelectric Generator*

To produce electricity by using thermoelectric module, it must be connected to two conjugate p-type and n-type semiconductor in series to increase the voltage [1]. It can be achieved through the concept of Seebeck's effect where voltage is produced when the module is put at different temperatures.

This is happening when one side of the semiconductor or material is heated and the other is cooled off. The effect occurs because of the movement of the charge carriers inside the material. The electrons are the charge carriers in n-type semiconductors and in p-type, the hole is the charge carrier [1]. Because of this, potential difference is created due to the build-up of the charge carriers at one end.

#### (B) *Boost Converter*

This is one of many important part of TEG, because it will increase the input voltage that it received from the TEG module. To build a boost converter, we must have an inductor, capacitor, resistor, transistor and diode when the switch turns on, the transistor or MOSFET in our case is turning on. Because of that, all the currents will flow to the MOSFET through the inductor. The current can flow through to the capacitor because the diode is in back biased [2]. When the MOSFET is turned off, the current will not flow to inductor, because the function of the induction is to make sure that our current flow is smooth. It will respond by generating a large voltage with opposite polarity of the supply source (voltage) [2]. The inductor suddenly acts like voltage source and the capacitor is in forward biased. Because of this, the capacitor is charged much higher than before. This also means that, we finally stepped up the low voltage DC voltage.

#### (C) *Buck Converter*

Buck converters work in a manner that is comparable with PWM 'dimming.' We've all heard of a PWM signal dimming lights. When the duty cycle is low, the load sees a low average voltage, and when the duty cycle is high, the load sees a high average voltage [1].

#### (D) *Direct and Indirect MPPT*

There are many type of MPPTs that been used in domestic and industry. Each of the design of the MPPT is based on the specifications, limitations and applications. Each

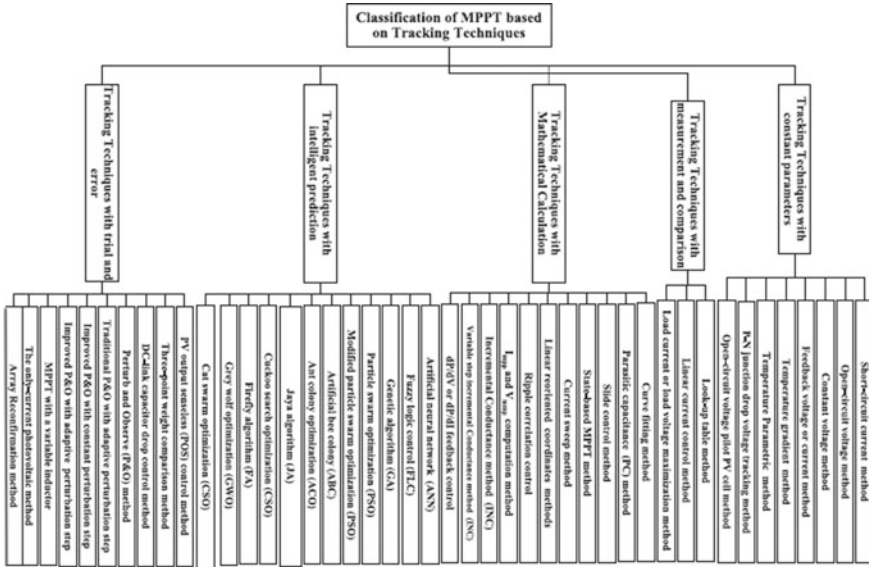


Fig. 1 General classification of MPPT [3]

of the methods can be classified based on the different factors, working principle and implementation [4]. However, we can classify these methods into two categories which are direct and indirect. Direct and indirect method fall under conventional method, because it relies on a relatively simple algorithm or calculations. Besides, it also has very low cost and is simple to build (Fig. 1).

## 4 Methodology

### (1) Flowchart

See Fig. 2.

### (2) Simulation and design for TEG modelling

In this project of FYP1, module from Hayati Mamur and Yusuf Coban, detailed modelling of the thermoelectric generator for maximum power point tracking is used problem [5] (Table 1).

By using this specification, the TEG model was designed and built in Simulink. Below is shown the block diagram for this project (Figs. 3 and 4).

In figure above, to increase the voltage, 20 TEG modules are used in series. Then, that TEG is connected to other TEG to increase the current in the design. After



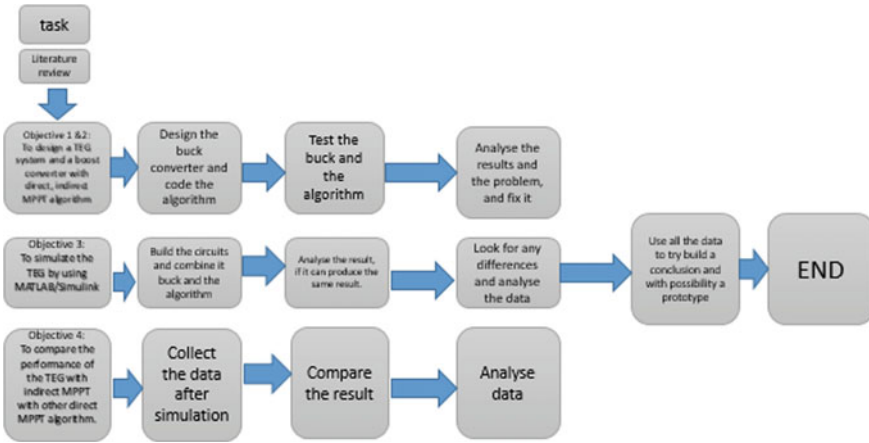


Fig. 2 Flowchart for the progress of the project

Table 1 Specification for the TEG

Description	Notation	Value
Hot temperature	°C	250
Cold temperature	°C	30
Seebeck coefficient	$\alpha$	$1.85 \times 10^{-4}$
Open-circuit voltage	$V_{oc}$	$4 \pm 0.4$
Short circuit current	$I_{sc}$	$5.8 \pm 0.6$
Matched load resistance	$R$	0.7
Matched load voltage	$V_{pmax}$	$2.0 \pm 0.2$
Matched load current	$I_{pmax}$	$2.9 \pm 0.3$
Matched load power	$P_{max}$	5.8

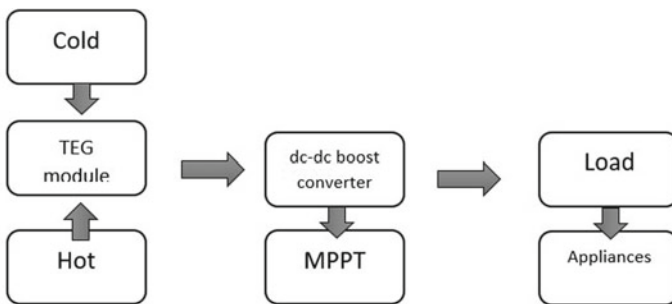


Fig. 3 Block diagram of TEG

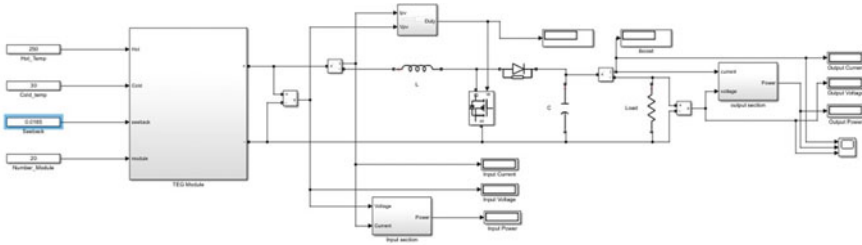


Fig. 4 TEG circuit

that, TEG was connected to the boost converter, and MPPT. The boost is fixed with components that have some value such as inductor (5 mH), capacitor (3300 F) and switching frequency (20 kHz).

To obtain the result that we desired in the TEG modelling, a specific value will put as input in the TEG module for Seebeck coefficient, the maximum and minimum temperature and the number of module used which is 20. To build this module, we need to dive deep into the internal structure of the TEG as shown in Fig. 5 (Figs. 6 and 7).

In the internal structure of the TEG model, the internal resistance is  $1.7 \times 20 = 34 \Omega$ . This is because we have 20 TEGs that are used. In the internal structure, we have two identical TEGs that are parallel to each other, so the overall internal resistance is  $17 \Omega$ .

### (3) Designing P&O MPPT

In this project, we only used the Perturb and Observe (P&O) MPPT, because we will use the data from the result to actually compare them with the data that we will get for future project or result in FYP2, which is the data from indirect MPPT.

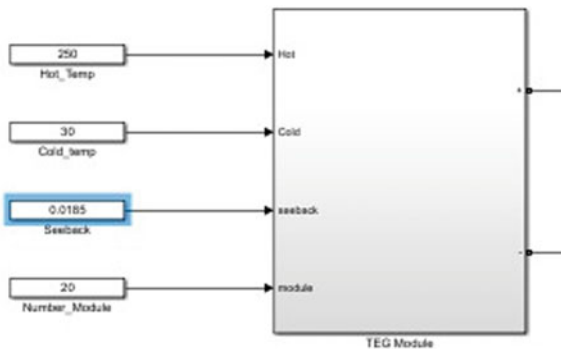


Fig. 5 TEG module

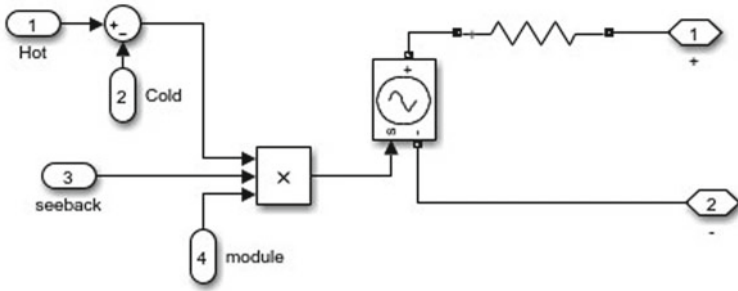


Fig. 6 Internal structure on TEG

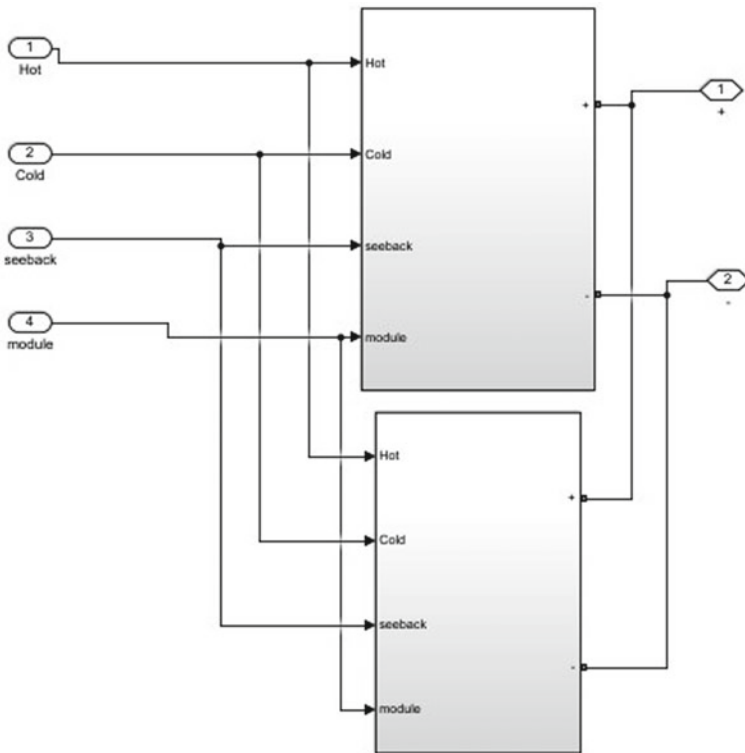


Fig. 7 Second layer of TEG module

This MPPT is designed to work with a boost converter that will help us to increase the small value of the voltage that it produced by the TEG itself. According to the block diagram, the input from the module will go to the converter and MPPT, where voltage and current will be measured. From there we can obtain the value for power. The data later was fed to the function block inside the MPPT internal circuit, where

our coding or source code was written. Inside the source code, the duty cycle was 0.7. If the duty cycle within limit was coded which was between zeros to one, if the power is more than zero, so the voltage also is more than zero. The duty cycle will be increased if the power is greater, but the voltage is lower than zero and reduced if both power and voltage are more than zero (Fig. 8).

(4) *First circuit MPPT*

See Figs. 9 and 10.

(5) *Second circuit MPPT*

See Figs. 11 and 12.

(6) *Algorithm for the three fixed constant voltage*

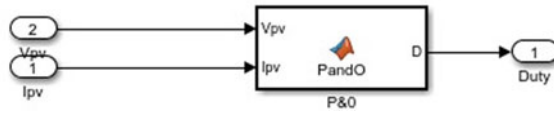


Fig. 8 MPPT block in Simulink

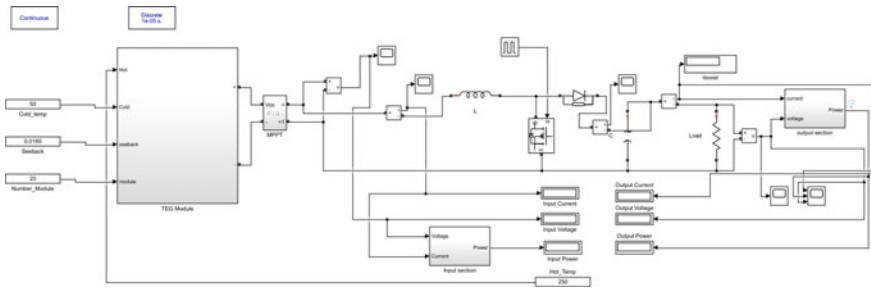


Fig. 9 Fractional constant voltage in Simulink

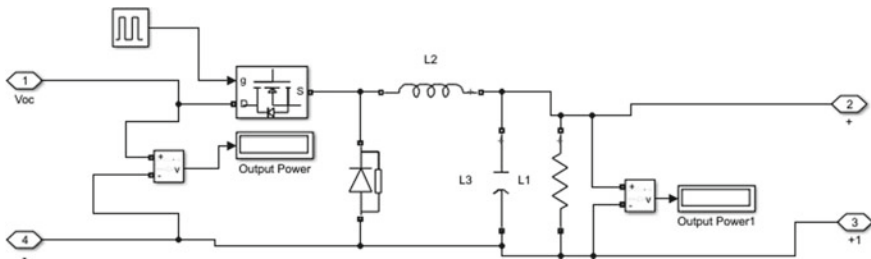


Fig. 10 MPPT

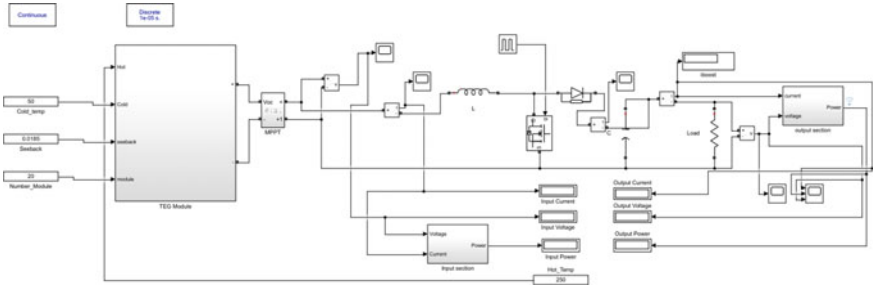


Fig. 11 Three fixed voltages in Simulink

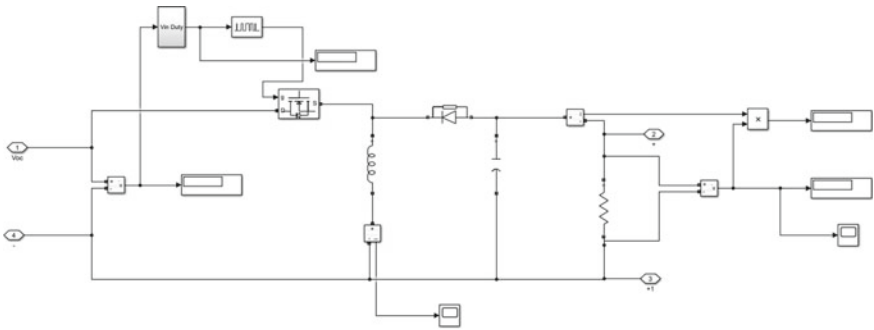


Fig. 12 MPPT block diagram for simulation

```

function D = Const (Vin)

persistent Dprev

if isempty(Dprev)
    Dprev = 0.5;
end
if (Vin>0)
    if (Vin>39)
        if (Vin>50)
            if (Vin>60)
                D=0.4478;
            else
                D=0.5195;
            end
        else
            if (Vin>45)
                D=0.5492;
            else
                D=0.5958;
            end
        end
    end
end
    
```

```

else
  if (Vin<39 && Vin>18)
    if (Vin>25 && Vin>33 )
      D =0.4032;
    else
      if (Vin>25 && Vin<33)
        D =0.4579;
      else
        if (Vin>20 && Vin<25)
          D=0.5297;
        else
          D=0.5747;
        end
      end
    end
  end
else
  if (Vin>10 && Vin<18)
    D=0.02525;
  else
    if (Vin>5 && Vin<10)
      D=0.4032;
    else
      D=0.5748;
    end
  end
end
end
end
end
else
  D =Dprev;
end

%Update internal values
Dprev = D;

```

## 5 Results

*This is the result for our fractional constant voltage in the table below. It is an indirect MPPT because we don't use V-I characteristics to achieve MPPT in the system.*

### (A) Fractional Constant Voltage

See Table 2.

### (B) Three Fixed Voltage

See Table 3.

### (C) Perturb and Observe

See Table 4.

**Table 2** Fractional constant voltage

Surface temp.		Load	Current		Voltage		Power		%eff
$T_H$	$T_C$		Input	Output	Input	Output	Input	Output	
60	50	17	0.2412	0.09573	0.982	1.627	0.2368	0.1558	65.7939
70			0.5508	0.2189	1.837	3.722	1.012	0.8149	80.5237
90			1.17	0.4653	3.547	7.911	4.149	3.681	88.7202
110			1.789	0.7118	5.256	12.1	9.404	8.612	91.5781
130			2.408	0.9582	6.906	16.29	16.78	15.61	93.0274
150			3.028	1.205	8.676	20.48	26.27	24.67	93.9094
175			3.802	1.513	10.81	25.71	41.11	38.9	94.6242
200			4.575	1.821	12.95	30.95	59.25	56.35	95.1055
250			6.123	2.437	17.22	41.42	105.5	100.9	95.6398

**Table 3** Three fixed constant voltage

Surface temp.		Load	Current		Voltage		Power		Eff%
$T_H$	$T_C$		Input	Output	Input	Output	Input	Output	
60			0.08544	0.06396	1.432	1.067	0.1224	0.06955	56.8219
70			0.2254	0.1688	2.78	2.869	0.6266	0.4843	77.2901
90			0.2563	0.1921	3.074	3.0266	0.7879	0.6275	79.6421
110			0.6144	0.4603	6.581	7.824	4.043	3.601	89.0675
130			1.084	0.8123	11.09	13.81	12.02	11.22	93.3444
150			1.371	1.027	13.86	17.46	19	17.92	94.3158
175			1.302	0.9755	13.27	16.58	17.28	16.18	93.6343
200			1.566	1.174	15.85	19.95	24.83	23.41	94.2811
250			2.802	2.099	27.71	35.69	77.64	74.93	96.5095

## 6 Discussion

### (A) Efficiency of Fractional Constant Voltage

This method is using buck converter to reduce the voltage it received from the TEG and set it at 75% of the original value before supplying it back to the boost converter. When the boost converter received a nice and stable voltage, it will reduce the amount of energy that it will waste during the process as in P&O.

**Table 4** Perturb and observe

P&O									
Surface temp.		Load	Current		Voltage		Power		Efficiency
$T_h$	$T_c$		Input	Output	Input	Output	Input	Output	
60	50	17	0.2131	0.1418	2.209	2.411	0.4706	0.3418	72.6307
70			0.4802	0.3119	4.039	5.302	1.939	1.654	85.3017
90			1.086	0.6489	7.201	11.03	7.817	7.159	91.5824
110			1.625	0.9857	10.82	16.76	17.59	16.52	93.917
130			1.956	1.324	15.91	22.51	31.12	29.81	95.7905
150			2.61	1.66	18.73	28.22	48.89	46.83	95.7865
175			3.077	2.082	24.71	35.4	76.04	73.7	96.9227
200			4.289	2.499	25.48	42.48	109.3	106.1	97.0723
250			5.147	3.345	37.97	56.86	195.4	190.2	97.3388

(1) *Voltage*

As we can see in the table below, the voltage of this MPPT is less than the normal P&O. This is due to the fact we already cut the input into 75% of the voltage that we received from the TEG. This method produced voltage as low as 0.982 V for the input and 1.627 V for the output and as high as 17.22 V input voltage and 41.42 V at its highest temperature. Due to the nature of this buck that will reduce the voltage input to produce lower output, this method will always produce a less voltage compared with the normal P&O.

(2) *Power*

If we compare the power from this MPPT, the power also reduce significantly. Power or energy loss from this MPPT is reduced due the fact that our voltage is oscillating less than normal MPPT due to the fact that it 'achieved' MPPT faster than normal one. At the highest temperature, the power it produced is about half of the P&O at the input which are 105.5 W and 195.4 W, respectively. At the lowest, it produces power input of 0.2368 W and output of 0.1558 W compared with the P&O of 0.4706 W at input and output of 0.3418 W.

(3) *Efficiency*

From the table above, we can see that the efficiency of this method is almost no different from the normal P&O. However, P&O has slightly better efficiency compared with the fractional constant voltage about from as low as 2% to as high as 7%. When this method is at highest temperature, it has 95.6388% efficiency compared with the P&O which is 97.3588. This is due to the low voltage produced



by this method compared with the P&O that produced the most effective voltage for the system. However, this difference or low efficiency is compensated by having a much less fluctuating voltage input waveform that can cause loss of energy in the system.

### (B) *Efficiency of three fixed voltage*

In this MPPT, we have an algorithm that will set the voltage input for the boost at three fixed voltage based on the voltage it received from the TEG. At the lowest, fixed voltage is 5 V, intermediate at 25 V and highest is at 50 V.

#### (1) *Voltage*

As we can see from the table above, this method produced voltage input of 1.432 V and output of 1.067 V at its lowest temperature. However, at its highest temperature, it produced an input voltage of 27.71 V and produced output of 35.69 V. This method performs better at highest temperature compared with low temperature, where it produced low voltage from the TEG. However, this method always produced a higher output voltage compared with the input, except when its at temperature 60 °C.

#### (2) *Power*

When we compare this method and normal P&O, the power it produced is much less, but the efficiency is slightly better than the fractional constant voltage method. At lowest temperature, it produced power input of 0.1224 W and output of 0.06955 W. This is very low in terms of number and compared with the P&O has produced which is input of 0.4706 W and output of 0.3418 W. At the highest temperature, it produced an input power of 77.64 W and output of 74.63 W. This is much better compared with when its at low voltage. Due to this result, we can suggest the application of this method is only applied to heavy industries where higher temperatures are often produced.

#### (3) *Efficiency*

From the table above, we can see a significant difference from this method compared with the normal P&O at the low voltage, which are only 56.8219% against P&O of 72.6507%. However, as the temperature increases, the efficiency is also increasing and the differences between the efficiency between these two methods also decreases. At its highest, this method has efficiency about 96.5095% compared with the P&O of 97.3588 and slightly better than the fractional constant voltage method that has 95.6388%. We can say that this method is suitable to be used at this temperature setting.

## 7 Comparing the Input Voltage Waveform

(A) *Fractional Constant Voltage*

See Fig. 13.

(B) *Three Fixed Voltage*

See Fig. 14.

(C) *Perturb and Observe*

See Fig. 15.

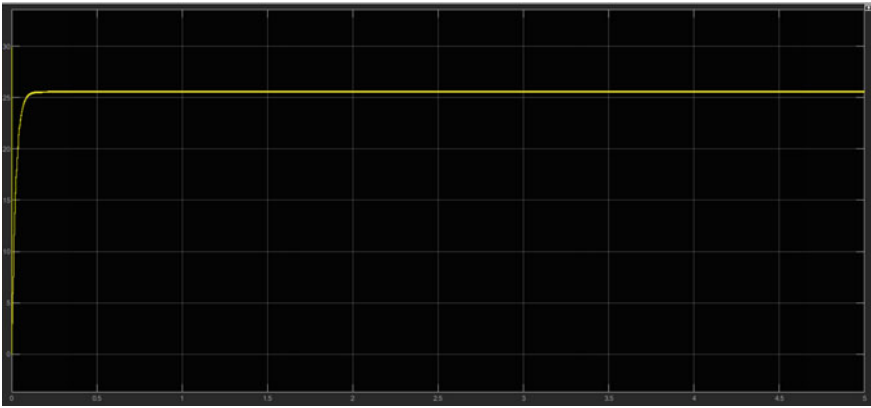
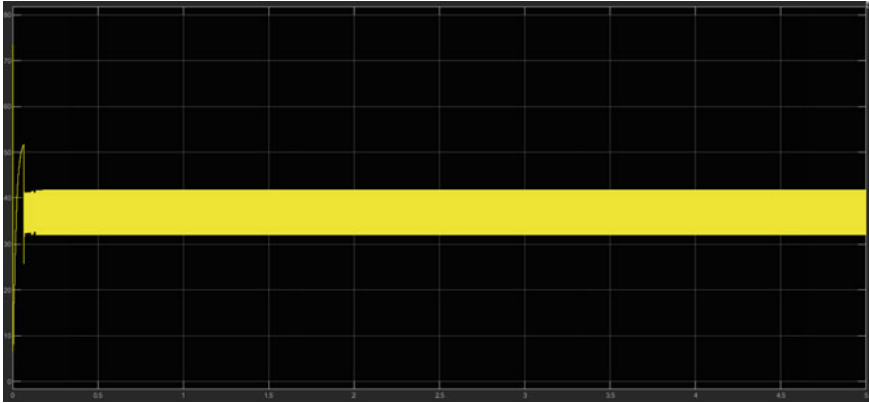


Fig. 13 Input voltage waveform for fractional voltage constant



Fig. 14 Input voltage waveform for three fixed voltage



**Fig. 15** Input voltage waveform for perturb and observe

Based on these three waveform of voltages at their highest temperature, we can see that, fractional and three fixed voltages have a very stable and constant input voltage. Almost there is no fluctuation at all. Compared with the P&O, the fluctuation is high and recorded at almost 10 V peak to peak. This will cause P&O loss a lot of energy and waste good amount of it in terms of heat. The appliances will become hot unnecessarily.

## 8 Conclusion

In conclusion, we can say that these two methods are not suitable to produce high and efficient power or voltage output for any loads. However, these methods are suitable to reduce the waste of energy, so that our hardware will not be unnecessary and waste the energy that it gains from the TEG. This is because the waveform it produces by these two methods is better compared with the P&O, but P&O still held a very good number in terms of power and voltage output. In addition, these two methods are also not suitable to be used in a very low voltage like 5 V, because it will produce the most inefficient output voltage and power among these methods. All in all, P&O still is the better choice method and has much potential if we can reduce the effect of changes to this MPPT.

**Acknowledgements** The authors would like to thank Universiti Teknologi, Malaysia (UTM) and Ministry of Higher Education, Malaysia (MOHE) for funding this research under UTM Encouragement Research (UTMER) Grant (Cost Centre No.: Q.J130000.3851.19J23).

## References

1. Beirnes B, Alfred, Friesen M, Asaf, Mohammad, Malalwa-Arachie JP, Pathak S, Arvenfal K, Shaner K, Naman (2020, Feb 19) How thermoelectric generators work. Applied Thermoelectric Solutions LLC. Retrieved Feb 3, 2022, from <https://thermoelectricsolutions.com/how-thermoelectric-generators-work/>
2. Boost converter: basics, working, design & operation. Components101 (n.d.). Retrieved Feb 3, 2022, from <https://components101.com/articles/boost-converterbasics-working-design>
3. Learnabout electronics. Boost Converters (n.d.). Retrieved Feb 3, 2022, from <https://learnabout-electronics.org/PSU/psu32.php>
4. Baba AO, Liu G, Chen X (2020) Classification and evaluation review of maximum power point tracking methods. *Sustain Futures* 2:100020. <https://doi.org/10.1016/j.sft.2020.100020>
5. Kahla S, Bechouat M, Amieur T, Feraga CE, Sedraoui M (2019) A comparison study: direct and indirect mode control of perturb and observe-MPPT algorithms for photovoltaic system. In: 2019 1st international conference on sustainable renewable energy systems and applications (ICSRESA), pp 1–6. <https://doi.org/10.1109/ICSRESA49121.2019.9182345>

# Comprehensive Review on AC-DC, DC-DC, DC-AC-DC Converters Used for Electric Vehicles and Charging Stations



Utkarsh Shukla, Shekhar Yadav, Nitesh Tiwari, and Aayushi Priyadarshini

**Abstract** The number of electric vehicles (EVs) has recently increased. For EVs, converters play a vital role. EVs have two main areas of research: EV drive systems and charging systems. In both systems, different power electronics converters need to be utilized. These converters are mainly used to convert the voltage, current, or power level. Hence, this paper reviews different converters, such as AC-DC converters, DC-DC converters, and DC-AC-DC converters. A generation of energy production is non-renewable based. DC grid as a base for EVs is more efficient than the AC-based grid system. It is also very reliable, power-efficient, easy to use, comparatively cheaper than AC, and easy to use with renewable energy sources (RESs) and integrated energy storage units (ESU). The EVs battery charging unit (BCU) power is powered with care using an energy management system (EMS) with proper control techniques. In charging stations, the converters perform a crucial role in charging EVs productively.

**Keywords** DC-DC converters · AC-DC converters · DC-AC-DC converters

---

U. Shukla · S. Yadav (✉) · N. Tiwari · A. Priyadarshini  
Department of Electrical Engineering, Madan Mohan Malaviya University of Technology,  
Gorakhpur, Uttar Pradesh, India  
e-mail: [syee@mmmut.ac.in](mailto:syee@mmmut.ac.in)

U. Shukla  
e-mail: [Shukloutkarsh475@gmail.com](mailto:Shukloutkarsh475@gmail.com)

N. Tiwari  
e-mail: [niteshwr1994@gmail.com](mailto:niteshwr1994@gmail.com)

A. Priyadarshini  
e-mail: [aayushipriyadarshini@gmail.com](mailto:aayushipriyadarshini@gmail.com)

## 1 Introduction

The EV charging station uses renewable energy as its source through an EV-PV converter linked with a PV microgrid, as PV is variable and regulated through a grid connection. It provides an uninterrupted power supply with high quality for that load which provides power when there is a deficiency in the utility grid. Microgrids used for EV charging are of different types [1]. The sliding mode control in the presence of external disturbance keeps the dc level at the desired value. It provides a power factor (PF) level close to 1 (more than 97%), which helps clarify the rectified output voltage that is not constant for the desired value [2]. Using a PI controller is difficult and not easy to tune. Therefore, using an artificial neural network (ANN), a genetic algorithm (GA) is taken into account for the packed U-cell (PUC) inverter. In this, ANN controls the switching, and GA controls the angle that provides the result with the constraint of a low total harmonic distortion (THD) value [3]. For the PV-based power system, transformerless inverter topology is introduced. In this, it is found that the T-type neutral point clamped performed better than the Neutral point clamped multi-level inverter [4]. For the NPC-MLI, use multi-carrier pulse width modulation (MCPWM). But it could not provide the DC link voltage balance to reduce the THD. Whereas to provide a better DC link voltage, the space vector modulation (SVM) technique is introduced, and the comparison is made with the 3L (three-level) SVM and the 5L SVM. The modern predictive control MPC is used with the DC link [5].

EVs can be charged by coupling of inductive or capacitive. Under Conductive coupling, EVs use the outlet plug for charging. Here, two types of the coil—one coil replicates receiving coil, whereas the other parking slot is interchanged with the power. Capacitive charging, 4 capacitive plates for charging. A level-based charging station (LB-CS) can decrease EV costs. At the same time, the time will be minimized by swapping technology [6]. The pulse width modulation (PWM) waveform is a reliable technique of switching [7]. The use of a Cuk converter in the EV charger with the use of single switch power factor correction operation during a supply cycle. It gives a better characteristic for the EV off-board charger, like high power density and less in price [8]. Using a multi-bi-directional Cuk converter for the photovoltaic (PV) system using MPPT with the salp swarm optimization technique helps maximize the output power from the PV array when there is a proper mismatch or partial shading [9].

The boost high gain buck-boost converter with the extended SCs makes a creditable position for a stand-alone PV system that helps operate above 300 V, which is impossible for the conventional buck-boost converter [10]. It works as a link between dc microgrid and EV battery packs. Introducing the ZVS helps achieve all the switching under a dual active boost converter (DABC) [11]. The low-speed EVs, recharging the battery pack rapidly is essential. It is obtained using an input series and output parallel converter [12]. DABC is to control the flow of power and minimization of that total power loss. By using the switching control strategy, minimizing the loss, efficiency improves by up to 10%, which is impossible with the conventional

control strategy [13]. There are many ways to reduce the charging cost. (i) By level-based charging station (LBCS). (ii) Reduced time by using swapping technology for a battery. The charger for EVs is of two types: off-board chargers and the other one is onboard chargers. As discussed, off-board charging has a higher transfer in KW and removes the weight of the vehicles, as the rate of energy transfer is high, whereas, for onboard charging, the transfer of KW is lower. A charging station is at different locations. There is a conformity of power reliability. EV batteries are charged by the use of the technique known as the battery swapping technique [14]. The comparison of power density with 100 kHz and 500 kHz of the LLC resonant converter and its improved design method is introduced. For the enhancement of that 500 kHz switching frequency power density, and also the mathematical modeling of the passive component like the transformer and the capacitor at the output is also performed. A converter is a proposed interleaved boost converter that reduces the ripple magnitude under input current and increases the magnitude of voltage gain by applying the voltage lift techniques or by replacing that conventional inductor with the coupled inductor of the IBC (interleaved boost converter) by using turn ratio [15]. EV charging is done with the help multileg interleaved boost converter that is digitally controlled, and experimental performance is seen in [16]. In the EV application, the reduction of electromagnetic interference is introduced with the help of the Sepic converter having an LC regenerating snubber. This technique helps reduce the component number and also helps in returning some of the switching energy for the Sepic converter [17]. The Sepic converter with PV inverter system is introduced, and the digital signal processing (DSP) is to produce the real-world environment of that proposed fuzzy logic controller (FLC) as well as the MPPT algorithm to control. It seems better than the conventional converter, the type of PI controller. The fuel cell EV application has a DC-to-DC converter with a three-phase high-voltage gain. The proposed converter decreases the magnitude of the voltage stress on the switches and the ripple in the input current in the introduced fuel cells (FCs). The Radial basis function network-based MPPT is set side by side with FLC, and the result favors that maximum power point tracking (MPPT) that tracks MPP is faster than FLC [18]. An interleaved boost converter helps reduce the current ripple, which helps increase the fuel cells' life span [19]. The use of the soft-switching in the interleaved boost converter with the six-phase, the use of the SiC semiconductors, and the coupled inductor technique for fuel cell vehicle (FCV) help significantly reduces the loss in power switching and weight reduction of the converter. The analysis of inherent soft switching for that potential transformer (PTs) is being performed in [20]. The substitute of the IBC, which is a multi-IBC, helps enhance the current capabilities at the module level, which can be achieved by operating several parallel power switches in sequence [21]. There is a comparison of the full bridge and half-bridge having a bi-directional dc to dc converter for the same application; the other topology is presented that has no device rating penalty, high efficiency that makes the new converter feasible for the use of the medium, and high-power related application [22]. A comparison of the inverter with the dc-dc converter is being performed. The inverter supplies the motor with high power and also the loads. But the converter supplies the low power to the load with low voltage. Therefore, in the future, the need for high power will

increase for EVs. Because of this, bi-directional dc-dc converters and many more will be studied [23]. It improves the DC-AC-DC converter efficiency using a Proton exchange membrane fuel cell (PEMFC) linked with EV's DC bus. The use of the high operating switching frequency helps in introducing the new technology that is synchronous rectification and also the use of SiC that helps in the loss depreciation and the increase the efficiency of the converter [24]. The EV charging station uses a DC microgrid and contains simple DC-to-DC conversion. The microgrid is controlled using the optimization technique (OT) based on an energy management strategy that improves the regulation and fast charging in EVs [25].

The main contribution of this paper is a comprehensive review of different power electronics convert. These converters are mainly reviewed for handling the application of EV drive and charging systems. It provides a review of:

- AC-DC converter such as asymmetrical two-device unidirectional boost converter, unidirectional multi-level converter, three-phase bridgeless boost converter, and three-level three-phase NPC converter.
- Bidirectional PV-Cuk converters, transformerless high gain boost and buck-boost DC-DC converters, single-ended primary inductance converters (SEPIC), multiple interleaved buck converters, full-bridge LLC resonant converters (LLCRC), and dual active bridge converters are examples of DC-DC converters.
- DC-AC-DC converter, such as inter-leaved 4-Phase Boost converter (IBC), and multi-device interleaved bidirectional converter.

This first section of this paper includes the introduction and literature review of different converters. The second section includes the AC-DC converter. The third section includes the DC-DC converter. The fourth section of this paper includes the DC-AC-DC converter. And in the last section of this paper covered the conclusion and future scope of this paper.

## 2 AC-DC Converters

Hybrid microgrids have advantages over AC and DC microgrids. DC power sources that can be used most of the time are photovoltaic (PV) systems, and they get connected through DC micro-grids and within the DC-DC boost converters, whereas EVs are linked with DC microgrid (DCMG) and DC-DC buck converters. On the other hand, the AC grid system is linked through a wind turbine generator (WTG). AC grid (230 V) having the load with AC as supply that is AC motors. Several advantages are there under that, the implementation of coordinated charging, and it also includes voltage regulation and frequency variation of the buses. To maintain grid balance, it uses a power-sharing module in this utility grid that absorbs energy from DCMG [25].



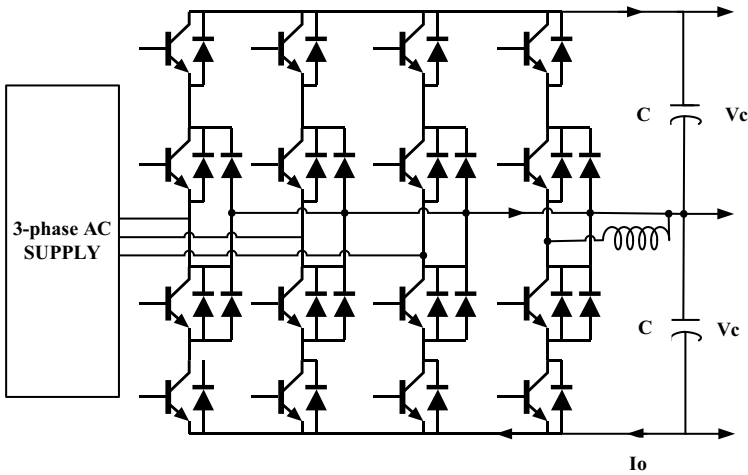


Fig. 1 Three-level three-phase NPC converter

### 2.1 Three-Level Three-Phase NPC Converter

Three level three-phase (TLTP) neutral point clamped multi-level inverter (NPC-MLI), as shown in Fig. 1 is widely used in the systems. In NPC-MLI arrangement defeats inconvenience in that leakage current and limits DC component which injects under microgrid. The TL-NPC-ML will help in motor control purposes. The NPC-MLI has several switches and various clamping diodes, providing for different phases with multiple voltage levels. The capacitor with the DC link is connected through series, separate from DC-linked voltage, and has an exact similar magnitude for that output. Boost under NPC-MLI because there was an increase in the capacitors having DC links. Also, there is the presence of clamping diodes with switches. Limits of the NPC-MLI is DC-link capacitor balancing. Hence it is only used for three levels. NPC-MLI mostly uses IGBT and diode to boost state voltage/current ratio to medium power range. It also uses one of the families of NPC-MLI, defined as T-N point MLI. It gives better efficiency for the above system. The efficiency for NPC-MLI will show a better response as compared to TNP-MLI. With dual MPPTs, the DC-Link checks out the conduction loss in an inverter [4].

### 2.2 Three-Phase Bridgeless Boost Converter

As shown in Fig. 2 indicates a kind of Bidirectional converter. The top-level switches show  $Q_{a, upper}$ ,  $Q_{b, upper}$ , and  $Q_{c, upper}$ , and the proposed nonlinear controller (NLC) leads to switching control signals  $u_a$ ,  $u_b$ , and  $u_c$ . Similarly, the bottom level switches which  $Q_{a, lower}$ ,  $Q_{b, lower}$ , and  $Q_c$  controlled similarly. Lower switches get off when

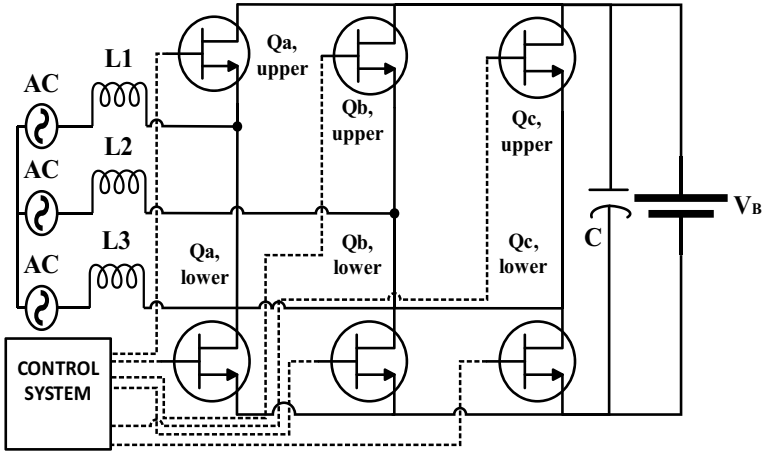


Fig. 2 Three-phase bridgeless boost converter

the upper circuit switches are ON, and vice versa. It contains around eight individual switching modes. For calculating the dynamic model of the converter, we derived all the dynamic modes with all different modes of operation. By performing KCL, Eq. (1) is obtained [9].

$$\begin{aligned}
 \frac{di_a(t)}{dt} &= \frac{1}{3L}(2v_a(t) - v_b(t) - v_c(t)) - \frac{2}{3L}V_B \\
 \frac{di_b(t)}{dt} &= \frac{1}{3L}(-v_a(t) + 2v_b(t) - v_c(t)) + \frac{1}{3L}V_B \\
 \frac{di_c(t)}{dt} &= \frac{1}{3L}(-v_a(t) - v_b(t) + 2v_c(t)) + \frac{1}{3L}V_B
 \end{aligned} \tag{1}$$

where  $v_a(t)$ ,  $v_b(t)$ , and  $v_c(t)$  replicate the voltage of the phases;  $i_a(t)$ ,  $i_b(t)$ , and  $i_c(t)$  replicate the current of the phases; and ' $V_B$ ' replicates battery voltage, whereas ' $L$ ' replicates the value of the inductor for individual phase, similarly for all three phases. A model can be derived from Mode 6, whereas the sign in the last variable under each Eq. (1) gets converted into Eq. (2) [9].

$$\begin{aligned}
 \frac{di_a(t)}{dt} &= \frac{1}{3L}(2v_a - v_b - v_c) + \frac{2}{3L}V_B \\
 \frac{di_b(t)}{dt} &= \frac{1}{3L}(-v_a + 2v_b - v_c) - \frac{1}{3L}V_B \\
 \frac{di_c(t)}{dt} &= \frac{1}{3L}(-v_a - v_b + 2v_c) - \frac{1}{3L}V_B
 \end{aligned} \tag{2}$$

Similarly, Modes 2 and 5 are obtained as Eq. (3) [9],

$$\begin{aligned}
\frac{di_a(t)}{dt} &= \frac{1}{3L}(2v_a - v_b - v_c) \mp \frac{1}{3L}V_B \\
\frac{di_b(t)}{dt} &= \frac{1}{3L}(-v_a + 2v_b - v_c) \pm \frac{2}{3L}V_B \\
\frac{di_a(t)}{dt} &= \frac{1}{3L}(-v_a - v_b + 2v_c) \mp \frac{1}{3L}V_B
\end{aligned} \tag{3}$$

The upper signs in the last term of the individual equations are for Mode 5. The dynamic model works under Modes 3 and 4, it is represented in Eq. (4) [9],

$$\begin{aligned}
\frac{di_a(t)}{dt} &= \frac{1}{3L}(2v_a - v_b - v_c) \pm \frac{1}{3L}V_B \\
\frac{di_b(t)}{dt} &= \frac{1}{3L}(-v_a + 2v_b - v_c) \pm \frac{1}{3L}V_B \\
\frac{di_a(t)}{dt} &= \frac{1}{3L}(-v_a - v_b + 2v_c) \mp \frac{2}{3L}V_B
\end{aligned} \tag{4}$$

In each equation, the upper part of the sign is from mode 4; Modes 0 and 7 give the following as Eq. (5) [9],

$$\begin{aligned}
\frac{di_a(t)}{dt} &= \frac{1}{3L}(2v_a - v_b - v_c) \\
\frac{di_b(t)}{dt} &= \frac{1}{3L}(-v_a + 2v_b - v_c) \\
\frac{di_a(t)}{dt} &= \frac{1}{3L}(-v_a - v_b + 2v_c)
\end{aligned} \tag{5}$$

The closed form is obtained by using all operating modes, from (1)–(5) get combined to give the following as Eq. (6) [9],

$$\begin{aligned}
\frac{di_a(t)}{dt} &= \frac{1}{3L}(2v_a - v_b - v_c) - \frac{1}{6L}(2u_a - u_b - u_c)V_B \\
\frac{di_b(t)}{dt} &= \frac{1}{3L}(-v_a + 2v_b - v_c) - \frac{1}{6L}(2u_a - u_b - u_c)V_B \\
\frac{di_a(t)}{dt} &= \frac{1}{3L}(-v_a - v_b + 2v_c) - \frac{1}{6L}(2u_a - u_b - u_c)V_B
\end{aligned} \tag{6}$$

it is simplified as a vector model that gives [9],

$$\frac{d}{dt}i = \frac{1}{3L}Kv - \frac{V_B}{6L}Ku \tag{7}$$

where,  $i = [i_a i_b i_c]^T$ ,  $v = [v_a v_b v_c]^T$ ,  $u = [u_a u_b u_c]^T$

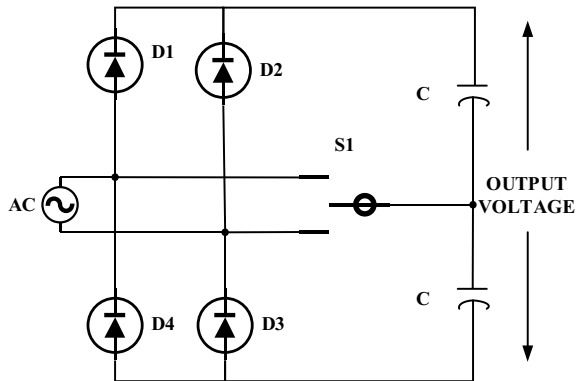
$$K = \begin{pmatrix} 2 & -1 & -1 \\ -1 & 2 & -1 \\ -1 & -1 & 2 \end{pmatrix}$$

Equation (7) is then utilized for a proposed controller [9].

### 2.3 Unidirectional Multi-level Converter

Rectifiers have dc inductors in them that are used for various reasons; a dc inductor is indicated as an ‘M’ inductor for unidirectional flow. The rectifier is one of the popular choices because of the single switch and standard rectifier diodes on the input side, cheapening its use. It sets the standard for comparing all types of 1-phase boost rectifiers. As represented in Fig. 3, the circuit is useful and gives high output voltages with more switch off-times compared with the 1-switch. Phase-adjusted unipolar (PAUP) PWM waveforms are obtained by a circuit using 2 switches rather than the 4 used in the H-bridge by rectifying the AC mains voltage, achieving a rectifier containing a standard rectifier diode (SRD) and using a dual series-connected boost circuit in which power is transferred through the output capacitor. The two dc-rails can contain the differential load. The value of ripple in the DC-link inductors is minimized by using a switching pattern. This performance gets converted using lower switching frequencies, low dc-rail inductors, and lower switch voltage stresses. These circuits are mainly used in universal power supplies (UPS), which are automatically connected to single gain or doubling rectifiers depending on the ac voltage [7].

Fig. 3 Unidirectional multi-level converter



### 2.4 Asymmetrical Two-Device Unidirectional Boost Converter

Figure 4 replicates AUIMLDDPC (Asymmetric unidirectional isolated multi-level DC-DC power converter). It comprises the half-bridge inverter (HBI), a single TWT, and dual (full bridge rectifier) FBRs, with the selective circuit and filter at the output containing L-C. The TWT (three-winding transformer) has the primary winding, which is represented by the number of the primary turns as ' $N_p$ ' and also with dual windings ( $N_s, N_t$ ) where ' $N_s$ ' indicates (secondary winding) and ' $N_t$ ' indicates (tertiary winding) at the secondary side. ' $V_{out_{FBR}}$ ' is the summation of  $V_{C3}$  and  $V_{C4}$  when two FBRs are connected in series (S3 is turned on) and  $V_{out_{FBR}} V_{C4}$  when two FBRs operate in stand-alone condition (S3 is turned off). When the duty ratio of the HBI switching is 0.5, it generates the voltage at the primary winding side, which is mostly a square wave in the TWT. A duty cycle with a fixed value of 0.5 for the HBI gives that square symmetrical wave with the winding having a primary number of turns represented by ' $N_p$ ' at the primary of that transformer. It also gives a dual output voltage waveform like a square shape with dual forward bridge inverter (FBRs) and gets two different voltages with not an equal number of windings.

The output voltage is not compulsorily fed toward that control circuit at the side of the primary with a proper value of the duty ratio for HBI. Then the isolation feedback gets avoided. Whereas both the designs of that transformer with the control of HBI are simple. The operation of AUIMLDDPC contains around four modes as follows [6],

- **Mode I**

Under mode I, the circuit is given below indicates that S1 gets ON, whereas S2, and S3 get off. And  $V_{out_{FBR}}$  as shown in Eq. (8) [6]

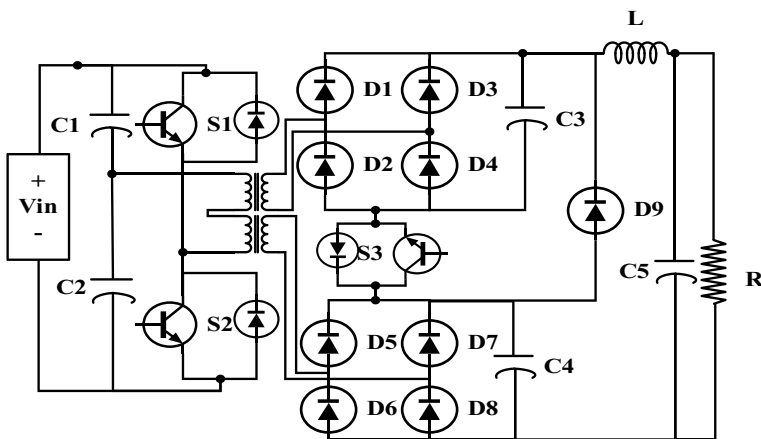


Fig. 4 Asymmetrical two-device unidirectional boost converter

$$V_{\text{outfBR}} = V_{C4} = \frac{V_{\text{in}n2}}{2} \quad (8)$$

- **Mode II**

Under mode II, as S2 gets OFF. And at the same time, S1 and S3 get ON. And  $V_{\text{outfBR}}$  as shown in Eq. (9) [6]

$$V_{\text{outfBR}} = V_{C3} + V_{C4} = \frac{V_{\text{in}n2}}{2} + \frac{V_{\text{in}n1}}{2} \quad (9)$$

- **Mode III**

Under mode III, S2 gets ON, but on the other hand, S1, with S3, gets OFF. And  $V_{\text{outfBR}}$  as shown in Eq. (10) [6]

$$V_{\text{outfBR}} = V_{C4} = \frac{V_{\text{in}n2}}{2} \quad (10)$$

- **Mode IV**

Under mode IV, S1 gets OFF, and S2 with S3 is turned ON. And  $V_{\text{outfBR}}$  can be represented as the voltage with the swing or varying value being less than that of the (unidirectional isolated multi-level DC-DC power converter) UIMLDDPC. Also, the capacity with the output filter proposed by the AUIMLDDPC is decreased when compared with the previous HBI type of UIMLDDPCs [6].

### 3 DC-DC Converters

It is differentiated into two switching types of converters: hard-switched converters and soft-switched converters. In recent years, converters have been mainly dc in nature. Therefore, mainly it is used as a soft-switched converter. Under these switching, it is mostly used as zero voltage or current switching (ZVS) and/or (ZCS), and almost every time, the parasitic with, if required, some additional component. At the same time, it can also classify the DC-DC converters under non-isolated as well as the isolated (transformer version), unidirectional, and bidirectional converters. Most of the converters that are mainly used in the charging station of the EVs to step-down with the help of the buck type of converter, step-up for the boosting purpose, buck-boost for performing both at the same time, also an improved kind of BB converter that is the SEPIC (single-ended primary inductor converter), having dual SEPIC know as Zeta, and Cuk converter comes under the isolated techniques. In flyback converter contains a transformer-type buck-boost converter. Isolated converters mainly contain Cuk, SEPIC, and dual SEPIC [23].

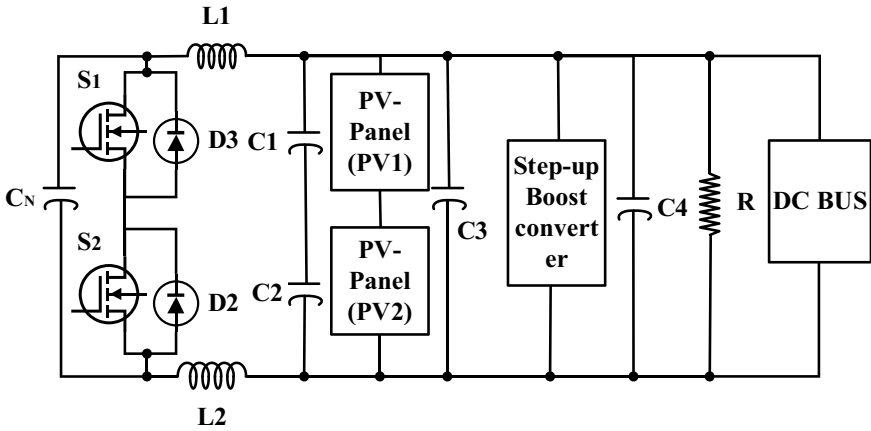


Fig. 5 Bidirectional PV-Cuk converter

### 3.1 Bidirectional PV-Cuk Converter

The Cuk converter circuit with the PV-PV is arranged in the given fashion, as shown in Fig. 5. It is composed of dual converters that indicate dual circuits. It used the capacitor  $C_n$  for energy-storing purposes and a buck-boost converter composed of the inductor. It shows a similar voltage transformation duty cycle ratio that is 'k'. The main issue is the non-continuation because the large capacitor affects the I/O current, and the converter terminal or PV connects to the shunt. Another positioning of the converter under which the primary is isolated with the secondary side is the flyback converter, which links each serially linked PV generator with conventional output with the DC bus, linking PV and the bus structure. The importance of that dual forms is that well-distributed solar irradiation, with no converter power loss. It still contains the same losses present at the time conversion when there is a use of a dc converter or another converter that is the dc to ac for the grid.

The two vital needs that can be fulfilled with the PV-to-PV alignment are made very challenging for controlling purposes. Firstly, it requires a reliable control scheme that leads the system to obtain the maximum power point (MPP). It keeps changing the PV [1].

### 3.2 Transformerless High Gain Boost and Buck-Boost DC-DC Converters

There is a valid reason for using the SC technique for conventional high gain boost and buck-boost converter (B-BBCs), as shown in Fig. 6 to decrease the switching ON time and also, at the same time, stabilize the output voltage due to this, it's

easy to compensate for ripple in the current across the input side as well as at the device side also, and this helps in reducing the conduction losses. A reverse-recovery problem arrived at the rectifier’s output end because the current with the short pulses is reduced extremely due to this duty ratio. Let’s keep things in mind that whether it uses the converter in the buck mode (BU-M), in boost mode (BO-M), or used in buck-boost mode (BU-BO-M) depends upon the SC-cell shown below with the red dotted line which is across the switch and the inductor. Whereas the arrangement used in Fig. 7 given below is used for high voltage gain, it cannot extend the SC cell for high voltage boost. In these extended SC-cells, we use a 2-stage SC-cell containing two diodes and a capacitor similar to that was in the double voltage circuit: In this, one operates under forward bias (FB) ( $C_{FB}$  and  $D_{FB}$ ), another under reversed-bias (RB) ( $C_{RB}$  and  $D_{RB}$ ). Whereas it shows that SC-cells work differently under conventional voltage double for the voltage extension under reverse-biased as there is no active involvement of that branch. The boosting ratio of the circuit can be increased by the increase in the number of extensions [10].

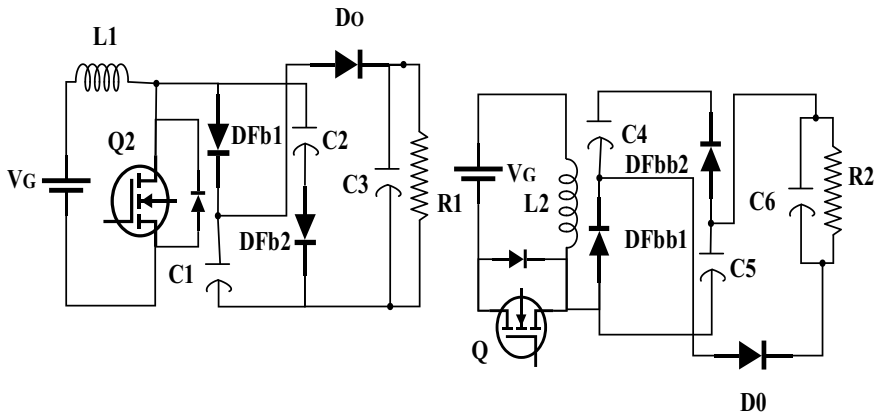
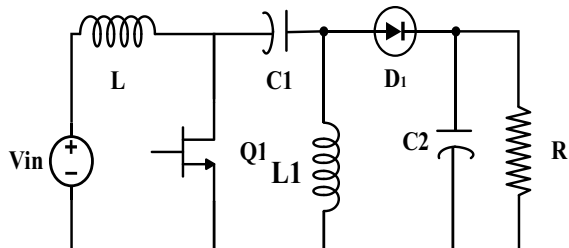


Fig. 6 Transformerless high gain boost and buck-boost DC-DC converters

Fig. 7 Single-ended primary inductance converter





### 3.3 Single-Ended Primary Inductance Converter (SEPIC)

It is one type that comes under (the BU-BO) dc-dc converter. The output voltage polarity of the converter is different compared with conventional converter. Under the SEPIC converter, the dual inductors' arrangement differs from the BBDC. This converter uses two coupled inductors instead of two separated inductors, which helps in reducing the inductance of the same half the inductance ripple in the current. SEPIC used dual coupled inductors as replicates in Fig. 7 represented as  $L_a$  and  $L_b$ . Like other DC/DC converters that use coupled inductors or transformers in the circuit. This converter is handled with the problem of energy stored of leakage inductance in a primary inductor. The voltage stress is because of the energy at the switch transistor at the off duration and also affects the MOSFET switch. To avoid it, we mostly use the snubber circuit, which helps us make a different path for energy so that the MOSFET switch can be protected easily. The snubber circuit helps reduce the electromagnetic interference (EMI) that helps us secure that switch with that stored energy inside the leakage inductance [17].

### 3.4 Multiple Interleaved Buck Converters

Let's take the  $N$  that indicates the legs number for an interleaved type of buck converter, as shown in Fig. 8. In  $V_{in}$  replicates voltage at the input side,  $V_o$  replicates voltage across the output, whereas the  $L_1, L_2 \dots L_n$  and  $i_1, i_2 \dots i_n$ , denote the leg of the inductances and currents to that of an inductor. Here,  $C$  shows filter capacitance for high-frequency ripple-providing switching operation, and the combination with the RL and RC shows parasitic series resistances (PSR) with inductors and capacitors. Load indicates the battery that's going to charge. Whereas  $n$  replicates the duty cycle of that signals, that is  $d_1, d_2 \dots d_n$  that help modulate the PWM signals that regulate buck converter's switches accordingly to the design of that proposed controller.

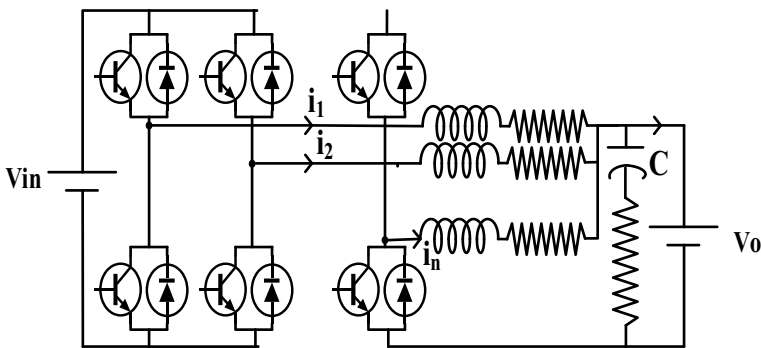
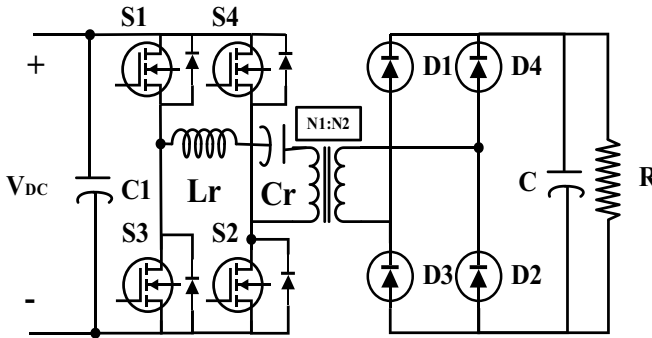


Fig. 8 Interleaved buck converter



**Fig. 9** Full-bridge LLC resonant converter

On considering the required amount of the voltage accumulated with the battery range  $DV_o$  and also having reference current with the constant  $I_{ref}$  that can select the load drop coefficient  $R$ , which is  $R = DV_o/I_{ref}$ . Also, the state space equations of the interleaved converter and k-leg power switch conduction losses indicate  $R_{S_{wk}}$ . Whereas  $R_{S_{wk}}$  is equivalent for both switches on the same leg [16].

### 3.5 Full-Bridge LLC Resonant Converter (LLCRC)

In LLCRC, the arrangement mainly contains dual series and parallel inductors. In Fig. 9 it can easily be seen that we have dual inductors with a single capacitor. It has an identical arrangement of the elements as present in a resonant converter that is connected in series with the transformer. It contains magnetization inductance (ML) within the transformer and works as a resonant element. As magnetizing current is cleared with SRC (series resonant converter), it handles the problem of having no-load control. A square wave voltage  $V_{ab}$  was found with various resonant converters because of the switching action. It behaves like a filter as IL for both SRI and SRC (series resonant capacitor/inductor). As discussed, a resonance capacitor also affects the magnetizing current that passes through ML. LLCRC is composed of dual resonant frequencies. It also contains  $L_r$  and  $C_r$  (resonant inductor and capacitor) as elements in high resonance frequency (HRF), whereas mutual inductor ( $L_m$ ),  $L_r$ , and  $C_r$  are for low resonance frequency (LRF) [14].

### 3.6 Dual Active Bridge

Figure 10 replicates the Bidirectional DAB (dual active bridge) converter. It has DAB converters, a dual filter, and a transformer with high frequency. It has a similar framework that permits the bidirectional power transfer through switching moments

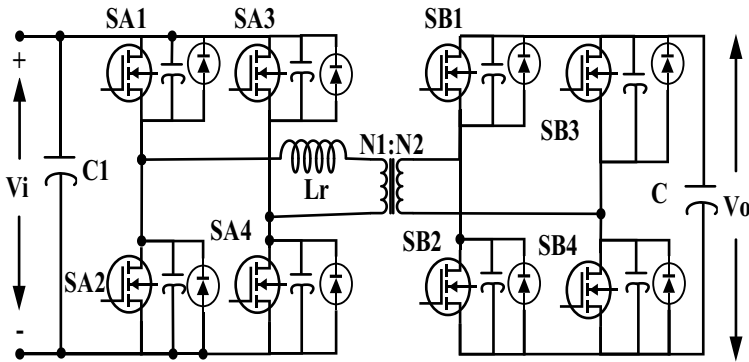


Fig. 10 Dual active bridge

of the dual bridges. In Fig. 10,  $v_p$  and  $v_s$  replicates, voltages across the transformer  $i_p$  indicate the primary current of the transformer as shown in Eq. (11) [11], and  $L_s$  indicates leakage inductance in a transformer. Whereas  $v_p$  and  $v_s$  show the quasi-square wave based on 4 parameters that can be controlled: The duty cycle of  $v_p$  ( $D_a$ ), a Duty cycle of  $v_s$  ( $D_b$ ), phase shift among  $v_p$  and  $v_s$ , and switching period ( $T_s$ ).

The control parameter is easily controlled to create a switching given to the modulator for all semiconductors. It can easily calculate the current at the side of the transformer’s primary end [11]. Where  $k$  symbolizes the transformer ratio.

$$i_p(t) = \frac{1}{L_s} \int_0^t (v_p - kv_s)dt + i_o \tag{11}$$

The transferred power ‘P’ as shown in Eq. (12) [11],

$$P = \frac{T_s V_A k V_B}{2L} \left( \frac{1}{4} - \left( \left( D_A - \frac{1}{2} \right)^2 + \left( D_B - \frac{1}{2} \right)^2 + \left( \varphi - \frac{1}{2} \right)^2 \right) \right) \tag{12}$$

### 4 DC/AC/DC Converter

The power converter mainly used as the DC-AC-DC is shown in Fig. 11 and described in [24]. In the circuit, the I-stage has a full bridge with a MOSFET and works as an inverter linked through a PEMFC with a high-frequency range with the capacitor filter. Because of capacitive input, and easily remove those harmonics. The temporized charge circuit connected at the input side allows that capacitor indicated with C to which linked with PEMFC without any current overload. The II-stage contains the planar technology with a very high transformer frequency. But because of that small

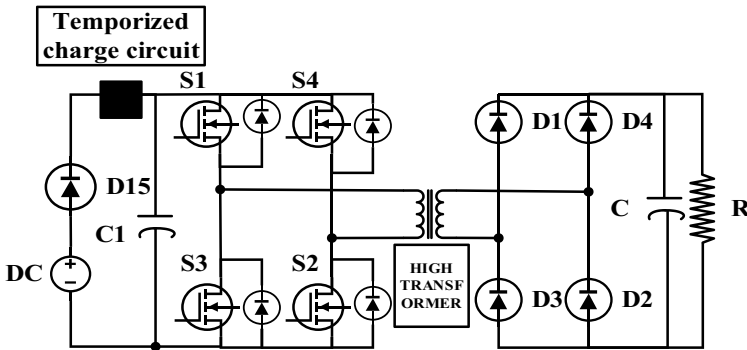


Fig. 11 DC/AC/DC converter

size (high power density) and higher frequency, both  $V$  and  $I$  produced eddy current loss of a lower amount, with an efficiency of around 98%. The last is the III-stage with a diode rectifier, low power factor LPF with LC that terminates the harmonic part before it is linked through the vehicle with the DC bus. Loss reduction can be made more efficiently by preferring the low voltage drop diode, that is, the Schottky diode, with the reverse recovery in a very low amount [24].

#### 4.1 Inter-leaved 4-Phase Boost Converter (IBC)

The arrangement of the circuit is as in Fig. 12 contains switches that are three in number ( $S1$ ,  $S2$ , and  $S3$ ) and diodes ( $D1$ ,  $D2$ , and  $D3$ ).  $L1$ ,  $L2$ , and  $L3$  filter the (1, 2, and 3) phases, respectively.  $V_{FC}$  is the (input voltage),  $V_o$  (output voltage), and  $RL$  (load resistor). The assumptions considered for the analysis of IBC are as follows:

- Inductors for every three phases are ideal ( $L1 = L2 = L3 = L$ ).
- Filtering capacitors took as same ( $C1 = C2 = C$ ).
- PC (proposed converter) is always under the Continuous Conduction Mode (CCM).
- The voltage, as well as the current ripple for the capacitor and inductor, are always assumed small. Switches  $S1$ ,  $S2$ , and  $S3$  are ON, with the double gate pulse having a phase shift of  $180^\circ$ . The first gate pulse is for switch  $S2$ , but that gate pulse has a  $180^\circ$  phase shift, which is for both switches  $S1$  and  $S3$  [19].

##### • Mode I ( $t_0 \leq t \leq t_1$ )

During mode I, switches in the circuit ( $S1$ ,  $S2$ , and  $S3$ ) get ON. Therefore, on the other hand, all diodes  $D1$ ,  $D2$ , and  $D3$  get under reverse bias, whereas capacitor ( $C$ ) disconnects with both load and supply.

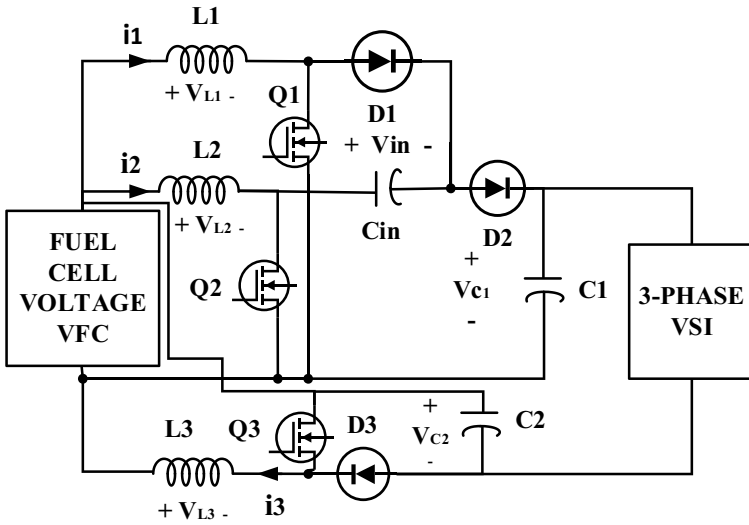


Fig. 12 3-phase high voltage gain IBC

- **Mode II** ( $t_1 \leq t \leq t_2$ )

During mode second, S2 is turned ON, whereas S1, and S3 get switched OFF. On the other hand, D1 and D3 represent a forward-biased diode, and D2 replicates the reverse-biased diode. The slope increases as the current through inductor L2 increases that is (VFC/L).

- **Mode III** ( $t_3 \leq t \leq t_4$ )

It works same as mode 1.

- **Mode IV** ( $t_4 \leq t \leq t_5$ )

During the fourth mode in the circuit, S2 is switched OFF, whereas S1, and S3 is switched ON. Whereas diodes are replicated with D1 and D3, which is reverse bias, but D2 conducts. The input voltage source VFC charges L1 and L3 (inductor), and as slop increases, the current through it gets increases, represented by (VFC/L). The C2 and C, which are used as circuit capacitors, supply energy to the load. On the other hand, the C1 (capacitor) gets charged through input voltage VFC [19].

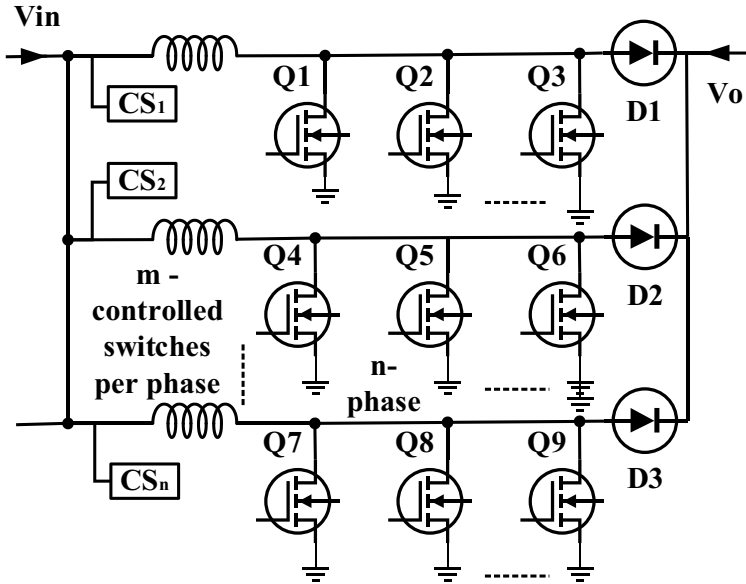


Fig. 13 Multi-device interleaved DC-DC bidirectional converter

## 4.2 Multi-device Interleaved Bidirectional Converter

The arrangement in Fig. 13, with that multiple-switch and the structures of multiple phases with DC/DC conversion of the multiple-phase application like multiple-switching, multi-phase structures (MPS) that deal with the converters of high power having 2-switch and the 2-phase boost converter in fuel cell hybrid electric vehicles (FCHEV).

Obtained with the help of the multi-switch and multi-phase structures, it can allow the same phase synchronization, and also, the multi-phase structure has those multiple configurations. It also considers parallel driving scheme (PDS), sequential driving scheme (SDS), and distributed driving scheme (DDS) under the module in conjunction to synchronize and, for each module, an interleaved mode. It mainly focuses on the multiple switch boost converter (MSBC) under DDS and the interleaved as it gets compromised with the current ripple at the input side and the part count. For clarity, it is named a Multi-Interleaved Boost Converter (MIBC) [21].

## 5 Conclusion

This paper indicates various types of converters that contain DC-DC converters and AC-DC converters and also involve DC-AC-DC converters. These converters in EVs are focused on improving efficiency, reducing size, enabling wireless charging, enabling bidirectional power flow, and improving power density. These developments

will help to make EVs more practical, efficient, and environmentally friendly, driving the growth of the EV industry in the years to come. It shows the design and use of these in EVs according to their condition, including the future trend of research. It focuses on multiple performances like the power that is obtained at the output side, the number of components, various converters switching frequency, EMI, different types of loss produced, performance of the converters related to the converter cost, and also with the reliability that always directly influence the selecting different types of converters for the BEV, PHEV. It also guides various automotive engineers and other PEC that design the passive components (capacitors and inductors) selection based on the powertrain's demand. Result validation and implementation of this converter for different EV drives and charging system is the future scope of this paper.

## References

1. Mao M, Zhang Li, Yang L, Chong B, Huang H, Zhou L (2020) MPPT using modified salp swarm algorithm for multiple bidirectional PV-Cuk converter system under partial shading and module mismatching. *J Solar Energy* 209:334–349
2. Ku HK, Jung JH, Park JW, Kim JM, Son YD (2020) Fault-tolerant control strategy for open-circuit fault of two-parallel-connected three-phase AC–DC two-level PWM converter. *J Power Electron* 20(1):731–742
3. Ali M, Tariq M, Lodi KA, Chakraborty RK, Ryan MJ, Alamri B, Bharatiraja C (2021) Robust ANN-based control of modified PUC-5 inverter for solar PV applications. *IEEE Trans Ind Appl* 57(4):3863–3876
4. Madasamy P, Verma R, Rameshbabu A, Murugesan A, Umamageswari R, Munda JL, Bharatiraja C, Mihet-Popa L (2021) Neutral point clamped transformer-less multi-level converter for grid-connected photovoltaic system. *J Electron* 10(8):977
5. Jayakumar V, Chokkalingam B, Munda JL (2021) A comprehensive review on space vector modulation techniques for neutral point clamped multi-level inverters. *IEEE Access* 09:112104–112144
6. Jou HL, Wu KD, Wu JC, Lin YZ, Su LW (2019) Asymmetric isolated unidirectional multi-level DC-DC power converter. *Eng Sci Technol Int J* 22(3):894–898
7. Javed K, Vandeveld L, De Belie F (2022) A novel current control scheme for grid-connected single-phase PWM bridgeless power converters. In: *Proceedings of seventh international congress on information and communication technology: ICICT 2022*, pp 155–169
8. Kushwaha R, Singh B (2019) A modified bridgeless Cuk converter-based EV charger with improved power quality. In: *2019 IEEE transportation electrification conference and expo (ITEC)*, pp 1–6
9. Sabzehgar R, Roshan YM, Fajri P (2020) Modeling and control of a multifunctional three-phase converter for bidirectional power flow in plug-in electric vehicles. *J Energies* 13(10):2591
10. Amir A, Che HS, Amir A, Khateb AE, Rahim NA (2018) Transformer-less high gain boost and buck-boost DC-DC converters based on extendable switched-capacitor (SC) cell for stand-alone photovoltaic system. *J Solar Energy* 171:212–222
11. Sun X, Wang Z, Zhang Q, Chen G (2021) Variable frequency triple-phase-shift modulation strategy for minimizing RMS current in dual-active-bridge DC-DC converters. *J Power Electron* 21(2):296–307
12. ElMenshaway M, Massoud A (2021) Development of modular DC-DC converters for low-speed electric vehicles fast chargers. *Alex Eng J* 60(1):1067–1083

13. Kim DH, Kim MS, Nengroo SH, Kim CH, Kim HJ (2019) LLC resonant converter for LEV (Light Electric Vehicle) fast chargers. *J Electron* 8(3):362
14. Revathi BS, Mahalingam P, Longatt FG (2019) Interleaved high gain DC-DC converter for integrating solar PV source to DC bus. *J Solar Energy* 188:924–934
15. Cuoghi S, Mandrioli R, Ntogramatzidis L, Gabriele G (2020) Multileg interleaved buck converter for EV charging: discrete-time model and direct control design. *J Energies* 13(2):466
16. Kasasbeh A, Kelleci B, Ozturk SB, Aksoz A, Hegazy O (2020) SEPIC converter with an LC regenerative snubber for EV applications. *J Energies* 13(21):5765
17. Reddy KJ, Sudhakar N (2018) High voltage gain interleaved boost converter with neural network-based MPPT controller for fuel cell-based electric vehicle applications. *IEEE Access* 6:3899–3908
18. Wang H, Gaillard A, Hissel D (2016) 6-phase soft-switching interleaved boost converter based on sic semiconductor for fuel cell vehicles. In: *IEEE vehicle power and propulsion conference (VPPC)*, pp 1–7
19. Zhang Z, Xie S, Wu Z, Xu J (2020) Soft-switching and low conduction loss current-fed isolated bidirectional DC–DC converter with PWM plus dual phase-shift control. *J Power Electron* 20(1):664–674
20. Depernet D, Gustin F, Hissel D (2017) High-efficiency DC/AC/DC converter based on synchronous rectifier for proton exchange membrane fuel cells. In: *International conference on fundamentals and development of fuel cells*, vol 17, no 2, pp 178–186
21. Abraham DS, Verma R, Kanagaraj L, Raman SRGT, Rajamanickam N, Chokkalingam B, Sekar KM, Popa LM (2021) Electric vehicles charging stations' architectures, criteria, power converters, and control strategies in microgrids. *Electronics* 10(16):1895
22. Tiwari N, Tiwari AN (2018) Performance analysis of unidirectional and bidirectional buck-boost converter using PID controller. In: *2018 2nd international conference on electronics, materials engineering & nano-technology (IEMENTech)*, pp 1–6
23. Tiwari N, Tiwari AN (2018) Design and control of buck converter using PID and fuzzy logic controller. In: *2018 international conference on power energy, environment and intelligent control (PEEIC)*, pp 557–564
24. Tiwari N, Yadav S, Arya SR (2022) Battery and super capacitor powered energy management scheme for EV/HEV using fuzzy logic controller and PID controller. *Int J Power Electron* 15(3–4):309–333
25. Tiwari N, Yadav S, Arya SR (2023) A comprehensive review of Indian market scenario and motor used in electric vehicle. *Recent Adv Electr Electron Eng* 16(4):347–361



# Control and Performance Analysis for Active Islanding Detection Using q-Axis Control in Renewable Energy Sources Based Microgrid: A Review



Avdhesh Kumar

**Abstract** In this paper, control and performance of an active islanding detection method have been analyzed using q-axis controller. The detection approach is based on disturbance injection via q-axis controller, which measures the mean absolute frequency variation of the voltage at the point of common coupling (PCC). Islanding identification provided by the q-axis controller method found to be efficient and reliable. The efficacy of the islanding identification method has been tested in the MATLAB/Simulink 18.0(a), for load of quality factor ( $Q_f = 2.5$ ) and analyzed. It offers the several contributions/benefits, viz. the islanding identification time is 180 ms (which is better than several other techniques in the literature), which correctly distinguishes between non-islanding and islanding scenarios, compatible with all international standards.

**Keywords** Renewable energy sources · Islanding detection technique · Distributed generator · Distributed generation

## 1 Introduction

Nowadays, the renewable energy sources (RES) based distributed generation (DG) has been increased substantially in the distribution grid. The most practical DG technology during the past ten years has been grid-connected photovoltaic systems, which have advantages in terms of installation, less maintenance cost, economical, sustainable sources, and green energy such as ecological friendly and can be harnessed for DG [1]. Despite the benefits of solar PV, they also pose some risks; as a result, the grid integration of DG necessitates protection and safety concerns in the distribution network [2].

---

A. Kumar (✉)

Electrical Engineering Department, Delhi Technological University, New Delhi, India  
e-mail: [avdhesh\\_phd2k17@dtu.ac.in](mailto:avdhesh_phd2k17@dtu.ac.in)

In order to ensure the safety, the detection of the island operations of distributed generators has become very important. Microgrid islanding arises as a consequence of breakers accidentally tripping, resulting in a significant threat to the safety of staff, damage to the equipment of utilities, consumers, etc. Islanding refers to a situation where energized DGs are disconnected from the bulk power grid, providing power only to the local loads for the time being [3, 4]. The rapid detection of an islanding activity is a compulsory requirement, for seamless connection to preserve the stability of the procedure and supplying likewise, critical demand of loads. Methods of island detection (IDMs) are broadly divided into remote and local categories. In the literature [5, 6], the remote islanding detection method has been proposed by Bayrak et where as remote IDTs which are not suitable for small microgrids because of the increased investment due to communication system. It is possible to apply these reliable and fast schemes to synchronous- as well as inverter-based DGs. However, the increased burden due to expense is recognized as the key constraint [7–9].

Local islanding detection technique (IDT) is usually limited to the common coupling point (PCC) and different parameters are monitored and evaluated for decision-making, such as voltage, current, frequency [10, 11]. There are three kinds of local IDTs: passive, active, and hybrid techniques. Recent passive approaches are illustrated by a few examples in the literature [12, 13]. Although these solutions can be applied easily and cheaply, they have a large non-detection zone (NDZ) or circumstances where power generation and consumption are nearly matched but not detected by islanding. Another difficulty is choosing a threshold value of algorithm for island detection, which is the trade-off between false tripping and minimum non detection zone (NDZ). To extract features from the frequency domain, a number of mathematical approaches have been employed. A magnitude of frequency-dependent impedance-related data for the passive IDT has been proposed in the literature [11]. To identify islanding, the inverter's output voltage's content of ripple is analyzed in the time domain [6]. In [11], the criteria for island detection are voltage and PCC harmonic characteristics. Including positive feedback to active IDT's different inverter control parameters, such as voltage, frequency, and phase angle, consequences an unstable system when the inverter is controlled and the grid is disconnected. To enhance the NDZ and PQ degradation, hybrid method including two local IDMs has been developed. Under standard operating circumstances, the standard of power has not been impacted [14, 15]. Nonetheless, difficulty and costs are still regarded as the biggest disadvantages in the hybrid methods of IDMs. For the purpose of detecting islands depending on reactive power and load control approach, Laghari et al. have presented a hybrid strategy [16].

In this paper, an active islanding detection islanding detection system using q-axis controller, has been developed and implemented in MATLAB/Simulink. Further, performance has been analyzed. Approach is based on  $i_{\text{dist}}$  injection via q-axis, which measures mean absolute frequency variation in PCC voltage that passes through the bandpass filter. Islanding identification technique has been analyzed and validated using MATLAB/Simulink 18.0(a), for loads with quality factor ( $Q_f$ ) of 2.5.

The following are the major contribution/benefits of the islanding detection method.

- (1) For the load of ( $Q_f = 2.5$ ), identification time is 180 ms.
- (2) Finds unintentional island creation more quickly than many earlier works.
- (3) Correctly distinguishes between non-islanding and islanding scenarios.
- (4) Compatible with all international standards.
- (5) It can identify islanding for all loads up to the quality factor ( $Q_f$ ) = 2.5.

## 2 Test System Configuration

Single-line diagram of RES-based microgrid is shown in Fig. 1 which comprises three DGs, out of which one is SPV-based, second is wind energy conversion-based, and third is fuel-cell-based DG, which are connected with parallel load at the PCC. Furthermore, in the present study, to analyze the control and performance of the islanding detection system, the test system has been developed for one DG, load, and grid to minimize the complexity. The test setup has been shown in Fig. 2, respectively, which comprises one DG (SPV system), and load at PCC is integrated to the grid. The load is adjusted to be in resonance with the 50 Hz system frequency. To facilitate the islanding identification capability, DG is integrated with the proposed islanding detection technique.

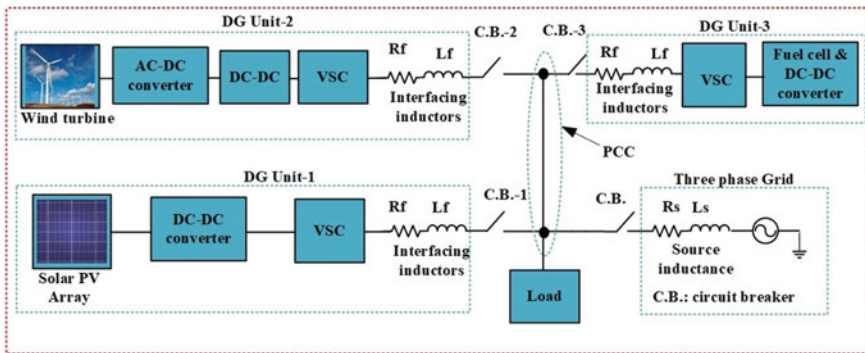


Fig. 1 Single-line diagram of RES-based microgrid

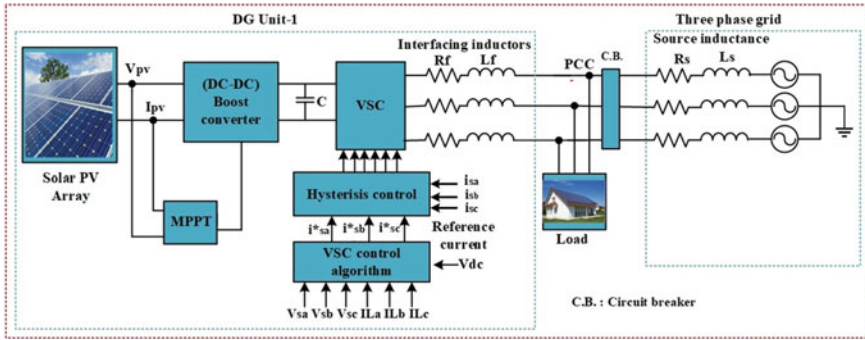


Fig. 2 Grid-integrated PV-based microgrid

### 3 d–q Control for Islanding Detection

d–q axes’ current controllers regulate real and reactive powers supplied by the VSC, respectively. The equations are given below:

$$p = \frac{3}{2} * (v_d * i_q), \tag{1}$$

$$q = \frac{3}{2} * (v_d * i_q). \tag{2}$$

The following are the current equations for the inverter output:

$$\begin{bmatrix} i_d \\ i_q \end{bmatrix} = \begin{bmatrix} i_{dref} \\ i_{qref} \end{bmatrix}. \tag{3}$$

In the present study, an investigation method is proposed along with the injection of a sinusoidal waveform working as a disturbance signal at a single frequency via q-axis controller. Disturbance signal frequency is injected into the grid, to test for the islanding formation. Furthermore, for an active islanding detection, the equations are reframed as:

$$\begin{bmatrix} i_d \\ i_q \end{bmatrix} = \begin{bmatrix} i_{dref} \\ i_{qref} + i_{dist.} \end{bmatrix}, \tag{4}$$

$$i_{dist.} = i_{dr} * \sin wdt. \tag{5}$$

In this investigation, a single 20 Hz signal of magnitude equal to 1% of rated  $i_d$  is applied to the VSC. To perform VSC at unity power factor,  $i_{dref}$  is set to 0. Under perfectly matched power conditions (between the solar PV system and load demand),

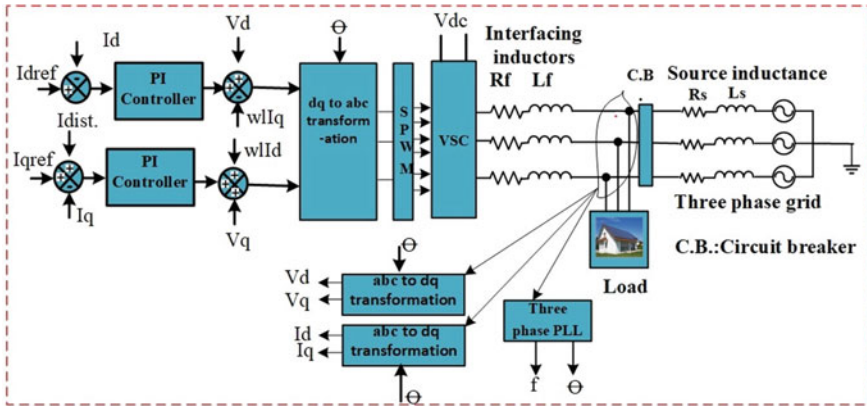


Fig. 3 Block diagram of d-q active control

frequency responses with and without injecting disturbance of current signal via q-axis show that without the injection of the current disturbance, the frequency variation on post-islanding is negligible. Because of this, the majority of passive islanding detection are inefficient at detecting the island formation. Only in post-islanding conditions, the current disturbance injection significantly changes the frequency of the voltage signal [17–19]. To determine whether the frequency variation is caused by islanded or non-islanded conditions, the frequency is further evaluated. Figure 3 depicts the entire block diagram for inverter’s d-q current controllers.

## 4 Active Islanding Detection Technique

A good research technique should be able to distinguish exactly between the island and non-island conditions in addition to being able to identify the islanding condition more quickly. Therefore, one such investigation technique based on the integration of BPF and  $AFV_{mean}$  is studied and validated in the present work.

### 4.1 Bandpass Filter

In the event that the grid frequency deviates more than 0.5 Hz, the active islanding detection technique identify whether island or mal- identify.

## 4.2 Absolute Frequency Variation (Mean)

Absolute output of BPF is used to calculate  $AFV_{\text{mean}}$ , which is presented as follows:

$$AFV_{\text{mean}} = \left(\frac{1}{T}\right) \left[ \int_{t-T}^t (AFV(t)) dt \right]. \quad (6)$$

$T$  is period of time of injected wave and  $t$  is instantaneous time.

## 4.3 Phase-Locked Loop (PLL)

The PLL is used to determine the frequency of the PCC voltage, angular frequency, and the theta needed for transformation from abc to dq0 and vice versa.

## 4.4 Threshold Settings

Figure 2 depicts the test system, simulated for solar PV and load ratings under perfectly matched power conditions (between solar PV system and load demand). Peak frequency variations are observed and recorded for post-islanding circumstances. The AFV and  $AFV_{\text{mean}}$  are then calculated using Eq. (6).

It is important to note that simulations show that peak frequency deviation for any well-matched solar PV system and load demand is roughly equal to  $Q_f = 2.5$ . As a result, the threshold is set at 95% of the derived  $AFV_{\text{mean}}$  values, as shown in Table 1. The following generalized expression to estimate peak variation in frequency with respect to  $Q_f$  under perfectly matched power state is given below in Eq. (7):

$$\text{Deviation in peak frequency} = -0.042 \ln(Q_f) + 0.1004. \quad (7)$$

The loads of  $Q_f = 2.5$  have been recommended for use by several standards and are therefore threshold 0.037 has been used in this paper.

**Table 1** Estimation of threshold value

S. no	Quality factor ( $Q_f$ )	Power rating (kW)	Peak deviation (Hz)	$AFV_{\text{mean}}$ (Hz)	Threshold
1	2.5	10.25	0.061	0.039	0.037

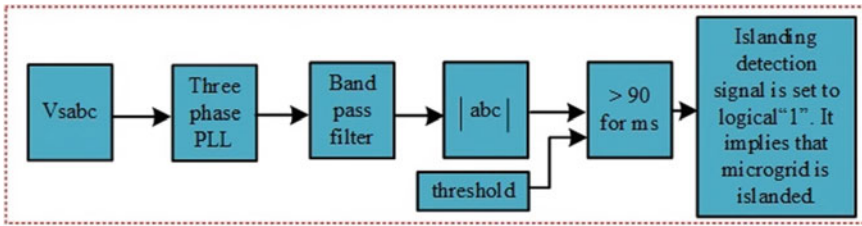


Fig. 4 Islanding detection technique

#### 4.5 Islanding Detection Signal

The PLL is used in simulations to determine the frequency of the  $V_{pcc}$  voltage. Furthermore, estimated frequency is passed through the BPF, and the output is taken as an absolute value.  $AFV_{mean}$  is then calculated using Eq. (6). For the purpose of comparing the stable value to the threshold,  $AFV_{mean}$  is computed. Logic 1 represents the islands' formation, if the  $AFV_{mean}$  surpasses the thresholds for the duration more than 90 ms, while remaining is at logical "0" if the estimated  $AFV_{mean}$  falls below the threshold and indicates the non-islanded state in less than 90 ms. Figure 4 depicts islanding detection system, the deliberate time delay is 90 ms, and it is calculated using simulations under adverse scenario and several literature surveys. The intentional time delay is required so that the islanding detection technique does not mistakenly identify transients as being on an island when they are not. The proposed technique's step-by-step process in Fig. 5 is depicted.

### 5 Case Study: Islanding Under Perfectly Matched Power Condition

Frequency deviation is negligible without current disturbance injection while island generation, the islanding detection technique is evaluated in this section under critical state (between the solar PV system and load, i.e., perfectly matched power). Consequently, the optimal power condition is tested for  $Q_f = 2.5$ . Solar PV system is islanded along with the local load from the distribution grid at 0.2 s. For the completely matched power condition in grid-connected and islanded modes, the waveform and response of frequency are shown in Figs. 6 and 7, respectively. Even in the case of a perfectly matched power state, islanding detection is proficient of locating the islanding development in less than 180 ms.

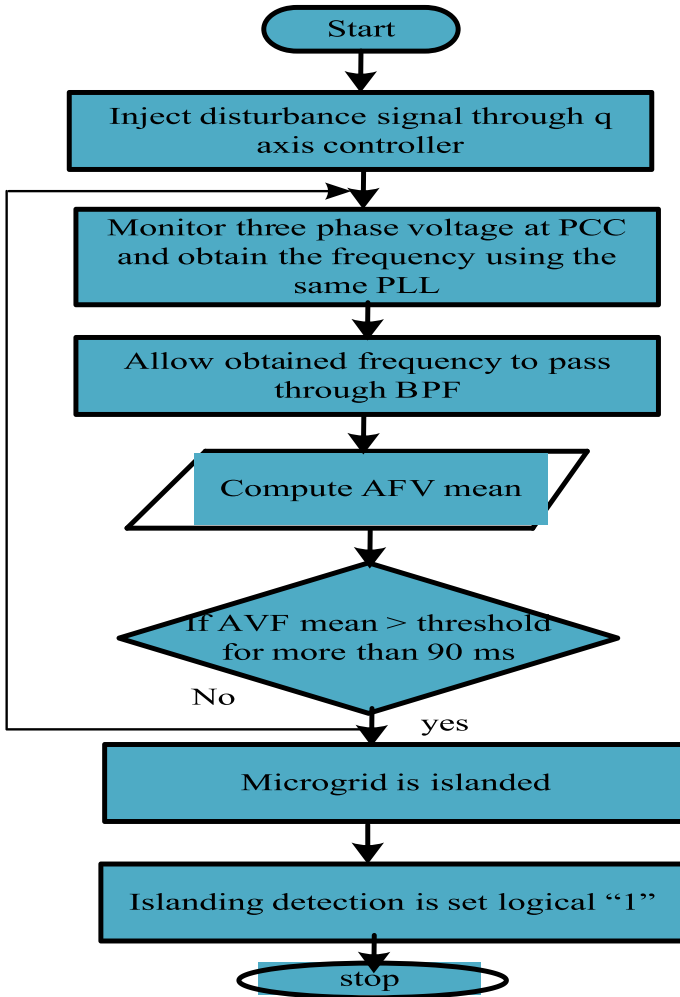


Fig. 5 Flowchart of control algorithm



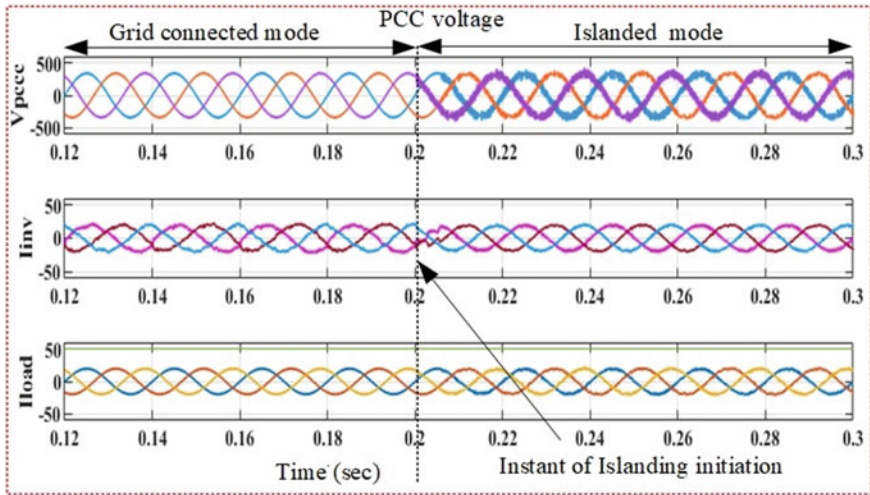


Fig. 6 Waveform: PCC voltage, inverter current, and load current

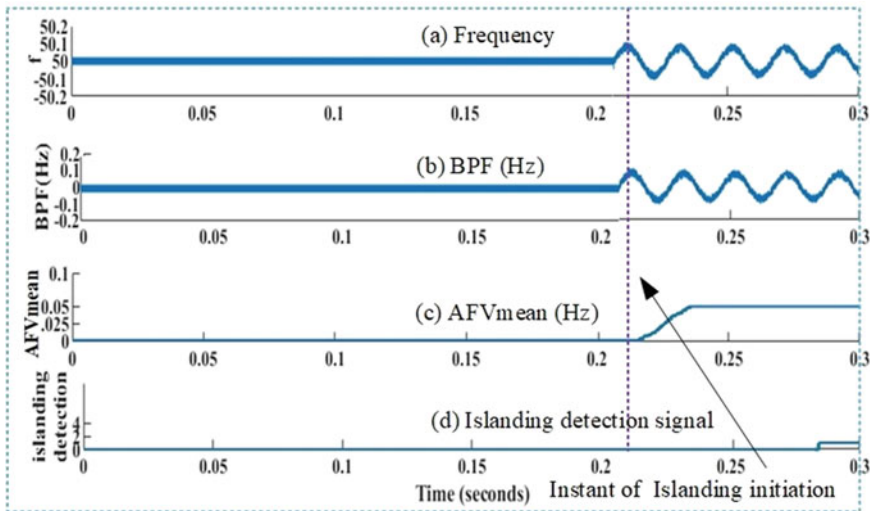


Fig. 7 Response: a PCC voltage, b inverter current, and c load current

## 6 Conclusion

In this paper, an investigation technique was analyzed along with the implementation of active islanding identification through q-axis control based on disturbance injection.

The islanding identification is provided by the q-axis controller method and tested in the MATLAB/Simulink 18.0(a), under the load quality factor ( $Q_f = 2.5$ ). It

offers the several benefits, viz. the islanding identification time is 180 milliseconds. Furthermore, correctly distinguishes between non-islanding and islanding scenarios, compatible with all international standards. It is found that islanding technique is very effective efficient and reliable. However, the islanding detection system can be employed for multiple DGs, and further research is being carried out to extend up to 33 and 66 bus systems.

## References

1. Kumar A, Garg R, Mahajan P (2022) Performance improvement of grid-integrated PV system using novel robust least mean logarithmic square control algorithm. *Electr Eng*. <https://doi.org/10.1007/s00202-022-01552-1>
2. Murugesan S, Murali V, Daniel SA (2018) Hybrid analyzing technique for active islanding detection based on d-axis current injection. *IEEE Syst J* 12(4):3608–3617. <https://doi.org/10.1109/JSYST.2017.2730364>
3. Mahdi M, Istemihan Genc VM (2019) A real-time self-healing methodology using model—and measurement-based islanding algorithms. *IEEE Trans Smart Grid* 10(2):1195–1204. <https://doi.org/10.1109/TSG.2017.2760698>
4. Alam MR, Muttaqi KM, Bouzderdoum A (2018) Characterization of voltage dips and swells in a DG-embedded distribution network during and subsequent to islanding process and grid reconnection. *IEEE Trans Ind Appl* 54(5):4028–4038. <https://doi.org/10.1109/TIA.2018.2833056>
5. Liu N, Diduch C, Chang L, Su J (2015) A reference impedance-based passive islanding detection method for inverter-based distributed generation system. *IEEE J Emerg Select Topics Power Electron* 3(4):1205–1217
6. Guha B, Haddad RJ, Kalaani Y (2016) Voltage ripple-based passive islanding detection technique for grid-connected photovoltaic inverters. *IEEE Power Energy Technol Syst J* 3(4):143–154
7. Merino J, Mendoza-Araya P, Venkataramanan G, Baysal M (2015) Islanding detection in microgrids using harmonic signatures. *IEEE Trans Power Del* 30(5):2102–2109
8. Colombage K, Wang J, Gould C, Liu C (2017) PWM harmonic signature-based islanding detection for a single-phase inverter with PWM frequency hopping. *IEEE Trans Ind Appl* 53(1):411–419
9. Reigosa D, Briz F, Blanco C, Guerrero JM (2017) Passive islanding detection using inverter nonlinear effects. *IEEE Trans Power Electron* 32(11):8434–8445
10. Makwana YM, Bhalja BR (2019) Experimental performance of an islanding detection scheme based on modal components. *IEEE Trans on Smart Grid* 10(1):1025–1035
11. Haider R, Hwan Kim C, Ghanbari T, Bukhari SBA, Zaman MS, Baloch S, Sik Oh Y (2018) Passive islanding detection scheme based on autocorrelation function of modal current envelope for photovoltaic units. *IET Gener Transm Distrib* 12(16):3911
12. Mishra RK, Choudhary A, Fatima S, Mohanty AR, Panigrahi BK (2022) A fault diagnosis approach based on 2D-vibration imaging for bearing faults. *J Vib Eng Technol*, 1–14
13. Palariya AK, Choudhary A, Yadav A (2016) Modelling, control and simulation of MPPT for wind energy conversion using Matlab/Simulink. *Eng J Appl Scopes* 1(2):9–13

14. Tomar A et al (eds) (2022) In: Proceedings of 3rd international conference on machine learning, advances in computing, renewable energy and communication: MARC 2021, vol 915, pp XV, 781, Springer Nature, ISBN: 978-981-19-2830-7. <https://doi.org/10.1007/978-981-19-2828-4>
15. Ahmad MW et al (eds) (2022) Intelligent data analytics for power and energy systems. Springer Singapore, pp XXII, 641. ISBN: 978-981-16-6081-8. <https://doi.org/10.1007/978-981-16-6081-8>
16. Murugesan S, Murali V (2020) Disturbance injection based decentralized identification of accidental islanding. *IEEE Trans Ind Electron* 67(5):37–67

# Harmonics Analysis of Triple-Phase Induction Motor Drive



Mohd. Rizwan Khan, Md. Nasim Akhter, and Mohd. Sartaj

**Abstract** Multi-phase machines have more than three phases. Induction motors have many advantages: low cost, robustness, rigid construction, no need for brushes and commutator segments (squirrel cage type), and longer life. In addition to these advantages of induction machines, multi-phase induction machines can drive a heavy load while decreasing torque pulsations and stator current ripple multi-phase machine drives are utilized in a wide range of applications, including but not limited to ship propulsion, electric aircraft, electric traction, hybrid electric vehicles, and various other industries. The present study uses a MATLAB/Simulink model in a stationary reference frame to examine induction motor drives' transient and steady-state characteristics with three, six, and nine phases. The present investigation undertakes a comparative analysis of the harmonics in the stator and rotor currents of induction motors with three, six, and nine phases, all of which possess identical power ratings. The motors were supplied with power directly from a balanced sinusoidal three-, six-, or nine-phase power source or through a three-, six-, or nine-phase inverter. This work aims to identify and contrast the differences in current harmonics between the various motor configurations. LC filters reduce the harmonics of inverter output voltage and stator and rotor current harmonics. The Simulink model of three, six, and nine-phase induction motors is developed using standard machine equations in this work. Speed, torque, flux, and current characteristic curves are compared for three-, six-, and nine-phase induction motors.

**Keywords** Multi-phase induction motor · Stator reference frame · MATLAB/Simulink · Inverter

---

Mohd. Rizwan Khan · Md. N. Akhter (✉) · Mohd. Sartaj  
Department of Electrical Engineering, Aligarh Muslim University, Aligarh, Uttar Pradesh, India  
e-mail: [md.naseemakhtar@gmail.com](mailto:md.naseemakhtar@gmail.com)

Mohd. Sartaj  
e-mail: [msartaj@myamu.ac.in](mailto:msartaj@myamu.ac.in)

# 1 Introduction

The use of mechanical energy is essential for both industry and everyday life. This can be accomplished with the assistance of a motor, which transforms the mechanical energy that we need into electrical energy. Induction motors are significant because they are inexpensive, dependable, and robust. To enhance the extent of understanding, a mathematical framework of a three-phase induction motor offers valuable perception of the transient and steady-state characteristics of the motor. According to [1], a model of a three-phase induction motor was developed in MATLAB/Simulink using Clarke's transformation in an arbitrary reference frame. Initially, multi-phase machines were not frequently employed since, at that time, multi-phase supply was not easily accessible. But, due to developments in power electronics technology, any number of balance phases can be created from a DC bus voltage by proper phase shifting. Multi-phase machines today play a significant role in research. Induction motors with five or six phases are frequently deemed the most suitable alternatives for high-power implementations, such as those in electric aircraft, ship propulsion, electric traction, textiles, and rolling mills. The performance of a five-phase induction motor is analyzed through dynamic modeling techniques, as described in reference [2]. It concludes that multi-phase drives are better than three-phase drives for several reasons, such as having less harmonic content and being able to work even if one phase is damaged. These advantages can be found in multi-phase drives. Induction motors may have both speed and torque controlled by adjustable-speed drives, including inverters.

Abrupt changes in the supply voltage, speed, and load torque significantly impact the transient performance of a machine. Utilizing a MATLAB/Simulink model that employs an arbitrary reference frame presents a sound approach for evaluating the transient responses of a three-phase induction motor to variations in the motor's load torque, as indicated by reference [3]. Compares the simulation findings with the experiment's findings and presents them.

Control strategies for induction motors may be classified into two groups: scalar control (which includes approaches like v/f control) and vector control. As a result of the scalar control approach maintaining a constant voltage-to-frequency ratio, the torque output by an induction motor is likewise maintained at a constant level throughout a broad spectrum of speed adjustments. A scalar controller is the simplest kind of controller, and although it does not need any speed feedback, this type of controller does not attain excellent precision for either the speed or the torque response. It is possible to regulate torque and speed using vector control independently [4] or field-oriented control (FOC).

The recent research showcases the utilization of a 16-bit microcontroller, specifically the dsPIC30F2010, for closed-loop scalar control in the context of three-phase induction motor drives. The study involves the design and analysis of said drives. The experiment showed that an inverter's output voltage is stable when a controller is used, and the ratio of stator voltage to frequency is kept the same. As a result, using DSP to regulate three-phase motors results in greater stability and efficiency

[5]. Multi-phase motor drives are well-suited for applications that require high power and high current due to their redundant assembly and lower-phase current for equal-rated power and voltage, which provides inherent fault tolerance [6]. This makes them suitable for applications that need a high current.

Multi-phase induction motors outperform three-phase models because their stator generates a field with fewer space harmonics. In an open circuit in any of the phases of a three-phase machine, the system will automatically transition into single-phase mode. Hence, it can run continuously, but it has to be de-rated since it needs help getting started and relies on certain other sources. The multi-phase machine may still self-start with just a little de-rating if an open circuit failure occurs on one of the lines [7, 8] As per prior research [9–13], the simulation of a three-phase induction motor's performance, as measured by stator current, rotor current, speed, and torque, demonstrates that the observed speed aligns with the anticipated speed. The voltage and current characteristics shift as the speed varies.

This study analyzes the harmonics produced by a three-, six-, and nine-phase induction motor, while electricity is supplied directly or through an inverter. Using the filter may drastically lower harmonic current in the stator and rotor.

## 2 Modeling of Multi-phase Induction Motor

The frame of reference works like an observer. Each frame of reference gives a different picture of the system. The system variable should be DC for control reasons, while the actual value is AC. The DC system variable may be obtained using the same speed of reference (frame) as the AC variable. This is referred to as a synchronously rotating frame of reference. Rotor-side disturbances, such as rapid changes in shaft load and moment of inertia, are estimated using the rotor frame of reference. This study models an induction motor using the stator frame of reference, where the reference frame is fixed on the stator, and all system variables are seen from the stator [11–13].

Matrix 1 is the transformation matrix from machine variables form to dqxy0 form for the odd number of phases. The first two rows give the dq axis components, the last row gives the zero sequence component, and the remaining  $2 \cdot [(m-1)/2 - 1]$  rows give the set of xy components. Nine-phase configuration has three sets of xy components. The three-phase configuration has no set of xy components, and the above-given formula for xy component rows validates the same. Only the dq components shown by the first two rows of Matrix 1 are torque-producing. For balance operating conditions, xy and zero sequence components are zero. For different types of faults, various combinations of xy and zero sequence components come into play according to the kind of faults.

$$\sqrt{\frac{2}{m}} \begin{bmatrix} 1 & \cos \alpha & \cos 2\alpha & \cos 3\alpha & \dots & \cos 3\alpha & \cos 2\alpha & \cos \alpha \\ 0 & \sin \alpha & \sin 2\alpha & \sin 3\alpha & \dots & -\sin 3\alpha & -\sin 2\alpha & -\sin \alpha \\ 1 & \cos 2\alpha & \cos 4\alpha & \cos 6\alpha & \dots & \cos 6\alpha & \cos 4\alpha & \cos 2\alpha \\ 0 & \sin 2\alpha & \sin 4\alpha & \sin 6\alpha & \dots & -\sin 6\alpha & -\sin 4\alpha & -\sin 2\alpha \\ 1 & \cos 3\alpha & \cos 6\alpha & \cos 9\alpha & \dots & \cos 9\alpha & \cos 6\alpha & \cos 3\alpha \\ 0 & \sin 3\alpha & \sin 6\alpha & \sin 9\alpha & \dots & -\sin 9\alpha & -\sin 6\alpha & -\sin 3\alpha \\ 1 & \cos 4\alpha & \cos 8\alpha & \cos 12\alpha & \dots & \cos 12\alpha & \cos 8\alpha & \cos 4\alpha \\ 0 & \sin 4\alpha & \sin 8\alpha & \sin 12\alpha & \dots & -\sin 12\alpha & -\sin 8\alpha & -\sin 4\alpha \\ \dots & \dots & \dots & \dots & \dots & \dots & \dots & \dots \\ 1 & \cos\left(\frac{m-1}{2}\alpha\right) & \cos 2\left(\frac{m-1}{2}\alpha\right) & \cos 3\left(\frac{m-1}{2}\alpha\right) & \dots & \cos 3\left(\frac{m-1}{2}\alpha\right) & \cos 2\left(\frac{m-1}{2}\alpha\right) & \cos\left(\frac{m-1}{2}\alpha\right) \\ 0 & \sin\left(\frac{m-1}{2}\alpha\right) & \sin 2\left(\frac{m-1}{2}\alpha\right) & \sin 3\left(\frac{m-1}{2}\alpha\right) & \dots & -\sin 3\left(\frac{m-1}{2}\alpha\right) & -\sin 2\left(\frac{m-1}{2}\alpha\right) & -\sin\left(\frac{m-1}{2}\alpha\right) \\ \frac{1}{\sqrt{2}} & \frac{1}{\sqrt{2}} & \frac{1}{\sqrt{2}} & \frac{1}{\sqrt{2}} & \frac{1}{\sqrt{2}} & \frac{1}{\sqrt{2}} & \frac{1}{\sqrt{2}} & \frac{1}{\sqrt{2}} \end{bmatrix}$$

**Matrix 1** Clark’s transformation for odd phase

Matrix 2 illustrates the decoupled transformation with an even number of phases to be considered. The first two rows of Matrix 2 stand for d-q components, while the latter two stand for zero-sequence components. The rows between define [(m-2)/2-1] sets of x-y components. Regarding six-phase machines, the first two rows stand in for the d-q axis component, the last two rows stand in for the zero sequence component, and one set stands in for the x-y components.

$$\sqrt{\frac{2}{m}} \begin{bmatrix} 1 & \cos \alpha & \cos 2\alpha & \cos 3\alpha & \dots & \cos 3\alpha & \cos 2\alpha & \cos \alpha \\ 0 & \sin \alpha & \sin 2\alpha & \sin 3\alpha & \dots & -\sin 3\alpha & -\sin 2\alpha & -\sin \alpha \\ 1 & \cos 2\alpha & \cos 4\alpha & \cos 6\alpha & \dots & \cos 6\alpha & \cos 4\alpha & \cos 2\alpha \\ 0 & \sin 2\alpha & \sin 4\alpha & \sin 6\alpha & \dots & -\sin 6\alpha & -\sin 4\alpha & -\sin 2\alpha \\ 1 & \cos 3\alpha & \cos 6\alpha & \cos 9\alpha & \dots & \cos 9\alpha & \cos 6\alpha & \cos 3\alpha \\ 0 & \sin 3\alpha & \sin 6\alpha & \sin 9\alpha & \dots & -\sin 9\alpha & -\sin 6\alpha & -\sin 3\alpha \\ 1 & \cos 4\alpha & \cos 8\alpha & \cos 12\alpha & \dots & \cos 12\alpha & \cos 8\alpha & \cos 4\alpha \\ 0 & \sin 4\alpha & \sin 8\alpha & \sin 12\alpha & \dots & -\sin 12\alpha & -\sin 8\alpha & -\sin 4\alpha \\ \dots & \dots & \dots & \dots & \dots & \dots & \dots & \dots \\ 1 & \cos\left(\frac{m-2}{2}\alpha\right) & \cos 2\left(\frac{m-2}{2}\alpha\right) & \cos 3\left(\frac{m-2}{2}\alpha\right) & \dots & \cos 3\left(\frac{m-2}{2}\alpha\right) & \cos 2\left(\frac{m-2}{2}\alpha\right) & \cos\left(\frac{m-2}{2}\alpha\right) \\ 0 & \sin\left(\frac{m-2}{2}\alpha\right) & \sin 2\left(\frac{m-2}{2}\alpha\right) & \sin 3\left(\frac{m-2}{2}\alpha\right) & \dots & -\sin 3\left(\frac{m-2}{2}\alpha\right) & -\sin 2\left(\frac{m-2}{2}\alpha\right) & -\sin\left(\frac{m-2}{2}\alpha\right) \\ \frac{1}{\sqrt{2}} & \frac{1}{\sqrt{2}} & \frac{1}{\sqrt{2}} & \frac{1}{\sqrt{2}} & \frac{1}{\sqrt{2}} & \frac{1}{\sqrt{2}} & \frac{1}{\sqrt{2}} & \frac{1}{\sqrt{2}} \\ \frac{1}{\sqrt{2}} & -\frac{1}{\sqrt{2}} & \frac{1}{\sqrt{2}} & -\frac{1}{\sqrt{2}} & \frac{1}{\sqrt{2}} & -\frac{1}{\sqrt{2}} & \frac{1}{\sqrt{2}} & -\frac{1}{\sqrt{2}} \end{bmatrix}$$

**Matrix 2** Clark’s transformation for even phase

### 3 Dynamic Equation of Multi-phase Induction Motor

D-q axis stator flux linkages can be written as the following equations:

$$\lambda_{ds} = L_s i_{ds} + L_m i_{dr}, \tag{1}$$

$$\lambda_{qs} = L_s i_{qs} + L_m i_{qr}. \tag{2}$$

x-y axis stator flux linkages can be written as the following equations:

$$\lambda_{xns} = L_{ls}i_{xns}, \quad (3)$$

$$\lambda_{y ns} = L_{ls}i_{y ns}. \quad (4)$$

d-q axis rotor flux linkages can be written as the following equations:

$$\lambda_{dr} = L_r i_{dr} + L_m i_{ds}, \quad (5)$$

$$\lambda_{qr} = L_r i_{qr} + L_m i_{qs}. \quad (6)$$

x-y axis rotor flux linkages can be written as the following equations:

$$\lambda_{xnr} = L_{ls}i_{xnr}, \quad (7)$$

$$\lambda_{y nr} = L_{ls}i_{y nr}, \quad (8)$$

$$L_s = L_{ls} + L_m, \quad (9)$$

$$L_r = L_{lr} + L_m. \quad (10)$$

The following equations give the equation for voltages along a stator's d and q axes.

$$V_{ds} = R_s i_{ds} - \omega_c \lambda_{qs} + p \lambda_{ds}, \quad (11)$$

$$V_{qs} = R_s i_{qs} + \omega_c \lambda_{ds} + p \lambda_{qs}. \quad (12)$$

The following equations give the equation for voltages along a stator's x and y axes.

$$V_{xns} = R_s i_{xns} + p \lambda_{xns}, \quad (13)$$

$$V_{y ns} = R_s i_{y ns} + p \lambda_{y ns}. \quad (14)$$

The equation for voltages along the d and q axes of a rotor is

$$V_{dr} = R_r i_{dr} - (\omega_c - \omega_r) \lambda_{qr} + p \lambda_{dr}, \quad (15)$$

$$V_{qr} = R_r i_{qr} + (\omega_c - \omega_r) \lambda_{dr} + p \lambda_{qr}. \quad (16)$$



The equation for voltages along the x and y axes of a rotor is

$$V_{xnr} = R_s i_{xnr} + p \lambda_{xnr}, \quad (17)$$

$$V_{ynr} = R_s i_{ynr} + p \lambda_{ynr}. \quad (18)$$

For the current in the stator's d-q axis, we have

$$i_{ds} = \frac{L_r \lambda_{ds} - L_m \lambda_{dr}}{L_s L_r - L_m^2}, \quad (19)$$

$$i_{qs} = \frac{L_r \lambda_{qs} - L_m \lambda_{qr}}{L_s L_r - L_m^2}. \quad (20)$$

For the current in the rotor's d-q axis, we have

$$i_{dr} = \frac{L_s \lambda_{dr} - L_m \lambda_{ds}}{L_s L_r - L_m^2}, \quad (21)$$

$$i_{qr} = \frac{L_s \lambda_{qr} - L_m \lambda_{qs}}{L_s L_r - L_m^2}. \quad (22)$$

The expression for electromagnetic torque can be formulated with flux linkage and current, as demonstrated below.

$$\frac{P}{2} (i_{qs} \lambda_{ds} - i_{ds} \lambda_{qs}). \quad (23)$$

Rotor speed is given by

$$\omega_m = \int \frac{(T_e - T_L)}{J}. \quad (24)$$

## 4 Nomenclature

$V_{ds}, V_{qs}, V_{dr}, V_{qr}$ : d-axis and q-axis stator and rotor voltages

$i_{ds}, i_{qs}, i_{dr}, i_{qr}$ : d-axis and q-axis stator and rotor currents

$\lambda_{ds}, \lambda_{qs}, \lambda_{dr}, \lambda_{qr}$ : d-axis and q-axis stator and rotor flux linkages

$p\lambda_{ds}, p\lambda_{qs}, p\lambda_{dr}, p\lambda_{qr}$ : d-axis and q-axis stator and rotor flux linkages derivative

$V_{xns}, V_{yns}, V_{xnr}, V_{ynr}$ : x-axis and y-axis stator and rotor voltages

$i_{xns}, i_{y ns}, i_{xnr}, i_{y nr}$ : x-axis and y-axis stator and rotor currents

$\lambda_{xns}, \lambda_{y ns}, \lambda_{xnr}, \lambda_{y nr}$ : x-axis and y-axis stator and rotor flux linkages

$p\lambda_{xns}, p\lambda_{y ns}, p\lambda_{xnr}, p\lambda_{y nr}$ : x-axis and y-axis stator and rotor flux linkages derivative

$R_s, R_r$ : stator and rotor resistances

$L_s, L_r, L_m$ : stator, rotor, and magnetizing inductances

$L_{ls}, L_{lr}$ : stator and rotor leakage inductances

$\omega_r$ : angular speed of the rotor in elect rad/sec

$\omega_m$ : angular speed of the rotor in mech rad/sec

$\omega_c$ : angular speed of reference frame in elect rad/sec

$T_e, T_L$ : electromagnetic and load torque in Nm

$J, P$ : are the moment of inertia and number of pole pairs

$m, n, \alpha$  number of the phase of the machine, number of pairs of x-y components, angle between adjacent phases

### 5 Equivalent Circuit

Figures 1 and 2 show the equivalent d- and q-axis circuits of the m-phase induction motor after applying the vector space decomposition given by matrices 1 and 2 for odd and even numbers of phases. By vector space decomposition, it is possible to control the d- and q-axis components of the m-phase drive, enabling it to function similarly to a three-phase machine. The d-axis part handles speed control, while the q-axis part handles torque regulation.

Figures 3 and 4 show the equivalent x and y circuits of the m-phase induction motor after applying the vector space decomposition given by matrices 1 and 2 for odd and even numbers of phases. Two sets of xy components with two zero-sequence

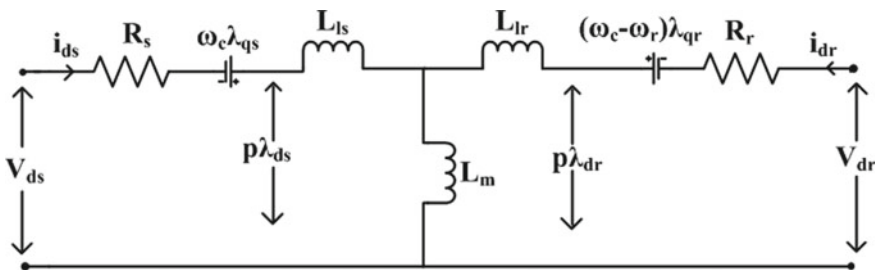


Fig. 1 Circuit corresponding to the d-axis

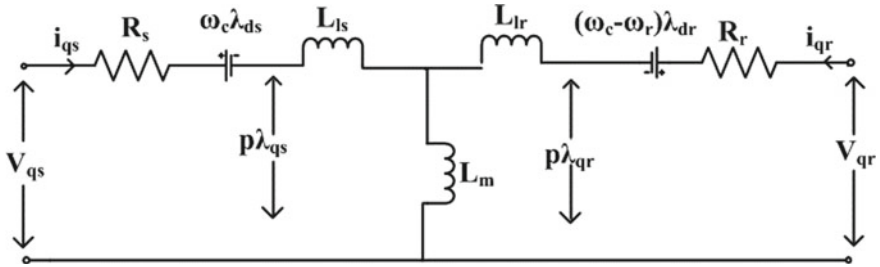


Fig. 2 Circuit corresponding to the q-axis

components are present for a six-phase machine. Three sets of xy components with one zero-sequence component are present for a nine-phase machine. Three-phase systems have one zero-sequence component and one set of torque-producing dq components.

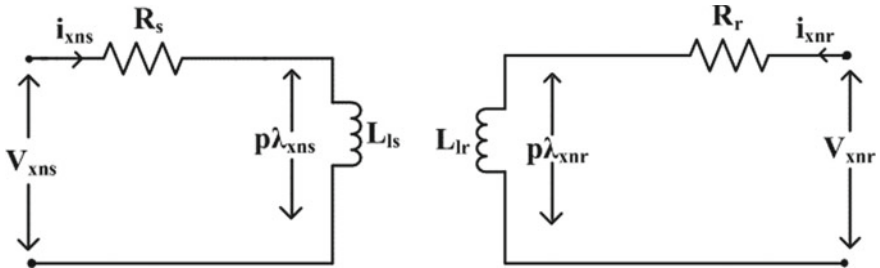


Fig. 3 Circuit corresponding to the x-axis

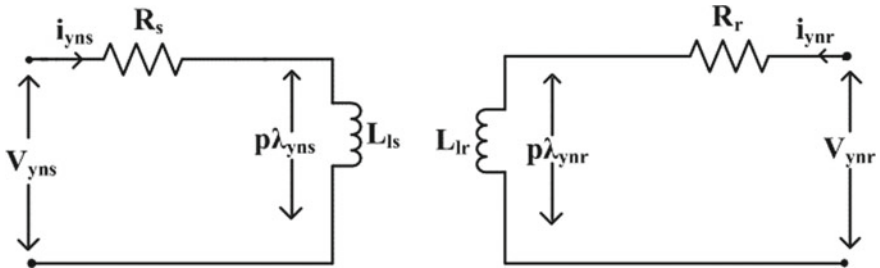


Fig. 4 Circuit corresponding to the y-axis

## 6 Simulation of Multi-phase Induction Motor

Figures 4, 5 and 6 each provide a single line schematic of a three-, six-, or nine-phase induction motor. The input to the motors is a balanced three-, six-, or nine-phase power supply, and the speed, torque, stator current, rotor current, and rotor flux of a multi-phase induction motor are seen on their scopes, accordingly (Fig. 7).

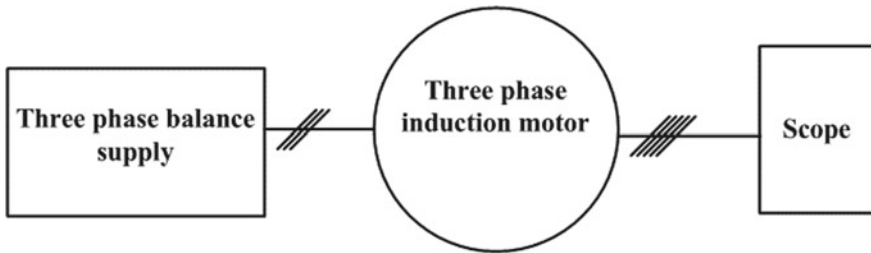


Fig. 5 Single line block diagram of three-phase induction motor

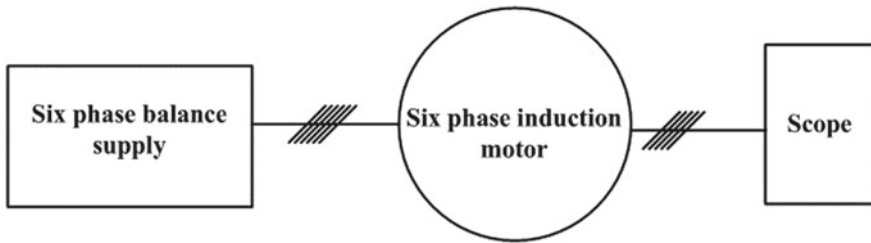


Fig. 6 Single line block diagram of six-phase induction motor

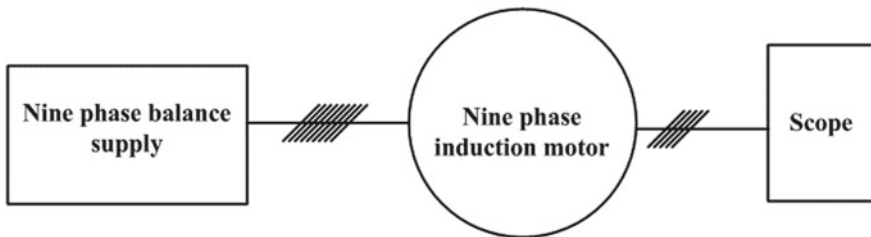


Fig. 7 Single line block diagram of nine-phase induction motor

## 7 Comparison of Response of Multi-phase Induction Motor

Figure 8 depicts the speed of the induction motor with three, six, and nine phases. The red curve depicts the speed of a three-phase induction motor, exhibiting the lengthiest transient time to reach a stable state. On the other hand, the blue line represents the speed of a nine-phase motor, which displays the shortest transient time to attain stability. At  $t = 1$  s, the induction motor experiences a significant speed droop when subjected to load torque in its three-phase configuration. In contrast, a comparatively smaller speed droop is observed in its nine-phase configuration.

Figure 9 illustrates the torque curves associated with induction motors of three, six, and nine phases. The red hue denotes the torque of the three-phase induction motor that exhibits the most extended transient period for stabilization. At the same time, the blue line signifies the torque of the nine-phase induction motor that displays the shortest transient period for stabilization. Figure 9 depicts the torque characteristics of induction motors with three, six, and nine phases. Upon application of a load torque of 3 Nm at  $t = 1$  s, all torque curves are modified to reflect the new load torque value.

Figure 10 illustrates the stator current characteristics of induction motors with three, six, and nine phases. The figure mentioned above depicts the stator current of a three-phase induction motor with the most prolonged transient settling time, as represented by the red curve. The stator current waveform of the nine-phase induction motor is depicted in Fig. 10. The transient period of the stator current in a nine-phase

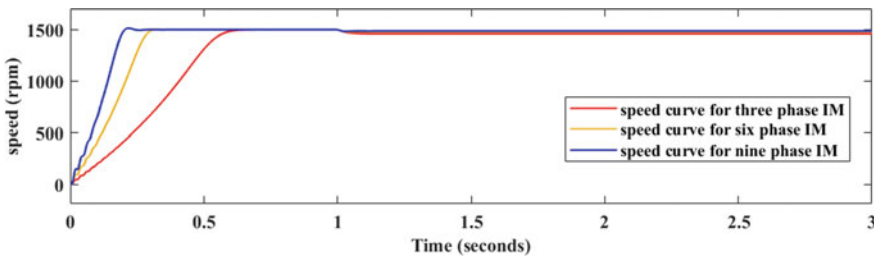


Fig. 8 Speed comparison of 3, 6, and 9 phase induction motor by direct supply

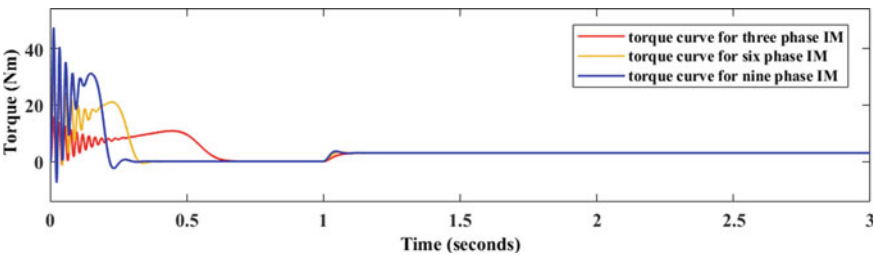
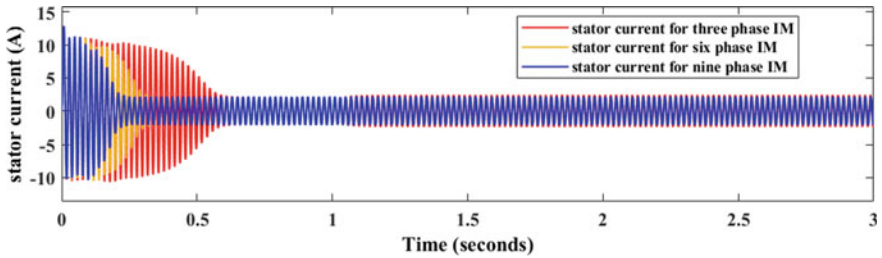


Fig. 9 Torque comparison of 3, 6, and 9 phase induction motor by direct supply



**Fig. 10** Stator current comparison of 3, 6, and 9 phase induction motor by direct supply

induction motor is shortest when the motor is subjected to a load torque at  $t = 1$  s, as indicated by the blue line, before reaching a steady state. The stator experiences an initial increase in current flow, followed by stabilization at a new level.

Figure 11 compares rotor current for three-, six-, and nine-phase induction motors run by a balanced sinusoidal multi-phase power supply. The red curve represents the rotor current of a three-phase motor, whereas the yellow curve illustrates the rotor current characteristics of a six-phase induction motor. The aforementioned graphical representation depicts the characteristics of the current in the rotor, specifically about nine distinct phases, as indicated by the blue curve. The curves above indicate that the initial transients of rotor current dissipate at an earlier stage in the nine-phase setup than in the three- and six-phase setups. Before  $t = 1$  s, the rotor current is almost equal to zero for all three machine connections. On load applications, the three-phase configuration has the highest magnitude of rotor current.

Figure 12 depicts the rotor flux for three-, six-, and nine-phase induction motors. The red curve depicts the rotor flux for a three-phase motor. This motor type has a lower flux value but a longer maximum settling time. On the other hand, the blue line depicts the rotor flux for a nine-phase motor. This type of motor has the highest flux value but the lowest settling time. As seen in the picture to the right, the value of the rotor flux goes down when the load torque is applied at time  $t = 1$  s.

Figures 13, 14, 15, 16 and 17 exhibit the speed, torque, stator current, rotor current, and rotor flux characteristics of a three-phase, six-phase, and nine-phase induction

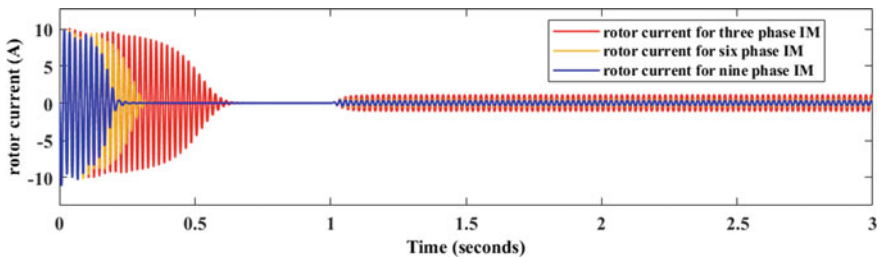


**Fig. 11** Rotor current comparison of 3, 6, and 9 phase induction motor by direct supply

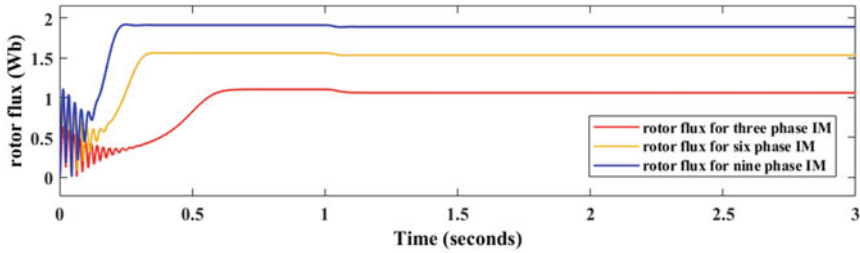


Fig. 12 Rotor flux comparison of 3, 6, and 9 phase induction motor by direct supply

motor powered by an inverter. The motor experiences a torque application at  $t = 1$  s, causing the speed to decrease from 1500 to 1000 rpm at  $t = 2$  s.

Figures 18, 19, 20, 21 and 22 depict the speed, torque, stator current, rotor current, and rotor flux characteristics of induction motors with three, six, and nine phases. These motors are supplied with power by an inverter incorporating an LC filter to mitigate the effects of harmonics on both stator and rotor currents. A torque is exerted at time  $t = 1$  s, resulting in a change in speed from 1500 revolutions per minute to 1000 revolutions per minute at time  $t = 2$  s.

Tables 1 and 2 compare harmonic content in stator and rotor currents for different input supply methods for different configurations of machines under different loading conditions. It is observed from Table 1 that the stator current harmonics are almost

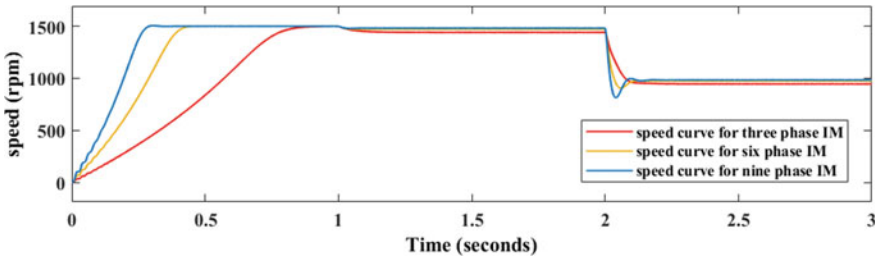


Fig. 13 Speed comparison of 3, 6, and 9 phase induction motor fed by the inverter

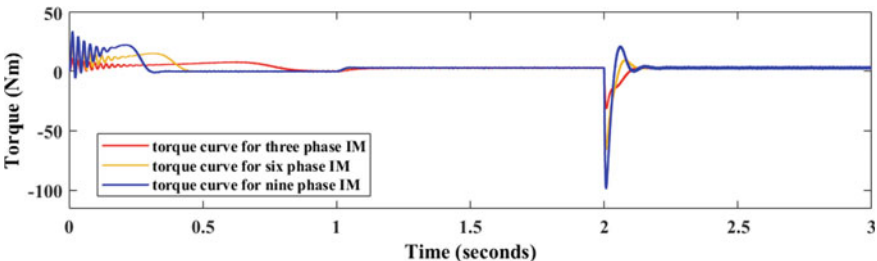


Fig. 14 Torque comparison of 3, 6, and 9 phase induction motor fed by the inverter

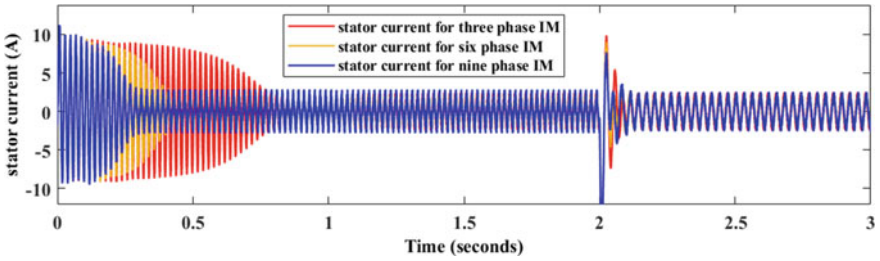


Fig. 15 Stator current comparison of 3, 6, and 9 phase induction motor fed by the inverter

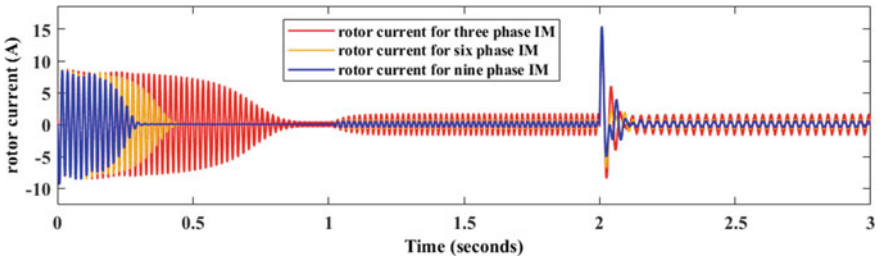


Fig. 16 Rotor current comparison of 3, 6, and 9 phase induction motor fed by the inverter

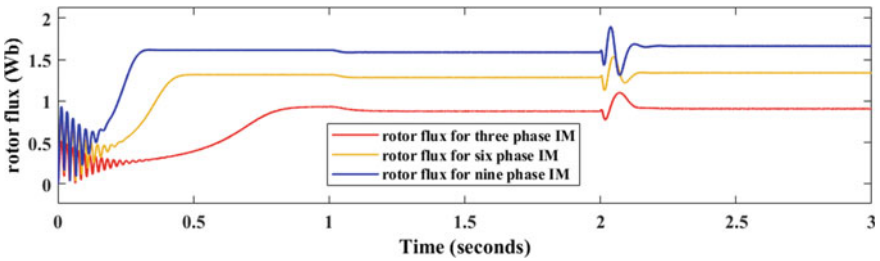


Fig. 17 Rotor flux comparison of 3, 6, and 9 phase induction motor fed by inverter

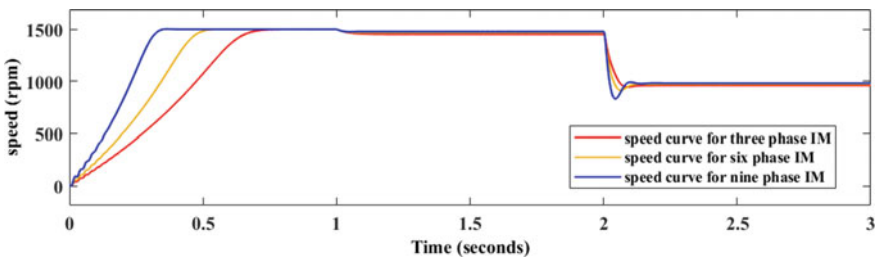


Fig. 18 Speed comparison of 3, 6, and 9 phase induction motor fed by inverter with filter



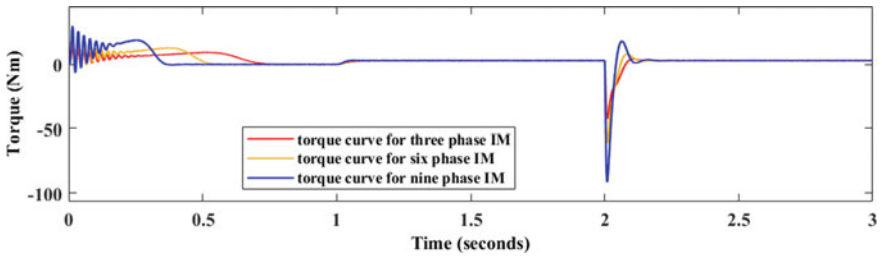


Fig. 19 Torque comparison of 3, 6, and 9 phase induction motor fed by inverter with filter

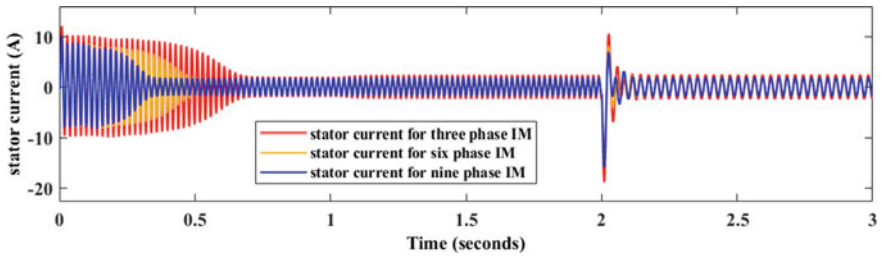


Fig. 20 Stator current comparison of 3, 6, and 9 phase induction motor fed by inverter with filter

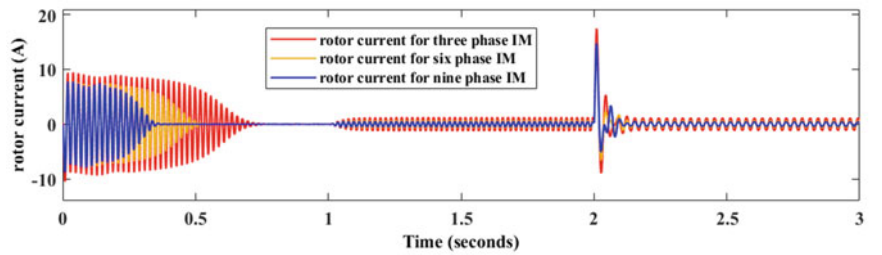


Fig. 21 Rotor current comparison of 3, 6, and 9 phase induction motor fed by inverter with filter

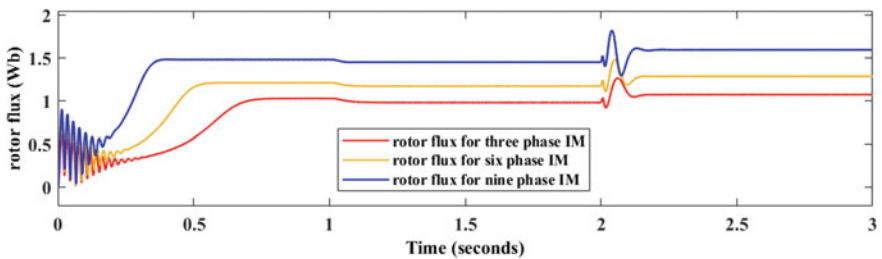


Fig. 22 Rotor flux comparison of 3, 6, and 9 phase induction motor fed by inverter with filter

equal for all the configurations of machine connections when supplied by a balanced sinusoidal supply. Harmonic content increases as the number of phases increases when the source is a power electronic inverter. For the same parameter of the LC filter, the stator current harmonic contents get reduced up to acceptable limits. Table 2 shows an interesting behavior: harmonic content in rotor current decreases with the number of phases for any input power configuration.

## 8 Conclusions

This study compares the performance of three-, six-, and nine-phase induction motors, and it has been observed that transient performances improve as we go for the higher number of phases from the three-phase. Applying mechanical load to the three-, six-, and nine-phase induction motor configurations shows that speed droop is the minimum for nine-phase configurations. As the number of phases increases, the rotor fluxes increase, but the stator current remains the same in all configurations. Tables 1 and 2 show the harmonic content in the stator and rotor currents under all configurations. If inverters supply these three configurations, harmonic content increases in stator current because the number of switches in the inverter increases as we go for more phases. Harmonic content gets reduced in rotor current even if supplied from an inverter. From this study, it can be concluded that the multi-phase machine performs better for high-performance applications with a balanced sinusoidal multi-phase power supply.

**Table 1** Stator current harmonics

Technique for providing power to the stator	Stator current THD at $t = 0.5$ s on no load			Stator current THD at $t = 1.5$ s on load			Stator current THD at $t = 2.5$ s on load		
	Three-phase	Six-phase	Nine-phase	Three-phase	Six-phase	Nine-phase	Three-phase	Six-phase	Nine-phase
Direct (%)	0.02	0.02	0.02	0.03	0.03	0.03	0.03	0.03	0.03
Through inverter (%)	14.52	27.0	29.66	12.23	21.44	29.1	9.11	13.8	17.40
Through inverter with filter (%)	2.02	3.63	5.98	1.75	2.63	4.34	0.96	1.51	1.54

**Table 2** Rotor current harmonics

Technique for providing power to the stator	Rotor current THD at $t = 0.5$ s on no load	Rotor current THD at $t = 1.5$ s on load			Rotor current THD at $t = 2.5$ s on load		
		Three-phase	Six-phase	Nine-phase	Three-phase	Six-phase	Nine-phase
Direct	The rotor current is zero	0.06%	0.04%	0.04%	0.06%	0.04%	0.04%
Through inverter		20.35%	4.86%	3.70%	15.90%	8.62%	8.55%
Through inverter with filter		2.99%	0.93%	0.28%	1.85%	0.52%	0.52%

## References

1. Ratnani PL, Thosar AG (2014) Mathematical modelling of a 3 phase induction motor using MATLAB/Simulink. *Int J Mod Eng Res* 4(6):62–67
2. Sarwer Z, Sartaj M, Khan MR, Zaid M, Shahajhani U (2019) Comparative performance study of five-phase induction motor, pp 1–6. *Innovations in Power and Advanced Computing Technologies (i-PACT)*, Vellore, India
3. Sandhu KS, Pahwa V (2009) Simulation study of three-phase induction motor with variations in the moment of inertia. *J Eng Appl Sci* 4(6):72–77
4. Aktaibi A, Ghanim D, Rahman MA (2011) Dynamic simulation of a three-phase induction motor using Matlab Simulink. In: 20th annual newfoundland electrical computer engineering conference, vol 5, no 12, pp 1–5
5. Aspalli MS, Asha R, Hunagund PV (2012) Three phase induction motor drive using igbts and constant V/F method 1(5):463–469
6. Singh GK (2002) Multi-phase induction machine drive research—a survey. *Electr Power Syst Res* 61(2):139–147
7. Bojoi R, Rubino S, Tenconi A, Vaschetto S (2016) Multi-phase electrical machines and drives: a viable solution for energy generation and transportation electrification. In: *Proceedings of 2016 international conference expo electrical power engineering EPE 2016*, pp 632–639
8. Devi K, Gautam S, Nagaria D (2014) Speed control of 3-phase induction motor using self-tuning fuzzy PID controller and conventional PID controller. *Int J Inf Comput Technol* 4(12):1185–1193
9. Patel JR, Vyas SR (2014) Simulation and analysis of constant V/F induction motor drive. *Int J Eng Tech Res* 2(4):290–293
10. Manjesh, Dabhade NS (2020) Temperature measurement of nine phase induction motor drive without load and various load conditions. *IJERT* 9(1):31–34
11. Tomar A et al (eds) (2022) In: *Proceedings of 3rd international conference on machine learning, advances in computing, renewable energy and communication: MARC 2021*, vol 915, pp XV, 781. ISBN: 978-981-19-2830-7. <https://doi.org/10.1007/978-981-19-2828-4>

12. Ahmad MW et al (eds) (2022) Intelligent data analytics for power and energy systems, pp XXII, 641. Springer Singapore. ISBN: 978-981-16-6081-8. <https://doi.org/10.1007/978-981-16-6081-8>
13. Krishnan R (2002) Electric motors drives modelling analysis and control. Prentice Hall of India, New Delhi

# Development of Witricity Based Wireless Power Transmission System



Kanhaiya Mishra, Arjun Kushawaha, Neetigya Chaurasia,  
Sudhanshu Kumar, Gautam Kr. Singh, and Mohammad Shahid

**Abstract** The creation of a wireless electricity transfer prototype has been a focus of active research in recent years due to its potential to completely alter the way of transmission and distribution of electrical energy. This prototype makes use of resonant magnetic coupling, which dispenses with the requirement of physical wires and enables the effective transfer of electrical energy across small distances. The transmitter and receiver units in this concept each have resonant coils that can resonate at the same frequency. Alternating current from the transmitter unit forms a magnetic field, which in turn causes a current to flow through the receiver unit's resonant coil. The electrical equipment or batteries can then be powered by this induced current. Optimizing the coils' resonance frequency, reducing electromagnetic interference losses, and assuring the security of the wireless energy transfer are just a few of the difficulties that had to be overcome during the creation of this prototype. The model has, however, demonstrated encouraging results in terms of its efficiency and dependability, and significant progress has been made in overcoming these issues. In the future, this technology may be used for a variety of purposes, such as wirelessly charging of electric vehicles, powering sensors and gadgets from a distance, and doing away with traditional power lines in homes and workplaces.

---

K. Mishra (✉) · A. Kushawaha · N. Chaurasia · S. Kumar · G. Kr. Singh · M. Shahid  
Department of Electrical Engineering, Galgotias College of Engineering and Technology,  
Knowledge Park-2, Greater Noida 201310, India  
e-mail: [Kanhaiya000002@gmail.com](mailto:Kanhaiya000002@gmail.com)

A. Kushawaha  
e-mail: [akushawaha17@gmail.com](mailto:akushawaha17@gmail.com)

N. Chaurasia  
e-mail: [412sarthak@gmail.com](mailto:412sarthak@gmail.com)

S. Kumar  
e-mail: [sonu16181037@gmail.com](mailto:sonu16181037@gmail.com)

G. Kr. Singh  
e-mail: [san127594@gmail.com](mailto:san127594@gmail.com)

M. Shahid  
e-mail: [mohd.shahid@galgotiacollege.edu](mailto:mohd.shahid@galgotiacollege.edu)

**Keywords** Electrical energy · Magnetic field · Resonance frequency · Electromagnetic interference

## 1 Introduction

A developing technology in the realm of mobile phones is wireless power transmission. Imagine arriving home and being able to charge your phone wirelessly in your living room, kitchen, or car. This eliminates the need to connect your phone to a wired charging source. In an emergency, one can use his free hand to speak while their phone charges. The ease of wireless power transfer via inductive coupling will alter how we charge cell phones and other electronics.

In 1890, Nicola Tesla made the discovery of wireless power transmission. He presumed using the Earth's ionosphere to send power across very long distances. Using the resonant transformer he utilized his demonstration, in the Tesla coil. In this coil, unwanted electric fields emit energy in all directions. Numerous technologies, including inductive coupling, capacitive coupling, microwaves, and laser techniques employ remote fields. However, this technique uses magnetic resonance coupling to transfer intermediate energy. That suggests that energy is transferred using non-radiative means and connector-free devices.

In order to replace lithium-ion batteries in home appliances and the field of medical science, wireless energy transmission, also known as witrlicity, is expanding its applicability. EVs are charged using magnetic resonance technology while being driven on a roadway. Since this technology can function in water, it can power underwater submarines for extended periods of time. Additionally, it satisfies the needs for safety and quick charging. Due to how simple and efficient inductive charging is, one may thank the development of power electronics for its success. The main benefit of using inductive charging is that there are no exposed conductors, interlocks, or connectors required for the system to function, significantly reducing the possibility of electric shock hazards. Medium-range (30–60 cm) application. In order to attain a range of meters to transfer power, WPT is a good option.

The physical separation of the primary and secondary windings causes losses due to proximity influence. Contactless transformers are not very efficient, given their inadequate coupling, wide air gaps between the primary and secondary windings, and high leakage inductances.

This article presents research on the energy transfer method known as witrlicity that uses inductive coupling technology. The abbreviation for wireless electricity is witrlicity. Theoretical analysis and numerical results show that mid-range (up to 1 m) wireless transmission of electricity is practically possible and efficient.

The organization of the paper is laid out in the following manner: Sect. 1 offers an introduction, while Sect. 2 outlines the main points. A complete literature review is provided in Sect. 3, with a discussion of the safety issues regarding wireless power transfer presented in Sect. 4. Section 5 describes the methodology and experimental results, as well as an explanation of the block diagram. An MRC-based theory is

explained in Sect. 6, and the outcomes of the experiments are then discussed in Sect. 7. The potential for future research is outlined in Sect. 8 and the conclusion can be found in Sect. 9.

## 2 Highlights of the Paper

- (a) Students have created the first research paper on wireless power transfer. This has a 1-m range and a maximum power output of 60 watts.
- (b) Resonant inductive coupling is utilized in this paper, where power is exchanged between two resonant circuits by magnetic fields.
- (c) It eliminates the maze of cords that keep devices tethered to an electrical socket.
- (d) The magnetic near field can also cover a number of metallic items that typically restrict magnetic fields.

## 3 Literature Survey

Wireless power transfer in the midrange via resonant coupling (witricity) has established itself as a major issue for both scientific exploration and engineering applications since it was invented by Tesla in the twentieth century. Great advancements have been made in recent years, particularly by an MIT research team whose achievements are especially noteworthy. In 2007, they were able to transmit 60W, achieving 40% efficiency over distances greater than 2 m. The idea behind witricity is that electromagnetic coupling between two systems of similar resonant frequencies is strongest. To boost transmission efficiency with this approach, it is best to operate in a “highly coupled” system. This involves using one resonator as the transmitter and another as the receiver, both having the same structure and resonant frequency. Maximum power then travels from sender to receive at resonance frequency. To even further improve transmission effectiveness, finding an exact resonance frequency is essential; this paper provides us with an effective method for doing so by way of equivalent circuits [1].

After the renowned scientist Sir Nikola Tesla proposed the concept of transferring energy without any wires, it has become a widely accepted technique and many applications nowadays have implemented this technology. Magnetic resonance coupling plays a major part in wireless energy transfer systems due to its various benefits compared with other methods. As the distance between the sender and receiver increases, however, its efficiency swiftly diminishes. The solution to this issue is frequency tracking, which is why the frequency tracking approach was conceptualized. With this paper, modern wireless power transmission technology is presented; in this method, high-frequency resonance is used at about 50 kHz for increased power transmission efficacy [2].



The goal of WiTricity is to draw a lot of interest due to its efficient and effective range of wireless power transfer. This research acted as a foundation for our study on the basics of resonance coupling in relation to wireless power transfer. Recently, magnetic resonant coupling was used to devise a powerful mid-range wireless power transfer. As the separation between the proposed antennas changes, so does the resonance frequency, according to research. In this examination, designers will employ an impedance matching network at 13.56 MHz to modify the frequency of the antennas. The permissible frequency is outlined in industrial, science, and medical (ISM) bands. To attain wireless charging, WPT technology must meet three requirements—high efficiency, big air gap, and high power—which it does successfully. The two most frequently used technologies for wireless transfer are microwave power transfer and electromagnetic induction; however, electromagnetic induction has limited range capabilities. Resonance coupling is a modern and highly effective way of transferring energy wirelessly through magnetic coupling between two resonating antennas in WiTricity. This paper is meant to elucidate how resonance coupling may be used to send electrical energy from a power source to an electrical load without the need for wires. We have also provided an overview of current technology, along with information on various aspects of WPT study areas and their benefits/drawbacks [3].

This reference paper explores the fundamentals of wireless power transmission, also known as WiTricity. Thanks to technological advances and more effective methods of power transfer, like inductive coupling through magnetic fields, we can now use WiTricity. To do this, we need a transmitting circuit with a DC-DC converter and an IRF 540 transistor for the receiving circuit, combined with a 9-V battery. We measured voltage and efficiency between 0 and 10 cm by varying the distance to get our readings. Our findings showed that when the distance is 10 cm, efficiency drops by up to 25%. In this paper, we have examined the use of inductive coupling for WPT over short distances [4].

To put the idea of wireless power transmission into practice, a power transmitter circuit on the sending side and a power output device on the receiving end were created. A self-resonating Royer oscillator was used on the sending side of the power transmitter circuit and both sides operate at 1.2 MHz as their standard frequency. With this type of wirelessly transmitted electricity, we mainly charged batteries for low-wattage emergency lights and cell phones, functioning effectively up to 1 m away. This method of transmitting power without connecting cables is called “wireless power transfer” (WPT). It is an appropriate option when a wired connection is not possible or feasible. There are a number of methods available for transmitting electrical power wirelessly, usually through an electromagnetic field, though non-radiative fields can be used for this purpose as well. Transformers are an incredibly useful example for this purpose. Highly resonant wireless power transfer (HR-WPT) increases energy transfer efficiencies at lower coupling rates by using high quality factor resonators [5].

Every human needs electricity, and wires are required for power transmission in order to provide that electricity. Nikola Tesla pioneered wireless power transfer in the early twentieth century. In addition to being dependable and effective, wireless power transfer (WPT) is also economical and environmentally benign. In addition to the previously published works and concepts of resonant coupling, the fundamental concept, design, and application of wireless electricity are presented in this paper. This non-radiative approach of wireless power transfer is efficient in terms of cost and it adheres to the mutual induction principle. This technique creates a magnetic field using a coil that is carrying current. When a second conducting coil is positioned close to the first, a portion of the oscillating magnetic field is absorbed by the second coil, causing the second coil to produce an electric current. Different gadgets can be powered by the current produced in the secondary inductive coil. According to how far apart the coils are from one another, the coil will receive an AC voltage ranging from 2.5 to 6 V in this situation. The secondary coil's output is further rectified, then coupled to a 4.5–6 V rechargeable battery. This can be immediately linked to any DC load. To display power load at output, any inverter with a 6-V, 20-W output can be used. For this, a CFL or tube light can be used. Future research in the field of wireless power can be rather significant. It is possible to create wireless power transmission systems that are smaller and more effective across long distances. In the future, it may be possible to transmit tens of thousands of kilowatts of electricity through distances of hundreds of miles using extremely efficient wireless power transmission technologies [6].

Wireless power transfer (WPT) can be either radiative or non-radiative, depending on the transfer technique. Far field influence determines the radiation power. An antenna can transmit power through an electromagnetic wave over a long distance through media such as air or vacuum. Resonant coupling and near-field inductive coupling are utilized for non-radiative WPT's short and medium-range applications. Electromagnetic induction via IWPT is employed to wirelessly transmit energy from the primary coil to the secondary coil. Generally, a transformer's magnetic field is confined to the high permeability core but with IWPT, there can just be air as a separation space between the primary and secondary loops. To increase efficiency at the receiver side, resonance coupling and resonant state of coils are utilized for optimization. Self-resonance of helix coils that resonate at a specific frequency using its self-inductance and parasitic capacitance can be used for resonance coupling, whereas an external capacitor must be added if the resonant coils' parasitic capacitance is insufficient to achieve resonance at the desired frequency. Near-field technology known as RWPT helps cover distances from few millimeters to few meters. RWPT modifies leakage inductance for increased power transfer efficiency by combining magnetic coupling with resonance approach; even when operating frequency isn't resonant, it behaves similarly to conventional IWPT by changing resonant operating frequency. Moreover, WPT model was subject to quantitative comparison analysis by using finite element analysis method ranging frequencies from 0.01 to 10 MHz. An optimizable WPT system which raised transfer efficiency up to 85% in a 10 cm distance and 45% in 20 cm has been recently proposed by authors. RWPT technology excelled in mid-range distances compared with IWPT due to superior efficiency and

was proven successful in experiments, where two self-resonant spiral coils with combined radius of 30 cm lit up a 60W bulb using 40–60% transmission efficiency over a 2 m air gap distance. WPT technology also has potential usage for kilowatt (KW)-scale high-power applications such as charging electric cars; more than 50 million wireless chargers sold in 2015 along with 140 million wireless receivers are expecting growth soon doubly so [7].

Wireless Power Transfer (WPT) can be either radiative or nonradiative, depending on the transfer technique. Far field influence determines the radiation power. An antenna can transmit power through an electromagnetic wave over a long distance through media such as air or vacuum. Resonant coupling and near-field inductive coupling are utilized for non-radiative WPT's short and medium-range applications. Electromagnetic induction via IWPT is employed to wirelessly transmit energy from the primary coil to the secondary coil. Generally, a transformer's magnetic field is confined to the high permeability core but with IWPT, there can just be air as a separation space between the primary and secondary loops. To increase efficiency at the receiver side, resonance coupling and resonant state of coils are utilized for optimization. Self-resonance of helix coils that resonate at a specific frequency using its self-inductance and parasitic capacitance can be used for resonance coupling, whereas an external capacitor must be added if the resonant coils' parasitic capacitance is insufficient to achieve resonance at the desired frequency. Near field technology known as RWPT helps cover distances from few millimeters to few meters. RWPT modifies leakage inductance for increased power transfer efficiency by combining magnetic coupling with resonance approach; even when operating frequency isn't resonant, it behaves similarly to conventional IWPT by changing resonant operating frequency. Moreover, WPT model was subject to quantitative comparison analysis by using finite element analysis method ranging frequencies from 0.01 to 10 MHz. An optimizable WPT system which raised transfer efficiency up to 85% in a 10 cm distance and 45% in 20 cm has been recently proposed by authors. RWPT technology excelled in mid-range distances compared to IWPT due to superior efficiency and was proven successful in experiments where two self-resonant spiral coils with combined radius of 30 cm lit up a 60W bulb using 40%-60% transmission efficiency over a 2 m air gap distance. WPT technology also has potential usage for kilowatt (KW)-scale high power applications such as charging electric cars; more than 50 million wireless chargers sold in 2015 along with 140 million wireless receivers are expecting growth soon doubly so [8–11].

Wireless Power Transfer (WPT) can be either radiative or nonradiative, depending on the transfer technique. Far field influence determines the radiation power. An antenna can transmit power through an electromagnetic wave over a long distance through media such as air or vacuum. Resonant coupling and near-field inductive coupling are utilized for non-radiative WPT's short and medium-range applications. Electromagnetic induction via IWPT is employed to wirelessly transmit energy from the primary coil to the secondary coil. Generally, a transformer's magnetic field is confined to the high permeability core but with IWPT, there can just be air as a separation space between the primary and secondary loops. To increase efficiency at the

receiver side, resonance coupling and resonant state of coils are utilized for optimization. Self-resonance of helix coils that resonate at a specific frequency using its self-inductance and parasitic capacitance can be used for resonance coupling, whereas an external capacitor must be added if the resonant coils' parasitic capacitance is insufficient to achieve resonance at the desired frequency. Near field technology known as RWPT helps cover distances from few millimeters to few meters. RWPT modifies leakage inductance for increased power transfer efficiency by combining magnetic coupling with resonance approach; even when operating frequency isn't resonant, it behaves similarly to conventional IWPT by changing resonant operating frequency. Moreover, WPT model was subject to quantitative comparison analysis by using finite element analysis method ranging frequencies from 0.01 MHz to 10 MHz. An optimizable WPT system which raised transfer efficiency up to 85% in a 10 cm distance and 45% in 20 cm has been recently proposed by authors. RWPT technology excelled in mid-range distances compared to IWPT due to superior efficiency and was proven successful in experiments where two self-resonant spiral coils with combined radius of 30 cm lit up a 60W bulb using 40–60% transmission efficiency over a 2 m air gap distance. WPT technology also has potential usage for kilowatt (KW)-scale high power applications such as charging electric cars; more than 50 million wireless chargers sold in 2015 along with 140 million wireless receivers are expecting growth soon doubly so [12–21].

## 4 Challenges for Safe Wireless Power Transmission

### A. Safety Concerns in Real Life

Environmental dynamics actually make it more challenging to guarantee EMR safety. To begin with, predicting and managing the wireless power density seems challenging. Taking signal from other wireless systems as an example, reflection and refraction can cause the radio exposure to exceed the safe level. Second, it can be difficult to ensure safety when end users are permitted to deploy new ETs and change the positions of current ETs/ERs in real time. In order to charge ERs cooperatively and meet the receivers' energy needs as quickly as feasible while maximizing the delivered energy, multiple ETs may be operational at once. On the other hand, if more ETs are used, radiation exposure to end users may increase. Providing simple ways to assure power transfer safety may help reduce RF exposure to some level, but in actuality, a number of adverse effects may occur.

### B. Safe Power Transfer Is Not Easy

The chosen quantity for millimeter wave safety rules is wireless power density, which does not rely on tissue absorption of power. However, due to its greater significance to dangerous damages, such as those to the eyes, temperature has a tremendous potential to become a quantity for safety requirements in the future. Because of this, current rules and actual efforts to achieve safe power transfer are insufficient, and the

possibility of health problems may seriously limit WPTN use. We think that in order to identify and stop unsafe power transfer operations in the real world, significant research is needed.

### (1) **Safety Attack**

Safety regulations may be abused to make ETs operate inefficiently while charging or even cease to exist altogether, which would constitute a denial of service. By controlling ET transmission parameters including power, frequencies, and transmission time in line with data from ERs about RF exposure, safe charging may be particularly ensured. If a wicked ER wants to avoid punishing its neighbors, it can easily claim that the RF radiation is beyond the safety limit. ETs should either stop transmitting altogether or limit the power of their transceivers in such a situation. Because of the potential for battery depletion, the higher safety attacks mean that ERs are charged less efficiently and operate for shorter periods of time. As was previously stressed, because of its susceptibility to environmental dynamics, it is nearly impossible to determine wireless power density properly. Better measurement and estimation methods are required to obtain the radio power distribution without response from ERs. This issue could be resolved by establishing a different sensor network that would gather measurements of environmental RF exposure without requiring ER feedback. However, this adds more administrative work and expense for WPTNs.

### (2) **Spoofing Attack**

The level of energy, device identity, and other information are all carried via beacons that ERs and ETs communicate across WPTNs. Malicious nodes are capable of listening in on the communications of other devices and using that information for their own benefit. For instance, a malicious node may send a request for energy right before another ER runs out of power in an effort to interrupt that node's operation and prevent ETs from delivering energy. Even worse, a rogue node may capture a charging request beacon from a specific ER, record it, and then imitate it by rebroadcasting to another ET in order to expose itself to more RF energy, cause interference, or degrade system performance. Digital signatures that provide both data integrity and authorization to detect impersonator nodes can be used as a traditional protection against spoofing attacks. However, developing and implementing such strategies for resource-constrained devices are difficult.

## **5 Work Methodology**

The load power and axial power transmission distance must be increased for resonant circuit WPT systems [22]. While strong resonance coupling can supply high power over a greater distance in kilowatts, microwave transmission cannot due to stability

and safety concerns. The active power, load, and coupling coefficient between the resonator and the quality factor of the drive circuit all depend on the electrical quantity parameter if it is fixed. Maximums for each can be determined as a result. The three characteristics mentioned above become important as load power increases. We can calculate the quality factor (QF) of the resonator using the equation ( $Q = \omega L/R$ ). We can improve the QF in two ways: first, by increasing the resistance-to-inductance ratio; and second, by elevating its natural resonant frequency. In this study, we saw an increase in the quality factor by employing smooth-surfaced, oxygen-free copper wire tubes of high quality because they have good conductivity and reduce skin effect. It just slightly improves the inductance to resistance ratio. The most effective method of raising the resonance frequency is to raise the greater quality factor. High power will be transferred directly by the resonator in our project.

**A. Design of the System**

The WiTricity system is composed of a driving loop, an output loop, and source and device resonators. The oscillator that provides energy to the system is linked to the generating loop, which then connects to the source resonator. The device’s resonator coil is attached to the output loop in order to power an external load. As shown in Fig. 1, here’s the block diagram of the system.

For wireless energy transfer, the planned WiTricity system uses a couple of identical rectangular spiral copper windings. An amplifier’s output with a 25 V amplitude at frequencies between 0.01 MHz and 10 MHz will produce an electric field in the load due to changes in the magnetic flux from the transmitter coil (which is also the receiver). We place emphasis on studying the voltage received by the receiver at numerous frequencies and distances to assess how energy is transmitted (Fig. 2).

**(A) Circuit Diagram**

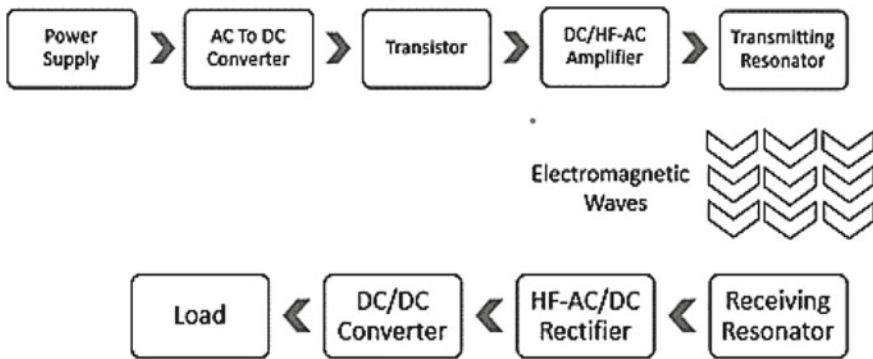


**Fig. 1** Wireless power transmission block diagram

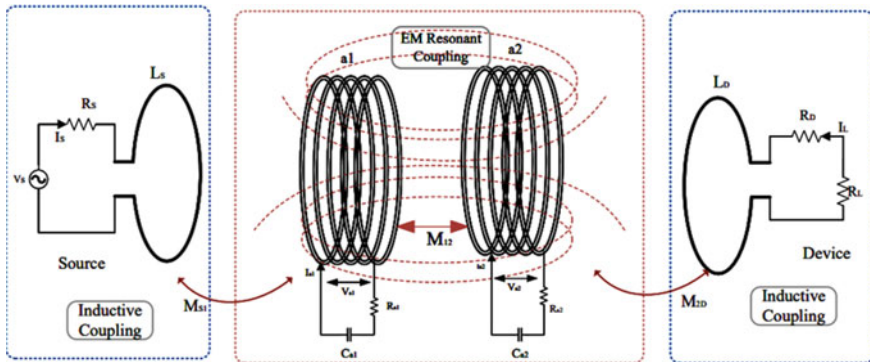


Fig. 2 Basic structure of WiTricity system

In this project, the transmitting resonator receives high-frequency power directly. According to Fig. 3 DDS generates the high-frequency signal, which MOS transistors M1 and M2 then amplify, C1 and C2 control dead time, D1 and D2 control freewheeling, while C3-C5 and L1 control impedance matching.

**(B) Parameters for Designing**

Resonance relates to phenomena; the LC circuit does not resonate on its own. Small driving perturbations have a big effect on the system in these phenomena. Resonance needs to be driven through the LC circuit, such as by an AC power source. The resonant frequency for a specific circuit is the frequency at which this equality holds true.

For the oscillator circuit to achieve a resonance frequency, the inductive and capacitive reactances of the resonant coil must be equal.

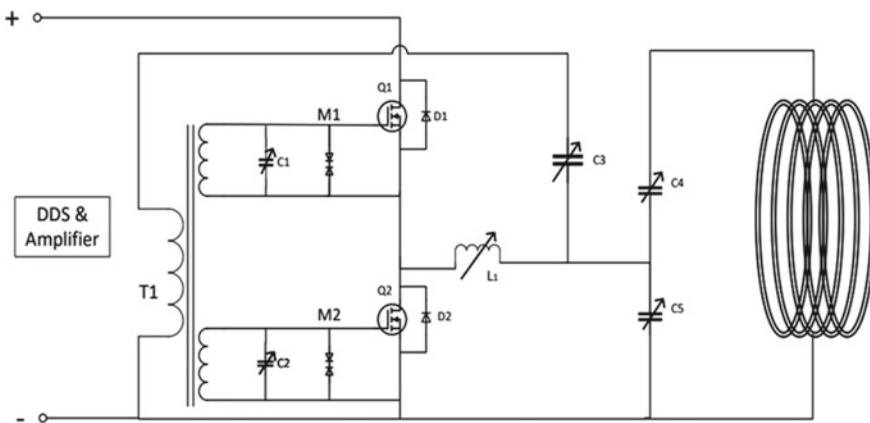


Fig. 3 Circuit diagram of three-coil power link

$$X_L = X_C \quad (1)$$

$$X_L = \frac{1}{\omega C} \quad (2)$$

$$\omega = 2\pi f \quad (3)$$

Capacitive resistance:

$$X_C = \frac{1}{2\pi f C} \quad (4)$$

Inductive coupling:

$$X_L = 2\pi f L \quad (5)$$

Resonant circuit formula:

$$4^2 f^2 LC = 1 \quad (6)$$

where,

$$f = \frac{1}{2\pi\sqrt{LC}} \quad (7)$$

$X_C$  = Capacitive reactance in ohms.

$X_L$  = Ohms of inductive reaction.

$f$  = Hertz-based frequency.

$L$  = Inductance in Henry.

$C$  = Farads of capacitance.

## 6 MRC-WPT Characteristics Based on Coupled Mode Theory

Figure 3 depicts the MRC-WPT system in a typical configuration. Power coupling, transformation, and transmission tasks are finished in three sections. By converting low voltage or high current to high voltage or low current between the resonators and the source or device coil, inductive coupling generates power for the resonators  $a_1$ ,  $a_2$ . A second time, when the system is configured in resonant states, power transfer between resonators couples via electromagnetic resonance, producing high



impedance performance and a relatively low transmission loss. The transmission and receiving coils' respective currents, resistances, and inductions are denoted as  $I_{1,2}$ ,  $RS$ , and  $L_{SD}$ .  $VS$  is the driving voltage; the mutual inductions between the coils are  $M_{S1}$ ,  $M_{1,2}$ , and  $M_{2D}$ , while  $RL$  is the load resistance. The coils have resonant inductances to one another. The connection between the device coil and the non-resonant source is disregarded. The general principles governing interactions between waves, including such sound and light waves are frequently described using coupled mode theory. It is ideal for modeling resonance energy transfer. For MRC-WPT lossless resonators systems, two equations in the form of various differential equations can be used to describe the flow of energy between the resonators.

$$\frac{da_1}{dt} = j_1 a_1 + k_{12} a_2 \quad (8)$$

$$\frac{da_2}{dt} = k_{21} a_1 + j \omega_2 a_2 \quad (9)$$

where  $k_{12}$  and  $k_{21}$  are mode coupling factors, 1, 2 is the native resonating angular frequency, and  $a_1$  and  $a_2$  stand for the resonator's front rotational mode, whose second parameter is the energy dimensions. Additionally, there is a connection between and the coefficient of coupling  $k$ , that is  $= k/2$ . Energy exchange between modes for a passively flawless system takes place and satisfies the energy's overall conserving requirement. Under weak coupling, any modification of the oscillation mode will resonate. Thus,  $a_1(t) = A(t) * \exp.[0.5j(1 - 2)t]$  is obtained, at which  $A(t)$  is a time domain function that progressively changes. Assuming the initial condition to be  $s t = 0, a_1(t) = 0$  leads to the solution (8) and (9), where  $\omega_1$  and  $\omega_2$  are estimated values,

$$a_1(t) = A(0) \left[ \frac{\cos(\Omega t) + j(\omega_1 - \omega_2)}{2\Omega \sin(\Omega t) e^{j\omega t}} \right] \quad (10)$$

$$a_2(t) = A(0) k_{21} \sin(\Omega t) / \Omega . e^{j\omega t} \quad (11)$$

The greatest energy exchange exists as long as  $\omega_1 = \omega_2$  according to the first requirement. This clarifies why the two circuits must tune in to resonance in a straightforward and counterintuitive way. Natural resonance will be offset and adjusted in angular frequency for lossy coupling systems. The formula for the resonating angular frequency  $\omega_1, \omega_2$  is  $\omega'_{1,2} = \omega_{1,2}(1 + j/2Q_{1,2})$ . When the quality factor is high enough, the Taylor expansion can be used to express eigenvalues as (3). Resonators are typically made to be similar in size, resonant frequency, and quality factors for more convenient impedance matching, resulting in  $Q_1 = Q_2 = Q$  and  $\omega_1 = \omega_2 = \omega$ .

$$\lambda_{1,2} = -\left(\frac{\omega}{Q}\right) \pm \sqrt{k_{12}k_{21}} \quad (12)$$

The parameters of the resonators are intended to be the same, thus  $Q_1 = Q_2 = Q$ ,  $\omega_1 = \omega_2 = \omega$ , and another satisfies the conditions that there is a positive root and the item inside the original sign is generally a real integer. After simplification, the preconditions are displayed as (4).

$$|k_{12}k_{21}| \gg \omega^2 / 4Q^2 \quad (13)$$

Two quality factors represent shortcomings, whereas two mode coupling variables represent the pace of energy coupling. In this regard, high-quality resonators must be used to build a low loss energy bridge between the supply and the receiver. The generalization of the connection between the energy transfer between both resonator, where  $|a_1|^2$ ,  $|a_2|^2$ , and  $|a_1 + a_2|^2$  signifies the energies of the individual resonators 1, 2, and the system overall. The cue's appearance is made up of the quality element. The entire energy rapidly degrades. Among the causes of attenuation is the linear system.

## 7 Result and Discussions

IWPT, a prospective near-field technology, is simple to use and has a small transmission range of only a few centimeters. The charging path between the transmitter and receiver still needs to be properly aligned even though power transfer efficiency is better. It operates at frequencies ranging from a few kHz to a few MHz. Applications that use RWPT, a near-field technology, can cover areas as small as a few millimeters up to as large as a few meters. Leakage inductance is adjusted in the RWPT method to boost power transfer efficiency by combining the magnetic coupling and resonance approaches.

While RWPT Fig. 4b normally has a switching frequency that is significantly greater than IWPT Fig. 4a, the effective power transfer efficiency (PTE) of RWPT technology can be attained over a few meters of distance (between a few MHz and several MHz). Because RWPT technology outperforms IWPT at mid-range distances, it is the subject of this study.

We created a testing environment for our wireless energy transfer system in order to do various measurements. The receiving coil, parted 1 m from the source coil connecting with 220 V power supply, induces with 220 V to transfer the 60W power wireless.

The output voltage, output current, and output power for both open circuit and closed circuit of the wireless energy transfer system were measured by varying the separation between the transmitter and receiver.

Experimental findings support the wireless energy transfer system and we developed proper functionality. More analysis shows that the wireless energy transfer system's effectiveness substantially declines as the transmitter and receiver's separation grows.

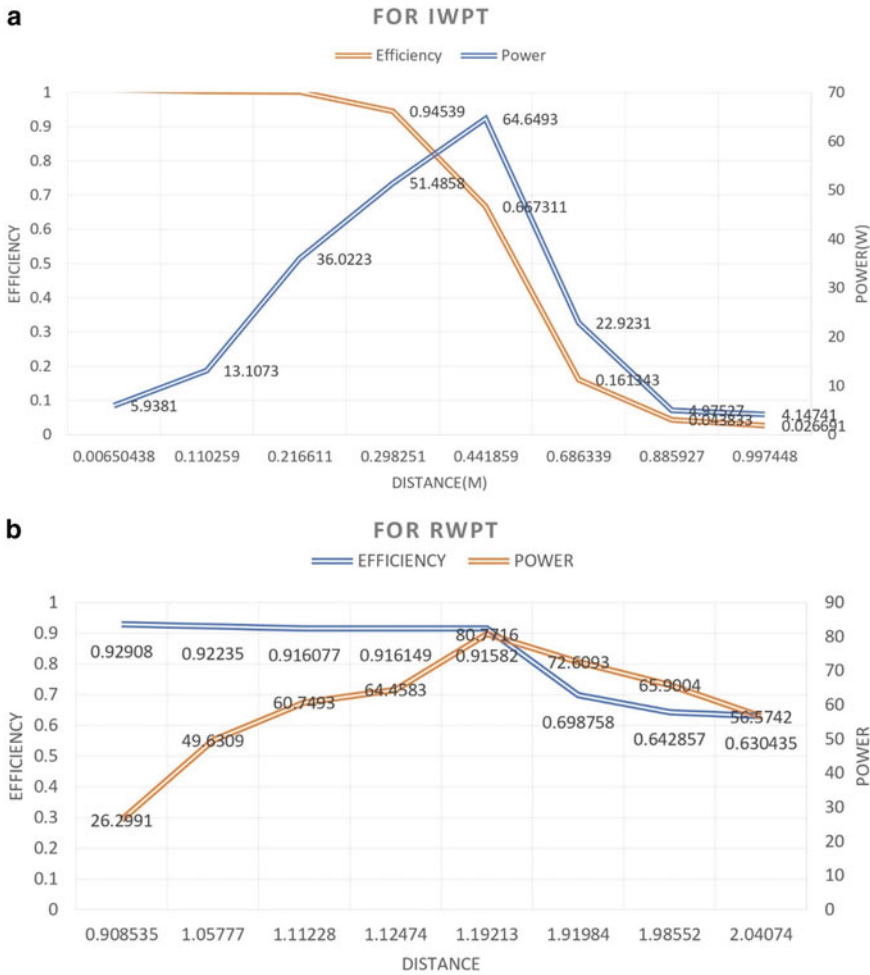


**Fig. 4** **a** Graph between power and distance in IWPT, **b** Graph between power and distance in RWPT

## 8 Future Scope

- (a) Many industries and application fields are interested in highly resonant wireless power transfer. Utilizing such technology has a variety of purposes, and these purposes frequently fall into one or more of the following categories.
- (b) By doing away with disposable batteries, electronics can be made more ecologically friendly. Compared with producing, shipping, and utilizing batteries based on conventional electro chemistries, employing grid electricity is far less expensive and environmentally harmful.

- (c) By removing connector circuit headers and wires that pass through roofs, wall, or other impediments (even skin tissue), you can make equipment water-proof and explosion-proof and reduce the risk of sparking at conductive interconnections.
- (d) It is the largest usage of WPT due to the utilization of satellites outfitted with enormous solar arrays and their placement in geosynchronous earth orbit. For the purpose of creating and transmitting microwave radiation to the ground, these satellites are necessary. Additional uses for WPT include wireless sensors, RF power adaptive rectifying circuits, and ubiquitous power sources.

## 9 Conclusion

The need for transferring energy through highly resonant coupling is demonstrated by the fact that at resonance, the resonator's angular frequency is equivalent, and coupling coefficients and quality factors are both much above 1. Greater efficiency was then identified with the help of  $Q/Q_L$  and  $K_{12}Q$ , which considered improvement by electric architecture and their spacing distances. The maximal active power of the loads is determined by the quality factor of a resonator with driving power and the coefficient of magnetic coupling between the resonator and the load. A recent device promises to boost transmission range and power while preserving a steady level of efficiency. It uses three-coil wireless energy transfer links. That explains a method for using a center feed technique to match the resonator's impedance appropriately. To test this theory, a 220v/60W light bulb can be used as the load. Wireless power transfer can be accomplished using a helical center feed coil and resonance coupling. A 60 w may be transferred without wire over a distance of 1 m with a 50–60% efficiency, as shown by an experiment. This method can be applied in the future to wirelessly power sensor networks.

## References

1. Beh T, Kato M, Imura T, Hori Y (2010) Wireless power transfer system via magnetic resonant coupling at fixed resonance frequency—power transfer system based on impedance matching EVS25 Shenzhen, China. *World Electr Veh J* 4. ISSN 2032-6653.
2. Kurs A, Karalis A, Moffatt R et al (2007) Wireless power transfer via strongly coupled magnetic resonances. *Science* 317(5834):83–86
3. Nguyen VT, Kang SH, Choi JH et al (2015) Magnetic resonance wireless power transfer using three-coil system with single planar receiver for laptop applications. *IEEE Trans Consum Electron* 61(2):160–166
4. Covic GA, Boys JT, Kissin M et al (2007) A three-phase inductive power transfer system for roadway-powered vehicles. *IEEE Trans Ind Electron* 54(6):3370–3378
5. Beh T, Kato M, Imura T, Hori Y (2010) Wireless power transfer system via magnetic resonant coupling at fixed resonance frequency—power transfer system based on impedance matching—EVS25. Shenzhen, China

6. Eekshita P, Sangeeth N, Narayana V, Jayaraman R (2021) Wireless power transmission system. In: International conference on computer communication and informatics (ICCCI—2021), Coimbatore, India, 27–29 Jan 2021
7. Beh T, Kato M, Imura T, Hori Y (2010) Basic study on improving efficiency of wireless power transfer via magnetic resonance coupling based on impedance matching. In: IEEE international symposium on industrial electronics, ISIE, IEEE, pp 2011–2016
8. Wang C, Xu W, Zhang C, Wang M, Wang X (2022) EURASIP. J Adv Signal Process 16. <https://doi.org/10.1186/s13634-022-00846-7>
9. Stephy VPT, Anbarasan A (2014) PV system with neutral point clamped inverter for suppression of leakage current and harmonics based fuzzy controller. Int J Adv Eng Res Sci 1(6):36–41
10. Zhang X et al. (2018) EURASIP. J Wirel Commun Netw. <https://doi.org/10.1186/s13638018-1148>
11. Imura A, Uchida T, Hori Y (2008) Experimental analysis of high efficiency power transfer using resonance of magnetic antennas for the near field—geometry and fundamental characteristics. In: IEEE Japan industry applications society conference, Kochi, Japan, No. 2–62, pp 539–542
12. Lee W, Yoon Y-K (Member, IEEE) Department of Electrical and Computer Engineering, University of Florida, Gainesville, FL 32611, USA Corresponding authors: Woosol Lee ([leewoosol@ufl.edu](mailto:leewoosol@ufl.edu)) and Yong-Kyu Yoon ([ykyoon@ece.ufl.edu](mailto:ykyoon@ece.ufl.edu)) 2020
13. Matias R, Cunha B, Martins R (2013) Modelling of inductive coupling for wireless power transfer to integrated circuits. IEEE, 198–201
14. Mokalkar BD, Tale CB, Idle CB (2012) Witricity: a novel concept of power transfer. Int J Eng Inven 1(1):51–59. ISSN: 2278-7461. [www.ijejournal.com](http://www.ijejournal.com)
15. Kumar A, Luthra SK, Ratan R (2015). Witricity: designed to change the world. Int J Innov Res Electron Commun 2(3):1–8. ISSN 2349-4042 (Print) and ISSN 2349-4050 (Online)
16. Shidujaman M, Samani H, Arif M (2014) Wireless power transmission trends. In: 3rd international conference on informatics, electronics & vision
17. Waffenschmidt E, Staring T (2009) Limitation of inductive power transfer for consumer applications. In Proceedings 13th Europe conference power electron application, pp 1–10
18. Tomar A et al (eds) (2022) In: Proceedings of 3rd international conference on machine learning, advances in computing, renewable energy and communication: MARC 2021, vol 915, pp XV, 781. ISBN: 978-981-19-2830-7. <https://doi.org/10.1007/978-981-19-2828-4>
19. Ahmad MW et al (eds) (2022) Intelligent data analytics for power and energy systems. Springer Singapore, pp XXII, 641. ISBN: 978-981-16-6081-8. <https://doi.org/10.1007/978-981-16-6081-8>
20. Kong S, Kim M, Koo K, Ahn S, Bae B, Kim J (2011) Analytical expressions for maximum transferred power in wireless power transfer systems. Electromagn Compat, 379–383
21. Salman A, Abbas A, Maqboo J, Liaqat Bhatti KM (2014) Efficient wireless electric power transmission using magnetic resonance coupling. Int J Sci Eng Res 5(1):2235. ISSN 2229-55
22. Xu W, Wang X, Li S, Lu S, Li W (2022) EURASIP. J Adv Signal Process, 20. <https://doi.org/10.1186/s13634-022-00852-9>

# Analysis of Three-Winding Transformer Configurations for Energy Storageless Dynamic Voltage Restorer



Muhammad M. Roomi, S. M. Suhail Hussain, Mohd Tariq,  
and Taha Selim Ustun

**Abstract** Dynamic voltage restorer (DVR) is considered as one of the best and cost-effective solution in addressing the power quality concerns in distribution systems. The integration of DVR with the reliable grid eliminates the need for external energy storage unit and can address the issue of compensating long/deep voltage sags. In this paper, a new topology, wherein the DVR taps in energy through a three-winding transformer connected to the grid is proposed. As different configurations are available for three-winding transformer, detailed analysis is conducted to find the best possible configuration of the three-winding transformer for a DVR integrated system. The studies are carried out in MATLAB/Simulink platform and the results are presented.

**Keywords** Power quality · Dynamic voltage restorer · Three-winding transformer · Current harmonics

---

M. M. Roomi  
Illinois at Singapore Pte Ltd, Singapore, Singapore  
e-mail: [roomi.S@adsc-create.edu.sg](mailto:roomi.S@adsc-create.edu.sg)

S. M. Suhail Hussain (✉)  
Electrical Engineering Department, King Fahd University of Petroleum and Minerals (KFUPM),  
Dhahran, Saudi Arabia  
e-mail: [suhail@ieee.org](mailto:suhail@ieee.org)

Interdisciplinary Research Center for Renewable Energy and Power Systems (IRC-REPS), King  
Fahd University of Petroleum and Minerals (KFUPM), Dhahran, Saudi Arabia

M. Tariq  
Department of Electrical Engineering, ZHCET, Aligarh Muslim University, Aligarh, India  
e-mail: [tariq.ee@zhcet.ac.in](mailto:tariq.ee@zhcet.ac.in)

T. S. Ustun  
Fukushima Renewable Energy Institute, AIST (FREA), Koriyama, Japan  
e-mail: [selim.ustun@aist.go.jp](mailto:selim.ustun@aist.go.jp)

# 1 Introduction

Due to the growing concerns on climate change the power generation systems are transitioning to renewable energy resources. Among the different renewable energy sources for power generation, solar-PV (photovoltaic) and wind constitutes predominantly towards renewable energy generation. Despite several advantages, renewable energy generation has certain challenges such as intermittent generation and unpredictable in nature. The variable power generation from renewable energy sources causes serious problems of voltage and frequency fluctuations that leads to power quality issues [1]. Furthermore, due to the incorporation of power electric converters with renewable generation systems, the issue of power quality becomes even more cumbersome [2]. The design and nature of power electronic devices introduce harmonics in the grid. Additionally, due to inherent load variation resulting in imbalance between reactive power generation and consumption causes voltage deviations, which can be impulses, transients, swells/sags, etc. These type of voltage deviations, if persisted may even lead to total voltage collapse [3]. Hence, power quality issues have a direct impact on the physical equipment in any electrical system [4].

By controlling the real and reactive power flows, the voltage and frequency fluctuations can be mitigated. Since voltage fluctuations can be controlled by reactive power compensation, numerous solutions have been proposed [5]. Among the solutions, custom power devices (CPDs) are considered as the cost-effective solutions for mitigating fluctuations [6]. These devices can be connected in series or in parallel or in series-parallel to compensate for the energy loss due to faults or voltage sags. Some of the common CPDs include battery energy storage system (BESS) [7], uninterruptible power supply (UPS) [8], dynamic voltage restorer (DVR) [9] or distribution static compensator (DSTATCOM) [10] or unified power quality conditioner (UPQC) [11]. Due to the size and cost, DVR emerges as the cost-effective choice to mitigate sag conditions [12].

DVR attenuates the deviation in the voltage significantly and has the ability to keep the voltage at the acceptable range. DVR consists of voltage source inverter (VSI) that adjusts the voltage, either through a transformer or without a transformer in series and injects the compensating voltage in synchronisation with the grid. Further, energy storageless DVR is considered as an economically viable solution. Therefore, a new topology is proposed in this paper, wherein the DVR is connected to a three-winding transformer and further, the ideal configuration to be employed in the three-winding transformer for a DVR integrated system is analysed.

The rest of the paper is organised as follows. Section 2 explains the overview of DVR, which includes power circuits and the compensation techniques employed in DVR. Section 3 presents the topology of DVR with three-winding transformer proposed in this paper. The simulation analysis and findings of different winding configurations for a DVR system is demonstrated in Sect. 4, followed by the conclusions in Sect. 5.

## 2 Dynamic Voltage Restorer

The main components of the DVR, as depicted in Fig. 1, comprise a source (DC source or an AC source with rectifier) providing DC voltage for a voltage source inverter (VSI), followed by a filter circuit, bypass switches and injection transformer. The required energy for the DVR can be fed through either an energy storage [13] or without energy storage [14]. The former energy delivery method is employed in cases of weak grids and latter is introduced only when the grid is reliable. An inverter is used irrespective of the energy source to convert the DC voltage, either from energy storage or a DC link, to three-phase voltage of desired magnitude, frequency and phase angle. The output of the inverter is fed into the grid through high voltage windings of the injection transformer. However, as the inverter is switched at high frequencies, the output of the inverter embodies high-frequency switching harmonics [15]. In order to eliminate these harmonics or to contain these harmonics within an acceptable range, low pass filters are connected at the output of the inverter [16]. These filters can be connected between the inverter and injection transformer (this avoids the transmission of harmonics into the injection transformer and thereby, no increase in the transformer rating is required) or between the injection transformer and the load (this leads to the injection of high-order harmonics into the injection transformer and thereby, increasing the transformer ratings). Finally, the bypass switches are incorporated in the DVR system as a protection measure. This set-up provides an alternative path for the current during faults, overloads or maintenance [17].

There are three modes of operation for a DVR. (i) Dormant/Standby mode—During this mode there are no voltage fluctuations detected and the output of the DVR remains zero. (ii) Active/Injection mode—DVR detects a voltage deviation during this mode and injects the desired voltage to mitigate the deviation. (iii) Protection/Isolation mode—During this mode, the DVR is protected from any over the limit fault currents through an alternative path [18, 19].

Similar to the modes of operation, there are three predominantly used voltage compensation methods for DVR. In the first pre-sag compensation method, the source voltage is constantly tracked for any voltage deviations. In cases of any detection, the difference in the voltage will be injected, thereby, adjusting the phase angle and magnitude and restoring the load voltage to pre-sag nominal voltage. In the second in-phase compensation method, the injected voltage should be in phase with the source voltage. This method mainly incorporated active power compensation. As this method does not address the phase jump, using it for sensitive loads is not advisable. The third method is the energy-minimised compensation method, wherein the injection or absorption is done from the power source to address the sag mitigation. In comparison with the first two compensation methods, this method does not involve active power exchange during the DVR active/injection mode [20, 21].

Fig. 1 Components of DVR





### 3 Proposed Energy Storageless Dynamic Voltage Restorer Configuration

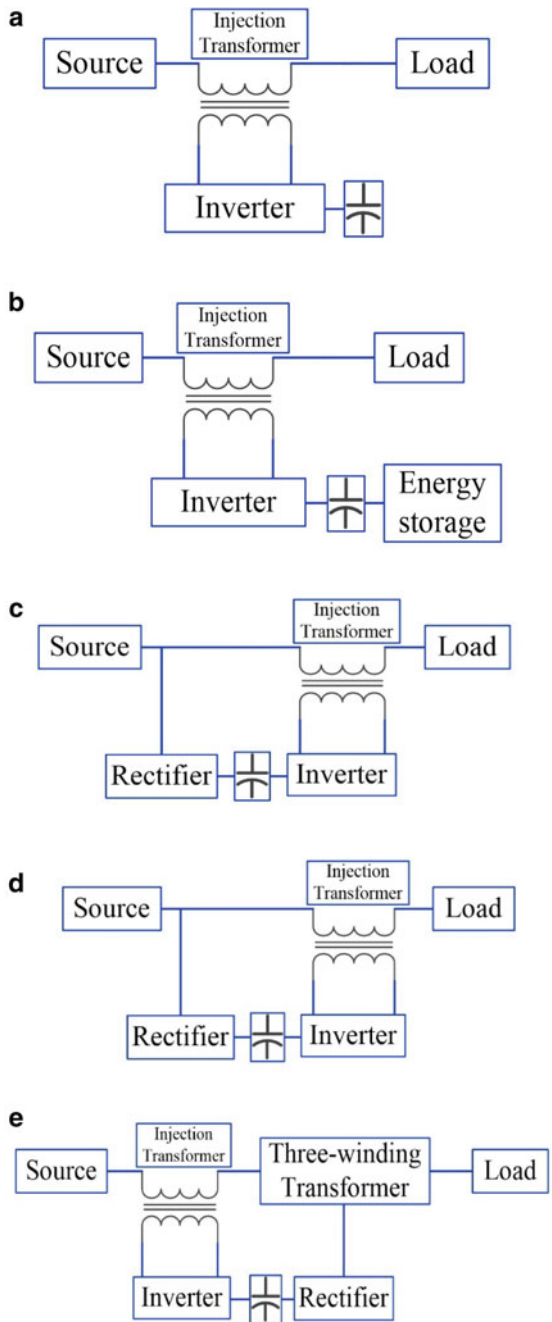
As aforementioned about the energy delivery for the DVR, the source can be categorised into two topologies. Firstly, for the DVR topology that consists of energy storage. In this type, the required energy is delivered through one of the two methods depicted in Fig. 2a, b. Figure 2a illustrates a direct DC link acting as a source to the DVR inverter [5] and in the second method in Fig. 2b, the energy is delivered through an external energy storage unit connected to the DC link [22]. In these cases, DC link voltage can be controlled to provide required energy to the DVR. Generally, these topologies involve storing of energy to storage unit when there is no disturbance in the supply. The second DVR topology constitutes no energy storage system. Therefore, the energy demand for the DVR is addressed through tapping in energy from the incoming energy source [23, 24]. The tapped in energy is fed to the DVR through either an AC/AC power converter or a combination of series and shunt converter. This converter topology can be connected in parallel to either the source side or the load side, as depicted in Fig. 2c, d, respectively.

Though DVR topologies with and without energy storage can be employed, there are advantages and drawbacks associated with these topologies. For instance, due to energy storage restriction with the capacitors, long duration voltage sags cannot be mitigated. This can be easily addressed with the energy storageless topology and this topology requires reliable grid. Further, this topology proves to be efficient with load side shunt-connected converter. Therefore, in this paper, as a modified strategy for tapping in energy from an incoming energy source, a three-winding transformer is connected to the load side. The primary winding is connected to the incoming source, the secondary winding is connected to the load and the tertiary winding is connected to the injection transformer of the DVR. The proposed system topology is illustrated in Fig. 2e. Prior to analysing the operation of the DVR with three-winding transformer, the study on the different configurations of the windings in order to find the suitable configuration for a DVR system is essential. Therefore, in this paper, the primary focus is to analyse the performance of different winding configurations of the three-winding transformer for integration with DVR.

### 4 Simulation Analysis

In order to analyse the performance of the three-winding transformer when integrated with the DVR, the system is built using MATLAB/Simulink. The model consists of a three-phase AC source that represents a grid feeding a three-phase load through DVR and three-winding transformer. The configurations of the three windings are depicted in Fig. 3. The analysis is carried out by introducing a sag in the source voltage. However, as the initial focus of the study is to find the best configuration for the DVR integrated system, the DVR is set to be in dormant mode in this paper

**Fig. 2** **a** Topology of DVR with DC link (capacitor). **b** Topology of DVR with external energy storage system. **c** Topology of energy storageless DVR (supply side). **d** Topology of energy storageless DVR (supply side). **e** Proposed energy storageless topology with three-winding transformer



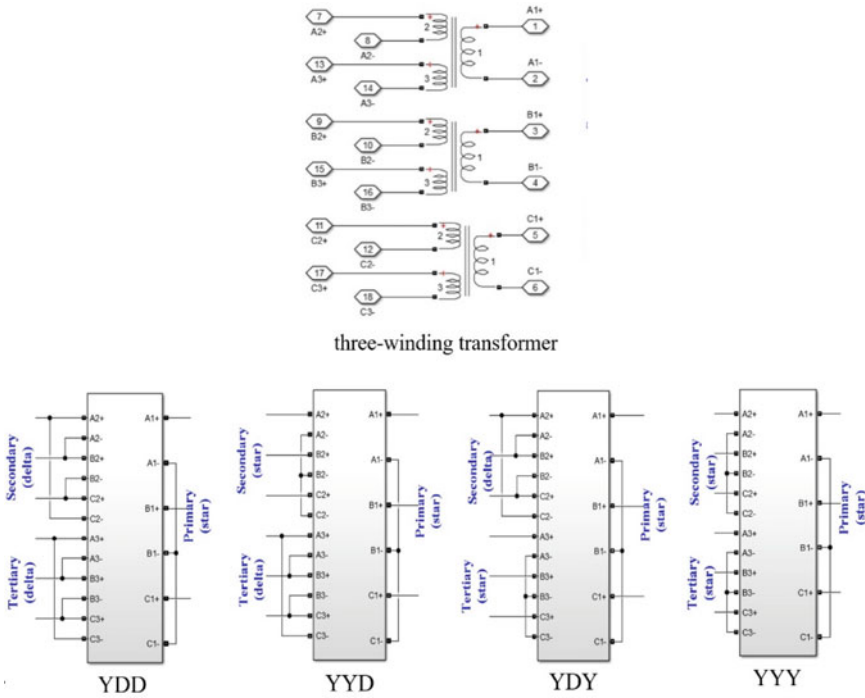


Fig. 3 Three-winding transformer configurations from Simulink

even during the sag condition. The primary side of the transformer is fixed to be a star configuration as it requires less number of turns and therefore, making the configuration economical for high-voltage transformers. Additionally, with the star connected the neutral can be grounded on the primary side of the transformer to avoid distortion.

Considering the primary side of the transformer to be star, the secondary and tertiary can be designed with both star and delta combinations. As such four combinations (star-delta-delta (YΔΔ), star-delta-star (YΔY), star-star-delta (YYΔ) and star-star-star (YYY)) of the primary, secondary and tertiary windings of the transformer are designed for the analysis. As aforementioned, DVR is fed through a DC source and a rectifier is necessary between this transformer and the DVR. This connection of rectifier to the tertiary side of the transformer will induce harmonics to the primary side. As such, the different configuration results are presented to identify suitable configuration for the integration of DVR with the grid.

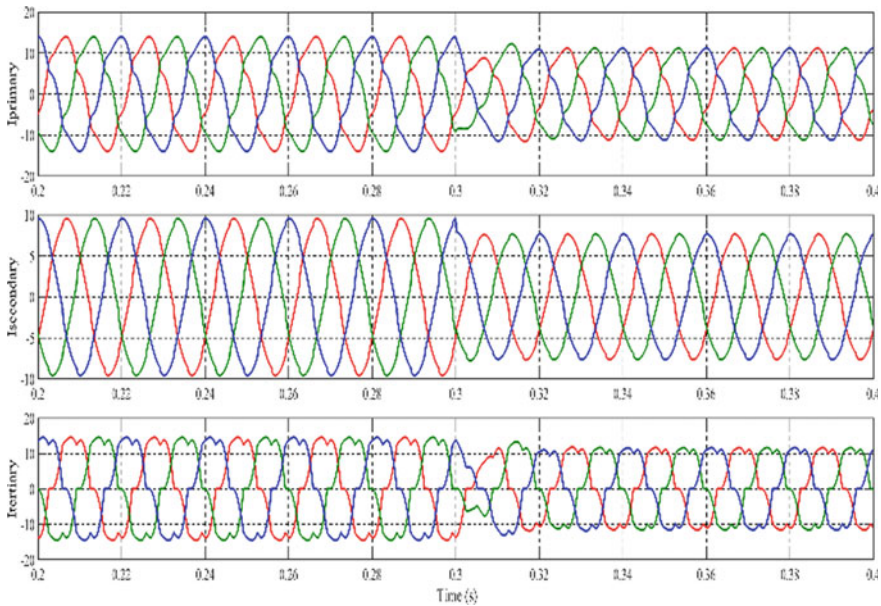
The parameters for the modelling of the system are tabulated in Table 1. The parameters that are the primary focus of this study are the primary, secondary and tertiary currents of the three-winding transformer, the tertiary voltage and the output DC voltage of the rectifier.

**Table 1** Specifications for the simulation

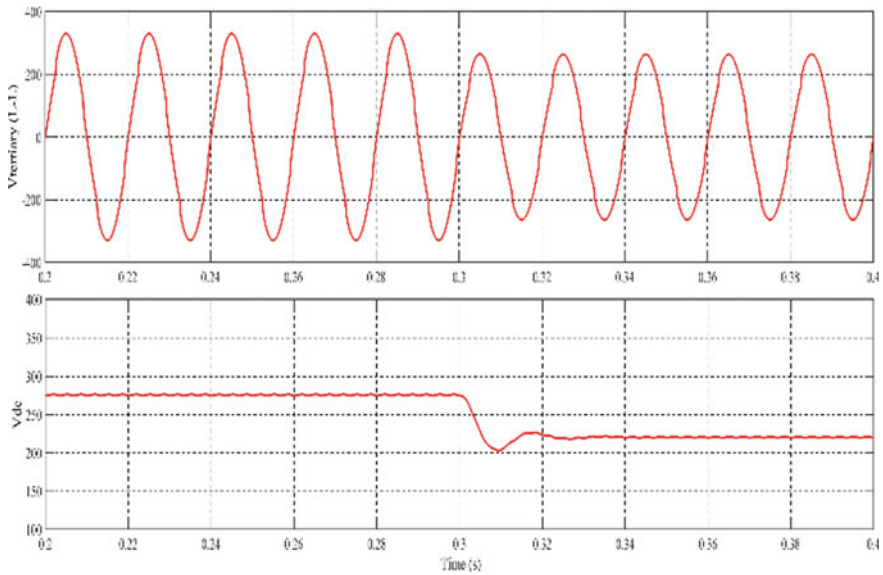
Parameter	Specification
AC line voltage	415 V
Nominal frequency	50 Hz
Injection transformer turns	1:1
Filter inductance	1 mH
Filter capacitance	2 $\mu$ F
Three-winding transformer turns	1:1:1
Switching frequency	10 kHz
Load active power	8 MW

Figure 4 depicts the current waveforms for the star-delta-delta configuration. As can be seen, the tertiary current has higher order harmonics and the same is reflected in the primary and secondary side of the transformer. The total harmonic distortion (THD) in the primary and secondary winding due to the distortion in the current waveforms of the third winding is found to be 8.64% and 3.39%, respectively. The tertiary voltage (phase-phase  $V_{ab}$ ) of the transformer and the corresponding DC link voltage is demonstrated in Fig. 5.

Similarly, in Fig. 6 the current of the transformer windings when connected in star-delta-star configuration is illustrated. When compared with star-delta-delta configuration, the primary current waveform is more distorted, signifying the impact of



**Fig. 4** Currents in star-delta-delta configuration



**Fig. 5** Line-to-line voltage in the tertiary windings and the rectified DC voltage to the DVR

the higher order harmonics from tertiary winding. Further, the primary current is higher (30 A peak) due to the star configuration of the tertiary winding. The THD of the primary and secondary winding for this configuration is calculated to be 9.47% and 8.59%, respectively. Though the primary side THD is relatively higher when compared with star-delta-delta configuration, the secondary side THD is much higher. The tertiary winding voltage and DC link voltage are plotted in Fig. 7.

The third configuration for this study is the star-star-delta configuration. The current waveforms of the windings is depicted in Fig. 8. As can be seen from the figure, the distortions in the primary and secondary side current waveforms are much lesser and the THD is calculated to be 8.64% and 3.39%, respectively, which is similar to star-delta-delta configuration. The voltage (phase voltage and DC link voltage) waveforms are exemplified in Fig. 9. The results of the final configuration, which is the star-star-star, is demonstrated in Fig. 10. From Fig. 11, though the primary winding of the transformer is not much distorted, the harmonics can be clearly seen in the secondary and tertiary side of the transformer. Further, due to the star configurations in the secondary and tertiary side of the transformer, the primary current is higher (40 A peak) compared with all other configurations. The THD for both the windings is found to be 9.47% and 8.59%, respectively. The voltage waveforms are presented in Fig. 11.

The fundamental frequency magnitude and the THDs for different configurations are tabulated in Table 2. Based on the analysis, the star configuration in the tertiary winding produces higher DC link voltage than the delta configuration. However, it induces more third-order harmonics than the delta-connected tertiary winding.

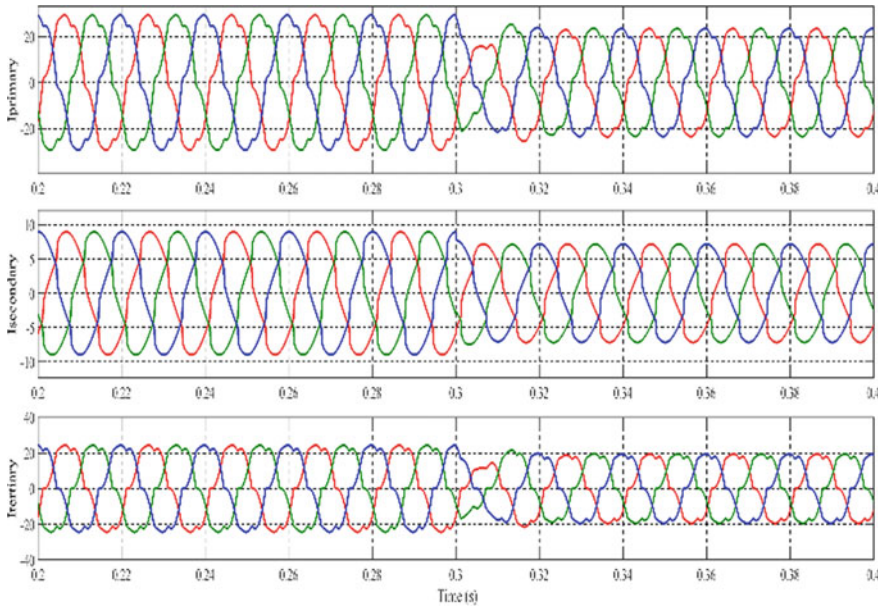


Fig. 6 Currents in star-delta-star configuration

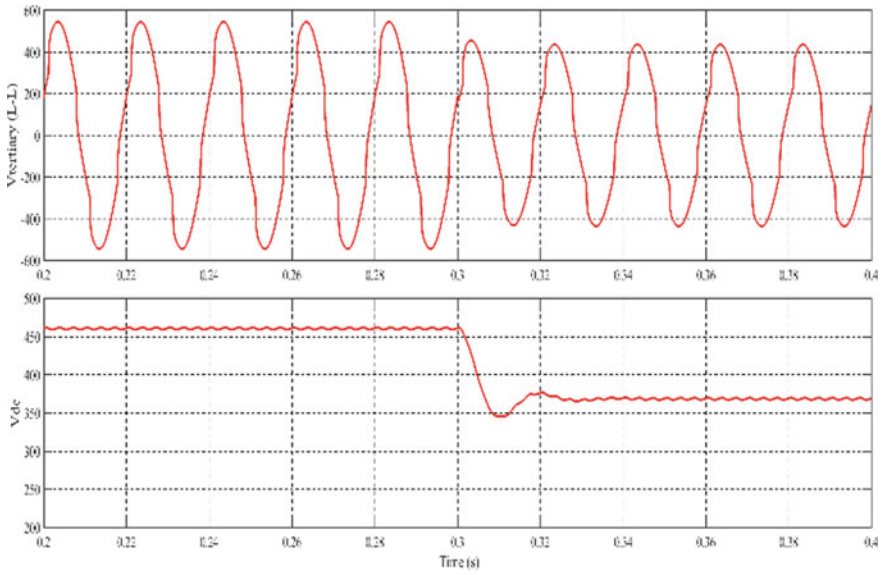
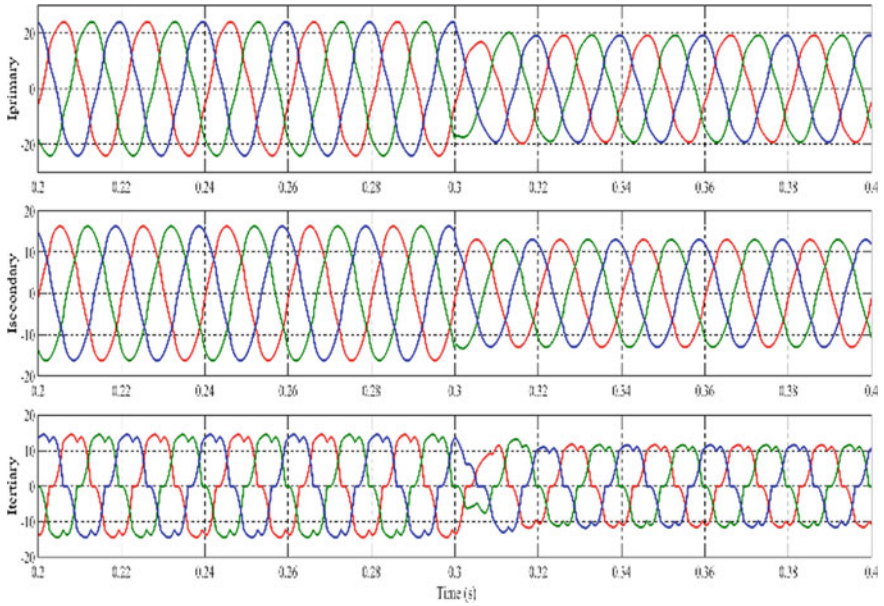
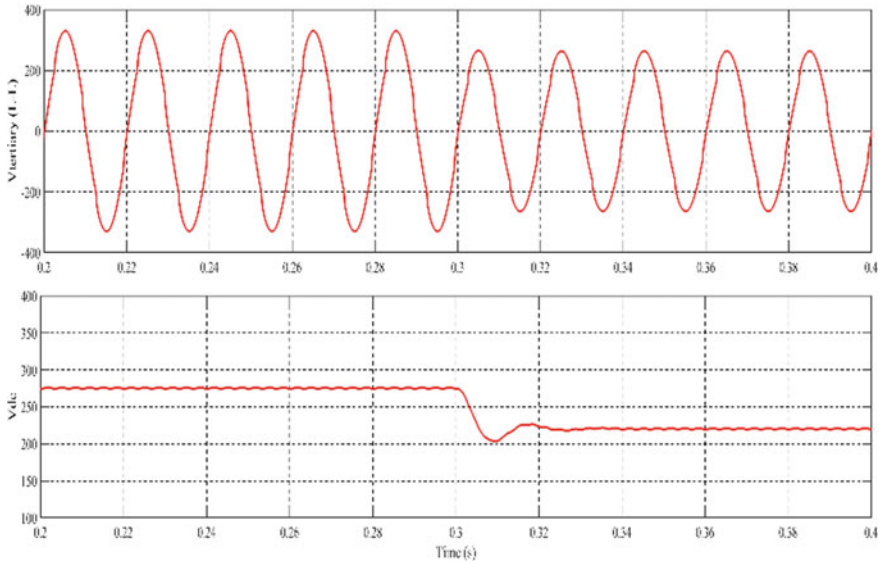


Fig. 7 Line-to-line voltage in the tertiary windings and the rectified DC voltage to the DVR





**Fig. 8** Currents in star-star-delta configuration



**Fig. 9** Line-to-line voltage in the tertiary windings and the rectified DC voltage to the DVR

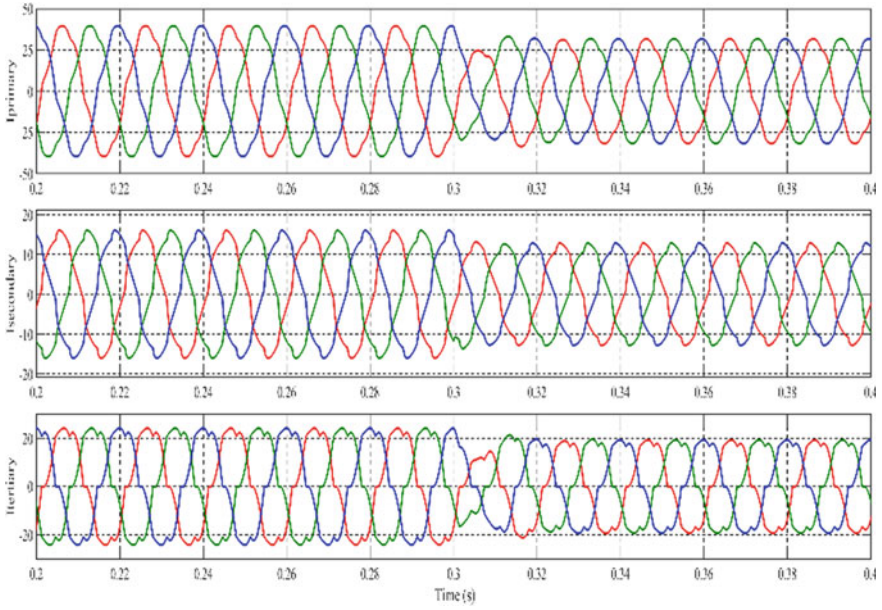


**Fig. 10** Currents in star-star-star configuration

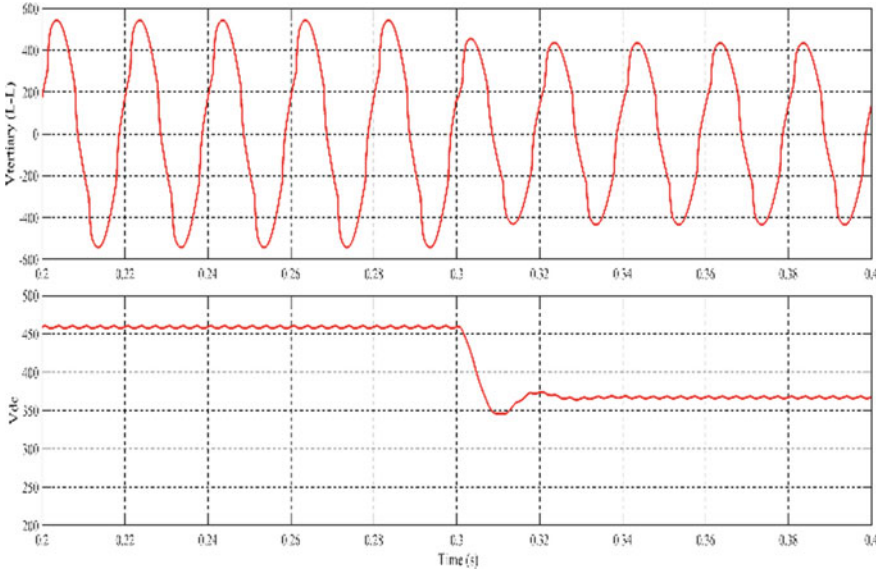


**Fig. 11** Line-to-line voltage in the tertiary windings and the rectified DC voltage to the DVR



**Table 2** Total harmonic distortions

Windings	Parameters	YDD	YDY	YYD	YYY
Primary	50Hz magnitude	13.71	29.6	13.71	29.6
	THD %	8.64	9.47	8.64	9.47
Secondary	50Hz magnitude	9.459	9.087	9.459	9.087
	THD %	3.39	8.59	3.39	8.59
Tertiary	50Hz magnitude	14.9	24.76	14.9	24.76
	THD %	13.97	11.49	13.97	11.49

Therefore, the possible considerations for the system are star-delta-delta and star-star-delta configurations. In addition, as the DVR is connected to protect the sensitive loads, it is necessary to consider the harmonics in the secondary winding. Therefore, with star-star-delta configuration these harmonics might be transferred to the sensitive loads. Based on the studies, star-delta-delta configuration will be most suited for DVR supported system.

## 5 Conclusion

In this paper, the primary focus is to analyse the performance of the three-winding transformer as a potential input source to DVR. As the model involves rectifier, introduction of harmonic components is unavoidable. Therefore, different configurations of the transformer are tested to determine a configuration that introduces lesser harmonics into the main grid. From the results, star-delta-delta configuration will be an ideal suggestion for the DVR integrated systems. Furthermore, as the end project taps in power from three-winding transformer, a sag in the source voltage may cause a sag in the DVR voltage. These scenarios can be used to find the rating of the DVR and hence helpful in designing the DVR. The output of the rectifier is fed to the DC link capacitors to provide a smooth input to the inverter. Any changes in the input voltage cause changes in the DC link voltage of the inverter. Therefore, these conditions can be used to analyse the behaviour of the capacitors in real-time scenarios.

## References

1. Masoud Farhoodnea AM, Shareef H, Zayandehroodi H (2013) Power quality impact of renewable energy based generators and electric vehicles on distribution systems. *Procedia Technol* 11(0173–2212):11–17
2. Aleem SA, Hussain S, Ustun TS (2020) A review of strategies to increase PV penetration level in smart grids. *Energies* 13(3):636

3. Church C, Morsi WG, El-Hawary M, Diduch C, Chang L (2011) Voltage collapse detection using ant colony optimization for smart grid applications. *Electr Power Syst Res* 81(8):1723–1730
4. Stump MD, Keane GJ, Leong FK (1998) The role of custom power products in enhancing power quality at industrial facilities. In: *Proceedings of EMPD'98, 1998 international conference on energy management and power delivery*, vol 2, pp 507–517
5. Moreno-Muñoz A (2007) *Power quality: mitigation technologies in a distributed environment*. Springer Science & Business Media
6. Ghosh A, Ledwich G (2012) *Power quality enhancement using custom power devices*. Springer Science & Business Media
7. Divya K, Østergaard J (2009) Battery energy storage technology for power systems—An overview. *Electr Power Syst Res* 79(4):511–520
8. Racine MS, Parham JD, Rashid M (2005) An overview of uninterruptible power supplies. In: *Proceedings of the 37th annual North American power symposium*, pp 159–164
9. Ranjan S, Das DC, Latif A, Sinha N, Hussain SS, Ustun TS (2021) Maiden voltage control analysis of hybrid power system with dynamic voltage restorer. *IEEE Access* 9:60531–60542
10. Latran MB, Teke A, Yoldaş Y (2015) Mitigation of power quality problems using distribution static synchronous compensator: a comprehensive review. *IET Power Electron* 8(7):1312–1328
11. Chen Y, Zha X, Wang J, Liu H, Sun J, Tang H (2000) Unified power quality conditioner (UPQC): the theory, modeling and application. In: *PowerCon 2000, 2000 international conference on power system technology*, proceedings (Cat. No. 00EX409), vol 3, pp 1329–1333
12. Brumsickle WE, Schneider RS, Luckjiff GA, Divan DM, McGranaghan MF (2001) Dynamic sag correctors: cost-effective industrial power line conditioning. *IEEE Trans Ind Appl* 37(1):212–217
13. Somayajula D, Crow ML (2014) An ultracapacitor integrated power conditioner for intermittency smoothing and improving power quality of distribution grid. *IEEE Trans Sustain Energy* 5(4):1145–1155
14. Jothibasu S, Mishra MK (2014) A control scheme for storageless DVR based on characterization of voltage sags. *IEEE Trans Power Deliv* 29(5):2261–2269
15. Kim H, Kim J-H, Sul S-K (2004) A design consideration of output filters for dynamic voltage restorers. In: *2004 IEEE 35th annual power electronics specialists conference (IEEE Cat. No. 04CH37551)*, vol 6, pp 4268–4272
16. Choi S, Li B, Vilathgamuwa D (2000) A comparative study of inverter-and line-side filtering schemes in the dynamic voltage restorer. In: *2000 IEEE power engineering society winter meeting. Conference proceedings (Cat. No. 00CH37077)*, vol 4, pp 2967–2972
17. Fitzer C, Arulampalam A, Barnes M, Zurowski R (2002) Mitigation of saturation in dynamic voltage restorer connection transformers. *IEEE Trans Power Electron* 17(6):1058–1066
18. Sadigh AK, Smedley K (2012) Review of voltage compensation methods in dynamic voltage restorer (DVR). *IEEE Power Energy Soc Gen Meet* 2012:1–8
19. Roomi MM, Raj PH, Zhao B (2020) Closed loop current control of dynamic voltage restorer for rectifier loads. In: *2020 IEEE international conference on power electronics, smart grid and renewable energy (PESGRE2020)*, pp 1–6
20. Moghassemi A, Padmanaban S (2020) Dynamic voltage restorer (DVR): a comprehensive review of topologies, power converters, control methods, and modified configurations. *Energies* 13(16):4152
21. Omar R, Rahim N, Sulaiman M (2011) Dynamic voltage restorer application for power quality improvement in electrical distribution system: an overview. *Aust J Basic Appl Sci* 5(12):379–396
22. Nielsen JG, Blaabjerg F (2005) A detailed comparison of system topologies for dynamic voltage restorers. *IEEE Trans Ind Appl* 41(5):1272–1280

23. Tomar A et al (eds) (2022) Proceedings of 3rd international conference on machine learning, advances in computing, renewable energy and communication: MARC 2021, vol 915, pp XV, 781. ISBN: 978-981-19-2830-7. <https://doi.org/10.1007/978-981-19-2828-4>
24. Ullah KMS, Roomi MM, Tariq M, Zhao B (2020) A unity power factor rectifier based dynamic voltage restorer for microgrid applications. In: 2020 IEEE 17th India council international conference (INDICON), pp 1–6

# Data Reliability Analysis for Early Fault Diagnosis of Air Handling Unit (AHU)



Hasmat Malik, Shahrin Md Ayob, Nik Rumzi Nik Idris, Awang Jusoh, Fausto Pedro García Márquez, and Abdulaziz Almutairi

**Abstract** The objective of this chapter is to analyze the reliability of the dataset for early fault diagnosis of air handling unit (AHU) of air conditioning and mechanical ventilation/heating, ventilation, and air conditioning (ACMV/HVAC) system. In this chapter, data reliability analysis for early fault diagnosis is performed for AHU only, which includes fan degradation and return air duct leakage fault conditions. Data of the said faults are generated through the use of an expert system platform, OpenStudio (OS) and sensitivity analysis is performed to identify the most sensitive parameters with respect to the fault severity level starting from zero to 30% of deviation from healthy condition. The most sensitive parameters are selected based on the rank of sensitivity analysis. A similar procedure was performed with real data obtained from measurement. The effect of parameters due to fault conditions in AHU is analyzed in terms of consistency of increasing, decreasing, both increasing and decreasing, and no correlation. The results of the analyzed data are documented and compared.

---

H. Malik (✉) · S. M. Ayob · N. R. N. Idris · A. Jusoh  
Department of Electrical Power Engineering, Universiti Teknologi Malaysia (UTM), Johor Bahru, Malaysia  
e-mail: [hasmat@utm.my](mailto:hasmat@utm.my)

S. M. Ayob  
e-mail: [e-shahrin@utm.my](mailto:e-shahrin@utm.my)

N. R. N. Idris  
e-mail: [e-nrumzi@utm.my](mailto:e-nrumzi@utm.my)

A. Jusoh  
e-mail: [awang@utm.my](mailto:awang@utm.my)

F. P. G. Márquez  
Ingenium Research Group, Universidad Castilla-La Mancha, 13071 Ciudad Real, Spain  
e-mail: [faustopedro.garcia@uclm.es](mailto:faustopedro.garcia@uclm.es)

A. Almutairi  
Department of Electrical Engineering, College of Engineering, Majmaah University, Al Majma'ah 11952, Saudi Arabia

**Keywords** Air handling unit (AHU) · Air conditioning and mechanical ventilation (ACMV) · Heating, ventilation and air conditioning (HVAC) · Data reliability · Early fault · Fault detection and diagnosis (FDD)

## 1 Introduction

The energy consumed for cooling contributes the most to a typical building energy consumption in tropical region like Malaysia. Faults and performance degradation in the air conditioning and mechanical ventilation/heating, ventilation, and air conditioning (ACMV/HVAC) system lead to energy wastage. As the cost of ACMV operation is already high, any efficiency losses would increase the cost further. In addition, electricity used to power the system is mainly generated from non-renewable sources in Malaysia and Singapore, which contributes to greenhouse gases when burned. As a result, there is a need for fault detection and diagnosis to minimize the impacts when a fault occurs. Faults can occur at any of the sub-systems of the ACMV and due to its size and complexity, it is a challenge to diagnose them accurately at low severity levels.

The ACMV or HVAC is a system that controls the temperature, humidity, fresh air, filtration, and movement of air through space. In Malaysia region, heating is not required, thus the system is known as ACMV, while regions that require heating use HVAC. The goal of such a system is to provide thermal comfort and acceptable indoor air quality for the occupants or to provide cooling for equipment. The ACMV can achieve this by conditioning the air through [1–5]: cooling, dehumidifying, cleaning, and ventilating. All these can be done based on the principles of thermodynamics, fluid mechanics and heat transfer. There are three subsystem that works together to perform the functions mentioned above. These three sub-systems are cooling tower, chiller plant, and AHU. Figure 1 depicts the interdependency of the three sub-systems and how heat is being transferred around the ACMV system.

The cooling tower removes the heat from the chiller plant's condenser through heat exchangers filled with water. This water loop is called the condenser water loop, the water is then pumped from the condenser to the tower. The water is cooled by pumping it up to the top of the cooling tower where the ambient air and wind can remove the heat from the water. Heat is removed from the water as it is sprayed on to thin film materials. As the water flows from the top to the bottom of the cooling tower, it is exposed to the ambient air and wind which cools it down. The cooled condenser water is then circulated back to the chiller plant's condenser to absorb heat again.

The chiller plant provides the cooling capacity for the building as the centralized cooling system. It provides cooling based on vapor compression which is the fundamental process in the refrigeration cycle. In the chiller plant, the compressor compresses the refrigerant which allows heat absorption at the evaporator and releases that heat at the condenser. The refrigerant circulates through an evaporator, compressor, condenser, and an expansion valve. A thermodynamic process at each

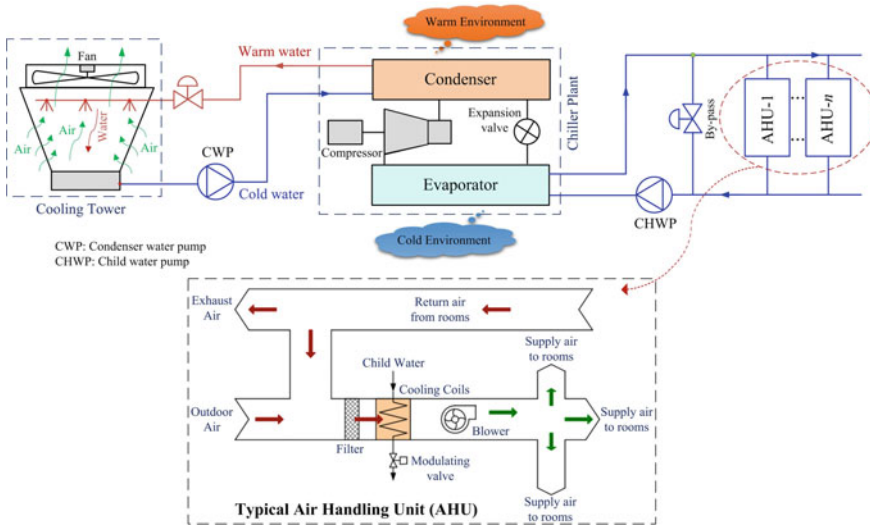


Fig. 1 Main components of central air conditioning system

component to ensure a continuous flow of cold refrigerant to absorb the heat from the chilled water loop. The cooled chilled water is then sent to the cooling coil for the AHU to cool the air.

The AHU is a system of ducts, filters, dampers, and fans to circulate cold fresh air and exhaust stale air. Fresh air is collected through an intake and cooled at the cooling coil as cold chilled water circulates the coil to absorb the heat from the air. The cooling coil dehumidifies the air as well by removing moisture in the air. The cold fresh air is then supplied to the various cooling zones in the building through the fans and ducts. Fans are used to aid in the circulation of conditioned air around the building as well as exhausting stale air through an outlet. Filters are used for cleaning and dampers regulate the amount of cold air entering each zone.

Cooling is provided through the removal of heat in spaces, the heat can be removed through radiation, convection, or conduction. The heat is transferred through a refrigeration system which uses a medium to absorb the heat and disperse it outdoors. The medium is known as the refrigerant, which can be water, air, or chemicals. This is possible by making use of a thermodynamic cycle called the refrigeration cycle. There is a compressor in the system that changes the pressure and state of the refrigerant to absorb or release heat.

Dehumidification of air drying is provided by the cooling coil as the temperature at the coil is below the dew point, thus moisture in the air will condense around the cooling coil. The moisture is then collected at the bottom of the coil and removed via piping.

Cleaning is done by air filtration at the AHU to remove particles, contaminants, vapors, and gases. This helps to remove air pollutants such as pollen and dust from the air, improving and regulating the air quality within the building. This is done by

implementing filters of various materials in the air ducts, especially the outdoor air inlets to prevent pollutants from entering the building. This also prevents ducts or fan blades from dust accumulation.

Ventilation is normally done mechanically through the AHU via the multiple fans within the duct system. Conditioned outside air is delivered into the building by a supply air fan and existing air is being exhausted to prevent carbon dioxide build-up. Ventilation is necessary as it is one of the most important factors for maintaining indoor air quality within the building. Without ventilation, stale air can happen which has an unpleasant smell and can become a health hazard for the occupants at higher levels.

ACMV has become an essential system and integrated into our society, both in residential and industrial. The ACMV system contributes to more than 60% of the total building energy consumption. Within the ACMV system, the chillers and fans are the two components that contribute significantly to energy consumption. Chiller consumes up to 55% and fans up to 35% of the total energy consumption [2–5].

Therefore, early FDD is very important for ACMV's health monitoring as well as optimal utilization of electrical energy, which is directly dependent on the optimal selection of the dataset and its severity level w.r.t. the fault condition. The main objective of this study is to analyze the severity and reliability of the dataset, which is used to detect and diagnose faults at low severity. By detecting faults at low severity, fixes, and maintenance can be done at a lower cost when compared with a more severe fault. This ensures the system operates optimally and reduces costs related to operation and maintenance. This in turn helps building owners to reduce electricity consumption and their carbon footprint.

The organization of this paper is comprised of seven sections. Section 1 represents the introduction. Brief information of AHU is represented in Sect. 2, which includes main components of the ACMV/HVAC and its related components. Section 3 represents brief information of AHU faults and its severity. The simulation of the model is shown in Sect. 4. Sections 5 and 6 represent the dataset collection and sensitivity analysis, respectively. Finally conclusion is represented in Sect. 7.

## 2 Brief Information of Air Handling Unit (AHU)

Figure 1 represents the main components of the central air conditioning (CAC) system, which includes mainly three sub-systems, i.e., cooling tower, chiller plant, and air handling unit (AHU).

The cooling tower is the point where the heat absorbed from the cooling zones are being dissipated into the atmosphere through the evaporative process. Warm condenser water is circulated to the top of the cooling tower, where the water is exposed and evaporated into the air passing through the cooling tower. As the water evaporates, the air absorbs heat and cools the remaining condenser water. The remaining condenser water will flow into a collection basin, where it can be pumped

back to the condenser to absorb heat at the chiller plant. There are five main components to a cooling tower, exhaust fan, drift eliminators, water distribution, fill, and basin. The hot condenser water is sprayed from the water distribution using a nozzle, it then flows on to the fill section which aids in the evaporation rate. The cooled water is then collected at the cooling tower basin which is then circulated back to the condenser. The hot air is exhausted by the fan and drift eliminators prevent droplets of water from being blown out of the tower [6].

The chiller operates on the vapor compression or vapor absorption concept. The most frequently used air conditioning cycle is the vapor compression. The low-pressure refrigerant evaporates in the evaporator to produce a cooling effect. A compressor, which often requires electrical energy, compresses the generated refrigerant vapor to condenser pressure. The high-pressure refrigerant condenses in the condenser, and the generated heat is discharged into the atmosphere/cooling tower. The condensed refrigerant is then expanded to evaporator pressure by an expansion valve to continue the cycle. There are two types of chillers, namely air-cooled and water-cooled chillers. Water-cooled chillers can be further categorized as absorption, centrifugal, helical rotary, and scroll [7]. The chiller plant consists of the compressor, condenser, expansion valve, power unit, control unit, and water box. The compressor increases the pressure of refrigerant vapor from the evaporator to the condenser. All the components are located centrally in a chiller plant room.

AHU is a main component of the central air conditioning system of commercial buildings to maintain zone temperature in a multi-zone application [1]. There are many different types of AHU, such as (1) as per location, (2) as per fan position, (3) as per mixing capability, (4) as per energy recovery, (5) as per service zone, (6) as per ducting, and (7) as per air volume. In our air conditioning and mechanical ventilation system (ACMV) context, the AHU is a draw-through, multiple zones, single duct variable air volume (VAV) AHU with mixing capability for energy recovery. The AHU is located indoors.

The variable air volume (VAV) system of the draw-through AHU modulates airflow according to the building's thermal load condition. Connected to the supply air ducts, the VAV box in each zone controls the temperature and amount of supply air necessary to maintain zone temperature in a multi-zone application [1]. A typical representation of VAV and CAV type systems is represented in Figs. 2 and 3, respectively. The main properties of the CAV system are: (1) chilled water flow to AHU coils is modulated based on return air temperature, (2) if the percentage change of cooling load of different rooms is not same, few rooms could be over-cooled or under-cooled. Similarly, the main properties of the VAV system are: (1) the opening of the VAV box damper is based on room temperature, (2) the speed of the fan is modulated based on duct pressure, (3) the chilled water valve is modulated based on the pre-set off-coil temperature of supply air, (4) suitable if the cooling load of different rooms is different.

Measurements are recorded from various points of interest within the AHU through the sensors installed. They include pressure, flow rate, temperature sensors, etc. The AHU's air handling controller (AHC) receives these readings and sends corresponding signals to the cooling coil, fans, and dampers for regulation to achieve



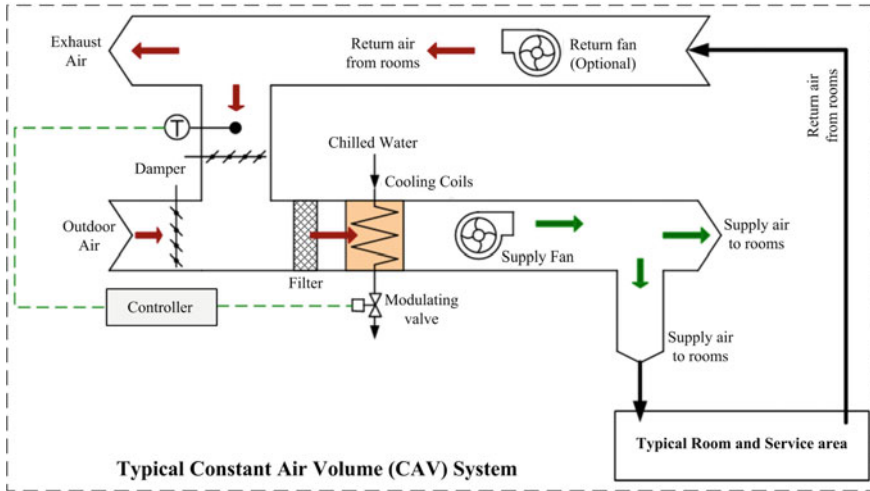


Fig. 2 Constant air volume (CAV) system’s type AHU

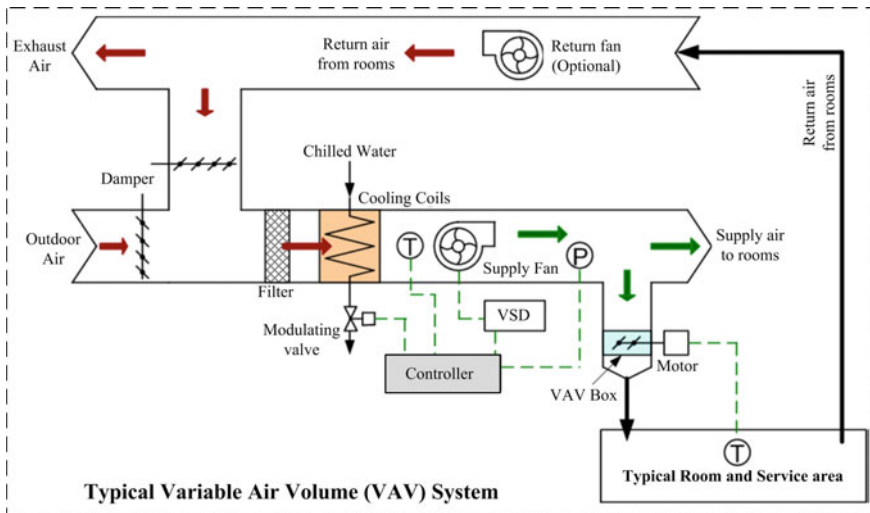


Fig. 3 Variable air volume (VAV) system’s type AHU

the designated supply air temperature and operating conditions—such as the indoor air quality (IAQ) standards. In Table 1, the functionality of each component is described.

Controlled automatically by the AHC, AHU dampers operate to conduct appropriate mixing of the air (outdoor and recirculated return air) to conserve energy by limiting heating or cooling and meeting the AIQ standards [8].

**Table 1** Summary of different functionality and location of AHU components

Component		Functionality	Location
Dampers	Outdoor air damper	Damper controls the amount of air entering the AHU	Outdoor air duct
	Exhaust air damper	Controls the amount of air exhausted from the system	Exhaust air duct
	Return air damper	Controls the amount of air mixed between the outdoor air and return air	Duct between fresh air and exhaust intake
Air ducts		For the delivery of cooled/ heat air and the path back to the AHU	Building
Filter		Trap dirt and dust to prevent them from entering the building and the build-up of dust within AHU's mechanical equipment and duct	Between mixing plenum and cooling coil
Fans (draw-through)	Supply fan	Ensures enough pressure to deliver cooled air to the various zones	Located supply air duct, after cooling coil
	Return fan	Ensures enough pressure to return air from the zones to the AHU for discharging or mixing	Located at return air duct
Cooling coil		Turned on for the purpose of cooling the room to the designated temperature	In the case of the project's draw-through fan system, cooling coil is located in between the filters and supply fan
Temperature sensor	T <sub>OA</sub>	Measure temperature at outdoor air duct	Outdoor air duct
	T <sub>RA</sub>	Measure temperature at return air duct	Return air duct
	T <sub>SA</sub>	Measure temperature at supply air duct	Supply air duct
	T <sub>MA</sub>	Measure temperature after mixing plenum	After mixing plenum
Pressure sensor	Filter pressure sensor	Differential pressure sensor measures the amount of blockage in the filter due to dirt, warning engineers for a replacement	Across filter
	Fan pressure sensor (used in BMS)	Differential pressure sensor used as a gauge for fan's performance and status	Across fan

(continued)

**Table 1** (continued)

Component		Functionality	Location
	Supply air duct static pressure	Measures the resistance to airflow caused by air moving through the duct. Information fed to VDS of supply fan	Supply air duct
Humidity sensor	Outdoor air humidity sensor	Measure the humidity of outdoor air	Before outdoor air
	After mixing chamber humidity sensor	Measure the humidity of mixed air	After mixing chamber
Airflow sensor	F <sub>1</sub>	Measure air flow of supply air duct. Information fed to VSD of return fan	Supply air duct
	F <sub>2</sub>	Measure air flow of return air duct. Information fed to VSD of return fan	Return air duct

$$\theta_{\text{outdoor}} = 1 - \theta_{\text{return}} = \theta_{\text{exhaust}} \quad (1)$$

where  $\theta_{\text{outdoor}}$  = angle of outdoor air damper,  $\theta_{\text{return}}$  = angle of return air damper, and  $\theta_{\text{exhaust}}$  = angle of exhaust air damper.

In the AHU, the control of mechanical cooling and heating is sequentially programmed to synchronize with the damper control [9]. It's worth noting that when the amount of outdoor air mixed is kept to a minimum, the outdoor air damper position is at its lowest, while the return air damper position is at its highest, as shown in Eq. (1).

During the heating mode, the heating coil valve is regulated for hot water supply from a boiler to maintain the designated supply air temperature, while the cooling coil valve is closed and the dampers are modulated to keep the amount of outdoor air being mixed to a minimum while meeting minimal ventilation requirements [9].

As the outdoor air temperature increases, the sequential operation switches from heating to free cooling, cooling the building with outdoor air. The air dampers modulate in this mode to maintain the appropriate supply of air temperature [9].

As the outdoor air temperature further increases, the AHU will be unable to cool the supply air to the desired temperature using only the outside air, triggering the cooling coil valve to carry out mechanical cooling [9].

The fans located at the supply and return air ducts are equipped with a variable frequency drive (VFD) which modulates its speed, influencing the airflow within the AHU as load condition varies. The purpose of each VFD however, differs. The supply fan is modulated with the purpose of maintaining duct static pressure, while the return fan is modulated with the purpose of maintaining the airflow difference between the supply and return fans. The control signal sent to the VFD of the supply fan is based upon the duct static pressure read from the pressure sensor at the supply air duct (P1), while the control signal sent to the VFD of the return fan is based upon

the airflow reading from flow sensors (F1 and F2) located at the supply and return air duct, respectively [8].

It is good to note that all AHU components complement each other to achieve the operating conditions dictated by the AHC [1]. In the context of this study, the heating coil is excluded due to its inapplicability in tropical climates like Malaysia.

### 3 Brief Information of AHU Faults

Faults that occur in AHU can lead to inefficient energy consumption, occupant discomfort, and safety issues. Thus, it is necessary to utilize FDD tools to locate faults automatically. According to Bruton et al., implementing FDD technologies resulted in a total savings of €104,000 per year in 18 AHUs across four testing sites [10]. The faults that occur in AHU are also listed in the NREL project “An Open-Based Platform for Whole-Building Fault Detection and Diagnostics.” According to the NREL, the faults are ranked by the amount of energy consumed, and duct leakage was identified as a major fault because it has the second-highest energy impact [11].

The IEA Annex 25 provides a list of faults for the air mixing section, filter-coil section, fan section, and VAV boxes that are listed without regard to severity or frequency of occurrence. A preliminary survey among designers, construction engineers, and commissioning engineers was conducted in Japan in 1992 to determine the importance of various faults in AHU. Before assessing whether or not a fault is critical, there are seven factors to consider which are environmental degradation and occupant complaints, increased energy consumption, serious secondary damage, frequent occurrence, difficult detection, lengthy repair time, and costly repair [12].

A list of AHU faults from the NREL, ASHRAE RP 1312, and IEA is shown in Fig. 4. The most impactful faults resulting in increased energy consumption are included in Table 2, which was compiled from the ASHRAE and NREL reports.

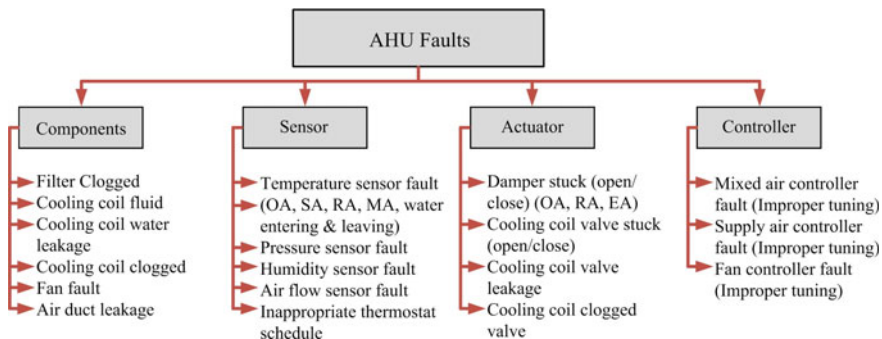


Fig. 4 List of all possible faults in AHU

**Table 2** Summary of AHU faults based on NREL, IEA, and ASHRAE RP-1312 [11–13]

S.no	Fault description	Source from
1	Air duct leakage	NREL
2	Damper stuck at certain position	NREL & ASHRAE, IEA
3	Cooling coil valve stuck/leak	ASHRAE & IEA
4	Fan motor degradation	NREL & IEA
5	Fan motor failure	ASHRAE
6	Supply air (SA) temperature sensor fault	NREL & ASHRAE
7	Outdoor air (OA) temperature sensor fault	NREL & ASHRAE
8	Inappropriate set point/schedule for thermostat	NREL
9	Supply air (SA) flow rate sensor reading fault	ASHRAE
10	Supply air (SA) pressure sensor reading fault	ASHRAE

Since these ten faults impact energy consumption and indoor thermal comfort, it is critical to conduct FDD so that the ACMV system will work efficiently with minimal operating costs and a high level of comfort for the occupants.

## 4 Simulation of ACMV Model

OpenStudio (OS) is an open source software development kit (SDK) for building energy modeling (BEM) that intends to significantly reduce the time and effort necessary to develop and maintain BEM-based applications, as well as to extend and support the ecosystem of end-user BEM tools and services [14]. Building fault models in OS can be used to quantify the impact of faults on building performance as well as create and test FDD techniques [15].

EnergyPlus (EP) inputs and outputs are presented in OS as a dynamic, object-oriented data model with an application programming interface (API), which is a much easier construct for programs to deal with [14]. The OS Platform includes a range of GUI programs that aid in the construction of mechanical systems, simulation job, and workflow management on local workstations and high-performance computing (HPC) clusters and result visualization [16].

The US Department of Energy (DOE) small office together with the tropical weather file is used as the reference base model. The small office reference building is a single-story building with five zones plus an attic. Certain parameters such as the scheduling of occupants will be modified to represent the typical office setting in Singapore more accurately. The US DOE contributes to the development of commercial and residential building energy codes and standards by taking part in industry review and update processes and providing technical assessments to support both published model codes and proposed modifications. DOE discloses its findings in

order to guarantee that its support is transparent and that its analysis is available for public examination and use [17].

OS application facilitates the design, simulation, and review of specific building energy models by building the model. Although, not all tabs are required for modeling a building, they are generally placed in the sequence in which they are utilized along the left-hand side of the window. The tabs are listed in Table 3 [60], along with a description of their functions. The maximum outdoor air flow rate was calculated as shown in Eq. (2).

$$\text{Flow Rate}_{\text{Outdoor Air}} = \text{Ventilation Rate} \times \text{Total Floor Area} \quad (2)$$

Figure 7 depicts the simulated operation on the base model with three parameters of interest, namely the outdoor air flow fraction, outdoor air temperature (system node 27) and the various zone temperatures. It is good to note Eq. (3). An increase in the amount ( $Q$ ) of return air being mixed is equivalent to a decrease in the amount of outdoor air being mixed within the mixing chamber.

$$Q_{\text{Supply Air}} = Q_{\text{Mix Air}} = Q_{\text{Outdoor Air}} + Q_{\text{Return Air}} \quad (3)$$

The designated zone temperatures are set at 23 °C from 18:00 h to 06:00 h and 25 °C otherwise. At 06:00 h, the ACMV strives to cool the zones to the designated 23 °C, mixing more return air to save energy while conducting mechanical cooling, resulting in a tremendous drop in the outdoor air flow fraction. From 06:00 h to 18:00 h, the various fluctuations are a result of the increase or decrease in infiltration levels (Fig. 8) and occupancy (Fig. 9). It is good to note that time is required for the zone to reach the designated temperature due to the thermal time constant, resulting in small modulations between the said time frame. For instance, from 13:00 h to 17:00 h, it can be seen that when the infiltration and occupancy levels remain constant, there were no modulations seen in the outdoor airflow fraction. After 18:00 h, the designated zone temperature changes from 23 to 25 °C. With the zones previously cooled to 23 °C, more outdoor air is introduced into the system for mixing, resulting in a spike in outdoor air flow fraction.

It is observed that from 20:00 h to 22:00 h, there was a linear increase in outdoor air fraction, suggesting more outdoor air being mixed. This is attributed to a drop in light scheduling seen in Fig. 10 at 20:00 h. With lesser lights present, the zones become relatively cooler compared with when more lights were on. In an attempt to maintain zone temperatures at 25 °C, more outdoor air is used for mixing resulting in an increase in outdoor air flow fraction.

**Table 3** Representation of OS tabs and description

Tabs	Description	Changes made to ASHRE-based model
Site	Specify weather, lifecycle costs, and utility bills	The weather file “tropical climate” applied to the model was obtained from the EP website
Schedules	Define schedules applied to building loads	People per space floor area which was required under the people definition was modified to 0.089699 people/m <sup>2</sup>
Constructions	Specify materials, construction assemblies, and sets	Converting cfm/ft <sup>2</sup> to m/s, it will lead to a value of 0.003048 m/s
Loads	Define individual building loads	The heating thermostat schedule under HVAC systems has to be removed to fit in the AMCV context as the heating was not required in Malaysia. The supply air temperature was modified to 21 °C under the cooling sizing parameters
Space types	Create profiles for how spaces are occupied	“Office WholeBuilding - Sm Office Ventilation” requires the outdoor air flow per floor area
Geometry	Define the building’s exterior and interior geometries	
Building	Assign building-level defaults and exterior items	
Spaces	Assign profiles to individual spaces	
Thermal zones	Group spaces into thermal zones and assign zone equipment	The zone cooling design supply air temperature was modified to 21 °C under the cooling sizing parameters, as specified in the “Schedule” tab and it is the same as the “Deck Temperature” schedule
HVAC	Specify heating, cooling, and water systems for the building	Total floor area for this model was 11,616 ft <sup>2</sup> . The maximum outdoor air flow rate was calculated as shown in Eq. (2). The finalized loop for the AHU can be found in Fig. 5
Variables	Specify additional simulation reporting variables	The variable tab informs the OS platform of the desired data to output during the simulation
Simulation settings	Customize simulation settings	

(continued)

**Table 3** (continued)

Tabs	Description	Changes made to ASHRE-based model
Measures	Assign OS measure scripts to a workflow	The measurements tab also enables importing of individual fault type model
Run simulations	Perform a single-energy simulation	After making all of the necessary adjustments, the model may finally begin the simulation, and it will take some time for the model to generate the required output variables as specified in the variables tab
Reports	Review simulation results for a single-energy simulation	The reports tab allows users to view various types of simulated summary findings, and the annual overview pie chart can be seen in Fig. 6

## 5 Dataset Collection for Further Study

For the purpose of sensitivity analysis and result demonstration, three different types of datasets have been collected such as (1) simulation datasets from our OS fault simulation model, (2) real datasets from the ASHRAE RP-1043 research project by Comstock et al. [18], and (3) real datasets from the Inventory of Data Sets for AFDD Evaluation by Jessica Granderson and Guanqing Lin [19].

The dataset from ASHRAE RP-1043 contains data measured and calculated based on a 90-ton centrifugal chiller. The experiment was designed with the specifications of air conditioning and refrigeration institute (ARI) Standard 550 for centrifugal and rotary screw water-chilling packages.

The dataset from the inventory contains performance dataset generated through simulation of physical experimentation. Both simulation and physical experimentation implement a VAV AHU for generating condition-based datasets. There are other differences between the dataset as well such as the total number of data points available for the parameters. The table below summarizes the difference between the two datasets, as given in Table 4.

It is good to note that the simulation and real data is vastly different. The real data was extracted from a heating, ventilation, and air conditioning (HVAC) system, which would suggest that both heating and cooling operations are involved. The simulated data, however, only operates in the latter operation.

## 6 Sensitivity Analysis and Result Demonstration

Data generation is done across the four faults once the base model is made. The data is used for data correlation analysis to determine any possible connection between the parameters and the fault. All the parameters related to the system, namely air system



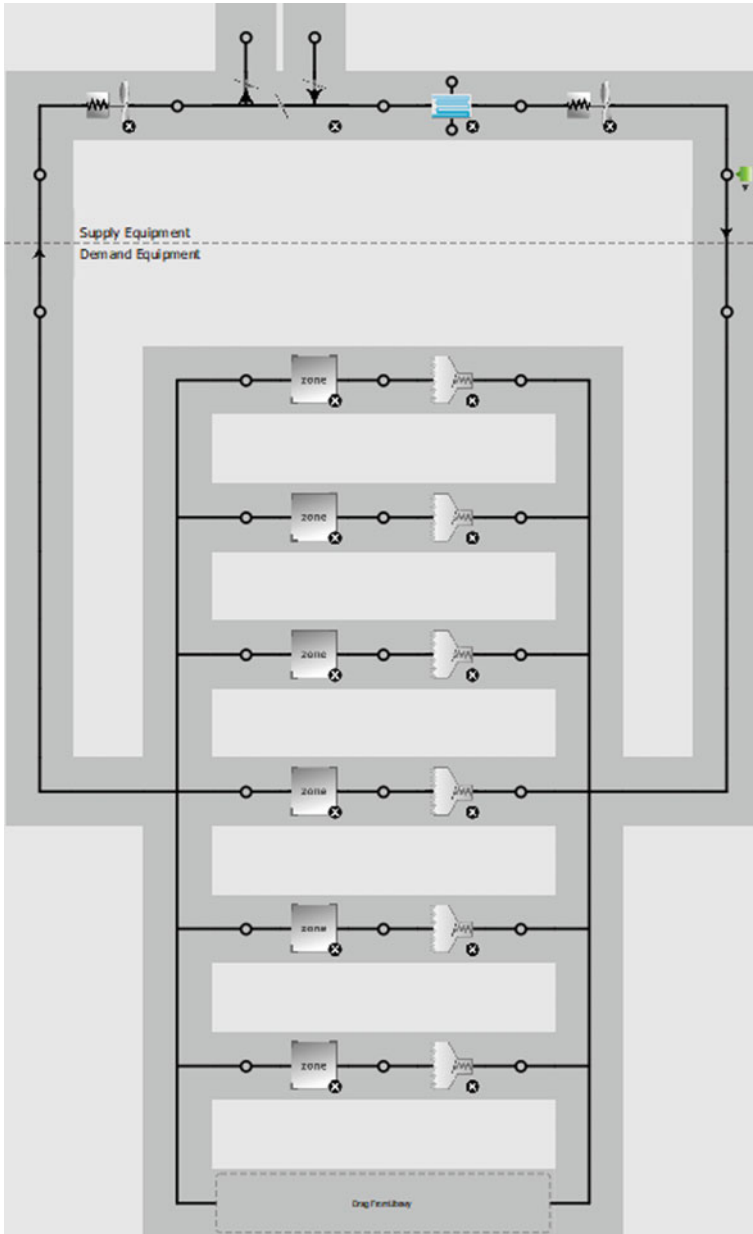


Fig. 5 Simulated AHU loop

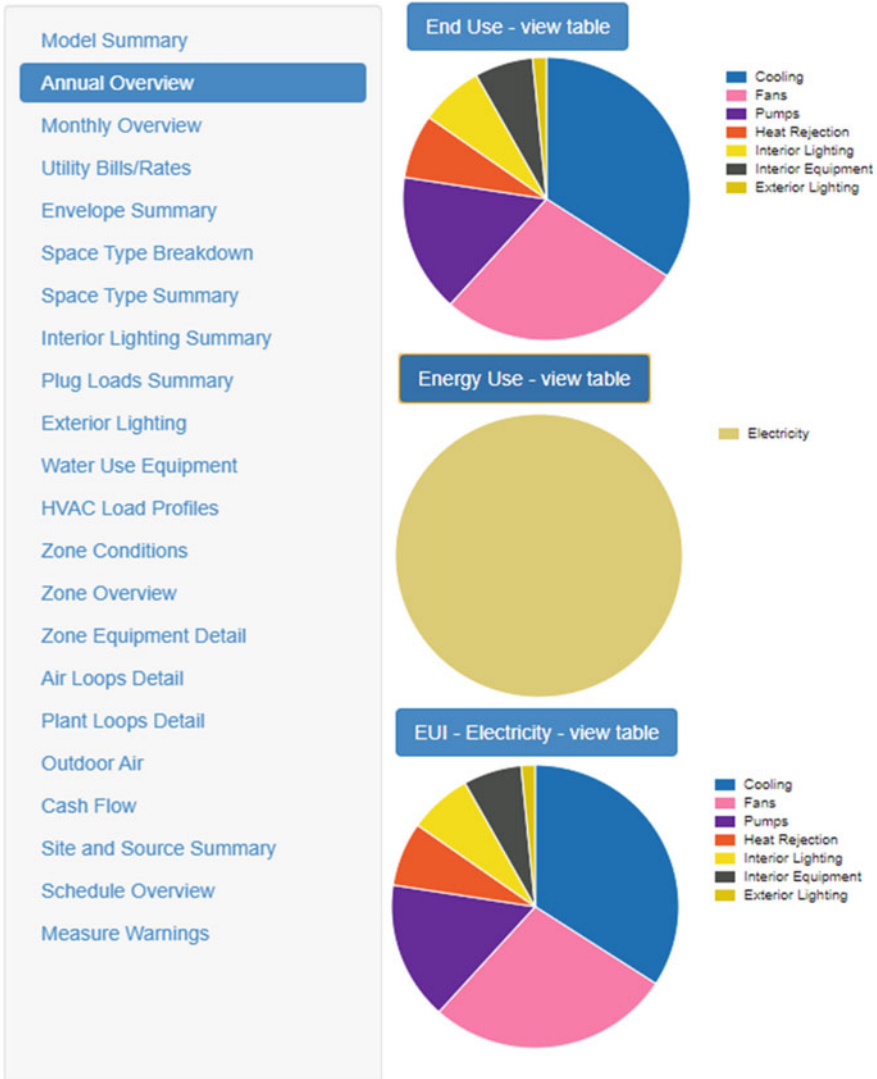


Fig. 6 Overview representation of the annual report of electrical consumption

were enabled for the analysis (in this study), followed by the model simulation. Fault propagation is captured through the enabling of parameters that are not explicitly within the system. For example, the data is generated with the consideration of the fault severity and the range of load. The range of load used is 0, 50, 100, 150, and 200% of the full load and the fault severity ranges from 0% (used as base value), 10, 20, 30, and 50% of the fault level. The collection of data is done for all the load variations and the fault severity. The collected dataset points are: (1) for cooling

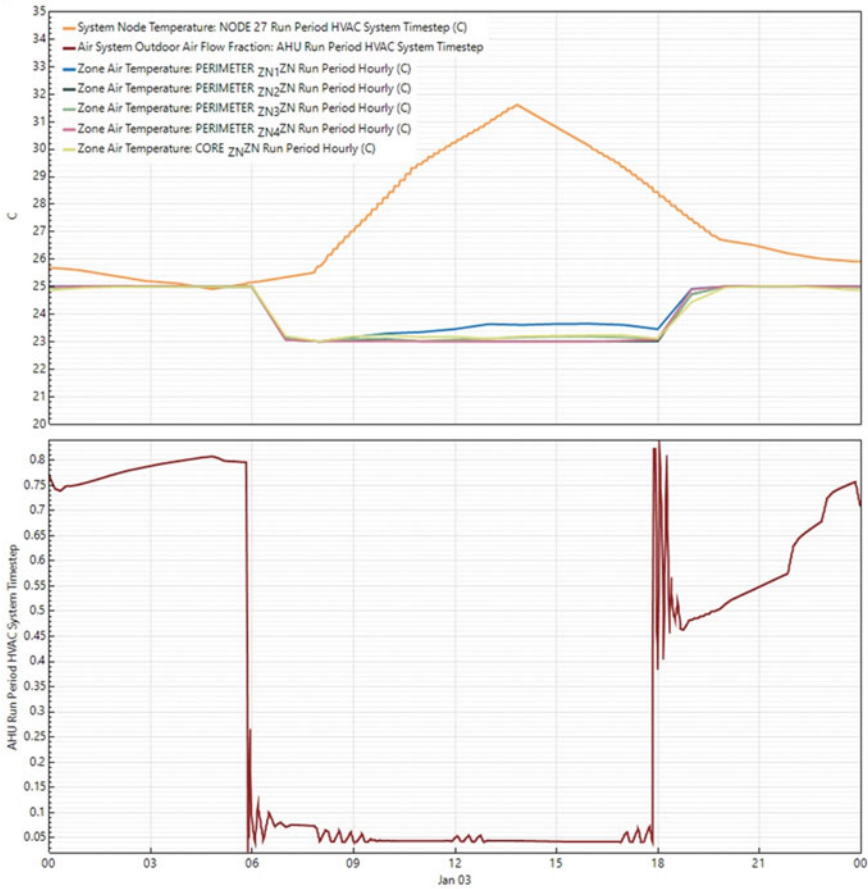


Fig. 7 Representation of outdoor air flow trends

coil (time, cooling coil total cooling energy, cooling coil source side heat transfer energy, cooling coil sensible cooling energy, cooling coil total cooling rate, cooling coil sensible cooling rate, cooling coil wetted area fraction), (2) for the fan (fan electricity rate, fan rise in air temperature, fan heat gain to air, fan air mass flow rate), and (3) air system (air system outdoor air heat recovery bypass minimum outdoor air mixed air temperature, air system outdoor air flow fraction, air system mixed air mass flow rate, air system outdoor air mechanical ventilation requested mass flow rate).

Once the data is extracted, parameters with changes according to the severity of fault and load variations are documented and arranged by its sensitivity to the varying fault levels. Sensitivity analysis is used to prioritize parameters for data dimension reduction based on the percentage difference between the average values of the parameters from the base value. The relative change formula is applied to calculate

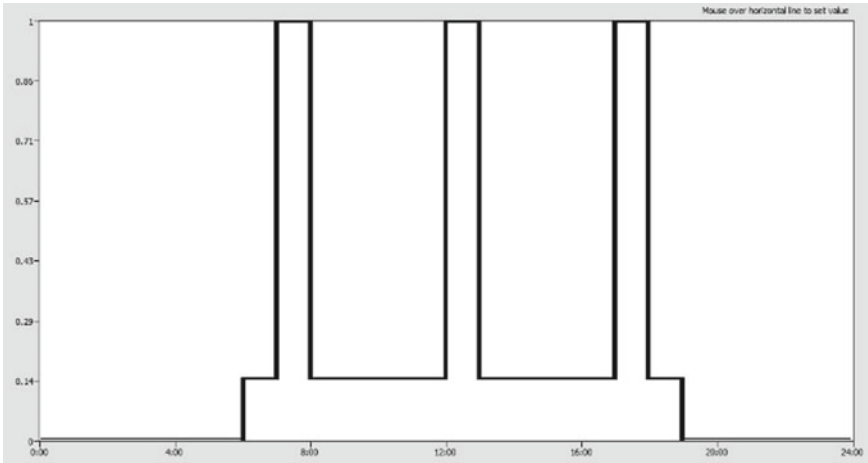


Fig. 8 Representation of door opening (infiltration) schedule

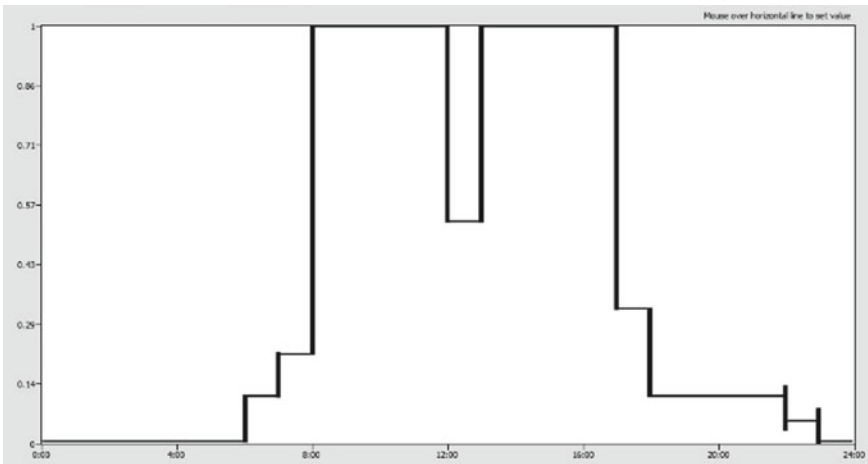
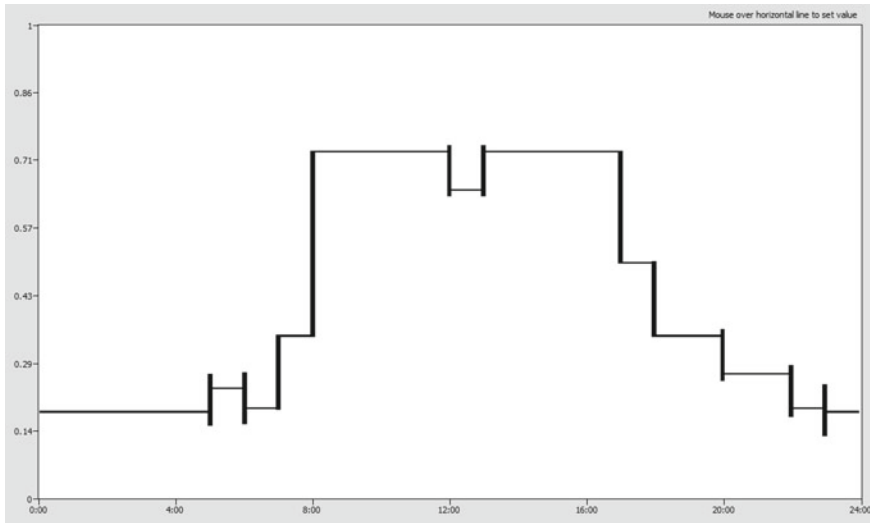


Fig. 9 Representation of occupancy schedule of building

the percentage difference between the severed parameter and the base parameter, where the final value is the average fault severed value and the initial value is the average base value for the parameter. For the case study of fan fault conditions, Table 5 gives how Eq. (4) is applied to the data, and Table 6 gives the compiled parameters with its respective sensitivity analysis.

$$\text{Relative Changes} = \left( \frac{\text{Final value} - \text{Initial value}}{\text{Initial value}} \right) \times 100 \quad (4)$$



**Fig. 10** Representation of building lights schedule

**Table 4** Representation of differences between simulation and real datasets

Dataset	OS-based emulated dataset for AHU faults	Real dataset for each AHU faults
Number of data points	36,000	175,200
Sampling rate	1 data per min	1 data per 15 min
Time period	1 day	1 year

Similarly, for the case study of sir system fault conditions, Table 7 gives how Eq. (4) is applied to the data, and Table 8 gives the compiled parameters with its respective sensitivity analysis.

This is done to rank and identify the most sensitive parameters which will be the input for artificial intelligence (AI) and machine learning (ML)-based diagnostic models [20–30]. This is important as it simplifies and improves the accuracy of data processing. For the real data, a similar method is done for its data correlation and sensitivity. From the real data, sensitivity analysis is done by collating the average values of the parameters, and Eq. 2 is applied to calculate the percentage difference between the fault severities and the base. The ranking is then done to identify the most sensitive parameters to input for AI/ML. The selected sensitive parameters (top 10) from the simulation data and real data are represented in Table 9.

Based on Table 9, the chosen sensitive parameters are different from the simulation parameters due to the availability of the data as not all parameters are being monitored for the real system as well as the difference in system, HVAC for real data, and ACMV for simulation. However, there are overlapping parameters that are directly or indirectly related to each other. For example, in the AHU system, real data contains

**Table 5** Representation of relative change formula applied for fan measurement

Fault level	M1	M2	M3	M4	M5	M6	M7	M8	M9	M10
0	2772.667	2772.667	0.941339	0.941602	2772.667	2772.667	9,981.601	9,981.601	2.767462	2.767462
0.1	3155.599	3155.599	1.048893	1.049177	3155.599	3155.599	11,360.157	11,360.157	2.774143	2.774143
0.2	3584.385	3584.385	1.177046	1.177354	3584.385	3584.385	12,903.786	12,903.786	2.749762	2.749762
0.3	4264.347	4264.347	1.352618	1.352962	4264.347	4264.347	15,351.648	15,351.648	2.766121	2.766121

M1: Fan Electricity Rate: VAR SPD FAN 3 Run Period Hourly (W), M2: Fan Electricity Rate: VAR SPD FAN 2 Run Period Hourly (W), M3: Fan Rise in Air Temperature: VAR SPD FAN 3 Run Period Hourly (delta C), M4: Fan Rise in Air Temperature: VAR SPD FAN 2 Run Period Hourly (deltaC), M5: Fan Heat Gain to Air: VAR SPD FAN 3 Run Period Hourly (W), M6: Fan Heat Gain to Air: VAR SPD FAN 2 Run Period Hourly (W), M7: Fan Electricity Energy: VAR SPD FAN 3 Run Period Hourly (J), M8: Fan Electricity Energy: VAR SPD FAN 2 Run Period Hourly (J), M9: Fan Air Mass Flow Rate: VAR SPD FAN 3 Run Period Hourly (kg/s), M10: Fan Air Mass Flow Rate: VAR SPD FAN 2 Run Period Hourly (kg/s)

**Table 6** Representation of ranked parameters based on the percentage difference for fan measurement

Percentage changes	Fault level	Sensitivity analysis									
		M1	M2	M3	M4	M5	M6	M7	M8	M9	M10
% change from base	0.1	13.81096	13.81096	11.42569	11.42477	13.81096	13.81096	13.81097	13.81097	0.24144	0.24144
	0.2	29.2757	29.2757	25.0396	25.0374	29.2757	29.2757	29.27572	29.27572	-0.63955	-0.63955
	0.3	53.79947	53.79947	43.69089	43.6873	53.79947	53.79947	53.79946	53.79946	-0.04844	-0.04844
% Change from 0.1	0.2	13.58809	13.58809	12.21794	12.21688	13.58809	13.58809	13.5881	13.5881	-0.87887	-0.87887
	0.3	35.1359	35.1359	28.9567	28.95454	35.1359	35.1359	35.13588	35.13588	-0.28918	-0.28918
% change from 0.2	0.3	18.97013	18.97013	14.9163	14.91546	18.97013	18.97013	18.97011	18.97011	0.594915	0.594915

**Table 7** Representation of relative change formula applied for air system measurement

Fault level	S1	S2	S3	S4	S5	S6
0	2.54E+01	4.60E-01	2.23E-02	3.85E-01	2.77E+00	1.87E-01
0.1	2.55E+01	4.58E-01	2.23E-02	3.85E-01	2.77E+00	1.87E-01
0.2	2.56E+01	4.57E-01	2.23E-02	3.85E-01	2.75E+00	1.87E-01
0.3	2.57E+01	4.55E-01	2.23E-02	3.85E-01	2.77E+00	1.87E-01

S1: Air System Outdoor Air Heat Recovery Bypass Minimum Outdoor Air Mixed Air Temperature: AHU Run Period Hourly (C), S2: Air System Outdoor Air Flow Fraction: AHU Run Period Hourly, S3: Air System Outdoor Air Minimum Flow Fraction: AHU Run Period Hourly, S4: Air System Outdoor Air Mass Flow Rate: AHU Run Period Hourly (kg/s), S5: Air System Mixed Air Mass Flow Rate: AHU Run Period Hourly (kg/s), S6: Air System Outdoor Air Mechanical Ventilation Requested Mass Flow Rate: AHU Run Period Hourly (kg/s)

**Table 8** Representation of ranked parameters based on the percentage difference for air system measurement

Percentage changes	Fault level	Sensitivity analysis					
		S1	S2	S3	S4	S5	S6
% change from base	0.1	0.3798	-0.26313	0	0	0.24144	0
	0.2	0.842727	-0.53961	0	0	-0.63955	0
	0.3	1.485053	-1.06611	0	0	-0.04844	0
% change from 0.1	0.2	0.461176	-0.27721	0	0	-0.87887	0
	0.3	1.101071	-0.8051	0	0	-0.28918	0
% change from 0.2	0.3	0.636957	-0.52936	0	0	0.594915	0

CE which is related to CCSCR in the simulation. Thus, the sensitivity analysis for simulation can be applied to a real system if the data or related data are available.

It can be noted that the real data did not contain parameter data from other sub-systems but solely on their respective sub-system, such as cooling tower data for chiller faults and pump data for AHU faults. In the simulation, Chiller and AHU faults occurring have a significant impact on the cooling tower and pump, respectively, as given in Table 9. The overall summary of effect of parameters due to fault conditions in AHU is represented in Table 10.



**Table 9** Representation of sensitive parameters (selected)

Simulation data-based top sensitive parameters		Real data-based top sensitive parameters	
FD	AHU	FD	AHU
CCTCR: CCC1	CCTCR: CCC1	RASEE	RASEE
CCSCR: CCC1	CCSCR: CCC1	RASGE	RASGE
FER: VSF3	FER: VSF3	CE	CE
FER: VSF2	FER: VSF2	EF	WBFTHEDP
FRIAT: VSF3	FRIAT: VSF3	WBFTHEDP	GF
FRIAT: VSF2	FRIAT: VSF2	RSFFEE	RHCHE
FHGTA: VSF3	FHGTA: VSF3	FE	HG
FHGTA: VSF2	FHGTA: VSF2	GS	N10SNRH
FEE: VSF3	FEE: VSF3	RHCHE	N3SNRH
FEE: VSF2	FEE: VSF2	HG	RSFOSNRH
CEMFR: CEE1	CEMFR: CEE1		
PER: PVS2	PER: PVS2		
PSP:PVS2	PSP: PVS2		
PFHGR: PVS2	PFHGR: PVS2		
PMFR: PVS2	PMFR: PVS2		

*CCTCR: CCC1*: Cooling Coil Total Cooling Rate: CHW CLG COIL 1 Run Period HVAC System Timestep (W), *CCSCR: CCC1*: Cooling Coil Sensible Cooling Rate: CHW CLG COIL 1 Run Period HVAC System Timestep (W), *FER: VSF2*: Fan Electricity Rate: VAR SPD FAN 2 Run Period HVAC System Timestep (W), *CEMFR: CEE1*: Chiller Evaporator Mass Flow Rate: CHILLER ELECTRIC EIR 1 Run Period HVAC System Timestep (kg/s), *FEE: VSF2*: Fan Electricity Energy: VAR SPD FAN 2 Run Period HVAC System Timestep (J), *FEE: VSF3*: Fan Electricity Energy: VAR SPD FAN 3 Run Period HVAC System Timestep (J), *FER: VSF3*: Fan Electricity Rate: VAR SPD FAN 3 Run Period HVAC System Timestep (W), *FHGTA: VSF2*: Fan Heat Gain to Air: VAR SPD FAN 2 Run Period HVAC System Timestep (W), *FHGTA: VSF3*: Fan Heat Gain to Air: VAR SPD FAN 3 Run Period HVAC System Timestep (W), *FRIAT: VSF2*: Fan Rise in Air Temperature: VAR SPD FAN 2 Run Period HVAC System Timestep (delta C), *FRIAT: VSF3*: Fan Rise in Air Temperature: VAR SPD FAN 3 Run Period HVAC System Timestep (delta C), *PER: PVS2*: Pump Electricity Rate: PUMP VARIABLE SPEED 2 Run Period HVAC System Timestep (W), *PFHGR: PVS2*: Pump Fluid Heat Gain Rate: PUMP VARIABLE SPEED 2 Run Period HVAC System Timestep (W), *PMFR: PVS2*: Pump Mass Flow Rate: PUMP VARIABLE SPEED 2 Run Period HVAC System Timestep (kg/s), *PSP: PVS2*: Pump Shaft Power: PUMP VARIABLE SPEED 2 Run Period HVAC System Timestep (W)

**Table 10** Representation of effect of parameters due to fault condition in AHU

Variable\Faults	Fan degradation	Return air duct leakage
<i>Overall</i>		
Electricity net: facility: site-run period hourly (J)	↑	↑
<i>In the case of fan fault analysis</i>		
Fan electricity rate: VAR SPD FAN 3 run period hourly (W)	↑	✓
Fan electricity rate: VAR SPD FAN 2 run period hourly (W)	↑	✓
Fan rise in air temperature: VAR SPD FAN 3 run period hourly (delta C)	↑	✓
Fan rise in air temperature: VAR SPD FAN 2 run period hourly (delta C)	↑	✓
Fan heat gain to air: VAR SPD FAN 3 run period hourly (W)	↑	✓
Fan heat gain to air: VAR SPD FAN 2 run period hourly (W)	↑	✓
Fan electricity energy: VAR SPD FAN 3 run period hourly (J)	↑	✓
Fan electricity energy: VAR SPD FAN 2 run period hourly (J)	↑	✓
Fan air mass flow rate: VAR SPD FAN 3 run period hourly (kg/s)	✓	✓
Fan air mass flow rate: VAR SPD FAN 2 run period hourly (kg/s)	✓	✓
<i>In the case of cooling coil fault analysis</i>		
Cooling coil total cooling energy: CHW CLG COIL 1 run period hourly (J)	↑	↑
Cooling coil source side heat transfer energy: CHW CLG COIL 1 run period hourly (J)	↑	↑
Cooling coil sensible cooling energy: CHW CLG COIL 1 run period hourly (J)	↑	↑
Cooling coil total cooling rate: CHW CLG COIL 1 run period hourly (W)	↑	↑
Cooling coil sensible cooling rate: CHW CLG COIL 1 run period hourly (W)	↑	↑
Cooling coil wetted area fraction: CHW CLG COIL 1 run period hourly	-	-
<i>In the case of air system fault analysis</i>		
Air system outdoor air heat recovery bypass minimum outdoor air mixed air temperature: AHU run period hourly (C)	↑	✓
Air system outdoor air flow fraction: AHU run period hourly	↓	↑
Air system outdoor air minimum flow fraction: AHU run period hourly	-	-
Air system outdoor air mass flow rate: AHU run period hourly (kg/s)	-	↑
Air system mixed air mass flow rate: AHU run period hourly (kg/s)	✓	✓

(continued)

**Table 10** (continued)

Variable\Faults	Fan degradation	Return air duct leakage
Air system outdoor air mechanical ventilation requested mass flow rate: AHU run period hourly (kg/s)	–	–
<i>In the case of system node</i>		
Temperature: node 29		↑
Air mass flow rate: node 28		↑

Legend: ↑: Consistent Increment At Increasing Fault Severity, ↓: Consistent Decrement At Increasing Fault Severity, ✓: Both Increment & Decrement Seen During Increasing Fault Severity, –: No Correlation Seen During Increasing Fault Severity

## 7 Conclusion

In this chapter, data reliability analysis for early fault diagnosis of AHU is performed by using two categories of datasets (category-1 dataset: emulated data, and category-2 dataset: real-data measurement). EnergyPlus<sup>+</sup>-based OpenStudio software platform is used to simulate the building envelope to generate the emulated dataset under different operating scenarios. In the simulation, building operation is fixed as per the working hours of the building's user, and a dataset is generated for different fault scenarios starting from healthy condition to the most severe fault condition. The fault severity is considered from 0 to 30% w.r.t. healthy situation, and different electrical and non-electrical signals were recorded for further analysis. Based on sensitivity analysis of different signals w.r.t. the fault severity levels, the most sensitive signals have been selected, which may be used for the development of the classifier/identifier of the faults at an early stage. For the real-recorded dataset, the chosen sensitive parameters are different from the simulation parameters due to the availability of the data as not all parameters are being monitored for the real system, as well as the difference in system, HVAC for real data, and ACMV for simulation. However, there are overlapping parameters that are directly or indirectly related to each other. In the AHU system, real data contains CE which is related to CCSCR in the simulation. Thus, the sensitivity analysis for simulation can be applied to a real system if the data or related data are available.

**Acknowledgements** This study was supported by the Universiti Teknologi, Malaysia—"Development of Adaptive and Predictive ACMV/HVAC Health Monitoring System Using IoT, Advanced FDD, and Weather Forecast Algorithms" (Q.J130000.3823.31J06).

## References

1. McDowall R (2009) Chapter 1—introduction to HVAC. In: *Fundamentals of HVAC systems: a course reader*. Elsevier, pp 1–10
2. Malik H, Panda SK, Pootla K, Spanos CJ (2022) Data-driven hybrid approach for early fault detection of AHU using electrical signals. In: *2022 international power electronics conference (IPEC-Himeji 2022- ECCE Asia)*, Himeji, Japan, pp 1365–1371. <https://doi.org/10.23919/IPEC-Himeji2022-ECCE53331.2022.9807260>
3. Chandra R et al. (2020) A survey of failure mechanisms and statistics for critical electrical equipment in buildings. In: *IECON 2020 the 46th annual conference of the IEEE industrial electronics society*, Singapore, pp 1955–1961. <https://doi.org/10.1109/IECON43393.2020.9254225>
4. Xinjie J, Malik H, Panda SK (2022) An optimized intelligent technique for bearing fault diagnosis using motor current signal analysis. In: *2022 international power electronics conference (IPEC-Himeji 2022-ECCE Asia)*, Himeji, Japan, pp 730–735. <https://doi.org/10.23919/IPEC-Himeji2022-ECCE53331.2022.9807128>
5. Malik H et al, Method and system for determining a condition of an airflow device. Patent, World Intellectual Property Organization, WO2022186770A1
6. U.S Department of Energy (2011) Cooling towers: understanding key components of cooling towers and how to improve water efficiency. Energy.gov. <https://www.coursehero.com/file/35758596/waterfs-coolingtowerspdf/>. Accessed 31 Mar 2022
7. Islam MR, Air-conditioning and mechanical ventilation (ACMV) systems. Institution of Engineers. [https://www.ies.org.sg/Tenant/C0000005/PDF%20File/Registry/SCEM/ACMV\(1\).pdf](https://www.ies.org.sg/Tenant/C0000005/PDF%20File/Registry/SCEM/ACMV(1).pdf). Accessed 24 Oct 2022
8. Seem J, House J, Kelly G, Klaassen C (2000) A damper control system for preventing reverse airflow through the exhaust air damper of variable-air-volume air-handling units. *HVAC&R Res* 6(2):135–148
9. Yu Y, Woradechjumroen D, Yu D (2014) A review of fault detection and diagnosis methodologies on air-handling units. *Energy Build* 82:550–562
10. Bruton K, Raftery P, O'Donovan P, Aughney N, Keane MM, O'Sullivan D (2014) Development and alpha testing of a cloud based automated fault detection and diagnosis tool for air handling units. *Automation in Construction*. <https://doi.org/10.1016/j.autcon.2013.12.006>. Accessed 24 Oct 2022
11. Kim J, Cai J, Braun JE (2018) Common faults and their prioritization in small commercial buildings. National Renewable Energy Laboratory. <https://www.nrel.gov/docs/fy18osti/70136.pdf>. Accessed 28 Mar 2022
12. Yoshida H (1996) Building optimization and fault diagnosis source book. In: *VAV air handling unit*, p 74. [http://www.iea-ebc.org/Data/publications/EBC\\_Annex\\_25\\_source\\_book.pdf](http://www.iea-ebc.org/Data/publications/EBC_Annex_25_source_book.pdf). Accessed 24 Oct 2022
13. Li T, Deng M, Zhao Y, Zhang X, Zhang C (2020) An air handling unit fault isolation method by producing additional diagnostic information proactively. <https://doi.org/10.1016/j.seta.2020.100953>. Accessed 24 Oct 2021
14. “OpenStudio,” Energy.gov, 28 Aug 2014. <https://www.energy.gov/eere/buildings/downloads/openstudio-0>. Accessed 24 Oct 2022
15. Cheung H, Braun JE (2016) Empirical modeling of the impacts of faults on water-cooled chiller power consumption for use in building simulation programs. *Appl Therm Eng* 99:756–764
16. Guglielmetti R, Macumber D, Long N (2011) OpenStudio: an open source integrated analysis platform. NREL. <https://www.nrel.gov/docs/fy12osti/51836.pdf>. Accessed 24 Oct 2022
17. Prototype building models. Building Energy Codes Program, 30 Oct 2021. <https://www.energycodes.gov/prototype-building-models>. Accessed 30 Oct 2022
18. Comstock MC et al, Experimental data from fault detection and diagnostic studies on a centrifugal chiller. In: *ASHRAE deliverable for research project 1043-RP fault detection and diagnostic (FDD) requirements and evaluation tools for chillers*, HL 99-18 Report #4036-1

19. Granderson J, Lin G (2019) Inventory of data sets for AFDD evaluation. Building Technology and Urban Systems Division Lawrence Berkeley National Laboratory
20. Azeem A et al (2022) Real-time harmonics analysis of digital substation equipment based on IEC-61850 using hybrid intelligent approach. *J Intell Fuzzy Syst* 42(2):741–754. <https://doi.org/10.3233/JIFS-189745>
21. Azeem A et al (2021) Design of hardware setup based on IEC 61850 communication protocol for detection & blocking of harmonics in power transformer. *Energies* 14(24):8284, 1–27. <https://doi.org/10.3390/en14248284>
22. Malik H, Mishra S (2017) Selection of most relevant input parameters using principle component analysis for extreme learning machine based power transformer fault diagnosis model. *Int J Electr Power Compon Syst* 45(12):1339–1352. <https://doi.org/10.1080/15325008.2017.1338794>
23. Malik H et al (2022) Data-driven hybrid approach for early fault detection of AHU using electrical signals. In: 2022 international power electronics conference (IPEC-Himeji 2022-ECCE Asia), Himeji, Japan, pp 1365–1371. <https://doi.org/10.23919/IPEC-Himeji2022-ECC53331.2022.9807260>
24. Malik H, Ahmad W, Kothari DP (2022) Intelligent data analytics for power and energy systems: advances in models and applications, 1st ed. Springer Nature, Berlin/Heidelberg, Germany. ISBN 978-981-16-6080-1
25. Malik H et al (2022) Power quality disturbance analysis using data-driven EMD-SVM hybrid approach. *J Intell Fuzzy Syst* 42(2):669–678. <https://doi.org/10.3233/JIFS-189739>
26. Fatema N et al (2022) Data driven intelligent model for quality management in healthcare. *J Intell Fuzzy Syst* 42(2):1155–1169. <https://doi.org/10.3233/JIFS-189779>
27. Fatema N, Malik H (2020) Data-driven occupancy detection hybrid model using particle swarm optimization based artificial neural network. In: Springer Nature book: Metaheuristic and evolutionary computation: algorithms and applications, under book series “Studies in computational intelligence”, pp 283–297. [https://doi.org/10.1007/978-981-15-7571-6\\_13](https://doi.org/10.1007/978-981-15-7571-6_13)
28. Fatema N et al (2019) Big-data analytics based energy analysis and monitoring for multi-story hospital buildings: case study. In: Springer Nature book: Soft computing in condition monitoring and diagnostics of electrical and mechanical systems, pp. 325–343. [https://doi.org/10.1007/978-981-15-1532-3\\_14](https://doi.org/10.1007/978-981-15-1532-3_14)
29. Fatema N et al (2019) Data driven intelligent model for sales prices prediction and monitoring of a building. In: Springer Nature book: Soft computing in condition monitoring and diagnostics of electrical and mechanical systems, pp. 407–421. [https://doi.org/10.1007/978-981-15-1532-3\\_18](https://doi.org/10.1007/978-981-15-1532-3_18)
30. Bist V et al (2022) A data-driven intelligent hybrid method for health prognosis of lithium-ion batteries. *J Intell Fuzzy Syst* 42(2):897–907. <https://doi.org/10.3233/JIFS-189758>

# Use of Solar Energy in Treatment of Pulp and Paper Industry Effluent with Hemp: An Experimental Study



Ambika Thakur, Deepak Juneja, and Yogyendra Narayan

**Abstract** The pulp and paper industries are one wastewater-intensive series around the world that produce a large quantity of wastewater. The effluent released from these industries is the major source of river pollution and aquatic pollution. This effluent consists of heavy metals, TSS, TDS, color, pH and a high number of BOD and COD. Different stages of papermaking produce different types of chemicals which are hazardous to health. Organic matter and suspended solids are considered as hazardous pollutants of the P&P industry. This paper is dealing with the experimental study of P&P industry effluent with hemp so that the desired results can achieve and effluent can safely discharge into rivers without impacting aquatic and environmental elements. The different treatment methods have been discussed in many research papers to treat the P&P industry wastewater and their remedial solutions, but the best result was given by the adsorption method of treatment as it was more versatile, effective, simple and economical in comparison to the other methods. Solar energy was tapped for the entire operation by 5 KW panels installed near the plant. After treatment, most of the parameters like pH, alkalinity, BOD, COD, TDS and TSS came in the range of Indian standards for effluent discharge.

**Keywords** Pulp and paper mills effluents · Water body pollution · Heavy metals · Adsorption · Treatment · Efficiency

---

A. Thakur · D. Juneja (✉)  
Department of Civil Engineering, Chandigarh University, Mohali, Punjab, India  
e-mail: [junejadeepash@gmail.com](mailto:junejadeepash@gmail.com)

A. Thakur  
e-mail: [ambika.e13703@cumail.in](mailto:ambika.e13703@cumail.in)

Y. Narayan  
Department of ECE, Chandigarh University, Mohali, Punjab, India  
e-mail: [yogendranarayan.cse@cumail.in](mailto:yogendranarayan.cse@cumail.in)

## 1 Introduction

Many industrial processes used around the world release large amounts of effluent into local water bodies and soils. These are the main source of contamination for aquatic life, public health and the environment [1]. The P&P industry is also considered to be one of the most polluting industries among them. The sudden increase in paper consumption increases the per capita demand as well as the number of pulp and paper industries, resulting in the generation of a large amount of wastewater. ASSOCHAM reported that the PPC of paper increased from 8.3 to 9.18 kg in 2009–2010 [2]. However, it is very low compared to the 350 kg per capita that was generated by several developed countries and 42 kg in China. Papermaking in India includes various methods, which are normally used in printing, bundling, typesetting and some exceptional papers. Paper for printing and typesetting comes in the form of copier paper, super printing paper, bond paper, creamy vellum paper, map litho paper (area and non-area size), covering the base paper and others. Bundling paper includes sheets, kraft paper, presentations and others. The different assortments are chromo paper/cardboard, craft paper/cardboard and others. In India, there are about 600 paper mills, twelve of which are real players and moreover widely acclaimed. In India, of all paper creations, 40% comes from hardwood and bamboo fiber, 30% comes from agricultural waste and 30% from reused materials [3]. The paper used for productions and newsprint checks to 2 million tons. 1.2 million tons of newsprint are produced and the rest is imported from various manufacturers [4]. This implies that around 40% of newsprint is acquired outside the country.

The papermaking practice uses a huge amount of water in the manufacturing processes, which is loaded into rivers and streams [5]. This wastewater from the pulp and paper industry contains a dark color, and an unusual state of BOD and COD due to the presence of lignin, chlorine compounds, sulfur compounds, TSS, TDS, etc. [6]. Most pulp and paper industries prefer the dilution method for wastewater discharge, which has serious environmental implications. Water bodies are the main springs that are used as the source of water for many practices. Contaminants inherent in pulp and paper waste streams include solid effluent, sediment, absorbable organic halides (AOX), chlorinated organic compounds, and chemical oxygen demand (COD) and biological oxygen demand contaminants (BOD) [7]. The dark color of pulp and paper industry effluents inhibits the photosynthesis process in the water and thus decreases the degradation process due to oxygen depletion. These contaminants are the main cause of pollution of water bodies. Water bodies are polluted and can be hazardous to aquatic and human life [6]. Thus, it is very important to develop economical techniques for the treatment of discharged effluents.

Use of solar power for all the electric operations helps in sustainable growth and also helps in optimizing the economic operations of the plant. Use of hemp for treatment of effluent also contributes to the green economy.

The paper first discusses the various parameters of influent (TSS, TDS, alkalinity, pH, BOD, COD, etc.) and then the parameters of effluents after treatment with hemp.

The parameters were found to be in the range of Indian standards for discharge into water bodies.

### ***1.1 Wastewater Creation in Pulp and Paper Processes and Its Qualities***

The quality of wastewater produced from various pulp and paper industries is different because of different processes adopted for manufacturing of paper [8]. So, two industries cannot have identical wastewater characteristics. Pulp and paper industry are generally having physical, chemical and biological characteristics. Suspended turbidity, black color, odor are the basic physical characteristics; TDS, TS, DO, BOD, COD, TOC, sulfur and its oxides, nitrogen and its oxides, toxic metals, etc., are the chemical characteristics of wastewater. If any pathogen or microorganism is present in water, then these are characterized under biological characteristics. Industrial wastewater is generally having physical and chemical characteristic. The major process of paper making, Digester process, generates black liquor and gland cooling water which consist of high amount of BOD in the range of 13,000 mg/l and other contaminants. Some of the processes and type of wastewater generated from pulp and paper industry are listed below in Table 1. These all processes show high amount of BOD and COD which are the major contaminant of pulp and paper industry wastewater, and its treatment is very important before its disposal in any water body or on land.

Characteristics of pulp and paper mill also depend upon the type and capacity of mill also. Table 2 is representing the characteristics of small mill and large paper mill effluent. Table 3 is representing pulp and paper pollution distribution from different sections. Ministry of Environment and forest has made some legislative rules for disposal of industrial effluent into natural water bodies. Indian standard values which are acceptable for discharge into rivers are listed in Table 4.

### ***1.2 Treatment of Pulp and Paper Industries' Wastewater***

Industrial wastewater is generally treated in three stages; physiochemical treatment, biological treatment and advance treatment. Physiochemical forms are utilized to evacuate suspended solids, colloidal pollutions, poisonous mixes, skimming matters and shading expulsion. Generally, screening, grit removal, sedimentation, coagulation and flocculation, ultrafiltration, ozonation and chlorination are the treatments that are used in primary, secondary and tertiary treatments. Ultrafiltration is the process in which great efficiency can achieved, but its cost is high. So generally, ultrafiltration process is avoided in P&P industrial wastewater [9]. The presence of lignin and its subsidiaries contributes dim dark shading to wastewater which is



**Table 1** Type of wastewater generated in various pulp and paper processes and their chemical characteristics

Process	Type of wastewater generated	Parameters					
		pH	TS (mg/l)	SS (mg/l)	BOD <sub>5</sub> (mg/l)	COD (mg/l)	N (mg/l)
Digester house	Black liquor, gland cooling water	11.6	51,583	23,319	13,088	38,588	–
Pulping	Unbleached decker wash	10	1810	256	360	–	–
Bleaching	1. Wastewater of low pH (chlorinated)	2.5	2285	216	140	–	–
	2. Wastewater with high pH (caustic process extraction) chlorolignin	10.1	–	37–74	128–84	1124–1738	2
Kraft mill	Black liquor	8.2	8260	3620	–	4112	350
Sulfite mill	Black Liquor	2.5	–	–	2000–4000	4000–8000	–
Paper making	White water includes fibers, talc and sizing agents	7.8	1844	760	561	953	11

Omid Ashrafi et al. 2015; Muna Ali, T.R. Sreekrishnan et al. 2001

**Table 2** Characterization of pulp and paper effluent

Parameters	Small mill	Large mill
Flow per day	330 m <sup>3</sup> /ton	222 m <sup>3</sup> /ton
pH	8.2–8.5	8.5–9.5
TS (mg/l)	–	4410
TSS (mg/l)	900–2000	3300
COD (mg/l)	3400–5780	716
BOD (mg/l)	680–1250	155

Source Table 10.1 Wastewater treatment written by M.N. Rao and A.K. Datta

the primary explanation behind high estimation of BOD and COD [10] audited the treatability of the Pulp and paper factory wastewater and execution of accessible treatment forms and in the wake of contrasting all the treatment methods, and he recommended that the joined procedures of both anaerobic and high-impact forms

**Table 3** Pulp and paper pollution distribution from different sections

Parameter	Plant size	Digester section	Bleaching section	Paper mill Section
Flow %	Small	45.5	16.2	10.8
	Large	9.75	27.8	16.7
BOD %	Small	66	18.4	2
	Large	32.5	32.5	1.43
SS %	Small	60	14.5	7.75
	Large	3	1.35	3.4

Source Table 10.2 wastewater treatment by M.N. Rao and A.K. Datta

**Table 4** Pulp and paper industrial effluent standards for discharge into rivers

Parameter	Limit (if specified)
BOD	+
	30 mg/L
COD	+
	350 mg/L
pH	+
	6.5–8.5
Chlorides	*
	1000 mg/L—surface waters and 600 mg/L—irrigation
Phenol	1000 µg/L*
Mercury	*
	0.01 mg/L
Suspended solids	+
	100 mg/L

\* General standard for pollutant discharge, Part A, Schedule 4, MOEF, 1993

+Minimum National Standards (MINAS) for large pulp and paper mills with chemical recovery

are successful in the expulsion of natural poisons. Fungal treatment, ozonation, coagulation and chemical oxidation are good for the color removal, whereas adsorption, ozonation and membrane filtration methods are recommended for the removal of the chlorinated compounds and adsorbable organic halides. Kumar et al. [11] studied the heavy metals (Zn and Pb) absorption by water hyacinth for 20 days. The technique is basically called as phytoremediation. The water hyacinth was collected, cleaned, grown and maintained in the laboratory conditions along with the effluent sample. They found that absorption ability of the plant depends on the duration, concentration of the effluent sample and the heavy metal ions' size. The plant absorbed more metal concentration at the low effluent concentration and vice versa. The reason for decreasing uptake rate by plant at the higher concentration of effluent was due to the toxicity of the effluents. The maximum uptake efficiencies for the duration (0, 5, 10,

15 and 20) in days and concentration of effluent in percentages (0, 5, 15, 20 and 25) were Pb (80.3%) and Zn (73.4%) [12]. They had done treatment of paper and board mill effluent using combined technique. The biological fed batch reactor (FBR) and sequence batch reactor (SBR) was followed by the coagulation and sand filtration. The FBR removed 93% COD and 96.5% BOD, whereas SBR removed 90% COD and 92% BOD. The toxicity of effluent was checked by exposing the effluent and the treated water to the fish for 72 h. The untreated wastewater was found toxic, whereas treated wastewater was not toxic for fishes [13]. They examined the reduction of color and phenolic compounds from kraft pulp industry. The treatment was done by ozonation and combined with some pretreatment. The single ozonation treatment reduces 70% color and phenolic compounds at pH of 3, whereas chemical coagulation/activated carbon followed by ozonation reduces greater than 90% at low pH. Activated carbon followed by ozonation reduces 72% even at high pH (10) [14]. They had reviewed the different techniques used for removal of heavy metal removal like evaporation, precipitation, ion exchange, etc. But those methods have disadvantages like toxic sludge production, etc. The adsorption technique was considered to be more advantageous because it is versatile, easily available and economical [15–17]. They used mixed adsorbent of coconut shell and silica gel to remove the organic pollutants from the pulp and paper mill. The batch method was used to test the adsorbent ability of adsorption with respect to contact time, pH and dosage amount. The most favorable result was obtained at the contact time of 45 min, dosage of 50 g/l and pH of 2. The efficiencies of pollutants removed were turbidity (72.51%), COD (88.6%), color (91.92%) and total carbon (92.5%). After getting the review from all the previous researches, one conclusion was made that adsorption technique is the best treatment method for pulp and paper industry effluent which gives good results in removal of TDS, BOD, COD, color and removal of toxic matter.

## 2 Material and Methodology

### 2.1 General

The treatment of P&P industry wastewater was done by an adsorption process. The hemp material used as an adsorbent and it is locally available. The industrial wastewater was taken from the—Kuantum Paper Limited|| industry located in the Saila Khurd area of Hoshiarpur district, Punjab, India. The physiochemical properties of the samples were tested by standards' methods. All the experiments were performed inside the environmental laboratory of Civil Engineering Department, LPU, Punjab. The hemp was freshly collected from the field. After collection, it was cut into small pieces of size around (1–2) cm and washed many times with the tap water and dried in the sunlight. After drying, the hemp was crushed into powder form with the help of crusher (grinder). The grounded hemp was again washed with tap and distilled water. The washed hemp powder was collected with the sieve and put into the oven for 24 h

at 105 °C in the oven dry. Later, it was cooled at room temperature and used as an adsorbent for adsorption process. The physical and chemical properties of hemp are shown in Tables 5 and 6. Wastewater samples taken from pulp and paper industry before and after treatments were analyzed, and their physiochemical characteristics are listed in Table 7. Power requirement for the entire plant is generated through 5 KW solar panels installed near the plant. (Fig. 1) It is a 10-panel plant with each panel generating half of a kilowatt. This is an online arrangement, so there is no need of batteries. All the powers generated are passed to the grid through a net meter. All power requirements are also through grid so there is no intermittency in operation. The online system offers many advantages. The main advantage is that the power supply is uninterrupted even on a cloudy day. Only one electricity bill comes in a year if there is net consumption of power. No money is credited to account in case there is net production. This helps in environment-friendly generation of electricity and also helps in tiding over power scarcity.

**Table 5** Physical properties of hemp

Color	Yellowish gray to deep brown
Length	4–7 feet
Tensile strength	Very strong fiber
Elastic recovery	Poor
Elongation at break	Easily stress
Moisture regain percentage	12%, i.e., > cotton and linen
Effect of heat	Excellent resistance to degradation heat
Effect of sunlight	Ability to prevent bad effect of sunlight
Luster	Highly bright

Source Textilefashion.com

**Table 6** Chemical properties of hemp

Effect of acid	Acid break the hemp fiber into small parts
Effect of alkali	Resistance to alkali
Effect of organic solvent	Not effected
Effects of insects	Not attacked by the crop insects like beetles, etc.
Effect of microorganism	Mostly attacked fungi and bacteria
Ability to dye	Not suitable to dye

Source textilefashionstudy.com

**Table 7** Physiochemical properties of influent and effluent samples and Indian standards for effluent discharge

S .no.	Parameters	P&P industry influent		P&P industry effluent		Indian standards for effluent discharge (BIS)		
1	pH		6.62		7.38		5–9	
2	Alkalinity		116.66		280		200	
3	Turbidity		64	NTU	20	NTU	10	NTU
4	Color		0.44	Nm	0.55	nm	–	
5	TSS		1500	mg/l	333	mg/l	100	mg/l
6	TDS		1,110,833	mg/l	978,000	mg/l	2100	mg/l
7	Conductivity		2.1		2.27		–	
8	COD		4000	mg/l	1984	mg/l	350	mg/l
9	BOD	5 day	66.66	mg/l	46.66	mg/l	30	mg/l
10	DO		10	mg/l	7	mg/l	–	
10	Sulfates		104	NTU	125	NTU	–	
11	Iron ion		5.26	ppm	4.21	Ppm	–	
12	Chloride		3126.69	mg/l	2789.20	mg/l	5	mg/l

**Fig. 1** Power plant installed at the plant site

## 2.2 Methodology

### 2.2.1 The Procedure of “Batch Experiment”

The adsorption was done by taking known amount of effluent solution filled into the conical flask having definite weighed amounts of the hemp of varying pH's (2, 4, 6 and 8) and adsorbent dosage of (0.5, 1, 1.5 and 2)g. The conical flasks containing

the mixture solution of adsorbent and adsorbate sample was shaken by an orbital shaker which was set to 150 rpm speed at room temperature. The shaking was done for 2 h, and after that, the mixtures was filtered through Whatman filter paper of 125 mm diameter to remove the suspended particles. Afterward, the physiochemical parameters of the filtered effluents were tested again to give the comparison of the result in laboratory. The whole adsorption experiment was done by the batch method. The adsorption was mainly done for the four physiochemical parameters of the industry effluents, namely **color**, **TSS**, **TDS** and **COD** by varying the contact time, dosage of adsorbent and pH of the industrial effluent solution. All the powers used in this operation are generated from solar power panels installed at rooftop of the plant.

#### Variation of Contact Time

The contact time was varied from (15, 30, 45 and 60) minute. It was done by adding fixed amount of hemp with the fixed amount of effluents in a 250 ml conical flask and mixed in the orbital shaker for 2 h at the speed of 150 rpm. After mixing, it was left to settle for (15, 30, 45 and 60) minute and then checked its efficiency. The best contact time was then used for dosage effect calculation.

#### Variation of Dosage

The dosage of hemp was varied from (0.5, 1, 1.5 and 2) g. The given varied amount of hemp was taken in four conical flasks with fixed amount of paper industry effluents. It was mixed in the orbital shaker for 2 h at the speed of 150 rpm and let it settle for the time we got in the experiment of contact time. The best dosage was then used for the pH effect calculation.

#### Variation of pH

The effluent's pH in the experiments was varied as (2, 4, 6 and 8). The pH was varied in the solution by adding required quantity of acid (HCL) and base (NaOH) solutions which was available at the laboratory. The effluent of desired pH at constant dosage was mixed and rotated at 150 rpm speed at room temperature for a contact time of 2 h.

### 3 Experimental Result

After samples' collection and testing, laboratories result for tested samples is given below.

As per the Indian standards, effluent discharge standards should be the same as mentioned in Table 7.

## 4 Results and Discussion

After physiochemical analysis of effluent generated from Industry, we came to know that these standards are not achieved properly. It required further treatment which was adopted in this research with the help of hemp. This material was used as an adsorbent which has the capacity to absorb impurities and purify the water impurities. These tests were performed only for three main parameters of wastewater physiochemical characteristics. These parameters were: color, TSS and COD. The following results are discussed below:

### 4.1 Changes After Treatment with Hemp

The graphs in Fig. 2 is showing the effect of time of contact and dose variation on color. The trend of the graph is showing that as the time of contact and hemp dose are increased, the color is removed from the effluent sample and maintained less value of color-balanced pH value 6. After this value, if the time of contact and hemp dose is increased, the value of color starts increasing and it also increases the pH of the sample. The pH value of effluent should be in-between 6 and 8 according to IS-10500. In this study, the pH value is fixed 6. So, the optimum amount of hemp dose and contact time at pH 6 are 1.5 g and 45 min, respectively, at which color value is obtained as 400 nm.

The above graph in Fig. 3 is representing total suspended solid variation when time of contact and dose change. Graph trend is showing that as we increase time of contact and dose, the value of TSS starts decreasing but in respect of pH increasing. At pH 6, the time of contact is 45 min, dose amount is 1.5 mg and TSS value is 110 mg/l. According to IS-10500, the value of TSS should be in-between 500 and 1000 mg/l.

The graph in Fig. 4 is showing the variation of COD and it is found that with increase in dose, the value of COD is decreasing, but after certain point, it starts increasing. The optimum result found to be at pH 6 is 450 mg/l and the amount of hemp dose is 1.5 mg. In this study, only three parameters were analyzed. The further studies will include effect of hemp on other parameters also.

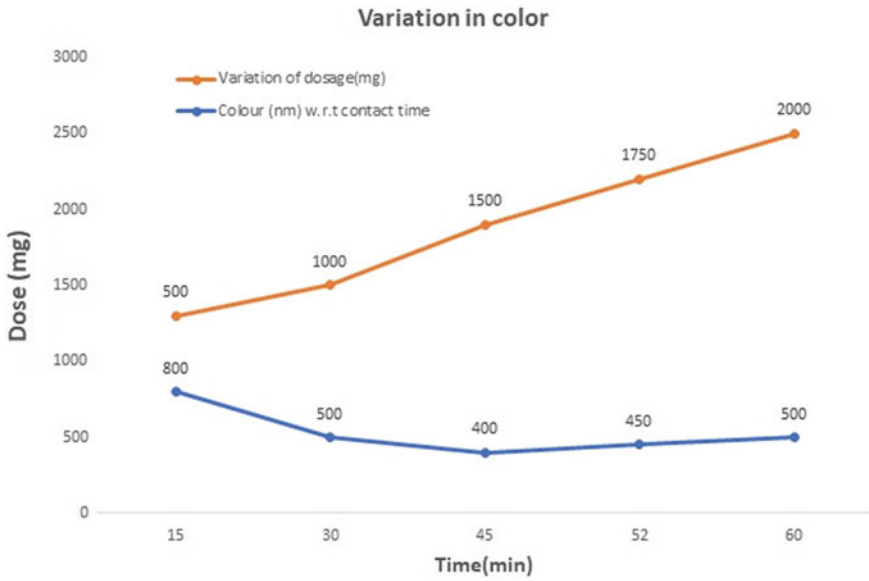


Fig. 2 Graph showing the color change in effluent with hemp after varying times of contact and dosage

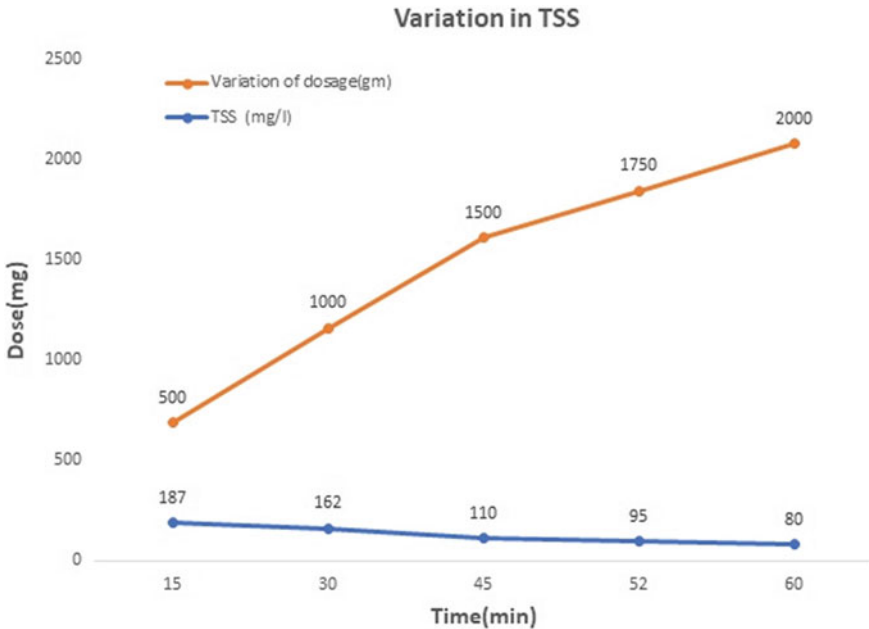
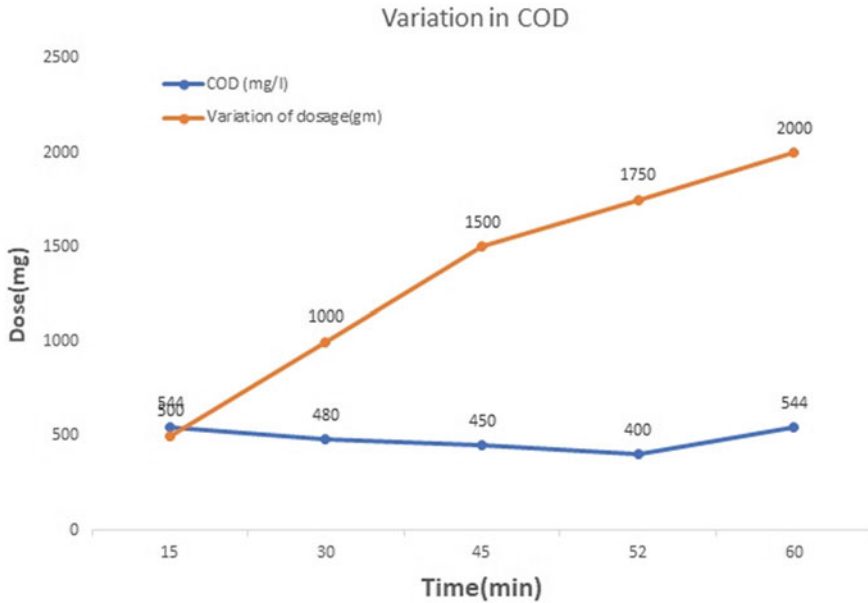


Fig. 3 Graph showing TSS removal with hemp treatment and effect of variation in contact time and dosage





**Fig. 4** Graph showing COD removal with hemp treatment and effect of variation in contact time, dosage and pH

## 5 Conclusion

The result of the experiments shows that we can add only particular amount of hemp in effluent for its treatment as after a certain point it starts to change the required results. From the above graphs, it was concluded that the optimum dose required for effluent treatment for one liter of the amount of effluent is 1.5 mg and its contact period should be 45 min. The addition of dose also changes the pH of the sample, so the pH maintained for this contact period was between 6 and 7. Hemp can be used as an absorbent and makes sure it should be dried properly before its use. Effluent from the paper and pulp industry can be safely discharged to water bodies after treating with hemp. There is an optimum dosage for treatment which was found in the experimental study. The absorption technique is best suited for the treatment of effluent. Discharging of effluent into water bodies is harmful for aquatic life and severely deters the various parameters of water. Water becomes unfit for irrigation or for public supplies. Treatment of effluent with hemp restores the quality parameters for water. In the future, we can research more adsorbent materials which can be find very effective for the treatment of effluent coming from pulp and paper industry and contribute for reduction in water pollution.

## References

1. Bhatnagar A (2015) Assessment of physicochemical characteristics of paper industry effluents. *Rasayan J Chem* 8(1):143–145
2. Grötzner M, Melchior E, Schroeder LH et al (2018) Pulp and paper mill effluent treated by combining coagulation-flocculation-sedimentation and fenton processes. *Water Air Soil Pollut* 229:364
3. Verma VK, Gupta RK, Rai JPN (2005) Biosorption of Pb and Zn from pulp and paper industry effluent by water hyacinth (*Eichhornia crassipes*). *J Sci Ind Res* 64:778–781
4. Gautham SK, Dhaneesh VV, Manu B (2018) Fenton's treatment of pulp and paper mill effluent. In: Singh V, Yadav S, Yadava R (eds) *Water quality management. Water science and technology library*, vol 79. Springer, Singapore
5. Medhi UJ, Talukdar AK, Deka S (2011) Impact of paper mill effluent on growth and development of certain agricultural crops. *J Environ Biol* 32:185–188
6. Gomathi S, Cibichakravarthy V, Ramanathan B, Sivaramaiah Nallapeta A, Ramanjaneya V, Mula R, Jayasimha Rayalu D (2012) Decolorization of paper mill effluent by immobilize cells of PHANEROCHAETE CHRYSOSPORIUM. *Int J Plant Animal Environ Sci* 2(1):141–146
7. Reddy KV, Vijayalakshmi T, Giri A, Bhavani AJG (2013) Effects of paper industry effluents on physicochemical and biological properties of soil. *Int J Innov Res Sci Eng Technol* 2(8):72–79
8. Afzal M, Shabir G, Hussain I, Khalid ZM (2008) Paper and board mill effluent treatment with the combined biological–coagulation–filtration pilot scale reactor. *Bioresour Technol* 99:7383–7387
9. Maheshwari R, Rani B, Saxena A, Prasad M, Singh U (2012) Analysis of effluents released from recycled paper industries. *J Adv Sci Res* 3(1):82–85
10. Pokhrel D, Viraraghavan T (2004) Treatment of pulp and paper mill wastewater: a review. *Sci Total Environ* 333(1–3):37–58
11. Kumar P, Kumar S, Bhardwaj NK, Choudhary AK (2011) Advanced oxidation of pulp and paper industry effluent. In: *International conference on environmental and agriculture engineering IPCBEE*, vol 15
12. Kumar P, Teng TT, Chand S, Wasewar KL (2011) Treatment of paper and pulp mill effluent by coagulation. *World Acad Sci Eng Technol Int J Chem Mol Eng* 5(8):729–734
13. Kesalkar VP, Khedikar IP, Sudame AM (2012) Physico-chemical characteristics of wastewater from Paper Industry. *Int J Eng Res Appl* 2(4):137–143
14. Sharma MC, Baxi S, Sharma KK, Singh M, Patel S (2014) Heavy metal ions levels and related physicochemical parameters in soils in the vicinity of a paper industry location in Nahan Area of Himachal Pradesh. *J Environ Anal Toxicol* 4(6):1358
15. Shivayogimath CB, Chidambarjoshi S (2015) Removal of organic pollutants from paper and pulp effluent using mixed adsorbents. *Int J Adv Sci Eng Technol* 3(3):1248
16. Ahmad MW et al (eds) (2022) *Intelligent data analytics for power and energy systems*. Springer, Singapore, p 641. <https://doi.org/10.1007/978-981-16-6081-8>
17. Tomar A et al (eds) (2022) *Proceedings of 3rd international conference on machine learning, advances in computing, renewable energy and communication: MARC 2021*, vol 915. Springer, New York, p 781. <https://doi.org/10.1007/978-981-19-2828-4>

# Design of Radar-Based Portable System for Monitoring of Human Vital Signs with Renewable Energy Resources



Pushparaj, Amod Kumar, and Garima Saini

**Abstract** This paper presents the design of a portable radar-based system for non-invasive monitoring of human vital signs, including heart rate (HR) and respiratory rate (RR) signals. The system is user-friendly and applicable in various settings, such as hospitals, clinics, and homes. The design process involves several stages, including submodules, system requirements identification, design, prototype development, data collection and analysis, optimization, and validation. It measures physiological signals, such as heart rate, breathing rate, and body movement, using electromagnetic waves. To minimize battery replacements or charging, the system integrates renewable energy systems like solar power or kinetic energy capture. Accuracy evaluation of the system is performed by collecting and analyzing data on vital signs, including heart rate, respiratory rate, and body movement, from a group of volunteers. The proposed system provides a sustainable, portable, and non-contact solution for monitoring HR and RR signals, which can enhance the accuracy of diagnosis and treatment in various biomedical applications.

**Keywords** Portable · Radar system · Heart rate (HR) · Respiratory rate (RR) signals · Non-contact · Electromagnetic waves · Renewable energy systems · Accuracy evaluation · Biomedical applications · Diagnosis and treatment

---

Pushparaj (✉) · A. Kumar · G. Saini  
National Institute of Technical Teachers Training and Research, Sector-26, Chandigarh, India  
e-mail: [pushprajpal@gmail.com](mailto:pushprajpal@gmail.com)

A. Kumar  
e-mail: [csioamod@yahoo.com](mailto:csioamod@yahoo.com)

G. Saini  
e-mail: [garima@nitttrchd.ac.in](mailto:garima@nitttrchd.ac.in)

# 1 Introduction

The design of a radar-based portable system for monitoring vital signs [1] in health-care applications with a renewable energy management device offers a new approach to non-invasive and continuous monitoring of human vital signs. This system utilizes radar technology to detect and measure small movements of the chest and heart, allowing for accurate calculation of vital signs such as heart rate (HR) and respiratory rate (RR).

In addition, the use of a renewable energy management device [2–4] ensures that the system is powered efficiently and sustainably. This device manages the energy consumption of the system, optimizes the use of available energy sources such as solar panels or wind turbines, and ensures that the system operates within safe and efficient limits. This type of system has significant potential to improve patient outcomes and quality of care in a variety of settings, including hospitals, clinics, and even in the home. By providing continuous and non-invasive monitoring of vital signs, medical professionals [5] can quickly detect and respond to changes in a patient's condition, leading to earlier interventions and better outcomes.

Biomedical applications have had a transformative impact on healthcare, particularly in the realm of non-contact human monitoring of vital signs. By harnessing cutting-edge technologies, healthcare professionals can now gather crucial health data without the need for physical contact or invasive procedures. This non-contact approach enhances patient comfort and compliance, reduces the risk of infections, and provides a more convenient monitoring experience.

One prominent non-contact technology utilized in monitoring vital signs [6] is thermal imaging. By capturing infrared radiation emitted by the human body, thermal cameras can measure body temperature with remarkable accuracy from a distance. This capability has been particularly valuable during the COVID-19 pandemic, enabling quick and contactless screening of individuals for fever, a common symptom of the virus.

Another non-contact method employed in vital sign monitoring is radar technology. Radar systems can detect subtle movements caused by respiration and heartbeats, allowing for precise measurement of respiration rate and heart rate without the need for any physical attachments or sensors. This non-intrusive approach is especially beneficial for patients who require continuous monitoring, such as those in intensive care units or individuals with chronic respiratory conditions [7].

Computer vision is yet another powerful tool used in non-contact human monitoring of vital signs. By analyzing video footage or images, sophisticated algorithms can extract vital sign information, such as heart rate, by observing subtle color changes in the face or other regions of interest. This non-contact approach is particularly useful in situations where direct physical contact may not be feasible or desirable, such as monitoring newborns, patients with sensitive skin, or individuals during sleep.

The real-time, continuous monitoring enabled by non-contact technologies offers significant advantages in detecting and responding to health emergencies promptly. Healthcare professionals can receive immediate alerts if there are any deviations or abnormalities in vital signs, allowing for timely intervention and improved patient outcomes [8].

Furthermore, non-contact human monitoring of vital signs has proven invaluable in scenarios where close physical proximity could pose risks, such as infectious disease outbreaks. By minimizing direct contact and reducing the potential for cross-contamination, these technologies enhance infection control measures and protect both patients and healthcare providers.

In summary, biomedical applications have paved the way for non-contact human monitoring of vital signs, revolutionizing healthcare. Through the use of thermal imaging, radar technology, and computer vision, healthcare professionals can gather crucial health data without physical contact or invasive procedures. This approach enhances patient comfort, improves infection control, and enables real-time, continuous monitoring for early detection of health issues, ultimately leading to better patient care and outcomes.

In the field of biomedical applications, radar-based portable systems have emerged as a promising technology for monitoring vital signs. These systems utilize radar sensors to detect and measure subtle movements caused by respiration and heartbeats, offering a non-contact approach that eliminates the need for physical attachments or invasive procedures. The portability of these systems allows for monitoring to be carried out in various settings, including hospitals, clinics, and even in remote or resource-limited areas.

One key advantage of radar-based portable systems is their ability to provide continuous, real-time monitoring of vital signs. By capturing and analyzing the radar signals reflected off the human body, these systems can accurately measure respiration rate and heart rate and even detect irregularities or anomalies. This continuous monitoring capability is especially crucial in critical care settings, where immediate intervention can be initiated in response to sudden changes in vital signs.

Furthermore, integrating a renewable energy management device into radar-based portable systems brings additional benefits. This device utilizes renewable energy sources, such as solar or wind power, to provide the necessary energy for the system's operation. By harnessing sustainable energy, these systems become more environmentally friendly and reduce dependence on conventional power sources. This is particularly advantageous in remote or underserved areas with limited access to reliable electricity grids, enabling vital sign monitoring to be conducted without significant energy constraints [9].

The combination of radar-based sensing technology with a renewable energy management device also enhances the system's portability and versatility. With a self-sustaining power source, the system can be easily transported and deployed in various locations, including field hospitals, disaster areas, and rural communities. This capability extends the reach of vital sign monitoring, ensuring that individuals in remote or resource-constrained regions can receive quality healthcare services.

Moreover, the use of renewable energy in these systems contributes to sustainability efforts within the healthcare sector. By reducing reliance on fossil fuel-based energy, the environmental impact is minimized, resulting in a greener and more sustainable healthcare infrastructure. This aligns with the growing recognition of the importance of sustainable practices in healthcare to mitigate climate change and promote environmental stewardship [10].

In this paper, we will discuss the design and implementation of a radar-based portable system for monitoring vital signs in biomedical applications with a renewable energy management device. We will explore the technical details of the system, including the radar technology used, the energy management device, and the feedback control loop used to optimize the system's performance. We will also discuss the potential applications of this system in various healthcare settings and the benefits it can bring to patients and healthcare providers.

### ***1.1 Human Vital Sign HR and RR Measurement***

Human vital signs, such as heart rate (HR) and respiratory rate (RR), are important indicators of a person's overall health and well-being. HR refers to the number of times the heart beats per minute, while RR refers to the number of breaths taken per minute. These vital signs are often used by medical professionals to diagnose and monitor various health conditions, such as cardiac and respiratory diseases.

Human vital signs, such as heart rate (HR) and respiratory rate (RR), are fundamental indicators of overall health and well-being. Heart rate refers to the number of times the heart beats per minute, reflecting the efficiency of the cardiovascular system. It is influenced by factors like physical activity, stress, and age. A normal resting heart rate for adults ranges from 60 to 100 beats per minute, although it may vary depending on individual characteristics. Deviations from the normal heart rate can indicate underlying medical conditions or physiological stress.

Respiratory rate, on the other hand, measures the number of breaths taken per minute and reflects the efficiency of the respiratory system. It is influenced by factors like exercise, emotions, and medical conditions. The average resting respiratory rate for adults is typically between 12 and 20 breaths per minute, but it can vary depending on age, health status, and other factors. Abnormal respiratory rates can indicate respiratory distress or respiratory disorders, such as asthma or pneumonia.

Monitoring heart rate and respiratory rate plays a crucial role in various healthcare settings. In clinical settings, healthcare professionals routinely assess these vital signs to evaluate a patient's overall health, response to treatment, or identify potential complications. In critical care units, continuous monitoring of heart rate and respiratory rate is particularly important for early detection of deteriorating conditions and prompt intervention [11].

Furthermore, monitoring heart rate and respiratory rate has extended beyond clinical settings with the advent of wearable devices and mobile health applications. These technologies allow individuals to track their vital signs in real-time and gain insights into their health and fitness levels. This self-monitoring approach empowers individuals to make informed decisions regarding their lifestyle, exercise routines, and overall well-being.

Moreover, advancements in technology have facilitated the development of non-contact methods for monitoring heart rate and respiratory rate. This includes the use of optical sensors, such as photoplethysmography (PPG), which measure changes in blood volume by shining light onto the skin. These non-contact approaches provide convenience and reduce patient discomfort, making them suitable for various applications, including remote patient monitoring and telemedicine [12].

In summary, heart rate and respiratory rate are essential vital signs that provide valuable information about an individual's health and well-being. Monitoring these parameters is crucial in clinical settings to assess patient health, guide treatment decisions, and detect early signs of deterioration. Additionally, wearable devices and non-contact technologies have enabled individuals to monitor their vital signs in real-time, promoting self-awareness and facilitating proactive healthcare management. As technology continues to advance, the monitoring of heart rate and respiratory rate will continue to play a vital role in maintaining and improving human health.

Traditionally, the measurement of heart rate (HR) and respiratory rate (RR) relied on manual methods, requiring individuals to physically count the pulse or breaths per minute. While effective, these manual measurements can be time-consuming and prone to human error. However, thanks to advancements in technology, automated methods for measuring HR and RR have gained widespread adoption.

Wearable devices, such as smartwatches and fitness trackers, have become increasingly popular for monitoring vital signs, including HR and RR. These devices use optical sensors or electrodes to detect changes in blood flow or electrical signals, providing continuous and real-time measurements. By leveraging sophisticated algorithms, wearable devices can accurately track HR and RR, allowing users to monitor their health and fitness levels conveniently. Furthermore, these devices often come with accompanying mobile applications that provide insights, trends, and personalized recommendations based on the recorded data [13].

In medical settings, more advanced devices are employed to measure HR and RR. For instance, electrocardiogram (ECG) devices are used to capture the electrical activity of the heart, enabling precise measurement of HR and detecting any abnormalities in cardiac rhythm. Pulse oximeters, another medical-grade device, combine a sensor placed on the fingertip or earlobe with infrared light to measure both HR and blood oxygen saturation levels. These devices provide accurate and reliable measurements, making them indispensable in clinical settings for diagnosing and monitoring various cardiovascular and respiratory conditions.

The integration of automated methods for HR and RR measurement brings numerous benefits. These methods provide objective and consistent measurements, minimizing the risk of human error associated with manual counting. The continuous monitoring capability of wearable devices allows for the detection of subtle changes

in vital signs that might go unnoticed during sporadic manual measurements. Additionally, the data collected from these automated devices can be stored, analyzed, and shared with healthcare professionals, supporting better diagnosis, treatment planning, and disease management [14].

In summary, the advent of automated methods for measuring HR and RR has transformed the way these vital signs are monitored. Wearable devices offer convenient and continuous tracking, empowering individuals to take charge of their health. Meanwhile, medical-grade devices like ECG and pulse oximeters provide highly accurate measurements for clinical use. With technology playing a pivotal role, automated HR and RR measurements offer greater precision, ease of use, and data insights, contributing to improved healthcare outcomes and personalized patient care.

In this paper, we will discuss the design and implementation of a radar-based portable system to monitor human vital signs, specifically HR and RR signals, for biomedical applications. The system will be designed to be portable and powered by a renewable energy management and control system, allowing for continuous and remote monitoring of vital signs in a variety of settings, including hospitals, clinics, and even in the home [15].

## ***1.2 Vital Sign Measurement Methods***

This measurement can be broadly classified into two categories: contact-based and non-contact-based methods.

**Contact-based methods:** Contact-based methods [16] for measuring vital signs require physical contact with the body through the use of sensors or devices. These methods provide accurate and precise measurements and are commonly used in clinical settings. Thermometers are contact-based devices used to measure body temperature. They can be placed under the tongue, in the ear, or on the forehead to obtain temperature readings. Blood pressure measurement involves using a blood pressure cuff wrapped around the arm, which inflates and deflates to measure the pressure exerted by the blood against the arterial walls.

Electrocardiogram (ECG) sensors are placed on the chest to measure the electrical activity of the heart. This method provides detailed information about heart rate, rhythm, and any abnormalities in the heart's electrical patterns. Respiratory sensors, on the other hand, are placed on the chest or nose to measure breathing rate and depth, providing insights into respiratory function and detecting any irregularities.

Blood glucose meters are contact-based devices used to monitor blood glucose levels in individuals with diabetes. A small sample of blood obtained from a finger prick is placed on a test strip, and the meter provides an instant reading of blood glucose levels.



Contact-based methods offer precise and reliable measurements, making them essential in diagnosing and monitoring various health conditions. However, they may be less convenient and require some level of patient cooperation and involvement. Nonetheless, advancements in technology have led to the development of more user-friendly and comfortable contact-based devices, improving the overall patient experience.

**Non-contact-based methods:** Non-contact-based methods [17] for measuring vital signs offer the advantage of not requiring physical contact with the body. These methods utilize various technologies to remotely measure vital signs by detecting changes in physical properties of the body or its surroundings.

Infrared thermometers are non-contact devices that measure temperature by detecting the thermal radiation emitted by the body. These thermometers capture the infrared radiation and convert it into temperature readings, making them convenient for quick and contactless temperature measurements, especially in large-scale screenings.

Pulse oximeters are another non-contact method used to measure oxygen saturation. These devices emit light through a body part, such as a finger or earlobe, and measure the amount of light that is absorbed by the oxygen-carrying hemoglobin in the blood. By comparing the absorbed light with the emitted light, pulse oximeters can determine the oxygen saturation level, providing valuable information about respiratory function and overall oxygen levels in the body.

Doppler radar is a non-contact technology that detects changes in the frequency of radio waves reflected off the body. This method can be used to measure heart rate and respiratory rate without any physical contact. By analyzing the changes in frequency caused by the movement of the body, Doppler radar modules can provide real-time and accurate measurements of vital signs.

Non-contact-based methods offer several advantages, including convenience, speed, and reduced risk of cross-contamination. These methods are particularly useful in situations where close physical proximity may pose risks, such as during infectious disease outbreaks or when monitoring individuals with compromised immune systems. Additionally, non-contact methods allow for continuous monitoring without causing discomfort or disturbance to the individual.

As technology continues to advance, non-contact-based methods for measuring vital signs are becoming more sophisticated and accessible. These methods have the potential to revolutionize healthcare by providing efficient and accurate monitoring solutions that enhance patient comfort and improve overall healthcare delivery.

Both contact-based and non-contact-based methods for measuring vital signs have their own distinct advantages and limitations, and the selection of a particular method depends on the specific application and context.

Contact-based methods generally offer high accuracy and precision in measuring vital signs. They allow for direct physical interaction with the body and provide reliable measurements. These methods, such as thermometers, blood pressure cuffs, and ECG sensors, are commonly used in clinical settings where accuracy is crucial for diagnosis, treatment, and monitoring of patients. Contact-based methods also tend to be well-established and have a long history of reliable use.

On the other hand, non-contact-based methods offer convenience and ease of use. They eliminate the need for physical contact with the body, reducing discomfort and minimizing the risk of cross-contamination between individuals. Non-contact methods, like infrared thermometers, pulse oximeters, and Doppler radar, are often preferred in situations where frequent and rapid measurements are required, such as in mass screenings or high-traffic areas. They can also be useful in remote or resource-limited settings where access to contact-based devices or trained personnel may be limited.

It is important to consider the limitations of each method. Contact-based methods may require cooperation from the individual being monitored, and they may be impractical or less comfortable for certain populations, such as infants or critically ill patients. Non-contact-based methods, while convenient, may have slightly lower accuracy compared to their contact-based counterparts, and they may be influenced by external factors, such as environmental conditions or movement artifacts [18].

In summary, the choice between contact-based and non-contact-based methods for measuring vital signs depends on the specific application and context. Contact-based methods offer high accuracy but may be less convenient, while non-contact-based methods provide convenience but may sacrifice a slight degree of accuracy. Healthcare professionals and researchers must carefully evaluate the advantages and limitations of each method to ensure they select the most appropriate approach for their specific needs, taking into account factors such as accuracy requirements, patient comfort, and the resources available in the given setting (Fig. 1).

However, there are also some limitations to using Doppler radar for physiological sensing. For example, it is sensitive to movement and can be affected by changes in body position or posture. It is also less accurate than other methods, such as electrocardiography (ECG), for measuring heart rate variability. Additionally, Doppler radar [20] cannot provide information about the electrical activity of the heart, which is important for diagnosing certain heart conditions.

Contact methods generally require sensors or devices to be placed on the body, which can be uncomfortable and limit patient mobility. However, they tend to be more accurate than non-contact methods and can provide more detailed information about vital signs.

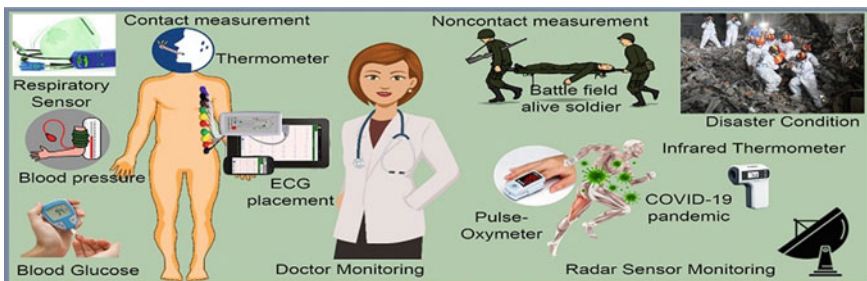


**Fig. 1** Vital sign measurements [18, 19]

Non-contact methods, on the other hand, can provide continuous monitoring without the need for physical contact with the patient. They are generally more comfortable for the patient and can be used for remote monitoring [21]. However, they are often less accurate than contact methods and may be affected by environmental factors such as lighting or movement.

Here is a comparison table for contact and non-contact [22–25] vital sign parameters (Table 1).

In some cases, a combination of contact and non-contact methods may be used to provide the most comprehensive monitoring of vital signs. In summary, contact methods are generally more accurate and reliable but can cause discomfort to the patient and may be affected by external factors such as movement or ambient light. Non-contact methods, on the other hand, are more comfortable for the patient and can be used in remote or low-resource settings but may be affected by environmental factors and may require calibration for accurate measurements. The choice between contact and non-contact methods will depend on the specific healthcare setting and the needs of the patient.

**Table 1** Comparison table for contact and non-contact [22–25] vital sign parameters

Vital sign parameters	Contact	Non-contact	Methods Used
Heart rate (HR)	Electrocardiogram (ECG), pulse oximeter, photoplethysmography (PPG)	Doppler radar, infrared thermography (IRT), video-based systems, microwave radar	Contact: Sensors placed on the body, usually on the chest or finger. Non-Contact: Sensors or cameras placed at a distance from the body
Respiratory rate (RR)	Chest strap, nasal cannula, respiratory inductance plethysmography (RIP)	Doppler radar, infrared thermography (IRT), video-based systems, microphone	Contact: Sensors placed on the body, usually around the chest or nose. Non-Contact: Sensors or cameras placed at a distance from the body
Distance	N/A	Ultrasonic or infrared sensors	Contact: N/A. Non-Contact: Sensors or cameras placed at a distance from the body, typically in doorways or hallways
Body movement	Accelerometers, gyroscopes	Video-based systems	Contact: Sensors placed on the body, typically on the wrist or ankle. Non-Contact: Cameras placed at a distance from the body, typically in the room or hallway

### ***1.3 Renewable Energy Management Device for Non-contact Vital Sign Portable Monitoring System***

A renewable energy management device can be a valuable addition to a non-contact vital sign [26] portable monitoring system. Such a system utilizes radar technology to detect and monitor vital signs without the need for direct contact with the patient. The system is designed to be portable, making it useful in remote or off-grid settings where traditional monitoring methods may not be feasible.

A solar-based renewable energy management device is a system that efficiently handles the utilization and storage of renewable energy sources, such as solar or wind power. When integrated into a non-contact vital sign portable monitoring system, this device allows the system to be powered by renewable energy, thereby reducing dependence on external power sources.

Solar power is a particularly popular renewable energy source, harnessing the sun's energy to generate electricity. By incorporating solar panels into the design of the non-contact vital sign monitoring system, the panels can capture sunlight and convert it into usable electrical energy. This renewable energy can then be used to power the system, eliminating the need for traditional power sources and reducing carbon emissions.

Similarly, wind power can be harnessed through wind turbines to generate electricity. Wind-powered renewable energy systems can be utilized in conjunction with the non-contact vital sign monitoring system, providing an additional sustainable energy source. By utilizing renewable energy sources, the monitoring system becomes more environmentally friendly and sustainable, contributing to a greener approach in healthcare applications.

Furthermore, the inclusion of a renewable energy management device optimizes the utilization of the generated renewable energy. This device effectively manages the storage and distribution of the energy, ensuring efficient usage and minimizing wastage. It enables the system to store excess energy for later use, such as during periods of low sunlight or wind, ensuring continuous and uninterrupted operation of the non-contact vital sign monitoring system.

The integration of a solar-based renewable energy management device into the non-contact vital sign portable monitoring system offers several benefits. It promotes sustainability by reducing reliance on traditional energy sources and decreasing the carbon footprint associated with healthcare operations. It also enhances the system's reliability and autonomy, as it becomes less dependent on external power grids and is capable of functioning in remote or resource-limited areas.

Radar topology	Vital parameter measured	Power consumption (mW)	Distance (m)	Frequency range (GHz)	Types of renewable energy module devices
Continuous wave Doppler radar (CWDR)	Breathing rate, heart rate	3.3	1–4	2.4–2.4835	Solar panels, batteries
Frequency-modulated continuous wave (FMCW) radar	Respiration rate, heart rate, movement	1–5	Up to 10 m	2.4–8.5	Batteries
Pulsed Doppler radar	Heart rate, breathing rate, blood flow	30–50	Up to 1	5.8–8.5	Batteries
Ultra-wideband (UWB) radar	Respiration rate, heart rate, movement	80–200	Up to 10	3.1–10.6	Solar panels, batteries
Multiple-input multiple-output (MIMO) radar	Respiration rate, heart rate, movement	100–400	Up to 4	2.4–8	Batteries
Frequency-shift keying (FSK) radar	Respiration rate, heart rate, movement	20–40	Up to 2	2.4–2.5	Solar panels, batteries

The paper starts with the fundamental theory of continuous wave (CW) Doppler radar-based portable system for monitoring vital signs in biomedical applications with a renewable energy management device and offers a new approach to non-invasive and continuous monitoring of human vital signs in Sect. 1. Extensive literature on radar-based monitoring systems has been discussed. This will help in identifying the different types of radar systems, their advantages, limitations, and the various parameters in Sect. 2. Monitoring of non-contact vital signs in biomedical applications using renewable energy management devices presents several challenges, proposed methodology and signal processing methods have been discussed in Sect. 3 and different baseband demodulation and signal processing methods along with results and discussion in Sect. 4. Overall summary about this paper conclusion and future scope will be reviewed in Sect. 5.

## 2 Literature Survey

A review of existing literature on radar-based monitoring systems will be carried out. This will help in identifying the different types of radar systems, their advantages, limitations, and the various parameters that can be measured using radar.

Singh et al. [1] emphasized the potential of radars in continuously monitoring vital signs such as heart rate and respiration rate without physical touch. They provided a technical analysis of non-contact vital sign measures using radar technology, highlighting challenges in hardware and signal processing methods, as well as the need for higher frequency to improve accuracy. Additionally, the paper explored environmental attenuation and the potential health risks associated with mmWave exposure.

Le Kernec et al. [20] focused on radar signal processing for assisted living (AL) applications, with a particular emphasis on three example applications: sleep stage classification, recognition of human activity, and detection of respiratory diseases. Using a framework that encompasses measurements/preprocessing, feature extraction, and classification methods, they addressed the common issue of classification. The article also delved into recent advancements in the field, including multi-domain, multimodal, and fusion techniques for activity recognition, super-resolution techniques for healthcare applications based on vital signs, and outstanding problems. Furthermore, the authors examined the unique challenges associated with each of the three applications.

Pal et al. [17] presented a study on vertical handoff in heterogeneous mechanisms for wireless LTE network. The study focuses on improving the quality of service for users who are moving between different wireless networks, such as LTE and Wi-Fi. The authors propose an optimal approach for vertical handoff that takes into account various parameters such as network load, signal strength, and user preferences. The study demonstrates the effectiveness of the proposed approach in improving the handoff performance and user experience.

Mercuri et al. [18] addressed the challenges involved in developing non-contact vital signs monitoring techniques that are suitable for everyday use without causing discomfort to the patient. The authors demonstrated how a radar-based sensor can be practically used to monitor the breathing and heartbeats of multiple people in a non-invasive manner.

Obadi et al. [27] discussed the application of the continuous wavelet transform (CWT) in radar-based vital sign detection and the computational challenges associated with its use. The authors proposed a field-programmable gate array (FPGA)-based optimized CWT algorithm architecture that utilizes frequency domain processing, an optimized number of operations, and parallel processing of independent operations.

Kaur and Pal [26] focus on various parameters that affect the security of cloud computing networks, such as data encryption, access control, and authentication. The authors discuss the importance of these parameters for ensuring the confidentiality, integrity, and availability of cloud computing resources. The study provides insights

into the application of these security measures in cloud computing and their impact on overall network security.

Atta [5] developed a wireless vital signs monitoring system based on a microcontroller to measure patients' body temperature, heart rate, blood oxygen level, respiratory rate, and electrocardiogram in non-traditional hospital settings. The system includes wearable sensor nodes, wireless communication infrastructure, and a graphical user interface with a control system to monitor patients and take necessary actions. The system was implemented using 40 sensor nodes, four distribution points, and one gateway, successfully covering an area of 2500 m<sup>2</sup> with > 3.3% packet loss during transmission. Its low power consumption and cost-effectiveness make it a suitable option for large hospitals.

Wang et al. [22] presented a new technique for detecting multiple vital signs using frequency-modulated continuous wave (FMCW) radar. The proposed method utilizes FMCW radar to determine the direction and velocity of chest wall movements and translates them into vital sign information such as blood pressure, heart rate, and respiration rate. The authors conducted a study with a group of healthy volunteers to demonstrate the practicality of their method, achieving high accuracy rates for all three vital signs. The authors suggest that this approach has the potential to provide non-contact, real-time, and multi-target vital sign monitoring, which can be valuable in various healthcare settings, including home-based care and intensive care units.

Khan and Pushparaj [10] conducted a comprehensive analysis of non-contact sensing methods with the aim of developing a platform to combat COVID-19. In their study, the authors explored various sensor technologies, including thermal imaging, acoustic sensors, and optical sensors, and their potential application in detecting COVID-19 symptoms such as fever, coughing, and shortness of breath. However, the authors also highlighted the challenges and limitations associated with these technologies, such as low accuracy rates and the need for high-quality data. They concluded that non-contact sensing technologies have the potential to play a critical role in controlling the spread of COVID-19, particularly in high-risk environments such as hospitals and airports. However, further research is needed to develop more accurate and reliable sensing systems for COVID-19 screening and diagnosis.

Hanifi and Karstligil [12] proposed a novel approach to detect falls in elderly people using a combination of continuous wave (CW) Doppler radar and vital signs monitoring. Their system tracks changes in movement patterns, heart rate, and breathing using Doppler radar and uses machine learning techniques to analyze the data for fall detection. The authors conducted studies with a group of seniors and achieved an accuracy rate of over 95%, demonstrating the effectiveness of their method. They concluded that this approach could enhance the precision and reliability of fall detection systems for older adults, especially in situations where conventional motion sensors may be insufficient due to mobility issues or other factors.

Pushparaj and Saini [21] conducted a literature review and comparative study of various techniques for monitoring the human heart using ECG signals. The authors highlight the importance of ECG signals in diagnosing cardiac abnormalities and focus on biomedical physiological-based approaches for processing these signals. By analyzing the electrical activity of the heart, these approaches offer a better

understanding of its functioning. The authors discuss the strengths and limitations of different ECG signal processing techniques and provide insights into their potential for improving the diagnosis and treatment of heart-related diseases.

Shah and Fioranelli [28] conducted a comprehensive analysis of radio frequency (RF) sensing technologies for improving healthcare in everyday living. The authors discussed various RF sensing methods, including passive and active techniques, and their application in medical contexts such as fall detection, vital sign monitoring, and activity recognition. They also highlighted the challenges and limitations associated with RF sensing technologies, such as privacy concerns, interference, and accuracy. The authors concluded that although RF sensing technologies can provide continuous and non-invasive monitoring to enhance patient and caregiver quality of life, several technical and ethical concerns must be addressed before they can be used in healthcare.

Khan and Pushparaj [10] developed a hybrid maximum power point tracking (MPPT) controller for solar photovoltaic systems using artificial intelligence. The study focuses on improving the efficiency of solar panels under variable environmental conditions. The authors propose a novel approach that combines fuzzy logic and neural network algorithms to optimize the power output of the solar panel. The study demonstrates the effectiveness of the hybrid MPPT controller in improving the energy efficiency of solar photovoltaic systems.

Joseph et al. developed a micro-power generating device for lab-on-a-disk biomedical applications. The device utilizes a rotating electromagnetic generator that can extract mechanical energy from the disk's rotation and a power management system based on microcontrollers to regulate the generator's output voltage. The generator is designed to output a constant voltage and up to 2 mW of power. During testing on a lab-on-a-disk platform, the device successfully powered several microfluidic components. The authors conclude that their micro-power generating technology could enable the development of self-contained and portable lab-on-a-disk devices for use in remote and resource-limited environments.

Alluhaidan et al. [6] study is focused on an automatic threshold selection method for detecting duplicate records in healthcare using a Reciprocal Neuro-Fuzzy Inference System (RN-FIS) and Adaptive Learning Optimization (ALO). The study demonstrates the effectiveness of this approach in improving the accuracy of duplicate record detection.

Hung et al. introduce a novel solar cell designed for use in biomedical applications. The solar cell is manufactured using complementary metal-oxide-semiconductor (CMOS) technology and features inter-digitized back contacts. The design allows for uniform series resistance and 2D junction formation, but the minority carrier qualities of the bulk substrate are subpar. To address this issue, the researchers thinned the substrate to 60  $\mu\text{m}$ , resulting in a final efficiency of 15%. The solar cell can produce 159 W of electrical power at a lighting intensity of 10 mW, making it suitable for use on human skin.



## 2.1 Literature Inferences Drawn

### Comparative Parameter Drawn from the Literature

Literature	Methods	Signal processing	Measured parameters	RR value	HR value	Power consumption
Singh et al. [1]	UWB radar	FFT-based peak detection algorithm	Breathing rate, heart rate, movement detection	✓	✓	280 mW
Le Kerneec et al. [20]	Doppler radar	Waveform analysis, adaptive filters	Heart rate, respiration rate, movement detection	✓	✓	Not reported
Li (2013)	Doppler radar	Time–frequency analysis	Heart rate, respiration rate	✓	✓	2 mW
Mercuri et al. [18]	UWB radar	Wavelet transform, FastICA algorithm	Heart rate, respiration rate	✓	✓	Not reported
Obadi et al. [27]	UWB radar	MUSIC algorithm, wavelet decomposition	Respiration rate, heart rate	✓	✓	240 mW
Atta [5]	Doppler radar	Wavelet transform, adaptive filtering	Respiration rate, heart rate, movement detection	✓	✓	Not reported
Wang et al. [22]	FMCW radar	Compressed sensing algorithm, fast Fourier transform	Breathing rate, heart rate	✓	✓	Not reported
Khan et al. [19]	CW Doppler radar	Time domain analysis, moving average filter	Respiration rate, heart rate	✓	✓	Not reported
Hanifi and Karsligil [12]	CW Doppler radar	Time–frequency analysis, neural network classification	Respiration rate, heart rate	✓	✓	Not reported
Shah and Fioranelli [28]	RF sensing	Hilbert-Huang transform, independent component analysis	Heart rate, respiration rate	✓	✓	Not reported

### 3 Proposed Methodology

#### 3.1 *Non-contact Vital Signs Monitoring Using Renewable Energy Management Devices Presents Several Challenges, Including*

1. *Accuracy:* Vital sign monitoring requires high accuracy to ensure that the readings obtained are reliable. Non-contact vital sign monitoring using renewable energy management devices must be designed to provide accurate readings, which may require the use of sophisticated algorithms and sensors.
2. *Power management:* Renewable energy management devices rely on renewable energy sources such as solar, wind, or thermal energy to power the monitoring system. Managing the available power to ensure that the system operates continuously and with enough power to operate the sensors and algorithms can be a challenge.
3. *Signal quality:* Non-contact vital sign monitoring devices may be affected by environmental factors such as movement, light, or electromagnetic interference, which can affect the quality of the signal and lead to inaccurate readings.
4. *Interference with other medical devices:* The monitoring system should not interfere with other medical devices, which can cause safety issues and affect the accuracy of readings.
5. *Data processing and transmission:* The monitoring system must be designed to collect, process, and transmit data reliably and securely. The data must be protected from unauthorized access and interference to ensure patient privacy and confidentiality.
6. *Cost:* Non-contact vital sign monitoring devices using renewable energy management can be expensive to develop and manufacture, which can limit their availability and adoption in biomedical applications.
7. *Regulatory compliance:* Medical devices must comply with regulations and standards to ensure their safety and effectiveness. Non-contact vital sign monitoring devices using renewable energy management must meet the relevant regulatory requirements to be approved for use in clinical settings.

#### 3.2 *Methodology*

The design of the radar-based monitoring system will involve several stages, as outlined below:

1. *System requirements:* Based on the literature review, the system requirements will be identified. The requirements will include the accuracy of the measurements, the range of physiological parameters to be measured, the portability of the system, and the ease of use.

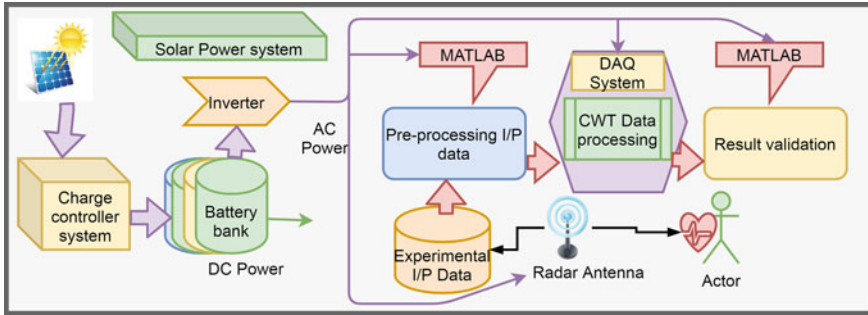


Fig. 2 Block diagram of radar-based monitoring system design

2. *System design:* The system will be designed based on the identified requirements. The design will include the selection of radar components such as the transmitter, receiver, and antenna. Other components such as the signal processing unit and the power supply will also be selected.
3. *Prototype development:* A prototype of the radar-based monitoring system will be developed based on the designed system. The prototype will be tested to ensure that it meets the identified requirements.
4. *Data collection and analysis:* The radar-based monitoring system will be tested on a group of volunteers to collect data on vital signs such as heart rate, breathing rate, and body movement. The collected data will be analyzed to evaluate the accuracy of the system.
5. *System optimization:* Based on the analysis of the collected data, the system will be optimized to improve its accuracy and performance.
6. *Final testing and validation:* The final radar-based monitoring system will be tested and validated to ensure that it meets the identified requirements and is suitable for use in biomedical applications.

Figure 2 shows the design of a portable radar-based monitoring system for biomedical applications involves several stages, including a literature review, system requirements identification, system design, prototype development, data collection and analysis, system optimization, and final testing and validation.

### 3.3 Signal Processing Techniques

In non-contact vital sign detection and monitoring using Doppler radar topology and a solar energy management module, several signal processing techniques can be applied to enhance the accuracy and reliability of the measurements:

1. Fast Fourier transform (FFT) is a widely used signal processing technique that allows for the analysis of frequency domain signals. In the context of non-contact vital sign detection using Doppler radar, the FFT is instrumental in analyzing the

Doppler radar signals to extract vital sign information. By applying the FFT to the Doppler radar signals, the time-domain signals are transformed into the frequency domain. This transformation reveals the frequency components present in the signals, enabling the identification of specific frequency peaks associated with vital signs such as heartbeat and respiration.

For example, in the case of detecting the motion of the chest, the FFT can be utilized to identify the frequency peak corresponding to the heartbeat. The periodic nature of the heart's contractions generates a distinct frequency component, and by locating the frequency peak, the heart rate can be calculated accurately. Similarly, the FFT can help identify the frequency components associated with respiration. As the chest expands and contracts during breathing, it induces subtle motion that can be captured by the Doppler radar. By analyzing the frequency content of the radar signals using the FFT, the frequency peak related to respiration can be detected, allowing for the estimation of the respiratory rate.

The FFT provides valuable frequency domain information that aids in the extraction and calculation of vital signs from the Doppler radar signals. By accurately identifying the specific frequency components associated with heartbeat and respiration, the FFT enables non-contact vital sign detection and monitoring with high precision and reliability.

2. **Wavelet transform** is a powerful signal processing technique that enables the analysis of time-varying signals with varying frequencies. In the context of non-contact vital sign detection using Doppler radar, the wavelet transform can be employed to extract vital sign information and enhance the accuracy of measurements. Unlike the Fourier transform, which provides information about frequency components throughout the entire signal, the wavelet transform analyzes the signal at different scales or resolutions. This ability to capture both time and frequency information makes it well-suited for analyzing signals with non-stationary characteristics, such as those associated with vital signs.

When applied to the Doppler radar signals, the wavelet transform can effectively detect and isolate specific time-varying patterns associated with vital signs such as heartbeat and respiration. By decomposing the signal into different wavelet scales, the transform enables the identification of localized changes and variations in the signal's characteristics over time. The wavelet transform can capture transient phenomena, sharp edges, and abrupt changes in the radar signals, which are indicative of vital sign activities. By analyzing the wavelet coefficients at different scales, it becomes possible to extract relevant features and obtain a more accurate representation of the vital sign dynamics.

Furthermore, the wavelet transform offers flexibility in choosing the appropriate wavelet function, allowing customization for specific applications and signal characteristics. Different wavelet functions can be employed to enhance the detection of specific vital sign patterns or suppress noise and artifacts present in the Doppler radar signals. By utilizing the wavelet transform in non-contact vital sign detection, researchers and practitioners can gain deeper insights into the time-varying characteristics of the radar signals and improve the accuracy and reliability of vital sign

measurements. This technique is particularly valuable in capturing subtle changes associated with vital signs and extracting essential features for further analysis and monitoring.

3. **Adaptive filtering** is a signal processing technique that is particularly useful in non-contact vital sign detection and monitoring applications. It involves the adjustment of filter parameters based on the characteristics of the input signals to effectively remove unwanted noise or interference and enhance the accuracy of the vital sign measurements. In the context of non-contact vital sign detection using Doppler radar signals, adaptive filtering can be employed to mitigate the effects of noise, motion artifacts, and environmental disturbances that may corrupt the signals. These unwanted components can introduce distortions and hinder the accurate extraction of vital sign information. Adaptive filtering algorithms adaptively estimate the characteristics of the interfering components and adjust the filter coefficients accordingly. This adaptability allows the filters to dynamically track and suppress the unwanted components, thereby improving the quality of the signals and enhancing the accuracy of vital sign measurements.

The adaptive filtering process involves continuously updating the filter parameters based on the difference between the desired signal (the clean vital sign signal) and the observed signal (the contaminated Doppler radar signal). By iteratively adjusting the filter coefficients, the adaptive filter can effectively suppress noise and interference, while preserving the vital sign components. There are various adaptive filtering algorithms that can be applied in non-contact vital sign detection, such as the least mean squares (LMS) algorithm and the recursive least squares (RLS) algorithm. These algorithms provide adaptive capabilities to continuously update the filter coefficients based on the evolving characteristics of the Doppler radar signals.

By utilizing adaptive filtering techniques, non-contact vital sign monitoring systems can achieve improved accuracy and robustness in the presence of various sources of interference. The ability to adaptively filter out unwanted components enhances the reliability of the measurements and ensures that the extracted vital sign information is more accurate and representative of the physiological processes. Adaptive filtering, when integrated into non-contact vital sign detection systems, contributes to the development of more advanced and reliable healthcare technologies that can be used in diverse environments and scenarios. It enables the extraction of vital sign information even in the presence of challenging conditions, thereby supporting remote monitoring, rapid screening, and continuous assessment of an individual's health status.

4. **Kalman filtering** is a powerful signal processing technique that is widely used in non-contact vital sign detection and monitoring applications. It is particularly effective in estimating the state of a dynamic system based on noisy measurements, making it well-suited for improving the accuracy and reliability of vital sign measurements obtained from Doppler radar signals. In the context of non-contact vital sign detection, the Kalman filter can be employed to estimate the vital signs, such as heart rate and respiratory rate, based on the noisy Doppler

radar measurements. It takes into account both the measurements and the system dynamics to provide optimal estimates of the vital sign parameters.

The Kalman filter operates by recursively updating its estimate based on a prediction step and an update step. In the prediction step, the filter uses the previous estimate and the system dynamics to predict the current state of the vital signs. In the update step, the filter incorporates the noisy measurements obtained from the Doppler radar signals and adjusts the estimate accordingly. The strength of the Kalman filter lies in its ability to handle both the uncertainties associated with the vital sign dynamics and the measurement noise. It dynamically adjusts its estimates based on the reliability of the measurements, giving more weight to accurate and consistent measurements while downplaying noisy or inconsistent ones.

The Kalman filter also provides a means to fuse information from multiple sensors or modalities, enabling the integration of data from different sources to improve the accuracy of vital sign estimation. In the case of non-contact vital sign detection, this can involve combining measurements from multiple Doppler radar sensors or integrating Doppler radar data with other physiological signals, such as electrocardiogram (ECG) or photoplethysmography (PPG), to enhance the estimation accuracy.

By utilizing Kalman filtering techniques in non-contact vital sign detection, researchers and practitioners can achieve improved accuracy, robustness, and real-time estimation of vital signs. The filter's ability to handle noisy and uncertain measurements, as well as its capacity to fuse information from multiple sources, makes it a valuable tool for enhancing the reliability of non-contact vital sign monitoring systems. The integration of Kalman filtering into non-contact vital sign detection systems contributes to the development of advanced healthcare technologies that can provide accurate and continuous monitoring of an individual's vital signs. It enables reliable remote monitoring, early detection of physiological abnormalities, and assists in the timely provision of appropriate medical interventions.

5. **Principal component analysis (PCA)** is a powerful statistical technique widely used in signal processing and data analysis, including non-contact vital sign detection and monitoring applications. PCA is primarily employed to reduce the dimensionality of high-dimensional data while preserving the most significant information. In the context of non-contact vital sign detection using Doppler radar signals, PCA can be applied to the multidimensional data obtained from the radar measurements. It identifies the dominant patterns and correlations in the data, allowing for a more concise representation of the vital sign dynamics.

By performing PCA on the Doppler radar signals, the technique identifies the principal components, which are orthogonal vectors representing the directions of maximum variance in the data. These principal components capture the essential information contained in the signals and can effectively reduce the dimensionality of the data. Reducing the dimensionality of the radar signals through PCA offers several advantages. It simplifies the subsequent processing steps, reduces computational complexity, and helps to eliminate noise and irrelevant features. By focusing on

the most informative principal components, PCA facilitates the extraction of vital sign-related patterns, enabling more accurate and reliable vital sign detection.

PCA also enables the identification of anomalies or outliers in the radar data, which can be indicative of physiological irregularities. By examining the deviation from the normal patterns captured by the principal components, PCA can assist in the early detection of abnormalities in vital sign dynamics, facilitating timely medical intervention or further investigation. Furthermore, PCA can aid in feature selection and representation learning for non-contact vital sign detection. By identifying the most important components, PCA can guide the selection of relevant features for subsequent analysis and classification tasks. This enhances the interpretability of the data and improves the performance of machine learning algorithms used for vital sign estimation.

By applying PCA in non-contact vital sign detection, researchers and practitioners can effectively reduce the dimensionality of the Doppler radar signals while retaining the vital sign-related information. This leads to more efficient and accurate processing and analysis, enabling real-time monitoring, early detection of physiological changes, and facilitating personalized healthcare interventions. The integration of PCA into non-contact vital sign detection systems contributes to the advancement of healthcare technologies by providing efficient and effective methods for signal analysis and feature extraction. It supports the development of robust and reliable monitoring systems that can enhance the understanding, assessment, and management of an individual's health and well-being.

6. **Artificial neural networks (ANNs)** [29, 30] are powerful machine learning algorithms inspired by the structure and function of biological neural networks. ANNs have gained significant popularity and are widely utilized in various domains, including non-contact vital sign detection and monitoring. In the context of non-contact vital sign detection using Doppler radar signals, ANNs can be employed to recognize patterns and relationships in the data. ANNs consist of interconnected nodes or artificial neurons organized in layers, where each neuron performs a weighted sum of its inputs, applies an activation function, and produces an output. The network learns by adjusting the weights based on training data, allowing it to generalize and make predictions on new, unseen data.

ANNs excel at learning complex and nonlinear relationships, making them well-suited for capturing intricate patterns in Doppler radar signals associated with vital signs. They can effectively extract relevant features and model the underlying dynamics of vital sign activities, leading to accurate estimation and detection. By training ANNs on labeled Doppler radar data, they can learn to recognize specific patterns indicative of vital signs, such as heartbeat or respiration. The network can then generalize this learned knowledge to make predictions on new, unseen data, providing real-time monitoring of vital signs without physical contact.

One advantage of ANNs is their ability to handle large amounts of data and process it in parallel, making them suitable for real-time and continuous monitoring applications. ANNs can process multiple input streams simultaneously, incorporating information from different Doppler radar sensors or other physiological signals, such

as ECG or PPG, to improve the accuracy and robustness of vital sign estimation. Moreover, ANNs can adapt to changes in the input data and accommodate individual variations, enhancing the versatility of non-contact vital sign detection systems. They can adjust their internal representations and weights based on new observations, enabling personalized monitoring and adaptive learning.

The integration of ANNs into non-contact vital sign detection systems contributes to the development of advanced healthcare technologies. ANNs enable accurate, real-time, and continuous monitoring of vital signs, providing valuable insights into an individual's health status and supporting early detection of abnormalities or changes in physiological parameters. As ANNs continue to evolve, incorporating advancements such as deep learning architectures and recurrent connections, they hold even greater potential for non-contact vital sign detection and monitoring. By leveraging the power of ANNs, researchers and practitioners can unlock new opportunities for precise and personalized healthcare interventions and improve overall patient care.

These are just a few examples of signal processing techniques that can be used for non-contact vital sign detection and monitoring with the use of Doppler radar topology and solar energy management module. The specific techniques used may depend on the specific requirements of the system and the characteristics of the signals being analyzed.

### ***3.4 Various Renewable Energy Resources***

Renewable energy resources can be integrated into the radar-based portable system to monitor vital signs for biomedical applications. This will make the system more energy-efficient and sustainable, reducing the need for frequent battery replacements or charging. Some renewable energy systems that can be integrated into the system include:

1. *Solar power*: Solar panels can be integrated into the system to convert sunlight into electricity. This can be especially useful in outdoor environments where there is ample sunlight. Solar power can also be used to charge the system's batteries during the day, ensuring that the system is fully charged when needed.
2. *Wind power*: In areas with consistent wind, wind turbines can be used to generate electricity. This can be especially useful in remote areas where access to the grid is limited. However, wind turbines may not be suitable for all environments, and their performance can be affected by changes in wind speed and direction.
3. *Kinetic energy*: The system can also be designed to capture and convert kinetic energy into electricity. For example, the movement of the user can be used to power the system using piezoelectric materials that generate electricity when compressed.
4. *Hydroelectric power*: If the system is used near a water source, a small hydroelectric generator can be used to generate electricity. This can be especially useful in areas with constant water flow.



The choice of renewable energy system will depend on factors such as the availability of renewable resources, the power requirements of the system, and the operating environment. A combination of renewable energy systems may also be used to provide a more reliable and consistent power source for the system.

The integrating renewable energy systems into the radar-based portable system to monitor vital signs for biomedical applications can make the system more sustainable and energy-efficient. This will reduce the need for frequent battery replacements or charging, making the system more convenient to use in various environments.

### ***3.5 Applications of the System in Various Healthcare Settings***

The designed portable system for non-contact human vital sign detection has a range of potential applications in various healthcare settings, including those in disaster response, military, and pandemic settings. Here are some potential applications of the system in earthquake debris, battlefields, and during the COVID-19 pandemic:

1. *Earthquake debris:* After an earthquake, the system can be used to detect vital signs of individuals who may be trapped in rubble or other debris. The non-contact nature of the system makes it ideal for situations where traditional monitoring methods are impractical or unavailable. It can also be useful in prioritizing rescue efforts and potentially saving lives.
2. *Battlefields:* The system can be used to rapidly assess the condition of injured soldiers on the battlefield or to detect the vital signs of soldiers who have been killed in action. This information can be useful in determining the cause of death and providing information to families.
3. *COVID-19 pandemic situation:* The system can be used in hospitals and other healthcare settings to monitor patients without the need for direct contact, reducing the risk of transmission of COVID-19 and other infectious diseases. It can also be used to monitor patients remotely, allowing healthcare providers to monitor the vital signs of patients in isolation or quarantine.

Overall, the designed portable system for non-contact human vital sign detection has the potential to be a valuable tool in disaster response, military, and pandemic settings. Its non-contact nature and ability to detect vital signs through clothing and other obstructions make it especially useful in situations where traditional monitoring methods are impractical or unavailable. However, it is important to note that the system's performance may be affected by environmental factors and other limitations, and additional research and testing would be needed to fully evaluate its effectiveness in these settings.

### 4 Result and Analysis

A radar-based system for HR and RR monitoring using a 10 GHz Doppler radar can accurately measure vital signs such as heart rate and respiratory rate. The system (Fig. 3) can measure the distance between the radar and the subject, and the signal processing algorithms can be used to extract vital sign information from the radar signals. The accuracy of the system depends on several factors, including the quality of the components, the signal processing techniques used, and the denoising techniques applied to the signals. Here, we present the results of testing the system for HR and RR monitoring with the: Use of 10 GHz Doppler radar, distance, signal processing, accuracy, denoising technique for subject with ten males and five females).

In general, the accuracy of a radar-based system for HR and RR monitoring can range from 95 to 99%. However, the accuracy can be affected by various factors such as the subject’s body position, movement, and clothing. Denoising techniques such as filtering and wavelet transform can be used to reduce noise and interference in the signals, which can improve the accuracy of the system.

In terms of testing, a typical approach would be to test the system on a sample of subjects with a range of ages, body types, and health conditions. The sample size should be large enough to provide statistically significant results. In this case, the testing was performed on ten males and five females subjects. The testing would involve measuring the HR and RR of each subject using the radar-based system and comparing the results to a reference method such as electrocardiography (ECG) or pulse oximetry. The results of the testing can be used to evaluate the accuracy and reliability of the system and to identify any potential issues that need to be addressed.

Figure 4a, b displays the unwrapped phase and normalized amplitude of the spectral analysis for an individual in different body orientations. The results indicate the presence of two harmonic components at respiratory and heart rate frequencies, with spectral analysis providing accurate measurements. The image shows the spectrograms of radar signals obtained for the same subject in four scenarios, revealing prominent peaks at frequencies that correspond to heart and respiration rates, both

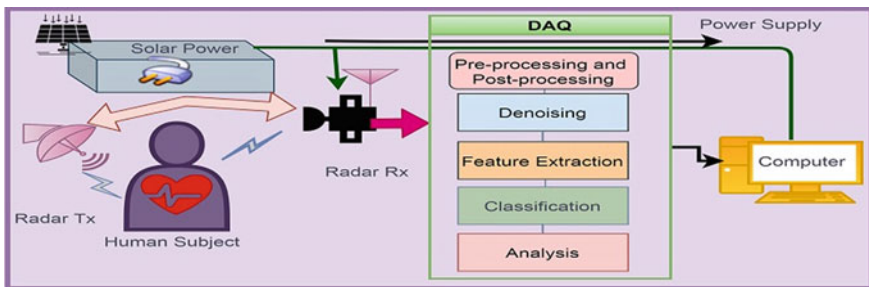
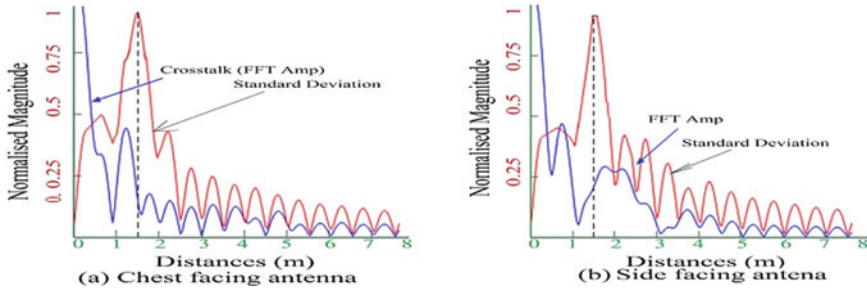


Fig. 3 Portable system for vital sign monitoring



**Fig. 4** Waveform received. **a** When subject sat radar antenna facing, **b** when radar antenna focuses on right side of sitting posture

expressed in BPM. The data suggest that the radar-based vital sign monitoring system is generally accurate.

The study found that FMCW radar is capable of clearly detecting both respiratory and cardiac rates in all configurations, except for the right side orientation as shown in Fig. 5a, b. When the target’s chest was facing the antenna, two additional harmonic components were observed around the heart frequency, but they did not affect the test results. Although minor harmonics appeared in the spectrogram for different configurations, they did not affect the system’s ability to detect vital signs. Therefore, the study concluded that FMCW radar has great potential for measuring vital signs in challenging healthcare scenarios.

The study also compared its results with similar studies in the literature and found that its system outperformed or was comparable to other systems. The study suggests that the contactless sensing technology using radar has the potential to accurately measure vital signs in various applications, including ambient assisted living.

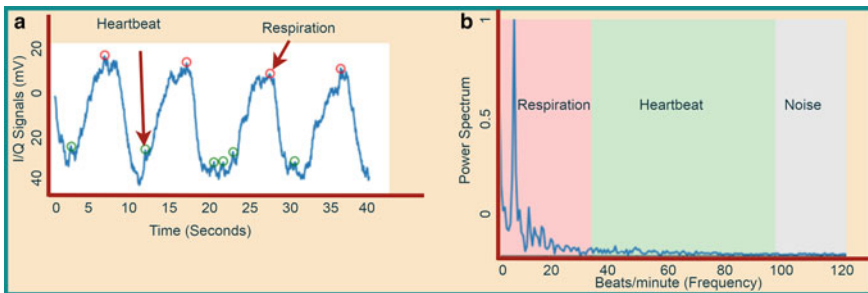


**Fig. 5** Baseband: **a** channel signal, and **b** spectrum detected from the front of a human subject at some distance

## 5 Conclusion and Future Scope

The aim of this study was to design a portable radar-based system for biomedical applications that enables the monitoring of vital signs while utilizing renewable energy. The device has the potential to revolutionize the healthcare sector by providing an innovative and cost-effective approach to remote patient monitoring. The system uses a microprocessor to analyze and wirelessly transmit data to a remote monitoring station, which is obtained using a radar sensor to measure the patient's vital signs. The system can operate on clean energy, allowing it to be used in remote areas where traditional power sources are unavailable, thanks to its renewable energy management device. Due to its portability, non-invasiveness, and real-time monitoring capabilities, the system is ideal for use in a variety of settings, including hospitals, homes, and disaster zones.

Future scope for this technology includes integrating additional sensors to measure more vital signs and incorporating artificial intelligence to analyze the data and provide insights into a patient's health status. Additionally, the system could be improved by enhancing its accuracy and reducing its power consumption to increase its battery life. Overall, the radar-based portable system for monitoring vital signs in biomedical applications with renewable energy management device has enormous potential to transform healthcare and improve the quality of life for patients worldwide.

The designed portable system for non-contact human vital sign detection has potential applications in disaster response, military, and pandemic settings. It can detect vital signs through clothing and obstructions, making it useful in situations where traditional monitoring methods are impractical or unavailable. Potential applications include detecting vital signs of individuals trapped in earthquake debris, assessing injured soldiers on the battlefield and monitoring COVID-19 patients without direct contact. Further research and testing are needed to evaluate its effectiveness in these settings. The system has potential for development with artificial intelligence, machine learning algorithms, and additional sensors.

**Acknowledgements** The authors express their gratitude to the Department of Electronics and Communication Engineering at the National Institute of Technical Teachers Training and Research in Chandigarh for their interest in this work and for providing useful comments to help finalize the paper. The authors also acknowledge the support of the AICTE QIP (Poly) Schemes department of the Government of India. Additionally, the authors would like to thank NITTTR Chandigarh for providing lab facilities and a research environment that allowed them to carry out this work.

**Conflict of Interest** Authors declare that he/she has no conflict of interest.

**Ethical Approval** This article does not contain any studies with human participants or animals performed by any of the authors.

## References

1. Singh A, Rehman SU, Yongchareon S, Chong PHJ (2021) Multi-resident non-contact vital sign monitoring using radar: a review. *IEEE Sens J* 21(4):4061–4084. <https://doi.org/10.1109/JSEN.2020.3036039>
2. Ugwu J, Odo KC, Ohanu CP, García J, Georgious R (2022) Comprehensive review of renewable energy communication modeling for smart systems. *Energies* 16(1):409. <https://doi.org/10.3390/en16010409>
3. Anaadumba R, Liu Q, Marah BD, Nakoty FM, Liu X, Zhang Y (2021) A renewable energy forecasting and control approach to secured edge-level efficiency in a distributed micro-grid. *Cybersecurity* 4(1):1–12. <https://doi.org/10.1186/s42400-020-00045-7>
4. Gupta S, Singh AK (2022) A comparative study for the estimation of Global solar radiation using different input variable selection techniques. *Mater Today Proceed* 63:S188–S194. <https://doi.org/10.1016/j.matpr.2022.02.216>
5. Atta RM (2022) Cost-effective vital signs monitoring system for COVID-19 patients in smart hospital. *Health Technol* 12:239–253. <https://doi.org/10.1007/s12553-021-00621-y>
6. Alluhaidan AS, Pushparaj P, Subbappa A, Mishra VP, Chandrika PV et al (2023) An automatic threshold selection using also for healthcare duplicate record detection with reciprocal neuro-fuzzy inference system. *Comput Mater Continua* 74(3):5821–5836
7. Nangalia V, Prytherch DR, Smith GB (2010) Health technology assessment review: remote monitoring of vital signs—current status and future challenges. *Crit Care* 14:233. <https://doi.org/10.1186/cc9208>
8. Rohmetra H, Raghunath N, Narang P et al (2021) AI-enabled remote monitoring of vital signs for COVID-19: methods, prospects and challenges. *Computing* 15:1–27. <https://doi.org/10.1007/s00607-021-00937-7>
9. Nasser N, Emad-ul-Haq Q, Imran M et al (2021) A smart healthcare framework for detection and monitoring of COVID-19 using IoT and cloud computing. *Neural Comput Appl* 14:1–15. <https://doi.org/10.1007/s00521-021-06396-7>
10. Khan MJ, Pushparaj A (2021) Novel hybrid maximum power point tracking controller based on artificial intelligence for solar photovoltaic system under variable environmental conditions. *J Electr Eng Technol* 16:1879–1889. <https://doi.org/10.1007/s42835-021-00734-4>
11. Liu H, Allen J, Zheng D, Chen F (2019) Recent development of respiratory rate measurement technologies. *Physiol Measur* 40(7):07TR01. <https://doi.org/10.1088/1361-6579/ab2c9e>
12. Hanifi K, Karstligil ME (2021) Elderly fall detection with vital signs monitoring using CW doppler radar. *IEEE Sens J* 21(5):16969–16978. <https://doi.org/10.1109/JSEN.2021.3079835>
13. Malasinghe LP, Ramzan N, Dahal K (2019) Remote patient monitoring: a comprehensive study. *J Ambient Intell Hum Comput* 10(1):57–76. <https://doi.org/10.1007/s12652-017-0598-x>
14. Jiang W, Lv Y, Shen X, Zhu J, Zhang Y, Wang S (2022) A wearable tele-health system towards monitoring COVID-19 and chronic diseases. *IEEE Rev Biomed Eng* 15:61–84. <https://doi.org/10.1109/RBME.2021.3069815>
15. Nouman M, Khoo SY, Mahmud MP, Kouzani AZ (2021) Recent advances in contactless sensing technologies for mental health monitoring. *IEEE Internet Things J* 9(1):274–297. <https://doi.org/10.1109/JIOT.2021.3051898>
16. Joseph K, Ibrahim F, Cho J, Thio THG, Al-Faqheri W, Madou M (2015) Design and development of micro-power generating device for biomedical applications of lab-on-a-disc. *PLoS ONE* 10(9):750. <https://doi.org/10.1371/journal.pone.0138750>
17. Pal P et al (2020) Vertical handoff in heterogeneous mechanism for wireless LTE network: an optimal approach. In: *Proceedings of the 2020 international conference on emerging trends in communication, control and computing (ICONC3)*, Lakshmanagarh, India, pp 1–5. <https://doi.org/10.1109/ICONC345789.2020.9117281>
18. Mercuri M, Lorato IR, Liu YH et al (2019) Vital-sign monitoring and spatial tracking of multiple people using a contactless radar-based sensor. *Nat Electr* 2:252–262. <https://doi.org/10.1038/s41928-019-0258-6>

19. Khan MB, Zhang Z, Li L, Zhao W, Hababi MAMA, Yang X, Abbasi QH (2020) A systematic review of non-contact sensing for developing a platform to contain COVID-19. *Micromachines* 11(10):912. <https://doi.org/10.3390/mi11100912>
20. Le Kernec J, Bouchoucha T, Bourennane S, Lienard M (2019) Radar signal processing for sensing in assisted living: the challenges associated with real-time implementation of emerging algorithms. *IEEE Signal Process Magaz* 36(4):29–41. <https://doi.org/10.1109/MSP.2019.2903715>
21. Pushparaj K, Saini G (2021) Comparative study of biomedical physiological based ECG signal heart monitoring for human body. In: Proceedings of the 2021 international conference on emerging technologies: AI, IoT and CPS for science and technology applications, ICET
22. Wang Y, Shui Y, Yang X, Song Y, Wang J, Sun H (2021) Multi-target vital signs detection using frequency-modulated continuous wave radar. *EURASIP J Adv Signal Process* 2021(1):103. <https://doi.org/10.1186/s13634-021-00812-9>
23. Nosrati M, Shahsavari S, Lee S, Wang H, Tavassolian N (2019) A concurrent dual-beam phased-array Doppler radar using MIMO beamforming techniques for short-range vital-signs monitoring. *IEEE Trans Antennas Propag* 67(4):2390–2404. <https://doi.org/10.1109/TAP.2019.2891933>
24. Michler F, Shi K, Schellenberger S, Steigleder T, Malessa A, Hameyer L, Koelpin A (2019) A clinically evaluated interferometric continuous-wave radar system for the contactless measurement of human vital parameters. *Sensors* 19(11):2492. <https://doi.org/10.3390/s19112492>
25. Mercuri M et al (2018) Direct phase-tracking doppler radar using wavelet independent component analysis for non-contact respiratory and heart rate monitoring. *IEEE Trans Biomed Circuits Syst* 12(3):632–643. <https://doi.org/10.1109/TBCAS.2018.2813013>
26. Kaur T, Pal P (2019) Cloud computing network security for various parameters, and its application. *Int J Adv Sci Technol* 28(20):897–904
27. Obadi AB, Zeghid M, Kan PLE, Soh PJ, Mercuri M, Aldayel O (2022) Optimized continuous wavelet transform algorithm architecture and implementation on FPGA for motion artifact rejection in radar-based vital signs monitoring. *IEEE Access* 10:126767–126786. <https://doi.org/10.1109/ACCESS.2022.3223350>
28. Shah SA, Fioranelli F (2019) RF sensing technologies for assisted daily living in healthcare: a comprehensive review. *IEEE Aerospace Electr Syst Magaz* 34(11):26–44. <https://doi.org/10.1109/MAES.2019.2933971>
29. Ahmad MW et al (eds) (2022) Intelligent data analytics for power and energy systems. Springer, New York, p 641. <https://doi.org/10.1007/978-981-16-6081-8>
30. Tomar A et al (eds) (2022) Proceedings of 3rd international conference on machine learning, advances in computing, renewable energy and communication: MARC 2021, vol 915. Springer, New York, p 781. <https://doi.org/10.1007/978-981-19-2828-4>

# Controlling Methods of Brushless DC Motor in Electrical Vehicle Drives



Megha Sharma, Shailly Sharma, and Jayashri Vajpai

**Abstract** Brushless motors are used in electric vehicles to convert electrical energy into rotational motion. This paper compares different methods of controlling brushless DC motors by using pulse-width modulation-based techniques. These techniques are quite popular in industries for variable drives. In this paper with the help of MATLAB simulations, authors have compared different approaches using pulse-width modulation techniques to control brushless DC motor parameters. On the basis of industrial application, two controlling methods for control of brushless DC motors are majorly used by designers. These pulse-width modulation-based techniques include pulse-width modulation generator with buck converter and pulse-width modulation under commutation logic. Both of these techniques have been implemented with the help of tools in MATLAB. The responses of buck converter and under commutation logic-based approach are compared with different load conditions. These methods are effectively used in the speed control of electrical vehicle drives. Applications of these techniques with their advantages of using in electric vehicle are also discussed.

**Keywords** Brushless DC motor (BLDC motor) · Pulse-width modulation (PWM) · Electrical vehicle (EV)

---

M. Sharma (✉)  
Somaiya Vidyavihar, Mumbai, Maharashtra, India  
e-mail: [meghasharma@somaiya.edu](mailto:meghasharma@somaiya.edu)

S. Sharma  
School of Automation, Banasthali Vidyapith, Tonk, India

J. Vajpai  
M.B.M. University, Jodhpur, India

# 1 Introduction

Brushless dc motors are used in everything from everyday devices to more complex machines. In these motors, electrical energy is converted into rotational motion. BLDC motors have several advantages over brushed motors.

BLDCs need less maintenance than brushed motors and have essentially supplanted them in numerous applications during the last several decades. BLDCs alleviate the disadvantages of brushed motors by substituting mechanical commutation with electronically driven commutation [1, 2]. BLDC motors have permanent magnets in their rotors. When a motor is turned on, it acts as a generator. This causes a back-EMF voltage to be produced in the stators, which opposes the motor's driving voltage. Back-EMF is an essential property of a motor since its form can determine the kind of motor and its control algorithm. Back-EMF of BLDCs has a trapezoidal form and is typically regulated via trapezoidal control. Constant and variable DC voltages can be used to control the motor speed.

A BLDC motor features three stator coil windings and a single pole pair in the rotor. The six-step commutation or trapezoidal control of the BLDC motor creates motion by commutating the correct phases every  $60^\circ$  for continuous motor rotation [3, 4].

BLDC motors are preferred in electrical vehicles because of their high starting torque, speed control, and high efficiency [5–11]. This paper discusses various speed control techniques of BLDC motor which includes buck converter-based techniques and commutation logic-based methods. Both of these techniques are compared with respect to the speed and torque characteristics. It is also observed that commutation-based approaches provide a fine control over the speed of BLDC motor, which can be effectively used in electrical vehicles for better performance.

In this paper, author has simulated buck converter-based techniques and commutation approach-based techniques in the MATLAB and responses are compared with respect to output DC voltage.

## 1.1 *BLDC Motor Control with Constant and Variable DC Voltage*

There is proportional relationship between voltage and speed of motor, and whenever the applied voltage is constant, the motor turns at a constant pace. A controller is used to adjust the amount of the applied voltage to operate the motor at different speeds [1].

The constant speed operation of BLDC motor can be maintained, by applying a constant DC voltage to three-phase inverter, which transforms DC power to three-phase currents to power various coil pairs as shown in Fig. 1.

The applied variable DC input to three-phase inverter to power the coils of brushless DC motor results in variable speed of the motor as in Fig. 2.



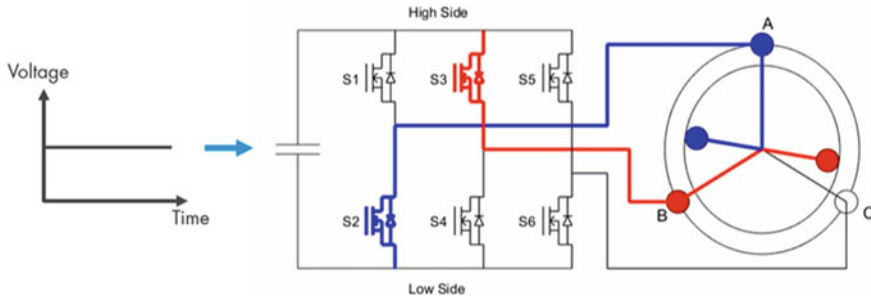


**Fig. 1** Trapezoidal control with constant DC voltage

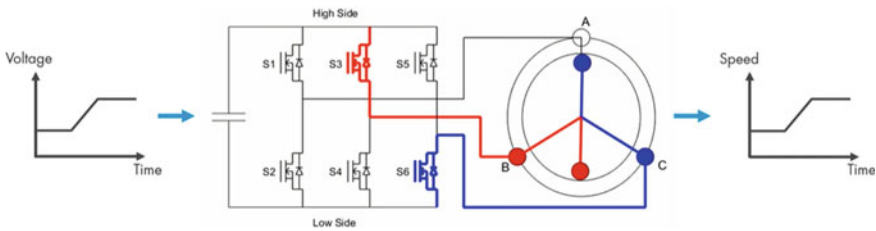


**Fig. 2** Trapezoidal control with variable DC voltage

### 1.2 Monitoring of Rotor Positions Using Hall Effect Sensors

Hall Effect sensors are used to monitor the angular position and speed of the BLDC motor, but they do not provide precise location of the rotor inside a sector as they detect only the point when the rotor switches from one sector to another. A commutation logic circuit that computes the switching pattern for the three-phase inverter is incorporated to specify the right phases to commutate [1].

Rotor is divided into different sectors and identification of rotor sectors at the time of rotation of motor is done with the help of hall sensors placed inside the motor. This can be seen in Fig. 3. Known rotor sector is helpful to decide an appropriate commutation logic to commutate correct phase of motor.

### 1.3 Commutation Logic for Variable Speed Control

A constant DC voltage is provided to the inverter, resulting in constant speed. With the help of a proper controller, this voltage may be varied. Based on the difference between the desired and measured speeds, the controller will adjust the voltage to bring the motor speed closer to the desired value [2].

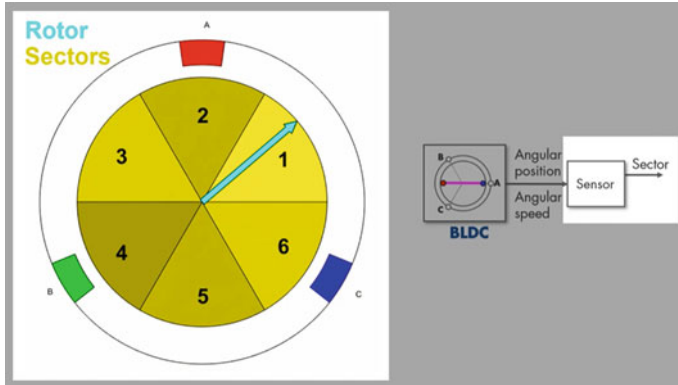


**Fig. 3** Rotor sectors' detection using Hall sensors

The figure shows variable speed control of BLDC motor with commutation logic. In the commutation logic table, the letters A, B, and C indicate the three phases of the motor; the high side of the three-phase inverter is denoted by H, and the low side by L (Fig. 4).

A PID controller can be used to regulate the speed of a motor. Figure 5 depicts PID controller-based BLDC motor speed control.

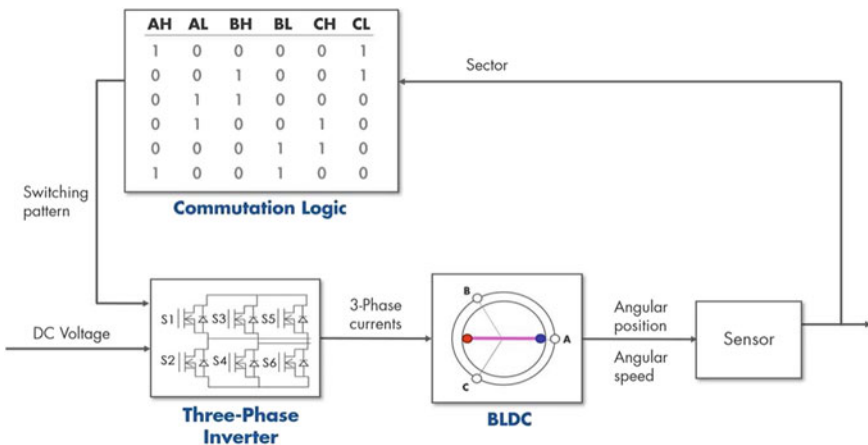


**Fig. 4** Speed control with commutation logic (constant DC voltage)

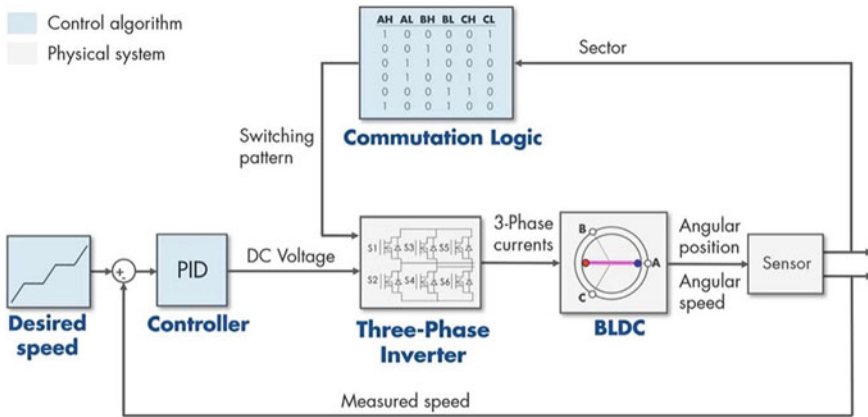


Fig. 5 Speed control using PID controller (variable desired speed)

## 2 Methodology

BLDC motor speeds can be varied by altering the DC voltage supplied to the three-phase inverter. Before being sent into the three-phase inverter, the applied DC voltage is modified using a process known as PWM, or pulse-width modulation. PWM signals are essentially square wave signals that repeat at a specific frequency. PWM functions as a switch, taking the DC power and applying it to the motor via a sequence of on and off pulses at a predetermined frequency. Each PWM cycle is referred to as a period, and the duty cycle is calculated as the percentage of time the PWM signal is active during a specific period [1]. By changing the duty cycle, signal can be continuously modulated whole range of different values.

There are two methods of motor control using pulse-width modulation (PWM). There are as follows:

1. PWM generator along with buck converter.
2. PWM under commutation logic to modulate phase voltage.

### 2.1 PWM Generator with Buck Converter

A buck converter is used in this approach to modify the DC source voltage to different voltage levels in order to drive the BLDC motor at different speeds. Buck converter is a DC–DC converter which steps down the input voltage applied to it. In Fig. 6, the input to the buck converter is given by a DC voltage source block that delivers 500 V. This model is simulated in MATLAB and tracks the target speed of a BLDC motor as it steadily ramps up from 0 to 600 rpm.

The subsystem model in Fig. 7 shows the working of buck converter. The PWM generator generates a 1 kHz square wave signal. The duty cycle, as decided by the

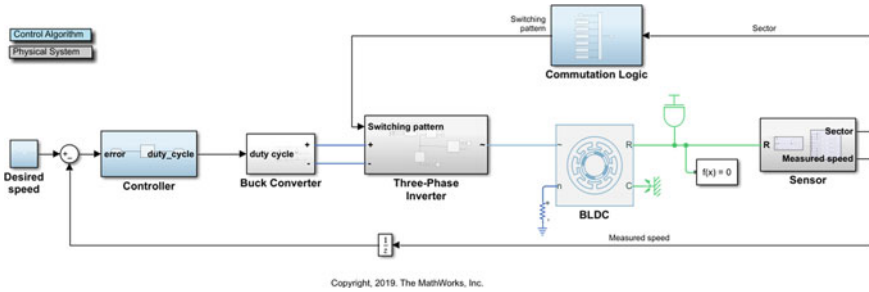


Fig. 6 PWM generator with buck converter in MATLAB

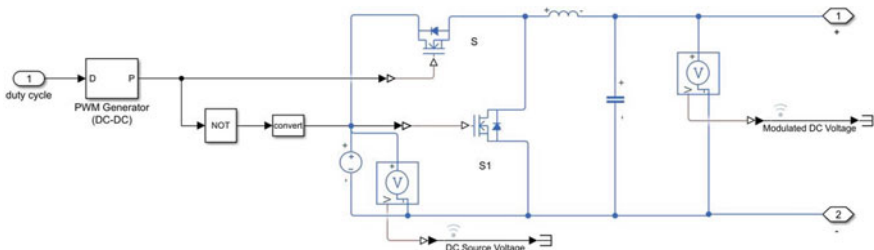


Fig. 7 PWM generator with buck converter (subsystem)

controller, is sent into the PWM generator. The PWM generator generates a signal that oscillates between 0 and 1 and regulates the on and off time of the buck converter’s two switches. Depending on this length, a varied amount of voltage drop at the buck converter’s output can be obtained.

The buck converter’s input is the DC source voltage, and the buck converter’s output is the modulated DC voltage supplied to the three-phase inverter (Fig. 7).

In Fig. 8 top trace indicates a DC source voltage of 500 V. The second one depicts the modulated DC voltage produced by the buck converter. The motor can be controlled at various speeds as a result of voltage modulation.

The observed speed is represented in orange, and it correctly tracks the target speed, which is indicated in green. In this setup, BLDC speed control is achieved by using a PWM generator in conjunction with a buck converter to supply a modulated DC voltage to the three-phase inverter.

### 2.2 PWM Under Commutation Logic

Another PWM-based approach for controlling a motor is by the commutation logic subsystem. The PWM generator output, according to this logic, ensures that the DC

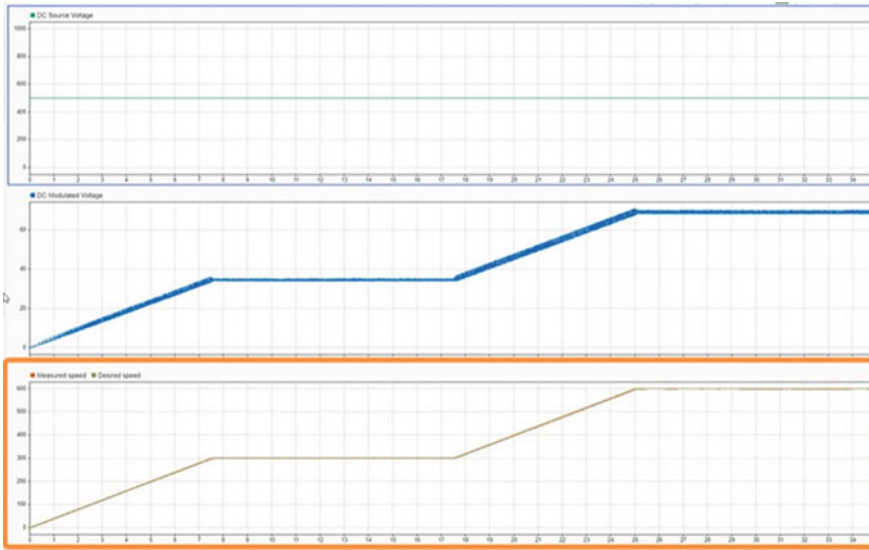


Fig. 8 Input DC voltage versus modulated DC voltage waveforms

source voltage is pulsed on and off to energize the right phases dependent on the sector that the rotor is shown in Fig. 9.

A commutation logic circuit is placed in between PWM generator and three-phase inverter. Commutation logic is based on the inputs of Hall Effect sensor. Hall Effect sensor senses the position of the rotor of BLDC motor. With the help of exact sector of rotor, commutation logic energizes the correct phase of three-phase inverter. The switching pattern of commutation logic depends upon rotor position.

The shift in phase voltages may be seen in the constant speed area. The motor runs at a steady pace. This logic selects a pair of inputs whenever the rotor is in any sector. This one requests a high and a low signal for two phases (A and C phases in

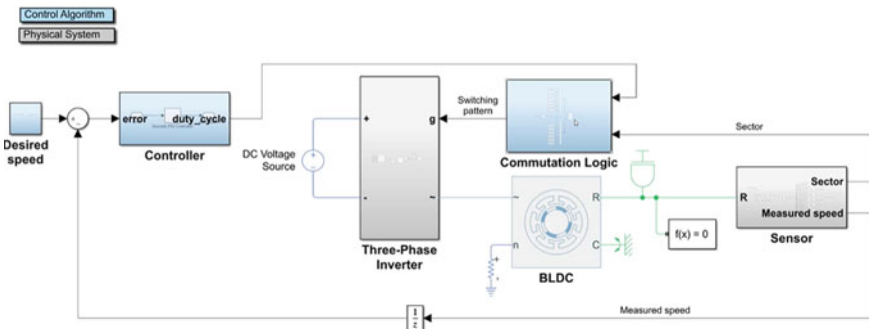
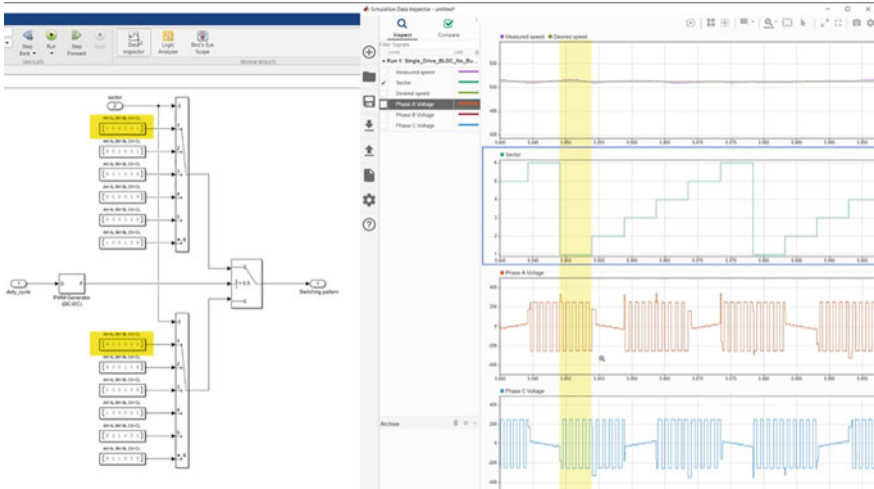


Fig. 9 Simulation of PWM under commutation logic



**Fig. 10** Selection of switching pattern under commutation logic and output waveform

Fig. 10), and this input, on the other hand, sends a low signal to A and a high signal to C. The PWM generator alternates between these two states dependent on its duty cycle, causing phase-A and phase-C voltages to pulse on and off between  $\pm 250$  V, which is  $\pm$  DC source voltage/2. The effective voltage sensed by the motor will be averaged when the phase voltages are adjusted in this manner.

### 3 Results and Discussions

Both the control methodologies are applicable in various industrial applications. Commutation logic-based controlling techniques provide a fine tuning of the speed of motor, whereas buck converter-based methods are easy to implement and not complicated.

Table 1 shows the comparison of both the methods:

This can be observed that six-step commutation for BLDC motor can be effectively used in control of BLDC motor in electric vehicles. It provides self-commutation characteristics of the motor also because of the effective use of Hall sensors placed inside the motor. This is recently proposed technique for electric vehicle control. Researches are also working in this area to find better results.

**Table 1** Comparison between buck converter and commutation logic-based approach for BLDC motor control

Sr. No.	PWM with buck converter	PWM with commutation logic
1	Its uses buck converter to modify DC input to the three-phase inverter	Commutation logic selects any two phases of inputs to three-phase inverter
2	Limitation to control the speed over the wide range	Fine control of speed is achieved for wide range
3	There is no role of sensor of BLDC motor, self-commutation is not possible	Self-commutation is possible with the help of sensor input

## 4 Conclusion

PWM control is known to have an averaging impact on the output voltage sensed by the motor. To achieve this averaging effect, the PWM frequency, which is calculated by  $1/\text{period}$ , must be properly chosen. If the switching frequency is too low, the motor will perceive a voltage that attempts to follow the square waveform rather than an averaged value. This will result in poor tracking of the reference speed, and the motor will continue to accelerate up and slow down. When the PWM frequency is increased to an acceptable level, the voltage is averaged out, which improves the speed control performance. Because of the switching nature of PWM, ripples will arise. PWM frequencies for controlling BLDC motors are typically in the kilohertz range and must be substantially higher than the reciprocal of the motor time constant. It is also observed that PWM under commutation logic provides better control, efficiency, and self-commutation to the motor, and these are preferred over buck converter-based methods for electrical vehicle drives. Commutation-based approaches can be used in the future to improve the efficiency and speed control of electrical vehicle drives and this work can be helpful in improving this.

## References

1. MATLAB. <https://www.mathworks.com>
2. Srivastava P, Tiwari VK (2020) Speed control of BLDC motor fed from solar PV array using particle swarm optimization. In: Proceedings of the 2020 9th international conference on system modeling and advancement in research trends, SMART 2020, pp 392–397. <https://doi.org/10.1109/SMART50582.2020.9337111>
3. LNCS Homepage. <http://www.springer.com/lncs>. Accessed 21 Nov 2016
4. Rameli M, Hais YR, Kadir REA (2017) Design of self-commutation BLDC motor with torque control strategy using fuzzy logic in hybrid electric vehicle (HEV). In: Proceedings of the 2017 international seminar on intelligent technology and its applications (ISITIA)
5. Sarojini Devi K, Dhanasekaran R, Muthulakshmi S (2016) Improvement of speed control performance in BLDC motor using fuzzy PID controller. In: Proceedings of the 2016 international conference on advanced communication control and computing technologies (ICACCCT), IEEE

6. Selmi T, Baitie HEK, Masmoudi A (2016) An approach to diagnose and remediate failures of Hall Effect sensors in BLDC motors. <https://doi.org/10.1109/SMART.2015.7399249>
7. Pindoriya RM, Rajendran S, Chauhan PJ (2016) Field programmable gate array based speed control of BLDC motor. <https://doi.org/10.1109/ISGT-Asia.2015.7387048>
8. Ahmad MW et al (eds) (2022) Intelligent data analytics for power and energy systems. Springer, Singapore, p 641. <https://doi.org/10.1007/978-981-16-6081-8>
9. Tomar A et al (eds) (2022) Proceedings of 3rd international conference on machine learning, advances in computing, renewable energy and communication: MARC 2021, vol 915. Springer, New York, p 781. <https://doi.org/10.1007/978-981-19-2828-4>
10. Mahendiran TV, Thanushkodi K (2013) A new improved algorithm for speed control of brushless DC motor. In: Proceedings of the 2013 international conference on current trends in engineering and technology, ICCTET 2013, pp 46–51. <https://doi.org/10.1109/ICCTET.2013.6675909>
11. Wang Z, Jin H, Guo J, Su J, Wang M (2017) Research on control system of three: phase brushless DC motor for electric vehicle. IOP Conf Ser Mater Sci Eng 274:012016. <https://doi.org/10.1088/1757-899X/274/1/012016>



# Effect of Number of Poles on IPMSM Performance for Electric Vehicle Drivetrain



Vinod Kumar Kuttey and Sravana Kumar Bali

**Abstract** Interior permanent magnet synchronous machine (IPMSM) has been widely used in different areas such as electric vehicles. The analysis and design process greatly affect the machine's performance. Especially, the selection of number of poles greatly affects the machine performance such as machine volume and machine losses. This paper deals with analysis of the three different pole numbers and slot numbers of IPMSM. Three types of design structures, 6-pole, 8-pole, and 10-pole, are compared using FEM. The results of these models are compared, and the trade-offs in selecting pole numbers are discussed. Finally, the most proper number of poles is selected after comparing three different models.

**Keywords** Pole number · Machine losses · FEM · IPMSM

## 1 Introduction

Interior permanent magnet synchronous motor (IPMSM) has performance characteristics such as high efficiency, high power density, and high torque density. These characteristics are greatly changed by the number of poles [1–3]. Therefore, the number of poles should be selected carefully in the initial design process to achieve high performance [4–8].

In this paper, the comparative analysis of interior permanent magnet synchronous motor (IPMSM) is used to investigate effect of number of poles on the IPMSM performance. Comparison analysis is performed according to various combinations of the number of poles and slots using FEM.

---

V. K. Kuttey (✉) · S. K. Bali  
GITAM Institute of Technology, Visakhapatnam 530045, India  
e-mail: [vkuttey@gitam.edu](mailto:vkuttey@gitam.edu)

S. K. Bali  
e-mail: [sbali@gitam.edu](mailto:sbali@gitam.edu)

This paper process is as follows: The first, three types of designs are analyzed using finite element method (FEM). Second, characteristics of these three types of designs are compared.

In the first part, 6-pole, 8-pole, and 10-pole designs are analyzed. These different machines are designed by keeping rotor outer diameter, air gap length, and stator inner diameter constant. The number of slots per pole is also kept constant so that 6-pole machine has 36 slots, 8-pole machine has 48 slots and 10-pole machine has 60 slots. All the machines have the same total slot area. Therefore, 6-pole machines have larger slot length than others. This allows more turns in one slot. For all designs, total ampere-turns are kept constant. The stator outer diameter is adjusted such that the maximum flux density in stator back iron, stator core connecting teeth, is 2 T at maximum current. The volume of magnets is kept constants for all designs. As the pole number increases, magnet width decreases such that all designs have the same torque and induced voltages [8].

## 2 Design of Three Types of IPMSM

The design of the three machines is performed referencing the Toyota Prius 2004 electrical motor. It has 8 poles and 48 slots. The 6- and 10-pole versions of these machines are designed in Ansys Maxwell environments. During the design stage, critical parameters of the original motor such as rated torque, speed, and current are kept the same. Three designs have the same stator inner diameter, air gap distance, and rotor outer diameter. On the contrary, stator outer diameter and rotor inner diameter change with respect to the pole number by keeping yoke flux density the same for all three designs. The number of slots per pole is kept the same such that 6-pole design has 36 slots, and 10-pole design has 60 slots. Three designs can be seen in the following figures [4].

As can be seen from the above figures, total magnet volume is kept the same by changing magnet length with respect to pole number such that 10-pole design has shorter magnets. By this way, induced voltages of all three designs kept the same for a fair comparison. It is seen that as pole numbers increase slot area decreases. By this way, total slot area is kept the same with increasing pole number.

The number of turns in a slot is adjusted by keeping current density in slots constant. Thus, 6-pole design has more turns in one slot since 6-pole design has larger slot area.

The parameters of the three different designs are given in Table 1.

The above parameters are calculated in such a way that the current density in a slot and torque are the same for all three designs. By considering that all designs have the same speed, it is shown that increase in pole number results in increasing electrical frequency.

**Table 1** Motor design parameters

	6-pole	8-pole	10-pole
Slot number	36	48	60
Slot area	× 20	× 15	× 12
Phase current	400 A	400 A	400 A
Number of turns per slot	12	9	7
Electrical period (ms)	13.3	10	8
Speed (rpm)	1500	1500	1500
Torque (Nm)	400	400	400

### 3 Comparison

In this section, three designs are compared in terms of size, induced voltage, loss, and other critical parameters by using FEM.

#### 3.1 Volume and Size

As the pole number increases, the magnet length decreases to keep total magnet volume same for all design. This results in less flux per pole. For all designs, saturation flux density is around 2 T for stator back yoke. By keeping maximum flux density at the back yoke close to this value, it is seen that as pole number increases, back core becomes thinner. This situation can also be seen in Figs. 1, 2, and 3. It is shown that 10-pole design has a smaller stator outer diameter due to this factor.

**Fig. 1** 6-pole design

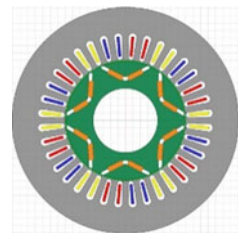


**Fig. 2** 8-pole design

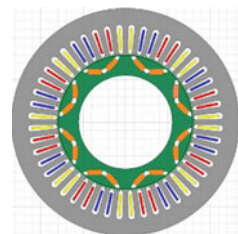


Fig. 3 10-pole design

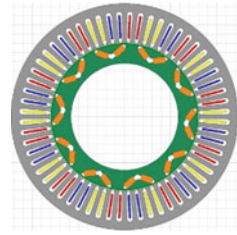
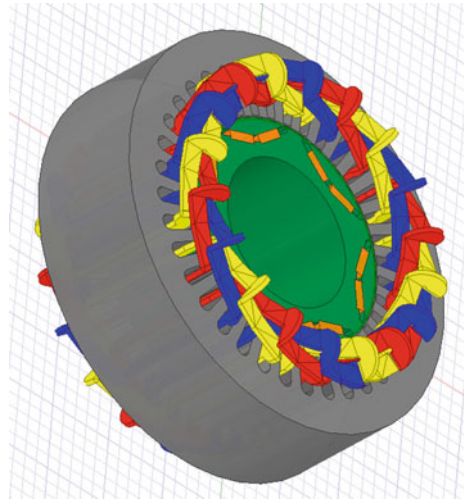


Fig. 4 Example of a figure caption



The other factor affecting volume is end winding length. The end winding is a portion of a turn that connects torque-producing effective parts of the windings. End windings don't contribute to the torque production, and they cause copper losses. The end windings of a 6-pole machine can be seen in Fig. 4.

As pole numbers increase, pole belts in mechanical degrees decrease. This results in smaller end winding length for designs with higher number of poles. However, it should be noted that as pole number increases, total number of end windings also increases due to the increases number of slots. For different number of poles, one turn with end windings is depicted in Fig. 5.

In Fig. 5, it is clearly seen that 10-pole design has shorter end winding length. This is better in terms of copper losses. Also, note that axial length of overall machine decreases as pole number increases. This factor affects the total volume of the machines. Total volume of the machine is calculated as in 1.

$$V = L * \pi * OD^2 / 4, \tag{1}$$

where  $V$  is the total volume of the motor,  $L$  is the axial length of the machine considering axial length of a turn as shown in Fig. 5, and  $OD$  is the outer diameter of

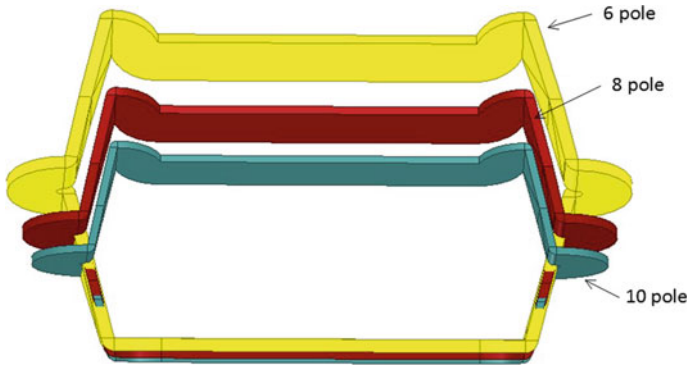


**Fig. 5** One 3D turns of 6–8–10-pole design

**Table 2** Volume comparison of the machines

	6 poles	8 poles	10 poles
Stator outer diameter (mm)	282	269	262
Axial length (mm)	165	157	152
Total volume (lt)	10.3	8.9	8.2

the stator. Using these design parameters, size, and volume data for different designs are tabulated in Table 2.

In Table 2, it is shown that volume decreases with increasing number of poles. This is an important outcome of this study. However, increasing pole numbers have some drawbacks, which will be studied in the next section.

### 3.2 Volume and Size

In a machine, there are mechanical losses, core losses, and copper losses. In this paper, the last two are analyzed. Firstly, three machines are run in a no-load case, i.e., when there are no phase currents, and core losses for machines are acquired using 2D FEM. The core losses under the no-load case are shown in Fig. 6.

It is shown that under no-load excitation core losses are almost ignorable. As pole numbers increase, electrical frequency also increases. It is known that core loss is proportional with material volume and square of the electrical frequency. This factor determines core loss in stator and rotor yoke. Since there is no excitation under this case, there are no copper losses.

Under rated current of 400A operation, core losses increase. Three designs have core and copper losses obtained from 2D FEM as in Figs. 7 and 8, respectively.

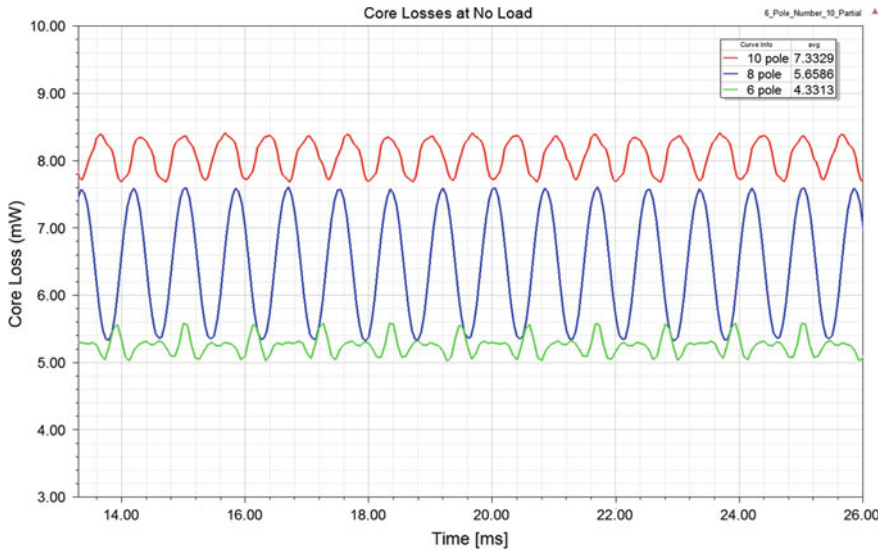


Fig. 6 Core losses under no-load case

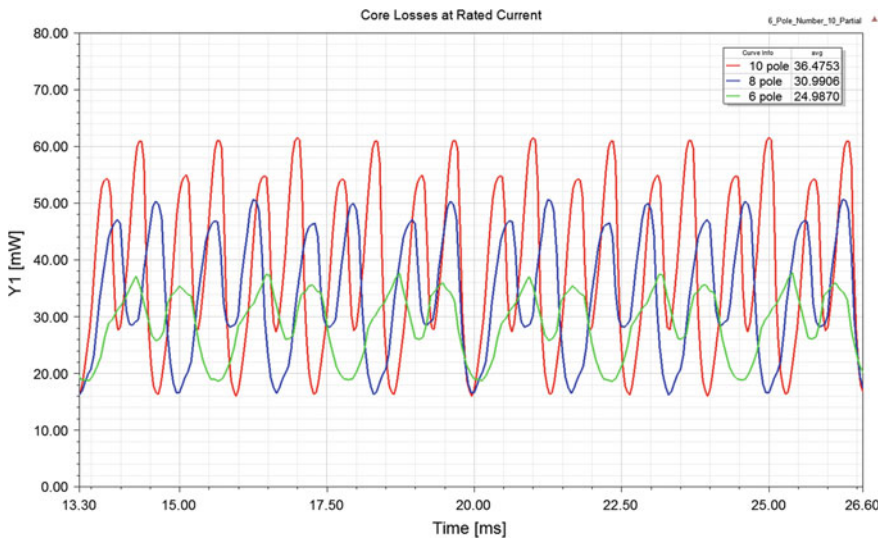


Fig. 7 Core losses under full load

It is shown that 10-pole design has the highest core and copper losses. This is another important outcome of this study. Increasing pole number also increases both copper and core losses. Thus, there is a trade of between volume and loss.

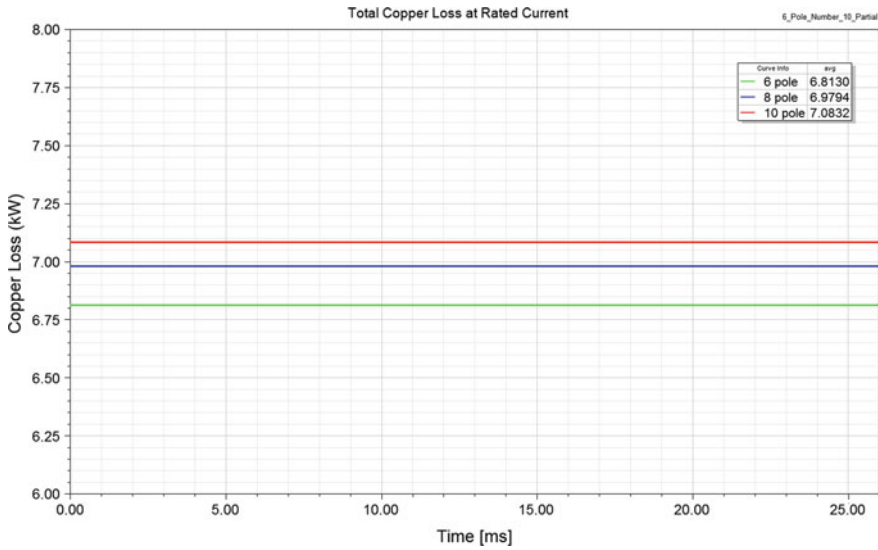


Fig. 8 Copper losses under full load

### 3.3 Induced Voltages

Induced voltages for three designs are compared under no-load excitation at 1500 rpm. In this case, there is no current in phases and voltage measured at the terminals is equal to the back emf, which results from flux linked by phases created by permanent magnets. Line-to-line induced voltages can be seen in Fig. 9.

As can be seen in Fig. 9, all designs have the same peak-to-peak magnitude of induced voltages. This is expected since total ampere-turns for all designs are the same, and the same magnet volume is used for all. Flux linkages are also the same.

It is stated that for lower number of poles, slot area is large and high number of turns are used although a total number of turns are the same for all designs. Another point to note in Fig. 9 is that designs have different periods. It is stated that as pole numbers increase, for the same speed, electrical frequency increases.

### 3.4 Other Parameters

In this subsection, some other critical parameters are compared for different machines. Torque produced under the same excitation and torque ripple are compared for all machines. For the comparison, all machines are run at 400 A of maximum phase current and load angle of 45°. The results are shown in Fig. 10.

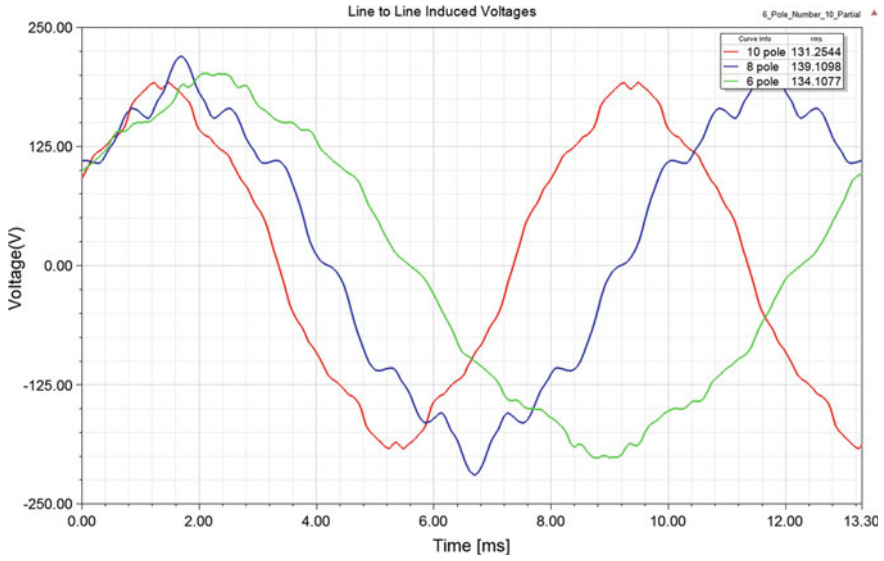


Fig. 9 Induced voltages under no-load

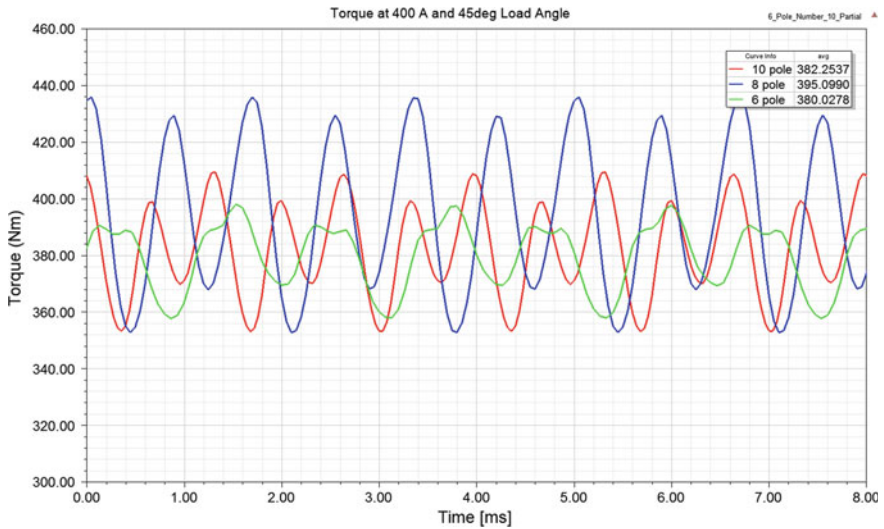


Fig. 10 Torque under rated current

It is known that pole and slot number selection have significant effect on torque ripples. In the analysis, it is shown that maximum torque ripple is observed for 8-pole design. All designs have almost the same average torque.



**Table 3** Magnet flux linkage and inductances

	6 poles	8 poles	10 poles
$\Psi_{PM}$	237 mWb	168 mWb	125 mWb
$L_d$	0.79 mH	0.54 mH	0.45 mH
$L_q$	2.3 mH	1.6 mH	1.3 mH

**Table 4** Base speeds in mechanical rad/s

	6 poles	8 poles	10 poles
$\omega_{base}$	150 rad/s	160 rad/s	166 rad/s

**Table 5** Electrical and proposed switching frequencies

	6 poles	8 poles	10 poles
Electrical frequency	75 Hz	100 Hz	125 Hz
Switching frequency	6 kHz	8 kHz	10 kHz

In this study, magnet flux linkage, direct and quadrature axis inductances of all designs are also compared. These parameters are calculated using finite element analysis on Maxwell. Magnetic flux linkage is peak flux linkage of any phase under no-load excitation. Quadrature and direct axis inductances are calculated from the inductance matrix obtained from Maxwell and using transformations. These values are tabulated in Table 3.

It is observed that inductances are higher for small number of poles. This is expected since there are higher number of turns per slot in designs with small number of poles. It is known that inductance is proportional with square of number of turns.

$$\frac{V_{DC}}{\sqrt{3}} = \sqrt{(-L_q i_q)^2 + (L_d i_d + \emptyset_p M)^2}, \quad (2)$$

where  $V_{DC}$  is DC link voltage and  $\omega$  is base speed in electrical radians per second. Using the electrical parameters calculated in Table 3, base speed of the machines is calculated as in Table 4.

Electrical frequency increases with increasing pole numbers. Electrical frequencies for all designs are tabulated in Table 5. Switching frequency is suggested to be around 20 times of electrical frequency, as a rule of thumb. The suggested switching frequency for each design is also tabulated in Table 5.

## 4 Conclusion and Future Scope

This paper deals with three types of IPMSM as the pole numbers of 6, 8, and 10. 10-pole machines have lower torque ripple than 6-pole and 8-pole machines. Since all three designs have the same flux linkages, they all have almost the same torque value

and almost the same induced voltages. The stator outer diameter and end winding length decrease as the number of poles increases. Therefore, the volume of machine decreases as the number of poles increases. So, the higher pole number means that higher torque density, higher power density. But the core losses increase as the pole number increases. 10-pole machine has an electrical frequency of 1.67 times of 6-pole machine's electrical frequency. On the other hand, a 6-pole machine's volume is equal to 1.26 times of 10-pole machine's volume. Core loss is proportional to square of frequency and proportional to volume. Thus, core losses increase as the number of poles increases. The copper loss also increases as the number of poles increases. This reduces machine efficiency. In conclusion, one should consider the trade-off when selecting the number of poles of IPMSM. It should be considered by design requirements. From the results obtained in this paper, the most proper pole number seems to be 8. Because its volume is not much > 10-pole, its core losses are much smaller than 10 poles.

## References

1. Jung J, Hong J, Kim Y (2007) Characteristic analysis and comparison of IPMSM for HEV according to pole and slot combination. In: Proceedings of the 2007 IEEE vehicle power and propulsion conference, Arlington, TX, pp 778–783
2. Cho CH, Jin CS, Jang IS, Lim SB, Lee J (2008) A comparative analysis of two kinds of poles for washing machines IPMSM with the same torque and output power. In: Proceedings of the 2008 international conference on electrical machines and systems, Wuhan, pp 3099–3101
3. Lee J, Kim J, Chang J, Chung S, Kang D, Hong J (2008) Determination of parameters considering magnetic nonlinearity in solid core transverse flux linear motor for dynamic simulation. *IEEE Trans Magnet* 44(6):1566–1569
4. Gaussens B, Boisson J, Abdelli A, Favre L, Bettini D (2017) Torque ripple mitigation of PM-assisted synchronous reluctance machine: de-sign and optimization. In: Proceedings of the 2017 20th international conference on electrical machines and systems (ICEMS), Sydney, NSW, pp 1–6
5. Mao Y, Zuo S, Cao J (2018) Effects of rotor position error on longitudinal vibration of electric wheel system in in-wheel PMSM driven vehicle. *IEEE/ASME Trans Mechatr* 23(3):1314–1325. <https://doi.org/10.1109/TMECH.2018.2818260>
6. Ahmad MW et al (eds) (2022) *Intelligent data analytics for power and energy systems*. Springer, Singapore, p 641. <https://doi.org/10.1007/978-981-16-6081-8>
7. Tomar A et al (eds) (2022) *Proceedings of 3rd international conference on machine learning, advances in computing, renewable energy and communication: MARC 2021*, vol 915. Springer, New York, p 781. <https://doi.org/10.1007/978-981-19-2828-4>
8. Zhou Y, Yan L, Ge L, Aboelhassan A (2022) Output performance comparison of surface-mounted PMSM based on conventional and modified segmented halbach magnet arrays. In: Proceedings of the 2022 IEEE 17th conference on industrial electronics and applications (ICIEA), Chengdu, China, pp 296–300. <https://doi.org/10.1109/ICIEA54703.2022.10006083>

# Offline Power Quality Management and Control Using Neural Networks



Papia Ray, Surender Reddy Salkuti, and R. Aditya Kumar

**Abstract** In this study, the power quality (PQ) of a single-phase system is evaluated using a neural network (NN). The NN-based backpropagation (BP) technique is used to do offline assessment. The disturbances are produced using Simulink in MATLAB. The dyadic analysis filter bank receives these disturbances to acquire signal's features. For training and testing NN, these extracted characteristics are used as input data. For single-phase evaluation without a filter bank, the conjugate gradient descent backpropagation algorithm (CGB) is initially utilized. However, training and accurate results require 100 neurons. For accurate findings, which are highly desired, the number of neurons is reduced by using a filter bank from 100 to 20. Hence, the feature extraction uses a filter bank. Using the same input data, seven backpropagation techniques train the network. The scaled conjugate gradient algorithm (SCGB)-based NN has been tested and shown to be superior to other algorithms. For training and testing the NN with the NN tool in MATLAB, the extracted features from the filter bank are utilized as the input data against the target data. The novelty to this work is that PQ disturbance signals are fed to a dyadic analysis filter bank and the number of neurons is reduced to 20. Also, here the SCGB-based NN is used for the first time for evaluating the accuracy of the algorithm. It is found from simulation results that SCGB-based NN gives 100% accuracy with minimum no. of neurons (20) and mean square error (MSE) during training (0.0034071).

**Keywords** Power quality · Neural networks · Dyadic analysis · Filter bank · Feature extraction · Gradient algorithm

---

P. Ray · R. Aditya Kumar  
Department of Electrical Engineering, Veer Surendra Sai University of Technology (VSSUT),  
Burla, Odisha, India  
e-mail: [papiaray\\_ee@vssut.ac.in](mailto:papiaray_ee@vssut.ac.in)

S. R. Salkuti (✉)  
Department of Railroad and Electrical Engineering, Woosong University, Daejeon, Republic of  
Korea  
e-mail: [surender@wsu.ac.kr](mailto:surender@wsu.ac.kr)

## 1 Introduction

Power quality (PQ) has become a vital issue for industrial and domestic consumers. A more straightforward and perhaps more concise definition might state: “Electric PQ is the degree to which the voltage, frequency, and waveform of a power supply system conform to established specifications”. Good PQ refers to a system that is free from the disturbances like harmonics, transients, sag, swell, flicker, noise, etc. [1, 2]. Any supply that deviates from this ideal is said to have poor PQ; whether the variation is necessary depends on the installation’s purpose, equipment’s design, and design.

These disturbances are called electromagnetic disturbances and can be very hazardous as per their intensity. These disturbances originated due to various reasons. These disruptions were caused by the increased usage of automatic systems, variable speed drives, and power electronics-based circuits. Insulation faults and breaking neutral conductors cause voltage sag (dip) and unbalance [3, 4]. The overvoltage and voltage swell are caused by lightning, switching, and ferro-resonance. The causes of voltage dips, imbalance, fluctuations, and harmonics are synchronous and asynchronous motors, welding equipment, arc furnaces, and welding machines.

For equipment like programmable logic controllers, televisions, microwaves, refrigerators, etc., electromagnetic problems like voltage dip and swell are dangerous. Compatibility issues can cause industries to lose market share, revenue, brand value, energy, and money. They can also damage equipment and increase energy usage [5, 6]. Customers may get dissatisfied when critical pieces of equipment malfunction in hospitals, airports, etc. Devices like dynamic voltage restorers, filters, uninterruptible power supplies, reactive compensators, etc., are utilized to correct PQ difficulties. It is vital to recognize and categorize the problems for this equipment to operate properly. The only option is compensation if the problem is correctly identified and categorized. Issues are identified and classified as part of PQ evaluation or monitoring. Some standards are set to evaluate the quality of power given by IEEE and IEC [7, 8]. These standards provide an everyday basis for assessing PQ concerns, system performance, and equipment performance. With the help of these standards, the characteristics of the power system and the needs of end-use equipment will be coordinated. According to these criteria, PQ is evaluated in this paper.

In the last two decades, most research has been done on a particular disturbance, i.e., voltage sag. Voltage sags occur more often because they are the secondary result of other disturbances broadcast over a larger area. When a fault (short circuit between any two phases of the transmission lines) occurs, a power outage in the general vicinity of the fault is produced [9]. The voltage level of a much broader grid area is dragged down as the entire grid tries to feed the fault. A voltage sag can last as long as the fault is in place. This condition is very hazardous for the whole of the power system. Hence, many researchers’ main goal is voltage sag assessment and its compensation. This paper also considers voltage sag a significant disturbance to be assessed [10]. Along with voltage sag, the disturbances monitored are voltage swell, interruption, and harmonics, sag with harmonics and swell with harmonics. In

Ref. [11], monitoring of the power quality of mono and polyphase AC power systems is reported, and consistent descriptions of conducted electromagnetic phenomena are included. This situation occurs due to deviation from nominal condition.

Summary of research gap from the aforesaid literature survey are:

- Proper training algorithm is not chosen till now for proper detection of PQ events.
- Number of neurons are not optimized to a minimal one.
- SCGB-based NN is not used till now for PQ event detection.

The novelty of the proposed work is:

- PQ disturbance signals are fed to a dyadic filter bank for first time and the number of neurons is reduced to a minimum value (20).
- Also, here the SCGB-based NN is used for the first time for evaluating the accuracy of the algorithm.
- The validation of the result is performed by examining seven training algorithms.

Remaining paper has Sect. 2 which focuses on work formulation and suggested approach, Sect. 3 depicts offline PQ assessment, Sect. 4 gives results and discussion and conclusion in Sect. 5.

## 2 Work Description and Proposed Approach

Power system has advanced to point that some issues, such as evaluating system performance, equipment compatibility, predictive or just-in-time maintenance, and improving PQ services need to be handled with extreme care. Evaluation of system performance is very important for the power producer [12, 13]. He can tailor the system performance to the client's needs after understanding the system performance. System characterization is a preventative method of PQ evaluation [14]. Understanding a system's typical PQ performance allows a provider to see issues immediately and provide information to his clients that will assist them in matching the features of their sensitive equipment with actual PQ characteristics.

PQ data accumulated over time can be examined to reveal details about the performance of particular equipment. For instance, repeated capacitor-switching restrikes may signal an impending failure of the capacitor-switching mechanism, just as repeated arcing faults from an underground cable may signal an impending cable failure. It is possible to swiftly request equipment repair to avert catastrophic failure, which would ultimately affect the functioning of PQ as a whole. To achieve the above objectives, reliable automatic recognition of PQ indices/disturbances is required [15]. Different algorithms have been defined to perform automatic detection and classification to relate the signal characteristic with the group they belong to. Some examples of automatic disturbance recognition algorithms are decision trees, fuzzy logic, NNs, support vector machines, etc. These methods can be used online if implemented in LabVIEW or a digital signal processor for PQ assessment. The NN is the best for offline assessment systems, due to its parametric model in

various applications [16, 17]. This parametric model can be used in LabVIEW if a mathematical model is established. Therefore, the suggested work attempts to build a mathematical model for LabVIEW for online PQ evaluation of the system while assessing PQ disturbances in offline mode with a NN.

The simulation study and comparison of the performance of seven different backpropagation algorithms are made to choose this backpropagation algorithm. The simulation study or offline power assessment is done in MATLAB. The disturbances are generated in MATLAB using programming and a simulation model. These disturbances are fed to the four dyadic analysis filter banks to extract the features of the voltage signal [18]. These extracted features are used as input data to train the network and test the NN. Initially, seven backpropagation algorithms are taken to train network with same data as input [19]. The NN based on scaled conjugate gradient algorithm (SCGB) is the best among Levenberg–Marquardt (LM), conjugate gradient (CGB), Bayesian regularization (BR), one step secant (OSS), gradient descent with momentum (GDM), and gradient descent with adaptive learning algorithms (GDx). The flowchart for performing the offline assessment is shown in Fig. 1.

Mathematical model of network trained by SCGB is developed and implemented in LabVIEW environment for online assessment. LabVIEW is interfaced with the experimental setup of the electromagnetic disturbance generator. For a single-phase system, the experimental setup is built with the help of various microcontrollers and solid-state relays (SSR). The controlling pulses to the SSR are controlled with a microcontroller [20, 21]. The disturbances considered for evaluation are voltage sag, swell, 5 under voltage, overvoltage, harmonics, sag, and swell with harmonics. For a three-phase system, three-phase programmable voltage source is used. Disturbance voltage is measured on the load side using voltage sensors and a data collecting system. DAQ assistant block is used in LabVIEW to acquire the signal. Along with implemented trained network, RMS and FFT measurement blocks are used. The experimental setup interfaced with LabVIEW gives the best online PQ assessment platform.

Many transformation techniques, such as Fast Fourier (FFT), Short Time Fourier (STFT), Wavelet (WT), Stockwell (ST), etc., are taken in signal analysis [22, 23]. Most of these methods are used in PQ analysis [24–27]. Fast Fourier transform is the primary and popular analysis method. The other ways are the modifications of fast Fourier transform methods which minimizes the drawback of FFT.

## **2.1 Training Commands**

The NN is trained with a backpropagation algorithm's help using specific MATLAB commands. The conjugate gradient backpropagation algorithm can be realized using the command “traincgb”. To train the network with a scaled conjugate gradient algorithm, “traincsg” is used. For LM algorithm, “trainlm” command is taken. “trainbr” is employed to train the network using the Bayesian regularization approach. To train the network with one step secant, “trainoss” command is used. Gradient descent with

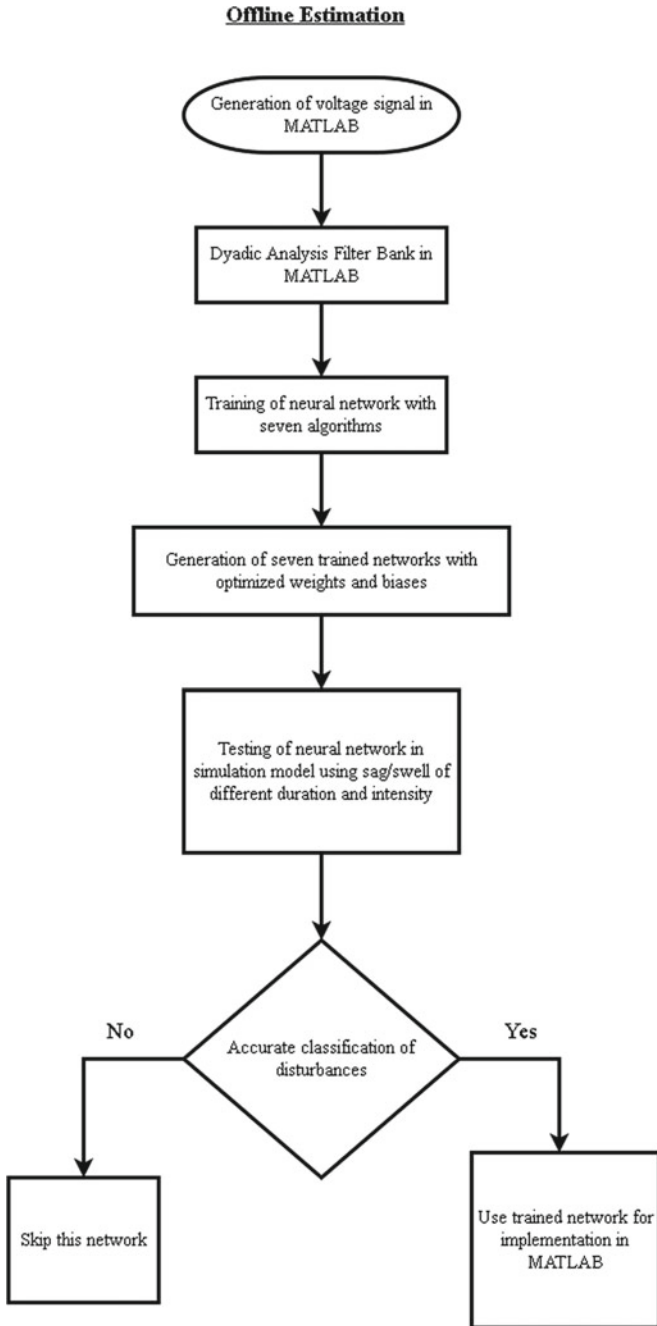


Fig. 1 Offline PQ assessment

momentum and an adaptive learning rate algorithm can be realized using “traingdm” and “traingdx”, respectively. These instructions with input and target matrix availability assist train network. In this study, the input matrix consists of generated disturbances and the target matrix is the desired output in the form of 0 and 1. The following sections explain the use of the NN for PQ assessment.

### **3 Offline PQ Assessment**

The aim of this work is to use the NN offline for PQ assessment. To achieve this, it is necessary to train and test network in offline mode. Data is required to train and test the NN. This data is in the form of generated disturbances saved in the matrix form. The general step 27 for using a NN for the application is the generation of data, feature extraction, training, and testing of the network. The feature extraction step is taken into account and seven algorithms are compared. The number of neurons required in the initial case is more than later case. A smaller number of neurons are desirable for less computation.

#### ***3.1 Production of Disturbances***

A simulation model is used to create the disturbances. An RMS voltage drop between 0.9 and 0.1 p.u. for 10 ms to 1 min is referred to as a voltage sag or dip. Voltage swell is an increase in RMS voltage between 1.1 and 1.8 p.u. for a duration of 10 ms to one minute. It comprises switches, a load, three voltage sources, and a measurement block. The voltage sources are used to generate normal voltage, or 230 V (RMS), as well as voltage dips and swells between 23 and 207 and 253 and 414 V (RMS), as well as various PQ disturbances, including voltage fluctuation, interruption, and transient (peak or surge) voltages. Switches switch the voltage levels provided to the loads according to the situation. An internal control timer is used to govern these switches. Voltage dips and swells can therefore be produced at any time and with any magnitude. These generated signals are fed into the feature extraction filter bank for dyadic analysis.

#### ***3.2 Voltage Signal Feature Extraction Using a Filter Bank***

Evaluation of electromagnetic disturbances is one example of a pattern recognition difficulty. One pattern class can be separated from another using feature vectors in pattern recognition. Pattern spaces frequently have a great degree of dimension. This categorization is essential. Another name for this procedure is “mapping pattern space



into feature space". The feature extraction method is used to complete this dimensionality reduction task. As a result, feature extraction (FE) reduces the dimension of existing features. If input signal  $c$  is provided by,

$$c = [c_1, c_2, c_3, \dots c_n] \quad (1)$$

FE process provides feature vector  $d$  after application,

$$d = f[c_1, c_2, c_3, \dots c_n] \quad (2)$$

The optimal transformation method for the feature extraction procedure is discrete wavelet transform (DWT). Feature vectors that are the same length as the input are generated after DWT. Almost all of the data in this vector are 0. This results from the signal's breakdown into a collection of wavelets orthogonal to its scaling. The decomposed wavelet spectrum is more effective than raw data for detecting patterns. This research implements DWT using a bank of dyadic analysis filters. The simulation model makes use of the MATLAB block for filter bank. The DWT is calculated, or signal is divided into subbands using this filter bank. This filter bank interprets the input as frames. If possible, the frame size should be more than or equal to  $2z$ , where  $z$  represents the appropriate level.

In many signal processing applications, the compactly supported orthogonal wavelet known as the Daubechies wavelet is employed. The suggested design has tested wavelets from the Daubechies family for the required application. The Daubechies wavelets D1–D8 are utilized for testing. The voltage signal is examined with various Daubechies wavelets D1–D8 and levels 1–8. It has been shown that the level three Daubechies three wavelet transformation of the voltage signal produced the best outcomes. Daubechies level being three, input vector is translated to an eight-frame signal. To do this, seven delay blocks are used to lengthen the signal. Discrete time input is delayed by specific no. of samples or frames in each delay block. Eight distinct wavelet coefficients are produced as the dyadic filter bank's output and are utilized for training. Figure 2 displays block diagram for DWT feature extraction step with filter bank. In Fig. 2, collected PQ signal is subjected to a sequence of dyadic filters (low and high pass) to extract low and high frequency coefficients, denoted, respectively, by letters " $a$ " and " $d$ ". Thereafter the reconstruction of the coefficients is done to get the total information of the signal. Further energy is extracted from the reconstructed coefficients using Eq. (3).

$$\text{Energy} = \sum_{i=1}^N \frac{D_i^2}{N} \quad (3)$$

where, ' $D$ ' denotes reconstructed detailed coefficient and ' $N$ ' is the level up to which the decomposition is done.

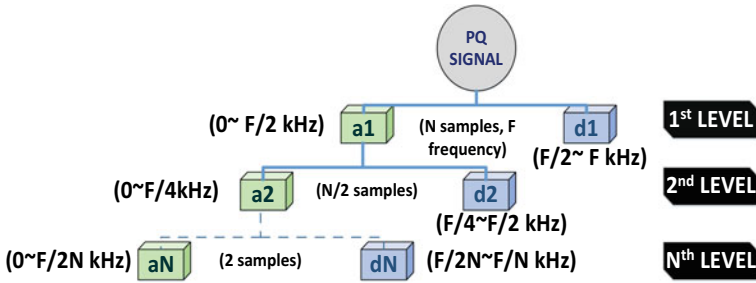


Fig. 2 Steps for DWT feature extraction

### 4 Results and Discussion

Input variables, an optimization algorithm, and the desired outcome are needed to train NNs. Thereafter, training with NNs in MATLAB is done. The retrieved features are used as input in this study. The best cross-validation method is the three-way data split-up approach. As a result, it is employed in cross-validation. A total of 60% of the input samples are utilized for training, 15% are used for testing, and remaining 15% are used for validation. Training is done using a backpropagation algorithm and feed-forward NN. Because the training pattern is supervised learning, disruption events are known beforehand. The backpropagation algorithm that performs the best for estimating electromagnetic disturbances has not been documented in the literature. To compare the backpropagation methods, an experiment is conducted. The performance of seven NNs trained using seven different algorithms is compared.

There are two hidden layers. During training, the number of neurons is chosen from 1 to 100. These are preserved together with 100 other training networks. Each network’s output is assessed. A network with 20 neurons produces accurate results. As a result, 20 neurons are the final number. The specified inputs, targets, and multiple neurons are employed with seven optimization techniques. 24 times are spent training each type of NN algorithm. Each time, the created trained network is saved for testing. The Simulink model of said approach is reported in Fig. 3. Figure 4 gives the graph of generated voltage disturbances. The training graphs for seven types of NNs are illustrated in Fig. 5.

From Fig. 5 it can be observed that SCGB-based NN gives least MSE during training and testing process when compared with other algorithms of NN. This is more clearly depicted in Table 1. Table 1 lists various parameters for seven different NN types. The optimized weights and biases values have a lower mean squared error. The number of neurons in a system increases its complexity. Therefore, while choosing a NN to be used for online assessment, mean squared error, the no. of neurons and accuracy are crucial factors to consider.

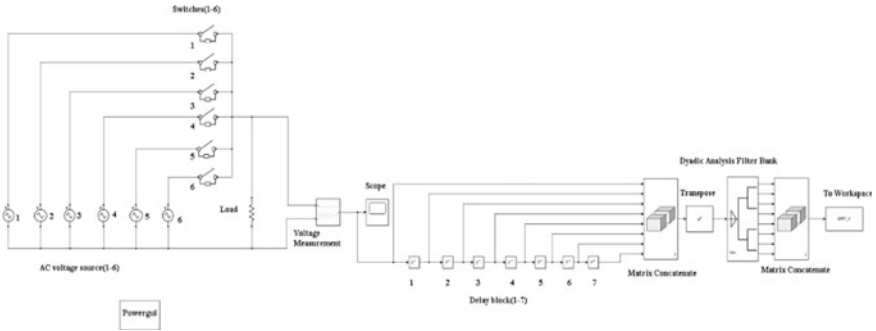


Fig. 3 Simulink model

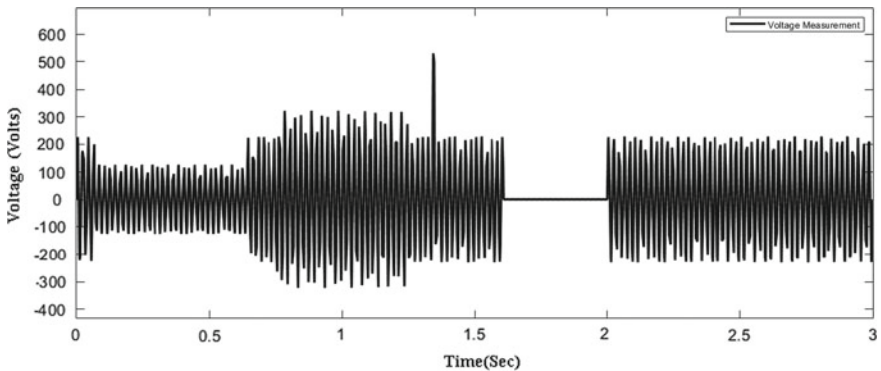
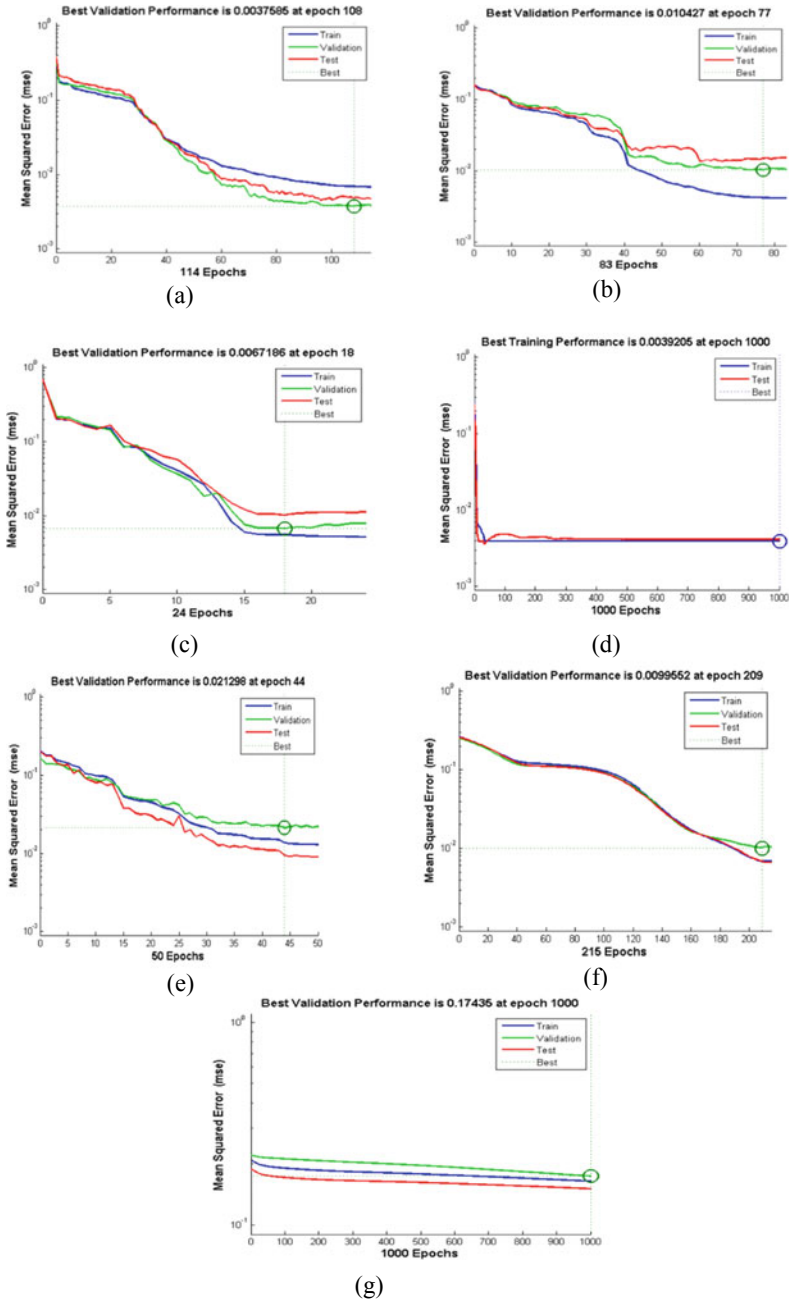


Fig. 4 Graph of generated voltage disturbances

From Table 1, it can be observed that SCGB training algorithm for neural network gives 100% accuracy with minimum MSE. In order to validate the result, the proposed work is compared with other researcher’s similar work and is depicted in Table 2.

It is depicted from Table 2 that the proposed scheme in this paper achieves maximum accuracy when compared with other researcher’s schemes. So, the proposed scheme, i.e., PQ analysis with SCGB-based NN is recommended and also other examples of NN are given in [31, 32].



**Fig. 5** Training graphs for seven types of NNs **a** SCGB, **b** CGB, **c** LM, **d** BR, **e** OSS, **f** GDX, **g** GDM

**Table 1** Various parameters for seven types of neural networks

Algorithms	Parameters			
	No. of neurons	Epochs	MSE in training set	Accuracy (in percentage)
SCGB	20	106	0.0034071	100
CGB	20	87	0.0163	93
LM	20	29	0.0078173	89
OSS	100	53	0.03241	63
BR	20	1000	0.004438	72
GDX	20	203	0.0850	82
GDM	> 100	1000	0.17813	32

**Table 2** Comparison with other researcher’s work

Scheme	MSE in training set	Accuracy (in percentage)
[28]	0.0089	99.8
[29]	0.326	96
[30]	0.563	94
Proposed one	0.0034071	100

## 5 Conclusion

In this paper, an offline assessment is performed by using the neural network (NN)-based backpropagation algorithm. The disturbances are generated in MATLAB using Simulink. The scaled conjugate gradient algorithm has the lowest mean squared error, while the gradient descent with the momentum algorithm has the highest mean squared error, which should be the minimum. According to test findings, SCGB algorithm offers greatest accuracy in terms of depicting voltage perturbations in PQ. The produced NN is saved, and the mathematical model of the NN can be developed using the mathematical model in LabVIEW for the online assessment of the PQ. The novelty to this work is that PQ disturbance signals are fed to a dyadic analysis filter bank and the number of neurons is reduced to 20. Also, here the SCGB-based NN is used for the first time for evaluating the accuracy of the algorithm. It is found from simulation results that SCGB-based NN gives 100% accuracy with minimum no. of neurons (20) and mean square error (MSE) during training (0.0034071). Future work includes validation of the proposed scheme with experimental setup dataset and applying recent optimization algorithms like extreme learning machine, histogram of oriented gradients, etc.

**Acknowledgements** This research work was supported by “Woosong University’s Academic Research Funding—2022”.

## References

1. Khadse CB, Chaudhari MA, Borghate VB (2017) Comparison of seven backpropagation algorithms for three phase power quality assessment. In: Proceedings of TENCON 2017—IEEE region 10 conference, Penang, Malaysia, pp 2548–2553. <https://doi.org/10.1109/TENCON.2017.8228291>
2. Heydt GT (1998) Electric power quality: a tutorial introduction. *IEEE Comput Appl Power* 11(1):15–19. <https://doi.org/10.1109/67.648490>
3. Das B, Panigrahi PK, Das SR, Mishra DP, Surender RS (2022) Power quality improvement in a photovoltaic based microgrid integrated network using multilevel inverter. *Int J Emerg Electr Power Syst* 23(2):197–209. <https://doi.org/10.1515/ijeeps-2021-0040>
4. Jurado F, Acero A, Ogayar B (2002) Application of signal processing tools for power quality analysis. In: Proceedings of IEEE Canadian conference on electrical and computer engineering, vol 1, pp 82–87. <https://doi.org/10.1109/CCECE.2002.1015179>
5. Hamid EY, Kawasaki ZI (2002) Wavelet-based data compression of power system disturbances using the minimum description length criterion. *IEEE Trans Power Delivery* 17(2):460–466. <https://doi.org/10.1109/61.997918>
6. Ray P, Salkuti SR (2020) Smart branch and droop controller-based power quality improvement in microgrids. *Int J Emerg Electr Power Syst* 21(6):2020. <https://doi.org/10.1515/ijeeps-2020-0094>
7. Angrisani L, Daponte P, Apuzzo MD (2001) Wavelet network-based detection and classification of transients. *IEEE Trans Instrum Meas* 50(5):1425–1435. <https://doi.org/10.1109/19.963220>
8. Ece DG, Gerek ON (2004) Power quality event detection using joint 2-D wavelet subspaces. *IEEE Trans Instrum Meas* 53(4):1040–1046. <https://doi.org/10.1109/TIM.2004.831137>
9. Gerek ON, Ece DG (2008) Compression of power quality event data using 2D representation. *Electr Power Syst Res* 78(6):1047–1052. <https://doi.org/10.1016/j.epsr.2007.08.006>
10. Mishra DP, Nayak AS, Tripathy T, Salkuti SR, Mishra S (2021) A novel artificial neural network for power quality improvement in AC microgrid. *Int J Power Electron Drive Syst* 12(4):2151–2159. <https://doi.org/10.11591/ijpeds.v12.i4.pp2151-2159>
11. P1159/D5—IEEE draft recommended practice for monitoring electric power quality, Dec 2018. ISBN: 978-1-5044-5395-0
12. Karimi M, Mokhtari H, Iravani MR (2000) Wavelet-based on-line disturbance detection for power quality applications. *IEEE Trans Power Delivery* 15(4):1212–1220. <https://doi.org/10.1109/61.891505>
13. Lin CH, Wang CH (2006) Adaptive wavelet networks for power-quality detection and discrimination in a power system. *IEEE Trans Power Delivery* 21(3):1106–1113. <https://doi.org/10.1109/TPWRD.2006.874105>
14. Subhash B, Rajagopal V, Salkuti SR (2022) Optimization of controller gains to enhance power quality of standalone wind energy conversion system. *Int J Emerg Electr Power Syst* 23(1):89–104. <https://doi.org/10.1515/ijeeps-2021-0024>
15. Yong DD, Reineri C, Magnago F (2013) Educational software for power quality analysis. *IEEE Lat Am Trans* 11(1):479–485. <https://doi.org/10.1109/TLA.2013.6502849>
16. Zhang H, Liu P, Malik OP (2003) Detection and classification of power quality disturbances in noisy conditions. *IEE Proc Gener Transm Distrib* 150(5):567–572. <https://doi.org/10.1049/ip-gtd:20030459>
17. Mokhtari H, Ghartemani MK, Iravani MR (2002) Experimental performance evaluation of a wavelet-based on-line voltage detection method for power quality applications. *IEEE Trans Power Delivery* 17(1):161–172. <https://doi.org/10.1109/61.974204>
18. Bruce LM, Koger CH, Li J (2002) Dimensionality reduction of hyperspectral data using discrete wavelet transform feature extraction. *IEEE Trans Geosci Remote Sens* 40(10):2331–2338. <https://doi.org/10.1109/TGRS.2002.804721>
19. Andrew JP, Ogunbona PO, Paoloni FJ (1994) Comparison of “wavelet” filters and subband analysis structures for still image compression. In: Proceedings of ICASSP '94. IEEE international conference on acoustics, speech and signal processing, Adelaide, SA, Australia, vol 5, pp 589–592. <https://doi.org/10.1109/ICASSP.1994.389443>

20. Salkuti SR (2022) Emerging and advanced green energy technologies for sustainable and resilient future grid. *Energies* 15(18):6667. <https://doi.org/10.3390/en15186667>
21. Babri HA, Tong Y (1996) Deep feedforward networks: application to pattern recognition. In: Proceedings of IEEE international conference on neural networks, 3 June 1996, pp 1422–1426. <https://doi.org/10.1109/ICNN.1996.549108>
22. Rodriguez MV, Romero-Troncoso R, de Jesus RRAO, Garcia-Perez A (2014) Detection and classification of single and combined power quality disturbances using neural networks. *IEEE Trans Ind Electron* 61(5):2473–2482. <https://doi.org/10.1109/TIE.2013.2272276>
23. Das SR, Mishra DP, Ray PK, Salkuti SR, Sahoo AK (2021) Power quality improvement using fuzzy logic-based compensation in a hybrid power system. *Int J Power Electron Drive Syst* 12(1):576–584. <https://doi.org/10.11591/ijpeds.v12.i1.pp576-584>
24. Lu Z, Bao G, Xu H, Dong X, Yuan Z, Lu C (2011) Battery energy storage system based power quality management of distribution network. In: Yang D (ed) *Informatics in control, automation and robotics. Lecture notes in electrical engineering*, vol 133. Springer, Berlin, Heidelberg. [https://doi.org/10.1007/978-3-642-25992-0\\_81](https://doi.org/10.1007/978-3-642-25992-0_81)
25. Giri AK, Arya SR, Guerrero JM, Kumar S (2023) Power quality: infrastructures and control. In: *Studies in infrastructure and control*, vol 1. Springer. ISBN: 978-981-19-7956-9
26. Benysek G, Pasko M (2012) Power theories for improved power quality. In: *Power systems (POWSYS)*, vol 1. Springer. ISBN: 978-1-4471-2786-4
27. Elbaset AA, Hassan MS (2017) Design and power quality improvement of photovoltaic power system, vol 1. Springer, Cham. ISBN: 978-3-319-47464-9
28. Topaloglu I (2022) Deep learning based a new approach for power quality disturbances classification in power transmission system. *J Electr Eng Technol* 18:77–88. <https://doi.org/10.1007/s42835-022-01177-1>
29. Wang S, Chen H (2019) A novel deep learning method for the classification of power quality disturbances using deep convolutional neural network. *Appl Energy* 235:1126–1140. <https://doi.org/10.1016/j.apenergy.2018.09.160>
30. Zhao W, Shang L, Sun J (2019) Power quality disturbance classification based on time-frequency domain multi-feature and decision tree. *Prot Control Mod Power Syst* 4(27):1–6. <https://doi.org/10.1186/s41601-019-0139-z>
31. Ahmad MW et al (eds) (2022) *Intelligent data analytics for power and energy systems*. Springer, Singapore, pp XXII, 641. ISBN: 978-981-16-6081-8. <https://doi.org/10.1007/978-981-16-6081-8>
32. Tomar A et al (eds) (2022) *Proceedings of 3rd international conference on machine learning, advances in computing, renewable energy and communication: MARC 2021*, vol 915. Springer Nature, pp XV, 781. ISBN: 978-981-19-2830-7. <https://doi.org/10.1007/978-981-19-2828-4>

# Optimized Integral Sliding Mode Load Frequency Control of an Isolated Power System



Neelam Kassarwani, Neelu Nagpal, Jagrat Sehgal, and Pierluigi Siano

**Abstract** This paper proposes optimized integral sliding mode approach as a load frequency control (LFC) for an isolated power system. The system integrates multiple sources including conventional generators, renewable energy sources (RESs), and energy reserves to supply power demand. This system experiences random and nonrandom disturbances as a result of uncertainty, transients, and noise that may be internal or external to the system. A novel integral sliding mode load frequency control (ISMLFC) using integral (PI) sliding surface is implemented for frequency regulation of the proposed system. The control variables of ISMLFC are optimally selected using particle swarm optimization (PSO) method. A Simulink model of the system in MATLAB is developed. A comprehensive simulation study is conducted considering different operating conditions with the variation in the levels of load and generations, time delay, disturbances, parameters, control structure, etc. The simulation results validate the robust performance of the optimized ISMLFC with the saturation function in the control law to provide better frequency response. Further, the comparative analysis with other alternative control approach, proposed controller outperforms for frequency regulation.

**Keywords** Load frequency control · Integral sliding surface · Sliding mode control · Optimized controller parameter · Random disturbance · Robust control

---

N. Kassarwani · N. Nagpal (✉) · J. Sehgal  
EEE Department, Maharaja Agrasen Institute of Technology, Delhi 110086, India  
e-mail: [nagpalneelu1971@ieee.org](mailto:nagpalneelu1971@ieee.org)

P. Siano  
Department of Management and Innovation Systems, University of Salerno, 84084 Fisciano, Italy  
e-mail: [psiano@unisa.it](mailto:psiano@unisa.it)

© The Author(s), under exclusive license to Springer Nature Singapore Pte Ltd. 2024  
H. Malik et al. (eds.), *Renewable Power for Sustainable Growth*,  
Lecture Notes in Electrical Engineering 1086,  
[https://doi.org/10.1007/978-981-99-6749-0\\_49](https://doi.org/10.1007/978-981-99-6749-0_49)

751



## 1 Introduction

Frequency variations in a power system (PS) are caused by a mismatch between the generation of electrical power and the load consumption. LFC as an essential component is in charge of establishing a power balance that is aimed to re-establish the synchronous generator's frequency [1]. This is done by tuning the governor in order to compensate for these changes faced by the PS. The increased entry of intermittent RERs, energy storage systems (ESSs), new forms of loads, distributed generation, and many such reasons have presented a challenge to LFC mechanism [2, 3]. In addition to measurement and model errors, both the generation and distribution, or both sides, must deal with random disturbances. In such situations, a conventional controller faces challenges to maintain the frequency within nominal range for a multi-source PS with stochastic disturbances and uncertainties. In addition, many LFC approaches have been reported such as  $H_\infty$  [4, 5], intelligent [1, 6], deterministic disturbance observer-based (DOB) and stochastic DOB [3, 7, 8], robust [9], and many more.

As an alternative, the SMC strategy is a variable structured control method. It is invariant to parametric variations and an effective robust control strategy. The design of SMC involves careful selection of sliding surface (SS) and switching function (fn.) to meet the reachability condition [10]. Various SMC schemes have been reported with different formulation of control laws. The frequency regulation of a traditional PS has been stabilized by selecting P-based SS in the SMC design and control parameters are optimized [11]. Considering similar PS model, an LFC problem has been formulated using P-based SS and Sgn fn. for SMC [12] and later work of same SMC has been extended considering RERs integrated PS [13] for frequency control. Using the PID-based SS and Sgn fn. in the control law, the optimal control parameters are obtained [14]. Likewise most of the work related to SMC for LFC problem has considered P-based SS and Sgn fn. for control law. In this present work, an optimized ISMLFC approach for an isolated PS is proposed as secondary frequency control. The SMC design incorporates PI-based SS along with considering both Sgn and Sat fns. type control law for performance comparison. The control variables are optimized using PSO to get improved frequency response. Further, an integral control action is performed to minimize the persistent steady state error,  $e_{ss}$ . The paper has the following contributions:

- Model development of an isolated area PS integrated with RESs and EV aggregators taking into account random and nonrandom disturbances.
- Formulation of PI-based sliding surface and saturation function in the control law for effective SMC design.
- Proposed optimized ISMLFC design and its implementation to regulate the frequency of the test system.
- Extensive simulation study at different operating scenarios for performance analysis considering different types of sliding surface, and switching functions in the formulation of control law.
- Assessment of the performance of optimized ISMLFC control methodology through a comparative analysis under diverse operating scenarios.

The paper is structured as: An introduction of the work is presented in Sect. 1, and system dynamics is discussed in Sect. 2. The proposed SMC approach and its implementation as optimized ISMLFC are discussed in Sect. 3 followed by simulation study in Sect. 4 to evaluate the performance of controller. Section 5 concludes the present study of LFC with sliding mode-based control method.

## 2 System Model

Figure 1 presents a scheme of an isolated PS considering its frequency response model. The system dynamics are expressed as:

$$\begin{aligned}
 \Delta \dot{f} &= \frac{1}{2H} \Delta P_r + \frac{1}{2H} \Delta P_e - \frac{1}{2H} \Delta P_d - \frac{D}{2H} \Delta f \\
 \Delta \dot{X}_g &= -\frac{K_g}{RT_g} \Delta f - \frac{1}{T_g} \Delta X_g + \frac{K_g \alpha_g}{T_g} \Delta P_c, \Delta \dot{P}_r = \frac{K_t}{T_t} \Delta X_g - \frac{1}{T_t} \Delta P_r \\
 \Delta \dot{P}_g &= \frac{K_t K_r}{T_t T_r} \Delta X_g + \frac{T_t - K_r}{T_t T_r} \Delta P_r - \frac{1}{T_r} \Delta P_g, \\
 \Delta \dot{P}_e &= -\frac{1}{T_e} \Delta P_e + \frac{1}{T_g} \Delta X_g + \frac{K_g \alpha_g}{T_g} \Delta P_c
 \end{aligned}
 \tag{1}$$

Various terms used in this dynamics are described in Table 1. It is obvious that the power system is subjected to disturbances. The dynamical model of PS (1) can be presented in state space matrix form as below:

**State vector,**  $X = [\Delta f \ \Delta X_g \ \Delta P_r \ \Delta P_g \ \Delta P_e]^T$ ; **Control input vector,**  $u = [\Delta P_c]$ ; and nonrandom and random disturbance vector,  $d = [\Delta P_d \ \delta_{ti}]$

$$\tag{2}$$

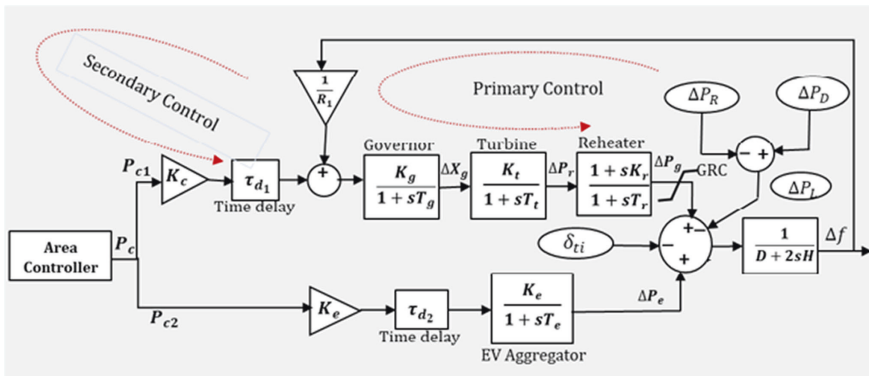


Fig. 1 Block diagram of LFC model of isolated PS

**Table 1** Description of parameters used in system model

Symbol	Notation	Value
$\Delta f$	Frequency deviation	Variable
$\Delta P_c$	Control input (local)	Variable
$R$	Governor droop characteristics	2.4
$\Delta P_{cg}, \Delta P_{ce}$	Control input for thermal turbine, control input for EVs	Variable
$\Delta P_e, \Delta P_g$	Differential changes in EVs power, turbine power	Variable
$\Delta P_r, \Delta X_g$	Differential changes in power of reheater, governor valve position	Variable
$\Delta P_L$	Local load demand	Variable
$k_e, T_e$	EVs gain and time constant	1 and 1
$k_g, T_g$	Speed governor gain and time constant	1 and 0.08
$k_r, T_r$	Reheater gain and time constant	1 and 10
$k_t, T_t$	Thermal turbine gain and time constant	1 and 0.03
$D, H$	Inertia constant, load damping coefficient	0.0083, 0.08335
$\tau_1, \tau_2$	Conventional generation system delay, EV generation system delay	0–0.1
$\alpha_g, \alpha_e$	Participation factor of conventional turbine, participation factor of EVs	0–1, 0–1

The random disturbance component comprises model error, time delay, parameter uncertainty, RER generation, etc. which is denoted by  $\delta_{ti}$  and non-random load deviation is denoted as  $P_{di}$ . The time delay includes the communication delay, and delay due to the governor setting. The model (1) considering both disturbance and noise can be represented as:

$$\dot{X} = A_1 X + B_1 U + d + \omega; Y(t) = C X \quad (3)$$

This model has a state vector,  $X \in \mathbb{R}^{n \times 1}$ , and output vector,  $Y \in \mathbb{R}^{m \times 1}$ . When control input vector  $U \in \mathbb{R}^{r \times 1}$  is applied to the model, the trajectory of the system changes. It is assumed to have modelling error in the form of noise,  $\omega$ . Further, lumped disturbance vector,  $d(t) \in \mathbb{R}^{q \times 1}$  is assumed to be bounded and can be estimated, i.e.  $d(t) \leq d^*(t)$  and  $\dot{d}(t) \leq \dot{d}^*(t)$  where,  $d^*$  (positive constant). In Eq. (3), different matrices represents:  $A_1$ —system,  $B_1$ —input,  $C_1$ —output,  $d$ —nonrandom component of disturbance,  $\omega$ —random component of disturbance respectively.  $\omega$  is in the form of white Gaussian noise (WGN) and has covariance, i.e.  $Q_0$ .

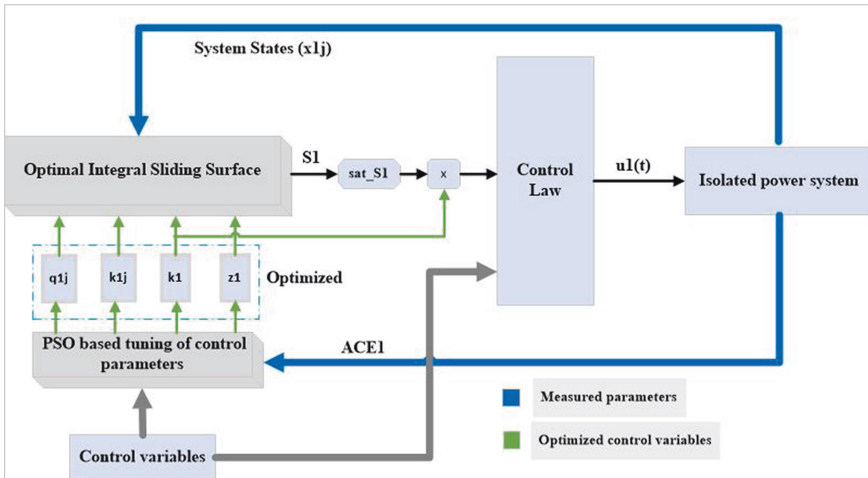


Fig. 2 Schematic diagram of optimized ISMLFC of an isolated power system

### 3 Proposed Optimized Integral Sliding Mode Load Frequency Control (ISMLFC) Approach

In this section, an optimized ISMLFC-based strategy for an isolated PS is developed to keep frequency deviations within acceptable limits. The SMC is characterized by its variable structured feature and is based on state feedback control law. Because of this unique feature, it is exploited for the effective control of nonlinear and inaccurate modelled PSs. An integral (I)-based sliding mode control approach is implemented to the isolated PS (refer Fig. 2) to regulate its frequency with in permissible limits for the stable operation. This ensures the system’s asymptotic stability under conditions such as selecting an appropriate SS for the desired trajectory, the existence of a reaching condition to have sliding mode, and the implementation of a control law so that the system trajectory drives to the surface and continues on it.

Considering  $Q_1 \in \mathbb{R}^{1 \times n}$ ,  $K_1 \in \mathbb{R}^{1 \times n}$ , and  $A_1 \in \mathbb{R}^{n \times n}$  as constant matrices, then PI-based SS is selected as:

$$SS_1(t) = Q_1 X(t) - \int Q_1 (A_1 - B_1 \times K_1) X(\tau) d(\tau) \tag{4}$$

In Eq. (4), sliding mode requires time,  $t$  and  $Q_1 B_1$  is non-singular. Using pole assignment approach, matrix  $K_1$  is designed in such a way that the eigenvalues of matrix  $(A_1 - B_1 K_1)$  are negative. The switching function in control law must meet the following criteria in order for the dynamic trajectory to enter sliding mode and remain in sliding mode.

$$SS_1(t) = 0; \dot{SS}_1(t) = 0; \quad \forall t \geq 0 \tag{5}$$

Further, an equivalent control is established to provide a switching law as control input. This switching function guarantees the Lyapunov stability condition such that the system remains in the sliding mode, i.e. system trajectory in regime. This is presented as:

$$SS_1(t)S\dot{S}_1(t) < 0 \tag{6}$$

This controller opts PI-based sliding surface as given in (4). The following condition (6) is fulfilled after substituting  $\dot{X}(t)$  from (3) in the derivative of  $S_1(t)$  of (4) as given below:

$$\begin{aligned} S\dot{S}_1(t) &= Q_1\dot{X}_1(t) = Q_1 [A_1X(t) + Q_1B_1u_1(t) + Q_1E_1d_1(t)] \\ &- Q_1 (A_1 - B_1 \times K_1) X_1(t) = 0 \end{aligned} \tag{7}$$

The equivalent control:

$$u_{eq}(t) = -K_1X_1(t) + (Q_1B_1)^{-1}Q_1E_1d_1(t) \tag{8}$$

Equation (8) refers the control required for ideal sliding mode. Also, the system Eq. (3) enters in sliding mode when  $u_{eq}(t)$  from (8) is put, i.e.

$$\dot{X}_1(t) = (A_1 - B_1K_1)X_1(t) + (I - B_1(Q_1B_1)^{-1}Q_1) E_1d_1(t) \tag{9}$$

where  $I$  denotes an identity matrix. When  $u_{eq}(t)$  is substituted, the derivative of SS changes as shown below:

$$\begin{aligned} S\dot{S}_1(t) &= Q_1\dot{X}_1(t) = Q_1 [A_1X(t) + Q_1B_1u_{eq}(t) + Q_1E_1d_1(t)] \\ &- Q_1(A_1 - B_1 \times K_1)x_1(t) \end{aligned} \tag{10}$$

Matrix  $Q_1B_1$  must be non-singular ( $Q_1B_1 \neq 0$ ), so the matrix  $Q_1$  is chosen in this manner. The control law has two terms:  $u_{eq}$ —equivalent control and  $\Delta u_1$ —the discontinuous term [15] as shown below:

$$u_1(t) = u_{eq} + \Delta u_1 \tag{11}$$

$\Delta u_1$  represents high-frequency switching function which in the discrete form can be expressed as:

$$\Delta u_1(n) = -k_1 \text{Sat}(SS_1(n)) \tag{12}$$

At  $n$ th instant,  $u_1(n)$  represents switching function,  $S_1(n)$  denotes SS, and  $k_1$ —switching gain matrix. The control input  $u_1(n)$  is formed from  $\text{Sat}(S_1(n))$  from the formation of the switching function  $\psi_1(n)$  which is given as:

$$\psi_1(n) = \text{Sat}(S_1(n)) = \begin{cases} +1, & \text{if } SS_1(n)X_1(n) > L; \\ \frac{SS_1(n)}{L}, & \text{if } SS_1(n)X_1(n) \leq L; \\ -1, & \text{if } SS_1(n)X_1(n) < -L. \end{cases} \quad (13)$$

In Eq. (13),  $L$  has a small value of 0.5 and referred as the boundary layer of Sat. fn. This control law takes into account a Sat. fn.-based ISMC, which is the product of SS and state tracking error. Further, the control law (12) and  $\Delta P_{c11}$  is in discrete form as:

$$\Delta P_{c11} = -K_1 X_1(n) - (Q_1 B_1)^{-1} Q_1 E_1 d_1(n) - (Q_1 B_1)^{-1} - k_1 \text{sat}(SS_1(n)X_1(n)) \quad (14)$$

The control law (14), i.e.  $\Delta P_{c11} = u_1(n)$ , drives the system trajectory on the SS (5) and afterwards, continues to slide on it. In addition, the persistent static frequency error in the system is minimized with the incorporation of integral control action (with  $z_1$  as integrator gain) which provides command to the speed changer. This is presented as:

$$\Delta P_{c12} = -z_1 \int \Delta f_1 dt \quad (15)$$

It is worth to mentioned that modified switching function  $\psi_1(n)$  puts the ISMC in the control loop that maintain the system frequency  $f_1$  and keep its deviation, i.e.  $\Delta f_1$  minimum. Also, implementation of optimal I-controller reduces  $e_{ss}$  in the output response. The control input  $\Delta P_{ci}$  is formulated from (14) and (15) as:

$$\begin{aligned} P_{c1} &= P_{c11} + P_{c12} \\ P_{c1}(n) &= -z_1 \left[ \sum \Delta f_1(n) \right] + u_1(n); \quad n - \text{sampling instant} \end{aligned} \quad (16)$$

The signum-function-based ISMC suffers chattering and oscillation problems. The optimal selection of the control variables decides the performance of proposed ISMLFC. Here, the isolated PS has five states; thus, the proportional gain of SS is:  $q_{11}, \dots, q_{15}$ , and integral gain is:  $k_{11}, k_{12}, \dots, k_{15}$ . Also, a switching function gain  $k_1$  and integral gain of the controller ( $z_1$ ) is considered for the control loop. These control variables are optimized using PSO technique selecting the parameters as: 12 control variables, 100 swarms, 150 iterations. The objective function ( $J$ ) is selected as integral square error (ISE) expressed as:

$$J = \int_0^{T_{\text{sim}}} (\Delta ACE_1^2) \quad (17)$$

**Table 2** Simulation scenarios for performance analysis of optimized ISMLFC

Scenario	Operating conditions	Details	Result
S1	Variations in non-random disturbance with different sliding surface	1–5% with P-based and PI-based	Figure 3a
S2	Switching function in control law	Sat versus Sig fn.	Figure 3b
S3	Variation in governor and turbine parameters	$\pm 10\%$ (Sat vs. Sig fn.)	Figure 3c
S4	Variation in EV-aggregator parameter	$\pm 10\%$ (Sat vs. Sig fn.)	Figure 3d
S5	Variation in generation (conventional and RERs) participation factor	0–100% (Sat vs. Sig fn.)	Figure 3e
S6	System states	$\Delta X = [\Delta f \ \Delta X_g \ \Delta P_g \ \Delta P_t \ \Delta P_c]$ (Sat vs. Sig fn.)	Figure 3f
S7	Variation in inertia constant ( $H$ )	$\pm 10\%$ with Sat fn.	Figure 3g
S8	Variation in damping constant ( $D$ )	0 to $\pm 10\%$ with Sat fn.	Figure 3h
S9	Variations in random disturbance (covariance)	$10^{-8}$ to $10^{-6}$ with Sat fn.	Figure 3i
S10	Changing distribution of measurement noise	Non-Gaussian (LD) keeping 0.02 loading	Figure 3j
S11	Variation in time delay	0.001–0.1 s	–

## 4 Simulation Study

In this section, a simulink model of isolated PS is developed using MATLAB version 2021A referring Fig. 2 and Eq. (1). The different parameter values used are marked in Table 1. For implementation of proposed optimized ISMLFC, the model is then simulated under different operating scenarios as presented in Table 2 for performance validation. The simulations are run for 30 s. Table 2 lists the numerous scenarios (S1–S11), and the results of these scenarios are displayed in Fig. 3. An analysis is performed based on the results to evaluate the performance of the current control scheme.

According to S1 and result Fig. 3a, it is inferred that using only P-based sliding surface (SS) in the SMC results: (i) more undershoots and overshoots, (ii) frequency deviations is not settled to zero, results more steady state error. With PI-based SMLFC, on the contrary, system achieves better transient as well as steady state  $\Delta f$ . Furthermore, the greater the loading step, the less favourable the transient and steady state response.

A performance comparison is made between SMC control law with Sat and Sgn switching fns. during cases S2–S6. The robustness of the proposed control approach is validated after running simulations with both types of functions under different load conditions, parameters, and contributions from conventional and EV reserves.

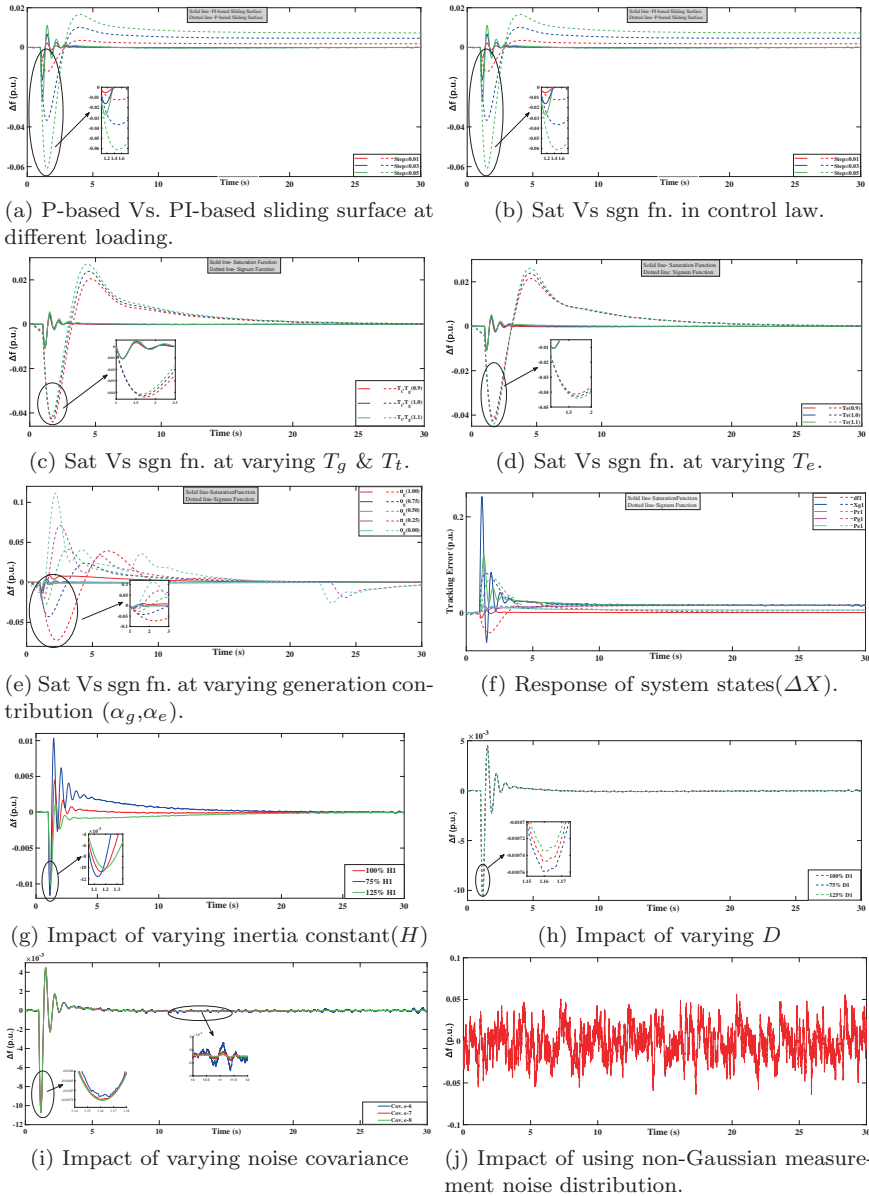


**Fig. 3** Frequency response plot for performance analysis of optimized ISMLFC

Figure 3b–e shows the corresponding results. From these plots, it can be seen that the performance of Sat fn.-based SMC is better in terms of transient response, frequency nadir ( $\Delta f_n$ ), settling time ( $t_s$ ) and  $e_{ss}$ .



**Table 3** Comparative analysis of control performance: P-based SS versus PI-based SS

Scenario, S1 ↓	$\Delta f_n$		$t_s$		$\Delta e_{ss}$	
	P-based	PI-based	P-based	PI-based	P-based	PI-based
1% loading	-0.012	-0.005	6.4 s	4.7 s	0.0018	$9.1 \times 10^{-7}$
3% loading	-0.037	-0.01612	9.37 s	4.8 s	0.0096	$3.5 \times 10^{-6}$

**Table 4** Comparative analysis of control performance: signum versus saturation function

Scenario, S2 ↓	$\Delta f_n$		$t_s$		$e_{ss}$	
	Sig fn.	Sat fn.	Sig fn.	Sat fn.	Sig fn.	Sat fn.
2% loading	-0.012	-0.005	10.05 s	3.1645 s	0.002	$-1.26 \times 10^{-5}$

It is obvious that incorporating RERs into the PS reduces system inertia, which affects system stability. The efficacy of proposed optimized ISMLFC (with Sat fn.) approach for frequency regulation under the influence of variation of inertia constant,  $M$  has been investigated in S7. In Fig. 3, the corresponding simulation result indicates that lowering  $M$  causes high-frequency overshoot and  $t_s$ . Although the frequency variation specially  $\Delta f_n$  is within permissible limit. In addition, the result Fig. 3h indicates that variations in damping constant introduces negligible impact on  $\Delta f$ .

It is noted from Fig. 3i that the variation of noise level (covariance) is varied and the frequency response is observed. It is found that  $\Delta f_n$  has no significant affected and  $e_{ss}$  is more in case of more noise covariance. Further, if it is considered that the sensor has non-Gaussian distribution say Laplacian distribution (LD). Then using function,  $y = 0 - (0.3 * \text{sign}(\text{rand} - 0.5)) * \log(1 - 2 * \text{abs}(\text{rand} - 0.5))$ , this noise is added in the output. The frequency response is not settled but it also not exceeding the range of  $\Delta f$ . The effect of delay time that may happen due to communication channel from control centre to generation is observed. On varying  $\tau_1 = \tau_2 = 0.001 - 0.1$  s, simulations are run. There is no effect of delay on the system response.

A comparative study is presented in Table 3. Likewise [11, 12] work, P-based SS is used in SMLFC for present model and its performance indices are compared with PI-based SS used in this paper. There is significant performance improvement in the later case. Further, another comparison is made considering the SMC approach using PI-based SS and Sgn fn. used by [13] with the proposed work using same type of SS but with Sat fn. The performance indices of the response are shown in Table 4.

## 5 Conclusion

An optimized ISMLFC strategy for a stochastic isolated PS is successfully developed and implemented. The proposed control strategy is designed using integral-based sliding surface and, further investigated using signum and saturation functions in

its control law. The incorporation of saturation function which is rarely used by the previous LFC work has shown improved performance. Further, the optimized control variables enhances the frequency control performance of ISMLFC for stable power operations. The performance validation of the proposed controller is done using diverse simulation scenarios. The test results indicate the present controller as robust secondary controller as compared with other control approaches. As future work, it is planned to implement a higher-order SMC with improved performance to regulate the frequency and/or voltage of isolated or multi-area interconnected power systems.

## References

1. Kumar N, Malik H, Singh A, Alotaibi MA, Nassar ME (2021) Novel neural network-based load frequency control scheme: a case study of restructured power system. *IEEE Access* 9:162231–162242. <https://doi.org/10.1109/ACCESS.2021.3133360>
2. Alhelou HH, Golshan MEH, Siano P (2021) Frequency response models and control in smart power systems with high penetration of renewable energy sources. *Comput Electr Eng* 96(Part A). ISSN 0045-7906
3. Aggarwal N, Mahajan AN, Nagpal N (2023) Dynamic state estimation of a multi-source isolated power system using unscented Kalman filter. In: Gupta D, Khanna A, Hassanien AE, Anand S, Jaiswal A (eds) *International conference on innovative computing and communications. Lecture notes in networks and systems*, vol 492. Springer, Singapore. [https://doi.org/10.1007/978-981-19-3679-1\\_10](https://doi.org/10.1007/978-981-19-3679-1_10)
4. Singh V, Mohanty SR, Kishor N (2013) H-infinity robust load frequency control in hybrid distributed generation system. *Int J Electr Power Energy Syst* 46:294–305
5. Singh VP, Mohanty SR, Kishor N, Ray PK (2013) Robust H-infinity load frequency control in hybrid distributed generation system. *Int J Electr Power Energy Syst* 46:294–305. ISSN 0142-0615. <https://doi.org/10.1016/j.ijepes.2012.10.015>
6. Jena A, Rout B, Saha N (2022) Modified particle swarm optimized load frequency control of renewable energy sources-based integrated power systems. In: Panda G, Naayagi RT, Mishra S (eds) *Sustainable energy and technological advancements. Advances in sustainability science and technology*. Springer, Singapore. [https://doi.org/10.1007/978-981-16-9033-4\\_36](https://doi.org/10.1007/978-981-16-9033-4_36)
7. Alhelou HH, Parthasarathy H, Nagpal N, Agarwal V, Nagpal H, Siano P (2021) Decentralised stochastic disturbance observer-based optimal frequency control method for interconnected power systems with high renewable shares. *IEEE Trans Ind Inform*
8. Alhelou HH, Golshan MEH, Hatziargyriou ND (2020) Deterministic dynamic state estimation-based optimal LFC for interconnected power systems using unknown input observer. *IEEE Trans Smart Grid* 11(2):1582–1592
9. Shendge PD, Patre BM, Phadke SB (2008) Robust load frequency sliding mode control based on uncertainty and disturbance estimator. In: Chan AHS, Ao SI (eds) *Advances in industrial engineering and operations research. Lecture notes in electrical engineering*, vol 5. Springer, Boston, MA. <https://doi.org/10.1007/978-0-387-74905-1-26>
10. Alhelou HH, Nagpal N, Kassarwani N, Siano P (2023) Decentralized optimized integral sliding mode-based load frequency control for interconnected multi-area power systems. *IEEE Access* 11:32296–32307. <https://doi.org/10.1109/ACCESS.2023.3262790>
11. Radosevic T, Vrdoljak K, Peric N (2008) Optimal sliding mode controller for power system's load-frequency control. In: *Proceedings of the universities power engineering conference*, pp 1–5. <https://doi.org/10.1109/UPEC.2008.4651435>

12. Mi Y, Wang C, Wang P (2013) Decentralized sliding mode load frequency control for multi-area power systems. *IEEE Trans Power Syst* 28(4):4301–4309. <https://doi.org/10.1109/TPWRS.2013.2277131>
13. Mi Y, Hao X, Liu Y, Fu Y, Wang C, Wang P, Loh C (2017) Sliding mode load frequency control for multiarea time-delay power system with wind power integration. *IET Gener Transm Distrib* 11(18):4644–4653. <https://doi.org/10.1049/iet-gtd.2017.0600>
14. Kumar A, Anwar MN, Kumar S (2021) Sliding mode controller design for frequency regulation in an interconnected power system. *Prot Control Mod Power Syst* 6(6):1–12. <https://doi.org/10.1186/s41601-021-00183-1>
15. Utkin (1977) Variable structure systems with sliding modes. *IEEE Trans Autom Control* 22(2):212–222. <https://doi.org/10.1109/TACCESS.2023.3262790.1977.1101446>
16. Kumar A, Asim M, Shadab MM, Akhtar I (2021) Review of various load frequency controllers. In: Iqbal A, Malik H, Riyaz A, Abdellah K, Bayhan S (eds) *Renewable power for sustainable growth. Lecture notes in electrical engineering*, vol 723. Springer, Singapore. [https://doi.org/10.1007/978-981-33-4080-0\\_26](https://doi.org/10.1007/978-981-33-4080-0_26)

# Implementation of Supercapacitor-Battery-Based Energy Storage System in Hybrid Power System Incorporating Renewable Energy Resources



Jahid, Manaullah, and Sheeraz Kirmani

**Abstract** As the globe is moving closer to using renewable energies (RERs), society is facing new difficulties. The current article proposes a system that is solar and wind energy based, a control system that combat with sporadic and unstable nature of the linked load as well as of wind and solar energy. In this paper, it is proposed that to counter mismatch between the power supplied by the renewable energy resources (RERs) and load connected to the system, a backup source/sink is needed. Generally, battery energy storage is used for this purpose. But this paper proposes a hybrid system of energy storage (HESS) comprising of battery and supercapacitor for solving the problem. Furthermore, the hybrid operation of these both storage systems provides better voltage and frequency regulation. The battery should be utilized to control the long-term power dysfunction between generation and demand by using a hybrid operation of a battery and supercapacitors and the supercapacitors to deal with the rapid changes and severe dysfunction between power production and consumption. With the suggested control method, HESS may be better controlled to offset power discrepancies that occur between the connected loads and the power generated by RERs. A main objective of the control system is to maintain at all times voltage at DC link, 3-phase voltage and frequency within required/specified range. Moreover, gap of electricity required and supply is minimized. To validate the findings, the suggested work is simulated in the MATLAB/Simulink environment.

**Keywords** Battery · Supercapacitor · Active power · PV system · Wind energy

---

Jahid (✉) · Manaullah  
Electrical Engineering Department, Jamia Millia Islamia University, New Delhi, India  
e-mail: [mdzahid4107@gmail.com](mailto:mdzahid4107@gmail.com)

Manaullah  
e-mail: [manaullah@jmi.ac.in](mailto:manaullah@jmi.ac.in)

S. Kirmani  
Electrical Engineering Department, Aligarh Muslim University, Aligarh, India

## 1 Introduction

Use of renewable sources of electricity is being promoted mainly because of two reasons: firstly, the reduction of harmful pollutants being emitted from fossil fuels for the generation of electricity, and secondly, as the rapid depletion of traditional resource reserves forces the world to move towards alternative energy sources. Increased emphasis on RERs accelerates this transition, which results in greater technical advances and a reduction of the cost of components as a consequence. RERs account for almost all energy produced in this area. According to the International Energy Agency (IEA), renewable sources will provide 50% of the global energy requirements by the year 2040. When comparing the different designs, the combination of battery with supercapacitor is regarded the most economic choice in places with no grid access accessible. The battery-supercapacitor system offers a variety of complimentary and supportive features including the ready-to-go, battery-sensitive and cost-effective [1–5]. The densities of energy and power of condensers and battery systems of different kind reflected as Ragone graph are displayed in Fig. 1. It can be realized from the figure that supercapacitors can produce high power in a short time and show that they have much good capacity to store power with 5000 W/kg density [6–9]. They can react efficiently to a minor power explosion and with a reaction time estimated in milliseconds because to their very rapid response time. These have a poor energy density, usually lower than 5 Wh/kg [10–13], making them inefficient. Due to its high energy density, BESS can generate low power levels for a long time, providing 10–1000 Wh/kg of energy density. On the other hand, BESS has a sluggish reaction time and cannot respond quickly after disruption. In addition, the discharge depth and the number of charging and discharging cycles have a major effect on battery life. The synergistic use of batteries and supercapacitors as a consequence of this advancement may find a good answer for a broad variety of applications. In addition to providing a long operational life for batteries, this combination may contribute to reducing the total system costs. While the supercapacitor's quick reaction time is excellent for correcting for rapid transients in RER output and load, the ability of a battery to compensate for the slow and lengthy transients is also beneficial [14–21].

Again, the BESS state of charge may be kept beyond the permitted limit to guarantee the device a long working life. Because they can be discharged in full and their discharge depth may be up to 100%, SCESS does not experience the low charge issue.

For RER-based power systems, batteries are traditionally used for energy storage medium. However, the rapid and frequent changes in the connected load, as well as external conditions, help to reduce the battery life. So, all RERS-based power system requirements cannot be met by batteries as a single storage device. Any additional energy storage technology that complements the batteries must be hybridized with batteries. Supercapacitors are an energy storage devices that may be better utilized for battery hybridization. Figure 1 showing the battery and supercapacitor characteristics.

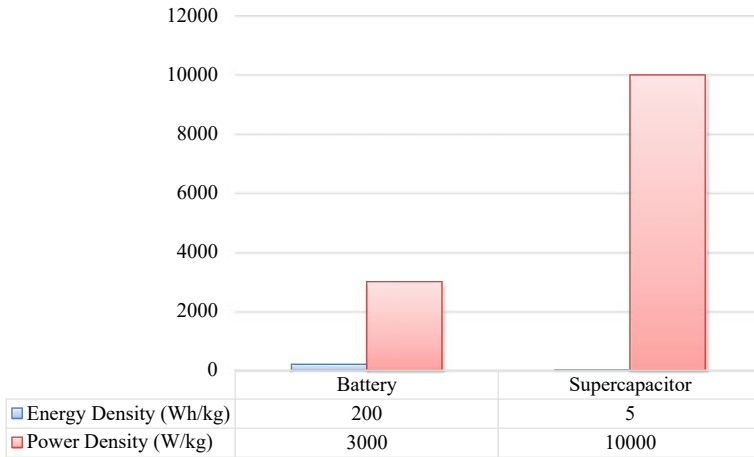


**Fig. 1** Comparison between power and energy density of supercapacitor and battery

The main objectives of the paper are:

1. Providing continues and good quality power to the load in every operating condition.
2. Reducing stress on battery energy storage system thus increasing its operating life.
3. Utilizing supercapacitor as other storage system for compensating sudden change in the demand and supply.
4. Maintaining voltage and frequency of the power fed to the load.

## 2 System Configuration and Modelling

The research system displayed in Fig. 2 is comprised of WECS, PV, the battery-supercapacitor combination, a dump load in form of DC load, AC load that have (i) non-critical as well as (ii) critical load as its sub-parts. The WECS consists of a synchronous generator which is run with the help of wind turbine. AC power is obtained from synchronous generator, and diode rectifier is used to convert AC power to DC. Converted DC as well as DC power output from PV system is made available to DC bus from where various connected loads are supplied. Supercapacitor as well as battery ESS make use of DC power to store and supply power through common DC bus. Thus, they are linked to the PCC through a two-way DC-to-DC converter. The two sources are used separately by the MPPT system to get maximum power from WECS and PV systems. BESS is responsible for the main backup function in case the production of the system is not adequate to satisfy the energy demand. On one hand, the BESS is highly dependable, but its lowering dynamics and delayed reaction time are the drawbacks of rapid transition events in sunshine, wind speed

and load. SCESS thus commits itself to rewarding the leniency of the battery. If RERs produce additional power and BESS is completely charged, the load of the dump is connected differently to the system. DC-to-AC converter or inverter is used to supply AC load having non-critical as well as critical load. Prime objective is to ensure that non-stop and quality forces are supplied to a vital load regardless of the input circumstances, while there are no non-critical load restrictions.

As shown in Fig. 2, a suggested system was developed in MATLAB and tested under different conditions to validate the control setup established for hybrid system incorporating renewable resources of energies that had been planned and executed in the previous step. Indicators that are examined, include voltage difference between cells, frequency change, reduction of distinction of generated power and requirement of power by the load, and keeping state of battery's charge constant. There is usually a discrepancy between the amount of power produced by making use of renewable resources and the amount of power supply needed by the various loads; as a result, either the generation exceeds the demand or the demand exceeds the generation.

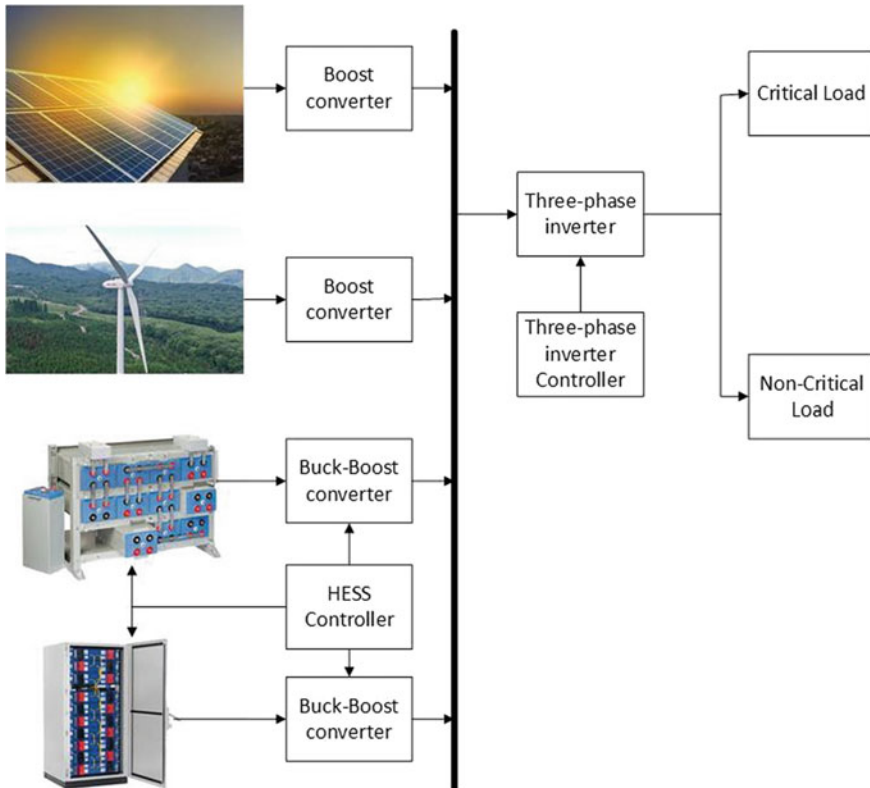


Fig. 2 Schematic diagram of HRES

### 3 System Control Strategy

Here HESS is exercised for compensation of active power in a power system where RERs are incorporated. Its control approach is represented in Fig. 3. Quantity of active power counterbalanced is decided by the error signal, i.e. difference between  $V_{DC}$  and  $V_{DCref}$ , wherein active power absorbed/injected from/to the system is determined by sign ( $\pm$ ) difference. For calculating the phase angle of ISE, a phase-locked loop (PLL) is exercised. Difference between  $V_{DC}$  and  $V_{DCref}$  is compensated by the PI controller thereafter that signal is further passed through a scale factor “K” for restricting the error in the range of  $\pm 1$ . The signal is thus obtained, and the output of the phase modulated sinusoidal signal is multiplied, which is further used in multiplication of the reference DC link voltage to generate control signals of the converter circuit.

#### 3.1 Simulation Results and Discussion

As per the control strategy, the HESS compensates the difference between power generated and demanded power either by releasing active power to the system or by charging itself. In case of deficit power, when generated power is lower than the demand then power is delivered by the Hybrid ESS, which is being studied in this section. Pattern of wind speed is represented by Fig. 4, where at  $t = 0$  s to  $t = 3$  s initially wind speed observed is 12 m/s, then it comes down to 9 m/s at 3 s, after that there is decrement and speed become 6 m/s at  $t = 5$  s and from  $t = 7$  s to  $t = 9$  s wind speed further comes down to 3 m/s and afterwards 0 m/s onwards. The waveform of output power of WECS corresponding to wind speed with respect to time is represented by Fig. 9. The irradiance of PV system is also changed with respect to time, as shown in Fig. 5. The power generated from utilization of solar irradiance through PV setup is also changed as power output of PV setup relies on the availability of sunlight and same can be seen in Fig. 9. Similarly, the load varies

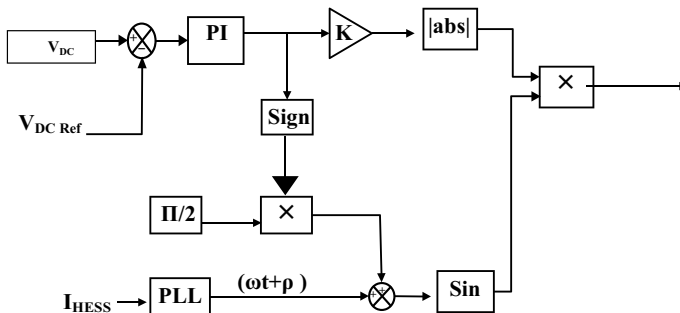


Fig. 3 Control strategy for HESS



with time and its requirement of power also changes which is also can be seen in Fig. 6.

As there are variations in the output power of the RERs and requirements of load, there is always mismatch between generation and demand. To compensate this mismatch, HESS comes into action and control strategy commands the HESS controller to activate the various converters. The difference between generation and demand is firstly, compensated by ESS incorporating supercapacitor as its response is much faster than BESS, thereafter gradually taken over by BESS as SCESS has lesser energy density as compared to BESS. The voltage waveforms of BESS and its SoC are shown in Fig. 7. Similarly, the current waveform of SCESS is demonstrated in Fig. 8. Figure 9 demonstrates the active power waveforms of RERs, HESSs, dump load, and load demand. From Fig. 9, it can be clearly seen that whenever there is a

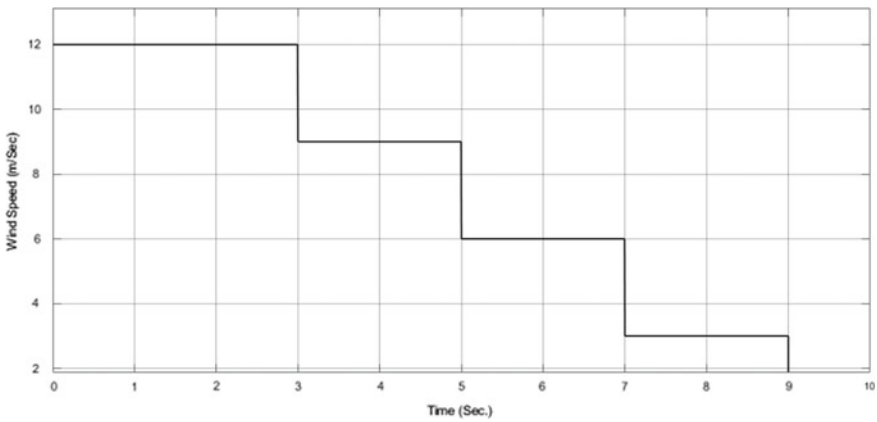


Fig. 4 Wind speed pattern

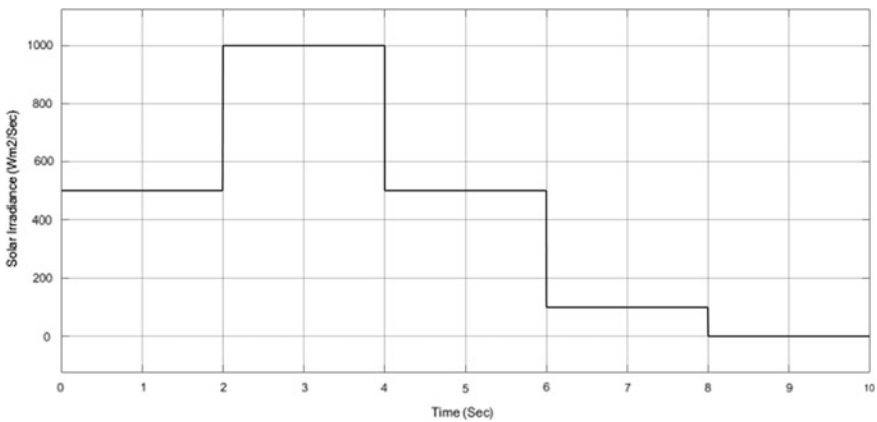


Fig. 5 Solar irradiance pattern

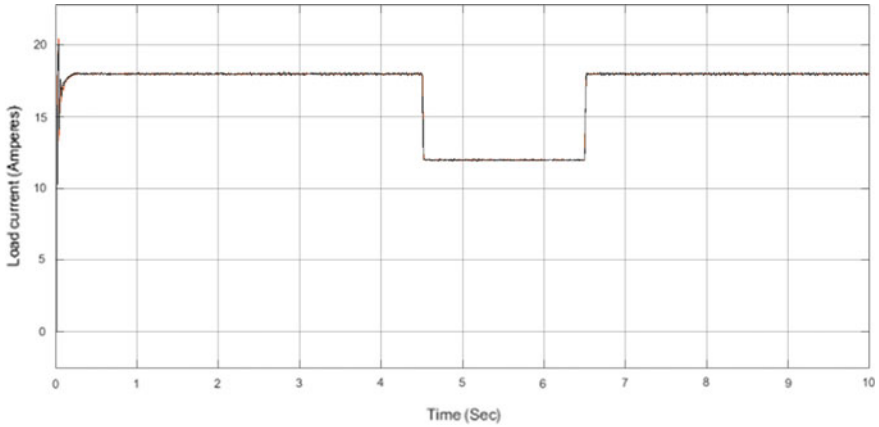


Fig. 6 Load pattern

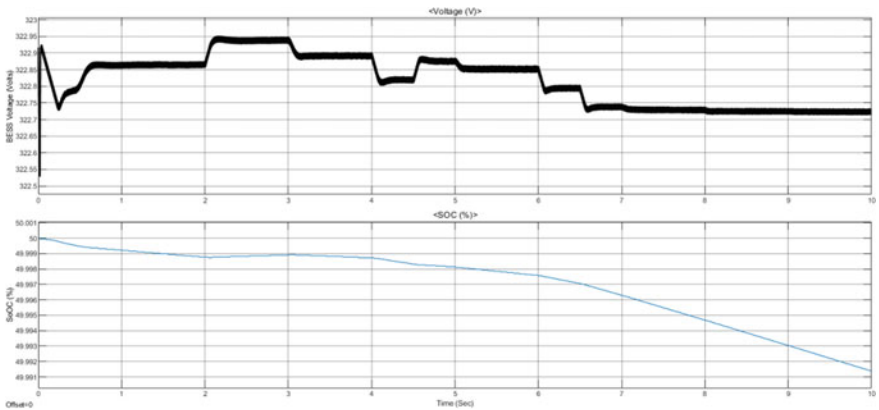


Fig. 7 BESS voltage and SoC waveform

variation occurs in the generation or load demand, HESS comes for the rescue and able compensate the difference between supply and demand effectively. Additionally, DC link voltage and 3-phase voltage waveform during different variations remain in the prescribed limits that can be clearly seen in Figs. 10 and 11, respectively.

### 4 Conclusions

In this work, a control strategy for a grid-isolated solar and wind-based power system incorporating hybrid renewable energy system combining batteries and supercapacitors is suggested and implemented. Testing of the control system was carried out

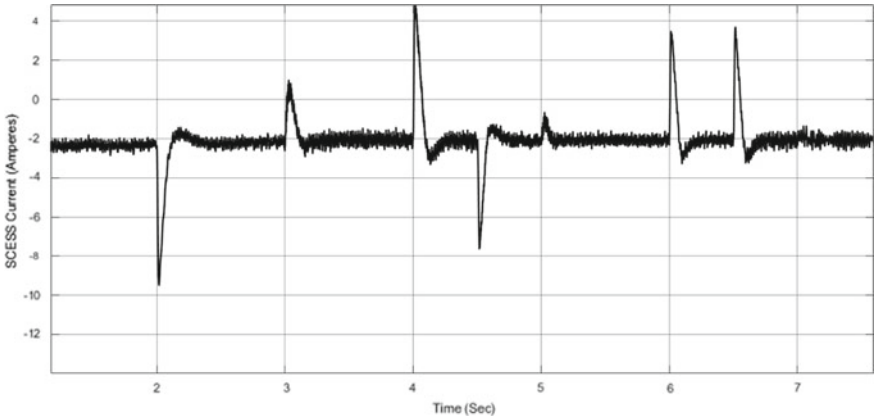


Fig. 8 SCESS current waveform

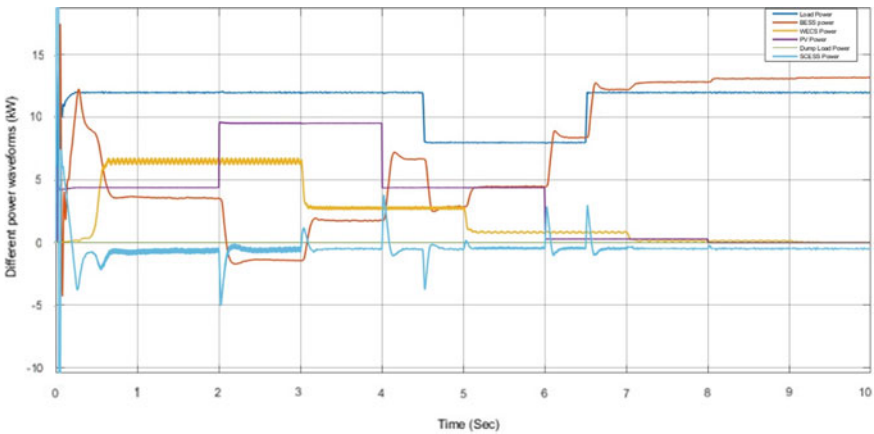
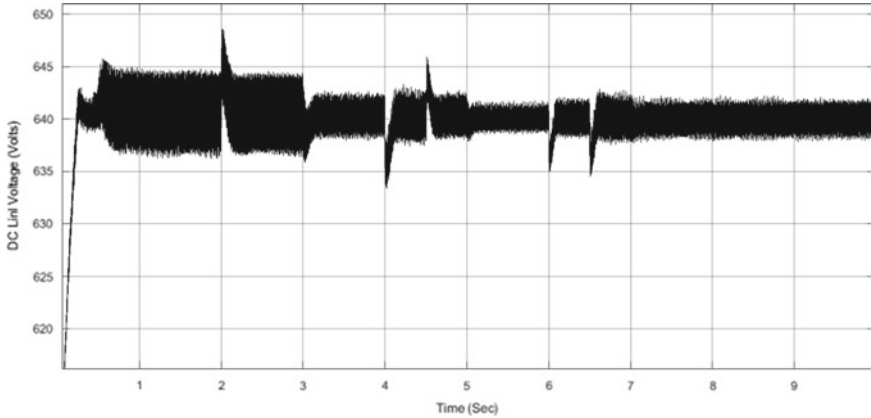
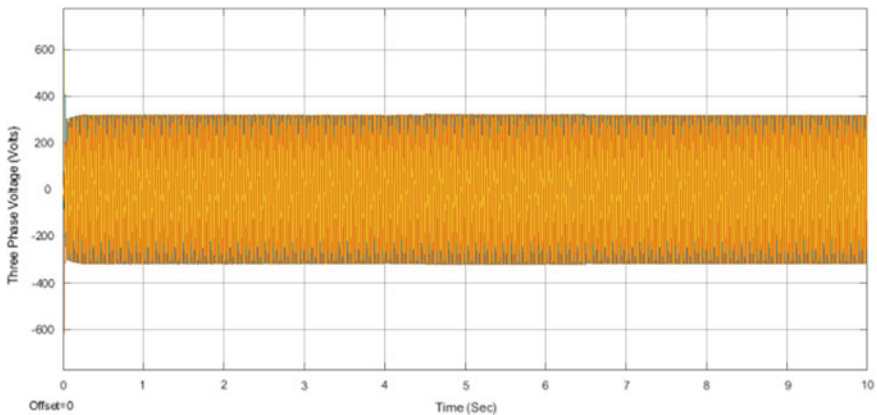


Fig. 9 Various waveforms of HRES

in both over generation and under generation scenarios, and the results show that the control strategy is able to keep up supplying quality power to load repeatedly. After testing the system under and over generation scenarios, the system was found to operate as anticipated and to be able to maintain its frequency, generation-to-demand difference and voltage at DC-connection inside shielded span when changes in circumstances occur. Moreover, BESS is progressively charged and discharged with the aid of supercapacitor ESS and supply of quick transients. BESS SoC may also be kept within acceptable limits by controller. In addition, three-phase voltage and frequency did not exceed allowed span. The work can be further extended when the proposed system is employed in grid-connected mode.



**Fig. 10** DC link voltage waveform



**Fig. 11** Three-phase voltage waveform

## References

1. Li B, Roche R, Miraoui A (2017) Microgrid sizing with combined evolutionary algorithm and MILP unit commitment. *Appl Energy* 188:547–562
2. Barelli L et al (2018) Dynamic analysis of a hybrid energy storage system (H-ESS) coupled to a photovoltaic (PV) plant. *Energies* 11(2):396
3. Choi M-E, Kim S-W, Seo S-W (2012) Energy management optimization in a battery/supercapacitor hybrid energy storage system. *IEEE Trans Smart Grid* 3(1):463–472
4. Aneke M, Wang M (2016) Energy storage technologies and real life applications—a state of the art review. *Appl Energy* 179:350–377
5. Lund PD, Lindgren J, Mikkola J, Salpakari J (2015) Review of energy system flexibility measures to enable high levels of variable renewable electricity. *Renew Sustain Energy Rev* 45:785–807

6. Krishan O, Suhag S (2018) An updated review of energy storage systems: classification and applications in distributed generation power systems incorporating renewable energy resources. *Int J Energy Res* 1–40
7. Lei J, Gong Q (2018) Optimal allocation of a hybrid energy storage system considering its dynamic operation characteristics for wind power applications in active distribution networks. *Int J Energy Res* 42(13):4184–4196
8. Nikolaidis P, Poullikkas A (2017) A comparative review of electrical energy storage systems for better sustainability. *J Power Technol* 97:220–245
9. Guney MS, Tepe Y (2017) Classification and assessment of energy storage systems. *Renew Sustain Energy Rev* 75:1187–1197
10. Akinyele DO, Rayudu RK (2014) Review of energy storage technologies for sustainable power networks. *Sustain Energy Technol Assess* 8:74–91
11. Rodrigues EMG, Godina R, Santos SF, Bizuayehu AW, Contreras J, Catalão JPS (2014) Energy storage systems supporting increased penetration of renewables in islanded systems. *Energy* 75:265–280
12. Krishan O, Suhag S (2020) Grid-independent PV system hybridization with fuel cell-battery/supercapacitor: optimum sizing and comparative techno-economic analysis. *Sustain Energy Technol Assess* 37:100625
13. Hredzak B, Agelidis VG, Demetriades G (2015) Application of explicit model predictive control to a hybrid battery-ultracapacitor power source. *J Power Sources* 277:84–94
14. Zoldy M, Csete MS, Kolozsi PP, Bordas P, Torok A (2022) Cognitive sustainability. *Cogn Sustain*
15. Kouchachvili L, Yaïci W, Entchev E (2018) Hybrid battery/supercapacitor energy storage system for the electric vehicles. *J Power Sources*
16. Kachhwaha A, Rashed GI, Garg AR, Mahela OP, Khan B, Shafik MB, Hussien MG (2022) Design and performance analysis of hybrid battery and ultracapacitor energy storage system for electrical vehicle active power management. *Sustainability*
17. Sanguesa JA, Torres-Sanz V, Garrido P, Martinez FJ, Marquez-Barja JM (2021) A review on electric vehicles: technologies and challenges. *Smart Cities*
18. Grujić I, Dorić J, Stojanović N, Abdullah OI, Grujić I, Stojanović N (2022) Numerical analysis of hydrogen fueled IC engine. Available online: <https://www.researchgate.net/publication/337898468>
19. Ahmad MW et al (eds) (2022) *Intelligent data analytics for power and energy systems*. Springer, Singapore, pp XXII, 641. ISBN: 978-981-16-6081-8. <https://doi.org/10.1007/978-981-16-6081-8>
20. Tomar A et al (eds) (2022) *Proceedings of 3rd international conference on machine learning, advances in computing, renewable energy and communication: MARC 2021*, vol 915. Springer Nature, pp XV, 781. ISBN: 978-981-19-2830-7. <https://doi.org/10.1007/978-981-19-2828-4>
21. Olabi AG, Abdelkareem MA (2022) Renewable energy and climate change. *Renew Sustain Energy Rev*

# Hybrid Waste to Energy Electricity Generation and Battery Storage System: The Economics and Environmental Emission in a Low-Income Community



Ahmed Abubakar Elwan, Mohd Hafiz Habibuddin, Yanuar Z. Arief, Ahmad Safawi Bin Mokhtar, and Rasyidah Binti Mohamad Idris

**Abstract** Waste and population growth have increased significantly, even in low-income and developing countries. Gombe metropolitan is the largest local government area in Gombe state, which is located in northern Nigeria. Gombe, like any other city in Nigeria, has seen an increase in population growth and land occupation, which has resulted in an increase in waste generation and a reduction in nearby land for land-filling activities. Using HOMER Pro optimization software, this study assesses the economic, environmental, and technical impact of a waste-to-energy (WtE) hybrid plant with a storage device. The system's net present cost (NPC) is estimated to be \$112,633 with a levelized cost of energy (LCOE) of 0.283\$/kWh. The total energy generated is estimated to be 62,084 kWh/year, with an excess of 1049 kWh/year expected after consumption of 60,386 kWh/year. The simulation results show that the proposed system has a very significant impact on the environment, with very low emissions. The hybrid WtE/storage device system is not economically viable because the cost of electricity from the system is higher than the grid price, but the results show strong viability in terms of environmental impact.

**Keywords** Net present cost · Waste-to-energy · Environmental emission · Municipal solid waste · Electricity

---

A. A. Elwan · M. H. Habibuddin · A. S. B. Mokhtar · R. B. M. Idris  
Department of Electrical Power Engineering, Universiti Teknologi Malaysia (UTM), Johor Bahru, Malaysia  
e-mail: [mdhafiz@utm.my](mailto:mdhafiz@utm.my)

A. S. B. Mokhtar  
e-mail: [safawi@utm.my](mailto:safawi@utm.my)

R. B. M. Idris  
e-mail: [rasyidahidris@utm.my](mailto:rasyidahidris@utm.my)

Y. Z. Arief (✉)  
Department of Electrical and Electronic Engineering, Faculty of Engineering, Universiti Malaysia Sarawak (UNIMAS), Kota Samarahan, Sarawak, Malaysia  
e-mail: [ayzulardiansyah@unimas.my](mailto:ayzulardiansyah@unimas.my)

## 1 Introduction

The world produces 2.01 billion tons of municipal solid waste per year, and this figure is expected to rise to 3.4 billion by 2050 [1]. If there are no changes, solid waste-related emissions will rise to 2.38 billion tons of CO<sub>2</sub> equivalent annually by 2050 [2]. High-income countries are expected to grow by 19 percent per day per capita by 2050, while low- and middle-income countries are expected to grow by 40% [3]. Dry wastes, such as plastic, paper, cardboard, metal, and glass, account for 51% of total waste generated. Additionally, solid waste adds to the world's greenhouse gas emissions. In 2016, solid waste accounted for 5–6.4% of all greenhouse gas emissions in the world, or roughly 1.6 billion tons of carbon dioxide (CO<sub>2</sub>) equivalent emissions [4]. The main factor causing emissions from solid waste is the manner of disposal, such as open dumps or landfills without mechanisms for collecting landfill gas [5].

An example of an integrated circular economy is waste-to-energy (WtE), which recovers energy from MSW. In addition to energy recovery, WtEs have other advantages, such as reducing the amount of waste transported to landfills, lowering air emissions typically experienced when open burning is used for waste disposal, increasing recycling rates, particularly during the preparatory stage of WtE, and, if harnessed, replacing fossil fuels in power generation, thus achieving the goal of environmentally friendly and sustainable energy generation. Reducing the amount of garbage that needs to be dumped, preventing water and air contamination, and replacing fossil fuels in the production of electricity are all advantages of hybrid waste management systems that incorporate energy recovery.

The majority of WTE feasibility studies fall into two broad categories: techno-economic and environmental analysis. The amount of heat or power recovered by WtEs was analyzed in terms of its relative environmental impact, as shown in [5–8]. Some of the most common elements used for economic analysis when performing feasibility studies are net present value, internal rate of return (IRR), and levelized cost of energy (LCOE) [9]. In feasibility studies, various combinations and architectures are developed using a variety of methods. Examples of such configurations include stand-alone, hybrid, stand-alone grid-connected, hybrid grid-connected, and so on, based on various renewable energy resources (PV, wind, and biomass), storage components (battery), and converters.

With the introduction of modern computer-based systems, the use of simulation tools has increased. Examples of such tools include MATLAB, PSIM, and HOMER. Hybrid Optimization Model for Electric Renewable (HOMER) software is widely used in determining likely configurations and implementation. The authors of [10] used HOMER to demonstrate the potential of optimized WtE technologies in conjunction with other renewable sources such as PV and wind in Bangladesh. Homer software was also used to assess the amount of electricity generated, as well as the economic and environmental impact on Hamadan [11]. HOMER was also used in hybrid off-grid feasibility studies in Australia, taking into account various climatic zones [11]. Liu et al. [12] used HOMER software to assess the feasibility of WtE in the Iraqi city of Najaf.

The authors of [13] use HOMER software to simulate the net present cost (NPC) and greenhouse gas emissions (GHG) of hybrid renewable energy systems. Heilig [14] investigated the techno-economics of replacing diesel generators and batteries in a hybrid with hydrogen. The results of the studies showed that it is technically possible to substitute; however, when economically evaluated, it shows that it has a high cost under current conditions; however, with advancements in hydrogen technologies, it is possible in the future. Heilig [14] used three (3) types of configuration to test the viability of options in off-grid rural electrification. According to the study's findings, PV is the most promising technology for rural electrification.

This paper presents a techno-economic and environmental assessment of a hybrid WtE and storage electricity generation plant to determine its viability as a grid electricity supply substitute for the selected community. The HOMER Pro software was used to model and simulate the hybrid system for feasibility analysis. The study area's estimated daily demand was used. An electricity generator was carefully chosen to match the amount of potential electricity available. For this study, gasification conversion technology was used for energy recovery.

## 2 Research Method

### 2.1 Study Area

The study area is a suburb of Gombe, the capital of Gombe state and one of the 11 LGA in Nigeria's northeastern region. When the insurgency was at its peak in 2014 and 2015, Gombe saw an influx of people from neighboring states [15]. Gombe, with an area of 52 km<sup>2</sup>, is between latitude 10° 17' 05.88'' N and longitude 11° 10' 36.78'' E, as shown in Table 1. Gombe's population was 26,210 in 1950, and it has grown at a rate of 4.07% per year since then [15], with an estimated population of 529,283 in 2021. These estimates represent Gombe's urban agglomeration, which typically includes Gombe's population as well as adjacent suburban areas that are usually included due to the rapid rate of expansion witnessed [16] (Table 1).

**Table 1** Gombe geographic information [20]

S. no.	Study area description (Gombe)		
	Item description	Unit	Value
1	Latitude	Degrees, minutes	10° 17' N
2	Longitude	Degrees, minutes	11° 10' E
3	Height above sea level	Meters	461 m
4	Population estimate (2021)	#	529,283



## 2.2 Waste Management and Waste Specifications

Gombe's solid waste management is not advanced and is frequently associated with data availability of the source, types of solid waste, composition, and generation rates. Gombe metropolis is the most advanced area of the state, but there is little record or knowledge of solid waste generated. For this study, we are using the most recent estimate from the state agency in charge of waste management in the city. According to estimates, the total amount of solid waste disposed of in open dump sites is around fifteen metric tons, which is equivalent to fifteen thousand kilograms (15,000 kg) daily in the Gombe metropolis [17]. Waste is generated in various parts of the Gombe metropolis, including residential households and other public areas such as shops, clinics, and schools. The community has a daily average waste generation capacity of 10 tons, which is disposed of in landfills or dumpsites for landfilling or open burning. The wastes can be classified as follows: Plastics, paper, wood, glass, polyethylene, organic waste/food, and others (uncategorizable waste) [18] as in Table 2.

## 3 Waste-to-Energy Conversion Technology

The selected conversion technology (gasification) and any other related parameters are based on the facility operating under all applicable regulations. The modular design technology approach was chosen. This concept will assist energy recovery systems in offsetting operating costs while also significantly lowering the capital costs of air pollution control equipment [19]. Figure 1 shows a typical gasification diagram. A modular gasification plant has two basic designs: a starved air combustor and an excess air combustor. The combustor is composed of two distinct combustion chambers known as the "primary" and "secondary" chambers. Waste enters the plant in batches via a hydraulically controlled ramrod from the primary chamber. When

**Table 2** Waste distribution composition [17]

S. no.	Waste distribution and classification	
	Composition	Average (%)
1	Fabrics	3
2	Metals	0
3	Organic	9
4	Paper	19
5	Polyethylene	40
6	Plastics	18
7	Wood	3
8	Others	7

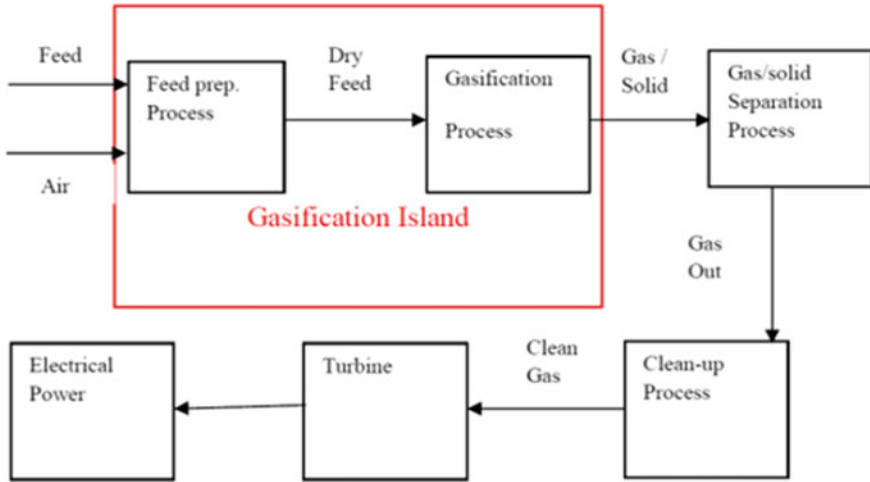


Fig. 1 Typical gasification diagram

waste is introduced into the primary chamber, it undergoes a retention period of up to 12 h.

## 4 Simulation and Modeling

### 4.1 Financial Modeling

HOMER uses (1–3) for financial analysis. The entire cost of plant components and installation costs is used to compute the capital cost of the WTE facility. For a small capacity, a gasification WTE facility can cost anywhere between \$15 and \$25 million on average [20]. Net present cost (NPC) and localized cost of electricity (LCOE) of the system are the financial parameters expected. Emission reduction and renewable fractions are employed in HOMER to assess environmental factors [21].

$$NPC = TAC/CRF \tag{1}$$

where

TAC = total annualized cost  
 CRF = capital recovery factor

$$LCOE = C_{ann,tot}/E \tag{2}$$

where

$C_{ann, tot}$  = annual cost in \$

$E$  = total electricity consumption in kWh/year

$$f_{WtE} = E_{WtE} / E_{ann,tot} \tag{3}$$

where

$E_{ann, tot}$  = annual total energy generation of the system

$E_{WtE}$  = electricity generation from the generator

### 4.2 Assumption for Simulation

Some basic assumptions must be made for HOMER simulations to be effective, as shown in Table 3.

Energy density refers to the amount of energy that can be stored in a single system per unit volume or weight. Battery efficiency is expressed as a percentage of charge and discharge efficiency (4) is used in sizing the number of batteries required.

$$BC = f_g * G * f \tag{4}$$

where

BC = BESS capacity in MW

$f_g$  = frequency gain

$G$  = governor drop

$f$  = system frequency in Hz.

Electrical energy recovered from the combustion of waste can be determined from (5).

**Table 3** Assumption parameters [17]

S. no.	Assumed parameters		
	Parameter	Unit	Value
1	Capacity factor	%	80
2	Carbon content at gasification	%	100
3	Gasification ratio	–	0.2
4	Grid unit price	\$/kWh	0.06
5	Hours of service	Hours	6970
6	Low heating value	MJ/kg	23
7	Moisture	%	15
8	Number of starts	Start/year	400
9	Operational life Genset	Year	20
10	Operational life storage	Year	4.21

$$\text{Electrical energy} = \frac{hv * \left[ \frac{2000ib}{\text{ton}} \right]}{\text{heat rate}} \tag{5}$$

where

hv = heating value of waste component *i*

heat rate = a measure of the efficiency of the plant, the number of Btu’s fuel needed to generate one kWh (Btu/kWh).

## 5 Results and Discussion

Based on impact categories, the simulation results from HOMER were presented and analyzed. Three impact levels, namely technical, economic, and environmental impact, were created from these categories. The subcategories for environmental are emissions, which are largely greenhouse gases (GHG). NPV, annualized costs, and LCOE were discussed at the economic impact level. Last but not least, the technical impact was reviewed concerning the contribution of electricity generation and consumption, excess electricity produced, and associated conclusions. Under each category, the results were displayed in figures and tables.

### 5.1 Economic Impact Assessment

Tables 4 and 5 show the cost impact results from the simulation. In Table 4, the generator has a capital cost of \$12,500, an operating cost of \$40,944, a replacement cost of \$42,156, and a salvage value of \$−283. Using net present cost indices, the total cost of the Genset is \$95,367. Table 5 shows the optimized cost on an annualized basis. The annualized capital costs for the generator are \$1594 as a capital cost, \$5375 as a replacement cost after its lifetime, and \$5227 to keep the generator in good working order. The highest cost is the replacement, followed by operation and capital costs.

The system converter is an exception to the preceding; it has no operating costs, low replacement costs, and a capital cost that is higher than its operating cost.

**Table 4** Economic simulation results (NPC)

S. no.	Net present cost (\$)					
	Parameter	Capital	Operating	Replacement	Salvage	Total
1	1 kWh lead acid	600	1725	7850	−17	16,159
2	25 kW capacity Genset	1,250	40,994	42,156	−283.1	95,367
3	Converter	952.4	0	174.01	−18.68	1108
4	Total	20,052	42,720	50,180	−318.8	112,634

**Table 5** Economic simulation results (annualized)

S. no.	Annualized cost (\$)					
	Parameter	Capital	Operating	Replacement	Salvage	Total
1	1 kWh lead acid	841.5	220	1001	-2.17	2060
2	25 kW capacity Genset	1.594	5,227	5375	-36.09	12,159
3	Converter	121.4	0	22.19	-2.38	141.24
4	Total	2557	5447	6398	-40.64	14,361

**Table 6** Environmental impact analysis

S. no.	Electrical production and consumption		
	Parameter	Unit	Value
1	Carbon dioxide	kg/year	119
2	Carbon monoxide	kg/year	0.54
3	Unburned hydrocarbon	kg/year	0.024
4	Particulate matter	kg/year	0.003
5	Sulfur dioxide	kg/year	0
6	Nitrogen dioxide	kg/year	0.52

According to the tables, the overall cost of replacement is high, accounting for the majority of the costs. The simulation’s NPC is \$112,630, and the LCOE is \$0.238/kWh.

### 5.2 Environmental Impact Analysis

The environmental impact of HOMER simulation for the WtE/storage hybrid system is shown in Table 6. Greenhouse gases (GHG) from the system total 120 kg/year and are composed of carbon dioxide, carbon monoxide, sulfur dioxide, and nitrogen dioxide. Unburned hydrocarbon emissions are as low as 0.024 kg/year, and particulate matter emissions are as low as 0.0032 kg/year. This demonstrates that hybrid WtE/storage can reduce GHG emissions as well as air emissions when compared to open burning or landfilling.

### 5.3 Technical Impact Analysis

Table 7 summarizes the system generation versus the required demand; the system is expected to generate a total of 62,084 kWh per year, with an annual load to serve of 60,386 kWh, and an excess of 1049 kWh per year, representing 1.6% of the total energy generated. There will be no capacity shortages or unmet loads from the system

**Table 7** Technical impact analysis

S. no.	Electrical production and consumption		
	Parameter	Unit	Value
1	Excess electricity	kWh/year	1049
2	Unmet electric load	kWh/year	0
3	Genset generation	kWh/year	62,084
4	Load consumption	kWh/year	60,386
5	Effective battery energy	kWh/year	3744
6	Battery losses	kWh/year	936
7	Converter maximum output	kW	2.88
8	Converter losses	kWh/year	187
9	Converter hours of operation	hrs	1791

because 100% of the energy demand is expected to be met. Because the system is a stand-alone hybrid system, excess energy can only be stored and not sold back to the grid.

When demand is low, the batteries are charged, and when demand exceeds generation, the batteries are discharged to power up the load. According to Table 7, the batteries have total energy supplied out that is 3744 kWh and a loss of approximately 936 kWh. Battery output is typically in DC form and cannot be used to power AC equipment, which is the most common load in every home. A system converter is used to convert the battery output back to alternating current (AC) for consumption. Table 7 shows that the converter loses 187 kWh/year, which is 5% of the total input energy (3744 kWh/year). The converter has a maximum output of 2.88 kW and a mean output of 0.41 kW.

## 6 Conclusion

This research is a techno-economic and environmental assessment of a hybrid WtE/storage system to supply a load demand from a Gombe metropolis suburb in Gombe state, Nigeria. The study concludes that:

- (1) While the amount of waste generated for this study is adequate for the purpose, the quality of the waste does not have the required heat value, affecting the overall optimization of the system.
- (2) Adopting WtE for suburban settlements in Northern Nigeria will help improve energy access to the population without electricity and waste management.
- (3) The cost of WtE energy is higher than the cost of energy from the government-owned grid. This is the case.

**Acknowledgements** This work was supported/funded by the Ministry of Higher Education under Fundamental Research Grant (Grant FRGS/1/2018/TK07/UTM/02/6).

## References

1. Population Estimates and Projections. <https://databank.worldbank.org/source/population-estimates-and-projections>. Accessed January 2020
2. Kaza S, Yao L, Bhada-Tata P, Van Woerden F (2018) What a waste 2.0: a global snapshot of solid waste management to 2050. World Bank Publications, December 2018
3. Trends in Solid Waste Management. [https://datatopics.worldbank.org/what-a-waste/trends\\_in\\_solid\\_waste\\_management.html](https://datatopics.worldbank.org/what-a-waste/trends_in_solid_waste_management.html). Accessed July 2021
4. Maria C, Góis J, Leitão A (2020) Challenges and perspectives of greenhouse gases emissions from municipal solid waste management in Angola. *Energy Rep* 6:364–369
5. Elwan A, Arief YZ, Adzis Z, Saad MHI (2014) The viability of generating electricity by harnessing household garbage solid waste using life cycle assessment. *Proc Technol* 11:134–140
6. Malav LC, Yadav KK, Gupta N et al (2020) A review on municipal solid waste as a renewable source for waste-to-energy project in India: current practices, challenges, and future opportunities. *J Clean Prod* 277:123–227
7. Fernández-Gonzalez JM, Grindlay AL, Serrano-Bernardo F, Rodríguez-Rojas MI, Zamorano M (2017) Economic and environmental review of waste-to-energy systems for municipal solid waste management in medium and small municipalities. *Waste Manage* 1(67):360–374
8. Viau S, Majeau-Bettez G, Spreutels L, Legros R, Margni M, Samson R (2020) Substitution modelling in life cycle assessment of municipal solid waste management. *Waste Manage* 1; 102:795–803
9. Islam MR, Al Rafi J, Hossain MS (2019) Operation planning of renewable energy-based hybrid system incorporating waste-to-energy (WtE) technologies. In: 2019 international conference on sustainable technologies for industry 4.0 (STI), IEEE, December 2019, pp 1–5
10. Alayi R, Jahangeri M, Monfared H (2020) Optimal location of electrical generation from urban solid waste for biomass power plants. *Anthropogenic Pollution J* 4(2):44–51
11. Anssari OM, Alkaldy EA, Almudhaffar N, AlTae AN, Ali NS (2020) A feasibility study of electrical energy generation from municipal solid waste in Iraq: Najaf case study. *Int J Electr Comput Eng* 10(4):2088–8708
12. Liu G, Rasul MG, Amanullah MTO, Khan MMK (2011) Feasibility study of stand-alone PV-wind-biomass hybrid energy system in Australia. In: 2011 Asia-Pacific power and energy engineering conference, pp 1–6. March 2011
13. Zoulias EI, Lymberopoulos N (2007) Techno-economic analysis of the integration of hydrogen energy technologies in renewable energy-based stand-alone power systems. *Renew Energy* 32(4):680–696
14. Heilig GK (2012) World urbanization prospects: the 2011 revision. United Nations, Department of Economic and Social Affairs (DESA), Population Division, Population Estimates and Projections Section, New York, vol 14, p 555
15. Abdullahi UY, Abbas AM, Abdullahi A (2018) Demographic and socio-economic determinants of house ownership in Gombe Local Government Area, Gombe State. *J Soc Sci Public Policy* 10(3)
16. Gombe State Environmental Protection Agency (2018) <https://moenv.gm.gov.ng/gosepa>
17. Imam A, Mohammed B, Wilson DC, Cheeseman CR (2008) Solid waste management in Abuja, Nigeria. *Waste Manage* 28(2):468–472
18. Mosiori GO, Onindo CO, Mugabi P, Tumwebaze SB, Bagabo S, Johnson RB (2015) Characteristics of potential gasifier fuels in selected regions of the Lake Victoria Basin. *S Afr J Sci* 111(5–6):1–6
19. Tchobanoglous G (2000) Integrated solid waste management engineering principles and management issues (No. 628 T3)

20. Barakat S, Samy MM, Eteiba MB, Wahba WI (2016) Feasibility study of grid connected PV-biomass integrated energy system in Egypt. *Int J Emerg Electr Power Syst* 17(5):519–528
21. Tomar A et al (eds) (2022) Proceedings of 3rd international conference on machine learning, advances in computing, renewable energy and communication: MARC 2021, vol 915), Pages XV, 781. ISBN: 978-981-19-2830-7. Springer Nature. <https://doi.org/10.1007/978-981-19-2828-4>



# Application of Solar Power in the Loopholes and Coverages of Buses in the Bus Rapid Transit System in Bhopal



Rajeev Kumar, Deepak Juneja, and Yogendra Narayan

**Abstract** Bhopal, more than any other city in India, has an extraordinary topographical design in which hillsides and lakes blend together to provide this area of Madhya Pradesh with an amazing appearance. The city of Bhopal, Madhya Pradesh, is a must-see destination with several monuments and attractive surroundings. It is one of MP's fastest-growing cities, situated on mountainous terrain in the Malwa Plateau. Bhopal is dealing with increasing population pressures on resources and infrastructure. To keep up with the rapid increase of fiscal, corporate, and commercial operations, the government has devised a number of reorganization plans and proposals. The Star City Bus or BRTS is one of the plans. It started with just 30 buses and later on grew up to 225 buses as of now. This study is majorly dedicated to knowing the plans, routes and transportation system of BRTS Bhopal to identify the coverage of areas, No. of stops and routes, congestion status, collision and parallel routes. It has been observed that the TR1 and TR4 schedules can be improved upon in order to maximize ridership and reduce complaints. Although it has the shortest trunk route distance, it also has the most bus stops, which causes delays and inconveniences to passengers.

**Keywords** Bus Route Transit System (BRTS) · Congestion · Route · Bhopal

---

R. Kumar (✉) · D. Juneja  
Department of Civil Engineering, Chandigarh University, Mohali, Punjab, India  
e-mail: [rkrajeev54321@gmail.com](mailto:rkrajeev54321@gmail.com)

D. Juneja  
e-mail: [deepakjuneja.civil@cumail.in](mailto:deepakjuneja.civil@cumail.in)

Y. Narayan  
Department of EC Engineering, Chandigarh University, Mohali, Punjab, India  
e-mail: [narayan.yogendra1986@gmail.com](mailto:narayan.yogendra1986@gmail.com)

## 1 Introduction

The transportation sector contributes significantly to the national economy. Nonetheless, public transportation has always been the most popular choice for the vast majority of people, and today, India boasts one of the world's busiest subway networks. The fundamental issue in metropolitan areas is passenger mobility and connecting the city periphery with the core section, and there are a few novel solutions to this problem. This is true of cities all over the world, including India. Compared to other Light Rail Transit (LRT) and Metro Rail options, urban planners, engineers, and administrators have found that Bus Rapid Transit Systems (BRTS) are more successful, cost-effective, and straightforward in providing a "lifeline" to the city. This is a form of mass transit that utilizes buses as a primary mode of transportation. BRTS sometimes referred to as a "surface subway", seeks to improve both the efficiency and accessibility of traditional bus systems. Because of its flexibility in operating in both light and heavy traffic conditions, BRTS is well suited for medium-sized cities like Bhopal, which have inadequate bus services but where the middle class constitutes the social structure. The idea behind BRTS is to reduce the number of single-occupant vehicles on the road by transporting those people in a more convenient and rapid means of public transportation.

The growth of cities depends on efficient transportation networks. With improved access and mobility, cities can run more smoothly. Transportation by passengers has a disproportionate impact on city operations. Growth necessitates better access to transportation options. Public transportation networks and the expansion of private transportation options like auto-rickshaws, private buses, and taxis are both viable options for making cities more accessible. Due to the significant contribution that urban sprawl and poor land use planning make to traffic congestion, air pollution, and greenhouse gas emissions; we can opt for a public transport system instead of a private one. Furthermore, public transportation aids in the prevention of sprawl by encouraging construction near transit stations, which in turn boosts patronage. In the light of this, urban mobility concerns were studied by transportation and community planning experts all over the world in an effort to find solutions. Their resurgence of interest in public transit is indicative of the growing awareness of environmental issues, as well as the need for viable alternatives to the gridlock on our nation's highways and the spread of our cities. A variety of transportation technologies, including Metro Rail Transit, Light Rail Transit (LRT), Mono Rail, etc., addresses these issues; however, they are expensive, inflexible, and have significant capital and operational costs. Because of these issues, public transportation providers are rethinking how they use technology and looking for novel, low-cost strategies to boost service quality. This is why BRTSs have cropped up all over the globe. BRTS may be created rapidly, gradually, and cheaply, and it offers operational flexibility.

## ***1.1 Vehicular Growth and Modal Split in India***

In recent decades, the number of cars on India's roads has skyrocketed. "Although the population of India's six major metropolises expanded by roughly 1.9 times during 1981–2001, the number of motor vehicles went up by about 7.75 times", it says in the "National Urban Transport Policy". At least 35% (27.76 million) of urban households had a motorized two-wheeler, and 9.7% (7.65 million) of urban households had a motorized four-wheeler, according to the 2011 Census. While the national average rise in registered motor vehicles from 2002 to 2011 was 10.2% each year, the annual rate of increase was 8.8% in the 19 metropolitan areas for which we have data for both years (Transport Research Wing 2012: 3–4). Vehicle ownership is on the rise, although there are still only 117 cars per every 1000 people. Yet, in the next years, India's rising car density will be a result of the country's ongoing strong economic growth. Large amounts of non-motorized transport are also present in India's urban areas, complementing automobiles (NMT). NMT refers to non-motorized transport, which includes 42% of all journeys made via walking and cycling and 16% made via public transport. The urban poor often has to resort to walking and cycling since they have no other options for getting around town. For a city to be an exemplar of sustainable transport, its motorized vehicle users, mostly those who commute by car (16%) and two-wheeler (21%), would need to transition to NMT. Cities with populations over eight million rely on the pedestrian, bicycle, and public transportation for 74% of all trips, whereas cities with populations over four million rely on these modes for 66% of all journeys. The percentage of two-wheeled motor vehicles ranges from 20 to 29% in cities with populations between 1 and 5 million, whereas the percentage of four-wheeled motor vehicles is between 10 and 12%. Urban transportation systems and regulations need to take this into account while still protecting the viability of walking and biking as viable modes of transportation for at least 50% of all journeys. Congestion and pollution have resulted from the inability of Indian cities' public transportation networks to meet rising demand, with many residents opting instead to use private vehicles or a hybrid form of public transit known as Intermediate Public Transport (Ministry of Urban Development, 2008). Weirder still, remedies to the aforementioned problem have been proposed, such as building flyovers and expanding roads, rather than enhancing public transportation. Municipal and state-run urban bus services are notoriously unstable, reliant on poorly maintained bus fleets, and underfunded and understaffed. Yet, no systematic efforts have been made to assist these services.

## ***1.2 Bus Rapid Transit System***

BRTS is defined as "a rubber-tired rapid transit mode that integrates stations, vehicles, services, running ways, and elements of the intelligent transportation system (ITS) to create a system with a strong positive character that creates a unique image". This

description emphasizes the adaptability of BRTS and the breadth of its applications, each of which is designed for a certain set of travel markets and physical surroundings. When it comes to transportation, the Bus Rapid Transit System (BRTS) is the best of both worlds: it offers the convenience and low cost of bus service while also matching or exceeding the effectiveness, efficiency, and adaptability of rail transit. Unlike rail-based rapid transit modes, the basic service unit of BRTS, a single vehicle, is relatively small. This allows BRTS vehicles (such as buses and specialized BRTS vehicles) to drive anywhere there is pavement. BRT systems can function with dedicated lanes, cleaner and quieter buses, off-vehicle fare collecting that takes just seconds, aesthetically pleasing stations, and minimal stops. It's estimated that a BRTS project can cost as little as a third as much as a Rail Transit one. It's a new kind of public transportation, a cross between a train and a bus.

Population growth is putting demand on Bhopal's already limited infrastructure and services. To accommodate the ever-increasing number of banking, corporate, and commercial enterprises, the government has proposed numerous reorganizational concepts and plans. The Star City Bus, or BRTS as it's more often known, is a feature in one of the concepts. Initially, there were just 30 buses; today, however, there are 225. The primary goal of this research is to get an understanding of the BRTS Bhopal system, including its plans, routes, and transportation system, in order to ascertain its coverage area, station count, route count, congestion rate, collision rate, and the number of parallel routes.

This paper analyses the loopholes and coverage of buses in the Bus Rapid Transit System in Bhopal. The first part contains an introduction to the transport system in Bhopal. The research approach adopted in this study is discussed in the second part. The research methodology adopted in this study is discussed in the third part. The finding of the study is discussed in the fourth part. The conclusions of the study obtained through the analysis are discussed in the fifth part, and the future scope is discussed in the last part of the paper.

### ***1.3 Solar Panel***

Solar panels on top of bus stops could be used to power sensors that could monitor traffic or pollution level in the air, which would be a huge benefits to commuters and passengers on the bus.

## 2 Proposed Approach

### 2.1 Public Transportation in Bhopal

Bhopal has a well-developed internal transportation system that connects it to the rest of the country by roads, railroads, and airways. To commute from one section of the town to another, there are a variety of options available, including City Link buses, minibuses, private cars, and automobiles.

### 2.2 Star Bus/BRTS

Star-adorned buses, the Bhopal City Link is run by Bhopal City Link Limited. The capital and second-largest city of Madhya Pradesh is Bhopal. The city is grappling with growing population pressure on its infrastructure and resources. To keep up with the city's rapid growth in fiscal, business, and commercial activity, the government has devised a number of plans and proposals to rebuild the city's transportation system. Bhopal City Link Limited (BCLL) is a state-owned road transportation company in Bhopal that operates a well-designed bus system that connects the entire city. Figure 1 shows the Bus Rapid Transit System of Bhopal.

Bhopal City Link Limited, which started operating in October 2006, is one of the city's most popular modes of transportation. BCCL, which has Bhopal Municipal Corporation and Bhopal Development Authority as shareholders, operates buses on all of Bhopal's major trunk and standard routes, linking the city's various nooks and crannies. BCCL, which was founded in October 2006, began serving more parts of the city more easily in March 2007, when it had enough buses to run on all key routes. The fare is nominal and is determined by the distance between the two points. BRTS system of town majorly consists of two categorical routes whereas in depth they are into four categories. Considering the major route categories is as follows:



Fig. 1 Solar panel in bus stop

- Trunk Routes

It connects key activity hubs. The farthest activity centre should be reachable in 45 minutes or less. There are 4 trunk routes in Bhopal.

- Standard Routes

These routes connect the city's principal origin and destination points. These are minibus routes that have been replaced. There are twelve standard routes in Bhopal as listed in Table 1. Details for all of them are given in Table 1.

To operate the above-mentioned buses on four routes corridors as shown in Fig. 2 are built in Bhopal.

1. Bairagarh to Misrod
2. Roshanpura-ORR
3. Board office to Raisen road
4. Bharat talkies to Taj-ul-masajid.

Figure 3 depicts the corridors along with their distance and the site map of it. The longest corridor is corridor one, whereas the shortest one is corridor 4.

**Table 1** BRTS Bhopal various buses details

S. No	Bus name	Origin	Destination	Route length (in km)	Bus stops
1	TR1	Chirayu Hospital (Bairagarh)	Akruti Eco city	42	46
2	TR2	Nadra Bus stand	HEG Mandideep	23	36
3	TR3	Bairagarh RS	Raisen Hoshangabad	28	56
4	TR4	Sehore naka	Misrod	23	47
5	SR1	Halalpur Bu stand	Chinchli Bairagrh	19	34
6	SR2	Nadra Bus stand	HEG Mandideep	23	36
7	SR3	Nariyal Kheda	Ayodhya nagar	26	56
8	SR4	Chinchli bairagrh	Over bridge Circle	30	41
9	SR5	Chirayu hospital	Avadhपुरी Vidyasagar college	40	50
10	SR6	Rajeev Gandhi college	Oriental college	40	44
11	SR7	Gandhi nagar	Patel Nagar Bypass	54	46
12	SR8	Chinchli Bairagarh	Coach factory	27	48



Fig. 2 Bus Rapid Transit System (BRTS), Bhopal



Fig. 3 BRTS corridor of Bhopal

### 3 Results and Discussion

The research methodology used in the study is statistical analysis. The major conclusion and results drawn in the study rely on secondary data. There are two types of data which are gathered for analysis. (1) Primary data refers to the first-hand data gathered by the researcher himself. This is a crude form of data available to the researcher. (2) Secondary data means data collected by someone else earlier, and it is usually refined for the researcher.

**Table 2** Demographic details

Parameter	Range	Frequency	Percentage (%)
Age	15–20	20	22.73
	20–25	27	30.68
	25–30	21	23.86
	30–40	12	13.64
	40 above	8	9.09
Gender	Female	59	67.05
	Male	29	32.95
Profession	Student	38	43.18
	Job	33	37.50
	Other	17	19.32
Transport service	Bus	37	42.05
	Own	20	34.09
	Other	21	23.86

### 3.1 Data Gathering and Analysis

88 people participated in the questionnaire and the questionnaire was shared by Google Form Link whose data description is as follows: Table 2 clearly represents participation in terms of percentage and frequency. It has been observed that 22.73% of people aged between 15 and 20, 30.6% of the responses aged between 20 and 25, 23% offer responses aged between 25 and 30, 14% aged between 30 and 40 and the remaining 9% is 40 and above. So maximum participation is from people aged between 20 and 25. Also, the table shows that 67% of participation is from females and 33% of participation is from males.

Data collected was shorted and then arranged in excel software, which then was edited, and coded as per the required procedure. In the analytical process, the nominal and ordinal scale was used for rating the questions. The relatively important index values are used in the study that they have commonly used tools for analysing attitudes towards surveyed variables in construction research.

### 3.2 Research Method

The statistical analysis methods utilized mean, which is all the more normally alluded to as the average. Mean is one of the important and most commonly used measures of central tendency.

Mathematical Equation:

$$\bar{x} = \Sigma f / \Sigma N, \quad (1)$$



where  $f$  states the sum of frequency and  $N$  is the total no. of operations.

### Regression

With regard to insights, regression is the connection between an independent variable and a dependent variable in the statistical analysis methods. The line utilized in regression analysis charts and graphs means whether the connections between the factors are solid or frail, notwithstanding showing patterns throughout a particular measure of time.

Mathematical Equation:

$$Y = a + bX + \epsilon, \quad (2)$$

where

$Y$ —is the dependent variable

$X$ —is the independent (explanatory) variable— $a$ —is the intercept  $b$ —is the slope

$\epsilon$ —and is the residual (error).

From Fig. 3, it is concluded that TR3 has the highest number of bus stops which is 56, whereas the longest distance covered by TR1 is 42 km. When being analysed it evaluates that for TR3 an average stop distance is 0.5 and 0.9 km for TR1. The formula used is Route distance/No of bus stops to calculate this. The difference between the two bus routes is noticeable and a point of consideration to reduce the no of stops which results in the reduction of total time in route coverage by bus.

From Fig. 4, it is concluded that SR3 has the highest no of bus stops which is 56, whereas the longest distance is covered by SR7 which is 54 km. When being analysed, it evaluates that for SR3 an average stop distance is 0.5 and 1.2 km for SR7. The formula used is Route distance/No of bus stops to calculate this. The difference between the two bus routes is noticeable and a point of consideration to reduce the no of stops which results in the reduction of total time in route coverage by Bus.

The below findings are based on ANOVA results, and Tables 3 and 4 depict the result for the same.

- TR1 and TR4 exhibit a positive association in the association test, indicating that TR1's timetable and plan can be used to improve TR4's overall timing.
- If the stop time of TR4 can be the way that the average stop time comes near to 0.5 or 0.6 km. It will increase the frequency of arrival time of TR4 at various bus stops.
- Overlapping of the buses on four stops was noticed in SR3 and SR2. Bus stops are Nadra Bus Stand, Sabji Mandi, Alpana Tiraha, and Bharat Talkies as shown in Fig. 5.
- Few other overlapping was also identified in the stated plans which are shown in Fig. 5.

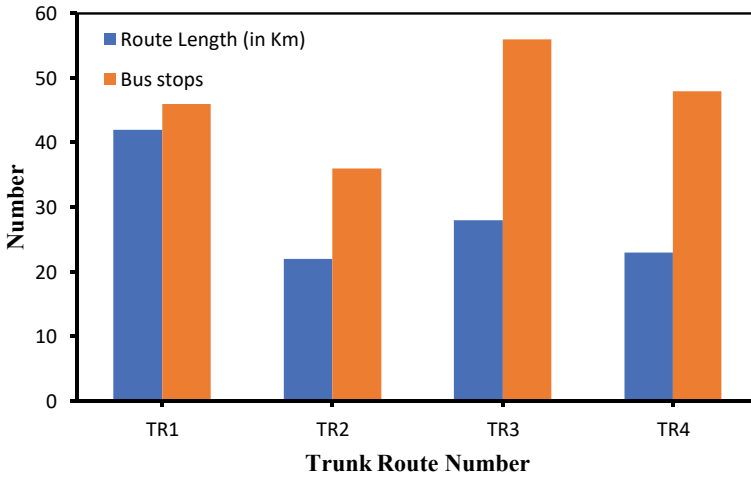


**Fig. 4** Route coverage and bus stops of various trunk routes

**Table 3** ANOVA test result for TR1 to TR4 in terms of waiting time

Dunnett’s multiple comparison test	Mean Diff	<i>q</i>	Significant, <i>P</i> < 0.05	Summary
TR1 versus TR2	– 3.333	5.774	Yes	–
TR1 versus TR3	1.333	2.309	No	ns
TR1 versus TR4	– 3.667	6.351	Yes	–

**Table 4** ANOVA test results between SR1 and SR8 in terms of waiting time

Dunnett’s multiple comparison test	Mean Diff	<i>q</i>	Significant, <i>P</i> < 0.05	Summary
SR1 versus SR2	– 2.667	4.438	Yes	–
SR1 versus SR3	– 2.333	3.883	Yes	–
SR1 versus SR4	0.3333	0.5547	No	ns
SR1 versus SR5	0.3333	0.5547	No	ns
SR1 versus SR6	0.6667	1.109	No	ns
SR1 versus SR7	0.6667	1.109	No	ns
SR1 versus SR8	1.333	2.219	No	ns

## 4 Conclusions

The arrival time, route overlapping, delay on bus stops, total time taken, and customer satisfaction to cover the route are significant characteristics in the Bhopal study region with regard to BRTS and its improved utilization (Fig. 6).

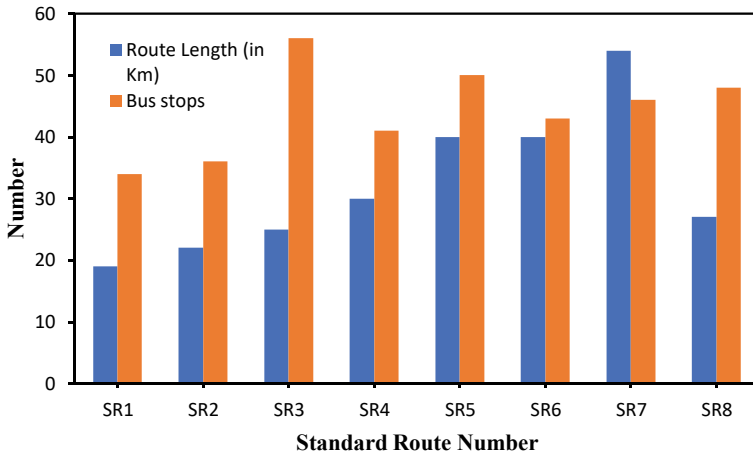


Fig. 5 Route coverage and bus stops of various standard routes

Junction	Bus Routes along the BRT corridor									
	BRTS	TR-1	TR-2	TR-3	SR-1	SR-2	SR-3	SR-4	SR-5	SR-6
Misrod										
Bagsewania										
RRL Tiraha										
Ganesh Mandir										
Mansarovar										
Baord Office										
Vyapam										
Shivaji Chowk										
New Market										
Roshanpura										

Fig. 6 Route overlapping of SR5, SR6, SR4, and TR2

- The study also finds that the TR1 and TR4 schedules might be improved upon in order to maximize service and delight riders.
- Although it has the shortest distance of any trunk route, its high frequency of stops has left passengers frustrated.
- The itinerary for SR2 and SR3 can be adjusted to improve their efficiency as a standard route because the difference of 3 kms between the two routes is equivalent to the difference of 20 stops.
- Since two routes share the four stops above, the latter can be eliminated.

- Solar panels on the top of bus stops can further be used to power sensors that can monitor traffic.

Or the level of pollution in the air, which will be a major benefit to the passengers and commuters on the bus. If the solar operate bus it introduce then it will effect the rate of fare on the passengers, which will also beneficial.

## 5 Future Scope

The study can be researched more in terms of traffic congestion, parallel routes, passenger utilization, road condition, the effect of metro lines on the road, and new deviations of the routes during the development period of metro. More association and advanced statistical tests like Chi-test and ANOVA can be applied for more precise and in-depth results. It can also be extended by suggesting better options for the existing resources of BRTS on the same with minimum revision and deviation.

## References

1. Saxena A, Gupta V, Shrivastava B (2021) An assessment of public transport accessibility levels for slums in Bhopal. *Int J Eng Adv Technol (IJEAT)* 10(5). ISSN: 2249-8958 (Online)
2. Anuj Jaiswal AR, Sharma A (2012) Optimization of public transport demand: a case study of Bhopal. *Int J Sci Res Publ* 2(7)
3. Solanki VS, Agarwal PK (2022) Performance improvement of bus transport system from user perspective. In: *Proceedings of the fifth international conference of transportation research group of India*
4. Krishna S, Sathvik S, Suchit S (2022) Advances in construction management evaluation of operational BRTS system in Bangalore. *Conference paper First Online*, pp 35–43, 19 Jan 2022
5. Samans R, Nelson J (2022) Corporate partnerships and systemic change. *Chapter Open Access Sustainable Enterprise Value Creation First Online*, 28 May 2022
6. Vuchic VR (1999) *Transportation for livable cities*. Centre for Urban Policy Research, New Brunswick, New Jersey
7. World Commission on Environment and Development (1987) *Our common future*. Oxford University Press, Oxford, UK
8. Moavenzadeh F, Hanaki K, Baccini P (2002) *Future cities: dynamics and sustainability*. Kluwer Academic Publishers, Norwell, MA
9. Bongardt D, Schmid D, Cornie H, Litman T (2011) *Sustainable transport evaluation*, GIZ, Eschborn, Germany
10. Miller P, de Barros AG, Kattan L, Wirasinghe SC (2016) Public transportation, and sustainability: a review. *KSCE J Civ Eng* 20(3):1076–1083
11. Gandhi S, Tiwari G, Joseph F (2013) Comparative evaluation of alternate Bus Rapid Transit System (BRTS) planning, operation and design options. *The Eastern Asia Soc Transp Stud* 9
12. Levinson HS, Zimmerman S, Clinger J, Gast J (2003) *Bus rapid transit: synthesis of case studies*. *Transp Res Rec* 1841(1):1–1
13. Panchoe V, Kushwaha N (2016) Performance evaluation of brts. *IJSTE-Int J Sci Technol Eng* 2(11):509–512

14. Miller P, de Barros AG, Kattan L et al (2016) Public transportation and sustainability: a review. *KSCE J Civ Eng* 20:1076–1083
15. Agarwal PK, Sharma A, Singh AP (2010) An overview on bus rapid transit system. *J Eng Res Stud*
16. Cidell J (2012) Sustainable transportation: accessibility, mobility, and derived demand. In: Theis T, Tomkin J (eds) *Sustainability: a comprehensive foundation*, pp 566–576
17. Dobranskyte-Niskota A, Perujo A, Pregl M (2007) Indicators to assess the sustainability of transportation activities. *Ispira: European Commission Joint Research Centre Institute for Environment and Sustainability*
18. Haghshenas H, Vaziri M (2012) Urban sustainable transportation indicators for global comparison. In: *Ecological indicators*, pp 115–121
19. Jewell C, Shah S, Patel K, Jaramillo J, Gorgas P, Vienckowski L, Bradbury G, Caceres R. A solar powered bus stop systems
20. Chowdhury N, Hossain C, Longo M, Yachi W (2018) Optimization of solar energy system for the electric vehicle at University Campus in Dhaka, Bangladesh. *Energies* 11:2433

# Forecasting of Carbon Emissions in India Using (ARIMA) Time Series Predicting Approach



Somesh Sharma, Amit Mittal, Manmohan Bansal, Bhagawati Prasad Joshi, and Ashish Rayal

**Abstract** After China and the USA, India is the third highest emitter of carbon dioxide (CO<sub>2</sub>). The research focuses on predicting carbon emissions in India using autoregressive integrated moving average (ARIMA) models. The study uses time series data from 1980 to 2021 to develop and validate the ARIMA models. The results of the analysis show that the ARIMA models are able to effectively capture the trend and seasonality of carbon emissions in India. The study also uses the ARIMA models to forecast future carbon emissions for the period 2022–2030. The forecasted value of CO<sub>2</sub> Emissions 3,616,149 (KT) as per ARIMA (0,2,1). The findings indicate that carbon emissions in India are likely to continue increasing in the future, despite efforts to reduce them. The research also investigates the impact of carbon emissions on renewable power generation in India. The study shows that the level of carbon emissions has a significant negative impact on renewable energy production, particularly solar and wind energy. The findings suggest that reducing carbon emissions is crucial for the growth and development of the renewable energy sector in India. The outcomes of this research have important consequences for decision-makers in government and stakeholders in the energy sector. The study highlights the need for effective policies and initiatives in order to lessen India's carbon footprint and encourage the growth of renewable energy sources. The ARIMA

---

S. Sharma

School of Management, Graphic Era Hill University, Bhimtal 263136, India

A. Mittal (✉)

Department of EVS, Graphic Era Hill University, Bhimtal 263136, India

e-mail: [amitforestry26@gmail.com](mailto:amitforestry26@gmail.com)

M. Bansal

School of Management, Invertis University, Bareilly 243123, India

B. P. Joshi

Department of Mathematics, Graphic Era Hill University, Bhimtal 263136, India

A. Rayal

Department of Mathematics, Uttarakhand University, Dehradun 248007, India

e-mail: [ashishrayal@uttarakhanduniversity.ac.in](mailto:ashishrayal@uttarakhanduniversity.ac.in)

© The Author(s), under exclusive license to Springer Nature Singapore Pte Ltd. 2024

H. Malik et al. (eds.), *Renewable Power for Sustainable Growth*,

Lecture Notes in Electrical Engineering 1086,

[https://doi.org/10.1007/978-981-99-6749-0\\_53](https://doi.org/10.1007/978-981-99-6749-0_53)

models developed in this study can serve as a valuable tool for forecasting carbon emissions and planning future energy policies in India.

**Keywords** ARIMA · Carbon emission · ADF · ACF · PACF

## 1 Introduction

The phenomenon of global warming has arisen as a significant environmental threat in contemporary times. Climate changes are now extensively recognized as the most stringent ecological concern affecting human society [1]. It will have far-reaching, significant, and unevenly distributed global ramifications and costs. Increased global carbon emissions are the principal factor contributing to climate change and global warming. GHG emissions, particularly CO<sub>2</sub> emissions, are the primary driver of global warming. Carbon dioxide is a heat-absorbing and radiating greenhouse gas [2]. Carbon dioxide accounts for roughly 77% of human greenhouse gases [3]. The ARIMA models to the task of forecasting carbon emissions in India contribute in:-

- Developing a reliable and accurate method for forecasting carbon emissions in India that can help policymakers and stakeholders make informed decisions about climate change mitigation strategies.
- Analyzing the drivers of carbon emissions in India and identifying the most significant factors that contribute to changes in emissions levels over time.
- Comparing the performance of ARIMA models with other forecasting methods to determine the most appropriate method for predicting carbon emissions in India.

Human activity, economic activity that involves burning fossil fuels, transportation, and energy supply all contribute significant amounts of carbon, methane, and other orangery airs globally, while the construction of buildings, forestry/deforestation, and agricultural sectors are also a major cause of increment of carbon, methane, and added orangery airs in the environment [1, 4, 5].

The research begins with an introduction that outlines the challenge posed by the changing climate and the importance of predicting carbon emissions in India. The literature review section will then provide an overview of previous research on carbon emissions and forecasting methods. The methodology section will describe the data sources, ARIMA models, and additional methods that were applied during the research. The analysis and discussion section will present the significant findings of the study, including statistical analyses or visualizations of the data. Finally, the conclusion section will summarize the most important findings, a discussion of their consequences, and some suggestions for the paths of future study.

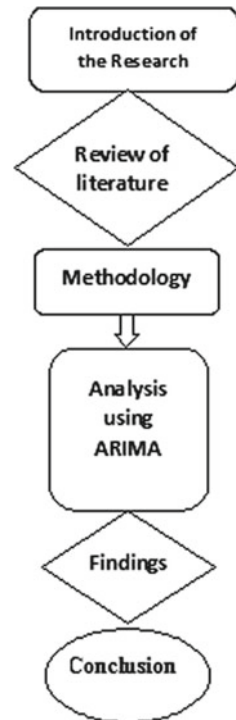
## 2 Proposed Approach

The proposed approach for predicting carbon emissions in India using ARIMA models involves following steps, Fig. 1. Proposed Research First, historical data on carbon emissions in India will be collected and analyzed to identify any patterns or trends. Next, the data will be pre-processed to remove any outliers or anomalies, and then the appropriate ARIMA model will be selected and fitted to the data. The model will be validated using statistical tests and performance metrics, and then used to forecast future carbon emissions in India. The impact of carbon emissions on renewable energy production will also be discussed. The results of the study will provide insights into the future trajectory of carbon emissions in India and inform policy decisions aimed at reducing carbon emissions and promoting renewable energy production.

### 2.1 Carbon Emission During COVID

The effects of COVID-19 were restricted to a short-term decrease in carbon emissions alone [6] because of government-mandated lockdowns, worldwide carbon dioxide emissions fell sharply during the COVID-19 epidemic [7]. The global average carbon

Fig. 1 Proposed research





dioxide content in the atmosphere in 2020 was 412.5 ppm, and, [2, 8] in 2021, the rise will be 1.5 billion tonnes, the second-largest in history. Despite the economic crisis induced by the COVID-19 outbreak, carbon emissions decreased by 17%, setting a new record low [9]. The 2.6 ppm rise above 2019 levels was the 5th highest on record in the 63-year history of the National Oceanic and Atmospheric Administration (NOAA). Since the year 2000, atmospheric CO<sub>2</sub> concentrations have risen by 12%, or about 43.5 parts per million (ppm). The COVID-19 outbreak led to 5.4% lower worldwide fossil carbon dioxide (CO<sub>2</sub>) emissions in 2020 [10].

India, China, and USA are among the main CO<sub>2</sub> emitters in the world, accounted for about half of global CO<sub>2</sub> emanations, with the top 20 emitters accountable for the outstanding 80% [11]. Several countries, including India, have committed to achieving net zero percent emissions by 2070 and have created milestones along the way [10, 12]. Deforestation is a significant source of greenhouse gases. More than 130 countries have pledged to end deforestation by 2030, and 105 countries have pledged to reduce methane emissions, by 2030. India remains heavily reliant on fossil resources such as oil and coal, and its economic interests are primarily domestic [13]. It necessitates national assessments of CO<sub>2</sub> emissions from primary sources and industries. India announced a transition to net zero emissions by 2070 at the COP26 climate change meeting in Glasgow. By the end of the decade, India's short-term goals include growing non-fossil fuel power capacity from 450 to 500 GW.

## 2.2 *Review of Literature*

Before forecasting carbon emission, there is a need to draw on the previous research as references to understand the models used by researchers to forecast carbon emission and the importance of controlling carbon emission and the factors that cause carbon emission.

Akyol and Uçar, 2021 predict Turkey's greenhouse gas emissions in 2030 and the economic consequences. According to the study, if Turkey continues on its current path of progressively growing greenhouse gas emissions, 728.3016 metric tonnes of CO<sub>2</sub> equivalent would be attained by 2030. These projections look below the pace of Turkey's Paris Climate Agreement pledges, which are seen as good for Turkey [14]. Mason et al., 2018 implement the covariance matrix adaptation evolutionary technique as an optimization methodology to estimate short-term electricity demand in Ireland, as well as wind power production and the amount of CO<sub>2</sub> intensity. Research predicts Ireland's energy consumption, wind power production, and CO<sub>2</sub> emission levels. The findings demonstrate that the CMA-ES is capable of making accurate predictions for each of these difficulties. As compared to other methods that are considered to be cutting-edge, CMA-ES surpasses them all by a significant margin [15]. Qiao et al., 2020 provide a unique hybrid approach that optimizes the standard LSSV machine model by combining a lion swarm optimizer with a genetic algorithm. The LSO-GA method has a better worldwide optimum capability in comparison with additional procedures because the optimum solution it obtains is the closest

to the genuine optimal solution. In addition, it features a quicker convergence speed [16]. Zhao et al., 2018 explain the MIDAS-BP model, which combines a regression model using mixed data sampling (MIDAS) with a neural network using back propagation (BP). To make predictions about carbon dioxide emissions in both the short term and long term, the MIDAS-BP model is [17]. In Xu et al., 2021 [18], the study proposes the utilization of a non-equigap generalized linear model (GM(1,1)) with conformable fractional accumulation (CFNGM(1,1)) to examine the association between energy consumption and CO<sub>2</sub> emissions. Based on the forecasted outcomes, it was observed that CO<sub>2</sub> emissions have increased to different extents in 30 countries and regions [18]. The COVID-19 pandemic has led to a short-term decrease in emissions; it may also result in long-term changes in energy and transportation systems that could lead to significant emissions reductions in the future [19]. Global carbon emissions decreased by approximately 7% in 2020 as a result of pandemic-related lockdowns and reduced economic activity [20]. The COVID-19 pandemic has had a noticeable impact on the carbon market, and the observed and inferred variations in the number of COVID-19 patients point to a more robust connection between the two variables. Policymakers, businesses, scientists, and members of civil society must all work together to turn COVID-19 into a sustainable opportunity [21, 22]. Time series forecasting is an essential approach utilized in several disciplines, such as finance, economics, engineering, and health care, to anticipate future patterns based on existing data. There are several techniques to time series forecasting, and numerous models have been created throughout the years to aid in making accurate forecasts. The statistical approach is one method for predicting time series; it uses numerous statistical approaches to assess past data and anticipate future trends. The machine learning method to time series forecasting entails the use of algorithms to automatically identify patterns and correlations in previous data and then use them to anticipate future trends. For time series forecasting, artificial neural networks, decision trees, fuzzy set logic, and support vector machines are utilized as machine learning models. In addition to these methods, there exist hybrid models that integrate statistical and machine learning methods [23–29]. Overall, the availability of several time series forecasting models enables practitioners to select the optimal technique for their particular needs, based on the data at hand, the required level of precision, and other variables.

### **2.3 Research Methodology**

This research aims to look at the history and current patterns in carbon emissions in India and predict emissions for the coming years. The study's primary goal is separated into two phases: (1) obtaining the best fit ARIMA model for CO<sub>2</sub> emissions forecasting and (2) projecting India's CO<sub>2</sub> emissions during the next eight years. This study aims to use the ARIMA method to forecast carbon emissions in India for 8 years from 2022 to 2030. This study's research technique involves using secondary data sources to investigate existing and future CO<sub>2</sub> emissions in India and anticipate future

CO<sub>2</sub> emissions. CO<sub>2</sub> KT is taken proxy of carbon emission in India. Statistics on CO<sub>2</sub> emissions are acquired from the World Bank's database. The existing proportion of carbon emanations in India was calculated using data of carbon emission taken from the database of World Bank. ARIMA is a time series approach which is used to project the level of carbon emissions. The Augmented Dickey–Fuller (ADF) test model is applied to adjust the presence of non-stationarity in data series of carbon emission. PACF, ACF plots, and the level of differencing are used to select an appropriate ARIMA model. AR (Auto regressive) (q) Integration (I) (d) and Moving average (MA) (p), parameters of Selected model are selected using PACF correlogram and correlogram. To confirm the legitimacy of selected model of ARIMA, the inbuilt function of Auto.Arima integrated within the R software is utilized. The analysis and prediction are conducted through the use of R software.

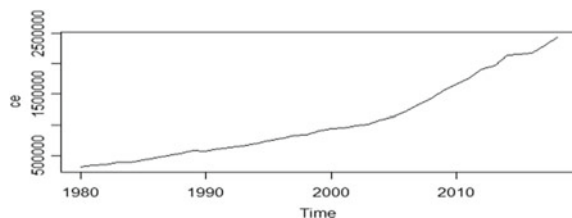
### 3 Forecasting of Emissions (KT) of CO<sub>2</sub> in India: Analysis and Discussion

Figure 2 shows a rising trend in CO<sub>2</sub> emissions, with only minor changes in recent years. Data series descriptive statistics do not appear persistent and are altered over the period frame, indicating that India's CO<sub>2</sub> emissions series does not track static outlines. A graphic analysis of Fig. 2 CO<sub>2</sub> emission (KT) the CO<sub>2</sub> emissions data series in India indicates a rising trend; consequently, it seems non-stationary. Time series is one the most accurate and reliable methods to forecast. The first requisite of time series analysis is that the data series should follow the stationary pattern.

Table 1 Statistics parameters for the Augmented Dickey–Fuller test show, the ADF test results that indicates the presence of Unit root at level in data series and accept the null hypothesis of unit root in data series.

A visual analysis of Fig. 3 CO<sub>2</sub> emissions (KT) at first of differencing indicates that original series differenced at first level of differencing does not follow the stationarity pattern, supported by results of the Augmented Dickey–Fuller (ADF) test. Now data series is differenced at second order to remove the unit root from the data series. In Fig. 3, diversification to the first order in CO<sub>2</sub> emissions (KT) shows the data series of CO<sub>2</sub> emissions differenced at second order. The data series seems stationary in this graph as descriptive statistics of data series seem constant. Data series of CO<sub>2</sub> emissions of India does track stationary patterns. ADF test results in Table 1 at second

**Fig. 2** CO<sub>2</sub> emission (KT)



**Table 1** Statistics parameters for the Augmented Dickey-Fuller method

1	2. At Level	3	4. At First difference	5	6. At second difference	7
8	9. t-statistics	10. Prob	11. t-statistics	12. Prob	13. t-statistics	14. Prob
15. ADF test statistics	16. 3.7243	17. 1	18. - 1.149889	19. 0.6846	20. - 6.941915	21. 0.01
22. Test Critical	24	25	26	27	28. - 6.941915	29
23. values						
30. 1% level	31. - 3.679322	32	33. - 3.6329	34	35. - 3.6329	36
37. 5% level	38. - 2.967767	39	40. - 2.948404	41	42. - 2.948404	43
44. 10%	46. - 2.622989	47	48. - 2.612874	49	50. - 2.612874	51
45. level						

order of differencing rejects the presence of unit root (null hypothesis); therefore, the Integrated (I) (d) parameter of ARIMA model (p,d,q) is 2 (Fig. 4).

Partial Auto Correlogram and Correlogram: By utilizing the PACF and ACF plots, the optimal parameters (p, q) for the ARIMA model can be identified.

A graphical examination and analysis of the PACF and ACF correlogram is a must to establish most appropriate specific values for the AR and MA (p and q) models. The AR and MA (p & q) values in ARIMA (p,d,q) are 0 and 1, as shown by the PACF and ACF correlogram in Figs. 5 and 6, respectively. The ARIMA model's forecasted parameters are (p,d,q)(0,2,1). Thus, the ARIMA model is the most appropriate for predicting India's CO<sub>2</sub> emissions (0,2,1).

**Auto.Arima Function:** (0, 2, 1) model of ARIMA model is identified with the help of visual inspection of ACF and PACF plots. The validity of the selected model can be determined with the use of Auto.Arima function, which is included in the R

**Fig. 3** Diversification to the first order in CO<sub>2</sub> emissions (KT)

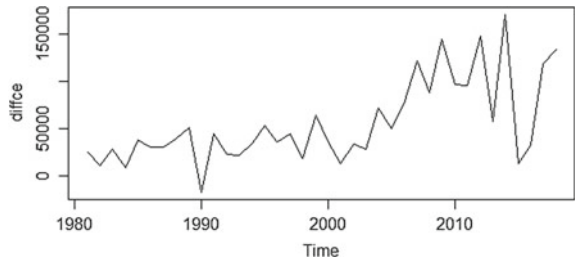


**Fig. 4** Diversification to the second order in CO<sub>2</sub> emissions (KT)

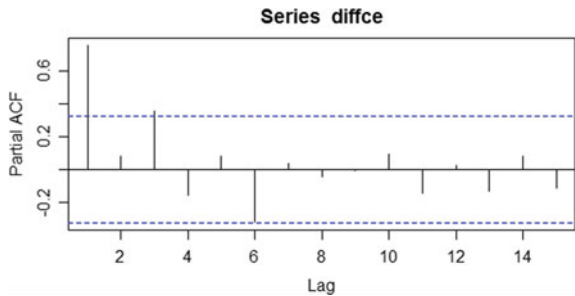


**Fig. 5** Diversification to the second order in the PACF plot

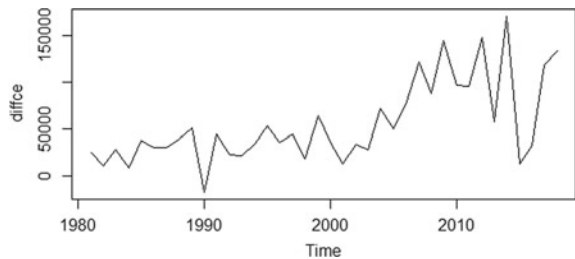
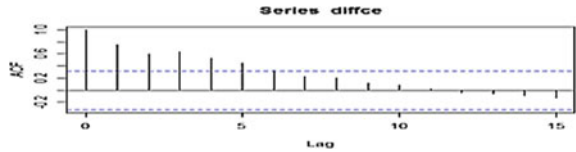


**Fig. 6** Diversification to the second order in the ACF plot



software and provides the best fit model. In terms of predicting, the “Auto.Arima ()” function recommended the identical (0, 2, 1) model of ARIMA for projection.

Table 2 Best fit ARIMA model shows the statistical results of the selected (0,2,1) model of ARIMA using “Auto.Arima()” function. Designated (0,2,1) model of ARIMA satisfies all the analytical scrutiny, like AIC and BIC criteria; hence, we used ARIMA (0,2,1) to forecast CO<sub>2</sub> emissions in India

Figures 7 and 8 show the residual graph based on ARIMA’s (0,2,1) model. Residual ACF plot in Fig. 6 displays the ACF plot of residuals inside the no autocorrelation bounds. Figure 8 illustrates that the change of the residual series does not transform substantially ended over the period since all of the spikes are contained inside the limits. It implies that the transformation in the residual series may be observed as infinite, that the suggested model fits the statistics well, and that the forecast made with this model would be precise. The chosen ARIMA model meets all residual diagnostics and validates all of the best fit ARIMA model’s property tests.

**Table 2** Best fit ARIMA model

Best fit ARIMA model	
Series-CO <sub>2</sub> emissions	
ARIMA (0,2,1)	
Coefficients	
ma1	- 0.724
s.e	0.1039
sigma <sup>2</sup> estimated as 1.355e + 09; log likelihood = - 441.37	
AIC = 886.73, AICc = 887.09	
BIC = 889.96	

**Fig. 7** ACF plot residuals of ARIMA (0, 2, 1) model

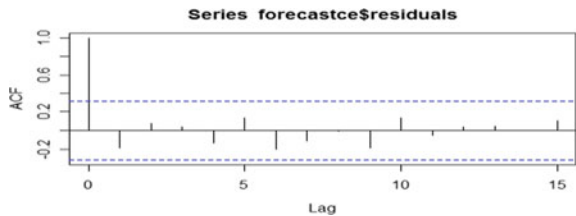
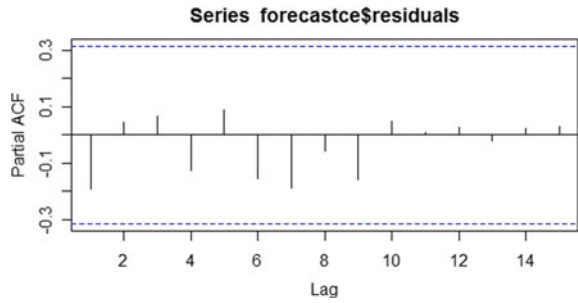


**Fig. 8** PACF plot residuals of ARIMA (0, 2, 1) model



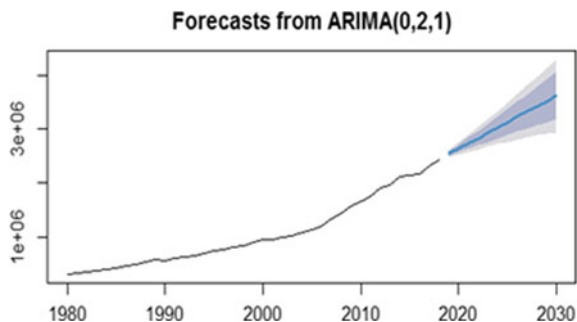
With the aid of the chosen (0, 2, 1) model of ARIMA, the predicted graph of emissions of CO<sub>2</sub> in India indicates an upward rising movement during the following 8 years. The probable CO<sub>2</sub> emissions amounts and trends are given in Table 3. The probable CO<sub>2</sub> emissions amounts and trends are shown in Table 3 and Fig. 9. It depicts a rising trend in CO<sub>2</sub> emissions during 8 years from 2022 to 2030. The anticipated value of CO<sub>2</sub> emissions with 80% and 95% confidence is shown in the shaded part of Fig. 8. The predicted values follow the movement of the previous data in the same way. CO<sub>2</sub> emanations in India are expected to upsurge in the same pattern as in past. The above findings projected that CO<sub>2</sub> emanations would endure to upsurge during the subsequent eight years.

**Impact of Carbon Emission on Renewable Energy Production:** The impact of carbon emissions on renewable energy production cannot be overstated. The increase in carbon emissions has led to a rise in global temperatures, which has resulted in more extreme weather patterns, such as heatwaves, droughts, and floods. These extreme weather patterns can have a significant impact on the efficiency and reliability of renewable energy sources, such as solar panels, wind turbines, and hydroelectric generators. High levels of carbon emissions can also result in increased costs and uncertainty for renewable energy production, which can hinder its growth and development. Addressing the issue of carbon emissions is crucial for the continued

**Table 3** Forecasted value of CO<sub>2</sub> emissions (KT)

Year	Forecasted value	Lo 80	Hi 80	Lo 95	Hi 95
2022	2,828,396	2,691,846	2,964,946	2,619,561	3,037,231
2023	2,926,865	2,758,054	3,095,677	2,668,691	3,185,040
2024	3,025,334	2,822,597	3,228,072	2,715,274	3,335,395
2025	3,123,804	2,885,474	3,362,133	2,759,310	3,488,297
2026	3,222,273	2,946,716	3,497,829	2,800,846	3,643,699
2027	3,320,742	3,006,365	3,635,118	2,839,944	3,801,539
2028	3,419,211	3,064,466	3,773,956	2,876,675	3,961,746
2029	3,517,680	3,121,064	3,914,296	2,911,108	4,124,252
2030	3,616,149	3,176,202	4,056,095	2,943,309	4,288,989

**Fig. 9** Forecasted value of CO<sub>2</sub> emission



growth and success of renewable energy, and policymakers and stakeholders must work together to reduce emissions and promote sustainable energy production.

## 4 Conclusions

This research paper has demonstrated the effectiveness of ARIMA models in predicting carbon emissions in India. The analysis showed that the ARIMA (0,2,1) model was the best fit for predicting carbon emissions in India, as it had the lowest Akaike Information Criterion (AIC) value and the highest accuracy in predicting future carbon emissions. The forecast of CO<sub>2</sub> releases in India would help the regime to plan policies and movements to decrease CO<sub>2</sub> releases and achieve the targets of the Paris Agreement's target of 40% non-fossil fuel power generation capacity, a 33–35% decrease in the economy's emission intensity compared to 2005, and the creation of a supplementary carbon sink of 2.5 billion to 3 billion tons of CO<sub>2</sub> equivalent.

This research contributes to the existing literature on carbon emissions prediction in India by providing an in-depth analysis of the best fitting ARIMA models. These models can help policymakers and stakeholders make informed decisions about carbon emission reduction policies in India. Future research could focus on developing more complex models that incorporate additional predictors and explore the effectiveness of different carbon reduction policies.

## References

1. Huisingh D, Zhang Z, Moore JC, Qiao Q, Li Q (2015) Recent advances in carbon emissions reduction: policies, technologies, monitoring, assessment and modeling. *J Cleaner Prod* 103:1–12
2. Lindsey R (2022) Climate change: atmospheric carbon dioxide. NOAA Climate.gov. Retrieved September 2022, from <https://www.climate.gov/news-features/understanding-climate/climate-change-atmospheric-carbon-dioxide>



3. Mehta PK, Meryman H (2009) Tools for reducing carbon emissions due to cement consumption. *Structure* 1(1):11–15
4. Friedlingstein P, O'sullivan M, Jones MW, Andrew RM, Hauck J, Olsen A, Zaehle S (2020) Global carbon budget 2020. *Earth Syst Sci Data* 12(4):3269–3340
5. Solomon S, Plattner GK, Knutti R, Friedlingstein P (2009) Irreversible climate change due to carbon dioxide emissions. *Proc Natl Acad Sci* 106(6):1704–1709
6. COVID-19 caused only a temporary reduction in carbon emissions—UN report, [Online] (2021). Available: <https://www.unep.org/news-and-stories/press-release/covid-19-caused-only-temporary-reduction-carbon-emissions-un-report>
7. Tollefson J (2021) Carbon emissions rapidly rebounded following COVID pandemic dip. *Nature* (Londn)
8. Zhongming Z, Linong L, Xiaona Y, Wangqiang Z, Wei L (2021) Greenhouse gas bulletin: another year another record
9. Newburger E (2020) Covid pandemic drove a record drop in global carbon emissions in 2020. *CNBC Environment*
10. UNEP U (2021) Emissions gap report 2020. UN
11. Mott G, Razo C, Hamwey R (2022) Carbon emissions anywhere threaten development everywhere. In: United Nations Conference on Trade and Development (UNCTAD). Available online at: <https://unctad.org/news/carbon-emissions-anywhere-threaten-development-everywhere>. Accessed 05 Feb 2022
12. Miglani S (2021) India rejects net zero carbon emissions target, says pathway more important. Reuters. <https://www.reuters.com/business/cop/india-says-net-zero-target-date-carbon-emissions-not-solution-2021-10-27/>
13. Choudhury S (2021) Can India achieve net zero carbon emissions by 2070? The road is long but not impossible. In: *CNBC*
14. Akyol M, Uçar E (2021) Carbon footprint forecasting using time series data mining methods: the case of Turkey. *Environ Sci Pollut Res* 28:38552–38562
15. Mason K, Duggan J, Howley E (2018) Forecasting energy demand, wind generation and carbon dioxide emissions in Ireland using evolutionary neural networks. *Energy* 155:705–720
16. Qiao W, Lu H, Zhou G, Azimi M, Yang Q, Tian W (2020) A hybrid algorithm for carbon dioxide emissions forecasting based on improved lion swarm optimizer. *J Cleaner Prod* 244:118612
17. Zhao X, Han M, Ding L, Calin AC (2018) Forecasting carbon dioxide emissions based on a hybrid of mixed data sampling regression model and back propagation neural network in the USA. *Environ Sci Pollut Res* 25:2899–2910
18. Xu Z, Liu L, Wu L (2021) Forecasting the carbon dioxide emissions in 53 countries and regions using a non-equivalent grey model. *Environ Sci Pollut Res* 28:15659–15672
19. Kalkuhl M, Fernandez Milan B, Brecha RJ (2020) Global carbon emissions in the post-COVID-19 era. *Environ Res Econ* 76(4):685–717. <https://doi.org/10.1007/s10640-020-00487-w>
20. Le Quéré C, Jackson RB, Jones MW, Smith AJP, Abernethy S, Andrew RM, Peters GP (2020) The impact of COVID-19 on carbon emissions: a review of the evidence. *Carbon Bal Manag* 15(1):16. <https://doi.org/10.1186/s13021-020-00161-y>
21. Lehmann P, de Brito MM, Gawel E et al (2021) Making the COVID-19 crisis a real opportunity for environmental sustainability. *Sustain Sci* 16:2137–2145. <https://doi.org/10.1007/s11625-021-01003-z>
22. Ghazani MM, Khosravi R, Barak S (2022) Nexus of COVID-19 and carbon prices in the EU emission trading system: evidence from multifractal and the wavelet coherence approaches. *Environ Sci Pollut Res* 29:41293–41308. <https://doi.org/10.1007/s11356-021-18304-6>
23. Ahmad MW et al (eds) (2022) Intelligent data analytics for power and energy systems. Springer Singapore, page XXII, 641. ISBN: 978-981-16-6081-8. <https://doi.org/10.1007/978-981-16-6081-8>
24. Tomar A et al (eds) (2022) Proceedings of 3rd international conference on machine learning, advances in computing, renewable energy and communication: MARC 2021, vol 915, Pages XV, 781. ISBN: 978-981-19-2830-7. Springer Nature. <https://doi.org/10.1007/978-981-19-2828-4>

25. Joshi BP, Kumar S (2012) Fuzzy time series model based on intuitionistic fuzzy sets for empirical research in stock market. *Int J App Evol Comp* 3(4):71–84
26. Joshi BP, Kumar S (2013) A computational method for fuzzy time series forecasting based on difference parameters. *Int J Mod Sim Sci Comp* 4(01):1250023
27. Joshi BP, Kumar S (2012) Intuitionistic fuzzy sets based method for fuzzy time series forecasting. *Cyb Sys* 43(1):34–47
28. Joshi BP, Kumar S (2012) A computational method of forecasting based on intuitionistic fuzzy sets and fuzzy time series. In: *Proceedings SocProS*, vol 2, Springer India, pp 993–1000
29. Joshi BP, Pandey M, Kumar S (2016) Use of intuitionistic fuzzy time series in forecasting enrollments to an academic institution. In: *Proceedings SocProS*, vol 1. Springer Singapore, pp 843–852

# Peak Shaving Through Battery Storage for Photovoltaic Integrated Building Considering the Time of Day Pricing



A. Sharma, P. Mahajan, and R. Garg

**Abstract** This paper has considered the feasibility of a battery storage system from peak demand reduction point of view under variable electricity energy pricing dynamics. The energy management approach described in this study seeks to reduce annual energy costs while maximizing battery energy throughput with grid restrictions acting as network demand limits for the performance evaluation of the investigated energy system in two scenarios. A typical building has been identified, where presently the PV system and grid supply is operated for meeting load requirements. The economics of the reference case with no battery storage (Case A) is compared with the economics of the battery storage plant that stores excess PV generation after self-consumption in the building (Case B). The analysis demonstrates that with an increase in storage size leads to a reduction in the energy cost till a certain point and any further increase beyond the critical point will increase the energy cost due to an increase in investment cost. The optimum value of battery storage in the present study is assessed as 1250 kWh and that result in annual financial savings of ₹7.3 lakhs under the time of day (ToD) regime. With falling battery storage prices, the payback period is anticipated to become shorter and more appealing in the near future. These comparative outcomes of the present study will provide input for government authorities and other stakeholders to develop regulations and policies for the promotion of battery storage. The active deployment of the battery energy storage systems within such types of installations, and its coordination with the other distributed energy resources will enhance the overall reliability, efficiency, and cost effectiveness of overall energy system. The modeling and simulation of the system are performed by General Algebraic Modeling System (GAMS).

**Keywords** Peak shaving · Battery energy storage system · Time of day · General algebraic modeling system (GAMS) · Photovoltaic integrated building

---

A. Sharma (✉) · P. Mahajan · R. Garg  
Department of Electrical Engineering, Delhi Technological University, Shahbad Daultapur, Main Bawana Road, Delhi 110042, India  
e-mail: [abhiabhi30@gmail.com](mailto:abhiabhi30@gmail.com)

# 1 Introduction

The recently concluded 26th meeting of Conference of the Parties (“COP26”) in Glasgow (U.K.) has provided a much-needed impetus to move away from fossil fuel-based energy sources. Aiming to meet 50% of India’s electricity needs with renewable energy, 500 GW of renewable energy capacity installation, reduction of cumulative carbon emissions by one billion tonnes between 2020 and 2030, and reduction of the carbon intensity of GDP by 45% over 2005 levels, were among the ambitious goals, the Indian Prime Minister set during the conference [1]. These are huge commitments from a country where coal has been the primary source of fossil fuel used to generate power in India, accounting for around 58% of total generation as on December 2022 [2]. Renewable energy sources like wind and solar are generally varying in nature and usually fail to provide a base load. However, with the advent of economical battery energy storage systems (BESS) at large-scale levels, the balancing process can be greatly aided by the use of renewable energy sources for base load. Moreover, batteries have other benefits, by storing the electricity generated during sunny hours and reusing it afterward, they raise the value and competitiveness of solar PV generation. Together with solar PV generation, battery storage appears to be one of the most economical methods of supplying isolated remote areas with inexpensive electricity. BESS and renewable energy-based power may offer a clean, cost-effective, and long-term replacement for coal-based power generation technologies [3]. Because of their favorable performance characteristics, high energy density, the flexibility of use, and, considerable cost reductions of battery modules, lithium-ion (Li-ion) batteries have supplanted other battery types as the preferred option for new BESS installations. Peak load though occurs normally for a small percentage of time usually resorted by generation capacity addition or by load shedding. ToD tariff is a crucial demand side management (DSM) measure that is used to encourage users to shift some of their non-essential loads from peak hours to off-peak hours, leading to improvement of system load factor through peak demand reduction. It is recognized widely across the energy industries. The ToD tariffs allow resources to be distributed more wisely and effectively by reflecting the true cost of producing, distributing, and supplying energy in price signals sent to customers [4]. The present study, apart from optimization of the BESS that maximizes the annual benefits to the building when the BESS and distributed energy resources like solar PV is used for peak load shaving under variable electricity energy pricing dynamics. The comparative outcomes will provide input for government authorities, policy-makers, investors, project developers, etc. to develop regulations and policies for the promotion of battery storage for such types of installations wherein distributed sources of energy and BESS are being used in coordination.

The paper proceeds as follows, analysis of the literature survey, along with gap identification is carried out in Sect. 2. The proposed approach for the study is discussed in Sect. 3. System modeling and analysis of the present load curves of building are discussed in Sect. 4. After a discussion on simulation results in Sect. 5, the conclusion of the study along with future work recommendations is discussed in Sect. 6.

## 2 Literature Survey

Due to growing environmental concerns and exponentially rising energy demands world over, the integration of decentralized energy sources like solar and wind into current conventional power systems has acquired greater significance. Decentralized sources at the user end decrease the demand for increased generation and transmission capacity as well as benefits like bill savings and reduced transmission congestion. However, solar PV and wind are variable sources, and there are several challenges associated to the temporal variability of its electricity output [5, 6]. Several energy storage technologies, including batteries [7], flywheels [8], super-capacitors [9], and fuel cell/electrolyzer hybrid systems [10], can be used to address this issue.

In the study [11], it has been demonstrated that with installation of battery system of capacity of 92 kWh in the sports building of Tampere University of Applied Sciences, Finland, the electric power taken from the grid was limited to 65 kW and in addition, latent heat thermal energy storage technique developed by Munich University of Applied Sciences was simulated for peak shaving of district heating. As per simulation results, thermal energy storage lead to shaving off of peaks of district heating power, subject to that the power limit is taken according to the total heat demand.

BESS helps in capacity firming, peak load shaving, power arbitrage, frequency regulation, and improving power quality [12, 13]. Storage systems lead to a reduction in the peak power and losses, but also will increase the investment cost however, the nation by significantly boosting production capacity and battery manufacturing competence can contribute economically in this crucial sector [14]. In the paper [15] optimization problem of renewable energy resources and the BESS in planning islanded micro-grids is solved using the general algebraic modeling system (GAMS).The effect of an increase in the Time of Use (ToU) as well as block rate tariff at Anhui province, China, has been studied for assessing the opportunity for building integrated photovoltaic system [16]. The effect of market-based energy pricing on the performance of the operation of the distributed network in coordination with renewable energy systems was studied in detail [17–19].

In the present study, the feasibility of a battery storage plant at the Delhi secretariat building has been carried out wherein presently PV system generation and grid supply are operated for supplying the load. Delhi owing to high percentage of domestic usage and harsh weather conditions in summer and winter seasons has unique load pattern and peak load issues. The peak electricity consumption in Delhi continuously exceeded that of Mumbai, Kolkata, and Chennai combined, and since 2000, the amount of electricity needed has virtually tripled. The annual share of combined domestic and commercial consumers during the period 2010–2017 made up almost 75–80% of share of Delhi's electricity consumption. An electrified household in Delhi uses roughly 260 units of electricity per month on average in 2016–2017, up from 155 units in 2000. Delhi's peak demand increased from 5028 (2011–2012) to 7409 MW (2019–2020). An average 3.27% increase in energy usage has been observed by about each year from 2011–2012 to 2019–2020, while energy consumption and peak

demand stayed at 29,534 MU and 6314 MW in 2020–2021 because of the Covid epidemic. There are currently 223.601 MW of installed solar systems at around 5800 locations, of which 21,557.53 kW at around 2134 locations are in the domestic sector [20, 21].

Various studies have already been conducted for the purpose of analyzing the performance of solar PV plants based on data of annual/monthly generation to cater to load profile characteristics [22]. However, only a few studies have examined the role of battery energy storage systems in coordination with a grid-connected PV-based system along with the determination of the optimal size of the BESS that maximizes the annual benefits to the building.

### 3 Proposed Approach

A study has been conducted in this paper to carry out the feasibility analysis of a combined solar PV and battery storage plant for the Delhi secretariat building. The contract demand of the building is 2742 kVA. Due to the limited rooftop area and land in the building, a solar PV plant has been installed on the vacant land near the Delhi secretariat building of decommissioned Indraprastha thermal power station. Out of the initial projected plant capacity of 3 MW, a 1 MW plant has been in service since 2015. The capacity was later enhanced to 2 MW in 2018. The output of solar plant is directly fed to building through 11 kV underground cable. The Solar Power Developer's (SPD) tariff rate for 25 years is set at Rs 4.50 per kWh. It was initially believed that this type of arrangement in which the grid provides limitless storage, and generated electricity is supplied directly into the grid will be sufficient hence no provision was kept for battery storage operations. This research paper is in continuation of earlier work done by the same authors [23] wherein a techno-economic analysis of the same plant was carried out. In this paper, two methodologies are analyzed and comparative analysis is represented for both ToD and flat tariff regime. In case A the analysis is made considering that there is no availability of BESS and is considered a reference case. In case B it is considered that whenever there is excess solar energy after self-consumption, it will be stored in the battery for usage in subsequent load cycles. Given the load profile of the building, the condition of surplus solar energy will happen during weekends and holidays and summer month offers an excellent opportunity for saving through battery storage. Charging of BESS from grid supply during off-peak hours has been disabled. The data set of 24 h for a typical summer day has been incorporated in GAMS resulting in saving in terms of daily energy charges. The battery charging from the grid is not permitted and if solar PV generation and load are available then the load is to be supplied in priority of solar/battery/grid. Direct supply of load through solar during the daytime has been accorded the highest priority. The remaining part of the load will be supplied through battery storage (given the conditions that the state of charge of battery is above the minimum state of charge). There may be the case that there is solar generation is available but the load is not available (particularly during

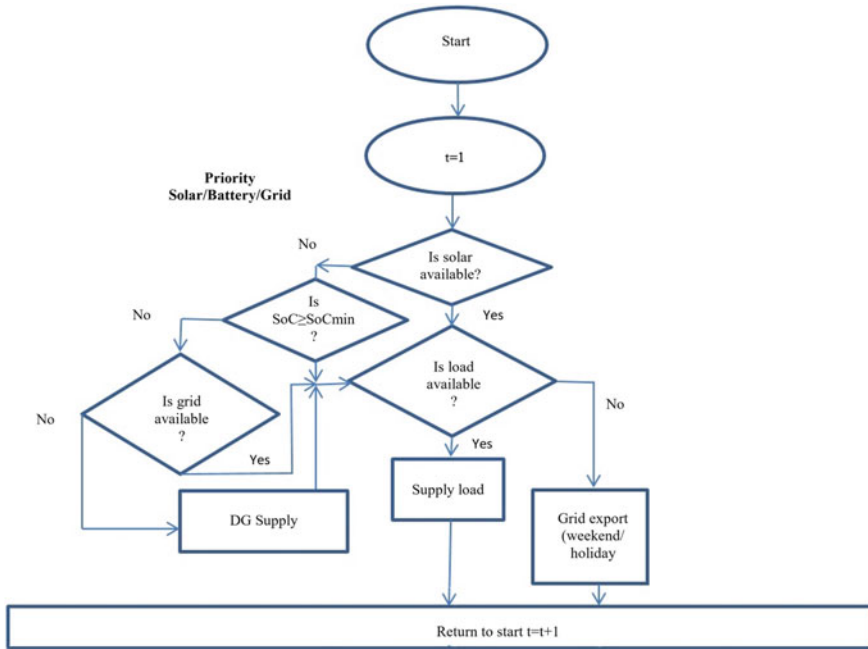


Fig. 1 Flow chart of methodology adopted

weekends and holidays) then solar generation will be utilized for battery charging and if the state of charge (SoC) of battery is sufficient then excess generation will be exported to the grid through net metering arrangement. The flow chart used for analysis is given in Fig. 1.

### 4 System Modeling

The generation output of the solar plant located at Indraprastha thermal power station is connected to the Delhi secretariat building for a distance of 2 km using an 11 kV, XLPE underground cable. Even though the Delhi secretariat building’s connected load exceeds the plant’s present installed capacity of 2 MWp, the system nevertheless delivers excess electricity beyond consumption levels to the utility grid during weekends and holidays using net metering. The tariff structure applicable to the building is tabulated below in Table 1.

Table 1 Applicable tariff structure

Category	Fixed charges	Energy charges
Non-domestic [HT] supply type HT (11 kV) < 3 kVA	₹250/kVA/month	₹8.50/kVAh

As per Delhi Electricity Regulatory Commission (DERC) regulations all consumers (other than residential) with a sanctioned load or maximum demand indicator (MDI) (whichever is higher) of 10 kW or 11 kVA and above are subject to the ToD tariff [24]. Table 2 provides the pertinent time slots for peak and off-peak hours, together with the percentage rebate and the surcharge rates.

Though electricity failure from the grid is very rare in building yet 3 DG sets of 750 kVA are installed in the Delhi secretariat for meeting the emergency load in case of grid supply failure. In the present study BESS is proposed for the Delhi secretariat to work in conjunction with the existing solar plant. The operation of the plant for power generation, storage and supply to load/grid can be controlled to target overall reduction in energy bill through peak shaving without compromise or major change in usage pattern. A common AC bus bar connects the solar PV panel, the grid, the diesel generator, the battery bank, and the load.

The conversion of the solar PV panel DC output to AC output at the AC bus bar is done by Inverter. An inverter/charger unit is installed between the battery and AC bus bar for conversion of DC to AC and AC to DC during the battery charging and discharging cycles respectively. DG sets are connected to a common AC bus bar for meeting the emergency load in case of power supply failure from the grid. Figure 2 shows the basic setup of the system that is used employed for the present study.

The Delhi Secretariat, which houses important offices of Delhi government such as those of the chief minister of Delhi and various cabinet ministers, provides an excellent range of battery storage systems for peak load shaving during summer seasons on account of the considerable variation of average weekday and weekend load. The typical building load profile indicates more energy consumption during working days (i.e. Monday–Friday) than weekends (i.e. Saturday–Sunday) and public holidays. The present study analyzed the energy bills from August 2021 to August 2022. The major load in building is due to chillers, AHU, pumps, lifts and room air conditioning units. Figure 3 and 4 display the load profiles of the building during weekdays and weekends on typical days of the winter season (January), summer season (May) and the rainy season (August). The high peak demand observed during summer and rainy weekdays is a result of the high use of the air conditioning systems in the building. It can be observed from Fig. 3 that during weekday's maximum demand reaches as high as 2250 kVA while during the weekend it varies between 50 and 750 kVA as shown in Fig. 4. It can be observed that in weekdays during 21:00–6:00 h the load is almost constant and is generally < 250 kVA and the load in building start increasing from 7:00 h to meet water pumping and cooling requirements in office rooms.

**Table 2** ToD tariff schedule as per DERC regulations

Peak hours (h)	Energy charges surcharge (%)	Off-peak hours (h)	Energy charges rebate (%)
1400–1700 and 2200–0100	20%	0400–1000	20%



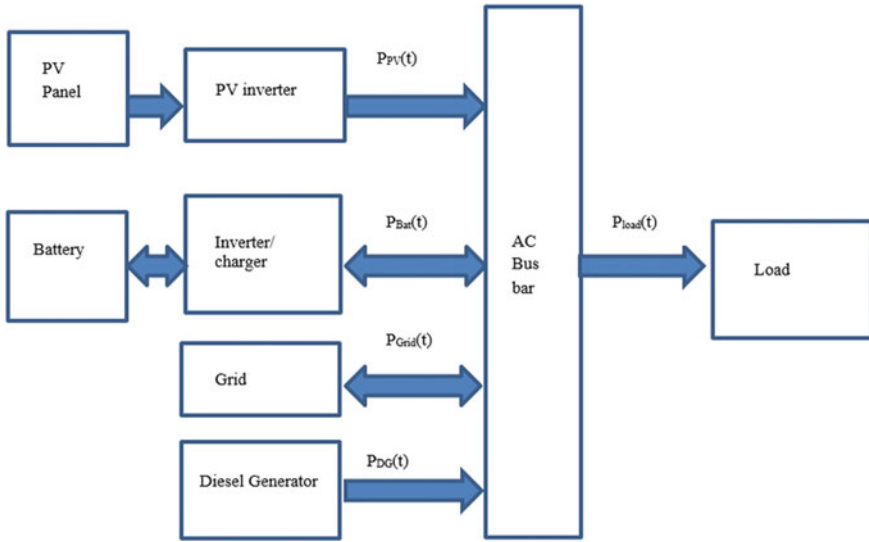


Fig. 2 Block diagram of basic system configuration

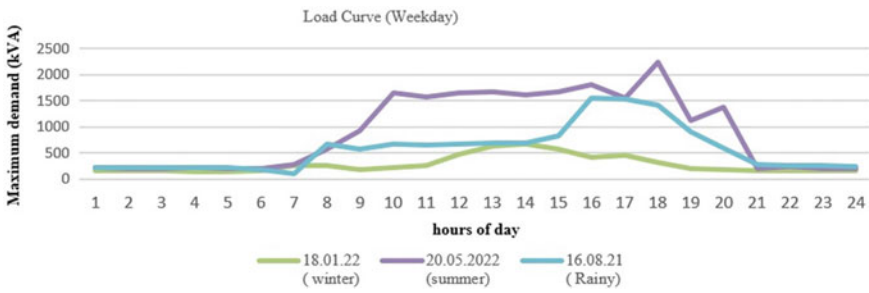


Fig. 3 Daily load curve profile (weekday)

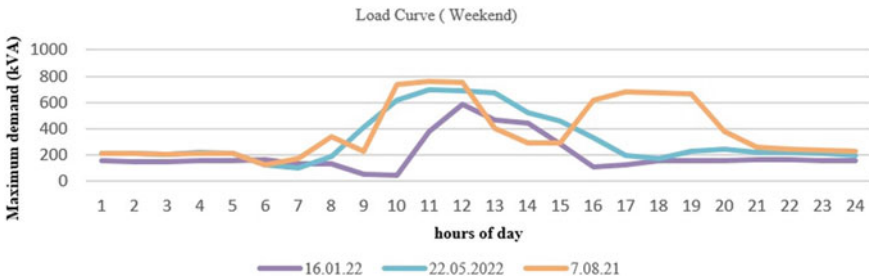


Fig. 4 Daily load curve profile (weekend)

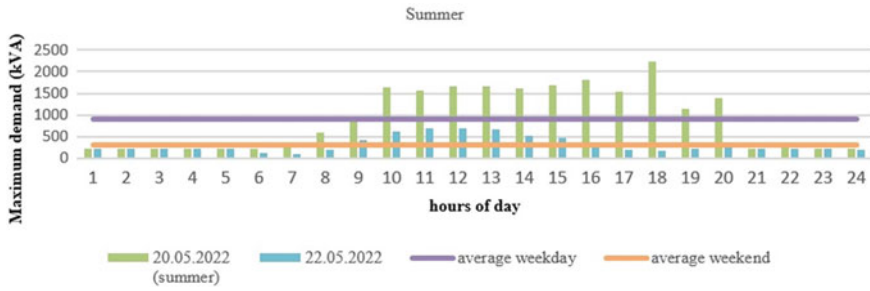


Fig. 5 Difference between weekday and weekend load for a typical summer day

Further examination of the daily load curve data of the building for a typical day yields that the difference between weekday and weekend load for a typical summer day is 600 KVA which is represented in Fig. 5 mainly on account of air conditioning requirements during weekdays. The corresponding values for winter and rainy seasons are 80 and 190 kVA respectively.

Figure 6 displays the solar PV generation profiles of the building during typical days of winter season (January), summer season (May) and the rainy season (August) taking into account the installed capacity of 2 MW. It can be observed that solar generation is comparatively more in rainy season during the study period. The high solar PV generation during rainy seasons can be attributed to absence of pollutants and natural cleaning of solar panels due to rain.

The size of the battery is optimised subject to the objective function of minimising energy charges, ensuring continuous supply while adhering to system constraints. The energy charges are given by Eq. 1.

$$\begin{aligned}
 \text{Energy Charges} = & \sum_{t=1}^{24} E_{\text{Grid}} \times T_{\text{Grid}} + \sum_{t=1}^{24} E_{\text{pv}} \times T_{\text{pv}} + \sum_{t=1}^{24} E_{\text{Bat}} \\
 & \times T_{\text{Bat}} + \sum_{t=1}^{24} E_{\text{DG}} \times T_{\text{DG}} + \sum_{t=1}^{24} \text{LOSS}_{\text{Bat}} \times T_{\text{Bat}} \quad (1)
 \end{aligned}$$

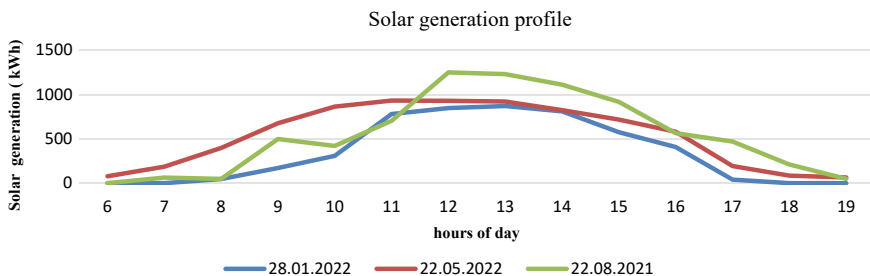


Fig. 6 Solar PV generation profiles during different seasons

where,  $E_{\text{grid}}$  is energy exchanged with grid in kWh,  $T_{\text{grid}}$  is grid tariff in INR/kWh,  $E_{\text{pv}}$  is energy received from solar PV plant in kWh,  $T_{\text{pv}}$  is solar energy tariff in INR/kWh,  $E_{\text{Bat}}$  is energy exchanged with BESS in kWh,  $T_{\text{Bat}}$  is BESS tariff in INR/kWh,  $E_{\text{DG}}$  is energy received from DG in kWh and  $T_{\text{DG}}$  is DG tariff in INR/kWh.

The objective function solution is determined using the following constraints. The battery state of charge at given time  $t$  is given by Eq. 2.

$$\text{SOC}(t) = \text{SOC}(0) + \text{SOC}(t - 1) + (P_{\text{Bat-c}} \times \eta_c) - (P_{\text{Bat-d}} \times \eta_d) \quad (2)$$

where, SOC is state of charge at  $t$  and  $t - 1$ ,  $P_{\text{Bat-c}}$  is battery power during charging in kW and  $P_{\text{Bat-d}}$  is battery power during discharging and  $\eta_c$  and  $\eta_d$  efficiency during charging and discharging respectively.

The power balance equation can be represented as given in Eq. 3.

$$P_G + P_{\text{pv}} + P_{\text{Bat-d}} + P_{\text{DG}} \geq P_{\text{load}} + P_{\text{Bat-c}} \quad (3)$$

where,  $P_G$ ,  $P_{\text{pv}}$ ,  $P_{\text{DG}}$  and  $P_{\text{load}}$  are grid power, solar PV power, DG power and load power in kW respectively.

The  $\text{loss}_{\text{Bat}(t)}$  is the cumulative hourly loss in battery capacity that can be calculated as given in Eq. 4 [25].

$$\text{Loss}_{\text{Bat}}(t) = \text{Loss}_{\text{Bat}}(t - 1) + (P_{\text{Bat-d}}(t) + P_{\text{Bat-c}}(t)) \times z \quad (4)$$

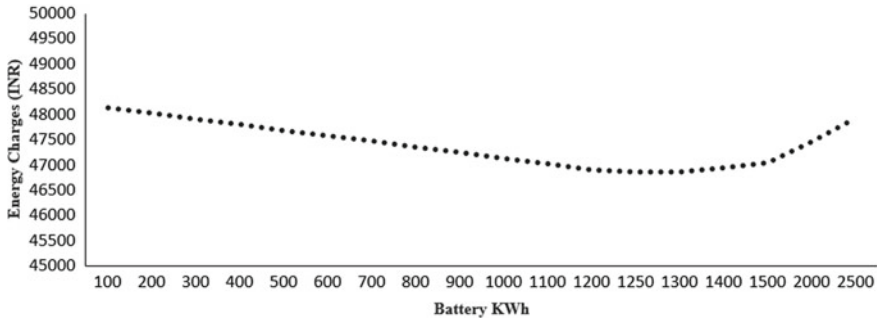
where,  $\text{loss}_{\text{Bat}}$  is battery loss at  $t$  and  $t - 1$  and  $Z$  is Ageing coefficient  $5 \times 10^{-4}$ .

Figure 7 shows the effect of BESS capacity on the daily energy charges using GAMS. GAMS's inbuilt CPLEX solver is used to solve mathematical equations. In order to obtain optimal battery size, the algorithm starts with an initial battery size of 100 kWh with the step size of 50 kWh. It is observed that that increasing the battery capacity will lead to reduction of energy cost. The curve will reach a minimum value and after that will start increasing signifies that any further increase in the capacity will increase the energy costs. From the given daily dataset, the optimal values selected for battery storage capacity come out to be 1250 kWh.

## 5 Simulation Results and Discussion

In the present study, two cases were simulated:

- A. This case is taken as reference case and has no provisions of battery storage for storing excess electricity. In the present case the excess energy during weekends and holidays is supplied to grid through net metering arrangement. The surplus energy exported to grid is tariffed at average power purchase charges (APPC) as fixed by regulator. The APPC charges for 2021–2022 are Rs. 3.85/kWh. In this



**Fig. 7** Annual energy charges as a function of the BESS capacity

reference case the daily energy cost is calculated under with and without ToD tariff regime.

- B. In this it is assumed that excess solar energy generation beyond consumption levels in building is stored in battery. The stored energy in battery will be utilised to supply load in subsequent cycles depending on state of charge. The present case forbids charging of battery through grid during off peak hours.

The simulation is carried out under the following assumptions:

1. Daily energy cost is calculated on basis of a data set of typical summer day during 2022 that offers the maximum opportunity of storage. The analysis can be further extended to monthly savings and annual saving by incorporating monthly and yearly datasets.
2. The battery charging and discharging efficiency are taken as 95 and 90% respectively.
3. Solar PV unit charges and battery energy charges are taken as ₹4.50 and ₹4.80/kWh.
4. DG tariff is taken as ₹15.00/kWh and grid tariff during normal hours is taken as 12.00/kWh.

For an optimum battery size of 1250 kWh. The results of simulation using GAMS linear programming are presented in Table 3 and Fig. 8.

The results demonstrate that the ToD regime offers more saving opportunities in comparison to the flat tariff rate regime.

There is a daily saving of in tune of ₹2000/- under the ToD regime which amounts to a saving of ₹7.3 lakhs per annum. Despite high payback time, the government of

**Table 3** Comparisons of simulation results

	Without BESS (case A)	With BESS (case B)
Daily energy cost (INR)	48,243 (with ToD)	46,852 (with ToD)
	47,339 (without ToD)	46,618 (without ToD)

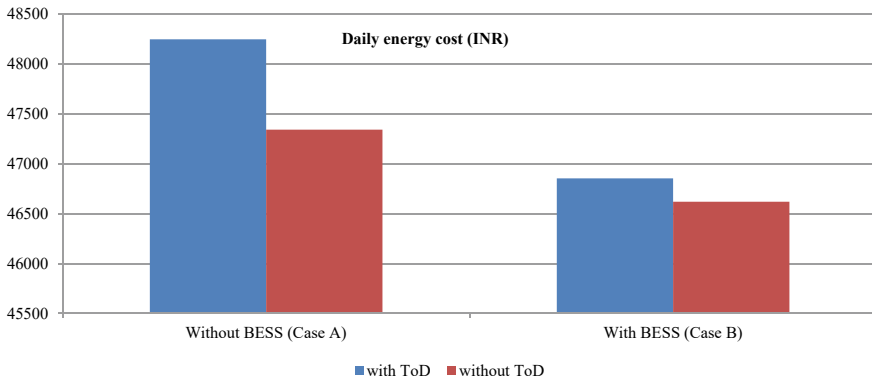


**Fig. 8** A comparison of daily energy cost

Delhi may consider installing the BESS on a pilot basis as a demonstration project. The payback time will be bound to come down with the falling price of BESS.

## 6 Conclusion

The current energy system is going through a phase of transition wherein traditional, centralized, and larger power plants are being replaced with smaller, distributed power plants. The world is looking for use of sustainable solutions for energy generation to mitigate climate change and rising global temperature issues. Due to variable nature of different renewable energy sources, the problem can be best addressed by use of BESS in coordination with battery energy storage. The present study conducted a techno-economic analysis for a grid-connected solar PV-BESS system with the objective of determining energy costs. From the analysis, it is observed that the ToD regime offers more saving opportunities in comparison to the flat tariff rate regime. Further, it is demonstrated that the sizing of the battery is a function of the ToD tariff, and input cost of power. The results present a saving scenario in which there is a daily saving of around ₹2000/- under the ToD regime which amounts to a saving of ₹7.3 lakhs per annum. In the present scenario though the payback period is high but with the government's thrust on battery storage and production link incentive schemes for batteries, the payback period is bound to become more attractive in the near future. The results demonstrate that the deployment of battery energy storage systems in coordination with distributed energy sources like PV will result in making the overall energy system more reliable, efficient, and economic without affecting usage patterns in building. The study will be broadened to achieve the net zero energy building target for same building for future research. The capacity of solar PV system and battery storage is required to be enhanced to achieve this objective.

## References

1. Press Information Bureau (2023) National Statement by Prime Minister Shri Narendra Modi at COP26 Summit in Glasgow. <https://pib.gov.in/PressReleasePage.aspx?PRID=1768712>. Accessed 28 Feb 2023
2. Ministry of Power (2023) Power sector at a glance ALL INDIA. <https://powermin.gov.in/en/content/power-sector-glance-all-india>. Accessed 28 Feb 2023
3. Govindarajalu C, De Sisternes F, Chavez S (2021) Stationary energy storage to transform power systems in developing countries. In: Live wire. World Bank, Washington, DC, p 116
4. Forum of Regulators (2023) Assignment on implementation and impact analysis of time of day (TOD) tariff in India. [http://www.forumofregulators.gov.in/Data/study/Implementation\\_Impact\\_Analysis\\_of\\_Time\\_of\\_Day\\_TOD\\_tariff\\_in\\_India.pdf](http://www.forumofregulators.gov.in/Data/study/Implementation_Impact_Analysis_of_Time_of_Day_TOD_tariff_in_India.pdf). Accessed 28 Feb 2023
5. Ueckerdt F, Brecha R, Luderer G (2015) Analyzing major challenges of wind and solar variability in power systems. *Renew Energy* 81:1–10
6. Clò S, D'Adamo G (2015) The dark side of the sun: How solar power production affects the market value of solar and gas sources. *Energy Econ* 49:523–530
7. Kawakami N, Iijima Y, Fukuhara M, Bando M, Sakanaka Y, Ogawa K, Matsuda T (2010) Development and field experiences of stabilization system using 34MW NAS batteries for a 51MW wind farm. In: Industrial electronics (ISIE), IEEE international symposium, Bari, Italy, pp 2371–2376
8. Díaz-González F, Sumper A, Gomis-Bellmunt O, Bianchi FD (2013) Energy management of flywheel-based energy storage device for wind power smoothing. *Appl Energy* 110:207–219
9. Abedini A, Nasiri A (2008) Applications of super capacitors for PMSG wind turbine power smoothing. In: Industrial electronics, 34th annual conference of IEEE, Orlando, FL, pp 3347–3351
10. Li X, Song YJ, Han SB (2008) Frequency control in micro-grid power system combined with electrolyzer system and fuzzy PI controller. *J Power Sour* 180(1):468–475
11. Korpela A, Kallioharju K, Mäkinen A (2023) Computational model to estimate new energy solutions in existing buildings. *Energy Syst* 13:1–14. <https://doi.org/10.1007/s12667-022-00557-w>
12. Omran WA, Kazerani M, Salama MMA (2011) Investigation of methods for reduction of power fluctuations generated from large grid-connected photovoltaic systems. *IEEE Trans Energy Convers* 26:318–327
13. Arunkumar CR, Manthathi UB, Punna S (2022) Supercapacitor-based transient power supply for DC microgrid applications. *Electr Eng* 104:463–472
14. Kumar CR, Majid MA (2020) Renewable energy for sustainable development in India: current status, future prospects, challenges, employment, and investment opportunities. *Energy Sustain Soc* 10(2):232. <https://doi.org/10.1186/s13705-019-0232-1>
15. Thang VV (2021) Optimal sizing of distributed energy resources and battery energy storage system in planning of islanded micro-grids based on life cycle cost. *Energy Syst* 12:637–656
16. Li L, Yao Y, Yang R, Zhou K (2018) Is it more effective to bring time-of-use pricing into increasing block tariffs? Evidence from evaluation of residential electricity price policy in Anhui province. *J Clean Prod* 181:703–716
17. Yang Y, Wang M, Liu Y, Zhang L (2018) Peak-off-peak load shifting: are public willing to accept the peak and off-peak time of use electricity price? *J Clean Prod* 199:1066–1071
18. Annala S, Lukkarinen J, Primmer E, Honkapuro S, Ollikka K, Sunila K, Ahonen T (2018) Regulation as an enabler of demand response in electricity markets and power systems. *J Clean Prod* 195:1139–1148
19. Abikarram JB, McConky K, Proano R (2019) Energy cost minimization for unrelated parallel machine scheduling under real time and demand charge pricing. *J Clean Prod* 208:232–242
20. Centre for Science and Environment (2023) CSE releases new analysis of electricity consumption in Delhi during the lockdown and un-lockdown phases. <https://www.cseindia.org/cse-releases-new-analysis-of-electricity-consumption-in-delhi-during-the-lockdown-10314>. Accessed 28 Feb 2023

21. Planning Department (2023) Government of NCT of Delhi: economic survey of Delhi, 2021–2022. [http://delhiplanning.nic.in/sites/default/files/E11\\_Energy.pdf](http://delhiplanning.nic.in/sites/default/files/E11_Energy.pdf). Accessed 28 Feb 2023
22. Twaha M, Ramli MAM (2018) A review of optimization approaches for hybrid distributed energy generation systems: off-grid and grid connected systems. *Sustain Cit Soc* 41:320–331
23. Sharma A, Mahajan P, Garg R (2016) Techno-economic analysis of Solar photovoltaic power plant for Delhi Secretariat building. *Intell Control Energy Syst ICPEICES* 128:1–5. <https://doi.org/10.1109/ICPEICES.2016.7853620>
24. Delhi Electricity Regulatory Commission (2023) Electricity tariff schedule for FY 2020–2021—BRPL, BYPL, TPDDL and NDMC. <http://www.derc.gov.in/sites/default/files/Tariff%20Schedule%202020-21.pdf>. Accessed 28 Feb 2023
25. Nayak C, Nayak M (2017) Techno-economic analysis of a grid-connected PV and battery energy storage system considering time of use pricing. *Turk J Electr Eng Comput Sci* 26:35. <https://doi.org/10.3906/elk-1703-35>

# Economic Analysis of Renewable Energy Systems for Rural Electrification



Nikita Yadav, Rahul Sharma, and Yashwant Sawle

**Abstract** The optimum hybrid energy system is described in this study in terms of emissions, price, and other aspects. All the calculations were performed by HOMER Pro software. With the use of HOMER software, this project aims to create an energy production model connected to an HRES combination at a location in Maharashtra, India. The outcomes of the study have been seen in NPC, O&M, COEs, and RF of energy systems. This study was conducted in Solapur, Maharashtra. Due to good data on wind and sun renewable energy resources, this area was chosen. The HOMER program, which is only adequate for these analyses, was used for all of the comparisons. This paper compares and demonstrates the ideal location for the suggested HRES model. The proposed hybrid renewable energy system is most suited for biofuel generators among the other two systems based on the following factors: initial cost, renewable fraction, COE, emission, and area of electricity generation.

**Keywords** Solar PV · Wind · Diesel generation · Biofuel generator · HOMER

---

N. Yadav

Chemical Engineering Department, Madhav Institute of Technology and Science Gwalior, Gwalior, India

R. Sharma · Y. Sawle (✉)

Electrical Engineering Department, Madhav Institute of Technology and Science Gwalior, Gwalior, India

e-mail: [yashsawle@gmail.com](mailto:yashsawle@gmail.com)



# 1 Introduction

In this rapidly growing country, the need of electrical energy is increasing day by day. Most of the production of electrical energy depends on fossil fuels due to which CO<sub>2</sub> emission increases which is not good for our environment. To cut off the emission of CO<sub>2</sub> and reduce the greenhouse gas effect, renewable energy is necessary for the environment and for the development of the country. Keeping this in mind, we have to pay attention to this problem so that we can eliminate the problems of energy crisis. Looking at the current situation, it is not very appropriate to use diesel generators. There are many reasons like increasing fuel prices, high maintenance of diesel generators, and transportation problems. Due to the lack of conventional resources like fossil fuels and also keeping environment issues in mind, renewable energy is the best alternative for power generation. It will reduce greenhouse gases like nitrogen dioxide, sulfur dioxide, and carbon dioxide which are very harmful for our environment and also harmful for health. We can have many renewable energies which we can implement in the hybrid systems like wind, PV, geothermal, biomass, hydro, etc. but for the area we opt for this study, the correct configuration will be wind, PV, and biomass which will increase the efficiency of the hybrid system and also reliable for the system [1].

In this paper, to provide renewable energy supply, we will develop a grid-connected hybrid system using solar, wind, PV, and biomass. Hybrid energy system which is connected with grid will reduce the cost by reducing the operational cost of grid supply. The objective of this project is to generate energy from easily available sources like solar and biomass in the rural areas. This system is made up of PV, wind, biomass, and grid system which is connected to the nearby rural area.

## Key Highlights of the Proposed Work

In this paper, author mainly focused on environmental benefits by reducing greenhouse gas emissions.

Through this paper, our main purpose is to select the best hybrid system by comparing three systems. In the first proposed system, author designed system by adding diesel generator, PV, and wind as a main component in second proposed system, author designed system using biogas, PV, and wind, and the third proposed system designed by using PV and wind as a renewable source. After comparing all three proposed systems, author gets the best system for the selected location Solapur, Maharashtra.

## Outlines of the Paper

In Section 1, author gives the introduction of the paper. Section 2 describes the software tool which is used to design the system. Section 3 discusses the methodology used for hybrid system design. Section 4 describes system designing by explaining all the components used in the system one by one for better understanding. Sections 5 and 6 explain result by comparing all the data on the basis of design, cost and system, emission, electricity, and cash flow. In the last, author concludes the whole work of paper.

## 2 Software Tools Used for the Systems

### HOMER Pro

Increasing problems like low fuel, pollution and many more we have to face, so get rid out of this problem HOMER is the best software. There are many advantages of this tool (HOMER) which help us to find the best combination of resources. HOMER is referred as Hybrid Optimization Model For Electrical Renewables. HOMER is a software that makes system modeling more reliable for grid-connected and standalone systems. HOMER made by Mistaya Engineering of Canada for the National Renewable Energy Laboratory (NREL). Sensitivity, behavior, and optimization are the three main principles in which HOMER software works [2]. Also, HOMER offers alternatives for selecting an ideal hybrid system from a huge collection of results organized from lowest to highest in terms of energy cost [3] (Fig. 1).

## 3 Methodology

The HOMER software from the National Renewable Energy Laboratory was used to design and measure the hybrid power system's components. It is easy to use software like HOMER. HOMER's main goal is to model a micropower system's durability [5]. While designing a power system, decisions regarding the components to use, their sizes, and other configuration options must be made. Due to the wide range of technological costs, the availability of energy sources, and the abundance of technological options, these decisions are difficult. The HOMER optimization and sensitivity analysis approaches facilitate the study of different system configurations [6].

For the higher-level capabilities of the system, its simulation capacity is essential for processes like sensitivity analysis and improvement. The simulation technique predicts how a certain control system, a set of system components of a specific size, and an operational strategy outlining how those components interact, will operate in a specific environment over an extended period of time. With the help of HOMER Pro software, solar plant with grid connectivity for a specific geographic location at SRFcamp in Solapur, Maharashtra, designed is optimized. A study has also been conducted to investigate how fluctuations in solar output affect the system's overall output. Using the three steps of simulation, sensitivity analysis, and optimization, HOMER Enhance its effectiveness determines the optimal solution.

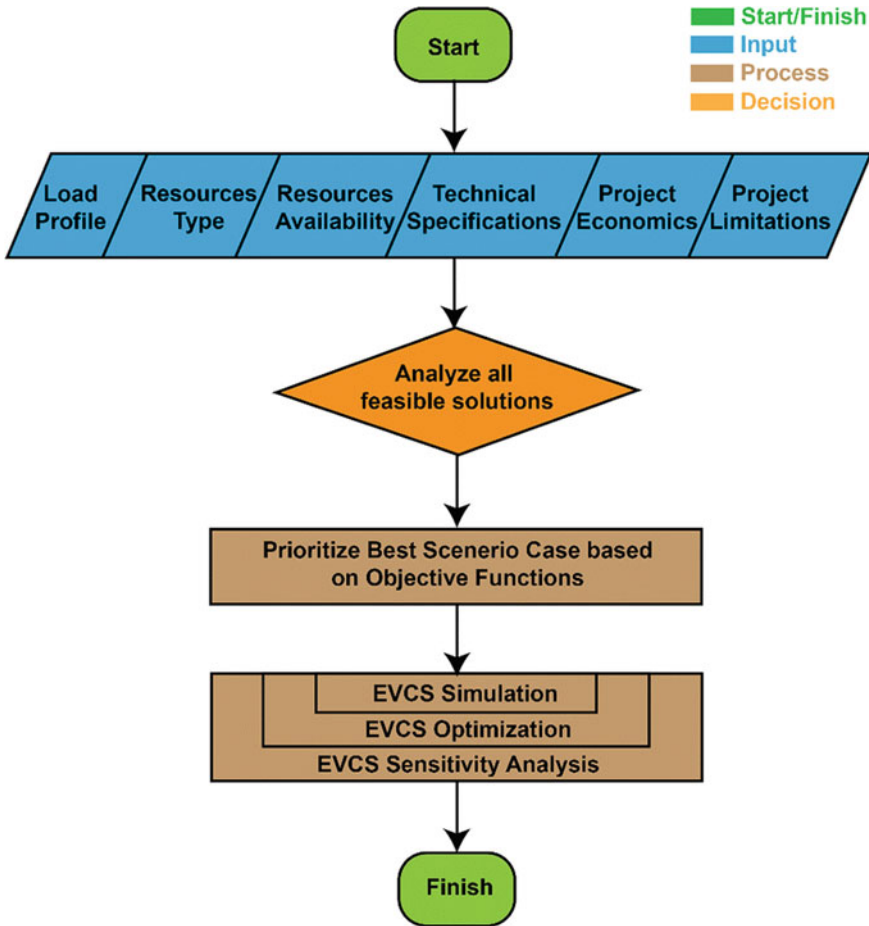


Fig. 1 Flow of HOMER system for achieving optimal system [4]

### 4 System Designing

The hybrid energy system is sized using a framework and the software HOMER. The AC and DC lines are connected together during the procedure using a converter. The suggested system combines backup secondary non-renewable sources like batteries/ diesel generators with primary renewable sources (wind/PV). With the help of the HOMER tool, the optimal configuration design and pre-feasibility study are generated. HOMER is employed to do an economic and environmental study of the system, which is meant to transmit all of its electricity into the grid. As a result, the utility will consume all the power produced [7].

Sensitivity analysis is considered during system design. For systems that use renewable energy, the designer has to select the optimal combination of wind, solar, battery, diesel generator, and converter elements to establish the appropriate size [8]. Also, the designer must add important information into HOMER Pro, including quantity, capacity, life expectancy, efficiency, average loads and average energy consumption, peak, and capital expense requirements.

**A. Resource Availability**

The proposed site location is located at this 21\*29.5'N latitude and 73\*24.4'E longitude in the HOMER Pro model. An average of 5.23 kWh/m<sup>2</sup>/day of horizontal solar radiation is received at this location annually. 5.67 m/s is the yearly average wind speed at this site. The location is Solapur, Maharashtra. Both wind speed and solar radiation are at their greatest at this site (Fig. 2).

**B. Load Profile**

11.26 kWh/day is the highest average intake based annual energy use, while 2.09 kW is the greatest peak load use. From January to December, it was seen that the load pattern remained constant. Monthly statistics form the basis for weekly and weekend loading condition. The constant increase in load was seen from January to December. HOMER designs and enhances hybrid energy power systems, which are off-grid power sources that generate electricity by combining wind and sun radiation. The simulation uses a typical home load. In a regular house, electricity is required for the lights, TV, air purifier, machines, and other equipment. Every month's daily load profiles may be created using HOMER, and weekday and weekend load profiles can be varied. During the whole year, the user can only select one profile. An individual's personal modified daily load

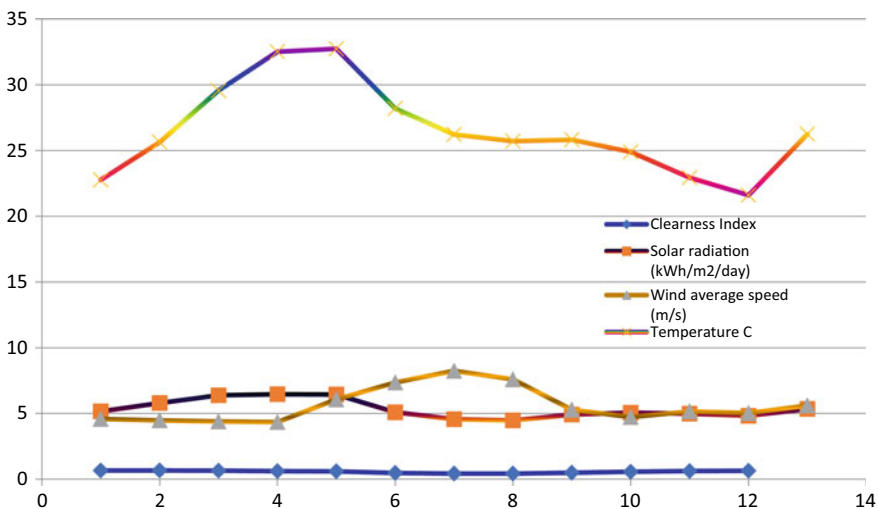


**Fig. 2** Data of solar, wind, and temperature

profile is transferred through to the following year. When the user initially opens the load window, the daily load profile for a weekday in January is carried over to subsequent months of the year, covering weekdays and weekends. In fact, the load profile is valid every day of the year.

### C. System Components

- i. **Wind:** Wind turbines have already been widely used since the Medieval Ages. The opponent of solar energy is wind power. The absorption of solar energy by the surface and atmosphere of the planet as well as the rotation of the globe about its axis and its circular orbit around the sun are the two processes that cause wind to occur. By turning the momentum of flowing air into mechanical movement, a wind turbine—which usually resembles a rotating shaft—can produce energy. Employing wind energy has the benefit of not polluting and having good potential as a power source. A simple model of a wind turbine with a hub height of 17 m is selected and created using HOMER in order to transform the wind’s motion energy into AC or DC electric power based on the power profile.
- ii. **Battery:** A regular lead-acid battery pack is utilized for this component. When RES is unable to handle the load and the battery size is exhausted, a backup diesel generator provides power. The system’s main components, the battery and controller, were also developed because it was anticipated that they would be used continuously. Over the battery’s lifespan, HOMER expects that the characteristics would not alter as a result of external factors like temperature.
- iii. **Solar PV:** The photovoltaic system transforms sun’s rays energy into photovoltaic energy to satisfy the need for power. It primarily runs on sunlight, and any surplus energy that the PV produces is utilized to charge the rechargeable systems, which may then be used to meet demand, especially at night when there’s no sunlight. The flat plate PV used in this research is standard.
- iv. **Diesel generator:** Hybrid systems use the diesel engine to add extra power when sources of clean energy fail to fulfill the real load demand. The cost of fuel varies based on where it is purchased due to transportation costs. As providing gasoline to some localities involves paying extra shipping costs, the price of fuel is typically higher in regional areas. An auto-size generator was the diesel generator employed for this experiment.
- v. **Converter:** In this study, a universal converter with a 95% efficiency and 100% rectified comparative capacity is used. DC power is converted into AC power using a converter circuit. It is anticipated to operate at a 95% effectiveness for all sizes. A standard inverter costs \$150, can last up to 15 years, and costs another \$150 to replace it [9, 11–17].
- vi. **Biofuel:** Biomass is a flexible renewable energy source. It may be converted into liquid fuels that resemble fossil fuels, such as petrol, diesel, and aviation fuel. Biopower technologies convert renewable fuels made from biomass into electrical energy and heat using methods akin to those employed with fossil fuels. The three stages that can extract the energy from biomass to

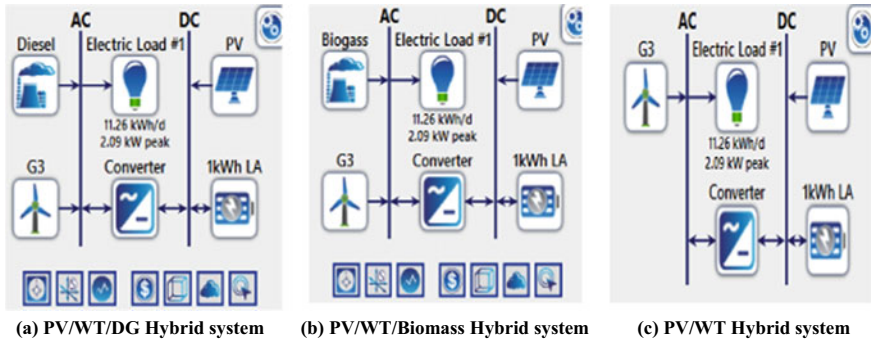


Fig. 3 a–c are proposed hybrid systems

produce biopower are burning, bacterial breakdown, and conversion into a fluid or gaseous form of fuel. The carbon impact on the generation of electricity can be decreased by using biopower to replace carbon-based fuels burned in power plants. The primary reason for selecting this kind of biomass-based hybrid system is that it can be easily and cheaply available in rural areas in the form of cowpats, pig manure, etc. The overall amount of power generated on a foggy day may be impacted by biomass [10] (Fig. 3).

### 5 Result and Discussion

In this research, there are three different proposed hybrid system which contains different components, whereas it gives the data about the NPC, COE, operating cost, initial cost, renewable fraction, production, and carbon emission. It also provides the data of cost summary, cash flow, compare economies, and carbon emission, and fuel summary. On the basis of result which comes from software, different model gives result, and it will compare on the basis of the following basis:

- a. **On the basis of architecture:** In the architecture portion of the final result, which is based on the simulated model’s architecture, the data for the PV, wind, converter, battery, and generator are displayed according to their unit (Fig. 4).
- b. **On the basis of cost and system:** In this portion, we address an established and significant element for attaining the most affordable hybrid system as it applies to HRES design. The findings for net present cost (NPC) and cost of energy (COE) are presented. The term “COE” refers to the typical cost per kWh of useable electrical power produced by HRES. The average cost per kWh of useful electrical power generated by HRES is referred to as COE. Also, it will provide information on production, startup costs, and running costs (Table 1).
- c. **On the basis of emission:** The planned HRES makes use of a diesel generator (DG), which releases a range of dangerous pollutants, including particulate matter, nitrogen oxides, carbon dioxide (CO<sub>2</sub>), and unburned hydrocarbons. The

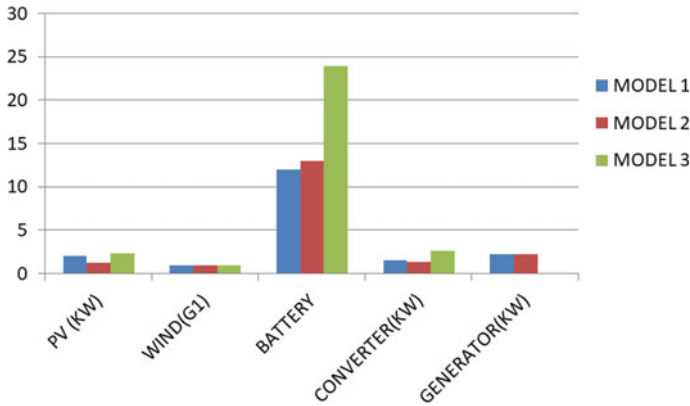


**Fig. 4** Result data of architecture section

**Table 1** Data of cost and system from final result for different locations

Models	NPC (\$)	COE (\$)	O&P (\$/year)	REN FRAC	Production (KWH)
Model 1	13,118	0.247	549	97	123
Model 2	15,750	0.293	774	100	518
Model 3	18,526	0.349	858	3,868	3,868

majority of emissions from dangerous gases are made up of carbon dioxide. As a result, in the suggested scenario, just the cost of the carbon dioxide penalty is considered. The cost of the CO<sub>2</sub> penalty is calculated using the tradable renewable energy certificate. CO<sub>2</sub> stands for carbon dioxide, Co for carbon monoxide, and NOX for nitrogen oxides in Table 2.

- d. **On the basis of electricity:** Based on the number of electricity parts, the production, and the consumption of power, it provides information on renewable energy sources that provide power under the section on electrical generation. It includes the principal AC load in the consumption. Also, it provides data on the amount of extra power (Fig. 5).

**Table 2** Data of emission of different locations

Models	CO <sub>2</sub> (kg/year)	CO (kg/year)	Unburned hydrocarbon (kg/year)	Particulate material (kg/year)	SO <sub>2</sub> (kg/year)	NOX (kg/year)
Model 1	148	0.93	0.0406	0.00564	0.361	0.874
Model 2	0	0.00374	0.000163	0.000023	0	0.00351
Model 3	0	0	0	0	0	0

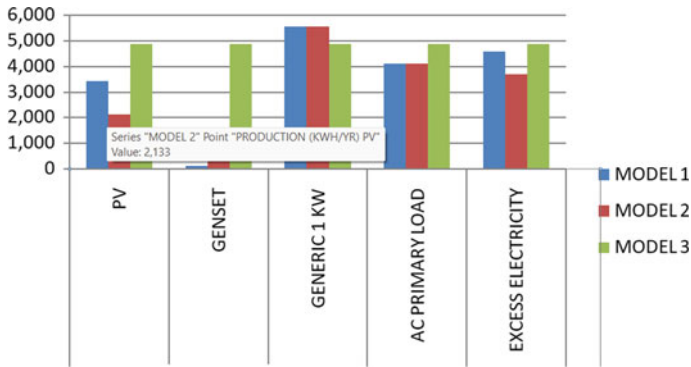


Fig. 5 Electrical data of different locations

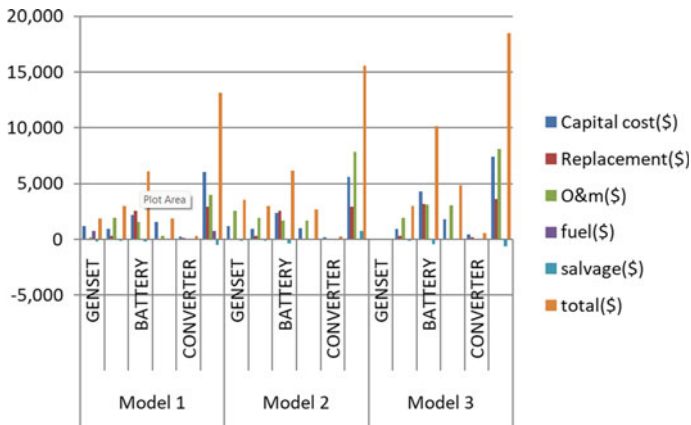


Fig. 6 Data of cash flow of different locations

- e. **On the basis of cost flow:** It provides information on every component used in the proposed model and also provides the price like replacement cost, capital cost, optimization and maintenance cost, salvage cost, fuel cost, and total cost for each component based on the cost summary from the final results of the proposed model for different locations (Fig. 6).

## 6 Conclusion

It is possible to determine which site for the proposed model is optimal using the following factors: architecture, cost and system, emissions, power, and cash flow. This information is also based on renewable energy sources such as solar and wind. It is obvious from the information on solar and wind that Solapur, Maharashtra, has



high average renewable energy data. However, considering additional factors such as budget and infrastructure, Solapur is viable and provides superior results, such as minimal COE in comparison to other locations, a higher REN proportion, and superior NPC. According to electrical location, Solapur has the largest annual total electrical output, as well as the biggest amount of surplus electricity.

## References

1. Pradhan SR, Kumar A, Sahoo A (2017) Optimization of grid-connected hybrid energy (solar and biomass) system using HOMER Pro software. *Int J InnoSci Res Tech* 2:50–57
2. Thirunavukkarasu M, Yashwant S (2021) A comparative study of the optimal sizing and management of off-grid solar/wind/diesel and battery energy systems for remote areas. *Front Energy Res* 9:752043
3. Chowdhury OR et al (2015) Optimization of a hybrid renewable energy system with HOMER. In: *Advances in computer science and ubiquitous computing: CSA and CUTE*. Springer, Singapore
4. Boddapati V et al (2022) Design and prospective assessment of a hybrid energy-based electric vehicle charging station. *Sustain Energy Technol Assessm* 53:102389
5. Sureshkumar U, Manoharan PS, Ramalakshmi APS (2012) Economic cost analysis of hybrid renewable energy system using HOMER. In: *IEEE-international conference on advances in engineering, science and management (ICAESM-2012)*. IEEE
6. Mohammed M et al (2013) Optimal sizing of photovoltaic systems using HOMER for Sohar, Oman. *Int J Renew Energy Res* 3(3):470–475
7. Kebbati Y, Baghli L (2022) Design, modeling and control of a hybrid grid-connected photovoltaic-wind system for the region of Adrar, Algeria. *Int J Environ Sci Technol* 13:1–28
8. Sawle Y (2022) An examination of the techno-economic viability of hybrid grid integrated and stand-alone generation systems for an Indian tea plant. *Front Energy Res* 8:806870
9. Thirunavukkarasu M, Yashwant S (2020) Design, analysis and optimal sizing of standalone PV/diesel/battery hybrid energy system using HOMER. In: *IOP conference series: materials science and engineering*, vol 937. IOP Publishing
10. Ileleji KE, Martin C, Jones D (2015) Basics of energy production through anaerobic digestion of livestock manure. In: *Bioenergy*. Academic Press
11. Thirunavukkarasu M, Yashwant S (2021) Smart microgrid integration and optimization. In: *Active electrical distribution network: a smart approach*, pp 201–235
12. Jain S, Sanjana B, Yashwant S (2022) Prefeasibility economic scrutiny of the off-grid hybrid renewable system for remote area electrification. In: *Proceedings of the international conference on paradigms of communication, computing and data sciences: PCCDS 2021*. Springer, Singapore
13. Shah S et al (2022) Optimal planning and design of an off-grid solar, wind, biomass, fuel cell hybrid energy system using HOMER Pro. In: *Recent advances in power systems: select proceedings of EPREC-2021*. Springer, Singapore, pp 255–275
14. Sawle Y (2022) Scrutiny of PV biomass stand-alone hybrid system for rice mill electrification. In: *Deregulated electricity market*. Apple Academic Press, pp 135–152
15. Sawle Y, Gupta SC (2018) Optimization of a standalone hybrid renewable energy system for telecom base station. *Prog Petrochem Sci Crimson J* 2(5):1–10
16. Ahmad MW et al (eds) (2022) *Intelligent data analytics for power and energy systems*. Springer, Singapore, p 641. <https://doi.org/10.1007/978-981-16-6081-8>
17. Tomar A et al (eds) (2022) *Proceedings of 3rd international conference on machine learning, advances in computing, renewable energy and communication: MARC 2021*, vol 915. Springer, New York, p 781. <https://doi.org/10.1007/978-981-19-2828-4>

# Improved Voltage Regulation in Hybrid Photovoltaic/Wind Using Modified Dynamic Voltage Restorer with Hybrid Control Scheme



Preeti Rani, Ved Parkash, and Naveen Kumar Sharma

**Abstract** The end-user load connected to micro-grid the highly sensitive to voltage disturbances. This study analyzed the improvement in the voltage regulation of hybrid PV/wind systems using Without Energy Storage (WES)-based Dynamic Voltage Restorer (DVR) by inserting voltage at a common point of the network to maintain the supply value at the load side. However, the controller of WES-based DVR is more important to improve the voltage regulation and Fault Ride through (FRT) capability in the hybrid network. The hybrid feedforward/feedback hysteresis control of WES-based DVR verifies the better response during various fault conditions as compared to open-loop control which is the novelty of this research. The positivity of the modified DVR and controller is verified through a test system modeled in MATLAB/Simulink-based simulation measures. The simulation results show better response during the transient and steady-state period and better voltage regulation during several three-phase fault conditions.

**Keywords** Grid · Solar · Wind · DVR · Hybrid control

## 1 Introduction

Electric power is energy that is distributed everywhere and is considered to be an end-user necessity. Based on the study, it is found that the use of switching converters is very normal at the local consumer level due to its various advantages available [1]. The performance of these converters affects the quality of power. By even a small variation in the reliability of the electric supply, in terms of any electrical parameters can put an unfavorable effect on the operation of the system or other apparatus for

---

P. Rani (✉) · V. Parkash  
MRSPTU, Bathinda, India  
e-mail: [pretty.singla15@gmail.com](mailto:pretty.singla15@gmail.com)

N. K. Sharma  
I. K. Gujral Punjab Technical University, Jalandhar, India

© The Author(s), under exclusive license to Springer Nature Singapore Pte Ltd. 2024  
H. Malik et al. (eds.), *Renewable Power for Sustainable Growth*,  
Lecture Notes in Electrical Engineering 1086,  
[https://doi.org/10.1007/978-981-99-6749-0\\_56](https://doi.org/10.1007/978-981-99-6749-0_56)

837

the switching device that has been utilized. Static components-based Flexible AC Transmission Systems (FACTSs) are frequently used to balance the power flow, control voltage regulation, and enhance power quality [2].

FACTS is also known as Custom Power Device (CPD) if the system is used at the end-user level for the benefits offered [3]. These devices are connected in the distributed network either in series, parallel, or a combination of both, and one of the CPDs, namely series connected DVR, which is the economic and fast way out available to compensate the various PQ issues arising from the change in magnitude of rated voltage such as voltage dip/swell. Out of these, voltage dip is the most common disturbance in power due to malfunctioning of remote area bus bars, switching of large electric loads, and starting of powerful motors [4]. In addition to the causes already described, intermittent sources used in hybrid PV/wind networks may also contribute to sag in a PV-wind power system.

In DVR, the energy demand can be met from a direct main DC supply of the network such as a solar plant, dc bus bar of a hybrid solar/wind network, using energy storage devices, namely supercharged capacitors, batteries, and super magnetic energy storage devices [5]. In the case of a hybrid network, DVR is mainly used to improve the PQ by using a suitable power electronic controller. If DVR is connected to the main source of supply of the network, it will be able to perform properly during any three-phase fault condition [6]. Considering the energy storage device as a main source of supply affects the simplicity and cost of the network and also due to the uneven capacity of the battery [7]. It means that the DC bus bar of the hybrid network is used alone as a supply source for the better to perform the DVR, but for short intervals, if the battery is used, the performance period will be slow even though it operates for a lengthy period of time. The hypothetical study of DVR with or without battery is a good research platform and its function in hybrid PV/wind micro-grid is a sustainable area of investigation [8].

A brief comparison of various DVR topologies and control strategies is discussed in [9]. In [10], a detailed analysis has discussed several control techniques of DVR to compensate for the effect of voltage sag. The DC link capacitor-based DVR for numerous PQ issues in the main supply is presented in [5]. To compensate for the effect of voltage sag, DVR performance with a high-frequency-based transformer is presented in [11]. The control scheme used in the DVR for the improvement of fault ride-through capability in a hybrid network discovers the efficacy of the device to compensate for most of the three-phase faults in the micro-grid [12]. Sensing, signal modulation, current and voltage regulation control, and reference signal are some of the procedures involved in controlling a DVR. With the help of the reference signal of DVR, a control modulator directly produces a gate pulse for the inverter, and this type of control scheme is called either open-loop or feedforward control [13]. Even though this control scheme has simplicity and stability during disturbances, but its poor response during the transient period gives the steady-state error due to high-voltage regulation [14]. To resolve these issues, hybrid feedback/feedforward control system is utilized with DVR to improve the voltage regulation. In the proposed control scheme, series-injected voltage of DVR is fed back to the control scheme.

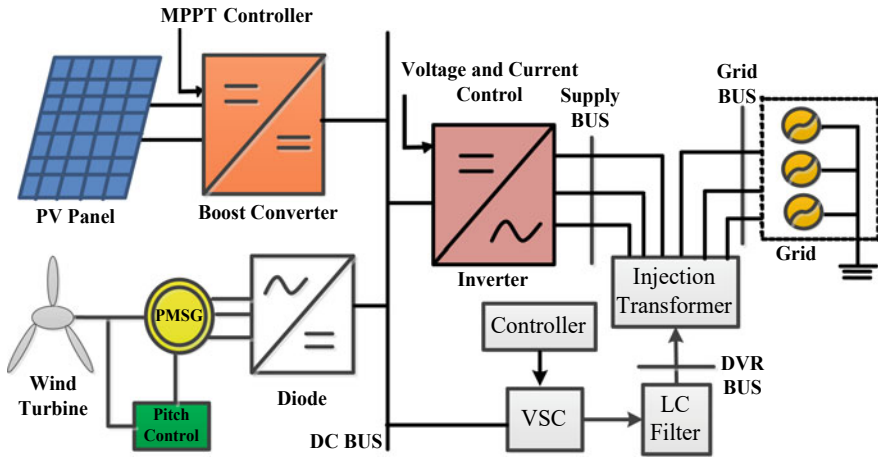


Fig. 1 Hybrid PV/wind micro-grid system with DVR

Systems using solar and wind energies are unstable and unable to produce consistent electricity production. In this research, an extensive and in-depth focus is put on the hybrid control-based DVR system’s critical function in delivering better PQ to the associated end-user-connected load and successfully utilizing micro-grid PV/wind energy [15]. This paper presented DVR to overcome several three-phase PQ issues and also to improve the FRT capability of micro-grid. The pulse-width modulation theory with feedback control is utilized with DVR. The simulation measures are based on the simulated model presented in this section for evaluating the efficacy of the proposed control with compensating device over traditional schemes. The proposed model based on MATLAB/SIMULINK based is depicted in Fig. 1.

Hybrid solar–wind networks (HSWNs) have gained significant attention in recent years due to their ability to harness renewable energy sources and provide a sustainable and reliable source of power. Here is a brief literature review of some of the recent research on HSWNs: an overview of the design, modeling, and control of HSWNs, including their potential advantages and challenges explained in [16]. Different optimization techniques that can be used to improve the performance and efficiency of HSWNs are discussed in [17]. Yadav et al. [18] presented a detailed design and simulation of an HSWN with battery storage, aimed at providing electricity to remote and rural areas. Rashid et al. [19] present an evaluation of the power output of an HSWN using simulation and experimental results. Kim and Kim [20] develop a mathematical model for an HSWN connected to the grid and analyze its performance under different operating conditions. Optimal control of hybrid solar–wind power generation systems using Model Predictive Control (MPC) is discussed in [21]. Saha et al. [22] present the design and implementation of a hybrid solar–wind energy system with battery storage for rural electrification. The authors used HOMER software to optimize the system design, considering the load demand and resource availability. Srinivasan and Panneerselvam [23] presented an improved particle swarm

optimization algorithm to determine the optimal sizing of a standalone hybrid solar–wind–battery system for rural electrification. Vinoth et al. [24], Yadav et al. [25], Jain et al. [26], Farooqi et al. [27], Tomar et al. [28], Ahmad et al. [29], Nielsen and Blaabjerg [30], Pal and Gupta [31], Asapu [32], Mukherjee and Banerjee [33], and Amalorpavaraj et al. [34] presented a study on the control and power management of a hybrid solar–wind power generation system for rural electrification. Overall, these studies demonstrate the potential of HSWNs as a reliable and sustainable source of power and highlight the importance of efficient design, optimization, and control strategies to improve their performance and efficiency. These studies often assume ideal conditions and do not account for real-world factors such as weather fluctuations and equipment degradation.

Despite the large number of studies on hybrid solar–wind networks, there are still several research gaps that need to be addressed. One area is the lack of studies on the environmental impacts of these systems. While hybrid solar–wind networks are generally considered to be environmentally friendly, the production and disposal of their components can have negative impacts on the environment. Another research gap is the need for more studies on the economic viability of these systems, particularly in developing countries where access to energy is a major challenge.

The novelty of mitigating power quality issues in a hybrid solar–wind network with a dynamic voltage restorer (DVR) lies in the integration of these two technologies to address multiple power quality issues simultaneously. Solar and wind power systems are inherently variable and intermittent, which can lead to voltage fluctuations, harmonic distortion, and unbalance in the power supply. The DVR is a power electronics-based device that can inject a voltage of appropriate amplitude and phase angle to correct voltage sags/swells, voltage unbalance, and reduce harmonic distortion in the system. The hybrid solar–wind network with a DVR can provide enhanced power quality to the system while ensuring a smooth integration of renewable energy sources into the grid. The DVR can dynamically adjust its output to match the varying renewable energy inputs, providing a robust and effective solution for mitigating power quality issues. Furthermore, the use of a hybrid solar–wind network can increase the overall reliability and resiliency of the system, as it reduces the reliance on a single source of renewable energy. This can enhance the overall energy security of the system, making it more resilient to potential disruptions.

1. The hybrid feedforward/feedback hysteresis control can provide faster response times to disturbances and voltage variations in the grid, as the feedback loop allows the system to quickly adjust the compensation provided by the DVR based on the actual voltage and current measurements.
2. Reduced the overshoot and undershoot associated with traditional feedforward control schemes, which can result in more stable and accurate compensation of voltage and current variations.
3. Designed to reject harmonics and other high-frequency noise in the grid, resulting in cleaner and more stable power output from the hybrid wind/solar network.

4. With more accurate and stable compensation provided by hybrid feedforward/feedback hysteresis control, the hybrid wind/solar network can operate more efficiently and with reduced energy losses. This can translate into lower operating costs and improved overall system performance.

The research work discussed in this statement is related to the mathematical modeling and simulation of a proposed system that includes a compensating device DVR and control schemes. The work is organized into four sections, with Sect. 2 discussing the WES-based DVR operation and its control and Sect. 3 describing the simulation results and discussion, while Sect. 4 provides a conclusion based on the findings of the study.

## 2 WES-Based DVR Operation and Its Control

Several voltage-based issues, such as PCC harmonic distortion, transients, under-voltage, and overvoltage, are primarily reduced by the DVR. The DVR offers regulated voltages even for linear/nonlinear loads connected with the DC bus through an inverter by injecting the necessary voltages between the grid bus and the grid [16]. The main goal of DVR is accomplished alone or in combination, depending on the system layout, demands, and control approach as required for the integrated network. Figure 1 shows the DVR structure connected with the micro-grid through the supply bus and grid bus. It consists of a converter, filter, controller, and injection transformer [17]. The converter, namely IGBT, analyzed the gate trigger pulse, and accordingly, the injected voltage magnitude was managed with the help of a controller, which is near to the required voltage magnitude.

### 2.1 WES-Based DVR Operation

The DVR is a switching converter connected to the grid in series through an injection transformer to inject appropriated voltage to overcome voltage disturbances and also to obtain nominal voltage regulation. The integration of a DC bus as a main source of DVR without an energy storage device is one of the good ways in PQ improvement. DC bus is used to provide electric energy in the compensating device during any kind of voltage disturbance in the supply voltage to maintain voltage regulation [18]. A combination of DC bus and DVR topology is very effective for effective performance to withstand any malfunctioning of end-user connected loads [19, 20, 33, 34].

Series injection transformer in DVR injected the controlled magnitude of voltage in series with the hybrid network to overcome the three-phase voltage disturbances and that voltage can be measured with the help of Eq. 1 and the rating of active power of DVR based in phase compensation scheme measured with Eq. 2 (Fig. 2).

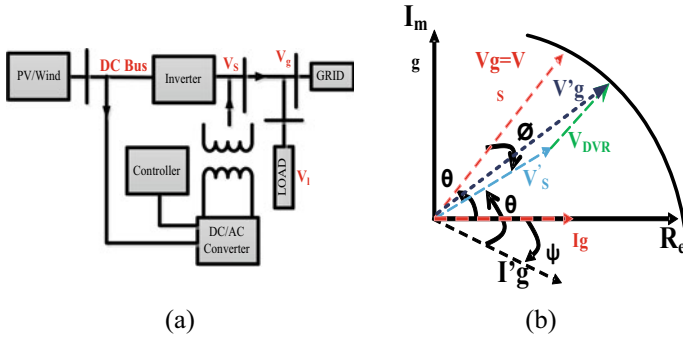


**Fig. 2 a** Schematic diagram of hybrid system with DVR **b** In-phase mitigation phasor

$$V'_g = V'_S + V_{DVR}, \tag{1}$$

where

- $V_{DVR}$  DVR-injected voltage (V).
- $V'_S$  Voltage across grid without DVR (V).
- $V'_g$  Voltage across grid with DVR (V).

$$P_g = \sum_{i=1,2,3} V_{DVR,i} * I'_g * \cos \theta, \tag{2}$$

where

- $P_{DVR}$  Active power of DVR (W).
- $V_{DVR,i}$  DVR-injected voltage in phase I (V).
- $I'_g$  Grid current (A).

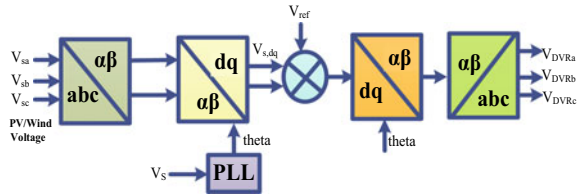
## 2.2 Feedforward Control

The conventional control technique in two axes' reference frame is also called either an open-loop controller or a feedforward controller as shown in Fig. 3. The reference voltage ( $V_{ref}$ ) represented the three-phase required voltage magnitude across grid bus, respectively [21]. The control scheme typically involves measuring the voltage at the load and comparing it to the desired voltage. Based on this comparison, compensating voltage can be generated and added to the supply voltage to achieve the desired voltage at the load.

$$V_{sa} = V_m \sin \omega t, \tag{3}$$

$$V_{sb} = V_m \sin(\omega t - 180), \tag{4}$$

**Fig. 3** Feedforward open-loop control



$$V_{sc} = V_m \sin(\omega t - 240). \tag{5}$$

The function of open-loop control in two axes’ reference frame allows clamping of compensating voltage and, therefore, allows DVR to preserve the sinusoidal insertion voltage level and mitigate deep voltage sags. Phase-Locked Loop (PLL) is used to preserve the phase angle of the reference voltage to synchronize with the phase angle of DVR-injected voltage. The controller transforms the three-phase to two-axis rotational frame and vice versa to generate the gate pulse for the inverter.

### 2.3 Hysteresis Control Scheme

The open-loop control detects the pre-fault condition of voltage at the supply bus before the grid bus during any disturbance in supply. A hybrid of open-loop and closed-loop controls can be used in a Dynamic Voltage Restorer (DVR) to compensate for the voltage drop across the components of the DVR, namely the filter circuit and injection transformer [22]. In a DVR system, the open-loop control is responsible for generating the compensating voltage waveform based on the voltage sag and harmonic distortion at the point of common coupling (PCC). The closed-loop control, on the other hand, is responsible for monitoring the voltage magnitude on the grid bus after the series injection voltage and adjusting the compensating voltage waveform as needed to maintain the desired voltage level. By using a hybrid control approach, the DVR system can provide better compensation for voltage sags and harmonics, while also compensating for the voltage drop across the components of the DVR. This can lead to improved performance and reliability of the DVR system (Fig. 4).

The use of feedforward with feedback hysteresis control (FF-FHC) in conjunction with a dynamic voltage restorer (DVR) can offer several advantages over traditional feedforward control schemes in a hybrid wind/solar network to improve power quality issues. Here are some potential advantages:

- **Improved Voltage Quality:** The feedforward with feedback hysteresis control scheme can significantly improve the voltage quality of the hybrid wind/solar network. The addition of feedback hysteresis control allows for more accurate control of the injected voltage, resulting in better voltage regulation and less voltage distortion.



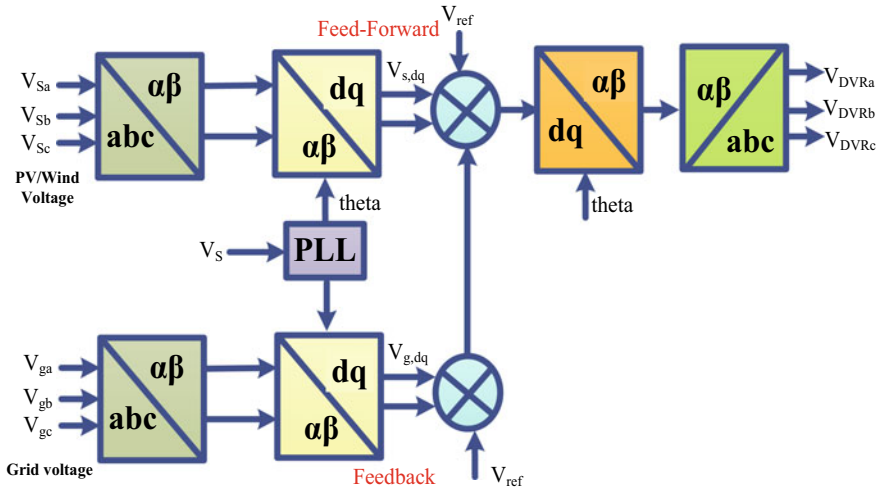


**Fig. 4** Hybrid feedforward/feedback control

- **Enhanced Stability:** The combination of feedforward and feedback hysteresis control provides improved stability of the hybrid wind/solar network during power quality disturbances. The feedforward control can quickly respond to changes in the network, while the feedback hysteresis control ensures that the system remains stable during the transition.
- **Increased Efficiency:** The use of feedforward with feedback hysteresis control in the hybrid wind/solar network can lead to increased efficiency. By controlling the voltage quality more precisely, the system can operate at optimal levels, leading to better energy conversion and reduced losses.
- **Reduced Cost:** The implementation of feedforward with feedback hysteresis control in the hybrid wind/solar network can lead to cost savings. The control scheme can help mitigate power quality issues, reducing the need for expensive equipment such as voltage stabilizers or transformers.
- **Flexibility:** The feedforward with feedback hysteresis control scheme is highly flexible and can be easily adapted to different types of power quality disturbances. This makes it a valuable tool for improving the performance of hybrid wind/solar networks in different operating conditions.

Overall, the use of feedforward with feedback hysteresis control in the hybrid wind/solar network can lead to improved power quality, enhanced stability, increased efficiency, reduced costs, and greater flexibility.

### 3 Simulation Results and Discussion

In this section, simulation results based on various three-phase fault conditions are presented using WES-based DVR. The results at three buses, namely the supply bus, grid bus, and DVR bus, of voltage, active power, and reactive power are measured in p.u. and rms, and also, harmonic distortion in THD% is discussed in detail during several PQ issues. The FRT performance of a micro-grid is being analyzed for faults and harmonics, specifically for balanced and unbalanced faults lasting between 0.3 and 0.4 s, and harmonics. The analysis includes the use of a hybrid controller-based DVR, and simulation results are presented in Figs. 5 and 6 for an unbalanced voltage sag of 0.3 per unit (p.u.) at the single line to ground.

Figure 5c and e represent the series-injected voltage and the regulated voltage across the grid, respectively, in root mean square (rms) and per unit (p.u.) units. The simulation results for these parameters are shown in Fig. 5d and f, respectively. In addition, Fig. 6a, b depict the active and reactive powers during a 0.3 p.u. unbalanced sag, while Fig. 6c, d show the injected power through DVR and the net regulated power across the grid, respectively. Finally, Fig. 6e, f represent the simulation results for the net regulated power across the grid during an unbalanced sag with two line-to-ground faults. Similarly, the simulation results for an unbalanced sag with two line-to-ground faults are presented in Figs. 7 and 8. These simulation results provide information about the behavior of the micro-grid during different fault conditions and the effectiveness of the hybrid controller-based DVR in regulating and stabilizing the voltage and power output of the system.

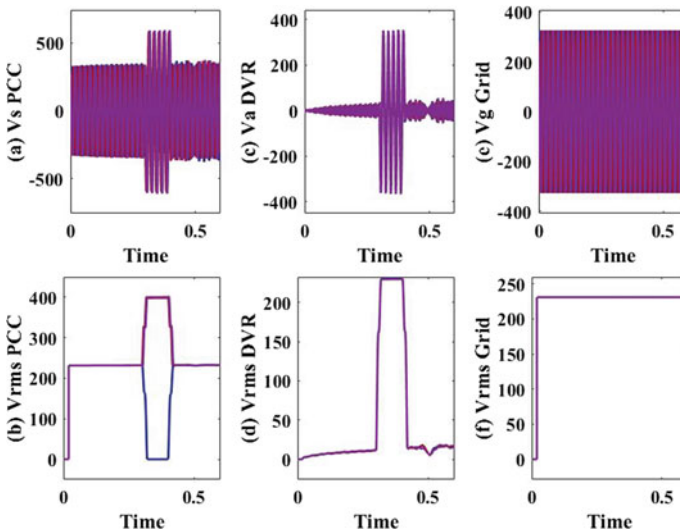


**Fig. 5** Hybrid power system voltage during L–G fault: **a** input voltage (pu), **b** input voltage (RMS), **c** DVR voltage (pu), **d** DVR voltage (RMS), **e** output voltage in (pu), **f** output voltage (RMS)

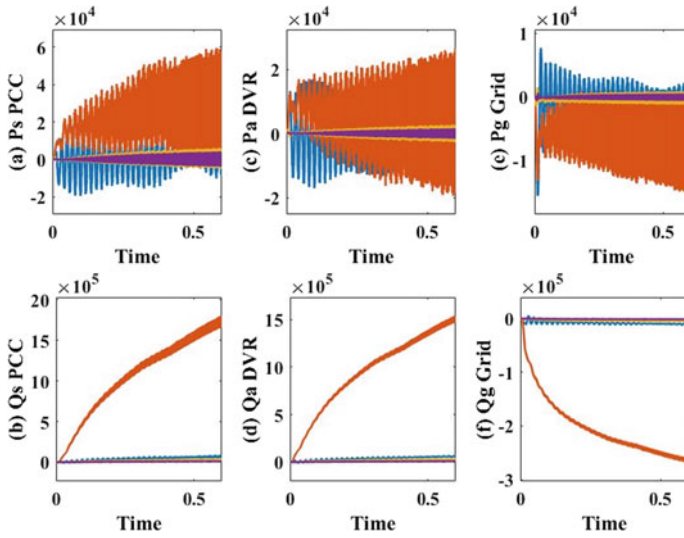


**Fig. 6** Hybrid energy system power during L-G fault: **a** input real power, **b** input wattless power, **c** DVR real power, **d** DVR wattless power, **e** output real power, **f** output wattless power

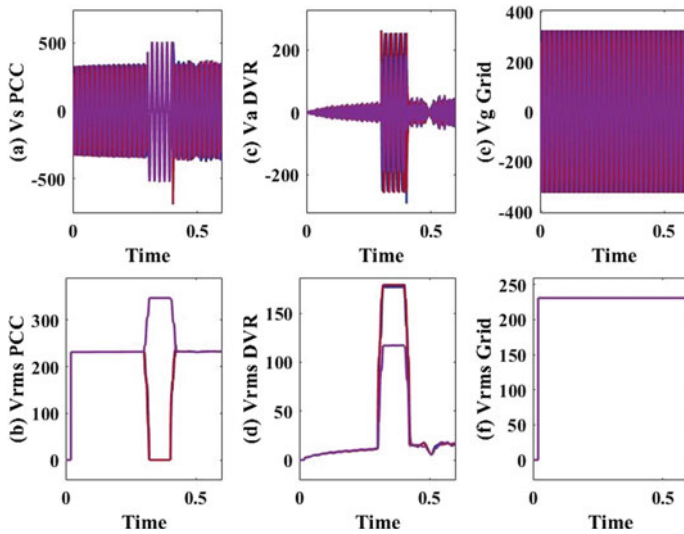


**Fig. 7** Hybrid energy system voltage during double line-to-ground fault: **a** input voltage (pu), **b** input voltage (RMS), **c** DVR voltage (pu), **d** DVR voltage (RMS), **e** output voltage in (pu), **f** output voltage (RMS)

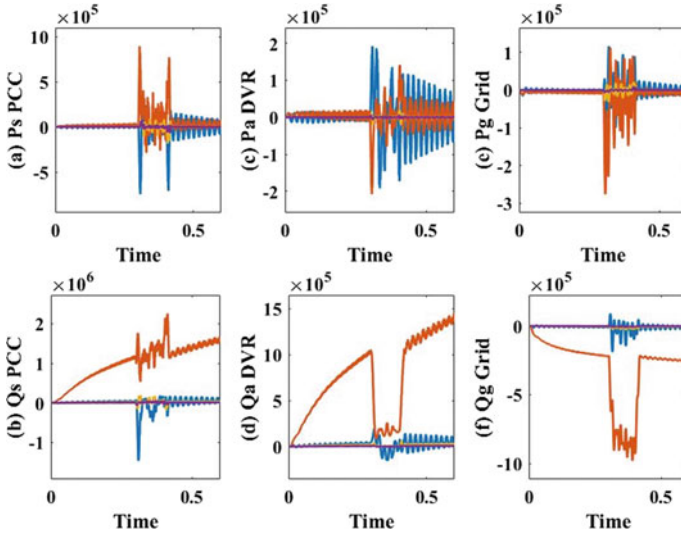


**Fig. 8** Hybrid energy system power during L–L–G fault: **a** input real power, **b** input wattless power, **c** DVR real power, **d** DVR wattless power, **e** output real power, **f** output wattless power

Figure 7 represents the source voltage during an L–L–G fault, the injected voltage, and the grid voltage—all in p.u. and rms of the hybrid control-based DVR. The unbalanced fault occurs for 0.3–0.4 s at 50 Hz frequency. The simulation results of real power and wattless power at the proposed buses are represented in Fig. 8.

Figures 9 and 10 represent the power outage fault for 0.3–0.4 s and this fault is also called L–L–L–G fault. This fault is one of the severe faults, and during this fault, power is zero that’s by it is called a power outage fault.

Figures 11 and 12 represent the simulation results of balanced faults, namely interruption duration 0.1–0.2 s, voltage sag duration 0.2–0.3 s, and voltage swell duration 0.3–0.4 s, at 50 Hz supply. These faults are carried out for 500 ms. Figure 11 represents the voltage waveform during the fault, injected voltage, and the voltage across the grid after the mitigation of these faults. Figure 12 represents the active power and reactive power during fault conditions, injected power, and the power across the grid for hybrid control with WES-based DVR.

Harmonics disturbs the stability of micro-grid-connected networks and many of the faults occurred with harmonics. Figure 13 represented the harmonic spectrums with THD% using open-loop feedforward control and hybrid control.

Harmonics analysis using open-loop control-based DVR is depicted in Fig. 13a and using hybrid control-based DVR is depicted in Fig. 13b. The hybrid control with WES-based DVR represented the lower THD% as per IEEE 519 standards.

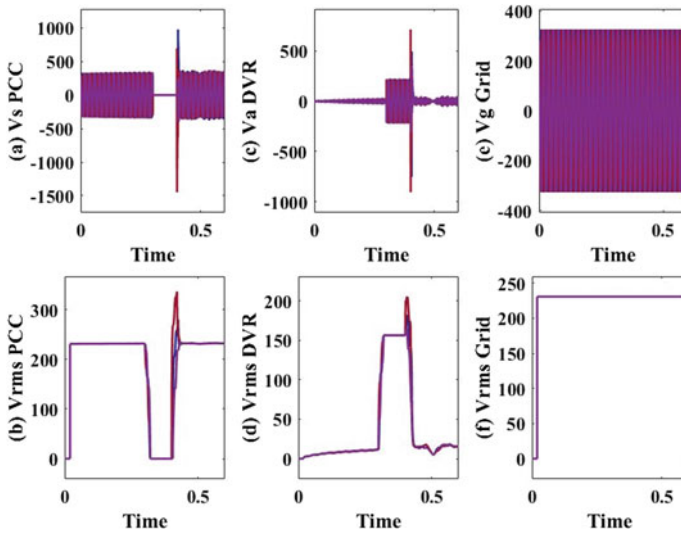


**Fig. 9** Hybrid energy system performance during power outage fault: **a** input voltage (pu), **b** input voltage (RMS), **c** DVR voltage (pu), **d** DVR voltage (RMS), **e** output voltage in (pu), **f** output voltage (RMS)

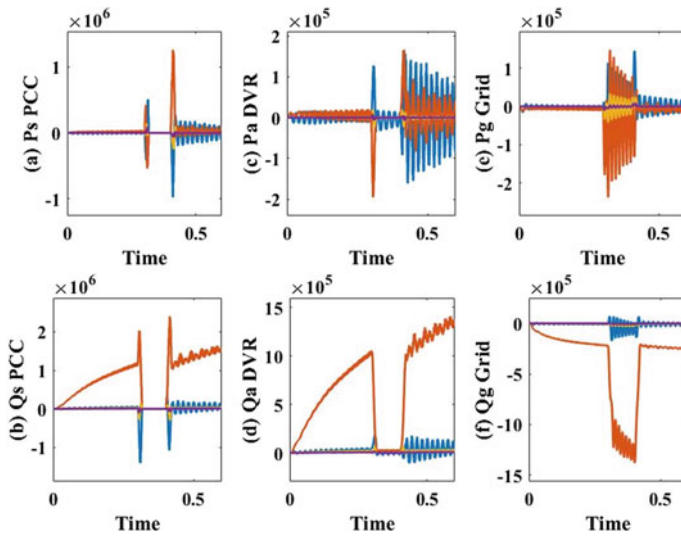


**Fig. 10** Hybrid energy system power during a power outage: **a** input real power, **b** input wattless power, **c** DVR real power, **d** DVR wattless power, **e** output real power, **f** output wattless power

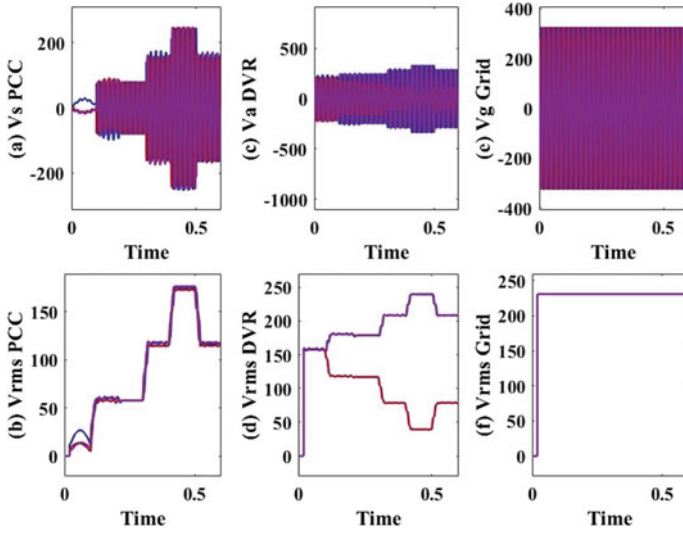


**Fig. 11** Hybrid energy system performance during various three-phase fault conditions: **a** input voltage (pu), **b** input voltage (RMS), **c** DVR voltage (pu), **d** DVR voltage (RMS), **e** output voltage in (pu), **f** output voltage (RMS)

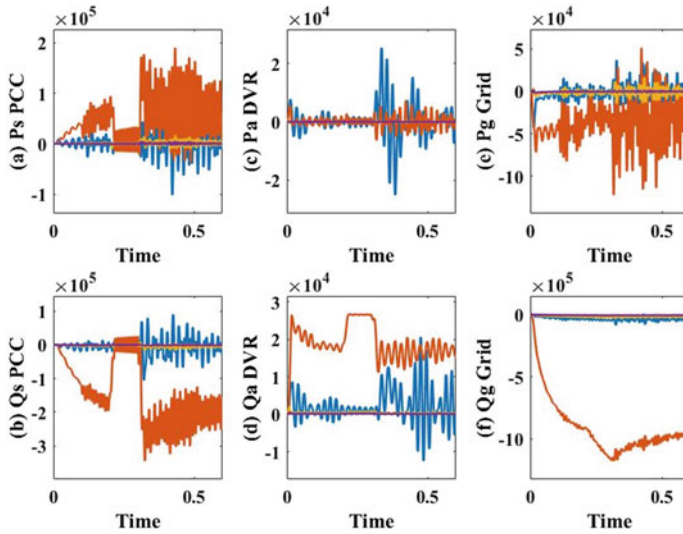


**Fig. 12** Hybrid energy system power during various three-phase fault conditions: **a** input real power, **b** input wattless power, **c** DVR real power, **d** DVR wattless power, **e** output real power, **f** output wattless power

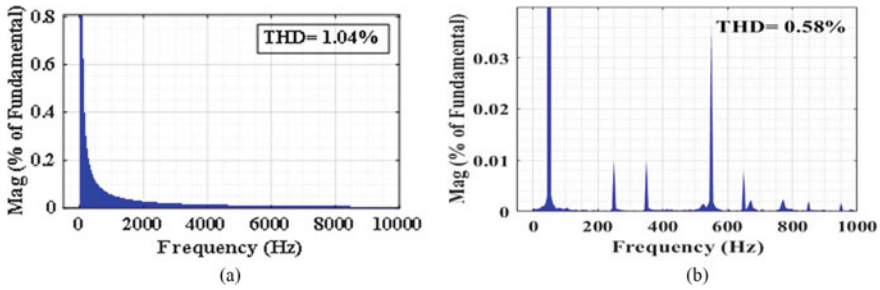


**Fig. 13** **a** Harmonic spectrum during fault, **b** harmonic spectrum with proposed hybrid control DVR

## 4 Conclusion

The effectiveness of WES-based DVR with hybrid control connected with a hybrid PV/wind network for several fault conditions is analyzed in this research. The performance of this topology is more efficient for the compensation of harmonic distortions in signals, to regulate the power and voltage across the grid. The simulation measures suggest that the performance of WES-based DVR is very effective for FRT improvement as per required grid code standards in hybrid wind/PV networks. The investigated hybrid control has many positive impacts such as limited complexity and better voltage regulation. The hybrid control with WES-based DVR is utilized to analyze the performance of the hybrid network while improving the voltage control and modifying the compensating device. This modified DVR and control scheme proves its effectiveness at several fault conditions as described in the simulation results and discussion section. Overall, the integration of a DVR with a hybrid solar–wind network represents a novel and effective approach to mitigating power quality issues and promoting the integration of renewable energy into the grid.

The future scope of a hybrid solar–wind network with DVR is promising and holds the potential in addressing some of the challenges faced by renewable energy systems. By using a combination of solar and wind energy, a hybrid solar–wind network can achieve higher levels of energy efficiency and reduce the variability of energy production. The addition of a DVR can help optimize the power output of the system, which can further improve efficiency and reduce energy waste.

## References

1. Varma SDK, Bhavani NVA (2016) Power quality improvement in standalone battery integrated wind energy system. In: International conference on signal processing, communication, power and embedded system, pp 642–647. <https://doi.org/10.1109/SCOPE5.2016.7955519>
2. Amutha N, Kumar BK (2013) Improving fault ride-through capability of wind generation system using DVR. *Int J Electr Power Energy Syst* 46:326–333. <https://doi.org/10.1016/j.ijepes.2012.10.040>
3. Naderi Y, Hosseini SH, Ghassemzadeh S, Ivatloo BM, Savagheb M, Vasquez JC, Guerrero JM (2020) Power quality issues of smart microgrids: applied techniques and decision making analysis. Elsevier Inc, pp 89–119. <https://doi.org/10.1016/B978-0-12-816445-7.00004-9>
4. Fekkak B, Menaoui A, Loukri A, Kouzou A (2020) Control of grid-connected PMSG-based wind turbine system with back-to-back converters topology using a new PIL integration method. In: International transactions on electrical energy systems, pp 1–25. <https://doi.org/10.1002/2050-7038.12882>
5. Chaudhary P, Singh G (2020) Fault mitigation through multi converter UPQC with hysteresis controller in grid connected wind system. *J Ambient Intell Hum Comput* 11:5279–5295. <https://doi.org/10.1007/s12652-020-01855-w>
6. Agalar S, Kaplan YA (2018) Power quality improvement using STS and DVR in wind energy system. *Renew Energy* 118:1031–1040. <https://doi.org/10.1016/j.renene.2017.01.013>
7. Benali A, Khiaat M, Allaoui A, Denai M (2018) Power quality improvement and low voltage ride through capability in hybrid wind-PV farms grid-connected using dynamic voltage restorer. *IEEE Access* 6:68634–68648. <https://doi.org/10.1109/ACCESS.2018.2878493>
8. Kasera J, Chaplot A, Maherchandani JK (2012) Modeling and simulation of wind-PV hybrid power system using Matlab/Simulink. In: Proceeding in conference on electrical, electronics and computer science, pp 1–4. <https://doi.org/10.1109/SCIECS.2012.6184769>
9. Bajaj M (2020) Design and simulation of hybrid DG system fed single-phase dynamic voltage restorer for smart grid application. *Smart Sci* 8:24–38. <https://doi.org/10.1080/23080477.2020.1748928>
10. Kumar TP, Subrahmanyam N, Sydulu M (2021) Power flow management of the grid-connected hybrid renewable energy system: a PLSANN control approach. *IETE J Res* 67:569–584. <https://doi.org/10.1080/03772063.2019.1565950>
11. Molla EM, Liu C, Kuo C (2020) Power quality improvement using microsystem technology for wind power plant. *Microsyst Technol* 26:1799–1811. <https://doi.org/10.1007/s00542-019-04726-3>
12. Muni V, Lalitha SVN (2017) Technical issues of Grid connected solar photovoltaic cell: a survey. *Int Sci Press* 10:913–920
13. Naidu R, Meikandasivam S (2021) Performance investigation of grid integrated photovoltaic/wind energy systems using ANFIS based hybrid MPPT controller. *J Ambient Intell Hum Comput* 12:5147–5159. <https://doi.org/10.1007/s12652-020-01967-3>
14. Kumar R, Singh SK (2018) Solar photovoltaic modeling and simulation: as a renewable energy solution. *Energy Rep* 4:701–712. <https://doi.org/10.1016/j.egyr.2018.09.008>
15. Sahoo B, Routray SK, Rout PK (2018) A new topology with the repetitive controller of a reduced switch seven-level cascaded inverter for a solar PV-battery based microgrid. *Eng Sci Technol Int J* 21:639–653. <https://doi.org/10.1016/j.jestch.2018.06.007>
16. Sayadi H, Taheri M (2019) A review of hybrid solar–wind power generation systems. *J Renew Sustain Energy Rev* 109:157–172. <https://doi.org/10.1016/j.rser.2019.04.045>
17. Hassan AH (2021) Optimization of hybrid wind-solar power systems: a review. *J Renew Sustain Energy Rev* 138:634. <https://doi.org/10.1016/j.rser.2020.110634>
18. Yadav SP, Yadav A, Yadav SK (2021) Design and simulation of a hybrid wind-solar energy system with battery storage for rural electrification. *J Energy Storage* 41:102986. <https://doi.org/10.1016/j.est.2021.102986>



19. Rashid MM, Asaduzzaman M, Hasanuzzaman M (2020) Evaluation of power output of a wind turbine and solar panel hybrid system. *Int J Energy Res* 44:11820–11838. <https://doi.org/10.1002/er.6122>
20. Kim TW, Kim JS (2016) Modeling and analysis of a grid-connected hybrid wind-solar energy system. *Energy* 114:840–849. <https://doi.org/10.1016/j.energy.2016.08.035>
21. Shinde S, Thakur S (2022) Optimal control of hybrid solar-wind power generation systems using model predictive control. *Lect Notes Electr Eng* 785:683–694. [https://doi.org/10.1007/978-981-16-3223-3\\_61](https://doi.org/10.1007/978-981-16-3223-3_61)
22. Saha A, Nambiar M, Subramanian KA (2021) Design and implementation of a hybrid solar-wind energy system with battery storage for rural electrification. *Lect Notes Electr Eng* 715:603–614. [https://doi.org/10.1007/978-981-33-6953-2\\_56](https://doi.org/10.1007/978-981-33-6953-2_56)
23. Srinivasan S, Panneerselvam L (2021) Optimal sizing of a standalone hybrid solar-wind-battery system for rural electrification using an improved particle swarm optimization algorithm. *Lect Notes Electr Eng* 715:583–593. [https://doi.org/10.1007/978-981-33-6953-2\\_54](https://doi.org/10.1007/978-981-33-6953-2_54)
24. Vinoth R, Saravanan T, Premalatha M (2021) Control and power management of hybrid solar-wind power generation system for rural electrification. *Lect Notes Electr Eng* 710:703–711. [https://doi.org/10.1007/978-981-16-0482-8\\_63](https://doi.org/10.1007/978-981-16-0482-8_63)
25. Yadav SP, Sharma A, Arora R (2021) Performance analysis of a hybrid wind-solar power system with energy storage for rural electrification. *Lect Notes Electr Eng* 710:137–147. [https://doi.org/10.1007/978-981-16-0482-8\\_13](https://doi.org/10.1007/978-981-16-0482-8_13)
26. Jain A, Shankar S, Vanitha V (2017) Power generation using permanent magnet synchronous generator (PMSG) based variable speed wind energy conversion system (WECS): an overview. *J Green Eng* 7:477–504
27. Farooqi A, Othman MM, MohdRadzi MA, Musirin I, Noor MSZM, Abidin IZ (2022) Dynamic voltage restorer (DVR) enhancement in power quality mitigation with an adverse impact of unsymmetrical faults. *Energy Rep* 8:871–882. <https://doi.org/10.1016/j.egy.2021.11.147>
28. Tomar A et al (eds) (2022) Proceedings of 3rd international conference on machine learning, advances in computing, renewable energy and communication: MARC 2021, vol 915. Springer, New York, p 781. <https://doi.org/10.1007/978-981-19-2828-4>
29. Ahmad MW et al (eds) (2022) Intelligent data analytics for power and energy systems. Springer, New York, p 641. <https://doi.org/10.1007/978-981-16-6081-8>
30. Nielsen JG, Blaabjerg F (2005) A detailed comparison of system topologies for dynamic voltage restorers. *IEEE Trans* 41:1272–1280. <https://doi.org/10.1109/TIA.2005.855045>
31. Pal R, Gupta S (2020) Topologies and control strategies implicated in dynamic voltage restorer (DVR) for power quality improvement. *Iran J Sci Technol Trans Electr Eng* 44:581–603. <https://doi.org/10.1007/s40998-019-00287-3>
32. Asapu S (2021) Modified hysteresis current control of multilevel converter for grid connected battery storage system. In: Material today proceeding, pp 1–9. <https://doi.org/10.1016/j.matpr.2021.07.290>
33. Mukherjee M, Banerjee A (2019) Power quality improvement by active shunt filter with hysteresis current controller. In: Proceeding in conference series: materials science and engineering, pp 89–97. [https://doi.org/10.1007/978-981-13-3450-4\\_11](https://doi.org/10.1007/978-981-13-3450-4_11)
34. Amalorpavaraj RAJ, Kaliannan P, Padmanaban S, Subramaniam U, Ramachandramurthy VK (2017) Improved fault ride through capability in DFIG based wind turbines using dynamic voltage restorer with combined feed-forward and feed-back control. *IEEE Access* 5:20494–20503. <https://doi.org/10.1109/ACCESS.2017.2750738>

# Contingency Analysis for a Solar Energy Generation System Using Real-Time Data Analysis



Vishal V. Mehtre, Shivani Jitendra Khare, Swapnil Namekar,  
and D. S. Bankar

**Abstract** Owing to being environment friendly, having a decrement in the amount of greenhouse emissions from fossil fuels, increment in the reliability of the current system, application and adoption of renewable energy systems has been escalating in electric generation systems. The major concern arises due to different faults occurring in the electric power system. The presence of certain harmonic contents and abnormalities can lead to major faults occurring in the power system, thereby causing an interruption in the distribution system of the grid. This greatly sways the efficiency of the electric power grid system. To address this challenge is the key to conducting contingency analysis. Numerous techniques have been enacted upon for identifying and truncating the occurrence of fault, thereby increasing the efficiency. This paper presents an overview of contingency analysis and the challenges faced in the field of renewable energy generation system. This paper focuses on analysis of solar energy generation system using real-time data which has been visualized on Google Colab platform using the Exploratory Data Analysis technique of machine learning. Thereafter, the results are taken into account to identify the possible contingencies that would be present in the solar energy generation system. Furthermore, challenges in renewable energy contingency analysis and an effective method to reduce the occurrence of contingency in the generation system have been proposed in this paper.

**Keywords** Electric grid · Exploratory data analysis · Renewable energy · Contingency analysis · Efficiency · Faults · Solar energy

---

V. V. Mehtre (✉) · S. J. Khare · S. Namekar · D. S. Bankar  
Department of Electrical and Computer Engineering, Bharati Vidyapeeth (Deemed to Be University) College of Engineering, Pune, Maharashtra, India  
e-mail: [vvmehtre@bvucoep.edu.in](mailto:vvmehtre@bvucoep.edu.in)

S. Namekar  
e-mail: [sanamekar@bvucoep.edu.in](mailto:sanamekar@bvucoep.edu.in)

D. S. Bankar  
e-mail: [dsbankar@bvucoep.edu.in](mailto:dsbankar@bvucoep.edu.in)

## 1 Introduction

Stability of power system has always been a major concern for the power system engineers, maintaining the said stability being the second major concern. Not only has there been an extensive amount of research in the field, but an equivalent number of techniques have been analyzed and implemented in attaining the same, one such tool being contingency analysis tool [1].

It is possible that the security and stability of the system will be maintained with the help of excellent fault forecasting using computer analytical tools when the use of renewable energy picks up speed in the process of producing electricity [2]. The stability of the system is defined by perpetuating the system parameters within the specified stable maximum limits and minimum limits. Hence, it is of utmost concern that the effect of outages is analyzed first hand in terms of the cause [3]. Once the analysis of outage situation is terminated, installation of redundant components such as generator, transmission line system, bus bars is crucial to ensure an uninterrupted supply process, when in case of interruption in the existing electrical model. According to the research done in [4], there is a long-term connection between carbon dioxide, economic growth, and non-renewable and renewable energy sources. New technological difficulties are emerging within the traditional and well-established technologies, such as solar, hydro, and biomass [5]. Contingency analysis enables the utility system to discover the impact of outage of the component, thereby structuring out the process of solving the contingency [6].

## 2 Contingency Analysis

### 2.1 *What is Contingency Analysis?*

In simpler terms, contingency analysis can be understood as a “what if” scenario wherein the simulator examines, reports, and prioritizes the impacts on electrical grid components in the situations of those what if scenarios [7]. It is a failure of a certain part of power system and hence is also termed as an “Unplanned Outage.” The “network model” is an electrical representation of the power system that is used in the contingency application. The complete real power system is represented in this network model. It is created by network experts as well as utility system planners. They translate the real-world equipment and connections of a power system into a power network mathematical model that can be solved using computer algorithms [8]. This network model includes electrical characteristics of the equipment as well as information about connections (topology and connectivity) (such as the impedance of transmission lines). The contingency analysis algorithm makes use of network “parameters,” which are network-related data. It makes use of the network model to simulate and compute the changes that occur when the equipment is removed from the power supply. When factors like income and expenses are taken into account,

they become more fragile than variations in applications and technological solutions [9].

## 2.2 Components of Contingency Analysis

The blocks carry out the following functions (Fig. 1).

### 2.2.1 Contingency Definition

This stage involves cataloguing different types of probable contingencies that might occur in the power grid utility. This stage serves to provide an overall journal of the contingencies that might occur in the future. This can be found out by performing analysis such as forecasting of load and demand using techniques of Exploratory Data analysis (a machine learning tool) [10]. A real-time data is taken into consideration which closely matches the working conditions of the present utility. The data is analyzed and results are generated.

### 2.2.2 Contingency Selection

This stage involves selection of the most severe type of contingency from the contingency definition. This stage acts as a filter, filtering out all the unnecessary contingencies from the contingency definition, thereby presenting a shortened list of all the probable occurrences that might affect the power system.

### 2.2.3 Contingency Evaluation

This stage is responsible for delivering a solution to the said contingency.

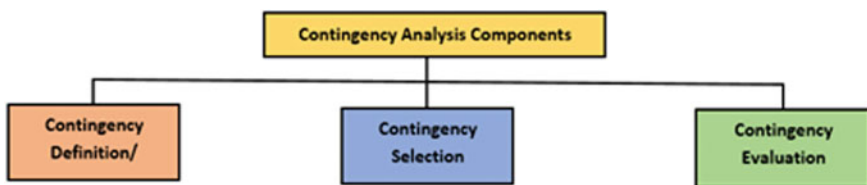


Fig. 1 Components of contingency analysis

### 3 Exploratory Data Analysis of Real-Time Solar Energy Dataset for Contingency Possibility

#### 3.1 About the Dataset

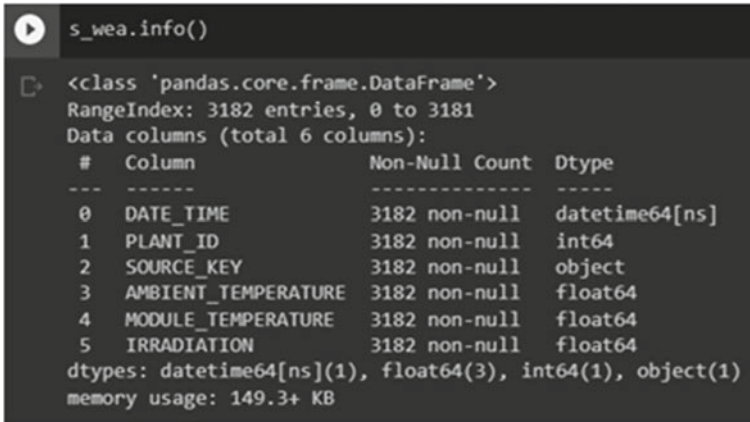
Data at the inverter level, where each inverter has several lines of solar panels linked to it, was used to compile the dataset. The sensor data was acquired using information from the plant level, where the array of sensors was positioned in the best possible way. During the course of 34 days, data from the dataset was collected at two solar farms in India. Each power plant has two data files: one for generation and the other for weather. Just the generation and weather data for plant 1 were taken into account in this article.

##### 3.1.1 Key Points About the Dataset

- The dataset contains 22 unique source key data. This means that the data has been gathered considering 22 inverters.
- Following code snippet in Fig. 2 shows detailed information about data type of the generation data of plant 1.
- **Column description: generation data**
  - **DATE\_TIME** Recorded at the intervals of 15 min.
  - **SOURCE\_KEY**: Represents inverter number (Inverter ID) as 22.
  - **DC\_POWER**: Represents the amount of DC power generated in the interval of 15 min (kW).

```
s_gen.info()
<class 'pandas.core.frame.DataFrame'>
RangeIndex: 68778 entries, 0 to 68777
Data columns (total 7 columns):
#   Column          Non-Null Count  Dtype
---  ---            -
0   DATE_TIME       68778 non-null  datetime64[ns]
1   PLANT_ID        68778 non-null  int64
2   SOURCE_KEY      68778 non-null  object
3   DC_POWER        68778 non-null  float64
4   AC_POWER        68778 non-null  float64
5   DAILY_YIELD     68778 non-null  float64
6   TOTAL_YIELD     68778 non-null  float64
dtypes: datetime64[ns](1), float64(4), int64(1), object(1)
memory usage: 3.7+ MB
```

Fig. 2 Generation dataset information



```
s_wea.info()
<class 'pandas.core.frame.DataFrame'>
RangeIndex: 3182 entries, 0 to 3181
Data columns (total 6 columns):
#   Column                Non-Null Count  Dtype
---  -
0   DATE_TIME             3182 non-null   datetime64[ns]
1   PLANT_ID              3182 non-null   int64
2   SOURCE_KEY            3182 non-null   object
3   AMBIENT_TEMPERATURE   3182 non-null   float64
4   MODULE_TEMPERATURE    3182 non-null   float64
5   IRRADIATION           3182 non-null   float64
dtypes: datetime64[ns](1), float64(3), int64(1), object(1)
memory usage: 149.3+ KB
```

**Fig. 3** Weather dataset information

- **AC\_POWER:** Represents the amount of AC power generated in the interval of 15 min (kW).
- **TOTAL\_YIELD:** Represents the total yield till the present time.
- **PLANT\_ID:** ID of the plant used to collect data—common for the entire dataset.
- Following code snippet in Fig. 3 shows detailed information about data type of the generation data of plant 1.
- **Column description: weather data**
  - **SOURCE\_KEY:** Represents the weather sensor ID—common for the entire dataset.
  - **AMBIENT\_TEMPERATURE:** Ambient temperature at the plant (°C).
  - **MODULE\_TEMPERATURE:** Represents the temperature of the solar module (°C).
  - **IRRADIATION:** Represents the amount of irradiation in the time interval of 15 min. Post-comparing the irradiation data with different research works, the unit for the data is kW/m<sup>2</sup>.
- No missing values were found in the dataset for both the generation data and the weather data. Hence, there is no requirement of dataset cleaning.
- Number of measurements per inverter range from (3104, 3155).

### 3.2 Determining Correlations

For determining the data distribution and correlation among the dataset parameters, we have considered constructing a heat map for generating suitable conclusions about

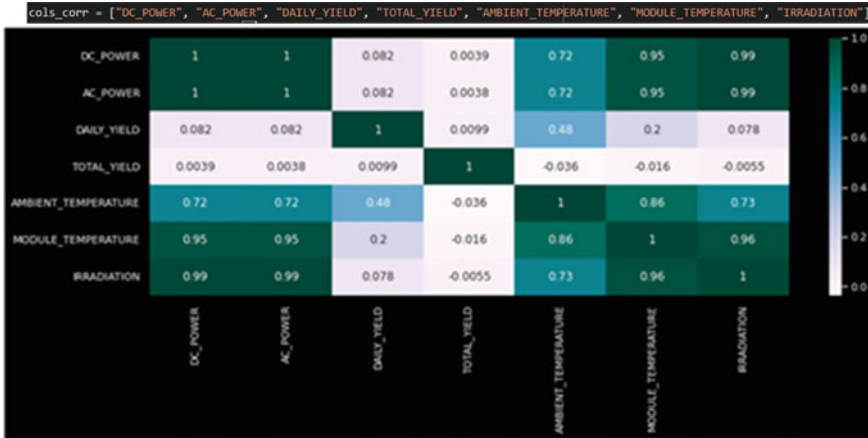


Fig. 4 Heat map for data correlation

the degree of correlation present in the dataset parameters. *Seaborn library* has been made use of for generating the heat maps.

### 3.2.1 Generating Heat Map

We have considered the following data for generating the heat map (Fig. 4).

### 3.2.2 Observations

From the heat map, we observe the following:

- On a scale of 0–1, matrix shows high correlation of 0.99 between **DC\_POWER** and **IRRADIATION**.
- On a scale of 0–1, matrix shows high correlation of 0.95 between **DC\_POWER** and **MODULE\_TEMPERATURE**.
- On a scale of 0–1, matrix shows high correlation of 0.99 between **AC\_POWER** and **IRRADIATION**.
- On a scale of 0–1, matrix shows high correlation of 0.95 between **AC\_POWER** and **MODULE\_TEMPERATURE**.
- Significant correlation is observed between **MODULE\_TEMPERATURE** and **AMBIENT\_TEMPERATURE**.
- On a scale of 0–1, matrix shows significant correlation of 0.85 between **IRRADIATION** and **AMBIENT\_TEMPERATURE**.
- On a scale of 0–1, matrix shows correlation of 0.48 between **DAILY\_YIELD** and **AMBIENT\_TEMPERATURE**.

### 3.3 Determining Outliers in the Parameters

The process of determining the outliers in the dataset will enable us to know the equipment responsible for contingency in the solar energy generation system.

#### 3.3.1 Generating Pair-Plots

For generating outliers in the system, we have plotted pair plots using *Seaborn library*. Figure 5 shows the pair-plots for outlier detection.

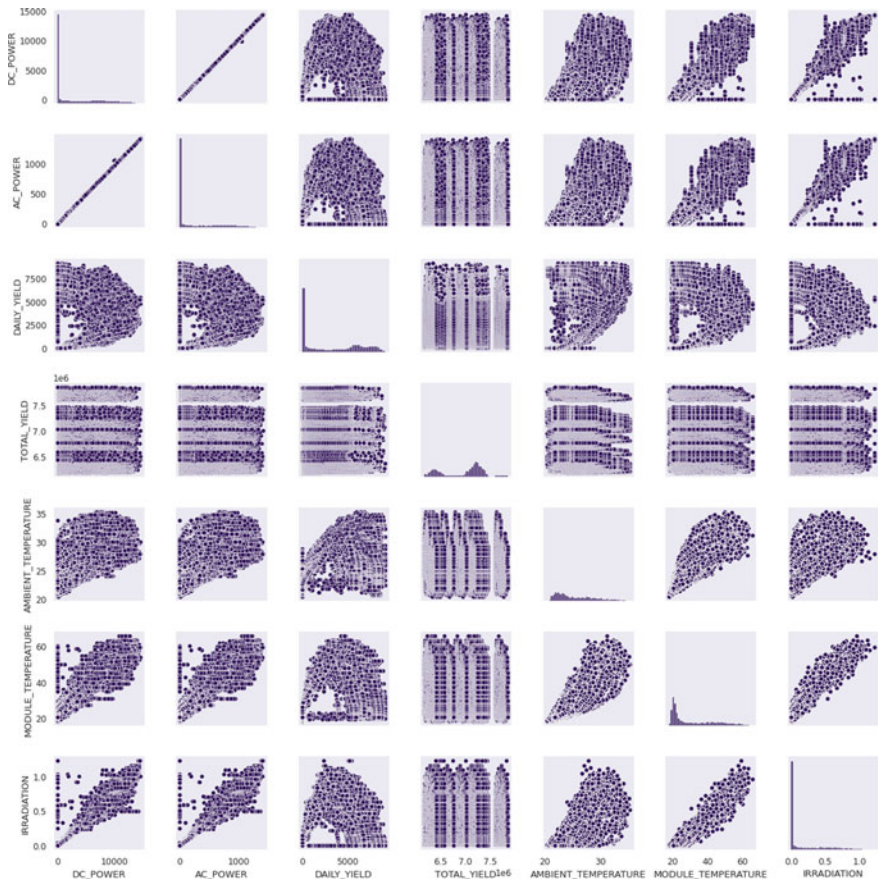


Fig. 5 Pair-plots for outlier detection



### 3.3.2 Observation

From the pair-plot generated above, the following conclusions can be drawn:

- Large number of outliers observed in **DC\_POWER** and **MODULE\_TEMPERATURE, IRRADIATION** plots.
- Large number of outliers observed in **AC\_POWER** and **MODULE\_TEMPERATURE, IRRADIATION** plots.
- Small number of outliers observed in **AC\_POWER** and **DC\_POWER** plot.

### 3.4 Detailed Analysis

In order to draw out more accurate conclusions, we have plotted pair-plots of the outlier parameters observed above with respect to the inverter source key. Figure 6 shows pair-plots for detailed analysis.

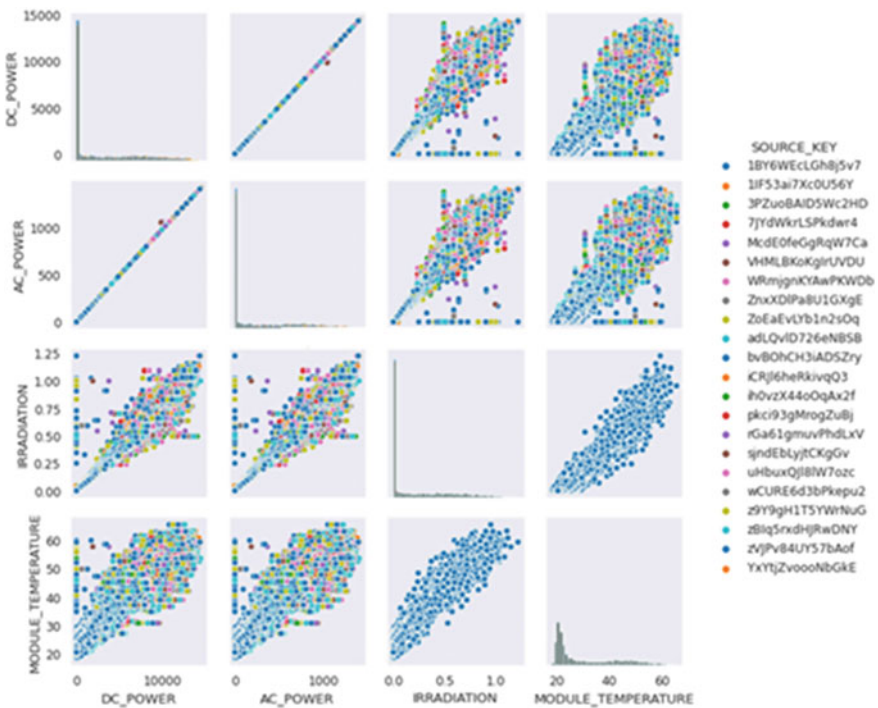


Fig. 6 Pair-plot for detailed inverter analysis

### 3.4.1 Observations

It can be observed that outliers are present due to a small number of faulty inverters present in the solar energy generation system due to which the overall efficiency of the solar energy generation system reduces.

## 3.5 Conclusions

- The outliers in **DC\_POWER**, **AC\_POWER** and **IRRADIATION**, and **MODULE\_TEMPERATURE** indicate the possibility of faulty photovoltaic cells in the solar array.

**Reason:** This is because even though there is energy falling on the solar cells, equivalent amount of power is not getting generated, and hence, this is one possible area of contingency in the solar power system [11].

- The outliers in **AC\_POWER** and **DC\_POWER** depict faults in the inverter system of the solar energy generation system.

**Reason:** This is because the total DC power being generated and the total AC power available at the conversion end are not equal. Losses are occurring during the conversion of DC power to AC power, and hence, this is another possible area of contingency in the solar power system.

## 4 Review of Contingency Analysis in Renewable Energy Systems

### 4.1 Renewable Energy Contingencies Challenges

Following are the metrics that categorize the various challenges related to contingencies which are posed to the renewable energy generation system.

#### 4.1.1 Challenge 1: Renewable Energy Contingency Size in Megawatts (MW) and Giga-Watt-Hour (GWh) and Duration in Days are Larger Than the Followed Power System Planning Standard ( $n - 1$ )

Renewable energy size and duration can be extensive in terms of both duration and size in comparison to what the current power system operator personnel's deal with. The largest contingency unit with which the typical power system operators operate

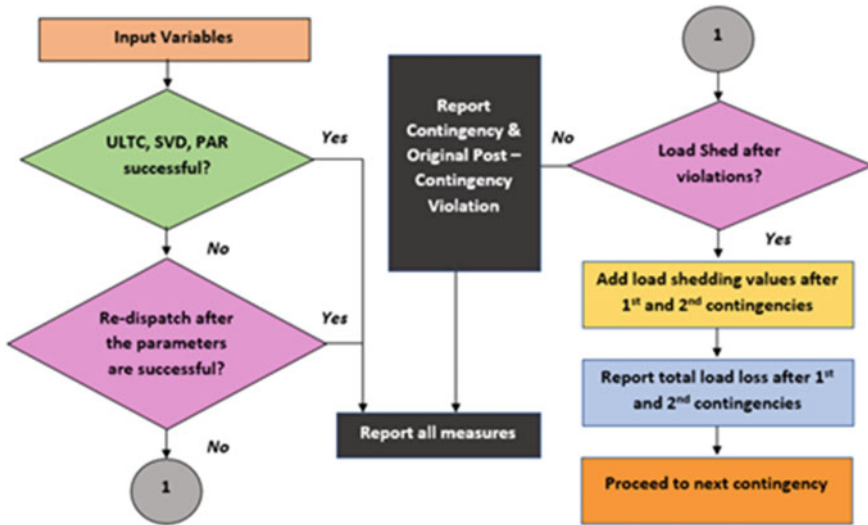


Fig. 7 Flowchart for  $(n - 1)$  contingency mitigation

is the standard  $(n - 1)$  contingency [12]. As the size of generating units evolved over time and reached Giga-watt generation state, this analysis has become an important constraint specially if the generating unit is not a part of the interconnected grid system or the distributive generation system [13].

Mitigation Process Post-First  $(N - 1)$  Contingency

The process followed for mitigation of standard  $(n - 1)$  contingency from the power system involves the following steps as shown in Fig. 7. Input variables such as load tap changing positions, voltage, load tap changers, line-to-voltage, phase angle are given to the system. Stage 2 checks conditions for under-load tap changing; Phase Angle Regulation Singular Value Decomposition is satisfied [14].

**Case 1: Condition Satisfied—Yes**

Result: All the measures are reported by the power system operators and the next step of contingency is evaluated.

**Case 2: Condition Satisfied—No**

Result: The parameters are re-dispatched again and checked if they are successful.

**Case 3: Condition Satisfied—Yes**

Result: All the measures are reported by the power system operators, and the next step of contingency is evaluated.

**Case 4: Condition Satisfied—No**

Result: Check if load shedding has occurred after all the violations.

**Case 5: Load Shedding occurred?—Yes**

Result: Add the load shedding result after the first and the second ( $n - 1$ ) contingency situations. Report total loss of load after the first and the second ( $n - 1$ ) contingencies and proceed to the next ( $n - 1$ ) contingency.

**Case 6: Load Shedding occurred?—No**

Result: Report contingency and original post-contingency violation values and proceed to next ( $n - 1$ ) contingency.

**4.1.2 Challenge 2: Small Amount of Research Conducted on Renewable System Contingency; Hence, Unavailability of Data for Analysis is a Rising Concern Leading to Non-Developed Technologies to Incorporate Mitigation Techniques in the System**

Conduction of small amount of research is a challenge when dealing with contingency analysis. Although data related to climate and climate change for a particular region has been conducted, but lack of research in inter-annual time duration poses as a shortcoming during contingency analysis as the analysis is predominantly based on the previously discussed “what-if” conditions [15].

The lack of research in the domain of vulnerability of variable renewable energy sources is one of the most severe disadvantages since this technique has been put forth as a part of diversification strategies for hydro-dominated systems [16].

**4.1.3 Challenge 3—Requirement of Significant Backup System and Huge Investments**

Contingencies accounting for wind and solar energies are significant as compared to line or generator outage. There is a significant amount of variation when contingency involves unpredictable failure of generator and predictable renewable energy system output [17]. Resources are required to be managed long before they are put into use [18]. This is necessary in order to reduce the gap between the generation and the demand by keeping the existing demand in check and having backups to renewable energy generation such as thermal power plants which are fuel ready and are effective in serving when solar and wind energy generation systems are down due to significant reasons [19–21]. The demand variations are another concern which significantly contributes in the renewable energy generation dips.

#### **4.1.4 Challenge 4: Catastrophic Events as a Part of Renewable Energy Contingencies**

The final challenge of renewable energy contingency is the catastrophic environmental events and natural disasters that result in damage to the transmission line system model (including transmission line towers and poles) resulting in interruption of the supply. With the cascaded system into pictures these days, this interruption can lead to major transmission side fault resulting in tripping of more and more generator models and grid collapsing. Insufficient planning leads to increased vulnerability of the power system components leading to contingency in the system [22]. System with more variable renewable energy sources is more inflexible and fragile, but this nature mainly depends on the nature of the transmission line and distribution line system.

### **5 Technique to Reduce Contingency Possibility in Generation System: Real-Time Data Analysis and Forecasting**

As discussed above, there is a need for reducing the contingency in the generation system. From the analysis conducted above, we have observed that contingency in the generation system occurs due to two possible factors, namely the cells which receive the source energy and the inverter system.

To reduce the possibility of occurrence of contingency in the generation system, a forecasting model that predicts the long-term equipment failure by taking in the real-time data as the input and performing analysis of the input data thereby comparing it with the standard data will prove to be beneficial in reducing the after-effects of contingency in the system. With proper forecasting model results and performing maintenance of the system, occurrence of contingency in the generation system can be reduced to a great extent.

### **6 Conclusion**

In this paper, we have analyzed the real-world data for determining the possibility of contingency in the solar energy generation system. Due to outliers in plots of DC power, AC power, irradiation, and module temperature, a fault is shown in solar cells. Due to the existence of outliers in both the DC power and the AC power, inverter system failures are seen. This paper also serves as a review of role of contingency analysis in renewable energy generation system. The research examines the issues encountered during the contingency analysis of renewable energy producing systems using real-world data from earlier studies. In addition, the forecasting approach that

has been explored to assist decrease contingency in the generating system has been suggested in this study. To raise the system's power quality, the future potential for contingency analysis for solar energy generation is used.

## References

1. Roy A, Jain S (2011) Contingency analysis in power system. Thesis of master of engineering in power systems and electric drives, Thapar University, Patiala. <https://doi.org/10.13140/RG.2.1.4481.4240>
2. Dong H, Cui L (2016) System reliability under cascading failure models. *IEEE Trans Reliab* 65:929–940. Author F, Author S, Author T (1999) Book title. 2nd edn. Publisher, Location
3. Danner P, de Meer H (2021) Location and solar system parameter extraction from power measurement time series. *Energy Inform* 4(Suppl 3):14. <https://doi.org/10.1186/s42162-021-00176-2>
4. Asiedu BA, Hassan AA, Bein MA (2021) Renewable energy, non-renewable energy, and economic growth: evidence from 26 European countries. *Environ Sci Pollut Res* 28:11119–11128. <https://doi.org/10.1007/s11356-020-11186-0>
5. Michopoulos A, Skoulou V (2020) Renewable energy (RES) technologies in building and built environment. Special Issue | Energy Efficiency | Springer
6. Feng W, Yanhong B, Jingjing R, Xiancheng R, Shaofeng L, Wang T (2019) Study on online recognition method of renewable energy cascading tripping evaluation based on machine learning. In: Proceedings of the 2019 4th international conference on power and renewable energy (ICPRE), pp 142–146. <https://doi.org/10.1109/ICPRE48497.2019.9034864>
7. Li N, Hedman KW (2015) Economic assessment of energy storage in systems with high levels of renewable resources. *IEEE Trans Sustain Energy* 6(3):1103–1111. <https://doi.org/10.1109/TSTE.2014.2329881>
8. Wu Y, Ye G, Chang L, Hsieh T, Jan B (2017) Capacity determination of a dynamic energy storage system in an island power system with high renewable energy penetration. In: Proceedings of the 2017 international conference on applied system innovation (ICASI), pp 1698–1701. <https://doi.org/10.1109/ICASI.2017.7988264>
9. Erdiwansyah M, Husin H et al (2021) A critical review of the integration of renewable energy sources with various technologies. *Prot Control Mod Power Syst* 6:3. <https://doi.org/10.1186/s41601-021-00181-3>
10. Jiang Y, Wang G, Roy S, Liu C-C (2016) Power system severe contingency screening considering renewable energy. In: Proceedings of the 2016 IEEE power and energy society general meeting (PESGM), pp 1–5. <https://doi.org/10.1109/PESGM.2016.7741564>
11. Khare SJ, Desai SG (2021) Microcontroller based solar tracking system design and grid connected photovoltaic systems. *Int J Sustain Energy Environ Res* 10(1):1–8
12. Ramesh AV, Li X (2021) Network reconfiguration impact on renewable energy system and energy storage system in day-ahead scheduling. In: Proceedings of the 2021 IEEE power and energy society general meeting (PESGM), pp 01–05. <https://doi.org/10.1109/PESGM46819.2021.9638033>
13. Chattopadhyay M, Chattopadhyay D (2020) Renewable energy contingencies in power systems: concept and case study. *Energy Sustain Develop* 128:25–35. <https://doi.org/10.1016/j.esd.2019.10.006>
14. Maihemuti S, Wang W, Wang H, Wu J, Zhang X (2021) Dynamic security and stability region under different renewable energy permeability in IENGs system. *IEEE Access* 9:19800–19817. <https://doi.org/10.1109/ACCESS.2021.3049236>
15. Xie X, Zhang Y, Meng K, Dong ZY, Liu J (2021) Emergency control strategy for power systems with renewables considering a utility-scale energy storage transient. *CSEE J Power Energy Syst* 7(5):986–995

16. Lamadrid AJ, Mount T, Zimmerman R (2013) On the capacity value of renewable energy sources in the presence of energy storage and ramping constraints. In: Proceedings of the 2013 workshop on modeling and simulation of cyber-physical energy systems (MSCPES), pp 1–7. <https://doi.org/10.1109/MSCPES.2013.6623322>
17. Meneses de Quevedo P, Contreras P, Rider MJ, Allahdadian J (2015) Contingency assessment and network reconfiguration in distribution grids including wind power and energy storage. *IEEE Trans Sustain Energy* 6(4):1524–1533. <https://doi.org/10.1109/TSTE.2015.2453368>
18. Dekeda B, Adonis M (2019) The case for integration of renewables in rail freight yards in South Africa. In: Proceedings of the 2019 international conference on the domestic use of energy (DUE), pp 156–162
19. Tomar A et al (eds) (2022) Proceedings of 3rd international conference on machine learning, advances in computing, renewable energy and communication: MARC 2021, vol 915. Springer, New York, p 781. <https://doi.org/10.1007/978-981-19-2828-4>
20. Ahmad MW et al (eds) (2022) Intelligent data analytics for power and energy systems. Springer, Singapore, p 641. <https://doi.org/10.1007/978-981-16-6081-8>
21. Sahraei-Ardakani M, Li X, Balasubramanian P, Hedman KW, Abdi-Khorsand M (2016) Real-time contingency analysis with transmission switching on real power system data. *IEEE Trans Power Syst* 31(3):2501–2502. <https://doi.org/10.1109/TPWRS.2015.2465140>
22. Toma R, Gavrilaş M (2016) Study on voltage dynamics in power grids with renewable energy sources integration. In: Proceedings of the 2016 international conference and exposition on electrical and power engineering (EPE), pp 760–765. <https://doi.org/10.1109/ICEPE.2016.7781441>

# Digital Twin in Extended Reality Applications for Industry 4.0



Ajune Wanis Ismail, Mohamad Yahya Fekri Aladin,  
and Nur Ameerah Abdul Halim

**Abstract** The technology of extended reality (XR) encompasses three distinct realities: virtual reality (VR), augmented reality (AR), and mixed reality (MR). Industry 4.0 has been defined by the enhancement in the industry that has been fulfilled using the digital information and communication technology. While XR has the potential to enhance and support industry 4.0 in diverse settings, head-mounted displays (HMD) devices are usually used in industry, and users get isolated themselves from the real world when they wear HMD. This chapter discusses the technologies involve in XR. XR allows user to feel the process and to be a part of the design process, especially when it involves interactive simulations and realistic three-dimensional (3D) visualizations. Additionally, the use of XR in conjunction with digital twins (DTs) can help designers examine the quality of surfaces under different lighting conditions. Despite the potential benefits of using XR and DT technologies in industry, presently there are very few papers or chapters that have focused on this topic. Therefore, this chapter presents the overview of XR technologies in industry 4.0, and DT has become the mirrored copy of physical objects in the digital environment. This chapter will discover the fundamentals of the XR applications implementation stages in the industry.

**Keywords** Augmented reality · Extended reality · Digital twin · Virtual reality · Mixed reality · Industry 4.0

---

A. W. Ismail · M. Y. F. Aladin · N. A. A. Halim (✉)  
Mixed and Virtual Reality Research Lab, ViCubeLab, School of Computing, Universiti Teknologi  
Malaysia, 81310 Johor, Malaysia  
e-mail: [new.ameerah@gmail.com](mailto:new.ameerah@gmail.com)

A. W. Ismail  
e-mail: [ajune@utm.my](mailto:ajune@utm.my)

M. Y. F. Aladin  
e-mail: [yahyafekri@gmail.com](mailto:yahyafekri@gmail.com)



# 1 Introduction

Extended reality (XR) technologies typically build upon mixed reality (MR), an immersive technology which is an immersive technology extends the reality by adding digital elements on a user’s surroundings to perform collaborative tasks. Combining AR and VR into one immersive world for new ways of perceiving things can only be achieved through immersion [1]. As defined by [2], MR has two subdivisions which are AR and Augmented Virtuality (AV). New terminology XR has arisen to define AR/VR/MR due these technologies have the capability to extend our reality, to extend sensing and user sixth sense such as touch, vision, hearing, smell, and taste. Figure 1 shows the XR continuum; XR has bounded AR, MR, and VR technologies which these technologies provide a different level of immersion and has the ability to deliver intuitive and natural interaction.

Three-dimensional (3D) images of organs have been rendered and displayed on flat screens have shown MR could help train surgeons [3]. XR across the Fourth Industrial Revolution (Industry 4.0) recently has given massive transformation in the future industrial developments from the conventional method to the digital and physical which has merged together. The advent of VR in the automotive industry has not only reduced the time and capital involved in the design and development of the vehicle [4] but also has enabled collaboration between teams in different locations and domains, thus creating a unified path for shaping better vehicles. The advent of AR/VR combined with the increase in computational power of PCs has influenced the automotive industry in its process of not only designing but also manufacturing, testing, and selling of vehicles [5]. A digital copy or digital twin (DT) can be overlaid, and modifications on the digital models can be done by using AR/VR [6]. This helps in better visualization, and reduces the cost and time consumed in the process. The usage of AR/VR applications for an industrial robot, manufacturing, and automotive industry through handheld devices, smart glass, and touch-screen interaction have superimposed realistic 3D visualizations [7, 8].

Another field that has potentially benefits from using digital twins is the renewable energy sector. In the renewable energy sector, digital twins are becoming increasingly

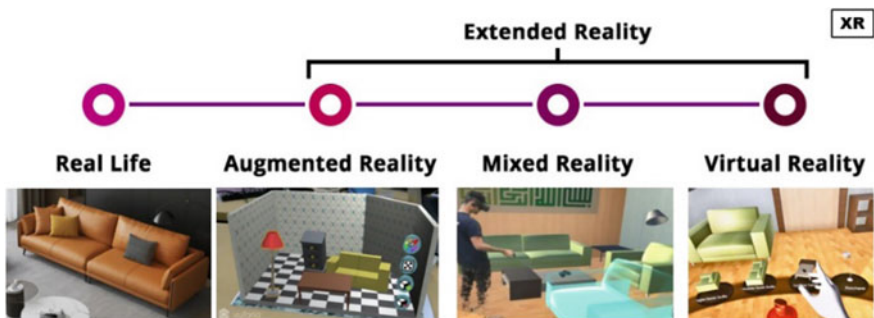


Fig. 1 Extended reality (XR)

popular due to their ability to optimize energy generation and reduce costs. For instance, wind turbines can be equipped with digital twins that can collect and analyze data on wind speed, direction, and turbulence, which can be used to optimize turbine performance and improve energy efficiency [9–11]. In addition, [12] presents an overview of how machine learning methods are utilized in energy systems that are integrated with phase change materials (PCMs). Other than that, [12] has provided an overview of the use of machine learning techniques in energy systems integrated with phase change materials (PCMs). Additionally, solar farms can use digital twins to track the movement of the sun and predict energy output, allowing for more efficient management of energy production within industry 4.0.

Industry 4.0 has been defined by the enhancement in the industry that has been fulfilled using the digital information and communication technology [13]. The next level in automation when the production classifications and simplification using computer technology and with the benefit of having a digital twin on the Internet [14]. Figure 2 shows the assisted reality (ASR) or AR has its digital twin representation [15]. ASR has been frequently used in industries where AR/VR has been functional. DT is a 3D model of products is a key component required in order to accomplish this representation of real object into its mirror digital copy [16]. The activities such as the product design and some other fields are required the real-time representation of physical assets or their mirror 3D images know as digital twin, DT. However, at present, very less papers or chapters have focused on DT with XR in the industry. Therefore, this chapter presents the overview of DT also the XR technologies in 4.0 industries.

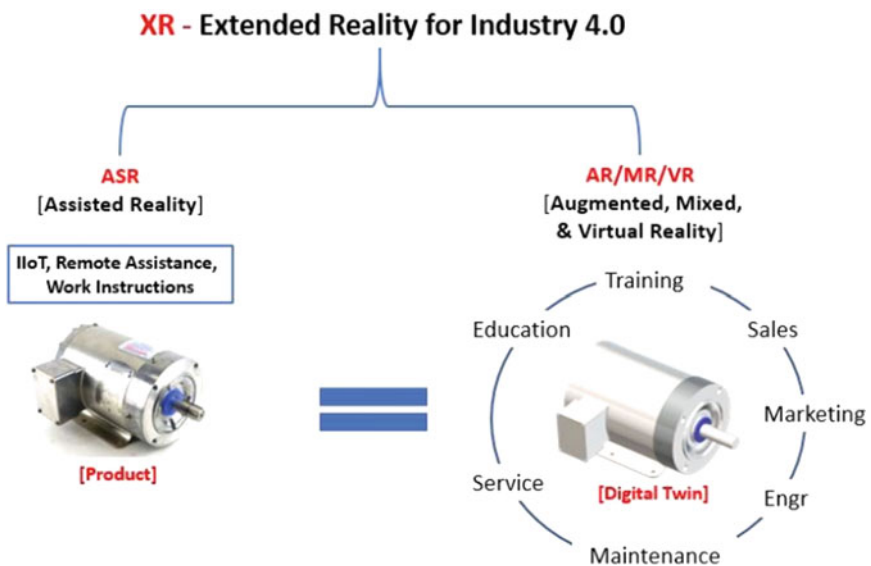


Fig. 2 Digital twins and XR for Industry 4.0 [15]

The integration of digital twins with XR technology can provide a powerful tool for Industry 4.0 by allowing users to visualize, manipulate, and interact with virtual representations of physical objects and systems. This can improve operational efficiency, reduce costs, and enhance productivity. The importance of digital twin in extended reality for Industry 4.0 is attributed to its capability of bridging the divide between the actual world and virtual world, providing a more immersive and interactive experience for users, and ultimately leading to better decision-making and improved outcomes in various industries. Therefore, throughout this chapter, we include several recent researches which have implemented DT in XR applications.

The remaining sections of this chapter are organized as follows. In Sect. 2, we provide the overview of DT in order to recreate the digital copy of industrial products or services. Section 3 reviews the important components to be considered if the industry wants to implement XR. Lastly, Sect. 4 presents our conclusions and outlines potential avenues for future research.

## 2 Digital Twin in XR Applications

DT is at the forefront of the Industry 4.0 because it is digital copy or assets in a VR world. We agreed with the DT concept that has been proposed by [18], and it has three main layers. Grieves [19] defined DT as a twinning in which the physical and virtual states were transferred during the cycle. Twinning enables the transmission of data between the physical and virtual world, as illustrated in Fig. 3. This process involves the transfer of information and operations from the virtual realm to the physical realm and vice versa. Essentially, DT is a framework that incorporates (a) tangible objects in the real world, (b) intangible products in the virtual realm, and (c) data and information that serve as a link between the physical and virtual objects. DT facilitates the acquisition of data in the physical world and its subsequent processing in the digital realm [20].

Data processing happened in digital world depending on the devices chosen by humans such as VR head-mounted display (HMD), and were linked to the DT information. With the devices, the standard interface for accessing the information is required. Next, the selected product types are instantiated, and the identification searching for information relating to them which is encompassed in the DT. Later, the users can access the information. Real-time interaction and modification of the DT is feasible, making it an ideal tool for simulation and testing purposes.

Figure 4 shows the real workstation in Fig. 4a has been replicated as the DT in Fig. 4c, Zed camera integrates with Kinect Azure as in Fig. 4b, has produced MR view. The DT now superimposed by the Zed camera (Fig. 4d, e). The actual user's posture was captured by the Kinect Azure camera, which was coupled to the Zed camera in order to provide an MR experience. The difference between the real user and the virtual manikin, on the other hand, is attributable to imperfections in the motion tracking system and camera calibration.

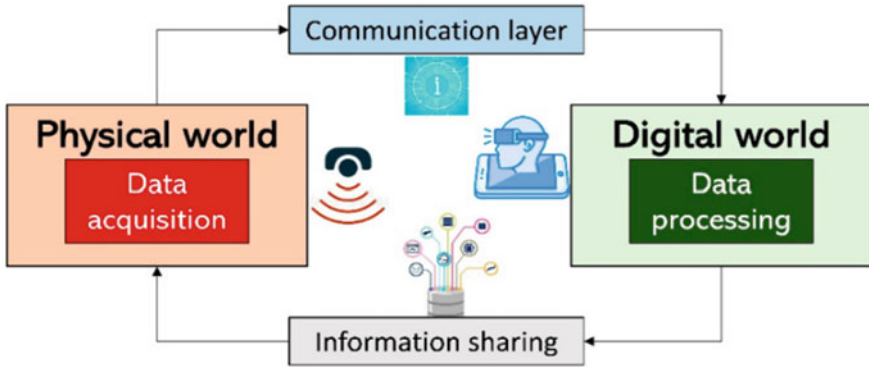


Fig. 3 DT concept in [18]

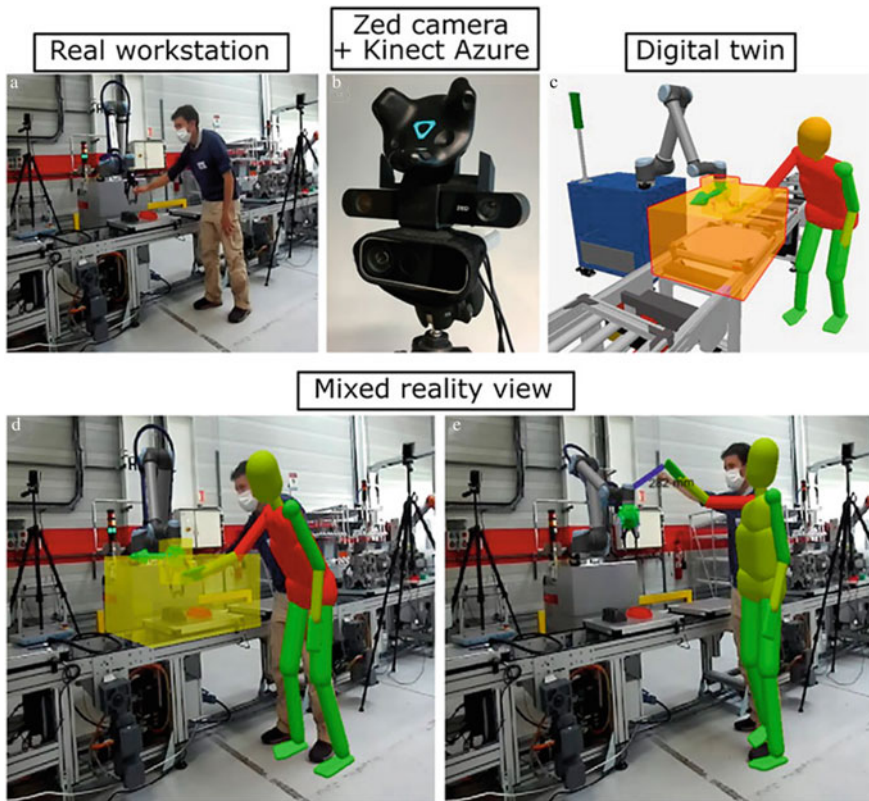


Fig. 4 First use case of MR application view for industry [21]

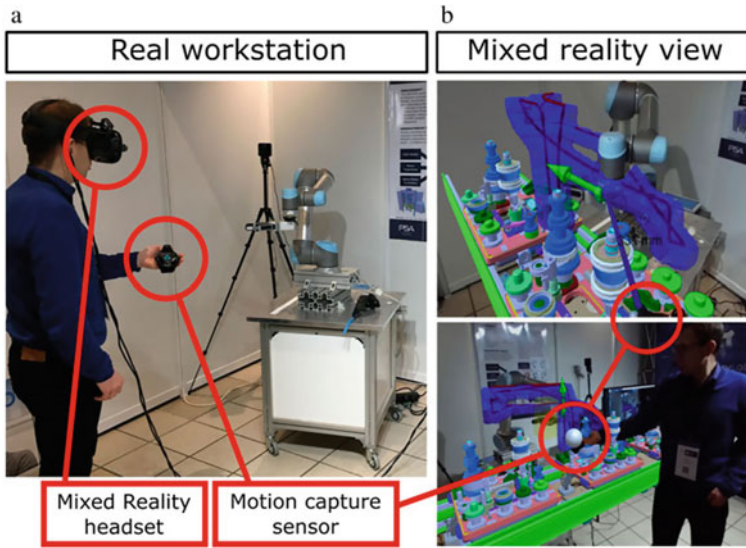


Fig. 5 Second use case of MR application for industry [21]

Figure 5 shows the real workstation with the real user wearing the MR HMD or headset and, on his hands, having the input controller device. Figure 5a is an improved virtual 3D environment with the safety criteria, while in Fig. 5b, the MR perspective of the digital twin where the user is being fully immersed in the environment. MR view requires user to wear a MR HTC Vive headset that attached with Zed mini camera. This way it can offset the real world. The HTC Vive incorporates a single motion capture sensor to track the user’s position. The sensors located on the user’s hand have been used to control or interact with the virtual object.

In Fig. 6, we can see the VR environment, which is different compared to MR because the user uses VR headset as in Fig. 6a, with attached with Zed camera. The result of VR world that viewed by user through VR headset is shown in Fig. 6b, while Fig. 6c presents the complete virtual space.

There are instances where the physical workstation is entirely absent, and the VR environment is entirely virtual. In contrast, MR is only partially immersive. VR creates a complete separation between the user and the real world, immersing them entirely within the virtual environment. In these scenarios, the digital realm is entirely composed of 3D models and avatars, and users experience it once they put on the VR headsets. Figure 7 shows the fourth use case for VR; it can be seen the user has worn VR headset Fig. 7a. The rendered scene has shown in Fig. 7b. VR is a suitable choice when collaborators desire to view the virtual environment from a distinct perspective. However, if the collaborators wish to converse in a face-to-face mode, while simultaneously observing the virtual image without disregarding the physical world, AR is the preferred option. By utilizing the MR interface, it is more feasible to achieve both scenarios.



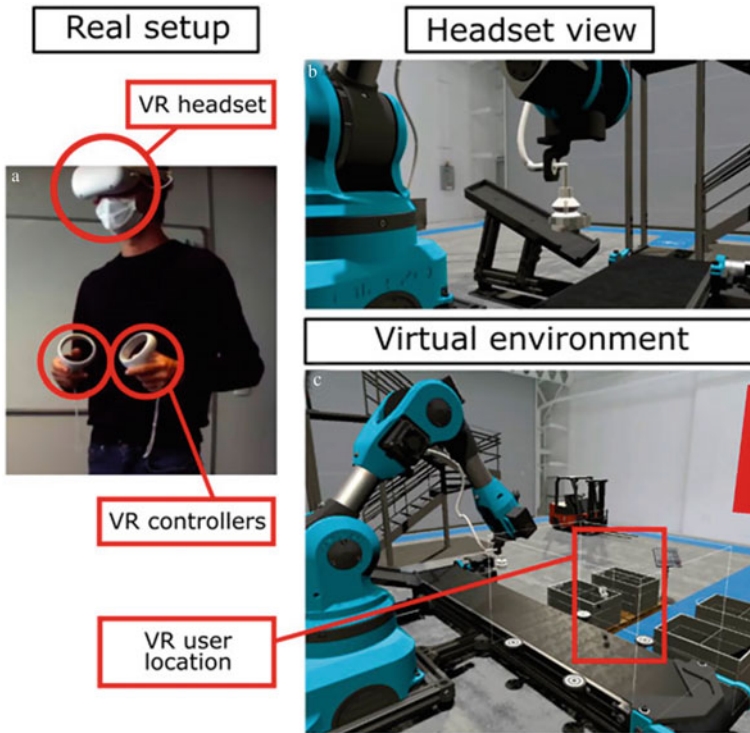


Fig. 6 Use case of VR application [21]

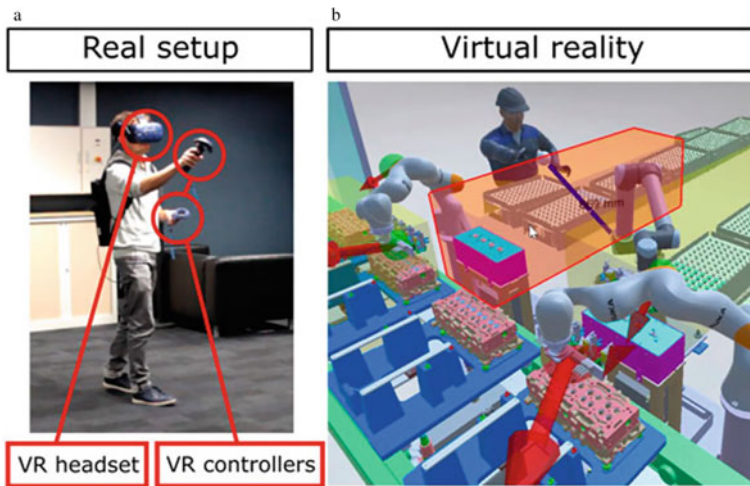


Fig. 7 Use case implemented in VR application [21]

Through the use of DT technologies, the system may continually gather and receive real-time data on the condition and operations of physical systems, which it uses to optimize, simulate, and predict the status of its physical twin in the future [17]. These predictions or optimized setups can be sent to actual devices. As a result, the coordination and management of the physical equivalents of DTs, such as energy converters and renewable energy sources, might be improved, resulting in reduced running costs.

### 3 XR Implementation

There are three fundamentals when designing or developing XR, besides the DT process, the system with the devices tracking and recognition is important. This section discusses the three important components that need to consider if the industry wants to implement XR.

(a) Display and sensing devices





HMD devices have been benefited a lot in most of XR applications. Table 1 shows the differences between Oculus Quest 2 and HTC Vive Pro. Both of these HMD supports full six-degree-of-freedom (6DOF). Their tracker is used for user interaction, but it also can work for motion detection.

The depth sensors (as in Fig. 8) such as Zed camera for MR occlusion-free environment [22] and Kinect Azure for human movement motion detection so the skeleton of human can be tracked in real-time [23]. Currently, these depth sensors are highly capable and can be seamlessly integrated with HMD devices. Figure 9 shows the guideline for workspace setup and apparatus setting, VR, and MR.

(b) Advanced Interaction

Interaction in XR is usually direct designed based on HMD devices. Natural interaction comes with a real hand gesture, and speech can sometimes consider advanced

**Table 1** HMD devices

	Oculus quest 2	HTC Vive Pro
		
Display	Opaque display	Opaque display
movement for activity	Full 6DOF, both rotation and translation 	Full 6DOF, both rotation and translation 

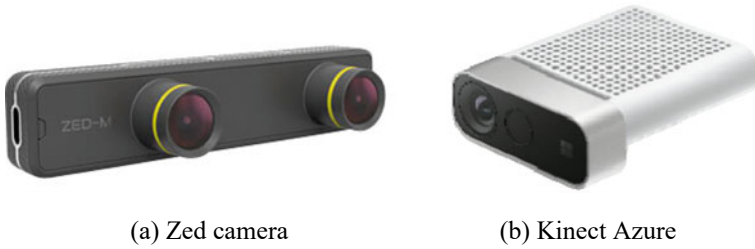


Fig. 8 Depth sensor devices

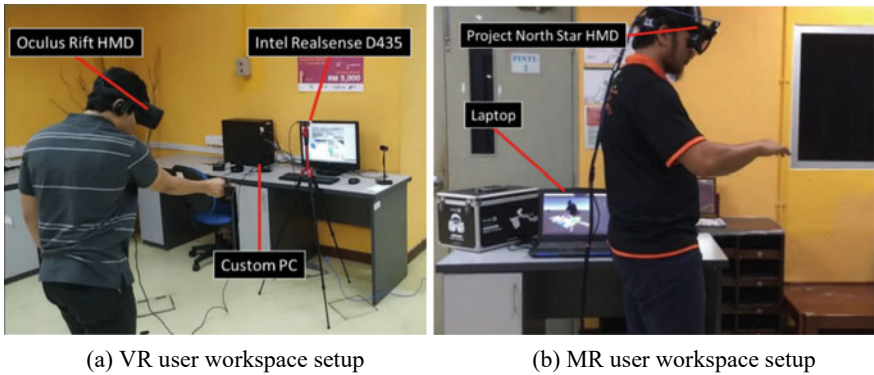


Fig. 9 XR devices setup for VR and MR systems [24]

interaction. Figure 10 shows the two common input devices Leap Motion and Oculus Touch (joystick). The common types of interaction, such as selecting, spawning, translating, rotating, release, and delete the object are presented in Table 2.

As presented in Fig. 11, it shows the interaction diagram from the input devices and sensors, such as Leap Motion or Oculus Touch, serve as a tool for a user to interact with the 3D object. Leap Motion controller understands and tracking human bare hands and creates a virtual hand. The virtual hands to the real hands were an image.

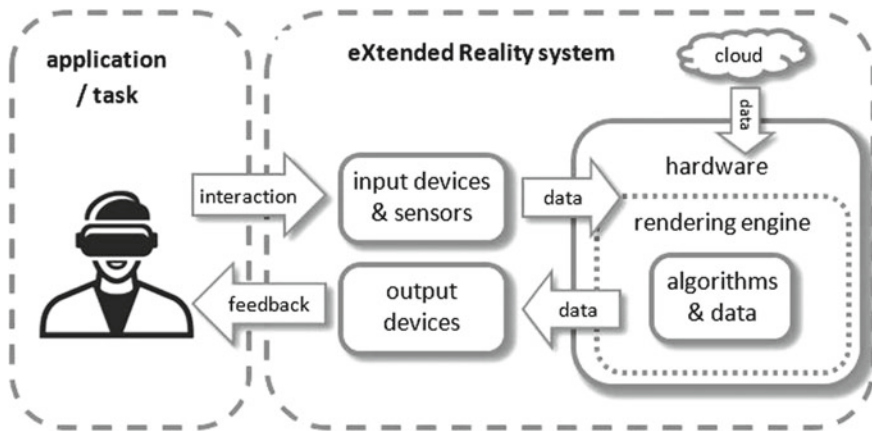


Fig. 10 Interaction input devices example



**Table 2** Common interaction commands

Interaction	Description
Select	Select the object by pressing the button on the Oculus Touch
Spawn	Instantiate the new object in the scene
Translate and Rotate	With the controller that contains motion, user can move the object to translate and change the orientation value for rotation
Release	When user was holding 3D object in hand, release can detach object from user’s hands
Delete	User can choose to erase or remove the object with delete command



**Fig. 11** Interaction in XR

Some hand movements such as tapping, and pinching can therefore be replaced by the virtual hand.

- **Application:** When the information displays on XR interface, user can response and give action. User may need to wear display device or glass headset. The XR application was depending on type of glasses that has been chosen—MR glasses, AR glasses, or VR glasses.
- **Interaction:** The recent devices and sensor user have many ways to interact with the application. However, when current HMD has come with their built-in sensors tracking and controller, it would be more easy to construct interaction techniques.
- **Processing and rendering:** XR environment required computer to render the scene and connect with the XR hardware. To connect more users, network connection is required. For rendering, the popular game engine Unity 3D usually was used.
- **Feedback:** User feedback could alert user that he/she has successfully clicked or pushed the button when the button gives indicator, message or sounds as the feedback.

In the context of the collaborative interface, where involve multi-user interaction, the interface with the sign-in information is required to connect both users, so they can join space. In a remote collaboration, both users need to exist in the same space. Therefore, MR space needs to be built for overlaying the VR user's virtual environment to the actual environment, and the VR environment is needed for projecting both users on the VR side. The application begins to prompt user to enter the pin; the network connection should be stable so both users can available in the same room.

### (c) Interfaces

Interface for the user to view the industry's information and data have to be designed based on the practical reasons or actual events in the industry. In some situations, the event only requires one user, and in some other situations, the industrial application needs more than one user. In this case, the collaborative interface may need to consider. The collaborative interface can bring two or more users into one single environment where they have shared the environment to perform collaboration tasks.

Figure 12 shows the interface when multi-user interactions may involve fundamental components. Networking is a crucial element in connecting the users from the different workspace. Intel Realsense D435 is used to teleport the user from different locations to exist in the application. This situation, there are two separate spaces local users, and remote users were merged. For natural user interaction some situations direct gesture interaction can make sense with the robust tracking device Leap Motion. In VR, if the user uses Oculus HMD, they would use the joystick named as Oculus Touch to perform interaction. An interface needs UI design (User Interface formerly known GUI—graphical user interface), and the database for the resource of the DT (3D model or digital copy of real product) is stored on networking to share with other users.

For users to be able to perform collaborative tasks in a shared space, a stable network is crucial to ensure a real-time shared environment. As depicted in Fig. 12, two clients were designated as local users (Client 1) and remote users (Client 2), and both participated in the shared space to carry out the cooperative tasks. Once both users have successfully entered the space, the input devices have been found such as the controller. The user will manipulate the object and modify the object. All users can see the changes have been made. The 3D data has sent to the cloud, and they can see what they do in real time [25].

## 4 Conclusion

In this chapter, DT and XR technologies for Industry 4.0 have been discussed. Looking at evolutionarily, the rapidly advancing technologies of 5G networks, as well as immersive technologies like AR/VR/MR and digital twins, hold great potential for the development of Industry 4.0, including in the renewable energy sector. A digital copy or digital twin (DT) can be overlaid, and modifications on the digital

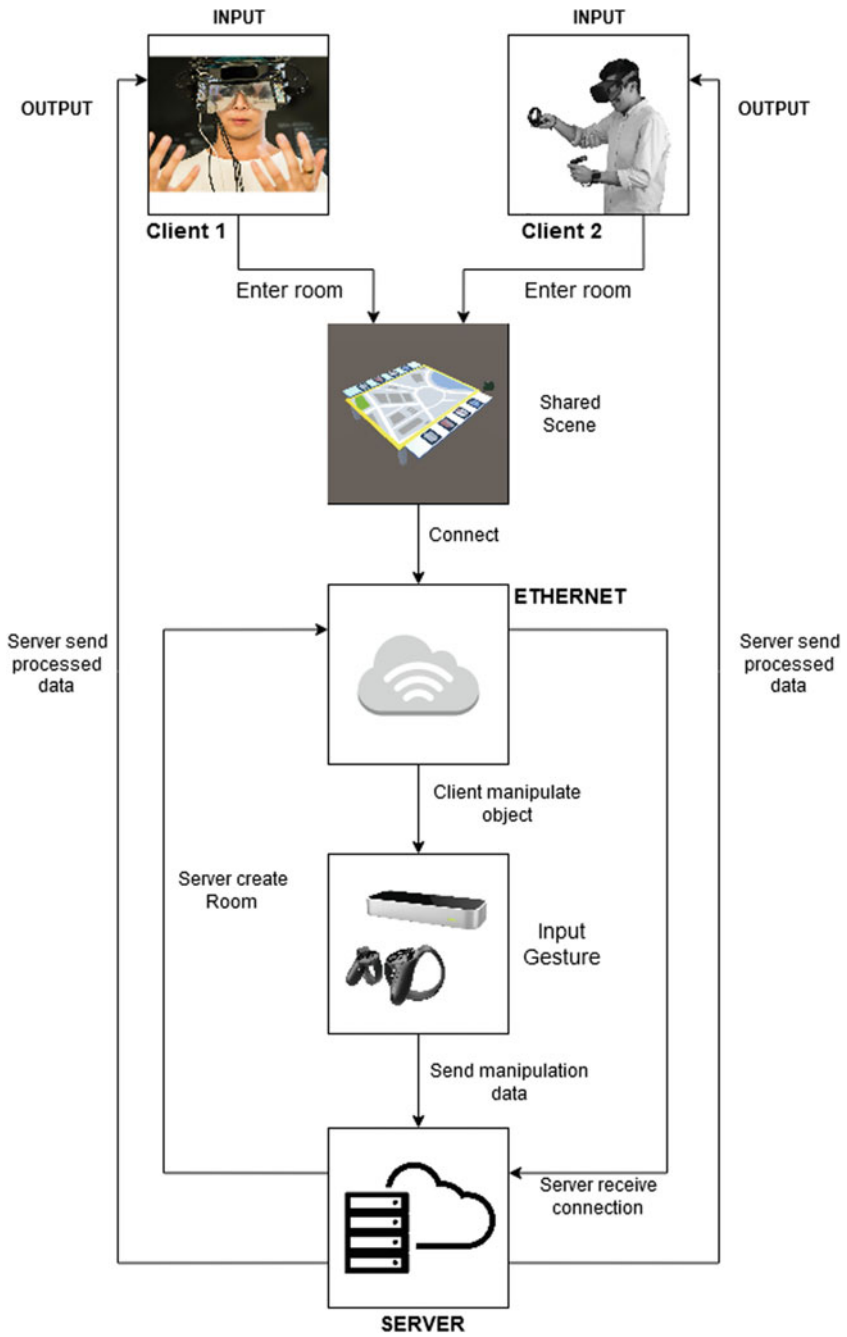


Fig. 12 Collaborative MR interface workflow [24]

models can be done by using AR/VR [6]. This helps in better visualization and reduces the cost and time consumed in the process. The usage of AR/VR applications for an industrial robots, manufacturing, and automotive industry through handheld devices, smart glass, and touch-screen interaction has superimposed the realistic 3D visualizations.

Four use cases have been presented in this chapter, for example, in VR and MR. Compared to VR, the user would fully have isolated from the real world. There are three fundamentals when implementing XR; this chapter has discussed about displays and sensing devices, the interaction, and the interfaces. Collaborative interface has been identified to cover multi-user interaction that would help industrial applications in more advance. Other than that, the wearable AR device such as a HoloLens is going to be the best device to use for these applications since they provide hands-free use. However, in a pinch, a phone or table could be used if the software supports it. When using a VR HMD, hands-free functionality can be achieved by incorporating the Leap Motion device. The fundamental in the XR applications implementation has been described. XR technologies for Industry 4.0 have their potentials to the sustainability; however, there are some barriers such as financial constraints, technical competency and talent to build the application, and digital data security. These constraints can further discuss in the future as a space for more researches, reviews, and surveys.

## References

1. Azuma RT (1997) A survey of augmented reality, presence: teleoperators and virtual environments, vol 6, pp 355–385. Accessed: 23 May 2022
2. Milgram P, Kishino F (1994) A taxonomy of mixed reality visual displays unconscious computing view project using stereoscopic video for defence teleoperation view project a taxonomy of mixed reality visual displays. IEICE Trans Inf Syst 12
3. Venkatesan M et al (2021) Virtual and augmented reality for biomedical applications. Cell Rep Med 2(7). <https://doi.org/10.1016/j.xcrm.2021.100348>
4. Berg LP, Vance JM (2017) Industry use of virtual reality in product design and manufacturing: a survey. Virtual Real 21(1). <https://doi.org/10.1007/s10055-016-0293-9>
5. Pantelidakis M, Mykoniatis K, Liu J, Harris G (2022) A digital twin ecosystem for additive manufacturing using a real-time development platform. Int J Adv Manuf Technol 120(9–10):6547–6563
6. Roldán JJ, Crespo E, Martín-Barrio A, Peña-Tapia E, Barrientos A (2019) A training system for Industry 4.0 operators in complex assemblies based on virtual reality and process mining. Robot Comput Integr Manuf 59
7. Ismail AW, Billinghamurst M, Sunar MS (2015) Vision-based technique and issues for multimodal interaction in augmented reality. In: ACM international conference proceeding series. <https://doi.org/10.1145/2801040.2801058>
8. Yıldız E, Møller C, Bilberg A (2021) Demonstration and evaluation of a digital twin-based virtual factory. Int J Adv Manuf Technol 114(1–2):185–203
9. Pimenta F, Pacheco J, Branco CM, Teixeira CM, Magalhaes F (2020) Development of a digital twin of an onshore wind turbine using monitoring data. J Phys Conf Ser 1618(2). <https://doi.org/10.1088/1742-6596/1618/2/022065>
10. Ebrahimi A (2019) Challenges of developing a digital twin model of renewable energy generators. In: IEEE international symposium on industrial electronics, vol. 2019. <https://doi.org/10.1109/ISIE.2019.8781529>

11. de Koning JDM, Stockman K, de Maeyer J, Jarquin-Laguna A, Vandeveld L (2021) Digital twins for wind energy conversion systems: a literature review of potential modelling techniques focused on model fidelity and computational load. *Processes* 9(12). <https://doi.org/10.3390/pr9122224>
12. Rashidi S (2023) Applications of machine learning techniques in energy systems integrated with phase change materials-A concise review. *Eng Anal Bound Elem* 150:237–245
13. Peças P, Encarnação J, Gambôa M, Sampayo M, Jorge D (2021) Pdca 4.0: a new conceptual approach for continuous improvement in the industry 4.0 paradigm. *Appl Sci (Switzerland)* 11(16). <https://doi.org/10.3390/app11167671>
14. Hu W, Zhang T, Deng X, Liu Z, Tan J (2021) Digital twin: a state-of-the-art review of its enabling technologies, applications and challenges. *J Intell Manuf Spec Equip* 2(1). <https://doi.org/10.1108/jimse-12-2020-010>
15. Agnusdei GP, Elia V, Gnoni MG (2021) Is digital twin technology supporting safety management? A bibliometric and systematic review. *Appl Sci (Switzerland)* 11(6). <https://doi.org/10.3390/app11062767>
16. Tao F, Zhang H, Liu A, Nee AYC (2019) Digital twin in industry: state-of-the-art. *IEEE Trans Industr Inform* 15(4). <https://doi.org/10.1109/TII.2018.2873186>
17. You M, Wang Q, Sun H, Castro I, Jiang J (2022) Digital twins based day-ahead integrated energy system scheduling under load and renewable energy uncertainties. *Appl Energy* 305. <https://doi.org/10.1016/j.apenergy.2021.117899>
18. Vachalek J, Bartalsky L, Rovny O, Sismisova D, Morhac M, Loksik M (2017) The digital twin of an industrial production line within the industry 4.0 concept. In: *Proceedings of the 2017 21st international conference on process control, PC 2017*
19. Grieves MW (2005) Product lifecycle management: the new paradigm for enterprises. *Int J Prod Dev* 2(1–2). <https://doi.org/10.1504/ijpd.2005.006669>
20. Liu M, Fang S, Dong H, Xu C (2021) Review of digital twin about concepts, technologies, and industrial applications. *J Manuf Syst* 58
21. Weistroffer V, Keith F, Bisiaux A, Andriot C, Lasnier A (2022) Using physics-based digital twins and extended reality for the safety and ergonomics evaluation of cobotic workstations. *Front Virtual Real* 3. <https://doi.org/10.3389/frvir.2022.781830>
22. Aladin MYF, Ismail AW (2019) Designing user interaction using gesture and speech for mixed reality interface. *Int J Innov Comput* 9(2). <https://doi.org/10.11113/ijic.v9n2.243>
23. Tölgyessy M, Dekan M, Chovanec L (2021) Skeleton tracking accuracy and precision evaluation of Kinect V1, Kinect V2, and the azure kinect. *Appl Sci (Switzerland)* 11(12). <https://doi.org/10.3390/app11125756>
24. Fadzli FE, Kamson MS, Ismail AW, Aladin MYF (2020) 3D telepresence for remote collaboration in extended reality (xR) application. *IOP Conf Ser Mater Sci Eng* 979(1):012005. <https://doi.org/10.1088/1757-899X/979/1/012005>
25. Vidal-Balea A, Blanco-Novoa O, Fraga-Lamas P, Vilar-Montesinos M, Fernández-Caramés TM (2020) Creating collaborative augmented reality experiences for industry 4.0 training and assistance applications: Performance evaluation in the shipyard of the future. *Appl Sci (Switzerland)* 10(24). <https://doi.org/10.3390/app10249073>

# Deep Image Coding in the Fractional Wavelet Transform Domain based on High-Frequency Sub-bands Prediction



Nadeem Ahmad, Zainul Abdin Jaffery, Irshad, and Shaheen Khan

**Abstract** This paper presents an image coding method using deep convolutional neural networks and the fractional wavelet transform (FrWT) algorithm. FrWT requires less memory than traditional discrete wavelet transform (DWT) methods. During the image transformation from the pixel domain to the wavelet domain, one low-frequency sub-band (LF-sub-band) and three high-frequency sub-bands (HF-sub-bands) are generated. The LF-sub-band is used to predict each HF-sub-band, reducing redundancy between them. The sub-bands are then fed into separate auto-encoders for encoding. Additionally, a conditional probability model is used to estimate the context-dependent prior probability of the encoded codes, improving entropy coding efficiency. A joint framework is used to train the auto-encoders and conditional probability model. Experimental results show that the proposed approach outperforms JPEG, JPEG2000, BPG, and some other neural network-based image coding techniques in terms of multi-scale structural similarity index measure (MS-SSIM). The proposed method generates better visual quality with more precise details and textures due to increased high-frequency prediction. The HF images exhibit average gains of 0.0011, 0.0027, and 0.0049 in MS-SSIM under low, middle, and high bitrates, respectively.

**Keywords** Deep neural networks · Image coding · Fractional wavelet transform · Discrete wavelet transform · Auto-encoder · Entropy coding

---

N. Ahmad (✉) · Z. A. Jaffery · Irshad · S. Khan  
Jamia Millia Islamia, New Delhi, India  
e-mail: [nadeemiete@gmail.com](mailto:nadeemiete@gmail.com).9540615092

Z. A. Jaffery  
e-mail: [zjaffery@jmi.ac.in](mailto:zjaffery@jmi.ac.in)

## 1 Introduction

Among other applications of computer vision and image processing, machine learning has made significant advances in image recognition [1–3], image segmentation [4, 5], and image classification [6, 7]. For the sake of training the network for dimension reduction [8], auto-encoder [9] is utilized in deep image coding. Nevertheless, the shallow auto-encoder is not appropriate for dimension reduction of deep networks because of the limitations of the hardware's ability to do computations. Deep image compression has seen a significant improvement thanks to a model that is built on top of deep neural networks [10] and (CNN) [11, 12]. A DNN-based recurrent neural network for image encoding was proposed for the first time by Toderici et al. [6] and utilized for images of size  $32 \times 32$ , produced a compression ratio that was equal to that of JPEG [7]. This result was achieved by using those images. The current state of the art in deep image coding can be broadly divided into three groups: conceptual image compression [13], end-to-end training of classical auto-encoder [14–17], and recurrent auto-encoder-based coding [15]. Conceptual image compression was first proposed in [15], and end-to-end training of classical auto-encoder was first proposed in [16] by Ballé et al., reference [18] proposed recurrent auto-encoder based image compression.

Encoder, quantization, entropy coding, and decoder are the four primary components that make up a deep image compression strategy. This structure is comparable to that of a conventional image compression approach. The encoder is the part that is responsible for reducing the dimensions of the input data and encoding it in a format that is more compact so that it can be compressed further. The discretization of the continuous values that are represented by encoded codes is accomplished by the lossy process of quantization, which also expresses each code using a finite number of bits. These quantized codes are prepared as the decoder's input, and the decoding process results in image reconstruction at the decoder's endpoints. The codes are further compressed using the lossless entropy encoding procedure. Knowing the prior likelihood of codes helps in computing the entropy.

The four main compression components of deep image compression are linked together via neural networks. Iterative parameter optimization is carried out via the neural network training model. We suggested deep image coding in this study using the fractional wavelet transform and high-frequency sub-band prediction. The trade-off between bit rates and distortion is managed with the aid of this deep model. Instead of using spatial pixels, the deep compression model is developed using features from fraction wavelet transforms. The advantage of a training model based on a fractional wavelet transform is the ability to distinguish between the input image's low- and high-frequency sub-bands. These sub-bands, which are processed based on several parameters, assist in maintaining high-frequency information and result in enhanced quality detail reconstruction. The probability distribution of high-frequency coefficients allows for the modeling of high-frequency coding prior probabilities after FrWT [21]. Neural networks are used to anticipate high-frequency sub-bands based

on low-frequency sub-bands in order to reduce redundancy between the two. The novelty in proposed work is as

- Instead of using the spatial pixel domain, the compression model employs fractional wavelet sub-bands, which has two major benefits.
- In order to process each sub-band according to its own features, the fractional wavelet transformations separate low-frequency and high-frequency information.
- The prior likelihood of high-frequency codes can be modified more easily because of the concentrated probability distribution of high-frequency coefficients produced by the FrWT.
- The model removes redundancy between the two sub-bands and enhances compression by using neural networks to anticipate HF-sub-bands from LF-sub-bands.
- The approach is inspired by wavelet zero tree compression and offers improved quality of detail reconstruction.

The proposed research work is organized further in remaining seven sections. The second section explained the deep image coding, the third section proposed the framework for image coding based on high-frequency sub-bands prediction, the fourth section proposed details about fractional wavelet transform and how its computation is different from conventional wavelet transform, the fifth section explained the details architecture of deep neural network used in the proposed work, the sixth section mentioned the experimental dataset set used for training the deep neural network, the seventh section explained the experimental and comparison results with the state-of-the-art present deep neural network, and the last eighth section explained the conclusion and future scope of proposed work.

## 2 Deep Image Coding

A deep image encoder includes an auto-encoder. This auto-encoder was developed using DNN as both the encoder and decoder. The encoder is responsible for converting the input image into codes, and the decoder is responsible for converting the codes back into the output images with as little distortion as is reasonably possible. In order to develop the very first deep compression model, a recurrent neural network (RNN)-based auto-encoder that underwent progressive training was utilized [16, 17, 19, 20]. This auto-encoder runs through a series of iterations, each of which creates a code that indicates the difference between the reconstructed image and the image that was fed into it. Iteratively adding the previously encoded bits from each recurrence to the total bits helps achieve the goal of producing a growing encoded bit stream. However, because residual value can shift and convergence speed can vary from iteration to iteration; this technique for deep compression was not found to be acceptable for within a single auto-encoder, you will need to make a choice between several alternative residuals. An additional way of deep image compression



was achieved by the utilization of a DNN-based auto-encoder that made use of end-to-end training [14–17, 21]. In this method, the encoder and the decoder do not have any recurrent structures, and encoded bits are simply retrieved from the encoder all at once. This method does not require gradually altering residual in the end-to-end training [14–17, 21], due to the fact that neither the encoder nor the decoder include any recurrent structures and the encoded bits are just immediately retrieved from the encoder. However, because high-frequency information is lost, image textures become overly smooth.

### 3 Proposed Framework for Image Coding Based on High-Frequency Sub-bands Prediction

In Fig. 1 that uses compression, the model is displayed. When the FrWT is applied to input image  $I$ , four sub-bands are created.  $\{I^{(s)}\}$ . Three of the four sub-bands are high-frequency (HF), and one is low-frequency (LF). As shown in Fig. 3, encoding and decoding these four sub-bands require the use of four parallel auto-encoders. Each sub-band goes through a mapping step for latent representation after the encoding phase.  $Y^{(s)}$ , followed by creating codes and the quantization step. Then, at the decoder end as shown in Fig. 2, the inverse mapping begins, producing a reconstruction of sub-bands  $\{Y^{\wedge(s)}\}$  finally, by employing the inverse discrete wavelet transform; we were able to reconstruct the image (IDWT)  $\hat{I}$  from reconstructed sub-bands. The aforesaid process is shown as follows in the following representation:

$$I^{(s)} = \text{FrWT}(I), \quad (1)$$

$$Y^{(s)} = E^{(s)} I^{(s)}, \quad (2)$$

$$Y^{(-s)} = Q^{(s)} Y^{(s)}, \quad (3)$$

$$I^{(-s)} = D^{(s)} Y^{(-s)}. \quad (4)$$

Finally, we were able to rebuild an image from recovered sub-bands using the inverse discrete wavelet transform (IDWT) procedure. The aforesaid process is shown as follows in the following representation  $\hat{I}$

$$Y^{(-s)} = Q^{(s)} Y^{(s)}, \quad (5)$$

$$\hat{I} = \text{IDWT}(\hat{I}^s), \quad (6)$$

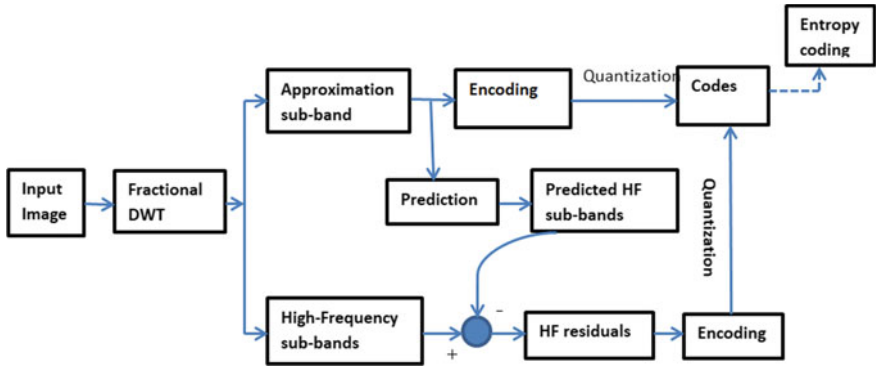


Fig. 1 Encoder

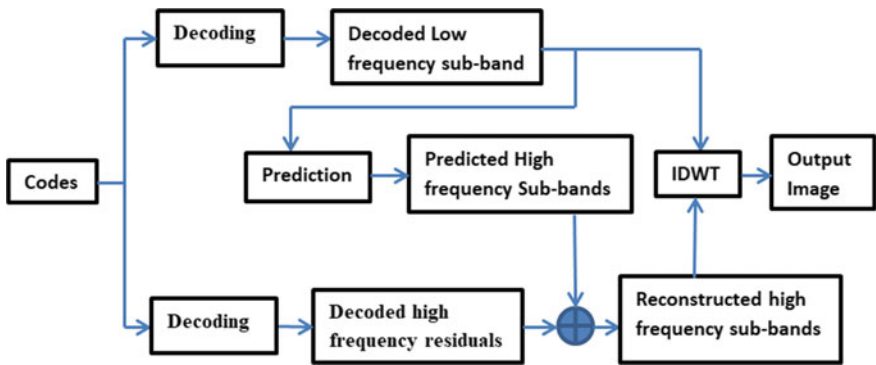


Fig. 2 Decoder

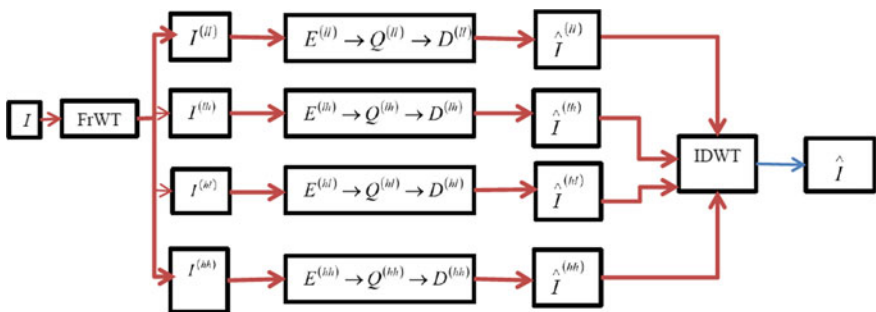


Fig. 3 Sub-bands parallel branches

where  $I^{(s)}$  represents the four sub-band after FrWT. The networks go through the steps listed below to encode and decode the input image:

$$(I^{(LL)}, I^{(H)}) = \text{FrWT}(I), \quad (7)$$

$$\hat{I}^{LL} = D^{LL}(Q^{LL}(E^{LL}(I^{LL}))), \quad (8)$$

$$\hat{I}^H = D^H(Q^H(E^H(r^H))) + P^H \hat{I}^{LL}, \quad (9)$$

$$\hat{I} = \text{IDWT}(\hat{I}^{LL}, \hat{I}^H). \quad (10)$$

Where subscript ( $LL$ ) denotes for LF-sub-band, subscript ( $H$ ) for different sub-bands of high frequency,  $r^{(H)}$  stand for the difference between high-frequency sub-band and residual and its prediction from LF-sub-band, whereas  $P^{(a)}(b)$  is the method for estimating the sub-band (a) frequency based on the sub-band (b). The context-correlated prior probability is calculated with the aid of conditional probability models, which aid in entropy coding to discover the entropy, in order to increase compression effectiveness even more. The probability framework and auto-encoders are trained together, and it is determined that the overall loss function is given by

$$\text{loss} = \text{loss}(P) + \text{loss}(\text{ac}). \quad (11)$$

## 4 Fractional Wavelet Transforms

In order to divide energy efficiently into a small number of low-frequency and small number of high-frequency coefficients, the wavelet transform has the capacity to decorrelate an image both in the spatial and frequency domain. The effectiveness of a wavelet-based image coding method depends on the proper wavelet filters selected and the coefficient quantization scheme. Wavelet transform's basis function is localized in both time and frequency. The need for a large amount of working memory is one of the main challenges in using the typical 2D-DWT to compress deep images. Deep image compression models cannot be used since the computation of image coefficients necessitates maintaining the entire image in memory. The image wavelet coefficients in the DNN-based model are computed using the fractional wavelet transform to get around this issue. In contrast to the traditional method, the fractional wavelet reads one row of an image at a time instead of an entire image from memory in  $M$  to compute the difference between two images.

In our model, FrWT is employed to calculate the coefficients for the low memory image DWT sub-bands. By modifying an end-to-end training model, the four sub-bands branches are trained together. When optimizing back propagation, sub-band

correlations are taken into account. As a result, the effectiveness of the reconstructed image can directly affect how well each sub-latent band’s representation is represented. Additionally, when the networks model and the entropy coding model are combined, the joint framework improves the optimization of bit allocation between sub-bands because it takes into account the optimization of correlation between sub-bands when bit-rate optimization is performed.

### 4.1 A Subsection Sample High-Frequency Sub-bands Prediction in FrWT Domain

It has been discovered that the coefficients of homonymous sub-bands from various stages exhibit high connections, which is motivated by the idea of wavelet zero tree-based image coding. The FrWT decomposition of the image yields LF- and HF-sub-bands. Due to the strong correlation that exists among the coefficients of high-frequency sub-bands at levels one, two, and three, any duplications that might have occurred among the expected homonymous sub-bands have been eliminated. In our proposed model, low-frequency sub-band  $I^{LL}$  decomposed continually by FrWT to produce one low  $I^{LL2}$  and three  $I^{H2}$ . Before or after the wavelet transform, no information is lost because the DWT computation is an invertible operation, and this conclusion can be drawn from the information theory background.

$$X(I^{LL}) = X(I^{LL2}) + X(I^{H2}|I^{LL2}) = X(I^{H2}) + X(I^{LL2}|I^{H2}), \quad (12)$$

where  $X(*)$  represents the self-information and  $X(*|*)$  represents conditional self-information from wavelet-tree theory, sub-band  $I^H$  is predictable by the sub-band  $I^{H2}$  due to the high correlation. As from Eq. (6.11), it is clear that the self-information of  $I^{LL}$  contains all the information of  $I^{H2}$ .  $I^{LL}$  may be utilized to make predictions of  $I^H$ . It is for this reason that we add a high-frequency prediction prior to encoding and that we encode the high-frequency residuals to increase coding effectiveness. Each high-frequency sub-residual bands can be discovered as follows:

$$r^H = I^H - P^H(I^{LL}). \quad (13)$$

During transmission from the encoder to the decoder in a lossy compression codec, some low-frequency data will be lost. Therefore, we can have  $X(\hat{I}^{LL}) < X(I^{LL})$  than there will also be  $X(P^H \hat{I}^{LL}) < X(P^H I^{LL})$ , i.e., some information from the high-frequency prediction will be lost at the decoder when comparing the high-frequency prediction at the encoder end. Before transmitting to the decoder, the encoder has already removed the loss information. An additional network is trained to address this issue together with anticipated high-frequency sub-bands at the encoder side.

The mask produced by these additional networks' training is depicted as having the same size as the forecast.

By  $Z^H$  where  $Z^H \in (0, 1)$  hence before subtracting the high-frequency prediction from  $I^H$  sub-band it is masked by  $Z^H$  and therefore Eq. (6.13) is represented now by

$$r^H = I^H - P^H(I^{LL}) \circ Z^H, \tag{14}$$

where Hadamard product is represented by  $(\circ)$ , which is given by element multiplication. Now high-frequency residuals from (6.14) are feed as input to the HF-encoder  $E^H$  after the prediction process and direct input of the LF-sub-band into the LF-encoder  $E^{LL}$ . The process of prediction of HF at the decoder side also took place as per to the decoded low-frequency sub-bands  $\hat{I}^{LL}$ . When we decode the signal, the format of the prediction network is exactly the same as when we encode it, but it will be without mask network reason being that at decoder side all predictions are used for HF reconstruction. Because of this, the reconstructed HF-sub-band is accomplished by combining the decoded HF residuals and the predictions for HF, which are presented as

$$\hat{I}^H = \hat{r}^H + P^H(\hat{I}^{LL}). \tag{15}$$

### 4.2 Different Sub-bands Auto-encoders

To reconstruct the proper sub-bands at the decoder end, numerous transpose convolutional layers with different strides are used.

### 4.3 Quantization

The system makes use of the non-uniform quantization in its operation. Suppose  $\Omega^{(s)} = \{\omega_1^{(s)}, \omega_2^{(s)}, \dots, \omega_q^{(s)}\} \in R^{1 \times q}$  indicates the centers of quantization for the sub-band. (s). These  $q$  quantization centers are optimized during training.

The 2-norm between filtering procedures is used to compute the outcomes of the quantization process and which can be represented as  $I(z^{(s)})$  and  $\Omega^{(s)}$  denoted as

$$z_i^{(-s)} = Q^{(s)}(I(z^{(s)})_i) = \arg \min_{w_j^{(s)}} \|I(z^{(s)})_i - \omega_j^{(s)}\|_2, \tag{16}$$

where  $i$  stands for each code's index and  $j$  for the quantization center's index.

### 4.4 Entropy Coding

Based on the idea of information entropy, entropy coding is a type of lossless coding where entropy may be applied to determine the bit cost of the codes. The quantized latent representations of the four sub-bands are obtained after the quantization process.

$$= E_{z^{(-s)} \sim p(z^{(-s)})} \left[ \sum_i -\log 2 \left( p \left( z_i^{(-s)} \right) \right) \right]. \tag{17}$$

The place where one’s anticipation the bit cost of  $z^{(-s)}$  is represented by  $E(R(z^{(-s)}))$ .  $i \in \{1, 2, \dots, L^{(s)}\}$  serve as each code’s index, and  $p(z^{(-s)})$  provides the prior likelihood of  $z^{(-s)}$ . In Eq. (17), the goal is to minimize the value of the expected loss as much as possible, which is achieved by training the likelihood model to maximize the likelihood. The cross-entropy loss function is commonly used for this purpose. The cross-entropy loss of the likelihood model can be computed by taking the actual probability  $p_r$  and the output probability  $p$  of the model and doing the following:

$$\begin{aligned} \text{Loss} &= \text{LOSS}_{\text{anecoder}} + \text{LOSS}_{\text{Probability model}} \\ \text{Loss} &= \lambda \cdot D(\hat{x}, x) + \sum_s R(I(z^{-s})) + \sum_s R(z^{-s}) \\ \text{Loss} &= \lambda \cdot D(\hat{x}, x) + \sum_s I(R(z^{-s})) + \sum_s R(z^{-s}). \end{aligned} \tag{18}$$

## 5 Architecture of Neural Networks

A number of models, including the FrWT model, the prediction model, the auto-encoder, and the probability model, are all components of the DNN-based compression system, and the CNN layers that control their development are used to create all of these models (Figs. 4, 5 and 6).

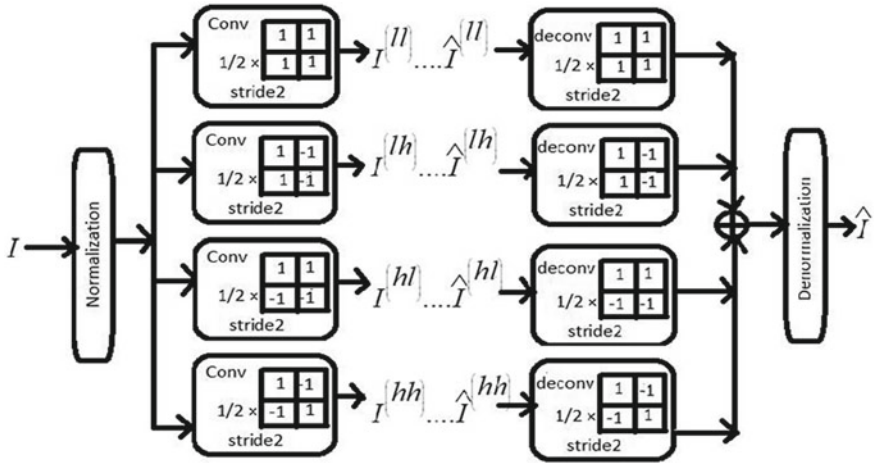


Fig. 4 Convolution implementation of fractional wavelet model

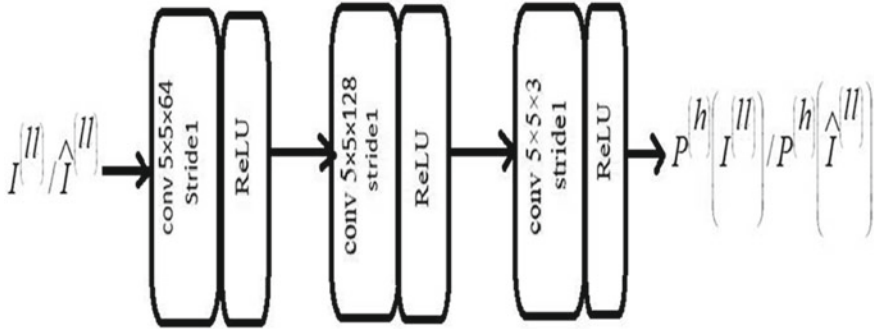


Fig. 5 High-frequency prediction model

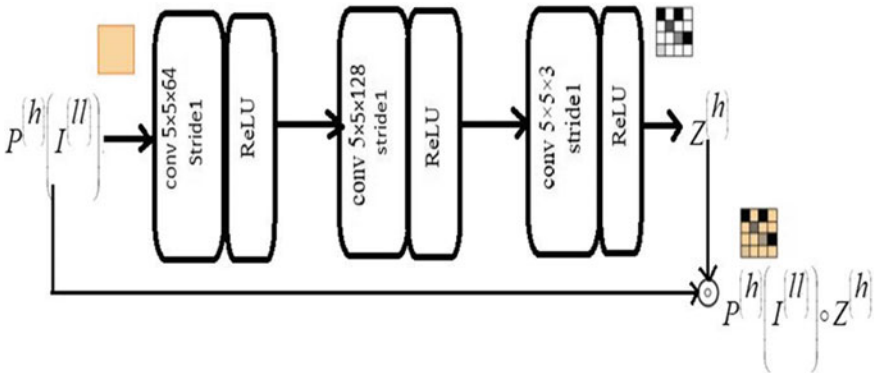


Fig. 6 Mask network architecture

## 6 Experiments

### 6.1 Datasets

The suggested image coding models were developed using roughly 440,000 3-channel RGB images from a subset of ImageNet. To conserve storage, each image that is included in the training dataset is scaled to  $256 \times 256$ . The Kodak Photo CD Image dataset [35] is used to test the models after they have been trained (Fig. 7).

The “conv/deconv  $5 \times 5 \times 64$ ” denotes convolutional or transpose convolutional layer with a kernel size of  $5 \times 5$ , the layer mentioned in the paragraph generates 64 output channels. Each  $N_z(s)$ 's channel count,  $n$ , has a different number depending on the sub-band. It is important to note that all conv and transpose-conv layers have the same padding, which has a value of 0 (Fig. 8).

“Conv3  $5 \times 5 \times 5 \times n$ ” denotes a convolution layer with  $n$  output channels and a 3D-kernel size of  $5 \times 5 \times 5$ , where  $n$  is the channel number of  $N_z(s)$ . Additionally, all of the convolution layers use “SAME” padding with a padding value of  $\omega_1^{(s)}$ .

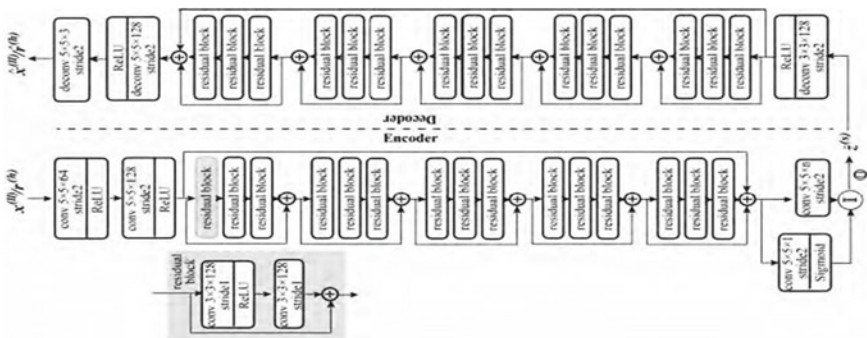


Fig. 7 Auto-encoder’s architecture

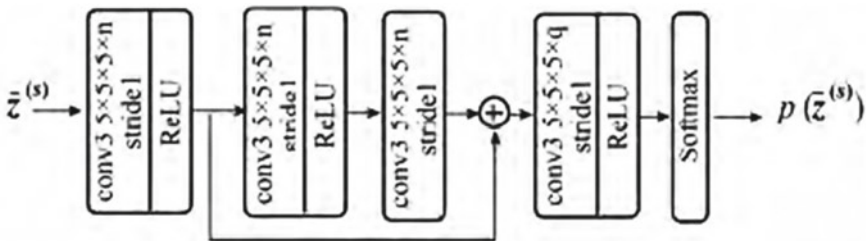


Fig. 8 Probability model’s architecture



## 6.2 Preprocessing Dataset

Random rotation is applied to the training set's images and divided into patches of  $160 * 160$  before being fed into the compression algorithm. We apply z-score normalization the input patch to each channel as part of the normalization process in accordance with the mean and variance obtained from the training set.

$$N(x_c) = \frac{x_c - \text{mean}_c}{\sqrt{\text{var}_c}},$$

where the input patch's various channels are indicated by the subscript  $c$ . Accordingly, the de-normalization of the image obtained by IDWT is applied to the decoder side to create the final reconstructed image.

## 6.3 Distortion Measurements

$D(I, \hat{I})$  reflects the difference in distortion between the input and recovered images. When compared to MSE, it is a metric for quality evaluation that has the potential to more properly reflect the image quality that can be seen by human eyes. The distortion during training is given by

$$D(I, \hat{I}) = 1 - \text{MS\_SSIM}(I, \hat{I}).$$

## 6.4 Parameter Training

The Adam optimizer [18] and a mini-batch size of 25 were used to optimize the model during training. The system's loss function, as indicated in Eq. (18), integrated the losses of the auto-encoder and the likelihood model to enable cooperative training. With a decay factor of 10 applied after every two epochs, the auto-encoder and likelihood model's starting learning rates were set at  $2 \times 10^{-4}$  and  $1 \times 10^{-4}$ , respectively. A bitrate threshold ( $R_t$ ) was designed to guarantee improved precision in managing the bit cost during training. Only when the bitrate loss surpassed  $R_t$  was this level used to impose penalties. As a result, Eq. (18) can be modified as follows:

$$\text{Loss} = \lambda \cdot \left(1 - \text{MS\_SSIM}(x, \hat{x})\right) + \max(R - R_t, 0),$$

where

$$R = \frac{1}{\sum_s L^{(s)}} \sum_s [I(R(z^{-(s)})) + R(z^{-(s)})]/2.$$

To make training easier, the weight parameter ( $\lambda$ ) was set to 100 after calculating the average bitrate loss for each code unit. A total of six models were trained, each corresponding to a specific bitrate ranging from 0.2 to 0.7 bits. During the quantization process, the value of  $q$  was established as 6, with the quantization centers initialized using uniform initialization within the range of  $(-2, 2)$ . To enhance the performance of the auto-encoders, batch normalization [22] was applied after every convolutional and transpose convolutional layer. All models were trained and tested on a GeForce GTX1070 GPU for a period of 6 epochs, which required approximately 30 h to complete.

## 7 Experimental and Comparison Results

The results of the rate-distortion (R-D) evaluations performed on the Kodak PhotoCD image dataset using various compression approaches are presented in Fig. 9. Using a variety of tools to get the results, the efficiency of our compression strategy was contrasted with that of traditional image compression techniques like JPEG, JPEG2000, and BPG. The JPEG2000 Toolbox for MATLAB given by Nikola Sprljan [23] was used to generate the JPEG2000 results, while the JPEG results were produced using the IrfanView program [24]. The results of the BPG were produced using the online BPG codec [25]. On our training set, we trained six models for each approach in order to compare them with [19, 26]. The target bpps stated in Table 1 were matched by these models. It is important to note that the results of these tests allowed us to evaluate the performance of our strategy and assess how effective it was in contrast to other approaches. In terms of bpp and MS-SSIM values, our results showed that our methodology performed better than the traditional methods. In conclusion, our method has shown to be competitive with cutting-edge deep compression techniques and has showed superior compression performance compared to conventional compression methods.

We have obtained the implementation of [19] from the authors and have verified that our experimental results align with the results reported in their paper. To ensure a fair and equitable comparison, we have set the number of codes of  $N^{(s)}$  to be equal in both the models of [19] and our models. This ensures that the same amount of information is carried by each model. It is important to keep in mind that the bpp values shown in Fig. 9 for both the [19] approach and our suggested method were determined using the associated coding models' predicted bit rates. To clarify, our implementation of the compression method outlined in [26] produces results that are consistent with those reported in [26]. The scale parameter of [26] has been set to 4 for all of the models in practical implementation, which is consistent with the scale utilized in our models. As we cannot reproduce the models described in

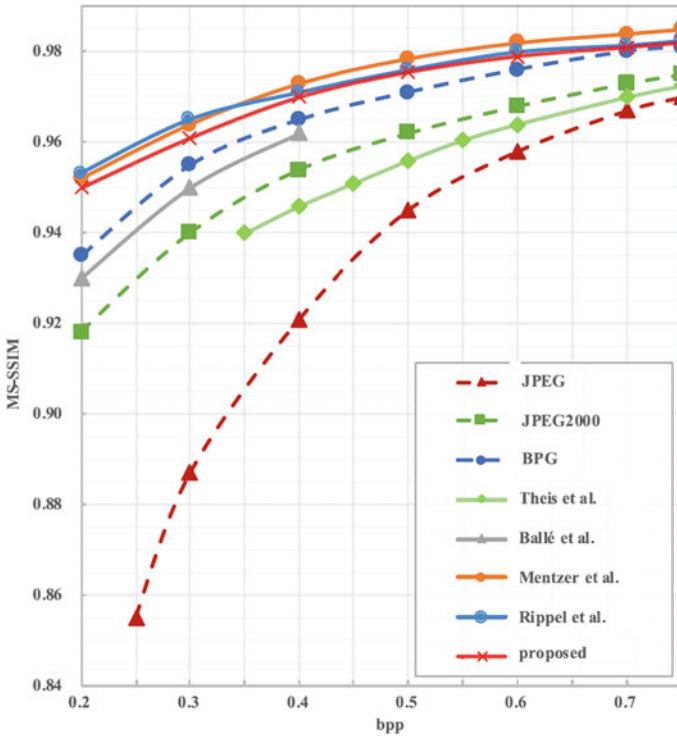


Fig. 9 Ratio-distortion curve for comparison to different methods

Table 1 Models channel allocation

bpp	$n^{(ll)}$	$n^{(lh)}$	$n^{(hl)}$	$n^{(hh)}$
0.2	28	8	8	4
0.3	36	12	12	4
0.4	44	12	12	4
0.5	56	12	12	4
0.6	64	16	16	4
0.7	72	20	20	8

[14, 15], we have collected the corresponding results from the papers based on the Kodak dataset and carefully transcribed them onto our R–D curves to ensure a meaningful comparison. Based on the information presented in Fig. 9, it is evident that the compression approach proposed in this study exhibits better performance than traditional compression methods, such as BPG, JPEG2000 and, specifically in terms of MS-SSIM at low bit rates. The proposed compression approach outperforms the deep compression methods of Ballé et al. [15] and Theis et al. [14], as shown in the comparison results.

While retaining the same level of reconstructive quality, the suggested method for image reduction offers notable improvements in bitrate savings. With up to 27% and 58% bitrate savings, respectively, it performs better than earlier techniques like [14, 15]. Furthermore, when compared to [19], which has pixel-based spatial training and performs better in terms of MS-SSIM, our suggested approach delivers comparable outcomes at the same bit-per-pixel (bpp) rate with just a somewhat lower MS-SSIM score of roughly 0.003. This is as a result of the suggested method's use of wavelet transform compression, which is a better technique for maintaining high-frequency features. When bitrates are higher than 0.4bpp, the results of our suggested method are equivalent to those of [26], especially when it comes to MS-SSIM. The use of adversarial training by [26] results in better performance at low bitrates, though. We compared the suggested methodology to the techniques described in [19, 26] while only comparing high-frequency (HF) images. To compare the models in [19, 26] performance with the suggested method, we breakdown the reconstructed images of [19, 26] using FrWT and produce the HF images in the same manner. The models in [19, 26] are both trained in the pixel domain. MS-SSIM is used to calculate the distortion of HF images. According to Table 2 comparison results, the proposed technique is better in terms of greater MS-SSIM values and lesser bitrates. Our proposed method shows average increases of 0.0011, 0.0027, and 0.0049 when compared to [19] in MS-SSIM of HF image at low, intermediate, and greater bitrates. The HF image of the suggested method shows remarkable MS-SSIM performance particularly for images with intricate features and textures. When HF images are processed using middle and high bitrates, respectively, our suggested approach provides an average gain in MS-SSIM of 0.0032 and 0.0048 in compared to [26]. In addition, our suggested method demonstrates a marginally better reconstruction of high-frequency information than [26] at low bitrates.

The results in Table 2 reveal that the MS-SSIM values of HF images in the methods of [19, 26] only exhibit marginal increases when the overall bitrates grow. As the total bitrates rise, the MS-SSIM values of HF images significantly rise, which indicates that our proposed technique performs significantly better at reconstructing fine details. This shows that the suggested method can recreate complex details precisely, which is important for maintaining image quality. Using different methods at low and high bitrates, Fig. 10 compares certain details visually. The findings for the suggested approach [19, 26] were attained using individual models trained at 0.3 bpp and 0.7 bpp, respectively. In conclusion, the suggested method for image reduction yields notable improvements in bitrate savings while preserving the same reconstructive quality.

## 8 Conclusion and Feature Scope

In this paper, a novel image coding system based on deep convolutional neural networks and the FrWT algorithm are presented. The system utilizes the advantages of FrWT in terms of low memory usage to compute DWT of images, resulting in a

**Table 2** Comparison of reconstructed high-frequency (HF) images using the proposed method with reference [23, 27] based on the MS-SSIM metric

Images	Proposed		Mentzer et al. [19]		Rippel et al. [26]		Wavelet transform	
	bps	MS-SSIM	bps	MS-SSIM	bps	MS-SSIM	bps	MS-SSIM
Kodim01	0.34	<b>0.9785</b>	0.36	0.9741	0.36	0.9757	0.34	0.9750
Kodim02	0.31	<b>0.9908</b>	0.31	0.9901	0.33	0.9903	0.31	0.9905
Kodim03	0.30	<b>0.9945</b>	0.28	0.9941	0.33	0.9943	0.30	0.9925
Kodim04	0.32	<b>0.9917</b>	0.31	0.9915	0.34	0.9915	0.32	0.9907
Kodim05	0.36	<b>0.9835</b>	0.38	0.9829	0.37	0.9831	0.36	0.9825
Kodim06	0.33	<b>0.9831</b>	0.33	0.9811	0.34	0.9813	0.33	0.9821
Kodim07	0.30	<b>0.9952</b>	0.30	0.9951	0.35	0.9953	0.30	0.9932
Kodim08	0.35	<b>0.9789</b>	0.36	0.9751	0.36	0.9770	0.35	0.9759
Kodim09	0.29	<b>0.9935</b>	0.27	0.9931	0.32	0.9934	0.29	0.9925
Kodim10	0.32	<b>0.9935</b>	0.30	0.9928	0.34	0.9936	0.32	0.9915
Kodim11	0.32	<b>0.9871</b>	0.33	0.9856	0.35	0.9862	0.32	0.9851
Kodim12	0.30	<b>0.9925</b>	0.30	0.9918	0.33	0.9919	0.30	0.9915
Kodim13	0.36	<b>0.9685</b>	0.38	0.9675	0.36	0.9666	0.36	0.9625
Kodim14	0.35	<b>0.9848</b>	0.36	0.9844	0.36	0.9842	0.35	0.9828
Kodim15	0.29	<b>0.9923</b>	0.28	0.9921	0.31	0.9921	0.29	0.9913
Kodim16	0.31	<b>0.9886</b>	0.31	0.9871	0.34	0.9874	0.31	0.9856
Kodim17	0.33	<b>0.9930</b>	0.31	0.9929	0.33	0.9932	0.33	0.9910
Kodim18	0.34	<b>0.9850</b>	0.35	0.9848	0.35	0.9844	0.34	0.9830
Kodim19	0.33	<b>0.9881</b>	0.32	0.9864	0.35	0.9867	0.33	0.9851
Kodim20	0.25	<b>0.9929</b>	0.23	0.9925	0.29	0.9929	0.25	0.9919
Kodim21	0.30	<b>0.9879</b>	0.30	0.9871	0.34	0.9872	0.30	0.9849
Kodim22	0.33	<b>0.9879</b>	0.37	0.9874	0.35	0.9874	0.33	0.9849
Kodim23	0.30	<b>0.9959</b>	0.27	0.9962	0.31	0.9963	0.30	0.9929
Kodim24	0.34	<b>0.9855</b>	0.35	0.9850	0.35	0.9963	0.34	0.9833
Ave	0.320	<b>0.9881</b>	0.318	0.9871	0.340	0.9873	0.320	0.9851

reduced memory requirement compared to traditional DWT methods. By utilizing FrWT, the suggested system separates the input image into sub-bands and performs encoding and decoding in the fractional wavelet transform domain, before creating the reconstructed image using IDWT. By using this approach, the system achieves better compression efficiency while maintaining high visual quality. Deep convolutional neural networks are utilized for the encoding and decoding of the sub-bands, and the context-dependent prior probability of the encoded codes for entropy coding is estimated using a conditional probability model. Experimental results show that the proposed system outperforms existing image compression methods, such as JPEG, JPEG2000, and BPG, in terms of SSIM, producing images with clearer details and textures. Therefore, the proposed system has the potential to be useful in applications

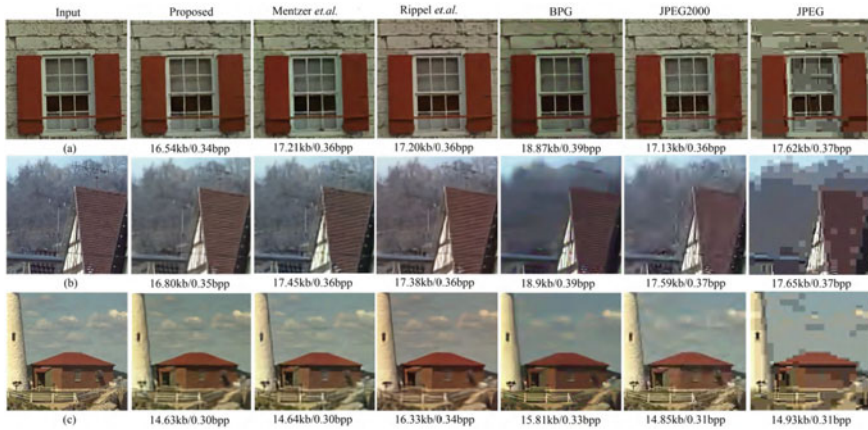


**Fig. 10** Visual comparison of several compression techniques at low bitrates is presented. Panels (a), (b), and (c), respectively, show the information sampled from the Kodak PhotoCD image datasets kodim1, kodim8, and kodim21

where efficient storage and transmission of large image files are required, such as in the fields of medical imaging, remote sensing, and multimedia communications.

## References

- Li R, Lu W, Liang H, Mao Y, Wang X (2018) Multiple features with extreme learning machines for clothing image recognition. *IEEE Access* 6:36283–36294
- Zhou B, Lapedriza A, Khosla A, Oliva A, Torralba A (2018) Places: a 10 million image database for scene recognition. *IEEE Trans Pattern Anal March Intell* 40(6):1452–1464
- Riggan BS, Reale C, Nasrabadi NM (2015) Coupled auto-associative neural networks for heterogeneous face recognition. *IEEE Access* 3:1620–1632
- Yang J, Li S, Xu W (2017) Active learning for visual image classification method based on transfer learning. *IEEE Access* 6:187–198
- Hinton GE, Salakhutdinov RR (2006) Reducing the dimensionality of data with neural networks. *Science* 313(5786):504–507
- Toderici G et al (2016) Variable rate image compression with recurrent neural networks (online). Available: <https://arxiv.org/abs/1511.06085>
- Wallace GK (1992) The JPEG still picture compression standard. *IEEE Trans Consum Electron* 38(1):18–34
- Theis L, Shi W, Cunningham A, Huszer F (2017) Lossy image compression with compressive autoencoders. Palais des Congrès Neptune, Toulon, France, Tech.Rep. ICLR 2017
- Toderici G et al (2017) Full resolution image compression with recurrent neural networks. In: *Proceedings of CVPR*, pp 5435–5443
- Covell M et al (2017) Target-quality image compression with recurrent, convolutional neural networks (online). Available: <https://arxiv.org/abs/1705.06687>
- Zmentzer F, Agustsson E, Tschannen M, Timofte R, Gool LV (2018) Conditional probability models for deep image compression. In: *Proceedings of CVPR*, pp 4394–4402
- Balle J, Laparra V, Simoncelli EP (2016) End-to-end optimization of non-linear transform codes for perceptual quality. In: *Proceedings of PCS, Nuremberg, Germany, Dec. 2016*, pp 1–5

13. Toderici G et al (2017) Full resolution image compression with recurrent neural networks. In: Proceedings of CVPR, Jul. 2017, pp 5435–5443
14. Theis L, Shi W, Cunningham A, Huszár F (2017) Lossy image compression with compressive autoencoders. Palais des Congrès Neptune, Toulon, France, Technical report on ICLR2017, 2017
15. Ballé J, Laparra V, Simoncelli EP (2016) End-to-end optimization of nonlinear transform codes for perceptual quality. In: Proceedings of PCS, Nuremberg, Germany, Dec. 2016, pp 1–5
16. Ballé J, Laparra V, Simoncelli EP (2017) End-to-end optimized image compression. In: Proceedings of ICLR, Aug. 2017, pp 1–27
17. Jiang F, Tao W, Liu S, Ren J, Guo X, Zhao D (2018) An end-to-end compression framework based on convolutional neural networks. *IEEE Trans Circ Syst Video Technol* 28:3007–3018
18. Tausif M, Kidwai NR, Khan E, Martin R (2015) FrWF-based LMBTC: memory-efficient image coding for visual sensors. *IEEE Sens J* 15(11)
19. Mentzer F, Agustsson E, Tschannen M, Timofte R, Gool LV (2018) Conditional probability models for deep image compression. In: Proceedings of CVPR, Feb. 2018, pp 4394–4402
20. Li M, Zuo W, Gu S, Zhao D, Zhang D (2018) Learning convolutional networks for content-weighted image compression. In: Proceedings of CVPR, Mar. 2018, pp 3214–3223
21. Gregor K, Besse F, Rezende DJ, Danihelka I, Wierstra D (2016) Towards conceptual compression. Barcelona, Spain, Technical report NIPS2016
22. Ioffe S, Szegedy C (2015) Batch normalization: accelerating deep neural training by reducing internal covariate shift. In Proceedings of ICML, Lille, France, June 2015, pp 448–456
23. *IrfanView*. Accessed 16 Feb 2019 (Online). Available: <http://www.irfanview.com>
24. *JPEG2000 for Matlab Ver.1.22*. (2016) (Online). Available: <https://github.com/nsprljan/ImageCodingResearchTools>
25. *BPG Format* (2018) (Online). Available: <https://bellard.org/bpg>
26. Rippel O, Bourdev L (2017) Real-time adaptive image compression. In: Proceedings on ICML, Long Beach, CA, USA, Jun, 2017, pp10–19
27. Gregor K, Danihelka I, Graves A, Rezende D, Wierstra D (2015) DRAW: a recurrent neural network for image generation. In: Proceedings of ICML, Jul. 2015, pp 1462–1471

# QIVIFS: Quaternion Approach of Interval-Valued Intuitionistic Fuzzy Sets with Applications in Renewable Energy System



Bhagawati Prasad Joshi, Madan Mohan Sati, Sanjay Oli, Deepak Kumar, Ashish Rayal, and Abhay Kumar

**Abstract** Interval-valued intuitionistic fuzzy sets (IFSs) are more useful than IFSs for modelling incomplete information about real-world issues. This manuscript effort is to incorporate the concept of “quaternion numbers (QNs)” to “interval-valued” IFS (IVIFS) and hence presents the concept of quaternion IVIFS (QIVIFS). These types of QIVIFS can capable of capturing mixed features and express multiple dimensional IVIF information through the interval functions of real-belongingness, imaginary-belongingness, real non-belongingness, and imaginary non-belongingness. Then, the logic operations and order relationships of the QIVIFSs are introduced based on QNs. We also present the distance function for QIVIF numbers. The composite feature of QIVIFS to express multiple dimensional IVIF information is a suitable tool to analyze problems in more details. Finally, we develop an approach for renewable energy system (RES) on the basis of QIVIFSs.

**Keywords** IFS · Interval-valued IFS (IVIFS) · Quaternion numbers · Accuracy function (AF) · Score function (SF) · Certainty function (CF)

---

B. P. Joshi (✉) · M. M. Sati

Department of Mathematics, Graphic Era Hill University, Bhimtal 263136, India

e-mail: [bpjoshi.13march@gmail.com](mailto:bpjoshi.13march@gmail.com)

S. Oli

Department of Mathematics, Dayananda Sagar College of Engineering, Bangalore 560078, India

D. Kumar

Department of Mathematics, Kumaun University Nainital, Nainital 263001, India

A. Rayal

Department of Mathematics, Uttarakhand University, Dehradun 248007, India

A. Kumar

Department of Industrial Engineering, University of Padova, 35131 Padua, Italy



## 1 Introduction

Most of the information is probabilistic and fuzzy while dealing with real-world problems, so that how to model reasonably is an important problem of knowledge representation. To address it, some researchers proposed many theories in the light of the unpredictability and ambiguity of the information, such as Dempster–Shafer evidence theory [1–3], “Fuzzy set” (FS) theory [4], “Rough Set” (RS) theory [5], entropy-based [6], evidential reasoning [7]. Due to these theories which have their own unique advantages, researchers have done a lot of work around them. Focusing on FS theory, Zadeh proposed FS theory in 1965 based on the characteristics of information fuzziness. Several hypotheses have been proposed since then to depict ambiguous information based on FS theory. In 1986, Atanassov proposed intuitionistic FS (IFS) [8]. Relative to FS, IFS values regarded as both belongingness function and non-belongingness function, which enables it to have stronger performance ability when dealing with fuzzy information, so as to describe the ambiguity nature of the physical universe more delicately and avoid information distortion. In 1989, Atanassov and Gargov extended the IFS and set up the conception of interval-valued IFS (IVIFS), by considering its belongingness and non-belongingness in interval forms [9]. The concept of IFS was applied in different approaches [10–15].

In 2002, Ramot et al. [16] presented the complex-FS (CFS). According to the polar illustration of complex numbers, in which the amplitude of the complex number is a fuzzy function and the phase of the complex number is a generic function, this formalism was developed. CFSs are excellent for solving complex problems [17]. Alkouri et al. [18, 19] used complex grades of belongingness and non-belongingness to develop “complex IFS”, a generalization of IFSs and CFSs (CIFS). The initial method for CIFS was based on the Ramot CFS [16]. In a complex plane, the range of the “complex degree” of belongingness is a unit disc. Alkouri and Salleh [20] exemplified the idea by offering a decision-making approach based on the CIFS distance metric.

Garg and Rani build up the notion of the complex IVIF (CIVIF) set [21] and their accompanying aggregation operations, stating that this form can more effectively capture two-dimensional information in a single set. With the addition of “imaginary” parts, this theory not only expands the description space of vague data, but also provides more flexibility. Moreover, Ngan et al. represented CIFS by QNs (IFS-Q), and the first time fuzzy set theory was expressed in “quaternion” form [22]. In this way, the “real belongingness function (BF)”, the “imaginary belongingness function (BF)”, the “real non-belongingness function (NBF)”, and the “imaginary non-belongingness function (NBF)” are each represented by a “quaternion”. As the emergence of “quaternion” numbers, the theory not only increases the amount of space that can be used to describe hazy information, but also makes the expression more adaptable, and it has the ability to both transmit multidimensional information and capture complex aspects. The RES selection issue was discussed by Gupta et al. [23] and was based on the language context of the IFS [23]. The challenge of deciding

where to construct a solar power plant was successfully met by Singh, who came up with a workable solution to the issue [24–26].

In algebra, quaternion is an expansion of complex numbers from two dimensions to three dimensions. Sir William Rowan Hamilton, an Irish mathematician, created quaternions and the rules for their operations in 1843 [27]. As a technique of describing three-dimensional mechanical issues, he invented them. Hamilton conceived of the idea of creating a fourth dimension after a lengthy search for mathematical operations that would maintain the typical characteristics of algebra. This allowed him to maintain the conventional rules of algebra with the exception of the commutative law for multiplication (generally,  $ab = ba$ ), so that the quaternions only form an associative group, more precisely a non-Abelian group. The quaternions are the most well-known and often employed hyper-complex numbers; however, they have been mostly replaced by matrix and vector operations. Unlike the complex number representation, which only has two dimensions, the quaternion number representation has four, allowing it to confine multiple characters and express ambiguous information. In this case, we employ the idea of “quaternion numbers” to merge the degrees of “real belongingness”, “imaginary belongingness”, “real non- belongingness”, and “imaginary non- belongingness” into a single degree of complex membership. These additional degrees of freedom provide a great deal of expressive space and allow for effective handling of ambiguity and uncertainty. Furthermore, as “quaternion” numbers can be expressed in both algebraic and polar form, this methodology offers flexibility in evaluating ambiguous information from many perspectives.

Due to the complication of decision-making difficulties, sometimes it is hard to express judgement in the form of single-valued belongingness and non-belongingness, despite the widespread usage of IFS-Q theory. As a result, an expansion of the existing theories could be very useful for depicting the uncertainties. Therefore, to provide decision-makers with greater flexibility, it is advisable to request that experts define their views using intervals. Motivated by this hypothesis, we present the conception of the quaternion interval-valued IFS in this manuscript (QIVIFS). Belongingness and non-belongingness degrees are expressed in terms of quaternion “interval-valued” according to this suggested theory. Consequently, a QIVIFS is a more extended extension of current theories like FSs, IFSs, IVIFSs, CFSs, CIFSSs, and IFS-Q. In view of the above analysis, we know that the quaternion model of IVIFSs is required to study due to its effectiveness as compared to quaternion model of IFSs. As a result, this manuscript focuses on solving the problem of how to describe interval fuzzy information by uniting the privileges of IVIFSs and quaternion numbers. Therefore, considering this motive, the following contributions are made by this study:

- The conception of quaternion IVIFS (QIVIFS) is proposed by incorporating QNs into IVIFS.
- This QIVIFS can capable of capturing mixed features and express multiple dimensional IVIF information. Therefore, it can be a suitable tool to analyze problems in more details.

- The logic operations and order relationships of the QIVIFSs are also introduced based on QNs.
- The distance function for QIVIF numbers is also established.
- Based on the proposed idea of QIVIFS, we develop an approach for RES selection problem presented.

This study is mainly providing the conception of QIVIFS and to provide a RES selection method under the QIVIFS environment. The manuscript is organized as: Sect. 1 “Introduction” provides background information and the relevant research on the topic, including studies on finding the research gap. The entire approach of the manuscript is presented under section “Proposed Approach”. The preliminaries consisting of some important definitions are presented under Sect. 3. The conception of QIVIFS along with its some important properties is outlined under Sect. 4. Section 5 provides an approach for RES selection based on proposed QIVIFS. Finally, key findings of this study are compiled along with future directions in Sect. 6.

## 2 Proposed Approach

The proposed approach for developing a RESS approach under AIFNs’ environment involves six steps as clearly depicted in Fig. 1. First section “Introduction” provides background information and the literature review presents relevant research on the topic, including studies on finding the research gap, which motivates us to carry this study. The preliminaries consisting of some important definitions are presented under Sect. 3. Section 4 outlines the conception of quaternion IVIFS (QIVIFS) by incorporating the concept of QNs into IVIFS. These types of QIVIFS can capable of capturing mixed features and express multiple dimensional IVIF information. Then, the logic operations and order relationships of the QIVIFSs are also introduced based on QNs. We also present the distance function for QIVIF numbers. The composite feature of QIVIFS to express multiple dimensional IVIF information is a suitable tool to analyze problems in more details. Based on the proposed idea of QIVIFS, we develop an approach for RES selection problem presented in Sect. 5. Finally, key findings of this study are compiled along with future directions.

## 3 Preliminaries

In this part, certain fundamental ideas are presented over the universal set  $X$ . The IVIFS was developed by extending the IFS concept [9] and its definition is given here as:

**Definition of IVIFS** An “IVIFS”  $A$  in  $X$  is characterized by having the following shape:  $A = \{(x, \tilde{\alpha}l_A(x), \tilde{\gamma}l_A(x)) : x \in X\}$ , where the functions  $\tilde{\alpha}l_A(x) = [\alpha l_A^-(x), \alpha l_A^+(x)] \subseteq [0, 1]$  and  $\tilde{\gamma}l_A(x) = [\gamma l_A^-(x), \gamma l_A^+(x)] \subseteq [0, 1]$  [0, 1] are called

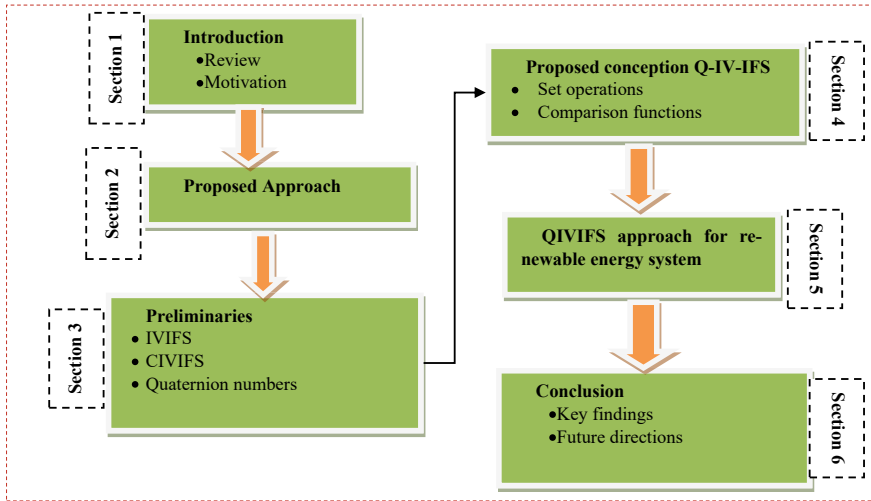


Fig. 1 Framework of presented approach

“interval-valued belongingness degree” and the “interval-valued non-belongingness degree” of  $x \in X$ , respectively, and  $\alpha l_A^+(x) + \gamma l_A^+(x) \leq 1 \forall x \in X$ .

**Definition (CIVIFS)** A “CIVIFS”  $C$  in  $X$  is characterized of the form  $C = \{ \langle x, \tilde{\alpha}l_C(x), \tilde{\gamma}l_C(x) \rangle : x \in X \}$ , where the functions

$$\tilde{\alpha}l_C(x) = [\alpha l_C^-(x), \alpha l_C^+(x)] = [r_C^-(x)e^{iwr_C^-(x)}, r_C^+(x)e^{iwr_C^+(x)}] \text{ and}$$

$$\tilde{\gamma}l_C(x) = [\gamma l_C^-(x), \gamma l_C^+(x)] = [s_C^-(x)e^{iws_C^-(x)}, s_C^+(x)e^{iws_C^+(x)}]$$

are called complex interval-valued belongingness degree and the complex interval-valued non-belongingness degree. Here,  $r_C^-(x), r_C^+(x), s_C^-(x), s_C^+(x) \in [0, 1]$  such that  $0 \leq r_C^+(x) + s_C^+(x) \leq 1$ , and  $wr_C^-(x), wr_C^+(x), ws_C^-(x), ws_C^+(x) \in [0, 2\pi]$  such that  $0 \leq wr_C^+(x) + ws_C^+(x) \leq 2\pi \forall x \in X$ .

**Definition (Quaternion Numbers)** Quaternion Number (QN) is a kind of “hyper-complex number” system, QN  $q$  have four terms: first term is the real part of QN  $q$  and rest three parts are imaginary parts of QN  $q$ . of the form of  $q = \text{Real Part } (a) + \text{Imaginary parts } (b \times i + c \times j + d \times k)$  or  $q = a + bi + cj + dk$ ,  $i, j, k$  are the “quaternion” units of square roots of  $-1$  depicted the multiplication cycle in Fig. 2. QN  $q$  can also be articulated by “Euler’s equation” as:  $q = |q|e^{\hat{n}\theta} = |q|(\cos \theta + \hat{n} \sin \theta)$ ,

where  $|q|$  is the module of  $q$ ,  $|q| = \sqrt{a^2 + b^2 + c^2 + d^2}$ .  $\theta$  is the rotation angle,  $\hat{n}$  is the rotation axis.

In addition,  $q$  can also be expressed as a vector,  $q = [a, b, c, d] = [a, \varpi]$ , where  $\varpi$  is the set of three imaginary part vectors. When  $a = 0$ ,  $q$  is a pure quaternion.

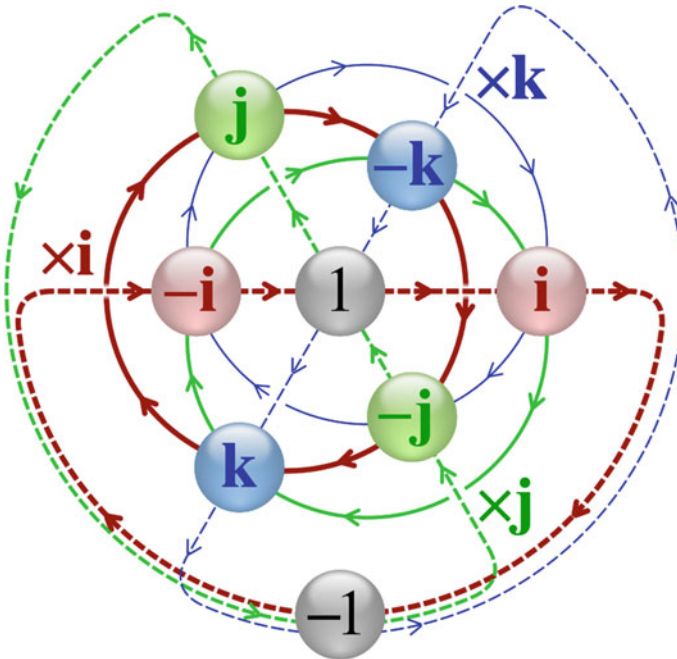


Fig. 2 Depicting the six cycles of  $i, j$  and  $k$  multiplication

Let, there are two quaternion  $q_1 = a_1 + b_1i + c_1j + d_1k = [a_1, \varpi_1]$  and  $q_2 = a_2 + b_2i + c_2j + d_2k = [a_2, \varpi_2]$ , then the following operations are valid:

- Hadamard product:  $q_1 * q_2 = a_1a_2 + b_1b_2i + c_1c_2j + d_1d_2k = [a_1a_2, \varpi_1\varpi_2]$ .
- Specially,  $q_1 * q_1 = q_1^{*2} = a_1^2 + b_1^2i + c_1^2j + d_1^2k = [a_1^2, \varpi_1^2]$ .
- Hybrid operation:  $q_1 \oplus q_2 = a_1a_2 + b_1b_2 + c_1c_2 + d_1d_2$ .
- Sqrt operation:  $\sqrt{q_1} = \sqrt{a_1} + \sqrt{b_1}i + \sqrt{c_1}j + \sqrt{d_1}k = [\sqrt{a_1}, \sqrt{\varpi_1}]$ .

### 4 Quaternion Interval-Valued IFS (Q-IV-IFS)

Let  $\text{Int}([0, 1])$  signify the collection of all “closed subintervals” of the interval  $[0, 1]$ . A quaternion “interval-valued” IFS (Q-IV-PFS)  $A$  in the universal set  $X$  is defined as an object of the form  $A = \{ \langle x, q(x) \rangle : x \in X \}$ , where  $q(x)$  represents the “quaternion function” of the element  $x \in X$  which is defined as  $q(x) = a_x + b_xi + c_xj + d_xk$ . Here, the real-belongingness function (RMF)  $a_x$ , imaginary-belongingness function (IMF)  $b_x$ , real non-belongingness function (RNMF)  $c_x$ , and imaginary non-belongingness function (INMF)  $d_x$  are taken to be closed subintervals of  $[0, 1]$  instead of discrete values in  $[0, 1]$ , i.e.  $a_x, b_x, c_x, d_x \subset [0, 1]$ , where

- $a_x = [\tau_{RM}^-(x), \tau_{RM}^+(x)]$  is the interval of RMF.
- $b_x = [\tau_{IM}^-(x), \tau_{IM}^+(x)]$  is the interval of IMF.
- $c_x = [\varsigma_{RN}^-(x), \varsigma_{RN}^+(x)]$  is the interval of RNMF.
- $d_x = [\varsigma_{IN}^-(x), \varsigma_{IN}^+(x)]$  is the interval of INMF.

Such that

$$\begin{aligned} \sup a_x + \sup b_x \leq 1 &\Rightarrow \tau_{RM}^+(x) + \tau_{IM}^+(x) \leq 1 \\ \sup c_x + \sup d_x \leq 1 &\Rightarrow \varsigma_{RN}^+(x) + \varsigma_{IN}^+(x) \leq 1 \\ \sup a_x + \sup c_x \leq 1 &\Rightarrow \tau_{E}^+(x) + \varsigma_{RN}^+(x) \leq 1 \\ \sup b_x + \sup d_x \leq 1 &\Rightarrow \tau_{IM}^+(x) + \varsigma_{IN}^+(x) \leq 1 \end{aligned}$$

Thus, a Q-IV-IFS  $A$  in the universal set  $X$  can also be defined as

$$A = \left\{ \left\langle x, [\tau_{RM}^-(x), \tau_{RM}^+(x)] + i[\tau_{IM}^-(x), \tau_{IM}^+(x)] \right\rangle + j[\varsigma_{RN}^-(x), \varsigma_{RN}^+(x)] + k[\varsigma_{IN}^-(x), \varsigma_{IN}^+(x)] : x \in X \right\}.$$

**Note:**

1. The quaternion function  $q(x) = a_x + b_x i + c_x j + d_x k$  can also be written as  $q(x) = (a_x + i b_x) + j(c_x - i d_x) = \varphi_{MF} + j\gamma_{NMF}$ . Here,  $\varphi_{MF} = a_x + i b_x$  can be the interval of complex belongingness function and  $\gamma_{NMF} = c_x - i d_x$  can be the interval of complex non- belongingness function.
2. Let we consider  $\Theta$  as the set of all Q-IV-IF numbers defined as

$$\Theta = \left\{ \left\langle [\tau_{RM}^-, \tau_{RM}^+] + i[\tau_{IM}^-, \tau_{IM}^+] \right\rangle : \begin{matrix} \tau_{RM}^+ + \tau_{IM}^+ \leq 1, \varsigma_{RN}^+ + \varsigma_{IN}^+ \leq 1, \\ \tau_{RM}^+ + \varsigma_{RN}^+ \leq 1, \tau_{IM}^+ + \varsigma_{IN}^+ \leq 1 \end{matrix} \right\}.$$

In other words,  $\Theta = \langle \tilde{q} = [\alpha^-, \alpha^+] + i[\beta^-, \beta^+] + j[\gamma^-, \gamma^+] + k[\delta^-, \delta^+] \rangle$  satisfying the following conditions:

1.  $\alpha^-, \alpha^+, \beta^-, \beta^+, \gamma^-, \gamma^+, \delta^-, \delta^+ \in [0, 1]$
2.  $\alpha^- \leq \alpha^+, \beta^- \leq \beta^+, \gamma^- \leq \gamma^+, \delta^- \leq \delta^+$
3.  $[\alpha^-, \alpha^+], [\beta^-, \beta^+], [\gamma^-, \gamma^+], [\delta^-, \delta^+] \subset [0, 1]$
4.  $\alpha^+ + \beta^+ \leq 1, \gamma^+ + \delta^+ \leq 1, \alpha^+ + \gamma^+ \leq 1, \beta^+ + \delta^+ \leq 1.$

Henceforth, it is understood that if  $\tilde{q}_r^{QI} \in \Theta$ , then  $\tilde{q}_r^{QI}$  has the illustration  $\tilde{q}_r^{QI} = \langle [\alpha_r^{QI-}, \alpha_r^{QI+}] + i[\beta_r^{QI-}, \beta_r^{QI+}] + j[\gamma_r^{QI-}, \gamma_r^{QI+}] + k[\delta_r^{QI-}, \delta_r^{QI+}] \rangle$  for  $r = 1, 2, 3, \dots$

### 4.1 Set Operations over Q-IV-IFNs

For two Q-IV-IFNs

$$\tilde{q}_r^{QI} = \langle [\alpha_r^{QI-}, \alpha_r^{QI+}] + i[\beta_r^{QI-}, \beta_r^{QI+}] + j[\gamma_r^{QI-}, \gamma_r^{QI+}] + k[\delta_r^{QI-}, \delta_r^{QI+}] \rangle (r = 1, 2),$$

the following operations are valid:

- (1)  $\tilde{q}_1^{QI} \leq \tilde{q}_2^{QI} \Leftrightarrow \alpha_1^{QI-} \leq \alpha_2^{QI-}, \alpha_1^{QI+} \leq \alpha_2^{QI+}, \beta_1^{QI-} \geq \beta_2^{QI-}, \beta_1^{QI+} \geq \beta_2^{QI+}, \gamma_1^{QI-} \geq \gamma_2^{QI-}, \gamma_1^{QI+} \geq \gamma_2^{QI+}$ , and  $\delta_1^{QI-} \leq \delta_2^{QI-}, \delta_1^{QI+} \leq \delta_2^{QI+}$ .
- (2)  $\tilde{q}_1^{QI} = \tilde{q}_2^{QI}$  when and only when  $\tilde{q}_1^{QI} \leq \tilde{q}_2^{QI}$  and  $\tilde{q}_1^{QI} \geq \tilde{q}_2^{QI}$ .
- (3) **Complement:**  $\tilde{q}_r^{QIc} = \langle [\gamma_r^{QI-}, \gamma_r^{QI+}] + i[\delta_r^{QI-}, \delta_r^{QI+}] + j[\alpha_r^{QI-}, \alpha_r^{QI+}] + k[\beta_r^{QI-}, \beta_r^{QI+}] \rangle$ .
- (4) **Union:**  $\tilde{q}_1^{QI} \cup \tilde{q}_2^{QI} = \left\langle \begin{aligned} &[\min(\alpha_1^{QI-}, \alpha_2^{QI-}), \max(\alpha_1^{QI+}, \alpha_2^{QI+})] \\ &+ i[\max(\beta_1^{QI-}, \beta_2^{QI-}), \min(\beta_1^{QI+}, \beta_2^{QI+})] \\ &+ j[\max(\gamma_1^{QI-}, \gamma_2^{QI-}), \min(\gamma_1^{QI+}, \gamma_2^{QI+})] \\ &+ k[\min(\delta_1^{QI-}, \delta_2^{QI-}), \max(\delta_1^{QI+}, \delta_2^{QI+})] \end{aligned} \right\rangle$ .
- (5) **Intersection:**  $\tilde{q}_1^{QI} \cap \tilde{q}_2^{QI} = \left\langle \begin{aligned} &[\max(\alpha_1^{QI-}, \alpha_2^{QI-}), \min(\alpha_1^{QI+}, \alpha_2^{QI+})] \\ &+ i[\min(\beta_1^{QI-}, \beta_2^{QI-}), \max(\beta_1^{QI+}, \beta_2^{QI+})] \\ &+ j[\min(\gamma_1^{QI-}, \gamma_2^{QI-}), \max(\gamma_1^{QI+}, \gamma_2^{QI+})] \\ &+ k[\max(\delta_1^{QI-}, \delta_2^{QI-}), \min(\delta_1^{QI+}, \delta_2^{QI+})] \end{aligned} \right\rangle$ .

It is straightforward to establish the authenticity of these operations.

### 4.2 Comparison Functions for Q-IV-IFNs

To compare Q-IV-IFNs with one another, we present three new scoring functions called score function (SF), accuracy function (AF), and certainty function (CF). These are defined below:

Let  $\tilde{q}_r^{QI} = \left\langle \begin{aligned} &[\alpha_r^{QI-}, \alpha_r^{QI+}] + i[\beta_r^{QI-}, \beta_r^{QI+}] \\ &+ j[\gamma_r^{QI-}, \gamma_r^{QI+}] + k[\delta_r^{QI-}, \delta_r^{QI+}] \end{aligned} \right\rangle$  be a Q-IV-IFN, then the SF (denoted by  $h(\tilde{q}_r^{QI})$ ), AF (denoted by  $\lambda(\tilde{q}_r^{QI})$ ), and CF (denoted by  $\wp(\tilde{q}_r^{QI})$ ) of  $\tilde{q}_r^{QI}$  can be defined as:

$$\begin{aligned} h(\tilde{q}_r^{QI}) &= \frac{1}{4} \left[ (\alpha_r^{QI-} + \alpha_r^{QI+}) + (\delta_r^{QI-} + \delta_r^{QI+}) \right. \\ &\quad \left. - (\beta_r^{QI-} + \beta_r^{QI+}) - (\gamma_r^{QI-} + \gamma_r^{QI+}) \right] \\ \lambda(\tilde{q}_r^{QI}) &= \frac{1}{2} [(\alpha_r^{QI-} + \alpha_r^{QI+}) - (\beta_r^{QI-} + \beta_r^{QI+})] \\ \wp(\tilde{q}_r^{QI}) &= (\alpha_r^{QI-} + \alpha_r^{QI+}) \end{aligned}$$

The SF, AF, and CF are helpful in assessing and comparing SVAN rankings. Below is a definition of how to compare two Q-IV-IFNs.

**Comparison between two Q-IV-IFNs:** For two Q-IV-IFNs  $\tilde{q}_r^{QI} = \left\langle [\alpha_r^{QI-}, \alpha_r^{QI+}] + i[\beta_r^{QI-}, \beta_r^{QI+}] + j[\gamma_r^{QI-}, \gamma_r^{QI+}] + k[\delta_r^{QI-}, \delta_r^{QI+}] \right\rangle (r = 1, 2)$ , then

- (1) If  $h(\tilde{q}_1^{QI})$  is lesser than  $h(\tilde{q}_2^{QI})$ , then  $\tilde{q}_1^{QI}$  is smaller than  $\tilde{q}_2^{QI}$  and can be expressed as  $\tilde{q}_1^{QI} < \tilde{q}_2^{QI}$ .
- (2) If  $h(\tilde{q}_1^{QI})$  is equal to  $h(\tilde{q}_2^{QI})$  and  $\lambda(\tilde{q}_1^{QI}) < \lambda(\tilde{q}_2^{QI})$ , then  $\tilde{q}_1^{QI}$  is smaller than  $\tilde{q}_2^{QI}$  and can be expressed as  $\tilde{q}_1^{QI} < \tilde{q}_2^{QI}$ .
- (3) If  $h(\tilde{q}_1^{QI})$  is equal to  $h(\tilde{q}_2^{QI})$ ,  $\lambda(\tilde{q}_1^{QI})$  is equal to  $\lambda(\tilde{q}_2^{QI})$  and  $\wp(\tilde{q}_1^{QI}) < \wp(\tilde{q}_2^{QI})$ , then  $\tilde{q}_1^{QI}$  is smaller than  $\tilde{q}_2^{QI}$  and can be expressed as  $\tilde{q}_1^{QI} < \tilde{q}_2^{QI}$ .
- (4) If  $h(\tilde{q}_1^{QI})$  is equal to  $h(\tilde{q}_2^{QI})$ ,  $\lambda(\tilde{q}_1^{QI})$  is equal to  $\lambda(\tilde{q}_2^{QI})$  and  $\wp(\tilde{q}_1^{QI}) = \wp(\tilde{q}_2^{QI})$ , then  $\tilde{q}_1^{QI}$  and  $\tilde{q}_2^{QI}$  represent the same information and can be expressed as  $\tilde{q}_1^{QI} = \tilde{q}_2^{QI}$ .

### 5 QIVIFS Approach for Renewable Energy System (RES)

Too much use and development of fossil fuels have caused problems with the environment and ecology that affect us every day. If we keep using fossil fuels, global warming could happen faster, which would be terrible. Global problems with the environment will have a big effect on how people all over the world use energy in the coming decades. Efforts to cut down on carbon emissions in the future are likely to change how the different types of energy affect the total amount of carbon emissions. Because the air is so dirty, some developing countries are starting to worry more and more about the environment. In this way, clean and renewable energy sources are becoming more appealing as a way to make energy more sustainable and cut pollution.

In this section, a renewable energy system (RES) having multiple wind generation systems (WGSs) is considered to compare WGSs on the basis of several criteria. Let the process is having  $\rho$  WGSs, i.e. alternatives  $\{\rho_1, \rho_2, \dots, \rho_\rho\}$  and  $o$  criteria  $\{o_1, o_2, \dots, o_o\}$  with weight vector is  $\omega = (\omega_1, \omega_2, \dots, \omega_o)^T$  satisfying  $\omega_i > 0, i = 1, 2, \dots, n$  and  $\sum_{o=1}^o \omega_o = 1$ . Let an expert committee provides his preferences of alternative  $\rho_\rho$  against the criterion  $o_o$  which is given by in the form Q-IV-IFNs. The adopted steps are presented below:

Step 1. Construct the Q-IV-IFNs preference table.

$$(\tilde{q}_{ij}^{QI})_{\rho \times o} = \left\langle [\alpha_{ij}^{QI-}, \alpha_{ij}^{QI+}] + i[\beta_{ij}^{QI-}, \beta_{ij}^{QI+}] + j[\gamma_{ij}^{QI-}, \gamma_{ij}^{QI+}] + k[\delta_{ij}^{QI-}, \delta_{ij}^{QI+}] \right\rangle_{\rho \times o} \quad (i = 1, 2, \dots, \rho; j = 1, 2, \dots, o)$$

by using the Q-IV-IFNs information of the alternative  $\rho_\rho (\rho = 1, 2, \dots, \rho)$  against criteria  $o_o (o = 1, 2, \dots, o)$  provided by the expert committee.

Step 2. Utilize the SF, AF, and CF to form the score table  $\hat{S} = \left\{ \hat{S}(\tilde{q}_{ij}^{QI}) \right\}_{\rho \times o} (i = 1, 2, \dots, \rho; j = 1, 2, \dots, o)$  from the preference table.



Step 3. (PIS and NIS): For each criteria, assume the + ve ideal solution (PIS) for the WGSs which is denoted by  $\rho_{\rho}^+ = \{[1] + i[0, 0] + j[0, 0] + k[1]\}$ , and the - ve ideal solution (NIS) for the WGSs which is denoted by  $\rho_{\rho}^- = \{[0, 0] + i[1] + j[1] + k[0, 0]\}$ . Then, find the score table-based separation measures of each WGS from these PIS and NIS, respectively, using the following equations:

$$\Delta_{\rho}^+(\rho_{\rho}^+, \widehat{S}(\tilde{q}_{\rho\sigma}^{QI})) = \text{SQRT} \left( \sum_{o=1}^o [\omega_o(1 - \widehat{S}(\tilde{q}_{\rho\sigma}^{QI}))]^2 \right),$$

$$\Delta_{\rho}^-(\rho_{\rho}^-, \widehat{S}(\tilde{q}_{\rho\sigma}^{QI})) = \text{SQRT} \left( \sum_{o=1}^o [\omega_o \cdot \widehat{S}(\tilde{q}_{\rho\sigma}^{QI})]^2 \right),$$

where  $\text{SQRT} = \sqrt{\quad}$ .

Step 4. Compute the mutual proximity of each WGS with respect to the PIS and NIS using the following equation:

$$\wp_{\rho} = \frac{\Delta_{\rho}^-\{\rho_{\rho}^-, \widehat{S}(\tilde{q}_{\rho\sigma}^{QI})\}}{\Delta_{\rho}^+\{\rho_{\rho}^+, \widehat{S}(\tilde{q}_{\rho\sigma}^{QI})\} + \Delta_{\rho}^-\{\rho_{\rho}^-, \widehat{S}(\tilde{q}_{\rho\sigma}^{QI})\}}.$$

Step 5. The highest value of mutual proximity  $\wp_{\rho}$  is the best WGS.

## 6 Conclusions

This manuscript effort is to incorporate the concept of quaternion numbers to IVIFS and hence presents the concept of Q-IV-IFS. This type of QIVIFS can capable of capturing mixed features and express multiple dimensional IVIF information via the interval functions of “real-belongingness”, “imaginary-belongingness”, “real non-belongingness”, and “imaginary non-belongingness”. Then, the logic operations and order relationships of the QIVIFSs are introduced based on quaternion numbers. We also present the distance function for QIVIF numbers. Overall, the key findings of this study are concluded as below:

- The conception of quaternion IVIFS (QIVIFS) is proposed by incorporating QNs into IVIFS.
- This QIVIFS can capable of capturing mixed features and express multiple dimensional IVIF information. Therefore, it can be a suitable tool to analyze problems in more details.
- The logic operations and order relationships of the QIVIFSs are also introduced based on QNs.
- The distance function for QIVIF numbers is also established.

- Based on the proposed idea of QIVIFS, we develop an approach for RES selection problem presented.

Future works will comprise to establish a series of operators based on different norms and with applications in addressing the engineering and environmental issues.

## References

1. Dempster AP (1968) Upper and lower probabilities generated by a random closed interval. *Ann Math Stat* 39(3):957–966
2. Smith AFM, Shafer G (1976) A mathematical theory of evidence. *Biometrics* 32(3):703
3. Shafer G (2016) A mathematical theory of evidence turns 40. *Int J Approx Reason* 79:7–25. <https://doi.org/10.1016/J.IJAR.2016.07.009>
4. Zadeh LA (1965) Fuzzy sets. *Inf Control* 8(3):338–353
5. Pawlak Z (1982) Rough sets. *Int J Comput Inf Sci* 11(5):341–356
6. Deng Y (2020) Uncertainty measure in evidence theory. *Sci China Inf Sci* 63(11):210201. <https://doi.org/10.1007/s11432-020-3006-9>
7. Almaghribi F, Xu DL, Yang JB (2021) An evidential reasoning rule based feature selection for improving trauma outcome prediction. *Appl Soft Comput*. 103:107112. <https://doi.org/10.1016/J.ASOC.2021.107112>
8. Atanassov KT (1986) Intuitionistic fuzzy sets. *Fuzzy Sets Syst* 20(1):87–96
9. Atanassov K, Gargov G (1989) Interval valued intuitionistic fuzzy sets. *Fuzzy Sets Syst* 31(3):343–349
10. Joshi BP (2019) Pythagorean fuzzy average aggregation operators based on generalized and group-generalized parameter with application in MCDM problems. *Int J Intell Syst* 34(5):895–919. <https://doi.org/10.1002/int.22080>
11. Joshi BP (2016) Interval-valued intuitionistic fuzzy sets based method for multiple criteria decision-making. *Int J Fuzzy Syst Appl* 5(4)
12. Joshi BP, Kumar A, Singh A, Bhatt PK, Bharti BK (2018) Intuitionistic fuzzy parameterized fuzzy soft set theory and its application. *J Intell Fuzzy Syst* 1–7. <https://doi.org/10.3233/JIFS-169805>
13. Joshi BP, Pandey M, Kumar S (2016) Use of intuitionistic fuzzy time series in forecasting enrollments to an academic institution. *AISC* 436
14. Joshi BP, Kumar S (2012) A computational method of forecasting based on intuitionistic fuzzy sets and fuzzy time series. *AISC* 131. [https://doi.org/10.1007/978-81-322-0491-6\\_91](https://doi.org/10.1007/978-81-322-0491-6_91)
15. Joshi BP, Gegov A (2020) Confidence levels q-rung orthopair fuzzy aggregation operators and its applications to MCDM problems. *Int J Intell Syst* 35(1). <https://doi.org/10.1002/int.22203>
16. Ramot D, Milo R, Friedman M, Kandel A (2002) Complex fuzzy sets. *IEEE Trans Fuzzy Syst* 10(2):171–186. <https://doi.org/10.1109/91.995119>
17. Ma J, Zhang G, Lu J (2012) A method for multiple periodic factor prediction problems using complex fuzzy sets. *IEEE Trans Fuzzy Syst*. 20(1):32–45. <https://doi.org/10.1109/TFUZZ.2011.2164084>
18. Alkouri AS, Salleh AR (2012) Complex intuitionistic fuzzy sets. *AIP Conf Proc* 1482(1):464
19. Alkouri AUM, Salleh AR (2013) Some operations on complex Atanassov's intuitionistic fuzzy sets. *AIP Conf Proc* 1571(1):987. <https://doi.org/10.1063/1.4858782>
20. Alkouri AUM, Salleh AR (2013) Complex Atanassov's intuitionistic fuzzy relation. *Abstr Appl Anal*
21. Garg H, Rani D (2019) Complex interval-valued intuitionistic fuzzy sets and their aggregation operators. *Fundam Inf* 164(1):61–101
22. Ngan RT, Son LH, Ali M, Tamir DE, Rishé ND, Kandel A (2020) Representing complex intuitionistic fuzzy set by quaternion numbers and applications to decision making. *Appl Soft Comput*. 87:105961

23. Gupta P, Mehlawat MK, Ahemad F (2022) Selection of renewable energy sources: a novel VIKOR approach in an intuitionistic fuzzy linguistic environment. *Env Dev Sust*
24. Singh S (2023) Knowledge and accuracy measure based on dual-hesitant fuzzy sets with application to pattern recognition and site selection for solar power plant. *Gran Comp*. 8:157–170
25. Ahmad MW et al (eds) (2022) *Intelligent data analytics for power and energy systems*. Springer, Singapore, pp 22, 641. ISBN: 978-981-16-6081-8. <https://doi.org/10.1007/978-981-16-6081-8>
26. Tomar A et al (eds) (2022) *Proceedings of 3rd international conference on machine learning, advances in computing, renewable energy and communication: MARC 2021*, vol 915. Springer Nature, pp 15, 781. ISBN: 978-981-19-2830-7. <https://doi.org/10.1007/978-981-19-2828-4>
27. Hamilton WR (1848) XI. On quaternions; or on a new system of imaginaries in algebra. *London Edinburgh Dublin Philos Mag J Sci* 33(219):58–60. <https://doi.org/10.1080/14786444808646046>

# Feminine Protection Wearable System Based on IoT



**Shubham Kumar Verma, Udai Raj Tiwari, Uttkarsh Rau, Khadim Moin Siddiqui, Sandhya Srivastava, and Jayati Vaish**

**Abstract** Nowadays, women well-being is as vital issue as any developed or developing country. Women security has arisen as one of the main necessities considering what is going on of the urban areas and other huge urban communities. To assist with settling this issue, in this paper, a GPS-based women's security stun gloves are proposed. The fundamental working of this venture is that whenever as women sense risk, all she needs to do and it to hang on the pushbutton of the gadget. When the gadget is enacted, it tracks the location of the women utilizing global situating framework (GPS) and sends crisis messages to currently enlisted portable number and the police control room and the security gadget likewise incorporates alarm, and a shock provider circuit gloves. The heartbeat rate and temperature are additionally shown on a connected liquid crystal display (LCD). The beats sensor checks the beat of casualty, and in strange circumstances, the gadget likewise sends current GPS location to rescue vehicle or enrolled portable number in form of SMS. This security gadget works for self-preservation and counteraction of wrongdoing. In case of unfavorable circumstances, this gadget will behave as shock generators which women can use against aggressors for self-protection. The fundamental benefit of this framework is that this gadget is simple to operate and can be used by any girl or woman for her safety.

**Keywords** Women protection system · Emergency pushbutton · GPS tracker · Self-defense · Stun gloves · Buzzer · Temperature sensor · Heart rate sensor

---

S. K. Verma · U. R. Tiwari · U. Rau · K. M. Siddiqui · S. Srivastava (✉) · J. Vaish  
Shri Ramswaroop Memorial College of Engineering and Management, Lucknow, India  
e-mail: [sandhya@srmcem.ac.in](mailto:sandhya@srmcem.ac.in)

J. Vaish  
e-mail: [jayati.en@srmcem.ac.in](mailto:jayati.en@srmcem.ac.in)

© The Author(s), under exclusive license to Springer Nature Singapore Pte Ltd. 2024  
H. Malik et al. (eds.), *Renewable Power for Sustainable Growth*,  
Lecture Notes in Electrical Engineering 1086,  
[https://doi.org/10.1007/978-981-99-6749-0\\_61](https://doi.org/10.1007/978-981-99-6749-0_61)

911

# 1 Introduction

In the twenty-first century, although technology is developing quickly, women and girls continue to have difficulties due to concerns about their safety. In our nation, women are not allowed to leave their homes at any time, particularly at night in the cities or the countryside. Hence, the technology needed to create a system that can provide protection and safety to the women. Even though this is an independent country, women do not feel safe traveling at night or occasionally even during the day in far-off places. The concept for this research work is based on news about women’s safety that is frequently read in newspapers or seen on news channels. The figures for crime involving them are rising daily which can be seen in Fig. 1.

- (i) Physical abuse of women accounts for almost 10% of all crimes in the nation.
- (ii) Among the estimated 876 million individuals worldwide who are illiterate in both reading and writing, two-thirds are women.
- (iii) Between 2001 and 2011, 30 lakh girl children died as a result of female infanticide.
- (iv) There are still one in three illiterate women in India even after 75 years of freedom.
- (v) In India, just 39.5% of women are employed, compared to 80% in China.
- (vi) 70% of the 1.3 billion individuals who live in absolute poverty worldwide are women.
- (vii) Women make up 10.9% of the population overall, while just 9.3% of agricultural workers (especially men) own land.

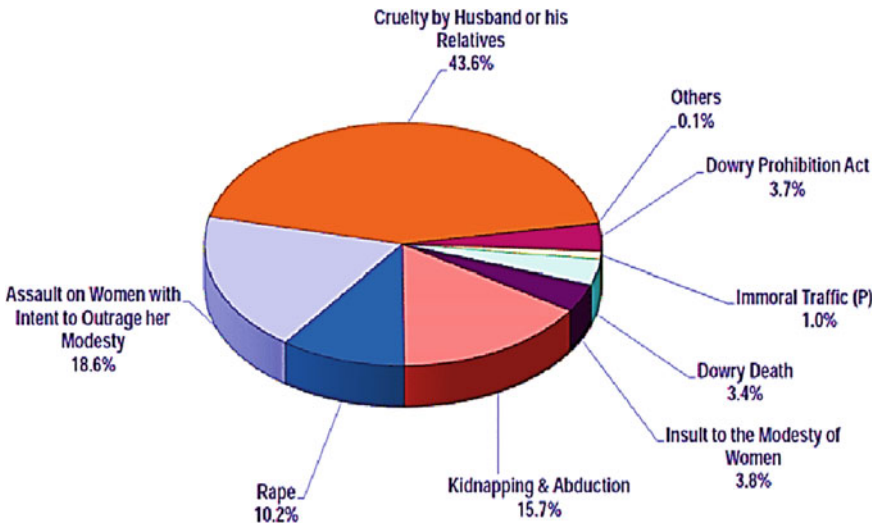


Fig. 1 Statistics of crime related to women

If authors talk about domestic violence, the statistics are as follows:

- (i) 12–15% of victims (women) say they have had their arms twisted, shook, kicked, pulled, beaten up, or had something thrown at them.
- (ii) In India, over two-thirds of married women were victims of domestic abuse, where one serious act of violence resulted in a woman's death.
- (iii) Every seventh woman who has ever been married has experienced bodily harm because of domestic abuse.
- (iv) The first two years of their marriage are when most women have ever encountered marital abuse regarding dowry, status, etc.

These types of incidents are generally carried out by first-time offenders who generally look like students, and hence, it is difficult to track them. Security measures taken by the police department include only monitoring through cameras in and around the city which includes some tips to alert the public only.

In the present time, where technology is more advanced such as global positioning system (GPS) tracker which can be used by government and police to track women in danger. This will not only track the women in danger but also alert the guardian or nearby police station by sending alert message and the location of women in every 2 min. The developed system is 100% secure and will try to overcome majority of the above-said crimes, thereby ensuring the safety of women. Nowadays, many applications are developed for the woman security but the main drawback of these applications are required to detect initial interaction of women and that it is not easily possible.

In this paper, an alternate solution is developed in the form of wearable women smart bands or gloves based on IOT and Android applications. It is an innovative technology that has been designed specifically for the safety and security of women [1–8]. The system consists of a pair of gloves that are equipped with technology and are connected to the Internet through Internet of things (IoT) technology. The wearable gloves are capable of delivering a high-voltage electric shock to an attacker when activated by the wearer. The IoT technology allows the gloves to be remotely monitored and controlled by a central system, providing an added layer of security [8–15]. The issue of women's safety has been a major concern for society for a long time, and with the advancement of technology, there have been efforts to develop innovative solutions to address this problem. The women wearable system based on IoT is a step toward providing women with a tool to protect themselves against physical harm. In this system, the stun gloves are not only a self-defense tool but also a means to alert the authorities and send distress signals in case of an emergency. The gloves are connected to a mobile application that can be activated by the wearer, triggering an alarm and notifying the emergency services. The IoT technology enables the gloves to transmit the wearer's location and other relevant information to the authorities, allowing them to respond quickly and efficiently.

Overall, the women wearable system based on IoT is a promising technology that has the potential to enhance the safety and security of women in various situations. It provides a practical and effective means of self-defense while also enabling women to call for help when needed. In this proposed work, pulse sensor and temperature sensor are also used to determine the real-time pulse and heartbeat data of women in danger. The proposed system is wearable and consists of advanced sensors and signal danger. The proposed system can also be used as a self-defense system which consists of shocks generator. The severity of shock is intense enough to scare the attacker away [1, 2]. This watch protects women or children during any vulnerable attack. The proposed watch works on the concept of heartbeat. Later, many devices were developed for safety purposes. They are as follows.

A ‘smart band’ is reported in [3] for the protection of women. The smart band continuously communicates with smartphone that must have access of Internet. A ‘Smart Girls security system’ has been reported in [4] for providing the security of women. It works on the pressure-based sensor. An IoT-based smart device is reported in [5] for providing security of women. This device sends the location of woman when she is in problem. It works on GPS and GSM systems. A smart intelligent security system for women is reported in [6]. In this work, the Raspberry Pi 2 controller was used. This technique gave protection for women via tear gas and live streaming video.

The inclusion of ‘Women Empowerment’s’ is one of the prime goals in the eight-millennium development. Goals underscore the relevance of this fact. Thus, in order to achieve the status of a developed country, India needs to transform its women forces into an effective human resource, and this is possible only through the safety and security of women.

The layout of paper is divided into five sections. Section 1 covers the introduction of the proposed safety device. The objective of the work is explained in Sect. 2. In Sect. 3, the methodology of the work is explained. The hardware implementation and results are covered in Sect. 4. The conclusion of the work is covered in Sect. 5.

## 2 Objective of the Work

In this work, a device has been developed for the women safety purpose. The objective of the proposed work is as follows:

1. The proposed device will intimate the parents and police about the current location of the women with the help of GPS system, and the GSM technology was also used to send messages in the pre-defined numbers.
2. In this work, a device has been used to give a tolerable current shock to culprit.
3. In our proposed system, an alarm device has also been used to warn neighbors.

4. The system has a GPS receiver, an umbrella controller, GSM modem, and GPS receivers for specific function purpose. Basically, the GPS system will be used to send the location of women, and GSM system will be used to send messages on the pre-defined numbers.
5. The suggested system contains security features that can assist women in need by allowing them to track emergency callers and provide information via notifications during situations by pushing the device's button right away. GPS tracking will be used to send updates on the victim's whereabouts to neighboring family members and police stations.

### 3 Methodology of the Work

The functional block diagram of the safety device is shown in Fig. 2. The solar panel and battery have been used for power backup. The solar panel will keep battery charged. The Arduino unit controller has been used for effective controlling purpose. The GPS module will send location of the victim, and GSM unit will send the message on the pre-define numbers. The temperature sensor will measure temperature of the victim, and heartbeat sensor will measure heartbeats of the victim. If both values will be more than the specified normal conditions, then the GSP module will send the location and message to the nearby police station and relatives. The buzzer is used for alarm purpose. The main novelty of this work is to provide a panic switch. When victim is in danger at that time, she can press panic button and culprit will get a current shock which will be unconscious for some moments. LCD display will be used for displaying purpose.

The electric shock in wearable gloves block diagram is shown in Fig. 3. In this system, a 9 V battery is used with resonator circuit and HFC transformer. This system will produce electric shock in case of emergency conditions [14, 15].

One can understand the operation of developed prototype from Fig. 4. The complete prototype can be understood via project flow diagram and shown in Fig. 5. The detailed operation is presented through the following chart in Fig. 6.

### 4 Hardware Implementation and Result Analysis

The proposed safety gadget is a cutting-edge instrument for offering security to women. This device is effective in determining a woman's real-time data, including her temperature, heartbeat, and GPS position. 38 °F and 75 beats per minute are the device's default settings. If these conditions alter in an emergency, a buzzer will turn on. Once it is turned on, it will use GSM to transmit the message to the police and any known relatives. Via a GPS location tracking gadget, the women's present location was included in the message. The gadget will record and display the temperature and heartbeat on the LCD display panel as shown in Fig. 7 when it is turned on and



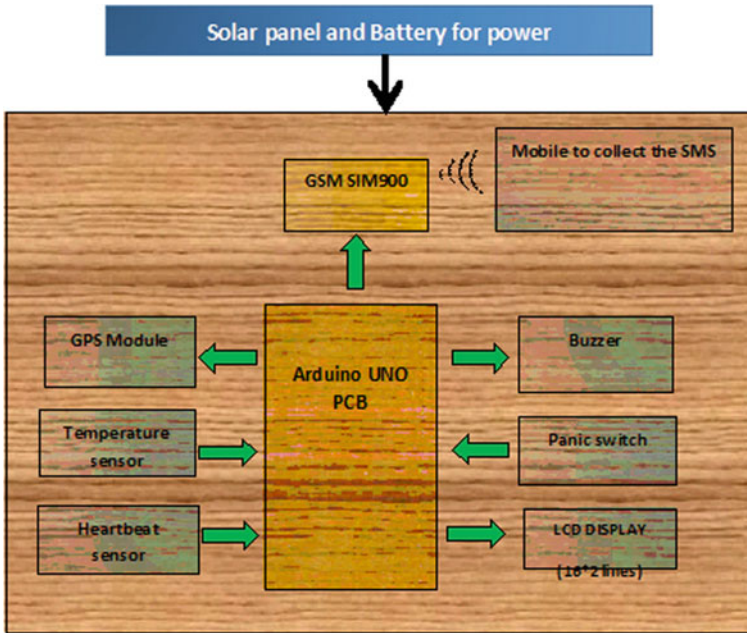


Fig. 2 Functional block diagram of the system



Fig. 3 Electric shock in stun gloves

in contact with the female body. This will demonstrate whether or not the women's condition is critical.

If a situation calls for an emergency, the women can press the shock button for their own safety. Also, the gadget contains a siren button that can alarm others in the immediate area. Also, if a gadget is switched ON by default, it may send a deactivation message or alert to the police or family members. The hardware prototype for an electric shock cannon is shown in Fig. 8. Figure 9 depicts the entire design of the wearable women safety device.

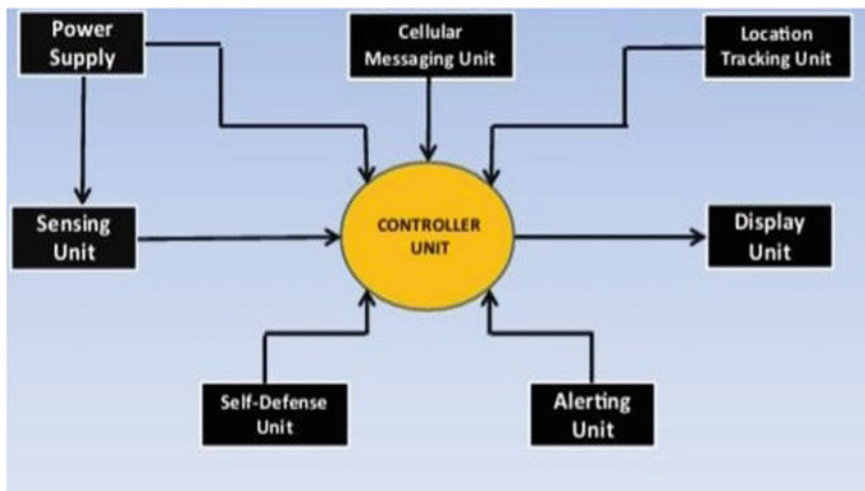


Fig. 4 Operational diagram of women safety device

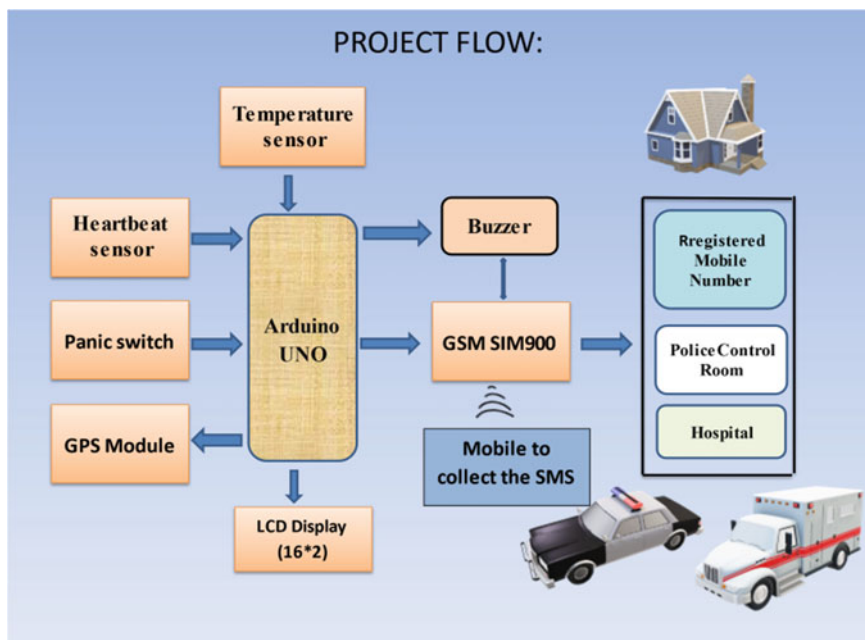


Fig. 5 Project flow diagram



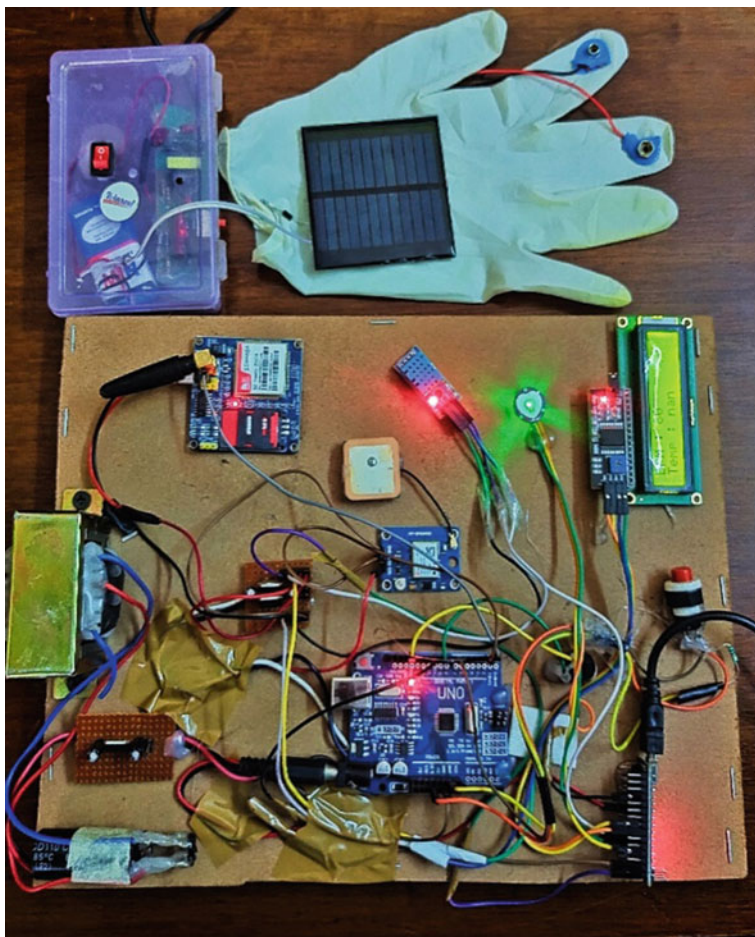


Fig. 7 Prototype of stun gloves-based protection system



**Fig. 8** Electric shock gun implementation



**Fig. 9** Prototype testing of shock circuit gloves

## 5 Conclusion

The development of women wearable safety device is a significant step toward addressing the issue of women's safety in public spaces. The smart gloves, which are equipped with IOT technology, provide a non-lethal defense mechanism that women can use in case of an emergency. The wearable safety device has the potential to empower women and gives them greater confidence to navigate public spaces without fear. The women safety device is discreet, easy to use, and can be worn as a regular accessory, making them a practical and accessible solution for women's safety. While the device offers a promising solution, there are still concerns that need to be addressed, such as the risk of misuse and the legal implications of using shock technology. It is important to ensure that the use of these smart safety devices is regulated and that they are only used in situations where self-defense is necessary.

Overall, women wearable safety device is a step in the right direction toward creating a safer world for women. As technology continues to advance, more innovative solutions that will help women will be developed so that they can feel more secure and protected in public spaces. It is important to continue to invest in the development of such technologies and to work toward creating a more inclusive and safe society for all.

## References

1. Karri V, Daniel Lim JS (2005) Method and device communicate via SMS after a security intrusion. In: 1st international conference on sensing technology, Palmerston North, New Zealand, 21–23 Nov 2005
2. Zhao Y, Ye Z (2007) Low cost IOT/GPRS based wireless home security system. *IEEE Trans Consum Electron* 56(4):546–567
3. Bing Z, Yunhung G, Bo L, Guangwei Z, Tian T (2001) Home video security surveillance. In: 2001 international conference on info-tech and infonet, 2001, proceedings, ICII 2001, Beijing, vol 3, pp 202–208
4. Ghoshal S (2009) *Embedded systems and robots projects using the 8051 microcontroller*, 1st edn. Cengage Learning
5. Pantelopoulos A, Bourbakis NG (2010) A survey on wearable sensor-based systems for health monitoring and prognosis. *IEEE Trans Syst Man Cybern Part C Appl Rev* 40(1):1–12
6. Anto Bennet M, Sankar Babu G, Natarajan S (2015) Reverse room techniques for irreversible data hiding. *J Chem Pharm Sci* 08(03):469–475
7. Anto Bennet M, Sankara Narayanan S, Sankar Babu G (2015) Performance & analysis of effective iris recognition system using independent component analysis. *J Chem Pharm Sci* 08(03):571–576
8. Monisha DG, Monisha M, Pavithra G, Subhashini R (2016) Women safety device and application FEMME. *Indian J Sci Technol* 9(10)
9. Miriyala GP, Sunil P VVNDP, Yadlapalli RS, Pasam VRL, Kondapalli T, Miriyala A (2016) Smart intelligent security system for women. *Int J Electron Commun Eng Technol (IJECET)* 7(2)
10. Hammed RT, Mohamad OAW, Tapus N (2016) Health monitoring system based on wearable sensors and cloud platform. In: 20th international conference on system theory, control and computing (ICTSCC)

11. Vahini S, Vijaykumar N (2017) Efficient tracking for women safety and security using IoT. *Int J Adv Res Comput Sci* 8(9)
12. Tomar A et al (eds) (2022) Proceedings of 3rd international conference on machine learning, advances in computing, renewable energy and communication: MARC 2021, vol 915. Springer Nature, pp XV, 781. ISBN: 978-981-19-2830-7. <https://doi.org/10.1007/978-981-19-2828-4>
13. Ahmad MW et al (eds) (2022) Intelligent data analytics for power and energy systems. Springer Singapore, pp XXII, 641. ISBN: 978-981-16-6081-8. <https://doi.org/10.1007/978-981-16-6081-8>
14. Verma R, Singh A, Choudhary A, Letha SS (2021) PV-grid based electric vehicle charging station with modified interleaved boost converter. *Aust J Electr Electron Eng* 18(4):277–287
15. Khan MJ, Choudhary A (2021) Maximum power point tracking techniques for PV framework under partial shaded conditions. In: Artificial intelligence, machine learning and data science technologies, 1st edn. CRC Press



# Marine Predictors Algorithm Optimization Technique to Estimate GMPP of PV Array Under Partial Shadowing Conditions



Rupendra Kumar Pachauri, Rajesh Singh, Ahmad Faiz Minai, and Shashikant

**Abstract** It is generally known that shadow circumstances negatively affect solar photovoltaic (PV) system performance, resulting in increased power loss (PL) and various power points (global and local) on P–V characteristics. This study examines PV array reconfiguration, an effective shadow reduction strategy. This metaheuristics-based reconfiguration method is compared to series–parallel and total-cross-tied PV array setups. The research uses MATLAB/Simulink and partial shading (PSCs). Comparative analysis, identification of performance metrics (e.g., global maximum power point (GMPP) locations, PL, power gain, fill factor (FF), and performance execution) would be better with the suggested PV array system reconfiguration approach. In the present investigation, two non-uniform irradiation patterns demonstrate the PV system’s nonlinear electrical performance. MPA-based PV array reconfiguration shows that PSCs perform better.

**Keywords** Solar PV system · Power loss · Metaheuristics approaches · Global maximum power · Fill factor

---

R. K. Pachauri (✉)

Electrical Cluster, School of Engineering, University of Petroleum and Energy Studies, Dehradun 248007, India

e-mail: [rpachauri@ddn.upes.ac.in](mailto:rpachauri@ddn.upes.ac.in)

Asian Institute of Technology, Khlong Luang, Pathum Thani, Thailand

R. Singh

Uttaranchal Institute of Technology, Uttaranchal University, Dehradun 248007, India

A. F. Minai

Electrical Engineering Department, Integral University, Lucknow, Uttar Pradesh, India

Shashikant

Electrical Engineering Department, Babu Banarasi Das University, Lucknow, India



# 1 Introduction

Fossil fuels—diesel, coal, gas—drive power demand. Scarcity and storage capacity encouraged alternative energy research. PV, wind, biofuel, and other alternative energy sources are best. PV system technology is becoming increasingly popular because to its ease of installation, particularly at stand-alone levels [1]. PV systems have poor power conversion efficiency, which has opened up research in materials, installation techniques, and sun-tracking [2]. PV system performance suffers from external factors like non-uniform irradiance [3]. PV array reconfiguration improves FF and GMPP locations under PSCs. Clouds, leaves, telecom towers, high-rise buildings, etc., generate shadows. PSCs' causes reduce the PV system's performance under shaded phenomena [4]. This study introduces the Marine predictor algorithm-based PV array reconfiguration, which has a greater GMPP output than standard methods [5–7].

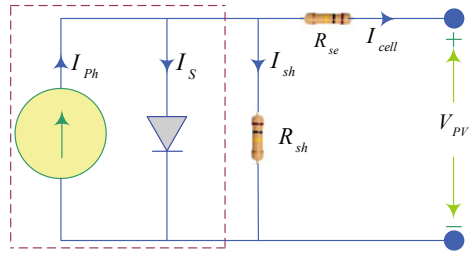
Newly published research articles are looked at in depth for the current study so that the research can be considered new. The experts in [8] studied and validated the performance improvements of honey-comb (HC), Ladder (LDR), bridge-link (BL), and TCT interconnections in a Su-Do-Ku (SDK) system. Moreover, the BL configurations are compared to conventional SP arrangements; the power increases are observed (11.92%, 17.24%, 12.77%, 12.77%, 12.04%, and 13.41%), respectively. SDK puzzle-based PV array increased shade dispersion capability within non-uniform solar irradiation levels as 100–700 to 1000 W/m<sup>2</sup> [9, 10]. The improvised SDK version is considered as re-configured PV array is considered and compared the performance with the conventional (SP, BL, HC, TCT), and game puzzle-based (SDK, and Optimal SDK) arrangements to check the feasibility the performance indices such as efficiency: 11.79%, FF: 65.8%, and PL: 11.25%. The authors of [11] have introduced the successive rotation approach of integer number-based PV array configuration and compared with conventional approaches under PSCs.

The following points from the research study establish the paper's uniqueness:

- MPA modifies the SP array setup to show the current balancing mechanism in shadowing scenarios.
- Existing SP and TCT arrangements are examined with MPA-based setups.
- MPA has greater performance than the lower PL and enhanced FF.

Section 1 introduces PV technology, and Sect. 2 covers PV array layouts. Section 3 examines performance parameters and shading instances. Section 4 covers findings and comments. Section 5 wraps up the study's findings.

**Fig. 1** PV cell (electrical circuit) [10]



## 2 PV Technology

### 2.1 Mathematical Modeling

Equation (1) shows PV cell voltage, while Fig. 1 shows the analogous circuit.

$$V_{PV} = \frac{AkT_C}{e} \ln\left(\frac{I_{Ph} + I_S - I_{cell}}{I_S}\right) - I_{cell}\left(\frac{R_{se}R_{sh}}{R_{se} + R_{sh}}\right), \tag{1}$$

where PV voltage and ideality factor approach for  $V_{PV}$  and  $A$ . Moreover,  $k$ ,  $I_{Ph}$ ,  $I_{cell}$ , and  $I_{DS}$  are shown for Boltzmann’s constant, photo-current, cell current, and saturation current (diode). Moreover, the series and shunt resistances are explored as  $R_S$  and  $R_{sh}$ .

In the present study, electrical specifications ( $V_m = 9.62$  V,  $I_m = 0.52$  A,  $V_{OC} = 11.25$  V, and  $I_{SC} = 0.55$  A) of 5 W PV module is considered for MATLAB/Simulation.

### 2.2 PV Array Systems

#### (i) SP and TCT configurations

A  $6 \times 6$ -size PV array system is constructed (Fig. 2a), and branch current is increased by cross-tied connections between parallel connection during PSCs as shown in Fig. 2b.

#### (ii) MPA-based configuration

Defining the optimization process’s primary goal is the first step. Researchers use a hybrid target function that is the total energy generated by the PV array divided by the absolute difference in row current to extract the most power from a typically shaded PV array surface. This is written as Eq. (2) as

$$\text{maximize}(\text{obj}(i)) = \frac{P_{array}}{|I_{max} - I_{min}|}, \tag{2}$$

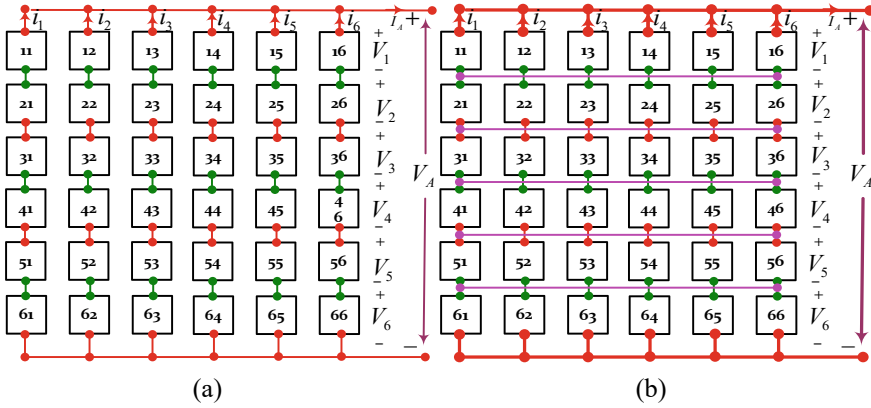


Fig. 2 Conventional a SP, b TCT arrangement (6 × 6 size)

where  $obj(i)$  stands for the fitness value of the  $i$ th element. Furthermore,  $I_{max}$  and  $I_{min}$  are the current values and the rows current vector is known as  $I = (I_1, I_2, I_3, I_4 \dots I_9)$ . The power generated from PV array is expressed in Eq. (3) [11] as

$$P_{array} = \sum_{n=1}^{n=9} I_{r_n} \times V_n, \tag{3}$$

where the voltage and current are expressed as  $I_{r_n}$  and  $V_n$  for the  $n$ th row in an array. The aforementioned mathematical criterion helps disperse the effect of shading throughout the full PV surface [9]. The dispersed shading impacts using MPA is shown in Fig. 3.

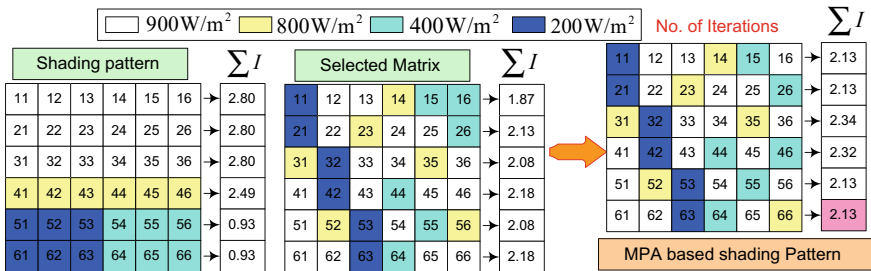


Fig. 3 Dispersed shading impacts using MPA

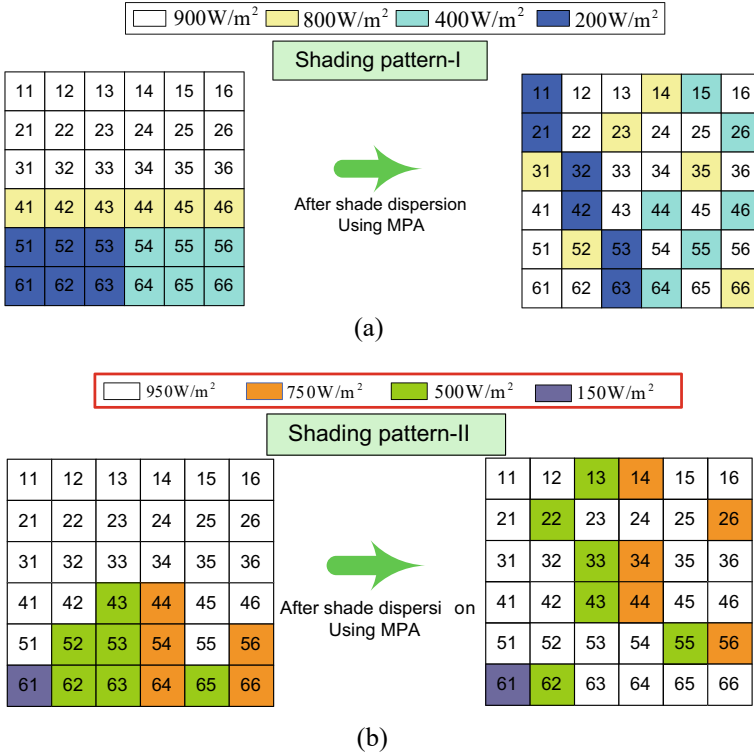


Fig. 4 Shading scenarios: I-II

### 2.3 Shading Scenarios

Two distinguished shading scenarios are considered to carry out study during the PV system performance investigation. Under shaded scenarios, the non-uniform irradiance levels (900, 800, 400, and 200 W/m<sup>2</sup>) are reported for performance study. Moreover, in the shading pattern comprised with different irradiation levels (950, 750, 500 and 150 W/m<sup>2</sup>). These shading patterns are shown in Fig. 4a, b.

## 3 Performance Indices for Comparative Study

### 3.1 Power at GMPP

PV curves have several power maxima points (LMPP and GMPP) due to non-uniform irradiance-based shading. This behavior reveals GMPP and LMPP power.

**Table 1** Theoretical analysis during shading pattern-1

Row	1	2	3	4	5	6
<i>SP</i>						
<i>V</i> (V)	$V_m$	$2V_m$	$3V_m$	$4V_m$	$5V_m$	$6V_m$
<i>I</i> (A)	$5.38I_m$	$5.38I_m$	$5.38I_m$	$4.78I_m$	$1.78I_m$	$1.78I_m$
<i>P</i> (W)	$5.38I_m V_m$	$10.76I_m V_m$	$16.14I_m V_m$	$19.12I_m V_m$	$8.9I_m V_m$	$10.68I_m V_m$
<i>TCT</i>						
<i>V</i> (V)	$V_m$	$2V_m$	$3V_m$	$4V_m$	$5V_m$	$6V_m$
<i>I</i> (A)	$5.38I_m$	$5.38I_m$	$5.38I_m$	$4.78I_m$	$1.78I_m$	$1.78I_m$
<i>P</i> (W)	$5.38I_m V_m$	$10.76I_m V_m$	$16.14I_m V_m$	$19.12I_m V_m$	$8.9I_m V_m$	$10.68I_m V_m$
<i>MPA</i>						
<i>V</i> (V)	$V_m$	$2V_m$	$3V_m$	$4V_m$	$5V_m$	$6V_m$
<i>I</i> (A)	$4.09I_m$	$4.09I_m$	$4.5I_m$	$4.40I_m$	$4.09I_m$	$2.13I_m$
<i>P</i> (W)	$4.09I_m V_m$	$8.18I_m V_m$	$13.5I_m V_m$	$17.6I_m V_m$	$20.45I_m V_m$	$12.78I_m V_m$

### 3.2 FF and PL Analysis

According to Eqs. (4) and (5) shows that the PL is the difference between uniform and non-uniform MPP,

$$FF = \frac{P_{GMPP}}{V_{OC} \times I_{SC}}, \tag{4}$$

$$PL = MPP_{at\ STCs} - GMPP_{at\ PSCs}. \tag{5}$$

Table 1 shows the theoretical row-wise voltage, current, and power under shaded case-I.

## 4 Results and Discussion

### 4.1 Analysis of P–V and I–V Curves at STCs

Ideal irradiation conditions provide P–V and I–V curves for a 6 × 6 configuration. The P–V curve in Fig. 5 shows that MPP power is 180.2 W under optimum circumstances.

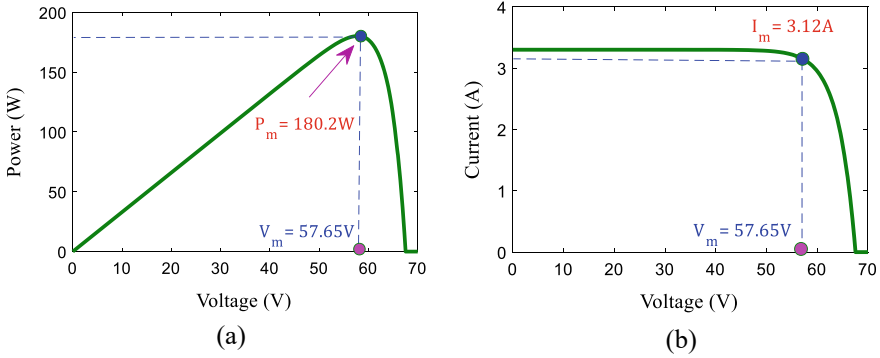


Fig. 5 P–V and I–V curves (STCs)

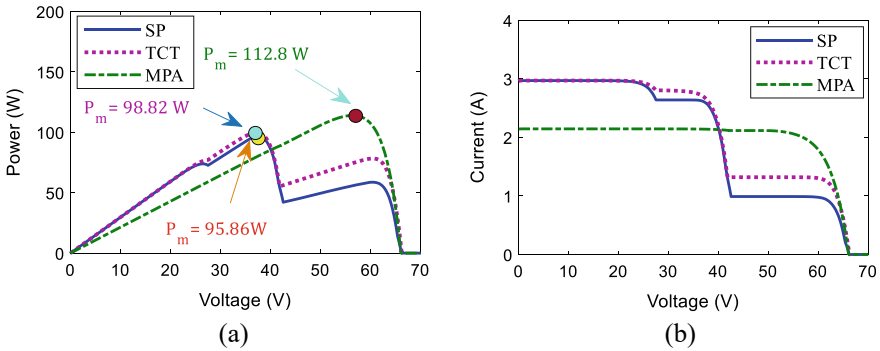


Fig. 6 Shade case-I: P–V and I–V curves

### 4.2 P–V and I–V Characteristics for PSCs

MPA PV systems outperform SP (95.86 and 112.1 W) and TCT (98.82 and 116.8 W) setups in terms of GMPP under shade situations (I–II). The functionality of P–V and I–V curves are shown in Figs. 6 and 7. Table 2 provides an overview of the study’s quantitative findings.

### 4.3 Power at GMPP and Execution Ratio: Analysis

Shaded GMPP power for SP, TCT, and MPA is shown in a bar chart in Fig. 8a (I–II). MPA-based PV systems produce higher power because of shadow dispersion.

Shade dispersion helps improve PV performance. MPA is better than standard designs in this context. In this work, MPA has a higher %ER (62.59 and 78.63%) than a conventionally constructed array as shown in Fig. 8b.

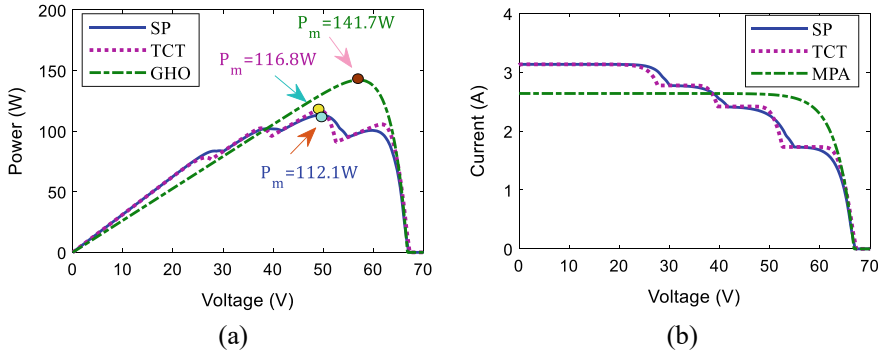


Fig. 7 Shade case-II: P–V and I–V curves

Table 2 Quantitative performance of PV array under PSCs: I–II

Parameters	PSC-I			PSC-II		
	SP	TCT	MPA	SP	TCT	MPA
$V_{OC}$ (V)	65.72	65.72	65.71	66.22	66.24	66.21
$I_{SC}$ (A)	2.84	2.87	2.09	3.10	3.12	2.55
$V_m$ (V)	37.2	37.18	56.62	49.44	48.62	57.23
$I_m$ (A)	2.57	2.65	1.99	2.26	2.40	2.47
$P_{GMPP}$ (W)	95.86	98.82	112.8	112.1	116.8	141.7
FF	0.513	0.523	0.821	0.546	0.551	0.839
PL (W)	84.34	81.38	67.4	68.1	63.4	38.5
%ER	53.19	54.83	62.59	62.2	64.81	78.63

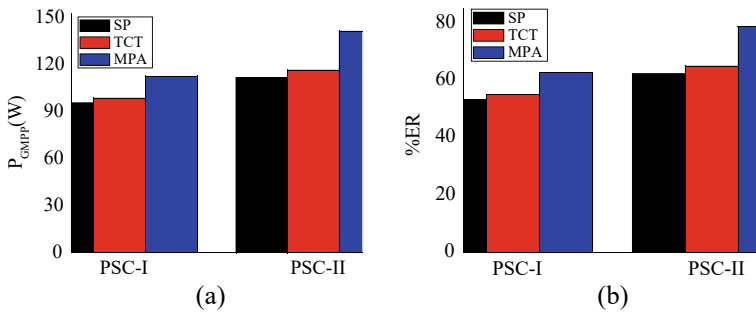


Fig. 8 a Power at GMPP, b %ER

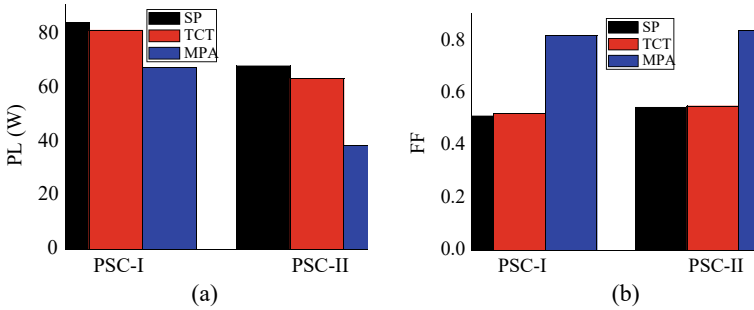


Fig. 9 a PL, b FF analysis

### 4.4 Analysis of FF and PL

PL for MPA-based PV systems is 67.4 and 38.5 W less than conventional PV systems. Under shading scenarios I–II, FF is greater for MPA-based PV array design than SP (0.513 and 0.546) and TCT (0.523 and 0.551). Figure 9a, b shows PL and FF analyses using bar charts.

## 5 Conclusion

SP, TCT, and MPA configurations (6 × 6) are studied. During shading instances (I and II), these observations are made:

- Under shade situations I–II, MPA configuration GMPP is 112.8 W, and conventional configurations are 141.7 W.
- In MPA-based designs, PL is 67.4 and 38.5 W, compared to SP and TCT.
- MPA-based PV setups have a better FF of 0.821 and 0.839 than traditional ones.

The research found that bigger shadow dispersion factors boost PV array performance. This research helps professional engineers and newcomers learn more. In this research, machine learning can find the best PV module position instead of MPA.

## References

1. Gupta A, Chauhan YK, Pachauri RK (2016) A comparative investigation of maximum power point tracking methods for solar PV system. *Sol Energy* 136:236–253
2. Bhadoria VS, Pachauri RK, Tiwari S, Jaiswal SP, Alhelou HH (2020) Investigation of different BPD placement topologies for shaded modules in a series-parallel configured PV array. *IEEE Access* 8:216911–216921
3. Bai J, Sun L, Pachauri RK, Wang G (2021) Investigate on photovoltaic array modeling and the MPPT control method under partial shading conditions. *Int J Photo Energy* 2021:1–16



4. Pachauri RK, Alhelou HH, Bai J, Golshan MEH (2021) Adaptive switch matrix for PV module connections to avoid permanent cross-tied link in PV array system under non-uniform irradiations. *IEEE Access* 9:45978–45992
5. Tao Y, Bai J, Pachauri RK, Sharma A (2020) Parameter extraction of photovoltaic modules using a heuristic iterative algorithm. *Energy Convers Manage* 224:1–18
6. Ahmad MW et al (eds) (2022) *Intelligent data analytics for power and energy systems*. Springer Singapore, pp XXII, 641. ISBN: 978-981-16-6081-8. <https://doi.org/10.1007/978-981-16-6081-8>
7. Tomar A et al (eds) (2022) *Proceedings of 3rd international conference on machine learning, advances in computing, renewable energy and communication: MARC 2021*, vol 915. Springer Nature, pp XV, 781. ISBN: 978-981-19-2830-7. <https://doi.org/10.1007/978-981-19-2828-4>
8. Vijayalekshmy S, Bindu GR, Rama Iyer S (2015) Analysis of various photovoltaic array configurations under shade dispersion by Su-Do-Ku arrangement during passing cloud conditions. *Indian J Sci Technol* 8(35):1–20
9. Babu TS, Ram JP, Dragicevic T, Miyatake M, Blaabjerg F, Rajasekar N (2018) Particle swarm optimization based solar PV array reconfiguration of the maximum power extraction under partial shading conditions. *IEEE Trans Sustain Energy* 9(1):74–85
10. Sai Krishna G, Moger T (2019) Improved Su-Do-Ku reconfiguration technique for total-cross-tied PV array to enhance maximum power under partial shading conditions. *Renew Sustain Energy Rev* 109:333–348
11. Pachauri RK (2022) Imperative role of optimization techniques to reconfigure solar photovoltaic array systems to diminish shading effects. *Int J Circuit Theory Appl* 50(1):317–353

# Artificial Intelligence-Based Bearing Fault Diagnosis of Rotating Machine to Improve the Safety of Power System



Mohmad Iqbal and A. K. Madan

**Abstract** To improve the safety of the power system in rotary machine like computer numerical control (CNC) and to minimize the risk of electrical hazards, early fault diagnosis of bearing is important. Artificial intelligence (AI) can play crucial role in optimizing the operation and management of manufacturing of any production plant. CNC machines are commonly used in the manufacturing and assembly of various components used in automotive, renewable power systems, aerospace, electronics, etc. Bearing is the main element and their failure is the common cause of machine tool failure. This study proposes sophisticated vibration-based bearing fault defects in CNC machine tools. Early fault detection can also help to identify energy-wasting issues such as electrical damage, and overheating. The approach develops a system to monitor and to quantify faults in rotating machine using investigative vibration data. The proposed technique aims to improve the reliability of the manufacturing system by detecting bearing faults early on. The method uses hybrid signal processing to decompose the vibration signal, and then weighted principal component analysis (WPCA) is applied to eliminate redundant features from the decomposed signal, and finally bi-directional long short-term memory (BLSTM) was used to predict the kind of bearing faults. AI algorithms can monitor manufacturing and power systems in real time, detecting faults or anomalies and triggering automatic responses to prevent system failure.

**Keywords** CNC machine tools · Bearing fault · Hybrid signal decomposition (HSD) · WPCA · BLSTM

---

M. Iqbal (✉) · A. K. Madan  
Department of Mechanical Engineering, Delhi Technological University, Delhi, India  
e-mail: [mohmadiqbal\\_86@yahoo.com](mailto:mohmadiqbal_86@yahoo.com)

© The Author(s), under exclusive license to Springer Nature Singapore Pte Ltd. 2024  
H. Malik et al. (eds.), *Renewable Power for Sustainable Growth*,  
Lecture Notes in Electrical Engineering 1086,  
[https://doi.org/10.1007/978-981-99-6749-0\\_63](https://doi.org/10.1007/978-981-99-6749-0_63)

933

## 1 Introduction

To run the machine tools, the power supply system plays a critical role in meeting the energy demands of modern industry and enabling economic growth and development. This includes protective relays, control systems, and other equipments that can detect and respond to faults or disturbances in the system. Bearing and control system are indeed crucial components of CNC machine. CNC machines are powered by electrical systems that are susceptible to faults and malfunctions, which can pose serious safety risks to operators and damage the equipment. The use of AI like machine and deep learning in manufacturing and power has been increasing rapidly over the past few years. AI can provide significant benefits to power and manufacturing industries by optimizing processes, reducing costs, improving safety, and increasing efficiency. A quick shift to a novel manufacturing age known as Industry 4.0 has been made possible by AI technologies [1]. Early component failure prediction to avoid the loss of power and unwanted shutdown of machine tools in any industry is necessary. In modern manufacturing system, CNC machines are usually used for manufacturing highly precise components. The use of CNC machines in these industries has revolutionized the manufacturing process by enabling highly precise and accurate production of complex parts and components. CNC machines use programmed instructions to control the movement of tools and machines [2]. Bearings are a fundamental component in many types of rotating machinery, including wind turbines power systems and CNC milling machines, and the diagnosis of these is necessary [3]. Fault diagnosis in rotating machinery is important to prevent economic losses and safety hazards caused by bearing failures. An intelligent fault diagnosis system in CNC machine tools can help improve the safety and reliability of mechanical components. This can be achieved by using various techniques like vibration analysis, thermal imaging, and ML algorithms. A single failure in a rotating component can result in significant economic losses due to downtime. Bearing failure is a common cause of breakdowns in various types of rotating machinery, both in high-speed and low-speed applications. It is important to use high-quality bearings, properly maintain and lubricate them, and regularly monitor their condition using techniques such as vibration analysis and thermal imaging [4–6]. CNC machine tools are complex systems that consist of multiple servo axes and data processing elements. Each servo axis is responsible for controlling the movement of a specific component, such as the cutting tool or the workpiece [7].

Teti et al. [8] investigated that mechanical failures in machines cause approximately 79.6% downtime in today's modern production. In this regard, a fault diagnostic technique based on cascading malfunction is presented to assure the safe functioning of CNC machines [9]. The failure of bearings in rotating machines for a short period could decline the performance or complete industrial damages. Luo et al. developed a classifier to choose the responses from vibration signals over 288 days. Dynamic features are then identified for the mechanical fault quickly in time-varying situations [10]. Fault detection in rotating machines is essential in terms of design

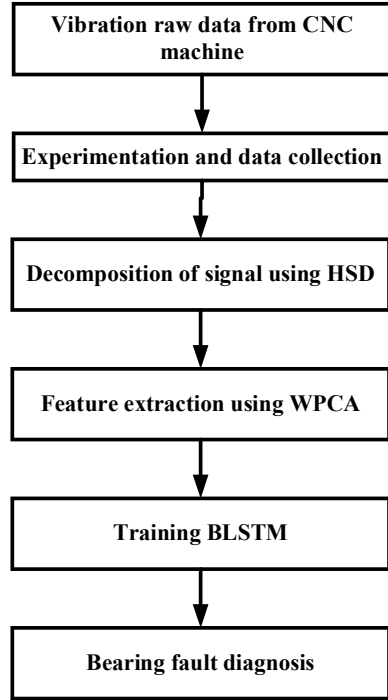
and maintenance. Jiao et al. [11] evaluate and describe the evolution of convolutional network-based fault diagnosis (CNFD) methods. Several well-known datasets for machine failure diagnostics are described like data gathering, model creation, feature learning, and decision-making. The calibration signals of rolling bearing faults are typically time-varying and nonlinear [12, 13]. Kumar and Kumar [14] proposed a method to identify automatic bearing fault damages in angular contact ball bearings. Later on a new method for separating the signals; SVD of the Hilbert spectrum provides singular values was presented [15]. SVM is then provided a classifier to improve machine stoppage problem. The advanced SWT approach is then used to putrefy the processed signal in succession of IMT function [16]. Different fault feature extraction methodologies based on data-driven ML approaches have been presented for various problems that have inadequate simplification capability [17, 18]. In engineering issues simple empirical features cannot offer an elevated accuracy although refined specialized skill in concern issues [19]. Various issues in rotating machine fault diagnosis were resolved using different deep learning techniques. The evaluation of defects due to the noise generated in the machines distress significant differences in dimension and characteristics that are complicated to extract throughout the procedure of real signal gathering [20, 21]. ANN [22, 23] and SVM [24–28] models are used in defect prediction and diagnosis in the field of condition monitoring most extensively. SVM models have their own merits and demerits. Overlearning is a difficulty. Although ANN is strong at predicting data used for training, it performs poorly when it comes to classifying test data. The outcomes of ANN produce superior results when the parameters are maximized. However, this increases the computation time, but the classification accuracy and efficiency are excellent. In a comparison of SVM, the ANN model is trained on behalf of feature extraction using HSD and then PCA is used for feature selection.

A previous study has revealed that most of the work on fault detection of bearings in CNC machine tools has been done thus far. However, power system faults primarily cause electrical damage in machines, resulting in severe mishaps in any production system. So far this idea is ignored by several researchers. Early critical component faults detection of the CNC machine, like bearing damages caused by electrical faults has been considered in this study. Contribution of this proposed work is as follows:

- (1) The major contribution of this study is the development of an experimental framework to predict bearing faults in CNC machine tools caused by electric power supply failure.
- (2) WPCA-based feature extraction technique was adopted as it combines both slow feature analysis and principal component analysis.
- (3) To classify the extracted feature, BLSTM is used to diagnose the kind of bearing faults or electrical faults in CNC machine.

Structure of the paper, Sect. 2 discusses the workflow. Section 3 discusses experimental setup and data acquisition. Section 4 discusses the methodology adopted to diagnose the faults in the system early on; Sect. 5 result and in Sect. 6 conclusions are provided.

**Fig. 1** Proposed workflow



## 2 Proposed Workflow

A brief explanation of this research work is presented in Fig. 1. The workflow diagram will provide basic information regarding the proposed work. First, the raw data is acquired from the bearing of the CNC machine tool and then a decomposition technique, HSD, was used to slice or decompose the huge vibration signals in to time frequency analysis. Then, a BLSTM model is used for feature extraction and model training.

## 3 Experimental Environment

The experimentation adopting during the vibration data acquisition is illustrated in Fig. 1. In the experimental environment, the hardware used is 3.6 GHz with RAM of 8 GB, a solid choice for running experiments for speedy execution of computational tasks. The codes needed for model used Matlab 2020. The data collected through accelerometer and feed to computer system, i.e., data acquisition system of this proposed work. This approach is used because traditional methods are not easy to

apply due to the dynamic structure of the CNC machine. During the data acquisition the motor speed is 700 RPM.

### 4 Methodology

Methodology implemented in this work is BLSTM-WPCA-based bearing failure prediction. The step-by-step description of proposed work methodology to improve the safety of machine is revealed in Fig. 2. This technique involves signal and data processing which are described in the following steps:

- Data collection from CNC machine that there was enough datasets accessible to appropriate bearing fault diagnoses.
- Hybrid signal decomposition was then used to decompose the collected data.
- Weighted principal component analysis (WPCA), a feature selection technique, was used to remove unnecessary features to enhance the accuracy.
- After this, BLSTM is used to diagnose the kind of bearing faults or electrical damage in the power system (Fig. 3).

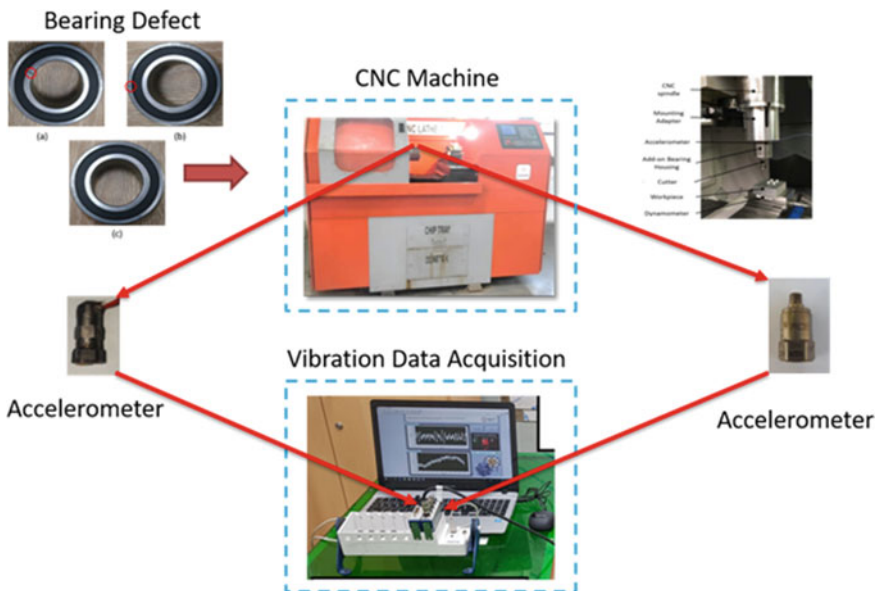


Fig. 2 Bearing fault diagnosis framework for CNC machine tool

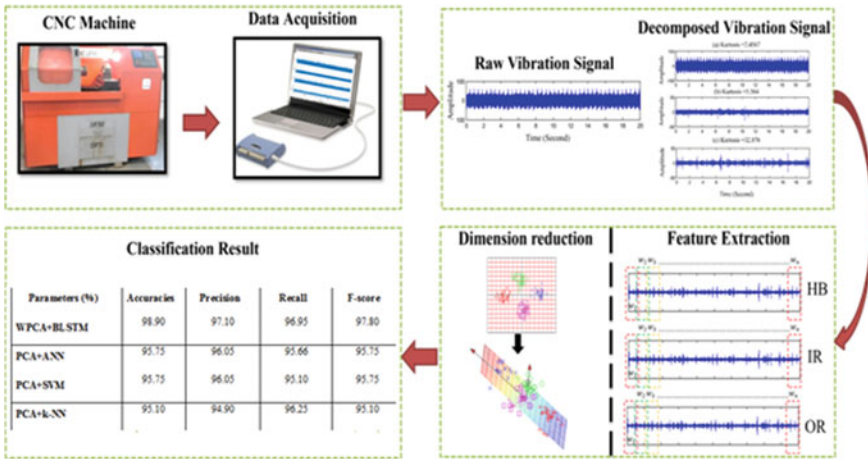


Fig. 3 Methodology adopted for bearing fault diagnosis

### 4.1 Hybrid Signal Decomposition Techniques

The use of hybrid signal decomposition in this proposed technique is used to filter nonstationary signals, which is important to handle the huge vibration data of CNC machine. HSD decomposed and sliced the raw data into useful decomposed signals. Figure 4 shows how well the huge raw vibration signal data is slicing or decomposing using HSD into desirable data.

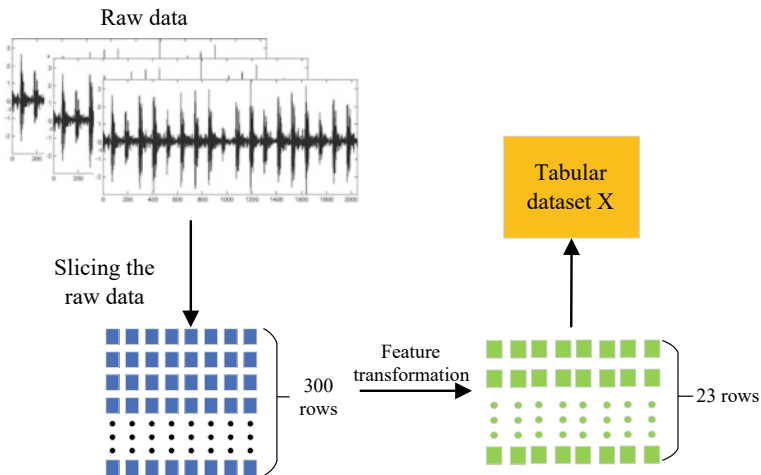


Fig. 4 HSD-based raw signal decomposition

## 4.2 *Weighted Principal Component Analysis*

Weighted principal component analysis (WPCA) is a variation of the standard PCA technique used in multivariate analysis and used when the variables of the dataset have different variances or when the variables are not equally important in explaining the total variance in the dataset. It is suitable for slow feature analysis and principal component analysis. The joint objective function of SFA and PCA can be resolved by WPCA discrete the same as,

$$I_1 = \max o^D Y Y^D o \quad (1)$$

$$\text{Min } \Delta x_i(d) = \min(x_i^2)_d \quad (2)$$

$X$  satisfies subsequent constraints:

$$(x_i)_d = o$$

$$(x_i^2)_d = 1$$

$$(x_j x_i)_d = o$$

## 4.3 *BLSTM*

Bi-directional long short-term memory (BLSTM) is a type of neural network architecture. BLSTM is a variation of the long short-term memory (LSTM) network, which is designed to overcome the vanishing gradient problem of traditional recurrent neural networks (RNNs). The convolutional neurons of RNN are improved by BLSTM model. From the beginning to the end and from the end to the beginning, we are using two separate LSTM layers. This allows the network to capture information from both the past and future contexts of the input sequence, resulting in better performance on sequence modeling tasks.

## 5 Experiment Results

The performance evaluation in this work is investigated by three kinds of datasets. Firstly, random numbers are created to select datasets for narrow faults with noise. Dataset related to vibration was recorded by accelerometer. Finally, the dataset related to faulty bearings and hazardous electrical systems from the sound signal was



**Table 1** Confusion matrix

True class	Proposed model BLSTM		
	H	IR	OR
H	98%	3%	1%
IR	1%	97%	1%
OR	4%	1%	96%

**Table 2** Evaluation of different performance parameters of the proposed model

Performance evaluation with other AI models				
Parameters (%)	Accuracies	Precision	Recall	<i>F</i> -score
WPCA + BLSTM	98.90	97.10	96.95	97.80
PCA + ANN	95.75	96.05	95.66	95.75
PCA + SVM	95.75	96.05	95.10	95.75
PCA + k-NN	95.10	94.90	96.25	95.10

recorded using different classifiers like SVM, ANN, K-NN, and BLSTM for different bearing states of machine. Confusion matrix of the presented work is represented in Table 1.

Table 2 evaluates the WPCA-BLSTM method with other methods. From this table, WPCA-BLSTM outperforms all other methods for all parameters like accuracy, precision, recall, and *F*-score. It was observed that WPCA-BLSTM achieved acceptable classification accuracies for different conditions, with 98%, 97%, and 96%, respectively that outperform other ML algorithms like SVM, ANN, and k-NN. In the proposed work, four repetitions were conducted to carry satisfactory results. From these preferred features we trained the model WPCA-BLSTM, ANN, SVM, and k-NN and results of proposed model are better.

## 6 Conclusion

Weighted principal component analysis (WPCA) feature selection technique was used to remove unnecessary features to enhance the accuracy. BLSTM is used to diagnose the kind of bearing faults or electrical damage in the power system of CNC machine. HSD decomposed and sliced the raw data into useful decomposed signals. Early fault detection can also help to identify energy-wasting issues such as poor lubrication or overheating.

Future scope: The main constraint of this study is signal overlapping and computational time is higher. In the future, these limitations could be studied, and the work can be expanded. Also, the power system that affects the electrical supply of the CNC machine can be considered in depth for future scope.

## References

1. Stetco A, Dinmohammadi F, Zhao X, Robu V, Flynn D, Barnes M, Keane J, Nenadic G (2019) Machine learning methods for wind turbine condition monitoring: a review. *Renew Energy* 133:620–635
2. Selvaraj V, Xu Z, Min S (2023) Intelligent operation monitoring of an ultra-precision CNC machine tool using energy data. *Int J Precis Eng Manuf-Green Technol* 10:59–69. <https://doi.org/10.1007/s40684-022-00449-5>
3. Stavropoulos P, Souflas T, Papaioannou C et al (2023) An adaptive, artificial intelligence-based chatter detection method for milling operations. *Int J Adv Manuf Technol* 124:2037–2058. <https://doi.org/10.1007/s00170-022-09920-8>
4. Boza P, Evgeniou T (2021) Artificial intelligence supports the integration of variable renewable energy sources into the power system. *Appl Energy* 290:116754
5. Xu G, Hou D, Qi H, Bo L (2021) High-speed train wheelset bearing fault diagnosis and prognostics: a new prognostic model based on extendable useful life. *Mech Syst Signal Process* 146:1–23
6. Malla C, Panigrahi I (2019) Review of condition monitoring of rolling element bearing using vibration analysis and other techniques. *J Vib Eng Technol* 7(4):407–414
7. Zhang K, Yuen A, Altintas Y (2013) Pre-compensation of contour errors in five-axis CNC machine tools. *Int J Mach Tools Manuf* 74:1–11
8. Teti R, Jemielniak K, O'Donnell G, Dornfeld D (2010) Advanced monitoring of machining operations. *CIRP Ann* 59(2):717–739
9. Zhang Y, Mu L, Shen G, Yu Y, Han C (2019) Fault diagnosis strategy of CNC machine tools based on cascading failure. *J Intell Manuf* 30(5):2193–2202
10. Luo B, Wang H, Liu H, Li B, Peng F (2018) Early fault detection of machine tools based on deep learning and dynamic identification. *IEEE Trans Ind Electron* 66(1):509–518
11. Jiao J, Zhao M, Lin J, Liang K (2020) A comprehensive review on convolutional neural network in machine fault diagnosis. *Neurocomputing* 5(417):36–63
12. Cui L, Mo D, Wang H, Chen P (2013) Resonance-based nonlinear demodulation analysis method of rolling bearing fault. *Adv Mech Eng* 2013:13 pages. Article ID 420694
13. Xiao M, Wen K, Zhang C, Zhao X, Wei W, Wu D (2018) Research on fault feature extraction method of rolling bearing based on NMD and wavelet threshold denoising. *Shock Vib* 2018:11 pages. Article ID 9495265
14. Kumar A, Kumar R (2018) Adaptive artificial intelligence for automatic identification of defect in the angular contact bearing. *Neural Comput Appl* 29(8):277–287
15. Wang M, Chen Y, Zhang X, Chau TK, Ching Iu HH, Fernando T, Li Z, Ma M (2021) Roller bearing fault diagnosis based on integrated fault feature and SVM. *J Vib Eng Technol* 24:1
16. Xin Y, Li S, Wang J (2019) A new fault feature extraction method for non-stationary signal based on advanced synchrosqueezing transform. *J Vib Eng Technol* 7(3):291–299
17. Gangsar P, Tiwari R (2017) Comparative investigation of vibration and current monitoring for prediction of mechanical and electrical faults in induction motor based on multiclass-support vector machine algorithms. *Mech Syst Signal Process* 94:464–481
18. Iqbal M, Madan AK (2023) Bearing fault diagnosis in CNC machine using hybrid signal decomposition and gentle AdaBoost learning. *J Vib Eng Technol*. <https://doi.org/10.1007/s42417-023-00930-8>
19. Glowacz A (2019) Fault diagnosis of single-phase induction motor based on acoustic signals. *Mech Syst Signal Process* 117:65–80
20. Othman MS, Nuawi MZ, Mohamed R (2015) Induction motor bearing fault detection using hybrid kurtosis-based method. *Int J Appl Eng Res* 10(13):33453–33456
21. Shifat TA, Hur JW (2020) An effective stator fault diagnosis framework of BLDC motor based on vibration and current signals. *IEEE Access* 8:106968–106981. <https://doi.org/10.1109/ACCESS.2020.3000856>

22. Iqbal M, Madan AK (2022) CNC machine-bearing fault detection based on convolutional neural network using vibration and acoustic signal. *J Vib Eng Technol* 10:1613–1621. <https://doi.org/10.1007/s42417-022-00468-1>
23. Ertunc HM, Ocak H, Aliustaoglu C (2013) ANN- and ANFIS-based multi-staged decision algorithm for the detection and diagnosis of bearing faults. *Neural Comput Appl* 22(1):435–446
24. Ahmad MW et al (eds) (2022) *Intelligent data analytics for power and energy systems*. Springer Singapore, pp XXII, 641. ISBN: 978-981-16-6081-8. <https://doi.org/10.1007/978-981-16-6081-8>
25. Tomar A et al (eds) (2022) *Proceedings of 3rd international conference on machine learning, advances in computing, renewable energy and communication: MARC 2021*, vol 915. Springer Nature, pp XV, 781. ISBN: 978-981-19-2830-7. <https://doi.org/10.1007/978-981-19-2828-4>
26. Wulandhari LA, Wibowo A, Desa MI (2015) Condition diagnosis of multiple bearings using adaptive operator probabilities in genetic algorithms and back propagation neural networks. *Neural Comput Appl* 26(1):57–65
27. Samanta BI, Al-Balushi KR, Al-Araimi SA (2003) Artificial neural networks and support vector machines with genetic algorithm for bearing fault detection. *Eng Appl Artif Intell* 16(7–8):657–665
28. Zhu K, Song X, Xue D (2014) A roller bearing fault diagnosis method based on hierarchical entropy and support vector machine with particle swarm optimization algorithm. *Measurement* 1(47):669–675

# Stability Enhancement of AC Microgrid Using Discrete Mode Controllers with Optimum Sampling Frequency



Amit Arora, Mahendra Bhadu, and Arvind Kumar

**Abstract** This paper examines the influence of discrete mode controllers with optimum sampling frequency to enhance the stability of the grid-integrated AC microgrid. The damping of low-frequency electromechanical oscillation performance of distributed generators of AC microgrid is analyzed. The AC microgrid is comprised of two renewable energy resources a photovoltaic (PV) farm, a variable wind speed type DFIG wind farm, and another two distributed generators hydro and diesel are based on synchronous generators. The diesel generator is used as a backup source to provide the load demand when the grid is subjected to disturbance and the generation of renewable power is not as per demand. This research investigates the effect of the execution of different discrete type's power system stabilizers with an optimum sampling frequency to enhance the stability of the AC microgrid. The discrete type time domain mode PSSs such as conventional PSS ( $\Delta\omega$ -PSS and  $\Delta Pa$ -PSS), MBPSS-4B, and LQG-based PSS controllers are executed on DGs of the AC microgrid for the damping of low-frequency electromechanical oscillation. The MATLAB/Simulink software gives a comparative analysis of the discrete mode controller's response to distributed generators of AC microgrid. The simulation result verified the system performance with an effective operational sampling frequency of discrete time domain mode controllers such as conventional PSSs, MBPSS-4B, and LQG controllers under fault conditions.

**Keywords** AC microgrid · Discrete mode controller · Power oscillation damping · Small signal stability · Distributed generators · Solar photovoltaic · Wind energy

---

A. Arora (✉) · M. Bhadu · A. Kumar  
Electrical Engineering Department, Engineering College Bikaner, Bikaner, Rajasthan, India  
e-mail: [amitarora8505@gmail.com](mailto:amitarora8505@gmail.com)

© The Author(s), under exclusive license to Springer Nature Singapore Pte Ltd. 2024  
H. Malik et al. (eds.), *Renewable Power for Sustainable Growth*,  
Lecture Notes in Electrical Engineering 1086,  
[https://doi.org/10.1007/978-981-99-6749-0\\_64](https://doi.org/10.1007/978-981-99-6749-0_64)

943

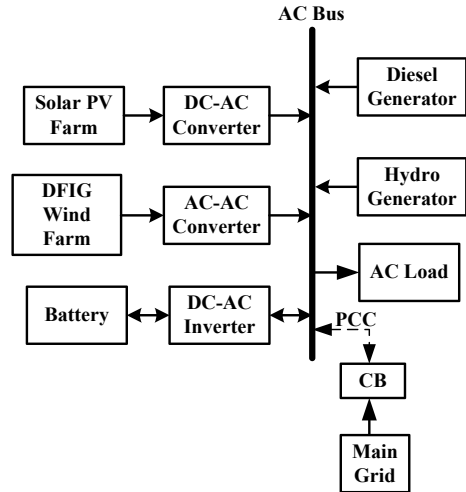
# 1 Introduction

In the present scenario, renewable energy sources-based microgrids are becoming increasingly in demand to generate clean energy. The generation of electricity from renewable energy sources (RESs) is only the key to decline the global warming. Interconnecting renewable energy generation sources with electrical power generation storage devices can be establishing a stable microgrid. The microgrid is an emerging field that offers to deliver reliable responses to the increase in stress on the main grid and transmission lines. The most effective general form for generation is, a microgrid integrated with both renewable energy sources (RESs) like wind, solar PV cells, and fuel cells also together with traditional energy sources like diesel generators, micro turbines, and micro or small hydro [1]. The integration of microgrid with renewable and traditional energy sources is controlled by the robust design controller, and it provides operational stability to the systems. In the interface of power electronics controller with RESs, there are many obstacles that are shown, such as continuing the power supply without any interruptions, integration of RESs with conventional grid, issues of power quality, stability, security, reliability, protection, and energy storage system, concerning the frequency and voltage deviation [2]. Therefore, researchers applied the technological advancement that is moving in the direction of implementation of renewable energy sources achieving maximum electricity generation to match the energy need. The major challenges with renewable energy sources are weather dependent so the generation of energy is variable in nature and utilization of these resources imposes a reduction in the inertia of the grid. Because of this, the problem of stability arises in power systems. Solar photovoltaic (SPV) energy and wind power are two main sources of renewable energy utilized in the generation of electricity, and they are free of pollution or carbon-free [3].

The voltage fluctuations, frequency oscillations, variance in generation and demand, etc., are a few main issues in the main power grid. The main focus of the researcher is to protect and maintain the stability of the main grid from the above discussed issues to construct a confined power generated grid that is known as a microgrid [4]. A microgrid provides electricity to rural, urban, and hilly areas if the failure or unavailability of the external grid. The advantages of a microgrid (MG) are provided energy at the time of peak load, environmentally friendly, and give an economical energy solution. The major problems for microgrids during the integration of intermittent renewable-based DGs are low inertia, change in voltage and frequency, stability, and protection [5].

The modes of operation in the microgrid are the following: the grid-connected, autonomous, or transited, and the reconnection operating modes. A microgrid in grid-connected mode can manage and interchange the generation of electricity with the conventional grid and maintain the power supply from renewable energy-based distributed generators of the microgrid, although the energy flows through a microgrid is bidirectional [6]. In the autonomous or stand-alone mode, the microgrid can sustain the balance in reactive power in the self-base without the existence of an infinite bus. So this mode has major challenges considering a proper voltage and frequency

**Fig. 1** Typical diagram of AC microgrid



magnitude, and another is proper power balance. The microgrid is classified into three major types as per power bus and load that is AC power, DC power, and hybrid (AC/DC) power microgrids [7].

Traditionally, a hierarchical architecture with primary, secondary, and tertiary supervisory control levels has been accomplished for the control of distributed generators (DGs), BESSs, the transition of operating modes, and the stability of the main grid and microgrid [8]. Figure 1 shows the diagrammatic block diagram of the AC microgrid with different distributed generators.

In the microgrid, the distributed generation resources are associated with the utility grid with an interface of a power electronics converter to operate as per their requirements and also to maintain the stability and quality of modern power systems [9].

The dynamic stability of the microgrid is the main issue because of the disturbances due to the fault, changes in load, and changes in voltage and frequency. For this reason, the research is focused on the stability of microgrids in terms of analysis of small signal stability. To measure, the dynamic stability of the microgrid, a small signal stability analysis gives an adjustment to the control variable of the microgrid [10].

The small signal stability in terms of low-frequency electromechanical oscillation of the distributed generators of the systems should be enhanced the system stability. The execution of power system stabilizers (PSSs) in the power generating distributed generator units dampens the electromechanical oscillations, which improves the system stability [11]. The different types of robust design oscillation damping controllers are executed in distributed generators of the systems to achieve better performance of the systems against low-frequency oscillations, and they are represented as traditional or local PSSs based on input speed and power, multi-band

PSS (MBPSS), PID-PSS, fuzzy logic-based PSS (FLPSS), H infinity ( $H \infty$ ), etc. [12–14].

However, type-1 fuzzy logic-based PSS controller techniques provide improve performance compared with conventional PID-based PSSs in terms of damping performance low-frequency oscillations of distributed generators of the systems; these standard type-1 fuzzy logic PSSs have shortcomings when it comes to handling significant levels of uncertainty and unpredictable disturbances in modern power systems. Have robustness in type-2 fuzzy logic-based PSS (FLPSS-II) to eliminate the uncertainties and unpredictable disturbance [15].

One of the best choices to get over these restrictions is a robust LQG controller. Its function's specificity makes it easier to manage uncertainty. According to a LQG-PSS with a distinctive estimation algorithm is successful at damping oscillations in the modern power system [16]. Continuous time domain LQG is a robust controller for damping the low-frequency oscillation (LFO) of distributed generators, and it also provides small signal stability to the system. This technique allows you to deal with regulation performance and provide the control signal to disturbances and measurement or random noise [17, 18].

The continuous time domain mode power system stabilizers are tuned by different tuning methods such as  $PV_r$ , GEP, and residue methods for selecting the optimal control values of gain and proper pole placements. Further, this tuned continuous time domain mode  $H(S)$  PSS transfers in the discrete time domain mode  $H(Z)$  PSS. The discrete transfer function of PSSs is used to easily dampen the low-frequency oscillations to achieve the small signal stability of the power system [19, 20].

The research gap is identified from the conclusion drawn from the literature survey on various aspects of the AC microgrid. Some domains need further attention such as comparative analysis of conventional lead-lag controllers in AC microgrid. The corresponding discrete mode controllers are also not armed systematically in any AC microgrid. There is also a need of investigating the performance of the AC microgrid at the optimal sampling frequency of discrete mode controllers.

The organization of the remaining article represents the following: Section 2 represents the proposed approach of the paper. Section 3 represents the modeling of the AC microgrid test system with the mathematical modeling of distributed generators, and Sect. 4 gives a brief discussion of discrete mode damping controllers and the mathematical modeling of robust discrete LQG controller. Section 5 represents the result section with the comparative analysis of the controller's validation. The paper ends with a conclusion in Sect. 6, followed by the references.

## 2 Proposed Approach

This paper proposed the design of damping robust discrete controllers to enhance the dynamic stability of the AC microgrid. The execution of discrete controllers in distributed generators of grid-integrated AC microgrid gives better performance against the disturbance of low-frequency electromechanical oscillations in a shorter

settling time. Overall the proposed approach of this research work is to raise the small signal stability of the AC microgrid using different types of discrete mode controllers with optimal sampling frequency.

The main objectives of the research paper are

- The robust design of discrete mode PSSs controllers is the main motive for a grid-connected AC microgrid to increase the system damping characteristics of low-frequency oscillation (LFO) mode for the stabilization of the microgrid.
- The performance of the different discrete mode PSSs such as CPSS ( $\Delta Pa$ -PSS and  $\Delta\omega$ -PSS), MBPSS (MBPSS-4B), and LQG has been compared to analyze the effectiveness of these discrete PSSs for improving the stability of AC microgrid under different varying operating conditions such as a three-phase line to ground fault.
- The discrete mode controllers give better damping performance against the disturbance at the optimal control sampling frequency.
- The compared controller's performance gives discrete time domain mode LQG is the most robust power oscillations damping (POD) controller to improve the dynamic small signal stability and damp the low-frequency electromechanical oscillations of the system.
- Validation of the proposed controllers in MATLAB/Simulink platform.

### 3 Test System

In this modeling of the test system total, 24.5 MW capacity of the distributed generators of the microgrid is connected to the AC grid where 20 kV, 50 Hz with a base MVA is 1000 MVA construct a grid-integrated AC microgrid. The proposed AC microgrid comprises four different power generating units with their installed capacity, a photovoltaic (PV) farm is 8 MW, a DFIG wind turbine is 4.5 MW, hydro is 6 MW, and diesel is 6 MW as a backup. The test system represents in single line grid-integrated AC microgrid illustration under fault conditions shown in Fig. 2 to examine the impact on DGs of electromechanical low-frequency oscillation in power systems. The main research concentrates on oscillations in a low frequency on a scale of 0.1–1 Hz because the focus of this investigation is how to increase the damping performance of modern power systems [21].

The power system stabilizers (PSSs) allow an auxiliary stabilization signal to distributed generators of AC microgrid, which measures the low-frequency oscillations (LFO) of the system and also increases the system stability. To dampen out the power oscillation of DGs of AC microgrid PSSs are used, this is attained with a voltage regulator to generate a torque in phase with speed [22]. The distributed generators connected with different PSSs using a multi-input and single-output switch are represented in Fig. 3.

The equivalent solar photovoltaic (SPV) circuit diagram with a load  $R_L$  is represented in Fig. 4. The output current of the SPV is represented by Eq. (1). Its circuit diagram has a current source, diode, and resistor and is present in [23].



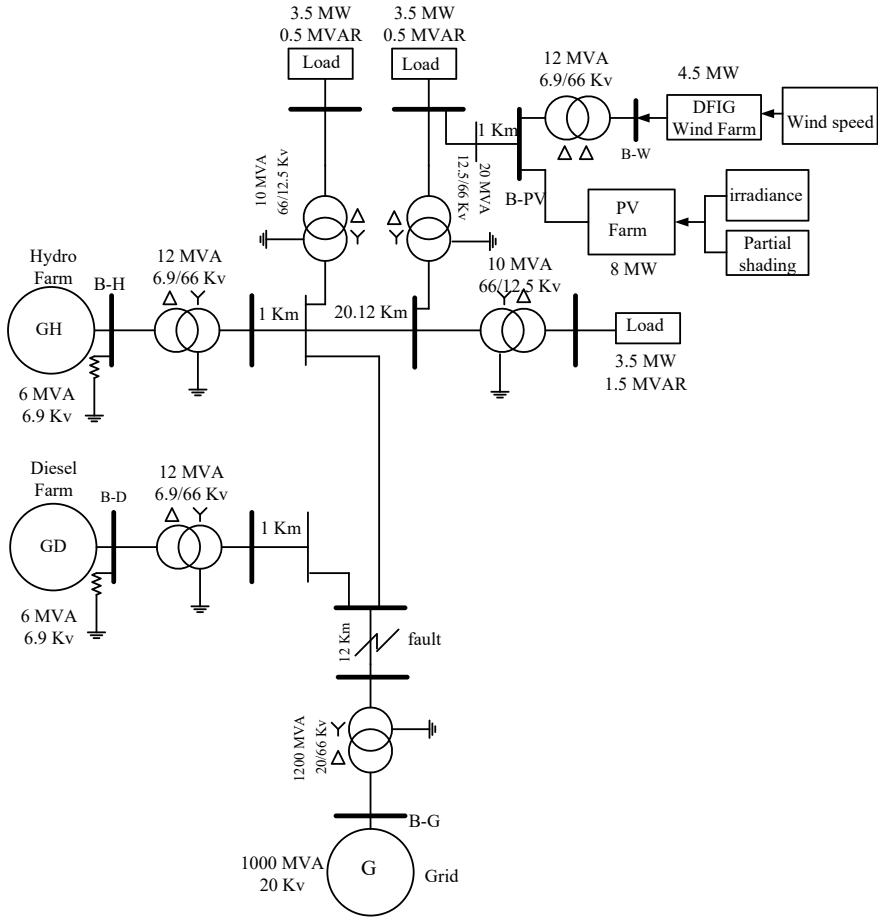


Fig. 2 AC microgrid single line diagram test system

$$I_{SPV} = I_{ph} - I_d - I_{Sh}, \tag{1}$$

where  $I_{SPV}$  is the total PV current,  $I_{ph}$  is photo current, and  $I_{sh}$  is the shunt current across shunt resistance.

The PN junction diode is used to get the unit exponential expression characteristics that represent a solar PV (SPV) system, and it is then expanded to obtain the solar PV total output current as shown below.

$$I_{SPV} = I_{SCA}(G) - N_P \times I_0 \left[ \exp\left(\frac{V_A + I_{SPV}R_S}{\eta N_S k T}\right) q - 1 \right]. \tag{2}$$

Here,  $I_{SPV}$  is total solar PV current (Amp.),  $V_A$  is solar PV voltage (Volt.),  $\eta$  is identity factor,  $I_0$  is reverse saturation current (Amp.),  $R_S$  is array series resistance

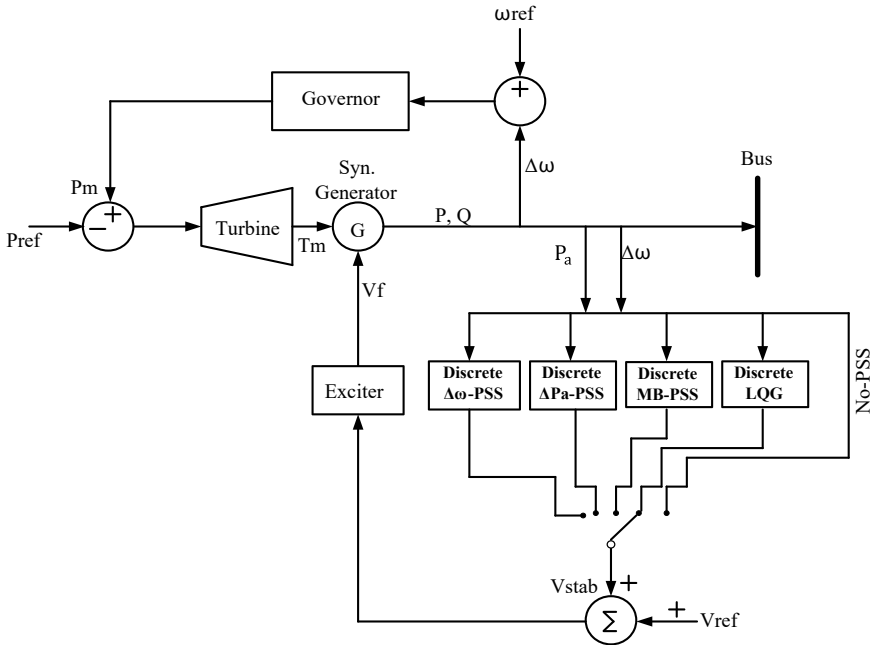


Fig. 3 Distributed generator arrangement with a discrete mode controller

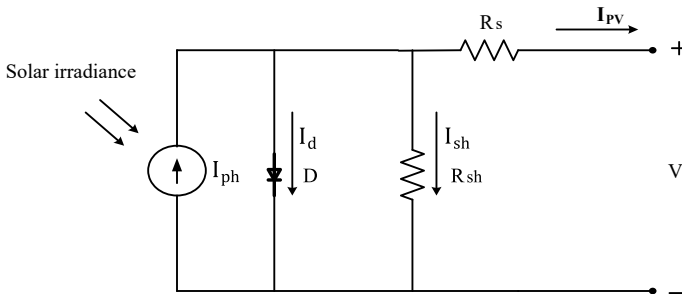


Fig. 4 Photovoltaic cell equivalent circuit

( $\Omega$ ),  $I_{SCA}(G) = N_P I_{SC}(G)$ ,  $I_{SC}$  is SPV short circuit current (Amp.),  $G$  is PV insolation ( $Wh/m^2$ ),  $N_P$  is the No. of modules in parallel,  $N_S$  is the No. of modules in series,  $k$  is represented as the Boltzmann constant, and  $q$  is the electron charge (C).

The DFIG-based wind turbine (DFIG-WT) to generate electrical power is depicted in Fig. 5, which is used for variable speed wind turbines. Its output power can be represented as follows:

$$p_{mech.} = \frac{1}{2} C_p(\beta, \lambda) \pi R^2 \rho v_{wind}^3 \tag{3}$$

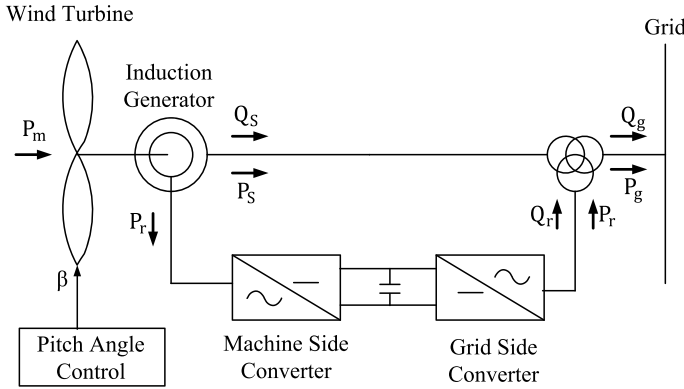


Fig. 5 DFIG configuration using wind energy conversion system

and generated torque due to the wind passing through the turbine blades is given as

$$T_m = 0.5 \frac{C_p(\beta, \lambda)}{\lambda} \rho \pi R^2 V_{wind}^3, \tag{4}$$

where  $C_p(\beta, \lambda)$  known as the coefficient of power is related to the pitch angle ( $\beta$ ) and tip velocity constant ( $\lambda$ ) of the turbine blades,  $\rho$  denotes air density,  $v_{wind}$  denotes the velocity of wind, and  $R$  is the radius of the turbine blade [24].

Equation 5 shows the relationship between the DFIG parameters which is the power coefficient  $C_p(\beta, \lambda)$  concerning relates with pitch angle ( $\beta$ ) of turbine blades, wind velocity ( $\omega_{wind}$ ) m/s, and tip velocity constant  $\lambda$ , respectively.

$$C_p(\beta, \lambda) = 0.517 \left( \frac{116}{\lambda_i} - 0.4\beta - 5.0 \right) \exp\left( -\frac{21}{\lambda_i} \right) + 0.0068\lambda. \tag{5}$$

The tip speed ratio ( $\lambda_i$ ) is given as in Eq. (6)

$$\frac{1}{\lambda_i} = \frac{1}{\lambda + 0.08\beta} - \frac{0.035}{\beta^3 + 1}. \tag{6}$$

### 4 Modeling of Damping Controllers

The power oscillation of the AC microgrid is dampened by the different types of continuous and discrete types of damping controllers and by this improved the performance of the overall system. The small signal stability problem in the distributed generators of the AC microgrid system such as rotor speed deviation, rotor angle deviation, frequency deviation, and voltage deviation, etc. are the disturbances due

to fault. The execution of various types of discrete PSS in DGs of AC microgrid provides the oscillation damping and improves the system stability. The main role of PSSs dampens the electromechanical low-frequency oscillations (LFO) of the microgrid [25]. The AC microgrid distributed generators are used different types of power oscillation damping controllers which are described as

- (i) Speed-based stabilizer
- (ii) Frequency-based stabilizer
- (iii) Power-based stabilizer
- (iv) Discrete mode PSS
- (v) Multi-band stabilizer (MBPSS-4B)
- (vi) Discrete LQG controller.

### 4.1 Discrete Time Domain Controllers

This block diagram’s function is to transform the continuous time domain ( $t$ ) signal to discrete time domain ( $z$ ) response signal using contained blocks as shown in Fig. 6, corresponding to input signal block, sample and hold circuit, pulse generator, gain, discrete transfer function, and desired response blocks. In this, the continuous transfer function  $H(s)$  converts into discrete transfer function  $H(z)$  to develop a desired controller with the help of a sample and hold circuit at the desired sampling frequency. Sample and hold are used to implement a signal sample and hold in discrete mode at desired sampling frequency to achieve optimum control response of the system. With these blocks function design, a discrete time domain controllers and improved the performance of systems and achieved optimum control response against disturbance at a sampling frequency consider 25 Hz ( $T = 0.04$  s) [26, 27].

While the estimation hold is zero-order hold (ZOH), at that time the discrete corresponding to  $H(s)$  is represented by Eq. (7).

$$H_{ho}(z) = (1 - z^{-1}) \left\{ \frac{H(s)}{s} \right\}, \tag{7}$$

where  $H(s)$  is known as the phase lead function shown in Eq. (8)

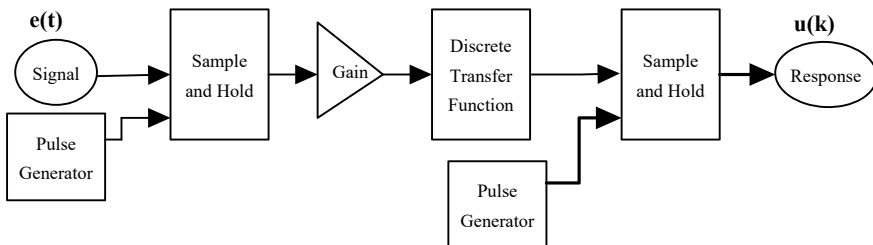


Fig. 6 Block diagram continuous to discrete mode controller conversion

$$H(s) = \frac{1 + sT_1}{1 + sT_2}. \tag{8}$$

So zero-order hold corresponding is represented by Eq. (9).

$$H_{ho}(z) = \frac{\frac{T_1}{T_2}z - \left(\frac{T_1 - T_2}{T_2} + e^{\frac{T}{T_2}}\right)}{z - e^{\frac{T}{T_2}}}. \tag{9}$$

### 4.2 Conventional Damping Controllers ( $\Delta\omega$ -PSS and $\Delta Pa$ -PSS)

The power oscillation damping controller is used to enhance the damping of the system. The basic functioning block model of the PSS damping controller is represented in Fig. 7. The deviation in rotor speed ( $\Delta\omega$ ) or accelerating power (Pa) is selected as input to enhance the damping by adding the feedback signal ( $V_S$ ) to excitation. The typical block diagram speed input-based PSS consists of different blocks considered as, a gain ( $K_{PSS}$ ), a washout time filter ( $T_w$ ) block, a phase angle compensation lead/lag with a time constant ( $T$ ) block, and a limiter ( $V_{max} - V_{min}$ ) [28–30].

The transfer function of the conventional power system stabilizer (CPSS) damping controller is given in Eq. (10) when the generator rotor speed ( $\Delta\omega$ ) is selected as a feedback signal.

$$V_S = K_{PSS} \frac{(sT_w)}{(1 + sT_w)} \frac{(1 + sT_1)}{(1 + sT_2)} \frac{(1 + sT_3)}{(1 + sT_4)} y. \tag{10}$$

The above equation represents speed ( $\Delta\omega$ ) or acceleration power (Pa) as the input signal as ‘y,’  $T_w$  represents as washout time constant,  $T_1, T_2, T_3,$  and  $T_4$  are represented as the time constant, and  $K_{PSS}$  represents as the gain of PSS.

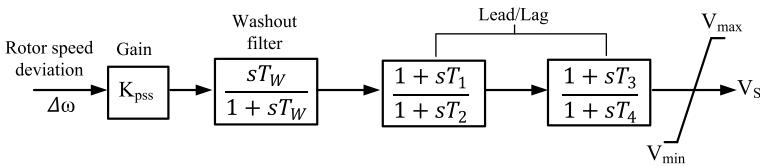


Fig. 7 Single input lead–lag power system stabilizer structure

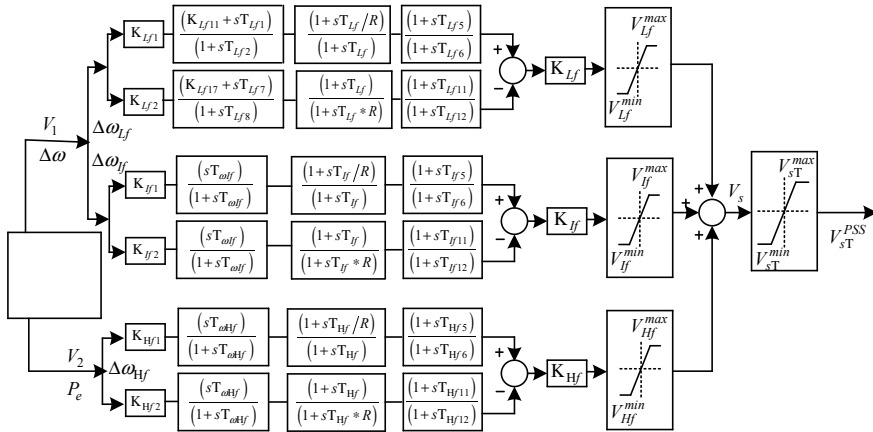


Fig. 8 Multi-input-based MBPSS-4B IEEE standard damping controller

### 4.3 Multi-band PSS (MBPSS-4B) Damping Controller

The MB-PSS damping controller structure is encountered by the IEEE St. 421.5 PSS-4B sort mode to achieve a wide range of electromechanical oscillation damping improvements. The structure of MBPSS-4B provides three adjustable tuning bands as the low-frequency band ( $F_L$ ) with a range of 0.01–0.1 Hz, the intermediate frequency band ( $F_I$ ) with a range of 0.1–1 Hz, and the high-frequency band ( $F_H$ ) with a range of 1–4 Hz modes of the oscillation, which are shown in Fig. 8 [31, 32].

### 4.4 Mathematics Modeling of Discrete LQG Controller

The system implemented with the LQG controller is used to stabilize and regulate the system. The system is influenced by disturbances or uncertainties and also in addition to communication noise is considered a feedback measurement signal which is described by the state space equation of the system [33, 34]. The discrete time domain linear quadratic Gaussian controller equation in discrete time is described by Eqs. (11) and (12).

$$x_{i+1} = A_i x_i + B_i u_i + v_i, \tag{11}$$

$$y_i = C_i x_i + w_i. \tag{12}$$

In the mathematical modeling of discrete LQG controller denotes  $A_i$ ,  $B_i$ ,  $C_i$  as the state matrix and ' $x_i$ ' is the state vector of ' $n$ ' dimensional ' $u_i$ ' is the vector of input of ' $m$ ' dimensional, and ' $y_i$ ' is the vector of the output of ' $q$ ' dimensional, and

here, ‘ $i$ ’ represents the discrete time index. The system needs to be, controllable, and observable, linear time-invariant. In input, ‘ $v_i$ ’ is the disturbance noise, whereas ‘ $w_i$ ’ is the measurement noise. Here,  $E(w_i w_i^T) = W_i$  and  $E(v_i v_i^T) = V_i$  are related to covariance matrices, respectively. The expectation operator of the system is denoted by  $E$ .

$J$  is the cost function corresponding to obtain the optimal control ‘ $u_i$ ’ on uncertainties in the system can be expressed by Eq. (13).

$$J = E \left[ X_N^T F x_N + \sum_{i=0}^{N-1} (X_i^T Q_i X_i + u_i^T R_i u_i) \right], \tag{13}$$

$$F \geq 0, Q_i \geq 0, R_i > 0. \tag{14}$$

The discrete time mode LQG controller is represented by given equations as

$$\hat{X}_{i+1} = A_i \hat{X}_i + B_i u_i + L_{i+1} \left( y_{i+1} - C_{i+1} \{ A_i \hat{X}_i + B_i u_i \} \right), \tag{15}$$

$$\hat{X}_0 = E[X_0], \tag{16}$$

where  $\hat{X}_i$  is analogous to the predictive estimate.

$$\hat{X}_i = E[X_i | y^i, u^{i-1}]. \tag{17}$$

The gain of the Kalman estimator is

$$L_i = P_i C_i^T (C_i P_i C_i^T + W_i)^{-1}, \tag{18}$$

where  $P_i$  is calculated by the given Riccati difference equation that moved in forward time,

$$P_{i+1} = A_i \left( P_i - P_i C_i^T (C_i P_i C_i^T + W_i)^{-1} C_i P_i \right) A_i^T + V_i, \tag{19}$$

$$P_0 = E \left[ (X_0 - \hat{X}_0) (X_0 - \hat{X}_0)^T \right]. \tag{20}$$

The feedback gain matrix is represented as

$$K_i = (B_i^T S_{i+1} B_i + R_i)^{-1} B_i^T S_{i+1} A_i, \tag{21}$$

where  $S_i$  is calculated by the given Riccati difference equation that moved in backward time,

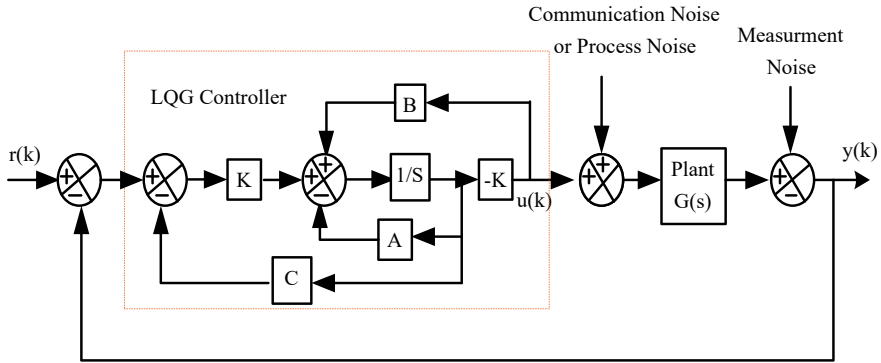


Fig. 9 Conventional model of LQG controller

$$S_i = A_i^T \left( S_{i+1} - S_{i+1} B_i (B_i^T S_{i+1} B_i + R_i)^{-1} B_i^T S_{i+1} \right) A_i + Q_i, \quad (22)$$

$$S_N = F. \quad (23)$$

The main functioning block diagram of the discrete mode LQG controller is represented in Fig. 9. The collective performance of Kalman estimator and linear regulator form the model of linear quadratic Gaussian controller which is used to provide effective performance against disturbances or uncertainties in the system [35]. In this work, the sampling time is 0.04 s. consider because controllers provide optimal control response against disturbances of low-frequency electromechanical oscillations, and discrete mode LQG controller gives better performance on this sampling frequency 25 Hz ( $T = 0.04$  s).

### 5 Simulation Results

The simulation results present that the stability enhanced the AC microgrid with the effect of discrete controllers at the optimal control sampling frequency. A 3- $\phi$  L-G fault, on the transmission line at a  $T = 1$  s. with spam of the fault is 0.15 s. in the AC microgrid test model. The implementation of the distinct types of discrete damping controllers at an optimum control sampling frequency of 25 Hz ( $T = 0.04$  s) is analyzed for the improvement of the constraint of low-frequency electromechanical oscillations in distributed generators of the grid-integrated AC microgrid. The responses of the diesel and hydro distributed generators with the effect of different types of discrete controllers with considered optimal sampling frequency are represented in Figs. 10, 11, 12, 13, 14 and 15 respectively with the variable such as rotor speed deviation ( $\Delta\omega$ ), rotor angle deviation ( $\Delta\delta$ ), and output active power ( $P_e$ ). Similarly, the responses of the DFIG-based wind farm and solar photovoltaic (SPV)



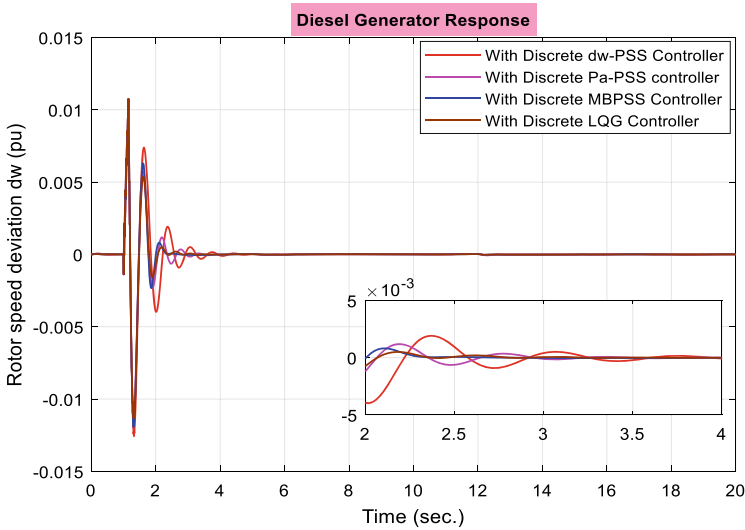


Fig. 10 Rotor speed deviation  $\Delta\omega$  (pu) of diesel generator

farm distributed generators with the influence of discrete controllers are represented in Fig. 16 with the parameter of rotor speed deviation ( $\Delta\omega$ ) of the DFIG-based wind farm distributed generator, and Fig. 17 PV bus voltage at PCC of photovoltaic (PV) farm distributed generator. The obtained response represents the enhanced stability in terms of damping the electromechanical low-frequency oscillation of AC microgrid distributed generators with the discrete controllers at the optimal sampling frequency. The robust design LQG controller is ideal and gives better results compared with conventional PSS ( $\Delta\omega$ -PSS and  $\Delta Pa$ -PSS) and MBPSS-4B controllers in the discrete time domain mode with considered optimal sampling frequency.

The summarized results show that the different discrete mode controllers at optimum control sampling frequency, i.e.,  $F = 25$  Hz ( $T = 0.04$  s), enhance the stability of the AC microgrid. The discrete LQG damping controller is more robust and improves the small signal stability of low-frequency electromechanical oscillations of the distributed generators of the AC microgrid.

## 6 Conclusion and Future Scope

This research work analyzed the enhancement of the stability of the AC microgrid with the design of the damping controller in a discrete time domain with optimum sampling frequency. In this, a microgrid integrated with four different distributed generators unit like a variable wind speed-based DFIG wind farm, photovoltaic (PV) farm, hydro, and one backup unit as a diesel generator. The execution of various types of damping discrete controllers such as conventional PSSs ( $\Delta\omega$ -PSS and  $\Delta Pa$ -PSS),

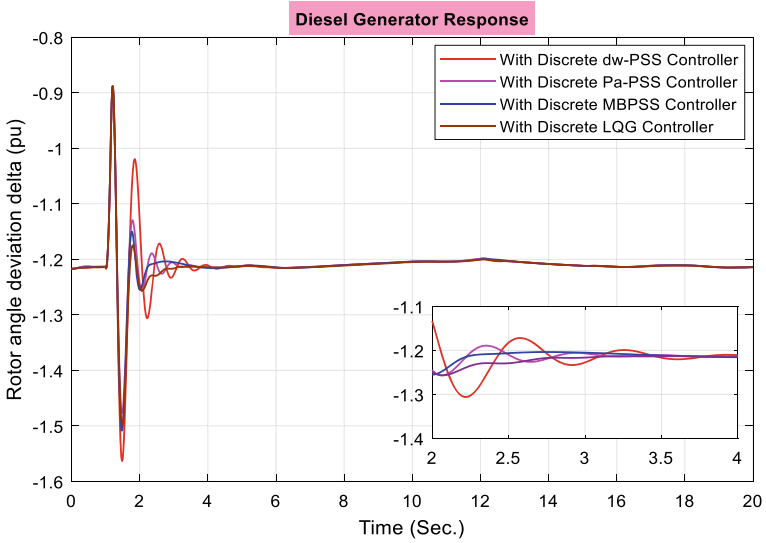


Fig. 11 Rotor angle deviation  $\Delta\delta$  (rad) of diesel generator

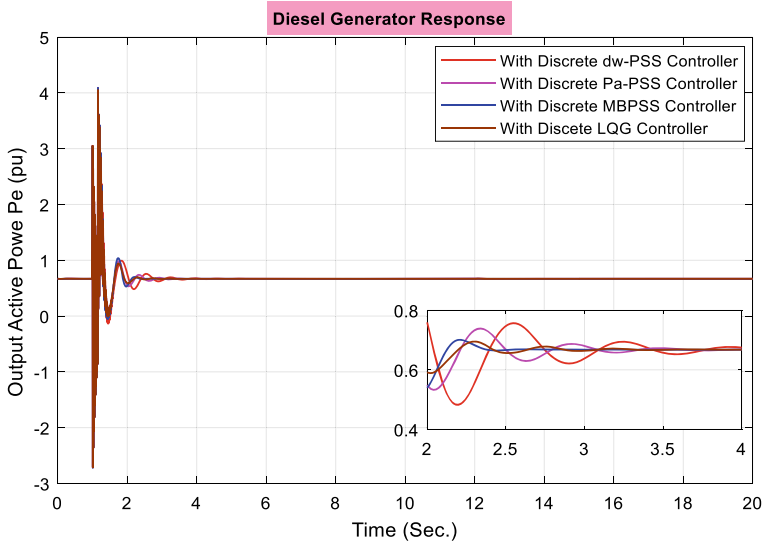


Fig. 12 Output active power ( $P_e$ ) of diesel generator

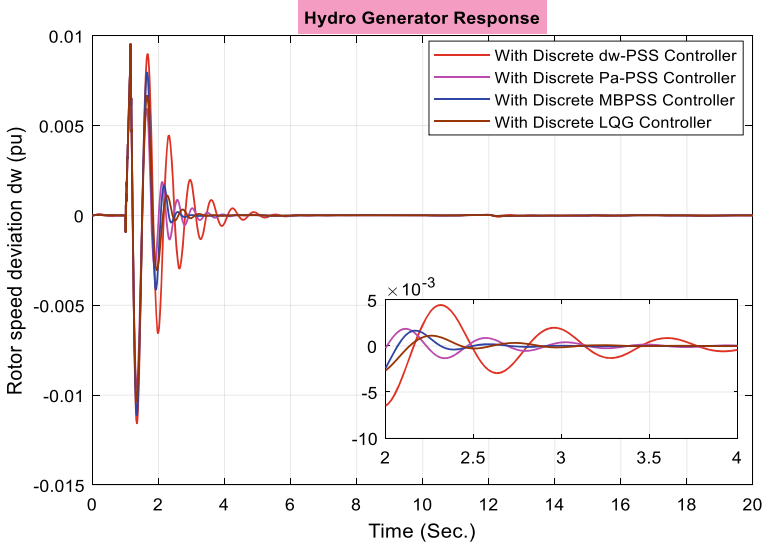


Fig. 13 Rotor speed deviation  $\Delta\omega$  (pu) of hydro generator

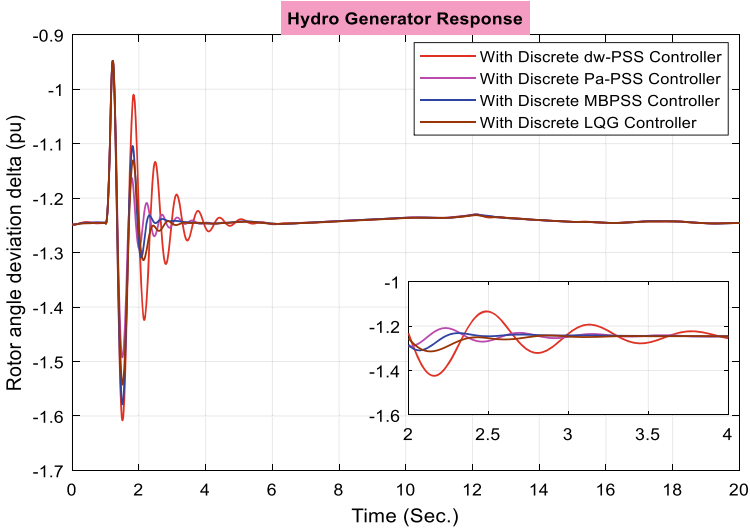


Fig. 14 Rotor angle deviation  $\Delta\delta$  (rad) of hydro generator

multi-band PSS4B (MBPSS-4B), and robust LQG controller at an optimum sampling frequency ( $T = 0.04$  s) executed on the distributed generators of the AC microgrid. Therefore examined and compared the performance of controllers with the disturbances and their effect to increase the dynamic small signal stability. The attained

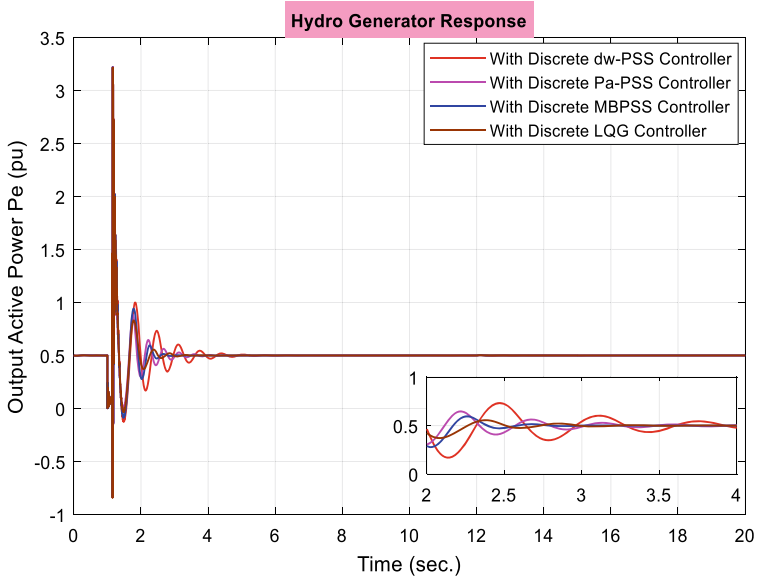


Fig. 15 Output active power ( $P_e$ ) of hydro generator (pu)

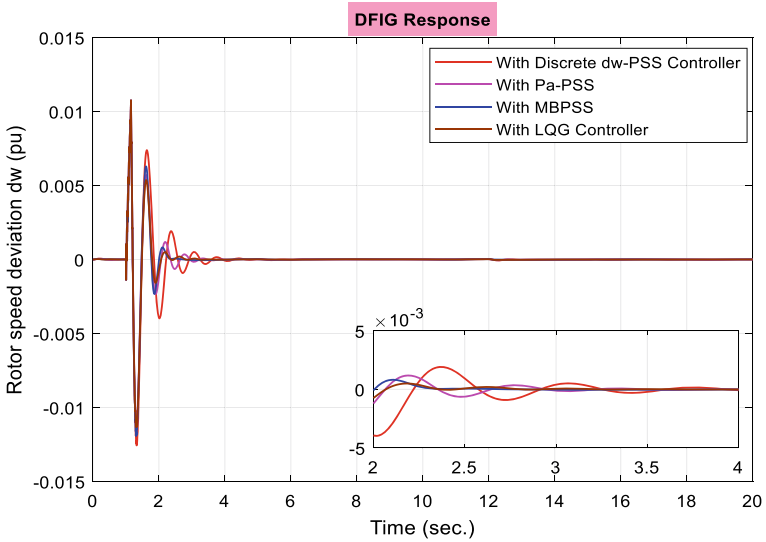
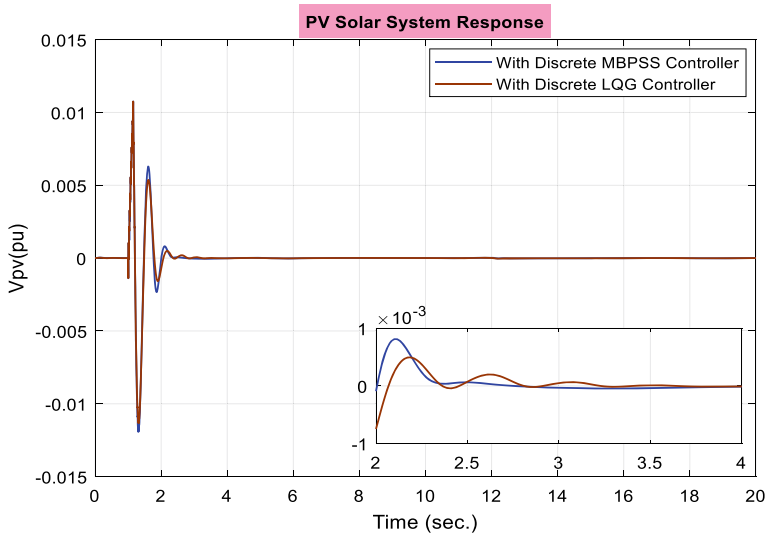


Fig. 16 Rotor speed deviation  $\Delta\omega$  (pu) of DFIG-based wind farm



**Fig. 17** PCC PV voltage (pu) of PV solar farm

responses of the DGs of the AC microgrid appear that the discrete time domain LQG controller is the more robust damping controller for dampening the low-frequency oscillations in a shorter settling time compared with the discrete conventional PSSs and discrete multi-band PSS4B (MBPSS-4B). Overall, we examined the performance of controllers in discrete time domain mode where the sampling frequency is considered 25 Hz ( $T = 0.04$  s), the performance shows that discrete time domain mode LQG is the most robust power oscillations damping controller to improve the dynamic small signal stability and damp the low-frequency electromechanical oscillations of the system in shorter settling time. This research work can be extended further for the implementation of all considered discrete types of controllers that can be used to investigate the performance of islanded mode AC microgrid.

## References

1. Shahgholian G (2021) A brief review on microgrids: operation, applications, modeling, and control. *Int Trans Electr Energy Syst* 31(6):e12885
2. Hossain MA, Pota HR, Hossain MJ, Blaabjerg F (2019) Evolution of microgrids with converter-interfaced generations: challenges and opportunities. *Int J Electr Power Energy Syst* 109:160–186
3. Abdelgawad H, Sood VK (2019) A comprehensive review on microgrid architectures for distributed generation. In: 2019 IEEE electrical power and energy conference (EPEC), pp 1–8
4. Mariam L, Basu M, Conlon MF (2016) Microgrid: architecture, policy and future trends. *Renew Sustain Energy Rev* 64:477–489

5. Mishra S, Malleshm G, Sekhar PC (2013) Biogeography based optimal state feedback controller for frequency regulation of a smart microgrid. *IEEE Trans Smart Grid* 4(1):628–637
6. Yang J, Yuan W, Sun Y, Han H, Hou X, Guerrero JM (2018) A novel quasi-master-slave control frame for PV-storage independent microgrid. *Int J Electr Power Energy Syst* 97:262–274
7. Sen S, Kumar V (2018) Microgrid modelling: a comprehensive survey. *Annu Rev Control* 46:216–250
8. Narayanan V, Kewat S, Singh B (2021) Control and implementation of a multifunctional solar PV-BES-DEGS based microgrid. *IEEE Trans Industr Electron* 68(9):8241–8252
9. Li Y, Xu Z, Xiong L, Song G, Zhang J, Qi D, Yang H (2019) A cascading power sharing control for microgrid embedded with wind and solar generation. *Renew Energy* 132:846–860
10. Hemanand T, Subramaniam NP, Venkateshkumar M (2018) Comparative analysis of intelligent controller based microgrid integration of hybrid PV/wind power system. *J Ambient Intell Humanized Comput* 1–20
11. Puchalapalli S, Tiwari SK, Singh B, Goel PK (2018) A microgrid based on wind driven DFIG, DG and solar PV array for optimal fuel consumption. In: 2018 IEEE 8th power India international conference (PIICON), pp 1–6
12. Singh B, Pathak G, Panigrahi BK (2018) Seamless transfer of renewable-based microgrid between utility grid and diesel generator. *IEEE Trans Power Electron* 33(10):8427–8437
13. Chang GW et al (2014) Modelling and simulation for INER AC microgrid control. In: 2014 IEEE PES general meeting | conference & exposition, pp 1–5
14. Hou X et al (2018) Distributed hierarchical control of AC microgrid operating in grid-connected, islanded and their transition modes. *IEEE Access* 6:77388–77401
15. Mohammed A et al (2019) AC microgrid control and management strategies: evaluation and review. *IEEE Power Electron Mag* 6(2):18–31
16. Baharizadeh M, Karshenas HR, Guerrero JM (2018) An improved power control strategy for hybrid AC-DC microgrids. *Int J Electr Power Energy Syst* 95:364–373. <https://doi.org/10.1016/j.ijepes.2017.08.036>
17. Das DC, Roy AK, Sinha N (2012) GA based frequency controller for solar thermal–diesel–wind hybrid energy generation/energy storage system. *Int J Electr Power Energy Syst* 43(1):262–279
18. Kumar A, Bhadu M, Arora A (2022) Coordinated wide-area damping control in modern power systems embedded with utility-scale wind-solar plants. *IETE J Res* 1–24. <https://doi.org/10.1080/03772063.2022.2082565>
19. Kumar A, Bhadu M (2022) A comprehensive study of wide-area damping controller requirements through real-time evaluation with operational uncertainties in modern power systems. *IETE J Res* 1–22. <https://doi.org/10.1080/03772063.2022.2043784>
20. Alnuman H (2022) Small signal stability analysis of a microgrid in grid-connected mode. *Sustainability* 14(15):9372
21. Paital SR, Ray PK, Mohanty A (2018) Comprehensive review on enhancement of stability in multimachine power system with conventional and distributed generations. *IET Renew Power Gener* 12(16):1854–1863
22. Rafique Z et al (2022) Bibliographic review on power system oscillations damping: an era of conventional grids and renewable energy integration. *Int J Electr Power Energy Syst* 136:107556
23. Kumar A, Bhadu M (2022) Wide-area damping control system for large wind generation with multiple operational uncertainty. *Electr Power Syst Res* 213(108755):01–23. <https://doi.org/10.1016/j.epr.2022.108755>
24. Mohammadzadeh A, Kayacan E (2020) A novel fractional-order type-2 fuzzy control method for online frequency regulation in ac microgrid. *Eng Appl Artif Intell* 90:103483
25. Mishra S, Patel S, Prusty RC, Panda S (2020) MVO optimized hybrid FOFPID-LQG controller for load frequency control of an AC micro-grid system. *World J Eng* 17(5):675–686. <https://doi.org/10.1108/WJE-05-2019-0142>
26. Bhadu M, Senroy N (2014) Real time simulation of a robust LQG based wide area damping controller in power system. In: IEEE PES innovative smart grid technologies, Europe. IEEE

27. Rahman M, Sarkar SK, Das SK, Miao Y (2017) A comparative study of LQR, LQG, and integral LQG controller for frequency control of interconnected smart grid. In: 2017 3rd international conference on electrical information and communication technology (EICT), pp 1–6. <https://doi.org/10.1109/EICT.2017.8275216>
28. Ranjan V, Arora A, Bhadu M (2022) Stability enhancement of grid connected AC microgrid in modern power systems. In: Proceedings of international conference on computational intelligence and emerging power system. Springer, Singapore
29. Kesraoui M, Lazizi A, Chaib A (2016) Grid connected solar PV system: modeling, simulation and experimental tests. *Energy Procedia* 95:181–188
30. Wang J (2021) Design power control strategies of grid-forming inverters for microgrid application: preprint. National Renewable Energy Laboratory, Golden, CO. NREL/CP-5D00-78874. <https://www.nrel.gov/docs/fy22osti/78874.pdf>
31. Kumar A, Bhadu M, Kumawat HC, Bishnoi SK, Swami K (2019) Analysis of sampling frequency of discrete mode stabilizer in modern power system. In: 2019 international conference on computing, power and communication technologies (GUCON), pp 14–20
32. Agrawal V, Rathor B, Bhadu M, Bishnoi SK (2018) Discrete time mode PSS controller techniques to improve stability of AC microgrid. In: 2018 8th IEEE India international conference on power electronics (IICPE). IEEE, pp 1–5
33. Kamwa I, Grondin R, Trudel G (2005) The limits of performance of modern power system stabilizers. *IEEE Trans Power Syst* 20(2):903–915
34. Kumar A, Sharma P, Bhadu M (2021) Performance analysis of multi-band PSS in modern load frequency control systems. *Reliab Theor Appl* 16(SI 1(60)):46–57. <https://doi.org/10.24412/1932-2321-2021-160-46-57>
35. Bhadu M, Senroy N, Narayan Kar I, Sudha GN (2016) Robust linear quadratic Gaussian-based discrete mode wide area power system damping controller. *IET Gener Transm Distrib* 10(6):1470–1478

# Performance Analysis of Grid-Integrated Solar System Through Interlinking Converter with Control Schemes



Preeti Rani, Ved Parkash, and Naveen Kumar Sharma

**Abstract** The output power of photovoltaic (PV) arrays is directly proportional to the solar irradiance level. Therefore, the results of a PV panel highly relies on the prevailing weather circumstances. This cause, the outcome of a PV system can fluctuate rapidly, making it difficult to maintain a stable power supply. This paper analyzed the performance of PV panel integrated with the grid through interlinking converters at different attributes is the novelty in this article. The primary objective of the research included in this thesis is to contribute to the increased implementation of photovoltaic (PV) systems into electric networks. This objective can be met by precisely assessing the performance of PV systems without underestimating the impacts of these systems on the electric network. Overestimating or underestimating the performance of PV systems can lead to issues with electric network planning and operation. Using various control techniques, such as MPPT, voltage and current control, and Pulse Width Modulation (PWM), helps to increase the system's performance and ensure a stable and efficient power supply. These control techniques are implemented in MATLAB/Simulink using control blocks and algorithms, which are connected to the simulation model of the network. Furthermore, the simulation measures performed using a 100 kW solar system connected to a power grid show better performance with various power electronics components and also verify the performance of the boost converter and the LCL filter with a reduction in harmonics in the output of the proposed network. A significant value of the LCL filter reduces Total Harmonic Distortion (THD) percentage, 0.06% for the grid.

**Keywords** Grid · Solar · Control · Boost converter · Interlinking converter

---

P. Rani (✉) · V. Parkash  
MRSPTU, Bathinda, India  
e-mail: [pretty.singla15@gmail.com](mailto:pretty.singla15@gmail.com)

N. K. Sharma  
I. K. Gujral Punjab Technical University, Jalandhar, India



## 1 Introduction

The use of distributed energy sources namely solar and wind power is becoming increasingly popular due to the environmental benefits they offer. Generating electricity from these sources can help reduce the carbon footprint and decrease the dependence on fossil fuels. Additionally, advancements in technology and government incentives have made these renewable energy sources more accessible and cost-effective [1]. Solar energy is a renewable resource that can be used to generate electricity through the energy conversion process. Utilizing the plentiful and cost-free energy from the sun is a fundamental benefit of photovoltaic (PV) networks. However, even though these systems have many benefits, they still face major obstacles preventing them from being widely used [2]. The main obstacles are poor efficiency and high cost when compared with other green technologies. Therefore, modeling PV systems is an important way to understand how they perform under different weather conditions. This helps to ensure that they will operate as intended during seasonal variations. However, it is worth noting that photovoltaic modules tend to be less efficient than other renewable energy resources [3].

A PV array's output power must be maximized by using an MPPT algorithm, which modifies the PV system's specific state to get peak power that the solar panels can provide. To enhance the performance of PV systems, MPPT algorithms have undergone extensive research. To assure the reliability and sustainability of the system, researchers have also concentrated on controlling the reactive and actual power production of PV systems in addition to MPPT management. Another crucial area of research to enhance the quality of the supply of solar power plants is to reduce current distortion [4]. There have been several MPPT algorithms proposed in recent years, but the Peter and Observe (P&O) and Incremental conductance (INC) MPPT algorithms are now highly used. Their procedures and principles are simple and easy to understand [5]. The main aim of P&O MPPT technology is to oscillate the tracking point, while the principle of INC MPPT technology is to create a zero power-to-voltage slope at the peak power point. By disturbing this slope, the INC MPPT technology can improve accuracy [6, 7].

In MPPT algorithms, DC/DC converters are typically used to convert the DC voltage that comes from the PV panels to a controlled supply voltage for the converter. To maximize the amount of power transferred from the photovoltaic cells to the load, the direct current to direct current converter modifies the frequency of duty cycle  $D$  to align the impedance of the loads with the source of PV impedance. To maintain the nominal voltage range for the demand, the resultant voltage is controlled. This makes it possible to harvest the most power possible from the photovoltaic (PV) system, which is essential for the system's effectiveness and performance [8]. To further elaborate on the previous comment, the converter that converts DC to DC often additionally contains a switching component, such as a field-effect transistor or an IGBT, to regulate the current passing through the inductive component and capacitor. The MPPT algorithm measures the frequency range of the switching device to sustain the MPP of the solar energy system, and the capacitors and inductors work to smooth

out any variations in voltage and current. The interlinking converter then receives the outcome of the DC to DC converter for additional processing before connecting to the grid [9].

Current-controlled interlinking converters regulate the current, which is inserted into the grid by adjusting the phase angle and value of supply of the converter output current in reference to the grid voltage. This control technique uses a single current control loop to regulate the supply introduced into the electric grid network, and it is usually implemented using a proportional-integral (PI) regulator. The choice of the right control algorithms depends on the particular application's requirements. Both voltage, as well as current control techniques, have benefits as well as drawbacks [10]. Both control circuits of a voltage-controlled interlinking converter help stabilize the current injected into the network and normalize the generated energy generated by the solar energy system to the 3-phase electrical grid. The voltage control at the DC bus method stabilizes the voltage at the interlinking converter input, allowing for more efficient operation of the inverter. An efficient and fast algorithm INC MPPT is used in the proposed network due to the high convergence speed and low complexity of the system [11].

A method for investigating the energy yield of a solar PV system integrated with an electric grid under dynamic atmospheric conditions using an artificial neural network (ANN) has been proposed in [12]. They used weather constraints such as solar insolation, temperature, and wind speed to test the ANN model, and achieved a high level of accuracy in predicting the energy yield of the system. An improved modified perturb and observe (IMPO) technique for MPPT of a PV system integrated with a grid is presented in [13]. In [14], an optimization technique is presented for figuring out the best place and size for electrically linked solar photovoltaic (PV) plants in the Kingdom of Saudi Arabia. They suggested a better Big Bang-Big Crunch algorithm to determine the best PV system configuration. The study discovered that the suggested algorithm was better than the traditional BB-BC algorithm at figuring out the best PV system configuration, leading to a higher energy yield and lower leveled cost of electricity (LCOE). A grid-connected photovoltaic system based on direct power control with an improved hysteresis control strategy was proposed in [15]. The authors aimed to address the problem of output power fluctuations caused by intermittent solar radiation and proposed a new method that can control the power output of the inverter in real-time to achieve a stable output. The study demonstrated that the presented method was effective in minimizing fluctuations in output power and improving the system's stability. Mapako and Dakwa [16] described a study that used a modified invasive weed optimization algorithm to optimize an electrically linked PV system. The authors modified the traditional algorithm by introducing a modified mutation operator and a new crossover operator to improve the algorithm's performance.

The research gap in the performance analysis of power plant-integrated solar power systems lies in the need to develop more accurate and reliable models to evaluate the system's operation under varying weather conditions, as well as to identify and address the factors that affect the system's efficiency and reliability. Identifying and addressing the issues related to system operation and maintenance, such as

module cleaning, monitoring, and fault detection, to improve system reliability and reduce downtime.

The novelty of simulating a grid-connected solar network with inverter and MPPT control lies in the ability to accurately model and analyze the effectiveness of the solar energy system under dynamic circumstances. The simulation can help identify the optimal design and operating parameters of the system, as well as potential issues and limitations:

- The simulation can also be used to test different control strategies and scenarios, such as changes in weather conditions, load demands, and system configurations. This can help identify the most effective control strategies and optimize the performance of the system.
- The proposed methodology adequately explains all the aspects that can have an effect on the various attributes of a solar power plant, such as power, current, and voltage as well as variation in solar insolation, and temperature.
- The absence of a step-by-step simulation technique is presented, which makes it easy for researchers to understand and do modeling independently.

In this work effectiveness of the solar power plant interconnected with the electric grid is analyzed under MATLAB/Simulink. The efficacy of the suggested work with interlinking converter and controller is verified through simulation results for different attributes. In Sect. 2 PV system modeling is explained. Section 3 described control schemes. Section 4 explains test system simulation and results. Section 5 concludes with a conclusion.

## 2 PV System Modeling

Figure 1 depicts the suggested grid-integrated PV model network. The model includes a photovoltaic (PV) panel, a boost converter, and additional components to regulate the outcome of the PV power plant. The PV panel generates electricity in response to incoming solar radiation, and the boost converter is utilized to increase the voltage of the generated electricity to a level suitable for grid integration. The boost voltage of the switching device is fed to the interlinking device between the grid and PV system, which is also called an inverter to change the DC to a 3-phase AC supply with minimum harmonic distortion due to the LC filter connected in between them.

Figure 2 shows an equivalent circuit of a solar energy cell with single diode, and the simultaneous equations characterize the characteristics of the PV module: [12]

$$I_D = I_0 \left[ e^{\frac{V_D}{V_T}} - 1 \right] \quad (1)$$

$$V_T = \frac{K_T}{q} * nI * N_{\text{cell}} \quad (2)$$

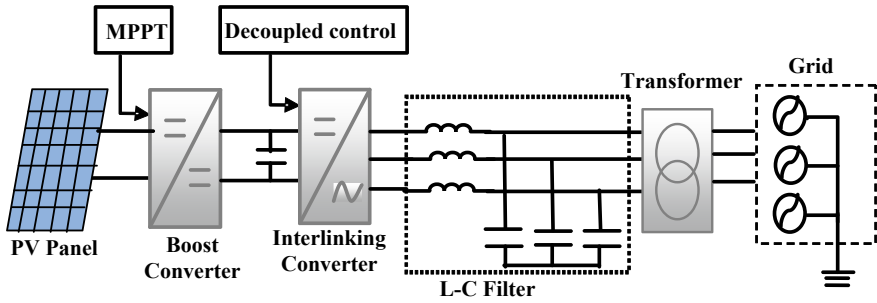
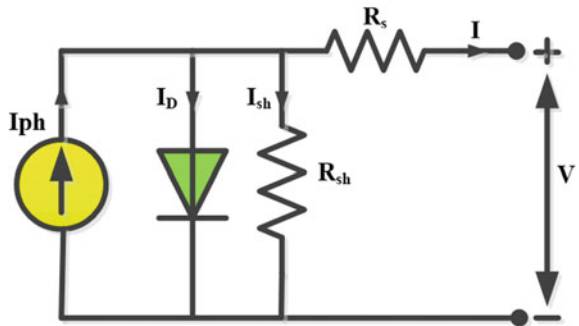


Fig. 1 Grid-connected PV model

Fig. 2 Equivalent model of PV array



where

- $I_D$  Diode current (A)
- $I_0$  Diode saturation current (A)
- $k$  Boltzman constant ( $1.3806e-23 \text{ J K}^{-1}$ )
- $nI$  Ideality factor, a number close to 1.0
- $T$  Cell temperature (K)
- $N_{\text{cell}}$  Cells connected in series in a module
- $V_D$  Diode voltage (V)
- $q$  Electron charge ( $1.6022e-19 \text{ C}$ )

### 2.1 Boost Converter Modeling

The schematic diagram of MPPT-based boost converter connected to the PV network is represented in Fig. 3. The following equations can be used to analyze the key boost converter components' values [14]:

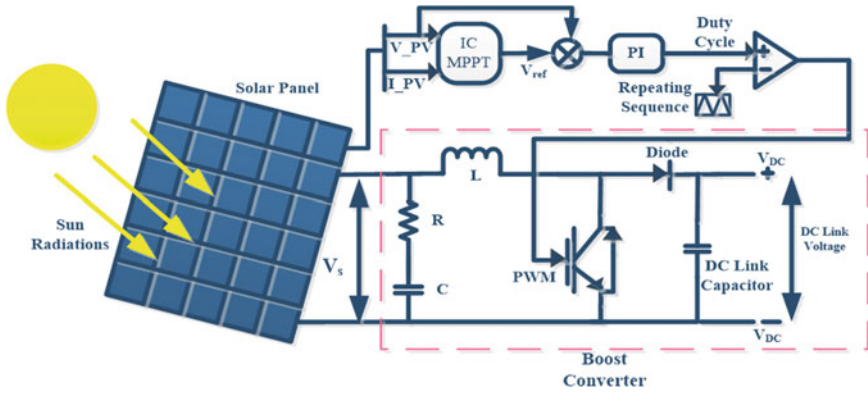


Fig. 3 MPPT with boost converter connected with solar panel

$$L = \frac{V_{ip}(V_0 - V_{in})}{f_{sw} V_0 \Delta I} \tag{3}$$

$$C = \frac{I_{op}(V_0 - V_{in})}{f_{sw} V_0 \Delta V} \tag{4}$$

where

- $V_{ip}$  Input voltage of boost converter
- $V_0$  Voltage across the capacitor of the boost converter
- $f_{sw}$  Switching frequency of boost converter 5 kHz
- $\Delta I$  Ripple boost current 1.4%
- $\Delta V$  Ripple voltage 0.4%.

### 2.2 Power LC Filter

The interface between the grid and inverter contains an LC filter to reduce harmonic distortion due to the conversion of supply from DC to a 3-phase AC supply. Figure 4 represented the model of the LC filter. The following equations can be used to analyze the values of  $L$  and  $C$ : [15]

$$C = \frac{0.05 \times S}{V^2 \times 2 \times \pi \times f} \tag{5}$$

$$L = \frac{0.2 \times V}{I \times 2 \times \pi \times f} \tag{6}$$

where

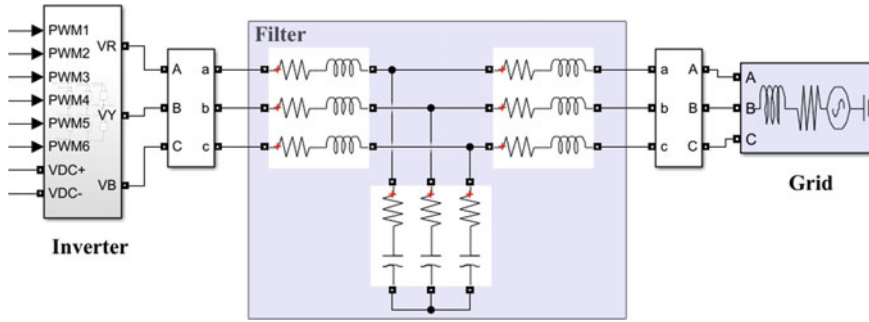


Fig. 4 Model of the LC filter

- $C$  is the filter capacitance (F)
- $L$  is the filter inductance (H)
- $S$  is rated power (W)
- $V$  is the grid voltage (V)
- $I$  is the grid current (A)
- $f$  is the frequency of supply (Hz).

### 3 Control Schemes

Two main control schemes are utilized in the proposed network one is the MPPT control scheme, which fed the control signal to the converter to regulate the input of the inverter [16, 17]. Another control scheme is decoupled control, it fed the six PWM signals to the switching converters to transform the DC supply to a 3-phase AC supply.

#### 3.1 INC MPPT Control

The MPPT block uses the INC algorithm to track the peak point of power with changes in the inputs of the PV panel. Figure 5 illustrates the flowchart of the INC algorithm. The flow chart demonstrated how to follow the peak point at every sampling frequency by comparing the supply parameters to the preceding sample. At the maximum, there is no power loss when the voltage changes. The power equation of the PV panel is [18]:

$$P = V \times I \tag{7}$$

Differentiate Eq. 7 with respect to  $V$

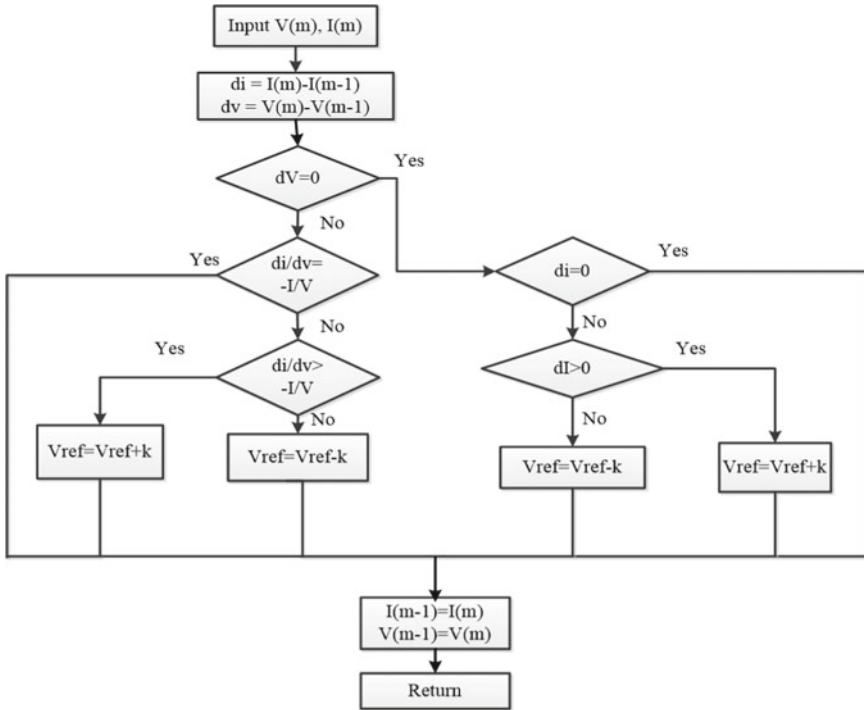


Fig. 5 Flow chart of INC MPPT algorithm

$$\frac{dP}{dV} = 1 + V \frac{dI}{dV} \tag{8}$$

At peak point [19]

$$\frac{dP}{dV} = 0 \tag{9}$$

$$\frac{dI}{dV} = -\frac{I}{V} \tag{10}$$

The condition of increasing conductance changes depending on where the operational point is on the curve. Change in incremental conductance according to position can find out by the following equations: [20]

On the curve’s right side

$$\frac{dI}{dV} < -\frac{I}{V} \tag{11}$$

On the curve’s left side

$$\frac{dI}{dV} > -\frac{I}{V} \quad (12)$$

The key benefit that this approach offers over the Peter and Observe method is that, when the operating point reaches the MPP, it can more precisely determine the peak point. This is because, while incremental conductance has a high tracking speed with changes in inputs of the PV panel, perturb and observe method operational point frequently oscillates about the MPP. Due to the employment of two sensors, a current and a voltage sensor, this method has the drawback of being more complicated than the perturb and observe method [21].

### 3.2 Interlinking Converter Control

The control architecture of a 3-phase interlink converter is shown in Fig. 6. For synchronizing the phase angle of the converter's electrical output with the grid voltage, a phase-locked loop (PLL) is used [22]. The control scheme consists of current and voltage regulators to match the synchronization needs and also to provide the optimized power with an improved power factor. The voltage regulator is designed to keep the DC voltage stable in spite of changes in weather conditions. It does this by using a PI controller to generate a command current  $(I_d)^*$ . The real DC voltage  $(V_{dc})^*$  is compared with this current. The voltage regulator modifies the current if the two values are not equal. Two PI controllers—one for the  $I_d$  current and another for the  $I_q$  current—make up the current regulator. The command current  $(I_d)^*$  is generated by the voltage regulator and compared to the grid current  $(I_d)$ . If there is a difference between the two, the current regulator will adjust the  $I_d$  current accordingly [23, 24].

The scheme is called decoupled control and includes a PI controller that receives an error signal and produces a voltage-measuring signal  $(V_d)$ . This signal is compared with the measured value of the inductor voltage  $(\omega L)$  to generate  $(V_d)^*$  [25]. This signal is then managed through another PI controller to generate an adding voltage signal  $(V_q)$  that is added to the inductor voltage  $(\omega L)$  to generate the command  $(V_q)^*$ . This control scheme is called decoupled because it separates the control of the real power  $(V_d)$  and reactive power  $(V_q)$  components of the inverter output. A 3-phase system output is then created from the  $(V_d)^*$  and  $(V_q)^*$  signals and sent to the PWM controller. In order to achieve optimal electrical power in terms of frequency and voltage that are in synchronization with the grid system, this device develops a switching pulse that regulates the inverter's operation [26–33].



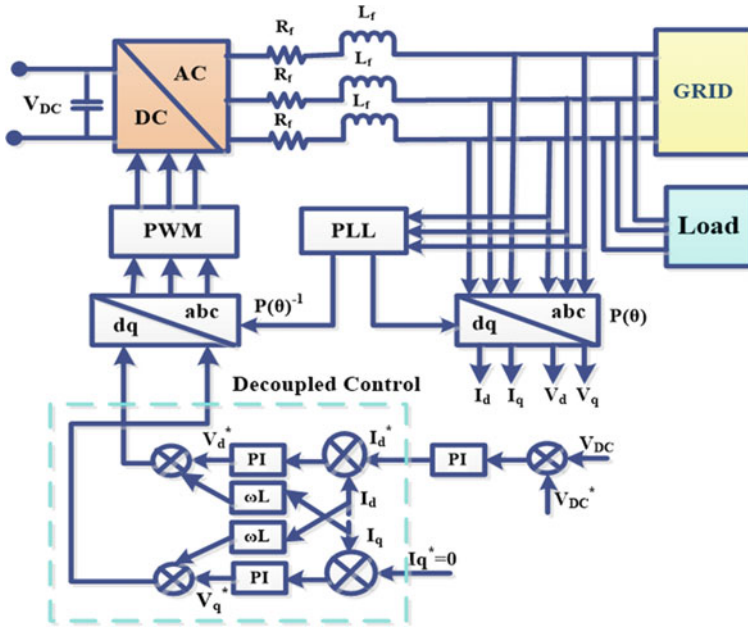


Fig. 6 Control scheme of interlink converter

### 4 Test System Simulation and Results and Discussion

This section examines the grid-integrated solar system’s actual performance using the MATLAB/Simulink environment. 100 kVA, 230 V (phase voltage), 50 Hz three-phase grid, use different converters and control schemes. Figure 7 depicts the model using Simulink of the grid-integrated solar system, and Table 1 provides a summary of the model’s key parameters. A PV panel, a converter that converts DC to DC to control the electrical voltage of the solar energy system’s output, an alternating current inverter that transforms DC electricity to AC power, and possibly additional components to synchronize the inverter’s electricity output with the electrical grid are all included in the Simulink model.

Figure 8 represented the performance of the proposed network at 1000 W/m<sup>2</sup> radiation intensity and 250 °C temperature in the form of characteristics. Figure 8a showed the 345.4 current and Fig. 8b depicted the 100 kW power at 290 V at the highest point of the curve.

Figure 9 represented the performance of the proposed network at fixed radiation intensity and variable temperature in the form of characteristics. Figure 9a represented the value of current and voltage decreases with the increase in temperature and Fig. 9b represented the decrease in power output of the PV panel with an increase in temperature input.

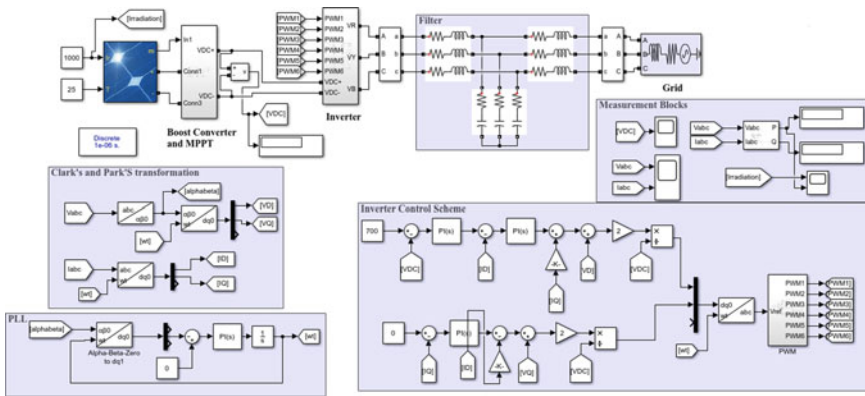


Fig. 7 Simulink model of the grid-integrated solar system

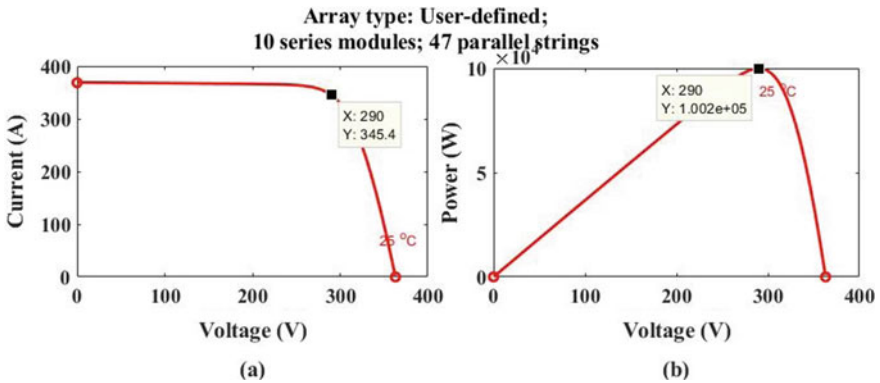


Fig. 8 Characteristics of PV panel at fixed inputs: a I/V characteristics, b P/V characteristics

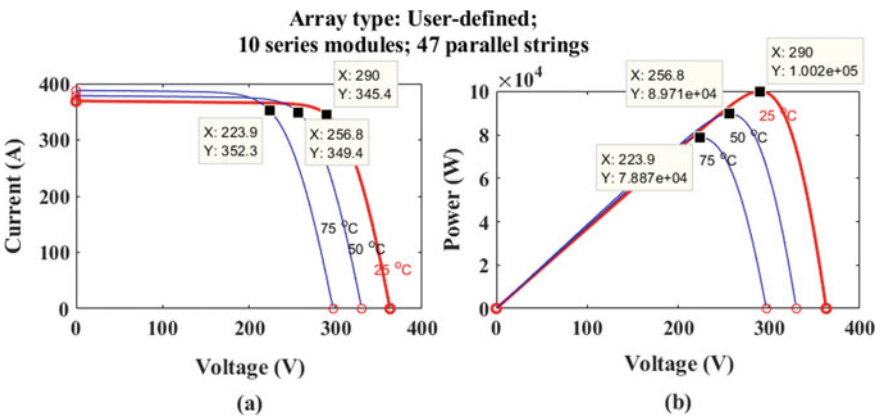
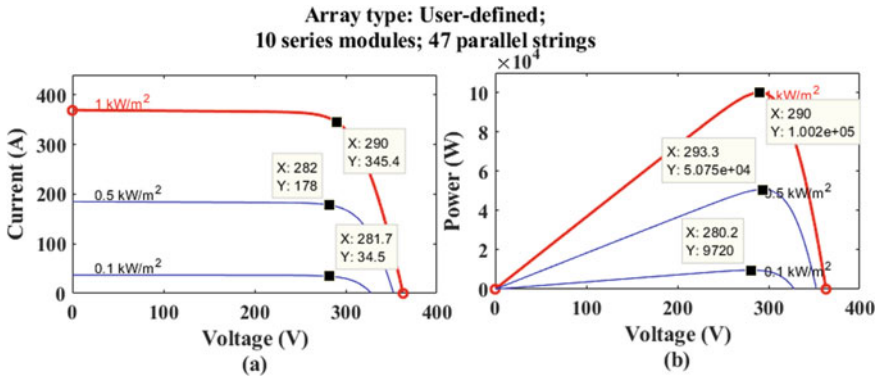
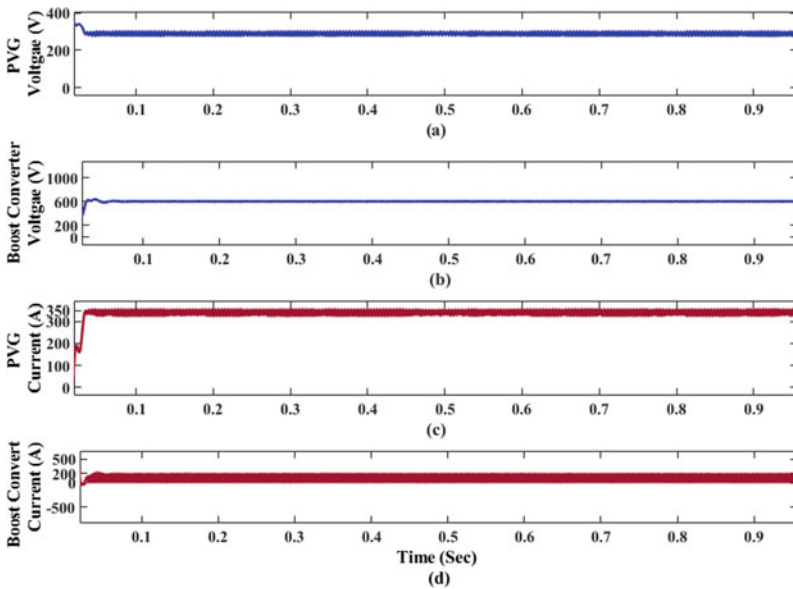


Fig. 9 Characteristics of PV panel at fixed radiation intensity and variable temperature: a I/V characteristics, b P/V characteristics



**Fig. 10** Characteristics of PV panel at variable radiation intensity and fixed temperature: **a** I/V characteristics, **b** P/V characteristics



**Fig. 11** Boost converter performance: **a** Photovoltaic generator (PVG) voltage, **b** boost converter voltage, **c** PVG current, **d** boost converter current

Figure 10 represented the characteristics of PV at fixed temperature and variable radiation intensity. Figure 10a represented the value of current and voltage decreased with decreases in radiation intensity from 1000 to 100 W/m<sup>2</sup> and also with a decrease in radiation intensity power output of the PV panel decreased.

Figure 11 represented the simulation waveform of voltage and current to analyze the performance of the INC-based boost converter. The boost converter increase the

voltage from 283 to 596 V as depicted in Fig. 11a, b and it step down the current from 353 to 171 A as depicted in Fig. 11c, d.

The output of the interlinking inverter without an LC filter is depicted in Fig. 12. Which shows the high amount of harmonic distortion in the simulation waveforms of voltage, current, real power, and wattless power of the grid.

The output of the interlinking inverter with an LC filter is depicted in Fig. 13. Which shows the least amount of harmonic distortion in the simulation waveforms of voltage, current, real power, and wattless power of the grid.

The main power quality issue in the utilization of power electronics components is harmonics distortion in the output of the interlinking converter. The suggested network's harmonic analysis without a filter is shown in Fig. 14, and with a filter is shown in Fig. 15. These harmonic spectrums represented the performance of the LC filter which reduces the THD% of the proposed topology. In the case of voltage, THD% improved from 106.70 to 0.06%, and in the case of current the THD% improved from 112.8 to 1.06%.

## 5 Conclusion

The objective of this paper is to analyze the effects of a proposed network, which consists of a PV arrays, an MPPT-based boost converter, and a 3-phase interlinking inverter employed with an LC filter. Two main control schemes namely INC tracker and decoupled control scheme employed in this network for the effectiveness of the system. Overall, the simulation of a grid-connected solar network with an inverter and MPPT control represents a novel and effective approach to designing and analyzing solar energy systems. By accurately modeling the performance of the system, the simulation can help optimize the system design, improve the energy yield, and enhance the overall reliability of the system.

The future scope of grid-connected solar networks is vast and holds significant potential for the global energy sector. Increased solar penetration: With the falling cost of solar PV systems and increasing efficiency, it is expected that solar energy will continue to gain a larger share of the energy mix. The future of grid-connected solar networks lies in increasing solar penetration and integration with the grid.

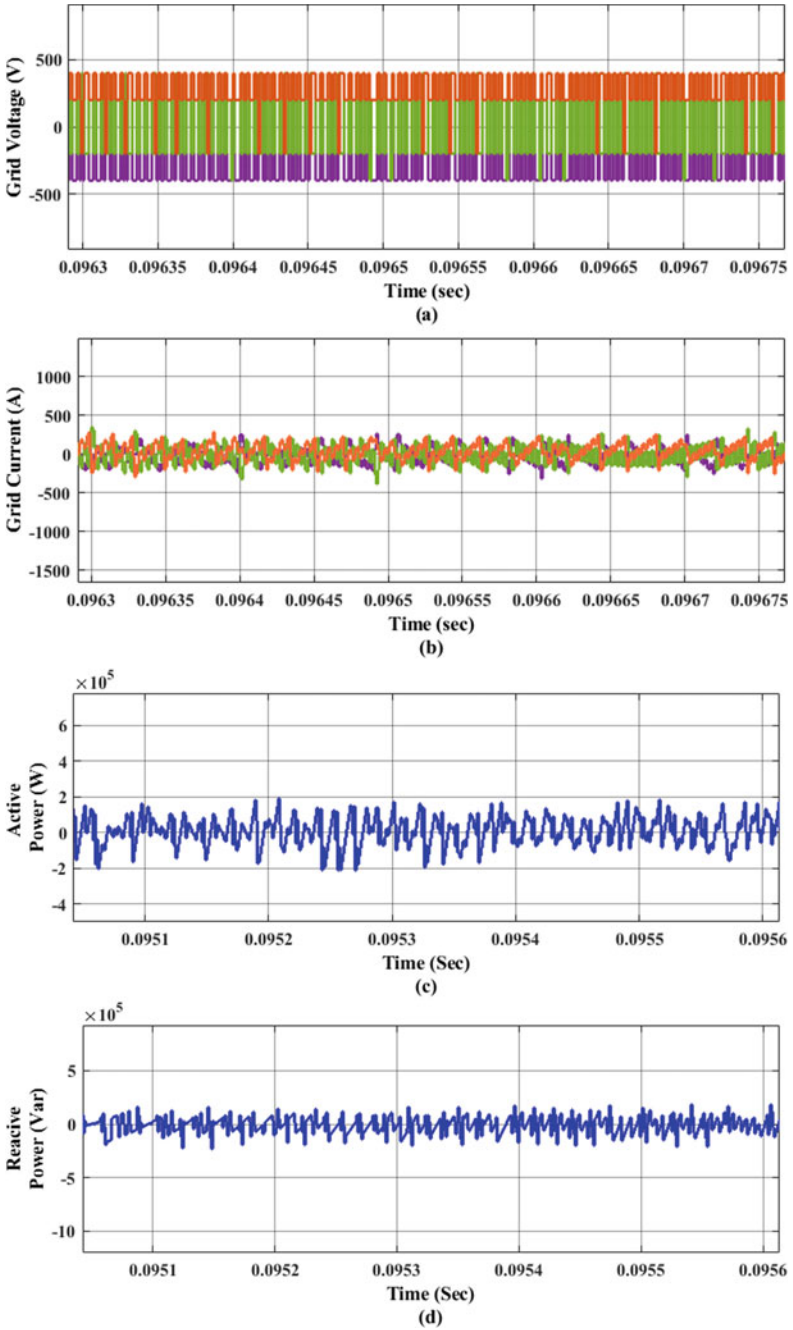


**Fig. 12** Grid output without filter: **a** Grid voltage, **b** grid current, **c** grid real power, **d** grid wattless power

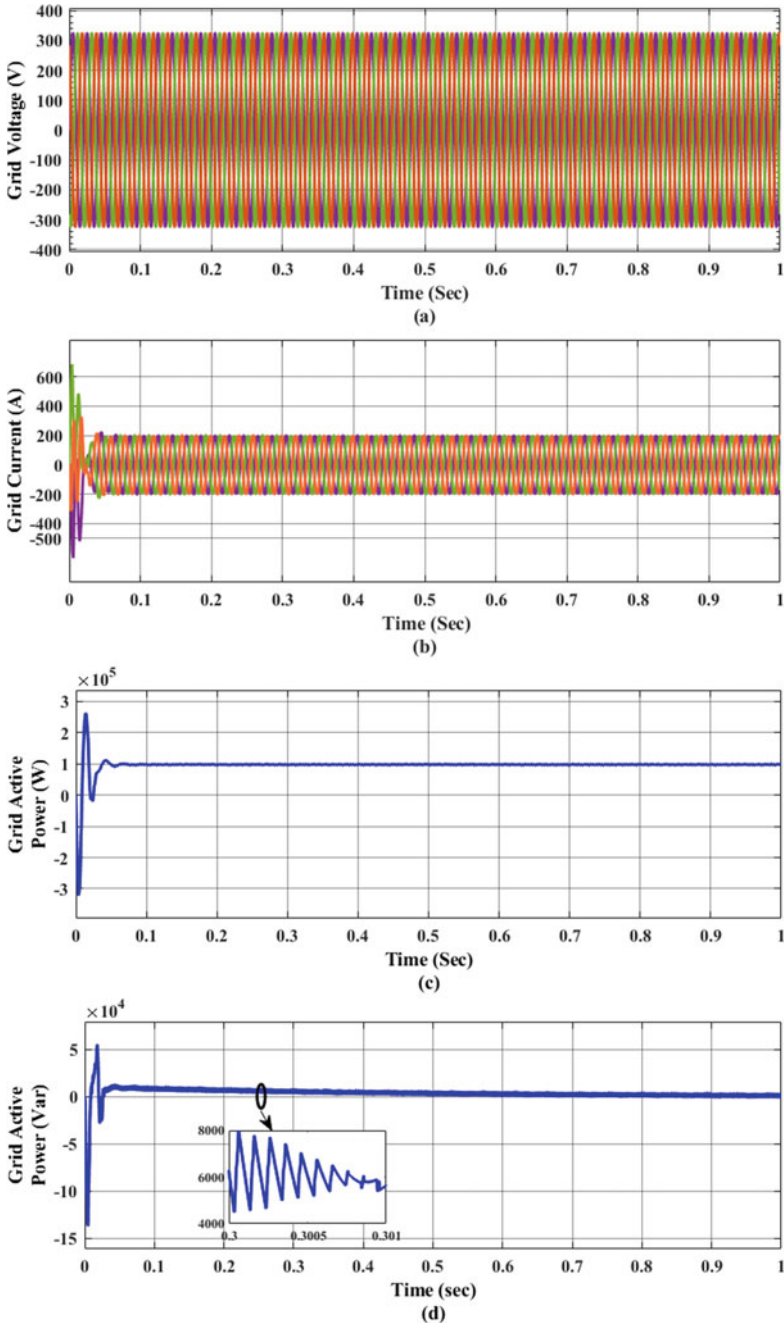


**Fig. 13** Grid output with filter: **a** Grid voltage, **b** grid current, **c** grid real power, **d** grid wattless power

**Fig. 14** Harmonic spectrum without filter

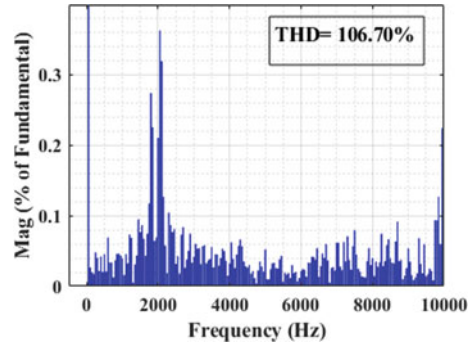
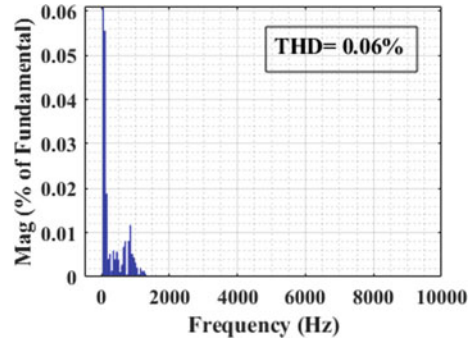


**Fig. 15** Harmonic spectrum with filter



## References

1. Castillo JP, Mafiolis CD, Escoba EC, Barrientos AG, Segura RV (2015) Design, construction and implementation of a low cost solar-wind hybrid energy system. *IEEE Lat Am Trans* 13:3304–3309. <https://doi.org/10.1109/TLA.2015.7387235>
2. Rini TH, Razzak MA (2015) Voltage and power regulation in a solar-wind hybrid energy system. In: *IEEE international WIE conference on electrical and computer engineering (WIECON-ECE)*, pp 231–234. <https://doi.org/10.1109/WIECON-ECE.2015.7443904>
3. Sujatha K, Nagaraj R, Ismail MM (2013) Real time supervisory control for hybrid power system. In: *International conference on green computing, communication and conservation of energy (ICGCE)*, pp 415–418. <https://doi.org/10.1109/ICGCE.2013.6823471>
4. Liwen C, Jiadan W, Qingtang D (2012) Simulation research of a novel wind and solar hybrid power system. In: *Power engineering and automation conference*, pp 1–4. <https://doi.org/10.1109/PEAM.2012.6612513>
5. Natsheh EM, Albarbar A, Yazdani J (2011) Modeling and control for smart grid integration of solar/wind energy conversion system. In: *Innovative smart grid technologies (ISGT Europe)*. *IEEE PES international conference*, pp 1–8. <https://doi.org/10.1109/ISGTEurope.2011.6162643>
6. Tiwari SK, Singh B, Goel PK (2018) Design and control of micro-grid fed by renewable energy generating sources. In: *International conference on power systems (ICPS)*, vol 54, pp 2041–2050. <https://doi.org/10.1109/TIA.2018.2793213>



7. Al-Salaymeh A, Al-Hamamre Z, Sharaf F, Abdelkader MR (2010) Technical and economical assessment of the utilization of photovoltaic systems in residential buildings: the case of Jordan. *Energy Convers Manage* 51:1719–1726. <https://doi.org/10.1016/j.enconman.2009.11.026>
8. Ho B, Chung H (2005) An integrated inverter with maximum power tracking for grid-connected PV systems. *IEEE Trans Power Electron* 20. <https://doi.org/10.1109/APEC.2004.1296072>
9. Zargar MY, Mufti MD, Lone SA (2016) Modeling and control of wind solar hybrid system using energy storage system. In: International conference on computing, communication and automation (ICCCA), pp 965–970. <https://doi.org/10.1109/CCAA.2016.7813855>
10. Kumar AVP, Parimi AM, Rao KU (2014) Performance analysis of a two-diode model of PV cell for PV based generation in MATLAB. In: IEEE international conference on advanced communications, control and computing technologies, pp 68–72. <https://doi.org/10.1109/ICA-CCCT.2014.7019191>
11. Sivagamasundari MS, Mary P, Velvizhi V (2013) Maximum power point tracking for photovoltaic system by perturb and observe method using buck boost converter. *Int J Adv Res Electr Electron Instrum Eng* 2:2433–2439
12. Kumar V, Bansal RC (2022) Energy yield prediction of a grid connected solar photovoltaic system under dynamic weather conditions using artificial neural network. *Lecture notes in electrical engineering*, vol 785, pp 613–622. [https://doi.org/10.1007/978-981-16-3223-3\\_55](https://doi.org/10.1007/978-981-16-3223-3_55)
13. Dandapat S, Datta S, Roy M (2022) An improved modified perturb and observe algorithm for maximum power point tracking of grid connected solar photovoltaic system. *Lecture notes in electrical engineering*, vol 785, pp 651–660. [https://doi.org/10.1007/978-981-16-3223-3\\_59](https://doi.org/10.1007/978-981-16-3223-3_59)
14. Khalil AB, Mohamad AA (2021) Optimal location and sizing of grid-connected solar PV systems in the Kingdom of Saudi Arabia using the improved big bang-big crunch algorithm. *Lecture notes in electrical engineering*, vol 715, pp 121–134. [https://doi.org/10.1007/978-981-33-6953-2\\_11](https://doi.org/10.1007/978-981-33-6953-2_11)
15. Jia Z, Li C, Li L, Li Q (2020) A grid-connected photovoltaic system based on direct power control with an improved hysteresis control strategy. *Lecture notes in electrical engineering*, vol 601, pp 207–215. [https://doi.org/10.1007/978-981-15-5584-3\\_20](https://doi.org/10.1007/978-981-15-5584-3_20)
16. Mapako M, Dakwa T (2021) Optimisation of a grid connected photovoltaic system using a modified invasive weed optimisation algorithm. *Lecture notes in electrical engineering*, vol 715, pp. 103–119. [https://doi.org/10.1007/978-981-33-6953-2\\_10](https://doi.org/10.1007/978-981-33-6953-2_10)
17. Jacob T, Arun S (2012) Maximum power point tracking of hybrid PV and wind energy systems using a new converter topology. In: International conference on green technologies (ICGT), pp 280–287. <https://doi.org/10.1109/ICGT.2012.6477986>
18. Benadli R, Khiari B, Sellami A (2016) Predictive current control strategy for a three-phase grid connected photovoltaic-wind hybrid system. In: International renewable energy congress (IREC), pp 1–6. <https://doi.org/10.1109/IREC.2016.7478901>
19. Hamadi MRA, Chandra A, Singh B (2014) Hybrid AC-DC standalone system based on PV array and wind turbine. In: IECON annual conference of the IEEE Industrial Electronics Society, pp 5533–5539. <https://doi.org/10.1109/IECON.2014.7049346>
20. Brano VL, Orioli A, Ciulla G, Gangi AD (2010) An improved five-parameter model for photovoltaic modules. *Solar Energy Mater Solar Cells* 94:1358–1370. <https://doi.org/10.1016/j.solmat.2010.04.003>
21. Lo Y-K, Lee T-P, Wu K-H (2008) Grid-connected photovoltaic system with power factor correction. *IEEE Trans Industr Electron* 55:2224–2227. <https://doi.org/10.1109/TIE.2008.921204>
22. Femia N, Petrone G, Spagnuolo G, Vitelli M (2009) A technique for improving P&O MPPT performances of double stage grid-connected photovoltaic systems. *IEEE Trans Indust Electron* 56:4473–4482. <https://doi.org/10.1109/TIE.2009.2029589>
23. Siddique MAB, Khan MA, Asad A, Rehman AU, Asif RM, Rehman SU (2020) Maximum power point tracking with modified incremental conductance technique in grid-connected PV array. In: International conference on innovative technologies in intelligent systems and industrial applications (CITISIA), pp 1–6. <https://doi.org/10.1109/CITISIA50690.2020.9371803>



24. Hua C, Lin J (2004) A modified tracking algorithm for maximum power tracking of solar array. *Energy Convers Manage* 45:911–925. [https://doi.org/10.1016/S0196-8904\(03\)00193-6](https://doi.org/10.1016/S0196-8904(03)00193-6)
25. Kumar AVP, Parimi AM, Rao KU (2015) Implementation of MPPT control using fuzzy logic in solar-wind hybrid power system. In: IEEE international conference on signal processing, informatics, communication and energy systems (SPICES), pp 1–5. <https://doi.org/10.1109/SPICES.2015.7091364>
26. Patsamatla H, Karthikeyan V, Gupta R (2014) Universal maximum power point tracking in wind-solar hybrid system for battery storage application. In: International conference on embedded systems (ICES), pp 194–199. <https://doi.org/10.1109/EmbeddedSys.2014.6953155>
27. Ahmad MW et al (eds) (2022) Intelligent data analytics for power and energy systems. Springer, Singapore, p XXII, 641. ISBN: 978-981-16-6081-8. <https://doi.org/10.1007/978-981-16-6081-8>
28. Tomar A et al (eds) (2022) Proceedings of 3rd international conference on machine learning, advances in computing, renewable energy and communication: MARC 2021, vol 915, p XV, 781. ISBN: 978-981-19-2830-7. Springer Nature. <https://doi.org/10.1007/978-981-19-2828-4>
29. Meza C, Biel D, Jeltsema D, Scherpen JM (2012) Lyapunov based control scheme for single-phase grid-connected PV central inverters. *IEEE Trans Control Syst Technol* 20:520–529. <https://doi.org/10.1109/TCST.2011.2114348>
30. Wai RJ, Wang W-H (2008) Grid-connected photovoltaic generation system. *IEEE Trans Circ Syst* 55:953–964. <https://doi.org/10.1109/TCSI.2008.919744>
31. Rani P, Arora VP, Sharma NK (2022) Performance investigation of solar-wind based grid-connected hybrid system under nonlinear load condition. In: 2022 1st international conference on sustainable technology for power and energy systems (STPES), pp 1–6. <https://doi.org/10.1109/STPES54845.2022.10006464>
32. Elbaset AA, Hassan MS, Ali H (2016) Performance analysis of grid-connected PV system. In: Eighteenth international middle east power systems conference, pp 675–682. <https://doi.org/10.1109/MEPCON.2016.7836965>
33. Rani P, Arora VP, Sharma NK (2022) An overview of the integration of PV system into electric grid. In: IOP conference series: materials science and engineering, vol 1228. <https://doi.org/10.1088/1757-899X/1228/1/012017>

# Towards Achieving Net Zero Emissions in India by 2070



Akash Midha and Anuradha Tomar

**Abstract** Problem regarding climate is one of the biggest problems which we are facing at present. In 2015, 194 parties adopted the Paris Agreement to limit the warming of Earth's surface to not more than 1.5 °C and to achieve the net zero globe by 2050 which means cutting the emissions of greenhouse gases such as carbon dioxide and methane to zero. India has set the target to reduce the emission intensity by 45% by 2030 and to achieve the net zero emission by 2070. India ranks third in carbon emissions in the world. The total carbon dioxide emissions in India in 2021 were around 2.8 billion tonnes. In 2022, these emissions saw an increase by 6%. Net zero would be possible in India by promotion of more and more non-fossil fuel sources instead of burning fossil fuels like coal and oil for the production of electricity and also by increasing deployment and integration of renewable sources in the sector of electricity production and transportation along with increase in production of green hydrogen. 100% renewables pathway can represent the truly decarbonized energy system. Globally, solar PV is needed to provide almost 70% of all primary energy by 2050 which means the solar capacity of 57.6 TW by 2050, and in the case of India, it is estimated that India should have 5630 GW of solar PV to achieve the target of net zero by 2070. To meet the target of net zero, there is requirement of large investments and strong policy framework in the nation.

**Keywords** Carbon dioxide emissions · Net zero emissions · Climate change · 100% renewable · Green hydrogen

---

A. Midha (✉) · A. Tomar  
Netaji Subhas University of Technology, Delhi, India  
e-mail: [akashmidha80@gmail.com](mailto:akashmidha80@gmail.com)

A. Tomar  
e-mail: [anuradha.tomar@nsut.ac.in](mailto:anuradha.tomar@nsut.ac.in)

# 1 Introduction

Problem regarding climate is one of the biggest problems which we are facing at present. Reduction of emission of greenhouse gases is the most appropriate approach which can limit the global warming [1, 2]. In 2021, the annual global carbon dioxide (CO<sub>2</sub>) emissions were 37.12 billion tonnes and the cumulative emissions by the end of 2021 were 1.7 trillion tonnes. Cumulative emissions are the sum total of all emissions since 1750 [3–5]. Over 40% of CO<sub>2</sub> emissions in energy CO sector are from power sector for the purpose of generation of electricity by fossil fuels such as coal, oil and gas which is responsible for CO<sub>2</sub> emissions—the gas primarily responsible for trapping of heat in the Earth’s atmosphere which is known as greenhouse effect and therefore causing global warming [5]. The power sector is followed by the transportation sector, and it is responsible for 20% of CO<sub>2</sub> emissions in the atmosphere [6]. In 2021, India emitted 2.71 billion tonnes of CO<sub>2</sub> in the atmosphere and is the third-largest emitter of CO<sub>2</sub> in the world by volume. However, the per capita emissions of India are 1.93 tonnes which is much less if compared to other countries like USA, China and Australia [3].

Over the past two centuries, CO<sub>2</sub> concentration rose from 280 to more than 380 parts per million (ppm) if we consider the ppm by volume due to which the temperature of Earth’s surface has increased by 0.74 °C over the past century and if CO<sub>2</sub> gets emitted in the atmosphere without any control, then there could be rise of 3.4 °C by the end of the century [7]. In 2015, the Paris Agreement came into force which is a legally binding international treaty in which 194 parties (193 states plus the European Union) had joined it and concluded to limit the warming of Earth’s surface to not more than 1.5 °C and to achieve the net zero emissions of greenhouse gases (and carbon dioxide) by 2050 [8].

If we see in the context of India till September 2022, the share of fossil fuel-based power plants is 236.068 GW (57.9%) while the share of renewables including energy from hydropower is 164.930 GW (40.4%) in the total capacity of India which is around 407 GW [9]. India has set the target to achieve 50% of power from non-fossil fuels and to reduce the emission intensity by 45% before 2030. However, the target has been set by the Government of India to achieve net zero emission by 2070 which is late if compared to other countries of the world which corresponds to global warming of 2.0 °C above pre-industrial levels [10]. At present time, the carbon emissions of India are continuously increasing and it is forecasted that India’s carbon emissions would be at their peak during 2040–2045 before sliding downwards [11].

The contribution of the paper is that it discusses the different studies done by several organizations and authors and on the basis of which comparative analysis of the situation of India has been done with other countries to provide the pathway of net zero emissions in India by 2070.

The paper is organized with Sect. 2 covering summary of India power sector and explaining the installed generation capacity and percentage share of different renewable and non-renewable sources in the Indian power sector. Section 3 discusses the contribution of different power supply technologies in emissions of carbon dioxide.

Section 4 explains about India's share in global CO<sub>2</sub> emissions. Comparative analysis of CO<sub>2</sub> emissions of India has been done in Sect. 5 with other major markets of the world such as USA and China to have a better understanding of the roadmap of India towards net zero emissions. Section 6 explains the pathway to 100% renewables which can represent the truly decarbonized energy system. Section 7 discusses the investment required and cost to achieve the net zero emissions in India, and the last Sect. 8 concludes with various steps required to achieve the target of net zero emissions in India.

## 2 Indian Power Sector

The development of power sector is the most important factor to develop the Indian economy. There are six regional grids in India which are Northern Region (NR) grid, Southern Region (SR) grid, Eastern Region (ER) grid, Western Region (WR) grid and North-Eastern Region (NER) grid. These grids are synchronized at the same frequency.

Total net generation capacity of the Indian power system by September 2022 is 407.797 GW of which 236.086 GW is from fossil fuels, 164.930 GW is renewable including hydropower and 6.780 GW is obtained from nuclear sources as shown in Table 1 [9].

**Table 1** Summary of Indian power system [9]

Category	Installed generation capacity (GW)	% of share in total
<i>Fossil fuels</i>		
Coal	204	50
Lignite	6.6	1.5
Natural gas	24.8	6.2
Diesel	0.5	0.1
<b>Total fossil fuels</b>	<b>236</b>	<b>57.9</b>
Hydropower	46.8	11.5
<i>Renewable</i>		
Solar	60.8	14.9
Wind	41.6	10.2
Cogen	10.2	2.5
Energy from waste	0.495	0.1
Hydropower (small)	4.9	1.2
<b>Total renewable (including hydro)</b>	<b>164.9</b>	<b>40.4</b>
<b>Nuclear</b>	<b>6.8</b>	<b>1.7</b>
<b>Total installed capacity</b>	<b>407.7</b>	<b>100</b>

### 3 Emissions of Carbon Dioxide from Power Supply Technologies

Electricity production is the main reason for emissions of carbon dioxide which accounts for more than forty per cent worldwide and is followed by the sector of transportation, industrial, residential and commercial. Traditional methods of electricity generation which are based on burning or combustion of fuels like coal, gas and diesel account for most of the CO<sub>2</sub> emissions. Burning or combustion of fuels also releases sulphur and nitrogen oxides which are primarily responsible for many environmental problems such as acid rain and also dangerous for human health causing various respiratory and heart diseases [7].

Nuclear power is a very good source to generate the low carbon electricity. Nuclear power has large density if compared with low carbon sources such as photovoltaics and wind. It has the power density of 4000 W/m<sup>3</sup> while photovoltaics and wind have the power density of 4–10 W/m<sup>3</sup> and 0.5–1.5 W/m<sup>3</sup> [12]. The main problem behind nuclear power is that it is controversial in many countries and is considered dangerous due to its radioactive emissions.

Renewable energy sources are environment-friendly sources but the main problem with them is that they are not available everywhere like photovoltaics are limited to places having good irradiation intensities, wind energy is limited to places having constant unidirectional wind speed and hydropower energy is stuck to dams. Photovoltaic systems release very low direct carbon dioxide emissions. However, if we also consider the indirect emissions still the emissions released by photovoltaics system are only one-fourth of fossil fuel emissions. The emissions released by wind energy are also very low, and emissions released by hydroenergy are six times more than the total emissions by the wind systems. Electricity generation based on biomass is carbon-neutral [7, 12]. Figure 1 shows the CO<sub>2</sub> emissions from various primary energy sources [12].

### 4 Carbon Dioxide Emissions in India

Considering the total CO<sub>2</sub> emissions, India ranks third and is followed by China and USA, although the per capita emissions of India are much less if compared to global per capita emissions. The total carbon dioxide emissions in India in 2021 were around 2.8 billion tonnes. In 2022, these emissions saw an increase by 6%. Figure 2 shows the CO<sub>2</sub> emissions in India and annual share of India in global emissions from 2000 to 2021. Burning of coal is the major source of release of emissions of CO<sub>2</sub> which released 1.8 billion tonnes of carbon dioxide in the year 2021 accounting for almost 34% of total release followed by oil (622.15 million t), cement (149 million t), natural gas (133.45 million t) and flaring (2.77 million t) as shown in Fig. 3 [3].

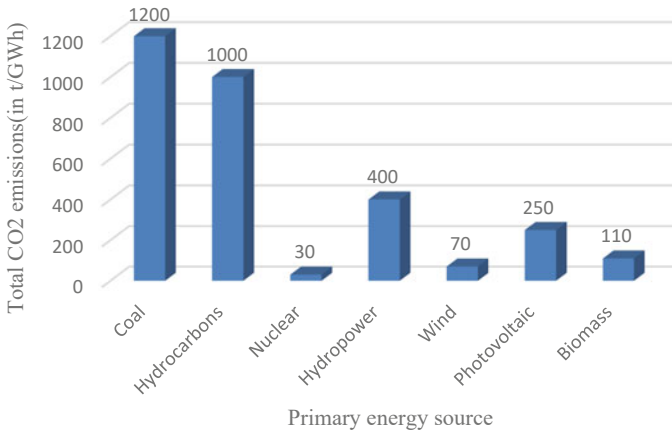


**Fig. 1** CO<sub>2</sub> emissions from primary energy sources [12]

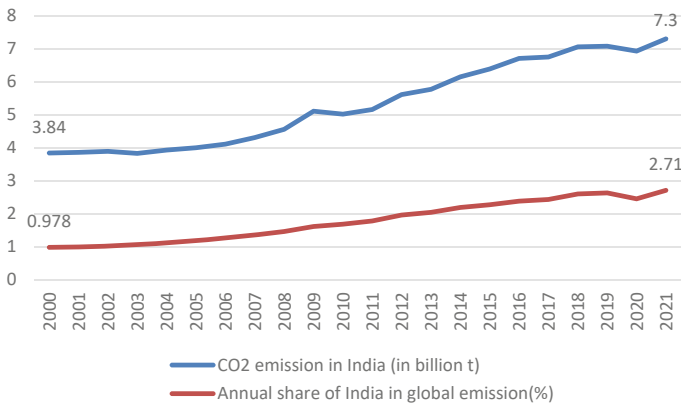


**Fig. 2** CO<sub>2</sub> emissions in India (in billion tonnes) and annual share of India in global emissions (in %) [3]

## 5 Comparative Analysis of CO<sub>2</sub> Emissions of India with Other Major Markets

Considering the total CO<sub>2</sub> emissions, India ranks third and is followed by China and USA. Although the emissions released by India are much less and not comparable to that of the emissions released by China and USA. In 2021, India released 2.79 billion tonnes of carbon dioxide emissions which make the cumulative emissions of 57 billion tonnes while China and USA released 11.80 billion tonnes and 5.12 billion tonnes emissions, respectively. The global emissions in the year 2021 were 41 billion tonnes accounting for the cumulative emissions of 1.74 trillion tonnes by

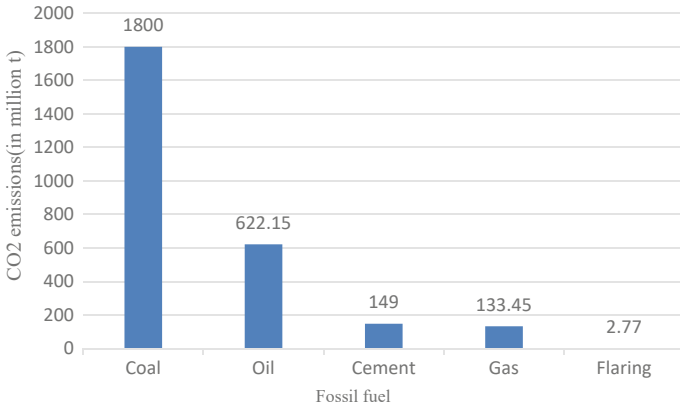


Fig. 3 CO<sub>2</sub> emissions in India from various fossil fuels [3]

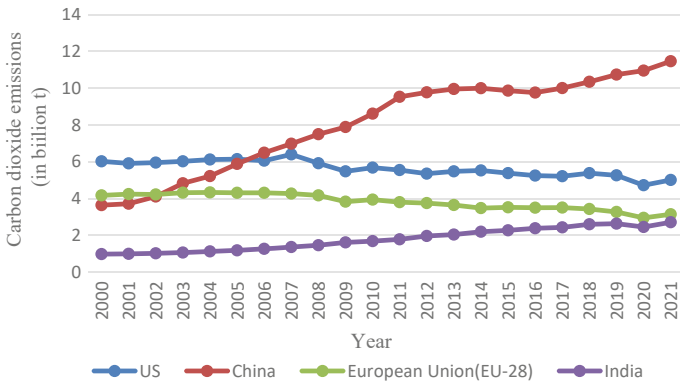


Fig. 4 CO<sub>2</sub> emissions (in bt) of major markets from 2000 to 2020 [3]

2021 [3]. Figure 4 shows the CO<sub>2</sub> emissions released by USA, China, EU and India in billion tonnes.

## 6 Towards 100% Renewables

100% renewables pathway can represent the truly decarbonized energy system. 100% renewables would overcome the concerns of global warming and depletion of fossil fuels. The target of 100% renewable energy would be achieved when all energy sources to meet all end-use energy needs in a certain location, region or country would be derived from renewable energy sources only 24 h per day, every day of the year [13]. Emission reduction could be possible if we double renewable energy

deployments by 2030 as per REMAP, 2014 [14]. Several analytical studies have been carried out by various organizations such as by Greenpeace in 2015 [15], by Energy Watch Group (EWG) [16]. The work done by Greenpeace in 2015 was refined and restated by the University of Technology Sydney (UTS) [17] which addresses the three scenarios: 5.0 °C (reference scenario), 2.0 °C, and 1.5 °C. To achieve the 1.5 °C, the net emissions must decline by 45% (relative to 2010 levels) by the end of decade and reach the net zero by 2050. The scenario of 1.5 °C assumes the electrification of transport and heating and cooling sectors at aggressive scale [13]. Solar PV’s share of the final energy supply should reach to 12,684 GW by 2050 [13]. The present global solar installed capacity has crossed 1 TW [18]. The EWG scenario projects that 90% (135,278 TWh) of all primary energy would come from power sector [16] in contrast to the International Renewable Energy Agency (IRENA). Therefore, solar PV is needed to provide 69% of all primary energy (76% of electricity) by 2050 which means the solar capacity of 57.6 TW by 2050 [13, 16] which is much greater than UTS 1.5 °C scenario [17]. In both, the studies achieving 100% renewable energy is technically feasible with the help of stronger policy support [13]. Figure 5 represents the share of primary energy supplies in the world in 1970, 2021 and 2050 [13, 19, 20].

In the case of India, it is estimated that India should have 5630 GW of solar PV in order to achieve its net zero target by 2070. At present, the present installed solar capacity of India is 40 GW only [21].

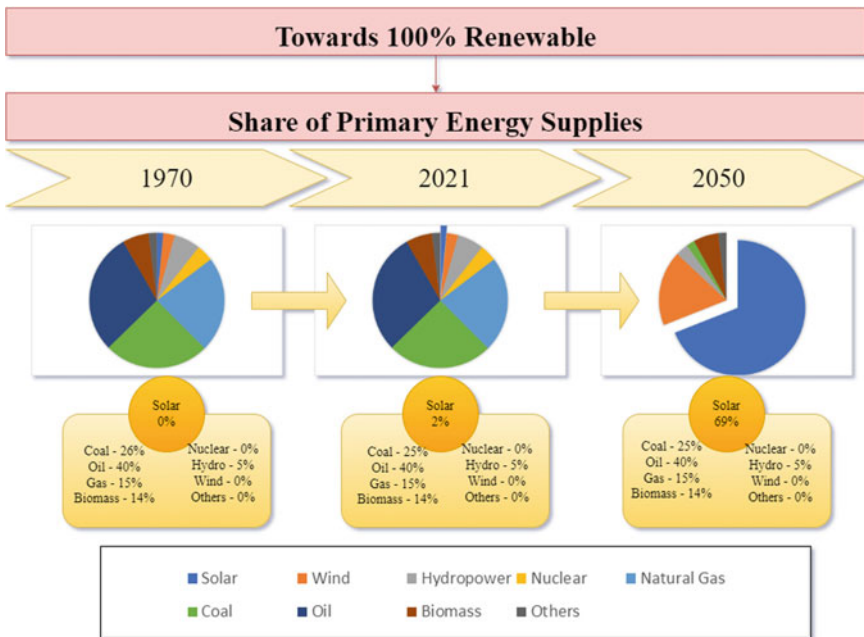


Fig. 5 Share of primary energy supplies in the world in 1970, 2021 and 2050 [13, 19, 20]



## 7 What's the Cost of Net Zero?

An estimated investment of around 125 trillion \$ is required by 2050 to achieve the target of net zero by 2050 globally. Developing economies make up about 40% of global GDP but account for 50–60% of the investment needs. More than half of the global investments are expected to take place in Asia Pacific with large levels of investment in key countries like China and India [22]. It is estimated that India needs the investment of \$10.1 trillion to achieve its net zero target by 2070 in which \$8.4 trillion is required to scale up power generation, transmission and distribution infrastructure, and \$1.5 trillion is required for green hydrogen power capacity.

The Indian government has introduced the production-linked incentives (PLI) scheme, and there is requirement of thousands of crore to promote the production of efficient solar modules. Various cement industries have committed Rs. 1400–1700 crore for waste heat recovery systems (WHRS) in FY 2022. Various investments are also being done in the domain of recycled steel. The government of India is also on its way to promote perform, achieve and trade (PAT) scheme to increase the efficiency in energy-intensive industries [23].

## 8 Conclusion

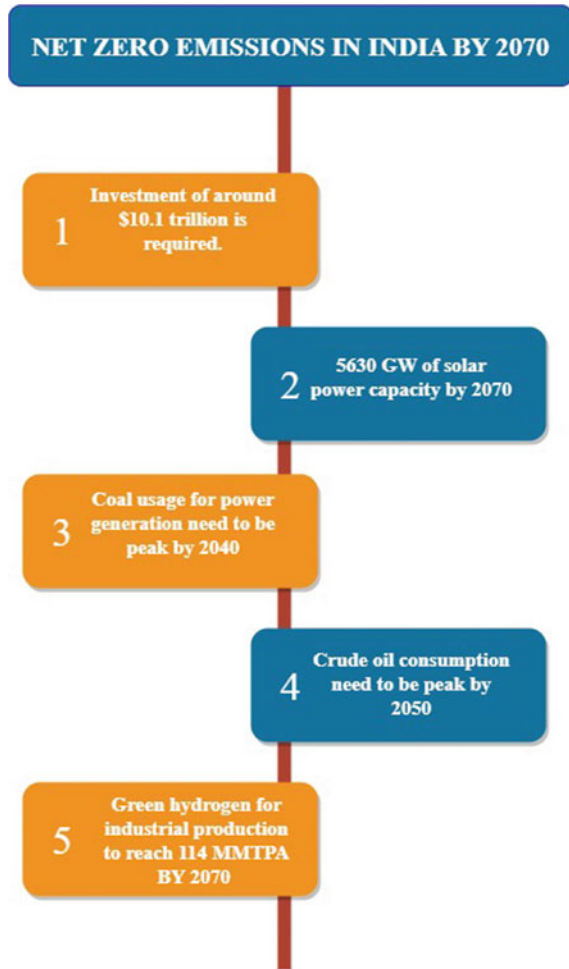
The Government of India has set the target to achieve the net zero emissions by 2070 which is very late as per the Paris Agreement according to which the target of net zero emissions is needed to be achieved by 2050. Net zero emissions by 2070 means the global warming of 2.0 °C by the end of century. Electricity production is the main reason for emissions of carbon dioxide which accounts for more than forty per cent worldwide and is followed by the sector of transportation, industrial, residential and commercial. Traditional methods of electricity production are responsible for a lot of CO<sub>2</sub> emissions while the emissions released by nuclear and renewable energy for the generation of the same amount of electricity which arise the need to promote renewable energy. Considering the total CO<sub>2</sub> emissions, India ranks third. In 2021, India released around 2.8 billion tonnes of CO<sub>2</sub> emissions.

To attain net zero emissions in India by 2070, the following are required:

- An estimated investment of around 10 trillion dollars.
- India should have the installed solar capacity greater than 5600 GW by 2070.
- Coal usage and crude oil consumption need to be peak by 2040 and 2050, respectively.
- Production of green hydrogen should be more than 100 MMTPA by 2070.

Net zero would be possible in India by promotion of more and more non-fossil fuel sources instead of burning fossil fuels like coal and oil for the production of electricity and also by increasing deployment of renewable energy sources in the sector of electricity production and transportation along with increase in the production of

**Fig. 6** India towards net zero emissions [22–24]



green hydrogen. In the studies done by UTS and EWG, 100% renewable globally is technically feasible with the help of strong policy framework (Fig. 6).

The economic aspects and investment required to achieve net zero emissions in India could be explored and studies could be done to achieve it early so to align the target of India with the global target as set up in the Paris Agreement. The policy framework is needed to be revised.

## References

1. United Nations Framework for Climate Change (2017, June 10) [Online]. Available: [https://unfccc.int/files/essential\\_background/background\\_publications\\_htmlpdf/application/pdf/con\\_veng.pdf](https://unfccc.int/files/essential_background/background_publications_htmlpdf/application/pdf/con_veng.pdf)
2. Chouhan BS, Rao KVS, Kumar Saxena B (2017) Reduction in carbon dioxide emissions due to wind power generation in India. In: 2017 international conference on smart technologies for smart nation (SmartTechCon), pp 257–264. <https://doi.org/10.1109/SmartTechCon.2017.8358379>
3. Ritchie H, Roser M, Rosado P (2020) CO<sup>2</sup> and greenhouse gas emissions. Published online at OurWorldInData.org. Retrieved from: <https://ourworldindata.org/co2-and-other-greenhouse-gas-emissions> [Online Resource]
4. International Energy Agency (IEA). Global energy review: CO<sub>2</sub> emissions in 2021 [Online]. Available: <https://iea.blob.core.windows.net/assets/c3086240-732b-4f6a-89d7-db01be018f5e/GlobalEnergyReviewCO2Emissionsin2021.pdf>
5. <https://www.world-nuclear.org/information-library/energy-and-the-environment/carbon-dioxide-emissions-from-electricity.aspx>
6. <https://www.statista.com/topics/7476/transportation-emissions-worldwide/>
7. Abdallah L, El-Shennawy T (2013) Reducing carbon dioxide emissions from electricity sector using smart electric grid applications. *J Eng* 2013(Article ID 845051):8 p. <https://doi.org/10.1155/2013/845051>
8. United Nations Paris Agreement (2016) [Online]. Available: <https://www.un.org/en/climatechange/paris-agreement>
9. Ministry of Power (GOI) (2022, October) [Online]. Available: <https://powermin.gov.in/en/content/power-sector-glance-all-india>
10. Vaughan A (2021) India's pledge on net zero. *New Scientist* 252(3359):10. [https://doi.org/10.1016/S0262-4079\(21\)01952-7](https://doi.org/10.1016/S0262-4079(21)01952-7)
11. <https://www.livemint.com/news/india/india-sees-carbon-emissions-peaking-in-204045-11635947031283.html>
12. Ciupăgeanu DA, Lăzăroiu G, Tîrșu M (2017) Carbon dioxide emissions reduction by renewable energy employment in Romania. In: 2017 international conference on electromechanical and power systems (SIEMEN), pp 281–285. <https://doi.org/10.1109/SIEMEN.2017.8123333>
13. Renné DS (2022) Progress, opportunities and challenges of achieving net-zero emissions and 100% renewables. *Solar Compass* 1:100007. <https://doi.org/10.1016/j.solcom.2022.100007>
14. IRENA (2014) Remap 2030: a renewable energy roadmap. International Renewable Energy Agency, Abu Dhabi, UAE. [https://www.irena.org/-/media/Files/IRENA/Agency/Publication/2014/IRENA\\_REmap\\_Report\\_June\\_2014.pdf](https://www.irena.org/-/media/Files/IRENA/Agency/Publication/2014/IRENA_REmap_Report_June_2014.pdf)
15. Teske S (Project Manager and Lead Author) (2015) Energy [r]evolution—a sustainable world energy outlook 2015. 100% renewable energy for all. Greenpeace International, Global Wind Energy Council, and Solar Power Europe. [https://www.researchgate.net/publication/310018861\\_Energy\\_Revolution\\_A\\_sustainable\\_world\\_energy\\_outlook\\_2015/link/582c1cea08aef19cb806d65d/download](https://www.researchgate.net/publication/310018861_Energy_Revolution_A_sustainable_world_energy_outlook_2015/link/582c1cea08aef19cb806d65d/download)
16. Ram M, Bogdanov D, Aghahosseini A, Gulagi A, Oyewo AS, Child M, Caldera U, Sadovskaia K, Farfan J, Barbosa L, Fasihi M, Khalili S, Dalheimer B, Gruber G, Traber T, De Caluwe F, Fell H-J, Breyer C (2019) Global energy system based on 100% renewable energy—power, heat, transport and desalination sectors study by Lappeenranta University of Technology and Energy Watch Group, Lappeenranta, Berlin
17. Teske S (2019) Achieving the Paris climate agreement goals. Springer-Open. <https://doi.org/10.1007/978-3-030-05843-2>
18. <https://www.pv-magazine.com/2022/03/15/humans-have-installed-1-terawatt-of-solar-capacity/>
19. Singer S, Denruyter J-P, Yener D (2017) The energy report: 100% renewable energy by 2050. In: *Towards 100% renewable energy: techniques, costs and regional case-studies*. Springer International Publishing

20. Renné DS (2022) The opportunities and challenges for 100% renewable energy. Sustainable energy development and innovation: selected papers from the World Renewable Energy Congress (WREC) 2020. Springer International Publishing, Cham
21. <https://economictimes.indiatimes.com/industry/renewables/india-needs-5630-gw-installed-solar-capacity-to-become-net-zero-nation-by-2070-report/articleshow/86984707.cms>
22. <https://climatechampions.unfccc.int/whats-the-cost-of-net-zero-2/>
23. <https://www.businesstoday.in/magazine/corporate/story/how-much-india-needs-to-spend-to-get-to-net-zero-340538-2022-07-06>
24. Tomar A et al (eds) (2022) Proceedings of 3rd international conference on machine learning, advances in computing, renewable energy and communication: MARC 2021, vol 915, p XV, 781. ISBN: 978-981-19-2830-7. Springer Nature. <https://doi.org/10.1007/978-981-19-2828-4>

# IOT-Based Monitoring and Controlling of Substation Parameters



P. Sai Kiran, B. Venkateswara Rao, G. Satyamohan Sarveswar,  
and P. Manikanta

**Abstract** Inevitably, electricity contributes to the development of the country. PLCs and SCADA systems are used to automate substations according to conventional methods, although this technology is incredibly expensive for a tiny substation. In order to automate a modest 11 kV substation, this study employs low-cost automation methods based on cutting-edge IoT innovations and embedded processors like the Raspberry PI. Using Raspberry PI, the smart substation is a modern automation solution that allows for the global control of device status and the main theme of the project is to control, monitor, and protect the power system network in the substation. The PZEM module, which is connected to a Raspberry PI (RPI), senses the parameters that need to be tracked in this situation. Data is delivered to the RPI, where it is analyzed so that tripping activities can occur. When the current sensor-measured value is processed with the help of predetermined programming in Raspberry PI, it will enable the relay to close, cut off the supply, and send a telegram alert to the authorized engineers. As the sensors identify the current or voltage values exceeding or falling behind some fixed threshold value.

**Keywords** Raspberry Pi · IoT · PZEM-004T · Smart substations

---

P. Sai Kiran (✉) · B. Venkateswara Rao (✉) · G. Satyamohan Sarveswar · P. Manikanta  
Department of EEE, V R Siddhartha Engineering College, Kanuru, Andhra Pradesh, India  
e-mail: [saikiranpolarathi@gmail.com](mailto:saikiranpolarathi@gmail.com)

B. Venkateswara Rao  
e-mail: [drbvrao@vrsiddhartha.ac.in](mailto:drbvrao@vrsiddhartha.ac.in)

© The Author(s), under exclusive license to Springer Nature Singapore Pte Ltd. 2024  
H. Malik et al. (eds.), *Renewable Power for Sustainable Growth*,  
Lecture Notes in Electrical Engineering 1086,  
[https://doi.org/10.1007/978-981-99-6749-0\\_67](https://doi.org/10.1007/978-981-99-6749-0_67)

993

## 1 Introduction

Electricity is very beneficial and readily available source of energy. It has a constantly expanding importance in our contemporary, industrialized world. Electrical power systems are tremendously vast, highly complex, and nonlinear systems. Such electric power systems are combined for operational, economical, and higher trustworthiness reasons [1]. They are among the most important components of the global and national infrastructure, and when these systems fail, the economy and national security are severely impacted both directly and indirectly. Generators, lines, transformers, loads, switches, and compensators are some of the parts that make up a power system. However, modern power networks frequently involve loads and power sources that are dispersed across a wide area. Electricity still endures power outages and blackouts today because of a lack of automated analysis and inadequate utility visibility over the grid [2]. The utility will receive the necessary view thanks to WSN, which will collect data from the various grid subsystems. While deciding whether to alert or slightly delay this, a sensor node (whether to immediately notify the sink about this information.). Automation of substations is now a must for every utility business in order to boost efficiency and enhance the quality of power being delivered as the complexity of the distribution network has grown [3]. By boosting test rates, the IoT-based continuous inspection system for managing and testing substations can be made better. This built-in technique can be used by administrators to confirm general conditions in a constant state and transient force substation scenarios. Additional points were tested using high-speed and lossless data from logs, the web, and disconnected analysis [4]. Therefore, distance between the generator and the load may be several miles, and the scale of the trade in huge force over a great distance has grown as a result of the low cost of electric force. Prior reform initiatives rarely ever generated concerns about the nature of the force. The desire for client-side power has sparked concern due to the widely used extension for it. Normal force transfer results in a sizable amount of energy loss, which points to a decrease in substation power [5]. By a different modification, the force's nature can be improved. It is required to determine the sort of requirement that has occurred [6]. The management of insurance, verification, or force structures is also flawless. It is not necessary for the structure to be intricate. The observation system is able to detect, filter out, and explain projected electrical line requirements as a result. Due to faults in the algorithmic evaluation process and the utterly futile utility system scam, blackouts and power shortages are currently difficult for the police to manage. Sense Information Assessment: You Must Correspond Confirmation Strategies Nothing else is done. In order to alert Sync about this information either immediately or after pausing the notification, the sensor hub will decide. The sink is used as a reference because it is thought to be truthful and advice should be offered [7]. It is crucial to keep in mind that the issue needs to be solved while keeping in mind the possibility of litigation. Idea as a result of the Internet of Things, Buzzer can transmit data for communication over a wired or remote connection (IoT). The integration of information preparation, communication, and retrieval within an organization is suggested by a thorough description of

IoT, or the industrial internet of things (IIoT). Presently, IIoT is linked to the development of wonderful networks for a diversity of submissions. As the Force System's activity is heavily time-based, less sluggishness post should be taken into account for the bulk of control and monitoring claims [8]. The use and control of the Force System are considered as being critically dependent on the IIoT's continued capabilities. A quick IIoT-based observation system with recording capabilities is created and put into use for the Force System substation [9]. IIoT can provide a mechanism for testing power substations line-to-line and many other reliable power device maintenance techniques. On the other side, it is challenging and exciting to trigger the checking sensor near the high-voltage (HV) equipment and force substation [10, 11]. If checking sensor performs well to ensure proper maintenance, it may be possible to reduce installation costs. The idea enables the transmission of data through wires or through remote associations for correspondence [12]. Planning, communication, and information retrieval are all integrated into one continuous organization by the Industrial Internet of Things (IIoT), a comprehensive IIoT concept. The development of perceptual matrices in numerous applications is increasingly linked to IIoT. The majority of control and testing applications should take into account low latency communication due to the Force System's heavily time-based activities. In order to guarantee power system discretion and account for all potential conditions, the ideal configuration model is described in the fundamental scenario. As a result, the state stays away from unfavorable semi-notable states. The substation modernization structure is the driving force behind the prediction and management of the force matrix. Data on activity status is gathered, tracked, and intercepted by the substation robotization system from both required and optional gears. The strategy lowers the cost of segments to accommodate the establishment's various financial and special needs as well as required substation outages. The Force System is expanding as a result of the introduction of new energy sources generally, especially power hardware switch systems, high-voltage direct current (HVDC) transmission, and environmentally friendly power sources. Environmentally friendly electrical assets will reportedly account for around 31.2% of the age of a politically relevant nation. A large portion of these riches will be provided by wind and solar energies.

## ***1.1 Research Motivation***

As the distribution network's complexity has grown, automation of substations has become a must for every utility company in order to increase efficiency and improve power quality. Electricity continues to experience power failures and blackouts today due to a lack of automated analysis and insufficient utility visibility over the grid. WSN will provide the utility with the required view by gathering data from the various grid subsystems. A sensor node will decide whether to notify or delay this slightly (whether to immediately notify the sink about this information). Since there may be hundreds of miles between the generators and the load, a lot of power must be exchanged across such a long distance on account of the poor quality of electric power.

Early on in development process, complaints about the quality of the power were rare. Concern over the quality of power being delivered on the user side has been raised as a result of the increase in customer demand for electricity. Due to the considerable amount of power lost during the transmission of the general electricity, the quality of the power received at the substation degrades. To enhance the effectiveness of power with suffering solutions, it is essential to comprehend the type of limitation that has occurred. In addition, if any aspect of a power system's monitoring, regulation, or protection is inadequate, there may be system instability. It is therefore necessary to have a monitoring system that can automatically identify, monitor, and classify the current limitations on electrical lines.

## 2 Solution Methodologies

The platform serves as a microprocessor for the current structure, which uses the voltage and current from the sensor to screen the three-phase electrical structure. It then purposefully uses another Android app to remotely broadcast the results to the screen. The supplied configuration confirms three voltage sensors and three current sensors using a Raspberry PI as a microcontroller. After estimation, it uses Bluetooth HC-05 to transfer this data to the client's Android mobile device. The constraints examined for the diffusion transformer are in conflict, and the transformer's evaluation is reversed. IoT has the ability to discreetly increase performance to a substantial level while also turning off the transformer to prevent harm. While monitoring and controlling substation using an IoT System, various sensors are employed to pinpoint the exact electrical restrictions. A temperature sensor, an AC voltage sensor, and a current sensor make up the sensors. Each sensor has a Raspberry PI microcontroller attached to it. The microcontroller receives the output from many sensors and delivers the current state of numerous linked boundaries for display on the LCD of the microcontroller interface. The Raspberry PI regulator and Bluetooth are the common currents, and the voltage and frequency are determined with voltage transformers, current transformers, and zero-intersection IDs, respectively. The Android app displays each microcontroller and remote device separately, along with the current, voltage, frequency, and force factors. The new Android mobile app uses App Finder programming to display voltage and current estimates. It seeks to investigate a number of initial base voltage power quality characteristics.

Learn about the various Raspberry PI sections in this area. Additionally, it is best to begin with technology and coding. Although most of the Raspberry PIs share a substantial fraction of these sections realistically speaking, a few sheets appear to be rather distinct in comparison to the ones below. Information was gathered and given to the Raspberry PI regulator based on a thorough conviction organization. These calculations for organizational structure are generative model that incorporate various degrees of stochastic, passive elements. Factors that are not active, often known as cover-up units, have dual properties. It is a test of all the variables, and the LCD has demonstrated that it is possible to utilize a serial port to regulate the



IoT's use and quality. This ringer is used to alert the sound caution structure when a system issue arises.

In AC, electrical energy is only produced, transmitted, and dissipated in the context of effective concepts. In any case, a DC supply is necessary for the majority of electronic devices and power supply circuits. For this purpose, dry cells and batteries can be utilized. They can almost likely profit from the advantages of comfort and freedom to swell. In any event, they have low voltage, require regular replacement, and cost more than a typical DC power source. One day, practically all electronic equipment will have a circuit that switches from an AC supply to a DC Supply. Hardware elements that perform the AC to DC conversion are called DC power supply. When all are said and done, the contribution of the power supply has a force transformer. The voltage control circuit is followed by a rectifier (diode circuit) smoothing channel. The four components from Square Profile that seize the required power supply are the transformer, rectifier, channel, and the controller set. Chronic Universal Serial Bus (USB) connectors are links that transfer data from a sequentially powerful device to a USB port. The sequential device is connected to the DB9 connector, which is arranged sequentially. The USB connector is connected to the computer's USB port or relevant USB center point. Direct transmission of the data reported by the serial device to the USB port allows programming to decrypt it.

A fundamental temperature sensor must have a Resistance Temperature Detector (RTD) in order to determine the temperature from an electrical output. The thermocouple is installed using two distinct metals, and it produces a direct electrical voltage that modifies the temperature. Since RTD is a variable resistor, it can adjust the electrical protection from temperature changes exactly and practically directly. The temperature sensor determines if an object is hot or cold. The functional basis for the sensors is provided by the voltage that circulates around the diode. The sensor monitors voltage formation, temperature rise, and voltage loss between the base and the terminals of the semiconductor maker. The device produces a simple signal that directly relates to the temperature if the voltage contrast is increased. As an electric current flows across a wire, a device known as a current sensor detects it and generates the corresponding sign. The measured data rating transmits the transformer's reverse growth to the controller if the transformer's pricing is confirmed. It is stated that the delivery indicator could be a straightforward voltage/current, or even a progressive output. Orchestral substations are being studied for the mechanical, rural, and urban sectors. Assessing sensors are employed for gauging, screening, locating shortcuts or ground defects, and selecting a course.

### **3 Problem Description**

#### ***3.1 To Improve Reliability and Compatibility***

One of the primary objectives of our paper is to make the paper as compatible and dependable as possible by immediately isolating the issue and maintaining a consistent voltage level, which will enhance the dependability of the power given.

#### ***3.2 Real-Time Supervision***

Every utility business now needs to automate substations in order to increase productivity and improve service quality as the distribution network's complexity has grown. Real-time supervision is one of the key focuses of our paper.

#### ***3.3 Distant Location Monitoring of the Observables***

We created this prototype with the transformers in mind because they are widely utilized in remote regions, even though this paper is meant for all substation equipment. Through this study, we hope to assure remote sensing of all observable characteristics.

#### ***3.4 To Maintain the Continuity of Supply***

By keeping an eye on current conditions, we want to maintain supply continuity. Decrease labor expenses, our paper's main objective is to somewhat reduce labor costs because doing so will improve the facility's economic viability (Fig. 1).

#### ***3.5 Hardware Design***

The hardware design is split into three parts due to diverse functionality of the system, and the key purpose of the system is to monitor, protect, and control. The entire substation electrical parameters can be viewed by the user on his/her mobile. This includes controlling ON and OFF of the feeders used in the substation.

The proposed approach to operate, monitor, and protect the substation is depicted in prototype form in Fig. 2. This circuit includes a Raspberry PI, a display, a relay, a current sensor, a voltage sensor, and a mobile. The primary benefits of this approach

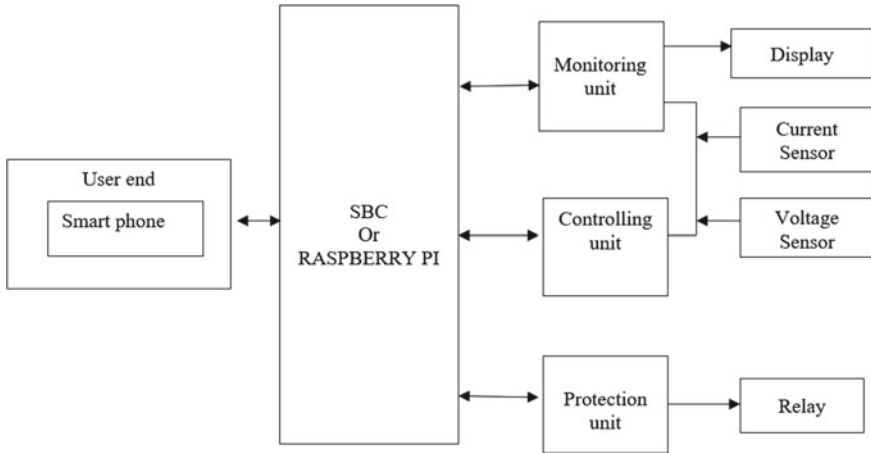


Fig. 1 Block diagram

are controllability and smart control via the internet or local host, cost-effectiveness and compact size, energy conservation through automation, replacement of fuses and MCBs with the suggested module, and finally, operating system independence.

When the current flowing through the substation exceeds the threshold value, then the substation will be shut down immediately by sending a notification. “Alert-OVER LOAD-Shutting Down” will be displayed. The substation parameters can be viewed in Telegram, and VNC viewer, and there is also a provision to monitor on display (Figs. 3 and 4).

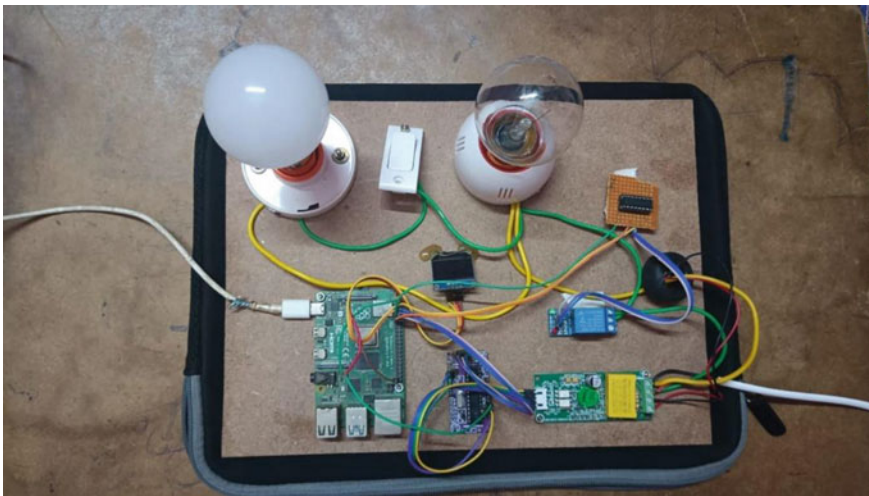


Fig. 2 Circuit connection



Fig. 3 Parameters monitoring on display

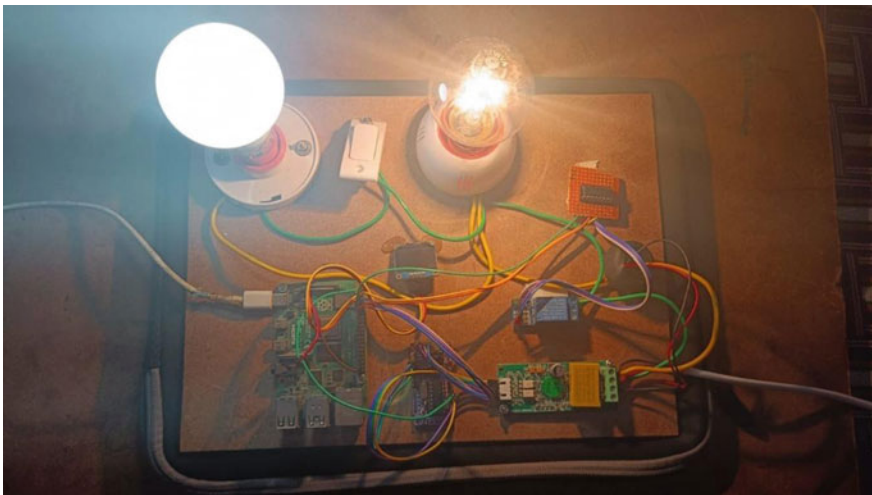


Fig. 4 Prototype model of smart substation using Raspberry PI

## 4 Conclusion

Businesses will transition to intelligent and optimized predictive maintenance as they upgrade their maintenance practices. The reduction of these expenses is a big problem because the investments made in the purchase of substation equipment monitoring systems incur extra costs to maintenance and operation. With Ethernet

cabling already present, the SMS is a low-cost option for implementing communications infrastructure in substations utilizing IEC 61,850 protocols. This allows it to be used in substations of any size and voltage level. The SMS makes use of data provided by IEDs and existing or provided communications network architecture for the SAS of the substation. The system's foundation consists of the same IEDs that are utilized for command, measurement, protection, and control. Compared to other monitoring tools like sensors or programmable logic controllers, they are more durable and reliable. They have the ability to intercept data transferred to the maintenance server, which then processes it and feeds the database. Because the IEDs are connected to the primary equipment via CTs, PTs, RTDs, and other devices, these functions can be carried out. The results of the practical experimentation, which was conducted in a lab with a station simulator and test rack, were entirely satisfying and demonstrated that the suggested solution is both feasible and affordable. The SMS influences additional expenses associated with the performance of equipment through the accurate and reliable prognosis of events, as well as to the planning of maintenance and subsequent reduction of undesired operating costs, such as employee overtime. According to a cost analysis, adding an SMS to an SAS network in order to modernize maintenance procedures will only add a modest percentage (10–15%) to the initial cost of digitalizing a small distribution substation. The expenditure to deploy the SMS is an even less incremental cost for a bigger and more complicated substation. By merely adding an additional control circuit, the system ensures the existing substation's efficient and reliable operation. The designed system has undergone numerous tests and has proven to be successful. With few adjustments, the produced equipment can be employed in industries and communication activities.

## References

1. Rajesh MV, Rao BV (2017) Artificial intelligence based machine learning assistance for self-driving car using Raspberry Pi. *Int J Adv Res Sci Eng* 6(11):1718–1724
2. Hajikhani M, Labeau F, Agba BL (2019) Power allocation for a self-sustainable power substation monitoring system using wireless transfer of energy. *IEEE Access* 7:141456–141465
3. Zhao L, Brandao Machado Matsuo I, Zhou Y, Lee W (2019) Design of an industrial IoT based monitoring system for power substations. *IEEE Trans Ind Appl* 55(6):5666–5674
4. Parikh P, Sindhu TS, Sharmi A (2013) A comprehensive investigation of wireless LAN for IEC61850 based smart distribution substation applications. *IEEE Trans Ind Inform* 9:1466–1476
5. Vinuta VK (2014) A case study: SCADA implementation in KPTCL. *IJERT* 3(10):45–53
6. Barbosa J, Gaspar C, Jost B, Frank M, Cardoso G (2017) A monitoring system for the LHCb data flow. *IEEE Trans Nucl Sci* 64(6):1191–1196
7. Vrushali RD, Umale VM (2012) Wireless monitoring of the green house system using embedded controllers 3(2)
8. Pankajavalli PB, Karthick GS, Sridhar M, Muniyappan A (2017) A system for monitoring electricity substation using IOT. *Int J Adv Res Sci Eng* 6:12
9. Albinali HF, Meliopoulos APS (2018) Resilient protection system through centralized substation protection. *IEEE Trans Power Deliv* 33(3):1418–1427
10. Ahmad MW et al (eds) (2022) *Intelligent data analytics for power and energy systems*. Springer, Singapore, p 641. <https://doi.org/10.1007/978-981-16-6081-8>

11. Tomar A et al (eds) (2022) Proceedings of 3rd international conference on machine learning, advances in computing, renewable energy and communication: MARC 2021, vol 915. Springer, New York, p 781. <https://doi.org/10.1007/978-981-19-2828-4>
12. Dambhare S, Soman SA, Chandorkar MC (2009) Adaptive current differential protection schemes for transmission-line protection. IEEE Trans Power Deliv 24(4):1832–1841

# Effectiveness of Resilience Index in Assessing Power System Performance



Hasna Satya Dini and Jasrul Jamani Jamian

**Abstract** The prediction of disaster increment in the upcoming year requires a proper strategy to prevent a widespread impact in electrical network. Quantitative, risk-based metrics are essential for capturing a power system condition during the planning, operating, and recovering stages of a disaster. Several studies have been conducted to develop strategy in quantifying resilience condition in electrical network. Yet, none of those indices nor method has been widely approved as a worldwide standard. Thus, this paper attempts to evaluate several resilience metrics, namely RICD,  $R_i$ ,  $R_t$ , and  $R_{time}$ , during a disaster in four different scenarios. The goal of this analysis was to seek the most appropriate index which will be able to capture the whole parameter of electrical system resilience. Typhoon Vicente is used as sample disaster on IEEE 6 bus power system which overlaid on South China area. The simulation shows that the resilience indices that are tested show significant different values for all resilience indices in each scenario. RICD and  $R_{time}$  have a strong influence from the comparison of typhoon duration and total repair time, while the amount of loss load has a stronger influence on  $R_i$  and  $R_t$ . Thus, a new index that is able to capture both phenomenon is needed to capture the full picture of power system during disaster.

**Keywords** Resilience · Index · Disaster · RICD · Transmission

---

H. S. Dini (✉) · J. J. Jamian  
Universiti Teknologi Malaysia, Skudai, Malaysia  
e-mail: [hasna@graduate.utm.my](mailto:hasna@graduate.utm.my)

J. J. Jamian  
e-mail: [jasrul@utm.my](mailto:jasrul@utm.my)

## 1 Introduction

Greenhouse gases emission causes an increase in air and water temperatures worldwide. Based on research, it is predicted that there will be an increase in the quantity and capacity of hurricanes, winter storms, heat waves, floods, and other disasters which are posing a threat to the global sustainability of environmental, infrastructure, and even economic system [1, 2]. For example, Hurricane Sandy caused the loss of access to electricity for 7 million people in 2012. This disaster destroyed over 100,000 main power lines. Several transformers at substations exploded and flooded substations. During 2010–2011, Queensland, Australia, experienced flooding, which affected six transformer substations. The disaster is estimated to have caused more than 150,000 customers to lose access to electricity. In 2008, China experienced an ice storm disaster that caused damage to 2000 substations and destroyed 8500 poles which caused a loss of access to electricity in 13 provinces and 170 cities [3].

The strong impact of natural disasters on access to electricity causes the need for a proper strategy to prevent the widespread of its impact. Conventional reliability calculations become irrelevant because they are based on the  $N - 1$ ,  $N - 2$ , or  $N - n$  contingency. Meanwhile, as mentioned in the paragraph above, natural disasters with a low probability and high impact can cause loss of components up to  $N-40$ . An index that can accommodate system readiness prior to these events is important so that prevention and mitigation can be carried out effectively by knowing the system's condition. In this case, resilience is offered as an index to quantify system readiness to face high-impact low-probability disasters.

Resilience in electricity is defined as the capability of a power system to plan to absorb, recover, and successfully adapting to adverse event [4]. Resilience in power system can be evaluated at infrastructure or electrical system level to develop methodologies which provide information to electrical operator and owner [5]. Quantitative, risk-based metrics are essential for measuring a system during the planning, operating, and recovering stages of a disaster. The results of this calculation will be the basis for determining policies, planning, operations, and investment in electric power systems [6]. Several studies have attempted to develop a metric for calculating resilience [7]. However, the metrics for calculating resilience in electric power systems have yet to agree on a standard.

Several resilience proposed indices were presented in [4] including resilience function which evaluate the system using trapezoidal performance or triangle performance. The paper gave a brief explanation about each of the index yet, and it did not simulate the disaster event to review the difference between those indices accurately. In [6], resilience indices which evaluate different aspect of resilience were assessed. It presented capacity resilience indices, speed recovery resilience indices, grid recovery resilience indices, and grid improvement parameter under Typhoon Boyalen and Typhoon Saba. The grid functionality difference between two events is used to observe system's improvement. These indices were meant to give a complete explanation of system resilience.



The development of some proposed resilience indices made it necessary to compare the effectiveness of them. Without this analysis, the reader will not be able to determine the difference between each indices and pick the proper index which properly captures the system’s resilience condition. Thus, this paper attempts to evaluate several resilience metrics during a disaster in four different scenarios. The disaster is simulated in the electrical system, and the system response will be evaluated. The value of each metric will be compared to see the effectiveness in a different disaster scenario.

The structure of this paper is as follows: Sect. 2 describes the concept of resilience in general, and Sect. 3 contains the steps taken in the simulation and scenario variations. Section 4 contains the procedures for modeling the components and sampled disasters. Section 5 displays the simulation data, and Sect. 6 contains an analysis of the simulation results. Section 7 contains a discussion of the result, and Sect. 8 is the conclusion and next steps to be taken.

## 2 Concept of Resilience

### 2.1 Definition of Resilience

A multi-phase resilience trapezoid curve can describe the impact of disturbances on the power system [8]. The trapezoidal curve in Fig. 1 depicts each phase of the disaster as follows:

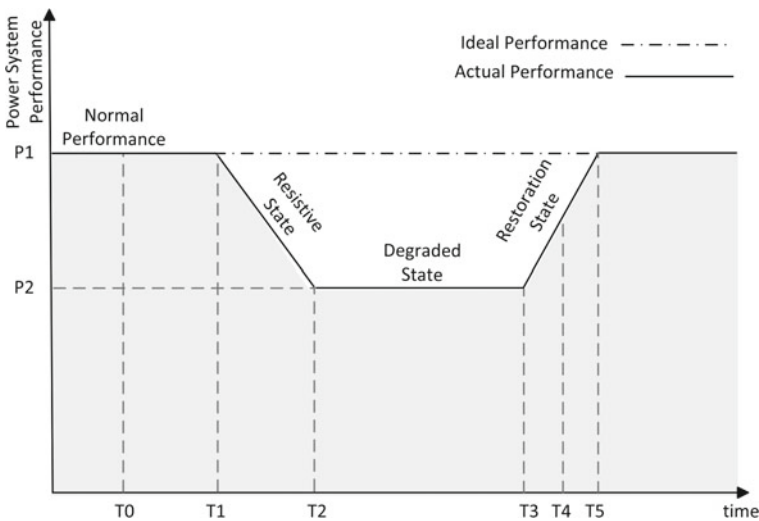


Fig. 1 Trapezoidal resilience curve

- Phase 1 is the initial phase of disturbance ( $T_0$ ), where the system can still maintain its performance as normal. Phase 1 ends when deterioration in system performance ( $T_1$ ) begins. In this phase, the system's strength is tested when a disturbance occurs. In a good system, phase 1 will last a long time; meanwhile, in a poor system, this phase occurs shortly since the component will instantly damage during the early phase of disturbance.
- Phase 2 is a resistive state which starts when a decrease in system performance occurs ( $T_1$ ) until the system reaches its minimum performance ( $T_2$ ). During this phase, the damage of the disturbance reaches the maximum point.
- Phase 3 is a degraded state. In this phase, the system waits for the repair team to make improvements ( $T_3$ ). The faster the repair team responds, the narrower this phase will be.
- Phase 4 is a restoration state, starting from  $T_3$  and ending when system performance returns to its normal state at  $T_5$ . The restorative steps include infrastructure repairs and system reconfiguration (network maneuvers, generator re-dispatch, and micro-grid formation).  $T_4$  is when the disturbance is over, which may occur before or after  $T_5$ . In this phase, system flexibility and speed of restoration will be seen.

## 2.2 Resilience Metrics

Based on the four phases mentioned, a resilience matrix needs to describe the conditions of each phase. The resilience calculation that has been developed attempts to describe the overall system resilience in a complete picture. In [8, 9], the traditional reliability index is used to represent system resilience, such as loss of load probability (LOLP), expected demand not served (EDNS), and expected energy not served (EENS). The calculation process employs the Monte Carlo method to produce those indices. While new indices were introduced in [10], the system's resilience performance was evaluated using (1).

$$R = E \left[ \frac{\sum_{n=1}^N T_u}{\sum_{n=1}^N T_u + T_D} \right] \quad (1)$$

Load outage duration is represented as  $T_D$ , while  $T_u$  stands for the load period during up-time, and the symbol  $N$  stands for the number of loads connected to the system. A different quantification approach was introduced in [11], and that resilience is the ratio of the area under the actual performance curve to the area under ideal performance, as shown in **Error! Reference source not found.**

$$R_t = E \left[ \frac{\int_{T_1}^{T_5} AP(t) dt}{\int_{T_1}^{T_5} IP(t) dt} \right] \quad (2)$$

Equation (2) misses to capture the system resistance [12]. A part of the system resistance is tested between  $[T_0, T_1]$ . The disaster has already occurred in this period, but the system can sustain its previous performance. Reference [13] has a quite similar approach to (2), yet it is able to consider the system resistance using the equation below:

$$R_i = E \left[ \frac{\int_{T_0}^{T_5} AP(t) dt}{\int_{T_0}^{T_5} IP(t) dt} \right] \quad (3)$$

AP in (3) represents the system's actual performance, and the performance may be represented using the supplied load. The actual and ideal performance (IP) is integrated from the beginning of the disturbance ( $T_0$ ) to the time during the system reaches its previous performance ( $T_5$ ). The resilience index presented in [12] (RICD) of a transmission network adds an essential part from (3) as follows:

$$R_{icd} = E \left[ \frac{\int_{T_0}^{T_5} AP(t) dt}{\int_{T_0}^{T_5} IP(t) dt} \frac{T_4 - T_0}{T_5 - T_0} \right] \quad (4)$$

Another approach is also introduced in evaluating system resilience to determine the impact of improvement. In [14], to measure system resilience during penetration of distributed generation using renewable energy sources, the system resilience is quantified using a fraction of the load buses whose voltage deviation is beyond  $\pm 5\%$  of its nominal voltage to all load buses.

### 3 Design of Methodology

Initial steps started with modeling the electric power system components, both on the structural and electrical sides. Infrastructure model of transmission line strength was employing normal logarithmic equation, while electrical network is using [15] model to simulate power flow analysis. The disturbances, in this case typhoon storms, are also modeled in spatial and temporal using a modified Rankine Vortex. The strength of the components is compared with the wind speed experienced per unit of time. The system's performance will be evaluated when a component cannot survive.

The resilience value was calculated using the Monte Carlo method, where the simulation was carried out 1000 times to ensure convergent results. The simulation steps can be seen in Fig. 2.

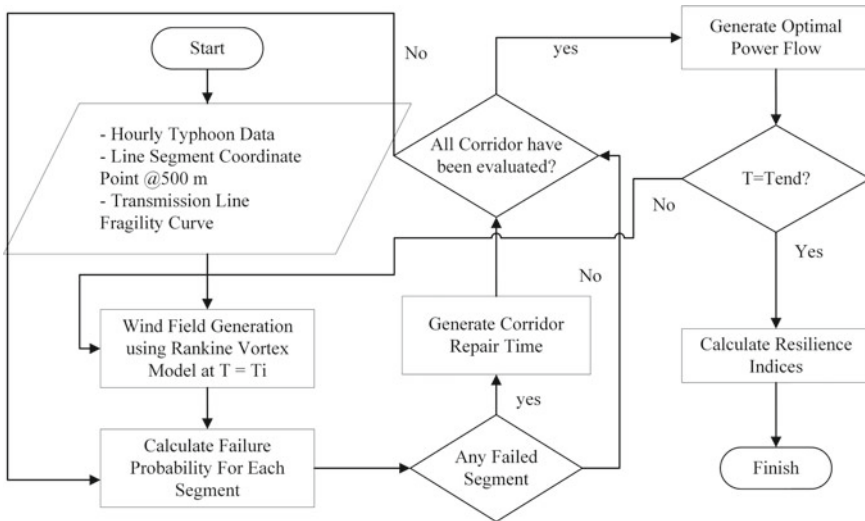


Fig. 2 Design of methodology

In this simulation, four scenarios will be used:

1. Scenario 1 (normal condition)

Under normal conditions, the number of teams is assumed to be only 1. If multiple outages occur, the next component shall wait until the repair team is available. The repair speed is 1 h per 500 m transmission line segment, and the speed of the repair team to arrive at the point of damage is 60 m/s.

2. Scenario 2 (component robustness variation)

In scenario 2, the strength variation of the transmission line is carried out where the strength is varied for normal (37 m/s), low (32 m/s), and strong (42 m/s) values. The four methods are calculated for each strength.

3. Scenario 3 (repair team variation)

The simulation is conducted for different numbers of repair teams. In normal conditions, only 1 team is available. For another case, we increase the number of the team into 2 teams, 4 teams, and in extreme conditions, 100 teams are employed.

4. Scenario 4 (repair speed variation)

In the last scenario, the repair speed is varied. For normal conditions, the repair speed is 1 h per transmission line segment (500 m). In other cases, the repair speed is simulated for 2 h per segment, 4 h per segment, and half an hour per segment.

The result of resilience indices between all four scenarios was then compared to see their effectiveness.

## 4 Evaluation of Typhoon Impact to Power System

### 4.1 Typhoon Modeling

Typhoon is a natural phenomenon that is difficult to be completely described. Even though wind measurements can be obtained from satellites or aircraft, it has yet to be possible to describe the three-dimensional model of the cyclone. Thus, a two-dimensional parametric model is often used to facilitate analysis in typhoon modeling. In [16], a parametric wind modeling method was compared: Rankine Vortex, Slosh, and Holland, where it was found that Rankine Vortex provided the best model when compared to the other two models.

Wind speed will be zero at the storm's center and increase as it gets closer to the maximum speed point, then decrease as the position is further away from the maximum point. The modified Rankine Vortex describes the wind speed distribution using Eq. (5).

$$\begin{aligned}
 V &= V_{\max} \left( \frac{r}{R_{\text{mw}}} \right)^X \quad \text{for } r < R_{\text{mw}} \\
 V &= V_{\max} \left( \frac{R_{\text{mw}}}{r} \right)^X \quad \text{for } r \geq R_{\text{mw}}
 \end{aligned} \tag{5}$$

The variable  $V_{\max}$  indicates the maximum speed of the typhoon in the specified time. While  $R_{\text{mw}}$  is the distance from the typhoon's center to its maximum velocity point,  $r$  is the distance from the typhoon's center to the observed point. Parameter  $X$  adjusts the wind speed distribution and has a value range of  $0.4 < X < 0.6$ . In this case, the average value is 0.5.

The calculated wind speed needs to be adjusted at a standard 10-m height using Eq. (6), with  $K_m$  being a correction factor of 0.8 in the modified Rankine Vortex modeling.

$$V_{10} = K_m V \tag{6}$$

The wind speed is assumed to have a circular wind flow, which is insufficient to depict the actual wind direction. The correction of wind direction shall be made using Eq. (7).

$$\begin{aligned}
 \beta &= 10^\circ \left( 1 + \frac{r}{R_{\text{mw}}} \right) \quad \text{for } 0 \leq r \leq R_{\text{mw}} \\
 \beta &= 20^\circ + 25^\circ \left( \frac{r}{R_{\text{mw}}} - 1 \right) \quad \text{for } R_{\text{mw}} \leq r \leq R_{\text{mw}} \\
 \beta &= 10^\circ \left( 1 + \frac{r}{R_{\text{mw}}} \right) \quad \text{for } 0 \leq r \leq R_{\text{mw}}
 \end{aligned} \tag{7}$$

The cyclone's forward motion shall be accounted for using Eq. (8).  $V_f$  is the forward velocity of typhoon movement, and  $U$  is the correction term.

$$U = \frac{R_{mw}r}{R_{mw}^2 + r^2} V_f \quad (8)$$

Thus, the total wind speed that affected the transmission line will be obtained in Eq. (9).

$$V_r = V_{10} + U \quad (9)$$

## 4.2 Component Modeling

The fragility curve will represent the strength of the transmission line when there is a typhoon. In [17], a logarithmic trend exists between wind speed and the probability of component failure. Thus, the failure probability of the transmission line can be represented by the normal logarithmic Eq. (10).

$$P_{1i} = \Phi(v) \quad (10)$$

With an average value of 37 and a standard deviation of 5 [12], this fragility curve represents the strength of the transmission line segments with a length of 500 m per segment.

## 4.3 Repair Process

The repair process of the components considers wind speed impact. A longer repair time (TTR) is needed at higher speed values. The total time to repair will include component repair time, waiting time, and time the repair team needs to reach the damaged area [12].

1. The wind speed impact is considered in the time to repair (TTR) using the
2. The TTR of the component will depend on the wind speed represented in the coefficient ( $k$ ) as stated in Eq. (11).

$$ttr_m = ttr_{norm} \times k \quad (11)$$

3. The repair team's required time to reach the repair area is added to the total repair time, where the length of travel time will depend on the distance of the repair team from the disturbance point ( $d$ ) and the speed of the repair team to

the disturbance point  $v_r$  as in Eq. (12).

$$t_r = \frac{d}{v_r} \quad (12)$$

4. Component repairs will be carried out alternately, with which the first failure will be served first so that the  $t_{\text{wait}}$  will be added to the total repair time as in Eq. (13).

$$t_{\text{total}} = (t_{\text{tr}} + t_r) \times k + t_{\text{wait}} \quad (13)$$

## 5 Simulation Data

The synthetic data is acquired using open-source data that is available online.

### 5.1 Typhoon Data

The simulated typhoon data is Vicente Typhoon that occurred from 21 June 2012 to 25 June 2012, taken from [18] and given in Table 1. Since forward motion data to solve (8) is not provided, it is estimated using the distance from the typhoon center between two consecutive data points divided by 6 h (time interval between two data points).

### 5.2 Electrical System Data

The tested system data is the reliability test system, IEEE 6 bus [19], which overlaid on the typhoon-impacted area. Figure 3 illustrates the IEEE 6 buses overlaid in the South China area, and Table 2 shows coordinate points of each bus.

### 5.3 Restoration Procedure

The system repair procedure is carried out based on sub-chapter IV-3, where the repair team is assumed to be on Substation 5 (113.06°E, 22.61°N). The value of the multiplier coefficient will depend on the wind speed by following the normal distribution in Eq. (14).

**Table 1** Simulated typhoon data

Time	Lat (deg.)	Long (deg.)	$V_{max}$ (knot)	$R_c$ (km)	$R_{max}$ (km)
2012-7-20 06:00	18	123	20	0	0
2012-7-20 12:00	19	122	20	0	0
2012-7-20 18:00	20	122	20	0	0
2012-7-21 00:00	20	120	25	315	83
2012-7-21 06:00	20	118	20	333	83
2012-7-21 12:00	19	117	30	333	83
2012-7-21 18:00	19	116	40	315	83
2012-7-22 00:00	19	116	45	333	65
2012-7-22 06:00	19	115	45	333	65
2012-7-22 12:00	19	115	45	333	56
2012-7-22 18:00	19	115	50	315	56
2012-7-23 00:00	20	115	50	333	37
2012-7-23 06:00	21	115	65	333	46
2012-7-23 12:00	21.10	114.20	80	291	28
2012-7-23 18:00	21.70	113.30	115	296	28
2012-7-24 00:00	22.30	112.30	85	296	28
2012-7-24 06:00	23	111	60	296	28
2012-7-24 12:00	23	109	45	0	0
2012-7-24 18:00	24	107	45	0	0
2012-7-25 00:00	24	105	20	0	0

**Fig. 3** IEEE 6 bus test system overlaid on South China

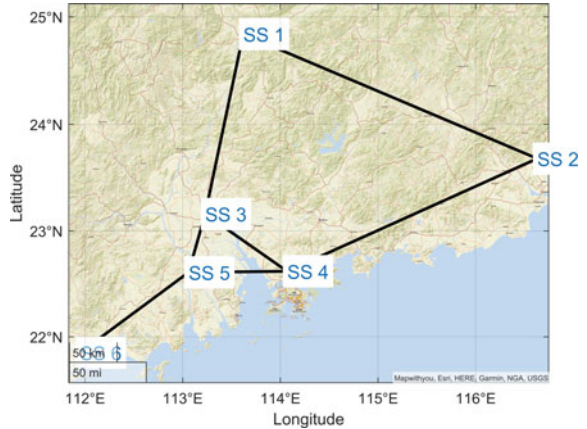




**Table 2** IEEE 6 bus substation coordinate

SS	1	2	3	4	5	6
Long	113.62°	116.63°	113.23°	114.07°	113.06°	111.95°
Lat.	24.84°	23.68°	23.16°	22.62°	22.61°	21.85°

$$k_w = \begin{cases} 1 & 0 \leq v \leq 10 \text{ m/s} \\ U(1, 2) & 10 \text{ m/s} < v \leq 20 \text{ m/s} \\ U(2, 3) & 20 \text{ m/s} < v \leq 40 \text{ m/s} \\ U(3, 4) & 40 \text{ m/s} < v \leq 60 \text{ m/s} \\ U(4, 5) & 60 \text{ m/s} < v \end{cases} \quad (14)$$

## 6 Analysis of Typhoon Impact

### 6.1 Scenario 1

Under normal circumstances, the resilience index is obtained using 1000 simulations to achieve convergence of values as shown in **Error! Reference source not found.** using Eqs. (2), (3), and (4) and the elements of Eq. (4) as shown in Eq. (15).

$$R_{\text{time}} = E \left[ \frac{T_4 - T_0}{T_5 - T_0} \right] \quad (15)$$

The typhoon is impacting the transmission line between Substations 5 and 6 (lines 5–6). During first simulation, 60 segments were failed and need immediate repair action, while other transmission line did not experience any failure in the segment. The failure in lines 5–6 causes system to loss load in Substation 6 (20 MW) due to unavailability of power generation back up in that substation. The system able to restore to its previous performance in hour 154 after disturbance in the first simulation is depicted in Fig. 4.

The simulation result is shown in Fig. 5, showing a similar value between  $R_{\text{icd}}(4)$ – $R_{\text{time}}$  and  $R_i(3)$ – $R_t(2)$ . The  $R_{\text{icd}}$  and  $R_{\text{time}}$  show a relatively low resilience index since restoration time is much longer than the typhoon duration.  $R_i$  and  $R_t$  have higher value because the system can sustain most of its load, and the restoration time does not significantly impact it.

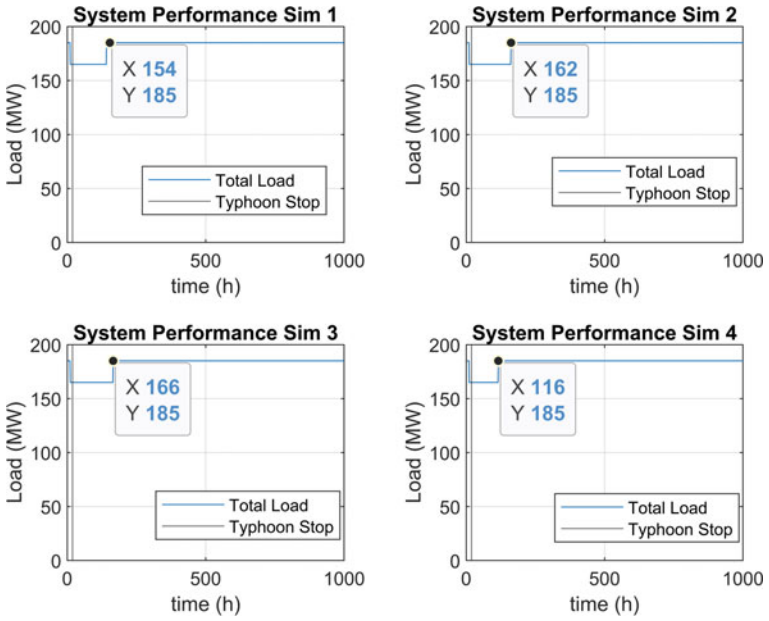


Fig. 4 Snapshot of system performance in normal condition for the first four iterations

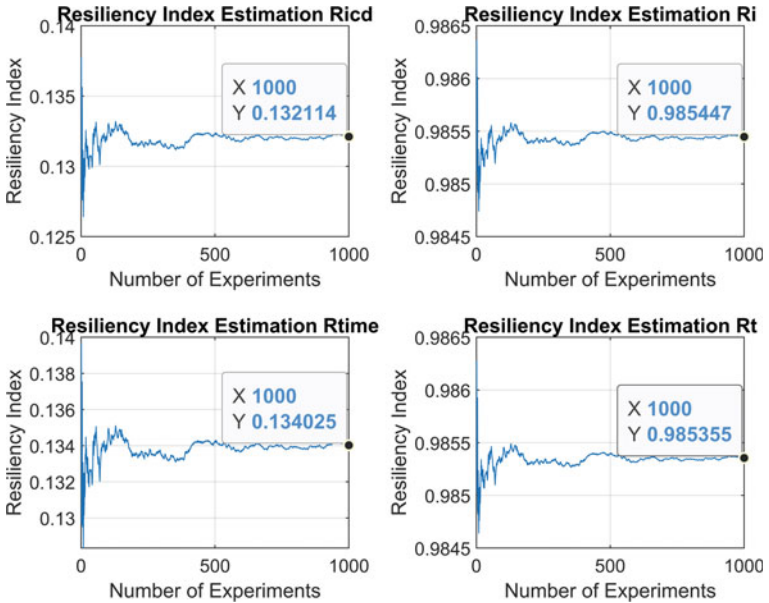


Fig. 5 Resiliency index estimation  $R_{icd}$ ,  $R_i$ ,  $R_{time}$ , and  $R_t$

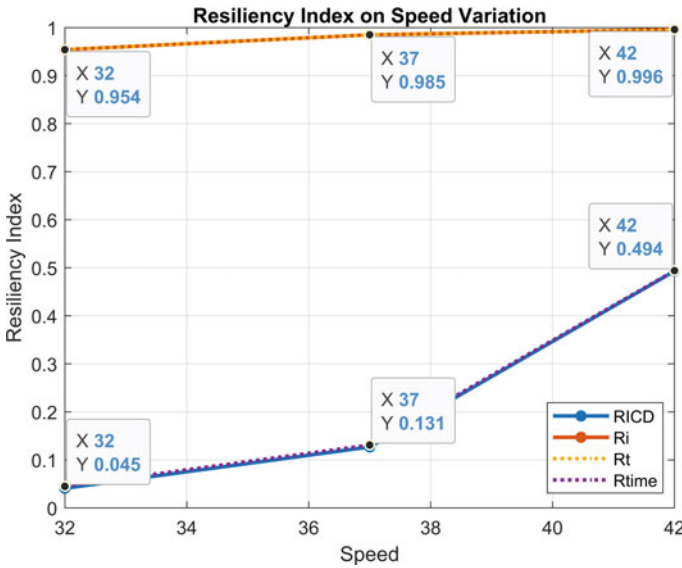


Fig. 6 Resilience index graph scenario 1

### 6.2 Scenario 2

In scenario 2, variations were made on the robustness of the transmission line. The scenario is done by changing the wind speed to 32 and 42 m/s so that the results are shown in Fig. 6. There is an increase in the value of the resilience indices in the four calculation methods when the strength of the transmission line increases. The significant difference to normal condition occurs in the RICD and Rtime values, which are 0.131–0.494, whereas in the Ri and Rt conditions, the value is not substantially different from 0.985 to 0.996. The insignificance occurs due to the loss of load in scenario 2, and normal scenario is similar, and the faulty segment only occurs in line 9 resulting unsupplied load in bus 6.

Meanwhile, when the transmission line strength drops by 5 m/s, the resilience values on Ri and Rt drop significantly to 0.045. The value is declining because the number of broken transmission line segment in the first simulation is 140 segments which result system able to restore its supplied load in hour 456.

### 6.3 Scenario 3

In scenario 3, variations are made on the number of repair teams using 2 teams, 10 teams, and an extreme case of 100 teams. In case of using 2 repair teams, it was seen that the repair was completed at 185 h, and the typhoon stopped at 20 h.

Meanwhile, an interesting thing occurred when 100 teams worked together to repair the faulty components. In Fig. 7, the repair finished in 15 h which preceded the typhoon duration. This phenomenon causes the resilience value on the RICD and Rtime methods to exceed the expected maximum value (1) to 1.343 as depicted in Fig. 8.

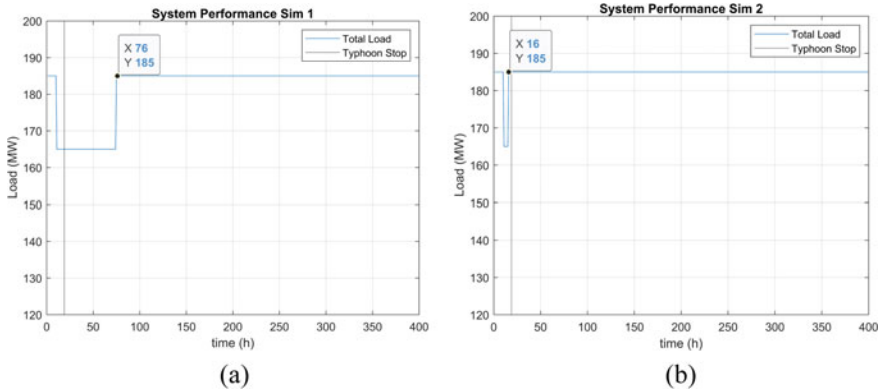


Fig. 7 Snapshot of single simulation a 2 repair teams b 100 repair teams

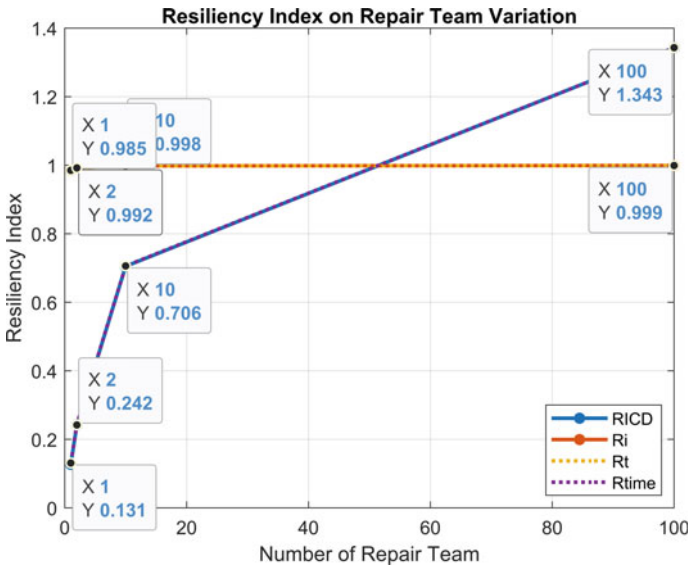


Fig. 8 Resilience index graph scenario 2

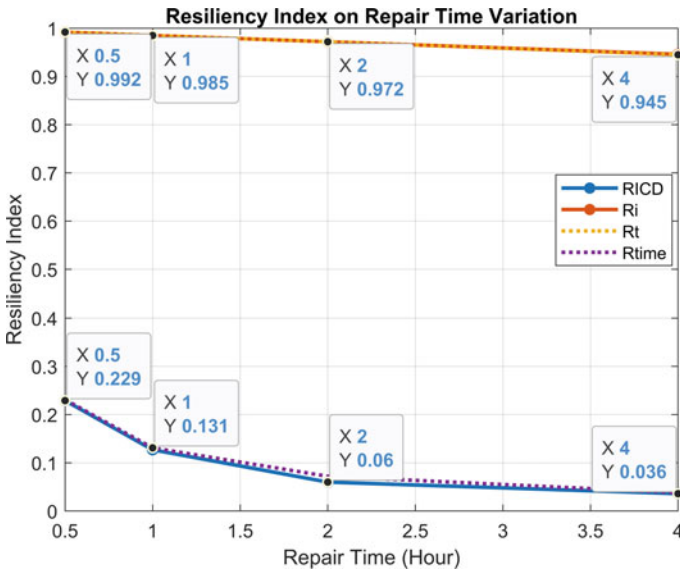


Fig. 9 Resilience index graph scenario 3

### 6.4 Scenario 4

In scenario 4, variations in repair time that are carried out with repair time per 500 m transmission line segment are 0.5, 2, and 4 h. The longer the repair time, the lesser resilience indices on the four methods. *Ricd* and *Ri* experienced a significant decrease of about 50% in value when the repair duration was 2 times longer than normal conditions. Meanwhile, the decline was insignificant for *Ri* and *Rt*, from 0.985 to 0.972 and 0.945 as shown in Fig. 9, respectively. When the repair time was accelerated to 0.5 h, the resilience increased significantly in *Ricd* and *Rtime* to 0.229 and 0.231 from the previous 0.127 and 0.131.

## 7 Discussion

Based on simulations in all scenarios, a very significant difference exists between *Ricd*–*Rtime* and *Ri*–*Rt*. The value of *Ricd* and *Rt* is greatly influenced by the comparison between the time of the typhoon duration and the total repair time  $\frac{T_{dur}}{T_5 - T_0}$ . *Ri* and *Rt* are more affected by the load lost during the disturbance. Even though the repair time is longer, the decrease in the value of resilience is not significant because the proportion of lost load is small compared to the load that survived when the disturbance occurred. However, the *Ricd* and *Rt* calculations show overly time-sensitive results. The resilience value is significantly low even though the load loss proportion is only 11% to the entire load.

## 8 Conclusion and Future Work

In this paper, we have tested the effectiveness of four methods of calculating efficiency using the Monte Carlo method. The simulation was conducted by simulating Typhoon Vicente on the overlaid IEEE 6 bus network in the South China area. In the four methods tested,  $RICD-R_{time}$  and  $R_t-R_i$  have similarities.  $R_{icd}$  and  $R_{time}$  are highly sensitive to the comparison of the typhoon duration to the total repair duration. Thus, even if the loss load is small, the resilience index value will be small if the repair time is much longer than the typhoon duration (loss of only 11% load but resilience could be  $< 0.01$ ). However, for  $R_t$  and  $R_i$ , the resilience values do not sufficiently reflect the repair time differences. These two indices highly influenced y amount of loss load; as long as the loss load is similar, the resilience indices will not have a significant difference.

Based on this simulation, it is necessary to have a resilience index that can fully describe the system's strength and the length of time for repairs proportionally. Thus, for future work, the author will do research to compose a resilience index that is able to capture both phenomena.

## References

1. President EOOT (2013) Economic benefits of increasing electric grid resilience to weather outages, T.W. House, Washington
2. Shammin MR, Haque AKE, Faisal IM (2022) A framework for climate resilient community-based adaptation. Climate change and community resilience. Springer, Singapore, pp 11–30
3. Panteli M, Mancarella P (2015) The grid: stronger, bigger, smarter? In: IEEE power and energy magazine. IEEE, pp 58–66
4. Izadi M et al (2020) A critical review on definitions, indices, and uncertainty characterization in resiliency-oriented operation of power system. Int Trans Electr Energy Syst 30(1):1–28
5. Alam MM, Eren Tokgoz B, Hwang S (2019) Framework for measuring the resilience of utility poles of an electric power distribution network. Int J Disast Risk Sci 15:270–281
6. Jufri FH, Widiputra V, Jung J (2019) State-of-the-art review on power grid resilience to extreme weather events: definitions, framework, quantitative assessment methodologies, and enhancement strategies. Appl Energy 239:1049–1065
7. Mathaios Panteli PM (2015) Influence of extreme weather and climate change on the resilience of power systems: impacts and possible mitigation strategies. Electr Power Syst Res 127:259–270
8. Panteli M et al (2017) Metrics and quantification of operational and infrastructure resilience in power systems. IEEE Trans Power Syst 32(6):4732–4742
9. Younesi A et al (2020) A quantitative resilience measure framework for power systems against wide-area extreme events. IEEE Syst J 16(1):915–922
10. Kwasinski A (2016) Quantitative model and metrics of electrical grids' resilience evaluated at a power distribution level. Energies 9(2):93
11. Ouyang M, Min X (2012) A three-stage resilience analysis framework for urban infrastructure systems. Struct Saf 36–37(2):23–32
12. Yang Y et al (2018) Quantitative resilience assessment for power transmission systems under typhoon weather. IEEE Access 6:40747–40756

13. Mousavizadeh S, Mahmoud-Reza S, Mohammad-Hossein A (2017) A linear two-stage method for resiliency analysis in distribution systems considering renewable energy and demand response resource. *Appl Energy* 211:443–460
14. Scala A, Mureddu M, Chessa A, Caldarelli G, Damiano A (2013) Distributed generation and resilience in power grids. In: Hämmerli BM, Kalstad Svendsen N, Lopez J (eds) *Critical Information Infrastructures Security*. Springer, New York, pp 71–79
15. Saadat H (1999) *Power system analysis*. The McGraw-Hill Companies, New York
16. Phadke AC et al (2003) Modeling of tropical cyclone winds and waves for emergency management. *Ocean Eng* 30:553–578
17. Krisy Murray KRWB (2014) Wind related faults on the GB transmission network. In: *Proceedings of the 2014 international conference on probabilistic methods applied to power systems (PMAPS)*, pp 1–6
18. Command NMO (2012) Best track western Pacific 12 June 2012. Mississippi
19. Billinton RKS, Chowdhury N, Chu K, Debnath K, Goel L, Khan E, Kos P, Nourbakhsh G, Oteng-Adjei J (1989) A reliability test system for educational purposes-basic data. *IEEE Trans Power Syst* 4(3):1238–1244

# Author Index

## A

Abdillah, Muhammad Hasya, 245  
Aditya Kumar, R., 737  
Adzmi, Megat Azri Irfan, 521  
Agarwal, Rashmi, 165  
Ahmad, Jawed, 85  
Ahmad, Nadeem, 881  
Ahmed, Subeyr Bashir, 99  
Akhter, Md. Nasim, 601  
Aladin, Mohamad Yahya Fekri, 403, 867  
Alankar, Bhavya, 85  
Al-Hakim, Rosyid R., 513  
Ali, Kesar, 495  
Almutairi, Abdulaziz, 649  
Anand, Rahul, 259  
Ansari, Md. Fahim, 319, 339, 347  
Arief, Yanuar Z., 271, 355, 367, 513, 773  
Arifin, A. K., 205, 229  
Arora, Amit, 943  
Arshad, Naseem Mohd, 535  
Asati, Ritika, 457  
Asija, Divya, 289  
Ayob, Shahrin Md., 99, 521, 535, 553, 649  
Ayop, Razman, 521, 535, 553

## B

Bajaj, Mohit, 75  
Bakare, Ganiyu Ayinde, 377  
Bali, Sravana Kumar, 177, 727  
Bankar, Deepak S., 457, 495, 853  
Bansal, Manmohan, 799  
Bhadu, Mahendra, 943

## C

Caesarendra, Wahyu, 245  
Chaurasia, Neetigya, 619

## D

Daud, Mohd Zaki, 521, 535, 553  
Deshmukh, Sheetal, 319  
Dhanalakshmi, R., 45  
Dinesh, Kantubhukta, 305, 431  
Dini, Hasna Satya, 1003  
Dixit, Anuj, 289

## E

Elwan, Ahmed Abubakar, 355, 367, 773  
Equbal, Md.Danish, 339  
Eteruddin, Hamzah, 271

## F

Fadzli, Fazliaty Edora, 403

## G

Garg, R., 813  
Govind, Kirti, 495  
Gupta, Anju, 165  
Gupta, Sushindra Kumar, 391  
Gupta, Vinay, 217, 469

## H

Habibuddin, Mohd Hafiz, 355, 367, 773  
Halim, Nur Ameerah Abdul, 867



Haruna, Yau Shuaibu, 377

Hashem, Hythem, 339

## I

Idris, Nik Rumzi Nik, 99, 649

Idris, Rasyidah Binti Mohamad, 355, 773

Imtiyaz, Rahil, 417

Iqbal, Atif, 1, 319, 347

Iqbal, Mohamad, 933

Irshad, 881

Islam, Shirazul, 319

Ismail, Ajune Wanis, 403, 867

## J

Jadoun, Vinay Kumar, 441

Jaffery, Zainul Abdin, 881

Jahid, 763

Jain, Samyak, 481

Jain, Sanyam, 481

Jamian, Jasrul Jamani Bin, 377, 1003

Javed, Saad, 85

Jayalakshmi, N. S., 441

Joshi, Bhagawati Prasad, 799, 899

Juneja, Deepak, 391, 675, 785

Jusoh, Awang, 99, 649

Justin, Ardrine, 553

## K

Kampara, Ravisankar, 431

Kassarwani, Neelam, 61, 751

Kaushik, Harsh, 481

Khalid, Syed Sibtain, 85

Khan, Akhlaque Ahmad, 259

Khanam, Ruqaiya, 417

Khan, Mohammad Junaid, 339

Khan, Shaheen, 881

Khare, Shivani Jitendra, 853

Khetarpal, Poras, 61

Kirmanani, Sheeraz, 763

Kumar, Abhay, 899

Kumar, Aman, 289, 417

Kumar, Amod, 689

Kumar, Arvind, 943

Kumar, Avdhesh, 193, 589

Kumar, Deepak, 899

Kumari, Deepa, 31

Kumar, Mahesh, 61

Kumar, Manoj, 289

Kumar, Mohit, 217

Kumar, Rajeev, 785

Kumar, Sanjay, 481

Kumar, Sudhanshu, 619

Kumar, Sujit, 75

Kumawat, Jitesh, 469

Kushawaha, Arjun, 619

Kuttey, Vinod Kumar, 727

## L

Lakshmi, D., 61

Lubis, Ahmad Husin, 245

## M

Madan, A. K., 933

Mahajan, P., 813

Malik, Hasmad, 1, 99, 649

Manaullah, 763

Mandake, Yogesh B., 495

Mangaraj, Mrutyunjaya, 305

Manikanta, P., 993

Márquez, Fausto Pedro García, 99, 649

Mehta, Gitanjali, 417

Mehetre, Vishal V., 853

Midha, Akash, 981

Minai, Ahmad Faiz, 217, 259, 923

Mishra, Kanhaiya, 619

Mishra, Sukumar, 1

Mittal, Amit, 799

Mokhtar, Ahmad Safawi Bin, 355, 773

Mustafa, Elfatih Elmubarak, 339

Mustapha, Musa, 377

## N

Nagpal, Neelu, 61, 481, 751

Namekar, Swapnil, 853

Narayan, Yogendra, 675, 785

Nezami, Md. Manzar, 339, 347

Nurulhak, Muhammad Syukri, 271

## O

Oli, Sanjay, 899

## P

Pachauri, Rupendra Kumar, 217, 259, 469, 923

Pandey, Anubhav Kumar, 441

Parkash, Ved, 837, 963

Pradhan, Aryadhara, 217

Praveena, A., 305

Priyadarshini, Aayushi, 569

Pushparaj, 689

Putra, Geordiano Devanaldy Khresna, 245

**R**

Radhiva, Muhammad, 245  
 Rana, Aditya, 391  
 Rani, Preeti, 837, 963  
 Rao, Naseem, 85  
 Rasid, Madihah Binti Md., 377  
 Rasid, Z. A., 205, 229  
 Rau, Utkarsh, 911  
 Ravisankar, Kampara, 305  
 Rayal, Ashish, 799, 899  
 Ray, Papia, 737  
 Riani, Sri, 513  
 Rizwan Khan, Mohd., 601  
 Rodriguez, Carlos, 99  
 Roomi, Muhammad M., 635  
 Roslan, S. A. H., 205, 229

**S**

Sai Kiran, P., 993  
 Saini, Garima, 689  
 Salkuti, Surender Reddy, 737  
 Sarfraz, 165  
 Sartaj, Mohd., 601  
 Sati, Madan Mohan, 899  
 Satish, Majji, 305, 431  
 Satyamohan Sarveswar, G., 993  
 Sawle, Yashwant, 827  
 Sehgal, Jagrat, 751  
 Shahid, Mohammad, 619  
 Shaikh, Arbaz Sher Khan, 495  
 Shaikh, Javid Navaj, 495  
 Sharan, Siti Nur Aisyah Mohd, 355  
 Sharma, A., 813  
 Sharma, Ashish, 31  
 Sharma, Megha, 717  
 Sharma, Naveen Kumar, 75, 837, 963  
 Sharma, Rahul, 827  
 Sharma, Ravi, 481  
 Sharma, Shailly, 717  
 Sharma, Somesh, 799  
 Shashikant, 217, 259, 469, 923  
 Shukla, Ashutosh, 217  
 Shukla, Utkarsh, 569  
 Siano, Pierluigi, 751  
 Siddiqui, Khadim Moin, 911

Singh, Gautam Kr., 619  
 Singh, Rajesh, 259, 923  
 Soelaiman, Nur F., 513  
 Sood, Y. R., 1  
 Srivastava, Sandhya, 911  
 Subbaramaiah, K., 431  
 Suhail Hussain, S. M., 635  
 Sumana, S., 45  
 Syahriar, Ary, 245

**T**

Tamvada, Karthik, 431  
 Tanweer, Safdar, 85  
 Tariq, Mohd, 635  
 Thakur, Ambika, 675  
 Tiwari, Nitesh, 569  
 Tiwari, Udai Raj, 911  
 Tomar, Anuradha, 981  
 Tomar, Tushar, 289  
 Tompala, Jyothi, 177

**U**

Umar, N., 205, 229  
 Ustun, Taha Selim, 1, 635

**V**

Vaish, Jayati, 911  
 Vajpai, Jayashri, 717  
 Venkateswara Rao, B., 993  
 Verma, Shubham Kumar, 911  
 Viral, R. K., 289  
 Vishwanath Nagarajan, V. S., 441

**W**

Wajdi, Muhammad Raihan, 245  
 Wulandari, Putri, 245

**Y**

Yadav, Nikita, 827  
 Yadav, Shekhar, 569  
 Yashaswini, H. K., 75